Konrad Solbrig | Dissertation

**Applied investigations on wood-based composites
in the context of X-ray densitometry**

Dissertation with the aim
of achieving the doctoral degree
Doctor of Natural Sciences (Dr. rer. nat.)

Applied investigations
on wood-based composites
in the context of
X-ray densitometry

at the

University of Hamburg

Faculty of Mathematics, Informatics and Natural Sciences

Department of Biology

Institute of Wood Science

submitted by

M.Eng. Dipl.-Ing. (FH) Konrad Solbrig

Lemgo, 2019

Gutachter: | Evaluators: Prof. Dr. Jörg B. Ressel

                                                   Prof. Dr. habil. Heiko Thömen

Eingereicht am: | Date of submission: 18th December 2019

Tag der Disputation: | Date of oral defence: 07th May 2020

URN: urn:nbn:de:gbv:18-ediss-89270

Dedicated to patience
and all those, who stood by my side,
kindly letting me share in this virtue.

Der Geduld und all den Menschen
an meiner Seite gewidmet,
die mir diese Güte zuteilwerden ließen.

"[…]
for, he reasons pointedly,
that which *must* not, *can* not [sic] be."

from
The Impossible Fact
translated by
Max Knight:
Gallows Songs and other Poems

„[…]
Weil, so schließt er messerscharf,
nicht sein *kann*, was nicht sein *darf*."

aus
Die unmögliche Tatsache
von
Christian Morgenstern:
Galgenlieder und andere Gedichte

Preface

After completing my studies in Wood Technology, I discovered my passion for both engineered wood products and all fields of science using technology to explore their inner properties. During my time as a scientific assistant at Ostwestfalen-Lippe University of Applied Sciences (now OWL University of Applied Sciences and Arts), Lemgo, Germany, in the Laboratory for Timber Engineering, Products and Production, I dealt with research topics in the field of radiometric investigations on wood-based composites by means of X-rays, neutrons, radar, ultrasonics, and other nondestructive methods. Accordingly, I gratefully took the chance to combine my fields of fascination with the main focus on wood-based composite panels and X-rays resulting in this dissertation.

Although writing such a doctoral thesis is ultimately the "tough fate" of the individual, it is by no means the achievement of a single person. Along the journey, the candidate – me – is the recipient of a tremendous outpouring of goodwill and support. Moreover, in a book[1] about "The invention of performance" I learned, that there is no individual human performance in the quasi-physical sense of power. Accordingly, an apparently solo endeavour such as this dissertation could only have been achieved thanks to the contribution of many, i. e., supervisors, colleagues, friends, and not least family members, who paved the way to this thesis. In this regard, perhaps most crucial to my final outcome, was the opportunity and freedom I was given to pursue my personal interests and, therefore, to discover my own field of research.

No road leading to a doctoral thesis is generic – neither was mine.

First and foremost, I owe a debt of gratitude to Prof. Katja Frühwald-König. As her scientific assistant, she gave me the opportunity to become a doctoral candidate and – after a period of initiation into the subject area – the freedom to independently focus on my research work. Moreover, she introduced me to manifold fields of research and education, where she encouraged me to broaden my horizons. Secondly, I owe a great deal to Prof. Dr.-Ing. Adrian Riegel. He was my first mentor in science and engineering and his supervision lent valuable direction to my academic career.

Scientific work can only transform into a dissertation through evaluation and most importantly supervision. My supervisor and first evaluator Prof. Dr. Jörg B. Ressel accepted my field of research for graduation and was always open for any request. I would like to offer my sincere thanks to Prof. Ressel for willingly supporting me as an external doctoral candidate, directly providing critical feedback as a valuable basis for keeping my work progressing on track, and finally helping me to take the big picture and focus it into a doctoral thesis. Prof. Dr. habil. Heiko Thömen did not hesitate to take on the requested role of the second evaluator. His clear feedback and effort for the examination is greatly appreciated.

Dr. Matthias Gruchot passed the baton on to me and, thereby, introduced me to the field of X-rays on wood-based composites. I would like to express my heartfelt gratitude for his ongoing interest and support in the ultimate completion of my thesis by keeping the pressure permanently high. Matthias Fuchs introduced me to the reality of (X-ray) measuring applications in an industrial and economic context and became my mentor in this field. I am deeply grateful, that he shared his outstanding experience in developing special equipment for a special branch and that he has encouraged me to have my own experience in this field. Thus, Matthias substantially contributed to the practical relevance of my research.

Beyond my appreciated advisors, I have some dear fellows, who substantially supported me on the way to graduation and to whom I would like to express my deep gratitude. Without Prof. Christian Kortüm as

---

[1] Verheyen, N. – Die Erfindung der Leistung. Hanser Berlin im Carl Hanser Verlag: München, 2018. 256 p.

a long-time companion at the Ostwestfalen-Lippe University of Applied Sciences, many a crucial situation would not have been overcome, many an idea would not have come to light in ongoing discussions, and many a light-hearted yet important "research discovery" would have been left unmade. Thank you, Christian, for being my wingman. My friend and associated wood academic Dr.-Ing. Richard Münder was always a highly-sophisticated discussion partner considering all fields of science and engineering as well as beyond. Dr.-Ing. Sebastian Horstmann willingly shared his experience in wood science and engineering and made me understand that the reality of graduation demands more than demonstrating scientific ability. Benjamin Krause was my appreciated colleague in a third-party funded research project at the Ostwestfalen-Lippe University of Applied Sciences. With his precise work and many an elaborate device construction he made an essential contribution to several of the performed investigations. Furthermore, my heartfelt appreciation goes out to my former colleagues at the DEPT 7 Production Engineering and Management – particularly the wood technology staff – and at further departments at the Ostwestfalen-Lippe University of Applied Sciences as well as the numerous student associates and all the secret helpers, who supported the sometimes obviously unusual work of a young research fellow.

As an external doctoral candidate at the University of Hamburg, I am also very grateful for various support from outside my home university in Lemgo and, therefore, for the opportunity to use various research facilities and equipment across Europe. Initially, I would like to express my acknowledgement to the board of examiners. Special gratitude goes out to the members of the Institute of Wood Science, Hamburg, Germany, who supported me and tolerated my work during several stays in Hamburg preferably X-raying in the institute's basement. I am pleased to acknowledge the rapid support of the Institut für Holztechnologie Dresden gemeinnützige GmbH (IHD), Dresden, Germany, where the competent and experienced local staff offered open-minded cooperation and willingness for any discussion. I am deeply grateful for the opportunity to have been able to perform some research at the Institute of Wood and Paper Technology, Technische Universität Dresden, Germany, with outstanding support by the local staff offering obliging and straightforward cooperation. Many thanks are also due to the Bundesanstalt für Materialforschung und -prüfung (BAM), Department of Non-destructive Testing (DEPT 8) Radiological Methods, for providing measuring equipment. Particularly the discussions with the former member Dr. Kurt Osterloh and his advice in some topics of the thesis are highly appreciated. I am very thankful to the staff members and management of the Electronic Wood Systems GmbH, Hameln, Germany, who made numerous measuring series possible and contributed to several results in terms of a cooperation project and beyond. Susan J. Ortloff did a great job proofreading this comprehensive thesis.

Part of the performed X-ray investigations are based upon experiments within the scope of the research project "Erforschung und Adaptierung von radiometrischen Verfahren zur Messung von Materialdichte und -feuchte an Holzwerkstoffen unter Berücksichtigung des strukturellen Aufbaus" funded by the German Federal Ministry of Economics and Technology on the basis of a decision by the German Bundestag by the lead partner AiF Projekt GmbH. A travel grant from the Stiftung Holzwirtschaft, Hamburg, Germany, served as valuable contribution to enable a conference visit in Brazil. A completion scholarship from the presidential board of the Ostwestfalen-Lippe University of Applied Sciences (now OWL University of Applied Sciences and Arts), Lemgo, Germany offered a good deal of freedom in the final stages of my research work. All funding is gratefully acknowledged.

Finally, my heartfelt gratitude goes out to my dear family and friends for their patience and encouragement. My parents and my sister gave me the freedom to journey down the dissertation road. They never made me feel like I might have chosen the wrong path. They left me no doubts about my work.

Ultimately, to my beloved future wife Dörthe. Your understanding and many sacrifices through the years are priceless. Now, I am totally yours.

Again, my deepest thanks to all of you!

Lemgo, October 2019   Konrad Solbrig

Declaration

Dissertation according to the Doctoral Degree Regulations of the Faculty of Mathematics, Informatics and Natural Sciences of the University of Hamburg (MIN-PromO as of 2nd May 2018).

Topic:

Applied investigations on wood-based composites

in the context of X-ray densitometry

Submitted by: M.Eng. Dipl.-Ing. (FH) Konrad Solbrig

Date of birth: 28th August 1984

Enrolment number: 6196555

Department: Biology, Institute of Wood Science

Date of submission: 18th December 2019

Day of oral defence: 7th May 2020

Evaluators: Prof. Dr. Jörg B. Ressel

Prof. Dr. habil. Heiko Thömen

This thesis comprises 453 pages.

Hiermit erkläre ich an Eides statt, dass ich die vorliegende Dissertationsschrift selbst verfasst und keine anderen als die angegebenen Quellen und Hilfsmittel benutzt habe.

I hereby declare, under oath, that I have written the present dissertation on my own and have not used any resources or aids other than those acknowledged.

(§ 8 (4) MIN-PromO as of 2nd May 2018)

Lemgo, 18th December 2019

English review testimonial

I certify that the English in the thesis:

Applied investigations on wood-based composites in the context of X-ray densitometry
by Konrad Solbrig
was reviewed and is correct.

Susan J. Ortloff (US citizen), freelance translator and editor

Susan J. Ortloff, October 8, 2019

Abstract

The industrial production of wood-based composites (WBCs) features the core processes in the forming and press line, which are characterised by densification and the curing of resin-blended furnish material to obtain a panel from a formed mat in a continuous or batch-wise process. Here, the reliable measurement of process parameters and panel properties is indispensable for monitoring and controlling production and quality. The in-plane area density (ρ_A) of the mat and the raw density (ρ) of the panel, along with its vertical raw density profile (RDP), are typically determined through nondestructive means of radiometric devices. X-ray systems for density measurement on WBCs are commonly used in both industry and research. They follow a similar basic principle of radiation transmission with specific setups depending on the measuring task at hand. Detector signals are evaluated regarding relative radiation transmission, which is well-known to follow Beer's law of exponential attenuation. Note here, particular conditions regarding radiation (energy and beam geometry) and material properties (consistent and homogeneous) are expected. These conditions, however, cannot be consistently achieved in applied radiometric investigations on WBCs. Therefore, X-ray transmission measurements in terms of densitometry on inhomogeneous and porous matter such as WBCs are fundamentally affected by

- material density,
- elemental composition,
- atomic numbers Z,
- beam geometry,
- energy level and spectrum, as well as
- energy-dependence of the individual attenuation processes,

with consequent radiation-physical effects such as beam hardening and radiation build-up.

Previous investigations by means of X-rays focus instead on the exclusive application of more or less established methods on wood and WBCs. The setup of respective X-ray devices contributes to the final validity of the measuring results, where general insufficiencies are found in preliminary studies. Hence, a fundamental but practice-oriented study on X-ray densitometry with explicit regard to WBCs as inhomogeneous and porous low-Z composite material considering both its composition and structure is currently needed.

According to the nature of X-ray application on WBCs, this thesis follows an interdisciplinary approach that brings together radiation physics and WBC technology. It examines radiation-physical aspects both experimentally as well as theoretically and analyses the fundamental material properties of WBCs, which are relevant for radiation interaction in a practice-oriented context due to a lack of such particular parameters for (lab-made) WBCs with predefined compositions in comparison to customary panels. Ultimately, individual findings are combined to draw conclusions on their radiation-physical interdependencies. An enhanced law of attenuation is deduced for practical description of X-ray transmission through WBCs.

In order to obtain mostly predefined material composition, both lab-made panels (labMDF) as well as furnish mats (cured in pre-densified state) were manufactured with particular focus on wood fibres and urea-formaldehyde adhesive resin (UF) as raw material. A practise-oriented range of customary industrial panels (indMDF) completes the sample sets.

Comprehensive material analyses with particular respect to properties relevant for radiation interaction were performed by means of

- gas pycnometry as most suitable method for true density determination of hygroscopic porous media,
- fibre and particle characterisation to qualify the actual members of the wood-particle-resin-matrix, as well as
- elemental and ash content analysis yielding the material composition on atomic level.

True density (ρ_t, i. e. solid density) determination on particularly prepared samples of labMDF, its raw fibres, cured UF resin, as well as indMDF and particleboard (PB) reveals similar results. For (lab-made) MDF a general value of $\rho_{t,labMDF} = 1515 \text{ kg/m}^3$ is derived from the measurements. Fibre morphology characterisation shows the utilised thermomechanical pulp (TMP) assortments to be dominated by two structural fibre types according to their volume fraction, i. e., mainly compact fibre bundles as well as short single fibres. Their distributions of dimensions (width and length) are found in a comparable order but rather below literature values. Elemental analyses complete with ash content determination reveal particular differences between the investigated materials. The results allow, however, a generalisation on the basis of the manufactured labMDF with 10 % UF resin content and $MC = 9.5$ % in consequence of 20/65 conditioning with mass fractions of H, C, N, O, and ash of 6.4 %, 45.0 %, 3.1 %, 45.2 %, and 0.3 % (S is neglected). Ash content of most of the customary MDF is found to slightly exceed the lab-made panels. Nitrogen content variations are particularly attributed to adhesive resin content and type, with values roughly one order of magnitude beyond clean wood in the case of common UF.

Based on the analysed material parameters, an explanatory beam path model is introduced, which makes it possible to describe radiation transmission through WBCs on distinct scales of interaction. The macroscopic scale [10^{-1} m] provides the measuring information of the radiometric investigations (X-ray densitometry) for an individually densified inhomogeneous solid body. On the contrary, actual radiation-matter interaction occurs on sub-microscopic, i. e., atomic level [10^{-10} m] defined by the elemental composition. Between macroscopic and sub-microscopic level, radiation propagation is considered to be affected by material structure of the porous body as (variably densified) wood-particle-resin-matrix on mesoscopic level [10^{-3} m], which is made up of cell-wall tissue with bound and free water as well as adhesive resin layers considering the microscopic scale [10^{-6} m]. Thus, an apparently simple radiation-matter interaction with consequent attenuation turns complex when both WBC structure and composition are considered along with the associated effective radiation transmission.

The conditions of the proposed concept were verified by exploratory transmission measurements on samples of both furnish mats and panels considering the practical applications, where X-ray devices with varying setups were employed. Particularly for RDP measurement on small specimens, a sufficient gravimetric reference method for non-radiometric direct determination was developed. Round robin test results reveal partly crucial deviations of the RDP shapes and surface-layer (SL) maxima between the devices as well as toward the reference method. Radiometric RDPs are concluded to be flattened in general. Deviations are found to increase with a more distinct RDP shape, i. e., increasing SL/CL ratio.

However, all transmission measuring series show individual deviations from the theoretical expectation under ideal conditions with varying extent due to the applied X-ray setups with different broad-beam conditions as well as the respective density range under investigation. Here, the mass attenuation coefficient is found to decrease with increasing area or raw density, contrary to the expectation to be a material constant per applied energy level. Consequently, radiation attenuation deviates from linear context with increasing absorber mass or thickness and Beer's law of attenuation breaks down for radiation transmission. Characteristic values quantify the individual deviations, and thus qualify the capability of the setups for X-ray densitometry. Radiation pre-hardening via individual pre-filter application yields the lowest deviation and radiation attenuation of the respective series approaches a linear context. The maximum deviation found in the case of an RDP setup at 35 kVp X-ray tube voltage and without pre-filter would yield up to -4 % measuring error in SL raw density considering an exemplary MDF-19 specimen, where only one mean mass attenuation coefficient is applied for calibration in common X-ray densitometry. Regarding radiometric determination of area density distribution of the formed furnish

mat, single-point calibration (one mass attenuation coefficient) for a wide measuring range can, in turn, cause measuring errors in the order of -47…+9 % at the limits. In addition to the fundamental non-linearities, differences between the mass attenuation coefficients of equivalent fibre mats and panels are verified due to the employed and practically typical broad-beam geometry setups. An exemplary difference compared to actual values is found in the order of +14 % of mat area density measurement based on panel calibration.

Beyond beam geometry and scattering issues, primarily X-ray spectra are well-known to cause such non-linearities. The majority of the applied setups is evaluated regarding their energy distribution via spectra measurements. Besides initial properties of the emitted beam, transmission spectra behind labMDF specimens with different raw densities but homogenous RDPs are determined to quantify the impact of such absorbers corresponding to RDP determination. A diminished beam hardening is found for some setups such that a more or less narrow initial spectrum is available, which is not considerably altered in terms of transmission through the total raw density range of the material under examination. However, an upward shift of the mean energy is superimposed by scattered radiation (rather low- and medium-energy) emitted from the specimens depending on their individual structure and further detector collimation. Spectra simulation considering the equivalent conditions is additionally performed.

Based on well-known X-ray application fundamentals, the performed material analyses, and the findings from X-ray measurements, theoretical evaluation and holistic discussion of X-ray attenuation in WBCs yields the following conclusions:

1. The computation of an effective atomic number Z_{eff} serves as a vivid measure to compare the X-ray attenuation potential of different compound substances and the effect of varying mixtures. The results are in good agreement with most of the rare literature values and empirically determined data of wood constituents. WBC Z_{eff} is found to be unaffected by MC variations (below fibre saturation) as well as resination (organic binders). A non-negligible impact of increasing ash content and variation of ash composition is, however, evaluated.

2. Mass-fraction-weighted total mean mass attenuation coefficient $\mu/\rho\,(E)_{\mathrm{mix}}$ computation with coincident radiation energy and spectra consideration provides a comprehensive data set based on the actual elemental composition and its virtual variation. Similar and partly almost congruent result plots of the applied WBCs and raw materials including water become obvious along the relevant energy range of $E = 5 \dots 100\,\mathrm{keV}$. However, total attenuation is dominated by the elements carbon and oxygen with a cumulated contribution of $\geq 85\,\%$. Therefore, a negligible impact of (organic) adhesive resins is proven. MC generally reveals minor but partly notable influence on $\mu/\rho\,(E)_{\mathrm{mix}}$ particularly on low and medium energy levels, where $\Delta MC = \pm 5\,\%$ around standard conditions causes not more than the relative deviation of $\pm 1.2\,\%$ of the corresponding mass attenuation coefficients. Ash content $\omega(a)$ is found to cause individual $\mu/\rho\,(E)_{\mathrm{mix}}$ differences between comparable materials, e. g., MDF of different industrial origins. An increment of up to $\omega(a) = 0.9\,\%$, i. e. three times that of clean wood from most of the European species, yields a significant impact on $\mu/\rho\,(E)_{\mathrm{mix}}$ in the order of $+1.5 \dots 13.4\,\%$, depending on the energy range. Accordingly, the differential mass attenuation coefficient $\delta\,\mu/\rho\,(E)_{\mathrm{mix}}$ $[\%/\Delta\mathrm{parameter}]$ is introduced to quantify a varying composition impact of individual parameters on attenuation by a single factor and to summarise the findings.

3. Despite a few exceptions, the computation results are generally found to exceed measuring data at equivalent energies. The differences are concluded to be systematically attributed to beam hardening and scattering. Ultimately, the study finds, that material structure, beam geometry, and radiation energy distribution primarily affect the measurement of μ/ρ values whereas variations in chemical composition yield minor influence as long as the main constituent elements are of similar atomic number.

The combination of all observations from measurements and findings from theoretical attenuation considerations supports further implications on interdependent radiation-physical effects like beam hardening, multiple scattering, and radiation build-up in the case of practical X-ray densitometry on WBCs:

4. Beam hardening is found to be particularly influential in the energy range $E < 24\,\mathrm{keV}$, above which scattering starts to dominate. For quantification of density-dependent energy variation, the beam hardening index $BHi(E, \rho_\mathrm{A})$ $[\%\Delta\bar{E}/\%\Delta\rho_\mathrm{A}]$ is introduced as a differential energy shift based on measuring or simulation data. Its evaluation verifies the findings from the comparison of the mass attenuation coefficients from measurement and computation, where non-constant μ/ρ measuring results fall below correspondingly computed values and decrease, in turn, with increasing area density. Beam hardening effects are concluded to cause considerable bias of X-ray densitometry results, where only one single mass attenuation coefficient is applied as a calibration parameter for a wide range of area density and for specimens featuring distinct raw density gradients.

5. The characteristic is, however, superimposed by scattering phenomena. Like beam hardening, scattering unavoidably occurs in the energy range of WBC X-ray applications. It may affect transmission measuring results such that non-linearities occur depending on the recorded scatter intensity superimposing the directly transmitted primary beam due to broad-beam geometry and setup conditions. Therefore, scattering yields an overestimation of the transmitted intensity in general. Besides energy and beam geometry, scatter recording depends on WBC structure, i. e., densification, since low-Z material with rather low true density tends to reveal lower self-absorption of secondary radiation in comparison to metals. However, radiation build-up in WBC transmission measurements is found to increase along increasing area density of the respective measuring series as well as with material densification, i. e., it increases more for panels than for furnish mats.

6. However, the proposed radiation transmission concept through WBCs comprising radiation-matter interaction on distinct scales is considered to be proven by the above findings.

7. The study ultimately concludes, that the conventional Beer's law of attenuation is no longer applicable to such X-ray densitometry applications on WBCs. Therefore, a power function approach for the relation between attenuation $\ln T^{-1}$ and area density ρ_A is determined to be the proper mathematic-physical solution of the biased linear context. Its inverse yields the double-exponential transmission function, which is consequently introduced as an enhanced law of attenuation. The additional exponent serves as a total index for the transmission conditions of the employed setup, including the material under investigation. The practice-oriented approach is applicable without particular requirements such as determination of X-ray spectra or computation of mass attenuation coefficients based on elemental composition. It involves just the appropriate evaluation of the transmission measurements employing the regular setup and utilising the explicit material under investigation. However, the approach is verified by application on the present transmission measuring results, where evaluated regression plots reveal good agreement with the individual data.

Since the present thesis aims to explore existing X-ray transmission setups and to describe the measuring conditions, improvements to the utilised devices are not explicitly made. Nevertheless, methodical implications on appropriate X-ray parameters for densitometry on WBCs are pointed out. Accordingly optimised X-ray measuring device hardware as well as improved calibration and data evaluation procedures are concluded to facilitate enhanced result accuracy with reliable absolute density values. Thus, practical X-ray densitometry on WBCs is able to yield reliable results under certain conditions. It requires, however, an enhanced understanding of radiation transmission from the X-ray beam's point of view and its propagation through the special material of WBCs. Therefore, the measuring data evaluation must consider such conditions by means of the double-exponential attenuation law. Here, the theoretical background is

provided by the present thesis. The practical implementation, however, must consequently be performed by the device manufactures. The users of such modern X-ray systems are enabled to obtain enhanced quality of their measuring results, which is relevant for both WBC science (wide range of partly new composites) and industry (increasing requirements on reliability and accuracy). Eventually, the proper application of capable nondestructive evaluation methods by valid and precise measuring systems for monitoring and controlling quality and process parameters in WBC production offers the possibility of achieving savings in raw materials and energy consumption as well as fundamental approaches for improving WBC production, thus, to optimise process conditions and material properties in general.

Die industrielle Produktion von plattenförmigen Holzwerkstoffen (HWS) wird maßgeblich durch die Kernprozesse in der Form- und Pressenstraße bestimmt. Die Plattenherstellung ist durch die Verdichtung und Aushärtung von geformten Matten aus beleimten Holzpartikeln gekennzeichnet, was in kontinuierlichen oder taktweisen Prozessen erfolgt. Dabei ist die zuverlässige Messung von Prozessparametern und Platteneigenschaften für die Überwachung und Steuerung von Produktion und Qualität unabdingbar. Die Bestimmung des Flächengewichts (Flächendichte ρ_A) der Matte und der Rohdichte (ρ) der Platte sowie des vertikalen Rohdichteprofils (RDP) erfolgt für gewöhnlich zerstörungsfrei mittels radiometrischer Geräte. Heute sind sowohl in der Industrie als auch in der Forschung Röntgensysteme zur Dichtemessung (Densitometrie) an Holz und Holzwerkstoffen verbreitet. Deren Grundprinzip zur Durchstrahlung ist ähnlich, wohingegen sich der jeweilige Aufbau in Abhängigkeit der Messaufgabe und auch in Bezug auf den Gerätehersteller unterscheidet. Die aus den gemessenen Detektorsignalen ausgewertete relative Durchstrahlung kann durch das hinlänglich bekannte Beer'sche Gesetz für die exponentielle Schwächung beschrieben werden. Die Gültigkeit setzt bestimmte Bedingungen in Bezug auf Strahlung (Energie und Strahlgeometrie) und Materialeigenschaften (konsistent und homogen) voraus, die bei radiometrischen Untersuchungen an HWS in der allgemeinen Praxis jedoch nicht angemessen erfüllt werden können. Demzufolge werden Röntgendurchstrahlungsmessungen zur Densitometrie an inhomogener und poröser Materie wie HWS grundlegend beeinflusst durch

- die Materialdichte,
- die elementare Zusammensetzung,
- die Ordnungszahl Z,
- die Strahlgeometrie,
- das Energieniveau und -spektrum sowie
- die Energieabhängigkeit der jeweiligen Schwächungsprozesse

mit den daraus resultierenden strahlungsphysikalischen Effekten wie Strahlaufhärtung und Strahlungsaufbau.

Bisherige Untersuchungen mittels Röntgenstrahlung an Holz und HWS konzentrierten sich eher auf die Anwendung praktisch bestehender Methoden als auf deren grundlegende Erforschung. Die Ausführung der jeweiligen Röntgengeräte leistet jedoch einen entscheidenden Beitrag zur Qualität und resultierenden Gültigkeit der Messergebnisse, wobei sich generelle Unzulänglichkeiten in Voruntersuchungen zeigten. Es bedarf daher einer grundlegenden aber gleichzeitig praxisorientierten Untersuchung der Densitometrie mittels Röntgenstrahlung an HWS unter besonderer Berücksichtigung der inhomogenen und porösen Struktur sowie der Zusammensetzung derartiger Verbundwerkstoffe aus Elementen mit niedrigen Ordnungszahlen.

Die vorliegende Arbeit folgt deshalb einem interdisziplinären Ansatz und verbindet dabei das Gebiet der Röntgenphysik mit der Holzwerkstofftechnologie. Strahlungsphysikalische Aspekte werden sowohl theoretisch als auch experimentell unter gezielter Materialanwendung untersucht. Grundlegende Eigenschaften von HWS mit Relevanz für die Strahlungswechselwirkung werden analysiert, da hier kaum Materialkennwerte von (labormäßig hergestellten) HWS mit vordefinierter Zusammensetzung im Vergleich zu handelsüblichen Platten vorliegen. Die jeweiligen Ergebnisse werden zusammengeführt und Schlussfolgerungen zu deren strahlungsphysikalischen Wechselbeziehungen vor einem praxisnahen Hintergrund gezogen. Für die anwendungsorientierte Beschreibung der Röntgendurchstrahlung von HWS wird ein erweitertes Schwächungsgesetz abgeleitet.

Für die Untersuchungen wurden sowohl HWS-Platten (labMDF) als auch Partikelmatten (mit Klebharzaushärtung im vorverdichteten Zustand) labormäßig hergestellt, um eine weitgehend vordefinierte Materialzusammensetzung zu erhalten. Dabei lag der Fokus auf Holzfasern und Harnstoff-Formaldehyd-Klebharz (UF) als

Ausgangsstoffe. Diese Probekörperreihen wurden durch handelsübliche Platten industriellen Ursprungs (indMDF) ergänzt.

Eine umfassende Materialanalyse unter besonderer Berücksichtigung der Eigenschaften mit Relevanz für die Strahlungswechselwirkung wurde durchgeführt mittels

- Gaspyknometrie als geeignetste Methode für die Reindichtebestimmung von hygroskopischen porösen Medien,
- Faser- und Spancharakterisierung zur Qualifizierung der tatsächlichen Strukturelemente der untersuchten Holzpartikel-Klebstoff-Matrix sowie
- Elementaranalyse und Bestimmung des Aschegehaltes resultierend in der Materialzusammensetzung auf atomarer Ebene.

Die Ergebnisse der Bestimmung der Reindichte (Feststoffdichte ρ_t) an eigens dafür vorbereiteten Proben von labMDF, dessen Rohfasern, ausgehärtetem UF-Harz sowie indMDF und Spanplatte zeigen ähnliche Werte. Aus den Messergebnissen wird für (labormäßig hergestellte) MDF ein verallgemeinerter Wert von $\rho_{t,labMDF} = 1515 \text{ kg/m}^3$ abgeleitet. Die Charakterisierung der Fasermorphologie zeigt, dass die verwendeten Sortimente thermomechanisch aufgeschlossenen Faserstoffs von den beiden Fasertypen kompakte Faserbündel sowie kurze Einzelfaser hinsichtlich ihres Volumenanteils dominiert werden. Die ermittelten Verteilungen von Breite und Länge liegen eher unter den verfügbaren Literaturwerten aber in einer vergleichbaren Größenordnung. Die Elementaranalyse in Kombination mit der Bestimmung des Aschegehaltes zeigt bestimmte Unterschiede zwischen den untersuchten Materialien. Die Ergebnisse erlauben jedoch eine Verallgemeinerung auf Basis der hergestellten labMDF mit 10 % UF-Festharzgehalt und einem Feuchtegehalt von $MC = 9,5 \%$ (Ausgleichsfeuchte nach 20/65 Klimatisierung) mit Masseanteilen der Elemente H, C, N und O sowie Asche von 6,4 %, 45,0 %, 3,1 %, 45,2 %, und 0,3 % (S vernachlässigt). Weiterhin stellte sich heraus, dass der Aschegehalt der handelsüblichen MDF den der labormäßig hergestellten im Mittel leicht übersteigt. Veränderungen im Stick-stoffgehalt sind insbesondere auf den Klebharzgehalt und -typ zurückzuführen und liegen im Fall von UF etwa eine Größenordnung über nativem Holz (ohne Rinde).

Unter Berücksichtigung der analysierten Materialeigenschaften wird ein Erklärungsmodell für die Durchstrahlung von HWS entwickelt und vorgestellt, das die Bedingungen entlang des Strahlwegs auf verschiedenen Ebenen der Wechselwirkung beschreibt. Die makroskopische Ebene [10^{-1} m] liefert die Messinformation der radiometrischen Untersuchung (Röntgendensitometrie) eines beliebig verdichteten inhomogenen Festkörpers. Im Gegensatz dazu erfolgt die tatsächliche Wechselwirkung zwischen Strahlung und Materie im submikroskopischen Maßstab [10^{-10} m], also auf atomarer Ebene, die durch die elementare Zusammensetzung bestimmt wird. Weiterhin ist davon auszugehen, dass die Ausbreitung der Strahlung auf den Betrachtungsebenen dazwischen von der Struktur des porösen Körpers beeinflusst wird. Dieser wird als (variabel verdichtete) Holzpartikel-Klebstoff-Matrix im mesoskopischen Maßstab [10^{-3} m] betrachtet, die wiederum auf mikroskopischer Ebene [10^{-6} m] aus Zellwandgewebe mit gebundenem und freiem Wasser sowie Klebharzschichten aufgebaut ist. Folglich umfasst die Schwächung der Strahlung infolge von Wechselwirkungen mit Materie komplexe Zusammenhänge hinsichtlich der Struktur und Zusammensetzung der HWS und der davon abhängenden effektiven Durchstrahlung.

Zur Verifizierung der Bedingungen des vorgestellten Erklärungskonzeptes werden orientierende Durchstrahlungsmessungen sowohl an Holzpartikelmatten als auch an Platten durchgeführt und die Messaufbauten hinsichtlich der Anwendung der Röntgengeräte in der Praxis variiert. Eigens für die RDP-Messung an kleinen Probekörpern wurde eine geeignete gravimetrische Referenzmethode zur direkten nicht-radiometrischen Bestimmung der Rohdichtegradienten entwickelt. Bei einem Ringversuche zeigen sich teilweise erhebliche Unterschiede der RDP-Verläufe und insbesondere der Deckschichtmaxima im Vergleich der Ergebnisse der eingesetzten Laborgeräte untereinander und jeweils ge-

genüber dem Referenzverfahren. Die Verfälschung spiegelt sich generell in einer Verflachung der RDP-Verläufe wider. Weiterhin ist festzustellen, dass die Abweichungen vom jeweiligen Referenzprofil mit ausgeprägterem RDP, d. h. größeren Verhältnissen von Deckschicht- zu Mittelschichtrohdichte, zunehmen.

Alle Reihen der Durchstrahlungsmessungen lassen jeweils Abweichungen im Verlauf der Messwerte über die untersuchte Dichtespanne von den theoretischen Erwartung unter idealen Bedingungen erkennen, wobei sich das Ausmaß unterscheidet und von den verschiedenen Röntgenmessaufbauten mit unterschiedlichen Parametern der ausgedehnten Strahlenbündel abhängt. Entgegen einer zu erwartenden Materialkonstante je Energieniveau sind dabei abnehmende Massenschwächungskoeffizienten innerhalb der jeweiligen Messreihe entlang zunehmender Flächengewichte oder Rohdichten zu beobachten. Folglich weicht die Strahlungsschwächung vom linearen Zusammenhang bei zunehmender Flächenmasse oder Dicke des Absorbers ab und das Beer'sche Schwächungsgesetz verliert seine Gültigkeit für diese Durchstrahlungsbedingungen. Die aus den Messergebnissen ermittelten Kenngrößen quantifizieren die jeweiligen Abweichungen und qualifizieren damit die Fähigkeit der eingesetzten Röntgenmesssysteme für die Densitometrie an HWS. Die Anwendung von Vorfiltern zur Aufhärtung der genutzten Strahlungsspektren führt dabei zu den geringsten beobachteten Abweichungen und die jeweiligen Messreihen nähern sich einem linearen Zusammenhang innerhalb einer gewissen Spanne von Dichtewerten an. Die maximale Abweichung zeigt sich beispielsweise bei einem RDP-Versuchsaufbau mit 35 kVp Röntgenröhrenspannung und ohne zusätzlichen Vorfilter. Dessen exemplarische Anwendung zur RDP-Bestimmung an MDF-19 würde aufgrund der beschriebenen Nichtlinearitäten in einem Messfehler von bis zu -4 % bei der Deckschichtrohdichte resultieren, sofern nur ein mittlerer Massenschwächungskoeffizient zur Kalibrierung herangezogen wird, wie allgemein üblich bei der Röntgendensitometrie. Auch bei der radiometrischen Bestimmung der Flächenge-

wichtsverteilung innerhalb einer geformten Holzpartikelmatte kann eine Einzelwertkalibrierung (nur ein Massenschwächungskoeffizient) zu Messfehlern führen und Abweichungen in der Größenordnung von -47…+9 % an den Grenzen eines großen Messbereiches nach sich ziehen. Neben den grundlegenden Nichtlinearitäten wurden bereits beobachtete Unterschiede zwischen den Massenschwächungskoeffizienten äquivalenter Fasermatten und -platten bestätigt, die auf unterschiedliche Streustrahlungsverhältnisse zwischen Matte und Platte bei den in der Praxis typischerweise zur Anwendung kommenden Durchstrahlungsgeometrien mit ausgedehnten Strahlenbündeln zurückzuführen sind. Wird die Kalibrierung anhand einer Platte für die Flächengewichtsmessung an einer Fasermatte herangezogen, ist beispielweise mit Abweichungen der Messwerte von etwa +14 % im Vergleich zum tatsächlichen Wert (gravimetrische Referenz) zu rechnen.

Über die Durchstrahlungsgeometrie und damit verbundene Streustrahlungsphänomene hinaus ist vornehmlich die beim Einsatz von Röntgenspektren auftretende Strahlaufhärtung dafür bekannt, derartige Nichtlinearitäten herbeizuführen. Deshalb werden neben den einfachen Durchstrahlungsmessungen (Bestimmung der Intensität ohne Energiediskriminierung) bei einem Großteil der eingesetzten Messaufbauten Röntgenspektren aufgenommen, um deren Energieverteilung zu bewerten. Neben den unveränderten Eigenschaften der Ausgangsspektren der Röhren (teils mit Filtern) werden Spektren nach der Durchstrahlung von labMDF mit verschiedenen Rohdichten aber homogenem RDP bestimmt, um den Einfluss derartiger Absorber in Bezug auf die RDP-Messung zu quantifizieren. Eine verringerte Strahlaufhärtung wurde bei einigen Messaufbauten derart festgestellt, dass ein mehr oder weniger enges Ausgangsspektrum bei der Durchstrahlung der gesamten untersuchten Rohdichtespanne keine nennenswerte Änderung erfuhr. Die Verschiebung der mittleren Energien der Spektren hin zu höheren infolge der Strahlaufhärtung wird jedoch durch Streustrahlung (vornehmlich niederer oder mittlerer Energie) überlagert, die als Se-

kundärstrahlung vom untersuchten Objekt emittiert wird, deren gemessene Intensität jedoch von der Materialstruktur sowie der Begrenzung des Strahlenbündels am Detektor abhängt. Ergänzend zu den Messungen werden Simulationen der Spektren unter Anwendung äquivalenter Bedingungen durchgeführt.

Auf Basis der allgemeinen Grundlagen von Röntgenanwendungen, der durchgeführten Materialanalysen und der Ergebnisse der Röntgenmessungen führen die theoretische Untersuchung und die ganzheitliche Diskussion der Durchstrahlung von HWS mittels Röntgenstrahlung zu folgenden Feststellungen:

1. Die Berechnung einer effektiven Ordnungszahl Z_{eff} dient als anschauliches Maß für den Vergleich des Strahlungsschwächungsvermögens verschiedener Verbundwerkstoffe und den Einfluss unterschiedlicher Zusammensetzungen. Die Ergebnisse der Berechnungen zeigen eine gute Übereinstimmung mit den meisten der jedoch kaum verfügbaren Literaturwerte sowie mit den empirisch bestimmten Daten der Holzbestandteile. Bei der Auswertung stellt sich heraus, dass Z_{eff} von HWS weder von Unterschieden im Feuchtegehalt (unterhalb des Fasersättigungsbereiches) noch der Beleimung (mit organischen Bindemitteln) beeinflusst wird. Der Einfluss eines zunehmenden Aschegehaltes sowie einer schwankenden Zusammensetzung der mineralischen Bestandteile ist jedoch nicht zu vernachlässigen.

2. Die Berechnung von mittleren Gesamtmassenschwächungskoeffizienten $\mu/\rho\,(E)_{\text{mix}}$ gewichtet anhand der Masseanteile der vorhandenen Elemente unter gleichzeitiger Berücksichtigung der Strahlungsenergien und -spektren liefert einen umfassenden Datensatz für HWS und deren Ausgangsstoffe auf Basis der tatsächlich bestimmten elementaren Zusammensetzung sowie deren virtueller Variation innerhalb extremer aber praxisnaher Grenzen. Die Darstellung der Ergebnisse in Diagrammen innerhalb der betrachteten Energiespanne von $E = 5 \dots 100\,\text{keV}$ ergibt augenscheinlich ähnliche und teilweise sogar deckungsgleiche Kurvenverläufe der eingesetzten HWS und Ausgangsstoffe inklusive Wasser. Die Gesamtschwächung in HWS wird

dominiert von den Elementen Kohlenstoff und Sauerstoff mit einem kumulierten Beitrag von $\geq 85\,\%$. Damit gilt ein vernachlässigbarer Einfluss von (organischen) Klebharzen als belegt. Der Feuchtegehalt zeigt generell einen geringen Einfluss auf $\mu/\rho\,(E)_{\text{mix}}$, ist aber insbesondere auf niederen und mittleren Energieniveaus durchaus zu berücksichtigen, wo Feuchteschwankungen von $\Delta MC = \pm 5\,\%$ um die Standardbedingungen jedoch lediglich relative Abweichungen der zugehörigen Massenschwächungskoeffizienten von $\pm 1{,}2\,\%$ nach sich ziehen würden. In Bezug auf den Aschegehalt $\omega(a)$ ergeben sich individuelle Unterschiede von $\mu/\rho\,(E)_{\text{mix}}$ zwischen vergleichbaren Werkstoffen wie beispielsweise MDF unterschiedlicher industrieller Herkunft. Eine Erhöhung des Aschegehaltes auf $\omega(a) = 0{,}9\,\%$, was dem Dreifachen von nativem Holz (ohne Rinde) der meisten Europäischen Arten entspricht, führt zu einem beträchtlichen Einfluss auf $\mu/\rho\,(E)_{\text{mix}}$ in der Größenordnung von $+1{,}5 \dots 13{,}4\,\%$ in Abhängigkeit des Energiebereiches. Zur Zusammenfassung der Berechnungsergebnisse und um eine dementsprechende quantitative Bewertung des Einflusses unterschiedlicher Materialzusammensetzungen anhand einzelner Kennwerte auf die Strahlungsschwächung zu ermöglichen, wird der differentielle Massenschwächungskoeffizient $\delta\,\mu/\rho\,(E)_{\text{mix}}\,[\%/\Delta\text{parameter}]$ als neue Kenngröße eingeführt.

3. Im Vergleich zwischen Messung und Berechnung der Massenschwächungskoeffizienten zeigt sich, abgesehen von wenigen Ausnahmen, dass die Berechnungsergebnisse im Allgemeinen über den Messwerten bei äquivalenten Energien liegen. Es wird geschlussfolgert, dass die Unterschiede systematisch den Auswirkungen von Strahlaufhärtung und Streustrahlung zuzuschreiben sind. Schließlich wird offensichtlich, dass vornehmlich Materialstruktur, Durchstrahlungsgeometrie und das Energiespektrum der Strahlung die Messung des Massenschwächungskoeffizienten μ/ρ beeinflussen, wohingegen Unterschiede in der chemischen Zusammensetzung der untersuchten Werkstoffe nur einen geringen Einfluss haben solange die Elemente der Hauptbestandteile eine ähnliche Ordnungszahl aufweisen.

Die Verknüpfung der Ergebnisse der theoretischen Betrachtungen zur Strahlungsschwächung mit den Beobachtungen bei den Messungen untermauert weitere Schlussfolgerungen zu den strahlungsphysikalischen Wechselbeziehungen der Effekte von Strahlaufhärtung, Mehrfachstreuung und Strahlungsaufbau in Bezug auf die praktische Anwendung der Röntgendensitometrie an HWS:

4. Eine erhebliche Strahlaufhärtung ist insbesondere im Energiebereich $E < 24\,\text{keV}$ vorzufinden, wo vornehmlich photoelektrische Absorption als Schwächungsprozess vorherrscht und erst mit weiter steigender Energie die Streuung zu dominieren beginnt. Zur Quantifizierung der dichteabhängigen Energieänderung wird eine Kennzahl für die Strahlaufhärtung (beam hardening index $BHi(E, \rho_\text{A})\,[\%\Delta\bar{E}/\%\Delta\rho_\text{A}]$) eingeführt, die als differentielle Energieänderung anhand von Mess- oder Simulationsdaten zu berechnen ist. Entsprechende Auswertungen bestätigen die Ergebnisse des Vergleichs der Massenschwächungskoeffizienten, wobei die nicht konstanten Messwerte von μ/ρ mit zunehmendem Flächengewicht abnehmen und unter den zugehörigen Berechnungsergebnissen liegen. Es lässt sich zusammenfassen, dass die Einflüsse der Strahlaufhärtung eine auffällige Verfälschung der densitometrischen Ergebnisse bewirken, solange für Röntgenmessungen nur ein mittlerer Massenschwächungskoeffizient zur Kalibrierung für große Flächengewichtsspannen oder Prüfkörper mit ausgeprägten Rohdichtegradienten herangezogen wird.

5. Die Beobachtungen werden darüber hinaus von Streustrahlungseffekten überlagert. Streustrahlung ist, wie die Strahlaufhärtung, unvermeidbar im Energiebereich der Röntgenanwendungen an HWS. Infolgedessen können bei Durchstrahlungsmessungen Nichtlinearitäten entstehen, wobei die aufgenommene Streustrahlungsintensität (Sekundärstrahlung) die Intensität des direkten Primärstrahls überlagert, was wiederum von den Parametern des Messaufbaus und der Geometrie des ausgedehnten Strahlenbündels abhängt. Demnach bewirkt Streuung im Allgemeinen eine Überbewertung der gemessenen Durchgangsintensität. Neben Energie und Durchstrahlungsgeometrie

hängt die aufgenommene Streuung auch von der HWS-Struktur ab. Hier spielt die Verdichtung eine entscheidende Rolle, da die Grundsubstanz des porösen Verbundwerkstoffes mit eher geringen Ordnungszahlen und niedrigen Reindichten tendenziell eine geringere Selbstabsorption der Sekundärstrahlung aufweist im Vergleich zu Metallen. Bei den Betrachtungen zur Streustrahlung stellt sich weiterhin heraus, dass ein zunehmender Strahlungsaufbau bei steigenden Flächengewichten innerhalb einer Messreihe sowie bei größeren Rohdichten des Materials vorliegt. Somit ist der Strahlungsaufbau an einer Platte größer im Vergleich zur äquivalenten Matte.

6. Alle Ergebnisse und Schlussfolgerungen sind als Beleg für das vorgestellte Erklärungsmodell zur Durchstrahlung von HWS auf den verschiedenen Ebenen der Wechselwirkung zu betrachten.

7. Schlussendlich zeigen die Untersuchungsergebnisse, dass das allgemeine Beer'sche Schwächungsgesetz für die Anwendung zur Röntgendensitometrie an HWS seine umfassende Gültigkeit verliert. Anstelle des verfälschten linearen Zusammenhangs wird folgerichtig mit einer Potenzfunktion ein geeigneter Ansatz zur mathematisch-physikalischen Beschreibung des Verhältnisses von Schwächung $\ln T^{-1}$ und Flächengewicht ρ_A gefunden. Die Umkehrfunktion bringt eine doppelt exponentielle Gleichung für die Durchstrahlung hervor, die folglich als erweitertes Schwächungsgesetz eingeführt wird. Der zusätzliche Exponent dient als Kennzahl für die Gesamtheit der vorliegenden Durchstrahlungsbedingungen des jeweils verwendeten Messaufbaus einschließlich des untersuchten Materials. Dieser praxisgerechte Ansatz ist anwendbar ohne besondere Anforderungen. Über die zweckmäßige Auswertung der mit dem regulären Durchstrahlungsaufbau und unter Verwendung des Untersuchungsmaterials aufgenommen Messdaten hinaus bedarf es keiner weiteren aufwändigen Informationen wie der Ermittlung von Röntgenspektren oder der Berechnung von Massenschwächungskoeffizienten aus Analyseergebnissen. Der Ansatz wird unter Anwendung der vorliegenden Ergebnisse der Durchstrahlungsmessungen überprüft, wobei die er-

mittelten Regressionsgleichungen gute Übereinstimmungen mit den Daten der jeweiligen Messreihen zeigen.

Die vorliegende Arbeit widmet sich vornehmlich der Untersuchung bestehender Röntgensysteme und der Beschreibung der jeweiligen Durchstrahlungsbedingungen unter Berücksichtigung von Messaufbau und Material. Deshalb werden keine Maßnahmen zur Verbesserung der eingesetzten Geräte durchgeführt. Dennoch werden anhand der methodischen Schlussfolgerungen geeignete Röntgenparameter für die Densitometrie an HWS verdeutlicht. Mit dementsprechend optimierten Röntgenmesssystemen und verbunden mit erweiterten Methoden zur Kalibrierung und Datenauswertung wird eine Steigerung der Genauigkeit der Messergebnisse mit zuverlässigen Dichtewerten ermöglicht. Damit wird die Röntgendensitometrie an HWS befähigt, belastbare Ergebnisse in der Praxis zu erzielen. Es bedarf jedoch eines erweiterten Verständnisses der Durchstrahlung von HWS aus Sicht des Röntgenstrahls sowie von dessen Ausbreitung durch dieses besondere Material. Daher müssen bei der Messdatenauswertung derartige Bedingungen unter Anwendung des doppelt exponentiellen Schwächungsgesetzes Berücksichtigung finden. Den theoretischen Hintergrund hierfür verschafft die vorliegende Arbeit. Die praktische Umsetzung obliegt hingegen den Geräteherstellern. Die Anwender solcher modernen Röntgenmesssysteme werden in die Lage versetzt, eine gesteigerte Qualität der Messergebnisse zu erzielen, was wiederum sowohl für die Forschung an HWS (breite Spanne an teilweise neuen Verbundwerkstoffen und Werkstoffverbünden) als auch für deren industrielle Produktion (steigende Anforderungen an Zuverlässigkeit und Genauigkeit) von besonderem Interesse ist. Die praxisgerechte Anwendung von nachweislich fähigen zerstörungsfreien Untersuchungsmethoden unter Einsatz von fundierten und genauen Messsystemen zur Überwachung und Steuerung von Prozess- und Qualitätskenngrößen bei der HWS-Produktion ermöglicht schließlich das Erzielen von Einsparungen bei Ausgangsmaterial und Energie und bietet weiterhin grundlegende Ansätze zur Optimierung von Prozessbedingungen und Materialeigenschaften.

Content

List of abbreviations and symbols

Abbreviation	Description
20/65	designation symbol for climate for technical applications (standard atmosphere) according to DIN 50014 (2018), here $\vartheta = 20\ ^\circ\mathrm{C}$ and $\phi = 65\ \%\ \mathrm{RH}$
3D	three-dimensional
AAPM	Association of Physicists in Medicine
ADC	analogue-to-digital converter
AE	acoustic emission
a. u.	arbitrary units
CFRP	carbon fibre reinforced polymer with epoxy resin as binder
CL	computed laminography
CL	core layer of a WBC panel
CLmat	CL particle mat samples, lab-made cured furnish mats out of resin-blended CL particles
CNR	contrast-to-noise ratio
Cox	Cox Analytical Systems AB, Mölndal, Sweden
CT	computed tomography
D	dust (fibre morphology characterisation)
Dc	dust coarse (fibre morphology characterisation)
EA	quantitative elemental analysis
EMB-12 EMCH	type of forming belt made by Habasit AG, Reinach, Switzerland
EMC	equilibrium moisture content
EPF	European Panel Federation
EW	earlywood
EWS	Electronic Wood Systems GmbH, Hameln, Germany
FA	formaldehyde, methanal, CH_2O
FBc	fibre bundle compact (fibre morphology characterisation)
FBs	fibre bundle split ends (fibre morphology characterisation)
Fmat	fibre mat samples, lab-made cured furnish mats out of resin-blended fibres (TMP)
FOV	field of view
FPL	Forest Products Laboratory – USDA Forest Service
FPO	PB with fine surface layer, old declaration for today's common PB
FSP	fibre saturation point
FWHM	full width at half maximum
F/U	molar ratio of formaldehyde to urea in the raw glue liquor of UF adhesive resin
GreCon	Fagus-GreCon Greten GmbH & Co. KG, Alfeld, Germany
GUI	graphical user interface
HCO	organic compounds containing the elements H, C, and O
HDF	high density fibreboard

Abbreviation	Description
IL	immersion liquid
IMAL	IMAL S. r. l., San Damaso (Modena), Italy
indMDF	customary industrial MDF
labMDF	lab-made MDF
LLD	lower level discriminator
low-Z	referring to matter (elements, compounds or mixtures) with low atomic numbers around carbon C with $Z = 6$, e. g. organic matter
LW	latewood
μCT, μXCT	computed tomography with voxel sizes in the micrometre range, with μXCT performed by means of X-ray
MC	moisture content
MCA	multichannel analyser
MCNP	Monte Carlo N-Particle Transport Code
MDF	medium density fibreboard
MDI	methylene diphenyl diisocyanate with its three isomers 2,2'-MDI, 2,4'-MDI, and 4,4'-MDI
MR	magnetic resonance
MUF	melamine-urea-formaldehyde adhesive resin
NDE	nondestructive evaluation, also nondestructive examination
NDI	nondestructive inspection
NDT	nondestructive testing
NIST	National Institute of Standards and Technology
n/a	not applicable, no action
n/s	not specified
OD	oven-dry
OSB	oriented strand board (strand board acc. to EN 300, structural board acc. to lexica)
PB	particleboard
PC	personal computer
PF	phenol-formaldehyde adhesive resin
PM	photomultiplier
PMDI	polymer of MDI
PMMA	poly(methyl methacrylate); poly(methyl 2-methylpropenoate); acrylic glass; Lucite®; Plexiglas®; Perspex®
qty.	quantity
R&D	research and development
raytest	raytest Isotopenmessgeräte GmbH, Straubenhardt, Germany
rem.	remainder
RH	relative humidity
ROI	region of interest
RT	room temperature
SAXS	small-angle X-ray scattering

Abbreviation	Description
SC	solid content
SFl	single fibre long (fibre morphology characterisation)
SFs	single fibre short (fibre morphology characterisation)
SL	surface layer of a WBC panel
SLmat	SL particle mat samples, lab-made cured furnish mats out of resin-blended SL particles
SNR	signal-to-noise ratio
TIFF	Tagged Image File Format
TMP	thermomechanical pulp; particular types for lab-made furnish mats (-F) and homogeneous fibreboards (-H), with milled type -H (-h)
WBC	wood-based composite
UF	urea-formaldehyde adhesive resin
USB	Universal Serial Bus
USDA	United States Department of Agriculture
XCOM	web program of the Photon Cross Section Database by NIST
XCT	computed tomography by means of X-rays
XRD	X-ray diffraction
XRF	X-ray fluorescence

Mathematical symbols and physical variables

Latin letters

Symbol	Units	Description
A	[Bq]	(radioactive) activity
A	[−]	mass number of a chemical element with $A = Z + N$
a	n/s	slope of a linear function $y = f(x) = a \cdot x + b$
B	[−]	build-up factor
b	n/s	ordinate intercept of a linear function $y = f(x) = a \cdot x + b$
c	n/s	factor in the general exponential equation $T = c \cdot e^{-d}$
CV	[%]	coefficient of variation as relative standard deviation
D	[mm]	diameter
d	n/s	exponent in general exponential equation $T = c \cdot e^{-d}$
DP_n	[−]	degree of polymerisation
ΔM	[μm, mm]	dimensional change
ΔMC	[% (abs.)]	MC change or difference (moisture content on oven-dry basis)
ΔT	[K]	temperature difference
E	[keV]	radiation energy
$\bar{E}$	[keV]	mean radiation energy, weighted by spectral distribution
E_{max}	[kVp]	maximum radiation energy, equivalent to effective maximum X-ray tube potential
E_{peak}	[keV]	intensity peak radiation energy of (a continuous) spectral distribution
f_z	[mm]	tooth feed rate with $v_f = n \cdot f_z \cdot z$
H_0	n/a	null hypothesis
H_1	n/a	alternative hypothesis
$h\nu_0$	[eV]	primary photon energy according to Planck's energy formula $E_{\mathrm{photon}} = h\nu_0$ with Planck's constant $h = 4.1357\ \mathrm{eV} \cdot s$ and photon's frequency ν_0 [s^{-1}] (lowercase Greek letter nu)
I	[a. u.]	intensity of radiation
I_{a}	[μA, mA]	tube current, accelerating current
k	n/a	number of classes
$L_p(x)$	n/s	Lehmer mean of the variables x with the exponent p
l	[mm]	length
l/w	[−]	slenderness ratio of fibres and particles
M	[kg/mol]	molar mass
m	[g]	mass
MC	[%]	moisture content defined as the mass of containing water in relation to the oven-dry mass $MC = m_{MC} - m_{\mathrm{OD}}/m_{\mathrm{OD}} \cdot 100$ [%]
mc^2	[MeV]	rest mass energy of the electron $mc^2 = 0.511$ MeV
N	[−]	neutron number of a chemical element with $N = A - Z$
N_A	[mol^{-1}]	Avogadro's number $N_A = 6.022140857 \cdot 10^{-23}\ \mathrm{mol}^{-1}$
n	[−]	sample size

Symbol	Units	Description
n	$[\text{s}^{-1}, \text{min}^{-1}]$	rotational speed
Q	$[-]$	quotient for the ratio of the respective quantities
q	$[\%/\%]$	differential shrinkage or swelling ration in % per 1 % ΔMC
R	n/s	measuring value range
r	$[\text{mm}]$	distance
r_j	n/s	class width
$r_{\text{U},j}, r_{\text{L},j}$	n/s	upper and lower class limit
SC_{UF}	$[\%]$	solid content of UF in the glue liquor, i. e., mass fraction of solid, dry UF resin on basis of the total glue liquor mass $\omega_{\text{UF,liq}} \cdot 100 \, [\%]$
$S(E)$	$[\text{a. u.}]$	spectrum of radiation energy
SPR	$[-]$	scatter-to-primary ratio
STR	$[-]$	scatter-to-total ratio
s	n/s	sample standard deviation
s_{S-D}	$[\text{mm}]$	distance from specimen backside to the detector surface
s_{T}	$[\text{mm}]$	transmission distance within the specimen corresponding to specimen depth or panel thickness
$s_{\text{X}-\text{D}}$	$[\text{mm}]$	distance from X-ray source (focal spot) to the detector surface
$s_{\text{X}-\text{S}}$	$[\text{mm}]$	distance from X-ray source (focal spot) to the sample surface
T	$[-]$	relative radiation transmission $T = \frac{I_{\text{T}}}{I_0}$
T	$[\text{K}]$	thermodynamic temperature (absolute temperature)
$\dot{T}$	$[\text{K/min}]$	rate of temperature variation $\dot{T} = T/t$
t	$[\text{mm}]$	thickness
$t_{1/2}$	$[\text{y}]$	half-life of a radionuclide
U_{a}	$[\text{kV}, \text{kVp}]$	tube voltage, tube potential, accelerating voltage
V	$[\text{cm}^3, \text{m}^3]$	volume
V_{S}	$[\text{cm}^3]$	solid matter volume
v_f	$[\text{mm/s}, \text{cm/min}]$	feed speed $v_f = n \cdot f_z \cdot z$
w	$[\text{mm}]$	width
x, y, z	n/s	coordinates for width and height (in detector plane) as well as depth (in transmission direction)
Z	$[-]$	atomic number of a chemical element with $Z = A - N$
$Z_{\text{eff}}(E)$	$[-]$	effective atomic number of a compound or mixture of chemical elements for a single radiation energy E
$Z_{\text{eff}}(\bar{E})$	$[-]$	spectral-weighted mean single-valued effective atomic number of a compound or mixture of chemical elements for the energy range $E_{\text{min}} \dots E_{\text{max}}$ of a radiation spectrum $S(E)$
$\bar{Z}_{\text{eff}}$	$[-]$	effective atomic number of a compound or mixture of chemical elements as electron-fraction-weighted mean computed via power law method
$\bar{\bar{Z}}_{\text{eff}}$	$[-]$	like $\bar{Z}_{\text{eff}}$ but with different computation
z	$[-]$	number of cutting edges

Mathematical symbols and physical variables

Greek letters

Symbol	Units	Description
δ	[%/%]	differential variation of a considered quantity with the corresponding range of a parameter
Δ	n/s	difference of two considered quantities
$\epsilon(i)$	[−]	electron fraction
η	n/s	beam hardening coefficient with varying definitions following BJÄRNGARD, SHACKFORD (1994) and KLEINSCHMIDT (1999), respectively
$\eta(i)$	[−, %]	mass-fraction-weighted contribution of a single constituent i to the total mass attenuation
ϑ	[°C]	temperature
θ	[rad]	scattering angle
θ_c	[mrad]	critical angle for total reflection
κ	[−]	introduced exponent kappa in the double-exponential law of attenuation
λ	[Å]	wavelength
$\mu_\mathrm{lin} = \mu$	[cm^{-1}, m^{-1}]	linear attenuation coefficient
μ/ρ	[cm^2/g, m^2/kg]	mass attenuation coefficient
$\overline{\mu/\rho}$	[m^2/kg]	mean mass attenuation coefficient from transmission measurement
$\mu/\rho\,(E)$	[m^2/kg]	mass attenuation coefficient for a single radiation energy E
$\mu/\rho\,(\bar{E})$	[m^2/kg]	spectral-weighted mean mass attenuation coefficient for the energy range $E_\mathrm{min} \ldots E_\mathrm{max}$ of a radiation spectrum $S(E)$
$\mu/\rho\,(E)_i$	[m^2/kg]	mass attenuation coefficients of the single component i for a single radiation energy E
$\mu/\rho\,(E)_\mathrm{mix}$	[m^2/kg]	total mean mass attenuation coefficient of a compound or mixture computed via mixture rule for a single radiation energy E
$\mu/\rho\,\big(S(E)\big)_\mathrm{mix}$	[m^2/kg]	spectral-weighted total mean mass attenuation coefficient of a compound or mixture computed via mixture rule for the energy range $E_\mathrm{min} \ldots E_\mathrm{max}$ of a radiation spectrum $S(E)$
μ_en/ρ	[cm^2/g]	mass energy-absorption coefficient
μ_tr/ρ	[cm^2/g]	mass energy-transfer coefficient
$\xi(i)$	[-, %]	fraction of single mechanism i of total mass attenuation
ρ	[kg/m^3]	raw density, bulk density
ρ_t	[kg/m^3]	true density
ρ_A	[kg/m^2]	area density, mass per unit area (also referred to as area weight, basis weight, or grammage)
Σ	$\left[\dfrac{\mathrm{cm}^2}{\mathrm{cm}^3} = \dfrac{1}{\mathrm{cm}}, \mathrm{m}^{-1}\right]$	interaction cross-section per volume element, total or macroscopic cross-section
σ	n/s	standard deviation of a statistical population
σ	[cm^2, m^2, Å^2, barn]	interaction cross-section
σ_a	[cm^2, m^2, Å^2, barn]	interaction cross-section per atom, atomic or microscopic cross-section

Symbol	Units	Description
$\sigma_{a,\text{tot}}$	$[\text{cm}^2, \text{m}^2, \text{Å}^2, \text{barn}]$	total interaction cross-section per atom as mean of a mixture
σ_e	$[\text{cm}^2, \text{m}^2, \text{Å}^2, \text{barn}]$	interaction cross-section per electron, electron cross-section
Φ	$[\text{a. u.}]$	fluence of photons
Φ	$[\%]$	porosity
$\varphi(i)$	$[-, \%]$	volume fraction of the single component i on basis of total mixture volume
$\omega(a)$	$[-, \%]$	ash content, mass fraction of the non-combustible (mineral or inorganic) residue based on OD mass of the considered mixture
$\omega(i)$	$[-, \%]$	mass fraction of the single component i typically based on OD mass of the considered mixture
$\omega(i)_{\text{mix}}$	$[-, \%]$	mass fraction of the single component i on basis of total mixture mass
$\omega(\text{UF})_{\text{liq}}$	$[-]$	mass fraction of solid, dry UF resin on basis of total glue liquor mass, i. e., $\text{SC}_{\text{UF}}/100$ $[\%]$
$\omega(\text{UF})_{\text{OD}}$	$[-, \%]$	mass fraction of UF on basis of oven-dry wood mass, i. e., resin content

Subscript	Description, referring to
0	initial state or condition, e. g. intensity I_0
A	area
a	ash content $\omega(a)$
coh	coherent scattering as particular attenuation mechanism, also referred to as inelastic or Compton scattering
D	detector-influenced
end	after the experiment or process
grav	gravimetric, i. e., determined by means of weighing and measurement
i, j	counting variable (general purpose)
in	scattered in
incoh	incoherent scattering as particular attenuation mechanism, also referred to as elastic or Rayleigh scattering
ini	initial, i. e., prior to the experiment or process
K	kernel of a data processing filter (e. g. Gaussian filter)
k	counting variable (number of stacked layers, specimen per sample, components of a mixture)
long	longitudinal solid wood direction
lin	linear
max	maximum value of the respective variable
MC	moist state with the respective moisture content
min	minimum value of the respective variable
mix	mixture or compound of chemical elements
n	counting variable (number of redundant images, sample size)
nom	nominal
OD	oven-dry state
opt.	optimal, aiming at ideal conditions
out	scattered out
P	primary (intensity)
p, q	counting variables for image array size (x;y)
peak	point of highest intensity, summit of a slope
ph	photon
phot	photoelectric absorption as particular attenuation mechanism
R	measuring value range
rad	radial solid wood direction
ref	reference
rel	relative
RT	room temperature
S	scattering (intensity)
S	solid matter
S1	state 1
S2	state 2

Subscript	Description, referring to
set	setpoint, desired value
T	transmission, transmitted
tan	tangential solid wood direction
tot	total

γ	gamma radiation
κ	enhanced law of attenuation with kappa as double-exponent

Subscript	Description, referring to
set	setpoint, desired value
T	transmission, transmitted

Chemical elements and radioisotopes

Symbol	Atomic number Z	Name (mass number A of the radioisotope)
Ag	47	silver
Al	13	aluminium
^{241}Am	95	americium (241)
Be	4	beryllium
C	6	carbon
Ca	20	calcium
Cd	48	cadmium
^{109}Cd	48	cadmium (109)
Cr	24	chromium
Co	27	cobalt
Cu	29	copper
^{137}Cs	55	caesium (137)
Fe	26	iron
^{55}Fe	26	iron (55)
Ge	32	germanium
H	1	hydrogen
He	2	helium
I	53	iodine
Li	3	Lithium
Mo	42	molybdenum
N	7	nitrogen
Na	11	sodium
Ni	28	nickel
O	8	oxygen
Pd	46	palladium
S	16	sulphur
Si	14	silicon
^{90}Sr	38	strontium (90)
Te	52	tellurium
Tl	81	thallium
W	74	tungsten
Zn	30	zinc

List of figures

List of tables

Section I
Introduction and background

For the most common wood-based composites, medium density fibreboard (MDF), particleboard (PB), and oriented strand board (OSB), the European Panel Federation (EPF) reports for 2017 a production volume of 49.1 million m³ in their member countries (excluding Russia and Turkey, cf. WIJNENDAELE (2018)), which represents a more or less consistent growth for nearly all panel types compared to the previous year (2016). According to common industry reporting, this generally positive trend continued in 2018. Likewise, North American, Chinese, and Southeast Asian production volumes are reportedly increasing with partly tremendous growth in capacities due to new or extended production lines (cf. SALO (2018)).

Notwithstanding global region, volume, and type with individual characteristics, the complex industrial production of furnish-based, panel-type, wood-based composites (WBCs) follows a similar process in most typical plants. Regardless of the still existing (multi-)opening presses particularly in the case of OSB, WBC production features a continuous process flow. After furnish generation, drying, and resination[2], the forming and press line, as illustrated in Figure I-1, comprises the core processes considered to be crucial for production capacity and product properties. Accordingly, numerous studies exist dealing with the context of processing, material, and final properties, which have been summarised over decades in just as many reports, theses, and textbooks such as

- RACKWITZ (1954),
- FAHRNI (1956),
- LAMPERT (1967)
- KELLY (1977),

- SUCHSLAND, WOODSON (1987),
- LOBENHOFFER (1990),
- DEPPE, ERNST (1991) as well as DEPPE, ERNST (1996),
- MALONEY (1993),
- HUMPHREY (1994),
- HAAS (1998),
- THOEMEN (2000),
- HASCH (2002),
- DUNKY, NIEMZ (2002),
- WINANDY, KAMKE (2003),
- CHAPMAN (2004),
- WALKER (2006b),
- THOEMEN (2010),
- ANSELL (2015), and
- PAULITSCH, BARBU (2015).

The common core processes start with spreading the resin-blended furnish material to form a mat (section B in Figure I-1) with a predefined area density[3] $\rho_A \, [\mathrm{kg/m^2}]$ on a mostly wetted forming belt (A) whereas the upper mat surface is individually wetted later (D). Densification of the loosely formed mat comprises two independent steps, where the mat with more or less equal area density is compressed to increasing raw density[4], i.e., two different continuous presses for

- (cold) pre-pressing (C) to reduce bulk height and to fix the mat (unheated press with upper mesh belt) and
- main hot-pressing (heating platens temperature in the range 180…240 °C) with rather fast densification down to target thickness in the infeed zone (E) and subsequent heat and mass transfer induced consolidation during the adjusting period (F) with final curing to maintain the final panel.

---

[2]   Note, the individual order of drying and resination depends on the WBC type.

[3]   Note, the technical term 'area density' with the symbol ρ_A and the unit $\mathrm{kg/m^2}$ is consistently utilised for the physical quantity 'mass per unit area' also referred to as 'area weight', 'basis weight', or 'grammage' particularly in the paper industry.

[4]   Note, the technical term 'raw density' with the symbol ρ and the unit $\mathrm{kg/m^3}$ is consistently utilised for the physical quantity 'density' considering mass per total volume including pores (refer to Chapter IV–1.5) also referred to as 'bulk density'.
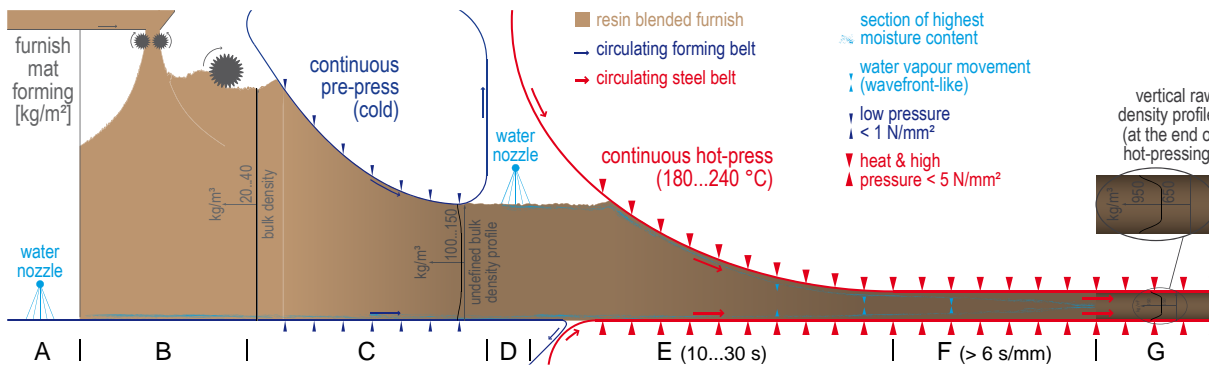
Figure I-1: Schematic illustration of continuous wood-based composite production (true to scale consolidation ratios) considering the common core processes in the forming and press line (lateral view of left-to-right production direction) with mat forming (B), pre-pressing (C), mat surface wetting (A+D), hot-pressing infeed (E) and consolidation (F), as well as final panel with typical RDP, exemplarily for MDF with one forming station.

Conventional hot-pressing featuring a wavefront-like water vapour movement[5] yields a typical raw density profile (RDP) across the panel thickness (G in Figure I-1) in consequence of varying plasticisation along the wavefront during the densification process, where this vertical density gradient is well-known to govern all physical and mechanical panel properties. Hence, reliable knowledge with valid results of relevant area and raw density gradients is indispensable for any WBC processing. In the forming and press line, however, measurement of such mat and panel parameters is consequently required for process and quality control (cf. PAULITSCH, BARBU (2015)) and performed in the industry employing different methods of varying extent (cf. NIEMZ, SANDER (1990) or HASENER, BARBU (2009)); i. e., determination of

- area density (distribution and basic dosing) of the pre-compressed furnish mat,
- area and raw density (mean and also distribution) of the ready-pressed panel, as well as
- raw density profile (RDP, also known as vertical density profile) on small specimens in the lab or inline after the hot-press

via densitometry by means of X- or gamma-rays with particular respect to the investigations of the present thesis. Obviously, densitometry and further measuring tasks are well-known to be preferably performed by nondestructive methods,

thus, impactless and partly contactless, where WELLING (1998) provides an overview for WBC industry and research.

In general, HELLIER (2001) defines nondestructive testing (NDT) as "[…] examination, test, or evaluation performed on any type of test object without changing or altering that object in any way […]" to determine the conditions or to measure characteristics of the object under investigation. Nondestructive examination (NDE), nondestructive inspection (NDI), and nondestructive evaluation (NDE) are further common expressions for such technologies. Besides the methods by means of ionising radiation such as radiographic testing, the main NDT techniques are visual, ultrasonic, acoustic emission, and thermal infrared testing, which are applicable to wood-based material, whereas eddy current, magnetic particle, and penetrant testing are preferably utilised for metal or partly limited to ferromagnetic materials (cf. HELLIER (2001)).

On wooden objects and timber, NDT is researched and practically performed by means of various methods beyond the aforementioned, where some of them are rather referred to as semi-destructive, e. g., the drill resistance technique (cf. RINN et al. (1996), TANNERT et al. (2014), and REINPRECHT, ŠUPINA (2015)). Note, also historical wooden goods, artworks, and cultural heritage items serve as objects under investigation. Accordingly, many reviews on wood

---

[5]　SOLBRIG et al. (2015b) confirm existing theory via quantitative neutron radiography in terms of exploratory studies.

NDT are available, which summarise the findings and applications, such as

- THUNELL (1955),
- NIEMZ (1995),
- NIEMZ et al. (1999),
- BEALL (2000) and likewise BEALL (2007),
- KASAL, ANTHONY (2004),
- BRASHAW et al. (2009),
- BUCUR et al. (1998), BUCUR (2003a), and more comprehensive BUCUR (2003b),
- WEI et al. (2011),
- NIEMZ, MANNES (2012) and furthermore LEHMANN, MANNES (2012),
- HASNÍKOVÁ, KUKLÍK (2014),
- WHITE, ROSS (2014) and likewise ROSS (2015),
- TIITTA (2006),
- RIGGIO et al. (2014), as well as
- VÖSSING, NIEDERLEITHINGER (2018).

Beyond such common studies, KUMAR (1958) considers the measurement of panel thickness to be a nondestructive method and provides, however, questionable implications, where a correlation between thickness, density, and bending strength is proposed for nondestructive evaluation of the bending strength based on thickness measurement. Nevertheless, common radiography, i. e., imaging by means of ionising radiation via film or digital image acquisition systems, is considered to be a well-established technique for material inspection in numerous fields. The like applies to wood applications, where POLGE (1978) provides a review on early research and development. For studies on later progress, reference is made to the aforementioned general wood-NDT reviews. In addition to imaging, densitometry is often applied on wooden drill cores, where methodical problems are already pointed out by LENZ et al. (1976), which are considered to cause biased results of the measured tree-ring structures. Besides X- and gamma-rays, KLEUTERS (1964) determines the local raw density of tree rings by means of beta radiation from a ^{90}Sr isotope source follow-

ing the fundamental law of attenuation and already employing a device for automatic measurement.

Likewise, in the initial research on WBCs, raw density gradients perpendicular to the panel plane were examined on small specimens, i. e., RDP determination by means of ionising radiation in the laboratory via densitometric evaluation of radiographs or later via direct radiation detection. Corresponding first studies primarily focused on the development of suitable RDP measuring devices and applicable direct scanning procedures. The initially applied radioisotopes – particularly with ^{241}Am as predominant source in this field for some decades (cf. MAY et al. (1976) and RANTA, MAY (1978)) – were partly already replaced[6] by X-ray tubes, which eventually became standard. The techniques introduced at that time still, however, serve as the basic principle of today's lab devices. Beyond the common radiometric RDP determination, special scientific applications on WBCs exist, e. g., in-situ investigations of RDP formation first by WINISTORFER et al. (2000) on single positions and later by GRUCHOT (2009) over the total (half during densification) cross-section. And WALTHER, THOEMEN (2009) utilise high-intensity X-rays from a synchrotron beamline for µXCT of MDF structures, to name just a few such studies, whereas several reports on common X-ray CT of WBCs exist. In addition, and with further respect to fundamental research at large-scale facilities, neutron radiography also needs to be mentioned as, e. g., a complementary method to X-rays for investigations on wood and WBCs. This is especially the case, where enhanced moisture contrast is required for the examination of

- water uptake in a trunk by BÜCHERL, LIERSE VON GOSTOMSKI (2011),
- diffusion processes in wood by MANNES et al. (2009), and
- water vapour movement in WBCs by SOLBRIG et al. (2015c).

---

[6] Note, the direct scanning X-ray devices for WBCs were introduced by the manufacturers in the mid-1990s, where, however, no references are available in the literature. Regarding wood densitometry, reference is made to HOAG, MCKIMMY (1988) as well as HOAG, KRAHMER (1991).

However, for a more comprehensive state of knowledge review on X-ray densitometry on WBCs, reference is made to Chapter II–3.

In the industrial context of WBC production, in turn, most of the applications differ from common radiography in NDT, since the employed inline devices instead generally feature continuous data acquisition for measuring purpose in contrast to imaging of static structures in terms of general NDT. Nevertheless, the determination of area density ρ_A and its distribution across the mat and panel plane by means of various inline measuring devices via ionising radiation has been common practice in WBC production for decades with, however, varyingly deep integration into process control depending on WBC type, installation country, as well as basic plant performance and age. Already GRETEN (1982), HÄNSCH et al. (1983) as well as KLEINSCHMIDT, HÄNSCH (1985) pointed out the necessity of such systems to achieve cost savings. The technologically important parameter of area density was first studied by WALTER, WIECHMANN (1961) employing both a radioisotope (^{90}Sr, beta radiation) as well as an X-ray tube. Accordingly, they consider the industrial application to be suitable for process control. Later, POLGE, LUTZ (1969) also investigate ρ_A as well as RDP determination via X-ray films. Subsequently, further research was performed, however, rather considering radiometric RDP than ρ_A determination methods, where virtually no further publications exist for the latter except FUCHS (2010) proposing a new calibration method and SOLBRIG et al. (2015d), who were first to quantify gauge capability of X-ray densitometry devices following common methods on basis of statistical measuring signal analysis. Today, inline X-ray devices for continuous measurements on furnish mats or panels are more or less state of the art in WBC production and commercially available from

- BST eltromat International GmbH, Bielefeld, Germany (former betacontrol GmbH & Co. KG, Freudenberg, Germany)
- Electronic Wood Systems GmbH, Hameln, Germany (EWS),
- Fagus-GreCon Greten GmbH & Co. KG, Alfeld, Germany (GreCon),

- IMAL S. r. l., San Damaso (Modena), Italy (IMAL), and
- Siempelkamp Maschinen- und Anlagenbau GmbH & Co. KG, Krefeld, Germany (SicoScan, made by EWS).

Some of the manufactures likewise provide a lab device for RDP determination, where reference is made to Table IV-22 for a detailed overview. Beyond that, comparable systems for similar measuring tasks exist for inline applications in paper production, however, from different manufactures such as

- Mahlo GmbH + Co. KG, Saal/Donau, Germany,
- Scienta Oy, Jorvas, Kirkkonummi, Finland, and
- Valmet Oyj, Espoo, Finland

whereas the area density measuring range considerably falls below WBC production due to the lower product thickness. Moreover, another measuring task performed by inline X-ray systems is the detection of foreign bodies like metal, rubber, or resin lumps in the furnish mat (cf. HILBERS (2006) or BARBU et al. (2014)), which is rather related to radiography with subsequent automated image data evaluation, thus, not further considered in the present thesis.

Notwithstanding apparently well-established X-ray techniques for densitometry on WBCs, during the decades of continuous development, individual device and component modifications were made, e. g., (monoenergetic) radioisotopes (such as ^{241}Am) were replaced by (polychromatic) X-ray sources, without particular adaption of corresponding methods and data evaluation procedures to the different radiation-physical requirements. Here, particular conditions regarding radiation and material properties were obviously left out of consideration. Accordingly, empiric experiments as part of preliminary studies to the present thesis considering both ρ_A as well as RDP measurement revealed fundamental insufficiencies and erroneous densitometry results with respect to hitherto X-ray measuring methods in WBC industry and science. Moreover, demand has grown for reliable, nondestructive measuring systems with regard to process and quality control in panel production due to both

economic and ecological reasons. The common aim is higher efficiency in raw material and energy consumption, hence, cost savings and reduced resource use. The like applies to corresponding research, where valuable X-ray devices for fundamental investigations in terms of product and process development are required. However, SOLBRIG et al. (2011) claim biased results for the RDP measurement with the applied X-ray measuring device and propose an alternative calibration procedure. Likewise already MOSCHLER JR, WINISTORFER (1990) and later RAUTKARI et al. (2011) point out the sample inhomogeneity itself to bias its radiometric determination. Eventually, there is a lack of comprehensive considerations similar to the theoretical wood densitometry from LIU et al. (1988) and OLSON et al. (1988), i. e., parametric models to obtain optimal radiation attenuation and energy conditions, and their practice-oriented transfer to X-ray densitometry on WBCs.

1 X-ray measuring systems

1.1 General setup and method

Regardless of individual technical realisation by the device manufacturers or in research setups, the basic principle of conventional X-ray densitometry systems for wood-based composites (WBCs) is similar considering the measuring process as illustrated in Figure II-1. Here, the general device setups employ X-ray tubes or partly still radioisotopes as radiation source with individual beam properties considering energy (Chapter II–1.2) and geometry (Chapter II–1.3). For measurement, radiation intensity I is acquired by either form of detection method. Source and detector are aligned on one linear axis with the material under investigation in between. The basic principle of transmission measurements features the evaluation of relative radiation transmission

$$T = \frac{I_\mathrm{T}}{I_0} \tag{II-1}$$

as ratio of the intensity after radiation transmission through the object under investigation, i. e., transmitted intensity I_T [a. u.], toward initial intensity I_0 [a. u.] from the source. Here, radiation intensity is commonly considered as number of photons within the beam cross-section or on a certain area (fluence), where acquired intensity rather refers to the fluence during the time interval of detection (fluence rate or flux density). Due to beam divergence in absence of attenuation during free propagation, photon fluence decreases following inverse-square law such that

$$I \propto \frac{1}{s^2} \tag{II-2}$$

where intensity I decreases with the square of increasing distance s from X-ray source (focal spot) to any point of interest, e. g., detector surface. Fundamentals considering radiation sources, propagation, interaction, and detection

with physical background and with particular regard to industrial measuring methods are available in numerous textbooks such as HUSSEIN (2003a), where HUSSEIN (2003b) provides manifold industrial applications as well as facts for device design and improvement. IEC 60050-395 (2014) defines different radiometric gauges. In contrast to transmission, backscatter imaging, and measuring methods feature a predefined angle between initial and transmitted beam as further discussed in Chapter II–2.5, where also wood-related applications even in WBC industry exist.

However, already NICKERSON (1958) reports fundamentals of differential radiation measurements on mathematical basis. Intensity differentiation in transmission measurement is attributed to material properties related to radiation-matter interaction and consequent radiation attenuation, which is defined and described in Chapter II–2. Here, the role of spatial resolution must be considered, since the measuring signal represents integration along beam path through the specimen as well as across detector area. The distinguishability of structural inhomogeneities depends on detector extension, i. e., size of smallest sensitive area element without further spatial discrimination of impinging radiation. Therefore, FRIEDMAN (2000) provides a detailed discussion and concludes on potential error in X-ray transmission measurement, where a determined density value represents the mean of local inhomogeneities. Likewise MOSCHLER JR, WINISTORFER (1990) explore the effect of specimen inhomogeneity and detector aperture size on accuracy of wood densitometry and finally consider the mass attenuation coefficient (refer to Chapter II–2.1) as erroneous depending on wood species, thickness, source strength, and aperture geometry.

$s_{\text{X}-\text{S}}$ $s_{\text{T}} = t$ $s_{\text{S}-\text{D}}$

radiation source with
broad-beam geometry

specimen

I_0 I_{T}

detector

$T = \frac{I_{\text{T}}}{I_0}$
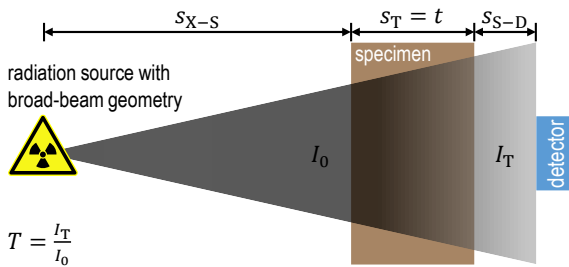
Figure II-1: Schematic illustration of common X-ray transmission measuring setups for densitometry on WBCs with radiation source (broad-beam geometry) emitting initial intensity I_0 and detector acquiring transmitted intensity I_{T} on one linear axis with material under investigation as specimen in between, complete with distance from X-ray source (focal spot) to sample surface $s_{\text{X}-\text{S}}$, transmission distance within specimen s_{T} (corresponding to specimen depth or thickness t), and distance from sample backside to detector surface s_{S-D}.

Eventually, radiation from both initial and transmitted beam is recorded by either form of detection method, which, however, yields an analogue or digital output signal corresponding to radiation intensity. Note, explicit investigation of detector impact and comparison of respective types in terms of X-ray densitometry is not part of this thesis, thus, fundamentals are not further pointed out and discussed, where reference is made to respective textbooks such as TSOULFANIDIS (1995) or LEROY, RANCOITA (2004). However, IEC 60050-395 (2014) names different detector types, where particularly

- scintillation detectors comprising a scintillating material, where ionising radiation is converted into visible light and for measuring purpose commonly a photomultiplier tube coupled via a photosensitive layer (photocathode) to yield an amplified electrical signal, referred to as photon-counting detectors, as well as
- semiconductor detectors for direct conversion of ionising radiation into electrical charge via the photoelectric effect

are found most relevant for X-ray densitometry on WBCs. Furthermore, ionisation chambers, where the impinging ionising radiation causes charged (gas) particles between collector electrodes are still applied in existing measuring devices for WBC industry. However, the different

detection methods are individually applied by the device manufactures or in terms of research and reveal their respective detector efficiency, which must be considered for the measuring process. HALMSHAW (1995) points out some requirements regarding basic concepts of radiometric methods with such design for specific applications like densitometry on WBCs, where a detector in combination with a recording device scans across the specimens. Accordingly, e. g.,

- sufficient source intensity,
- narrow beam collimation corresponding to detector size, and
- scanning spot size and detector integration time in coordination with appropriate signal statistics

have to be individually defined for each particular X-ray measuring application.

Finally, the relationship between measurement and physical properties of the object under investigation needs to be established (cf. HUSSEIN (2011)). Therefore, calibration is performed to transform an analogue or digital signal with arbitrary units to an intended measuring information in terms of density, i. e., raw density ρ or area density ρ_{A}, where a simple linear approximation may be found as valid. The relationship may, however, be affected by individual impact factors of both irradiation setup and material, as well as particular interdependencies such that the linear model becomes ill-posed considering the total measuring range.

1.2   X-rays

In November 1895 during his investigation of cathode rays, Röntgen (1898b) discovered a "new kind of rays" emitted from a Hittorf's vacuum tube or a well-exhausted Crookes' or Lenard's tube[7] with the potential to penetrate any kind of matter. Today, X-rays, also referred to as roentgen radiation, are widespread in various medical and technical applications. For common purposes, radiation generation is carried out by means of X-ray tubes, i. e., vacuum tubes, where accelerated electrons by high voltage from a cathode hit the target material (e. g., tungsten $_{74}$W) of the anode, where their deceleration, in turn, causes emission of ionising radiation as continuous bremsstrahlung spectrum superimposed by characteristic lines from fluorescent emission if present. In order to specify X-ray devices regarding parameters of the tube and their emitted radiation, several standards and guidelines exist such as

- DIN EN 12543-1 (1999) and further parts for characteristics of focal spots in industrial X-ray systems,
- DIN EN 12544-2 (2000) for determination of emission constancy from X-ray tubes,
- DIN EN 12544-3 (1999) for determination of maximum energy,
- DIN EN 13068-1 (2000) for evaluation of radioscopic devices, as well as
- VDI/VDE 5575-2 (2015) for determination of beam-geometric and spectral quantities of X-ray optical systems.

Further sources[8] are particle accelerators, where high-intensity X-rays are, e. g., available from synchrotrons at large-scale facilities. X-radiation is well-known as electromagnetic radiation in the spectrum beyond visible light with wavelengths $\lambda \leq 12.4 \, \mathrm{nm} = 124 \, \text{\AA}$ corresponding to radiation energies $E \geq 0.1 \, \mathrm{keV}$ whereas often its particle character, thus, consideration as photons, is

practically utilised to describe various phenomena. For NDT on wood and WBCs, an energy range of $E = 5 \dots 100 \, \mathrm{keV}$ is found to be commonly applicable depending on specimen size, thus, the amount of matter to be irradiated. However, the basic energy level in this range, in turn, facilitates X-rays to penetrate matter and to ionise the very same, thus, to release electrons inside. Obviously, interaction occurs during X-ray propagation through material, which is further pointed out in Chapter II–2.1. Besides X-rays, radioisotopes serve as sources of gamma radiation emitting monoenergetic or discrete polyenergetic ionising radiation with one or a few discrete wavelengths depending on the type of radioisotope such as ^{241}Am with $E_\gamma = 59.5 \, \mathrm{keV}$ or ^{137}Cs with $E_\gamma = 662 \, \mathrm{keV}$. Beyond that, special ways to generate monochromatic radiation by means of X-ray tubes exist (cf. Küstner (1931)), which are, however, generally accompanied by a considerable loss of radiation intensity. However, radioisotopes are still relevant in common NDT due to their simple availability without further resources like power supply or cooling apart from radiation protection issues. For WBC densitometry, such radiation emitters are partly still utilised in older gauges but rather substituted by X-ray tubes in current devices. Thus, the focus of this thesis is more or less exclusively on X-rays.

Röntgen (1898a) already observed phenomena, which are now described as the well-known polychromatic character of X-rays. The shape of such X-ray energy spectra $S(E)$ as radiation intensity distribution over the considered energy range mainly depends on target material (atomic number) and angle as well as tube voltage (peak voltage) U_a [kVp] whereas total intensity is proportional to tube current I_a. Further possibilities to influence X-ray spectra such as filtration are discussed in Chapter II–2.4.2. However, Figure II-2 shows common X-ray spectra from a W-target tube with 45° target angle and inherent pre-

---

[7]   The mentioned tubes are early experimental electrical discharge tubes to explore cathode rays named after the respective physicist.

[8]   Supposedly beyond relevance in general NDT, Camara et al. (2008) observe X-ray emission as nanosecond pulses around $E_{\mathrm{peak}} = 15 \, \mathrm{keV}$ in consequence of triboelectric effects during peeling of common adhesive tape in moderate vacuum.
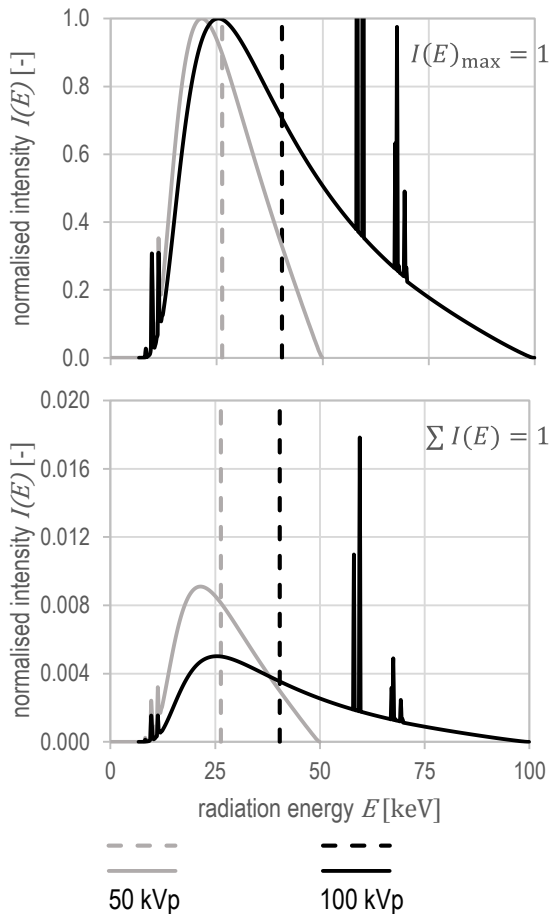
Figure II-2: X-ray spectrum of a conventional X-ray tube with tungsten (W) as target material (45° angle, 0.2 mm Be tube window, 0.635 mm Al pre-filter) as common energy distribution on two energy levels $U_a = E_{max} = 50$ kVp and $U_a = E_{max} = 100$ kVp with simulated bremsstrahlung including characteristic K and L lines[9] (via XRayTools, Chapter IV–4.2.6.2) as normalised intensity to maximum of bremsstrahlung with $I(E)_{max} = 1$ (top) or to unity such that $\sum I(E) = 1$, respectively, both incl. mean energies $\bar{E}$ (dashed lines).

filtering on two energy levels, where the characteristic lines[9] superimposing the bremsstrahlung occur in dependence of the applied tube voltage U_a. Beyond U_a representing the (nominal) maximum energy E_{max} of the spectrum, its mean energy is commonly applied to quantify radiation characteristics and penetration potential. For the energy range $E_{min} \dots E_{max}$ of the considered radiation spectrum $S(E)$, the spectral-weighted mean energy $\bar{E}$ [keV] is evaluated via

$$\bar{E} = \int_{E_{min}}^{E_{max}} E \cdot S(E) dE \qquad \text{(II-3)}$$

for continuous and

$$\bar{E} = \sum_{j=0}^{n} E_j \cdot S(E_j) \qquad \text{(II-4)}$$

for discrete spectra with both $S(E)$ normalised to unity such that $\int_E S(E) dE = 1$ and $\sum_n S(E_j) = 1$, respectively.

Moreover, knowledge of the employed X-ray spectra is required to consider variations of the very same owing to radiation-physical effects, e. g., beam hardening as pointed out in Chapter II–2.4. Accordingly, ZHUKOVSKIY et al. (2012) regard determination of utilised radiation spectra as an important problem in NDT. TSOULFANIDIS (1995) provides comprehensive basics of measurement and detection of radiation including the determination of spectra. KRIEGER (2013) describes the physical background for energy analysis of ionising radiation (referred to as spectrometry) via pulse-height determination and subsequent representation of the energy distribution (referred to as spectroscopy) with calibration against standard radioactive sources. Therefore, measurement of X-ray spectra is fundamentally carried out by means of partly elaborate energy- or wavelength-discriminating detection methods, which is, however, rather more common in gamma spectroscopy or fluorescence analysis than simple X-ray transmission investigations. Nevertheless, convenient methods for practice-oriented performance of spectra measurement exist. To this end, scintillation photon-counting detectors with subsequent pulse height analysis are commonly applied, where detector events are distinguished according to their amplitude corresponding to the energy of incident photons. Such devices feature certain restrictions regarding precision and efficiency, which is discussed in terms of application in Chapter IV–4.2.6.1 and Chapter IV–4.3.3.1. Measured X-ray spectra are also available from

---

[9]   Note, height of characteristic lines may be truncated owing to energy resolution of the simulation and is, however, out of range in the upper 100 kVp chart. For characteristic energies of tungsten or further elements, reference is made to KORTRIGHT, THOMPSON (2009) or elsewhere.

numerous investigations, e. g., ANKERHOLD (2000) with regard to predefined setups whereas individual transmission measuring conditions require particular energy considerations. Furthermore, energy- or wavelength-dispersive radiation detection is performed in terms of X-ray spectrometry for analytical purpose, where TSUJI et al. (2004) report on recent advances. Besides spectra measurement, simulation methods on the basis of physical laws exist whereas one is considered not to replace the other. TILLACK, BELLON (2000) introduce and discuss a model utilising tabulated interaction cross-section data to describe the bremsstrahlung spectra including characteristic radiation from X-ray tubes, which takes all relevant parameters into account. Likewise, further researchers propose algorithms for simulation of X-ray spectra, e. g.,

- TUCKER et al. (1991),
- ACOSTA et al. (1999),
- POLUDNIOWSKI, EVANS (2007) as well as POLUDNIOWSKI (2007), and
- DERESCH et al. (2010),

where their individual peculiarities and validity is discussed elsewhere. Eventually, the application of both a customary spectrometer and available spectra simulation software is part of this present thesis and further discussed in Chapter IV–4.2.6 (methods) as well as Chapter IV–4.3.3 (results).

Beyond more or less direct measurement and simulation, methods for spectra estimation by means of transmission data exist commonly without special demand on equipment. BAYER (2005) explored an approach for spectra estima-

tion via filter curves determined by the actual investigation setup. He applies a model from RUTH, JOSEPH (1997) based on TUCKER et al. (1991), where emitted spectra from particular target materials are modelled and fitted to transmission measurements by means of metal absorbers with increasing thickness. Spectra estimation on the basis of distinct transmission data was already proposed by SILBERSTEIN (1932) and applied by SILBERSTEIN (1933), who suggests the application of easily acquired filter curves for theoretical spectra determination in contradiction to laborious direct experimental recording in due time. The latter describes, in turn, a rigorous solution considering a particular form of $I(E)$ representing actual filtration curves, which, accordingly, cover many cases. The fundamental approach involves the following roughly summarised procedure. The investigated radiation wavelength interval $\lambda_{\min} \dots \lambda_{\max}$ is divided into n parts of $\Delta\lambda = (\lambda_{\max} - \lambda_{\min})/n$ with $\lambda_1 \dots \lambda_n$ representing the mean wavelength of the sub-interval. By following this discrete consideration, actual integral equation for total transmission $T(t)$ $[-]$ in dependence of thickness t $[\mathrm{m}]$, where the radiation beam goes through, is approximated via

$$T(t) = \frac{I_\mathrm{T}}{I_0} = \Delta\lambda \sum_{i=1}^{n} e^{-\mu(\lambda_i)\cdot t} \cdot f(\lambda_i) \qquad \text{(II-5)}$$

with transmitted I_T $[\mathrm{a.\,u.}]$ and initial intensity I_0 $[\mathrm{a.\,u.}]$, wavelength-dependent linear attenuation coefficient $\mu(\lambda_i)$ $[\mathrm{m}^{-1}]$ and specific intensity $I_\lambda = f(\lambda_i)$ of the particularly considered wavelength λ_i within the spectrum. Subsequently, n unknowns $f(\lambda_i)$ are established by a system of n linear equations

$$
\begin{aligned}
f(\lambda_1) + f(\lambda_2) + \cdots + f(\lambda_n) &= 1 = T_1 \\
e^{-\mu(\lambda_1)\cdot t_2} \cdot f(\lambda_1) + e^{-\mu(\lambda_2)\cdot t_2} \cdot f(\lambda_2) + \cdots + e^{-\mu(\lambda_n)\cdot t_2} \cdot f(\lambda_n) &= T_2 \\
&\cdots \quad \cdots \\
e^{-\mu(\lambda_1)\cdot t_n} \cdot f(\lambda_1) + e^{-\mu(\lambda_2)\cdot t_n} \cdot f(\lambda_2) + \cdots + e^{-\mu(\lambda_n)\cdot t_n} \cdot f(\lambda_n) &= T_n
\end{aligned}
\qquad \text{(II-6)}
$$

corresponding to a set of transmission data T_n by means of $n-1$ predefined filters of well-chosen layer thickness and more or less free transmission T_1 through air without any absorber corresponding to $i = 1$. Particularly, consistently equivalent nominal single layer thickness, thus,

$t_3 = 2 \cdot t_2$ etc., appears advantageous. However, SILBERSTEIN (1932) points out a closer approximation with increment layer number n. He furthermore suggests for filter thickness definition at least some layers chosen as thin as fea-

sible to allow consideration of spectra low-energy share by the method. Since filters serve as predefined absorbers, material is analogously chosen considering radiation penetration potential.

Henceforth, the approach was applied and refined in numerous investigations, where DELGADO (2007) accordingly reviews the studies as difficult considering the reconstruction of spectral distributions from attenuation data. Here, he distinguishes two methodical groups, i. e.,

- mathematical approaches solving the system of linear equations and
- physical concepts employing additional spectral models.

For details and citations, reference is made to DELGADO (2007). He concludes hitherto studies that they have in common to draw on a priori knowledge. The consequently derived robust iterative expectation-maximisation reconstruction method was validated via simulation as well as measurement, likewise imposes a priori positiveness of evaluated spectral distributions within the energy range limited by application parameters. Despite consideration as ill-conditioned problem, DELGADO (2007) and furthermore DELGADO (2009) revisit the SILBERSTEIN (1932) approach for spectra determination from attenuation data aiming at fundamental enhancement by imposing satisfiable a priori conditions. The more sophisticated solution to the inverse problem, i. e., the reconstruction of initial spectra from simple transmission measurements, is introduced by ZHUKOVSKIY et al. (2012). As aforementioned and beyond exemplarily discussed studies, numerous further contributions regarding spectra estimation by means of attenuation data exist, where applications with respect to wood research are underrepresented so far.

1.3   Beam geometry

Attributed to the physics of electron interaction with the target material of the tube anode, X-ray tubes are considered as quasi-point sources with particular extent of the focal spot. The emit-

ted beam continuously diverges. Thus, consequent exceeding of the focal spot dimensions commonly yields cone (circular focal spot) or fan (line focus) beams in further dependence of target alignment. Hence, no radiation with consistently parallel beam geometry can be generated by means of convenient X-ray sources for industrial or simple laboratory application. As a matter of fact, exclusively the beam axis perpendicularly impinges on the specimen surface. Furthermore, beam extent is commonly limited by means of respective source apertures, which, however, solely crop the beam to size and shape. To this end, hole or slit dimensions are predefined with respect to the region of interest (ROI) of the specimens under investigation. Therefore, sufficient material and thickness of the aperture is particularly chosen considering E_{max} to consistently establish practically total absorption (like radiation shielding), i. e., approximation via $T(E_{\mathrm{max}}) = I_{\mathrm{T}}/I_0 \approx 10^{-4} \dots 10^{-3}$. Owing to cropped beam, aperture collimation causes loss of radiation flux corresponding to aperture size and covered beam. Furthermore, the emitted beam starts to diverge again after transmission through an aperture.

Regarding beam geometry, DIN 6814-2 (2000) distinguishes between narrow and broad beam and defines the prior as a more or less parallel radiation beam with small diameter impinging perpendicularly on a considered material layer, where the detector registers only such transmitted radiation parallel to this beam axis. On the contrary, broad-beam geometry considers large diameters for irradiation and detection of transmitted radiation from any direction. The practical adaption of a broad-beam geometry as illustrated in Figure II-1 to narrow-beam conditions would, e. g., require respective source and detector collimation to yield a pencil beam corresponding to primary beam axis perpendicularly hitting the detector. The phenomena of narrow- and broad-beam geometries and consequently narrow- and broad-beam attenuation are comprehensively researched and discussed in numerous studies and fundamental background is explained in respective textbooks such as ATTIX (2004). Moreover, narrow-beam attenuation in combination with further energetic requirements

is also referred to as ideal or "good-architecture" conditions for transmission measurements (cf. Liu et al. (1988)). Eventually, the relevance of broad-beam geometry for radiation attenuation particularly considering scattering is discussed in Chapter II–2.5. At this, e. g., Midgley (2006) determines the maximum angular width of a more or less narrow beam considering an acceptable amount of scattered radiation reaching the detector.

Contrary to beam collimation by apertures, particular methods exist to actually focus or quasi-parallel align divergent X-rays. Principles of respective types of X-ray optics are attributed to particular wave-like characteristics of X-rays (cf. Als-Nielsen, McMorrow (2011)). Corresponding components are, however, commonly more elaborate compared to focussing of visible light, since radiation properties differ remarkably owing to the energy range. Whereas simplistic collimation via apertures is commonly applied for convenient and robust purposes, special beam optics are primarily utilised in laboratory environments for analytical issues. Besides refractive X-ray lenses (cf. Bruno et al. (2005)), capillary optics are common for beam focusing or collimation for different analytical setups, where Bjeoumikhov et al. (2005) provide an appropriate overview.

Capillary optics as capillary X-ray lenses are part of X-ray optical systems and further specified in VDI/VDE 5575-3 (2018). Accordingly, capillary optics for either beam focussing or collimation are methodically based on total external reflection on smooth inner surfaces. Total refection was already demonstrated by Compton (1923) and Rindby (1986) practically studied X-ray intensity after transmission through capillary glass fibres. Besides single capillaries, polycapillary optics are henceforth discussed and, however, shortly denoted as capillary optics. They consist of numerous hollow glass tubes within an array of certain shape, where multiple total reflections along each of the capillaries occur. For comprehensive fundamentals, reference is made to Gao, Janssens (2004). The most significant parameter for practical application is the critical angle θ_c [mrad] for total reflection without intensity loss, which depends on radiation energy and can

be approximated for convenient glass capillaries via

$$\theta_c \approx \frac{30}{E \,[\text{keV}]} \tag{II-7}$$

resulting in $\theta_c \approx 1 \dots 3$ mrad for $E = 10 \dots 30$ keV, i. e., $< 0.2°$. Within the considered energy range, X-rays under grazing incidence with angles below θ_c are totally reflected, where multiple repetitions yield quasi-parallel beams with the diameter of the capillary array and divergence angle corresponding to θ_c. Consequently, capillary optics feature energy-dependent transmission efficiency, where their individual application is designated for a corresponding energy range. Gao, Janssens (2004) exemplarily present transmission efficiency as function of radiation energy due to critical angle energy dependence. Here, transmission efficiency drops beyond particular energy, which can individually be designed to a certain extent via capillary geometry with parameters according to VDI/VDE 5575-3 (2018). Owing to energy dependence of θ_c, Rindby (1986) concludes capillary optics as appropriate for filtering of high-energy X-rays of the applied spectrum. However, radiation intensity can significantly be enhanced at certain distance from radiation source compared to simple aperture collimation with equivalent geometry in consequence of diminished divergence of quasi-parallelly collimated radiation by capillary optics. Eventually, collimating capillary optics yield quasi-parallel beams, where their respective performance is particularly characterised by

- output beam dimensions,
- output beam divergence angle, and
- intensity gain.

The latter compares radiation intensity of collimated beam by capillary optics toward simple apertures of the same dimensions.

Beyond predominant round or hexagonal geometries, where Bjeoumikhov et al. (2009) pointed out recent developments, flat capillary optics exist as applied by Bergsten et al. (2001) and Croudace et al. (2006) obtaining emitted beam dimensions $< 0.2 \times 200 \text{ mm}^2$. Notwithstanding hitherto progress, Engström et al. (1996) point out controversies and unsolved problems regarding actual processes inside the capillaries.

Amongst others, capillary optics were comprehensively investigated by BALAIC et al. (1995), BILDERBACK, FONTES (1997), VINCZE et al. (1998), and BJEOUMIKHOV et al. (2005). However, the only wood-related utilisation of capillary optics for sophisticated tree-ring analysis of drilling cores are attributed to BERGSTEN et al. (2001). Several investigations exist (refer to tree-ring analysis in Chapter II–3.1) by means of the consequently applied X-ray scanner model based on the device introduced by RINDBY et al. (1989) whereas CROUDACE et al. (2006) and further researchers employ the respectively adapted device for sediment core analyses. Notwithstanding that, SOLBRIG et al. (2010) report on the adaption of a respective device with capillary optics for measurements of the vertical raw density profile on WBCs. Regardless of advantageous flat beam collimation, capillary optics accordingly require demanding and repetitive maintenance of beam alignment.

2 Radiation-matter interaction

2.1 General radiation attenuation fundamentals

The intensity of ionising radiation is well-known to decrease along the beam path of propagation through matter in consequence of interaction between radiation photons and the atomic electron shell with various mechanisms, i. e., in general absorption and scattering in the energy range with respect to wood and WBC applications. This radiation attenuation, in turn, depends on different parameters regarding both radiation and material, i. e., in general energy characteristics as well as thickness (penetration distance), density, and kind of matter. Considering that, fundamental physics are available in textbooks such as EVANS (1955) or KOHLRAUSCH et al. (1996). Terms and definitions are furthermore provided in standards and guidelines such as DIN 6814-2 (2000), IEC 60050-881 (1983) or ISO 5576 (1997). However, the attenuation of initial radiation intensity I_0 [a. u.] within material layers of the thickness t [mm, cm, m] yielding the transmitted intensity I_T [a. u.] of the very same radiation beam is commonly quantified by the linear attenuation coefficient $\mu_\mathrm{lin} = \mu$ [cm^{-1}, m^{-1}] and basically described by exponential intensity decrement following well-known Beer's[10] law of attenuation

$$I_\mathrm{T} = I_0 \cdot e^{-\mu(E) \cdot t} \tag{II-8}$$

with the energy-dependent linear attenuation coefficient $\mu(E) = \mu_\mathrm{lin}$ as measure for the diminution of radiation beam intensity along propagation path through the absorber. Owing to its density dependency, μ_lin is commonly related to the density ρ [g/cm^3, kg/m^3] of the considered material, where

$$\mu_\mathrm{lin} = \frac{\mu}{\rho} \cdot \rho \tag{II-9}$$

defines the mass attenuation coefficient μ/ρ [cm^2/g, m^2/kg], which is preferably applied as material constant[11] due to its theoretical independence from density. Consequently, eq. (II-8) turns into

$$I_\mathrm{T} = I_0 \cdot e^{-\frac{\mu}{\rho}(E) \cdot \rho \cdot t} \tag{II-10}$$

and with $\rho_\mathrm{A} = \rho \cdot t$ it becomes

$$I_\mathrm{T} = I_0 \cdot e^{-\frac{\mu}{\rho}(E) \cdot \rho_\mathrm{A}} \tag{II-11}$$

where $\mu/\rho\,(E)$ is still an energy-dependent material constant. Moreover, the mass attenuation coefficient is defined by means of the atomic cross-section[12] σ_a [m^2, barn] as common measure for interaction probability of a radiation beam with an absorber such that

$$\frac{\mu}{\rho} = \frac{N_A}{M} \cdot \sigma_a \tag{II-12}$$

with Avogadro's number N_A and molar mass M [kg/mol], where the product is also referred to as total or macroscopic interaction cross-section Σ [cm^{-1}, m^{-1}] per mass unit (cf. KRIEGER (2012)). Note, beyond linear and mass attenuation coefficients, there exist the mass energy-transfer coefficient μ_tr/ρ [cm^2/g] and the mass energy-absorption coefficient μ_en/ρ [cm^2/g]. The values take energy transfer from radiation on the charged particles of the attenuating material into account These quantities are, thus, rather of dosimetric interest and considered as less relevant in terms of material testing.

Radiation attenuation along the beam path through the object under investigation occurs due to interaction of photons with matter, where, e. g., TSOULFANIDIS (1995) fundamentally describes the interaction processes and their individual dependencies on photon energy E and atomic number Z of the material (referred to as low-Z matter). Here, PARETZKE (1987) provides

---

[10] Note, the shortest designation of this historically evolved physical law (cf. PERRIN (1948)) was chosen.

[11] Note, henceforth in this thesis, the unit m^2/kg is exclusively utilised for the mass attenuation coefficient μ/ρ, due to correspondence to area and raw density units kg/m^2 and kg/m^3, respectively, commonly applied in wood industry, notwithstanding that cm^2/g is commonly to be found in μ/ρ tabulations.

[12] HOLLOWAY, BAKER (1972) report on origin of the barn as unit for cross-sections defined as 10^{-24} cm^2.

the theory of radiation track structures, which is important particularly in case of material with low atomic numbers Z. Therefore, GROSSWENDT (1999) presents a summary of "[…] the physical background of photon interactions with matter from the point of view of track structure formation in water", and thus provides basic aspects of radiation propagation through matter. For detailed fundamentals of mechanics, kinematics, and cross-sections of radiation-matter interaction reference is made to HUSSEIN (2007). Aspects of radiation propagation, interaction mechanisms, and attenuation as well as their dependencies are comprehensively reviewed and summarised in further textbooks such as

- ATTIX (2004),
- LEROY, RANCOITA (2004),
- ALS-NIELSEN, MCMORROW (2011),
- HUSSEIN (2011),
- KRIEGER (2012), and
- RUSSO (2018).

Beyond attenuation as consequence of radiation-matter interaction, FENGEL, WEGENER (1983) report on changes of structural, chemical, physical, and mechanical wood properties initiated by ionising radiation of rather high energy and dose rates, which has, however, no relevance in case of NDE owing to low dose rates and short irradiation duration, where no impact on transmission measuring results is expected.

In an energy range of $E = 5 \dots 100 \text{ keV}$ with respect to wood and WBCs, three relevant interaction mechanisms occur, which are exemplarily illustrated in Figure II-3 for two distinct chemical elements, i. e.,

- photoelectric absorption (photo),
- coherent, i. e., elastic, scattering (coh), also referred to as Rayleigh scattering, and
- incoherent, i. e., inelastic, scattering (incoh), also referred to as Compton scattering,

where only photoelectric absorption is considered to remove the attenuated radiation portion from the beam of certain extent whereas scattering solely changes the direction and partly the energy of the respective photons. Obviously, scattering occurs as an elastic (coherent) or inelastic (incoherent) process, where the prior is as-
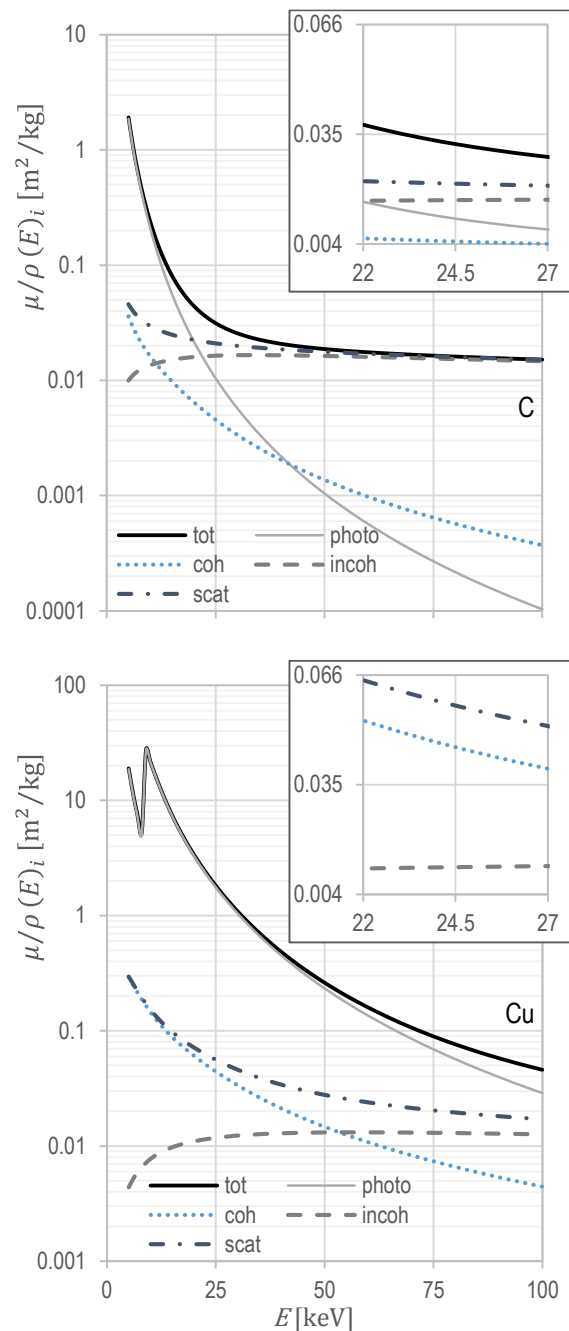
Figure II-3: Total mass attenuation coefficients $\mu/\rho\,(E)$ over radiation energy E incl. single attenuation processes photoelectric absorption, coherent and incoherent scattering, as well as scattering (scat = coh + incoh) of the elements carbon $_6\text{C}$ (top, equal to Figure VII-30, with corresponding data in Table VII-4) and copper $_{29}\text{Cu}$ for a practice-oriented energy range determined via XCOM (2010).

sociated without and the latter with release of energy from the incident and subsequently scattered photon (cf. DIN 6814-2 (2000)). Thus, the energy of scattered radiation E' from incoherent

interaction remains below initial energy E and can be computed via

$$E' = \frac{E}{1 + (1 - \cos\theta) \cdot E/mc^2} \tag{II-13}$$

as function of the scattering angle θ with the rest mass energy of the electron mc^2 (cf. TSOULFANIDIS (1995)). However, in the way total radiation attenuation of a beam through matter results from all interaction processes along the path, a total energy-dependent mass attenuation coefficient $\mu_{\text{tot}}/\rho\,(E)$ comprising all single mechanisms is well-known to be considered as sum

$$\frac{\mu_{\text{tot}}}{\rho}(E) = \frac{\mu_{\text{photo}}}{\rho}(E) + \frac{\mu_{\text{coh}}}{\rho}(E) + \frac{\mu_{\text{incoh}}}{\rho}(E)$$
$$= \frac{\mu}{\rho}(E)$$
$$\tag{II-14}$$

of the single mass attenuation coefficients $\mu_i/\rho\,(E)$ of the all relevant i processes. Consequently, the contribution of each single attenuation mechanism to the total process can be empirically computed as simple ratio

$$\xi(i) = \frac{\frac{\mu_i}{\rho}(E)}{\frac{\mu_{\text{tot}}}{\rho}(E)} \tag{II-15}$$

with the i-th attenuation fraction $\xi(i)\,[-]$ such that $\sum_k \xi(i) = 1$. At this, $\xi(i)$ varies with the radiation energy for one and the same material.

The energy dependence of both single mechanisms and total attenuation becomes obvious from the continuously decreasing slope of $\mu/\rho\,(E)$ over radiation energy E in Figure II-3, where its non-linearity needs to be pointed out with considerable incline toward low energies (note, logarithmic ordinate axis). Hence, $\mu/\rho\,(E)$ increases with decreasing radiation energy, where particularly the attenuation fraction of photoelectric absorption $\xi(\text{photo})$ distinctly increases and starts to dominate attenuation below an individual energy level considering absorber material. Such energy-dependent characteristics cause, in turn, radiation-physical effects, where reference is made to Chapter II–2.4 for further context and practise-oriented discussion. However, the continuous slope of $\mu/\rho\,(E)$ is commonly superimposed by absorption edges at

characteristic energies for the respective chemical element (cf. RINDFLEISCH (1937)), which occur with respect to the WBC-relevant energy range $E_{\max} < 100\,\text{kVp}$ for all elements $_{13}\text{Al}\ldots_{82}\text{Pb}$ (except low-Z elements such as $_6\text{C}$), where, e.g., $_{29}\text{Cu}$ reveals its K-edge at $E = 8.98\,\text{keV}$ according to HUBBELL, SELTZER (2004) or XCOM (2010) as easily can be seen in Figure II-3. Thus, radiation energy must be taken into account for any transmission measurement and densitometry consideration. For practical computation following eq. (II-10), $\mu/\rho\,(E)$ is applied representing a value of one particular energy E. For X-ray measurements, a mean energy $\bar{E}$ is commonly utilsed to describe penetration potential of the present energy spectrum. By according consideration of presumed or determined radiation spectra $S(E)$ (refer to Chapter II–1.2) with the energy range $E_{\min}\ldots E_{\max}$, a spectral-weighted mean mass attenuation coefficient is commonly computed via

$$\frac{\mu}{\rho}(\bar{E}) = \int_{E_{\min}}^{E_{\max}} \frac{\mu}{\rho}(E) \cdot S(E)\,dE \tag{II-16}$$

for continuous spectra with regard to eq. (II-3) and

$$\frac{\mu}{\rho}(\bar{E}) = \sum_{j=0}^{n} \frac{\mu}{\rho}(E_j) \cdot S(E_j) \tag{II-17}$$

for discrete spectra with regard to eq. (II-4) with both $S(E)$ normalised to unity. Beyond practise-relevant $\mu/\rho\,(\bar{E})$ representing mean attenuation conditions, its variation due to energy shift during X-ray transmission must be considered as to be discussed in Chapter II–2.4.

The energy dependency of $\mu/\rho\,(E)$ is often expressed along with its dependence on absorber matter in terms of the atomic number Z. In this regard, $\mu/\rho\,(E)$ is well-known to generally increase with increasing Z of pure substances, which likewise applies to an effective atomic number Z_{eff} of a compound or mixture, where reference is made to Chapter II–2.2 for a more detailed discussion. Figure II-4 illustrates the context between $\mu/\rho\,(E)$ and Z considering a relevant range of atomic numbers up to $_{30}\text{Zn}$ (zinc) for three exemplary energy levels. Note, the selected energies correspond to particular devices
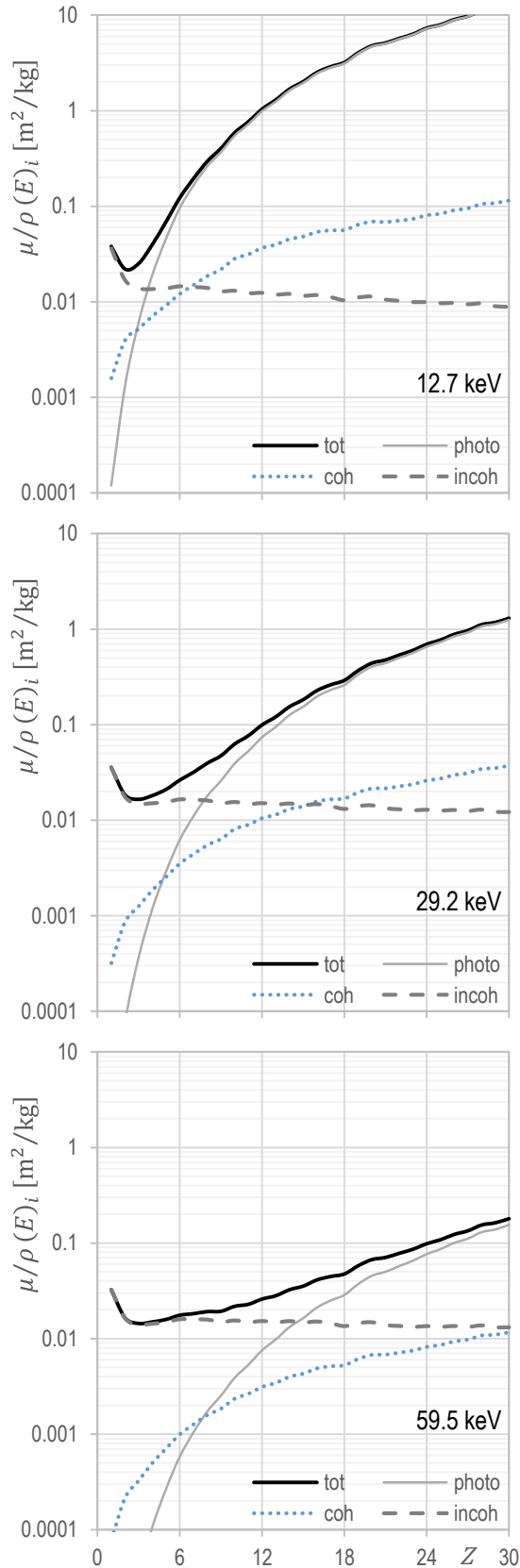
Figure II-4: Total mass attenuation coefficients $\mu/\rho\,(E)$ over atomic number Z incl. single processes photoelectric absorption, coherent and incoherent scattering on three energy levels (acc. to Table IV-34) with data determined via XCOM (2010).

as later utilised in this thesis (refer to Table VII-2) and represent the low, medium, and high level of the relevant energy range of $E = 5\ldots100\,\mathrm{keV}$ for WBC applications. In addition to the total attenuation, individual plots are shown for the single attenuation processes. Obviously, an exception of the continuous increment of $\mu/\rho\,(E)$ occurs for the element hydrogen $_1\mathrm{H}$ (and partly helium $_2\mathrm{He}$ at higher energies). This is exclusively attributed to incoherent scattering, which dominates the interaction of hydrogen with X- and gamma-rays, where the scattering share increases with increasing radiation energy.

However, early expressions to describe Z dependence reveal the empirical context

$$\mu_{\mathrm{photo}} = 2.64 \cdot 10^{-26} \cdot Z^{3.94} \cdot \lambda^3 \qquad \text{(II-18)}$$

with further dependence on the wavelength λ likewise representing radiation energy E, where, however, λ decreases with increasing E. The common concept dates back to WALTER (1929), who investigated several formulae for X-ray absorption (i. e., attenuation including scattering) in arbitrary matter based on mass content of the present elements. In this regard, he points out the dependency of μ/ρ on Z at certain wavelengths λ with the approach to compute $\mu/\rho\,(E)$ accordingly. However, the exclusive validity for real absorption was already considered. More precisely, BARRETT, SWINDELL (1996) found a dependence of the individual attenuation processes on energy E and atomic number Z for photoelectric linear absorption coefficient following

$$\mu_{\mathrm{photo}} \approx k \cdot \frac{Z^m}{(h\nu_0)^n} \cdot \frac{\rho}{A} \qquad \text{(II-19)}$$

with a constant k depending on the atomic shell involved, primary photon energy $h\nu_0$, density ρ, and atomic mass number A, where the exponents m and n are, in turn, slowly varying functions of Z and ν_0 with $m = 4$ and $n = 3$ as rule of thumb. Likewise, Z dependence of the linear incoherent scattering coefficient becomes obvious from the definition of BARRETT, SWINDELL (1996) given by

$$\mu_{\mathrm{incoh}} = \sigma_{\mathrm{incoh}} \cdot N_A \cdot Z \cdot \frac{\rho}{A} \qquad \text{(II-20)}$$

with Avogadro's number N_A, density ρ, and atomic mass number A as well as the incoherent (Compton) scattering cross-section, which is according to JACKSON, HAWKES (1981), frequently expressed by

$$\sigma_{\text{incoh}} = Z \cdot \sigma_{\text{KN}} \qquad (\text{II-21})$$

where σ_{KN} represents Klein-Nishina formula following KLEIN, NISHINA (1929), who describe the scattering cross-section for a single free electron by an complex equation and corresponding derivation. However, such μ/ρ definitions based on E and Z are applied by LINDGREN (1991) in the field of wood densitometry, where reference is made to Chapter II–2.2 for general discussion of the fundamental concept. Accordingly, SINGH et al. (1996) consider the knowledge of μ/ρ as required to utilise its individual relation toward Z as well as density of both absorption and scattering. Eventually, Z dependence becomes obvious from the different levels of carbon $_6\text{C}$ and copper $_{29}\text{Cu}$ plots of $\mu/\rho\,(E)$ over radiation energy E in Figure II-3 with $\Delta Z = 23$, where C plots considerably fall below Cu such that the attenuation by copper is up to 95 times that of carbon at low energy just above the K-edge whereas the differences converge down to three times at the end of the considered energy range.

Beyond E and Z, the dependence of μ_{lin} as well as its single mechanisms on the material density ρ becomes already obvious in the previous equations, which is, in turn, considered as dependence on atomic density in condensed matter. Hence, increasing density yields increasing macroscopic cross-section $\Sigma\,[\text{cm}^{-1}]$, i.e., interaction probability along the beam path; thus, radiation attenuation increases. According to BRADLEY et al. (1991), density dependence of attenuation mechanisms can commonly be approximated via

$$\mu_{\text{photo}} \propto Z_{\text{eff}}^{3.5} \cdot \rho \qquad (\text{II-22})$$

for photoelectric interaction of linear attenuation μ_{photo} and via

$$\mu_{\text{incoh}} \propto \rho \qquad (\text{II-23})$$

for corresponding incoherent scattering share μ_{incoh}, where both are obviously proportional to material density.

process	variation of σ_a with Z	variation with increasing E	kind of interaction
$\boldsymbol{\mu_{\text{photo}}}$	$Z^4 \ldots Z^5$	rapidly decreasing	complete energy [1] absorption during one process
	$Z^4 \ldots Z^{4.5}$	$E^{-3.5}$	[2]
$\boldsymbol{\mu_{\text{coh}}}$	$Z^2 \ldots Z^3$	rapidly decreasing	no energy loss [1] with bound electrons
	$Z^{2.5}$	E^{-2}	[2]
$\boldsymbol{\mu_{\text{incoh}}}$	Z	relatively slow variation	partly energy loss [1] depending on energy and angle
	Z	$E^{-0.5} \ldots E$	[2]

Table II-1: Summary of the approximate dependencies of the main radiation-matter interaction processes photoelectric absorption as well as coherent and incoherent scattering during attenuation of X- or gamma-rays within an wood- and WBC-relevant energy range of $E = 5 \ldots 100\,\text{keV}$ (with further proportionality to density), following Schätzler (1979) [1] and Krieger (2012) [2], respectively.

To conclude on radiation-matter interaction and attenuation dependencies, Table II-1 provides a summary considering the relevant single interaction processes photoelectric absorption as well as coherent and incoherent scattering within a wood- and WBC-relevant energy range of $E = 5 \ldots 100\,\text{keV}$, which is, moreover, similar to the range of medical application apart from CT. As easily can be seen, there is a strong dependence on radiation energy E and material composition expressed via atomic number Z, which can commonly be described by the power law $Z^m \cdot E^{-n}$ as introduced by BRAGG, PEIRCE (1914) for photoelectric absorption (cf. MIDGLEY (2004) and JACKSON, HAWKES (1981)). However, the context is considered to also apply to the scattering processes with individually lower exponents. Moreover, MIDGLEY (2004) develops and employs a parametrisation scheme for μ_{lin} considering the dependencies at energies above respective K-edges, which utilises four coefficients for low-Z elements in the energy range $E = 30 \ldots 150\,\text{keV}$. Further expressions to summarise dependencies of the linear attenuation coefficient are more or less related to the above and utilised in numerous studies. Finally, Figure II-5 schematically illustrates the fundamental understanding

of radiation propagation through matter considering the single interaction processes resulting in a total mass attenuation coefficient $\mu_{\text{tot}}/\rho\,(E)$ according to eq. (II-14) and the application for transmission measurements following Beer's law of attenuation eq. (II-10). Beyond the fundamental dependencies of radiation attenuation with particular respect to monoenergetic narrow-beam radiation and pure substances consisting of one chemical element, further dependencies are considered to occur in case of X-ray application on compounds or mixtures such as WBCs as to be discussed in the consequent chapters.

Eventually, required attenuation data for theoretical considerations is commonly available in tabulations from respective sources (cf. GERWARD (1993)). At this, HUBBELL, SELTZER (2004) provide values of mass attenuation coefficient $\mu/\rho\,(E)$ as well as mass energy-absorption coefficient $\mu_{\text{en}}/\rho\,(E)$ as tabulated data with, nevertheless, rather coarse energy steps but including individual absorption edges in the range $E = 1\,\text{keV} \dots 20\,\text{MeV}$ for elements $Z = 1 \dots 92$ complete with 48 additonal substances of dosimetric interest. Furthermore, the database XCOM (2010) provides both single process values and total mass attenuation coefficients for elements with $Z \leq 100$ as well as predefinable compounds or mixtures with standard or individual energy grids in the range $E = 1\,\text{keV} \dots 100\,\text{GeV}$, which is more flexible and avoids own data interpolation. Figure II-3 presents exemplary attenuation data of the elements carbon $_6\text{C}$ and copper $_{29}\text{Cu}$ within a wood- and WBC-related energy range $E \leq 100\,\text{keV}$ determined via XCOM (2010) complete with plots of the single attenuation processes μ_{photo}/ρ, μ_{coh}/ρ, and μ_{incoh}/ρ. Note, all utilised mass attenuation coefficients in the present thesis are comprehensively listed in Appendix VII–4. Beyond that, further programs exist for $\mu/\rho\,(E)$ computation such as GERWARD et al. (2001), MuPLOT (2006), and EL-KHAYATT (2011) based on equivalent physical background and mostly utilising the same interaction cross-section resources. Regarding accuracy of available attenuation data, MIDGLEY (2005) points out that there is an ongoing debate. He measures the linear attenuation coefficient of several compounds
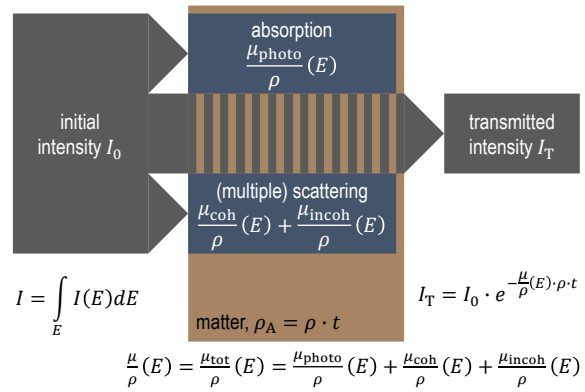
Figure II-5: Schematic illustration of the fundamental understanding of radiation transmission through matter and the application for transmission measurements, with integrated radiation intensity I, total mass attenuation coefficient $\mu_{\text{tot}}/\rho\,(E)$ as sum of the single interaction processes acc. to eq. (II-14), and Beer's law of attenuation following eq. (II-10).

by means of monoenergetic X-rays from secondary targets. In comparison to tabulated values from HUBBELL, SELTZER (2004), he found the measurements generally to be lower by about $-1\,\%$ on average. Already HAWKES, JACKSON (1980) discuss the accuracy of available data and develop a parametric model to compute linear attenuation coefficients explicitly considering the three attenuation processes in the energy rang of medical relevance $E \leq 150\,\text{keV}$. However, evaluation of theoretical data from different sources is assigned to fundamental physics and not part of the present thesis. Tabulated values available from HUBBELL, SELTZER (2004) and, thus, the database XCOM (2010), are eventually considered to be widely used as a source of (single) $\mu/\rho\,(E)$ and consequently employed for all theoretical attenuation considerations as well as computations in the present thesis.

2.2   Effective atomic number of compounds and mixtures

2.2.1   General approach

Within the considered energy range, X-ray photon interaction with matter occurs in the atomic electron shell and, thus, generally corresponds to the atomic number Z of the individual element. Real radiation absorption, i. e., photoelectric absorption, strongly depends on Z of the single-elemental absorber and varies approximately as Z^4, which, according to ALS-NIELSEN, MCMORROW (2011), fundamentally facilitates X-rays for imaging applications based on a contrast between the structural members. Additionally, scattering processes complete the total attenuation as aforementioned. However, regarding chemical compounds or mixtures of different elements, effective X-ray attenuation at a particular energy level is attributed to a corresponding electron configuration, which, in turn, results in an effective atomic number Z_{eff}. Here, diverse approaches to computationally describe radiation interaction with arbitrary matter date back to the first decades of applied X-ray research, where WALTER (1929) describe the history and evaluate the validity of several formulae. According to MURTY (1965), the concept virtually considers a compound as "[…] fictitious element having an effective atomic number Z_{eff}." Likewise, JACKSON, HAWKES (1981) denote Z_{eff} as "[…] convenient parameter for representing the attenuation of X-rays by a complex medium […]". Meanwhile, MANOHARA et al. (2008) observe a renewed interest toward Z_{eff} for radiation interaction characterisation with low- and medium-Z matter compounds and mixtures in various fields of research.

2.2.2   Simplistic power law method

In fundamental considerations to re-define the physical unit for radiation quantity and dose, MAYNEORD (1937) carries out calculations of real energy absorption with respect to a variety of substances including carbohydrates and water. Here, he refers to the findings of WALTER (1929) regarding the absorption of an individual atom with the atomic number Z according to

eq. (II-18). From that, MAYNEORD (1937) derives the computation of an effective atomic number

$$Z_{\mathrm{eff}}^m = \sum_{i=1}^{k} \epsilon(i) \cdot Z_i^m \qquad (II-24)$$

for compounds, where the electron fraction $\epsilon(i)$ is determined via

$$\epsilon(i) = \frac{\omega(i) \cdot \dfrac{Z_i}{A_i}}{\sum_{i=1}^{k} \omega(i) \cdot \dfrac{Z_i}{A_i}} \qquad (II-25)$$

based on the single atomic number Z_i in relation to the corresponding mass number A_i of all respective k elements weighted by the elemental mass fractions $\omega(i)$ in the compound or mixture such that $\sum_k \epsilon(i) = 1$. Hence, eq. (II-25) serves as the transformation of $\omega(i)$, regardless whether from theory or elemental analysis, toward $\epsilon(i)$ considering respective atomic electron abundance Z_i/A_i. Since PHELPS et al. (1975) point out a strong correlation between attenuation parameters (here Hounsfield units) and electron density (electrons per unit volume) of the investigated material by polychromatic X-rays within a medically relevant energy range, the electron-fraction-based weighting appears sufficient. However, their computations follow MAYNEORD (1937) and they discuss the influence of polychromatic X-rays and predominant Compton interactions with $E > 30\,\mathrm{keV}$. Inferring from this, Z_{eff}, which merely considers photoelectric absorption, is biased due to increment presence of incoherent scattering, which, in turn, is inherently included in tabulated total μ/ρ. Returning to Z_{eff} power law according to eq. (II-24), MAYNEORD (1937) suggests $m = 2.94$ henceforth representing the most common value. The exponent m is found to vary between hitherto studies, since it is derived by fitting the individual investigation results. Subsequently, $\sqrt[m]{Z_{\mathrm{eff}}^m}$ with $m = 2.94$ is abbreviated with $\bar{Z}_{\mathrm{eff}}$ denoting the electron-fraction-weighted mean atomic number of a mixture or compound. This is to distinguish, furthermore, from energy-dependent $Z_{\mathrm{eff}}(E)$ and its single-valued representation $Z_{\mathrm{eff}}(\bar{E})$ as energy-weighted mean. Beyond $\bar{Z}_{\mathrm{eff}}$, Table II-2 provides an overview considering selected methods of Z_{eff} determination complete with exemplary

method	Z_{eff}	E [keV]	source
eq. (II-24), $m = 2.94$	7.42	n/s	own computation
eq. (II-24), $m = 2.94$	7.24	n/s	MAYNEORD (1937)[13]
eq. (II-24), $m = 3.1$	7.45	n/s	HINE (1952)
eq. (II-24), $m = 3.4$	7.49	n/s	TSAI, CHO (1976)
eq. (II-26)	7.95	n/s	HUSSEIN et al. (1997)
σ-based	5±0.3	30	PARTHASARADHI (1968)
σ-based	7.46	20	YANG et al. (1987)
σ-based	6.17	10	KUMAR, REDDY (1997)
Auto-Z_{eff} software	6.14	10	TAYLOR et al. (2012)
	5.78	20	

Table II-2: Effective atomic numbers Z_{eff} of water (H_2O with $\omega(_1H) = 11.19\ \%$, $\omega(_8O) = 88.81\ \%$) determined via the respective method as compilation of reported values from selected hitherto literature or accordingly re-computed; radiation energy E for mean single value or n/s if method is independent.

water values. Moreover, SPIERS (1946) determines $\bar{Z}_{\text{eff}}$ of unknown substances via Z_{eff} calibration on known compounds and measures μ/ρ by means of pre-filtered 60 kVp X-rays. Despite differing derivation but based on the same empirical expression (alike eq. (II-18)) for photoelectric absorption by WALTER (1929), SPIERS (1946) defines the same formula, here eq. (II-24), as applied by MAYNEORD (1937). Eventually, both fundamental studies were performed with primary respect to dosage considerations during radiotherapy or radiographic investigations of the human body. However, detailed derivation of the approach on expressions for determination of mass attenuation coefficients based on the atomic number can be found there and complete with holistic discussions of its validity elsewhere.

MURTY (1965) reviews Z_{eff} determination via power law, whereupon, at given energy, radiation interaction with a single element is proportional to its Z^m with apparent variations in m owing to the respective study. At that, MURTY (1965) evaluates the different expressions and concludes the potential requirement for distinct Z_{eff}

expressions corresponding to individual attenuation mechanisms whereas an approximation of a single $\bar{Z}_{\text{eff}}$ for the investigated heterogeneous material appears suitable. Accordingly, elemental mixtures with neighbouring Z yield comparable Z_{eff} values independent from the calculation approach. However, the expression he derived shows similarities to eq. (II-26) but appears to be erroneous. HINE (1952) suggests $m = 3.1$ corresponding to photoelectric absorption and, nonetheless, points out the limitation of $\bar{Z}_{\text{eff}}$ expression as a single number. Accordingly, each present interaction process with the constituent elements must be considered by individual weighting. Consequently, more advanced Z_{eff} computations explicitly take energy-dependent attenuation processes into account. Nevertheless, simplistic power law according to eq. (II-24) provides in this thesis a vivid evaluation of WBCs regarding their attenuation potential without demand of complex input data.

Furthermore, HUSSEIN et al. (1997) carry out both Monte Carlo simulations (by common MCNP radiation transport code) and laboratory experiments aiming at the detection of narcotics in cargo containers. However, for Z_{eff} determination of their various materials they define the effective atomic number[14] $\bar{\bar{Z}}_{\text{eff}}$ of a mixture as

$$\bar{\bar{Z}}_{\text{eff}} = A_{\text{eff}} \cdot \sum_{i=1}^{k} \omega(i) \frac{Z_i}{A_i} \qquad \text{(II-26)}$$

with $A_{\text{eff}} = \sum_{i=1}^{k} \omega(i) \cdot A_i$. Despite similar electron-fraction-based weighting, the expression with apparent exponent $m = 1$ particularly represents Compton scattering owing to high energy level employed from a ^{60}Co source with $\bar{E} = 1.25\ \text{MeV}$ within their investigations. Nonetheless, explorative comparison (Table II-2) with eq. (II-24) approach reveals merely slight differences, where, as an extreme example, $\bar{\bar{Z}}_{\text{eff,H}_2O} = 7.95$ is 1.07 times that of $\bar{Z}_{\text{eff,H}_2O} = 7.42$ and WBC values are rather equal. Consequently, the more simplistic eq. (II-26) approach is, however, omitted henceforth.

---

[13] Apparently transposed digits by original author cannot be reproduced due to missing intermediate values.

[14] Here, Z is labelled with double-bar for distinction.

Derived from fundamental X-ray physics, JACKSON, HAWKES (1981) introduce both simple formulae and accurate parametrisation of the attenuation coefficient. As part of their study, they report Z_{eff} basics referring to further primary work and provide valuable conclusions on hitherto fundamental investigations. Thus, their comprehensive work is henceforth preferably cited. However, JACKSON, HAWKES (1981) revisit the concept of Z_{eff} determination as electron-fraction-weighted sum of Z_i, where exponent m in eq. (II-24) has to be distinguished regarding photoelectric absorption and coherent scattering. At this, they summarise $m_{\mathrm{photo}} = 3 \dots 4$ and $m_{\mathrm{coh}} = 1 \dots 2$ both depending on radiation energy and material composition. In case of small scattering contribution, one $\bar{Z}_{\mathrm{eff}}$ figure with m_{photo} is sufficient to characterise the investigated elemental composition. Regardless of attenuation process distinction, they conclude $\bar{Z}_{\mathrm{eff}}$ definition according to eq. (II-24) as invalid for wide energy ranges as well as for compounds comprising atoms with very different Z_i. Nevertheless, the approach provides practical approximations with consistent results in certain cases. On the contrary, regarding medical energy ranges and low-Z biological tissue under investigation, they consider coherent scattering neglection as suspect and resulting in poor accuracy. Inferring from this, a single-valued atomic number $\bar{Z}_{\mathrm{eff}}$ is crucially limited to narrow Z_i as well as E ranges and consequently lacks holistic validity. Notwithstanding that, $\bar{Z}_{\mathrm{eff}}$ serves as vivid measure to estimate and compare compounds and mixtures regarding their attenuation potential caused by varying compositions particularly due to single neighbouring constituents. Likewise JACKSON, HAWKES (1981) conclude insufficient accuracy for precise clinical studies and many researchers critically discuss the simplistic power law according to eq. (II-24). Particularly TAYLOR et al. (2008), who point out the initial dedication of the approach by MAYNEORD (1937) to low-energy attenuation measurement, hence, high energy level require energy-related considerations. Eventually and according to TAYLOR (2011), the method is of "[…] questionable scientific validity[…]" for applications with energy ranges across several orders of magnitude.

2.2.3   Energy-related effective atomic numbers

For explicit consideration of both actual radiation energy and related interaction processes individually corresponding to the investigated elemental mixture, more comprehensive Z_{eff} determination methods exist compared to conventional power law. Moreover, the procedures are more elaborate and require extensive input data. Based on the mixture rule as to be defined in Chapter II–2.3, which determines via eq. (II-31) the mass-fraction-weighted mean mass attenuation coefficient $\mu/\rho\,(E)_{\mathrm{mix}}$ of the considered compound or mixture, TAYLOR et al. (2012) suggest determining the total atomic cross-section via

$$\sigma_{a,\mathrm{tot}} = \frac{\dfrac{\mu}{\rho}(E)_{\mathrm{tot}}}{N_A \cdot \sum_{i=1}^{k} \dfrac{\omega(i)}{A_i}} \qquad \text{(II-27)}$$

with Avogadro's number N_A. Cross-sections serve as measure for the likelihood of interaction where $\sigma_{a,\mathrm{tot}}$, in turn, additively comprises photoelectric absorption, coherent, and incoherent scattering cross-sections. Subsequently, by further means of total electron cross-section $\sigma_{e,\mathrm{tot}}$, $Z_{\mathrm{eff}}(E)$ is computed for each energy conventionally requiring complex interpolations over a matrix of energy- and Z-dependent cross-section data. However, particular differences in computation concepts occur between the respective researchers. The same applies to employed cross-section and mass attenuation data per chemical element regarding chosen source or own measurement. Notwithstanding that, the methods both exploit the correlation between Z_{eff} and interaction cross-sections (cf. PARTHASARADHI (1968)), which generally appears as

$$Z_{\mathrm{eff}} = \frac{\sigma_a}{\sigma_e} \qquad \text{(II-28)}.$$

Eventually, for comprehensive overview, MANOHARA et al. (2008) provide a practicable compilation of formulae for Z_{eff} determination on photon cross-section basis. They conclude, among others, the energy and interaction process dependency of Z_{eff} with its maximum values to be found in the low-energy range with

dominating photoelectric effect as radiation attenuation mechanism.

SINGH et al. (1996) perform $Z_{\mathrm{eff}}(E)$ calculations based on both tabulated $\mu/\rho\,(E)$ data and own attenuation measurements. Their study comprises a variety of compounds, but none of them is similar to WBCs, just boric acid H_3BO_3 with $\bar{Z}_{\mathrm{eff,H_3BO_3}} = 7.38$ in a comparable order to WBCs and rather close to H_2O. However, they distinguish $Z_{\mathrm{eff}}(E)$ with respect to the individual attenuation mechanism, which unveils particular findings especially in the range $E < 100\,\mathrm{keV}$ for investigated medium-Z compounds. This is for the respective compounds,

- $Z_{\mathrm{eff}}(E)_{\mathrm{photo}}$ with characteristic jumps,
- $Z_{\mathrm{eff}}(E)_{\mathrm{coh}}$ with non-similar fluctuations, and
- $Z_{\mathrm{eff}}(E)_{\mathrm{incoh}}$ is increasing with energy increment but remains also constant for some compounds.

Notwithstanding that, $Z_{\mathrm{eff}}(E)_{\mathrm{H_3BO_3}}$ reveals no significant, but in case of incoherent scattering, slight variations along the considered energy range compared to the compounds above. Moreover, since interaction cross-sections are strictly additive, $Z_{\mathrm{eff}}(E)$ corresponding to total attenuation comprises the sum of all respectively observed phenomena. However, already YANG et al. (1987) consider the cross-section-based method as the most accurate determination concept. In their low-energy Z_{eff} study of human tissues ($E = 10 \dots 200\,\mathrm{keV}$), they conclude their definition of $Z_{\mathrm{eff}}(E)$ for the total radiation-mater interaction process as more appropriate. For further theoretical as well as experimental investigations by means of materials with elemental compositions and energy ranges in a comparable order to WBC applications, reference is made to EL-KATEB, ABDUL-HAMID (1991), KUMAR, REDDY (1997), KAUR et al. (2006), and TAYLOR et al. (2008).

Beyond that, TAYLOR et al. (2012) introduce a valuable tool – referred to as Auto-Z_{eff} software – for $Z_{\mathrm{eff}}(E)$ computation fundamentally employing energy-related radiation attenuation data, thus, exploiting the smooth correlation between σ and Z. Following eq. (II-27), the program routines draw on particular cross-section and mass attenuation data from individual sources. Computation basically requires the input of $\omega(i)$ such that $\sum_k \omega(i) = 1$ of the substance to be investigated. For composite materials typically with $Z \lesssim 30$, Auto-Z_{eff} software facilitates the rapid computation of energy-dependent atomic numbers as the particular value $Z_{\mathrm{eff}}(E)$ for any requested energy ranging $E = 10\,\mathrm{keV} \dots 1\,\mathrm{GeV}$ as well as spectral-weighted mean single-valued $Z_{\mathrm{eff}}(\bar{E})$ for inbuilt or user-defined energy spectra $S(E)$. The latter is simply evaluated via

$$Z_{\mathrm{eff}}(\bar{E}) = \int_{E_{\min}}^{E_{\max}} Z_{\mathrm{eff}}(E) \cdot S(E)\,dE \qquad \text{(II-29)}$$

for continuous and

$$Z_{\mathrm{eff}}(\bar{E}) = \sum_{j=0}^{n} Z_{\mathrm{eff}}(E_j) \cdot S(E_j) \qquad \text{(II-30)}$$

for discrete spectra with both $S(E)$ normalised to unity such that $\int_E S(E)\,dE = 1$ and $\sum_n S(E_j) = 1$, respectively. Far from absorption edges, uncertainties are stated in the order of $1 \dots 2\,\%$, however, increasing with decreasing energies. Moreover, reference is made to TAYLOR et al. (2012) for comprehensive details upon the Auto-Z_{eff} software, which is, furthermore, freely available. Manifold applications are reported elsewhere with diverse purposes and investigated materials from human tissues, corresponding phantoms, dosimetric materials, and shielding substances to particular composites. Amongst other methods, SINGH et al. (2014a) assess Auto-Z_{eff} software and compare results to available experimental data for human organ and tissue substitutes, where their methodical remarks are of poor precision. However, the study is fairly congruent to SINGH et al. (2014b). Despite initial purpose for medical physics, the Auto-Z_{eff} software appears as promising tool for both fundamental and practice-oriented radiation-physical considerations on wood and WBCs due to, however, the aforementioned methodical similarities.

2.2.4   Wood-related applications

Beyond studies in medical and related physical fields as well as material science, particular Z_{eff} considerations regarding wood and WBCs are fairly rare. Nevertheless, LU, LAM (1999) theoretically consider $\bar{Z}_{\text{eff}}$ determined via eq. (II-24) with $m = 3.4$ but fail to present respective results corresponding to their lab-made panels of aspen strands. LINDGREN (1991) computes linear attenuation coefficients $\mu(E)$ at $\bar{E} = 73\,\text{keV}$ and subsequent Hounsfield units following the model of TSAI, CHO (1976) on the basis of eq. (II-14) with distinction of photoelectric absorption and Compton scattering. For his calculations on dry and wet wood, $\mu(E)_{photo}$ requires $\bar{Z}_{\text{eff}}$, which is determined via eq. (II-24) with $m = 3.4$ accordingly suggested by TSAI, CHO (1976) for biological material with $Z < 16$ and $\rho < 2000\ \text{kg/m}^3$ at $E < 150\,\text{keV}$. However, he bases electron fraction determination on elemental composition of prevalent cell-wall constituents and weights $\mu(E)_{\text{mix}}$ volumetrically, where true density is equally assumed with common $\rho_{\text{t}} = 1500\ \text{kg/m}^3$ and typical chemical wood composition complete with mineral content are taken from general literature. Eventually, intermediate values of $\bar{Z}_{\text{eff}}$ for individual cell-wall constituents are lacking. HUSSEIN et al. (1997) present for maple wood ($\rho = 700\ \text{kg/m}^3$, unknown composition) $\bar{Z}_{\text{eff,maple}} = 6.66$ amongst other comparison materials for their investigations toward detection of narcotics. More recently and specifically, SARITHA, NAGESWARA RAO (2012) investigate the Z dependence of photon radiation interaction with soft- and hardwood samples from several Indian species. Their impression of less focus on Z related studies on wood appears true to reality compared to other materials. However, based on determined elemental composition, they compute $\bar{Z}_{\text{eff}} = 6.9 \ldots 8.0$ via eq. (II-24) with $m = 3.54$ at $E = 59.5\,\text{keV}$. The exponent is fitted from measuring results determined by transmission experiments aiming at $\mu/\rho\,(E)_{\text{mix}}$ in comparison to computed values from tabulated data. Particular studies on mangrove wood (*Rhizophora*

spp.) emerge in the early 1990s. BANJADE et al. (2001) evaluate hardwood[15] ($\rho = 1040\ \text{kg/m}^3$, BRADLEY et al. (1991)) regarding its applicability as water-equivalent phantom at high radiation energies (MeV). Computed via eq. (II-24) with $m = 3.5$ they present $\bar{Z}_{\text{eff,mangrove}} = 7.09$. On low-energy level, however, MARASHDEH et al. (2015) likewise conclude mangrove wood to potentially serve as a solid water- or tissue-equivalent phantom for photon dosimetry. Beyond solid wood, they preferably apply binderless particleboard (PB) owing to its homogeneity and further advantageous properties reported by MARASHDEH et al. (2011). $Z_{\text{eff}}(E)$ is theoretically determined via σ-based method with $\mu/\rho\,(E)$ from simulation (MCNP) over $E = 10 \ldots 60\,\text{keV}$ with fractional abundance of constituent elements omitting $\omega(\text{H})$ provided by MARASHDEH et al. (2011) and in comparison to poor data for mangrove raw wood utilised by BANJADE et al. (2001). Consequently, results reveal considerably differing $Z_{\text{eff}}(E)$ with increasing energy between the sample types due to divergent elemental compositions. On the contrary, they match the results of BANJADE et al. (2001) at E_{min}, where all samples settle around $Z_{\text{eff}}(10\,\text{keV}) \approx 7.25$. Beyond that, results are discussed in comparison to breast tissue and water, where remarkable discrepancies are observable with increasing energy again. Regardless of their conclusions toward inadequate water and tissue equivalence of mangrove PB whereas raw wood is apparently rather close to water and breast, the $Z_{\text{eff}}(E)$ results for mangrove PB obtained by MARASHDEH et al. (2015) are obviously invalid. This insufficiency is clearly caused by the poor data basis with elemental composition lacking H. Moreover, wood matter – regardless of species – with certain MC as well as in oven-dry condition comprising no H is fundamentally non-existent. However, these implications were proven by recalculation via Auto-Z_{eff} software and doubtless found valid.

---

[15] From an internal master thesis, they report a questionable elemental composition with $\omega(\text{H}) = 5.43\ \%$, $\omega(\text{C}) = 40.16\ \%$, $\omega(\text{N}) = 0.03\ \%$, and $\omega(\text{O}) = 54.38\ \%$ for mangrove.

2.2.5   Concluding remarks

Obviously, Z_{eff} conduces as a vivid measure to compare X-ray attenuation potential of different compound substances and the effect of varying mixtures. Nevertheless, individual approaches reveal particular limitations (e. g. Z and E range) and yield partly poor accuracy, which, however, depends on purpose of application. Moreover, Auto-Z_{eff} software by Taylor et al. (2012) claims to surpass the simplistic power law method, where, accordingly and obvious from Table II-2, the latter yields systematic overestimation of Z_{eff}. Likewise pointed out by Phelps et al. (1975), energy-independent $\bar{Z}_{\text{eff}}$, which merely considers photoelectric absorption, receives growing distortion with increasing radiation energy due to increment presence of Z-independent Compton scattering, which, in turn, is inherently included in tabulated $\mu/\rho\,(E)$. Hence, σ-based $Z_{\text{eff}}(E)$ or direct $\mu/\rho\,(E)_{\text{mix}}$ determination appear as rather promising regarding particular quantification of radiation attenuation with explicit energy consideration. To this end, tabulated data of energy-dependent elemental mass attenuation coefficients is available elsewhere (cf. Hubbell, Seltzer (2004)) or Auto-Z_{eff} software enables convenient computation. On the contrary, $\bar{Z}_{\text{eff}}$ determination following eq. (II-24) is capable of rapid estimation with little preconditions. Notwithstanding the above, valid knowledge of the elemental composition of investigated composite material applies as fundamental requirement for all approaches to estimate and compare attenuation potential. In this regard, elemental mass fractions $\omega(i)$ may originate from both

- theoretical or tabulated data basis in case of well-known compounds (e. g. H_2O) or predefined mixtures (e. g. tissue-equivalent phantom), respectively, or from
- actual elemental analyses to be performed in case of complex compound mixtures (e. g. WBCs).

Beyond that and quasi reverse to σ-based method, knowledge of Z_{eff} facilitates computation of the mean mass attenuation coefficient of investigated compounds or mixtures via cross-sections for photon interaction (refer to II–2.1, eq. (II-12) for total attenuation and, e. g.,

eq. (II-20) considering incoherent scattering). Therefor, e. g., Jackson, Hawkes (1981) provide a parametrisation expression for total atomic cross-section $\sigma_{a,\text{tot}}$ based on fundamental theory for X-ray attenuation coefficients explicitly considering all photon interaction mechanisms in a medically relevant energy range, i. e., taking photoelectric absorption as well as coherent and incoherent scattering cross-sections into account. However, omitting this indirection, the theoretical total mass attenuation coefficient $\mu/\rho\,(E)_{\text{mix}}$ of compounds and mixtures under investigation is to be approximated directly via common mixture rule as fundamentally pointed out in Chapter II–2.3.

2.3   Radiation attenuation in compounds and mixtures

2.3.1   General approach

Material beyond pure substances, which consist of more than one chemical element, can be described by an effective atomic number Z_{eff} of the considered compound or mixture, where reference is made to Chapter II–2.2. Here, total radiation attenuation following eq. (II-14) comprises individual attenuation potential of all constituents expressed by the energy-dependent mass attenuation coefficient $\mu/\rho\,(E)_i$ of each chemical element i corresponding to its atomic number Z. Single $\mu/\rho\,(E)_i$ take in particular energy dependency into account and may, in turn, considerably differ within the compound. Notwithstanding actual radiation-matter interaction occurs on atomic level, there is no distinction between the members in terms of the scale of conventional transmission measuring applications, thus, the processes are additive along the beam path. Hence, total radiation attenuation in compounds and mixtures can be understood as sum of attenuation processes from radiation-matter interaction of all constituents according to their fractional abundance, as widely known. The context presumes no local agglomeration of single constituents with respect to investigation geometry, i. e., size of structural inhomogeneities in comparison to spatial resolution. Accordingly, the approach primarily applies to mixtures which are

more or less homogeneous on the corresponding level of consideration for transmission and interaction of penetrating radiation along the beam path. However, already WALTER (1929) performed first computations of a total mean mass attenuation coefficient (comprising real absorption and scattering) for chemical compounds based on own derivations of $\mu/\rho\,(E)$ for particular elements as aforementioned and the known mass fractions of the few elements.

2.3.2   The mixture rule

The approach implies the additivity of attenuation processes and was already applied by PARTHASARADHI (1968) and elsewhere. Beyond their comprehensive study on Z_{eff} as well as single-mechanism attenuation determination, JACKSON, HAWKES (1981) provide a comprehensive report on the mixture rule. Accordingly, MCCULLOUGH (1975) points out that a total mean mass attenuation coefficient $\mu/\rho\,(E)_{\mathrm{mix}}\;[\mathrm{m^2/kg}]$ "[…] can be approximately evaluated […]" via

$$\frac{\mu}{\rho}(E)_{\mathrm{mix}} = \sum_{i=1}^{k} \omega(i) \cdot \frac{\mu}{\rho}(E)_i \qquad \text{(II-31)}$$

as sum of all present single mass attenuation coefficients $\mu/\rho\,(E)_i$ of all respective k elements weighted by the elemental mass fractions

$$\omega(i) = \frac{m_i}{m_{\mathrm{mix}}} \qquad \text{(II-32)}$$

in the compound or mixture such that $\sum_k \omega(i) = 1$. Thus, the contribution of each single element of the compound or mixture to total radiation attenuation corresponds to its respective mass fraction within the substance multiplied by its individual mass attenuation coefficient. Analogously to attenuation fraction $\xi(i)$ in eq. (II-15), let

$$\eta(i) = \frac{\omega(i) \cdot \dfrac{\mu}{\rho}(E)_i}{\dfrac{\mu}{\rho}(E)_{\mathrm{mix}}} \qquad \text{(II-33)}$$

be the mass-fraction-weighted contribution $\eta(i)\;[-]$ of the ith single member to total mass attenuation such that $\sum_k \eta(i) = 1$. Here, high-attenuating constituents of low concentration may have a crucial impact on the total mass attenuation of the considered material, such as high-Z

minerals in organic matter even though their mass fraction $\omega(i)$ is low. Eventually, the mixture rule serves as basis for energy-related Z_{eff} computation as already introduced in Chapter II–2.2.3 and, e. g., applied by PARTHASARADHI (1968).

An extension of eq. (II-31) further enables taking polychromatic radiation into account. For any requested energy range $E_{\mathrm{min}} \dots E_{\mathrm{max}}$ considering presumed or determined radiation spectra $S(E)$, the spectral-weighted total mean mass attenuation coefficient $\mu/\rho\,\big(S(E)\big)_{\mathrm{mix}}\;[\mathrm{m^2/kg}]$ of the compound or mixture is evaluated analogously to eq. (II-16) and eq. (II-17), respectively, via

$$\frac{\mu}{\rho}\big(S(E)\big)_{\mathrm{mix}} = \int_{E_{\mathrm{min}}}^{E_{\mathrm{max}}} \left(\sum_{i=1}^{k} \omega(i) \cdot \frac{\mu}{\rho}(E)_i \right) \cdot S(E)\,dE$$

$$\text{(II-34)}$$

for continuous and

$$\frac{\mu}{\rho}\big(S(E)\big)_{\mathrm{mix}} = \sum_{j=0}^{n} \left(\sum_{i=1}^{k} \omega(i) \cdot \frac{\mu}{\rho}(E_j)_i \right) \cdot S(E_j)$$

$$\text{(II-35)}$$

for discrete spectra with both $S(E)$ normalised to unity such that $\int_E S(E)\,dE = 1$ and $\sum_n S(E_j) = 1$, respectively. Therefore, this enhanced $\mu/\rho\,\big(S(E)\big)_{\mathrm{mix}}$ computation facilitates consideration of both actual radiation energy spectrum and related interaction processes individually corresponding to the investigated elemental mixture. Hence, spectral-weighted total mean mass attenuation coefficient determination via eq. (II-34) and eq. (II-35), respectively, is supposed to yield more appropriate estimation compared to simple application of eq. (II-31) employing $\mu/\rho\,(\bar{E})_i$ for $\bar{E}$ from eq. (II-3) and eq. (II-4), respectively, since the latter by means of $\bar{E}$ not explicitly takes individual attenuation characteristic along the energy range of every element present into account.

For solution of either of the above mixture rule equations, tabulated $\mu/\rho\,(E)_i$ (cf. HUBBELL, SELTZER (2004)) are commonly utilised. Since theoretical data considers isolated atoms, the applicability of these values for $\mu/\rho\,(E)_{\mathrm{mix}}$ computations has to be discussed. Limitations of the mixture rule eq. (II-31) are, e. g., pointed out by

McCullough (1975). Accordingly, it ignores changes in molecular, chemical, or crystalline environment of the considered atoms, hence, their chemical bindings, electron structure, and state of aggregation. In the energy range $E > 10\,\mathrm{keV}$, however, McCullough (1975) estimates errors of less than a few percent. At this, Deslattes (1969) provides a comprehensive discussion on hitherto knowledge of mixture rule validity. Jackson (1982) additionally points out that its validity range is not well-established. All authors found considerable errors to be expected for energies close to (below) absorption edges of the respective constituents. Differently with energies far above the very same, where, e. g., low-Z compounds and mixtures like organic matter without trace elements are considered not be affected in terms of common X-ray applications. Moreover, potential light metal elements within an organic mixture such as aluminium $_{13}\mathrm{Al}$ or calcium $_{20}\mathrm{Ca}$ with their K-edge at $E = 1.56\,\mathrm{keV}$ and $E = 4.04\,\mathrm{keV}$, respectively, (cf. Hubbell, Seltzer (2004)) are not supposed to cause considerable bias of $\mu/\rho\,(E)_{\mathrm{mix}}$ from absorption edge effects with respect to transmission measurements at $E \gtrsim 10\,\mathrm{keV}$. Notwithstanding that, validity of the mixture rule was evaluated in several studies, where its results were both,

-   verified, e. g., by Murty (2004) for particular alloys at medium ($E = 22.1\,\mathrm{keV}$) and high ($E = 59.5\,\mathrm{keV}$) energy level and
-   found invalid, e. g., by Turgut et al. (2002) for various compounds at low energy levels ($E = 4.51 \dots 11.21\,\mathrm{keV}$).

The latter summarise that mixture rule breaks down for radiation energy ranging approximately 0.1 keV below and 1.5 keV above the K-edge of at least one element in the compound or mixture. Likewise, Kerur et al. (1993) found both good agreement within 1 % and deviations of about 11 % between computed and measured $\mu/\rho\,(E)_{\mathrm{mix}}$ depending on the chemical environment of the investigated compounds and the presence of absorption edges near the applied radiation energy. Moreover, discussion of mixture rule validity is still part of recent research, such as Akça, Erzeneoğlu (2014), in terms of

μ/ρ measurements particularly in biomedical science.

The impact of chemical structure is always named but rarely clarified using particular examples in literature. However, Jackson (1982) points out validity of the mixture rule in cases, where there are only negligible effects of molecular binding and chemical or crystalline environment on the atomic wave function, in other words, the electron structure. She reviews an example, where a shift of K-edge position in iron $_{26}\mathrm{Fe}$ is found in consequence of changed oxidation state of the atoms. Barrett, Swindell (1996) confirm the approach of eq. (II-31) to be applicable in cases, where chemical binding energies are small compared to applied X-ray energies. Consequently, chemical compounds may be treated as elemental mixtures. Beyond that, more detailed derivation of the approach and comprehensive restrictions regarding its validity can be found elsewhere. Eventually, mixture rule is found to be widely applied – partly in comparison to transmission measurements – on studies regarding chemical composition dependency of mass attenuation coefficient of, e. g.,

-   HCO-materials (cf. El-Kateb, Abdul-Hamid (1991), Singh et al. (1993)),
-   soil (cf. Coppola, Reiniger (1974)),
-   building materials (cf. Singh et al. (2004)),
-   and common compounds (cf. Singh et al. (1996)),
-   or even air (cf. Veigele (1970)).

2.3.3   Wood-related applications

Wood and consequently WBCs are likewise no single-elemental material. Therefore, theoretical evaluation of the composition impact on radiation attenuation is part of hitherto studies, where computation results are partly compared to practical transmission measurements. However, in contrast to manifold practice-oriented X-ray applications in wood science and industry, such fundamental research is rather underrepresented and partly yields questionable conclusions. Table II-3 compiles selected $\mu/\rho\,(E)_{\mathrm{mix}}$ from literature available for $E = 60\,\mathrm{keV}$ (incl. $E = 59.5\,\mathrm{keV}$ corresponding to $^{241}\mathrm{Am}$). As far as

source	$\mu/\rho\,(E)_{\mathrm{mix}}\,[\mathrm{m^2/kg}]$		
	wood	resins	water
OLSON, ARGANBRIGHT (1981)	0.0192 0.0193		
KOURIS et al. (1981)	0.0193 0.0201 0.0196		
LAUFENBERG (1986)*	0.0183	0.0181 0.0182 0.0178	0.0196
SALINAS et al. (2006)	0.0189		
SARITHA, NAGESWARA RAO (2013)	0.0195 ... 0.0209		
HUBBELL, SELTZER (2004)			0.0206
XCOM (2010)	0.0191		0.0206

Table II-3: Computed mass attenuation coefficients $\mu/\rho\,(E)_{\mathrm{mix}}$ of wood (oven-dry as far as specified), adhesive resin, and water via mixture rule eq. (II-31) for $E = 60\,\mathrm{keV}$ (* and $E = 59.5\,\mathrm{keV}$ corresponding to ^{241}Am) as compilation of reported values from selected hitherto literature and computation by means of XCOM (2010).

known, the values were individually computed via mixture rule eq. (II-31) by means of actual analysis data or assumed elemental compositions. Compilation is completed with computation results via XCOM (2010) at $E = 60\,\mathrm{keV}$ of commonly generalised wood composition (refer to Table IV-14) and water (H_2O). WBC and adhesive resin values are rare. At this, wood values obviously reveal a concurrent order but, however, range within $\mu/\rho\,(E)_{\mathrm{wood}} = 0.0183\,...$ $0.0209\,\mathrm{m^2/kg}$ ($\pm\,6.6\,\%$) supposedly depending on both underlying elemental composition and applied $\mu/\rho\,(E)_i$ of the single constituents.

Already OLSON, ARGANBRIGHT (1981) computationally predict mass attenuation coefficients of various wood species and found certain variations for radiation with $E < 40\,\mathrm{keV}$, whereas $\mu/\rho\,(E)_{\mathrm{mix}}$ is considered as equal above this energy level. Calculations for $E = 10\,...\,1500\,\mathrm{keV}$ via eq. (II-31) are based on elemental compositions from several sources partly including ash content where the latter is found to have increasing impact on attenuation coefficient with increasing ash content at decreasing radiation energies. They compare theoretical estimation to experimental data acquired by means of monoenergetic radioisotopes revealing differences ranging <10 %, where measured $\mu/\rho\,(E)$ fall consistently below computation owing to beam geometry and scattering impact. OLSON, ARGANBRIGHT (1981), however, conclude theoretical estimation via mixture rule to be a suitable alternative to elaborate measurements. Likewise KOURIS et al. (1981) perform $\mu/\rho\,(E)_{\mathrm{mix}}$ calculations to evaluate the influence of trace element abundance on densitometry and found measurable attenuation changes despite negligible effects on gravimetric raw density. Moreover, in terms of development of a fast RDP determination method, LAUFENBERG (1986) investigate the influence of adhesive and moisture content on radiation attenuation by WBCs. Prediction of $\mu/\rho\,(E)_{\mathrm{mix}}$ at $E = 59.5\,\mathrm{keV}$ corresponding to employed ^{241}Am radiation source and based on elemental composition (with appropriate values but no particular sources named) yields similar values of wood and resin but significant differences between wood and water μ/ρ. He estimates the potential error by application of wood $\mu/\rho\,(E)_{\mathrm{mix}}$ values excluding adhesive resin of common content as negligible for measurements on WBCs. On the contrary, $MC = 12\,\%$ causes about 1 % error related to dry wood $\mu/\rho\,(E)_{\mathrm{mix}}$ application. LAUFENBERG (1986) concludes, however, that there is no significant impact on radiometric RDP determination from variations of resin content, wood species, and ambient moisture conditions within normal ranges. In their theoretical study, LIU et al. (1988) consider wood to be a polyatomic absorber, where, in the case of homogeneous density distribution, the linear attenuation coefficients are consequently additive. Following the definition of μ/ρ of eq. (II-9) they likewise deduce mass-fraction-weighted $\mu/\rho\,(E)_{\mathrm{mix}}$ according to eq. (II-31) for polyatomic mixtures. Considering heterogeneous material, they moreover propose taking both local density $\rho(x;y;z)_j$ and corresponding local mass-fraction $\omega(x;y;z)_j$ of each jth constituent into account, where integration along the beam path finally yields the related $\mu/\rho\,(E)_{\mathrm{mix}}$. Also LINDGREN (1991) computes linear attenuation coefficients and subsequent CT-numbers of

compounds consisting of different materials following the approach of WILSON (1980) for quantitative computed tomography (CT) as specialised technique at that time. As already pointed out in Chapter II–2.2.4, the prediction of LINDGREN (1991) under application of general wood compositions considering prevalent cell-wall constituents (cellulose, hemicellulose, and lignin) complete with mineral content, utilises tabulated data omitting own analyses and takes further assumptions into account such as density of all constituents equals $\rho = 1500 \text{ kg/m}^3$. Calculations yield total μ_{lin} and subsequent CT-numbers for $\bar{E} = 73 \text{ keV}$ at $U_{\text{a,nom}} = 120 \text{ kVp}$ tube potential for dry wood as well as wood containing water with $MC = 6 \dots 117 \%$ range. Finally calculated CT-numbers are employed as calibration for wood raw density measurement by means of a medical CT scanner, where LINDGREN (1991) claims to obtain an accuracy of $\pm 4 \text{ kg/m}^3$ for dry wood and $\pm 13.4 \text{ kg/m}^3$ for wood containing water. In agreement with the theoretically computed results from LINDGREN (1991), MACEDO et al. (2002) found $\mu/\rho\,(E)$ independent from wood species in terms of their attenuation measurements at $E = 28.3 \text{ keV}$ and $E = 59.5 \text{ keV}$ (and $E = 662.0 \text{ keV}$) and further point out the influence of chemical composition on μ_{lin} even at constant raw density. Ash content, in turn, is considered by BROWN et al. (1974) to be negligible with respect to chosen radiation energy, where they already estimate $\mu/\rho\,(E)_{\text{mix}}$ with calculations corresponding to high energy levels such as $E = 662.0 \text{ keV}$ emitted from ^{137}Cs. However, mixture rule is applied also in further more recent studies to compute $\mu/\rho\,(E)_{mix}$ of wood species in comparison to measurements mostly by means of monoenergetic radiation such as SARITHA, NAGESWARA RAO (2013) at $E = 59.5 \text{ keV}$ with estimations via XCOM (2010) based on elemental analyses with, nevertheless, questionable results.

Beyond first investigations from LAUFENBERG (1986) on influence of MC and adhesive resin on radiation attenuation following OLSON, ARGANBRIGHT (1981), there is a lack of fundamental studies related to WBCs. Two decades later, HILBERS (2006) applies the approaches in an industrial context on WBCs with practice-oriented but obviously inconsistent investigations. Omitting own elemental analyses on particular material, composition of WBC constituents (wood, adhesive resin, additives, and water) based on respective assumptions and single sources is utilised. Varied resin content and type are applied for lab-made panels and correspondingly computed $\mu/\rho\,(E)_{\text{mix}}$ in comparison to X-ray measuring results at assumed $\bar{E} = 30 \text{ keV}$. For both computation and measurement, HILBERS (2006) concludes apparent differences between μ/ρ of UF- and PMDI-bonded MDF whereas various paraffin, melamine, and water content has a minor effect on total attenuation. Further investigations on WBCs are performed by MARASHDEH et al. (2012) and TOUSI et al. (2014) but within a totally different field of application, i. e., biomedical science.

2.3.4   Concluding remarks

Obviously, $\mu/\rho\,(E)_{\text{mix}}$ computed based on known elemental mass fractions serves as a clear means of quantifying radiation attenuation within a compound or mixture. There is exclusively one fundamental approach following eq. (II-31). In addition, the mixture rule can be extended considering presumed or determined radiation spectra $S(E)$ by eq. (II-34) and eq. (II-35), respectively. Hence, the quality of results is not effected by the method itself (like Z_{eff} determination, refer to Chapter II–2.2.5) but can only be as accurate as the validity of the utilised elemental composition for the material under investigation. The same applies to the considered radiation energy regarding both single-valued mean energy $\bar{E}$ or as a spectrum $S(E)$ and the correspondingly utilised single values $\mu/\rho\,(E)_i$ of the involved constituents. Here, XCOM (2010) and HUBBELL, SELTZER (2004), respectively, appear as a commonly used data basis for mass attenuation coefficients and interaction cross-sections of elements, compounds, and mixtures. Contrary to the simplistic power law method following eq. (II-24) for Z_{eff} computation, which is error-prone in case of predominant Compton interactions on corresponding energy levels, mass-fraction-weighted $\mu/\rho\,(E)_{\text{mix}}$ comprises all

present attenuation mechanisms on the energy level under investigation, which are inherently included in tabulated $\mu/\rho\,(E_i)$. Moreover, XCOM (2010) facilitates particular attenuation considerations related to single interaction mechanisms since the database provides respective values for photoelectric absorption and coherent as well as incoherent scattering.

Like Z_{eff} determination (Chapter II–2.2.5), $\mu/\rho\,(E)_{\mathrm{mix}}$ computation is, nevertheless, just a theoretical evaluation considering as many as known material, radiation, and setup conditions. Thus, potential discrepancies between computations and measurements may occur, where hitherto investigations reveal different findings depending on both validity of applied elemental mass fractions and quality of measuring conditions, i. e., how the setups meet monoenergetic narrow-beam requirements. To conclude limitations beyond practical insufficiencies, JACKSON (1982) found the mixture rule "[…] valid if molecular and chemical effects are negligible." Moreover, several investigations facilitate to imply that absence of medium- to high-Z elements of considerable mass fraction with absorption edges within the applied energy range of the X-ray spectrum enable the mixture rule not to break down. However, JACKSON (1982) generally concludes validity of the mixture rule as "[…] very uncertain in the soft X-ray region […]" whereas a particular energy range is not defined. In contrast to scientific attenuation studies employing monoenergetic radiation, practical X-ray applications with polychromatic spectra $S(E)$, which may cover several critical energies, are more error-prone. Notwithstanding the above, beyond low-energy range, i. e. $E > 15\,\mathrm{keV}$, only small errors of less than a few percent are to be expected (cf. McCULLOUGH (1975)). The mixture rule is henceforth applied for WBC considerations without respect to chemical state of the considered compound or mixture, which is too complex to be evaluated and explicitly considered in this thesis.

2.4 Attenuation of polychromatic radiation

2.4.1 General background

Owing to the energy dependence of radiation attenuation, i. e., increasing attenuation with decreasing energy (refer to Figure II-3), transmission and associated attenuation of polychromatic radiation such as X-rays with a more or less wide energy spectrum (refer to Figure II-2) yields particular effects, which have to be considered in terms of transmission measurements. In consequence of radiation transmission through any matter, the initially emitted spectrum of bremsstrahlung (potentially superimposed by characteristic lines), undergoes variation in continuous energy distribution such that the low-energy share of the transmitted spectrum typically decreases. Therefore, an upward energy shift with increasing mean energy can be observed, whereas maximum energy (peak energy) remains constant such that $E_{\mathrm{max}} = U_{\mathrm{a}}\,[\mathrm{kVp}]$. The effect is well-known as beam hardening, since high radiation energy is commonly referred to as hard due to penetration potential (in contrast to soft low-energy radiation).

However, in the field of radiological technique, DIN 6814-2 (2000) defines hardening as variation of the spectral particle fluence rate while heterogeneous X-rays propagate through a material layer by diminution of relative photon share to which a higher linear attenuation coefficient applies. With regard to CT in NDT, DIN EN 16016-1 (2011) and likewise ISO 15708-1 (2017) define the term beam or spectrum hardening as "spectral change of a polychromatic beam caused by preferential attenuation of lower energy photons". Moreover, DIN EN 16016-3 (2012) and likewise ISO 15708-3 (2017) refine the definition of this effect and point out consequent artefacts, which may occur in the reconstructed image. VDI/VDE 2630-1.1 (2016) definition focusses on shift of energy distribution and therefore the median of the spectrum up to higher energies. Beyond definitions in standards and guidelines from both medical as well as technical field considering beam hardening, reference is made to respective fundamental literature such as

- HALMSHAW (1995),
- BARRETT, SWINDELL (1996),
- HUSSEIN (2003a),
- ATTIX (2004),
- HERTRICH (2005),
- KRIEGER (2012), as well as
- SCHIEBOLD (2015)

for comprehensive, detailed, and practice-oriented explanations of the phenomenon. Eventually, beam hardening unavoidably occurs in terms of transmission measurements by means of polychromatic radiation such as X-rays. Note, already varying distances between X-ray source and investigated specimen s_{X-S} as well as between specimen and detector surface s_{S-D}, i. e., respective air layer thickness (for attenuation coefficients refer to VEIGELE (1970)), may influence applied X-ray spectra as pointed out by ANKERHOLD et al. (1999), where long distances have to be considered to cause slight beam hardening.

As fundamental consequence of upward energy shift, it is well-known that mass attenuation coefficient decreases with energy increment due to its energy-dependency (refer to Figure II-3). Beam hardening, in turn, increases with increasing attenuation potential of the absorber, i. e., its thickness at its simplest. Coincidently, mass attenuation coefficient further decreases along the beam path, which is basically, however, expected to be constant for the material under consideration. Generally, decreasing attenuation coefficients along a certain measuring range are to be found in several studies and consequently attributed to the beam hardening effect. Accordingly, KOTWALIWALE et al. (2007) report in a simple study on the effect with respect to their calibration of a digital X-ray imaging system ($E_{max} = 50\,kVp$) for biological material and conclude that attenuation coefficient decreases with increasing thickness of homogeneous layers of polystyrene. Likewise KOTWALIWALE et al. (2006) found attenuation coefficients of pecan nut and shell to vary with sample thickness. Already TSAI, CHO (1976) evaluate the effective linear attenuation coefficient $\tilde{\mu}_{lin}$ from X-ray transmission measurements of different materials, where they likewise consider an effective energy $\tilde{E}$, which is found to

differ between the materials despite equal transmission distances. Consequently, they compute the error of $\tilde{\mu}_{lin}$ resulting from variable beam hardening between the considered material and water as reference via the simple difference of the material's $\tilde{\mu}_{lin}$ at the very same effective energy $\tilde{E}$ toward $\tilde{\mu}_{lin}$ at water $\tilde{E}$. Eventually, it is concluded and verified via measurements on PMMA in comparison to water as reference that the error is a strong function of both energy level and spectrum.

With respect to quantitative X-ray transmission measurements in hitherto research applications, variation of the attenuation coefficient in dependence of the object under investigation is the most significant consequence of beam hardening. In this regard, the divergence from initially linear slope of radiation transmission is commonly pointed out. As presented in Figure II-6, KASPERL (2005) illustrates the difference between linear slope of transmission values from a monoenergetic source through an aluminium step wedge in contrast to the concave plot measured by means of a polyenergetic source. Obviously, the linear context

$$\ln(T^{-1}) = \ln\left(\frac{I_0}{I_T}\right) = \mu_{lin}(E) \cdot t \qquad (II\text{-}36)$$

deduced from exponential law of attenuation eq. (II-8) with the linear attenuation coefficient $\mu_{lin}(E)$ as proportionality factor along increasing layer thickness t (of homogeneous absorber material) fails owing to energy dependency of
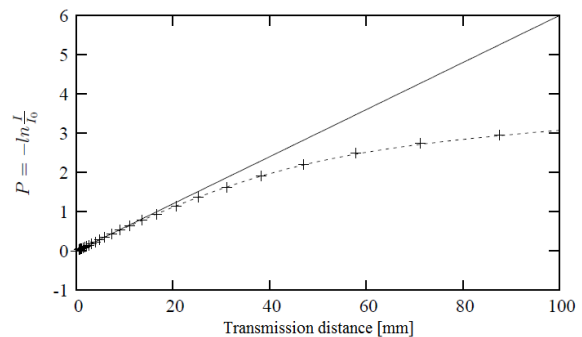
Figure II-6: Non-linear slope of X-ray projection data P (+ with dashed line) measured by means of an aluminium step wedge at $U_a = 224\,kVp$ compared to ideal expectation (solid line) as basis for CT beam hardening correction via linearisation method, acc. to KASPERL (2005).

$\mu_{\mathrm{lin}}(E)$. The same applies to mass attenuation coefficient $\mu/\rho\,(E)$ (refer to eq. (II-9)). Beyond beam hardening, further reasons for potential non-linearities in transmission measurements come in addition such as scattering superimposition and detector non-linearity, which can, however, hardly be distinguished and will be discussed elsewhere. Eventually, DAVIDSON et al. (2003) consider beam hardening to cause insufficiencies regarding flat field correction (i. e., I_0 determination) with respect to detector type and gain settings, which, in turn, could cause artefacts in medical imaging. Their experimental results yield different detector gain settings in dependence of PMMA object transmission distance. Nevertheless, their theoretical approach with changes in energy distribution from acquired initial I_0 toward transmitted I_{T} intensity, where the latter may further vary within the object, is comparable to aforementioned bias of linear context referring to eq. (II-36). For attenuation coefficient applications in quantitative X-ray measuring practice, such as densitometry or also CT, beam hardening can be concluded to cause local or global deviations from expected true values in dependence of structure and homogeneity of the measuring object, e. g., distinctness of the investigated density gradient as well as the applied reference objects.

Beyond attenuation considerations within the specimens, beam hardening already affects commonly applied initial spectra from X-ray tubes due to inherent filtering of the components as exemplarily illustrated in Figure II-7 following well-known representations (cf. HERTRICH (2004)) by means of particular spectra simulations via XRayTools (refer to Chapter IV–4.2.6.2). Note, similar spectral distributions, however, at higher energy levels are presented by TILLACK, BELLON (2000), who discuss a model, which describes the generation of bremsstrahlung. Obviously, the $0.2\,\mathrm{mm}$ beryllium (Be) window truncates more or less total energy fraction $E < 2\,\mathrm{keV}$ (refer to 'at tube' plot in Figure II-7). Moreover, initial radiation emission within the vacuum tube ('at target' plot in Figure II-7) is, in turn, affected by inherent radiation absorption within the W target. At this, the absorption edges
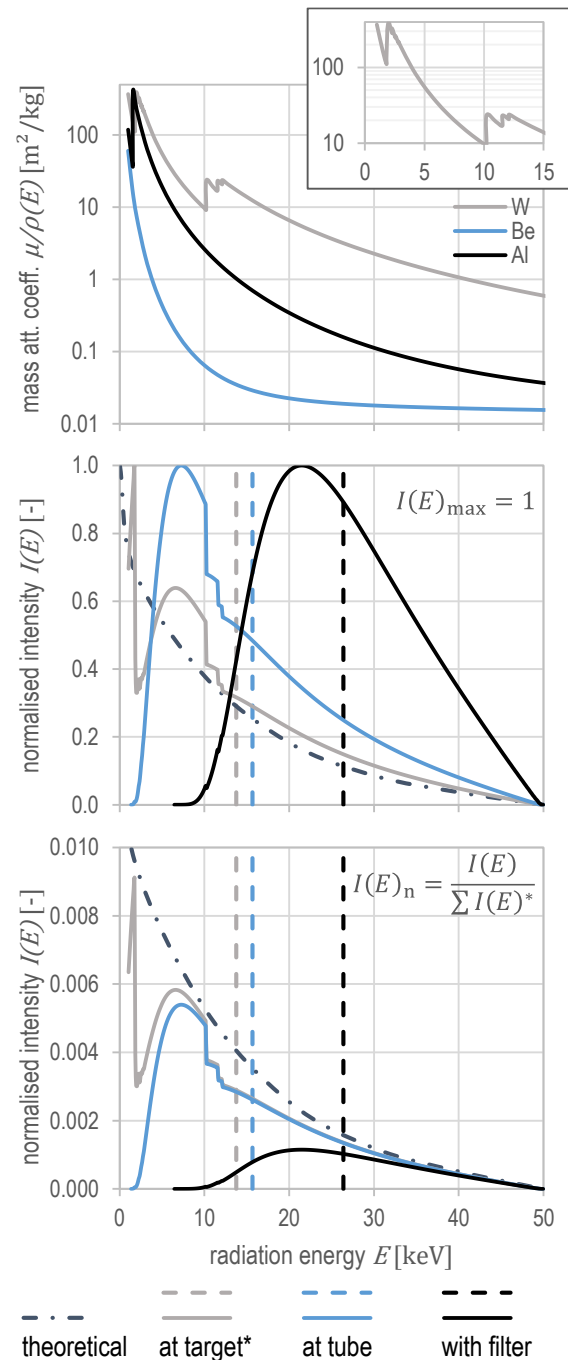
Figure II-7: Comparison of theoretical X-ray spectra (conventional W-target tube at $U_{\mathrm{a}} = E_{\mathrm{max}} = 50\ \mathrm{kVp}$) with simulated bremsstrahlung excluding characteristic lines (via XRayTools, Chapter IV–4.2.6.2) considering initial emission (at target), inherent filtering of $0.2\,\mathrm{mm}$ Be window (at tube), and additional $0.635\,\mathrm{mm}$ Al pre-filter (spectrometer lid Chapter IV–4.2.6.1; with filter) as well as theoretical expectation without any attenuating impact (dash-dotted line), as normalised intensity with $I(E)_{\mathrm{max}} = 1$ (middle) or to I at target (bottom) both incl. mean energies $\bar{E}$ (dashed lines), complete with respective mass attenuation coefficients $\mu/\rho\,(E)$ over radiation energy (top, with inset around W absorption edges) determined via XCOM (2010).

(upper chart with inset in Figure II-7) cause a correspondingly characteristic low-energy distribution, which is, however, continuous but features respective jumps at the absorption edges. Furthermore, TILLACK, BELLON (2000) point out that an increasing target angle leads to longer radiation transmission distance through the target and, therefore, higher inherent absorption. Thus, an increment of the target angle must be considered to yield increasing beam hardening. However, consequent pre-filter application enables rather predefined lower energy limits and yields considerable upward shift of mean energy (dashed lines in Figure II-7 and 'with filter' plot with exemplary 0.635 mm Al layer). Hence, a theoretical distribution of bremsstrahlung (dash-dotted plot) without any attenuation impact can be assumed as continuously increasing slope of the intensity plot from $I(E_{\mathrm{max}}) = 0$ along decreasing energy toward a certain intensity maximum. Already NICKERSON (1958) considered the intensity to be proportional to the number of photons of a particular energy and showed a similar representation. ATTIX (2004) deepens the theoretical background of unfiltered bremsstrahlung energy spectra. He points out, that the shown simple triangular spectra (in Figure II-7, more or less exponential slope assumed) are, however, practically never observed, since characteristic X-rays may superimpose bremsstrahlung depending on the energy range and the inherent filtration of at least the target and tube window removing the low-energy radiation.

2.4.2   Application for pre-filtering

The practical utilisation of the beam hardening effect for X-ray pre-filtering to influence the spectral composition of the applied radiation was already mentioned (refer to Figure II-7 'with filter'). Basically in NDT, X-ray radiography applies radiation filters in the primary beam to obtain sufficient film density gradation (blackening), thus, grey-scale range within total image, in case the objects under investigation have considerable thickness variations (cf. STEGEMANN (1995)). Moreover, SCHIEBOLD (2015) points out to consider potential contrast reduction in consequence of beam hardening.

Per definition according to VDI/VDE 5575-1 (2017), X-ray filters are a defined material layer, "[…] which changes the spectral composition of the transmitted radiation only by absorption". In general and according to DIN EN 1330-11 (2007), filters are devices reducing unwanted radiation. Moreover, ISO 5576 (1997) and likewise DIN EN 1330-3 (1997) refine the definition considering an uniform material layer of usually higher atomic number than specimen matter and particularly purposing soft X-ray absorption. Inherent filtration is, in turn, the very same caused by components of X-ray tube, setup or housing penetrated by the primary beam. Eventually, IEC 60050-881 (1983) considers filtration as "modification of the characteristics of ionizing radiation" and, therefore, defines technical terms, where reference is made to the very same. Accordingly, also compound filters are applicable like the Thoraeus filter, which is composed of predefined layers of Al, Cu, and Sn and provides enhanced radiation transmission yield. However, in the context of X-ray optical systems, the guideline VDI/VDE 5575-9 (2018) exists with focus on X-ray filters. Notwithstanding primary application in analytical X-ray devices (e. g. for diffraction or XRF, cf. ALS-NIELSEN, MCMORROW (2011)), the described basic physical principals, properties, and parameters can be transferred to densitometric applications in industry. Accordingly, an X-ray filter, which normally represents one (or several) homogeneous material layer(s), is quantitatively characterised by its transmission function (here, adapted from wavelength λ to energy E) following eq. (II-1) with energy consideration, thus,

$$T(E) = \frac{I_{\mathrm{T}}(E)}{I_0(E)} \qquad (\text{II-37})$$

which leads with well-known $\mu_{\mathrm{lin}}(E)$ to the exponential attenuation function eq. (II-8). Moreover, it is pointed out that spectral transmittance $T(E)$ increases along increasing energies for one and the same filter but decreases with filter thickness increment, where, e. g., 1 mm Al is considered to more or less totally suppress low-energy fraction $E < 10\,\mathrm{keV}$ of the spectrum. However, pre-filter application diminishes total intensity as integral over the spectrum. Hence, pre-filters are to be optimised via selection of material and thickness

to yield both desired threshold for low-energy suppression and appropriate total radiation intensity. VDI/VDE 5575-9 (2018) finally introduces the factor of relative suppression

$$Q = \frac{T(E_1)}{T(E_2)} \qquad \text{(II-38)}$$

to compare the intensities of particular energies within the spectrum, thus, to evaluate filter efficiency. Eventually, DIN 6814-2 (2000) differentiates filtering regarding the variation of spectral fluence rate distribution, direction distribution or the intensity distribution along beam cross-section via absorption or scattering within a material layer. Therefore, filters are distinguished depending on the pre-dominant effect, i. e., photon absorption, scattering or local attenuation, and regarding the designated application, i. e., hardening, scattering, and attenuating, respectively.

Beyond standard and guideline definitions, pre-filter application is more or less common in technical and medical X-ray devices. Furthermore, special applications exist, where, e. g., RITCHINGS, PULLAN (1979) propose a method for simultaneous dual-energy X-ray scanning. To this end, they cover alternating detector collimator slits by, e. g., 0.5 mm Sn foil at $U_{a,nom} = 120$ kVp and separate the corresponding data from the projections.

However, particularly for medical applications, appropriate suggestions exist in X-ray diagnostics aiming at dose reduction for the patient (cf. HERTRICH (2004) and KRIEGER (2012)) as well as image enhancement, where typical pre-filtering yields energy distributions with $\bar{E} \approx 0.5 \cdot E_{max}$ as a rule of thumb (cf. KRIEGER (2013)). Legally defined filter thicknesses depending on the application are well-known in diagnostic radiology (cf. KAUFFMANN et al. (2006)). Layer thickness pre-definition is commonly given as Al equivalent, which considers individual inherent filtration and further allows filter material variations. Initially defined by the withdrawn standard DIN 6811-1 (1987) and now to be found in DIN EN 60601-1-3 (2014), exemplary minimum values for total layer thickness Al equivalent are available with

-   $t_{Al} = 1.5$ mm for $U_{a,nom} \leq 70$ kVp and
-   $t_{Al} = 2.5$ mm for $U_{a,nom} > 70$ kVp

(both regarding dental radiographs). Furthermore, ANKERHOLD (2000) lists approved pre-filter materials and layer thicknesses to produce the radiation qualities, i. e., X-ray spectra under standard experimental conditions, as specified in DIN 6818-1 (2004), ISO/DIS 4037-1 (2017) or further standards, e. g., considering narrow- and wide-spectrum series. Moreover, ANKERHOLD (2000) measured and evaluated all respective spectra from a W-target tube (for further details reference is made to the very same), lists characteristic data, and additionally provides charts of the energy distributions. According to this, Table II-4 lists an exemplary selection of four radiation qualities (label) complete with the unfiltered spectra on two energy levels regarding nominal tube voltage $U_{a,nom}$ sorted according to increasing mean energy $\bar{E}$ [keV]. Furthermore, the width of the spectra on the respective energy level maintaining E_{max}, however, decreases along the displayed order, which becomes obvious from Figure II-8 likewise illustrating the upward shift of $\bar{E}$ due to beam hardening. Although emitted spectra are attributed to the applied X-ray tube and irradiation conditions, pre-filter definition by means of total filtration in mm Al and Cu provides an appropriate orientation to obtain predefined X-ray properties also for the desired non-medical application. Beyond discussion of Al equivalence, NAGEL (2003) compares the pre-filter effect with respect to different materials and their respective slope of $\mu/\rho\,(E)$, where he points out ideal filter materials in dependence of application and intended effect, which are basically counter-balanced between maximum low-energy suppression and minimum reduction of total intensity, i. e., a kind of high-pass filter. Moreover, high-Z filter materials with an absorption edge in the considered energy range yield certain band-pass characteristics – specifically utilised around characteristic lines – where, e. g. in the field of X-ray diffraction, DIN EN 1330-11 (2007) defines the beta filter as absorber removing most of the K_β line from the applied X-ray spectrum. Further coefficients to quantify radiation quality exist besides eq. (II-38), e. g., as regulations from the American Association of Physicists in Medicine (AAPM). For general basics regarding radiation

$U_{a,nom}$	radiation quality	total filtration]		$\overline{E}$
[kVp]	label[16]	[mm] **Al**	[mm] **Cu**	[keV]
30	unfiltered	–	–	13.9
	H-30, C 30	0.5	–	19.5
	W-30, B 30	2.0	–	22.9
	N-30, A 30	4.0	–	24.6
	L-30	4.0	0.18	26.7
60	unfiltered	–	–	21.2
	H-60, C 60	3.9	–	38.0
	W-60, B 60	4.0	0.3	44.8
	N-60, A 60	4.0	0.6	47.9
55	L-55	4.0	1.2	47.8

Table II-4: Examples for total filtration to produce the radiation qualities specified in DIN 6818-1 (2004) and ISO/DIS 4037-1 (2017) as compiled by ANKERHOLD (2000) with corresponding mean radiation energy $\overline{E}$ from X-ray spectra measuring and evaluation data (W-target tube, 20° anode angle, 1.0 mm Be window, 250 µm Kapton® (polyimide) foil).

qualification, reference is made to KRIEGER (2012) or elsewhere.

Regarding industrial or general technical practice, pre-filter utilisation highly depends on the more various applications mainly aiming at both image enhancement as well as diminution of detection signal bias and consequent artefacts (in CT) due to non-linear attenuation. Regarding radiometry, RÓZSA (1987) describes several industrial applications, however, without explicit pre-filter consideration, since radioisotopes predominated as radiation source, where no beam hardening of the preferably monoenergetic energy distributions can occur. The like applies to the wood industry, where previous systems utilised nuclear sources instead of today's X-ray tubes. However, pre-filter definition is commonly more or less part of the individual setup particularly of analytical X-ray devices and rarely reported on in research. Appropriate suggestions in standards and regulations like for aforementioned medical applications only partly exist for technical radiography in the field of nondestructive
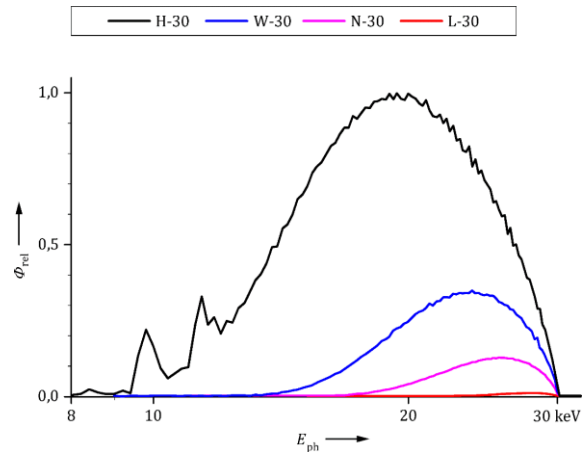
Figure II-8: Exemplary X-ray spectra of four radiation qualities on the 30 kVp energy level (Table II-4) with relative fluence Φ_{rel} [a.u.] (normalized to the air kerma at the same tube current and distance) over photon energy E_{ph}, acc. to ISO/DIS 4037-1 (2017).

testing preferably of metal objects. Particular definitions, however, with respect to low-Z material are lacking. According to DIN 54113-1 (2018), where technical requirements for macro-structural analysis X-ray devices with $U_a \leq 1$ MVp are defined, the radiation source must be equipped with an additional filter of at least 2 mm Al equivalent, however, with respect to technical safety requirements. For quantification purpose of imaging properties in terms of radioscopic testing (NDT), DIN EN 13068-1 (2000) defines, e.g., (7 ± 0.5) mm Al at $U_{a,nom} = 50$ kVp to ensure respective radiation quality. DIN EN ISO 5579 (2014) as the follow-up document to the withdrawn DIN EN 444 (1994) only recommends filters between object and detector to avoid low-energy scattered radiation but describes no particular action with regard to beam hardening prevention. The standard, however, rather applies to high-energy radiographic testing of metal materials. Note, reduction of scatter radiation in front of the detector is referred to as intermediate-filtering by DIN EN 16016-3 (2012) and likewise ISO 15708-3 (2017). For determination of basic spatial resolution, DIN EN ISO 16371-2 (2018), DIN EN ISO 17636-2 (2013), as well as

---

[16] The respective quality label comprises a number for the tube voltage and a letter regarding the respective standard for the radiation quality 'high air-kerma' (H, C), 'wide-spectrum' (W, B), 'narrow-spectrum' (N, A), as well as 'low air-kerma' (L) series. Kerma (acronym for kinetic energy released per unit mass) is a dosimetric measure for the energy transfer from ionising radiation to matter. For detailed definitions, equations, and applications, reference is made to DIN 6814-3 (2016), KRIEGER (2013) or elsewhere.

further standards for radiographic inspection define radiation transmission conditions with, e. g., 1 mm Al pre-filter at $U_{\mathrm{a,nom}} = 90\,\mathrm{kVp}$ for investigation of light alloys. For CT in the field of NDT, DIN EN 16016-2 (2012) and likewise ISO 15708-2 (2017) recommend filtration to reduce low-energy radiation and consequent scattering as well as beam hardening effects, thus, to enable image quality enhancement, e. g., by means of 0.25 mm Cu at $U_{\mathrm{a,nom}} = 90\,\mathrm{kVp}$ to yield a transmission of $T = 0.1$ (eq. (II-1)) through 100 mm of water, 95 mm PMMA or 25 mm Al. Beyond this rough guideline, DIN EN 16016-3 (2012) and likewise ISO 15708-3 (2017) add, that optimal transmission conditions can be obtained by pre-filter application, where the very same have to be considered to diminish radiation intensity. VDI/VDE 2630-1.1 (2016) distinguishes between pre-filter (source filter) and intermediate-filter (detector filter). The guideline series in the field of dimensional measurement via CT, however, provides no particular recommendation for filter material and thickness considering the respective tube voltage and application. Notwithstanding that, VDI/VDE 2630-1.2 (2018) considers energy-related interaction, i. e., beam hardening (and scattering), as one of numerous influence factors with effects on dynamic range and results of measurement such that reconstruction yields wrong material density and biased object geometry unless corrected or influenced by pre-filtering. The latter is, however, pointed out as part of measuring strategy to obtain beam correction favourably by physical beam hardening. In the context of spectra evaluation (E_{max}), DIN EN 12544-3 (1999) provides recommendations for filter thickness and material selection considering tube voltage, e. g., 1 mm Al at $U_{\mathrm{a,nom}} = 20\,\mathrm{kVp}$ or 1 mm Fe at $U_{\mathrm{a,nom}} = 40\,\mathrm{kVp}$, to obtain sufficient low-energy absorption. Beyond standards and guidelines, Halmshaw (1995) points out filtering in the context of radiographic techniques in industrial radiology and likewise distinguishes filters close to the X-ray tube window to produce harder radiation as well as the very same behind specimen to reduce amount of scattered radiation on the film (or detector). Owing to the considered applications on high energy levels, e. g., 0.25 mm Pb at $U_{\mathrm{a,nom}} = 150\,\mathrm{kVp}$ are

recommended. Accordingly, filters generally extend the thickness latitude of the specimen and, however, require longer exposure times. Eventually, Attix (2004) deepens theoretical aspects behind X-ray filtration and beam quality.

In conclusion, pre-filter application in the context of attenuation of polychromatic radiation, equivalent definitions are available in several standards and guidelines. The application is prevalent in both medical and technical X-ray devices whereas the necessity and purpose partly vary. Accordingly, recommendations or actual requirements for pre-filter material as well as layer thickness markedly differ and, nevertheless, highly depend on the respective case of application. Regarding industrial or general technical X-ray systems, appropriate specifications are less noticeable and rather part of individual device design. Particularly for radiographic testing, i. e., X-ray imaging, of metal objects as NDT discipline, pre-filter definition aiming at beam hardening prevention is underrepresented. Eventually, X-ray densitometry on low-Z material such as wood is not explicitly considered at all.

2.4.3   Beam hardening quantification

X-ray spectra and their penetration potential can be characterised by parameters for radiation quality such as tube voltage, effective energy, and filtration following the definition in IEC 60050-881 (1983) as well as by the aforementioned factor of relative suppression Q eq. (II-38) according to VDI/VDE 5575-9 (2018). The quantification of beam hardening, in turn, is often associated with the correction of the very same. Particularly in the field of CT considering both medical and technical applications, beam hardening is a central issue, since it causes different artefacts in image reconstruction. A historically famous example is the "Hounsfield bar" (cf. Brüning et al. (2006)), where after reconstruction without any correction a structure in the human skull is displayed, which, however, does not exist. The cupping effect is a general consequence, where grey values within the CT image of an homogeneous object decrease from surface toward centre according to the definition of DIN EN 16016-1 (2011) and likewise ISO 15708-

1 (2017). Hence, beam hardening correction methods preferably refer to CT applications.

DIN EN 16016-3 (2012) and likewise ISO 15708-3 (2017) point out proper technical possibilities to consider beam hardening artefacts, which, however, have to be corrected in terms of the reconstruction process. A typical correction procedure comprises X-ray measurements on a step wedge of the same material covering a sufficient thickness range. Subsequently, conversion of the transmission data into true thickness values yields correction factors. The method, however, is considered to be invalid in the case of composite samples. From KALENDER (2011) it can be concluded, that beam hardening correction is possible for more or less homogeneous (soft) tissues and elaborate for high-contrast structures like bone in tissue. Beam hardening correction was the subject of numerous hitherto investigations considering both medical and technical applications, where first approaches refer to medical CT (cf. KIJEWSKI, BJÄRNGARD (1978) or HERMAN (1979)) and the technical field is lacking in wood-related studies. However, beam hardening correction by several methods, e. g., via linearisation algorithms or employing a priori knowledge of the energy spectrum, is state of the art in modern CT systems, thus, reference is made to common literature (cf. BARRETT, SWINDELL (1996), ALS-NIELSEN, MCMORROW (2011), KALENDER (2011)). Nevertheless, particular work and respective findings have to be highlighted owing to their relevance for the present thesis. WICKIZER et al. (1976) provide comparison of four hitherto beam hardening models, where intensity of the emerging polychromatic beam is related to absorber thickness. They found already beam hardening to yield inconsistent data if simple exponential attenuation is assumed. TSAI, CHO (1976) analyse and report on the physics of contrast and linear attenuation in medical CT, where they more or less quantify beam hardening via error computation of the effective attenuation coefficient as already pointed out in Chapter II–2.4.1. HERMAN (1979) establishes linearisation method. RUTH, JOSEPH (1997) consider beam hardening and its correction in terms of their X-ray spectra estimation approach from transmission measurements and

find the knowledge of X-ray spectra to be important for correction of beam hardening artefacts as do SIDKY et al. (2005). BAYER (2005), in turn, performs beam hardening correction in terms of the utilised iterative reconstruction algorithm on the basis of X-ray spectra determined via Al and Cu filter curves and further application of fitting parameters for the semi-empirical model described by RUTH, JOSEPH (1997). Although the methods are applied for investigations of water dynamics in porous media, the structure of the latter is not explicitly considered. KASPERL (2005) finds beam hardening artefacts as inherent to the system whereas non-linearity from beam hardening and detector can, however, not be distinguished as already pointed out by BUCK (1996). Furthermore, KASPERL (2005) comprehensively reports on beam hardening occurrence and corrections and consequently develops own algorithms, which are only applicable to homogeneous objects (likewise his scattering correction approaches). However, KRUMM et al. (2010) present an iterative correction method for multi-material objects, where neither knowledge of the initial spectrum nor the material absorption characteristics are required; likewise KRUMM et al. (2008) already did, which is now available as "Iterative Artifact Reduction IAR" from Fraunhofer EZRT (IIS). ZHOU et al. (2009) combine pre-filtering and a linearisation method for beam hardening correction of linear accelerator industrial CT, where they obtain $< 2\,\%$ error in density measurement of several plastics and metals. Note, for the high-energy beam, $5\,mm$ Cu filter at $U_{a,nom} = 9\,MVp$ from linear accelerator are applied yielding a spectrum mainly in the range $E = 0.3 \ldots 3.0\,MeV$. Beyond linearisation, ZHANG et al. (2015) propose an exponential correction model based on projection raw data of CT reconstruction. Again without the requirement of a reference, WÜRFL et al. (2018) perform calibration-free beam hardening correction. Their fully-automatic artefact reduction is based on redundantly measured raw data and concluded as robust to, e. g., scatter and misalignment. CAO et al. (2018) follow dual-energy correction method of ALVAREZ, MACOVSKI (1976) as proposed effective means in industrial CT and evaluate the very same by variation of the applied X-ray spectra.

KERMANI, FEGHHI (2018) take beam hardening correction into account in terms of their scattering quantification. Obviously, beam hardening correction is still part of current research particularly regarding industrial or general technical CT applications. The same applies to the still emerging discipline of micro-CT, where DAVIS, ELLIOTT (2006) point out the role of beam hardening and scatter for the occurrence of artefacts beyond others. In this regard, they also point out the necessity for individual evaluation of the beam hardening effect to find optimal pre-filters for the respective experimental conditions. Regarding scatter, they add for consideration that it may cause overcorrection of beam hardening by means of attenuation measurements on step wedges via linearisation method. Such correction, nevertheless, coincidently includes a certain degree of scatter correction.

Beyond quantification in terms of beam hardening correction and besides factors for pre-filter efficiency, further methods exist to quantify beam hardening considering the respective application and, however, mostly to verify the applied correction algorithm. A formal concept for beam hardening considering mean linear attenuation coefficient decrement along penetration depth is proposed by KLEINSCHMIDT (1999) employing, however, high-energy beams from medical accelerators. Accordingly, a beam hardening coefficient should quantify spectral variations along the beam path in the considered body. Therefore, he defines the negative relative change of mean linear attenuation coefficient $\bar{\mu}_{\mathrm{lin}}(t)$ along penetration depth t as beam hardening coefficient

$$\eta(t) = -\frac{\frac{d\bar{\mu}_{\mathrm{lin}}(t)}{dt}}{\bar{\mu}_{\mathrm{lin}}(t)} \qquad \text{(II-39)}.$$

Moreover, KLEINSCHMIDT (1999) points out the difference to the definition of BJÄRNGARD, SHACKFORD (1994), which takes the integral linear attenuation coefficient into account. Accordingly, beam hardening coefficient η is part of attenuation law eq. (II-8) such that

$$T(t) = \frac{I_{\mathrm{T}}(t)}{I_0} = e^{-\mu \cdot t \cdot (1 - \eta \cdot t)} \qquad \text{(II-40)}$$

where both coefficients are determined from measurements. However, KLEINSCHMIDT (1999) concludes his approach to be likewise applicable to quantify beam hardening in filters or (step) wedges beyond his application in terms of radiation therapy. ALLES, MUDDE (2007) take, in turn, aforementioned concepts into consideration in their analytical study on beam hardening and the effective attenuation coefficient, however, with respect to medical X-ray CT. For the employed polychromatic spectrum, they discuss the concept of a mean attenuation coefficient, which decreases with penetration depth due to beam hardening and propose a model for approximation of the very same, utilising a simple fit of the function $\mu(E)$ over the relevant energy range. An extension of the analytical model, in turn, is found to provide "a rather good description of beam hardening" in dependence of penetration depth, which is exemplarily evaluated for X-ray transmission through water. Note, ALLES, MUDDE (2007) restrict their beam hardening analysis to homogenous media, since general consideration of heterogeneous material is regarded as much more complicated. The effect of beam hardening on CT numbers, which correspond to linear attenuation coefficient, is reviewed by HUDDLESTON (1988). For estimation and empirical correction in terms of bone mineral content measurement IMAMURA, FUJII (1981) introduce the term $e^{-\rho^2 \cdot t} \cdot 10^7$ with the density ρ and X-ray path length or material thickness t as "beam hardening index", which quantifies deviation from actual CT numbers in an uncorrected reconstruction. Another version of beam hardening index is introduced and applied by LIN, SAMEI (2014) to validate their proposed fast poly-energetic iterative filtered backward projection algorithm (piFBP) for CT reconstruction including beam hardening correction. In CT reconstruction, they point out that beam hardening effect causes both visible artefacts (e. g. cupping) and invisible voxel value deviations. By focussing on quantification of voxel accuracy, they consider the computed voxel value as sum of theoretical value plus errors from beam hardening and noise (scattering). Consequently, LIN, SAMEI (2014) define their beam hardening index $BIdx$ as percentage of normalised mean error, which

computes the mean deviation of voxel values from theoretical expectation. ARUNMUTHU et al. (2013) quantify the beam hardening effect and, therefore, applied pre-filtering and correction by linearisation in their simulation study by means of evaluation of the occurring cupping artefacts. To this end, they calculate the percentage of beam hardening via

$$Cupping = \frac{\left(\frac{(a+b)}{2}\right) - m}{m} \cdot 100 \ [\%] \qquad \text{(II-41)}$$

within the considered cylinder cross-section, where a and b are the grey levels from monochromatic radiation transmission and m is the minimum grey level at the cupping region in consequence of attenuation of polychromatic radiation.

To conclude on beam hardening quantification, the methods are often associated with its correction with particular respect to CT applications. Beam hardening correction methods primarily following linearisation approach are part of modern CT systems and reconstruction algorithms. Simple linearisation is elaborate in the case of inhomogeneous material and composite structures. Furthermore, knowledge of the applied X-ray spectra is regarded as advantageous. Quantification methods and respective beam hardening indices beyond correction in CT reconstruction preferably refer to decrement of attenuation coefficient along beam path and consequently non-linear radiation transmission. However, non-linearity from beam hardening and further effects like scattering as well the detector itself must be considered as inherent of the employed X-ray system.

2.4.4   Concluding remarks

Radiation spectra, their variation, and consequent effects must be considered in the context of X-ray transmission measurements. Beam hardening biases any quantitative X-ray application, where physical quantities are determined or displayed based on the material's attenuation coefficients, which are expected as constant but actually vary along the beam path through the specimen due to upward energy shift. Particularly in the fields of both medical and technical

CT, correction of consequent non-linearities of radiation transmission is required likewise SINKA et al. (2004) carry out for their CT measurements of density variation in tablets.

Beyond density measurement via CT, further quantitative investigations exist, where beam hardening is found to be considered but not necessarily corrected by elaborate algorithms. MINCONG et al. (2008) evaluate mass thickness (i. e., area density ρ_A [g/cm^2]) measurement of aluminium by means of X-rays as substitution for gamma radiation. They conclude on their experimental results from transmission measurements by application of 0.2 mm Ni as suitable pre-filter at $U_{a,nom} = 30$ kVp as well as $U_{a,nom} = 45$ kVp to agree well with theoretical data from simulation and point out that a relative error of <1 % can be obtained for a certain mass thickness range of aluminium alloy samples. Beyond their conclusions, both presented plots are, however, found to obviously tend toward non-linearity, i. e., degressive increment of measured attenuation $\ln(I_0/I_T)$ [−], which is supposed to reveal more considerable downward deviation from expected linear slope particularly in the case of 45 kVp plot and beyond the shown attenuation range $0 < \ln(I_0/I_T) \le 1.6$. Moreover, since their theoretical pre-evaluation with transmission data based on simulation reveals appropriate linear fit, the observation must further be considered to be attributed to scattering or detector non-linearity phenomena. For further details of simulation and experiment, reference is made to the very same paper of MINCONG et al. (2008). Furthermore, PEASE et al. (2012) include also wood in their X-ray attenuation studies of moisture movement in building materials, where they introduce and discuss the inconsistency of polychromatic X-ray application for quantitative measurements. Owing to beam hardening, they point out that linear attenuation coefficient μ_{lin} [m^{-1}] is no longer a constant along increasing material layer thickness but rather asymptotically aproximates toward the very same at considered E_{max}. It can further be presumed that the like applies to mass attenuation coefficient μ/ρ [m^2/kg] along increasing area density ρ_A. However, PEASE et al. (2012) review that thickness dependency of the

mean linear attenuation coefficient $\bar{\mu}(t) = \bar{\mu}_{\text{lin}}(t)$ can, in turn, be described by, e. g.,

$$\bar{\mu}(t) = \frac{\mu_0}{(1 + \lambda \cdot t)^2} \qquad \text{(II-42)}$$

following KLEINSCHMIDT (1999) and ALLES, MUDDE (2007) with the beam hardening coefficient $\lambda \, [m^{-1}]$ and the initial mean attenuation coefficient $\mu_0 \, [m^{-1}]$ considering an infinitely thin material section, which is, thus, complex to be determined. In their transmission measurements on porous materials employing X-rays on varying energy levels $E_{\text{max}} = 30 \ldots 85 \, \text{keV}$, PEASE et al. (2012) utilise no pre-filters. Their results illustrate the influence of material thickness on the attenuation coefficient, where they found μ_{lin} decreasing with increasing material thickness. At this, also wood results are presented as plot from $E_{\text{max}} = 60 \, \text{keV}$ measurements along the thickness range $t = 5 \ldots 80 \, \text{mm}$ and they, nevertheless, conclude minimal impact of wood on μ_{lin} values compared to the utilised building materials, e. g., clay brick or concrete. Accordingly, the deduced beam hardening coefficients yield $\lambda_{\text{brick}} = 0.863 \, \text{m}^{-1}$, $\lambda_{\text{concrete}} = 9.0 \, \text{m}^{-1}$, and $\lambda_{\text{wood}} = 0.863 \, \text{m}^{-1}$ as well as $\lambda_{\text{water}} = 0.888 \, \text{m}^{-1}$. The beam hardening effect is, eventually, considered with the term $1 + \lambda \cdot t$ in the denominator of the equations and equals one with zero thickness. Moreover, with respect to their moisture movement studies aiming at evaluation of the proposed interdependency between radiation attenuation in porous substrate and included water, PEASE et al. (2012) introduce the coupled effective attenuation coefficient of water, which considers water within basic material and the influence of the latter on beam hardening. Thus, the coefficient is recommended to be directly measured for the respective investigation instead of utilisation of tabulated water values.

Beyond human tissue, there are only few investigations on low-Z material considering beam hardening effect such as aforementioned studies of KOTWALIWALE et al. (2006). With regard to wood-related quantitative X-ray applications, beam hardening likewise occurs whereas the explicit consideration of its effects on measuring results can be concluded to be underrepresented

so far. HOAG, KRAHMER (1991), e. g., discuss the utilisation of polychromatic radiation sources and the calibration of X-ray densitometers, however, without any regard to potential bias in consequence of beam hardening. HILBERS (2006) interprets some observed phenomena in X-ray area density measurement and deviations between predicted and measured mass attenuation coefficients to be attributed to the beam hardening effect. DU PLESSIS et al. (2013) found in their quantitative CT density determination on polymeric materials that object dimensions, i. e., transmission distances, change the density measuring results owing to beam hardening artefacts. Beam hardening considerations in X-ray densitometry and investigations on the consequences for measuring results are available from SOLBRIG (2012) and deepened by SOLBRIG et al. (2014a) for determination of the vertical raw density profile on WBCs. Moreover, SOLBRIG et al. (2015a) provide comprehensive discussion on the radiation-physical effects in WBCs and propose an approach for explicit consideration with regard to the employed X-ray transmission measuring setup.

Beyond beam hardening, further radiation-physical effects influence the transmitted spectrum in consequence of attenuation of polychromatic radiation; and thus, may affect the recorded beam intensity. Since coherent and incoherent scattering is part of attenuation process within the considered energy range with increasing scattering fraction $\xi(\text{scat})$ toward higher energies (refer to Figure II-3), scatter radiation must be considered as part of transmitted radiation in case of common broad-beam geometry (refer to Figure II-1). Hence, scattered energy fraction contributes to transmitted energy spectrum whereas its rather low energy is supposed to counteract beam hardening.

To conclude on the relevance of beam hardening effects for X-ray densitometry, two different issues can be pointed out regarding initial beam as well as radiation attenuation within the material under investigation:

- energy shift, which enables low-energy adjustment of X-ray spectra by application of defined pre-filters for more or less predefined pre-hardening with consequent lower threshold $E_{\min}$ and

- non-linearity of attenuation $\ln(T^{-1})$, which is supposed to yield deviations of evaluated measuring results from true values.

A practise-oriented application of the prior enables to avoid the latter. Moreover, proper pre-filter application facilitates to adapt X-ray spectra according to the requirements of the transmission measurement considering radiation penetration potential. Notwithstanding the above, pre-filter application diminishes but does not eliminate beam hardening effects as already pointed out by BROOKS, CHIRO (1976) and discussed by PEASE et al. (2012) or elsewhere.

2.5   Scattering as radiation attenuation process

2.5.1   General background

In terms of radiation transmission, DIN 6814-2 (2000) generally defines scattering as variation of angular distribution of the radiation behind the material in comparison to the initial beam as a result of interactions along the beam path through the material layer. With respect to a point of interest, the standard further considers scattered radiation as ionising radiation occurring from interaction of an initial beam within matter. Hence, scatter reveals the same type as the initial radiation but differs regarding directional as well as usually spectral distribution. More general, DIN EN 1330-3 (1997) defines scattered radiation as radiation, which is subjected to a directional change with or without energy variation while passing through matter. Obviously, scattered radiation in X-ray applications occurs from both coherent and incoherent scattering as interaction mechanisms, which are part of total attenuation according to eq. (II-14). The contribution of both scattering processes to total attenuation depends, in turn, on radiation energy due to energy dependency of single mechanism mass attenuation coefficients. However, the ac-

tual effect from scattering depends on further aspects. Beyond general definitions and knowledge considering scattering as attenuation process, reference is made again to respective basic literature such as

- HALMSHAW (1995),
- BARRETT, SWINDELL (1996),
- HUSSEIN (2003a),
- ATTIX (2004),
- HERTRICH (2005),
- HUSSEIN (2011),
- KRIEGER (2012), as well as
- SCHIEBOLD (2015)

for comprehensive, detailed, and practice-oriented explanations of the phenomenon. Obviously, scattering unavoidably occurs in terms of transmission measurements, where particular conditions yield respective significance of the effect.

There is a strong angular dependency of scattering intensity, which is again dependent on radiation energy. Figure II-9 shows typical polar diagrams of both coherent (top) as well as incoherent (bottom) scattering cross-sections [barns/electron] according to MIDGLEY (2006), which correspond to resulting intensity distribution of scattered radiation in consequence of interaction within matter. With particular regard to incoherent scattering of the exemplary data for
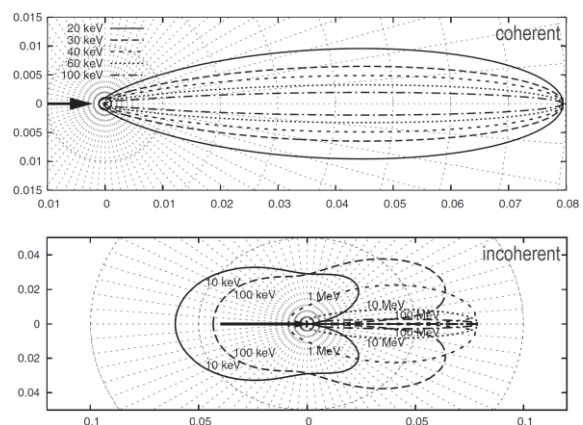
Figure II-9: Angular distribution of scattering via polar representation of coherent (top) as well as incoherent (bottom) differential scattering cross-section [barns/electron] exemplarily for the element oxygen $_8O$ at different radiation energies, acc. to MIDGLEY (2006).

the element oxygen $_8O$, distribution strongly depends on radiation energy. On low energy level (10 keV plot), scattering mainly occurs in backward direction with a further forward preference around the polar angle $\theta = 45°$. With increasing energy, in turn, angular distribution predominantly changes toward forward direction, however, still off the primary beam axis (considering 100 keV plot). On the contrary, scattering exclusively occurs in forward direction along and around the beam axis regarding coherent interaction, where divergence increases with decreasing energy. Furthermore and particularly in case of incoherent forward scattering, angular distribution varies for different chemical elements, thus, likewise compounds or mixtures, where reference is made to MIDGLEY (2006). In terms of a review, GROSSWENDT (1999) analyses angular photon scattering. He found rather wide angular distribution for coherent scattering at $E < 50$ keV, which must, thus, be taken into account. On the contrary, coherent scattering can be neglected at high energies due to strong forward scattering, which may be regarded as part of the primary radiation of the transmitted beam. With regard to incoherent interaction, increasing forward scattering with increasing radiation energy can be concluded from the review of GROSSWENDT (1999), however, less strong compared to coherent scattering and with wider angular distributions even at higher energies as well as increased backward scattering. Considering, e. g., radiation interaction in water at $E = 50$ keV, there is a cumulated distribution of 85 % coherent scattering in an angular range $\theta \leq 45°$ and 99 % within $\theta \leq 90°$ as well as 19 % incoherent scattering in the range $\theta \leq 45°$ and 53 % within $\theta \leq 90°$. Note, azimuthal angle is assumed to be uniformly distributed in the range $0° < \varphi \leq 360°$. Cumulated values at $E = 10$ keV fall respectively below. Hence, scattered radiation in the exemplarily considered energy range is still part of the extended beam and may consequently hit the detector depending on its dimensions and distance to the irradiated body without further collimation. Eventually, DIN 6814-2 (2000) likewise concludes an individual directional distribution for both scattering processes.

Regarding energy dependency, the contribution of scattering (scat = coh + incoh) to total attenuation considering one particular energy can be quantified via eq. (II-15), thus $\xi(\text{scat}) = \frac{\mu_{\text{scat}}}{\rho}(E)\big/\frac{\mu_{\text{tot}}}{\rho}(E)$, where Figure II-3 provides an exemplary illustration with respect to the elements carbon $_6C$ with, e. g., $\xi(\text{scat}) = 0.51$ at $E = 20$ keV or $\xi(\text{scat}) = 0.89$ at $E = 40$ keV (for particular data, refer to Table VII-4) and copper $_{29}Cu$ with, e. g., $\xi(\text{scat}) = 0.02$ at $E = 20$ keV or $\xi(\text{scat}) = 0.07$ at $E = 40$ keV. Likewise, BRADLEY et al. (1991) note beginning domination of incoherent scattering at energies around $E \approx 30$ keV in case of water.

However, effective scattering contribution to total attenuation must be considered to, moreover, depend on individual conditions of the employed transmission measuring setup. Thus, scattering considerations are basically related to present beam geometry and potentially utilised apertures for both source and detector collimation (refer to Chapter II–1.1). Eventually, practical X-ray transmission measuring conditions with respect to the investigated cases of application in wood and WBC densitometry do not necessarily feature ideal narrow-beam geometry. Hence, any kind of scattered radiation from any irradiated point of the specimen may reach the detector, which is, in turn, considered as broad-beam attenuation, where several geometries are possible (cf. ATTIX (2004)). Such conditions are likewise referred to as "poor geometry" by EVANS (1955), who attributes every practical problem in radiology to non-narrow-beam geometry.

Scattered radiation belongs to secondary radiation, which is defined according to IEC 60050-881 (1983) as "radiation emitted by matter as a result of an interaction of the primary radiation with the […]" specimen under investigation whereas primary radiation, in turn, originates, e. g., from an X-ray tube target. Likewise DIN 6814-2 (2000) distinguishes primary and secondary radiation. Moreover, scattered radiation may be subjected to further interaction processes along the beam path within the material, which is commonly known as multiple scattering. DIN 6814-2 (2000) notes, that multiple interactions usually occur as different types along the

beam path resulting in particular energy and directional distribution of the radiation finally emerging from the material under consideration. A comprehensive discussion of multiple scattering theory within various physical applications is available from GONIS, BUTLER (2000) following the fundamental idea to calculate scattering properties of a complex system considering corresponding properties of its constituent parts. Already EVANS (1955) provides an illustrative overview on "the extremely complicated family of secondary radiation", which may undergo consequent stages of interaction. PARETZKE (1987) discusses theory of radiation track structures in consequence of consecutive interaction processes within the specimen. Eventually, the attenuated beam diverges from initial axis and turns more inhomogeneous, i. e., reveals a wider energy distribution, where, however, mean energy is considered to rather decrease.

Consequently, scattered radiation must be taken into account to additionally occur within the extension of the initially attenuated beam. Following EVANS (1955), Figure II-10 shows a well-known broad-beam representation, where scattered radiation from interaction in the specimen may superimpose the primary beam on the detector (scattered in) or exceed the beam path of interest (scattered out), i. e., yield real attenuation. Accordingly, acquired transmitted intensity I_T is considered as sum of primary I_P and a portion of scatter I_S intensity, thus,

$$I_\text{T} = I_\text{P} + I_\text{S} \qquad \text{(II-43)}.$$

In radiography, scattered radiation is a well-known source of image noise, which comprises no information, and reduces, in turn, image contrast (cf. MIETTUNEN, KORHOLA (1991)). Hence, scatter reduction is considered to result in enhanced signal-to-noise ratio (SNR) as well as contrast-to-noise ratio (CNR), where MIETTUNEN, KORHOLA (1991) and further investigations report on methods to obtain the very same.

For quantification of scattering conditions of the transmission geometry with regard to eq. (II-43), scatter-to-primary ratio

$$SPR = \frac{I_\text{S}}{I_\text{P}} \qquad \text{(II-44)}$$

radiation source with broad-beam geometry

$I_\text{T} = I_\text{P} + I_\text{S}$
$I_\text{S} = I_\text{S,coh} + I_\text{S,incoh}$
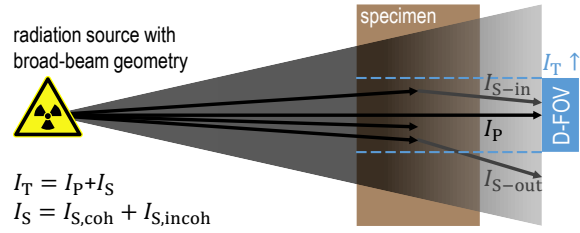
Figure II-10: Broad-beam geometry following EVANS (1955) illustrating (based on Figure II-1) radiation interaction in the specimen with both processes absorption as well as scattering, with secondary (scattered) radiation I_S superimposing primary beam I_P on the detector field of view (FOV, scattered in) or exceeding the beam path of interest (scattered out).

is computed as ratio between scatter I_S and primary I_P intensity impinging on the detector, where scatter intensity is, in turn, considered as aforementioned sum

$$I_\text{S} = I_\text{S,coh} + I_\text{S,incoh} \qquad \text{(II-45)}$$

of scattered radiation from both coherent and incoherent interaction with regard to the applied energy range $E_\text{max} < 100\,\text{keV}$. SPR is a common index for comparison of experimental results in both medical and technical X-ray research, where particular conclusions correspond to general scattering effects. MIETTUNEN et al. (1991) found increasing SPR with an increment of layer thickness (i. e. radiation absorption) as well as with increasing radiation energy in terms of tube voltage. MIDGLEY (2006) points out that detection of scattered radiation causes errors in μ/ρ measurement. On the presented mathematic-physical basis, he evaluates SPR from both coherent and incohenrent scattering for low-Z elements ($Z \leq 20$) and water as exemplary material in the energy range $E = 5 \dots 1000\,\text{keV}$ with particular respect to the angular scatter distribution. Accordingly, acceptable SPR strongly depends on both elemental composition of the specimen as well as radiation energy. For SPR dertermination via individual measurement of either scatter or primary signal, various methods exists with particular benefits and limitations (cf. SCHÖRNER et al. (2011) or KERMANI, FEGHHI (2018)). A similar quantity for scatter conditions evaluation is the scatter-to-total ratio

$$STR = \frac{I_\text{S}}{I_\text{T}} = \frac{I_\text{S}}{I_\text{P} + I_\text{S}} \qquad \text{(II-46)}$$

which relates scatter intensity I_S toward total intensity $I_T = I_P + I_S$. *STR* is also denoted as scatter fraction and applied by SCHÖRNER et al. (2011) for comparison of different scatter correction methods.

The increment of radiation intensity with increasing material layer thickness owing to scattered radiation impinging on a region of interest is commonly known as radiation build-up. With regard to medical physics, DIN 6814-2 (2000) attributes the build-up effect to an increment of secondary radiation from scattering in dependence on penetration depth. Moreover, IEC 60050-881 (1983) defines the phenomenon as increment of absorbed dose rate with increasing penetration depth due to electron release and scattered radiation. Therefore, build-up effect and occasionally computed build-up factor appears to be rather of dosimetric interest, which is, e. g., applied in brachytherapy for dose calculations (cf. ANAGNOSTOPOULOS (2006)). However, in the field of industrial radiographic testing, DIN EN 1330-3 (1997) in accordance with ISO 5576 (1997) and likewise IEC 60050-395 (2014) define the build-up factor considering a point of interest as intensity ratio of total (scattered plus non-scattered) toward primary (non-scattered) radiation. This well-known definition takes scatter-to-primary ratio *SPR* eq. (II-44) into account, i. e., $(I_P + I_S)/I_P = 1 + I_S/I_P$ with $I_P + I_S = I_T$ according to eq. (II-43) at the point of interest. ATTIX (2004) considers build-up factor approach as useful to quantitatively describe broad-beam attenuation, which is applicable to any specified geometry, attenuator or physical quantity in radiological physics. The already introduced build-up factor B [−] takes intensity increment by scattering into account and extends attenuation law eq. (II-10) to

$$I_T = B \cdot I_0 \cdot e^{-\frac{\mu}{\rho}(E) \cdot \rho \cdot t} \qquad \text{(II-47)}$$

where different expressions exist to determine B. ANAGNOSTOPOULOS (2006) as well as further researchers draw on *SPR* according to eq. (II-44) and apply

$$B(t) = 1 + SPR(t) = 1 + \frac{I_S(t)}{I_P(t)} \qquad \text{(II-48)}$$

where B is considered as function of specimen thickness t equal to transmission distance s_T. This definition of the build-up factor is already presented by EVANS (1955), who further points out, that B linearly increases with increasing absorber thickness t. Obviously, for conventional broad-beam applications $B > 1$ whereas $B = 1$ in the special case of ideal narrow-beam attenuation, where no scattered radiation is registered on the detector (cf. ATTIX (2004)). HALMSHAW (1995) employs the term to industrial radiology and concludes in contrast to EVANS (1955) that this simple linear relationship can only be proven by experiments within a limited range of radiation energy. KORNELSEN, YOUNG (1981) employ

$$B(t) = 1 + k_a \cdot (\mu_{\text{lin}} \cdot t)^{k_b} \qquad \text{(II-49)}$$

where k_a and k_b are constants to be determined by fitting of experimental data and found both in the range 0.9…1.6 for the applied radioisotopes. SHANI (2001) likewise mentions this parametrised representation of B as a function of transmission distance, which is, therefore, a limitation of the physically acceptable model described by eq. (II-47). According to KRIEGER (2012), build-up factor can be approximated by

$$B = 1 + \mu \cdot t \qquad \text{(II-50)}$$

where, obviously, above constants of eq. (II-49) equal one. For derivation, reference is made to the respective publication. Considering continuous bremsstrahlung spectra, VOROB'EV et al. (1971) propose an equation for $B(t, E_{\max})$ depending on layer thickness t as well as energy spectrum and found spectra impact to yield slower increment of $B(t, E_{\max})$ along increasing t. Moreover, TSOULFANIDIS (1995) provides further equations for build-up factor calculation, which are, nevertheless, based on above approaches. Already, MUSÍLEK et al. (1980) discuss different empirical formulae for computation of B and compare corresponding results with experimental data, where they found varying agreement with a maximum error of $< 20\,\%$. With respect to theoretical computation, they, nevertheless, question the usefulness of B due to partly elaborate preconditions. SUTEAU, CHIRON (2005) introduce an iterative computation method for build-up factors of multi-layer material such as shieldings based on an empirical double-layer

formula. However, the representation of B according to eq. (II-48), which draws on SPR, appears as most common definition and can, thus, be found in numerous textbooks also regarding NDT such as STEGEMANN (1995) or SCHIEBOLD (2015). Eventually, practical and accurate B determination is non-trivial. Supported by an example, KRIEGER (2012) points out that simple approximation is often not sufficient, since there is a complex dependency of B on

- transmission distance through the specimen $s_\mathrm{T} = t$,
- beam cross-section,
- distance from specimen backside to detector surface s_{S-D},
- material and composition of the specimen, and
- radiation energy spectrum.

Numerous studies regarding determination, dependencies, and further relations of the build-up factor are available. Regarding HCO-materials, BRAR, MUDAHAR (1996) continue the work of BRAR et al. (1994) and found increasing B with increasing penetration length, since probability for multiple scattering likewise increases, hence, yielding higher fraction of multiply scattered low-energy radiation. They further conclude on energy dependency that B is rather small at $E < 30\,\mathrm{keV}$ owing to predominance of photoelectric absorption. Along increasing energy of the initial radiation, an increment of B is found up to a broad peak around $E = 80 \ldots 150\,\mathrm{keV}$ and decreasing values beyond depending on layer thickness as well as material composition. However, their investigated materials with nearly equal Z_eff reveal nearly similar B up to a respective energy rather on low to medium level again depending on transmission distance. Hence, particular dependency on material composition becomes obvious, which turns negligible beyond a certain energy level. BRAR et al. (1999) confirm the latter findings. With respect to the investigation of six wood species, however, by means of $E = 1332\,\mathrm{keV}$ radiation from a $^{60}\mathrm{Co}$ isotope source, KUMAR et al. (2006) report on similar findings particularly regarding geometrical dependencies of B, i. e., detector collimation diameter and specimen thickness. Considering the

observed differences in B with identical collimator and thickness, they conclude on Z_eff dependency, which appears questionable, since wood elemental composition is similar in a rather narrow range (as to be pointed out in Chapter IV–2.4.2), where only ash content (Chapter IV–2.3.2) may particularly vary with respect to tropical hardwoods. For more detailed discussions on the effects of wood composition on Z_eff as well as $\mu/\rho\,(E)_\mathrm{mix}$, reference is made to Chapter II–2.2.4 and Chapter II–2.3.3, respectively. Despite lacking botanical names as well as raw density values of the investigated species, the results from KUMAR et al. (2006) are supposedly attributed to varying raw densities between the species due to well-known density dependency of scatter intensity. Further results regarding biological samples such as Chlorophyll, Muscle, and tissue with Z_eff in the order of wood and water are presented by SIDHU et al. (1999) as well as SIDHU et al. (2000). Additional data for some polymers is available from SINGH et al. (2009). All three investigations conclude that B depends on both initial radiation energy and Z_eff of the considered material, since interaction processes depend, in turn, on the very same. Energy dependency is already discussed above with congruent findings. In contrast to the questioned conclusion of KUMAR et al. (2006), the three studies reveal an obvious context between Z_eff and B. In this regard, B markedly decreases with increasing energy particularly in the range $E \leq 100\,\mathrm{keV}$. The trend, however, slows down with increasing energy, where practically no variation can be found at $E \geq 1\,\mathrm{MeV}$. Beyond organic matter, B is likewise evaluated considering soil or rock samples with similar findings (cf. KURUDIREK et al. (2011)).

Finally, BARRETT, SWINDELL (1996) deepen scattering considerations and consequent effects referring to both theoretical background and mathematical description as well as practice-oriented discussion, however, with respect to radiological imaging in the medical field. Furthermore, for a comprehensive review on incoherent scattering theory, reference is made to BERGSTROM JR, PRATT (1997). To conclude on scattering funda-

mentals, INANC (1999) performs simulation studies and points out dependencies of scattering phenomena such as

- X-ray tube voltage,
- considered volume in the specimen,
- specimen material, and
- distance from specimen backside to detector surface s_{S-D},

which are partly similar to aforementioned impact factors.

2.5.2   The role in X-ray applications

Scattering in medical application is also an issue of dosimetric interest, as NAGEL (2003) points out, since backscattered radiation increases dose rate near the surface on front of the investigated human body (incident beam). Regarding X-ray imaging, however, scatter-to-primary ratio SPR eq. (II-44) must be taken into account, since scattering diminishes contrast by the very same factor. Furthermore, NAGEL (2003) summarises well-known dependencies that scattering intensity on the detector is essentially governed by body thickness and beam geometry (field of view, FOV). Accordingly, contrast reduction for, e. g., FOV = 250 cm² is about factor 3 for 100 mm body thickness and factor 6 for 200 mm human body at $U_a = 100\,\mathrm{kVp}$. Scattering impact can be reduced by means of scatter grids but not totally eliminated.

Scattering in general technical applications, where narrow-beam geometries are not applicable, is fundamentally taken into account, to be part of the recorded beam via detection or imaging, hence, increasing the radiation intensity beyond expected linear attenuation according to $\mu_{\mathrm{tot}}/\rho\,(E)$ in eq. (II-10). Furthermore and particularly regarding X-ray imaging, there is a certain distribution of scatter intensity across the image, or, in general, the FOV (cf. HUSSEIN (2011)). Beyond image blur, an increment of recorded intensity in comparison to expectation following eq. (II-10), where only real attenuation is considered, is a serious bias of transmission measurement. Already NICKERSON (1958) proposed that any radiation reaching the detector besides the unaltered transmitted beam yields errors in the

accuracy of attenuation law eq. (II-10), thus, transmission measurement. To this end, his setup features both (isotope) source and detector collimation to minimise external scattering and the registration on detector. Moreover, the utilisation of thin material layers for investigation reduces internal scattering in forward direction to low probability. In general, KASPERL (2005) points out that scattering processes are complex and recorded scatter intensity on detector yields further non-linearity of $\ln(T^{-1})$ according to eq. (II-36) in addition to beam hardening effect as illustrated in Figure II-6. Consequently, artefacts occur in CT reconstruction like cupping or anisotropic artefacts, i. e., dark stripes. Eventually, scattering considerations are still subject of current research such as the studies from KERMANI, FEGHHI (2017) and KERMANI, FEGHHI (2018). With respect to quantitative applications, radiation build-up as systematic bias of detector signal is of primary interest in transmission measurements. In exemplary addition to numerous investigations already discussed in Chapter II–2.5.1, SHIRAKAWA (2000) performs gamma-ray thickness gauging of steel plates by means of $^{137}\mathrm{Cs}$, where application of the proposed model for build-up consideration is found to yield good agreement with experimental data.

Ways to reduce the amount of scatter radiation impinging on the detector (or film), thus, to diminish B, are described and discussed by HALMSHAW (1995) considering industrial radiology, i. e.,

- masking and collimation,
- filters,
- anti-scatter grids, and
- distance.

In addition to these technical solutions, KASPERL (2005) points out appropriate choice of energy spectrum, where – if possible considering penetration potential – energy range should be dominated by photoelectric absorption. However, masking is defined by ISO 5576 (1997) as application of material to limit irradiated area to a particular region of interest considering the object under investigation. Limitation of the beam to minimum required area is good practice in radiography (cf. HALMSHAW (1995)), i. e., both

source and detector collimation, which is like-wise applied in transmission measurement. Filters in front of film or image detector are recommended by several standards for radiography in NDT, where respectively high energies are applied. In this regard, DIN EN ISO 16371-2 (2018) points out 0.5…2 mm Pb filter as well as reasonable masking for reduction of scattered radiation on the imaging system (film or detector). Considering further filter effects, reference is made to Chapter II–2.4.2, where beam hardening is discussed. Utilisation of anti-scatter grids in medical radiography is, e. g., described by HERTRICH (2005). For diagnostic X-ray imaging particularly in mammography, DIN EN 60627 (2016) defines and specifies characteristics of linear anti-scatter grids. Regarding industrial applications, HALMSHAW (1995) notes that anti-scatter grids are rarely utilised, owing to no appropriate design at that time, which is supposedly still the case. Air gaps behind the object are further actions reducing scattered radiation. According to HALMSHAW (1995), the increment of s_{S-D} reveals a marked effect and causes, however, loss of sharpness in case of X-ray imaging with rather large focal spot sizes (e. g., owing to increasing penumbra). NEITZEL (1992) compares the application of grids and air gaps in (medical) digital radiography utilising a theoretical model. The results evaluated via SNR reveal $s_{S-D} = 200\,\text{mm}$ to yield about the same scattering reduction as a highly selective grid in case of high scatter fraction. Considering low and medium scatter conditions, NEITZEL (1992) found the air gap with better SNR results than any grid. Hence, appropriate object detector distance s_{S-D} is considered as advantageous toward the application of anti-scatter grids. SHAH et al. (1996) evaluate effectiveness of different methods for scatter reduction on imaging contrast at 60, 100, and 140 kVp. They found grid to be superior to air gap and beam area reduction for contrast improvement, which is contrary to the findings of NEITZEL (1992), who, however, considered SNR results. Obviously, all discussed methods take aforementioned (Chapter II–2.5.1) dependencies of scatter occurrence and intensity individually into account.

Technical methods for reduction of scatter radiation recording are typically only applicable to a certain extent and respective consequences of broad-beam applications are unavoidable. Accordingly, KASPERL (2005) concludes for CT applications that correction methods are required subsequently to the measuring process. Beyond beam hardening and other common effects in CT applications, DAVIS, ELLIOTT (2006) describe also artefacts in consequence of scattered radiation and consider the very same as crucially dependent on the specimen and utilised X-ray energies. Accordingly, scatter principally causes a lowering of image contrast, hence, yields underestimation of the linear attenuation coefficients in terms of reconstruction particularly in small highly-attenuation regions. As already pointed out in Chapter II–2.4.3 regarding beam hardening, scattering affects linear transmission measurements, e. g., on step wedges, which may lead to overcorrection of beam hardening artefacts. Obviously, there is a demand for appropriate scattering correction, where numerous methods as well as investigations exist. However, only exemplary studies are discussed below. According to DIN EN 16016-2 (2012) and likewise ISO 15708-2 (2017), scattering correction is besides beam hardening part of the allowed correction in terms of reconstruction in the field of technical CT, since scatter is potential reason for artefacts. Moreover, due to the common application of flat panel detectors in technical CT, a rather high amount of scattered radiation occurs owing to non-narrow beam geometry and wide detector extension. Here, DIN EN 16016-3 (2012) as well as ISO 15708-3 (2017) refine the problem, where scattered radiation, which was removed from the initial beam in consequence of interaction, may be registered by another detector element. It is pointed out that this scattered radiation cannot be easily distinguished from true signal and consequently biases the measurement. By means of proper collimation, the scattering effects can be reduced but, as commonly known, not eliminated. Since scattering intensity depends on radiation energy and material density, signal non-linearities occur, which cannot necessarily be corrected by software, thus, must be avoided by setup re-design. In technical practice

and particularly with respect to quantitative applications, SINKA et al. (2004) consider non-linearities in consequence of scattering effects beyond beam hardening to be corrected for their X-ray CT density measurement in tablets, where scatter effects are initially minimised by means of collimation. In contrast to beam hardening correction as discussed in Chapter II–2.4.3, KASPERL (2005) points out that scattering correction is crucially affected by the geometry of the object under investigation. In consequence of discussion of hitherto correction methods, he develops an own approach, which is part of "Iterative Artifact Reduction IAR" from Fraunhofer EZRT (IIS) in addition to beam hardening correction. However, the approach of KASPERL (2005) performs a length based scattering approximation, which takes object shape into account whereas multiple scattering is neglected and a homogenous specimen is assumed. To perform scattering correction in CT, various possibilities exist, where some methods are based on *SPR* determination (cf. SCHÖRNER et al. (2011)). WÜRFL et al. (2018) propose their already mentioned beam hardening correction methods furthermore as robust to scatter. ZHOU et al. (2009) found scattered radiation to complicate density measurements likewise beam hardening does as non-linear effects.

Eventually, correction methods are rather part of CT applications and considered as common practice in current devices for both medical and technical applications. Methods to reduce the occurrence of scattering within the specimen as well as registration on the detector depend on the respective application, where the way of performance is particularly related to the individual X-ray setup. However, any scatter impinging on the detector is considered to bias the transmission measuring results.

2.5.3 Beneficial applications

The occurrence of scatter radiation in technical applications is not only an issue to be considered regarding signal bias or image blur, and thus to be taken into account or even to be corrected. Moreover, approaches exist, where scattering effects are utilised for particular applications.

X-ray scattering techniques like small-angle X-ray scattering (SAXS) or X-ray diffraction (XRD) are fundamental research methods for analysis of crystalline structures (cf. ALS-NIELSEN, MCMORROW (2011) and REIMERS et al. (2008)). Microstructure analysis applications exist also in the field of wood science (cf. LICHTENEGGER et al. (1999) and DONALDSON (2008)), where furthermore the well-known SilviScan® device introduced by EVANS (1994) was updated by EVANS (1999) with XRD to measure wood microfibril angle (cf. LANVERMANN et al. (2013)). Notwithstanding the above, such scattering techniques are beyond the scope of this thesis dealing with X-ray transmission densitometry, thus, henceforth neglected.

Also medical applications exist (cf. HARDING (1997)) whereas the following review focusses on technical approaches to utilise scattering effects. In this regard, HARDING (1997) fundamentally discusses the principles with respect to both fields and provides a respective review on scattering applications. According to HUSSEIN (1989), scattered radiation is applicable for many NDT and imaging issues since it carries valuable information on density, composition, and geometry. In further discussion of the physical principles, he, however, concludes, that results from scattering measurements are difficult to interpret. Nevertheless, this alternative approach is considered to provide advantageous measuring conditions compared to conventional transmission methods with respect to particular NDT or imaging applications. Thus, scattering, especially backscatter methods in general NDT are to be found in numerous textbooks such as STEGEMANN (1995). Backscatter imaging is well-established in NDT preferably for inspection of low-Z materials such as light-weight composites and commonly considered as viable and advantageous method for applications with limit access, since it is only required from one side. Accordingly, numerous studies in a variety of technical fields exist, where only exemplary methods are named in the following. For material testing, KOSANETZKY, HARDING (1987) introduce an apparatus to measure backscatter intensity with variable focus on particular material layers for subsequent depth-dependent imaging. BOSSI et

al. (1988) apply backscatter X-ray imaging as an inspection tool for material characterisation and obtain good sensitivity toward small changes in material conditions supported by appropriate energy adaption, which can, in turn, be used to control penetration depth. Furthermore, ComScan is denoted as a commercially available NDT X-ray backscatter imaging system (cf. ANON. (1992), HARDING, HARDING (2010)). EWERT et al. (2008b) compare two techniques, i. e., flying spot as well as twisted slit diaphragm, regarding inspection of light-weight materials. Application of twisted slit collimator is further described by OSTERLOH et al. (2010). Backscatter images of a wooden log likewise acquired by means of the twisted slit camera are presented by OSTERLOH et al. (2007) in comparison to respective transmission data. JAENISCH et al. (2016) report on the quantitative simulation of backscatter X-ray imaging by a proposed Monte Carlo model in comparison to experimental results aiming at optimisation of a backscatter system considering

- angle between source and detector,
- shielding in between both,
- slit collimator system, and
- type of detector as well as
- object parameters with corresponding interaction conditions.

Beyond imaging, HOLT et al. (1984) consider (gamma-ray) scattering techniques to facilitate direct real-time density measurements within a specific region of interest (ROI). By means of simulations and experiments, HUSSEIN et al. (1997) investigate scattering intensities in relation to material density and Z_{eff} (refer to Chapter II–2.2.2), where they found the ratio of scatter intensity at low toward high energy to be a promising indication for distinguishing the considered materials covering both a range of densities and compositions. Moreover, HO, HUSSEIN (2000) propose a model for the numerical estimation of scattering signal intensity on the detector considering, e. g., flaws in an aluminium block, thus, to apply Compton-scatter quantification for NDT. Regarding low-Z material, MCFARLANE et al. (2000) examine the measurement of scatter profiles across the specimen cross-section via simulation and found close agreement to experimental studies with respect to inspection of the

density variation in food material. They conclude that scatter application for void detection in polystyrene spheres yields a high contrast but low SNR due to the low scatter signal count rate compared to transmission measurement. Thus, scatter application is considered not to compete with transmission technique in the case of homogeneous samples but to provide useful results for inhomogeneous objects. Eventually, HARDING, HARDING (2010) consider scatter-based densitometry as the ultimate goal beyond qualitative imaging yielding a quantitative spatial distribution of the material density. To this end, they review various techniques to determine the attenuation factors.

Furthermore, some few studies on wood exist following the approach to determine local specimen raw density via backscatter intensity. ELDRIDGE et al. (1990) investigate this promising method by means of energy-dispersive X-ray fluorescence analysis. Over a wide range of wood densities ($\rho = 184 \dots 755 \ \mathrm{kg/m^3}$, oven-dry specimens), they found an approximately linear relationship between wood raw density and Compton-scatter intensity at incident radiation energy $E = 22 \ \mathrm{keV}$ (^{109}Cd) and a scattering angle of $\theta = 135°$. DIVÓS et al. (1996) present similar findings in their study on gamma backscatter densitometry. Their investigation of three European wood species at $MC \approx 12 \ \%$ by means of a radioisotope ring source(^{241}Am, $E_\gamma = 59.5 \ \mathrm{keV}$) and a low-energy scintillation detector reveals linear relationship between backscatter intensity and wood raw density within the range of $\rho = 350 \dots 900 \ \mathrm{kg/m^3}$. DIVÓS et al. (1996) further conclude on the influence of MC on the resulting scattering intensity and some limitations of the method, where they examine minimum specimen thickness of about 70 mm not to affect the measuring signal as well as the minimum specimen edge distance of 10 mm to obtain reliable results. Beyond applications in wood technology, TAJUDDIN et al. (1996) evaluate forward scattering intensities in an angular range of $10 \dots 45°$ utilising a ^{241}Am point source with a NaI(Tl) scintillator. Their investigated range of hardwoods ($\rho = 548 \dots 1065 \ \mathrm{kg/m^3}$) includes mangrove wood (*Rhizophora* spp.) and was submerged in water before measurement. From the results,

they compute the ratio of total scattering toward transmission intensity and found a linear relationship across the raw density range of the samples, where a decrement of the scattering angle, in turn, progressively increases the measured scatter intensity. TAJUDDIN et al. (1996) conclude based on their results, that the hardwood reveals similar scattering and transmission properties like coincidently investigated water. Likewise, SHARAF (2001) presents experimental results from 90° scatter intensity measurements for tissue-equivalent materials including wood and plastics as well as water as reference material. The experiments employing a monoenergetic fluorescent radiation ($E = 25.2\,\mathrm{keV}$) from a secondary Sn target (exited by $55\,\mathrm{kVp}$ Mo-target tube), a collimated pencil beam, and a SiLi detector perpendicular to initial beam axis through the specimens reveal again scattering proportional to material density with a remarkable linear agreement. Furthermore, the performed experiments serve to demonstrate validity of the method, where mathematic-theoretical basics are presented and practical aspects are discussed. Accordingly, SHARAF (2001) concludes that scatter densitometry is a useful technique for precise measurement of material density. However, different scattering angles were utilised. PAKI AMOUZOU et al. (2006) measure the angular distribution of inelastic scattering intensity from organic materials including wood, water, and further substances at energy levels $E \leq 80\,\mathrm{keV}$ employing a cooled CdTe detector for energy discrimination in the acquired data. Their results reveal good agreement with theoretical calculations considering the employed tube spectra. Moreover, SCHÄTZLER (1979) discriminates coherent and incoherent scattering intensity in his measurements of forward (68°) scatter intensity on samples of organic compounds by means of a $^{241}\mathrm{Am}$ source and a pure Ge detector, which displays energy spectra. Since low-Z elements reveal a strong dependency of the ratio of coherent toward incoherent scattering intensity, SCHÄTZLER (1979) follows this approach to utilise such measurements to determine the chemical composition of binary organic systems, i. e., substances of two major compounds such as water content in milk products.

Beyond the discussed rather scientific applications, further utilisation of scattered radiation for densitometry was investigated, where industrial applications arose from. Here, measuring systems exist for inline inspection of the vertical raw density profile (RDP) in the production process of WBCs. The device introduced by DUEHOLM (1996) with the first test installation in a German MDF plant in 1995 is still commercially available as StenOgraph from Fagus-GreCon Greten GmbH & Co. KG, Alfeld, Germany. The measuring principle becomes obvious from the illustration in Figure II-11 (top). The primary beam penetrates the running panel in an angle of 45° and a fixed detector on the beam axis records transmitted intensity. A second detector is aligned perpendicularly to the beam axis and is moveable along the very same with a collimator focused on this flying spot within the panel, where scattered radiation intensity is registered. After data acquisition along total panel cross-section,
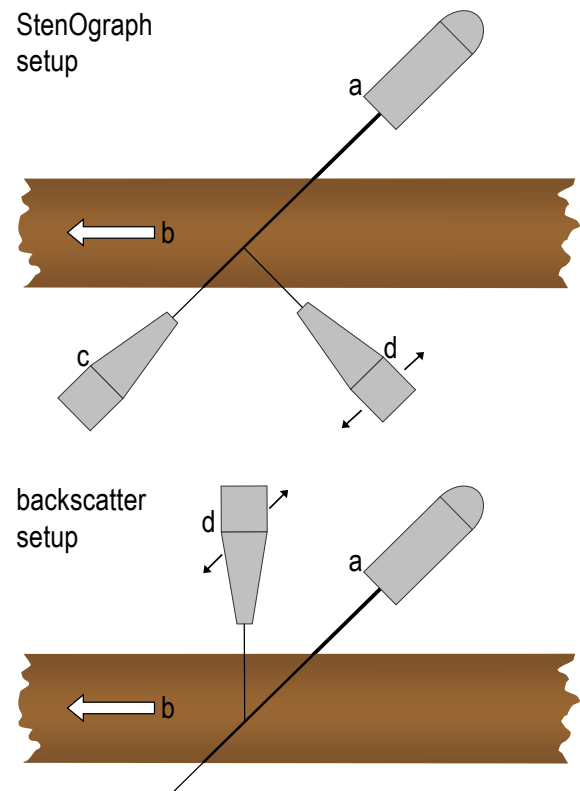
Figure II-11: StenOgraph (top) and backscatter (bottom) measuring setup for inline RDP determination on WBCs, with X-ray tube (a), panel and feed direction (b), fixed transmission detector (c), and movable scattering detector (d), acc. to DUEHOLM (1995) and FERNÁNDEZ et al. (2007a), respectively.

evaluation of both signals yields raw density of each scanned volume element with a spatial resolution of 0.01 mm in diameter according to the manufacturer GRECON (2018). A further but similar approach for the same measuring task is presented by FERNÁNDEZ et al. (2007a), where the device, however, does not comprise a transmission detector and both the tube as well as the movable scattering detector are located on one side of the panel. The device is commercially available as CDP700 from IMAL SRL, San Damaso, Italy. As illustrated in Figure II-11 (bottom), the 45° primary beam irradiates the material and the collimated scattering detector is aligned in an angle of 90° to the panel surface, thus, 135° to the primary beam axis, creating a backscatter geometry in contradiction to the 90° scattering setup of the StenOgraph. The proposed algorithm yields RDP unfolded from measurement of integrated scattering signal with a graph resolution of 0.01 mm according to the manufacturer IMAL (2018). FERNÁNDEZ et al. (2007b) add a multiple scattering correction, which is computed offline for several panel thicknesses assuming known chemical composition and raw density. Finally, corrected RDPs are found to be in good agreement with profile results determined via transmission measurement by DPX200 device (refer to Chapter IV–4.2.5).

2.5.4   Concluding remarks

In radiography, scattering is well-known to reduce image quality in terms of increasing noise and decreasing contrast as well as sharpness. EWERT et al. (2008a), in this regard, compare the effects considering film and detector utilisation. Regardless of the beneficial applications (Chapter II–2.5.3), the occurrence of scattered radiation in quantitative transmission measurements is considered to have a consequent impact on measuring results particularly in terms of radiation build-up on the detector, where non-narrow-beam geometries are employed. Thus, scattering biases any quantitative X-ray application, where physical quantities are determined or displayed based on the materials attenuation coefficients, which do not expect any presence of secondary radiation, where its intensity actually varies along the beam path through the specimen due to multiple interaction. Hence, correction – or at least explicit consideration – of consequent non-linearities of radiation transmission is required and commonly performed in the field of both medical and technical CT, e. g., SINKA et al. (2004) for CT measurements of density variation in tablets.

Regarding build-up factor B, no particular values are available for wood or other low-Z materials beyond some data for steel (cf. HALMSHAW (1995) or SCHIEBOLD (2015)). However, HALMSHAW (1995) expects B in the case of materials other than steel to follow the same pattern as found for steel. Notwithstanding that, actual B values for individual measuring setups depend on their respective conditions considering

-   beam geometry,
-   collimation,
-   energy level and spectrum,
-   detector type and dimensions,
-   distances,

as well as composition of the material under investigation. As a general consequence for X-ray densitometry by means of non-narrow-beam geometry, it can be inferred that attenuation law eq. (II-10) breaks down, since transmitted beam and consequently registered radiation intensity comprises a certain scattering share. In this regard, a few particular studies are available with regard to quantitative transmission measurements and mass attenuation coefficients. In contrast to theoretical mass attenuation coefficient, COPPOLA, REINIGER (1974) consider scattered radiation to be expected on the detector in addition to primarily transmitted intensity likewise already pointed out by GRODSTEIN (1957). ELDRIDGE et al. (1990) prove increasing scattering intensity along with increasing wood raw density of different species. SARITHA, NAGESWARA RAO (2013) consider scattered radiation to bias the attenuation coefficient determination of their wood samples. They evaluate the impact of specimen thickness and found reduced scattered radiation reaching the detector with increasing thickness by consequently increased scattering angles. KIM et al. (2013) found de-

creasing mass attenuation coefficients with in-
creasing radiation penetration depth in terms of
X-ray CT on some softwood specimens and de-
duce an equation for depth-dependent μ/ρ
based on simple linear regression of the very
same over logarithmic thickness. Furthermore,
they exclusively attribute the observed phenom-
ena to (multiple) scattering, however, without
consideration of beam hardening effects, which
appears questionable with regard to their applied
X-ray energy range $E \leq 37\,\mathrm{keV}$, where attenua-
tion is considered still to be affected by photoe-
lectric absorption besides coherent and incoher-
ent scattering (refer to Figure II-3 and Table
VII-4). Eventually, OSTERLOH et al. (2007) con-
sider wood moisture as the main source of scat-
tered radiation. Thus, effects from scattered ra-
diation in WBC densitometry are surmised to de-
pend on material MC. As already mentioned in
Chapter II–2.4.4, SOLBRIG et al. (2015a), how-
ever, provide the first comprehensive discus-
sions on practice-relevant effects including scat-
tering, which bias measuring results in X-ray
densitometry on WBCs.

3 X-ray densitometry on wood and wood-based composites

3.1 General background

Aspects of radiation-matter interaction with wood and WBCs under investigation by means of X-rays are presented above considering an effective atomic number, the mass attenuation coefficient of the compound, beam hardening, and radiation scattering. However, the common applications of transmission measurements by means of ionising radiation serve for material density determination and its distribution in the object either as absolute measurement (densitometry) or for visualisation (imaging and CT). Here, X-ray applications on wood as inhomogeneous, porous, and anisotropic material are well-known to differ from general NDT, where several reviews exist as pointed out in Chapter I. A first study regarding the theory of densitometry on wood is available from LIU et al. (1988), OLSON et al. (1988), and LIU, TIAN (1991), who provide fundamental discussions of aspects relevant for density measurements on wood. Furthermore, HUSSEIN (2003b) reviews manifold applications of radiation gauging, imaging, and analysis even with regard to wood. Regardless of the generally possible techniques, the particular applications in WBC production comprise the measurement of area and raw density (mean values and gradients), where the manufacturers of inline X-ray systems for continuous measurements on furnish mats or panels as well as laboratory devices for RDP determination on small panel specimens are already mentioned in Chapter I. In wood science, however, numerous X-ray applications exist, where a selection is outlined below with a focus on densitometry and the studies relevant for WBCs as well as particularly the advances in the context of RDP determination (Chapter II–3.2).

Structural investigations on solid wood exist from large-scale characterisation (e. g. timber CT) to microstructural analysis (e. g. microfibril angle), which are not the main subject of this review. However, X-ray studies on wood are primarily performed by means of established and commercially available devices, particularly in the

case of CT application in the laboratory. Nevertheless, also special CT devices exist in the lab (cf. LINDGREN et al. (1992)) and for investigation of large logs (cf. LISTER (2004)). OH et al. (2009) apply an own X-ray evaluation system for the characterisation of knots via two-dimensional digital imaging with subsequent raw density computation. For microtomography (µXCT) with high spatial resolution, high-flux synchrotron radiation is often utilised, e. g., by ILLMAN, DOWD (1999), who evaluate fungal wood decay of the cell wall on microscale. Such beamlines allow, moreover, 3D imaging and low-Z material analysis with high density resolution of about 1 % at low radiation energy according to LAUTNER, BECKMANN (2012), which, in turn, facilitates the differentiation of structures and material types in the specimen as shown by BECKMANN et al. (2008).

Obviously, structural investigations are typically performed via CT in order to obtain 3D information. Here, for basic CT principles refer to KAK, SLANEY (1988) and for a comprehensive review on the utilisation for determining wood properties including raw density measurement and moisture content monitoring to WEI et al. (2011). Furthermore, DAVIS, WELLS (1992) review CT on wood with comprehensive information about the fundamentals. They point out some CT limitations and the relevance of correct calibration by means of appropriate phantoms containing regions of known attenuation coefficients in due consideration of artefacts, which can affect the final voxel values, thus, the measuring accuracy. RINNHOFER et al. (2003) claim the obtainable density accuracy of a CT to be better than 5 % and reproducibility better than 1 % whereas absolute values of density are considered as less important in the case of log studies, where differences between the structures are evaluated. However, X-ray CT on logs (cf. LINDGREN (1992), GRUNDBERG et al. (1995)) reveals considerable advances (cf. LAUDON et al. (2013), SAUTER et al. (2015), STÄNGLE et al. (2015)) particularly in consequence of the introduction of a CT scanner for the sawmill industry by GIUDICEANDREA et al.

(2011), since WEI et al. (2011) found medical CT scanners to be inappropriate for industrial applications.

Likewise, there is an increasing interest in microstructural analysis (cf. ILLMAN, DOWD (1999), WALTHER, THOEMEN (2009), LAUTNER, BECKMANN (2012), STANDFEST et al. (2013), TAYLOR et al. (2013)) on both wood and WBCs as well as the examination of effects in consequence of special wood treatment, where, e. g., raw density profiles are evaluated on CT data basis after thermo-hydro treatment by BIZIKS et al. (2019). Also, wood-like material is studied via CT such as cork by OLIVEIRA et al. (2016). Beyond structural investigations and measurements, numerous CT applications for 3D imaging of wooden objects exist particularly related to cultural heritage (cf. LEHMANN, MANNES (2012), WAGNER et al. (2018)). Eventually, the review of CT applications for solid wood investigations with a focus on investigations, where the density is evaluated (i. e., quantitative analysis rather than simple imaging of structures only considering the relative contrast in the image) is not further deepened. However, approaches from technical as well as medical CT regarding radiation-physical effects are considered in the previous chapters.

Wood densitometry has a history starting in the 1960s and 1970s. Here, POLGE (1970) describes the method based on X-ray imaging with subsequent recording of the optical film density (blackening) and POLGE (1978) provides a review on early advances. However, already KLEUTERS (1964) points out the need for precise methods to analyse the raw density distribution in wood and its annual ring structure. He continued the work of KEYLWERTH, KLEUTERS (1962) with a laboratory device applying beta-rays and a respective detector to directly perform the density measurement. More common than beta-rays, gamma-ray absorptiometry through a given specimen thickness is applied, where LOOS (1961) claimed that raw density can be determined nondestructively if the MC is known and vice versa. However, film densitometry appears to have been more or less prevalent in the first decades of X-ray applications on wood. RUDMAN et al. (1969) perform densitometry with 23 kVp

X-rays and a long distance of $s_{X-D} = 2.5$ m between tube and film such that a cellulose acetate step wedge is simultaneously irradiated on the X-ray film as calibration object. PARKER et al. (1973) introduce a computerised scanning densitometer, where X-ray negatives are converted in profiles of density values [kg/m³] with intervals of 0.01 mm. Calibration wedges are simultaneously exposed on the same film. The radiographs are acquired with 20 kVp on film by means of the X-ray scanning machine developed by PARKER, JOZSA (1973). Already LENZ et al. (1976) report about methodical problems regarding calibration and the feasible accuracy of tree-ring width and raw density measurement by means of the radiographic-densitometric procedure. ESCHBACH et al. (1995) describe a commercially available new device for optical densitometry on radiographs (or even directly on wood samples) comprising partly automated measurement and data evaluation by means of a software.

Beyond X-ray films, BROWN et al. (1974) apply photon-counting detectors for automatic and continuous gamma-ray densitometry on wood in order to study its thermal decomposition. HOAG, MCKIMMY (1988) present an X-ray device including a scintillation detector for direct scanning densitometry (without initial film exposure). HOAG, KRAHMER (1991) apply the refined densitometer and discuss the utilisation of polychromatic radiation sources and the calibration of X-ray densitometers, however, without any regard to potential bias in consequence of beam hardening. Further direct scanning densitometers were developed and applied employing appropriate radioisotopes rather than X-ray tubes in the early decades (cf. COWN, CLEMENT (1983) or MOSCHLER, DOUGAL (1988)).

MALAN, MARAIS (1992) perform gamma-ray densitometry studies on various wood species covering a wide raw density range. They found high radiation energy (from a ^{137}Cs radioisotope with $E_\gamma = 662$ keV) to be less sensitive to potentially different mass attenuation coefficients $\mu/\rho\,(E)$ corresponding to the constituents of the wood species. At a lower energy level (^{241}Am with $E_\gamma = 59.5$ keV), in turn, varying equilibrium moisture

content (EMC) is considered to have a low impact on the accuracy of the method due to the very similar $\mu/\rho\,(E)$ of wood and water. Comparatively low radiation energy with $E_\gamma = 5.9\,\mathrm{keV}$ from a ^{55}Fe source is applied by Cown, Clement (1983) with 5 mm increment cores or radial wood block cross-sections and later by Tiitta et al. (1996) in their automated setup to measure the raw density distribution in samples of 1.5 mm and 2.8 mm spruce veneer sheets. Schajer (2001) describes a multi-channel X-ray scanner to measure lumber raw density distribution in order to identify knots, which is applied for strength grading. Macedo et al. (2002) present a procedure for densitometry from CT scans with calibrations at three different X- and gamma-ray energies $(E = 28.3, 59.5, 662\,\mathrm{keV})$ and apply the method to different wood species and sample dimensions. Freyburger et al. (2009) utilise a medical CT scanner (X-ray tube at 80 kVp and 120 kVp) and found the relation between Hounsfield numbers and wood density to be linear within in wide range of $\rho = 133 \ldots 1319\,\mathrm{kg/m^3}$ of tropical species. The calibration data is verified with an independent validation set of mainly temperate species in the range of $\rho = 364 \ldots 821\,\mathrm{kg/m^3}$, where an error of $\rho = 5.4 \ldots 7.7\,\mathrm{kg/m^3}$ is reported. Lehmann, Mannes (2012) compare radiation transmission techniques by means of X-ray tubes and synchrotrons as well as employing neutrons regarding obtainable resolution and contrast, where exemplary results from corresponding applications are shown. X-ray densitometry is often performed in combination with the evaluation of other material parameters such as mechanical properties (cf. Viguier et al. (2017)). Apart from intact wood or WBCs, this is also relevant for other lignocellulosic material, e. g., biomass pellets as investigated by Tenorio et al. (2015).

Wood densitometry is obviously often applied for tree-ring analysis, which is a common purpose particularly in the field of dendrochronology or dendroclimatology. Besides radiometric methods, simple procedures for tree-ring counting and width measurement exist as well as optical methods (cf. Clauson, Wilson (1991)). However, the analysis of annual rings with focus on

densitometry has been performed by numerous researchers, e. g.,

- Hapla (1985),
- Lewark (1986),
- Bucur, Lewark (1987),
- Hoag, McKimmy (1988),
- Schweingruber et al. (1988),
- Worbes et al. (1995),
- Lindeberg (2004),
- Grudd (2008),

as well as the already aforementioned. Moreover, Leban et al. (2016) initiate the XyloDensMap project, to measure the wood density variations in thousands of drill cores from French trees. Jacquin et al. (2019) develop a software to semi-automatically evaluate the raw density along drill cores by CT scans (medical 80 kVp device) of numerous specimens arranged in one set and obtain an error of determination of 1.7 % for 5 mm drill cores. Likewise, Steffenrem et al. (2014) describe a procedure to measure tree-ring width and relative density differences between the drill cores by means of a medical CT system, where the up to 441 specimens are mounted in a cassette made of balsa. Bergsten et al. (2001) analyse the effects of X-ray intensity, specimen thickness, fibre direction, and extractives content on microdensitometry on pine and spruce (young and old) drill cores considering contrast and resolution by means of a Cu-target flat-beam X-ray scanner including capillary optics and a 1024 pixel (25 × 25 µm²) linear diode array as directly operating detector. Beyond drilling core measurements, Solbrig et al. (2010) introduce the application of this device, however, with a Ag-target tube, for RDP measurement on the typical 50 × 50 mm² WBC specimens following the work of Solbrig (2009), where reference is made to Chapter II–3.2. Note here, another version of the scanner is described by Croudace et al. (2006) for application on sediment drill cores. Besides X-ray transmission measurements, the scanner employed by Bergsten et al. (2001) facilitates the analysis of trace elements in wood by means of X-ray fluorescence (XRF). For analytical applications on wood samples, furthermore, the SilviScan® device exists as introduced by Evans (1994) and updated by Evans (1999), which comprises

X-ray diffraction analysis (XRD) for microfibril angle measurement beyond X-ray absorption densitometry combined with optical image analysis. Numerous such wood analyses on microscopic level exist particularly in combination with other properties or methods, e. g., VAHEY et al. (2006), WU et al. (2009), KEUNECKE et al. (2010), LANVERMANN et al. (2013), and BLOHM (2015). Ultimately, X-ray applications for tree-ring analysis and wood densitometry including structural investigations reveal a wide range from simple film radiography, over automated direct scanning densitometry and CT with quantitative evaluation, to special X-ray devices and utilisation of large-scale facilities with synchrotron or neutron radiation.

3.2   Determination of density gradients on wood-based composites

Densitometry applications on wood-based composites (WBCs) have to be distinguished regarding the object under examination and the direction of the density gradient to be measured, i. e.,

- the raw density profile (RDP, also known as vertical density profile) on small specimens in the laboratory or inline on the total panel after the hot-press or
- the lateral area and raw density distribution of the furnish mat or ready-pressed panel along and across the production direction.

Regarding radiometric RDP determination methods and devices, several investigations exist and a history can be outlined. However, this is not a review of RDP determination in terms of general WBC research such as by MAY (1983), BOEHME (1992), KRUSE et al. (1996), WONG et al. (1999), BELINI et al. (2014), BENTHIEN, OHLMEYER (2017), and HUNT et al. (2017). Regardless of the non-destructive radiometric methods, destructive gravimetric methods were applied featuring direct raw density determination of the respective layers, where reference is made to Table IV-21 in Chapter IV–4.2.4.1 for a detailed compilation. Note, such methods are elaborate, but still considered to serve as direct reference methods for the radiometric techniques. Furthermore, semi-

destructive (non-radiometric, indirect) methods were proposed for RDP determination, e. g., by PAULITSCH, MEHLHORN (1973), HELMS, NIEMZ (1993) as well as WINISTORFER et al. (1995) via drill resistance technique, which, however, never became prevalent in WBC industry (inline) and research.

Nevertheless, NEARN, BASSETT (1968) acquire simple radiographs of MDF and PB cross-sections but evaluate only the relative density variation according to the blackening of the X-ray film. HENKEL (1969) also performs X-ray radiography, however, with subsequent densitometric evaluation and reports, furthermore, on first applications of direct detection of the transmitted radiation via an ionisation chamber as detector scanning along the specimen cross-section. POLGE, LUTZ (1969) explore X-ray film based methods including densitometric evaluation known from tree-ring analysis for RDP determination on PB. RANTA, MAY (1978) refine the approach of MAY et al. (1976) and introduce an automated measuring device employing a scintillation detector and the radioisotope ^{241}Am with $E_\gamma = 59.5\,\text{keV}$ as henceforth common radiation source in this field of gamma-ray densitometry on WBCs. However, STEINER et al. (1978) modify an X-ray scanning-densitometer originally designed by PARKER et al. (1973) for tree-ring analysis and obtain accurate and detailed RDP data also on waferboard. To this end, X-ray negatives acquired with 35 kVp on film are scanned at increments of 0.01 mm for conversion in density values [kg/m³] by a computer. Together with the specimen, a calibration wedge made of waferboard with known density steps is radiographed on the same sheet of film. LAUFENBERG (1986) presents a study, where a simple and fast RDP determination method is developed aiming to replace the tedious gravimetric procedures via incremental planing or sanding. To this end, radiation transmission from an ^{241}Am source is directly measured by means of a 2'' NaI(Tl) scintillation detector through the specimens, which are moved in steps of 0.001'' (25.4 µm). After amplification by a photomultiplier tube, the signals are discriminated for a minimum energy level. The measurement is computer controlled and radiation intensity is recorded along with the individual

specimen position. Variations in the measured RDPs from the random nature of the radiation source depending on scanning time are discussed. Beyond the development, LAUFENBERG (1986) provides first essential conclusions regarding the mass attenuation coefficients of WBCs as discussed elsewhere. WINISTORFER et al. (1986) present a direct scanning gamma densitometer with adjustable collimation slits in front of both source (^{241}Am) and scintillation detector. Exemplary gamma-ray measuring results (with 15 µm detector aperture, 19 µm step size, and 10 s integration time per step) utilising a mass attenuation coefficient reported by MOSCHLER, DOUGAL (1988) in comparison to the RDPs obtained by gravimetric method (face milling with 80 µm increments per layer) on the same samples reveal the scanning densitometer to be ideally suited for RDP measurement. Near the panel surface, however, misalignment of the specimen and beam may cause erroneous measuring results. Nevertheless, WINISTORFER et al. (1986) consider already such direct densitometry systems as becoming the standard technique for lab RDP determination and regard the gravimetric method as obsolete. THOMPSON et al. (1989) report about design and construction of an RDP measuring system for the WBC industry. Again, the setup comprises a linear table with a stepper motor to move the specimens with 0.001'' (25.4 µm) increments through the gamma-ray beam from an ^{241}Am radioisotope source, a NaI scintillation detector with photomultiplier tube for photon conversion, a single channel analyser to discriminate against background radiation limiting the signal to the relevant energy range of the source, and a subsequent pulse counter connected to a computer. The acquired raw data is smoothed twice by a three value wide moving mean filter. GIBBON, TUNDAK (1989) describe a ready-to-use "density profilometer"[17] comprising a computer operated gamma radiation source (^{241}Am), detection system, sample positioning, and operator terminal with monitor and printer. They point out, that

such RDP measuring devices eliminate the human impact causing errors of the manual method. Obviously, there were similar device developments in the 1980s preferably employing the radioisotope ^{241}Am and photon-counting detectors with a stepper motor to scan the specimen in small increments. Beyond initial research and developments, SOINÉ (1990) reports about a commercially available RDP lab device, where an accuracy of 1 % is claimed but no further technical details are provided. Finally, SOLBRIG et al. (2010) introduce a commercially available tree-ring analysis device modified for RDP measurement in consequence of the adaptions by SOLBRIG (2009) as well as GRUCHOT (2009). The X-ray scanner runs a Ag-target tube at 55 kVp with flat-beam collimation via capillary optics (refer to II–1.3).

However, the basic principle of gamma- or X-ray RDP determination, which is illustrated in Figure II-12, is similar for all available laboratory devices for decades. Accordingly, the specimen is moved in small adjustable increments (commonly less than 100 µm) through the beam[18] by means of a manipulation unit with, e. g., a stepper motor and typically a sample holder able to carry several specimens for automated batch measurement. The specimens of individual thickness are cuttings with the prevalent in-plane dimensions 50 × 50 mm² corresponding to other test specimens for the quality assurance of mechanical parameters and panel properties such as internal bond following DIN EN 319 (1993) in WBC industry. However, the initial beam is limited to a reasonable extent or may even be collimated via a narrow slit aperture or capillary optics as a flat fan or quasi-parallel beam, respectively (refer to Chapter II–1.3). Today, X-ray tubes dominate as radiation sources commonly with tungsten W as anode target material, operated at a more or less appropriate tube voltage, and partly with any type of pre-filter. Contrary to this, radioisotopes – primarily ^{241}Am – are still employed in existing devices but are no longer

---

[17]   The RECOM 8900/DA density analyser is found to be no longer available.

[18]   Note, the movement of the beam plus detector along the stationary specimens rarely exists only in the case of radioisotopes.
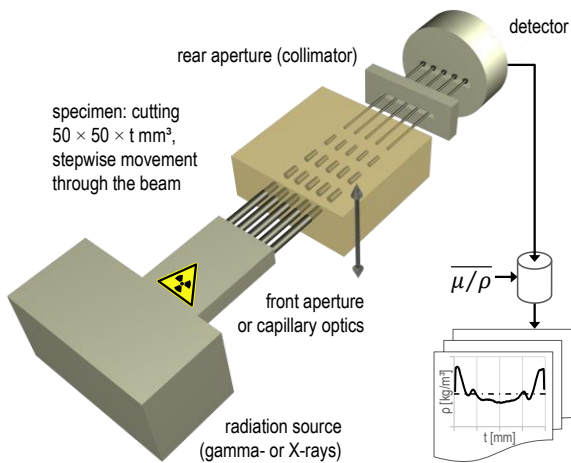
Figure II-12: Basic principle of radiometric raw density profile (RDP) determination by means of laboratory devices on small specimens of wood-based composite (WBC) panels, extended schematic illustration following to RANTA, MAY (1978).

Figure II-13: Definition of the raw density profile (here, of particleboard) with mean density (MD), peak density (PD), core density (CD), peak area (PA), central line (CL), gradient factor* (GF), peak distance* (Pdi), peak base* (Pb), *values expressed as percent of total panel thickness, acc. to WONG et al. (1998) and WONG (1999).

part of the commercially available devices supposedly due to transport and disposal restrictions and other practical reasons. After radiation attenuation within the specimen, the detector converts the impinging intensity into a count rate or an arbitrary signal (refer to Chapter II–1.1) depending on the type employed by the individual device manufacturer without further spatial discrimination except it is a line camera. In front of the detector, there is typically a rather narrow slit aperture (e. g. 50 µm), which is relevant for the effective spatial resolution, i. e., the actual thickness of the measured layer regardless of the step size. Nevertheless, SOLBRIG et al. (2014a) point out that partly considerable differences exist regarding the components relevant for valid measuring results such as radiation source, aperture design (for collimation), and detector type as well as data acquisition and evaluation. The common calibration of such devices is discussed in Chapter II–3.3. Ultimately, SOLBRIG et al. (2013) as well as SOLBRIG et al. (2014a) unveil partly considerable deviations between RDP measuring results of the same set of specimens in terms of their round robin test employing several devices as well as a reference method. The detailed study is part of the present thesis and described in detail in Chapter IV–4.2.5 with the developed reference method in Chapter IV–4.2.4 and the results in Chapter IV–4.3.1.

Beyond measuring data acquisition and display of the result plot, further evaluation of the RDP is possible. JENSEN, KEHR (1995) propose a definition for board regions along the thickness in order to numerically evaluate the RDP symmetry and respective values within the outer and transition zones as well as the inner zone of the cross-section. WONG et al. (1998) and likewise WONG (1999) introduce a definition of the RDP in greater detail via variables in order to quantify typical points or sections in the profile (to establish correlations to panel processing parameters), which is presented in Figure II-13. WINISTORFER et al. (1996) apply nonparametric regression analysis of RDP measuring data in order to model and statistically compare the accordingly smoothed RDP curves. Nevertheless, neither official rules or standards for RDP measurement on WBCs were established, nor, so far, is there a consistent definition of characteristic values of the typically U-shaped slope of customary panels. However, the prevalent data evaluation depends on the device manufacturer but is well-known to focus on the surface layer (SL) peaks and the core layer (CL) raw densities with respectively simple parameters, i. e., the left and right (or upper and lower) SL max as well as the CL min both with the raw density value and the respective position along the panel thickness. Additionally, the RDP slope in the transition zone

between SL and CL is often visually evaluated regarding intermediate peaks.

The application of X-ray CT on wood and WBCs primarily serves for structural investigations on different scales, which is, however, beyond the scope of this thesis and not further reviewed in detail. Here, e. g., SUGIMORI, LAM (1999) analyse the macro-void distribution in strand-based wood composites but do not evaluate the CT data regarding the raw density gradients in the specimens. Likewise, the µXCT studies of STANDFEST et al. (2013) on compressed wood and TAYLOR et al. (2013) on beech wood regarding shrinkage examine the microstructure without explicit density evaluation. Based on their segmentation of CT data for estimation of porosity and average fibre dimensions, LUX et al. (2006) retrieve the raw density of the studied insulation fibreboards with partly good accuracy assuming 1530 kg/m³ cell-wall density. Beyond that and the well-established lab devices, CT is also applied for RDP determinations in WBC science. GAO (1990) proposes and evaluates RDP determination by means of X-ray CT, where the specimen is scanned only with limited angles through the panel surface (i. e. incomplete rotation) and the developed models are found to be feasible for raw density estimation with mean standard errors of 56.9 kg/m³ and 42.4 kg/m³, respectively. STANDFEST et al. (2009) compare RDP determination by means of a common lab device and industrial CT on MDF, PB, and OSB specimens (30 × 30 mm²). The grey-scale CT data is transformed to density values such that the mean grey value corresponds to the mean raw density displayed by the lab device. The results reveal good agreement in the CL section whereas differences of the SL values occur due to boundary effects in the case of CT reconstruction. Here, the position of SL maximum is found to be shifted inwards and the values fall up to 200 kg/m³ below the common lab device results, where the RDP slopes converge within 1…2 mm from the panel surface. PLINKE et al. (2018) state that a CT scan provides the calibrated density distribution in all three dimensions and for selectable sub-volumes as long as the atomic number Z and the mass attenuation coefficient μ/ρ is constant and the global mean raw density $\bar{\rho}$ of the

specimen is known. Accordingly, such data is considered to reveal more information about the specimen under investigation, i. e., in-plane raw density distribution or particle distribution and orientation depending on the applied resolution. Furthermore, they show different RDP shapes within one 50 × 50 mm² specimen depending on the considered region of interest (ROI).

Since WBCs and other wood material commonly occur as panel-type objects, a complete CT scan with all 360° projections appears impossible in cases where the initially large objects are to be examined and no small specimens may be cut. Accordingly, incomplete methods such as limited-angle CT or computed laminography (CL) may generally be applied on flat objects (cf. EWERT et al. (2008b), MAISL et al. (2010)). A reliable reconstruction of valid density data is considered to be challenging and has not yet been proven. SANABRIA et al. (2011) perform also limited-angle reconstructions of their full CT scans for comparison purpose but do not quantitatively evaluate the density distribution in their glued timber specimens. Although GAO (1990) concludes the feasibility of limited angle CT with two mathematical models for estimation of RDPs, the aforementioned standard errors of the experiments with relative deviations in the order of 5.6…7.6 % for standard MDF is considered to be much too high to regard the technique as reliable RDP measurement. Moreover, an unpublished study (in 2015) revealed that the reliable reconstruction of the RDP within lab-made homogeneous MDF (refer to Chapter IV–1.2) cannot be obtained from laminography (CL) data within appropriate tolerances. However, impurities in the panel such as resin lumps or other foreign bodies with higher densities or atomic numbers Z than the WBC matter can easily be displayed via CL.

In WBC industry, X-ray systems for RDP determination exist also for inline installation after the hot-press. To this end, two devices employing scattering technologies are commercially available, which are already explained in Chapter II–2.5.3 and illustrated in Figure II-11, i. e.,

- the StenOgraph as introduced by Dueholm (1996) and available from Fagus-GreCon Greten GmbH & Co. KG, Alfeld, Germany as well as
- a backscatter device presented by Fernández et al. (2007a) and available as CDP700 from IMAL SRL, San Damaso, Italy.

However, there is a lack of further scientific studies regarding the measuring accuracy and general capability of such inline inspection systems. Practical experiences reveal a spatial resolution of the measuring spot in the order of 0.4 mm along the panel thickness. Regardless of the scattering systems, the device introduced by Warnecke (1995), which is intended to perform an angled transmission measurement through the front edge of the panel, never became prevalent in the WBC industry. Ultimately, as is commonly known, none of the available inline systems is able to replace the more or less exact RDP measurement by means of a capable laboratory device.

Beyond the measurement of the final RDP by means of the common lab devices or otherwise, few in-situ investigations of the RDP formation during the hot-pressing process exist on a laboratory scale. Winistorfer et al. (2000) present first results from OSB lab-fabrication employing the device introduced by DePaula (1992) with radiometric raw density determination on single positions (25 %, 50 %, and 75 % of the press opening distance) by means of ^{137}Cs radiation sources ($E_\gamma = 662\,keV$) and scintillation detectors in a 700 × 700 mm² laboratory press. Later, Gruchot (2009) develops a miniature densification unit installed in a Ag-target flat-beam X-ray scanner including capillary optics, which makes it possible to continuously observe the hot-pressing process over the total cross-section (only the lower half during densification).

Besides the RDP measurement vertically to the panel plane by any method, the horizontal density gradients are also determined, where particularly the area density distribution across the plane of the panel or furnish mat is evaluated with regard to the mat forming process. To this

end, inline X-ray devices for continuous measurements are more or less prevalent in the WBC industry (refer to Chapter I). However, Walter, Wiechmann (1961) perform first radiometric investigations of area density distributions within WBCs. Likewise, Polge, Lutz (1969) explore horizontal profiles via densitometric evaluation of X-ray films. Later, inline devices for industrial application were developed and installed, where not necessarily corresponding studies are published. However, Lu, Lam (1999) evaluate the horizontal density distribution and wood particle overlap in their robot formed flakeboards by means of a laboratory line array X-ray scanner. Furthermore, they point out that the applied calibration materials (aluminium and PMMA) have an effect on the obtained X-ray measuring results. Wang et al. (2005) examine the feasibility of X-ray systems application for NDE of density distribution in panels (MDF, PB, and OSB) utilising the 60 kVp laboratory scanner on 1.22 × 2.44 m² panels with final spatial resolution of 12.5 mm in comparison to gravimetric raw density determination on small specimens. They imply that the method has great potential for the desired application, but further research is required to improve the accuracy of the technique by enhancement of image resolution and scanning sensitivity as well as the calibration procedure considering the various WBCs. The Dieffensor – a fan-beam X-ray scanner for foreign body detection and area density distribution determination in the forming line commercially available from Fagus-GreCon Greten GmbH & Co. KG, Alfeld, Germany – is applied by Hilbers (2006) to investigate the impact of adhesive resin type and content as well as paraffin (hydrophobic agent) on area density measurement by means of respective laboratory panels. Based on the determined mass attenuation coefficients he concludes an apparent influence of PMDI content and type compared to the UF resins. Furthermore, Hilbers (2006) performs a field experiment in MDF production to evaluate the effect of modifications in the forming line on area density variation along and across the fibre mat. Likewise, Hilbers et al. (2011) examine the raw density distribution (assuming constant thickness for evaluation of X-ray data) of lab-made

MDF, PB, and OSB and the effect on air-coupled ultrasonic transmission. SANABRIA et al. (2013) apply such X-ray data to model and predict the raw density distribution based on ultrasonic measurements on lab-made PBs with different raw densities but homogenous (vertical) RDPs. CHEN et al. (2010) evaluate MDF, PB, OSB, and plywood horizontal density distribution employing a 60 kVp digital X-ray system with approx. 1.4 mm pixel pitch across the panel width and automatically adjusted sampling rates with synchronisation to the feed speed in order to obtain equivalent resolution in longitudinal direction. Image processing with calibration curves from aluminium plates (refer to Chapter II–3.3) as well as panel mass and thickness yields the raw density distributions. However, FUCHS (2010) proposes a new calibration method for traversing inline X-ray measuring systems on furnish mats in the forming line. Accordingly, the calibration should be performed on the equivalent furnish mat instead of previously common specimens of ready-pressed panels to obtain appropriate measuring accuracy. FUCHS (2010) found differences in radiation attenuation between a panel and the corresponding mat with equal area density. Finally, SOLBRIG et al. (2014b) evaluate an optimised X-ray measuring system for inline measurement of the furnish mat area density distribution regarding its capability for process and quality control in WBC production and propose related methods for measuring systems qualification to the requirements in WBC industry.

3.3   Calibration and attenuation coefficients

Regardless of former radiographic methods, densitometry devices for wood and WBCs are direct scanning systems, which require proper calibration in order to obtain repeatable and verifiable results as pointed out by MOSCHLER, DOUGAL (1988). To this end, they propose a calibration procedure for their gamma-ray device with a low ($E_\gamma = 5.9$ keV from ^{55}Fe) and a high ($E_\gamma = 59.5$ keV from ^{241}Am) radiation energy. Blocks of various wood species with a raw density range of $\rho \approx 300 \dots 900$ kg/m^3 (equilibrated to room

conditions) are scanned for determination of transmission intensity I_T at twelve evenly spaced positions and the mean raw density is individually determined via gravimetric method. With mean count rate and specimen thickness the linear attenuation coefficient μ_lin is computed following eq. (II-8). The results are correlated to ρ and the slope of the regression line yields the mass attenuation coefficient μ/ρ following eq. (II-9), which is applied for direct densitometry. In former film densitometry, it was common to simultaneously irradiate step wedges with known densities and thicknesses on each acquired X-ray image (cf. RUDMAN et al. (1969)). Later, KRUGLOWA et al. (2010) extend the approach and manufacture a calibration wedge out of 14 different wood species representing a raw density range of $\rho \approx 390 \dots 800$ kg/m^3 for in-situ assessment of timber structures. Calibration is performed on the basis of the grey-scale values, where no mass attenuation coefficients are evaluated. Note here, a portable pulsed 150 kVp X-ray tube and image plates (with a digitalisation system subsequent to exposure) are applied, which is still relevant in general NDT. However, step wedges were also applied for direct scanning X-ray densitometry and measured before each specimen measurement, e. g., by HOAG, KRAHMER (1991). For direct calibration on the basis of mass attenuation coefficient values, MEDVED et al. (1998) determine the mean $\overline{\mu/\rho}$ corresponding to the gravimetric mean raw density $\bar{\rho}$ by transmission measurements of PB specimens perpendicular to the panel plane with their gamma-ray RDP device, likewise already MAY et al. (1976). Obviously, for the general calibration procedure for densitometry on inhomogeneous material with various raw densities, where no universal densities and attenuation coefficients are tabulated, the attenuation law eq. (II-10) is applied and transformed in order to yield an individual mass attenuation coefficient μ/ρ on the basis of the gravimetrically determined raw density ρ of the specimen and corresponding transmission measurements with the ratio of the intensities $T = I_\mathrm{T}/I_0$ as result according to eq. (II-1). This is commonly performed such that the mean value $\overline{\mu/\rho}$ is computed as

constant of proportionality corresponding to assumed linear attenuation or the principle of step wedges is applied, where another fitting can be determined.

Nevertheless, most of the current (and even former) laboratory devices for direct RDP measurement perform the calibration automatically on each 50 × 50 mm² specimen taking account of its gravimetric raw density. The general context is illustrated in Figure II-14 and can be referred to as self-calibration, since no further action is required than the automated X-ray measurement and the gravimetrical raw density determination per specimen as regular part of the RDP measuring procedure. Here, the mean measured attenuation

$$\overline{\ln T^{-1}} = \frac{1}{n} \cdot \sum_{i=1}^{n} \ln\left(\frac{I_0}{I_{T_i}}\right) = \frac{1}{n} \cdot \sum_{i=1}^{n} \ln T_i^{-1} \qquad \text{(II-51)}$$

is computed as mean value of the logarithmic of reciprocal transmission $\ln T_i^{-1}$ with T_i following eq. (II-1) as relative transmission per measuring step i along the profile. Note, arithmetic averaging must take the logarithm $\ln T_i^{-1}$ into account, which is considered to follow a linear context, whereas a mean directly computed on the basis of the single transmission ratios T_i is found to yield minor deviations. Subsequently, the mean measured attenuation $\overline{\ln T^{-1}}$ [−] is related to the mean gravimetric raw density $\bar{\rho}_{grav}$ [kg/m³] and the transmission distance s_T [m] of the individual specimen such that the transformation of attenuation law eq. (II-11)

$$\overline{\mu/\rho} = \frac{\overline{\ln T^{-1}}}{\bar{\rho}_{grav} \cdot s_T} \qquad \text{(II-52)}$$

yields the mean mass attenuation coefficient $\overline{\mu/\rho}$ [m²/kg] for the specimen under investigation. On the contrary, GIBBON, TUNDAK (1989) describe a device, where calibration is carried out once for each category of material. They point out that calibration serves to yield appropriate raw density values, i. e., quantitatively correct results, whereas the RDP shape is considered not to be affected by calibration, i. e., the qualitative shape is always correct. However, the growing requirements in modern WBC research and in-
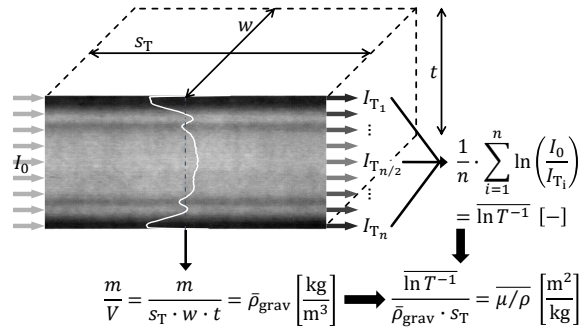
Figure II-14: Illustration of the common self-calibration for RDP measurement with determination of a mean mass attenuation coefficient $\overline{\mu/\rho}$ according to eq. (II-52) based on the mean measured attenuation $\overline{\ln T^{-1}}$ according to eq. (II-51) and the mean gravimetric raw density $\bar{\rho}_{grav}$ of the specimen.

dustry must consequently have reliable densitometry results from the applied measuring devices.

Obviously, the studies on WBC calibration and the procedures of the practice-oriented devices preferably take only one $\overline{\mu/\rho}$ value for a certain measuring range into account, where it is considered to be (more or less) constant. Nevertheless, the aforementioned non-linearities from beam hardening, scattering, and detector phenomena are supposed to bias the slope of measured density gradients in consequence of non-linear radiation attenuation along increasing density or material layer thickness. Already STEINER et al. (1978) found a curvilinear relationship between cross-sectional specimen raw density (waferboard) and X-ray film blackening in terms of their calibration with a waferboard step wedge. GRUCHOT (2009) applies lab-made MDF with homogenous RDPs to manufacture specimens with transmission distances $s_T = 5 \dots 70$ mm and 5 mm increments for calibration measurements at four different moisture conditions, i. e., step wedges with correspondingly nominal $\rho = 90 \dots 1260$ kg/m³ at virtually equal $s_T = 50$ mm. The evaluation of the acquired data yields a second-degree polynomial fitting for each MC level, which are further combined with a function for MC dependent μ/ρ following the mixture rule to finaly obtain a calibration function considering both the raw density and moisture dependency of μ/ρ. It is applied for in-situ meas-

urement of the RDP formation during hot-pressing of MDF. For area density calibration on furnish mats, FUCHS (2010) fits a function with up to 20 sampling points of increasing area density ρ_A to consider beam hardening effects and points out that different adhesive resins (UF, PMDI) have a minor influence on the calibration in contrast to additives like fire retardants. For the application of a single mean mass attenuation coefficient $\overline{\mu/\rho}$ by the common RDP lab devices, insufficiencies are observed by SOLBRIG et al. (2011) on WBCs and likewise reported by RAUTKARI et al. (2011), where the RDPs are found to be flattened in general owing to the invalid single $\overline{\mu/\rho}$ along the raw density range. Accordingly, SOLBRIG et al. (2011) and also SOLBRIG (2012) propose to apply individual calibration functions as second-degree polynomial fitting for μ/ρ over the measuring signal from conditioned MDF step wedges considering the moisture content.

Densitometry by X- or gamma-rays requires calibration and, therefore, mass attenuation coefficients μ/ρ by either form of determination method to solve the attenuation law eq. (II-10) for the raw density ρ or eq. (II-11) for the area density ρ_A, respectively, based on the acquired transmission measuring data. Here, only a few values are explicitly given for WBCs in the literature mostly as part of RDP measuring studies. Regardless of experimental values from transmission measurements, which are discussed below, theoretical mass attenuation coefficients $\mu/\rho\,(E)_{\mathrm{mix}}$ of a compound with known elemental composition can be computed via the mixture rule as clarified in Chapter II–2.3. However, the suitability of such values for calibration requires comprehensive knowledge of the individual radiation conditions of the applied densitometry device and becomes more complicated in the case of polychromatic X-rays due to radiation-physical effects such as beam hardening. Hence, the application of $\mu/\rho\,(E)_{\mathrm{mix}}$ for calibration purpose of X-ray densitometry devices appears questionable at all. However, LINDGREN (1991) computes linear attenuation coefficients and CT-numbers for dry and wet wood. The data is applied as calibration for wood raw density measurement by

means of a medical CT scanner, where an accuracy of ± 4 kg/m^3 for dry wood and ± 13.4 kg/m^3 for wet wood is claimed to be obtained as already discussed in Chapter II–2.3.3. Note here, no particular WBC densitometry studies are known, where theoretical $\mu/\rho\,(E)_{\mathrm{mix}}$ values are utilised for calibration.

Most of the former experimental μ/ρ data was measured by means of devices employing an ^{241}Am radioisotope source with (monochromatic) $E_\gamma = 59.5$ keV. Likewise, the computed values via mixture rule in Table II-3 correspond to this energy level, where not many explicit WBC values are available. However, for particleboard, MAY et al. (1976) experimentally determine $\mu/\rho = 0.0172$ m^2/kg (via transmission measurements perpendicular to the panel plane) and RANTA, MAY (1978) apply the measured $\mu/\rho = 0.0189$ m^2/kg for all RDP investigations as calibration. LAUFENBERG (1986) determines experimental values of oven-dry material in comparison to corresponding computation data (Table II-3). For solid wood, the measurement results in $\mu/\rho = 0.0182$ m^2/kg (red oak) and $\mu/\rho = 0.0183$ m^2/kg (douglas-fir). MACEDO et al. (2002) perform wood raw density determination by means of X- and gamma-ray CT at different energies, where a range of $\mu/\rho = 0.0173 \ldots 0.0193$ m^2/kg is measured by means of an ^{241}Am source and a NaI(Tl) scintillation detector over eight species with the mean $\overline{\mu/\rho} = 0.0180$ m^2/kg. Although they conclude the data not to show a significant variation, a slight trend of increasing μ/ρ with decreasing raw density is obviously identifiable. For adhesive resins, LAUFENBERG (1986) determines $\mu/\rho = 0.0186$ m^2/kg (PF), $\mu/\rho = 0.0189$ m^2/kg (UF), and $\mu/\rho = 0.0179$ m^2/kg (PMDI). Likewise, RANTA, MAY (1978) measure resin values with $\mu/\rho = 0.0189$ m^2/kg (UF) and $\mu/\rho = 0.0186$ m^2/kg (PF). Obviously, all values measured by means of ^{241}Am setups are in a comparable order considering both wood and adhesive resins. Further WBC μ/ρ measuring data is only available for other (polychromatic) energy levels, since radioisotopes are preferably replaced by X-ray tubes in current devices. Note here, the validity of the μ/ρ values may be vaguer depending

how detailed the X-ray setup including pre-filters and its consequent energy parameters are described whereas radioisotope applications yield attenuation data for discrete energies. However, HILBERS (2006) provides no detailed X-ray specifications for the performed area density measurements by means of the aforementioned Diefensor. The determined range of $\mu/\rho = 0.03475 \dots 0.0352$ m^2/kg for lab-made MDF is found to apparently depend on the applied adhesive resin type with differences between PMDI- as well as UF-bonded panels and no considerable impact of paraffin, melamine, and water content. GRUCHOT (2009) applies the same Ag-target device like SOLBRIG et al. (2010) including capillary optics (without further pre-filter) and diode line-array detector at 55 kVp and determines $\mu/\rho = 0.048 \dots 0.055$ m^2/kg for the MC range below FSP measured on lab-made MDF with varying transmission distances s_T. Employing the same X-ray setup, SOLBRIG et al. (2011) present a comparable range of $\mu/\rho = 0.043 \dots 0.072$ m^2/kg for MDF (industrial origin) measured by means of step wedges. The data unveils non-constant values over the measuring range, where μ/ρ decreases with increasing raw density (i. e. area density due to virtually equivalent thickness of the steps s_T). Moreover, FUCHS (2010) found different μ/ρ values for fibre mats and MDF with equal area density. Obviously and as already discussed in Chapter II–2.3.3, μ/ρ values correspond to the respective study and depend on the individual conditions of both

- the measuring setup regarding radiation properties and beam parameters as well as
- the material considering its composition and structure.

Accordingly, there are no generally valid values of the energy dependent mass attenuation coefficient $\mu/\rho\,(E)$ for WBCs. Therefore, the commercially available X-ray densitometry systems come with individual calibrations and corresponding procedures of the manufacturers, where the self-calibration (Figure II-14) is commonly applied for RDP determination by means of laboratory devices.

However, regarding the calibration procedures and approaches, also questionable studies exist.

GUAN et al. (2001) regard specimen orientation in terms of radial, tangential, and longitudinal wood direction and the corresponding scanning direction to have a considerable effect on the calibration. Their measurements for verification of the theoretical considerations obviously reveal raw density variations between and within the annual rings as well as the applied aperture size (cf. MOSCHLER JR, WINISTORFER (1990)) as reason for the deviations between the determined μ/ρ values rather than the wood grain direction. For the analysis of WBC horizontal raw density distribution, CHEN et al. (2010) acquire calibration curves by means of aluminium plates (0…4 layers), which are considered to yield equivalent attenuation like the wood material applying a non-linear curve fitting algorithm. However, they regard their procedure as appropriate with periodical verification of adequate accuracy of about 1.5…2.7 % via comparison of the X-ray scan of a panel with its gravimetric reference results from cutting respective specimens. Nevertheless, aluminium $_{13}$Al instead of wood as calibration material for WBC densitometry must obviously be considered to reveal different attenuation characteristics in the applied energy range up to 60 keV owing to the different scattering fraction as attenuation mechanism, where reference is made to the comparison of carbon $_6$C and copper $_{29}$Cu in Figure II-3 as well as corresponding Al data in Figure VII-33. KIM et al. (2013) derive an equation for a specimen thickness dependent μ/ρ on the basis of their CT data, in order to convert the very same into density results, i. e., a kind of calibration. They attribute decreasing μ/ρ along the penetration path to scattering phenomena without consideration of obviously present beam hardening in the applied energy range up to 37 keV. KIM et al. (2014) apply the same approach and claim to yield an error of 41 kg/m³. Eventually, the calibration procedure and the individually found context may yield appropriate results in the respective study but cannot be considered to be generally valid.

Beyond device calibration procedures and mass attenuation coefficients for RDP measurements partly considering varying moisture content (MC) of the specimens, the determination of the moisture distribution in the WBC or wood material is

examined via X-ray densitometry to some extent. BAETTIG et al. (2006) determined MC profiles in Norway spruce boards during drying in a laboratory kiln for 5…10 days with X-ray scans every 30 minutes and perform differential data evaluation by means of the measured μ/ρ of the oven-dry wood and water. Likewise, CAI (2008) computes MC gradients along the board thickness for three wood species via the difference between raw density profiles from measurements at moist and oven-dry conditions (employing a commercially available RDP measuring device). Such differential methods are common to accomplish MC (profile) determination via X-ray densitometry on wood (cf. WATANABE et al. (2008), TANAKA et al. (2009)) as well as on WBCs (cf. MEDVED et al. (1998), XU et al. (1996)) and also via CT (cf. HANSSON, CHEREPANOVA (2012), LI et al. (2016)). Note, data evaluation must consider the specimen shrinkage during drying below FSP. Besides the oven-dry state, also other conditions with known EMC are partly applied as reference for the calculation. TIITTA (2006) explores different NDT methods with particular focus on the measurement of moisture gradients, where TIITTA et al. (1993) present an automated gamma-ray equipment (^{241}Am) for the measurement of moisture and raw density distributions in wood also via difference of the attenuation coefficients between moist and dry state with the concluded disadvantage that the specimens must be dried in order to measure the oven-dry raw density distribution, which is required to estimate the absolute MC. Other procedures evaluate MC variations from density changes determined via CT scanning during drying by means of respectively developed algorithms (cf. LINDGREN (1992), WIBERG, MORÉN (1999)). PERRE, THIERCELIN (2004) apply wedges of air-dry wood (sorbus torminalis due to its homogeneity) and water (within sheets of Mylar film) to determine the attenuation depending on material layer thickness. However, JENSEN et al. (2002) point out that simultaneous assessment of MC and ρ is sensitve toward small variations in the setup due to the chemical similarity of wood and water. For in-situ investigations of dynamic processes in WBCs or wood such as the RDP formation and water vapour movement

during hot-pressing or moisture sorption with swelling and shrinkage in general, the differential evaluation may not be feasible due to successive variation of the local raw density and the overall geometrical conditions (e. g. lateral expansion), i. e., moisture and wood matter variation processes are superimposed. Here, GRUCHOT (2009) was not able to provide a clear discrimination between the movement of wood matter and water in his in-situ investigations of the MDF hot-pressing process. For the examination of such superimposed processes, SOLBRIG et al. (2015c) propose the application of neutron radiography in WBC research, which may be utilised as quantitative method and combined with other techniques such as X-ray densitometry. Here, neutron radiation in comparison to X-rays yields considerably higher contrast between water and wood matter due to the high cross-section of the element hydrogen $_1$H (cf. MANNES et al. (2009), LANVERMANN et al. (2014b)), which is even applicable to large wooden objects by means of fission neutrons (cf. OSTERLOH et al. (2008)).

Obviously, the radiation attenuation potential of wood matter and water for X- or gamma-rays is in a similar order. The like applies to organic adhesive resins as shown above by means of the exemplary mass attenuation coefficients for UF, PF, and PMDI. However, the low contrast between the WBC constituents and water was always an issue in examinations aiming at the discrimination of the very same or in respective structural investigations. In medical applications, contrast agents such as iodine are utilised, where no sufficient contrast can be obtained between similarly attenuating human tissues (cf. NAGEL (2003), HERTRICH (2005)). Likewise, contrast agents as particles or solutions can support special imaging or measuring tasks in technical X-ray applications. WANG et al. (2007) utilise chemically inert gold particles to improve the imaging contrast between the constituents of wood plastic composites, to explore the inner structure, deformation, and damage accumulation of the final material under load or other environmental conditions. LI et al. (2016) apply $CsCl$ with 2.5 % concentration in demineralised water for absorption analysis in MDF and OSB and point out similar penetration behaviour of the solution

like pure water. Nevertheless, the particle size (molecules, ions) of the contrast agent must fundamentally be considered in comparison to pore sizes and potential interaction with the wood matter, which may bias the regular sorption characteristics. In their CT investigations of wood-adhesive bondlines, PARIS et al. (2015) found customary adhesive-resin polymers to have similar chemical characteristics and density compared to wood cell-wall polymers and consequently apply iodine as contrast agent in the adhesive recipe. VAZIRI et al. (2011) measure the weld line density between wood specimens welded together via linear vibration welding, where no adhesive is applied and no contrast agent may be injected. However, contrast agents are not yet very common in WBC research by means of X-rays but may enhance the distinguishability between the constituents of WBCs as well as water whereas their impact on the investigated characteristics must be considered.

Besides wood and conventional WBCs, other lignocellulosic material as well as respective composites are researched regarding their raw density properties in terms of material testing and product development. Here, neither coniferous nor deciduous wood but bamboo, palm wood or annual plants are utilised. RDPs are determined by SCHEFFLER, BLÜTHGEN (2017) within the culm wall of different bamboo species and by KRÖCKEL (2017) on panels made of bamboo scrimber. Bark is also applied for panel manufacturing in the laboratory, where GÜNTHER et al. (2015) analyse the inner structure of wood bark insulation boards by means of CT regarding the distribution of bark components with different raw densities. The raw density distribution of biomass pellets is investigated by TENORIO et al. (2015) via 7 kVp X-ray imaging and densitometry for RDP determination in both longitudinal and transversal direction of the pellets made of different lignocellulosic material (i. e. wood and agricultural crops). Besides organic adhesive applications, cement-bonded particleboards are industrially produced and further investigated, where DIRESKE et al. (2017) evaluate appropriate measuring conditions and accuracy for this rather highly-attenuating composite. Note here,

such lignocellulosic raw material and the corresponding composites differ in the elemental composition from clean (European) wood species particularly considering the mineral content, which is comprehensively discussed in Chapter IV–2.3.2.

Beyond wooden or more generally lignocellulosic raw material, similar studies regarding radiometric density determination on comparable low-Z, polymeric, and partly porous materials exist. KOTWALIWALE et al. (2007) utilise 22 layers of polystyrene sheets with consequently $s_\mathrm{T} = 0.08 \ldots 6.03$ mm in order to predict the μ/ρ via X-ray imaging at 15…50 kVp, where the calibration material is considered to be similar to the biological material under investigation regarding ρ and Z. DU PLESSIS et al. (2013) propose a calibration method for X-ray CT on polymeric low-Z materials, where a linear function is fitted between the average CT grey values and the corresponding range of actual density values ($\rho \approx 900 \ldots 2200$ kg/m^3). They regard, nevertheless, differences in chemical composition of the measured compared to the calibration material as reason for deviations between experimental and actual density values. SINKA et al. (2004) consider non-linearity effects from beam hardening and scattering (refer to Chapter II–2.4.4 and II–2.5.4) in their calibration for the determination of density distributions in tablets by means of X-ray CT at 40 kVp. The tables were manufactured using microcrystalline cellulose powder with 100 μm particle size and 1520 kg/m^3 solid matter density, which is pressed under different conditions resulting in tablet raw densities ranging from 1189…1221 kg/m^3. Obviously, other porous objects are similarly investigated like WBCs, where the densification is relevant for the final product properties.

X-ray densitometry on wood and WBCs of common sizes is mainly performed in an energy range, which is similar to medical applications. Moreover, the two different sectors feature comparable requirements such as to obtain appropriate imaging or measuring contrast within similarly attenuating material or tissue as well as water. For both imaging and measuring purposes, X-ray applications on WBCs may be considered to correspond to medical applications rather than

to common X-ray NDT predominantly on metal samples, i. e. coarse structure analyses such as qualitative imaging investigation of weldings or castings regarding processing failures. Beyond diagnostic radiology, i.e., medical X-ray imaging, also densitometry applications exist particularly with measurements of the bone density (cf. HUDDLESTON (1988)) but also considering soft tissue and the accuracy of CT values in dependence on beam hardening (cf. SCHMITT et al. (1987)). Z_{eff} considerations are common in the context of phantom material selection, i. e., tissue substitutes, (cf. SINGH et al. (2014a)). Here, even wood and WBCs are evaluated by BANJADE et al. (2001) and MARASHDEH et al. (2015), respectively as already discussed in Chapter II–2.2.4. The latter examine the radiation-physical properties of mangrove wood PB and MARASHDEH et al. (2012) measure RDPs of the manufactured specimens. MARASHDEH et al. (2015) discuss their results in comparison to breast tissue, which is comparable to (moist) WBC matter regarding its Z_{eff} (cf. TAYLOR et al. (2012)) and, therefore, its attenuation potential, but shows increased hydrogen mass fraction $\omega(\text{H})$, which is well-known to be relevant regarding scattering. Eventually, mammography deals with corresponding methodical issues like WBC densitometry considering the low radiometric contrast between the structural members with similar elemental compositions. Hence, the research in such medical applications is considered to provide appropriate approaches adaptable to densitometry on WBCs.

3.4   Concluding remarks

Comprehensive reports on the early developments of techniques and procedures for wood densitometry as well as RDP determination on WBCs by means of X- and gamma-rays exist in the literature. Likewise, X-ray CT applications for structural investigations have been comprehensively examined, however, with a focus on imaging rather than densitometry. Moreover, modern CT research investigates and implements special technologies, which are increasingly available due to the general technical progress and en-

able further insights such as phase contrast imaging (cf. ALS-NIELSEN, MCMORROW (2011)), where, e. g., DEROME et al. (2011) utilise the method for the CT investigation of wood swelling hysteresis at the cellular scale. PLANK et al. (2017) report on 4D-XCT applications, where the time domain is implemented in CT data evaluation and, e. g., in-situ investigations become feasible with 3D information. Regarding conventional X-ray densitometry in WBC industry and science, however, there is a certain lack of investigations considering the development and evaluation of existing recent improvements and few corresponding scientific studies are available. However, general insufficiencies were observed in the measuring practice in WBC industry and also unveiled in terms of preliminary investigations. Obviously, the effects of the former replacement of radioisotopes by X-ray tubes as well as beam hardening and further radiation-physical phenomena, which are well-known to cause non-linearities in the measuring results, were not holistically considered. Thus, previous and current X-ray densitometry devices may yield more or less accurate results under certain conditions in a limited range. Their radiation-physical design appears, nevertheless, questionable to some extent.

Fundamental investigations of the X-ray transmission measuring methodology and its results on wood and WBCs are rare. LIU et al. (1988) confirm the area density ρ_A to be a "[…] significant parameter that determines the degree of attenuation." Furthermore, they clarify "good-architecture" conditions for densitometry on wood to comprise

- linear source-absorber-detector alignment with vertical radiation incidence,
- convergent, narrow collimated beam (prior and behind absorber),
- absorber of uniform thickness, and
- monochromatic radiation with optimal energy (according to OLSON et al. (1988)),

where radiation attenuation is described by exponential intensity diminution following Beer's law eq. (II-10). In applied radiometric WBC investigations and common densitometry by

means of X-rays, these conditions cannot be reasonably met in any case.

Beyond the measuring architecture, the application range regarding the area density of the material under investigation is relevant in order to obtain ideal attenuation conditions. From the aforementioned theoretical wood densitometry and some further studies a range of "ideal transmission" around $T = 1/e$ becomes obvious, which is henceforth considered to provide appropriate measuring conditions. Nevertheless, WBCs are inhomogeneous and porous low-Z material, which features partly considerable raw density differences

- between the various panel types,
- within one panel as vertical RDP or
- between the processing steps due to densification of the furnish mat to the final panel.

Finally, all these conditions must be considered for X-ray densitometry on WBCs and need consequently to be investigated in order to yield reliable and valid measuring results.

In the field of X-ray measurements on wood-based composites (WBCs), general insufficiencies are empirically known and were unveiled via preliminary investigations for the present thesis. Obviously, technological improvements are required regarding design and pre-setting of previous X-ray densitometry devices. In addition, increasing requirements in WBC production have generated a practice-oriented demand to also increase the accuracy (as well as precision) and to make the X-ray measuring systems adaptable to the particular requirements of the application, i. e., the specific measuring tasks. Moreover, regarding the actual influence of varying material compositions on densitometry results depending on, e. g., type, wood species, glue liquor, and moisture content, some proposals exist but a fundamental study is lacking. Past studies, however, have focused on the exclusive application of more or less established nondestructive testing (NDT) methods rather than on fundamental considerations. Because X-ray spectra govern radiation attenuation in the material under investigation, particularly the consideration of poly-chromatic radiation character with explicit determination of transmission spectra from varying WBCs is still pending. The complex relationship between material and radiation parameters and their impact on measuring results has yet to be holistically explored. Fundamentally, a well-known connection exists between the attenuation of ionising radiation and the density of the irradiated material, where this proportionality serves as the basis for density measurement (referred to as densitometry). Considering the attenuation of polychromatic X-rays in porous and inhomogeneous low-Z matter, however, radiation-physical effects occur, which are considered to bias the basically linear context, and thus to yield biased densitometry results under certain conditions. Note, the impact of

- X-ray setup and beam geometry,
- radiation spectrum and beam hardening,

- scattering and radiation build-up, as well as
- material type and composition

is generally known for X-ray transmission measurements. Their explicit impact and, furthermore, their interdependencies with respect to WBCs have, however, yet to be comprehensively described.

The aim of the present thesis is to investigate the context of material and radiation aspects, which are considered to be relevant for X-ray densitometry on WBCs. Therefore, an interdisciplinary approach in the field of NDT on wood and WBCs is followed. To this end, the detailed objectives are to combine both

- fundamental investigations and analyses including their critical discussion to characterise the applied material regarding relevant properties for interaction with ionising radiation and
- experimental as well as theoretical investigation of interaction of X-rays with the characterised matter.

Accordingly, a fundamental but practice-oriented contribution is provided as scientific basis for required improvements. The focus is on the development of approaches used to describe the irradiation conditions by means of the employed X-ray transmission setups. Implications on appropriate X-ray parameters for densitometry on WBCs are provided. However, no explicit improvements of the utilised X-ray devices are performed.

First, the utilised material is described. The same set of lab-made MDF and furnish mats (fibres and particles) as well as the same customary industrial panels are utilised throughout the study. The aim is to yield a more or less comprehensive data set for the applied material. To this end, analytical investigations are subsequently performed, i. e.,

- determination of solid matter density (true density) and porosity,
- characterisation of furnish morphology, and
- analysis of elemental composition complete with ash content.

Based on fundamental knowledge and particularly supported by the analysis data, an empirical radiation transmission concept through inhomogeneous and porous low-Z composites, i. e., WBCs, is developed from the radiation beam's point of view on distinct scales. A round robin test of raw density profile (RDP) measurement on customary industrial WBCs is included in this thesis as an initial part of the main X-ray investigations to verify the proposition of erroneous RDP measuring results. X-ray measurements are performed by means of different setups, which basically correspond to current devices as applied in WBC industry and research. The investigations comprise both

- more or less regular X-ray transmission measurements to evaluate radiation attenuation in dependence of material and radiation parameters as well as
- X-ray spectra determinations with modified setups, where the detectors are replaced by a spectrometer.

The latter measurements are furthermore completed with corresponding simulations of the spectra. Beyond measurements and due to the lack of fundamental studies on the attenuation of polychromatic radiation in WBCs, comprehensive theoretical investigations are performed with computations considering

- an effective atomic number Z_{eff} and particularly
- the energy-dependent mass-fraction-weighted total mean mass attenuation coefficients $\mu/\rho\,(E)_{\text{mix}}$ via mixture rule

employing the determined elemental compositions with subsequent evaluation of the computation results and virtual variation of the compositions to explore the boundary conditions. The computation results are consequently compared to corresponding measuring values of the mean mass attenuation coefficient μ/ρ. Ultimately, all results from measurements and theoretical considerations are combined to show the impact of

beam hardening, scattering, and radiation energy on the X-ray densitometry on WBCs and to draw further conclusions on their radiation-physical interdependencies complete with material parameters, i. e., composition and structure of WBCs. Finally, an enhanced law of attenuation is deduced in order to provide an appropriate radiation-physical description for radiation transmission through WBCs and related material with regard to the applied broad-beam X-ray attenuation. The thesis closes with final implications and prospects considering the methods and applications of X-ray densitometry on WBCs.

Note, the thesis focuses on the examination of X-ray transmission through WBCs. To this end, no extensive measuring series but rather exploratory tests are performed to conclude the complex relations to a central approach, which needs, in turn, to be verified with subsequent test series. Among others, MDF is preferably utilised in such fundamental investigations because it is the most homogenous WBC and has further advantageous properties. Regarding adhesive resins, there is a further focus on urea-formaldehyde-based systems (UF) owing to their major commercial relevance. Beyond various radiation parameters for the X-ray measurements, no variation or independent evaluation of the detector characteristics are carried out, which is, however, instead considered to be an existing part of the setups. For statistical considerations, tests on the distribution type are deliberately omitted and preferably robust methods are applied, i. e., nonparametric tests, due to the partly small sample sizes and the exploratory character of this study. Ultimately, regarding the radiation-physical effects on densitometry, no existing correction methods, e. g., from medical or technical computed tomography (CT), are applied, since the present thesis aims to provide a fundamental investigation of the radiation-physical phenomena and to deduce practice-oriented conclusions for X-ray densitometry on WBCs.

1   Material

1.1   Lab-made furnish mats

Among others, common X-ray measuring applications in WBC production are to be found in the forming line on the pre-compressed furnish mat (refer to Figure I-1, after section C). Hence, respective furnish mats were manufactured with predefined parameters in the laboratory to make such material available for various X-ray measurements and further examinations. To distinguish the furnish mats based on their particle types, the term fibre mats exclusively refers to MDF and the term particle mats to PB, respectively. Thermomechanical pulp (TMP) fibrous material was provided originating from a Central European panel manufacturer primarily made of softwood (labelled TMP-F, different from Chapter IV–1.2). Further information regarding wood species composition or outward transfer, however, is not explicitly detailed. For particle mats, both surface (SL) and core layer (CL) particles with undefined wood species composition were drawn out prior to the blender resination from a Scandinavian particleboard production line during manufacturing of regular 16 mm panels. However, the size of all particle types is analysed in Chapter IV–2.2. Mats of resin-unblended particles were manually formed in boxes whose dimensions do not disturb the respective beam paths. Homogeneous lateral material spread was considered via mat height and manual pre-pressing – in the case of SL particles by means of a parallel aligned and vibrating force plug as shown in the setup in Figure IV-1. Even material distribution is also challenging during fibre mat forming whereas mechanical homogenisation is less feasible at this scale. Additionally, varyingly strong mat springback makes it difficult to obtain constant mat thickness along samples of the same area density. Notwithstanding that, han-

dling of only loosely formed furnish mats complicates the reproducibility of both radiometric and gravimetric measuring results. Any method and condition variation on one and the same sample seems unachievable. To enable a comprehensive study of radiation attenuation behaviour in specifically pre-densified wood-particle-resin-matrices, cured furnish mats were produced with a predefined composition, area density, and equilibrium moisture content. Consolidation ratio and subsequent mat raw density were empirically adapted to individual practice-oriented conditions after cold pre-press (refer to Figure I-1) aiming at raw densities ρ listed in Table IV-1 at finally 9 % MC.
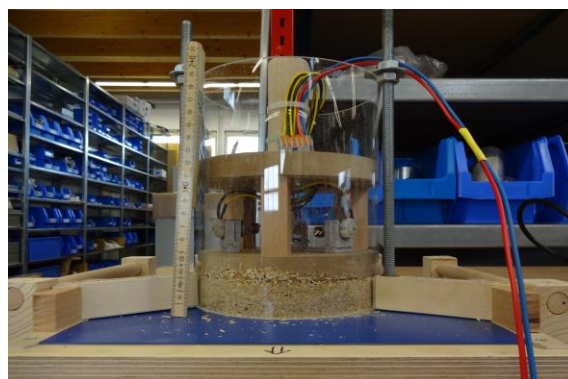
Figure IV-1: Setup for forming and measuring of particle mats (here SL particles) on actual forming belt (dark blue bottom cover) including parallel aligned and vibrating force plug within PMMA cylinder (inner diameter 172 mm).

furnish particles	ρ_A [kg/m^2]	ρ [kg/m^3]	t [mm]	quantity [pc.]
fibres	1	125	8	9
fibres	2	125	16	16
SL	1	300	3.3	6
CL	2	200	10	13

Table IV-1: Target parameters of the lab-made cured furnish mats at $MC = 9$ %.

Furnish material was blended per type with urea-formaldehyde adhesive resin (resin content on dry furnish mass basis $\omega(\mathrm{UF})_{\mathrm{OD}} = 10\,\%$, type UF2, refer to Table IV-3), 1 % hardener (40 % ammonium sulphate solution), and additional water (15 % target MC) without the use of further additives like hydrophobing agents in the glue liquor individually considering the actual furnish MC. Resination was carried out using a two-media nozzle with 1.5 bar atomisation pressure in a rotating drum with $n = 50\,\mathrm{min}^{-1}$. In the case of fibres, post-blending time was minimised to avoid felted agglomerations and both dry and blended material was fluffed pneumatically. Gravimetrical dosing and homogeneous mat forming was directly performed within steel cylinders (inner diameter 174 mm) with subsequent isochoric consolidation therein according to target parameters in Table IV-1. Considering laterally bounding cylinder walls, respective mat expansion during pressing and corresponding density drop-off toward mat edges is not expected to occur. All furnish mats fixed in this manner by round blanks of steel on both faces (with parchment paper in between) were stored in an air-circulating furnace at $\vartheta_{\mathrm{furnace}} \approx 110\,°\mathrm{C}$ for 50 min (1 kg/m²) and 60 min (2 kg/m²), respectively, for resin curing. Durations originate from preliminary tests considering resin curing time. For exemplary photographs of the densification setup, reference is made to Appendix VII–1.1. Note, the presence of cured resin instead of typically blended furnish by raw glue liquor is assumed to have a negligible influence on the total elemental composition at the same MC and final radiation attenuation considering X-ray measurements in Chapter IV–4.3.2.2, where these specimen are exclusively used for. Because cured mat disk diameter serves as intended specimen size, no further sample processing was necessary.

Figure IV-2 shows the final mat disks made of TMP fibres (top and middle, henceforth labelled Fmat), SL (middle, SLmat), and CL (bottom, CLmat) particles. Due to cold compression, slow through-heating, and consequently uniform plas-ticisation, homogeneous vertical RDP was intended. However, the RDP actually obtained differs significantly from the aim as exemplarily shown in Figure IV-3. Corresponding to the considerable raw density drop-off toward lower surface ($t = 15\,\mathrm{mm}$), the face appears

- wavy,
- concave,
- manually more compressible, i. e. softer, and
- coarse with more teared out fibres

compared to the upper one which is more compact and smooth but not as consolidated as a ready-pressed panel. At the edge, the region around $\rho_{\max}$ at $t \approx 12\,\mathrm{mm}$ is less compressible than the surrounding but no distinct differences regarding to densification are visible. This is caused by interdependent reasons. During fibre mat forming, fine (and potentially worse resin-blended) material trickles down leading to worse internal bond of lower surface layer. The effect of poor surface soundness is emphasised by faster heating and subsequently earlier curing and, in turn, earlier cracking (thermally-induced hydrolysis) of resin. Consequently, poor bonding quality results in considerable spring-back and loosening of fibrous material within the lower surface. During un-heated fibre mat consolidation to target thickness within the steel cylinder, air exhaust was only enabled at the upper face through the gap between the steel blank and inner pipe wall. Thus, higher densification occurs in the upper surface layer. However, the phenomenon is similar to real scale WBC production where especially fibre mats are considered actually not to reveal a homogeneous densification profile[19] after cold pre-pressing. Here, furnish mats are transported by an air-impermeable forming belt (e. g. made of mesh coated with thermoplastic polyurethane) whereas the upper permeable mesh belt enables air exhaust. Beyond furnish mat manufacturing, considerable fibre material tear outs can be observed at lower surface edges during specimen cutting (50 × 50 mm² for RDP measurement) by circular saw. Nevertheless, no RDP measurements were

---

[19] Refer to the respective remark in Figure I-1 (section C), where the considered vertical bulk density profile of the furnish mat was, however, not explicitly examined so far.

Figure IV-3: Exemplary vertical RDPs of the cured 2 kg/m² fibre mats (Fmat2) measured by the Ag-target RDP device (Chapter IV–4.2.2) at standard conditions 20 °C/65 % RH with the mean profile calculated from four single measurements (specimens 1…4), all single charts aligned at upper surface ($t = 0$).

1.2 Lab-made homogeneous fibreboards

Predefined material for X-ray measurements and further investigations is likewise required as ready-pressed panels in addition to the furnish mats (Chapter IV–1.1) whereas laboratory manufacturing is, however, limited to MDF. As distinction from customary industrial MDF, the abbreviation labMDF is introduced for the lab-made homogeneous fibreboards described hereafter. Despite partially manufactured mean panel raw densities $\bar{\rho} > 850 \ \mathrm{kg/m^2}$, lab-made panels are referred to as MDF nominally on all raw density levels without distinction between MDF and HDF. Fibreboards are exclusively utilised as lab-made means of choice because of the respectively highest obtainable homogeneity and consequently lowest property standard deviation amongst all WBC types. Thus, MDF allows reduced sets of samples in general and their application for exploratory studies such as the present one.

All manufactured panels (Figure IV-4) follow a well-defined pattern of raw density ρ, thickness t, and, consequently, area density ρ_A in mutual relation (multiplier $13/8$) as obvious from Table IV-2. Accordingly, samples with equal ρ_A and varying densification ratios are obtained covering a practise-oriented range. Predefinition of sample variation is based on the kernel element with $t = 19 \ \mathrm{mm}$ and $\bar{\rho} = 650 \ \mathrm{kg/m^3}$ more or less

Figure IV-2: Final lab-made furnish mats as cured disk-shaped bodies made of resin-blended TMP fibres (top and middle, henceforth labelled Fmat), SL (middle, SLmat), and CL (bottom, CLmat) particles.

carried out on the fragile particle mats where specimen preparation was not feasible. Actual moisture and density parameters of all furnish mat samples are presented in Table IV-5 in Chapter IV–1.5.

Figure IV-4: Lab-made MDF (labMDF) specimens with the nominal dimensions of $50 \times 50 \times t_{\mathrm{panel}}$ mm^3 as set of all manufactured types according to Table IV-2 (further photographs in Appendinx VII–1.1).

ρ	t [mm]			
[kg/m^3]	11.7	19	30.9	
400	4.7	7.6	12.4	
650	7.6	12.4	20.1	ρ_{A}
1056	12.4	20.1	32.6	[kg/m^2]

Table IV-2: Target parameters of the lab-made homogeneous MDF (without sanding allowance) at EMC at 20 °C/65 % RH in mutual relation (multiplier 13/8) with equal area densities ρ_{A} along the upward diagonals.

representing the most common panels MDF and PB regarding to t, ρ, and ρ_{A}, whereas no distinct vertical RDP is intended. Quantity is kept to one panel per modification because of elaborate manufacturing as follows and rather small required specimen sizes. However, the applied nondestructive methods enable repeated measurements on one and the same specimen. To obtain monolithic matter for irradiative purposes in terms of a specifically densified wood-particle-resin-matrix of more or less precisely known composition, homogeneous panels without raw density gradients in any direction are required. Manufacturing of such panels is only feasible on a lab scale with particular pressing process considerations.

TMP fibres primarily made of softwood (labelled TMP-H, different from Chapter IV–1.1) were provided as dry raw material. Despite their origin from a Central European panel manufacturer, no further information regarding wood species composition or outward transfer is available. However, fibre size is analysed in Chapter IV–2.2. For panel manufacturing, fibres were blended batch-wise with urea-formaldehyde adhesive resin (resin content on dry furnish mass basis $\omega(\mathrm{UF})_{\mathrm{OD}} = 10$ %, type UF1, refer to Table IV-3) and additional water (12 % target MC) in the glue liquor without the use of further additives like hydrophobing agents considering actual fibre MC of the respective batch. In this case, adhesive resin type did not require additional hardener. Batch-wise resination was carried out unsing a two-media nozzle with 1.7 bar atomisation and

0.5 bar liquid pressure in a horizontal plough-share blender ($n = 66\ \mathrm{min}^{-1}$) with an additional radially aligned chopper (Gebrüder Lödige Maschinenbau GmbH, Paderborn, Germany) within 2…4 min followed by 5 min post-blending time. To disintegrate felted agglomerations initially present and caused by blending, both dry and resinated fibres were fluffed pneumatically. Gravimetrical dosing and homogeneous in-plane mat forming was directly carried out on the (cold) lower aluminium pressing plate (with parchment paper in between) surrounded by a simple forming box. At this, specific edge overmetering was performed to counteract lateral expansion during pressing because of missing resistance around panel edges and resulting density drop-off at the very same. To reduce the height of fluffily formed mats restricted by hot-press daylight (max. 250 mm), pre-compression was performed via hydraulic unheated pre-press – in the case of high ρ_{A} up to the pressure limit. Afterwards, each pre-consolidated fibre mat was equipped with a thermocouple (type J) with its tip in the centre for process control via core temperature. Covered with the upper aluminium pressing plate, the whole package was positioned within the hydraulically driven and electrically heatable laboratory press (Siempelkamp, Krefeld, Germany) at room temperature. Temperature gradient within the mat has to be minimised during pressing to obtain the intended homogeneous vertical RDP. To this end, a pressing schedule suggested by HAAS (1998) was applied with slight modifications. Accordingly, unheated fibre mats were compressed down to target thickness (including sanding allowance of totally 1.5 mm) within 50 s. To unify start point, rather fast heating up to 30 °C followed. Subsequently, pressing platen temperature was increased with a setpoint ramp

of $\dot{T} = 1$ K/min up to $\vartheta_{\mathrm{press}} = 110\,°\mathrm{C}$ aiming at a mat core temperature $\vartheta_{\mathrm{CL}} > 105\,°\mathrm{C}$. To ensure even through-heating and resin curing, a 5 min retention time was added. Likewise, WONG et al. (1999) perform homogenous PB manufacturing via cold densification to target thickness. They, however, heat the press platens up to 160 °C, which is considered to support cracking (thermally-induced hydrolysis) of resin due to rather long total press time, and thus can result in more distinct mellow surface areas. After press opening, individual panels were stored vertically for smooth conditioning. The pressing procedure took > 85 min per panel. However, the degree of cure is assumed to differ from customary industrial panels corresponding to through-heating conditions. Likewise regarding industrial panels, actual resin molecule structure varies whereas their influence on total elemental composition at the same MC and final radiation attenuation needs to be assumed as negligible, in turn. Due to cold compression where particles are not plasticised, high mat counter pressure occurs which, in turn, increases with increasing target raw density. A range of 2.1…5.3…16.6 N/mm² was observed whereas maximum specific pressure typically does not exceed 4…5 N/mm² in case of hot-pressing. Thus, in-plane dimensions of the 1056 kg/m³ panels had to be reduced according to hydraulic pressure limit of the employed lab press. Finally, panels of 400 × 600 mm² (regular) and 350 × 350 mm² (reduced), respectively, were manufactured. Besides samples for other research purposes, basically two nominal specimen sizes were respectively cut from panel centre after calibration sanding to target thickness (Table IV-2):

- 105 × 105 mm² and
- 50 × 50 mm² (additionally one respective non-sanded set).

Table IV-2 shows one such set of specimens. Despite edge overmetering, density drop-off is unavoidable. Thus, a 50 mm wide surrounding margin was squared up per panel. Further individual sampling operations are pointed out in the respective method chapter. Figure IV-5 shows examples of the obtained homogeneous vertical RDPs (one plot per nominal thickness and raw density). Obviously, not all panels show a totally
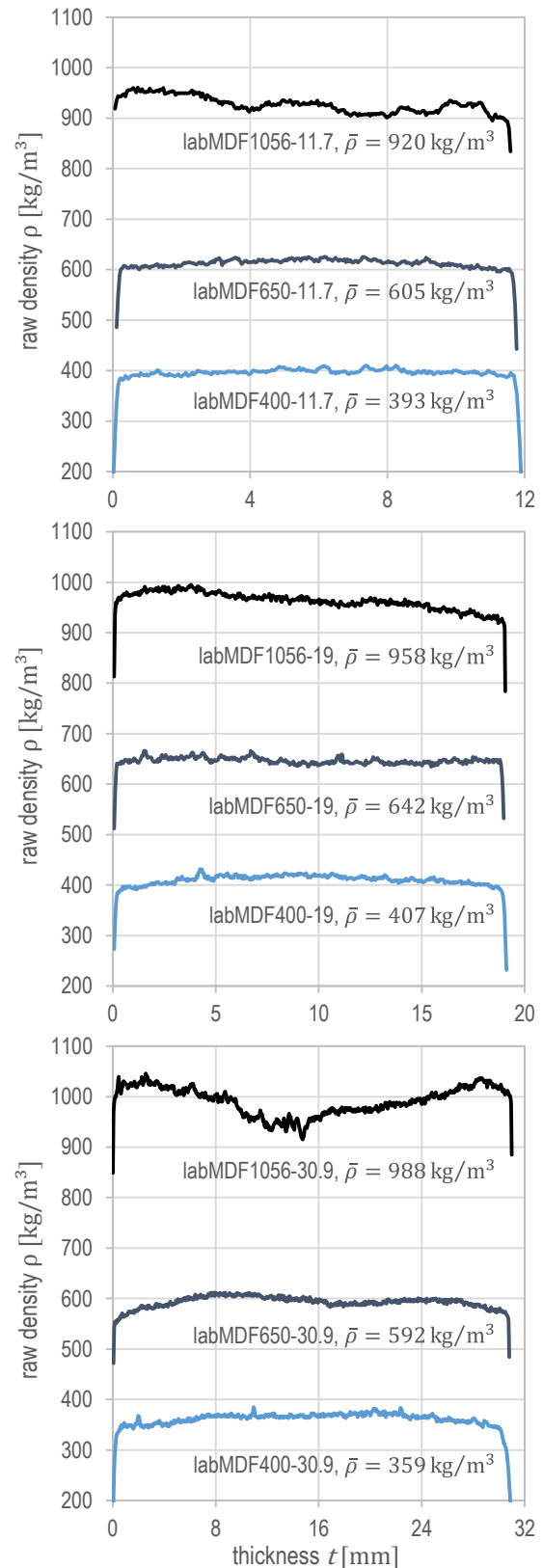
Figure IV-5: Exemplary homogeneous vertical RDPs of labMDF after calibration sanding with one plot per nominal thickness and raw density acc. to Table IV-2, measured by the W-target RDP device (Chapter IV–4.2.3) at standard conditions 20 °C/65 % RH with mean specimen raw density $\bar{\rho}$ (all panel values in Table IV-5); $t = 0$ corresponding to upper surface.

homogeneous RDP. Nevertheless, except for the 1056-30.9 specimen, no labMDF yields higher surface than core raw density. Thus, the adapted temperature set-point ramp ($\dot{T} = 1\ \mathrm{K/min}$) resulted in steady mat through-heating with minimised ΔT along thickness and consequent uniform plasticisation. Likewise, HAAS (1998) concludes regarding his manufactured panels and finally suggests a temperature increase just slightly above 1 K/min, particularly in the case of high raw densities where he observes $\Delta T_{\max} = 5\ \mathrm{K}$ between surface and core of a 20 mm panel. Actual moisture and density parameters of the labMDF samples are presented in Table IV-5 in Chapter IV–1.5.

1.3 Customary industrial panels

In contrast to predefined lab-made composites, customary industrial panels of random origin were utilised. However, their concisely selected type, structure, and thickness variations cover a practice-oriented range. Investigations considering X-ray RDP determination particularly focus on 19 mm panel thickness due to commercial relevance of the very same thickness range 16…19 mm (except flooring) and representative RDP characteristics. Oriented strand board (OSB) was excluded for structural reasons. Full size raw particles (strands $l > 50\ \mathrm{mm}$, $t < 2\ \mathrm{mm}$, acc. to DIN EN 300 (2006), up to $25 \times 150 \times 0.7\ \mathrm{mm^3}$, cf. THOEMEN et al. (2010)) exceed the most common specimen size, i. e., $50 \times 50 \times t\ \mathrm{mm^3}$. In the case of regular RDP determination, measurements were practicable whereas the conditions are disadvantageous for fundamental investigations. However, structural result deviations generally superimpose measuring dispersion itself. The applied panel types with varying utilisation frequencies regarding the respective measurement focus on MDF. Here, several nominal thicknesses with $t_{\mathrm{nom}} = 2, 3, 6, 8, 10, 12, 19, 25, 30\ \mathrm{mm}$ are utilised. A further type of MDF-19 as well as PB-19 come in addition for round robin test and other analyses.

Wood-fibre insulation board with $t_{\mathrm{nom}} = 40\ \mathrm{mm}$ is utilised with regard to light panels. All customary MDF samples are henceforth summarised with the abbreviation indMDF. For exemplary RDPs complete with photographs of the specimens, reference is made to Appendix VII–1.3. Whereas insulation boards are bonded with MDI adhesive resins, glue liquor is assumed to be based on UF in the case of MDF and PB. Respective specimens were cut after sufficient trimming from total half-sized panels or appropriate residuals. Actual moisture and density parameters of the industrial panel samples are presented in Table IV-5 in Chapter IV–1.5. Note, MDF-3 was artificially created by symmetrical removal of the surfaces via sanding (calibration finish) of an MDF-8 panel. Thus, a virtually homogeneous RDP (see Figure VII-7) was obtained corresponding to the more uniform core layer.

1.4 Adhesive resin

Owing to its commercial and technical relevance, exclusively urea-formaldehyde (UF) adhesive resins, the most important adhesive systems in the WBC industry, were applied on lab-made material. For several analytical purposes on isolated adhesive resin, samples of both applied types of Kaurit glue liquid, BASF SE, Ludwigshafen, Germany[20], were prepared in various different ways as follows and summarised in Table IV-4, complete with their labels. The delivered liquid glue liquor was utilised for sample preparation without any further additives except hardener. Table IV-3 provides selected properties of both glue liquors according to the individual technical date sheet complete with their particular applications. The raw liquid resin (label L in Table IV-4) consists of UF pre-polymers dispersed in water with predefined solid content (SC). A second batch was mixed with additional 1 % of 40 % ammonium sulphate $(NH_4)_2SO_4$ solution as hardener (LH). There was no further water addition. From both batches, samples nominally comprising 60 g were dosed in 250 ml beakers for further preparation. Besides liquid samples

---

[20] Their repeated and obliging provision of adhesive resin is highly appreciated. Note, particular Kaurit types are known but not further pointed out.

property (at 20 °C)	UF1	UF2
SC_{UF} [%]	68 ± 1	66.5 ± 1
$\rho_{liq,UF}$ [kg/m^3]	1288...1294	1288...1298
viscosity [mPa · s]	300...500	350...600
storability [weeks]	1	4.5...5.5
F/U	n/s	n/s
application and investigation (in this thesis)	labMDF elemental analysis	furnish mats true density ash content elemental analysis

Table IV-3: Properties of delivered liquid glue liquor of both applied UF adhesive resins Kaurit glue liquid, BASF SE, Ludwigshafen, Germany, according to technical data sheet, complete with particular applications and investigation methods within this thesis.

UF#-* * label	additive (NH₄)₂SO₄	treatment ϑ	duration	state
L	-	n/a	n/a	liquid
LH	1 %	n/a	n/a	liquid
D	-	20 °C	weeks	solid, dried
DH	1 %	20 °C	days	solid, dried
C	-	103 °C	16.5 h	solid, cured
CH	1 %	103 °C	0.5 h	solid, cured
	re-conditioning and interim storage always at 20/65 to constant mass			
...-OD	further oven-drying to constant mass (controlled) for individual analysis prior to measurement			

Table IV-4: Summary of preparation types for analytical purposes on isolated UF adhesive resin with respective labelling for both applied types #1 and #2.

for elemental analysis (Chapter IV–2.4; UF-L, UF-LH), solid resin is required such as present on blended and subsequently dried furnish as well as within the final panel referred to as wood-particle-resin-matrix. Notwithstanding the common procedure for SC determination (discussed in Chapter IV–2.1.2), solid resin bodies were prepared with particular structural considerations. To avoid pores as consequence of evaporating water from drying as well as polycondensation, drying of both glue liquors was performed at $\vartheta_{RT} \approx 20\,°C$ for several days (with) or weeks (without hardener), respectively, aiming at as void-free as possible moulded solid resin blocks (UF-DH, UF-D). Long-lasting duration corresponds to the rather compact volume and minor surface compared to thin resin layers spread on furnish material. Whereas the air-dried solid samples represent conditions prior to hot-pressing, actually cured resin was prepared in an exhaust air furnace at $\vartheta_{furnace} \approx 103\,°C$ for 30 min (with) or 16.5 h (without hardener), respectively (UF-CH, UF-C). In the latter case, the resin was still completely liquid after 30 min and the final block was significantly shrunken. Curing temperature was chosen with respect to actual conditions within panel core layer during hot-pressing, where vapour temperature as predominant heat transfer mechanism corresponds to just slightly increased ambient pressure conditions. Contrary to slowly dried samples, cured resin blocks include cracks and coarse pores. After several days of re-conditioning at 20/65, all solid resin

blocks were crushed and provided for individual sampling as well as further preparations as needed. Despite slightly differing glue liquor properties (Table IV-3) between UF1 and UF2 and inherently included hardener in the case of UF1, respectively obtained analytical results will be comparable and can, in turn, be transferred to similarly composed UF adhesive resins under particular consideration of respective curing conditions.

1.5 Moisture content and density

Because wood and WBCs are inhomogeneous, porous, and hygroscopic materials, all physical and elasto-mechanical properties are more or less related to moisture content and density, which are commonly determined in terms of the performed experiments. Moreover, present X-ray investigations draw on density determination with further focus on moisture impact. To this end, these basic parameters are, however, not explicitly measured on a specific set of samples but, as usual, determined in the context of all main investigations on the respective specimens. Thus, the data is compiled in this chapter. Related methods and facilities are pointed out.

All utilised material was conditioned at a predefined temperature and relative humidity (RH) to constant mass according to the requirements of the respective investigation and in accordance

with corresponding standards resulting in an individual equilibrium moisture content (EMC) depending on the material itself. For externally performed experiments, conditioning or likewise drying was performed in advance and material was sealed for transport due to limited access to respective sample environmental equipment at the experimental stations as henceforth individually noted in the chapter of the respective investigation. However, the main conditions were 20 °C and 65 % RH (20/65), which is commonly referred to as standard conditions. Regarding wood and WBCs, such conditioning is typically applied for material testing and fundamental aspects (cf. ISO 13061-3 (2014), DIN EN 310 (1993), DIN 68100 (2010), and DIN 68364 (2003)). In general technical applications, 20/65 is one of the standard atmospheres (intermediate level) defined by (withdrawn) DIN 50014 (1985). Notwithstanding that there is no official international representation and DIN 50014 (1985) was withdrawn without direct substitution[21], 20/65 is considered to serve as standard condition in the (European) wood industry and in research. Moreover, in international relationship with DIN 50014 (1985), ISO 554 (1976) defines standard atmospheres for conditioning and/or testing, which holds 20/65 to be "used in certain fields of application" whereas ISO 291 (2008) as further corresponding standard specifies 23/50 as standard for conditioning and testing of plastics (for non-tropical countries), which is, in turn, the recommended atmosphere in ISO 554 (1976). DIN EN ISO 1 (2016) predefines the standard reference temperature for the specification of geometrical and dimensional properties with 20 °C. However, 20/65 is in the order of regular indoor ambient conditions, thus, around medium EMC range. In addition, a moist level is applied with increased relative humidity, i. e., 20 °C and 83 % RH (20/83), which is close to the typical upper limit of application range of wood products (cf. DIN 68100 (2010)). Conditioning was performed in a constant climate chamber in the case of 20/65 as predominant conditions for all X-ray measurements and in a variable climate

cabinet at 20/83 for a selected set of samples. Furthermore, oven-dry (OD) conditions were obtained by means of an exhaust air drying furnace at $\vartheta_{\mathrm{furnace}} = (103 \pm 3)\,°C$, which is relevant as more or less moisture-free state for some X-ray measurements and particularly for the analyses in Chapter IV–2.

Moisture content MC [%] is defined as the "amount of moisture contained in wood, expressed as a percentage of its oven-dry mass" according to ISO 13061-1 (2014), which specifies oven-dry determination method with regard to small clear wood specimens. The same applies to WBCs where DIN EN 322 (1993) specifies procedure and calculation, i. e.,

$$MC = \frac{m_{MC} - m_{\mathrm{OD}}}{m_{\mathrm{OD}}} \cdot 100 \ [\%] \qquad \text{(IV-1)}$$

with mass of specimen in initial (moist) m_{MC} [g] and oven-dry m_{OD} [g] state. Note, the utilised symbols are considered to be more common and self-explanatory, and thus, introduced here in difference to both standards. However, determination of MC was always performed in accordance with DIN EN 322 (1993) for all material types, i. e., furnish or panel specimens, since DIN EN 322 (1993) solely requires initial mass of at least $m_{MC} = 20$ g regardless of dimensions and shape. Drying to constant mass was carried out by means of an exhaust air drying furnace at $\vartheta_{\mathrm{furnace}} = (103 \pm 3)\,°C$. Beakers were utilised to carry all types of loose material such as fibres and particles during weighing and drying. Likewise, lab-made furnish mats were reduced to small pieces and stored in beakers. In some cases, fluffy fibre material caused weighed portions with $m_{MC} < 20$ g. However, results were verified in additional tests, where appropriate mass loss was found with regard to precision of the applied scale.

Density of material is well-known to be defined (cf. DIN 1306 (1984)) as ratio of mass m to the volume V of a sample, i. e., the quotient

$$\rho = \frac{m}{V} = \frac{m}{l \cdot w \cdot t} \qquad \text{(IV-2)}$$

---

[21]   Note, with DIN 50014 (2018), a follow-up document was meanwhile published, which is, however, fundamentally based on ISO 554 (1976) with some modifications.

commonly expressed in $\mathrm{kg/m^3}$ in the field of wood and WBCs. The determined density applies to the present temperature and pressure, where, in the case of hygroscopic wood and WBCs, MC becomes an additional material parameter influencing the density. Moreover, wood and WBC density generally refers to the raw density (also referred to as bulk density), where total volume comprises both solid matter and pore volume as defined in, e.g., DIN 51918 (2012) or DIN 66137-1 (2003). Furthermore, considering loose or bulk material such as powder or particles, bulk density takes the total volume of solid matter and pores inside as well as between the particles into account (cf. DIN 66137-1 (2003)), which is relevant with regard to bins or un-compressed furnish mats in the WBC process. In contrast to raw and bulk density, the true density ρ_t according to eq. (IV-4)[22] only considers solid matter density of porous material, which is, in turn, defined as quotient of oven-dry mass and solid substance (mainly cell wall) excluding pores. However, unless otherwise specified, ρ henceforth exclusively refers to the raw density, since all regular determinations on wood or WBCs in accordance with ISO 13061-2 (2014) or DIN EN 323 (1993), respectively, take total volume including pores into account. Furthermore, without consideration of specimen thickness in eq. (IV-2), the area density

$$\rho_\mathrm{A} = \frac{m}{A} = \frac{m}{l \cdot w} \tag{IV-3}$$

is defined as mass m per unit area A with the context $\rho_\mathrm{A} = \rho \cdot t$ and commonly expressed in $\mathrm{kg/m^2}$. For area density ρ_A no explicit standards exist with respect to WBCs except former TGL 11369 (1977), where also the today common $100 \times 100 \mathrm{\,mm^2}$ specimens for gravimetric ρ_A determination in production and quality control are already specified. However, the determination of ρ and ρ_A was always performed in accordance with DIN EN 323 (1993) for all material types with weighing by means of sufficiently precise balances considering nominal mass of the individual specimen types. Dimensions for volume and

area determination were measured in accordance with DIN EN 325 (2012) via digital callipers (partly with interface and footswitch to minimise operator influence) or outside micrometre on demand, e.g., in the case of thin specimens. For dimensions >150 mm a steel ruler was applied. The determination was mainly carried out as part of RDP measurement on specimens with nominal dimensions $50 \times 50 \times t \mathrm{\,mm^3}$ (thus, often repeated per specimen in the measuring series) and, furthermore, on particular cuttings with dimensions corresponding to the respective beam geometry of other X-ray measurements. Here, the length and width measuring procedure with measuring jaws at an angle of about 45° to the panel plane and preferably covering the total cross-section as specified in DIN EN 325 (2012) is found to be best for obtaining valid results particularly considering panel types with low raw density or coarse structure.

Table IV-5 compiles all results from moisture content (MC) and density determination (raw density ρ and area density ρ_A, complete with thickness t) at standard conditions (20/65), which is the predominant conditioning level for all X-ray measurements. Additionally, OD and 20/83 results are available for resin-unblended pure SL particles, which were utilised for manual mat forming (Figure IV-1). Beyond the tabulated values, exemplary RDPs are shown in Figure IV-3 (Fmat) and Figure IV-5 (labMDF) as well as in Appendix VII–1.3 in Figure VII-5 (insulation) and Figure VII-7 (indMDF). However, Table IV-5 comprises data for the lab-made material (panels and furnish mats), corresponding raw furnish (fibres and particles), as well as selected industrial panels (MDF and insulation). The results represent the arithmetic mean and the coefficient of variation (CV) per set of samples with at least $n = 3 \dots 5$ each. The material properties for labMDF (Chapter IV–1.2) are listed with individual mean values and CVs per nominal raw density (400, 650, 1056 kg/m³) and thickness (11.7, 19, 30.9 mm).

---

[22] The true density of all relevant materials is determined and further discussed complete with data from literature in Chapter IV–2.1.

material	MC [%] mean	CV [%]	t [mm] mean	CV [%]	ρ [kg/m³] mean	CV [%]	ρ_A [kg/m³] mean	CV [%]
TMP-H	10.8	0.5	n/s		n/s		n/s	
400-11.7			11.65	3.5	396	1.6	4.6	4.3
400-19	9.4	0.6	19.23	0.3	404	1.7	7.8	1.9
400-30.9			31.15	0.4	362	1.1	11.3	1.3
650-11.7			11.89	0.4	620	2.4	7.4	2.6
650-19	9.5	1.4	19.18	0.2	630	3.2	12.1	3.3
650-30.9			31.22	0.3	583	1.2	18.2	1.1
1056-11.7			11.70	0.2	932	2.9	10.9	3.0
1056-19	9.5	1.9	19.11	0.1	974	1.6	18.6	1.6
1056-30.9			31.06	0.1	990	0.8	30.7	0.8
labMDF	**9.5**	**1.3**		**0.6**		**1.8**		**2.2**
CV(**mean**)	**0.7 %**							
TMP-F	11.1	1.0	n/s		n/s		n/s	
Fmat1	9.7	0.5	8.53	1.9	122	1.6	1.04	0.6
Fmat2	9.0	1.4	16.75	1.8	120	5.5	2.03	4.7
Fmat	**9.4**	**0.9**		1.9	121	3.6		2.6
CV(**mean**)	**5.1 %**				**1.0**			
SL, 20/83	13.8	0.4	2.4...27.9	n/a	245	6.3	0.5...7	n/a
SL, OD	2.0	5.7	2.0...29.4	n/a	233	2.4	0.5...7	n/a
SL	10.8	0.7	2.2...27.5	n/a	238	4.5	0.5...7	n/a
CL	11.7	0.6	n/s		n/s		n/s	
SLmat	10.5	1.3	4.83	2.0	217	2.2	1.05	0.5
CLmat	11.3	1.1	10.73	2.4	197	2.1	2.11	2.2
MDF-2	7.7	2.3	1.99	0.4	869	1.2	1.7	1.1
MDF-3	8.2	0.9	3.19	0.6	774	1.9	2.5	2.1
MDF-6	8.0	1.4	6.15	0.7	893	0.9	5.5	1.2
MDF-8	7.9	1.5	8.03	0.6	811	0.8	6.5	0.7
MDF-10	8.3	1.8	10.10	0.5	774	1.3	7.8	1.0
MDF-12	8.2	2.3	12.09	0.4	764	0.6	9.2	0.6
MDF-19	8.2	1.9	19.17	0.4	746	0.5	14.3	0.5
MDF-25	8.1	1.2	25.21	0.4	742	0.8	18.7	0.7
MDF-30	8.2	1.0	29.98	0.3	775	1.0	23.2	0.9
indMDF	**8.1**	**1.6**		**0.5**	**794**	**1.0**		**1.0**
CV(**mean**)	**2.5 %**				**6.7 %**			
insulation	9.1	0.9	41.99	0.3	212	0.6	8.9	0.8

Table IV-5: Compilation of all results from determination of fundamental material properties at standard conditions 20 °C and 65 % RH (unless otherwise stated) with moisture content MC acc. to eq. (IV-1), thickness t (perpendicular to specimen plane), raw density ρ acc. to eq. (IV-2), and area density ρ_A (in specimen plane) acc. to eq. (IV-3) for lab-made material (panels and furnish mats), corresponding raw furnish, and selected industrial panels (mean with CV per set of samples and CV(mean) of single sample mean values).

MC results represent the mean per raw density, since the determination was mainly performed in terms of ash content analysis (Chapter IV–2.3), where the thicknesses per raw density level were combined due to the limited number of the elaborately lab-made panels and the more or less destructive nature of oven-drying with potential cracks in the panel plane. TMP fibre results are to be distinguished regarding the types, i. e., raw material utilised for panels (TMP-H, Chapter IV–1.2) and fibre mats (TMP-F, Chapter IV–1.1). Here (and likewise for CL particles), only MC

was determined since the density properties are not reasonably measurable on the loose and bulky furnish material and not required from the raw material. The properties of the cured fibre mats (Fmat, Chapter IV–1.1) with nominal area densities of $\rho_{\mathrm{A,nom}} = 1 \ \mathrm{kg/m^2}$ and $\rho_{\mathrm{A,nom}} = 2 \ \mathrm{kg/m^2}$ obviously depend on the individual forming and densification. The MC values, however, can be combined to one Fmat mean due to simultaneous manufacturing of the specimens. Likewise, the cured particle mats (SLmat and CLmat) reveal a structural impact. Furthermore, resin-unblended SL particles were conditioned on a moist (20/83) and dry (OD) level in addition to the standard conditions. Consequently, MC significantly differs from 20/65 level, where, however, $MC = 2 \ \%$ represents the effective EMC of the OD but hygroscopic material during the, nevertheless, rapidly performed X-ray measurements. Accordingly, the results are found to vary more considerably with $CV = 5.7 \ \%$ (of the measuring values, i. e., 0.11 % MC). Moreover, the shown ρ values and ranges of t and ρ_{A} represent the results of manual mat forming (Figure IV-1), which was exclusively performed by means of varyingly conditioned SL particles. Finally, the properties of the utilised MDF of industrial origin (indMDF) are listed according to the nominal panel thickness and the values are found to range in common orders. Regardless of the typical raw density differences between the individual MDF (or HDF) types, MC values are similar with a rather low variation of $CV(\mathrm{mean}) = 1.7 \ \%$.

The range of variation of all determined material properties in Table IV-5 is found to be in a typical order and CV tendentially more or less decreases with increasing panel thickness. Moreover, CV of the thickness is expectedly low due to calibration sanding of the panels except the cured furnish mats owing to the compressible (Fmat) and partly coarse (SLmat and CLmat) structure of the specimens, where the variations are rather attributed to measurement. All differences from typical CV ranges, e. g. in the case of labMDF400-11.7, were double-checked and are considered to be attributed to panel processing. The like applies to ρ and ρ_{A}, where the industrially obtained homogeneity (indMDF) de-

pends on the panel type (application) and manufacturer and the lab-made materials (labMDF and all furnish mats) reveal the human impact despite all the care taken. Accordingly, the mean CVs of labMDF exceed the indMDF values.

Obviously, the actual properties of lab-made samples individually differ from their target values (Table IV-1, Table IV-2). Differences of the panel and particularly the mat thickness t correspond to the unpredictable springback after consolidation as well as the swelling and shrinkage behaviour of the final specimens. However, the setpoint for panel calibration sanding was rather kept beyond target thickness not to yield too thin panels. In consequence of thickness calibration, the density values partly fall below the target (particularly in the case of labMDF1056) although an appropriate sanding allowance of 1.5 mm was considered in the gravimetrical furnish dosing. However, ρ_{A} differences from the target may further be attributed to not double-checking the resulting MC of the furnish after blending, where, in turn, the actual dry forming mass is affected by the very same. Furthermore, a defined forming allowance was not applied and lateral expansion during hot-pressing of the labMDF was just considered via fibre distribution (edge overmetering). Note here, the cured furnish mats were formed and consolidated in steel cylinders. Eventually, the aforementioned human impact particularly regarding manual mat forming variations is unavoidable in the case of lab-made material.

Beyond sample manufacturing, the human influence affects also the specimen measurement, where both systematic and random errors may occur during gravimetrical raw density determination. FREYBURGER et al. (2009) compute the relative error $\Delta\rho/\rho = 0.1 \ldots 0.15 \ \%$ depending on specimen size, where questionable single errors are assumed corresponding to the division (displayed digits) of the utilised calliper and scale. Nevertheless, KORTÜM, RIEGEL (2017) point out the potentially high range of variation of the measuring device and explore the gauge capability in woodworking. Moreover, own unpublished capability investigations reveal measuring related deviations particularly due to oper-

ator influence considering the mechanical dimension determination of the specimen with further dependence on the material structure. The results determined via repeat measurements ($n = 100$) on common MDF and PB specimens clarify the practically achievable accuracies by means of a calliper in the order of $CV = 0.03 \ldots 0.08$ %, where typically right-skewed dimension distributions occur. Therefore, truncated volumes are mechanically measured. However, specimen mass determination is less error-prone by operator impact. Consequently, gravimetrically determined raw densities are empirically assumed to exceed the actual values of the solid body in general. Here, final accuracies of gravimetric raw density determination are computed (via Gaussian propagation of uncertainties) in the order of $CV = 0.07 \ldots 0.15$ %, which is just the potential error of the manual measuring process regardless of the material variations. In the case of rather soft WBC material such as insulation boards, the compressibility comes in addition and results in apparently diminished volumes and increased raw densities, where the measuring error is considered to exceed above figures. Therefore, DIN EN 12085 (2013) defines the maximum measuring pressure of the applied gauge. In contradiction, teared out fibres or particles in the edge region reduce the specimen mass resulting in apparently decreased raw densities, where the influence decreases with increasing specimen size. Hence, gravimetrical raw density determination with contacting dimension measurement is inherently erroneous regarding reasons such as

- operator influence (handling of the measuring device),
- material influence (compressibility), and
- material preparation influence (rectangular cutting and teared-out particles),

which has rarely been pointed out yet. The actual impact is, finally, hardly quantifiable and depends on the individual material and measuring conditions including operator skills.

2 Material characterisation

2.1 True density and porosity

2.1.1 Sampling and method

Purposing both general material characterisation and particular true density (i. e. solid matter density) determination of the wood-particle-resin-matrix as actually radiation attenuating matter, gas pycnometry was carried out in accordance with DIN 66137-2 (2004). Measurements were exclusively performed on labMDF ($t_{nom} = 19\,\mathrm{mm}$, all raw density levels) and MDF-19 as well as PB-19 (both from round robin test) as industrial comparison samples. Specimens were prepared following the recommendations of ZAUER et al. (2013). Accordingly, thin slices in the tangential-radial plane, i. e. $t_{\mathrm{long}} < 3\,\mathrm{mm}$, are required to facilitate free access of displacement gas to all pore spaces, which can here additionally be inhibited by the applied adhesive resin. Since MDF and PB are composed of randomly in-plane-aligned TMP fibres or particles, respectively, considerably less wood fibres are assumed to be cut by preparing respective cross-sectional slices compared to described solid wood slices. Nevertheless, specimens were cut from two distant areas of the respective panels with nominal dimensions of $2 \ldots 3 \times 10 \times 19\,\mathrm{mm}^3$ ($l \times w \times t_{\mathrm{panel}}$). One sample comprises three random specimens from each panel area (6 pieces in total). Additionally, raw TMP fibres (resin-unblended) of labMDF were investigated to evaluate both adhesive resin and hot-pressing influence. Therefor, cluster sampling was performed directly from the bag at representative positions and the obtained material was remixed again. For size reduction of fibrous material and cutting of its cell lumina, the sample was milled by means of a laboratory rotor mill (Ultra Centrifugal Mill ZM 200, RETSCH GmbH, Haan, Germany) with a 12-tooth rotor at $n = 14'000\,\mathrm{min}^{-1}$ utilising a ring sieve with 0.5 mm trapezoid holes. Fibre morphology characterisation in Chapter IV–2.2 reveals that milling evidently was efficient by cutting wood cells as intended, which obtained crucially reduced fibre lengths with values below 1200 μm as upper quartile Q3 (< 2400 μm, 97.5 % quantile). Note, milled fibres actually originate from bulk sample for elemental analysis (Chapter IV–2.4.1). Here, five samples were withdrawn again via cluster sampling from the milled material with individual masses around 0.5…0.8 g (OD). After sampling was performed at EMC in consequence of common conditioning at 20 °C and 65 % RH (20/65), all samples were oven-dried to constant mass and individually vacuum-sealed for transport. Measurements on $n = 3(5)$ samples as repeat determination with maximum ten iterations each were carried out by means of the device ULTRAPYCNOMETER 1000T, QUANTACHROME GmbH & Co. KG, Odelzhausen, Germany with Helium (He) as displacement gas. For illustrated specimen preparation, sampling, and measuring equipment, refer to Appendix VII–2.1. Device was calibrated for bulk volumes around 1.9 cm³. After appropriate conditioning at room temperature, samples were unpacked and weighed (m_{OD}) immediately prior to measurement and positioned vertically preferably free-standing within measuring cell of the pycnometer to facilitate gas flow around. Specimens of the samples were handled without skin contact very rapidly to avoid moisture absorption. For solid matter volume $V_{\mathrm{S}}\,[\mathrm{cm}^3]$ determination, standard procedure of the laboratory[23] with established device settings was carried out per sample with ≤ 10 iterations aiming at repeat deviation < 0.1 %. At this, V_{S} is derived from correspondingly measured pressure differences based on ideal gas equation at isothermal conditions (Boyle-Mariotte law). For methodical details, reference is made to DIN 66137-2 (2004) and particularly to ZAUER et al. (2013) regarding measurements on wood. Special procedures for applications on, e. g., carbonaceous materials or plastics are standardised in DIN 51913 (2013)

---

[23] True density determinations were performed at the Institute of Wood and Paper Technology, Technische Universität Dresden, Germany, with outstanding support by the local staff. Their obliging and straightforward cooperation allowing own performance of the analyses is highly appreciated.

and DIN EN ISO 1183-3 (2000), respectively. Both state requirements for repeatability in the order of 0.1…0.2 % likewise predefined here.

Finally, true density ρ_t [kg/m³] is computed via

$$\rho_t = \frac{m_{OD}}{V_S} \qquad (IV\text{-}4)$$

per sample. Furthermore, porosity Φ [%] is calculated according to

$$\Phi = \left(1 - \frac{\rho_{OD}}{\rho_t}\right) \cdot 100 \; [\%] \qquad (IV\text{-}5)$$

with global mean oven-dry raw density ρ_{OD} [kg/m³] of the respective material. Local (oven-dry) raw density and porosity based on bulk volume measurements via calliper on each single (tiny) specimen were not determined because a valid volume measurement cannot be ensured regarding to partly soft and fibrous, thus compressible, material showing holes and non-parallel surfaces from simple cutting. Alternatively, respective global values were taken from Table IV-5 in Chapter IV–1.5.

In order to complete furnish and WBC material, cured adhesive resin was analogously investigated, i. e. exclusively preparation type UF2-CH according to Table IV-4. To this end, crushed material was further milled by rotor mill as above. The powder enables enhanced displacement gas accessibility to potential pores occurred from evaporating water during curing. Assuming a certain hygroscopicity of solid UF resin, a sample of milled solid resin was dried due to requirement of DIN 66137-2 (2004) and further related standards. To avoid over drying in the oven, which is associated with post-curing of adhesive resin, emission of free formaldehyde, and, on the other hand, thermally-induced hydrolysis with cracking of the macromolecules, process control is required. Thus, drying at approximately 103 °C and simultaneous MC determination was carried out by means of a rapid lab device (CM easy plus, C.M. Instruments, Oerlinghausen, Germany) including a balance (0.0001 g displayed digits) besides radiative heat source. Here, controlled drying stops when constant mass of the weighed portion is reached. However, considerable mass loss exceeding potential MC was observed supposedly owing to aforementioned effects during drying. Thus, besides oven-dry material (UF2-

CH-OD), two samples conditioned at 20/65 (UF2-CH) were prepared and individually vacuum-sealed again. Pycnometric V_S measurements with weighed portions of nominally 1.33 g corresponding to powder bulk volume of approximately 1.9 cm³ were performed as repeat determination with $n = 2$ samples each. Subsequent ρ_t calculation according to eq. (IV-4) yields density of the cured resin which appears as solid non-porous matter. Hence, Φ computation according to eq. (IV-5) is dispensable.

In addition to gas pycnometry, exploratory measurements on dry adhesive resin as solid body were performed by immersion method. Following DIN EN ISO 1183-1 (2013), density determination was carried out via Archimedes' principle (i. e. buoyancy method) within purified water (without wetting agent) as immersion liquid (IL). To this end, analytical balance XS205DU, Mettler-Toledo GmbH, Giessen, Germany, equipped with a convenient density kit was utilised at uncontrolled surrounding conditions with $\vartheta_{RT} = 25.7\,°C$. Therefore, actual density of the immersion liquid H_2O determined via an appropriate sinker yielded $\rho_{IL} = 997.177$ kg/m³, which is in good agreement with tabulated value $\rho_{H_2O,25.7} = 996.89$ kg/m³ (cf. DIN CEN/TS 15405 (DIN SPEC 1152) (2010)). For further performance description, reference is made to DIN EN ISO 1183-1 (2013). Accordingly, specimen density ρ_S [kg/m³] at ϑ_{RT} is calculated via

$$\rho_S = \frac{m_{S,A}}{m_{S,A} - m_{S,IL}} \cdot \rho_{IL} \qquad (IV\text{-}6)$$

with apparent specimen mass in air $m_{S,A}$ [mg] and within immersion liquid $m_{S,IL}$ [mg], respectively. The specimens with irregular shapes but without undercuts and visually free of pores were fragments with $m_{S,A} = 297 \ldots 1613$ mg of the solid resin blocks prepared according to Chapter IV–1.4. Coarsely crushed material was utilised without further milling. Here, density measurements were again exclusively carried out on UF2 where samples were taken from preparation types UF2-D and UF2-DH according to Table IV-4. Re-conditioning and interim storage was carried out at 20/65. Considering potentially bound water, part of UF2-DH sample was oven-

dried (with mass control as above) and consequently stored in a desiccator at $\vartheta_{RT} \approx 20\,°C$ (UF2-DH-OD). Here, fine cracks occurred immediately within the still intact specimens. All samples were re-conditioned to ambient temperature of the analytical balance prior to measurement.

2.1.2　Results and discussion

Figure IV-6 shows measured true density ρ_t [kg/m³] results of WBC samples comprising labMDF (three raw densities) and customary MDF and PB as well as raw TMP-H fibres and UF2-CH resin (cured with hardener). Table IV-6 summarises all mean values and dispersion parameters complete with mean porosity Φ [%] per sample type. Note regarding wood-based samples, all values refer to oven-dry conditions alike at measurement and cannot directly be transferred to total true density at particular MC including adsorbed water. Sample no. 1 of PB (shaded in Figure IV-6) was rejected due to significant result deviation from the others (statistically proven by Shapiro-Wilk test, $\alpha = 0.01$ and Hampel's test $\alpha = 0.01$) presumably because of a systematic processing error. Nevertheless, all

sample type (oven-dry)	mean ρ_t $\left[\frac{kg}{m^3}\right]$	$s(\rho_t)$ $\left[\frac{kg}{m^3}\right]$	$CV(\rho_t)$ [%]	global mean ρ_{OD} $\left[\frac{kg}{m^3}\right]$	global mean Φ [%]
labMDF	**1454**	10.6	0.7	n/a	n/a
400	1447	11.6	0.8	374	74.1
650	1452	2.5	0.2	592	59.2
1056	1463	10.7	0.7	917	37.3
TMP-H	**1516**	56.3	3.7	n/a	n/a
MDF19	1437	1.5	0.1	709	**50.7**
PB19	1473	9.9	0.7	607	58.3
UF2-CH-OD	1514	6.4	0.4	n/a	n/a
UF2-CH	**1501**	3.2	0.2	n/a	n/a
UF2-DH-OD	1455	2.1	0.1 buoyancy method		
UF2-DH	1454	1.7	0.1 buoyancy method		
UF2-D	1422	8.7	0.6 buoyancy method		
UF resin*	1400	*unofficial information, WBC industry			
UF1*	1498	*theoretical value acc. to eq. (IV-10)			
UF2*	1520	*theoretical value acc. to eq. (IV-10)			
labMDF* **10 % UF**	1515	*theoretical value acc. to eq. (IV-13) with ρ_t of TMP-H and UF1			

Table IV-6: Results of true density ρ_t [kg/m³] (solid density) determination by He pycnometry on exemplary WBCs with labMDF (three raw densities) and customary MDF and PB as well as raw fibres TMP-H and cured UF resin (with hardener) with mean values per set of samples n, standard deviation s [kg/m³], and coefficient of variation CV [%] as well as oven-dry raw density ρ_{OD} (global mean from total panel) and computed global mean porosity Φ [%] per sample type; additional solid resin density buoyancy method; complete with computed ρ_t for UF and labMDF on theoretical basis.

Figure IV-6: Results of true density ρ_t [kg/m³] (solid density) determination by He pycnometry on exemplary WBCs with labMDF (three raw densities) and customary MDF and PB as well as raw fibres TMP-H and cured UF resin (with hardener) as mean values per set of samples n; mean of labMDF $\bar{\rho}_t = 1454$ kg/m³.

measurements provide reproducible results. The number of automatic iterations varied between 3…10 runs until reaching repeat limit, where the maximum (10) was just required in some cases of labMDF400 and TMP-H. Furthermore, except raw fibres, all material types reveal minor variations within the respective set of samples with $CV(\rho_t) < 1\,\%$. Notwithstanding the reliable measuring procedure, likewise pointed out by ZAUER et al. (2013), variations in the case of milled raw fibres are caused by inappropriate filling of the measuring cell leading to poor gas accessibility and potentially considerable moisture absorption during handling due to major furnish surface.

However, $\bar{\rho}_t$(TMP-H), i. e. clean wood result, is in good agreement with the common value for oven-dry wood and in the order of previously published work (Table IV-7), where variations result from the respective determination method. Since actual process parameters of TMP generation are unknown, the magnitude of heat impact on wood matter cannot be quantified. However, ZAUER et al. (2013) observe a slight decrease of cell-wall density of about $30 \ldots 40$ kg/m^3 (spruce) in consequence of their 'mild' thermal treatment at $\vartheta = 200\,°C$ for 4 h whereas PFRIEM et al. (2009) conclude true density increment of modified spruce at equal conditions. However, according to both implications based on findings of WINDEISEN et al. (2007), true density decrease is caused by primary degradation of hemicelluloses increasing the lignin share. Higher temperatures, in turn, induce lignin degradation along with cell-wall density increase alternating the ratio again. Actually, thermal modification processes are beyond typical industrial thermal conditions during defibration process with $3 \ldots 7$ min digester retention time at $\vartheta = 175 \ldots 195\,°C$ and subsequent mechanical refining (cf. THOEMEN et al. (2010)). Thus, the comparatively short thermal impact implies negligible influence on cell-wall density. Finally, varying TMP generation conditions within typical industrial range can be neglected regarding true density for this first approach either. Since variations rather depend on apparent chemical composition corresponding to wood species, tabulated common values (Table IV-7) serve as appropriate data for TMP fibres and other raw furnish material in the case of lacking measuring values. Fundamental considerations of heat and vapour impact during generation of fibrous material on its properties are contributed by LAMPERT (1967) based on hitherto investigations. Regarding the currently common thermo-mechanical defibration method, he points out less degradation in consequence of hydrolysis and loss of wood substances compared to steam explosion defibration by Mason gun for Masonite process.

Obviously from result presentation, labMDF ρ_t values differ from corresponding raw fibres. However, due to $\vartheta_{press} \leq 110\,°C$ and above-

matter (oven-dry)	ρ_t $\left[\frac{kg}{m^3}\right]$	Φ [%]	method (displ. medium)	source
wood (all species)	1500	n/s	n/s	[1, 2, 3, 6]
	1480...1510	n/s	n/s	[6]
	1560	n/s	salt sol.	[3]
spruce	1426	n/s	xylene	[8]
	1430	64	He	[9]
	1470	71.4	He	[10]
	1460	n/s	He	[4]
	1533		H_2O	
	1444		Benzene	
pine	1519	68	H_2O	[7]
	1429	66	Toluene	[7]
wood fibres				
Masonite	1456	n/s	xylene	[8]
defibrator fibreboard (wet process)	1452			
porous f.	n/s	78...94	n/s	[5]
intermediate f.		53...68		
hardboard		32...40		
cellulose	1528	n/s	xylene	[8]
	1560	n/s	n/s	[1]
	1580	n/s	n/s	[3]
	1553...1592	n/s	n/s	[6]
	1611	n/s	H_2O	[6]
hemicellulose	1500	n/s	n/s	[6]
	1535	n/s	xylene	[8]
lignin	1305	n/s	xylene	[8]
	1406	n/s	He	[4]
	1422		H_2O	
	1388		Benzene	
	1350...1460 ...1500	n/s	n/s	[1]

Table IV-7: Common values of true density ρ_t [kg/m^3] (solid density) and porosity Φ [%] determined via the respective method (by displacement medium) on different kinds of wood matter; sources [1] AUTORENKOLLEKTIV (1988), [2] LOHMANN (2010), [3] KOLLMANN (1951), [4] STAMM, HANSEN (1937), [5] LAMPERT (1967), [6] BOSSHARD (1974), [7] RACZKOWSKI, STEMPIEŃ (1967), [8] SEIFERT (1972), [9] PFRIEM et al. (2009), [10] ZAUER et al. (2013).

noted implications on thermal treatment conditions, considerable cell-wall modifications beyond plasticisation processes are empirically excluded during panel manufacturing. Despite consolidation reduces lumina volumes, it, nevertheless, coincidently enhances gas accessibility by

wood-cell deformation (cracks) anyway. Owing to varying densification ratios and atypical cold consolidation with subsequent through-heating during labMDF manufacturing, results do not allow any valid conclusion for hot-pressing influence in general. The obvious difference between ρ_t of raw fibres TMP-H and labMDF can, however, not significantly be proven by Welch's t-test[24]. Here, null hypothesis $H_0: \bar{\rho}_{t,\text{TMP-H}} = \bar{\rho}_{t,\text{labMDF}}$ vs. $H_1: \bar{\rho}_{t,\text{TMP-H}} \neq \bar{\rho}_{t,\text{labMDF}}$ is rejected at $\alpha = 0.07$. However, poor significance level arises from considerably high standard deviation of raw fibre measuring values $\rho_{t,\text{TMP-H}}$ and small sample sizes. Thus, more appropriate nonparametric Mann-Whitney U test unveils the difference more significantly where H_0 is rejected at $\alpha = 0.05$.

On the contrary to the apparent influence of resination on total true density, as a matter fact, true density of resin-bonded WBC is expected not to differ significantly from $\rho_{t,\text{wood}}$ due to similar density of cured solid UF adhesive resin $\rho_{t,\text{UF}} = 1481 \dots 1542 \, \text{kg/m}^3$ determined on theoretical basis as follows. Technical literature and data sheets solely provide density values of the liquid glue liquor in the range of $\rho_{\text{liq,UF}} = 1.26 \dots 1.3 \, \text{g/cm}^3$ with UF resin solid content $\text{SC}_{\text{UF}} > 60 \, \%$ (cf. PIZZI, MITTAL (2003), ZEPPENFELD, GRUNWALD (2005), SHEIKH et al. (2008)). As described by BANDEL (1995) or PIZZI, MITTAL (2003), resin solid content is typically determined via drying for a predefined duration (e. g. 2 h) at $\vartheta = 120 \, °\text{C}$. Simultaneously, polycondensation is expected to proceed, resin nearly cures, and respective amount of water evaporates as well as DUNKY (1998) points out. Thus, density of cured state can be derived, where resin is considered to be a non-porous solid body. Furthermore, liquid glue liquor is considered to be an ideal solution assuming a heterogeneous mixture without interaction on the molecular level. Accordingly, volumes are strictly additive – likewise masses even in non-ideal cases (cf. WITTENBERGER, FRITZ (1991)). Hence, resulting density of the mixture

$$\rho_{\text{mix}} = \frac{\sum_k m_i}{\sum_k V_i} \tag{IV-7}$$

in general equals the quotient of the respective sum of component's masses m_i and volumes V_i – likewise common to compute the mixture density of dispersions (cf. VÖLZ (2001)). Beyond those assumptions, DUNKY, LEDERER (1982) denote UF adhesive resins as partly aqueous solutions and partly dispersions therein. Furthermore, already DANKELMAN et al. (1976) suppose colloidal resin particles instead of molecules in solution. Their considerations support the concept of the glue liquor as quasi-ideal mixture without volume interaction of the components. With corresponding mass fractions

$$\omega(i)_{\text{mix}} = \frac{m_i}{m_{\text{mix}}} \cdot 100 \, [\%] \tag{IV-8}$$

and component volumes represented by individual density ρ_i eq. (IV-7) turns into

$$\rho_{\text{mix}} = \left(\sum_k \frac{\omega(i)_{\text{mix}}}{\rho_i} \right)^{-1} \cdot 100 \, [\%] \tag{IV-9}.$$

With the liquid UF resin solid content $\text{SC}_{\text{UF}} = \omega(\text{UF})_{\text{liq}} \cdot 100 \, [\%]$ eq. (IV-9) turns into

$$\rho_{\text{liq,UF}} = \left(\frac{1 - \omega(\text{UF})_{\text{liq}}}{\rho_{\text{H}_2\text{O}}} + \frac{\omega(\text{UF})_{\text{liq}}}{\rho_{\text{t,UF}}} \right)^{-1} \tag{IV-10}$$

for the binary ideal mixture of dry UF adhesive resin and water yielding the density of the liquid glue liquor. Accordingly, solving of eq. (IV-10) for $\rho_{\text{t,UF}}$ with $\rho_{\text{liq,UF}}$ and SC_{UF} from Table IV-3 and $\rho_{\text{H}_2\text{O},20} = 0.9982 \, \text{g/cm}^3$ at room temperature $\vartheta_{\text{RT}} = 20 \, °\text{C}$ yields $\rho_{\text{t,UF1}} = (1498 \pm 17) \, \text{kg/m}^3$ as well as $\rho_{\text{t,UF2}} = (1520 \pm 22) \, \text{kg/m}^3$ as true density of cured UF adhesive resin on a theoretical basis. Note, actual solid density is expected to depend on the cross-linking level of cured resin depending, in turn, on the curing conditions such as temperature, pH-value, and surrounding MC. However, neglecting the volume effects of glue liquor with dispersed colloidal UF pre-polymers, theoretical considerations finally provide appropriate $\rho_{\text{t,UF}}$ values as first approximation in the order of common $\rho_{\text{t,wood}}$. (Table IV-7) and measured $\rho_{\text{t,TMP-H}}$ (Figure IV-6 and Table IV-6).

---

[24] Unequal variances proven by F-test in advance, where null hypothesis H_0 was rejected at $\alpha < 0.001$.

Moreover, according to unofficial information from the R&D department of a German WBC manufacturing company, $\rho_{t,UF} = 1400 \ \mathrm{kg/m^3}$ is taken into account as a general value for solid ordinary UF adhesive resin.

Beyond theoretical considerations for lack of technical data from literature, measuring results of variously prepared resin types in Table IV-6 as well as exemplary UF-CH in Figure IV-6 prove the order of magnitude of computationally derived values. Gas pycnometry measuring results $\rho_{t,UF2\text{-}CH\text{-}OD} = 1514 \ \mathrm{kg/m^3}$ and $\rho_{t,UF2\text{-}CH} = 1501 \ \mathrm{kg/m^3}$ are in good agreement with theoretical values for both adhesive resins. Both mean values from repeat determination do not reveal any significant difference regarding sample treatment, where its actual impact is indefinable. However, displacement gas accessibility is considered as appropriate due to fineness degree of milled powder. Despite buoyance method was intentionally employed to double-check previous values, the method seems suitable for convenient density determination on void-free solid resin fragments in general. Particularly in case of UF2-DH sample (refer to Table IV-4 for clarification of abbreviations), an appropriate repeatability was obtained. Compared to theoretical and pycnometric values, buoyancy results drop slightly below, which clearly corresponds to the accomplished curing states at room temperature. Obviously equal results of UF2-DH-OD and UF2-DH samples reveal no considerable impact of gently attempted drying of rather huge crystalline resin fragments. The apparent difference between UF2-D samples with and without hardener is confirmed to be significant by Mann-Whitney U test, where the null hypothesis $H_0: F(\mathrm{UF2\text{-}DH}) = F(\mathrm{UF2\text{-}D})$ vs. $H_1: F(\mathrm{UF2\text{-}DH}) \neq F(\mathrm{UF2\text{-}D})$ (i. e. samples are from the same population) is rejected at $\alpha = 0.001$. Beyond that, in the case of the samples UF2-DH-OD (with desiccation cracks) and UF2-D, an upward or downward shift of displayed values was observed during immersed weighing. Thus, short submersion duration and immediate reading of first stable mass value was ensured. However, observed phenomena are obviously caused by the respective structural conditions of both samples. Fine

cracks within UF2-DH-OD sample induce capillary water uptake with consequent apparent mass increase. In the contrary case of the UF2-D sample, the dissolution of poorly cured resin results in decreasing specimen mass, where the impact on ρ_{IL} is negligible. A sticky surface of the removed specimens supports this assumption. In both cases, specimen volume variations and correspondingly altering buoyant forces make a minor contribution.

Considering oven-dry WBC matter again as a binary ideal mixture, i. e. heterogeneous mixture with assumed no atomic interaction, of cell-wall substances and cured adhesive resin, the resulting true density of this oven-dry WBC matrix is computed according to eq. (IV-7) by

$$\rho_{t,WBC} = \frac{m_{wood,OD} + m_{UF}}{V_{S,wood,OD} + V_{S,UF}} \qquad \text{(IV-11)}$$

as ratio of simply added single masses and solid volumes. Consequently, with actual UF resin mass fraction based on total WBC mass

$$\omega(\mathrm{UF})_{WBC} = \frac{\omega(\mathrm{UF})_{OD}}{100 \ [\%] + \omega(\mathrm{UF})_{OD}} \qquad \text{(IV-12)}$$

eq. (IV-11) turns into

$$\rho_{t,WBC} = \left(\frac{\omega(\mathrm{wood})_{WBC}}{\rho_{t,wood}} + \frac{\omega(\mathrm{UF})_{WBC}}{\rho_{t,UF}} \right)^{-1} \quad \text{(IV-13)}.$$

Accordingly calculated true density of labMDF with nominal resin fraction $\omega(\mathrm{UF})_{WBC} = 0.091$ and single true densities $\rho_{t,UF} = 1498 \ \mathrm{kg/m^3}$ as well as $\rho_{t,wood} = \rho_{t,TMP\text{-}H} = 1516 \ \mathrm{kg/m^3}$ yields $\rho_{t,labMDF} = 1515 \ \mathrm{kg/m^3}$ as mean value. Consequently, pycnometric measuring data of all WBC types does not represent actual true density of the oven-dry wood-particle-resin-matrices and is invalid, in turn. The apparently lower ρ_t values result from falsified higher V_S measuring values corresponding to diminished accessibility to the lumina and micro-pores caused by resin covering of cracks and pits of uncut fibres. The minor difference between MDF from laboratory and industry is not significant but seems to correspond to more capable industrial resination process accomplishing a more even adhesive resin distribution and fibre covering finally leading to worse gas accessibility. Additionally, the slightly higher resin solid content – evaluated via elemental

analysis, refer to IV–2.4.2 – supports these implications. Beyond those theoretical considerations regarding WBCs, influence of practical specimen preparation causes partly uncut fibres. Thus, inaccessibility to the respective wood-cell lumina for displacement gas He in case of closed pits[25] leads to falsely too high V_S values resulting, in turn, in decreased ρ_t according to eq. (IV-4) likewise ZAUER et al. (2013) conclude for their in fibre direction thick specimens ($t_{long} = 6$ mm).

Likewise normatively required, solid volume determination by gas pycnometry was carried out on oven-dry material. Despite rapid handling during sample unpacking, weighing, and measuring device loading, moisture absorption from surrounding air by the peculiarly hygroscopic oven-dry wood cannot be prevented. As control measurements immediately after the respective pycnometry cycle reveal, sample masses solely increased about 0.2 % on average. However, total sample manipulation cannot be evaluated, e. g. vacuum sealing. Hence, an infinitesimal MC in the early chemisorption state has to be considered. Thus, biased measuring results occur in a manifold but undistinguishable way. DIN 66137-2 (2004) points out that evaporating water vapour influences equilibrium pressure during measurement. As a consequence, too low values of V_S are displayed and, in turn, too high values of ρ_t are calculated via eq. (IV-4). Beyond insufficiencies related to measuring procedure, structural impact of adsorbed water layer on cell wall results in apparently higher ρ_t whereas a ρ_t decrease of this mixed matrix is expected due to eq. (IV-9) with $\rho_{H_2O,20} = 0.9982$ g/cm^3. ZAUER et al. (2013) likewise discuss this phenomenon based on the findings of STAMM, SEBORG (1934), SEIFERT (1972), and further hitherto investigations. Accordingly, high apparent volume compression of adsorbed water layers on cellulosic material at low MC levels is reported leading to $\rho_{H_2O} > 1$ g/cm^3. Additionally, ZAUER et al. (2013) and hitherto publications assume enhanced gas accessibility of micro-pores due to swollen cell wall corresponding to MC. Thus, superimposing

moisture effects rather yield decreased V_S resulting in increased ρ_t due to eq. (IV-4). Beyond discussed wood-chemical and methodical dependencies of V_S determination, RACZKOWSKI, STEMPIEŃ (1967) propose increasing ρ_t with increasing ρ_{OD}. Accordingly, the context is attributed to variations on sub-microscopic scale in cell-wall structure, i. e., intra- and interfibrillar micro-pores. However, verifications of the found relation are pending so far. Hence, established concepts considering compositional differences between species are rather taken into account.

To summarise the contribution of interdependent influence factors of practical relevance on validity of ρ_t determination on WBC via He gas pycnometry, the following relations of practice-oriented relevance result in respective ρ_t deviations:

- TMP fibre generation → no impact,
- furnish resination → ρ_t ↓,
- $MC > 0$ % → ρ_t ↑, and
- inaccessible lumina → ρ_t ↓.

Those potential falsifications have to be taken into account regarding evaluation and further processing of true density data from gas pycnometry. However, already KOLLMANN (1951) considers He as most appropriate displacement medium. For further methodical discussions, reference is made to the very same as well as ZAUER et al. (2013).

2.2   Fibre and particle morphology

2.2.1   Sampling and method

Fibrous raw material for lab-made furnish mats (TMP-F) and homogeneous fibreboards (TMP-H) was investigated regarding fibre length and width to take actual values into account for radiation-material interaction considerations. To this end, respective evaluations on both resin-unblended TMP fibre types were carried out utilising an optical analysis method developed and provided by IHD, Dresden, Germany. Complementary investigations were carried out by

---

[25] Well-known pit aspiration inhibits access to softwood tracheid lumina.

means of the FibreCube device at that time available at TI, Hamburg, Germany, where reference is made to Appendix VII–2.2. Beyond regular fibre material, milled fibres type H (TMP-h) were likewise investigated with particular regard to fibre length considerations in terms of true density determination.

Comprehensive concepts toward manifold TMP characteristics and resulting WBC properties are provided by WENDERDEL, KRUG (2011). However, former results available from literature are rare and viable general data is lacking. Furthermore, PLINKE et al. (2012) critically point out poorly representative results of classical sieve methods applied on fibres. On the contrary, via image processing and evaluation, they consider particle-wise contour determination as well as explicit differentiation of present fibre and particle types within the furnish assortment as more valuable, where both result in respectively weighted frequency distributions. The same applies to particles, where likewise particular length determination is not feasible via sieve screening. Consequently, WENDERDEL et al. (2014) consider furnish assortments as a mixture of structural elements. They therefore explicitly suggest to fundamentally distinguish present TMP fibre types regarding their morphology characteristics. Subsequently defined model particles on wood-anatomical basis serve with sub-classes as criteria for fibre classification. Thus, WENDERDEL (2015) concludes an undifferentiated analysis as major insufficiency of other methods. In addition to his implications on found correlations regarding final MDF properties, a distinctive evaluation beyond solely one mean figure appears valuable for the present purpose of fibre characterisation, i. e. structural considerations of material penetration by ionisation radiation. For holistic fibre morphology considerations and critically discussed state of the art in characterisation of TMP furnish, reference is made to WENDERDEL (2015).

For all performed furnish morphology analyses, cluster sampling was realised directly from the bag at representative positions and obtained material was blended again. Subsequently, individually required samples were withdrawn from these bulk samples resulting in the nominally requested weighed portions. The same applies to milled fibres remaining from true density determination (Chapter IV–2.1.1). Material was consistently stored at standard conditions (20/65) and vacuum-sealed for transport. For visual comparison, Appendix VII–2.2 provides photographic documentation of all utilised fibres and particles.

TMP morphology characterisations aiming at actual dimensions (length and width) of all fibres in the respective sample were carried out by means of the method developed and introduce by IHD (2014) and refined regarding several aspects by WENDERDEL (2015), referred to as IHD method henceforth. The actually performed procedure and primary data evaluation was equivalent to the descriptions of WENDERDEL (2015), whereon reference is made to for particular details. The employed device involves components of both QualScan and CamSizer system for image acquisition on separated particles. Here, nondestructive fibre separation and feed through modified FlowCell ensues via suspension of the respective sample in degassed water. Automated image acquisition of the respective material portion within the FlowCell is followed by data evaluation beginning with flat field image correction. For exemplary raw images, see Appendix VII–2.2. Complex data evaluation and fibre morphology characterisation algorithms are specified in detail by WENDERDEL (2015). Explicit distinction of fibre types according to implemented parameters for characterisation of the particular structural elements is performed, as one among other outstanding features of the system. Finally, the procedure yields the parameters length, width, and volume of each individual fibre where weighted frequency distributions on volume basis and further descriptive statistics can be derived considering the individual structural fibre types

- dust (D),
- dust coarse (Dc),
- single fibre short (SFs),
- single fibre long (SFl),
- fibre bundle compact (FBc), and
- fibre bundle split ends (FBs).

Here, automated separation and classification follows the predefinitions by WENDERDEL et al. (2014). By default, evaluation features frequency distributions on volume fraction basis of the respective fibre types complete with dust, rather than quantity- or mass-based evaluation. However, fibre morphology analyses were performed following the established procedure of the laboratory[26]. To this end, repeat determinations with $n = 3$ samples each nominally comprising a weighed portion of 1 g per run were carried out. Advantageously, comprehensively available initial measuring data enabled own evaluations.

Beyond statistics, the moisture conditions require certain corrections. Total immersion in water causes wood MC beyond fibre saturation point (FSP) and consequently TMP fibres in totally swollen state during measurement. However, fibre dimensions at standard (20/65) or oven-dry conditions are requested. On the contrary, applied fibre analysis method is expected to yield systematically increased fibre widths. Thus, downward correction is indispensable. Here, no particular differential shrinkage ratio q [%/%] is available for individual TMP fibres. Hence, MC-related correction of fibre dimensions – particularly the width – considering cell-wall shrinkage perpendicular to the grain appears non-trivial owing to structural conditions. Since TMP fibres are released from their native tissue, swelling and shrinkage ensues freely with assumingly higher extent. Moreover, q_w alterations across the annual ring along earlywood (EW) and latewood (LW) as well as between cell types are commonly known; i. e. $q_{w,EW} < q_{w,LW}$. Therefor, LANVERMANN et al. (2014a) provide figures for spruce determined on cross-sections of the nominal dimensions $40 \times 40 \times 5$ mm³ (tan, rad, long) with $\rho_{OD} = 365$ kg/m³ in the order of

- $q_{\mathrm{rad,LW}} = 0.25$ %/%,
- $q_{\mathrm{tan,LW}} = 0.33$ %/%,
- $q_{\mathrm{rad,EW}} = 0.07$ %/%, and
- $q_{\mathrm{tan,EW}} = 0.33$ %/% as well as

- $q_{\mathrm{rad}} = 0.14$ %/%,
- $q_{\mathrm{tan}} = 0.33$ %/%

for the bulk sample. Comparison of tabulated bulk wood values of differential shrinkage ratio of pine

- $q_{\mathrm{rad,pine}} = 0.15 \ldots 0.19$ %/% and
- $q_{\mathrm{tan,pine}} = 0.25 \ldots 0.36$ %/%

or beech

- $q_{\mathrm{rad,beech}} = 0.19 \ldots 0.22$ %/% and
- $q_{\mathrm{tan,beech}} = 0.38 \ldots 0.44$ %/%

in radial and tangential, respectively, direction as well as MDF

- $q_{\mathrm{t,MDF}} = 0.71 \ldots 0.93$ %/%

perpendicular to the panel plane (cf. DIN 68100 (2010)) unveils common softwood-hardwood differences and WBC processing impact, where increased MDF values correspond to densification ratio amongst others. Notwithstanding that, dimensional changes along the grain of single fibres are evidently neglected. Furthermore, DEROME et al. (2012) investigated hysteretic swelling and shrinkage by means of phase contrast X-ray tomography on spruce wood specimens with dimensions of $500 \times 500 \times 8000$ µm³ (tan, rad, long). They point out the differences between earlywood and latewood again – likewise comprehensively researched on spruce below macroscopic scale by LANVERMANN (2014) – and consider both single wood cells and the respective total fibre bundle. For their observed samples, they provide values in the order

- $q_{\mathrm{rad,LW}} = 0.30$ %/%,
- $q_{\mathrm{tan,LW}} = 0.35$ %/%,
- $q_{\mathrm{rad,EW}} = 0.06$ %/%, and
- $q_{\mathrm{tan,EW}} = 0.20$ %/%.

Apparently, there is no expected impact of reduced cross-sections revealed. Regardless of their particular samples, the share of latewood within an annual ring crucially varies across the log cross-section and depends on ring width, and thus growing conditions, and increases up to 50 % with increasing tree age, i. e., in outer tree

---

[26] Fibre morphology analyses were performed at the Institut für Holztechnologie Dresden gemeinnützige GmbH (IHD) Dresden, Germany, by the competent and experienced local staff. Their obliging and open-minded cooperation ready for any discussion and rapid support is highly appreciated.

rings (cf. TRENDELENBURG (1939)). However, a general share of latewood in, the order of one third, appears to be sufficient for rather young roundwood applied in WBC industry. Beyond that, tan/rad alignment of each measured TMP fibre as well as within a formed fibre mat ensues by chance, which inhibits, in turn, distinction of cross-sectional directions. Consequently, with an empirical ratio EW : LW = 2 : 1, a weighted mean and virtually isotropic

- $q_{\text{tan/rad,spruce}} \approx 0.2\ \%/\%$

is derived from the CT results above, obviously in the order of common spruce or pine values but rather toward the lower limit. Considering analogously a common hardwood (beech) content of 10 % in industrial MDF, mean differential shrinkage ratio for fibre width of a corresponding TMP mixture is respectively increased. Regardless of poor generalisation conditions, present data facilitates a first approximation according to which a mean and virtually isotropic differential shrinkage ratio is defined in the order

- $q_{w,\text{TMP}} = 0.22\ \%/\%$

on empirical basis for individual but randomly aligned TMP fibres regarding their cross-sectional direction (fibre width). Note, considering drying below FSP, estimation involves slight decrease of $q_{w,\text{TMP}}$ toward FSP beyond actually linear range within $MC = 5 \dots 20\ \%$. According to the common classification of wood species by TRENDELENBURG (1939) regarding their typical FSP as well as impact from thermal modification during TMP processing, assumed $MC_{\text{FSP}} = 27\ \%$ appears sufficient. Aiming at standard conditions with $MC_{20/65}$ from Table IV-5 in Chapter IV–1.5, MC decrease is about $\Delta MC = MC_{\text{FSP}} - MC_{20/65} = 16.2\ \%$. Finally, correction of dimensional changes ΔM [μm] of the actual fibre width N_w in consequence of water immersion is carried out following DIN 68100 (2010) via

$$\Delta M_w = N_w \cdot \frac{\Delta MC \cdot q_{w,\text{TMP}}}{100\ [\%]} \qquad\qquad \text{(IV-14)}$$

yielding relative changes of $\Delta M_w = 3.56\ \% \cdot N_w$.

Furthermore, both surface (SL) and core layer (CL) particles were characterised via simple sieve analysis. The investigations were carried out immediately after material withdrawal with

appropriate conditioning in between at the Scandinavian particleboard production plant by means of locally established and generally common method. To this end, analytical Sieve Shaker VS 1000 Retsch GmbH, Haan, Germany, was employed complete with test sieves of 200 mm diameter and mesh sizes 0.25, 0.315, 0.5, 0.8, 1.0, 2.0, 4.0, 8.0 mm (DIN ISO 3310-1 (2017)). One sample for single determination of nominally 100 g of SL and CL particles each was screened for 15 min at 50 % amplitude. Discussion of analysis methods are available from HARTMANN et al. (2006) or elsewhere.

2.2.2   Results and discussion

Table IV-8 presents selected TMP fibre size data of published results from hitherto investigations. Obviously, no general data is available supposedly owing to significant dependency of fibre morphology characteristics on defibration conditions as well as neither standardised nor even established capable analysis methods prior to appreciable developments of the recent years. Moreover, considerable material related and methodical differences in consequence of varying

- wood species,
- defibration conditions,
- analysis method, and
- way of mean determination

as well as inherently wide fibre size range inhibit to summarise typical morphology parameters of TMP fibres from literature. Nevertheless, purposed radiation-physical considerations require a generalisation to facilitate a schematic model concept based on model particles of WENDERDEL et al. (2014) and actual measuring data.

Table IV-9 provides summarised results of fibre morphology characterisation via IHD method with volume-weighted mean width w [μm] and length l [μm] as well as computed slenderness ratio l/w [−] per structural fibre type of TMP-F and TMP-H, respectively. Here, the values involve ΔM_w swelling correction of fibre width correction via eq. (IV-14). Relative frequencies were computed as volume fraction $\varphi(i)$ [%] of each analysed fibre related to total volume of either individual structural fibre type or whole sample for

analysis method	fibre width[27] [µm]	fibre length [µm]	mean type	source
n/s	40... 250	4000... 7000	n/s	LOHMANN (2010)
sieve	166	4182	(1)	LAMPERT (1967) recalculated
QualScan µCT	400 n/s	2050 3000 ...5000	(2) n/a	WALTHER (2006)
QualScan	400	2050	n/s	GRUCHOT (2009)
FibreLab	30.9	1680	n/s	ROFFAEL et al. (2009)
air-jet sieve QualScan	340 380	n/s 2490	(2)	KRUG (2010) lab-made
air-jet sieve QualScan	330 390	n/s 2240	(2)	KRUG (2010) industrial
air-jet sieve	700	n/s	(2)	WENDERDEL, KRUG (2010)
FibreCube	n/s	2900	(3)	BENTHIEN et al. (2014b)
IHD	304	3580	(4)+(2)	WENDERDEL (2015)
model SF model FBc	40 600	3200 6000	n/a	WENDERDEL et al. (2014)

Table IV-8: Compilation of more or less representative mean dimensions of TMP fibres (as far as known from pine), selection of previous analysis results at typical medium defibration conditions determined by the respective method; mean calculation (1) mass-based weighted, (2) mean of 16, 50 und 84 % quantile, (3) double-length weighted, (4) volume-based weighted.

structural fibre type	width w [µm]	length l [µm]	l/w [−]	$\varphi(i)$ [%]	TMP type
D*	18	61	4	0.2	F
	18	61	4	0.2	H
Dc*	56	98	2	3.9	F
	55	102	2	5.5	H
SFs	**44**	**925**	**23**	**15.8**	**F**
	43	**805**	**20**	**22.3**	**H**
SFl	47	3971	88	0.3	F
	47	3929	87	0.2	H
FBc	**224**	**2049**	**10**	**76.1**	**F**
	237	**1988**	**9**	**69.6**	**H**
FBs	278	8665	33	3.8	F
	284	8434	31	2.2	H
Σ	191	1756	11	100.0	F
	181	1498	10	100.0	H
Σ'	198	1859	11	95.9	F
	191	1622	11	94.3	H
SFs	**44**	**850**	**19**	**21**	**M**
FBc	**230**	**2020**	**9**	**79**	**M**

Table IV-9: Results of fibre size determination by IHD method on both raw TMP fibre types F and H and computed slenderness ratio l/w with combined data from $n = 3$ samples after ΔM_w swelling correction via eq. (IV-14) of fibre width summarised as median values from volume-based weighted frequency distribution per individual structural fibre type i and its volume fraction $\varphi(i)$; complete with undifferentiated values respectively weighted with (Σ) and without (Σ') dust; * partly below camera resolution limit (15 µm pixel size); added empirical figures for structural TMP fibre model (M).

the purpose of appropriate mean value weighting and frequency distribution representation. Notwithstanding the IHD procedure for final evaluation, individual data classification considering actual value range $R = max - min$ per measuring sub-series (structural fibre type) with the number of classes k according to

$$k = 1 + \frac{10 \cdot \log(n)}{3} \tag{IV-15}$$

in dependence of the number of measuring values n as well as with exponentially increasing individual class widths r_j ($j = 1 \dots k$) computed via

$$r_j = r_{\text{U},j} - r_{\text{L},j} \tag{IV-16}$$

with upper

$$r_{\text{U},j} = max^{j \cdot k^{-1}} \cdot min^{(k-j) \cdot k^{-1}} \tag{IV-17}$$

and lower

$$r_{\text{L},j} = max^{(j-1) \cdot k^{-1}} \cdot min^{(k-j-1) \cdot k^{-1}} \tag{IV-18}$$

class limit with r_j corresponding to w_j and l_j, respectively, was carried out to facilitate convenient distinction of the wide-ranging values by logarithmic representation of frequency distribution. Relative volume-based frequency

$$\Delta Q_{3,j} = Q_3(r_{\text{U},j}) - Q_3(r_{\text{L},1}) \tag{IV-19}$$

---

[27]   Note, width considers henceforth any cross-sectional dimension of the fibre whereas two-dimensional image acquisition allows no explicit distinction.

was normalised and transformed to logarithmic abscissa via

$$\bar{q}_{3,j}^* = \frac{\Delta Q_{3,j}}{\log(r_{U,j}/r_{L,j})} \qquad \text{(IV-20)}$$

following DIN ISO 9276-1 (2004), where subscription 3 denotes volume-based distributions. However, further descriptive statistics have to be unaffected from appropriate classification. Mean results per individual structural fibre type i were determined as median values from each volume-weighted frequency distribution, which are exemplarily shown in Figure IV-7 for selected predominant structural fibre types. Likewise WENDERDEL et al. (2014) already suggested, the volume-based weighting of both measured fibre dimensions is to be preferred in contrast to number-weighted distributions. Mean values were computed by volume-weighted median instead of arithmetic mean, which is considered as robust measure of location in general and particularly appropriate for the present right-skewed distributions. In this regard, median as middle value of distribution density is not affected by both single coarse fibres (shives) and certain amount of fine dust. It properly represents investigated furnish mat structure in general, which is of central importance for purposed radiation-physical considerations.

Presented results in Table IV-9 and Figure IV-7 comprise combined data of the initial $n = 3$ samples of repeat determination. Moreover, re-combination was appropriate due to sampling from blended bulk samples, obviously congruent single results in comparison of the three samples, and established repeatability of the method according to WENDERDEL et al. (2016). Note, determined fibre width represents solely one extent of the structural element perpendicularly to the length as most extensive dimension owing to two-dimensional image acquisition. However, it is considered to denote fibre thickness or depth, thus, diameter likewise, which is analogously as-

sumed by device software for fibre volume determination. Dust particles (D) largely fall below camera resolution limit (15 μm pixel size). Notwithstanding that, their volume fraction is consequently not assumed to be underestimated and actually heads toward negligibility. Coarse dust class (Dc) ranges in measurable sizes, but shows low content, in turn. Despite its respectively minor relevance as amount of matter for radiation attenuation, total fines content is crucial regarding resin consumption. However, WENDERDEL (2015) likewise neglects minor volumetric dust content. Furthermore, Table IV-9 (bold figures) reveals that two structural fibre types dominate both TMP assortments, respectively, according to their volume fraction $\varphi(i)$, where compact fibre bundles (FBc) show major content besides short single fibres (SFs). As easily can be seen from Figure IV-7, both fractions respectively govern the shape of volume-weighted frequency distributions considering both width and length. Thus, dimensions of the distinctly most frequent types of structural elements FBc and SFs are henceforth exclusively taken into account for structural considerations on the formed or consolidated furnish mat regarding radiation transport through WBC matter. With respect to the remarkable SFs content, WENDERDEL (2016) empirically assumes respective hardwood (beech) content and/or comparatively new refiner discs with respectively high cutting impact. Finally, he endorses assumed industrial origin based on experience. Accordingly, occurrence of long single fibres (SFl) with high l/w is rare within such industrial TMP. Nonetheless, their relevance for mechanical panel properties is unquestionable. Eventually, typically low volume fraction of fibre bundles with split end (FBs) WENDERDEL (2016) likewise attributes to assumed industrial conditions of mechanical pulping with long cutting paths through high disk diameters compared to lab refiners.
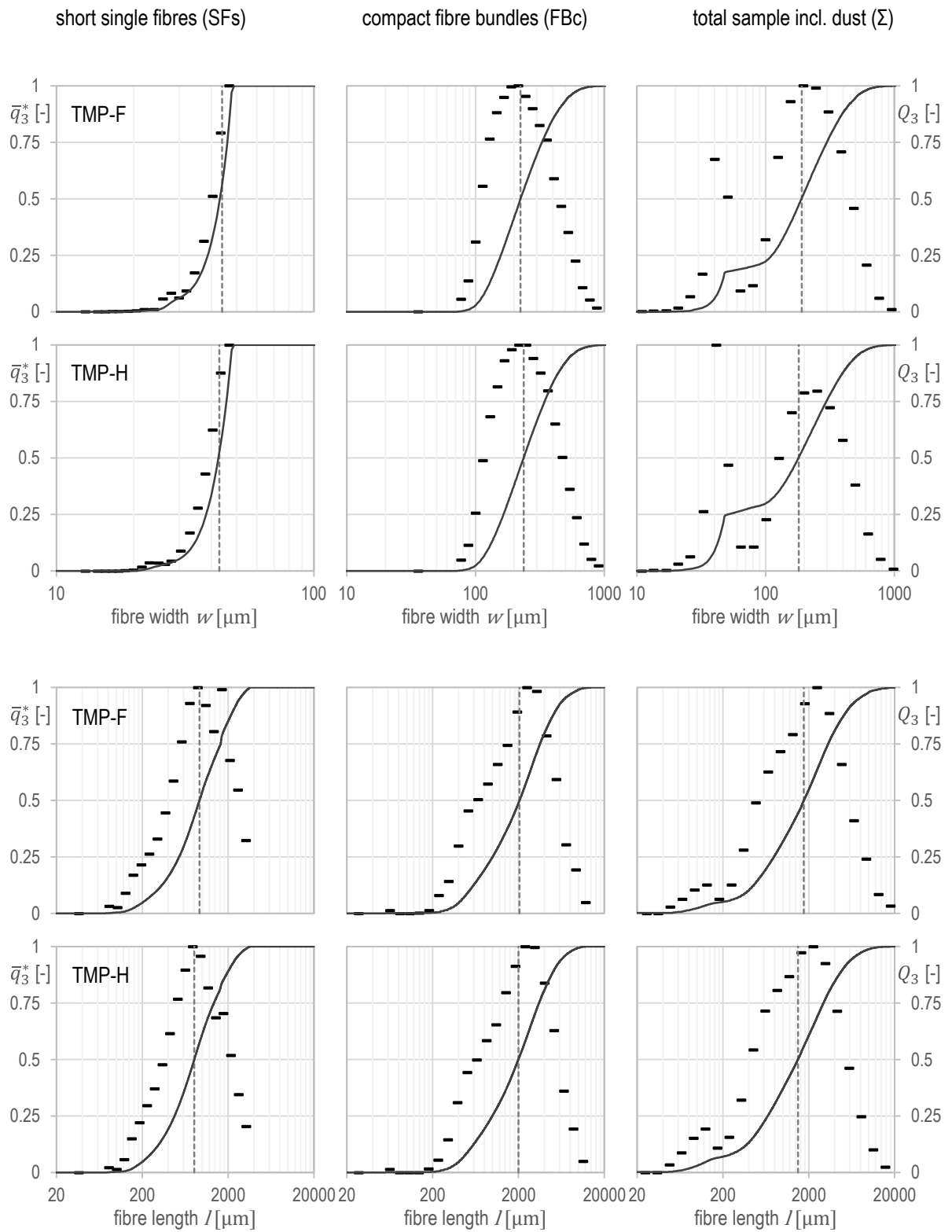
Figure IV-7: Results of fibre size determination by IHD method as normalised frequency $\bar{q}_3^*$ $[-]$ (bars, transformed on logarithmic abscissa) as well as cumulative frequency Q_3 $[-]$ (solid line) distributions of volume fraction of fibre width w and length l $[\mu m]$ following DIN ISO 9276-1 (2004) complete with median (vertical dashed line); TMP-F and TMP-H data of selected predominant structural fibre types short single fibres (SFs) and compact fibre bundles (FBc) as well as total sample incl. dust (Σ).

Evidently, ascertained variability in volume fractions of fibrous sample components clarifies necessity of distinction between structural fibre types in context of morphology characterisation. The same applies to measured characteristics of fibre dimensions. Additionally to distinguishing evaluation, a combined representation of all frequencies on volume basis is provided in Figure IV-7, which appears advantageous in particular cases of investigation as WENDERDEL (2015) points out and serves for comparative purposes here. At this, a volume fraction of total fibrous sample of $\varphi(\Sigma) = 70\,\%$ in the case of TMP-H exceeds fibre widths of $w \geq 100\,\mu m$ whereas TMP-F batch contains less Dc as well as SFs and solely $\varphi(\Sigma) = 23\,\%$ fall below $w < 100\,\mu m$. To distinguish classified fibre types again (Figure IV-7, left and middle column), distribution of SFs width is rather narrow and significantly bounded above owing to classification criteria ($w \leq 48\,\mu m$). The obviously symmetrical FBc distribution on logarithmic abscissa shows positive skewness. The same applies to volume-weighted frequency distribution of both total samples (Figure IV-7, right column), where an additional peak of fine fibres (SFs, Dc, SFl, and D) respectively occurs. Regarding fibre length of both TMP types, charts illustrate a comparable bimodal total distribution with less distinct peaks of lower lengths in contrast. Maximum length was found $l_{\mathrm{max}} = 21117\,\mu m$ (TMP-F) and $l_{\mathrm{max}} = 18213\,\mu m$ (TMP-H), respectively, where fibres were classified as FBs in both cases. On the contrary, the highest extent in fibre width was determined on FBc with $w_{\mathrm{max}} = 1065\,\mu m$ (TMP-F) and $w_{\mathrm{max}} = 1100\,\mu m$ (TMP-H), respectively. Maximum slenderness ratio $l/w_{\mathrm{max}} > 150$ occurs within SFl classes each, which are, nonetheless, totally underrepresented with $\varphi(\mathrm{SFl}) < 0.3\,\%$. Finally, considering numbers (Table IV-9) of composition $\varphi(i)$ as well as fibre dimensions w and l, both TMP fibre batches are apparently similar. Likewise, charts of volume-weighted frequency distributions (Figure IV-7) of both width and length unveil certain conformities. Accordingly, they are almost congruent regarding fibre morphology characteristics.

To summarise, SFs and FBc as predominant characteristic structural types are considered for general fibre size values, where $\varphi(\mathrm{SFs})$ depends on hardwood content and $\varphi(\mathrm{FBc})$ with $l/w \approx 9 \ldots 10$ dominate TMP furnish. Accordingly, a mean empirical assortment of TMP fibres comprises $\varphi(\mathrm{FBc}) = 79\,\%$ with $w = 230\,\mu m$, $l = 2020\,\mu m$, and $l/w = 9$ as well as $(\mathrm{SFs}) = 21\,\%$ with $w = 44\,\mu m$, $l = 850\,\mu m$, and $l/w = 19$ as added in Table IV-9 (TMP-M).

Beyond regular fibres, summarised measuring results in Figure IV-8 of milled material TMP-h reveal considerably reduced fibre lengths. Here, volume-weighted majority of values comes below 2400 μm (upper whisker) with the median 782 μm. Evidently, milling was efficient by cutting wood cells as intended for true density determination (Chapter IV–2.1).

To conclude fibre morphology characterisation, WENDERDEL et al. (2014) summarise TMP fibres for MDF manufacturing as heterogeneous mixture of distinct structural elements such as dust, single fibres, and fibre bundles, where the former is considered as negligible regarding its typically low volume fraction. Both utilised TMP assortments are found to be dominated by two structural fibre types according to their volume fraction, i. e., mainly compact fibre bundles as well as short single fibres. Regardless of similar magnitude, present fibre characterisation results (Table IV-9) rather fall below literature values (Table IV-8) due to industrial origin of the utilised material. However, apparent morphological similarity of both TMP fibre types considering dimension distributions is found, where complementary illustrations of size variations are provided in
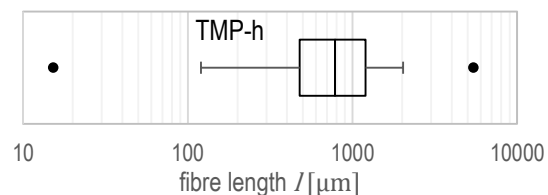
Figure IV-8: Summary of fibre length l [μm] variation within total assortment (incl. dust) of milled fibres TMP-h determined by IHD method as box plot with (all volume-weighted) $Q1 = 478\,\mu m$, $med = 782\,\mu m$, and $Q3 = 1197\,\mu m$, 5 % quantiles as whiskers $Q(0.05) = 120\,\mu m$ and $Q(0.95) = 2015\,\mu m$, as well as $min = 15\,\mu m$ and $max = 5419\,\mu m$ (bullets).

Appendix VII–2.2. Moreover, the applied concept of distinction of predefined structural elements is considered to be a valuable procedure, which facilitates purposed generalisation without losing accuracy and, ultimately, unveils the predominant structural elements regarding fibre dimensions. Both used batches of fibrous material were chosen without any particular purpose regarding common panel properties. However, typical industrial assortments were intended. For previously found relations between defibration conditions, fibre sizes, and final WBC properties by means of the utilised characterisation methods, reference is made to WENDERDEL, KRUG (2010) and BENTHIEN et al. (2014b), where WENDERDEL (2015) develops holistic model concepts. In comparison of analysis results toward compiled values in Table IV-8, the way of mean computation is of crucial impact in addition to actual structural differences. Note, there are several particular mean types facilitating to weight results according to intention; e. g., Lehmer mean

$$L_p(x) = \frac{\sum_{i=1}^{n} x_i^p}{\sum_{i=1}^{n} x_i^{p-1}} \qquad \text{(IV-21)}$$

as variable general measure of location, which enables to emphasise small values by exponent $p < 1$ and to shift the mean toward high values by $p > 1$. However, volume-based instead of double length-based (TI method, Appendix VII–2.2) weighting of present evaluation appears reasonable and practice-oriented regarding present purpose considering bulk volume including fibre width and not only fibre length. Beyond that, volume-based weighing is to be preferred toward number-based frequency distributions as already pointed out by WENDERDEL et al. (2014) with exemplary comparative calculations. Regarding mechanical properties, volume-based computation rather represents the amount of bulk material. The like applies to radiation-physical considerations, where the amount of matter, i. e., mass per unit area, thus, volume assuming equal raw density, is relevant for radiation attenuation. Hence, number-based evaluation is considered not to provide representative figures. However, a simplified generalisation of common fibre dimensions based on the present TMP

batches finally yields for the predominant fibre bundle compact (FBc) $l \approx 10 \cdot w$ single fibre short (SFs) $l \approx 20 \cdot w$ corresponding to the individual slenderness ratio l/w, where similar ratios become obvious from the data of WENDERDEL (2015). Note, both figures serve as rough estimate for further conceptional application of the data for a rather schematic model concept of radiation transmission through WBC matter.

In addition to fibre data, Figure IV-9 shows the sieve analysis results of SL and CL particle characterisation with particle size distributions as mass fraction per class according to eight sequential mesh sizes and residue (< 0.25 mm). Evidently, an explicit distinction between particle thickness and length is not feasible owing to screening mechanism. Though particularly slender particles tend to remain in sieves beyond their proper classes, the results provide a rough estimation of thickness distributions within both particle assortments. However, the obtained results just represent a classification of the particles but do not reveal actual dimensions (length and width) by absolute numbers. Due to complementary purpose, no further highly sophisticated analysis methods were performed for SL and CL particles. Therefore, determined particle characteristics are not applied further.
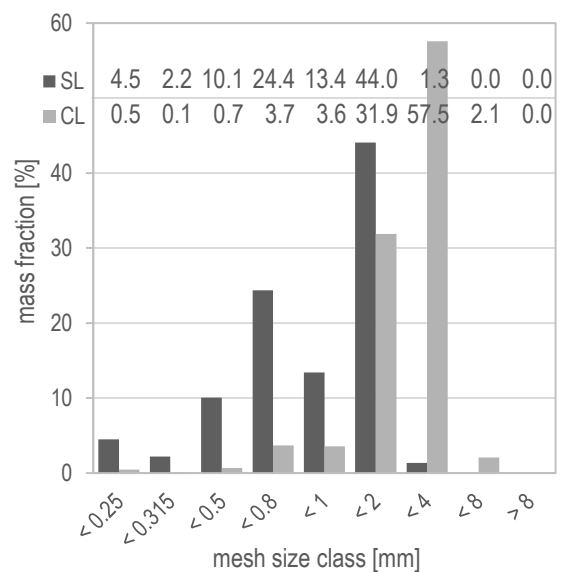
Figure IV-9: Sieve analysis results of SL and CL particle characterisation by Sieve Shaker with classes acc. to eight sequential mesh sizes and residue.

2.3 Ash content

2.3.1 Sampling and method

The non-combustible, mineral or inorganic, respectively, component residue as mass fraction of oven-dry sample mass is referred to as ash content $\omega(a)$ [%] (cf. KALTSCHMITT et al. (2009)). Furthermore, DIN 51719 (1997) annotates acc. to RUHRKOHLE-VERKAUF GMBH (1984) for solid fuels that determined ash content is non-identical to actual mineral matter content of the initial substance due to chemical reactions during combustion. LASKE (1961) likewise distinguishes between "true ash" and diminished residue on ignition. Accordingly, the latter deviates in amount and composition from natural mineral matter content. Depending on combustion temperature and type of mineral compound, mineral mass increase or decrease occurs, respectively, during combustion process. However, the content of metallic (e. g. Ca) and metalloid (e. g. Si) elements is of primary interest for the present study as contribution to WBC matter compositions on atomic level.

For ash content determination on wood and WBCs via direct single-stage combustion, no particular European standards are present. However, respective regulations exist for similar materials like paper and board (DIN 54370 (2007)), adhesives (DIN EN 1246 (1998)), plastics (DIN EN ISO 3451-1 (2008) and further parts), solid fuels (DIN 51719 (1997)), and carbonaceous materials (DIN 51903 (2012)). As exemplary application on cokes, the latter defines as method parameters for expected $0.1 < \omega(a) \leq 1\,\%$

- 2…20 g weighed portion
- with previous oven-drying and
- 10…20 h combustion
- at $\vartheta_{furnace} = (800 \pm 20)\,°C$
- in oxidising atmosphere.

Note, DIN 51903 (2012) points out decreasing ash content with increasing combustion temperature. Moreover, TAPPI T 211 (2016) as well as TAPPI T 413 (2017) define procedures on two different temperature levels for the pulp and paper industry, where ASTM D1102-84 (2013) is a corresponding adaption to wood. Regarding

wood fibre building boards, ISO 3340 (1976) regulates sand content determination. Here, the complete combustion of

- (200 ± 2) g weighed portion of
- conditioned samples (20/65)
- at $\vartheta_{furnace} = 500 \ldots 600\,°C$
- after pre-ignition

is followed by acid and water treatment as well as filtration to extract any remaining sand particles (≥ 40 μm). Supposedly following ISO 3340 (1976), SCHRIEVER, BOEHME (1984) investigate mineral components in coated PB by combustion of 50 g oven-dry samples with subsequent sand extraction (≥ 50 μm) and analysis of Si and Al content, respectively. While they determine an ash content of $\omega(a) = 0.58 \ldots 1.09\,\%$, the corresponding sand content $\omega(sand) = 0.006 \ldots 0.142\,\%$ ranges one order of magnitude below. IVANOVA (2009) applies the method as reference procedure for her investigations on indirect determination of mineral impurities. The ISO method followed by both is commonly applied in the WBC sector for sand content determination with company-internal adaptions. Here and elsewhere, multi-stage ignition processes with external (incomplete) pre-combustion and subsequent (complete) combustion within a crucible in a respective muffle furnace are performed. With their focus on sand content (i. e. especially SiO_2 from impurities) "[…]to obtain an indication of machinability by cutting tools" (ISO 3340 (1976)) and the way of pre-combustion, the procedures are supposed to be error-prone regarding the consideration of highly-dispersed trace elements. DEETZ (2009) preformed a single-stage combustion of annual plants with $\omega(a) > 5\,\%$ in general. Furthermore, he worked with considerably reduced weighed portions down to 10…15 g owing to bulk volume.

Considering previously reported investigations, the procedure performed in this study was developed, evaluated, and optimised with further respect to present equipment. Accordingly, a single-stage process within a lid-covered voluminous crucible was carried out without pre-combustion as gradually listed in Table IV-10. Thus, ash particle discharge during intense early pyrolytic combustion step is avoided. Note, despite

porcelain discolouration, removed lids did not show any ash aggregation. The procedure is less laborious and total ash mass without further performance for acid-soluble silica determination is intended. As exhaust air high-temperature furnace, the microwave laboratory system StarT Pyro T-1640, MLS GmbH, Leutkirch, Germany was employed. Porcelain combustion crucibles with lid, a capacity of 270 cm³, and heat stability up to 1000 °C were manipulated exclusively by clean crucible tongs even in cold state to avoid contamination and weighing result falsification by skin particles and moisture. Finally, ash content $\omega(a)$ [%] is computed via

$$\omega(a) = \frac{m_a}{m_{\mathrm{OD}}} \cdot 100 \ [\%] = \frac{m_{a,2} - m_{a,0}}{m_{a,1} - m_{a,0}} \cdot 100 \ [\%]$$

$$(\text{IV-22})$$

per sample with respective masses $m_{a,i}$ following Table IV-10. Due to combustion of oven-dried material with coincident MC determination, no correction of the very same is required. Unless specified otherwise, results from eq. (IV-22) refer to oven-dry state of the material.

Comprehensive measurements were carried out on all employed WBC types and (raw) furnish materials as well as one adhesive resin type (UF2-D) with $n = 3 \dots 5$ each. In comparison to several established methods (except ISO 3340 (1976)) for combustion of comparable materials, weighed portion was crucially increased in case of typically densified panels with $\bar{\rho} > 500 \ \mathrm{kg/m^3}$ to enhance weighing accuracy by coincidently increasing residual ash mass after combustion with respect to expected minor ash content $\omega(a) < 0.5 \ \%$ in relation to sample mass and major crucible tare. Here, by means of maximum available (covered) crucible volume, oven-dry weighed portions of nominally (65 ± 2) g were obtained. Bulky loose fibres ($\approx 9 \dots 13$ g) and particles ($\approx 30 \dots 40$ g) as well as low-density panels ($\approx 20 \dots 30$ g) and mats ($\approx 9 \dots 13$ g) required a respective reduction. To increase surface for enhanced combustion and to facilitate proper crucible filling, panel material was reduced to small pieces (approx. $5 \times 10 \times 15 \ \mathrm{mm^3}$) by cutting via band-saw to save material again. For illustrated specimen preparation, sampling, and measuring equipment see Appendix VII–2.3. Note, in the

step	action	parameters; output duration	
1	sample cutting from distinct panel areas		
2	re-conditioning and interim storage	20/65; > 1 week	
3	pre-sampling and oven-drying in a beaker with coincident MC determination (DIN EN 322 (1993))	(75 ± 2) g, (103 ± 2) °C; 72 h	**MC**
4	crucible cleaning and drying	900 °C; 1 h	
5	cooling-down crucible in desiccator and weighing	RT; 1 h	**$m_{a,0}$**
6	crucible filling with sample and weighing	(65 ± 2) g, RT; rapidly	**$m_{a,1}$**
7	(incomplete) combustion	900 °C; 1 h	
8	lid removal, coincidently fresh air into combustion chamber		
9	(complete) combustion	900 °C; 5 h	
10	pre-cooling down in furnace	< 900 °C; 0.5 h	
11	cooling-down crucible in desiccator and weighing	RT; 1 h	**$m_{a,2}$**
12	mass double-check	after > 12 h	**$m_{a,2+}$**
13	compute ash content	eq. (IV-22)	**$\omega(a)$**

Table IV-10: Elaborate gradual performance of ash content $\omega(a)$ determination according to own procedure, with total duration (steps 3 to 11) > 9 h.

case of indMDF samples, sampling was actually performed on cuttings directly neighbouring the X-ray measuring positions within the total panel. Adhesive resin UF2-D (see Table IV-3 and Table IV-4) was taken from residual material with totally exceeded duration of storage inside the canister. However, gentle drying of the solid block was completed for 96 h at 60 °C and material was reconditioned at 20/65 afterwards. In contrast to all other ash content samples, crushed UF2-D material was combusted in conditioned state (20/65) omitting oven-drying in advance due to aforementioned impact on resin structure by cracking of macro molecules, which, in turn, causes water and formaldehyde evaporation. Consequently and owing to non-porous coarse powder with $\rho_t \approx 1400 \dots 1500 \ \mathrm{kg/m^3}$, an increased weighed portion in crucible of $m_{a,1} - m_{a,0} \approx 110$ g was obtained without the necessity of accordingly increased combustion duration due to assumed rapidly evaporated volatile components along with thermally-induced hydrolysis. Nonetheless, expected ash content of adhesive

resin toward zero is considered to be unaffected by actual moisture conditions.

To summarise in general, complete combustion and actual ash content $\omega(a)$ determination is methodically influenced by

- specimen cutting size,
- sample MC,
- weighed portion,
- furnace temperature,
- combustion duration,
- presence of oxygen,
- particle discharge, and
- cleanliness during performance.

However, temperature control and duration of the respective combustion stages is worth to be evaluated elsewhere considering stages of wood combustion in general (cf. MARUTZKY, SEEGER (2002) and KALTSCHMITT et al. (2009)) and particularly element oxidation, which, in turn, might increase mass of non-combustible residue.

2.3.2   Results and discussion

A selection of common ash content $\omega(a)$ values and previously reported research results are compiled in Table IV-11. Beyond that, FENGEL, GROSSER (1975) provide from a bibliographical review a comprehensive compilation of the chemical composition of soft- and hardwoods on molecular level complete with their ash content. Furthermore, ROWELL (2005) composes data of hardwoods and softwoods in the USA, which have been analysed by USDA FPL from 1927 to 1968. As easily seen, ash content differs considerably with respect to the composition of the sample (e. g. including bark) and the wood habitat. Nonetheless, tremendous upward differences are considered as erroneous regarding clean wood from temperate zones. The statement from WALKER (2006a), that "the inorganic ash content is usually 0.1…0.3 % […] and rarely exceeds 0.5 %, except in some tropical hardwoods […]" with high Si content, unveils an appropriate general value range.

Ash, in turn, comprises several elements, where EHRENBERGER (1991) describes composition of combustion residues in general. Accordingly, ash from ignition in air atmosphere comprises both stable free metals (e. g. Co, Ni) as well as metal or metalloid oxides (e. g. Al_2O_3, Fe_2O_3, SiO_2) and metal sulphates (e. g. $CaSO_4$). Regarding the present study and owing to infinitesimal S concentration in wood (despite known 1 % hardener $(NH_4)_2SO_4$ in labMDF) and combustion at 900 °C, Ca as major ash component is assumed to be present as CaO instead its sulphate. According to LOHMANN (2010), ash of European wood species mainly consists of cations Ca^{2+} (25…35 %), K^+ (10…15 %), Mg^{2+} (3…7 %), and Fe^{3+}, Mn^{2+}, Al^{3+} (10 %) as well as anions CO_3^{2-} (25…35 %), SO_4^{2-}, PO_4^{3-}, and $(Si_xO_y)^{4x-2y}$ (10 %). MÖRATH (1950) points further out, that partly ash components are firmly bound to grain matter. Moreover, a comprehensive study on the occurrence of trace elements in wood was performed WAŻNY, WAŻNY (1964). They basically determined ash content (at $\vartheta_{furnace} = 500\,°C$) ranging $\omega(a) = 0.13\ldots1.64\,\%$ for 34 European wood species with subsequent ash analyses. Doubtless, crucial variations are considered to be caused by methodical and sampling reasons. Implications on significant differences between respective species in general seem unconvincing. However, radial distributions of minerals across stems of Norway spruce are, e. g., available from ÖSTERÅS (2004).

Regarding WBCs, less numerous investigations exist (Table IV-11), which, in turn, rather purpose determination of sand content with a certain particle size as abrasive medium. In this regard, IVANOVA (2009) concludes the origin of mineral inclusions fundamentally as impurities from raw material or production process. However, actual ash content of all WBC types is inferred to be affected by manifold conditions, such as

- wood-yard cleanliness,
- debarking quality,
- potential chip washing (MDF),
- waste-wood content, and
- coating including abrasive particles,

thus, the WBC type in general where $\omega(a)_{MDF} < \omega(a)_{PB}$. Influence of typical adhesive resins (without filler) is negligible owing to its purity. Finally, in comparison to wood (pure matter, clean, without bark), ash composition of WBCs shows a higher Si content from external impurities, which markedly occurs in PB.

material	remarks	$\omega(a)$ [%]	source
bark		3...4	[14]
	beech	2.6	[14]
	beech	3...4	[1]
	pine	1	[1]
	spruce	1.8	[14]
	spruce	1...3	[1]
	mean	**2.4**	**comp.**
beech		0.363	[20]
		0.4	[12]
	mean sap- & heartwood	0.435	[6]
		0.5	[14]
		0.55	[17]
		0.57	[8]
		0.67	[22]
	mean	**0.5**	**comp.**
pine		0.17	[12]
	mean sap- & heartwood	0.17	[6]
		0.26	[17]
		0.32	[22]
	mean	**0.23**	**comp.**
spruce		0.21	[20]
	mean sap- & heartwood	0.23	[6]
		0.23	[12]
		0.26	[2]
		0.37	[8]
		0.4	[14]
		0.79	[22]
	mean	**0.46**	**comp.**
hardwood	chips	0.465	[18]
softwood	chips	0.366	[18]
wood		0.4	[20]
	mean from 14 citations	0.4	[21]
		0.3...1.0	[10]
		0.5...1	[14]
	all species	0.2...0.6	[11]
	all species	0.2...0.6	[15]
	all species	0.2...0.8	[1]
	all species	0.5...1.5	[5]
	temperate zones	0.2...0.5	[7]
	temperate zones	0.2...0.6	[4]
	temperate zones	0.2...0.8	[13]
	mean	**0.5**	**comp.**

material	remarks	$\omega(a)$ [%]	source
tropical wood		< 4	[4]
	range 0.08...6.5		[19]
	mean from 43 species	0.98	[19]
		1.5...8.0	[13]
	mean	**3.2**	**comp.**
MDF		0.295	[3]
PB	PF	0.305	[3]
PB	UF	0.31	[3]
PB	PMDI	0.32	[3]
PB	mean 5 manufacturers	0.84	[16]
	SL	0.9	[16]
	CL	0.72	[16]
WBCs	uncoated	0.5...3	[14]
WBCs	coated	1...3	[14]
WBCs	MDF or PB with UF/MUF	0.6	[14]
WBCs	MDF or PB with PF	2.0*	[14]
WBCs	MDF or PB with PMDI	0.8	[14]
WBCs	**general mean**	**0.8**	**comp.**
Lit.	AUTORENKOLLEKTIV (1988)		[1]
	BEYER et al. (2018)		[2]
	BETZ et al. (2002)		[3]
	BLAŽEJ et al. (1979)		[4]
	BUNBURY (1925)		[5]
	DAUBE (1883)		[6]
	FENGEL, WEGENER (1983)		[7]
	GOTTLIEB (1883)		[8]
	HÄGGLUND (1951)		[9]
	KNIGGE, SCHULZ (1966)		[10]
	KOLLMANN (1951)		[11]
	[10] acc. to [6] as cited in [9]		[12]
	LOHMANN (2010)		[13]
	MARUTZKY, SEEGER (2002)		[14]
	MÖRATH (1950)		[15]
	SCHRIEVER, BOEHME (1984)		[16]
	SERGEJEWA (1959)		[17]
	TAPPI T 211 (2016)		[18]
	TORELLI, ČUFAR (1995)		[19]
	TRENDELENBURG (1939)		[20]
	TZSCHERLICH (1988)		[21]
	WAŻNY, WAŻNY (1964)		[22]

Table IV-11: Compilation of common values of ash content $\omega(a)$ [%] for selected wood species and WBCs (from literature) with general mean computed (comp.) per material from reliable literature data; * questionable deviation.

Compared to the suggestion of SCHRIEVER, BOEHME (1984) regarding combustion until bright ash is present, the obtained final ash in the crucibles appeared rather brownish. Only fibres (TMP-F) showed a bright cover and both particle types (SL and CL) white speckles (see Appendix VII–2.3). However, no black carbon particles indicating incomplete combustion remained in any case. The results of ash content $\omega(a)$ determination are summarised in Table IV-12 with corresponding illustration Figure IV-10. To this end, raw data was evaluated as follows.

Hampel's test was carried out to identify potential outliers per sample type. Accordingly, only a couple of single measurements had to be rejected at $\alpha = 0.05$, which occurred rather from methodical insufficiencies than local inherent material extremes due to representative weighed portion. Here, labMDF, in turn, appeared noticeably consistent without any outliers per set of samples (= raw density level including panels of each thickness). Thus, laboratory manufacturing was continually clean. Partly adjusted sets of samples with $n \leq 5$ were subsequently evaluated. At this considering residue masses (Table IV-10), F-test of equality of variances with $H_0: \sigma^2(m_{a,2}) = \sigma^2(m_{a,2+})$ vs. $H_1: \sigma^2(m_{a,2}) \neq \sigma^2(m_{a,2+})$ failed to reject the null hypothesis at $\alpha = 0.05$ for each respective sample type. Notwithstanding that, normality cannot be ensured and sample sizes are small. Hence instead of Student's t-test, more robust and nonparametric Mann-Whitney U test of equality of $m_{a,2}$ and $m_{a,2+}$ per set of samples with the null hypothesis $H_0: F(m_{a,2}) = F(m_{a,2+})$ vs. $H_1: F(m_{a,2}) \neq F(m_{a,2+})$ was applied. As result for all sample types, H_0 cannot be rejected at $\alpha = 0.05$ again. Consequently, no statistically significant differences between both mass measurements exist; thus, solely the first value $m_{a,2}$ is henceforth taken into account. Beyond that, the slight general difference $m_{a,2+} > m_{a,2}$ is assumed to be caused by moisture uptake (despite storage in desiccator) and further oxidation of the metals. The same statistical testing was applied toward equality of all labMDF samples, which is likewise significantly proven. Hence, due to equal variances and no significant differences between

measurements of the respective samples, values of the three raw density classes (i. e. consolidation levels) are combined and total mean as well as CV of labMDF are computed (Table IV-12, bold figures). On the contrary, H_0 was rejected at $\alpha = 0.05$ considering both fibre types, which are evidently not from the same population – already regarding ash content. Equality evaluation of $\omega(a)$ of industrial panels is dispensable due to obvious differences between the panel thicknesses in Figure IV-10. Nevertheless, total mean of indMDF is computed for generalisations reasons whereas the high CV between sample mean values has to be considered, which, in turn, unveils the variations and doubtless different origins of the panels. Note, regardless parameter dispersion within the material, the rather low CVs per sample type are considered to represent appropriate repeat accuracy of the method as well as the reproducibility of the procedure, which was performed by three alternating operators. On the contrary, TAPPI T 211 (2016) provides such data from an interlaboratory trial (round robin test), where $CV = 1 \ldots 27\,\%$ between the labs partly crucially exceed the present values and are found to decrease with increasing mean ash content, supposedly owing to rater low nominal weighed portion of at least 1 g OD material to yield, in turn, at least 10…20 mg ash.

Beyond statistical implications, determined WBC ash content is in the order of common wood range. The same applies to particles and corresponding mats in relation to PB theory considering increased impurities. However, tremendous deviations occur in case of fibrous raw material. Due to considerable CV values, variations are evidently caused by methodical insufficiencies. Primarily, distinctly decreased weighed portion of fibrous material decreases weighing accuracy of coincidently minor ash mass. However, accuracy loss does not cause systematic upward offset. Assumed rapid moisture absorption of oven-dry material during crucible filling would bias the results downwards by virtually increasing weighed portion. Incomplete combustion, which apparently increases ash mass, is methodically excluded owing to reduced material amount but unaltered combustion parameter.

| material | $\omega(a)$ [%] | | |
	$\mathbf{mean}(n)$	CV	adjusted n
TMP-H	0.455	23.8 %	4
400	0.309	2.5 %	5
650	0.305	3.5 %	5
1056	0.311	2.5 %	5
labMDF	**0.309**	**2.8 %**	
$CV(\mathbf{mean})$	**0.9 %**		
TMP-F	0.701	14.9 %	4
Fmat1	0.589	n/a	1
Fmat2*	0.448	5.0 %	3
Fmat*	**0.495**	**5.0 %**	
$CV(\mathbf{mean})$	**19.2 %**		
SL	0.497	0.2 %	2
CL	0.359	3.4 %	3
SLmat	0.484	1.7 %	3
CLmat	0.350	2.7 %	3
UF2	0.044	9.4 %	3
MDF-3	0.337	2.5 %	2
MDF-6	0.368	5.8 %	3
MDF-8	0.340	3.5 %	4
MDF-10	0.303	3.8 %	5
MDF-12	0.291	1.6 %	4
MDF-19	0.358	4.4 %	4
MDF-25	0.336	6.8 %	5
MDF-30	0.419	4.8 %	4
indMDF	**0.344**	**4.1 %**	
$CV(\mathbf{mean})$	**11.6 %**		
insulation	0.274	2.8 %	6
TMP	**0.35...0.45**		**generalisation**
MDF	**0.30...0.40**		**generalisation**

Table IV-12: Results of ash content $\omega(a)$ [%] determination via complete combustion at 900 °C following Table IV-10 as mass fractions on OD basis for lab-made material (panels and furnish mats), corresponding raw furnish, and adhesive resin as well as selected industrial panels (mean per partly adjusted set of samples, $n \leq 5$); mean per material type and CV of single sample mean values (bold); * double-weighted Fmat2 value in mean and CV due to two resination batches (one for Fmat1) acc. to Table IV-15.

The analysis results of solid adhesive resin with $\omega(a)_{\text{UF2-D}} = 0.044$ % range one number of magnitude below furnish and panel material, which seems to approximate toward detection limit but determined ash mass, however, of $m_a \approx 0.05$ g was in a sufficient order regarding applied balance. Hence, $\omega(a)_{\text{UF2-D}}$ results are not neglected
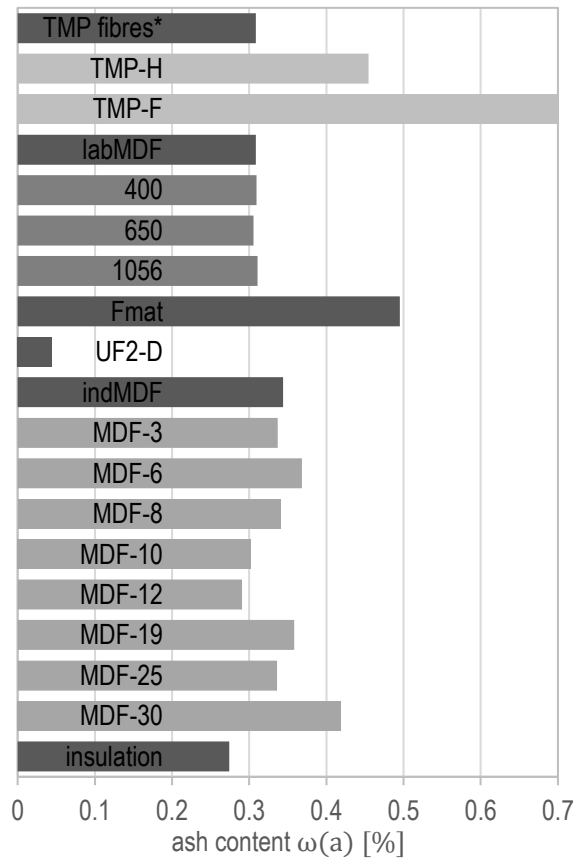
Figure IV-10: Results of ash content $\omega(a)$ [%] determination from Table IV-12, compilation of mean values per representative material types; * mean adjusted to labMDF for general computations.

and explicitly taken into account for further computations as contribution to total $\omega(a)_{\text{WBC}}$. However, due to infinitesimal ash content of adhesive resin, resination computationally decreases ash content of final WBC but just in the order of -0.05 % (abs.) in case of virtually added 10 % UF content. Hence, accordingly adjusted ash content of raw TMP fibrous material is generalised in the range $\omega(a)_{\text{TMP}} = 0.35 ... 0.45$ % (refer to last rows in Table IV-12). As mentioned above, ash composition comprises varying mass fractions of minerals or their oxides, respectively. Within the obtained combustion residues, metal oxides and SiO_2 are assumed to predominate whereas mineral compounds such as $CaCO_3$ are decomposed owing to high ignition temperature (likewise during elemental analysis). Here, a fundamental distinction between mineral matter and ash content is dispensable henceforth. In this study, ash content determination primarily

serves to complete elemental analysis and to facilitate oxygen content deduction as described in Chapter IV–2.3. To conclude more general, TMP fibre based WBCs such as MDF feature an ash content in the range $\omega(a) = 0.3 \ldots 0.4 \,\%$, which comprises residual metal oxides dominated by CaO after complete combustion at high temperatures. For further discussions in terms of comprehensive elemental analysis, reference is made to Chapter IV–2.4.2.

2.4   Elemental composition

2.4.1   Sampling and method

Quantitative elemental analysis (EA) yields the mass fraction of the non-metallic chemical elements C, H, N, and S. A comprehensive method for simultaneous CHNS analysis is based on catalytic tube combustion at up to 1200 °C with oxygen feed for quantitative sample digestion. Subsequently transported by carrier gas (He), the combustion gases are separated via purge and trap chromatography columns and quantified by thermal conductivity detector. For method details, reference is made to ELEMENTAR (2016) and EHRENBERGER (1991).

Obviously, content of the element O is not determined in this manner. Amongst other direct methods (cf. EHRENBERGER (1991)), LASKE (1961) suggests subtractive oxygen determination owing to error-prone direct procedures. Accordingly and henceforth to complete the present elemental analyses, oxygen content $\omega(O)$ is computed via the sum

$$100 \,[\%] = \sum_k \omega(i) + \omega(O) + \omega(a) \qquad \text{(IV-23)}$$

with mass fractions $\omega(i)$ of present non-metallic $k = 4$ elements H, C, N, and S respectively quantified via EA as well as ash content $\omega(a)$ (Chapter IV–2.3.2).

In this study, EA is carried out aiming at actual elemental composition of all radiometrically investigated materials

- to compare analysis results with tabulated common values (from literature),
- to deduce a generalisation for WBCs,

- to particularly evaluate the impact of applied adhesive resin and its content

and finally,

- to provide data for theoretical radiation attenuation considerations.

Regarding performance of EA on wood and WBCs, no particular European standards are present. However, respective international regulations for similar materials like coal and coke (ASTM D 5373 (2014)) exist. Furthermore, DIN EN 16785 (2014) draws on results from elemental analysis. Notwithstanding a lack of comprehensive normative regulations, the applied EA method is common in the chemical, agricultural, and energy sector. For EA in this study, vario MACRO cube CHNS, Elementar Analysensysteme GmbH, Hanau, Germany, was employed. Oxygen content $\omega(O)$ was computed according to eq. (IV-23) considering elsewhere determined ash content (Chapter 2.3.2). CHNS+O analyses were carried out on all employed WBC types and (raw) furnish materials as well as the two adhesive resins in different conditions. Though the method requires oven-dry samples, material was conditioned at 20/65 in advance to measurement owing to long-lasting handling during sampling preparation (weighing, pelletising). The huge surface of milled and cut particles is prone to moisture absorption anyway. Thus, analyses were performed explicitly considering known MC of each sample type, where global values from Table IV-5 were taken into account for.

Following device restrictions, small weighed portions, and their packing in thin tin foil, require fine and even powder. To this end, shavings from the panels were generated by means of a fine-toothed saw. Sampling was performed in distant areas of the respective panel and obtained powder material was blended again. Note likewise for ash content determination (Chapter IV–2.3), in the case of indMDF samples, sampling was performed on cuttings directly adjacent to the X-ray measuring positions within the total panel. Beyond final panels, bulky and partly coarse furnish material was milled by means of a laboratory rotor mill (Ultra Centrifugal Mill ZM 200, RETSCH GmbH, Haan, Germany) with a

12-tooth rotor at $n = 14'000\ \text{min}^{-1}$ utilising a ring sieve with 0.5 mm trapezoid holes (equally in Chapter IV–2.1.1). In advance, accordingly treated bulk samples were respectively blended per furnish type from cluster samples withdrawn directly from the bag at representative positions. Note, milled fibres for true density determination (Chapter IV–2.1.1) originate from the very same bulk sample. On the completion of furnish and WBC material, both liquid and cured adhesive resin was analogously investigated. Here, analyses were carried out on both UF types (Table IV-3), where samples were withdrawn in consequence of particular preparation UF-L, UF-LH, UF-C, and UF-CH according to Table IV-4. In case of cured resin (-C and -CH), crushed material was further milled by rotor mill as above. Generally, any contamination was avoided at best, which, in turn, potentially biased analytical results. Powder bulk samples were reconditioned (20/65) until analysis. For illustrated specimen preparation, sampling, and measuring equipment see Appendix VII–2.4.

For EA, $n = 5$ (lab) or $n = 8$ (ind.), respectively, samples were withdrawn again via cluster sampling from each prepared powder bulk sample and nominally comprise a weighed portions of (20 ± 2) mg. Individual sample mass was determined and transferred to device software. Powder material was manually packed in tin foils and pelletised by manual press diminishing air pockets, whereas specific tin capsules with press are provided for liquid samples. After sample feeder loading, analyses were performed fully automated by vario MACRO cube yielding concentration of the elements H, C, N, and S in relation to individual sample mass [wt. %]. Furthermore, device internal operating method was set considering expected elemental composition, which controls, e. g., amount of oxygen feed for combustion. Regarding WBCs, preventively chosen method "plastic waste" with tremendous oxygen feed was meanwhile changed to more resource-efficient "plant" while ensuring proper combustion. For liquid resin samples, however, method "liquid waste" was unexceptionally set. Prior to

measuring cycles, device was calibrated by means of a provided substance of precisely known elemental composition (i. e. sulphanilamide $C_6H_8N_2O_2S$).

Note, obtained mass fractions $\omega(i)_{MC}$ of the i-th element refer to conditioned sample state, thus, comprise respective MC (refer to Table IV-5). In contradiction, $\omega(a)$ is determined on oven-dry basis[28]. Hence, MC correction of EA data prior to $\omega(O)$ computation is required. Therefor, the measured H content is reduced by included fraction of absorbed water as follows. Let the mass at MC of an individually analysed sample m_{MC} equal to 100 [-]. Then,

$$\omega(i)_{MC} \equiv m(i)_{MC} \qquad \text{(IV-24)},$$

i. e. the mass fraction of the i-th element is equivalent to its mass in the compound sample, both at the same MC. Regarding H in the moist sample, the total mass results from

$$m(\text{H})_{MC} = m(\text{H})_{\text{OD}} + m(\text{H})_{\text{H}_2\text{O}} \qquad \text{(IV-25)}.$$

According to definition of MC (eq. (IV-1)), oven-dry sample mass is calculated, in turn, by

$$m_{\text{OD}} = m_{MC} \cdot \frac{100}{100 + MC} \qquad \text{(IV-26)}.$$

With the mass fraction of hydrogen in water molecules $\omega(\text{H})_{\text{H}_2\text{O}} = 0.1119$ and eq. (IV-26), eq. (IV-25) turns into

$$m(\text{H})_{\text{OD}} = m(\text{H})_{MC} - (m_{MC} - m_{\text{OD}}) \cdot \omega(\text{H})_{\text{H}_2\text{O}}$$
$$\text{(IV-27)}$$

and yields H mass in the oven-dry substance. Beyond hydrogen, other elements present require no absolute mass adjustment, thus,

$$m(i)_{MC} = m(i)_{\text{OD}} \mid i = \text{C,N,S} \qquad \text{(IV-28)}.$$

Finally, all $m(i)_{\text{OD}}$ are referred to oven-dry basis total mass m_{OD} yielding

$$\omega(i) = \frac{m(i)_{\text{OD}}}{m_{\text{OD}}} \cdot 100\ [\%] \qquad \text{(IV-29)}$$

as mass fraction of the i-th element present. Subsequently, $\omega(O)$ is computed following eq. (IV-23) with corresponding $\omega(a)$ values from Chapter 2.3.2.

---

[28] Note in general, mass fraction ω without any subscript explicitly refers to oven-dry mass as basis.

To summarise the procedure in general, data output from EA device requires MC correction and subsequent oxygen content deduction considering associated ash content.

2.4.2   Results and discussion

To evaluate the obtained analysis results and to deduce a potential generalisation with regard to a radiation transmission concept through porous composites, a comprehensive literature review aimed at hitherto investigations of the elemental composition of wood, WBCs, and their components. Table IV-14 compiles a selection from most appropriate as well as historical sources, where elemental mass fractions $\omega(i)$ [%] appear sufficiently reliable. Beyond mass fractions from numerous analytical studies, MARUTZKY, SEEGER (2002) and KALTSCHMITT et al. (2009) provide the empirical formula $C_1H_{1.4}O_{0.66}$ for the main elements of wood in general (not further specified), which is commonly applied for combustion reaction equations. However, first EA investigations by DAUBE (1883) and GOTTLIEB (1883) of common European species already unveiled minor variations of their elemental composition. Nonetheless, several general figures in subsequently published specialised books differ in detail. Thus and to facilitate an overview, own research was required.

Despite remarkably similar elemental composition on atomic level of dry wood matter, significant differences occur on the molecular scale. Content and distribution of the main macromolecular components (i. e. cellulose, hemicelluloses, and lignin) as well as extractives differ significantly between soft- and hardwood species, along height and diameter of the trunk, within one annual ring, and finally between parts of the cell wall. In the latter case, e. g., lignin content of hardwood ranges from 17…26 % in the secondary wall S_2-layer up to 70…92 % in the middle lamella (cf. BLAŽEJ et al. (1979) and WALKER (2006a)). For further details, reference is made to commonly known wood chemistry textbooks such as HÄGGLUND (1951), FENGEL, WEGENER (1983) or ROWELL (2005). Beyond that, FENGEL, GROSSER (1975) provide from a bibliographical review a comprehensive compilation of the chemical composition of soft- and hardwoods on molecular level. However, owing to the occurrence of radiation-matter interaction on atomic level, molecule types are not further considered. Nevertheless, true density of the respective matter has to be taken into account regarding radiation penetration. Several former researchers point out, not falsely to conclude from almost equal elemental composition on respective chemical identity of wood species. Notwithstanding that, similarities occur particularly from an X-ray beam's point of view as proved and quantified in Chapter IV–5.2.2.

Beyond wood EA, WBC values are sparsely represented and rather related to solid fuel investigations so far. However, considerable differences occur in case of N content corresponding to type and amount of adhesive resin in WBC. Whereas according to KOLLMANN (1951) $\omega(N) > 0.26$ % is erroneous for clean wood, values for UF-bonded WBCs extent to $\omega(N) = 4.8$ %, which originates from predominant N in urea molecules. Consequently, minor N content in MDI monomer causes just a slight increase in respectively bonded WBCs, where, furthermore, the resin content with a typical range $\omega(PMDI)_{WBC,OD} = 2\ldots6(\ldots10)$ % (cf. RESSEL (2008) as cited in THOEMEN et al. (2010)) is lower in general. To complete the most relevant basic adhesive resin types, PF-bonded panels are not expected to show any alteration of $\omega(N)$ corresponding to absence of N in the very same PF glue liquor.

Regardless whether on an empirical basis or analytically determined, elemental composition data on adhesive resins is rarely available so far. Apparently, any reporting was dispensable by institutional research and had to be avoided by manufacturers. Furthermore, a general estimation of the actual mass fractions of adhesive resin elements is non-trivial owing to considerable structural dependencies of both glue liquor and cured resin. Already DUNKY, LEDERER (1982) come upon little information about the molecular structure of UF adhesive resins. Today, remarkable progress in holistic characterisation is still lacking. However, considering UF resin regard-

ing cured state, the three-dimensional macromolecular structure depends on its cross-linking level depending, in turn, on curing conditions such as

- temperature,
- pH, and
- ambient MC

likewise considered for true density (Chapter IV–2.1.2). In the case of glue liquor, gelled state of pre-polymer depends on its molar ratio of formaldehyde to urea in the raw glue liquor (F/U ratio), desired manner of reaction, and viscosity resulting from degree of pre-polymerisation via condensation duration. Notwithstanding that, following empirical considerations yield values for elemental composition in an appropriate order of magnitude, as summarised in Table IV-14. Under simplified assumption of a linear macromolecular structure (cf. ROFFAEL (1982) and BUDDRUS (1990)) and $F/U = 1$, stoichiometrically balanced UF polycondensation product consists of the aligned monomer $[CO(NH)_2CH_2]_n$ where $n\,H_2O$ are eliminated. This first approximation yields the atomic ratio $H : C : N : O = 4 : 2 : 2 : 1$. With exemplary macromolecular molar masses determined as a function of condensation duration and F/U ratio by BILLIANI et al. (1990) ranging in the order $M_n \approx 1'000 \dots 100'000\,g/mol$, a corresponding degree of polymerisation $DP_n \approx 14 \dots 1400$ for $M_{UF} = 72.1\,g/mol$ can be estimated. Notwithstanding that, the sole knowledge about molar mass distribution within the cured resin does not reveal its composition. More sophisticated considerations regarding reaction mechanisms and molecule structures are provided by MEYER (1979). Although no general macromolecule can be defined, according to a model of cured UF resin illustrated by VOLLMERT (1985), the respective ratio $H : C : N : O = 3.94 : 2.29 : 1.71 : 1$ can be deduced. Obviously and likewise stated by DUNKY (1998), a simple UF resin unveils a broad variety of possible reactions and structures. Due to X-ray interaction mechanisms, however, the actually resulting structural characteristics of resin matter are dispensable again (refer to wood con-

Literature		
	AUTORENKOLLEKTIV (1988)	[1]
	BETZ et al. (2002)	[2]
	BOSSHARD (1974)	[3]
	BUNBURY (1925)	[4]
	DAUBE (1883)	[5]
	FENGEL, WEGENER (1983)	[6]
	GOTTLIEB (1883)	[7]
	KALTSCHMITT et al. (2009)	[8]
	KNIGGE, SCHULZ (1966)	[9]
	KOLLMANN (1951)	[10]
	LOHMANN (2010)	[11]
	MARUTZKY, SEEGER (2002)	[12]
	MÖRATH (1950)	[13]
	POLLER, KNAPPE (1988)	[14]
	ROBERTS (1964)	[15]
	ROWELL (2005)	[16]
	TRENDELENBURG (1939)	[17]
	TZSCHERLICH (1988)	[18]
	VOLLMERT (1985)	[19]
	WAGENFÜHR (1989)	[20]
	WAGENFÜHR, SCHOLZ (2012)	[21]
	WALKER (2006b)	[22]

Table IV-13: List of citiations corresponding to the sources in Table IV-14.

siderations above) as long as stoichiometric ratios are known or not considerably affected by varying H_2O or formaldehyde (FA) elimination.

material, substance	remarks	mass fraction $\omega(i)$ [%] of the chemical element $_Z i$ (with atomic number Z) in oven-dry substance						source
		$_1$H	$_6$C	$_7$N	$_8$O	$_{16}$S	ash	
bark	trunk wood	5.9	52.9	n/s	41.2	n/s	n/s	[14]
		6.0	52.6	0.6	39.0	0.063	1.800	[12]
		5.8	50.1	0.5	40.9	0.079	2.600	[12]
		5.7	51.4	0.5	38.7	0.085	n/s	[8]
	mean	**5.8**	**51.6**	**0.5**	**39.8**	**0.075**	**2.192**	**comp.**
beech	mean of sap- and heartwood	5.9	49.0	0.2	44.5	n/s	0.435	[5]
		6.1	49.1	0.1	44.2	n/s	0.570	[7]
		6.3	48.5	1.0	44.2	n/s	n/s	[4]
		6.2	48.0	n/s	45.3	n/s	0.500	[15]
		5.1	50.9	0.9	42.1	n/s	n/s	[9]
		6.1	49.0	0.3	44.3	0.007	0.500	[12]
	with bark	6.2	47.9	0.2	45.2	0.015	n/s	[8]
	mean	**6.0**	**48.9**	**0.5**	**44.2**	**0.011**	**0.501**	**comp.**
pine	mean of sap- and heartwood	6.2	52.3	0.2	41.2	n/s	0.170	[5]
		6.3	49.9	1.0	42.8	n/s	n/s	[4]
	pine and spruce	6.1	51.4	0.9	41.6	n/s	n/s	[9]
	mean	**6.2**	**51.1**	**0.7**	**41.8**	**n/s**	**0.170**	**comp.**
spruce	mean of sap- and heartwood	6.1	49.8	0.2	43.7	n/s	0.230	[5]
		6.2	50.3	0	43.1	n/s	0.370	[7]
		6.4	49.6	1.0	43.0	n/s	n/s	[4]
	pine and spruce	6.1	51.4	0.9	41.6	n/s	n/s	[9]
		6.2	50.3	0.2	43.1	0.005	0.400	[12]
	with bark	6.3	49.8	0.1	43.2	0.015	n/s	[8]
	mean	**6.2**	**50.1**	**0.4**	**42.9**	**0.010**	**0.333**	**comp.**
wood		6.1	49.6	0.1	43.8	n/s	0.400	[17]
	all species	6.1	50.0	0.1…0.2	43.0	n/s	0.2…0.6	[13]
	all species	6.1	50.0	rem. < 0.26 %	> 43	n/s	rem. 0.2…0.6	[10]
	dry, approx.	6.0	50.0	< 1*	43.0	n/s	< 1*	[9]
	mean, various species	6.0	50.0	< 1*	43.0	n/s	< 1*	[6]
	trunk wood	6.8	49.3	n/s	43.9	n/s	n/s	[14]
	mean of 14 citations	6.1	49.8	0.2	43.5	n/s	0.400	[18]
	softwood, empirically comp.	6.0	50.2	0.2	43.2	n/s	0.400	[18]
	hardwood, empirically comp.	6.1	48.7	0.2	44.6	n/s	0.400	[18]
	all species	6.4	50.5	0.1	43.0	n/s	0.300	[1]
	all species	6.1	50.0	0.2	43.4	n/s	0.300	[20]
	compilation	6.0	49.4	0.1	44.1	0.016	0.337	[2]
	$C_1 H_{1.4} O_{0.66}$, empirical	5.9	50.1	0	44.0	0	0	[8, 12, 22]
	all species	6.0	50.0	0.1…0.3	44.0	n/s	0.2…0.8	[11]
	all species, common generalisation	6.0	50.0	n/s	44.0	0	trace amounts	cf. [3, 16]
	mean	**6.1**	**49.8**	**0.2**	**43.5**	**0.005**	**0.383**	**comp.**

continued from page 110

material, substance	remarks	$_1$H	$_6$C	$_7$N	$_8$O	$_{16}$S	ash	source
		mass fraction $\omega(i)$ [%] of the chemical element $_zi$ (with atomic number Z) in oven-dry substance						
cellulose		6.2	44.4	0	49.4	n/s	0	[17]
	$(C_6H_{10}O_5)_n$, $DP_n = 4000 \ldots 5000$	6.2	44.4	0	49.4	0	0	[1]
	trunk wood holocellulose	7.0	43.9	n/s	49.1	n/s	n/s	[14]
		6.2	44.4	n/s	49.4	n/s	n/s	[21]
	all kinds of hemicelluloses	6.0	45.0	n/s	49.0	n/s	n/s	[21]
	mean	**6.3**	**44.4**	**0**	**49.3**	**0**	**0**	**comp.**
lignin		5.0…6.5	62…69	0	26…33.5	n/s	0	[17]
		5.5…6.0	63…67	0	27…34	0	0	[1]
	softwood, mean	5.9	62.7	0	31.1	0	0	[6]
	hardwood, mean	6.0	59.1	0	34.7	0	0	[6]
	trunk wood	6.1	64.6	n/s	29.3	n/s	n/s	[14]
	mean	**5.8**	**63.6**	**0**	**30.6**	**0**	**0**	**comp.**
WBCs	MDF or PB, UF, NH_4Cl	n/s	48.0	3.0…4.5	42.0	0.100	0.600	[12]
	MDF or PB, UF, $(NH_4)_2SO_4$	n/s	48.0	3.0…4.5	42.0	0.200	0.600	[12]
	MDF or PB, PF	n/s	50.0	0.3…0.5	44.0	0.100	2.0**	[12]
	MDF or PB, PMDI	n/s	49.0	0.6	43.0	0.100	0.800	[12]
	PB, UF	6.1	47.8	2.5	43.3	0.015	0.310	[2]
	PB, PF	6.3	49.6	0.1	43.4	0.015	0.305	[2]
	PB, PMDI	5.9	50.5	0.7	42.5	0.015	0.320	[2]
	MDF	6.0	46.6	4.8	41.9	0.014	0.295	[2]
	mean, UF	**6.0**	**47.6**	**3.7**	**42.1**	**0.105**	**0.499**	**comp.**
	mean, other resin	**6.1**	**49.7**	**0.4**	**43.3**	**0.066**	**0.474**	**comp.**
water	H_2O	11.2	0	0	88.8	0	0	comp.
formaldehyde	CH_2O	6.71	40.0	0	53.3	0	0	comp.
urea	CH_4N_2O	6.7	20.0	46.7	26.6	0	0	comp.
MDI[29]	$C_{15}H_{10}N_2O_2$	4.0	72.0	11.2	12.8	0	0	comp.
paraffin	alkane C_nH_{2n+2}, $n = 18 \ldots \underline{25} \ldots 32$	14.9	85.1	0	0.0	0	0	comp.
PMMA	$(C_5H_8O_2)_n$	8.1	60.0	0	32.0	0	0	comp.
UF glue liquor	$SC_{UF} = 66$ %, with 50 % urea, 25 % FA, 25 % H_2O, unofficial information WBC industry	7.8	20.0	23.3	48.8	0	n/s	comp.
UF glue liquor	$F/U = 0.87$	7.5	21.7	27.1	43.7	0	n/s	comp.
UF glue liquor	$F/U = 1.13$	7.6	22.0	24.1	46.3	0	n/s	comp.
UF cured resin	$[CO(NH)_2CH_2]_n$, simplified linear condensation polymers	5.6	33.3	38.9	22.2	0	n/s	comp.
UF cured resin	macromolecular model	5.6	38.5	33.5	22.4	0	n/s	[19]

Table IV-14: Compilation of common values of elemental composition as mass fraction $\omega(i)$ [%] of the i elements H, C, N, O, and S on oven-dry basis for selected wood species, WBCs, and adhesive resins (as liquor incl. water) as well as their molecular components complete with ash content $\omega(a)$ (Table IV-11), acc. to literature (list in Table IV-13) or own empirical considerations with general mean computed (comp.) per material from reliable literature data; * both N and ash together, ** questionable deviation.

---

[29] With its three isomers 2,2'-MDI, 2,4'-MDI, and 4,4'-MDI. Note, there is no further considerations of potential three-dimensional structure of the cured adhesive resin.

The results of elemental analysis (EA) with subsequent MC correction yielding mass fractions $\omega(i)$ [%] on oven-dry basis of the i elements H, C, N, and S as well as subtractive $\omega(O)$ determination are summarised in Table IV-15 complete with ash content $\omega(a)$ from Table IV-12. An additional illustration of mean values per selected material types is provided in Figure IV-11. In advance of compilation, raw data was evaluated as follows.

Hampel's test per chemical element of each sample with $n = 5$ (lab) or $n = 8$ (ind.), respectively, identified just few potential outliers at $\alpha = 0.05$. Values typically became critical, where CV of the sample were distinctly low (without the outlier) or particularly for N and S with inherently major variations. Notwithstanding the observed statistical significance, none of the values were rejected. Moreover, and due to no observed irregularities during sampling and analysis, EA results alone do not help to distinguish the reason whether the significant value was caused by methodical insufficiencies (e. g. incomplete combustion) or by actually extreme local compositions (e. g. lignin-cellulose ratio in wood). Regarding the individual sample, coefficient of variation (CV) as standardised measure of dispersion enables implications on both method and material. Considering C, low $CV < 1\,\%$ indicates appropriately complete combustion in general. Actually, the range (with median) $CV = 0.1 \ldots (0.4) \ldots 1.7\,\%$ of all analyses (without UF) reveals no systematic impact in respect thereof. On the contrary, distinctly varying $\omega(N)$ with the dispersion range (with median) $CV = 1.0 \ldots (2.4) \ldots 10.9\,\%$ of all resin blended materials indicates partly inappropriate resin distribution. Moreover, each weighed portion comprises varying shares of furnish and UF from the milled initial wood-particle-resin-matrix. Furthermore, this becomes obvious from comparably high CV of the $\omega(N)$ mean values (CV(mean) in Table IV-15), particularly in the case of indMDF. The latter represents the differently predefined typical resin contents of the respective MDF type and thickness.

Owing to steady analysis method and purposed scale of investigation, i. e. sub-microscopic elemental composition and not macroscopic properties, it would be justified to assume Gaussian distributed values. Already KOLLMANN (1965) concludes the assumption of Gaussian distribution also for sub-microscopic cell-wall substances, which allows to imply on Gaussian distributed populations of the elemental composition likewise. To evaluate homogeneity of variances, *F*-test was performed at significance level $\alpha = 0.05$ considering the analysis results per element of each set of samples tested against each other with the following summarised findings. Considering raw furnish and the respective lab-made material made out of it, the equality of variances was tested according to $H_0 : \sigma^2(\omega(i)_{\mathrm{furnish}}) = \sigma^2(\omega(i)_{\mathrm{labWBC}})$ vs. $H_1 : \sigma^2(\omega(i)_{\mathrm{furnish}}) \neq \sigma^2(\omega(i)_{\mathrm{labWBC}})$. Regardless of individual exceptions, null hypothesis failed to reject at α in general. Thus, origination from same populations is indicated despite treatment (blending and hot-pressing) of the raw furnish. Note, particular value dispersion comprises superimposition of both material and measurement variations. The same applies to *F*-test within the group of labMDF with nine sets of samples. On the contrary, in case of industrial panels, the null hypothesis $H_0 : \sigma^2(\omega(i)_{\mathrm{furnish}}) = \sigma^2(\omega(i)_{\mathrm{indMDF}})$ had to be rejected at α in favour of the alternative hypothesis $H_1 : \sigma^2(\omega(i)_{\mathrm{furnish}}) \neq \sigma^2(\omega(i)_{\mathrm{indMDF}})$ in case of all sample units. However, both TMP fibre types as well as all industrial panels came certainly not from the same origin. Analogously to labMDF, samples of indMDF were tested against each other. At this, *F*-test revealed roughly equal variances in all cases for the respective elements. Despite knowingly different origins of particular panels, test results appear reliable. They are caused by higher CV within individual sets of samples owing to more distinct sampling areas across the whole production width of the panel compared to several points of one lab-made panel each. To conclude all *F*-tests, findings reveal an ambiguous picture owing to commonly rather low CV caused by steady analysis method but individual exceptions and potential outliers (see Hampel's test above) occur resulting from

superimposition of material irregularities and insufficiencies in method performance. Accordingly but regardless of justifiable normality assumption, more robust and nonparametric Mann-Whitney U test of equality of respective sets of samples was again performed at significance level $\alpha = 0.05$ instead of Student's (equal) or Welch's (unequal variances) t-test to compare sample means. Notwithstanding known different origins of TMP fibres, U test of the two types via $H_0 : F(\omega(i)_{\text{TMP-H}}) = F(\omega(i)_{\text{TMP-F}})$ vs. $H_1 : F(\omega(i)_{\text{TMP-H}}) \neq F(\omega(i)_{\text{TMP-F}})$ failed to reject H_0 at α and thereby failed to support the alternative hypothesis H_1. Hence, values from both analyses can be combined to general means for elemental composition of TMP fibres (bold figures TMP in Table IV-15). Note, $\omega(\text{O})$ was adjusted with +0.3 % considering apparently falsified ash content determination of both raw fibres. Beyond that, EA data of all WBCs was evaluated regarding significant influence of treatment, i. e., resination and panel or mat, respectively, processing. To this end, U testing was again carried out with the following summarised findings at significance level $\alpha = 0.05$. Regarding respectively processed lab-made material (blended furnish, mats, and panels), significant differences from corresponding raw furnish are indicated; i. e., $H_0 : F(\omega(i)_{\text{furnish}}) = F(\omega(i)_{\text{labWBC}})$ was rejected at α in favour of $H_1 : F(\omega(i)_{\text{furnish}}) \neq F(\omega(i)_{\text{labWBC}})$. Notwithstanding that generalisation, partly equal $\omega(\text{H})$ occurs where total share remains roughly constant regardless of added UF. Evaluation of equality of raw TMP fibres and indMDF is dispensable analogously to unequal variances. Within the group of all labMDF, all sample units are statistically equal to each other despite individual exceptions. Here, labMDF1056-11.7 differs evidently in particular detail due to apparently poor resination effectiveness obvious from low $\omega(\text{N})$. Likewise, resin application and curing are generally responsible for all more or less slight differences between lab samples due to batch-wise blending and panel-wise consolidation. Furthermore, individually evaluated industrial panels regarding equality toward each labMDF via U test reveal an ambiguous picture tending to reject H_0; thus, to differ from each other. Within the industrial panel

group, partly no statistically significant differences between the sample units are revealed by U test. Evidently, $\omega(\text{H})$ is always equal. Apparent differences in total elemental composition depend particularly on $\omega(\text{N})$, hence, resin content, with subsequent $\omega(\text{C})$ and $\omega(\text{O})$ variations. On the contrary, the elemental composition of MDF-30 is significantly unequal to all other industrial panels due to distinctly different $\omega(\text{N})$ caused by comparably high resin content, which appears typical for this panel type. Further statistical testing via Hampel's test of both lab-made and industrial sets (with mean values per sample type, i. e., presented data in Table IV-15) unveils consistent EA data and verifies U test findings – particularly remarkable for industrial panels. Outlier tests $n = 9$ (lab) or $n = 8$ (ind.), respectively, per element identify at $\alpha = 0.05$ solely few irregularities, i. e. apparently prominent values (Table IV-15 with #). In this regard, contamination in the case of $\omega(\text{S})$ appeared and $\omega(\text{N})$ differs due to obtained effective resination of the respective batches (labMDF) as well as inherently varying resin content of industrial panels due to thickness and designated use, as mentioned above. Hence, the computation of respective mean elemental contents regarding employed lab-made and industrial, respectively, panels is eligible on statistical basis. In the latter case, values conduce as global mean for MDF regardless of the origin. Nonetheless, a certain range of $\omega(\text{N})$ and $\omega(a)$ has to be considered. Regarding evaluation of both applied resin types with the respective preparations, analysis results of UF2-CH attract attention. Evidently, EA (H, C, N, and S) and subtractive O results are biased due to systematic deviations of all samples ($n = 5$) with $\omega(\text{O})$ far beyond expected order of magnitude and H, C, and N contents out of proportion. U test proves the obvious difference where $H_0 : F(\omega(i)_{\text{UF1-C}}) = F(\omega(i)_{\text{UF2-CH}})$ was rejected at $\alpha = 0.05$ in favour of $H_1 : F(\omega(i)_{\text{UF1-C}}) \neq F(\omega(i)_{\text{UF2-CH}})$ for all elements without exception. Therefore, even in the virtual case of totally overdosed hardener and correspondingly atypical cross-linking levels, the determined ratio $\text{H} : \text{C} : \text{N} : \text{O} = 2.26 : 0.66 : 0.63 : 1$ can stoichiometrically not be obtained via reaction of any F/U ratio of the resin. Potentially crystalline bound water would have been in

the highly unlikely order of $MC \approx 40\,\%$. Hence, erroneous UF2-CH data is henceforth not considered. Further analogous hypothesis testing of the remaining resin preparation types reveals an ambiguous picture likewise for furnish and processed material. Despite individual exceptions, variances are equal due to *F*-test. Apparently comparable elemental compositions of liquid and cured, respectively, adhesive resins are not supported by *U* test results, where null hypothesis is rejected at $\alpha = 0.05$ of the majority. All three liquid samples appear similar, but UF1-L differs from both UF2-L and UF2-LH due to supposedly different molar F/U ratio. The differences between liquid UF2 preparation types may be caused by additional hardener and subsequent pre-curing reactions within glue liquor. EA results of UF1-C and UF2-C are in the same order of magnitude but unequal according to *U* test; evidently, since the former inherently contains hardener resulting in specific macromolecular structure. Notwithstanding that, valid EA data of both cured adhesive resins is again combined (UF-C) for generalisation purpose. However, tests of equality between liquid and cured resin samples is dispensable. Finally, the ambiguous picture of iteratively applied two-sample hypothesis tests enables, nonetheless, particularly to combine data and to reliably compute total means as well as CV of the individual sample means within the respective material groups (Table IV-15, bold figures) as generalisation thereof.

Beyond implications on statistical basis, EA data facilitates empirical considerations. As specified in Table IV-14, sulphur content of clean wood is infinitesimal low with $\omega(S) < 0.01\,\%$. Regarding WBCs, values up to one order of magnitude above are possible but still make a minor contribution to total composition. Possible sources are bark, waste wood, general impurities, and ammonium sulphate $(NH_4)_2SO_4$ as common catalyst. Regarding utilised fibre-based material, considerable bark and waste wood content is excluded. Extra hardener was added during processing of the furnish mats, but not for labMDF. Further application is assumed in the case of industrial UF-bonded panels, because $(NH_4)_2SO_4$ is commonly used instead of NH_4Cl to avoid chlorine compounds in emission or combustion gases. Thus, a certain S contend is accordingly expected. Regarding adhesive resins, increased $\omega(S) \approx 0.1\,\%$ indicates the required $1\,\%$ hardener addition in case of UF2-LH and UF2-CH. Consequently but diminished by total mixture, $\omega(S)_{Fmat} > \omega(S)_{labMDF}$. The same applies to indMDF. Beyond that, methodical causes are partly present. Increased $\omega(S)$ is observed in case of first sample(s) within analysis sequence after daily calibration by sulphanilamide despite $4 \ldots 5$ blank cycles to purge the system prior to actual analyses. MDF-3 is a prominent example. However, considerably high CV values and analysis results close to detection limit allow to neglect sulphur content in case of $\omega(S) < 0.1\,\%$.

Likewise sulphur, increased nitrogen content in WBCs originates from bark, waste wood, general impurities, and resination depending on type, since $\omega(N) < 0.26\,\%$ is expected in clean wood. Additionally, in the case of analysed TMP fibres of unknown origin, a slight falsification cannot be avoided. Despite disabled resination (blowline) for fibre withdrawal, uptake of adhesive resin residues in pipe system is conceivable. In case of CL particles, urea powder was process-related added regularly prior to resinating blender which, in turn, was located nearby the point of withdrawal. Potential contamination cannot be excluded. The atypically higher $\omega(N)$ in SL particles is assumed to be caused by process-related addition of sanding dust from final panel (for particle analysis reference is made to Figure IV-9). Finally, all prepared samples potentially contain air (incl. $78.08\,\%$ N_2) in pelletised specimen (packed in tin foil), which may systematically increase $\omega(N)$. As already discussed in terms of statistical tests, considerably higher CV is caused by both differently effective resin content between panels and variations in actual resin distribution on blended furnish (cf. THÖMEN, VIEMEISTER (2015)) within respective weighed portion of milled material. In case of samples from MDI-bonded insulation boards, $\omega(N)$ just slightly exceeds TMP values as common. Subsequently, compound ratios are shifted due to high $\omega(C)$ content in MDI. Eventually, nitrogen content serves as indicator for adhesive resin type and content in WBCs. With further

knowledge of the actual resin composition in present curing state, a precise quantification of effective resin content in the final panel is feasible, which will prospectively be pointed out elsewhere .

Oxygen content via subtractive determination is considered as indirect result. Consequently, accuracy depends on summed deviations of single analyses and particularly ash content determination. Thus, its dispersion is considered as sum of single variances under linear conditions, which is commonly described by Gaussian propagation of uncertainties. Nevertheless, as pointed out above, difference method is considered as more precise compared to direct determination procedures. However, standard deviation of $\omega(a)$, in turn, is one order of magnitude below standard deviation of $\omega(C)$ and $\omega(O)$ (e. g. labMDF: 0.009 % vs. 0.1479 % or 0.2055 %, respectively). Hence, method related variations of ash content are comparatively negligible in relation to total elemental composition, but finally considerable with respect to radiation attenuation (refer to Chapter IV–5.2.2).

Regarding carbon content, potential impact of incomplete combustion owing to poor oxygen feed caused by inappropriate device internal operating method was discussed earlier. Here, no further exceptions were observed. The same applies to hydrogen content.

Sample MC directly affects initially determined $\omega(H)_{MC}$ and, consequently, analysis results of further elements as mass fractions of weighed portion. Hence, elemental composition in standardised oven-dry state is obtained by MC correction of all values. In this regard, validity of applied MC contributes to final accuracy of determination, in turn. Analyses were performed on 20/65 conditioned material with corresponding EMCs (refer to Table IV-5). Notwithstanding sample preparation (weighing and pelletising) was carried out in a lab without air-conditioning, considerable MC variations are not expected owing to comparably typical ambient conditions (during not too hot summer and early autumn) and rapid processing. Thus, systematic adaptions of elsewhere determined sample MC for correction

were not required. Note, even though EMC accommodates slowly, a variation of ± 1 % EMC due to virtual ± 5 % RH would result in (exemplarily for labMDF650-11.7)

- $\omega(H) = (5.9 \pm 0.05)$ %,
- $\omega(C) = (49.2 \pm 0.45)$ %,
- $\omega(N) = (3.4 \pm 0.03)$ %, and
- $\omega(O) = (41.1 \pm 0.43)$ %.

Whereas H and N values are uncritical, the ranges of C and O are beyond 95 % confidence intervals of the mean. However, potential MC-related error of EA performed on oven-dry material would even be worse due to more rapid moisture absorption during handling. Thus, the not precisely quantifiable impact of material re-conditioning has to be accepted. Consequently, potential systematic result deviations in the above estimated order of ± 1 % (rel.) have to be considered at worst case. For UF resin EA data, no MC correction was carried out prior to subtractive $\omega(O)$ determination due to intended inherent elemental composition of both glue liquor and cured resin. In the latter case, only infinitesimal amount of crystalline bound water is assumed. However, required MC determination by oven-dry method would cause falsifying mass changing modifications of macromolecular UF structure as pointed out earlier. Additionally, data of liquid resin samples was virtually dried by MC correction according to SC_{UF} (see Table IV-3). The values (labelled (SC)* in Table IV-15) tend toward actual analysis results, but differ in the order of 10 % MC corresponding to assumingly evaporated water amount during polycondensation reaction.

Ultimately, investigated materials are organic compounds containing the elements H, C, and O in general, which are referred to as HCO-material following SINGH et al. (1993). Since wood is predominantly composed out of the very same elements, the term was found to serve as a well-suited summary. Note, here, the acronym HCO referring to the described materials should not be confused with hydrogen carbonate HCO_3^- or an aldehyde HCO- (functional group rather denoted as -CHO). Moreover, owing to fractional abundance of N in case of WBCs bonded with

UF-based adhesive resin, the term is respectively extended to HCNO-materials, which clearly concludes the present matter composition. Here, sulphur is neglected. Beyond combined data resulting in mean values per material type, more vivid empirical formulae with the respective stoichiometric ratios of the predominant elements in the HCNO-compound are derived. Approximate calculations aiming at $C = 1$ yield the stoichiometric ratios $H : C : N : O =$

-   $1.39 : 1 : 0.01 : 0.62$ (TMP),
-   $1.43 : 1 : 0.06 : 0.63$ (labMDF),
-   $1.42 : 1 : 0.05 : 0.61$ (Fmat),
-   $1.45 : 1 : 0.07 : 0.61$ (indMDF), and
-   $1.34 : 1 : 0.01 : 0.58$ (insulation).

The TMP figures are in good agreement with common wood ratio (Table IV-14) $H : C : N : O =$

-   $1.40 : 1 : n/s : 0.66$ (wood)

with a slight shift of TMP ratio toward carbon due to increasing lignin share with comparably high $\omega(C)$ in consequence of thermal treatment during defibration as likewise considered in Chapter IV–2.1.2. Regarding processed lab-made and industrial material, all particularly discussed findings become obvious. To conclude in general:

-   type and amount of applied adhesive resin individually shift the elemental composition;
-   HCO-ratio remains more or less unchanged by adding UF resin;
-   nitrogen content enables to estimate UF resin content with knowledge of its composition, in turn;
-   additionally, ash content has to be taken into account;
-   indMDF composition can be distorted by further additives whereat no particular knowledge is present.

In the case of mean results of cured resin UF-C, computations toward $O = 1$ yield the stoichiometric ratio $H : C : N : O =$

-   $3.2 : 1.4 : 1.4 : 1$ (UF-C),

which evidently differs from the aforementioned linear molecule model with

-   $4 : 2 : 2 : 1$ (UF empirical)
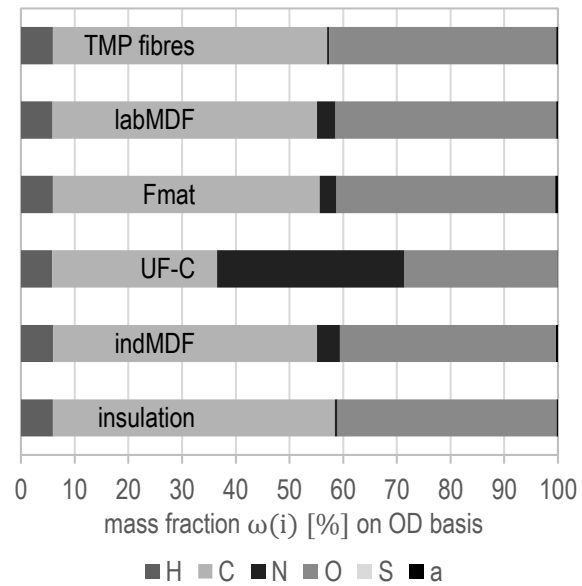
Figure IV-11: Results of elemental analysis (EA) as mass fractions $\omega(i)$ [%] on OD basis of the i elements H, C, N, and S, MC correction acc. to eq. (IV-27), subtractive $\omega(O)$ determination acc. to eq. (IV-23), complete with ash content $\omega(a)$ from Table IV-12; compilation of mean values per representative material types.

owing to initial molar ratio $F/U > 1$ and obtained cross-linked macromolecular structure in dependency of actual curing conditions.

Finally, the elemental composition of the analysed HCNO-materials at any requested MC can be computed via MC correction procedure according to eq. (IV-24) to eq. (IV-29), but vice versa. To this end, MC-related $m(H)_{H_2O}$ as well as $m(O)_{H_2O}$ are added and all $m(i)_{MC}$ are referred to m_{MC} yielding $\omega(i)_{MC}$. Alternatively, desired MC is separately considered for theoretical radiation attenuation considerations in Chapter IV–5. However, respective values of the henceforth commonly applied summarised compositions at EMC in consequence of 20/65 conditioning are exemplarily presented in Table IV-16.

OD	$\omega(i)$ [%]					
material	$_1$H	$_6$C	$_7$N	$_8$O	$_{16}$S	a
TMP fibres	**5.9**	**51.0**	**0.4**	**42.3**	**0.007**	**0.309**
TMP-H	5.9	51.1	0.5	42.0	0.007	0.455
TMP-H+UF1	5.8	50.2	4.0	39.8	0.012	0.300
400-11.7	5.8	49.2	3.4	41.2	0.061	0.309
400-19	5.8	49.4	3.4	41.0	0.028	0.309
400-30.9	5.8	49.3	3.5	41.1	0.017	0.309
650-11.7	5.9	49.2	3.4	41.1	0.029	0.309
650-19	6.0	49.2	3.6	40.9	0.016	0.309
650-30.9	5.9	49.1	3.6	41.0	0.010	0.309
1056-11.7	6.0	49.5	#2.9	41.3	0.004	0.309
1056-19	5.9	49.2	3.5	41.1	0.002	0.309
1056-30.9	5.9	49.2	3.5	41.1	0.001	0.309
labMDF	**5.9**	**49.3**	**3.4**	**41.1**	**0.019**	**0.309**
CV(mean)	1.0 %	0.2 %	6.3 %	0.3 %	102 %	0.9 %
TMP-F	5.9	51.0	0.3	42.0	0.065	0.701
TMP-F+UF2	6.1	48.6	2.9	42.1	0.0	0.300
Fmat1	6.0	50.0	2.9	40.5	0.043	0.589
Fmat2	5.9	49.6	3.2	40.8	0.031	0.448
Fmat2	5.9	49.4	3.3	40.9	0.029	0.448
Fmat	**5.9**	**49.7**	**3.2**	**40.7**	**0.034**	**0.495**
CV(mean)	0.5 %	0.6 %	6.4 %	0.5 %	22 %	16 %
SL	5.9	50.2	1.0	42.4	0.050	0.497
CL	5.9	50.0	0.5	43.1	0.095	0.359
SLmat	6.0	48.8	3.0	41.9	0.028	0.300
CLmat	6.0	48.9	2.6	42.2	0.037	0.300
UF1-L	7.5	20.9	25.5	46.0	0.000	0.044
UF2-L	7.5	21.7	23.7	47.0	0.005	0.044
UF2-LH	7.7	20.5	22.7	49.0	0.093	0.044
UF1-L(SC)*	6.3	27.6	33.7	32.3	0.000	0.044
UF2-L(SC)*	6.3	28.9	31.6	33.1	0.006	0.044
UF2-LH(SC)*	6.6	27.3	30.3	35.7	0.124	0.044
UF1-C	5.7	29.8	35.6	28.8	0.007	0.044
UF2-C	5.9	31.7	34.2	28.3	0.001	0.044
UF2-CH**	6.5	22.5	25.1	45.7	0.126	0.044
UF-L	**7.5**	**21.3**	**24.6**	**46.5**	**0.002**	**0.044**
UF-C	**5.8**	**30.7**	**34.9**	**28.5**	**0.004**	**0.044**
MDF-3	6.0	49.8	3.8	39.9	#0.166	0.337
MDF-6	6.0	48.8	4.7	40.1	0.059	0.368
MDF-8	6.0	49.4	3.7	40.5	0.057	0.340
MDF-10	6.0	49.6	3.7	40.3	0.048	0.303
MDF-12	6.0	49.7	3.5	40.5	0.040	0.291
MDF-19	6.0	49.4	4.0	40.1	0.039	0.358
MDF-25	6.0	48.7	4.4	40.5	0.023	0.336
MDF-30	5.9	47.6	#6.1	40.0	0.027	0.419
indMDF	**6.0**	**49.1**	**4.2**	**40.2**	**0.042**	**0.344**
CV(mean)	1.0 %	1.5 %	20 %	0.6 %	33 %	12 %
insulation	**5.9**	**52.5**	**0.5**	**40.8**	**0.003**	**0.274**

Table IV-15: Results of elemental analysis (EA) as mass fractions $\omega(i)$ [%] on OD basis of the i elements H, C, N, and S for lab-made material (panels and furnish mats), corresponding raw furnish, and adhesive resin as well as selected industrial panels (mean per set of samples, $n = 5$ and $n = 8$, respectively), MC correction acc. to eq. (IV-27), subtractive $\omega(O)$ determination acc. to eq. (IV-23), complete with ash content $\omega(a)$ from Table IV-12; mean per material type and CV of single sample mean values (bold figures); * virtually dried by MC correction acc. to SC_{UF} (Table IV-3); ** erroneous; # outlier identified by Hampel's test but not removed (except MDF-3).

20/65	$\omega(i)$ [%]					
material	$_1$H	$_6$C	$_7$N	$_8$O	$_{16}$S	a
TMP fibres	6.5	46.0	0.4	46.9	0.006	0.278
labMDF	6.4	45.0	3.1	45.2	0.017	0.282
Fmat	6.4	45.4	2.9	44.8	0.031	0.453
indMDF	6.4	45.4	3.9	43.9	0.038	0.318
insulation	6.4	48.1	0.5	44.8	0.003	0.251

Table IV-16: Elemental compositions at EMC (Table IV-5) in consequence of 20/65 conditioning computed via inverse MC correction acc. to eq. (IV-24) to eq. (IV-29) for selected material types.

2.5 Concluding remarks

All comprehensive investigations for material characterisation were performed exclusively on furnish-based WBCs (fibres and particles) and their corresponding raw materials with a particular focus on MDF because of its advantageous homogeneity and more uniform structural conditions for basic examinations. A practice-oriented variety of sample types and conditions was utilised whereas their origin was both lab-made with predefined compositions as well as customary industrial. The structural members, i. e., TMP fibres, of the lab-made mats and panels are distinguished regarding their morphological conditions and reveal comparable distributions of their dimensions (width and length) on a volume-fraction basis. Accordingly, the structural types compact fibre bundles (FBc) as well as short single fibres (SFs) mainly dominate the present TMP furnish with 79 % and 21 %, respectively, as generalisation neglecting the further members. How-

ever, any mechanical impact during WBC processing (refer to Figure I-1), such as densification, is considered to affect the fibre morphology, thus, the total porosity comprising intra- and inter-cellular lumina and voids. Porosity was determined from both panels and raw material via true density (i. e. solid density) measurement by means of gas pycnometry. The results are found in more or less good agreement with well-known literature values, where the WBC constituents range in a comparable order of magnitude and allow a more or less comprehensively valid generalisation for oven-dry WBC matter with $\rho_{\text{t,labMDF}} = 1515 \text{ kg/m}^3$. At regular MC, true density values are error-prone in determination. Moreover, direct computation, i. e., MC correction, is non-trivial, in turn, due to density increment of bound water. Hence, OD values are commonly applied. Notwithstanding that, true density of the WBC matter under investigation is considered not to be significantly affected by any typical WBC processing. Thus, solid matter of furnish mat and final panel remains accordingly equivalent during panel production and even in global comparison.

This does not apply to the composition of WBCs. However, particularly the results from elemental analysis (EA) complete with ash content determination via combustion are of primary interest for subsequent computations in terms of theoretical attenuation considerations. Regardless of particular differences between the investigated materials, a generalisation is deduced on basis of the manufactured labMDF with 10 % UF resin content at $MC = 9.5$ % in consequence of 20/65 conditioning with mass fractions of H, C, N, O, and ash of 6.4 %, 45.0 %, 3.1 %, 45.2 %, and 0.282 % (note, sulphur content is negligibly low). Moreover, elemental composition of wood (TMP) is dominated by C and O, i. e., $\omega(\text{C+O})_{\text{TMP}} = 93$ % (OD). During WBC processing, resination with 10 % UF (OD basis) causes slight shift toward N resulting in $\omega(\text{C+O})_{\text{labMDF}} = 90$ % (OD). Eventually, $MC = 9.5$ % representing common MDF at standard ambient (20/65) conditions yields equivalent $\omega(\text{C+O})_{\text{labMDF,9.5 % MC}} = 90$ %, where the ratio is shifted toward O. The results are found in more or less good agreement with hitherto investigations of elemental composition

(Table IV-14) and ash content (Table IV-11). Though well-established methods were applied and, however, partly modified, particular interdependency of elemental analysis and ash content determination have to be discussed. The former with combustion at crucially high temperatures considers all non-metal atoms even in mineral matter. The latter results in ash as complete combustion residue, where metal and metalloid atoms supposedly appear as oxides arising from oxidation processes during cool-down period in furnace and desiccator. In comparison to established and standardised methods for ash content determination, combustion temperature ($\vartheta_{\text{furnace}} = 900$ °C) was preferably increased toward the very same of elemental analysis ($\vartheta_{\text{tube}} = 1200$ °C) aiming at similar decomposition conditions. Hence, minerals (e. g. $CaCO_3$) are cracked and actual O content is revealed. Regarding the performed subtractive oxygen determination via eq. (IV-23), LASKE (1961) likewise points out that O is present in both organic and inorganic matter as well as water, where the latter is, however, considered via MC correction. Accordingly, an accurate difference method for O determination based on EA and ash content would require the actual mineral content of the sample excluding bound O. A clear specification of the individually present conditions along with particular mineral content determination is, however, not possible, since ash composition was not further analysed after sample combustion. Therefore, a corresponding but obviously minor potential error of oxygen content $\omega(\text{O})$ results has to be accepted. However, the present study is rather aiming at practical application than detailed discussion of analysis results. Consequently, ash is considered to be an oxide of metals and metalloids with a mean atomic number (refer to Chapter II–2.2) for further examinations based on elemental analysis. The distinction between ash and mineral matter content as well as their composition is henceforth dispensable. For generalisation, an effective atomic number was empirically determined as $Z_{\text{eff}}(a) \approx 19 \dots 20$ based on available literature data for wood ash composition (Chapter IV–2.3.2), where calcium $_{20}\text{Ca}$ as predominant element is found to represent the mean of all present metal and metalloid

constituents. Thus, C_a and corresponding data is henceforth generally utilised for any computation based on EA results unless otherwise specified. Notwithstanding that discussion, the relevance of such method-related variations of ash or mineral content for WBC processing, subsequent panel machining, and mechanical properties is neglectable. Regarding X-ray attenuation, in turn, a certain impact has to be considered with respect to radiation energy as to be pointed out in Chapter IV–5.2.2 based on comprehensive theoretical examinations. Finally, the consideration of customary WBCs as HCNO-materials complete with a general ash content considered as C_a vividly concludes and simplifies the investigated matter in terms of transmission of ionising radiation. Beyond elemental composition, structural conditions of the inhomogeneous and porous composites have to be taken into consideration for holistic radiation transmission concepts on distinct scales, which can, however, not explicitly be characterised and quantified.

3 Radiation transmission concept through porous composites

3.1 Introduction

Notwithstanding manifold hitherto radiographic investigations of porous material by means of different kinds of radiation such as X-rays or neutrons, particular considerations of the very same porous body as impact on radiation attenuation is pending. Regardless of comparably young neutron radiography, practise-oriented investigations of X-ray attenuation mechanisms regarding quantitative applications are found not as yet to consider porosity and inhomogeneity of the respective absorbers explicitly. The same applies to radiometric investigations of WBC.

Hence, from the radiation beam's point of view, an empirical model based on common knowledge as well as supported with actual data from sophisticated material characterisation (Chapters IV–2.1 to IV–2.4) on distinct levels of consideration for transmission and interaction of penetrating corpuscular radiation through porous compound media such as WBCs is developed and illustrated in Figure IV-12. The proposed radiation transmission concept aims at the objective to serve as simplified illustrative model but to explicitly consider generalised material parameters, thus, to provide an abstraction of WBC characteristics to be taken into account regarding radiometric investigations. The structural considerations upon radiation propagation through resin bonded WBCs are, however, limited to schematic visualisation roughly true to scale and do not claim to conduce as precise holistic modelling of neither wood-particle-resin-matrices nor radiation-matter interaction within the very same. Furthermore, the provided two-dimensional illustrations (Figure IV-12) as cross-sectional views representing the plane of radiation transmission are sufficient since interaction effects, particular scattering, appear rotationally symmetrical around primary beam axis. To some extent, the explanatory conceptual beam path model was published by SOLBRIG et al. (2015a) in advance. The concept is primarily developed for X-rays but is considered to be analogously

applicable for neutrons, where, nonetheless, experiments are required to verify the proposed model. Regarding radiation propagation and interaction in this explanatory model and henceforth, X-rays are considered as photons. Thus, their corpuscular character is taken into account.

However, while radiation corpuscles of particular energy, travel through WBCs, their interaction with matter and the related information content of measurement have to be considered on distinct scales. As a result in Figure IV-12, correspondingly derived describing functions of the energy-dependent mass attenuation coefficient $\mu/\rho\,(E)$ represents attenuation conditions with close respect to the individual level of consideration. Purposing the description of irradiated WBC matter from a more or less divergent, polychromatic beam's point of view, the concept assumes each transmitted photon to be counted on detector of certain extent, where the origin of each detected radiation corpuscle has to be considered in the context of metrological, i. e., quantitative applications. Accordingly, structural levels below visual perception have to be investigated regarding radiation transmission and interaction. Consequently, the beam path model illustrated in Figure IV-12 follows the fundamentally present structure of resin-bonded WBCs and distinguishes between

- macroscopic,
- mesoscopic,
- microscopic, and
- sub-microscopic

scale for evaluation. Note, idealised considerations are initially focussed on but not necessarily restricted to MDF and are assumed to be transferable to further WBCs, where particular conditions (e. g. particle size) have individually to be taken into account.

fibre mat (cold pre-pressed)

MDF (hot-pressed)

level of consideration

cross-section (thickness) — homogeneously formed

panel plane

SL

CL

SL

cross-section (thickness)

panel plane

macroscopic scale $[10^{-1}\ \mathrm{m}]$

$$\frac{\mu}{\rho}(E) = \frac{\int_E \int_t \mu(t)\,dt\,dE}{\overline{\rho}}$$

- apparently solid body with distinct densification
- equilibrium MC
- **measuring information** from transmitted intensity $I_\mathrm{T}(\rho_A, E)$ of penetrated matter

$$\rho_A = \rho \cdot t$$

$$\frac{\rho_\mathrm{MDF}}{\overline{\rho}_\mathrm{mat}} = \frac{650\ldots\mathbf{750}\ldots1100}{125} = \frac{6}{1}$$

cross-section (thickness)

panel plane

cross-section (thickness)

panel plane

mesoscopic scale $[10^{-3}\ \mathrm{m}]$

$$\frac{\mu}{\rho}(E) = \omega_\mathrm{WBC} \cdot \frac{\mu}{\rho}(E)_\mathrm{WBC} + \omega_\mathrm{voids} \cdot \frac{\mu}{\rho}(E)_\mathrm{voids}$$

- porous body as (densified) wood-particle-resin-matrix
- MC distribution in furnish
- WBC processing impact

$\overline{\Phi}_\mathrm{mat} = 92\ \%$
$\overline{\Phi}_\mathrm{MDF} = 50\ \%$
SFs: 21 %, 44 × 850 μm²
FBc: 79 %, 230 × 2020 μm²

across the grain

along the grain

across the grain

along the grain

$\mathrm{H_{\diagdown}O_{\diagup}H}$

$\mathrm{Ca^{2+}}$

—Si-O— (ash)

$C_n H_{2n+2}$

microscopic scale $[10^{-6}\ \mathrm{m}]$

$$\frac{\mu}{\rho}(E) = \sum_j \omega(j) \cdot \frac{\mu}{\rho}(E)_j$$

- j = dry wood matter, water, resin, additives, impurities
- consistent cell-wall tissue & resin layers; (densified) lumina
- bound water layers, free vapour
- WBC composition

$\rho_{t,\mathrm{TMP}} = 1516\ \mathrm{kg/m^3}$
$\rho_{t,\mathrm{UF\text{-}CH}} = 1501\ \mathrm{kg/m^3}$
$\rho_{t,\mathrm{H_2O}} > 998.2\ \mathrm{kg/m^3}$

sub-microscopic scale $[1\ \text{Å}]$

$$\frac{\mu}{\rho}(E) = \sum_i \omega(i) \cdot \frac{\mu}{\rho}(E)_i$$

- i = H, C, N, O, Ca (ash), ...
- condensed matter with total elemental composition $\omega(i)$ independent from structure
- bound or free water molecules as fraction of total composition
- actual **radiation-matter interaction** with atoms, i. e. e$^-$ shell (X-rays) or core (neutrons)

matter	$\omega(i)\ [\%]$				
	$_1$H	$_6$C	$_7$N	$_8$O	ash
TMP OD	5.9	51.0	0.4	42.3	0.3
labMDF OD	5.9	49.3	3.4	41.1	0.3
labMDF 9.5 % MC	6.4	45.0	3.1	45.2	0.3

Figure IV-12: Schematic illustration of the empirical concept of radiation-matter interaction on distinct scales considering the actual beam path of ionising (corpuscular) radiation during transmission through WBCs as both (cold) pre-compressed furnish mat (left column) as well as consolidated final panel (right column) exemplarily for MDF; resulting attenuation $\mu/\rho\,(E)$ as respective mathematical representation, complete with actual parameters from material characterisation (Chapters IV–2.1 to IV–2.4) relevant/representative for the respective scale.

3.2   Macroscopic level

The irradiated specimen appears on macroscopic, i. e. visual, scale as a solid body featuring a certain raw density ρ [kg/m³] with, in turn, a potentially three-dimensional distribution. The homogeneously formed initial fibre mat commonly results in MDF with a distinct raw density profile (RDP) along panel cross-section with $\rho_{\max} = 900 \dots 1200$ kg/m³ in SL and rather uniform ρ_{CL}. The close-up position in the MDF sub-image (Figure IV-12) with exemplary $\rho = 850$ kg/m³ represents the transition area between $\rho_{\max}$ and homogeneous CL. Fibre mat is considered to be cold-densified by pre-press with $p_{\max} < 1$ N/mm² resulting in $\rho \approx 125$ kg/m³ (refer to Table IV-1) whereas previous bulk density after forming is in the common order of $\rho = 15 \dots 30$ kg/m³ (cf. KRUG (2010)). Table IV-17 summarises macroscopic conditions for individual manufacturing, thus, densification states with nominal values, where reference is made to Table IV-5 in Chapter IV–1.5 for actual data of the employed material. Obviously, macroscopic scale is characterised by densification ratios (dr), which, in turn, average in the order of factor 6 from pre-pressed TMP fibre mat to final MDF with particular variations along panel thickness whereas a further factor of 5…6 is found in relation to the loosely formed mat. Relating to softwood as raw material, typical densification ratios are in the order $\bar{\rho}_{\mathrm{MDF}}/\bar{\rho}_{\mathrm{softwood}} \approx 5/3$ on average. Nevertheless, this level of consideration refers to the mat or panel in its actual representation, i. e., as recorded after the beam has passed the specimen. In this regard, the cumulated radiation transmission is governed by the amount of matter along the beam path, i. e., area density ρ_{A} [kg/m²]. This corresponds to the measuring scale whose resulting information content equals a line integral from radiation source to detector surface averaging the information weighted along the travelled path. Integration of the linear attenuation along transmission is required in the case of inhomogeneous porous media, where the amount and compositions of the penetrated substance alter along the beam path.

ρ_{A}	1 kg/m²	40 kg/m²	state	dr
ρ [kg/m³]	20...25		loosely formed mat	
t [mm]	40...50	1600...2000		5
ρ [kg/m³]	100...150		(cold) pre-pressed mat	
t [mm]	7...10	270...400		6
ρ [kg/m³]	600...850		hot-pressed final panel	
t [mm]	1.25...	...60		

Table IV-17: Potential radiation transmission conditions on macroscopic scale at the respective densification state exemplarily for MDF within industrially possible ranges of area density ρ_{A} with corresponding mat height resp. panel thickness t and raw density ρ, complete with rough densification ratios (dr) between the states; nominal figures as mean values of the total body based on common literature data and practical experience.

3.3   Mesoscopic level

Between the macroscopic and microscopic level, but still within the range of visual perception, WBCs require a mesoscopic scale for structural considerations to be characterised by a porous body as individually consolidated wood-particle-resin-matrix including inter-cellular pores, i. e., voids, filled with moist air. In case of MDF and further flat-pressed WBC panels, furnish particles are typically flat but randomly aligned within panel plane. However, for simplification reasons, respective schematisations in Figure IV-12 were solely made of fibres aligned along one in-plane direction and all structural members are illustrated in their ideally straight appearance. Related to blending performance and parameters, fibres of the matrix are both covered incompletely or totally by adhesive resin, where manifold investigations are available elsewhere (cf. THÖMEN, VIEMEISTER (2015)). Subsequently, structural members touch each other either directly or with intermediate bond-line as intended. TMP fibres with the typically predominant structural types short single fibre (SFs) and compact fibre bundle (FBc) show varying morphology characteristics with dimensions within a range related to the pulping process and particular volume fractions, where FBc type commonly dominates. However, consolidation ratio causes final porosity and resulting raw density. With esti-

mated $\bar{\rho}_{\text{softwood}} \approx 450 \text{ kg/m}^3$ for common softwood assortments in MDF production, the formed mat with porosity $\Phi_{\text{mat}} = 92 \%$ is volumetrically composed of 28 % TMP fibres with, in turn, $\Phi_{\text{softwood}} \approx 70 \%$ and 72 % air as voids in between where densification of individual fibres is assumed as negligible. Considerably decreased mean $\Phi_{\text{MDF}} = 50 \%$ originates from both compaction of voids (inter-cellular pores) and compression of TMP fibres, hence, reduced intra-cellular pores. The latter significantly depends on the local densification ratio and the former causes almost eliminated voids in the consolidated wood-particle-resin-matrices.

In consequence of porosity, radiation does not travel constantly through condensed matter but the beam path shows permanent alternations of resinated moist TMP fibres and intermediate air during transmission through WBCs. Depending on occurrence and void size, thus, densification ratio, (moist) air-filled voids enable comparably free radiation propagation off the initial beam axis after first interaction with any kind of WBC matter present. Slightly free beam path in between consolidated matter on account of comparatively low interaction probability with moist air, in turn, facilitates divergence of scattered radiation. Hence, the transmitted share of scattered radiation is related to WBC porosity along the beam path.

Obviously, the coarse structure at the mesoscopic scale is denoted by fibre morphology characteristics as well as densification ratio (global and local) and, therefore, resulting porosity Φ (global and local), which comprises intra- and inter-cellular pores, where the former actually belongs to microscopic level as described hereafter. However, WBC processing impact refers to whole production starting from fibre generation to resination, mat forming (fibre alignment), pre-pressing, and finally to hot-pressing followed by conditioning as well as individual MC variations. Already mentioned global figures for densification ratios (dr, Table IV-17) considerably vary on this scale locally, since initial raw density of extracted single fibres and fibre bundles, i. e., TMP, ranges around mean softwood raw density. Moreover, local cold as well as hot consolidation of the wood-particle-resin-matrix

depends on multiple material- and process-related parameters such as MC, cross-sectional position, and plasticisation and their actual characteristic. Beyond performed empirical descriptions, particular investigations with partly precise dimensional measurements and vivid presentations of WBC structures are reported and manifoldly available in literature. In this regard (representative selection),

- HEYDEN (2000) models a network of pure cellulose fibre fluff (dry-shaped) for mechanical studies on theoretical basis,
- FAESSEL et al. (2005) contribute a comprehensive study on low-density wood-based fibreboard ($\rho = 45 \dots 250 \text{ kg/m}^3$) with µXCT data acquisition and subsequent 3D modelling,
- WALTHER (2006) investigates the microstructure of MDF from wood and further lignocellulosic fibrous material by microscopic and µXCT methods with additional evaluation of adhesive resin distribution,
- LUX et al. (2006) distinguish porosities on two spatial scales, i. e., air volume within and outside the fibres,
- STANDFEST (2011) provides broad evaluations of the microstructure of MDF, PB, and OSB with particular focus on the void structure mainly by means of µXCT,
- SANABRIA et al. (2013) classify inter-particle porosity into flat voids between non-touching pressed particles and edge voids dominating during consolidation at particle-fragment-ends in accordance with the concept of DROLET, DAI (2010) for their measurements and modelling of air-coupled ultrasound propagation through PB, and
- SLISERIS et al. (2017) simulate fibre network microstructure with different densification ratios calibrated by means of µXCT data from standard lab-made MDF for estimation of elasto-mechanical panel properties and consequent optimisation of manufacturing technology.

Note, commonly denoted microstructures of the investigated WBCs refer to fibre or particle structures, i. e., mesoscopic scale as defined in the present case. However, the present simplification of WBC mats and panels as porous bodies

in terms of individually densified wood-particle-resin-matrices appears sufficient for all consequent radiation attenuation considerations.

3.4   Microscopic level

Wood is well-known not to be a homogeneous material. Thus, radiation interaction alternates on the microscopic scale representing the wood-cell structure characterised by intra-cellular pores filled with moist air surrounded by condensed matter. In general, dimensions of softwood tracheids (e. g. pine) range in the order of $w = 14 \ldots 46\ \mu\text{m}$ and $l = 1800 \ldots 4500\ \mu\text{m}$ according to TRENDELENBURG (1939). Solid cell-wall substance comprises constituents (e. g. celluloses and lignin) whose true density ρ_t is independent from the raw density ρ of the porous body and solely varies within a natural range. Independent from wood species, cell-wall substance averages an approximately equal dry true density $\rho_\text{t} \approx 1500\ \text{kg/m}^3$ (Table IV-7).

Considering resin-bonded WBCs, intermediate resin layers complete the solid structure with specific ρ_t again. Regarding bond-line thickness of resin-blended fibres, WALTHER (2006) provides typical values between touching fibres of his lab-made MDF samples $t_\text{UF} = 0.05 \ldots 0.186\ \mu\text{m}$ in dependence of densification ratio (MDF800…MDF400) whereas the resin layer on fibres without contact to each other averages $t_\text{UF} \approx 0.08\ \mu\text{m}$. Furthermore, he describes a resin aggregation referred to as adhesive resin meniscus in consequence of fibre consolidation. Beyond resin coating, XING et al. (2005) report an average distance of resin penetration into tissue of $6.5\ \mu\text{m}$ for their investigated industrial MDF fibres, which mainly occurs towards the lumina. Besides basic adhesive resin, glue liquor possibly contains further additives (e. g. hydrophobic agents or fire retardants), which likewise partly penetrate into the wood-cell structure and contribute to layer thickness.

Wood as a hygroscopic material contains water as vapour within air-filled intra-cellular lumina and, predominantly, adsorbed as bound water within surrounding cell-wall tissue in equilibrium

with ambient conditions. In this regard and owing to both WBC processing and application conditions, the relevant MC ranges below FSP with, as already in Chapter IV–2.2.1 sufficiently assumed, $MC_\text{FSP} = 27\ \%$, where cell walls are fully saturated with water as vividly illustrated by SKAAR (1988). Initially designated as FSP by TIEMANN (1906), the saturated state, however, rather refers to a certain MC range than a particular value. Although water is expected to be exclusively found in bound state below FSP, e. g., PASSARINI et al. (2015) actually discover liquid water entrapped within their investigated wood structures at EMC but only at moist ambient conditions of 21 °C and 90 % RH. Eventually, free liquid water can occur in the WBC structure accordingly and owing to poor distribution of liquid glue liquor as well as potentially wetted surfaces in the case of formed furnish mats.

However, at identical ambient conditions, decreased EMC is typically found in the case of WBCs compared to untreated wood due to manifold material- and process-related influence parameters and their superimposition such as TMP generation, heat impact during drying, and resination, as commonly known and still explicitly investigated, e. g. by HOSSEINPOURPIA et al. (2016). Beyond EMC, further phenomena occur on the microscopic consideration level. As already pointed out in the context of true density result discussion in Chapter IV–2.1.2, particularly during moisture uptake into WBC matter in early stages, the adsorbate water undergoes a volume contraction as bound to the surface of the adsorbent cell-wall tissue. Accordingly reasoned by SEIFERT (1972), with increasing MC, true density of wood furnish, and eventually also of WBC matter, initially just infinitesimally diminishes up to $MC \approx 4\ \%$ and concavely decreases thereafter. Since volume contraction of adsorbed water layers evidently occurs, the provided (increased) density values of adsorbed water have to be taken into account for theoretical beam path modelling. For water adsorbed on defibration fibres (TMP), SEIFERT (1972) reports densities in the order of $\rho_\text{t,H}_2\text{O} = 1390\ \text{kg/m}^3$ at $MC = 0 \ldots 3\ \%$ decreasing, in turn, toward $MC \approx 13\ \%$, whereupon its naturally free character with

$\rho_{H_2O,20} = 998.2 \; \text{kg/m}^3$ remains. Therefore, radiation propagation ensues through both free vapour as well as compressed bound water predominating at standard conditions (20/65) with mean $MC_{\text{labMDF}} = 9.5 \, \%$ and $MC_{\text{indMDF}} = 8.1 \, \%$ (refer to Table IV-5 in Chapter IV–1.5).

Cell-wall structure by itself is primarily characterised by microfibrillar structure within the dominating secondary wall S$_2$-layer (cf. KOLLMANN (1951) p. 121), where the width of the interfibrillar micro-pores range in the order of $w \approx 100 \, \text{Å}$ (perpendicular to the grain). The questionable dependency of ρ_t on ρ_{OD} associated with intra- and interfibrillar micro-pores as proposed by RACZKOWSKI, STEMPIEŃ (1967) was already discussed regarding true density determination in Chapter IV–2.1. Notwithstanding their presence but owing to infinitesimal short potentially free propagation within micro-pores in comparison to cell lumina (three orders of magnitude above) as well as inter-cellular voids on the scale beyond, the fibrillar structure is not further considered for conceptual beam path model, which moreover regards the cell wall as a consistent tissue. However, from a chemical point of view, BOSSHARD (1974) denotes the wood cell-wall as a mixed body.

Finally, according to the mass fraction $\omega(j)$ of the structural constituents along the beam path, i. e., mainly cell-wall tissue, adhesive resin, and bound water, total attenuation equals the respectively weighted sum of individual attenuation contributions. Surrounding the cell lumina, the matter penetrated by radiation is considered to be more or less consistent owing to continuously alternating composition along the beam path and varying alignment of the very same toward wood grain. Accordingly, true density averages about $\rho_{t,\text{labMDF}} = 1515 \; \text{kg/m}^3$ exemplarily for the employed labMDF (Table IV-6) with $\omega(\text{UF})_{\text{OD}} = 10 \, \%$ at oven-dry conditions, which cannot directly be transferred to the actual MC level as discussed earlier. Despite condensed matter, the comparably free beam path through the lumina affects radiation propagation off the primary beam axis on the microscopic scale as well as on the mesoscopic level through inter-cellular voids.

3.5   Sub-microscopic level

Finally, actual radiation-matter interaction occurs on the sub-microscopic, i. e. atomic, scale. Depending on the type, radiation interacts with electron (e^-) shells (X-ray photons) or atomic cores (neutrons). Regardless of molecular WBC constituents, the explanatory model exclusively considers the elemental composition which the present matter is made of. Moreover, for simplification purpose, a more or less homogeneous distribution of the predominant low-Z elements is presumed on this level of consideration. Here, the elemental composition of the total matter is taken into account for subsequent attenuation-related computations on this basis and no distinction between chemical constituents with comparable elemental contents (Table IV-14) is made, in turn. Furthermore, mineral components from wood itself, bark or process-related impurities (Table IV-11) with varying amounts due to WBC type contribute to radiation attenuation. Nonetheless, a general value of $\omega(a)_{\text{MDF}} = 0.3 \ldots 0.4 \, \%$ is sufficient to be taken into account for MDF (Table IV-12), where a slight increase potentially occurs in the case of other WBCs with comparably less sophisticated raw material cleaning. Beyond highly-dispersed inorganic elements, impurities, e. g., sand from bark, may occur as single particles spread within WBC matter, which are of particular interest regarding radiographic and tomographic methods (e. g. causing artefacts) in dependence of the employed radiation type and properties. Furthermore, total elemental composition is considered to comprise water whether bound or free due to MC as respective H and O fraction, where $\omega(i)$ of all components is adaptable to requested MC following inverse MC correction procedure according to eq. (IV-24) to eq. (IV-29). This viable adjustment is contrary to true density, where respective computations are non-trivial, moreover, not feasible. Apparently, MC variations directly contribute to respective alterations in radiation attenuation but actual impact considerably depends on radiation type and properties, thus, attenuation parameters, where X-ray attenuation corresponds to present atomic numbers within the mixture (refer to Chapter IV–5.1).

However, a closer consideration of the elemental composition of WBCs – as already denoted as HCNO-materials – enables the derivation of mass attenuation coefficients on a theoretical basis by means of tabulated data for X-ray applications (Chapter IV–5.2) with particular respect to radiation energy spectra. Accordingly performed computations are respectively compared to measured attenuation data. Hence, WBCs are exclusively considered to be a mixture of HCNO-elements inclusive of some minerals dominated by calcium (Ca) on this scale, which depicts the actual geometric level of radiation-matter interaction in contradiction to macroscopic scale, which provides measuring information of radiometric investigations. Subsequently, on elemental composition basis, the effective atomic number Z_{eff} (cf. MURTY (1965)) is derived in Chapter IV–5.1 providing an illustrative figure, to compare the impact on X-ray attenuation. Finally and beyond elemental composition, there is no influence of any WBC production process-related structural variations such as consolidation on radiation-matter interaction on the sub-microscopic scale. Hence, independent from material (coarse) structure, sub-microscopic level exclusively involves elemental- and energy-related interaction mechanisms of the respective radiation with the investigated matter.

3.6   Conclusion

With the objective to be introduced as an explanatory beam path model, the concept is not entitled to claim precise quantitative description of three-dimensional WBC structures like aforementioned models do (refer to Chapter IV–3.3). However, partly good agreement is found in comparison of relevant details. Moreover, a qualitative illustration of structural aspects on distinct scales relevant for radiation transmission and attenuation is intended considering both WBC composition and processing across the wide range from mat forming of resinated furnish to the cured final panel.

Designated as a central issue, the WBC structure comprising inter- as well as intra-cellular pores, i. e., voids and cell lumina, respectively, is

considered to directly affect transmitted radiation intensity. Since an equal amount of irradiated identical matter is expected to cause equal attenuation, transmitted radiation intensity through WBCs considerably depends on consolidation of the porous matter. The densification ratio and resulting total porosity affect radiation propagation off the primary beam axis. Moreover, the impact of the WBC structure on effective radiation attenuation is considered to be quantifiable regarding metrological applications.

Based on practice-oriented objectives, the conditions of radiation transmission through WBCs are both

- simple to generalise regarding low-Z elemental composition embedded in virtually consistent solid matter with constituents of similar true density and
- complex to model precisely regarding beam path geometry with respect to potential structural members as well as radiation-matter interaction considering actual inhomogeneity.

Radiation-matter interaction and corresponding attenuation related to elemental composition, are subsequently computable, wherefore reference is made to Chapter IV–5.2. On the contrary, radiation propagation, thus, effective attenuation and resulting transmission, are considered to be attributed to structural conditions on the mesoscopic and microscopic scale, particularly porosity, owing to consistent true density of the condensed matter present. Hence, both composition and structure are relevant for radiation attenuation on all considered scales below macroscopic appearance as solid body.

To conclude in short with reference to Figure IV-12, radiometric density measuring results $\rho\,[\mathrm{kg/m^3}]$ or $\rho_A\,[\mathrm{kg/m^2}]$ based on transmission intensity detection represent the macroscopic conditions of irradiated WBC matter whether furnish mat or final panel, whereas on the one hand their mesoscopic and microscopic structures affect total effective radiation transmission and on the other hand actual radiation-matter interaction ensues on sub-microscopic (atomic) scale. Independent from consolidation ratio of wood furnish,

the true densities of relevant constituents present, i. e., cell-wall tissue, resin, additives, and water, remain constant. Thus, penetrated matter undergoes no alteration in relation to individual densification. Consequently and regardless of apparent structural impact, transmitted radiation is expected to primarily contain information about irradiated mass of matter, i. e., its area density ρ_A, expecting, in turn, a homogeneous non-porous absorber. Accordingly, the computed mean attenuation data via weighted sum of tabulated mass attenuation coefficients $\mu/\rho\,(E)_i$ [m^2/kg], which refer to atomic cross-sections, exclusively yields valid ρ_A results for consistent bodies and is not applicable for direct densitometry on porous media. Hence, radiation transmission-based raw density evaluation requires effective $\mu/\rho\,(E)$ values determined with a priori knowledge of the structural conditions. Though radiation-matter interaction ensues on atomic level, measuring information is attributed to macroscopic level of the inhomogeneous body with considerable impact of structural conditions on mesoscopic and microscopic scales below. The latter are characterised by alternations along the beam path of (moist) air and various solid constituents, i. e., radiation is considered not to constantly travel through condensed matter, which facilitates potentially free radiation propagation off the primary beam axis, where radiation photons or corpuscles undergo minimised likelihood of interaction within pores and voids.

Finally, the developed conceptual beam path model illustrates actual transmission conditions of WBC whether furnish mat or final panel obviously not fulfilling good-architecture conditions (i. e., monochromatic narrow-beam, refer to Chapter II–1.3). However, in an ideal case, radiation attenuation is described by exponential intensity diminution following the well-known Beer's law according to eq. (II-10) and eq. (II-11), respectively, where initial intensity I_0 [a. u.] is exponentially attenuated yielding transmitted intensity I_T [a. u.] in dependence of mass attenuation coefficient $\mu/\rho\,(E)$ [m^2/kg], transmission distance t [m], and raw density ρ [kg/m^3] or area density ρ_A [kg/m^2], respectively. In applied radiometric WBC investigations by means of X-rays or other forms of radiation, the conditions for full validity of Beer's law cannot be reasonably met in any case leading to biased exponential context. Subsequently, the explanatory beam path model is revisited and refined in Chapter IV–6.5, where particular consequences of WBC structure and composition as well as further related effects on quantitative measurements are discussed.

4 X-ray measurements

4.1 Sampling and sample preparation in general

All performed X-ray measurements require a more or less similar specimen cutting and preparation. The number of specimens, however, depends on the respective measuring series. Note here, sample sizes are considered to be rather small due to the exploratory character of this study. However, material manufacturing and general specimen preparation were already described in the respective sections in Chapter IV–1 considering the individual material types lab-made furnish mats and homogenous fibreboards as well as customary industrial panels. Before and after cutting, all material was stored at standard conditions 20 °C and 65 % RH (unless otherwise stated) as primarily applied for the X-ray measurements. Additionally, SL particles were stored at dry (OD) and moist (20/83) conditions. The individual conditioning to constant mass was ensured prior to each measuring series. In the case of any transport to external measuring facilities, the material was vacuum-sealed to avoid changes in EMC. The actual MC is evaluated after conditioning and summarised in Table IV-5 complete with the further properties thickness t, raw density ρ, and area density ρ_A, which are furthermore discussed with description of their determination in Chapter IV–1.5. For measurements with regard to area density ρ_A determination on furnish mats (Fmat, SLmat, and CLmat), not total real-size mats like in the industrial production but sufficiently large specimens (174 mm diameter) are utilised as manufactured according to Chapter IV–1.1. The like applies to the lab-made and particularly the customary industrial panels (labMDF, Chapter IV–1.2 and indMDF, IV–1.3, respectively). All indMDF specimens were randomly cut from the panels with the required dimensions. In due consideration of the individual X-ray beam geometries as well as detector sizes, it was verified that the respectively employed specimens sufficiently cover the core beam and a relevant surrounding area in order to obtain appropriate radiation transmission and scattering conditions like on real-size material. Given the nondestructive nature of X-ray measurements, most of the sample sets could be employed for numerous measurements on the different devices and setups or as repetition for verification of observations before they were partly utilised for the destructive material analyses (Chapter IV–2) or RDP determination via reference method in terms of the round robin test (Chapter IV–4.3.1). Eventually, specific details on sampling and sample preparation are provided at the beginning of each respective result presentation chapter.

4.2 Methods

4.2.1 Overview

The following subchapters point out the employed methods for X-ray measurements with particular purposes. However, basically two X-ray devices with either Ag (Chapter IV–4.2.2) or W (Chapter IV–4.2.3) as tube-target material were utilised for manifold applications, where the latter was furthermore varied in its application-oriented setup. Regardless of control and data acquisition software as well as sample manipulation, descriptions rather focus on radiation-related components and their parameters to keep reproducibility of results and related implications. Note, some components cannot be further specified owing to their origin from a bilateral research project and to keep proprietary data. Accordingly, brand and manufacturer names as well as detailed pictures are partly omitted.

Notwithstanding basically similar transmission setups, Ag- and W-target device differ tremendously from each other considering components and interconnection. Accordingly, the same applies to raw data processing and evaluation. However, equivalent output of measuring results is eventually obtained regardless of device-specific procedures.

Both devices were furthermore part of a round robin test (Chapter IV–4.2.5) with several customary measuring devices involved for raw density profile (RDP) determination. Demanding verification of radiometric raw density measuring results in the case of RDP determination required the development of a gravimetric reference method as pointed out in Chapter IV–4.2.4. Beyond actual measurements, X-ray spectra determination (Chapter IV–4.2.6) was performed by means of simulation methods with explicit consideration of the respective measuring parameters.

4.2.2   Ag-target device

Notwithstanding particular modifications, the first of the two utilised X-ray devices is equivalent to the Itrax Multiscanner (without XRF unit) by Cox Analytical Systems, Mölndal, Sweden as described by COX (2016) and hitherto likewise referred to as Itrax Woodscanner. Besides the aforementioned regular tree-ring analysis applications, this device was initially employed for WBC investigations by GRUCHOT (2009) with additional specimen-modifying installations. However, SOLBRIG (2009) finalised, evaluated, and optimised his adaptions for RDP determination, which is likewise reported by SOLBRIG et al. (2010). For a detailed description with comprehensive focus on control and data acquisition software, reference is made to the very same. Hereinafter, the particularly adapted Itrax device was exclusively applied for investigations regarding vertical RDP determination on 50×50 mm² specimens (as exemplarily shown in Figure IV-19 with the round robin test samples). Figure IV-13 shows the internal space with the main radiation-related components of the device and Table IV-18 compiles selected specifications. Here, a water-cooled glass diffraction X-ray tube with long fine focus on the Ag target serves as radiation source. Moreover, the Ag-target device particularly features capillary optics made of quartz glass for flat-beam collimation (refer to Chapter II–1.3). Detailed specifications of the actually involved polycapillary optics are, however, not available. Since device setup was

initially not designed for variable pre-filter installation, a respective additional fastener was mounted directly after beam emission from capillary optics. Subsequent impact on beam geometry in terms of more distinct divergence can, however, not be excluded. Nevertheless, due to primary application for RDP measurement, the parallel alignment of the flat beam toward specimen plane was carefully maintained. To this end, the capillary optics gimbal mounting provides two translational and three rotational degrees of freedom as illustrated in Figure IV-13. The rotation around the beam axis (Z via C) was furthermore horizontally aligned toward the detector slit aperture. Moreover, sophisticated beam alignment facilitates precise spatial resolution of the specimen in terms of measuring values true to thickness position. Therefore, poor beam alignment potentially causes non-parallel and layer-crossing radiation transmission through the specimen, which obviously emerges as surface raw density decrement, where actually no distinct gradient is present. Beyond manipulation, stability is likewise considered. In dependence of temperature, thus also of operating time, variations in beam alignment were observed via the detector signal of radiation intensity. The regular variations are primarily not attributed to focal spot drift but are rather caused by thermal expansion of the tube housing with mounted capillary optics and further related components. Consequently, in addition to so-called tube warm-up in terms of gradually high-voltage and current increment lasting up to 30 min, a two-hour device warm-up at regular high-voltage settings was consistently performed in advance of each measuring cycle.

Notwithstanding preliminary trials with parameter and setup variations, presented results will be limited to regular Itrax device settings referring to SOLBRIG (2009) at $U_{\mathrm{a,nom}} = 55$ kV and $I_{\mathrm{a,nom}} = 40$ mA without pre-filter unless otherwise stated. The utilised upper tube power limit enables maximum photon flux yield, which is required by the employed detector. For the purpose of at least one energetic variation, 1.5 mm Al was applied as additional pre-filter likewise shown in Figure IV-13 (e). For the two exclusive configurations of Ag-target device, the correspondingly derived
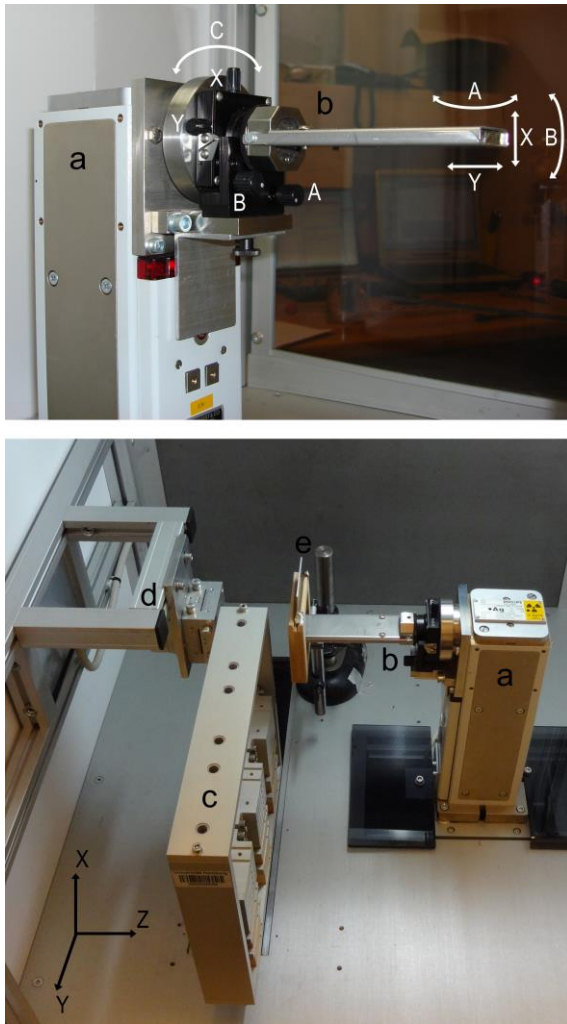
Figure IV-13: Internal space of the modified Itrax Woodscanner (Cox (2016)), referred to as Ag-target device), with long fine focus X-ray tube with Ag target (a), capillary optics with gimbal mounting for beam adjustment (b and arrows with two translational and three rotational axes in upper picture), sample holder for < 24 specimens (c), detector unit comprising adjustable slit collimator and line camera (d), mounting for variable pre-filter installation (e), and high-voltage generator and sample-holder manipulation axes (x, y) in lower section; illustration partly following SOLBRIG (2009).

device setup	Ag-RDP
X-ray tube	
target material	$_{47}$Ag
take-off angle	6°
focal spot	0.4 × 12 mm²
tube window	0.3 mm Be
$E_{\max}$ via $U_{\mathrm{a,nom}}$	55 kVp
current $I_{\mathrm{a,nom}}$	40 mA
max. power	2200 W
cooling	water
beam geometry	
collimation	capillary optics
beam shape	flat beam
take-of size (w × h)	15…22 × 0.05…0.1 mm²
$s_{\mathrm{X-S}}$	263 mm
s_{T}	50 mm
$s_{\mathrm{S-D}}$	48 mm
photon detector	
collimation	parallel slit, adjustable
type	line camera, 1024 pixel
size (w × h)	25.6 × 2.5 mm²

Table IV-18: Selected specifications of Ag-target device with one setup; radiation-related component parameters as specified by manufacturers or particularly determined, with distance from X-ray source (focal spot) to sample surface $s_{\mathrm{X-S}}$, transmission distance within sample s_{T} (corresponding to specimen depth), and distance from sample backside to detector surface s_{S-D}.

abbreviations and figure labels following the pattern "setup-$U_{\mathrm{a,nom}}$-add. pre-filter" are

- "Ag-RDP-55-w/o" and
- "Ag-RDP-55-w/".

Beyond the influence from capillary optics on the X-ray spectrum (Chapter II–1.3), no further inherent materials with pre-filter character need to be considered. The predominance of character-

istic Ag-target K lines within the utilised X-ray energy range as well as the energy-dependent transmission efficiency of the employed capillary optics, however, restrict further considerable influenceability of initial radiation properties, which will be discussed elsewhere. Therefore, the resulting mean energy level proved itself to be sufficient but by no means optimal for the specimen transmission distance $s_{\mathrm{T}} = 50$ mm.

For data acquisition, detector integration time (intra-software exposure time) was empirically adapted to initial beam path conditions, e. g. pre-filtering, ranging 50…250 ms but kept respectively equal for repeated measuring series. Measuring data is basically stored in a 16 bit TIFF file per measured specimen. Here, the data array corresponds to the scanned ROI and can

be displayed as grey-scale image. Horizontal image width of 21.375 mm originates from reasonable detector collimation and further software masking of boundary pixels resulting in 855 used pixels of 25 µm width each. Vertical image height depends on specimen height (panel thickness) and applied scanning step size with 50 µm as a default value. Variations in the order of 50…125 µm facilitated shortened measuring time particularly performed in the case of thick panels such as insulation whereas solely spatial resolution became coarser since the integration time per measuring step remained equal. Thus, vertical pixel height likewise varies where, however, each array row represents one scanning step and virtual specimen layer. Each pixel value, in turn, comprises the measuring information of radiation transmission $T = I_\mathrm{T}/I_0$ following eq. (II-1) multiplied by a constant (> 30,000, here not further specified) to cover half 16 bit range. For further technical and software details on the Itrax device, reference is made to SOLBRIG (2009). For subsequent measuring data evaluation, the mean per horizontal image row is computed from raw data ($T \cdot$ constant) and respective horizontal spatial resolution not further considered.

4.2.3   W-target devices

Whereas the Ag-target device is considered as a complete setup with slight modifications toward the delivered system, the second of the two utilised X-ray devices features particularly different and individually prepared setups. However, all setups share, in turn, radiation source and detector type. A passively conduction-cooled metal-ceramic X-ray tube with conventional point focus on the W target serves as radiation source. Radiation detection is performed via photon counting without spatial resolution across a predefined area by means of a scintillator with subsequent photomultiplier (PM) tube and corresponding read-out electronics. This principle of X-ray detection yields remarkably higher efficiency in comparison to ionisation champers and semiconductor detectors. The applied detector units, nonetheless, vary in scintillator size and

type, thus, energy efficiency, and further particular details, which were actually withheld by the detector manufacturer but correspond to the energy range of application. Beyond radiation source and detection, three setups of the W-target device are to be distinguished (and labelled) regarding their application for

- vertical RDP determination on 50 × 50 mm² specimens (W-RDP),
- measurement of horizontal area density distribution on furnish mats (W-mat-ρ_A), and
- measurement of horizontal area density distribution on panels (W-panel-ρ_A),

where Table IV-19 compiles selected specifications and Figure IV-14 exemplarily shows the W-mat-ρ_A setup. Accordingly, the setups mainly differ in beam geometry considering radiation transmission distances, beam shape with corresponding apertures, and consequently irradiated specimen volumes. Beam alignment was initially performed as an individual part of the basic setup but not adjusted further during the respective measurements since the beam path is not as prone to drift as in the case of the Ag-target device. However, to maintain sufficient stability, the X-ray tube was consistently operated for at least one hour at the respective high-voltage settings in advance of each measuring cycle. Variable pre-filters were installed on demand of each application directly after beam emission either from X-ray tube or subsequent aperture. Owing to the basically less tightly collimated and generally divergent cone or fan beams, additional divergence in consequent of pre-filtering was not further considered and consequently neglected. Eventually, all applied setups of the W-target device appear more robust, and thus, practice-oriented.

Within the utilised energy range, the exclusive bremsstrahlung spectra without predominant characteristic lines of the W-target tube facilitate a variety of influences on the initial radiation properties by means of variation of tube potential $U_\mathrm{a,nom}$ in coordination with pre-filter application. Accordingly, resulting energy levels were specifically predefined considering the particular material conditions of the desired application – e. g.,

Figure IV-14: Exemplary W-mat-ρ_A setup of the W-target device with X-ray tube (a), aperture (b), any WBC specimen (c), and detector (d) as well as high-voltage generator (e), without installed pre-filters.

in terms of sample area density ρ_A and transmission distance s_T. Respective tube current $I_{a,nom}$ adaption was performed aiming at appropriate photon flux for reasonable detector signal yield. Here, the applied parameter variations are based on prior practice-oriented experience with the experimental setups and particularly the applied detectors, where, however, specific values are not further pointed out. Table IV-20 compiles nominal X-ray tube potential settings and pre-filter variations for all W-target device setups. Corresponding abbreviations and figure labels were derived following the pattern "setup-$U_{a,nom}$-add. pre-filter", e. g. "W-mat-25-w/". Note, inherent materials within the beam path besides additional pre-filters are attributed to the setup itself and consequently taken into account in terms of all energetic considerations. A piece of forming belt (type EMB-12 EMCH, Habasit AG, Reinach, Switzerland) was required to carry the furnish material likewise in practise whereas the panel samples were freely mountable within the beam path.

device setup	W-RDP	W-mat-ρ_A	W-panel-ρ_A
X-ray tube			
target material			$_{74}$W
take-off angle			21°
focal spot			0.2 × 0.2 mm²
tube window			0.3 mm Be
E_{max} via $U_{a,nom}$			< 50 kVp
current $I_{a,nom}$			< 0.3 mA
max. power			40 W
cooling			passive via conduction
beam geometry			
collimation	hole	slit	slit
beam shape	cone	fan	fan
take-of size [mm²]	Ø 6 mm	6 × 14	8 × 40
s_{X-S} [mm]	60	150	1661…1688
s_T [mm]	50	< 400	3…30
s_{S-D} [mm]	53	70…470	36
photon detector			
collimation	slit, 50 µm	none	none
type		scintillator with PMT	
(energy range)	(high)	(low-mid)	(low-mid)
size (w × h) [mm²]	25.4 × 25.4	25.4 × 101.6	25.4 × 101.6

Table IV-19: Selected specifications of W-target device with three setups; radiation-related component parameters as specified by manufacturers or particularly determined, with distance from X-ray source (focal spot) to sample surface s_{X-S}, transmission distance within sample s_T (corresponding to specimen thickness or depth), and distance from sample backside to detector surface s_{S-D}.

W-device setup	$U_{a,nom}$ [kV]	pre-filter inherent	additional
RDP	35	w/o	1.96 mm Al
	50	w/o	1.96 mm Al
mat-ρ_A	16	belt + 1.0 mm CFRP	w/o
	20	belt + 1.0 mm CFRP	w/o
	25	belt + 1.0 mm CFRP	1.5 mm Al
panel-ρ_A	16	1.2 mm CFRP	w/o
	20	1.2 mm CFRP	w/o
	25	1.2 mm CFRP	1.5 mm Al
	35	2.0 mm Al	0.05 mm Cu

Table IV-20: Nominal X-ray tube potential settings and pre-filter variations of the three W-target device setups; inherent pre-filters are attributed to basic setup and respectively always present; 'belt' corresponds to EMB-12 EMCH by Habasit; derived abbreviations and figure labels "setup-$U_{a,nom}$-add. pre-filter", e. g. "W-mat-25-w/".

X-ray signal acquisition per measuring position was performed as a directly integrated signal without spatial distinction across the respectively sensitive area owing to the detector type (in contrast to Ag-RDP device line camera). Intra-detector integration time (gate time) was consistently set to 100 ms. Further intra-software integration time of commonly 1000 ms ensured noise reduction and thus provided more reliable mean measuring signals. In the case of transmission measurements by means of W-ρ_A setups, the displayed recording of detector count rates per time period [cpp] represent impinging radiation intensity from initial I_0 or transmitted I_T beam. Subsequently computed transmission data $T = I_T/I_0$ following eq. (II-1) was stored independently from X-ray device and utilised for consequent measuring data evaluation. The same applies to W-RDP setup, which furthermore features automated data recording. To this end, specimens move continuously through the beam with an adjustable step size along the height (panel thickness) governed by manipulation velocity (variable) and detector integration time (constant). The parameter was, nevertheless, consistently set to mid-level velocity resulting in 0.044 mm step size as a reasonable compromise between measuring speed and result quality in terms of signal noise, which is diminished with decreasing manipulation velocity, thus, increasing integration time per virtual measuring step.

4.2.4   Gravimetric reference method

4.2.4.1   Background and general remarks

Since radiometric methods solely provide indirect raw density results based on respective data evaluation, the fundamental demand for a reference method to be independent from any calibration is obvious. Hence, the verification of relative X-ray measurements requires an absolute value determination method. In the case of investigations on in-plane distribution within a panel, sampling and subsequent gravimetric area density determination appear rather convenient, where commonly 100 × 100 mm² specimens are successively cut. Thus, the henceforth discussed methods exclusively focus on vertical RDP determination.

To this end, former non-radiometric and preferably gravimetric RDP determination methods (Table IV-21) were evaluated, particularly optimised, and an appropriate reference method was developed based on the well-known principle as described in Chapter IV–4.2.4.2. Here, thin layers are cut parallel to the panel plane to measure their mass and volume for direct raw density determination per layer. Hitherto methods fundamentally differ regarding layer removal processing whereas raw density per layer is commonly determined by differential mass and volume measurement with one exception (sawing in Table IV-21). However, SOLBRIG et al. (2011) report on first experiences with the hereinafter adapted microtome. Regarding data processing, they already perform a smoothing of the results per layer via mean calculation with predecessor and successor. Attributed to the applied procedure, they finally conclude erroneous mass determination of potentially incomplete layers as the reason for the blurred RDP slope, whereas sufficient correlation between radiometric and gravimetric data was found.

However, the literature review (Table IV-21) unveils certain insufficiencies in the destructive RDP determination methods. WINISTORFER et al. (1986) found crucial RDP data variability and conclude the gravimetric method as erroneous due to numerously repeated specimen positioning and mechanical measurement. PLATH, SCHNITZLER (1974) likewise state the propagation of measuring uncertainties in consequence of frequently consecutive determination of differential mass and thickness as considerable. In the case of sawing method, low number of data points with consequently rather coarse spatial resolution and certain loss of information due to saw blade thickness is pointed out. According to MAY (1977), measuring uncertainties increase with decreasing layer thickness. Nevertheless, the actual RDP shape is falsified particularly within the surface area due to excessive layer thickness. Eventually, STEVENS (1978) regards the surface structure after slicing as limiting for thickness measuring accuracy and further considers particle tear-outs to cause errors in the mass of removed layers. For 0.25 mm slicing of

method	characterisation	applied or described by
gravimetric, direct		
milling or sanding	- more or less defined removal (chips and dust) of thin layers of the specimen - differential mass and thickness determination via residual mass and thickness measurement of the specimen for raw density calculation per removed layer	HENKEL (1969), POLGE, LUTZ (1969), PLATH, SCHNITZLER (1974), MAY (1977), WINISTORFER et al. (1986)
sawing	- cutting of intact layers (slices of approx. 2 mm) by precision circular saw - direct raw density determination of removed layer by mass and dimension determination of the intact slice - interpolation of saw cut gap	POLGE, LUTZ (1969), PLATH, SCHNITZLER (1974)
slicing (thick)	- cutting of slices as thin as 0.25 mm (MDF) or 1.0 mm (PB) by knife of slicing apparatus - specimen positioning against reference surface - differential mass and thickness determination via residual mass and thickness measurement of the specimen for raw density calculation per removed layer	STEVENS (1978)
slicing (thin)	- removal (slicing by regular microtome knife) of thin layers (nom. 50 µm) of the specimen - collection and mass determination of removed slices per layer - assumption of constant layer thickness - raw density calculation per removed layer	SOLBRIG et al. (2011)
non-gravimetric, relative		
drilling resistance	- vertical drilling (predefined needle or bit) through the panel by means of a respective device - relation between density and cutting force, determined via required torque or motor power - result: relative profile over drilling distance	PAULITSCH, MEHLHORN (1973); WINISTORFER et al. (1995), HELMS, NIEMZ (1993), Appendix VII–3
acoustic emission	- recording of acoustic emission (AE) during panel processing by a tool along its thickness - two principles: rotating specimen, fixed tool with AE transducer; rotating tool, fixed specimen with AE sensor - relation between density and signal intensity (AE level) - calibration via mean signal level and mean specimen raw density	LEMASTER, DORNFELD (1990), LEMASTER, GREEN (1992)

Table IV-21: Compilation of non-radiometric and partly destructive laboratory methods for vertical raw density profile (RDP) determination on WBCs, distinction regarding density determination per layer.

material with $\bar{\rho} = 800 \ \mathrm{kg/m^3}$ he states a maximum error of ±11 % for layer raw density, where a major portion is attributed to thickness measurement.

Beyond layer-removing methods, Table IV-21 is completed by further non-radiometric possibilities for RDP determination, which, on the contrary, solely yield relative results. In the case of drilling resistance, own exploratory studies by means of a handheld device (a rather old model with only a profile print-out) confirmed the method to be inappropriate as absolute reference. For exemplary results, reference is made to Appendix VII–3. Hence, all listed non-gravi-

metric methods are considered not viable as reference methods due to likewise required calibration to obtain absolute density values beyond the relative profile.

4.2.4.2   Setup and procedure

The developed device for non-radiometric RDP determination is fundamentally based on evaluated and consequently enhanced former methods with the main focus on a repeatable cutting process for gravimetric raw density determination per predefined layer. Preliminary examinations unveiled face milling to be an advantageous cutting method. Contrary to peripheral

milling (cf. RIEGEL (1997)), face milling facilitates to achieve appropriate surface quality with little microstructural damage and waviness. Beyond milling, conventional sanding may furthermore cause surface densification particularly in the low-density core layer of MDF and undefined dust residues within the pores and voids. Sanding was examined and found insufficient regarding predefined layer removal by means of customary machine equipment.

However, for face milling, a hand router (Festool OF 1000) equipped with a Ø 30 mm cutter (two edges) was run at $n = 21700 \ \mathrm{min}^{-1}$. Since face cutting edges are concavely angled, only their outer corners process the final surface. The router was mounted on a sliding microtome (Modell K, R. Jung AG, Heidelberg, Germany) instead of the regularly fixed knife block as shown in Figure IV-15. The microtome was further modified to obtain a rapid and repeatable sample fixing by means of a well-designed specimen holder clamped on the original slide. The milling plane was aligned parallel to the specimen plane. In addition, specific equipment and details are presented in Appendix VII–3. Constant and sufficiently repeatable thickness of layer removal was achieved by the present elevating mechanism of the microtome's slide. To this end, face milling of each intended 50 µm layer was performed in two stages due to the built-in maximum elevation around 30 µm. The effective layer thickness of 50 µm was predefined following common X-ray RDP measuring devices considering their average step size. For equivalent milling, the variable feed speed of the microtome slide was adjusted at $v_f = 53.3 \ mm/s$, hence, generating $f_z = 0.074 \ mm$ tooth feed rate.

Ordinary RDP samples were processed as follows. The specimens of originally 50 × 50 mm² (w × l) and nominal panel thickness were separated in the middle by sawing in the direction of the passing X-ray beam with regard to the maximum cutting diameter < 30 mm. Left halves of the specimens were fixed on an aluminium baseplate by PVA glue providing appropriate strength and allowing subsequent easy removal (not water resistant). The panel surface for measurement was individually selected regarding interesting characteristics along the RDP and

Figure IV-15: Setup of the gravimetric reference method with slide of the modified microtome (a), sample holder with specimen (b), hand router Festool OF 1000 (c) incl. face milling cutter (Ø 30 mm), and baseplate (d) to fasten router instead of knife block.

radiometric data was accordingly matched. Consequently, the reference method is limited to one half of the specimen thickness (≈ 10 mm in case of usual 19 mm panels) as restricted by the sample holder and potential glue penetration into the lower surface. Width and length as mean along panel thickness of each specimen half were measured prior to gluing via digital calliper. Initial mass of the fixed specimens was determined after repeated conditioning at 20/65 to constant mass.

After each 50 µm layer milling with aforementioned parameters and gentle pneumatic dust removal, residual mass and thickness (mean of three points) of the fixed specimen were measured including the baseplate. Subsequently, raw density per layer was computed from differential values. The particular equipment is shown in Appendix VII–3. The elaborate performance of this destructive procedure with 200 iterations lasting 6 h per 10 mm thickness is only of interest for special purposes. Gravimetric RDP reference

measurements were exclusively performed on common 19 mm panels, i. e., total set of samples from the round robin test (Chapter IV–4.2.5) and further 19 mm labMDF specimens for method evaluation (Chapter IV–4.2.4.3). During application, the method was continuously improved considering practicability of the procedure aiming at enhanced convenience and repeatability with more uniform results and reduced disturbances.

Note, the second (right) halves of all specimens were kept for result verification on demand but not further required. Finally, to visualise the inner structure, photographs were acquired from every layer after milling on selected specimens of both MDF and PB. For exemplary image sequences, reference is made to Appendix VII–3.

4.2.4.3   Method evaluation

As part of continuous improvement, gravimetric reference method was finally evaluated by means of labMDF of 19 mm nominal thickness including all three raw density levels (refer to Table IV-2). Beyond advantageous structural homogeneity and smaller particle size, lab panels were applied due to their homogeneous RDP without distinct gradients. Results of reference method evaluation are presented in Figure IV-16 (raw data plots), which obviously show partly considerable variations between adjacent measuring points notwithstanding all improvements of the procedure. Note, all presented reference RDPs solely comprise the upper half of the panel thickness due to aforementioned limitations.

Potential sources of errors and their effect on the results are attributed to the layer processing method itself. In this regard, an obvious pattern of value scattering along processing direction (surface to core) is characterised by repetitions of immediate raw density increments followed by equivalently decreasing values until the data reach their mean slope again. Owing to comparably stable thickness values, the crucial variations are caused by respectively apparent mass
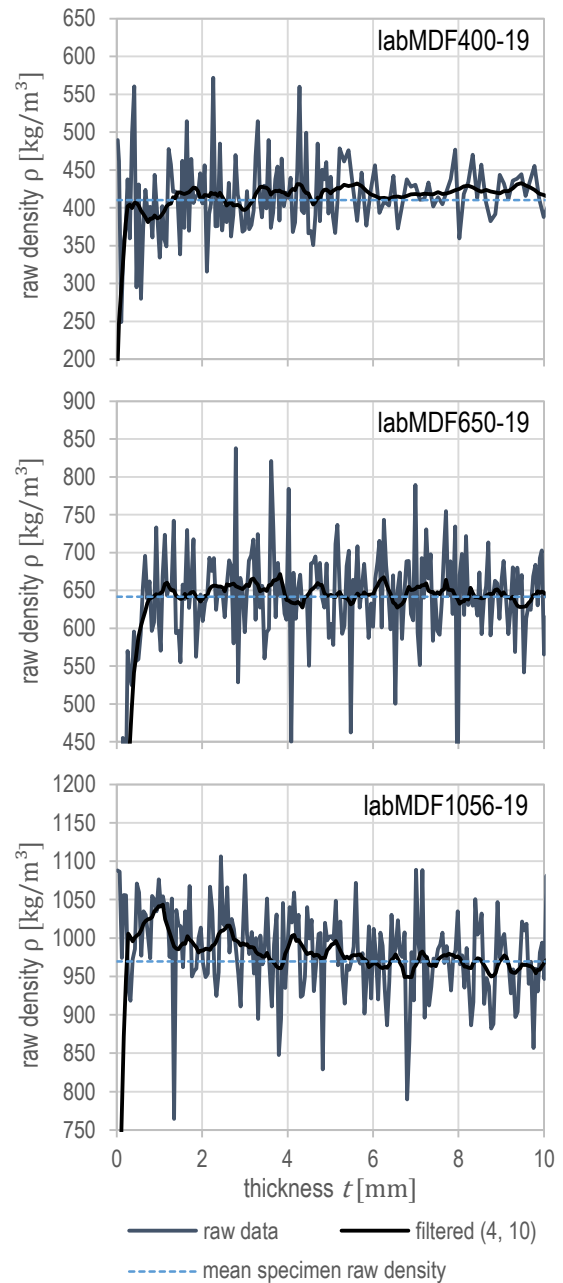
Figure IV-16: Gravimetric RDP of 19 mm labMDF[30] for method evaluation purpose as raw data and filtered via Gaussian smoothing by convolution kernel $\sigma = 4$, $w_K = 10$, with mean gravimetric raw density of the specimen (dashed line).

differences. The observed phenomenon is considered to correspond to irregular particle tear-out from the following layer(s) in the geometrical order of fibre bundles considering MDF. In the case of PB, likewise separated fibre bundles but especially total particles are withdrawn, where

---

[30] In case of labMDF400-19 for $t > 5$ mm, layer thickness was empirically doubled because of observed considerably fibrous milling surface.

rather loose fine fractions with inappropriate bond as well as dust and residues of bark are considered. For exemplary image series of the layers after milling, reference is made to Appendix VII–3. In addition to general plane tear-out and particularly in the case of PB, edge chipping and loss of total chips occur on the boundaries due to horizontal cutting forces. Embedment in respective material likewise common for microtome thin section cutting would minimise the problem but has an impact on the results owing to mass infiltration. However, the fluctuations increase in core layer with commonly decreasing local internal bond and increasing porosity. Nevertheless, both effects are not directly quantifiable. Beyond methodical reasons, typical uncertainties of thickness measurement and weighing process additionally occur.

Nevertheless, the effects from milling cause a form of value noise for the gravimetric raw density results, which obviously superimposes the actual RDP. Though there is no strict regularity observable, the values alter with extreme extent around the mean slope of the profile. The phenomenon was found to be comparable to statistical noise in digital imaging or signal processing. Hence, respective filtering methods for noise reduction were considered. In contrast to simple median filtering, Gaussian smoothing was found to provide sufficiently effective filtering yielding a more consistent slope of the profile. Beyond Gaussian filtering, utilisation of more sophisticated methods such as Kalman filter, which, practically spoken, enables information to be restored, requires a priori knowledge, which is not available for this short data set of 201 values. However, data processing for Gaussian smoothing was performed by means of MATLAB® where a 1D Gaussian convolution filter was built. Smoothing character of the filter is adjustable via width of the kernel w_K and standard deviation σ of its Gaussian distribution in terms of the number of considered values. The strength of noise reduction was empirically counterbalanced toward keeping the character of the actual RDP. Therefore, half the width of the Gaussian window $w_K/2$ follows the size of potentially torn out fibres. As shown in Table IV-9, labMDF fibre assortment is dominated in the order of $\varphi(\mathrm{FBc}) =$

79 % by compact fibre bundles (FBc) with $w = 230\,\mu m$ mean width. Hence, the applied kernel was defined by $\sigma = 4$ and $w_K = 10$ with regard to nominally 50 µm distance between the data points. Accordingly, Figure IV-17 shows the gravimetric RDP of labMDF650-19 as raw data with the respective filter variations around the finally applied one. The wide kernel with $\sigma = 4$ and $w_K = 40$ causes smoother slope but a considerably rounded boundary edge ($t = 0\,\mathrm{mm}$) whereas (1, 10)-filter yields still too noisy results. Eventually, filtering was carefully applied in order
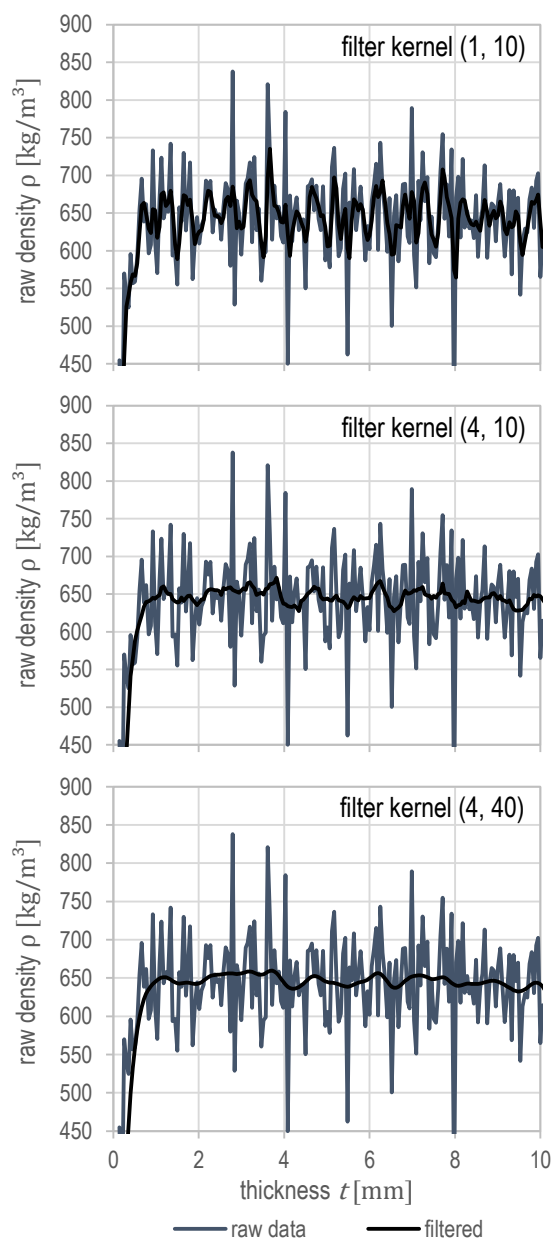
Figure IV-17: Gravimetric RDP of labMDF650-19 as exemplary raw data with filter variations around the applied (4, 10) convolution kernel (σ, w_K).

to avoid biased reference data. The same applies to PB results. However, beyond basic statistical noise, raw data is superimposed by few points of paired outliers with more extreme values compared to MDF. The immediately consecutive and considerably distinct measuring values with $\Delta\rho \approx 500\ldots800\text{ kg/m}^3$ are attributed the to sudden loss of huge particles in size and mass. Notwithstanding crucially different particle geometry, equivalent filtering was applied to PB data since appropriate results were obtained. Accordingly, Figure IV-18 exemplarily presents successfully smoothed reference profiles in comparison to the respective raw data of both a MDF and PB specimen. All final results are shown as part of round robin test in Chapter IV–4.3.1. Though filtered data still comprises fluctuations related to the reference method itself, the actual RDP shape becomes obvious between the local peaks of the plot.

Beyond noisy raw data caused by random influences, a potential systematic impact is attributed to the considered specimen area. Whereas X-ray measurements cover the middle of the of the $50 \times 50\text{ mm}^2$ specimens with certain extent depending on the beam geometry of the measuring device, the divided reference specimens take only one respective half into account. In cases of crucial structural inhomogeneities such as resin agglomerations, these specimen area conditions may cause deviations between gravimetric and radiometric results beyond insufficiency reasons of the latter. Further methodical reasons are local or global changes in equilibrium moisture content (EMC) during long-lasting layer milling and measurement. Accordingly, frictional heat at the face milling cutter or varying surrounding conditions, respectively, consequently cause mass and volume changes as well as swelling and/or shrinkage. Potential friction heat was quantified with specimen surface temperature increment of $\Delta T \approx 2.5\text{ K}$ determined after milling whereas warming directly within cutting zone was supposedly higher. Actual dehydration from heat impact was not quantifiable. In consequence of rather warm and dry surrounding conditions, a mass loss was determined per total specimen in the order of 0.1 g, hence, re-
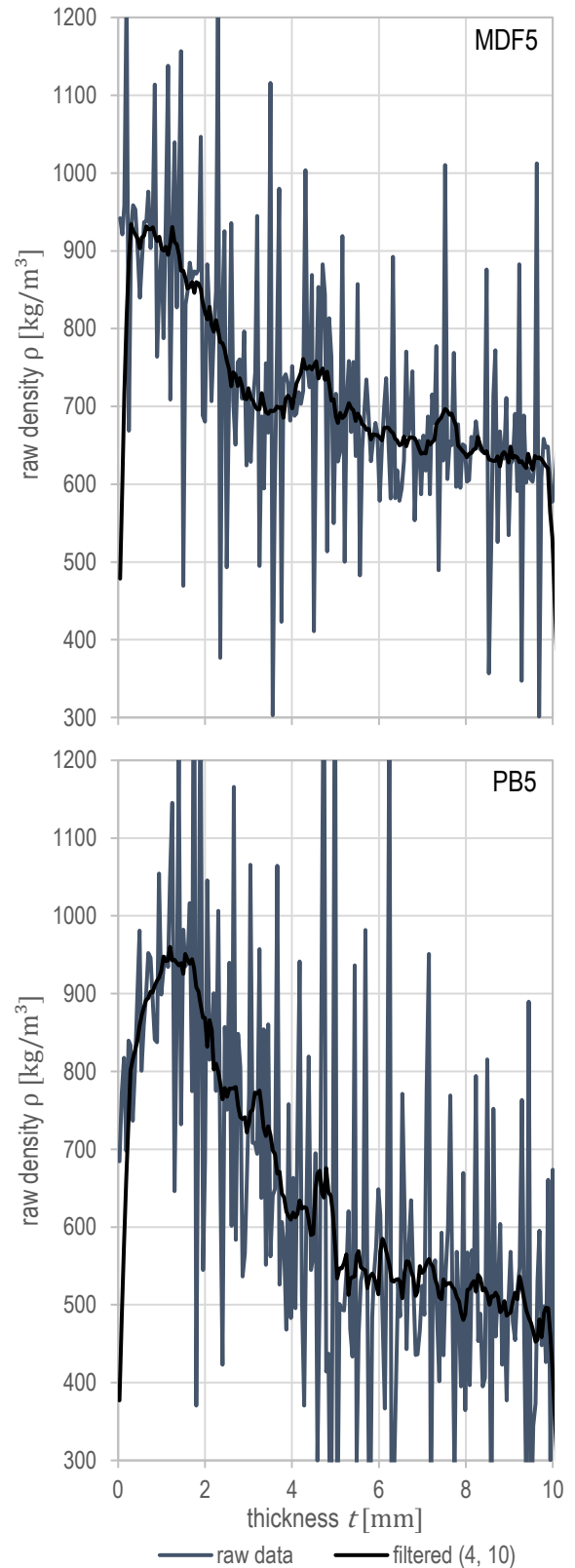
Figure IV-18: Exemplary gravimetric RDPs of MDF-19 (top) and PB-19 (bottom) from round robin test as raw data and filtered via Gaussian smoothing by convolution kernel $\sigma = 4, w_K = 10$; note, selected specimens respectively represent found raw data noise of extreme extent.

sulting in a negligible share per layer. Further-more, data evaluation unveiled an apparent op-erator impact since extent of noise varies. De-spite all standardisations, no particular reasons could clearly be identified. Eventually, the ap-plied Gaussian filter was, however, able to smooth even the most distinct noise as exempla-rily shown in Figure IV-18. For further charts, ref-erence is made to Appendix VII–3.

Notwithstanding the discussed insufficiencies caused by milling and the elaborate total method itself, the performed procedure with subsequent data smoothing was eventually found to yield ap-propriate reference results for vertical RDP de-termination on 50×50 mm² specimens. How-ever, no alternative reference method is consid-ered to be available, which is comparably practi-cal and provides respective spatial resolution. For future applications, the reference method is preferably suggested for RDP measurements on MDF due to its rather homogeneous structure and smaller particle size.

4.2.5   Round robin test

Since generally observed insufficiencies in radi-ometric RDP determination were, amongst oth-ers, the central motivation for this thesis, the pre-sent situation needed to be investigated to pro-vide an explicit overview considering common measuring devices in current laboratory applica-tions. To this end, an exploratory round robin test was carried out within a small group of partici-pants to compare the results of different RDP gauges. Note, the device selection excluded in-line gauges, which basically differ from lab gauges regarding their measuring principle. However, all utilised devices follow the well-known measuring principle based on attenuation of transmitted radiation as schematically shown in Figure II-12. Nondestructive measurements were carried out in an interlaboratory trial on one and the same set of MDF and PB samples ($n = 5$ each, Figure IV-19) involving eight gauges from five manufactures in seven laboratories of
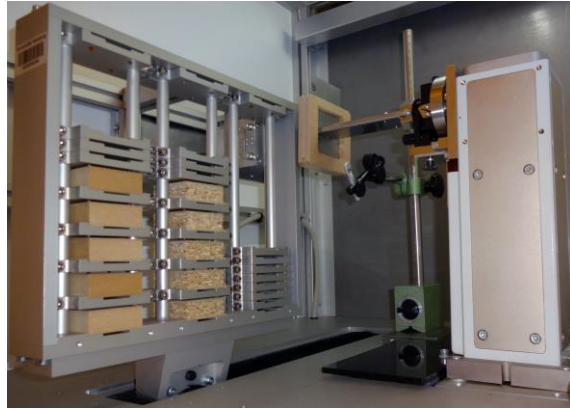
Figure IV-19: Set of MDF-19 and PB-19 samples ($n = 5$ each) of the round robin test during measurement by Itrax Woodscanner.

different European institutions and WBC produc-ers as well as one measuring device manufac-turer. A compilation of the employed RDP meas-uring devices is given in Table IV-22 in alpha-betic order with technical data as specified at this time by the manufacturers.

The measurements were performed[31] according to the regular procedure with typical settings of the respective lab, whereby the identical X-ray penetration direction through the specimens and upper/lower surface alignment was ensured. The device-specific data output was converted into a uniform manufacturer-neutral representa-tion in random order (devices A…H) for compa-rability and anonymisation. In addition to radio-metric measurements and to quantify their accu-racy, the aforementioned (Chapter IV–4.2.4) gravimetric reference method was the final and destructive member of the round robin test.

---

[31] Note, the measurements were successively performed in 2013 by a skilled worker of the respective lab or the author himself. The contribution of all industry and institute partners, which made the round robin test possible at all, is highly appreciated.

manufacturer	Cox	EWS	GreCon	IMAL	raytest
device	Itrax	DENSE-LAB	DAX	DPX	Dichteprofil-
models (qty.)	Woodscanner (1)	Mark2 (1)	DA-X (2)	200 (1)	messgerät (1)
		Mark3 (1)	5000 (1)		
radiation source	X-ray tube (Ag target)	X-ray tube (W target)	X-ray tube (W target)	X-ray tube (n/s)	radioisotope (^{241}Am)
U_a	≤60 kV	≤50 kV	33 kV	25 kV	$E_\gamma = 59.5$ keV
I_a	≤40 mA	<1 mA	<1 mA	0.25 mA	$A_0 = 1.66$ GBq
detector type	line camera	scintillator	semi-conductor	scintillator	scintillator
measuring range	< 1500 kg/m³	< 1500 kg/m³	< 1500 kg/m³	< 1500 kg/m³	n/s
accuracy	0.5 %	±1 % of measuring range	±0.5...1 % of measuring range	±0.1 % repeating accuracy	1 %
step size	≥ 5 µm	10...100 µm	20 µm	10...50 µm	≥ 75 µm
measuring time	≥ 0.025 s/step	0.03...1 mm/s	0.1...1 mm/s	0.01...0.5 mm/s	12.2 s/step

Table IV-22: Selected radiometric laboratory devices for raw density profile (RDP) measurement on 50 ×50 mm² specimens employed for round robin test, with technical data as specified at this time by the manufacturers.

4.2.6   Radiation spectra

4.2.6.1   Measurement

As already pointed out in Chapter II–1.2, the character of the employed X-ray spectra is relevant for occurring radiation-physical effects and, moreover, alters during radiation transmission. Regardless of the alike performed convenient spectra simulations (Chapter IV–4.2.6.2), explicit knowledge of the actual conditions requires verification via measurements. To this end, the X-ray NaI(Tl) spectrometer digiBASE 905-3 with MAESTRO-32 MCA emulation software, ORTEC, Oak Ridge, USA, was applied[32]. The detector consists of a 2" × 2" thallium-activated sodium iodide NaI(Tl) scintillator, a subsequent photomultiplier (PM) tube, and a digital multi-channel analyser (MCA, 1024 channels) connected via USB to a PC, where the software is running and for power supply. The aluminium (Al) lid of the NaI(Tl) detector with 0.635 mm (0.025") thickness was henceforth considered for all employed filter materials, with reduced thickness accordingly. Via MAESTRO, the following acquisition parameters were set for all spectra measurements:

- high voltage 1100 V,
- amplifier gain 1.0,

- shaping time 2 µs, and
- lower level discriminator (LLD) of the analogue-to-digital converter (ADC) at channel 35 to crop low-energy noise peaks.

To obtain dead-time losses < 10 % during data acquisition as well as appropriate counting statistics, total count rates were typically kept to around 10,000 cps. Consequently, the measuring setup was individually adapted to the respective conditions, i. e., especially photon flux emitted by radiation source, which, however, had to be kept rather low via appropriately diminished tube current I_a as well as additional detector apertures individually adapted by means of lead material. Furthermore, both distance (due to inverse-square law of intensity $I \propto 1/r^2$) and aperture size of the particular source and detector collimation were adjusted. Subsequently, acquisition time was chosen typically between 10…20 min and in special cases up to 60 min aiming at 'good statistics'. However, maintained conditions per level of energy and pre-filter variation as pointed out below facilitate approximate intensity comparison within one set of varied absorbers. Figure IV-20 exemplarily shows the most elaborate spectra acquisition setup by means of the partly dismantled Ag-target device

---

[32] Long-term provision of the equipment by Division 8.3: Non-destructive Testing, Radiological Methods, BAM Federal Institute for Materials Research and Testing, Berlin, Germany is gratefully acknowledged.
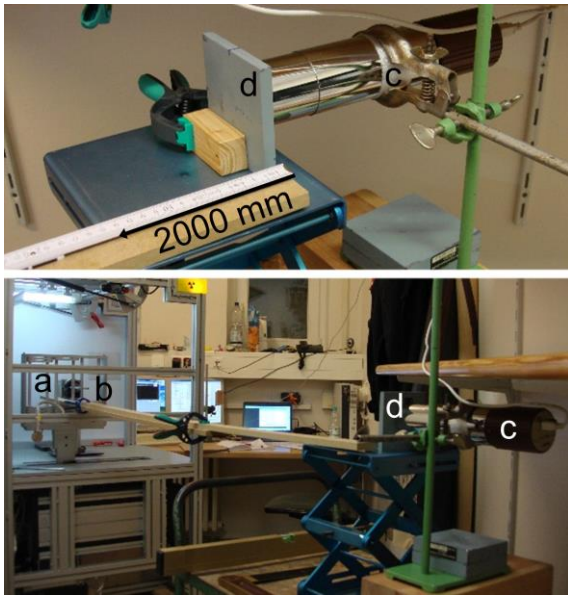
Figure IV-20: Exemplary measuring setup for radiation spectra determination with Ag-target tube (a), capillary optics w/o additional pre-filtering (b), spectrometer digiBASE 905-3 (c) behind Pb-collimator (d) with aperture ⌀ 1.5 mm, $r = 2000$ mm, free beam path without specimen; bar for alignment.

(refer to Chapter IV–4.2.2). Due to time-consuming data acquisition, the material and measuring conditions and their combination were carefully considered and specifically varied in practice-oriented ranges; i. e.,

- E_{max} [kVp] via $U_{a,nom}$ [kV],
- with/without pre-filtering additionally to 0.635 mm Al detector lid, and
- with/without specimen labMDF (400, 650, and 1056 respectively) as predefined absorbers ($z_{nom} = 50$ mm).

Accordingly, spectra measurements were performed by means of both X-ray devices comprising Ag- and W-target tubes, respectively (Chapters IV–4.2.2 and IV–4.2.3), where the initial detector was generally substituted by the spectrometer. For the Ag-target device, the original setup was further dismantled to enable data acquisition without capillary optics to evaluate their impact on radiation spectrum of the parallelly focused beam. On the contrary, simple beam collimation of W-target devices by apertures are, however, not expected to influence the energy distribution. Filters were installed directly behind the radiation exit of the source and specimens at the original sample position to maintain radiation

transmission conditions with respect to regular measuring application. Due to the employed devices referring to RDP measurement, corresponding specimens with radiation penetration lengths $z_{nom} = 50$ mm in direction of the panel plane were utilised as additional absorbers to likewise evaluate their spectra interference. To this end, the individual specimen was moved ±5 mm around the middle of panel thickness in steps of 1 mm during acquisition time, where raw density of homogenous labMDF is most uniform (for local mean values refer to Table IV-23) to avoid particular structural influence. As usual, 20/65 conditioning was performed previously to the measurements resulting in $MC = 9.5\,\%$ (Table IV-5). Due to rather warm and dry unregulated ambient conditions, the common slight specimen dehydration was observed via mass loss, which is, however, negligible regarding distinct impact on evaluated spectra.

Despite hardware pre-configuration of digiBASE MCA for an energy range < 70 keV, individual energy calibration via evaluation software, which is valid for all measurements with the same parameters, needs to be performed by means of a radiation source of known energy. Hence, Americium ^{241}Am ($t_{1/2} = 432.2$ y) with its most intense characteristic gamma-energy $E_{peak} = 59.54$ keV was utilised. Intensity calibration was omitted. Figure IV-21 shows an acquired spectrum of ^{241}Am, where the intensity peak at channel no. 784 corresponds to 59.54 keV. Though the actual energy spectra of radioisotopes are expected to show discrete line(s), blurred discretisation of the energy spectrum by the MCA becomes obvious. In this regard, the parameter 'full width at half maximum' (FWHM), which generally

labMDF	total panel thickness t [mm]	mean raw density in ROI $\bar{\rho}$ [kg/m^3]	penetration length z [mm]
400	19.27	420.07	50.61
650	19.12	655.54	50.61
1056	19.10	1007.25	50.00

Table IV-23: Particular properties of the labMDF specimens for spectra measurements within the ROI section ±5 mm around the middle of panel thickness.

describes the extent of distributions by the difference between two extremes around a peak, is applied to evaluate the spectrometer resolution. Let the measured intensity $I(E)$ at the intensity peak energy E_{peak} (radiation energy of highest intensity) be the considered maximum; then FWHM [keV] is determined via

$$\text{FWHM} = |E_1 - E_2| \tag{IV-30}$$

with the extreme energies E_i fulfilling the condition

$$I(E_1) = I(E_2) = \frac{1}{2} \cdot I(E_{\text{peak}}) \tag{IV-31}.$$

Accordingly, the characteristic ^{241}Am line of the exemplary calibration spectrum in Figure IV-21 yields $\text{FWHM}_{\text{Am}} = 7.1\,\text{keV}$. Since energy resolution in terms of FWHM commonly approximates 10 % of the spectrometer energy range (here $\Delta E = 70\,\text{keV}$), the achieved resolution is found in an appropriate order and the obtained spectral distributions represent a usual shape. The same applies to X-ray spectra including characteristic energies within the considered range, where the evaluated Ag spectra yield at the best $\text{FWHM}_{\text{Ag}} = 4.5\,\text{keV}$, which, apparently, reveals enhanced energy discrimination potential in the mainly applied low-energy range. However, data acquisition and evaluation yield energy spectra $S(E)$ in general and the initially emitted $S_0(E)$ or through an absorber transmitted $S_{\text{T}}(E)$ spectrum particularly as distribution of intensities $I(E)$ over the considered energy range E. Although the measured spectra represent the actual impact of the respective attenuating object, they are furthermore biased by an energy-dependent characteristic detector output considered as detector response function $D(E)$ of the spectrometer, which is different from the individually applied regular measuring device detectors. Thus, all measured spectra have to be considered as detector-influenced spectra $S_{\text{D}}(E)$ according to

$$S_{\text{D},0}(E) = S_0(E) \cdot D(E) \tag{IV-32}$$

for emitted spectra and

$$S_{\text{D,T}}(E, \rho_{\text{A}}) = S_{\text{T}}(E, \rho_{\text{A}}) \cdot D(E) \tag{IV-33}$$

for transmitted spectra, which furthermore depend on type and area density ρ_{A} of the respective absorber.
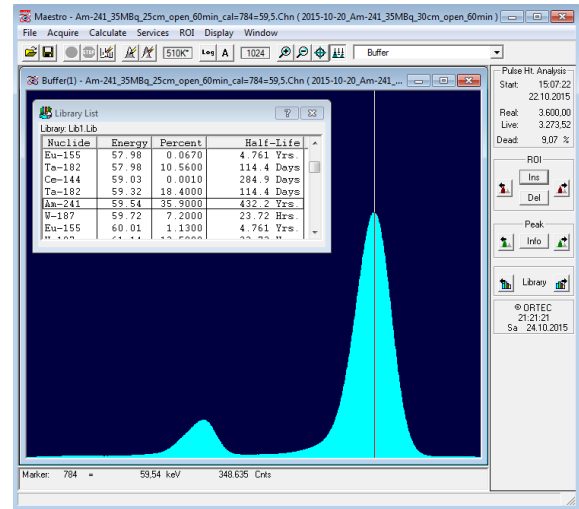
Figure IV-21: Calibration spectrum of ^{241}Am with $E_{\text{peak}} = 59.54\,\text{keV}$ and FWHM $= 7.1\,\text{keV}$ acquired by spectrometer digiBASE 905-3 with 3,600 s real measuring time incl. 9.07 % dead time, and mean 12885 cps; GUI of MAESTRO-32 MCA software.

Beyond energy-related detector influence $D(E)$, acquired spectra $S_{\text{D}}(E)$ comprise further distortion owing to both MCA energy resolution as well as inherent detector noise. Whereas the latter is attributed to Compton blur within the scintillator leading to respective background intensity, the former corresponds to spectrometer capability and set parameters causing fussy spectra representation particularly in case of characteristic lines as obvious from Figure IV-21. The smooth slope toward limit values if furthermore attributed to pile-up, where detector is unable to discriminate rather coincident events. Consequently, maximum energy E_{max} of the acquired X-ray spectra and further particular energies are less distinctly definable. However, E_{max} determination is carried out by common procedure following the suggestions of ZSCHERPEL (2015) and the regulations of DIN EN 12544-3 (1999), where the latter describes the spectrometric method for measurement and evaluation of X-ray tube voltage. Accordingly, the threshold energy E_{max} of energy-calibrated measuring results by means of an appropriate energy-dispersive photon detector is defined, where the linearly falling slope of the spectral plot intersects the abscissa as illustrated by the blue dashed line in Figure IV-22. As easily can be seen from the exemplarily shown raw-spectrum evaluation, determined

W tube, $U_{a,nom} = 35$ kV
open (0.635 mm Al)
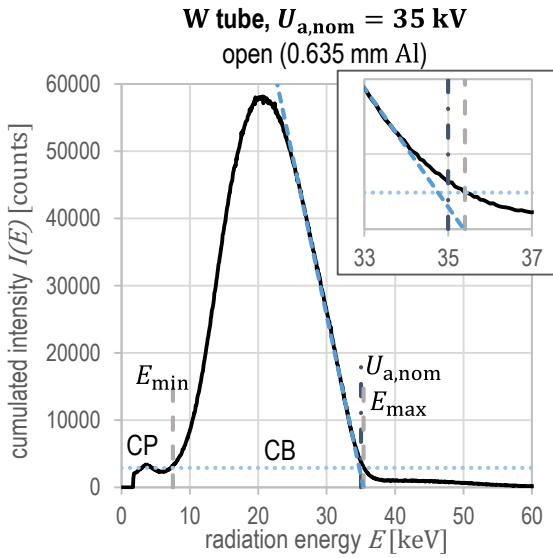
Figure IV-22: Exemplary X-ray spectrum of a W-target tube at $U_{a,nom} = 35$ kV (dash-dotted line), without additional pre-filter (except 0.635 mm Al detector lid) as energy-calibrated raw data; illustrated evaluation with tangential auxiliary line (blue dashed line) downward to $E_{max} = 35.4$ kVp (right grey dashed line) as abscissa intersection and obviously defined $E_{min} = 7.5$ keV (left grey dashed line) for upper and lower energy threshold determination as well as subsequent detector Compton blur reduction comprising total Compton background (CB, blue dotted line) $I_{CB} = 2936$ counts and a low-energy Compton peak (CP); inset: detail around E_{max}.

$E_{max} = 35.4$ kVp (right grey dashed line) exceeds nominal tube voltage $U_{a,nom} = 35.0$ kV (dash-dotted line). Regardless of the individual performance for each acquired raw spectrum, threshold energies were summarised and equally defined per energy level. Eventually, measured intensities $I(E)$ above the determined upper threshold E_{max} are not directly attributed to the investigated beam and, hence, not further considered. Analogously, lower threshold energy is required to adjust biased low-energy spectrum whereas its determination is not pointed out in DIN EN 12544-3 (1999). Therefore, lower limit value is obviously defined, where the downward slope toward low energies is heading for its vertex (left grey dashed line in Figure IV-22) at $E_{min} = 7.5$ keV. Regardless of

the potentially erroneous estimations, slight variations were found to be negligible regarding the finally evaluated spectra and their characteristic parameters. Measuring data below the lower threshold E_{min} is not further considered, where, subsequently, Compton peak (CP) is eliminated. Note, the CP with $E_{CP} \approx 4$ keV does evidently not correspond to the characteristic L lines of a W target with the most intense $E_{L\alpha 1} = 8.40$ keV and $E_{L\beta 1} = 9.67$ keV (cf. KORTRIGHT, THOMPSON (2009)) and furthermore likewise occurs in the acquired Ag spectra. Finally, the intensity of Compton background I_{CB} (CB, dotted line in Figure IV-22) is individually defined via $I(E_{max}) = I_{CB}$ and subtracted from measuring values; i. e.,

$$I(E) = I(E)_{raw} - I_{CB} \qquad (IV-34)$$

where, e. g., $I_{CB} = 2936$ counts. Consequently, exclusively $I(E)$, thus, $S_{D,0}(E)$ and $S_{D,T}(E)$, within the energy limits is henceforth taken into account for further spectra-based considerations.

4.2.6.2   Simulation

Computer-aided modelling of X-ray spectra with explicit consideration of both actually present and virtually varied transmission setups provides a convenient possibility to gain knowledge about radiation energy distribution emitted by X-ray tubes and, furthermore, the energy-dependent attenuation by varying absorbers with subsequently transmitted spectra. To this end, the software XRayTools for spectrum modelling and visualization with its graphical frontend XRayGUI Version 1.3.7.0 by BAM was employed[33]. Exemplarily shown in Figure IV-23 by the GUI, the program suite features the generation of both continuous and characteristic radiation from X-ray tubes with nearly arbitrary target material. Regardless of certain restrictions, XRayTools software comprises valuable subroutines facilitating to model particular radiation-physical phenomena during subsequent radiation transmission through predefinable absorbers. For detailed remarks on the fundamental background, reference is made to DERESCH et al. (2010), where, in

---

addition, performance details are pointed in the correspondingly delivered software manual.

Regarding the present application, modelling of initial, pre-filtered, and transmitted (through specimen) spectra was comprehensively carried out considering manifold radiation and material parameters owing to the convenient performance. Nonetheless, for the purpose of result comparison, simulations were particularly focussed on specifically varied conditions of actual spectra measurements (Chapter IV–4.2.6.1). All component properties were set in the closest agreement with available data. Amongst the comprehensive parameters, the following were basically required for modelling of sources by means of

- target material via Z,
- target angles of incident electrons and emitted X-rays,
- E_{max} [kVp] equivalent to $U_{a,nom}$ [kV],
- energy resolution [keV], and
- (constant) inclusion of both bremsstrahlung and characteristic energies

as well of filters or absorbers, respectively, by

- composition via $\omega(i)$ of Z_i,
- density,
- thickness of vertical transmission, and
- inclusion of scattered radiation

with individual variations due to virtually investigated transmission setup. Further adjustable parameters such as I_a [mA] rather result in radiation intensity variations and were, accordingly, maintained aiming at spectra in a comparable order. The same applies to typical default values. For precise labMDF absorber modelling, actually corresponding elemental compositions including ash content (Table IV-15) at $MC = 9.5\,\%$ (Table IV-5) due to common 20/65 conditioning previous to measurement as well as mean raw density and penetration length in accordance with spectra measuring specimens (Table IV-23) were taken into account. Moreover, detector modelling was omitted owing to a lack of explicit information about the required complex parameters. Thus, simulation yields initial $S_0(E)$ or transmitted $S_T(E)$ spectra, respectively, without explicit consideration of detector response function
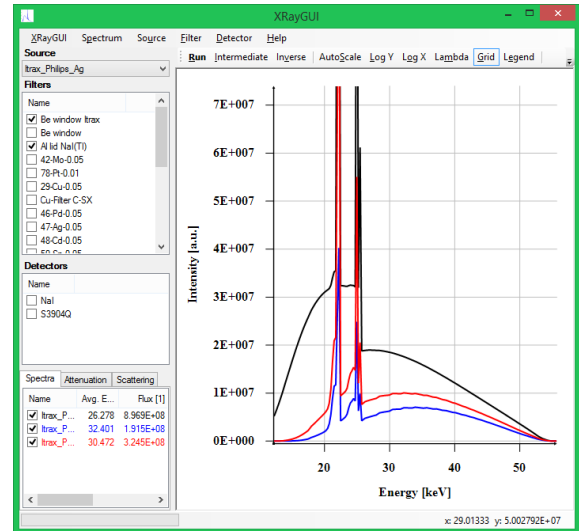
Figure IV-23: Exemplary Ag-target spectra modelled by XRayTools on the frontend XRayGUI, with lists of sources, filters, and resulting spectra (left).

$D(E)$ according to eq. (IV-32). However, energy-dependent transmission through labMDF absorbers $S_T(E, \rho_A)$ is thoroughly evaluated. Furthermore, the sophisticated impact of capillary optics beyond beam alignment was unfeasible to be validly modelled by XRayTools. However, simulations were performed inherently including 0.635 mm Al detector lid from the applied spectrometer (Chapter IV-4.2.6.1), where additional simulations provide actually emitted spectrum from the respective tube without any absorber on theoretical basis. Finally, all data was saved with predefined energy resolution as a text file for subsequent processing.

In contrast to the measuring data evaluation, modelled spectra did not require elaborate threshold energy determination owing to non-consideration of detector effects such as pile-up and energy resolution and the consequent absence of detector Compton background and further distortion. Nonetheless, simulated raw datasets exceed predefined energy limits and range downward to $E > 0\,\text{keV}$ with $I(E) \approx 0$, hence, require adjustment. Thus, the upper limit value was ideally set as $E_{max} \equiv U_{a,nom}$ likewise predefined. However, the lower limit is attributed to beam hardening and was individually defined at $I(E_{min}) \geq 1\,\text{cps}$ corresponding to the energy E_{min} with at least one countable event per second.

4.3   Results

4.3.1   Round robin test

A manufacturer-neutral representation in random order (devices A…H) shows the round robin test results per panel type MDF in Figure IV-27 and PB in Figure IV-28 (page 152 et seq.). Here, the RDP measurements per chart were nondestructively performed on one and the same specimen. Both result overviews with RDP plots from all devices are completed by corresponding data from reference method. Due to the reference method range, all charts are limited to the RDP of half panel cross-section ($t = 0 \dots 10$ mm) of the specimens. Data evaluation was done considering the assignment of panel top (labelling) as position $t = 0$ mm because this context differs from one device to another. Note, in the case of the measurements on MDF2 by device A, the fundamentally biased results owing to the failed performance in an external laboratory were rejected (n/a in Table IV-24). However, Figure IV-27 comprises the biased chart with parallel shifted plot for comparison. Supposedly, incorrect specimen mass input falsified the gauge-internal data evaluation. From device H as an additional member during the round robin test, measurements were limited to the specimens four and five of both MDF and PB. Variations in MC, hence specimen mass, were avoided by vacuum-sealed transport and in the meantime re-conditioning at 20/65 to constant mass. In the case of supposedly critical transport by mail, slight dehydration was observed in the order of 0.1…0.2 % specimen mass and found to be negligible, in turn. Thus, results can be considered free of further method-related disturbances.

In addition to the presentation of RDP charts and visual comparison, characteristic values were evaluated following common practice extended by own approaches and adapted to RDP conditions present. To this end, Figure IV-24 illustrates the determination of selected characteristic RDP values on an RDP from the round robin test (half panel cross-section). Accordingly, determination of mean values within a predefined region of interest (ROI) per panel layer serves as preferred evaluation tool. Owing to the rather uneven CL slope of both utilised panel types with
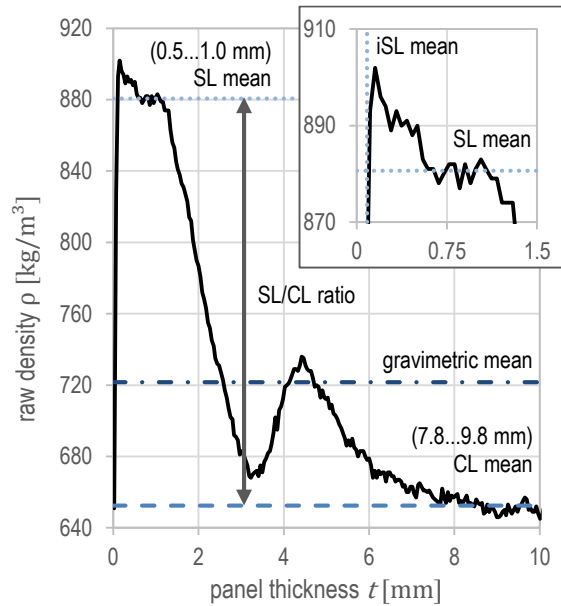
Figure IV-24: Exemplary raw density profile (RDP, solid black line, half panel cross-section) as result of round robin test (MDF-19, random specimen and device) with representation of selected characteristic values (refer to Table IV-24 and Table IV-25); inset with magnification of intersection of increment surface edge and SL mean value.

slightly decreasing raw density toward panel core, ROI for CL mean value calculation was kept comparatively narrow at $t = 7.8 \dots 9.8$ mm representing an even section. Since boundary effects occur in both cases, i. e., radiometric as well as gravimetric determination, the section for SL mean value calculation starts below the surface at $t = 0.5$ mm. To focus, nevertheless, on the outer SL area, where raw density maximum is supposed particularly in case of MDF, computation ROI ends at $t = 1.0$ mm. To further evaluate SL data, the point of intersection (iSL mean [mm]) of increment surface edge and SL mean value was found to appropriately quantify the obvious differences in RDP plots of the particular devices and to provide a characteristic value describing the surface edge steepness. Notwithstanding the different SL RDP shapes, the described ROIs for mean value computation were applied to both MDF and PB. Additionally, extremes were determined considering the respective cross-section half with core-layer minimum (CL min) and surface-layer maximum (SL max) raw density as well as the position of the latter from surface [mm]. Moreover, gravimetric mean

raw density determined via specimen mass and dimensions serves as fundamental input parameter for common self-calibration of the applied laboratory X-ray devices (refer to Figure II-14). Eventually, distinctness of RDP is not only considerable in terms of particular mechanical panel properties, this profile characteristic introduced as raw density contrast directly affects RDP evaluation from X-ray measuring data as discussed elsewhere. In the present case with respect to the particular devices as well as reference data, raw density extremes (SL max and CL min) are partly blurred. Hence, for the surface to core layer ratio (SL/CL ratio [-]) computation as figure for the raw density contrast, respective mean values (SL mean and CL mean) are taken into account. Table IV-24 and Table IV-25 compile all characteristic RDP values for MDF and PB, respectively, with actual raw density values ρ $[\text{kg/m}^3]$ from gravimetric reference method. In case of radiometric results (devices A…H), characteristic figures were computed as raw density difference $\Delta\rho$ $[\text{kg/m}^3]$ toward respective reference values for comparison purposes.

In comparison between all X-ray devices, their results differ in varying extent from each other. No radiometrically determined RDP shape equals another. Beyond summarising charts, Figure IV-26 provides a more detailed view on the RDP of two exemplary specimens MDF4 and PB5, respectively. Considering the obvious RDP shape, the gradient from the panel surface to SL max differs considerably between the gauge results. The introduced characteristic value iSL mean (Table IV-24, Table IV-25) quantifies the surface edge steepness, where low values represent a steep surface edge gradient. The insets in Figure IV-26 with magnification of SL region illustrate the differing slopes toward SL max of all devices. Accordingly, in the case of MDF, devices C, E, and H provide the most inappropriate surface edge steepness with iSL mean averaging around $t \approx 0.43\,\text{mm}$ whereas device F features the steepest gradient with close position of iSL mean to panel surface around $t \approx 0.11\,\text{mm}$. Regarding PB, devices C and E show poor steepness again, where, however, less clear tendencies between the devices and more

variations between specimens with generally higher iSL mean can be observed.

Methodical reasons for distinct iSL mean figures can be found in geometrical misalignment of the respective X-ray beam axis, aperture, and specimen within device setup. Consequently, RDP slope starting from $\rho = 0$ kg/m^3 or with respective low values beyond, as commonly known, is usually not existent. A raw density drop toward the panel surface is limited to an extent corresponding to typical sanding allowance owing to mellow surface areas; thus, cannot come close to zero. However, customary sanded panels were utilised for the round robin test. Hence, distinct mellow areas were already removed and can, in turn, be excluded. Therefore, the extent of apparently well-known surface edge gradients is actually attributed to geometrical conditions regarding radiation transmission through the specimens and corresponding gauge setup, i. e., parallel alignment of relevant components, specimen plane, and X-ray beam axis. Eventually, iSL mean is more convincing for RDP measuring result comparison than commonly used SL max position, which instead corresponds to panel processing. However, the iSL mean is affected by both panel conditions and measuring device performance whereas the latter plays a greater role than commonly supposed. Beyond geometrical conditions, a horizontal shift of total raw density values on the x-axis depends in addition on the evaluation software, which commonly determines the panel surface through a threshold for the surrounding air.

The extreme values CL min and SL max as well as the position of the latter are primarily considered as panel-typical characteristic. Their measured occurrence is, nonetheless, particularly superimposed by device-specific measuring signal quality. Unsteady but slender variations within the profile per device (A, C, E, G, and H) are not caused by panel structures but rather result from measuring signal or count rate fluctuations, i. e., signal noise. Typical structural inhomogeneities in the scale of particles or possible inclusions are partly visible only within PB RDPs (Figure IV-26 bottom and Figure IV-28). Since X-rays are transmitted through a specimen depth of 50 mm

with subsequent radiation acquisition by the detector, fine variations along the beam path are finally homogenised in terms of averaging signal integration (refer to macroscopic scale in Figure IV-12 as well as Chapter–3.2). Hence, solely heavy impurities, i. e., high-density objects exceeding mean layer raw density as well as with distinct extension in beam direction, result in significant variations of RDP slope, which are clearly attributed to panel structure. Accordingly, RDP plots measured on, e. g., OSB reveal coarse structural variations, since full size raw particles (strands $l > 50$ mm, $t < 2$ mm, acc. to DIN EN 300 (2006), up to 25 × 150 × 0.7 mm³, cf. THOEMEN et al. (2010)) may cover total specimen plane and, thus, govern raw density of the considered layer. However, a more detailed view on the RDPs of exemplary specimens in Figure IV-26 unveils respective differences between MDF and PB plots. The well-known shape of MDF RDPs due to inappropriate second densification during hot-pressing (cf. MEYER (2007) or GRUCHOT (2009)) with local peaks in the passage slope between SL and CL is obvious from all MDF specimens in Figure IV-27. In the case of MDF4 (Figure IV-26), the REF chart reveals a narrow local peak around $t = 4.75$ mm, which is attributed to the reference method and its insufficiencies as discussed elsewhere. Contrary to this, a more or less distinct local peak around $t = 5.0$ mm occurs in all PB5 charts in Figure IV-27. This variation is considered to correspond to a high-density impurity on the beam path through the specimen. Distinctly varying slopes around the peak are attributed to individual irradiation geometry in terms of lateral beam dimensions and effective spatial resolution of measurement; i. e., not solely step size but, moreover,

- aperture size in front of the detector,
- effective projection extension on the very same, and
- parallel alignment of beam axis and panel plane with perpendicular impingement on the detector.

Eventually, measuring value resolution of each device fundamentally limits reliable distinguishability between raw density variations. Consequently, the impurity in PB5, appears with varyingly clear contrast, e. g., not visible in the plots

from the devices C and G and with blurred shape from the devices A and E. Regardless of upward shift of device B data, it provides most distinct indication of the impurity. Finally, the reference plot shows the peak with a slight lateral shift. Moreover, the visualisation in Figure IV-25 with an X-ray image acquired by the Ag-target device (Chapter IV–4.2.2) as well as images per layer of the reference method (Chapter IV–4.2.4.2, for further image series, refer to Appendix VII–3) unveils the local raw density peak to actually comprise two impurities more or less within the same panel layer.
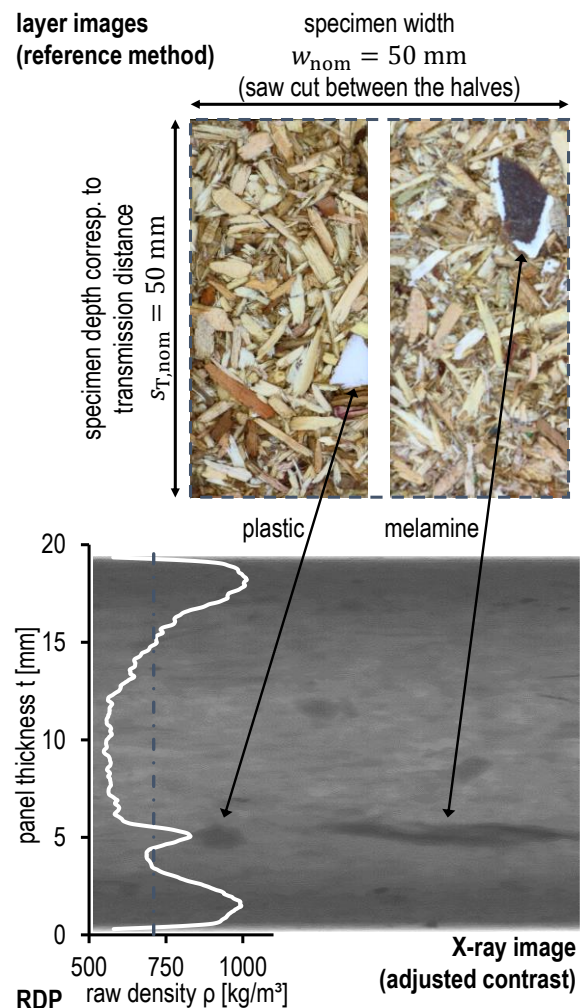
Figure IV-25: Visualisation of the impurities in the round robin test specimen PB5 with two objects in the X-ray image (bottom, acquired by Ag-target device, Chapter IV–4.2.2) superimposed by the RDP, likewise visible in corresponding layer images (top, acquired in terms of face milling per 50 μm layer by reference method (Chapter IV–4.2.4.2) separately for left and right half of the specimen, further image series in Appendix VII–3).

The magnitude of the differences between measuring results of the X-ray gauges depends on the cross-section position. Core layer values are in the same range considering both panel types – except device E, which exceeds the others. By tendency, devices C and F come slightly below the other with differences in CL mean around $\Delta\rho = -20 \text{ kg/m}^3$. On the contrary, maximum deviations between radiometric results can be observed within SL section regarding both SL mean and SL max. Again, device E results drop far below all other plots. The majority of RDPs is, however, in a comparative order in SL, where the values of device F and particularly device C exceed the remaining plots, in turn. The maximum total distance of SL mean is found between device C and E with $\Delta\rho = 62 \text{ kg/m}^3$ for MDF and with $\Delta\rho = 109 \text{ kg/m}^3$ for PB determined on one and the same respective specimen. Obviously, all device B plots are systematically beyond the others, where distance increases with increasing specimen number (equals measuring order). Therefore, signal drift during measurement is considered as apparent reason with tremendous impact in case of PB measured subsequent to MDF.

In comparison toward the reference RDPs, differences of all X-ray devices in similarly varying extent like between each other can be observed whereas certain tendencies are found. Notwithstanding data enhancement of reference method via Gaussian smoothing, slight insufficiencies remain in measuring results as discussed in Chapter IV–4.2.4.3. However, the real RDP shape becomes obvious between local peaks of the reference plot. A comparison of the radiometric and reference plots reveals minor differences in the CL section likewise between each other with crucial deviations of device E results, in turn. According to the ΔCL mean in Table IV-24 and Table IV-25, CL raw density consistently exceeds reference values regardless of particular exceptions, which are considered to be attributed to partly remaining noise in reference data. Here, devices C and F for MDF and devices C, D, F, and H for PB yield the lowest deviation from the reference data averaging $\Delta\rho < +10 \text{ kg/m}^3$. Devices B and E, in turn, feature the highest differences from the reference for both panel types.

On the contrary, deviation of all radiometric RDPs from the gravimetric reference is considerable regarding the SL section. As quantified by the ΔSL mean in Table IV-24 and Table IV-25, SL raw density measured by all X-ray devices except device C can be summarised to generally fall below the reference despite particular exceptions, which are, in turn, attributed to partly remaining noise in reference data. Maximum differences from reference can be found for device E with $\Delta\rho \approx -45 \text{ kg/m}^3$ (MDF) and $\Delta\rho \approx -68 \text{ kg/m}^3$ (PB). The differential results of all remaining devices range around $\Delta\rho \approx -30 \ldots -20 \text{ kg/m}^3$ for both panel types, where PB RDPs tend to yield higher deviations. Devices F and H, however, feature the comparatively lowest ΔSL mean and closest slope toward the reference plot. The aforementioned obvious upward shift of device B plots results in apparently diminished deviations from the reference. Nonetheless, the considered signal drift has increased impact on evaluated measuring data in the case of high-density, thus more attenuating, panel SL. Since device C plots feature certain signal noise with spatially coarse fluctuations, their ΔSL mean characteristic is complex with both negative and positive deviations from the reference. The SL RDP slope of device C can, nevertheless, be concluded as close to and slightly beyond the reference plot.

A comparison between MDF and PB results eventually confirms the proposed theory of increasing deviations with a fundamentally more distinct RDP shape, since SL/CL ratio of PB with $\mathrm{SL/CL\,(REF)} = 1.84$ (Table IV-25) exceeds MDF values with $\mathrm{SL/CL\,(REF)} = 1.41$. (Table IV-24). Furthermore, the considered values for raw density contrast fall below the reference data for all radiometric RDPs. Device E again shows the highest deviations with $\mathrm{SL/CL\,(E)} = 1.59$ (PB) and $\mathrm{SL/CL\,(E)} = 1.29$ (MDF) in consequence of its previously discussed differences to the reference plots. To conclude in general, all radiometric RDP shapes appear flattened toward the reference profile; i. e., increased CL, decreased SL, and diminished extreme values. Hence, the actual raw density contrast along the vertical cross-section of the panel is diminished. Regarding customary WBC panels, inherent impact of

falsification of total RDP increases with increasing SL/CL ratio. The like applies to particular points on RDP, where validity of their raw density values decreases with increasing distance from gravimetric mean raw density. Hence, mean radiometric raw density is more or less equal to the gravimetric value. Eventually, sample heterogeneity itself biases its radiometric determination likewise MOSCHLER JR, WINISTORFER (1990) and RAUTKARI et al. (2011) point out. Moreover and owing to the state of employed RDP measuring devices, round robin test results illustrate metrological consequences of radiation-physical effects from interaction of polychromatic X-rays with inhomogeneous porous low-Z material, which is clarified hereafter in Chapter IV–6 with particular respect to Figure IV-76 illustrating the context of diminished accuracy in RDP measurement.
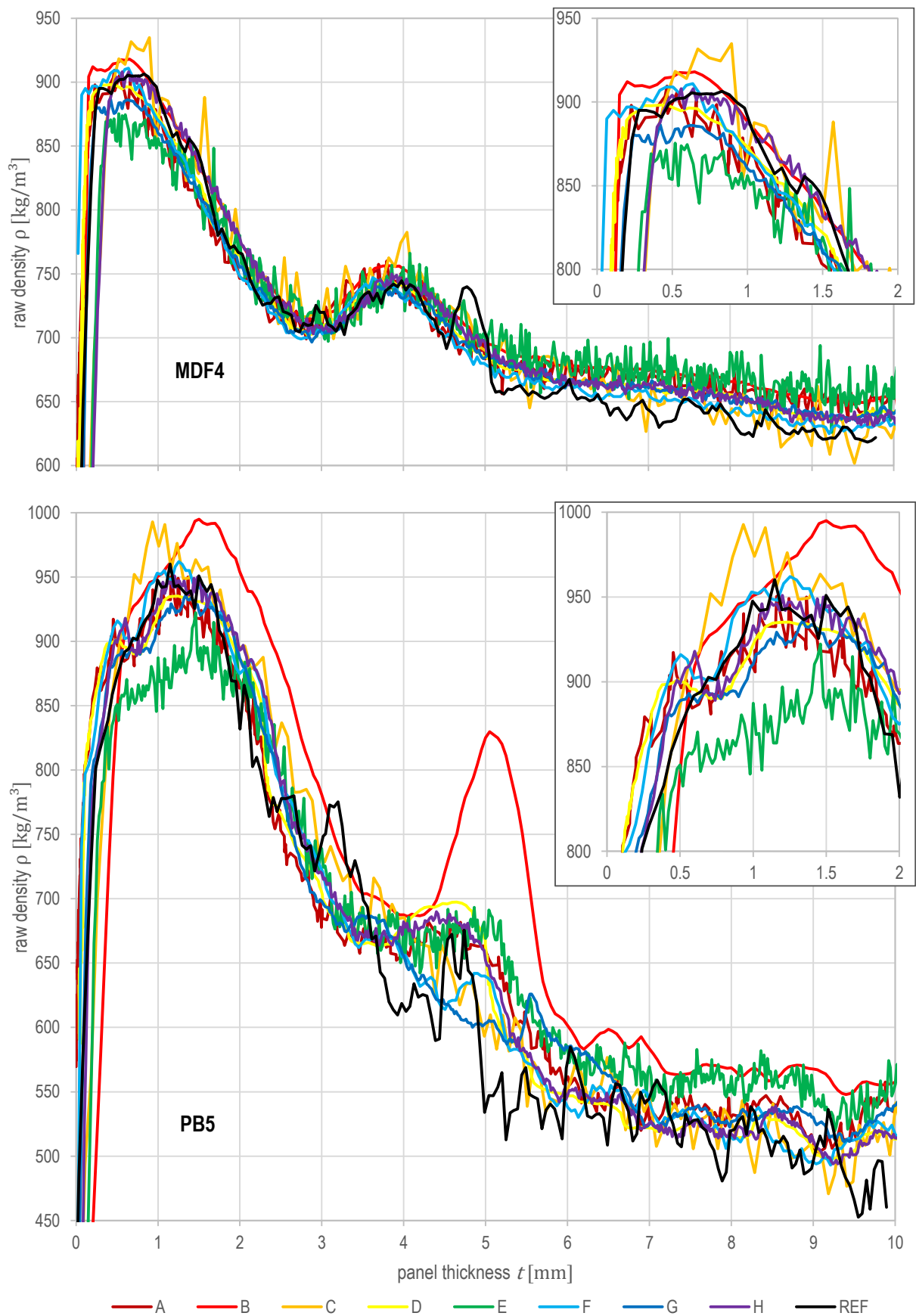
Figure IV-26: Results of round robin test (all devices A…H, coloured lines) and reference method (REF, black line) of one and the same exemplary specimen MDF4 (top) resp. PB5 (bottom) as RDP of half panel cross-section (0…10 mm) of the specimen due to reference method limits; insets with magnification of SL region.

device	SL mean	CL mean
A	-27	+16
B	-3	+24
C	+10	+5
D	-17	+11
E	-45	+28
F	-13	+4
G	-27	+11
H	-0	+19
REF	gravimetric reference	

difference to REF $\Delta\rho$ [kg/m³]
mean value $n = 5$ (2) per device
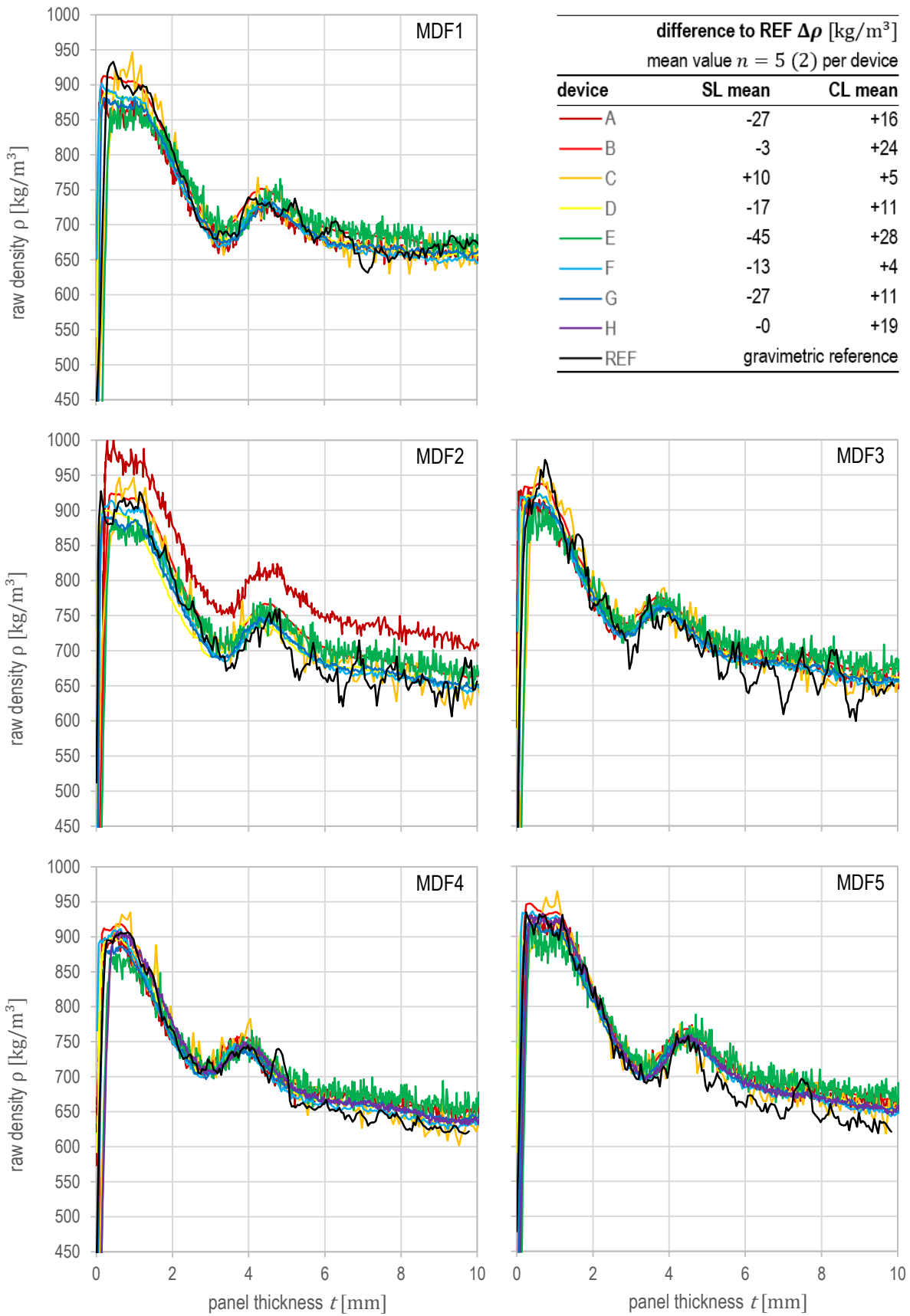
Figure IV-27: Results of round robin test as overview of all devices (A…H, coloured lines) and reference method (REF, black line) of all MDF specimens (one and the same each) as RDP of half panel cross-section (0…10 mm) of the specimen due to reference method limits; caption with selected characteristic RDP values from Table IV-24.

char. value	spec. #	grav. reference ρ [kg/m³]	device A	B	C	D	E	F	G	H
			$\Delta\rho$ [kg/m³] (toward reference)							
SL max	1	933	-41	-20	+14	-44	-50	-31	-52	n/a
	2	927	n/a	-3	+19	-27	-36	-13	-37	n/a
	3	971	-40	-34	-10	-50	-62	-48	-60	n/a
	4	906	+3	+12	+29	-8	-31	+5	-20	+2
	5	935	-4	+12	+30	-8	-11	+1	-14	-2
	mean		**-21**	**-7**	**+16**	**-28**	**-38**	**-17**	**-37**	**+0**
SL mean	1	902	-42	+4	+15	-20	-47	-21	-32	n/a
(0.5…1	2	911	n/a	+0	+14	-21	-46	-12	-32	n/a
mm)	3	941	-43	-27	-8	-30	-60	-32	-39	n/a
	4	901	-21	-8	+1	-14	-41	-10	-23	-2
	5	914	-1	+16	+29	+2	-31	+11	-10	+1
	mean		**-27**	**-3**	**+10**	**-17**	**-45**	**-13**	**-27**	**-0**
CL min	1	622	+21	+49	+8	+32	+30	+24	+29	n/a
	2	606	n/a	+56	+11	+48	+45	+33	+39	n/a
	3	598	+50	+70	+38	+58	+47	+52	+54	n/a
	4	585	+50	+63	+16	+50	+40	+40	+50	+46
	5	565	+88	+101	+54	+88	+83	+78	+84	+80
	mean		**+52**	**+68**	**+25**	**+55**	**+49**	**+45**	**+51**	**+63**
CL mean	1	666	-7	+10	-7	-7	+11	-13	-4	n/a
(7.8…9.8	2	654	n/a	+17	-3	+4	+20	-3	+3	n/a
mm)	3	650	+15	+27	+6	+15	+32	+9	+15	n/a
	4	628	+25	+29	+3	+17	+34	+8	+17	+15
	5	636	+32	+39	+24	+26	+41	+17	+24	+23
	mean		**+16**	**+24**	**+5**	**+11**	**+28**	**+4**	**+11**	**+19**
SL mean/	1	1.35	1.31	1.34	1.39	1.34	1.26	1.35	1.31	n/a
CL mean	2	1.39	n/a	1.36	1.42	1.35	1.28	1.38	1.34	n/a
ratio	3	1.45	1.35	1.35	1.42	1.37	1.29	1.38	1.36	n/a
[–]	4	1.44	1.35	1.36	1.43	1.38	1.30	1.40	1.36	1.40
	5	1.44	1.37	1.38	1.43	1.38	1.30	1.42	1.37	1.39
	mean	**1.41**	**1.34**	**1.36**	**1.42**	**1.36**	**1.29**	**1.39**	**1.35**	**1.39**
position from surface [mm]										
SL max	1	0.45	0.17	0.20	0.96	0.27	0.70	0.15	0.20	n/a
	2	0.13	n/a	0.40	0.98	0.18	0.84	0.37	0.26	n/a
	3	0.74	0.30	0.55	0.57	0.29	0.48	0.59	0.68	n/a
	4	0.83	0.47	0.65	0.90	0.43	0.52	0.64	0.42	0.56
	5	0.25	0.39	0.35	1.07	0.43	0.46	0.42	0.32	0.68
iSL mean	1	0.26	0.10	0.10	0.43	0.16	0.48	0.07	0.14	n/a
intersec-	2	0.07	n/a	0.30	0.45	0.09	0.32	0.15	0.12	n/a
tion with	3	0.58	0.04	0.10	0.42	0.18	0.32	0.07	0.20	n/a
SL mean	4	0.48	0.21	0.10	0.45	0.19	0.34	0.15	0.22	0.46
	5	0.20	0.30	0.20	0.92	0.26	0.30	0.11	0.24	0.30

Table IV-24: Results of round robin test for MDF specimens (#1…5) as comparison of characteristic RDP values computed as raw density difference $\Delta\rho$ [kg/m³] toward gravimetric reference values ρ [kg/m³] with position [mm] of characteristic SL points; mean of $n = 5$ specimens (bold line) per device (only of relative values $\Delta\rho$, since allocation of specimen's upper and lower surface varied).

device	SL mean	CL mean
A	-28	+17
B	+20	+46
C	-1	+4
D	-21	+3
E	-68	+39
F	-10	+1
G	-30	+14
H	-8	+5
REF	gravimetric reference	
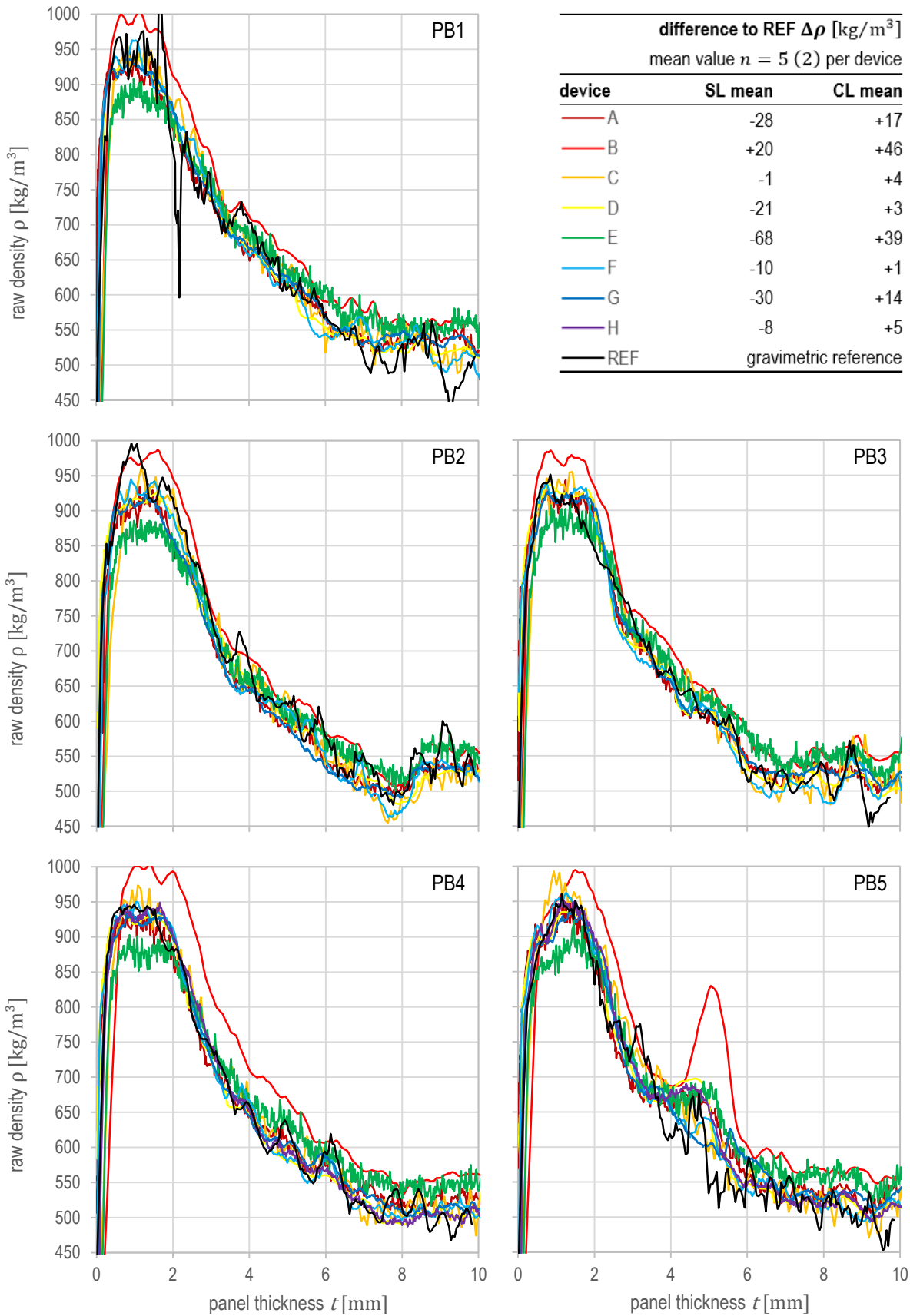
Figure IV-28: Results of round robin test as overview of all devices (A…H, coloured lines) and reference method (REF, black line) of all PB specimens (one and the same each) as RDP of half panel cross-section (0…10 mm) of the specimen due to reference method limits; caption with selected characteristic RDP values from Table IV-25.

char. value	spec. #	grav. reference ρ [kg/m³]	A	B	C	D	E	F	G	H
					$\Delta\rho$ [kg/m³] (toward reference)						
SL max	1	976	-29	+28	-22	-37	-68	-13	-39	n/a
	2	996	-58	-9	-34	-71	-109	-51	-73	n/a
	3	951	-8	+34	+4	-14	-41	-12	-24	n/a
	4	946	-10	+58	+27	-13	-43	+4	-13	+3
	5	960	-10	+35	+33	-25	-38	+2	-24	-9
	mean		**-23**	**+29**	**+2**	**-32**	**-60**	**-14**	**-35**	**-3**
SL mean	1	943	-20	+47	-11	-14	-61	-2	-20	n/a
(0.5…1	2	976	-77	-4	-58	-61	-105	-49	-69	n/a
mm)	3	932	-14	+41	-5	-6	-59	-7	-21	n/a
	4	940	-22	+8	+10	-14	-65	-3	-21	-11
	5	913	-9	+9	+56	-11	-52	+10	-19	-6
	mean		**-28**	**+20**	**-1**	**-21**	**-68**	**-10**	**-30**	**-8**
CL min	1	437	+79	+115	+51	+74	+87	+50	+76	n/a
	2	480	+11	+27	-25	+2	+19	-17	+11	n/a
	3	449	+47	+84	+32	+43	+58	+33	+51	n/a
	4	460	+47	+74	+14	+30	+57	+36	+41	+27
	5	453	+51	+95	+18	+45	+67	+40	+59	+41
	mean		**+47**	**+79**	**+18**	**+39**	**+58**	**+28**	**+48**	**+34**
CL mean	1	506	+30	+54	+19	+17	+49	+14	+32	n/a
(7.8…9.8	2	537	-12	+13	-30	-21	+16	-29	-12	n/a
mm)	3	503	+18	+52	+21	+9	+41	+5	+18	n/a
	4	505	+19	+49	+7	-2	+39	+5	+6	-4
	5	501	+28	+61	+6	+14	+49	+11	+26	+14
	mean		**+17**	**+46**	**+4**	**+3**	**+39**	**+1**	**+14**	**+5**
SL mean/	1	1.86	1.72	1.77	1.78	1.78	1.59	1.81	1.72	n/a
CL mean	2	1.82	1.71	1.77	1.81	1.77	1.58	1.83	1.73	n/a
ratio	3	1.85	1.76	1.75	1.77	1.81	1.60	1.82	1.75	n/a
[–]	4	1.86	1.75	1.71	1.86	1.84	1.61	1.84	1.80	1.86
	5	1.82	1.71	1.64	1.91	1.75	1.56	1.80	1.70	1.76
	mean	**1.84**	**1.73**	**1.73**	**1.83**	**1.79**	**1.59**	**1.82**	**1.74**	**1.81**
					position from surface [mm]						
SL max	1	1.24	0.86	1.15	0.83	1.01	0.98	0.95	0.86	n/a
	2	0.91	1.35	1.60	1.18	1.55	1.16	0.90	1.28	n/a
	3	0.84	1.24	0.85	1.42	0.80	1.36	0.73	0.78	n/a
	4	0.98	0.81	1.40	1.08	0.69	0.86	1.03	0.78	1.66
	5	1.15	1.16	1.50	0.93	1.25	1.46	1.25	1.34	1.20
iSL mean	1	0.44	0.84	0.55	0.61	0.73	0.64	0.81	0.74	n/a
intersec-	2	0.81	1.09	0.75	0.95	0.85	0.86	0.81	1.00	n/a
tion with	3	0.54	0.60	0.65	1.27	0.67	0.68	0.59	0.64	n/a
SL mean	4	0.77	0.46	0.60	0.63	0.54	0.64	0.64	0.72	0.60
	5	0.80	0.76	0.65	0.78	0.43	0.80	0.81	0.66	0.52

Table IV-25: Results of round robin test for PB specimens (#1…5) as comparison of characteristic RDP values computed as raw density difference $\Delta\rho$ [kg/m³] toward gravimetric reference values ρ [kg/m³] with position [mm] of characteristic SL points; mean of $n = 5$ specimens (bold line) per device (only of relative values $\Delta\rho$, since allocation of specimen's upper and lower surface varied).

4.3.2   Transmission measurements

4.3.2.1   General remarks on performance and results

Aiming at qualification of X-ray transmission conditions as well as quantification of radiation attenuation in dependence of material and radiation parameters, the presented transmission measuring results serve as basis for consequent theoretical attenuation considerations in Chapter IV–5.

The results presented in Chapter IV–4.3.2.2 (Figure IV-30 to Figure IV-36) are attributed to measuring applications for the determination of area density distribution across furnish mats or panels. Therefore, measurements were performed on stacked layers of cured furnish (Chapter IV–1.1) and panel material (Chapter IV–1.3) as well as cumulatively formed particle mats (Chapter IV–1.1). Accordingly, material with respectively equivalent raw density was utilised whereas thickness, thus, radiation transmission distance s_T [mm] within the sample increased per measuring step. Hence, the results are presented as charts in dependence of area density ρ_A [kg/m^2] with expectably equivalent raw density.

Contrary to this, the results shown in Chapter IV–4.3.2.3 (Figure IV-44 to Figure IV-50) correspond to RDP determination perpendicular to the panel plane. For that purpose, measurements were performed on specimens with nominally equal depth, thus, radiation transmission distance $s_T = 50$ mm but increasing raw density of the employed panels type labMDF (Chapter IV–1.2). Owing to the lab-made material, variations are limited to the three available raw density steps (Table IV-2). However, results are accordingly plotted in dependence of raw density ρ [kg/m^3] corresponding to area density dependent attenuation since ρ_A [kg/m^2] equivalently varies at nominally constant transmission distance s_T. Hence, actually varied raw density, thus, material structure, is consequently considered an impact on effective transmission as to be concluded in consequence of the measurements (Chapter IV–4.3.2.4) and further pointed out in Chapter IV–6. Beyond result plots, attenuation is quantified via computed mean mass attenuation

coefficients $\overline{\mu/\rho}$ [m^2/kg] in Table IV-27, where measuring results from labMDF are completed by respective mean values from indMDF.

Measuring data was acquired via transmission measurements by means of the devices described in Chapter IV–4.2.2 and Chapter IV–4.2.3. Beyond the stated methods, data evaluation comprises the following interdependent parameters:

- ρ_A [kg/m^2] as well as ρ [kg/m^3], respectively, from individually performed gravimetric measurements (refer to Chapter IV–1.5,
- ratio of measured transmission and initial radiation intensity $I_T/I_0 = T$ [–] following eq. (II-1) as relative transmission provided by all devices after respective raw data evaluation,
- therefrom calculated logarithmic of reciprocal transmission $\ln T^{-1} = \ln(I_0/I_T)$ [$-$] henceforth referred to as measured attenuation,
- and consequently per measuring point computed quotient of attenuation $\ln T^{-1}$ divided by corresponding area density ρ_A yields mass attenuation coefficient μ/ρ [m^2/kg] following Beer's law of attenuation eq. (II-11).

Figure IV-29 comprises all aforementioned data evaluations as exemplary template for all respective charts below. To this end, theoretically expected transmission measuring results were exemplarily computed via Beer's law of attenuation eq. (II-11) as illustrated in Figure II-5 for a virtual measuring device at medium energy level under ideal conditions; i. e., good-architecture conditions according to the discussions in Chapter II–1.3 (cf. LIU et al. (1988)) with

- monoenergetic radiation,
- narrow-beam transmission setup without scattered radiation impinging on the detector,
- no further bias from components like detector non-linearity, and
- homogeneous non-porous material.

Accordingly, the computed attenuation $\ln T^{-1}$ represents the linear transformation of exponentially decreasing measured transmission T,

ideal medium-energy device
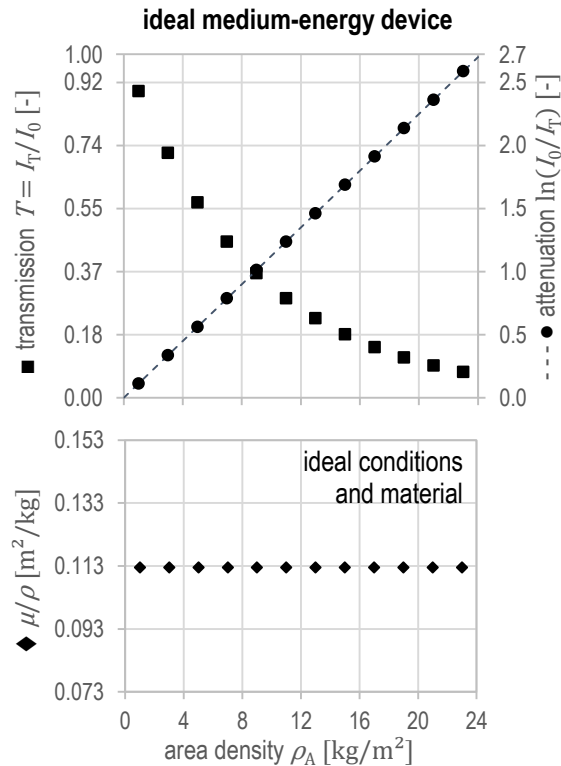
Figure IV-29: Theoretically expected transmission measuring results under ideal conditions in dependence of area density ρ_A $[\mathrm{kg/m^2}]$, with measured relative transmission T, therefrom calculated attenuation $\ln T^{-1}$ with its expected linear slope (dashed line estimation via $\mu/\rho_{\max}$) and consequently computed mass attenuation coefficients μ/ρ $[\mathrm{m^2/kg}]$; determined by means of an exemplarily assumed medium-energy device at $E_{\max} = \bar{E}$ (monoenergetic) on stacked specimens of homogeneous non-porous low-Z material.

where ideal measuring results fulfil the mathematical context. The relation of attenuation and transmission becomes further obvious in the intersection of both plots in Figure IV-29 (top) at $T = e^{-1}$ and $\ln T^{-1} = 1$. This level of transmission and attenuation, respectively, is also considered as appropriate measuring conditions, where reference is made to Chapter II–2.1. Since mass attenuation coefficients show equal values per material and energy, μ/ρ in Figure IV-29 (bottom) is constant over the total range of area density ρ_A. At the point of intersection of T and $\ln T^{-1}$, in turn, area density equals reciprocal mass attenuation coefficient $\rho_A = (\mu/\rho)^{-1}$.

The radiation parameters already stated in the figure caption respectively correspond to the initial X-ray spectrum emitted from the complete radiation source including inherent and potentially additional pre-filters of the setup. Besides nominal X-ray tube potential $U_{a,\mathrm{nom}}\,[\mathrm{kV}]$, the actual radiation properties maximum $E_{\max}\,[\mathrm{kVp}]$ and mean energy $\bar{E}\,[\mathrm{keV}]$ originate from radiation spectra measurements (Chapter IV–4.2.6.1), where reference is made to Chapter IV–4.3.3.1 for comprehensive results and particular discussions.

4.3.2.2 Results from area density measuring applications

All measurements for the results presented in this chapter were performed by exclusive application of the W-target device ρ_A setups (Table IV-19). To evaluate both effects from radiation properties and WBC structure impact, the measurements comprise three series with WBC material variation considering fibre mats (Fmat, Figure IV-30 to Figure IV-32), conventional MDF (indMDF, Figure IV-33 to Figure IV-35), and furnish mats from surface (SLmat, Figure IV-38) as well as core layer particles (CLmat, Figure IV-39 and Figure IV-40). Each material series covers again three radiation energy conditions (Table IV-20). Consequently, W-mat-ρ_A setup (Table IV-19) was employed for measurements on both furnish mat types as well as W-panel-ρ_A setup on panels. Beyond those variations, MC impact was evaluated utilising loosely formed SL particle mats conditioned to constant mass on three predefined moisture levels (Figure IV-41 to Figure IV-43). Notwithstanding that, exclusively the standard conditions 20/65 were applied to the material of all other measurements in the present chapter. Eventually, resulting mass attenuation coefficients of all measurements are compiled in Table IV-26 for comparison purpose. Note, measurements were not performed on total real-size furnish mats or panels but utilising appropriately small specimens covering the detector and actually exceeding the divergent beam path. Specimen dimensions were, however, evidently wide enough not to bias the measuring results, thus, to cause identical radiation-physical effects like respective real-size WBC material.

The first measuring series presented in Figure IV-30 to Figure IV-32 was determined on stacks of lab-made cured fibre mats (Fmat, Chapter IV–1.1). To this end, both nominal 1 kg/m² as well as 2 kg/m² samples (Table IV-1) were utilised resulting in respective measuring steps, where the actual area densities ρ_A (Table IV-5) are in good agreement with the target values. Mean raw density of the fibre mats was $\rho_1 = 122$ kg/m³ and $\rho_2 = 120$ kg/m³, respectively, at $MC_1 = 9.7$ % as well as $MC_2 = 9.0$ % ($\overline{MC} = 9.4$ %) as likewise shown in Table IV-5 and discussed in Chapter IV–1.5. For the Fmat measuring series, W-mat-ρ_A setup (Table IV-19) was employed with pre-defined tube potential and pre-filter variation as pointed out in Table IV-20. On all three energy levels of the series, Fmat transmission measurements were performed across a respectively wide ρ_A range. Thus, result charts in Figure IV-30 to Figure IV-32 feature certain overlappings.

However, transmission T plots of all three energy levels respectively reveal a continuously decreasing slope of the measuring results along increasing area density ρ_A with apparently exponential character. Contrary to theoretical expectation (Figure IV-29), backward-extrapolated trend of the transmission data yields no ordinate intercept at $T = 1$ but more or less distinctly below, whilst, however, the actual point of intersection varies between the three energy conditions and also the slope of the plots. Here, minimum deviation can be found for 25 kV level with pre-filter application (Figure IV-32) with $T = 0.98$ whereas 16 kV (Figure IV-30) and 20 kV level (Figure IV-31) plots (both without pre-filter) intersect ordinary axis at $T = 0.90$ and $T = 0.82$, respectively. Hence, the 20 kV level transmission plot reveals maximum deviation from the expected exponential character. Based on empirical observations as part of experiment preparations, it was found that the detector non-linearity starts to considerably increase for $T < 0.15$, which, in turn, biases the slope in the upper ρ_A range. Nevertheless, no distinct outliers can be identified in all three T plots.

The like applies to attenuation $\ln T^{-1}$ result plots. On all three energy levels, a continuously increasing slope can be found unveiling, however, an obviously non-linear context. For comparison purpose, an expected linear plot of $\ln T^{-1}$ was accordingly drawn in each figure (dashed line), which was respectively computed as estimation with $(0; 0)$ intersection via $\mu/\rho_{\max}$ as theoretically constant mass attenuation coefficient. Here, a degressive increment of the measured attenuation varies between the applied energy conditions. However, the downward deviation from the expected linear slope respectively increases with increasing ρ_A, hence, decreasing radiation transmission T through the stacked Fmat specimens. Particularly, minimum deviation can be found for 25 kV level, where setup comprises an additional 1.5 mm Al pre-filter. In comparison to 16 kV, the 20 kV level reveals a more distinct (actual maximum) non-linear $\ln T^{-1}$ slope, where this energy level was actually obtained by solely increment of $U_{a,nom}$ without further pre-filter addition.

The plots of mass attenuation coefficients μ/ρ correspond to the observed non-linear $\ln T^{-1}$ characters and unveil no constant values across the measuring range in no performed case. Along increasing ρ_A, μ/ρ reveals a fundamentally decreasing slope whilst difference from constancy varies in comparison between the three energy conditions. To this end, Figure IV-36 summarises μ/ρ results from all ρ_A measurements. Particularly the upper chart, where its relative variation was computed toward $\mu/\rho_{\max}$ at $\rho_{A,\min}$, unveils the differences. Note that, μ/ρ at 25 kV level is more or less close to constancy across the lower area density range and starts to decline at $\rho_A > 21$ kg/m² (refer also to Figure IV-32). On the contrary, 16 kV as well as 20 kV level plots (Figure IV-30 and Figure IV-31) consistently show distinctly decreasing μ/ρ values along the total ρ_A measuring range with a relative slope in a comparable order as obvious from Figure IV-36 (top). However, in comparison to T and $\ln T^{-1}$, μ/ρ plots generally reveal less straight slopes with particular outliers such as $\rho_A = 2.1$ kg/m² value in Figure IV-30. The observed

W-mat-16-w/o

W-mat-20-w/o

Figure IV-30: Transmission measuring results in dependence of area density ρ_A [kg/m^2], with measured relative transmission T, therefrom calculated attenuation $\ln T^{-1}$ with its expected linear slope (dashed line estimation via μ/ρ_{max}) and consequently computed mass attenuation coefficients μ/ρ [m^2/kg]; determined by means of W-mat-ρ_A device (Table IV-19) at $U_{a,nom} = 16$ kV (measured $E_{max} = 16.9$ kVp, $\bar{E} = 12.7$ keV) on stacked fibre mat specimens (Fmat) with $\overline{MC} = 9.4$ %.

deviations are attributed to material inhomogeneity rather than to X-ray measuring issues. Therefore, the gravimetrically determined area density as mean value per fibre mat specimen does not ultimately represent the actual ρ_A value at the particular radiation transmission position.

Figure IV-31: As Figure IV-30; determined by means of W-mat-ρ_A device (Table IV-19) at $U_{a,nom} = 20$ kV (measured $E_{max} = 21.2$ kVp, $\bar{E} = 15.5$ keV) on stacked fibre mat specimens (Fmat) with $\overline{MC} = 9.4$ %.

W-mat-25-w/

Figure IV-32: As Figure IV-30; determined by means of W-mat-ρ_A device (Table IV-19) at $U_{a,nom} = 25$ kV (E_{max}, $\bar{E}$ not measured) on stacked fibre mat specimens (Fmat) with $\overline{MC} = 9.4$ %.

Analogous character of measuring result plots can be observed for the indMDF series presented in Figure IV-33 to Figure IV-35, which were determined by means of the W-panel-ρ_A setup, where energy conditions were, in turn, varied according to Table IV-20. Note, less overlapping of the ρ_A ranges per energy level was obtained, since measurements by means W-panel-ρ_A setup were performed in connection with its practice-oriented application in an industrial context. Particularly in the case of 20 kV and 25 kV series, measurements do not cover the complete transmission range $0 < T < 1$. However, measurements were consequently focused on application-oriented ρ_A ranges per energy level according to experience. Therefore, transmission results are roughly limited to $0.1 < T < e^{-1}$. Eventually, measurements were performed on customary MDF (indMDF, Chapter IV–1.3), where various measuring steps in terms of ρ_A are attributed to respective panel thickness and were further obtained by predefined combination (stacking) of the very same. To this end, the aforementioned WBC material (Chapter IV–1.3) MDF-6, MDF-8, MDF-10, MDF-12, MDF-19, MDF-25, and MDF-30 (likewise applied for e. g. EA, Chapter IV–2.4) as well as additionally MDF-2 (not yet present for further analyses) was utilised. For the determined material properties MC, t, ρ, and ρ_A at 20/65 conditioning, reference is made to Table IV-5.

The result charts in Figure IV-33 to Figure IV-35 reveal, in turn,

- apparently exponential transmission T plots,
- non-linear slope of attenuation $\ln T^{-1}$, and
- consistently decreasing mass attenuation coefficients μ/ρ along increasing area density ρ_A

whilst distinctness again varies in comparison between the three energy levels. Notwithstanding the above, differences of the indMDF results can be observed toward the transmission measurements on Fmat stacks regardless of congruent ρ_A ranges and energy levels as well as equivalent material composition (where reference is made to EA, Chapter IV–2.4).

For T plot of 25 kV level (Figure IV-35), ordinate intercept is close to expectation at $T = 0.99$. In case of 16 kV (Figure IV-33) and 20 kV level (Figure IV-34), plots intersect ordinary axis at $T = 0.95$ and $T = 0.83$, respectively; i. e., above corresponding values from W-mat-ρ_A measurements. In comparison to Fmat results, only particular measuring points in case of 20 kV series fall below the considerable detector non-linearity threshold around $T = 0.15$. Hence, indMDF transmission measuring results appear less different from theoretical expectation, which is further supposed to be attributed to the lower number of measuring points and respectively poor estimation in comparison to Fmat data. Nevertheless, 20 kV level transmission plot reveals maximum deviation from expected exponential character again.

The like applies to indMDF attenuation $\ln T^{-1}$ plots in Figure IV-33 to Figure IV-35 with minimum deviation from linear estimation in the case of 25 kV level data and maximum non-linearity of attenuation at 20 kV energy conditions. In direct comparison to Fmat $\ln T^{-1}$ plots from W-mat-ρ_A measurements (Figure IV-30 to Figure IV-32), the slope of indMDF plots apparently reveals slightly lower distance toward respective linear estimation along increasing area density ρ_A

Consistently lower μ/ρ values are found for indMDF in comparison to Fmat likewise obvious from the summary in Table IV-26 and Figure IV-36 (bottom), where all panel values fall below respective fibre mat data. The relative comparison of computed μ/ρ at $T = e^{-1}$ per energy level yields indMDF is 86 % that of Fmat at 16 kV, 84 % at 20 kV, and 91 % at 25 kV level. However, steadily decreasing slope along increasing ρ_A with minimum deviation from constancy in the case of 25 kV level (Figure IV-35) can again be observed. In comparison to Fmat plots with particular reference to Figure IV-36 (top), indMDF μ/ρ decrement appears relatively flatter along increasing ρ_A on all energy levels, where only 16 kV level data appears indistinguishable.

Eventually, a similar situation regarding outliers can be concluded as already pointed out in the case of Fmat data. Furthermore and particularly in the case of the 25 kV level plot in Figure IV-35, deviations between consequently computed μ/ρ values on the same nominal ρ_A measuring step

W-panel-16-w/o

W-panel-20-w/o

Figure IV-33: Transmission measuring results in dependence of area density ρ_A [kg/m^2], with measured relative transmission T, therefrom calculated attenuation $\ln T^{-1}$ with its expected linear slope (dashed line estimation via $\mu/\rho_{\max}$) and consequently computed mass attenuation coefficients μ/ρ [m^2/kg]; determined by means of W-panel-ρ_A device (Table IV-19) at $U_{a,nom} = 16$ kV (measured $E_{\max} = 16.9$ kVp, $\bar{E} = 12.7$ keV) on stacked industrial MDF specimens (indMDF) with $\overline{MC} = 8.1$ %.

Figure IV-34: As Figure IV-33; determined by means of W-panel-ρ_A device (Table IV-19) at $U_{a,nom} = 20$ kV (measured $E_{\max} = 21.2$ kVp, $\bar{E} = 15.5$ keV) on stacked MDF specimens (indMDF) with $\overline{MC} = 8.1$ %.

become obvious. Note, the data was acquired on redundant specimens, hence, differences are again attributed to material inhomogeneity.

To briefly summarise comparison results, transmission measurements on pre-densified fibre mats and ready-pressed panels yield comparable results regarding transmission and attenuation characteristic, respectively, whereas actual mass attenuation differs. Moreover, the results unveil that structural conditions have an impact on radiation-physical effects from interaction of polychromatic X-rays with inhomogeneous porous low-Z material, which is clarified hereafter in Chapter IV–6.

W-panel-25-w/

Figure IV-35: As Figure IV-33; determined by means of W-panel-ρ_A device (Table IV-19) at $U_{a,nom} = 25$ kV ($E_{\max}$, $\bar{E}$ not measured) on stacked MDF specimens (indMDF) with $\overline{MC} = 8.1$ %.

W-panel-16-w/o   W-panel-20-w/o   W-panel-25-w/

W-mat-16-w/o   W-mat-20-w/o   W-mat-25-w/
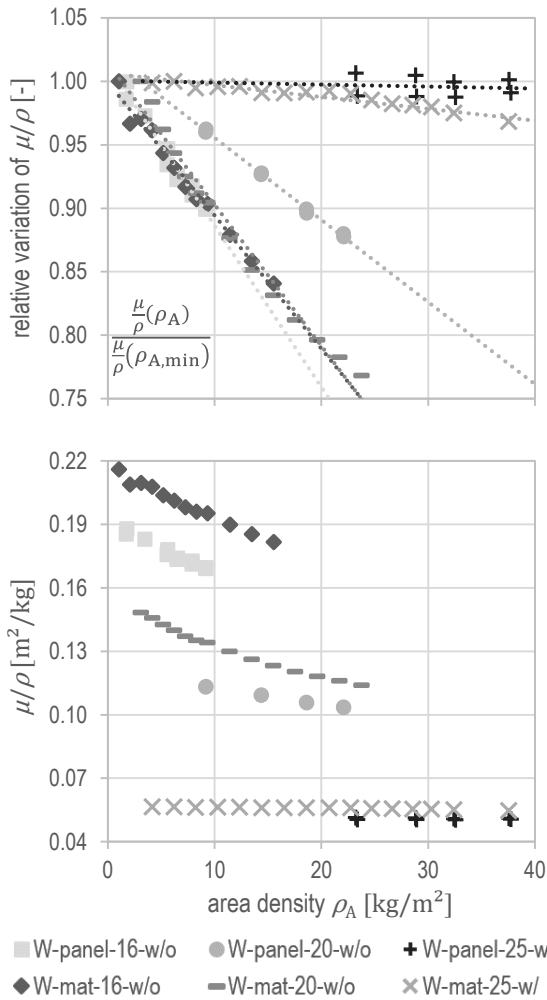
Figure IV-36: Summary of transmission measuring results by area density devices (W-mat and W-panel) as mass attenuation coefficient μ/ρ [m^2/kg] (bottom) in dependence of area density ρ_A [kg/m^2] and its relative variation (top) computed toward $\rho_{A,min}$ from W-mat device measurements (plots normalised to unity with $\frac{\mu/\rho(\rho_A)}{\mu/\rho(\rho_{A,min,mat})} = 1$), with linear regression (dashed lines, top) indicating the trend.

Contrary to the consistent energy settings above (see also Table IV-20), a further W-panel-ρ_A setup was employed with 50 µm Cu pre-filter after X-ray tube and additional 2.0 mm Al as mechanical covering of the detector likewise serving as inherent pre-filter of the setup. Note, the nominal tube potential was set to $U_{a,nom} = 35$ kV, yielding measured $E_{max} = 35.1$ kVp, $\bar{E} = 27.3$ keV. X-ray measurements were performed on customary MDF (indMDF, Chapter IV–1.3), where the measuring steps in terms of ρ_A are again attributed to the respective panel thickness, whereas stacking was omitted. However,

setup: **W-mat** (except indMDF: W-panel)			
E_{max} [kVp] via $U_{a,nom}$	**16**	**20**	**25**
Al pre-filter $t = 1.5$ mm	w/o	w/o	w/
$\bar{E}$ [keV]	12.7	15.5	n/a
material	μ/ρ [m^2/kg] @ $T = e^{-1}$		
	ρ_A [kg/m^2] @ $T = e^{-1}$		
indMDF (W-panel)	0.1749	0.1154	0.0508
	5.7	8.7	19.7
Fmat	0.2039	0.1369	0.0559
	4.9	7.3	17.9
SL-/CLmat	0.2189	0.1384	0.0591
	4.6	7.2	16.9
SL, OD	0.1989		
	5.0		
SL, 20/65	0.2047		
	4.9		
SL, 20/83	0.2064		
	4.8		

Table IV-26: Summary of transmission measuring results by W-panel (only indMDF) and W-mat device in varying configuration, with μ/ρ [m^2/kg] and ρ_A [kg/m^2] at $T = e^{-1}$ (appropriate measuring conditions) computed via interpolation of measuring data.

the employed set of samples is equivalent to the aforementioned W-panel-ρ_A device measurements comprising MDF-3, MDF-6, MDF-8, MDF-10, MDF-12, MDF-19, MDF-25, and MDF-30 (Chapter IV–1.3).

Obviously, the result charts in Figure IV-37 unveil distinctly differing attenuation conditions in comparison to low- and medium-energy results (Figure IV-33 to Figure IV-35). The higher energy level causes higher penetration potential, hence, high transmission T and low attenuation $\ln T^{-1}$. A rather wide but too low area density range of the presented measuring series fails to obtain appropriately high attenuation, however, resulting in a limited transmission range $e^{-1} < T < 1$. Notwithstanding that, high sensitivity is expected at around $T = e^{-1}$, which will be discussed elsewhere.

Transmission T plot at this energy level appears almost linear, since the range does not fall below $T < e^{-1}$. Nevertheless, the expected exponential character can be observed. Backward-extrapolated data yields ordinate intercept at $T = 1.002$,
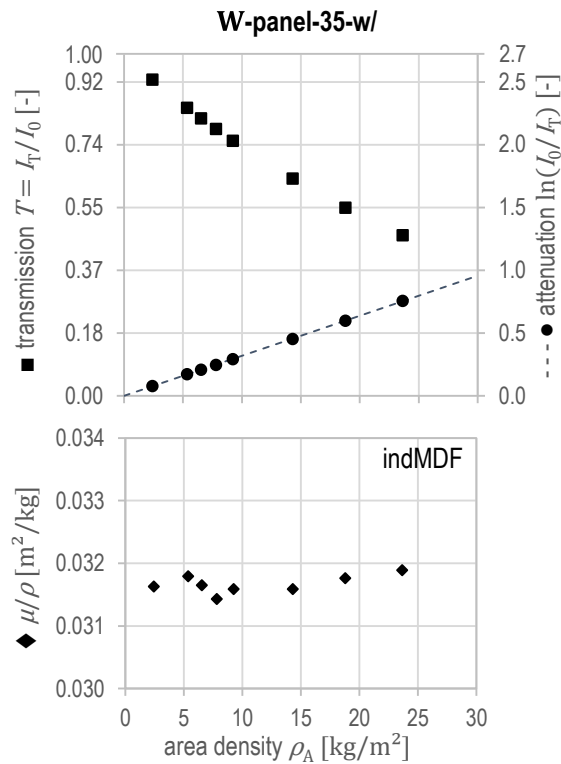
Figure IV-37: Transmission measuring results in dependence of area density ρ_A [kg/m^2], with measured relative transmission T, therefrom calculated attenuation $\ln T^{-1}$ with its expected linear slope (dashed line estimation via $\mu/\rho_{\max}$) and consequently computed mass attenuation coefficients μ/ρ [m^2/kg]; determined by means of W-panel-ρ_A device (Table IV-19) with 50 µm Cu pre-filter (X-ray tube) and additional 2.0 mm Al (detector covering) at $U_{a,\text{nom}} = 35$ kV (measured $E_{\max} = 35.1$ kVp, $\bar{E} = 27.3$ keV) on single panels of industrial MDF specimens (indMDF) with $\overline{MC} = 8.1$ %.

which is considered to be equivalent to theoretical expectation. Accordingly, the 35 kV attenuation $\ln T^{-1}$ results in Figure IV-37 with continuously increasing slope do not unveil any obviously non-linear context. Moreover, the slope is apparently congruent to linear expectation (dashed line) within the considered range. Both T and $\ln T^{-1}$ plots are again free of any outliers. Eventually, the plots of mass attenuation coefficients μ/ρ correspond to the observed linear $\ln T^{-1}$ character. Data in Figure IV-37 (bottom) reveal no downward trend and remain, moreover, constant over the measuring range with mean $\overline{\mu/\rho} = 0.0317$ m^2/kg regardless of slight variations of $\Delta\mu/\rho = \pm0.0002$ m^2/kg (±0.7 %). The latter are rather attributed to insufficiencies

in gravimetric ρ_A determination as mean value across the specimen not considering, in turn, local inhomogeneities as already discussed above. However, lower μ/ρ values in comparison to all W-panel-ρ_A measurements above correspond to increased energy of this particular setup.

To summarise the additional measuring series results for indMDF in short, higher energy level causes increased penetration potential. Comparably distinct pre-filter application with respective layers of Cu and Al yields linear attenuation in good accordance with expectation and more or less constant mass attenuation coefficients μ/ρ along the measured ρ_A range. Moreover, deviations from linearity are considered to occur as a results of extended measuring ranges with $T < e^{-1}$ and $\ln T^{-1} > 1$, respectively.

Beyond the comparison between pre-compressed furnish mats and consolidated panels made of resin-blended fibres, an additional measuring series (Figure IV-38 to Figure IV-40) was performed utilising both surface (SL) and core layer (CL) particles. Aiming at variations in furnish structure, i. e., fibres and particles, rather than composition and consolidation, investigations were focused, in turn, on pre-compressed particle mats to be compared with fibre mat results. Again, both nominal 1 kg/m² (SLmat) as well as 2 kg/m² (CLmat) samples (Table IV-1) made of cured particle mats (Chapter IV–1.1) were utilised as stacks with consequent measuring steps. Here, the actual area densities ρ_A (Table IV-5) are again in more or less good agreement with the target values. The mean raw density of the particle mats, however, was $\rho_{1,\text{SL}} = 217$ kg/m^3 and $\rho_{2,\text{CL}} = 197$ kg/m^3, respectively, at $MC_{1,\text{SL}} = 10.5$ % as well as $MC_{2,\text{CL}} = 11.3\%$ as shown in Table IV-5 and discussed in Chapter IV–1.5. The employed W-mat-ρ_A setup (Table IV-19) was identical to the respective measurements on fibre mats (Fmat, Figure IV-30 to Figure IV-32), likewise radiation energy and pre-filter conditions (Table IV-20). Particle mat measurements cover a comparable but slightly limited ρ_A range particularly in the case of 16 kV and 25 kV energy level owing to limited availability of the fragile specimens.
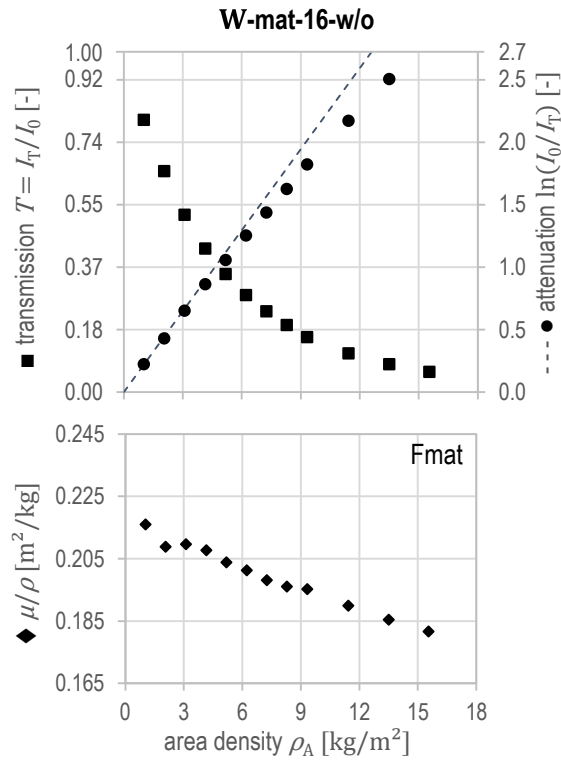
W-mat-16-w/o

W-mat-20-w/o

Figure IV-38: Transmission measuring results in dependence of area density ρ_A [kg/m^2], with measured relative transmission T, therefrom calculated attenuation $\ln T^{-1}$ with its expected linear slope (dashed line estimation via $\mu/\rho_{\max}$) and consequently computed mass attenuation coefficients μ/ρ [m^2/kg]; determined by means of W-mat-ρ_A device (Table IV-19) at $U_{a,nom} = 16$ kV (measured $E_{\max} = 16.9$ kVp, $\bar{E} = 12.7$ keV) on stacked SL particle mat specimens (SLmat) with $\overline{MC} = 10.5$ %.
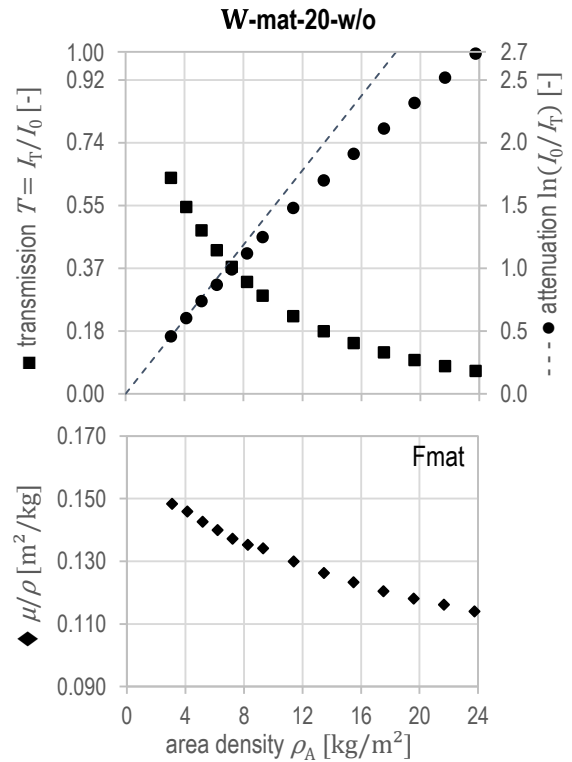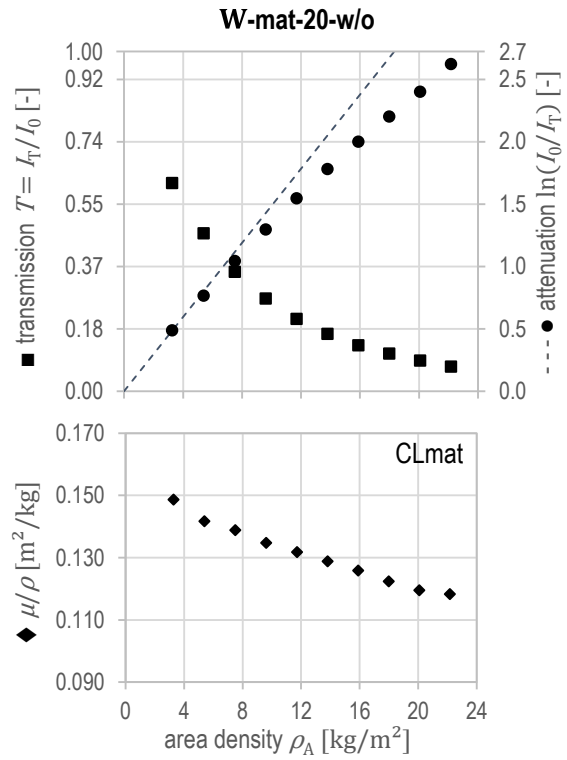
Figure IV-39: As Figure IV-38; determined by means of W-mat-ρ_A device (Table IV-19) at $U_{a,nom} = 20$ kV (measured $E_{\max} = 21.2$ kVp, $\bar{E} = 15.5$ keV) on stacked CL particle mat specimens (CLmat) with $\overline{MC} = 11.3$ %.
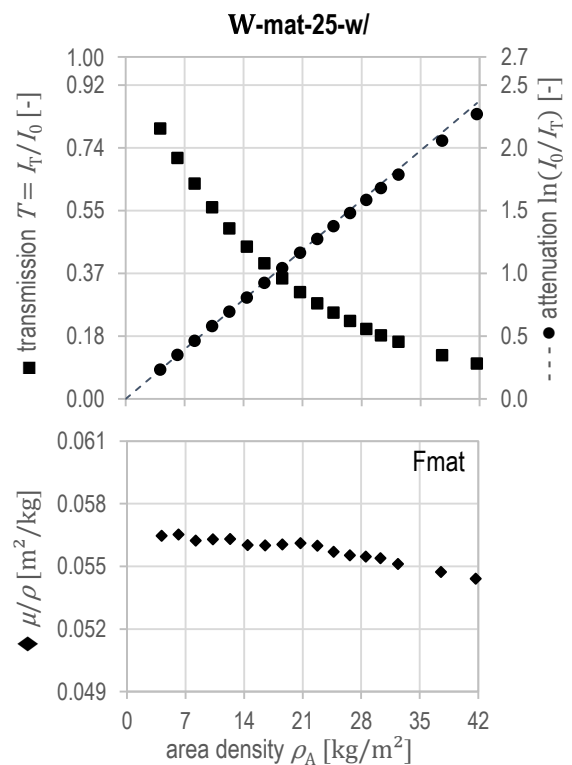
W-mat-25-w/
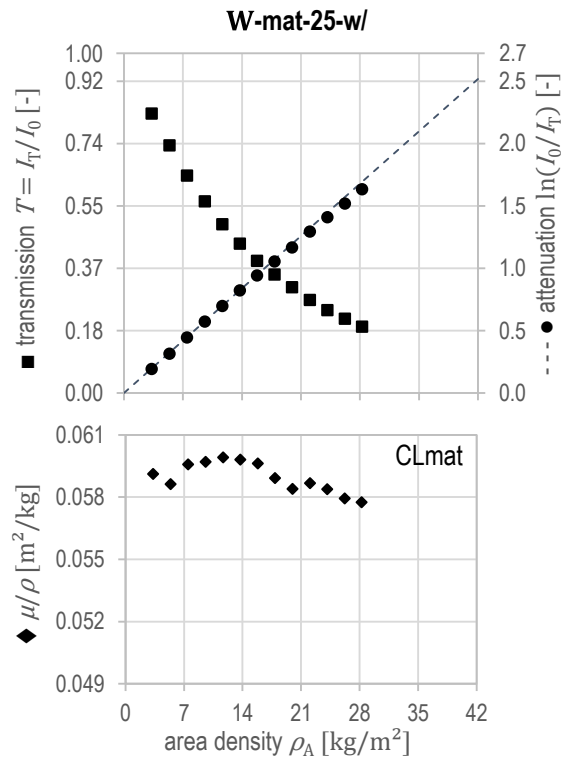
Figure IV-40: As Figure IV-38; determined by means of W-mat-ρ_A device (Table IV-19) at $U_{a,nom} = 25$ kV ($E_{\max}$, $\bar{E}$ not measured) on stacked CL particle mat specimens (CLmat) with $\overline{MC} = 11.3$ %.

In general, SLmat and CLmat result charts in Figure IV-38 to Figure IV-40 reveal analogous characteristics in comparison to Fmat charts (Figure IV-30 to Figure IV-32) but at the same time certain peculiarities. Transmission T plots again reveal continuously decreasing slope, where the exponential character can be observed. Regardless of 16 kV level with slightly limited transmission range $0.25 < T < 1$, the data from all measurements appropriately falls below $T < e^{-1}$. Backward-extrapolation of the transmission consistently yields ordinate intercepts below $T = 1$, particularly with rather low deviation of $T = 0.98$ at 25 kV and $T = 0.99$ at 16 kV level as well as the most distinct intersection $T = 0.83$ at 20 kV. Except 16 kV level, the points of intersection correspond to aforementioned Fmat data of the respective energy level. Thus, 20 kV level transmission plots reveal again maximum deviation from expectation, i. e., simple exponential slope. The apparently low deviation from $T = 1$ in comparison to the 16 kV Fmat chart ($T = 0.90$) is considered to be attributed to the limited measuring data range toward $\rho_A > 7$ kg/m^2, where the transmission plot regularly starts to converge. Hence, no significant differences in transmission characteristics can be observed in comparison of fibre and particle mats with similar composition and pre-densification whereas the latter actually varies in a nominal raw density range of $\rho_{nom} = 125 \ldots 200 \ldots 300$ kg/m^3 (fibres, CL, SL) as summarised in Table IV-1. However, the like applies to attenuation $\ln T^{-1}$ plots, where comparable deviations from theoretically expected linearity can be found.

Mass attenuation coefficients μ/ρ of particle mats, in turn, slightly exceed the respective values determined on fibre mats. The summary in Table IV-26 unveils maximum difference of 16 kV values 9 % above Fmat results, 5 % at 25 kV level, and negligible 1 % at 20 kV. However, their slope is likewise characterised by decreasing μ/ρ values along increasing ρ_A with varying distinctness between the energy levels, in turn. Whilst again no considerable outliers are apparent in the case of T as well as $\ln T^{-1}$ plots, they are obviously present in the μ/ρ charts particularly in the case of 16 kV and 25 kV level

measurements. Beyond specimen inhomogeneity, there were worse conditions compared to fibre mats for gravimetrical area density determination owing to coarse and more fragile structure of both particle mats, which tended to loose particles during handling.

Whilst the above presented results were determined on material within an equivalent MC range in consequence of identical conditioning at nominal standard conditions 20/65, the following measuring series (Figure IV-41 to Figure IV-43) takes varying equilibrium moisture conditions on three levels into account. To this end, resin-unblended pure SL particles (Figure IV-9 in Chapter IV–2.2) were conditioned to constant mass at oven-dry (OD), standard (20/65), and moist (20/83) level; note in case of OD state, moisture uptake of hygroscopic particles could not be avoided during handling and measurement despite rapid performance and sealed storage in desiccated bags. Consequently, mean MC at the three conditioning levels was $MC_{SL,OD} = 2.0\%$, $MC_{SL,20/65} = 10.8\%$ as well as $MC_{SL,20/83} = 13.8\%$ as shown in Table IV-5 and discussed in Chapter IV–1.5. To obtain, in turn, furnish structure equivalent to industrial process conditions, particle mats from the conditioned material were manually formed and pre-densified immediately before X-ray measurements (Figure IV-1 in Chapter IV–1.1). The resulting mean bulk density of the growing particle mats was $\rho_{SL,OD} = 233$ kg/m^3, $\rho_{SL,20/65} = 238$ kg/m^3, and $\rho_{SL,20/83} = 245$ kg/m^3, respectively (Table IV-5, Chapter IV–1.5). The accordingly employed W-mat-ρ_A setup (Table IV-19) was identical to the respective measurements on cured fibre and particle mats whereas radiation energy and pre-filter conditions were limited to low energy level with exclusive measurements at 16 kV (Table IV-20).
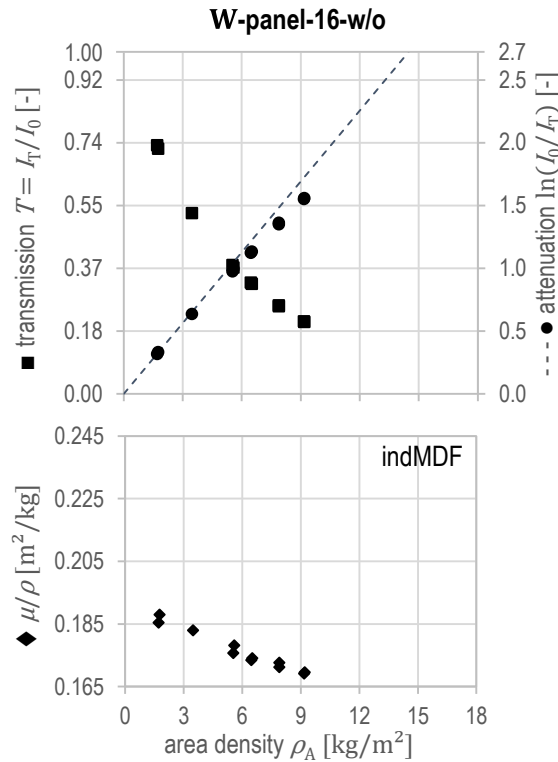
Figure IV-41: Transmission measuring results in dependence of area density ρ_A [kg/m^2], with measured relative transmission T, therefrom calculated attenuation $\ln T^{-1}$ with its expected linear slope (dashed line estimation via $\mu/\rho_{\max}$) and consequently computed mass attenuation coefficients μ/ρ [m^2/kg]; determined by means of W-mat-ρ_A device (Table IV-19) at $U_{a,nom} = 16$ kV (measured $E_{\max} = 16.9$ kVp, $\bar{E} = 12.7$ keV) on a loosely formed and growing particle mat (Figure IV-1) made of resin-unblended SL particles with $\overline{MC} = 2.0$ % representing oven-dry conditions (OD).
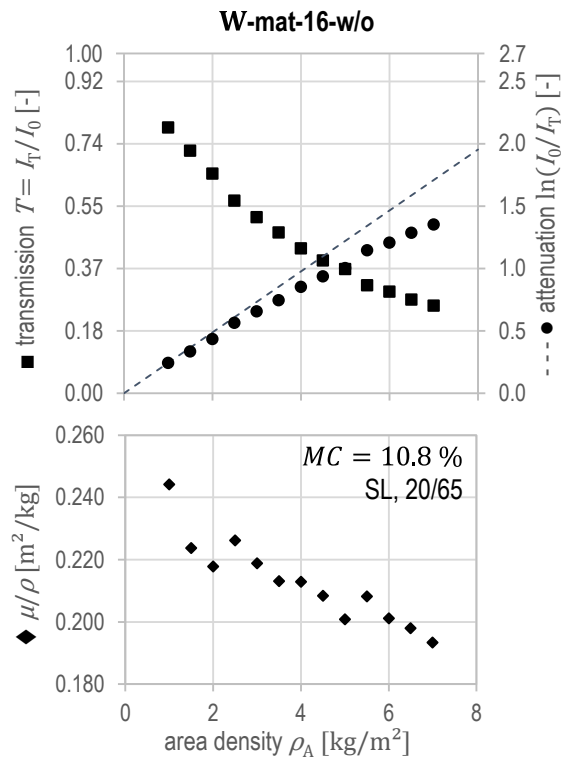
Figure IV-42: As Figure IV-41; with $\overline{MC} = 10.8$ % representing standard conditions (20/65).
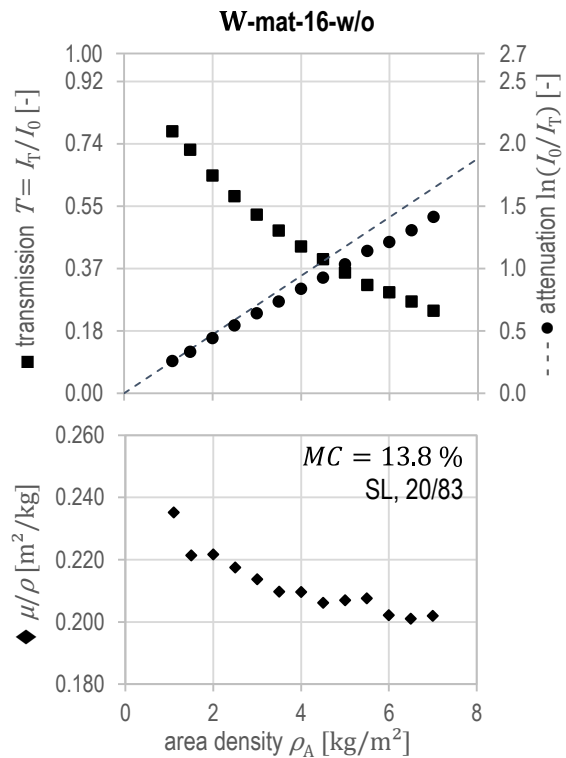
Figure IV-43: As Figure IV-41; with $\overline{MC} = 13.8$ % representing moist conditions (20/83).

In general, all result charts (Figure IV-41 to Figure IV-43) on the three MC levels reveal the already well-known characteristics on 16 kV radiation energy level with particular differences between the EMC conditions. In the transmission T plots, however, no obvious differences between OD, 20/65, and 20/83 charts can be found. Regarding obtained transmission range $0.25 < T < 1$, data of all measurements appropriately falls below $T < e^{-1}$. Backward-extrapolation yields again ordinate intercepts below $T = 1$, with $T = 0.94$ at OD, $T = 0.93$ at standard (20/65), and $T = 0.95$ at moist (20/83) conditions; i. e., all slopes unveil more or less equivalent differences from theoretical expectation. The attenuation $\ln T^{-1}$ plots, in turn, reveal particular differences between the MC levels. Here, the increment deviation from expected linear slope with increasing MC from OD to 20/65 state can be observed. Eventually, the mass attenuation coefficients μ/ρ of the varyingly conditioned SL particles are in a comparable order of magnitude. Nevertheless, particular consideration of the summarised figures in Table IV-26 unveils more or less increasing values with increasing MC; i. e., $\mu/\rho_{20/65}$ is 2.9 % higher than μ/ρ_{OD} and $\mu/\rho_{20/83}$ is 3.8 % beyond OD level. Hence, there is just a slight increment between standard and moist conditions of 0.9 % of the μ/ρ values, where their respective MC is closer to each other than toward OD level. Considering single values of all MC dependent results, outliers are again rather apparent in μ/ρ plots particularly owing to repeated manual particle mat forming.

Eventually, observed MC dependency in the charts as well as the summary in Table IV-26 had to be verified. Therefore, data was compared by means of statistical hypothesis testing. Since X-ray measuring data was acquired in equivalent ρ_A steps obtained by respectively precise individual material dosing, the three data sets of this series at predefined moisture conditions can mathematically be understood as dependent samples. Taking $\mu/\rho\,(\rho_A)_{condition}$ data accordingly into account, Wilcoxon matched pairs signed rank test was performed which is furthermore robust against non-Gaussian distributed data. The test enables to compare paired observations by assessing whether within-pair differences are symmetrically distributed around their median, which equals zero. In this regard, the comparison between standard and moist conditions with the null hypothesis $H_0: F(\mu/\rho\,(\rho_A)_{20/65}) = F(\mu/\rho\,(\rho_A)_{20/83})$ vs. $H_1: F(\mu/\rho\,(\rho_A)_{20/65}) \neq F(\mu/\rho\,(\rho_A)_{20/83})$ reveals no significant differences between the $\mu/\rho\,(\rho_A)$ series since it fails to reject H_0 on all significance levels α. On the contrary, both $H_0: F(\mu/\rho\,(\rho_A)_{OD}) = F(\mu/\rho\,(\rho_A)_{20/65})$ vs. $H_1: F(\mu/\rho\,(\rho_A)\ ) \neq F(\mu/\rho\,(\rho_A)_{20/65})$ as well as $H_0: F(\mu/\rho\,(\rho_A)_{OD}) = F(\mu/\rho\,(\rho_A)_{20/83})$ vs. $H_1: F(\mu/\rho\,(\rho_A)\ ) \neq F(\mu/\rho\,(\rho_A)_{20/83})$ are rejected at $\alpha = 0.001$ (two-tailed); hence, in keeping with obvious perception, equivalent $\mu/\rho\,(\rho_A)$ series at standard (20/65) and moist (20/83) conditions, respectively, are distinctly different from the very same at OD state considering the measurements at 16 kVp energy level.

4.3.2.3   Results from raw density profile measuring applications

Beyond the different versions for area density ρ_A measurements presented in Chapter IV–4.3.2.2, further setups of the W-target device (W-RDP setup, Table IV-19) were employed for X-ray transmission measurements in terms of conventional raw density profile (RDP) determination on small specimens. To this end, two energy levels $U_{a,nom} = 35$ kV and $U_{a,nom} = 50$ kV with and without 1.96 mm Al pre-filter were applied (Table IV-20). Likewise, the Ag-target device was utilised with its exclusive setup (Ag-RDP, Table IV-18) regularly operated at $U_{a,nom} = 55$ kV without pre-filter and with additional 1.5 mm Al as variation. The setup configurations of both devices and the respectively applied energy levels of all measurements correspond, however, to X-ray spectra determination described in Chapter IV–4.2.6.1 with the results presented in Chapter IV–4.3.3.1

According to the common application and in contrast to the aforementioned ρ_A results, all result charts in Figure IV-44 to Figure IV-50 are presented as plots over the raw density $\rho\;[\mathrm{kg/m^3}]$ as gravimetrically determined mean value per

specimen. Eventually, Table IV-27 summarises the measurements by means of consequently computed mean mass attenuation coefficients $\overline{\mu/\rho}$ [m^2/kg] per specimen type and configuration (energy level and pre-filter). All measurements were exclusively performed on small specimens with nominal transmission distance $s_T = 50$ mm parallel to the panel plane cut into squares. The measuring process was carried out as stepwise scan across the respective panel thickness. To this end, labMDF with predefined densification steps (Table IV-2) was utilised aiming at transmission plots corresponding to ρ_A results (Chapter IV–4.3.2.2) and to likewise evaluate raw density dependency of radiation transmission and attenuation, respectively, as well as mass attenuation coefficients. The applied setup configuration and material variations purpose again to evaluate both effects from radiation properties as well as WBC structure impact. Beyond these comprehensive measuring series on lab-made WBC material with homogeneous RDP, further measurements on customary industrial panels (indMDF) as well as insulation board (both utilised for elemental analysis, refer to Chapter IV–2.3 and IV–2.4) were performed to evaluate and compare their $\overline{\mu/\rho}$ [m^2/kg] (Table IV-27) complete with the samples (MDF and PB, $t_{nom} = 19$ mm) from round robin test. Nevertheless, exclusively standard conditions 20/65 were applied to the material of all measuring series in the present chapter. For the determined material properties MC, t, ρ, and ρ_A, reference is made to Table IV-5.

The first of the labMDF measuring series presented in Figure IV-44 and Figure IV-45 was determined by means of the Ag-target device without (Ag-RDP-55-w/o) and with (Ag-RDP-55-w/) additional pre-filter. Owing to the limited raw density steps of the lab-made panels compared to finely graduated furnish mat and panel stacks known from area density measurements in Chapter IV–4.3.2.2, the plots respectively comprise solely three distinct data points. However, corresponding character of the measurements becomes obvious. Moreover, in case of larger sample sizes such as in Figure IV-44, densification variations between the specimens support the slope of the plot.

Notwithstanding some limitations, RDP measurements reveal in general analogous results and transmission as well as attenuation characteristics in comparison to ρ_A results in Chapter IV–4.3.2.2. In particular, Ag-RDP transmission T plots show continuously decreasing slope with obviously exponential character. Considering backward-extrapolated trend of the data, only in case of the series without pre-filter, ordinate intercept drops below theoretically expected $T = 1$ with $T_{w/o} = 0.90$ (Figure IV-44) whereas pre-filtering yields point of intersection actually at $T_{w/} = 1.0$ (Figure IV-45). Hence, Ag-RDP-55-w/ setup and configuration appear to more or less meet ideal conditions (Figure IV-29) regarding transmission plot. However, all presented RDP measurements do not cover the complete transmission range $0 < T < 1$ but take a comparable section limited around $T \leq e^{-1}$ into considerations; i. e., $0.11 < T_{w/o} < 0.39$ in case of Ag-RDP-55-w/o and $0.18 < T_{w/} < 0.49$ for the additional measurements with pre-filter (Ag-RDP-55-w/).

The like applies to attenuation $\ln T^{-1}$ plots with continuously increasing slope. In the case of Ag-RDP-55-w/o, i. e., without pre-filter, an obviously non-linear slope, in turn, can be observed with deviation from linear estimation (dashed line in Figure IV-44) particularly in the higher raw density range. Contrary to this, attenuation of pre-filtered radiation from Ag-RDP-55-w/ by labMDF in the applied raw density range yields results close to linearity.

The plots of mass attenuation coefficients μ/ρ correspond, in turn, to observed T as well as $\ln T^{-1}$ characters and the present peculiarities. In case of the results in Figure IV-44 (Ag-RDP-55-w/o), μ/ρ plot unveils no constant values across the measuring range with a fundamentally decreasing slope along increasing ρ. Particular outliers primarily within the $\rho_{nom} = 400$ kg/m^3 samples are mainly attributed to gravimetrical raw density determination, which is more error prone on light fibrous specimens. The tendency becomes, however, clearly obvious. On the contrary, Ag-RDP-55-w/ results reveal μ/ρ values more or less close to constancy across the measured ρ range. For a more direct comparison, reference is made to Figure IV-50,
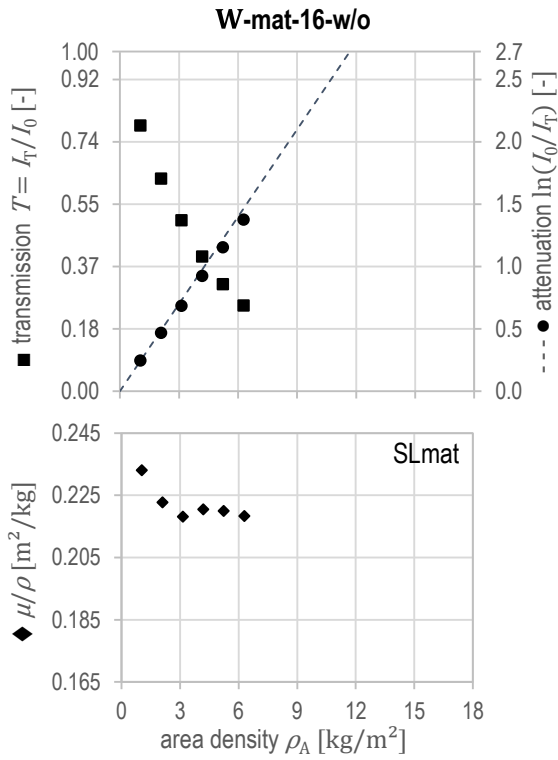
Ag-RDP-55-w/o

Ag-RDP-55-w/
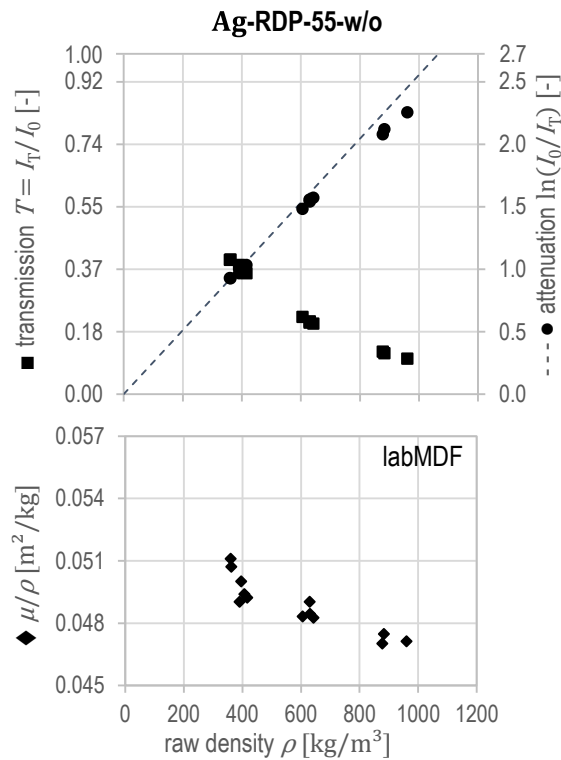
Figure IV-44: Transmission measuring results in dependence of raw density ρ [kg/m^3], with measured relative transmission T, therefrom calculated attenuation $\ln T^{-1}$ with its expected linear slope (dashed line estimation via $\mu/\rho_{\max}$) and consequently computed mass attenuation coefficients μ/ρ [m^2/kg]; determined by means of Ag-RDP device (Table IV-18) without pre-filter at $U_{a,nom} = 55$ kV (measured $E_{\max} = 51.3$ kVp, $\bar{E} = 21.1$ keV) on single labMDF specimens (nominal transmission distance $s_T = 50$ mm) with $\overline{MC} = 9.5$ %.

Figure IV-45: Transmission measuring results in dependence of raw density ρ [kg/m^3], with measured relative transmission T, therefrom calculated attenuation $\ln T^{-1}$ with its expected linear slope (dashed line estimation via $\mu/\rho_{\max}$) and consequently computed mass attenuation coefficients μ/ρ [m^2/kg]; determined by means of Ag-RDP device (Table IV-18) with additional 1.5 mm Al pre-filter at $U_{a,nom} = 55$ kV (measured $E_{\max} = 51.3$ kVp, $\bar{E} = 21.5$ keV) on single labMDF specimens (nominal transmission distance $s_T = 50$ mm) with $\overline{MC} = 9.5$ %.

which summarises μ/ρ results from all RDP devices and their respective relative variation in dependency of ρ. Here, a continuous downward trend of measured μ/ρ from all setups can be found except Ag-RDP-55-w/ with apparently increasing values, however, in the absence of any clear trend. Since there is no reasonable explanation for increasing μ/ρ ($\rho_A = \rho \cdot t$) under the present radiation-physical conditions, the determined values are considered not to increase but rather vary around an equivalent mean value over the present raw density range. The low-density value can further be understood as outlier again affected by fundamental insufficiencies of gravimetric raw density determination on compressible fibrous specimens. Regarding

Ag-RDP-55-w/o, relative variation of μ/ρ [–] decreases, in turn, about $\Delta\mu/\rho_{rel} = -5.4$ % along the utilised nominal raw density range $\rho_{nom} = 400\ldots1056$ kg/m^3.

Eventually, the configuration of Ag-target setup with additional pre-filter (Ag-RDP-55-w/) apparently facilitates to meet ideal conditions (Figure IV-29) with respect to the obtained measuring results. This might apply to the present radiation properties, since capillary optics and collimators diminish the occurrence of scattered radiation. Furthermore, a more or less narrow-band energy distribution was obtained as to be pointed out in Chapter IV–4.3.3. The material, nevertheless, remains inhomogeneous and porous. Moreover,

further bias from measuring components particularly the detector of this setup causing non-linearity was diminished by parameter setting but can, however, not totally be excluded.

The result charts of the W-target device measuring series on labMDF in Figure IV-46 to Figure IV-49 reveal, in turn,

- apparently exponential transmission T plots,
- non-linear slope of attenuation $\ln T^{-1}$, and
- consistently decreasing mass attenuation coefficients μ/ρ along increasing raw density ρ

whilst distinctness varies in comparison between the two energy levels and pre-filter variations, which are consequently presented and evaluated at once.

Considering transmission T plots, all W-RDP measurements cover comparable transmission ranges around $T \le e^{-1}$, particularly,

- $0.10 < T < 0.36$ (W-RDP-35-w/o),
- $0.17 < T < 0.46$ (W-RDP-50-w/o),
- $0.16 < T < 0.47$ (W-RDP-35-w/), and
- $0.23 < T < 0.55$ (W-RDP-50-w/).

Note here, the increasing transmission potential of the applied X-ray spectra becomes obvious in consequence of increasing energy level and pre-filter application. The continuously decreasing slope of the transmission T plots may partly appear linear owing to the limited measuring steps whereas their exponential character is, however, a priori presumed. The actual slope is, in turn, attributed to the respective measuring data and is considered to correspondingly differ from the ideal expectation (Figure IV-29). Consequently, the backward-extrapolated trend of the data yields no ordinate intercept at theoretically expected $T = 1$ in all cases of the W-target device measuring series whilst the plots actually intersect the ordinary axis at

- $T = 0.83$ (W-RDP-35-w/o),
- $T = 0.88$ (W-RDP-50-w/o),
- $T = 0.94$ (W-RDP-35-w/), and
- $T = 0.96$ (W-RDP-50-w/),

hence, consistently but varyingly distinct below $T = 1$. Compared to the aforementioned Ag-RDP plots, the respective series without additional pre-filter (Ag-RDP-55-w/o) yields the point of intersection $T = 0.90$ more or less directly between the W-RDP series without and with pre-filter. Moreover, Ag-RDP-55-w/ achieves the closest fit to the theoretical expectation with $T = 1$. However, T plots from W-RDP measurements under application of an additional pre-filter (W-RDP-35-w/ and W-RDP-50-w/) yield lower deviation from expectation than the very same without pre-filter (W-RDP-35-w/o and W-RDP-50-w/o). Beyond that, comparison of the applied radiation energies reveals ordinate intercepts closer to $T = 1$ in case of the respectively higher energy level ($U_{a,nom} = 50\,\text{kV}$) whereas $35\,\text{kV}$ level values considerably drop below.

Analogous observations can be found regarding attenuation $\ln T^{-1}$ plots with again continuously increasing but obviously non-linear slope. Here, the highest deviation from expected linear estimation (dashed lines), i. e., W-RDP-35-w/o, corresponds to minimum T intercept value and vice versa, i. e., W-RDP-50-w/. The same context applies to the series in between.

Moreover, observations from measuring charts are reflected in the plots of consequently computed mass attenuation coefficients μ/ρ, which consistently decrease with increasing raw density. The downward slope, in turn, differs between the configurations with its steepest characteristic in the case of W-RDP-35-w/o and comparably the lowest decrement for W-RDP-50-w/. The plots of relative variation of μ/ρ in Figure IV-50 (top) unveil no crucial differences in slope between the energy levels but, however, between the series with and without pre-filter where the pre-filter yields less strongly decreasing values. Potential but less obvious outliers are again considered to be attributed to gravimetrical raw density determination. Since identical ρ values were utilised for immediately consecutive measuring series, a congruent pattern can be found in Figure IV-48 and Figure IV-49 whilst the slope differs due to present radiation-physical conditions. Eventually, none of the W-RDP results is as close to theoretically expected transmission measuring results under ideal conditions (Figure IV-29) as the Ag-RDP-55-w/ plot featuring more or less constant μ/ρ over the ρ range. Notwithstanding that, W-RDP-50-w/ results reveal the

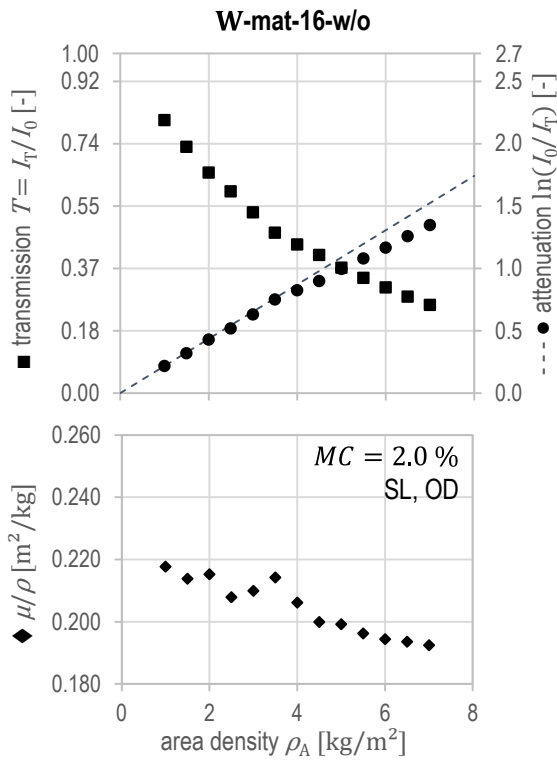**W-RDP35-w/o**

W-RDP-50-w/o
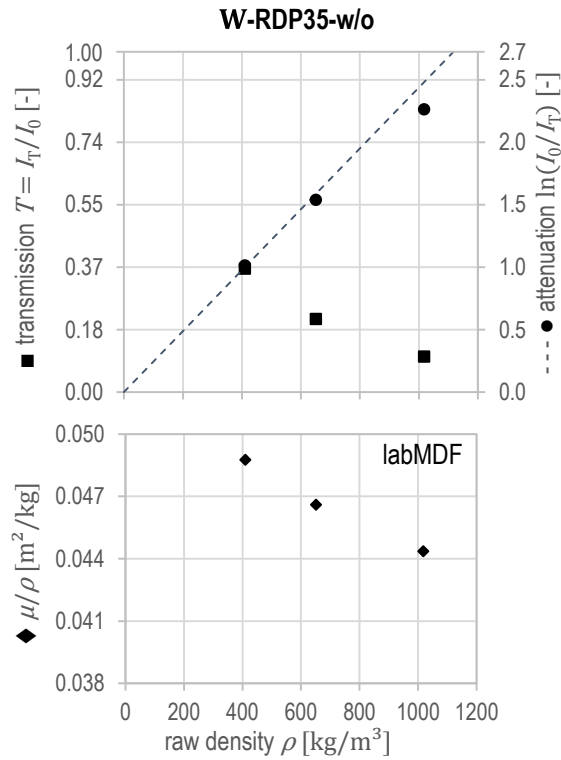
Figure IV-46: Transmission measuring results in dependence of raw density ρ $[\mathrm{kg/m^3}]$, with measured relative transmission T, therefrom calculated attenuation $\ln T^{-1}$ with its expected linear slope (dashed line estimation via μ/ρ_{max}) and consequently computed mass attenuation coefficients μ/ρ $[\mathrm{m^2/kg}]$; determined by means of W-RDP device (Table IV-19) without pre-filter at $U_{\mathrm{a,nom}} = 35$ kV (measured $E_{\mathrm{max}} = 35.4$ kVp, $\bar{E} = 21.5$ keV)[34] on single labMDF specimens (nominal transmission distance $s_{\mathrm{T}} = 50$ mm) with $\overline{MC} = 9.5$ %.

highest similarity with the ideal expectation. Note with reference to Figure IV-50, relative variation of μ/ρ $[-]$ decreases just slightly about $\Delta\mu/\rho_{\mathrm{rel}} = -2.9$ % along the utilised nominal raw density range $\rho_{\mathrm{nom}} = 400 \dots 1056$ $\mathrm{kg/m^3}$. The like applies to W-RDP-35-w/ with $\Delta\mu/\rho_{\mathrm{rel}} = -3.7$ %. On the contrary, μ/ρ results from transmission measurements without additional pre-filter reveal on both energy levels much steeper decrement along increasing ρ with $\Delta\mu/\rho_{\mathrm{rel}} = -8.2$ % (W-RDP-50-w/o) and $\Delta\mu/\rho_{\mathrm{rel}} = -9.0$ % (W-RDP-35-w/o), respectively.
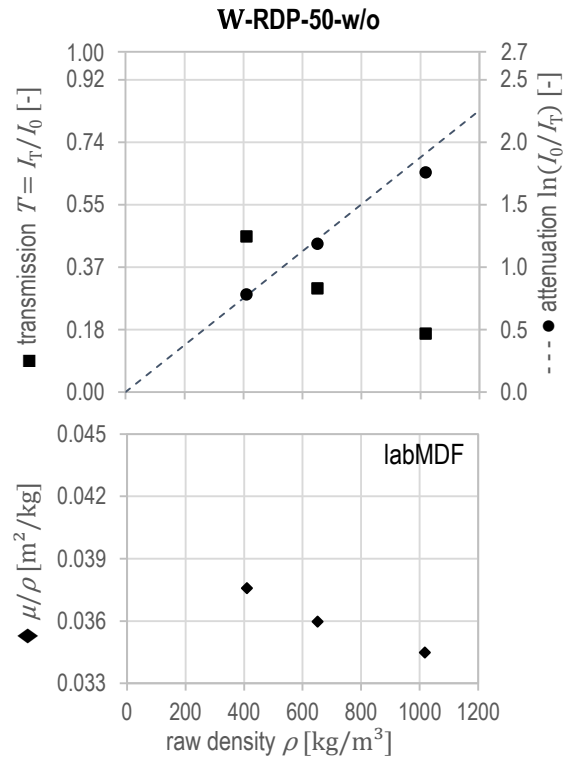
Figure IV-47: As Figure IV-46; determined by means of W-RDP device (Table IV-19) without pre-filter at $U_{\mathrm{a,nom}} = 50$ kV (measured $E_{\mathrm{max}} = 50.9$ kVp, $\bar{E} = 26.3$ keV)[34] on single labMDF specimens (nominal transmission distance $s_{\mathrm{T}} = 50$ mm) with $\overline{MC} = 9.5$ %.

Finally, Table IV-27 summarises all computed mass attenuation coefficients as mean value $\overline{\mu/\rho}$ $[\mathrm{m^2/kg}]$ per labMDF specimen type and configuration (energy level and pre-filter), which verify the obvious perception in Figure IV-44 to Figure IV-50. Corresponding to maximum energy E_{max} [kVp] and pre-filter application, the mean radiation energy $\bar{E}$ [keV] of the applied X-ray spectrum (refer to Chapter IV–4.2.6 and IV–4.3.3) increases in the presented order of columns. Accordingly, $\overline{\mu/\rho}$ decreases with increasing $\bar{E}$ within the respective device series. Eventually, the labMDF results reveal both raw density and energy dependency of mass attenuation coefficient where $\overline{\mu/\rho}$ generally decreases with increasing ρ and E. Considering density, the observation applies to both raw and area density which are equivalent in consequence of equal nominal transmission distance $s_{\mathrm{T}} = 50$ mm.

---

[34] Note, measured values correspond to spectra determination on open X-ray beam without additional pre-filter but including 0.635 mm Al detector lid.

W-RDP-35-w/

W-RDP-50-w/
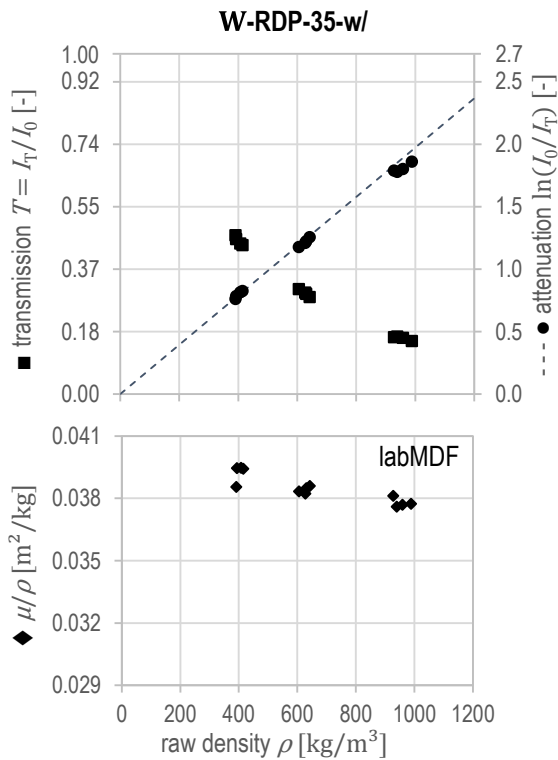
Figure IV-48: Transmission measuring results in dependence of raw density ρ [kg/m^3], with measured relative transmission T, therefrom calculated attenuation $\ln T^{-1}$ with its expected linear slope (dashed line estimation via $\mu/\rho_{\max}$) and consequently computed mass attenuation coefficients μ/ρ [m^2/kg]; determined by means of W-RDP device (Table IV-19) with 1.96 mm Al pre-filter at $U_{a,\text{nom}} = 35$ kV (measured $E_{\max} = 35.4$ kVp, $\bar{E} = 24.2$ keV) on single labMDF specimens (nominal transmission distance $s_\text{T} = 50$ mm) with $\overline{MC} = 9.5$ %.

Figure IV-49: As Figure IV-48; determined by means of W-RDP device (Table IV-19) with 1.96 mm Al pre-filter at $U_{a,\text{nom}} = 50$ kV (measured $E_{\max} = 50.9$ kVp, $\bar{E} = 29.2$ keV) on single labMDF specimens (nominal transmission distance $s_\text{T} = 50$ mm) with $\overline{MC} = 9.5$ %.

Nevertheless, there is furthermore a structural impact along the raw density steps to be discussed elsewhere.

Analogous observations considering energy dependency of $\overline{\mu/\rho}$ can be found in the case of data from customary panels indMDF as well as round robin test samples (MDF and PB), which complete the compilation in Table IV-27 (all conditioned at 20/65, Table IV-5). On the contrary, raw density dependency becomes not clearly obvious, since the present range is comparably small and further effects from panel structure and composition as well as uncertainty of the measurement itself are considered to predominate. Whilst results from W-RDP device reveal only slight variations between the indMDF samples with

$CV = 0.6 \ldots 0.9$ %, the results from Ag-RDP device vary more considerably with $CV = 2.7$ % and $CV = 4.9$ %, respectively, which is considered to be caused by insufficient repeatability and radiation energy drift between the measurements.

For comparison of $\overline{\mu/\rho}$ of labMDF and indMDF, in turn, virtual labMDF values were computed by linear interpolation for $\bar{\rho} = 765$ kg/m^3 of the indMDF samples. The resulting differences apparently depend on the device. In the case of Ag-RDP, indMDF values are approximately 95 % that of labMDF. On the contrary, indMDF results from all W-RDP setups exceed (virtual) labMDF $\overline{\mu/\rho}$ values about $1 \ldots 2$ %. There is apparently no consistent tendency comparing lab-made and customary panels. The latter, however, feature a slightly higher ash content (refer to Table IV-12), which can be considered to cause this insignificant $\overline{\mu/\rho}$ increment at equivalent raw densities in the case of W-RDP results. The actual impact of elemental composition including ash content will comprehensively be discussed in Chapter
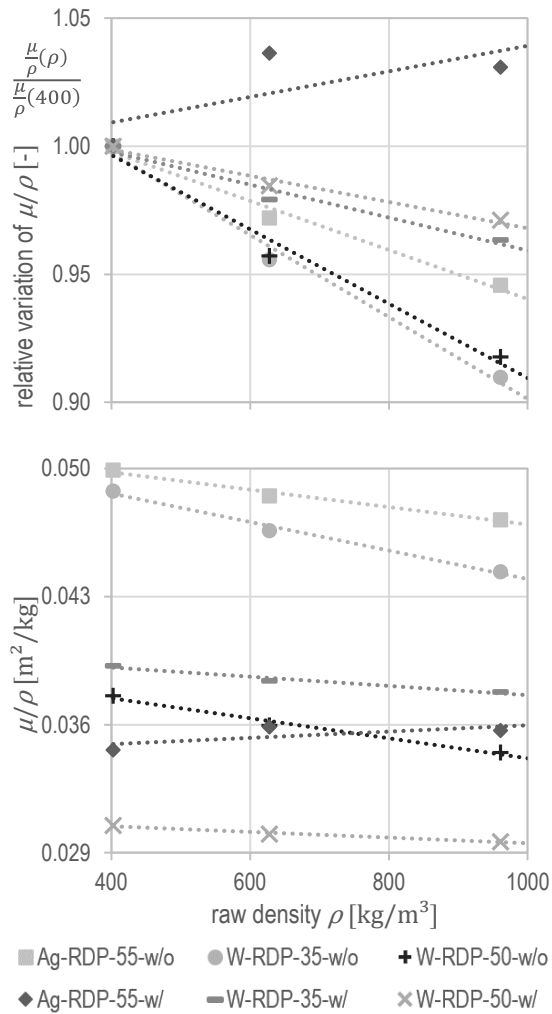
Figure IV-50: Summary of RDP devices transmission measuring results as mass attenuation coefficient μ/ρ [m^2/kg] in dependence of raw density ρ [kg/m^3] and its relative variation computed toward minimum $\rho_{\mathrm{nom}} = 400$ kg/m^3 (plots normalised to unity with $\frac{\mu/\rho(\rho)}{\mu/\rho(400)} = 1$), with linear regression (dashed lines) indicating the trend; for labels and data refer to Table IV-27.

IV–5.1 and IV–5.2. Nevertheless, Ag-RDP $\overline{\mu/\rho}$ variations are attributed to the aforementioned methodical insufficiencies rather than to particular material conditions. Beyond that, the samples from the round robin test facilitate a direct comparison between $\overline{\mu/\rho}$ of customary MDF and PB in general. Accordingly, exemplary PB mass attenuation coefficients are 5…8 % higher than MDF values depending on the device. The consistent differences are, however, primarily attributed to correspondingly lower raw density and respective structural material conditions whereas potential variations in adhesive resin

and additive content are considered to have minor impact as to be pointed out elsewhere.

Besides WBC panels on common densification levels, additionally investigated low-density insulation board reveals increased $\overline{\mu/\rho}$ compared to labMDF as well as indMDF. With respect to the W-RDP device, insulation $\overline{\mu/\rho}$ exceed indMDF values about 10 … 12 % in case of configuration without pre-filter and about 4 … 5 % with pre-filtered beam on both energy levels, respectively, whilst insulation raw density is 28 % that of indMDF. The magnitude of insulation $\overline{\mu/\rho}$ deviation was found to be in an analogous order comparing labMDF400 toward labMDF1056; i. e., about 9 … 10 % (without pre-filter) and about 3 … 4 % (with pre-filter) on both energy levels beyond, respectively, at corresponding 58 % raw density decrement of the specimens. Hence, $\overline{\mu/\rho}$ obviously increases with decreasing raw density at equal composition. The like applies to Ag-RDP device measurements (without pre-filter). The elemental composition (refer to Table IV-15) of the investigated MDI-bonded insulation boards differs, in turn, from all applied UF-bonded MDF. The $\overline{\mu/\rho}$ differences are, however, considered not to be an issue of material composition, which will be comprehensively discussed in Chapter IV–5.1 and IV–5.2 again. Considering insulation vs. indMDF and likewise labMDF400 vs. labMDF1056, the corresponding raw density and $\overline{\mu/\rho}$ differences are in a comparable order per X-ray setup, hence, attributed to structural material conditions. Accordingly, it is rather an issue of radiation spectra, scattering, and propagation, which will comprehensively be discussed in Chapter IV–6.

device			Ag-RDP	Ag-RDP	W-RDP	W-RDP	W-RDP	W-RDP
E_{max} [kVp] via $U_{a,nom}$			55	55	35	35	50	50
Al pre-filter thickness [mm]			w/o	1.5	w/o	1.96	w/o	1.96
$\overline{E}$ [keV]			21.1	21.5	21.5	24.2	26.3	29.2
material (specimen type)	$\overline{\rho}$ [kg/m³]	$\overline{\rho}_A$ [kg/m²]	$\overline{\mu/\rho}$ [m²/kg]					
400	403	20.3	0.0499	0.0346	0.0488	0.0392	0.0376	0.0305
650	628	31.7	0.0485	0.0359	0.0466	0.0384	0.0360	0.0300
1056	961	47.9	0.0472	0.0357	0.0444	0.0378	0.0345	0.0296
labMDF	664	33.3	0.0485	0.0354	0.0466	0.0385	0.0360	0.0300
labMDF virtually @ $\overline{\rho}_{indMDF}$	765	38.2	0.0480	0.0358	0.0457	0.0381	0.0353	0.0298
MDF-3	785	39.3	0.0443	0.0346	0.0454	0.0380	0.0357	0.0300
MDF-8	802	40.1	0.0453	0.0327	0.0455	0.0383	0.0355	0.0300
MDF-10	757	37.9	0.0482	n/a	0.0459	0.0384	0.0359	0.0302
MDF-12	758	37.9	0.0451	0.0321	0.0460	0.0387	0.0361	0.0304
MDF-19	741	37.1	0.0454	0.0322	0.0462	0.0387	0.0360	0.0303
MDF-25	745	37.3	0.0457	0.0358	0.0465	0.0389	0.0363	0.0305
MDF-30	766	38.3	0.0455	n/a	0.0463	0.0389	0.0361	0.0305
indMDF	765	38.2	0.0457	0.0335	0.0460	0.0385	0.0359	0.0303
MDF round robin test	725	36.2	0.0463	0.0388	0.0454	0.0383	0.0343	0.0299
PB round robin test	665	33.2	0.0485	0.0407	0.0491	0.0413	0.0367	0.0319
insulation	218	10.9	0.0468	n/a	0.0514	0.0403	0.0394	0.0314

Table IV-27: Summary of transmission measuring results by both RDP devices Ag-RDP and W-RDP in varying configuration, with $\overline{\mu/\rho}$ [m²/kg] determined as mean mass attenuation coefficient via eq. (II-52) at nominal transmission distance $s_T = 50$ mm of the specimens cut from lab-made (labMDF) and customary (indMDF, round robin test, and insulation) panels, all conditioned at 20/65 with EMC acc. to Table IV-5; for $\overline{E}$ [keV] refer to Chapter IV–4.2.6 and IV–4.3.3.

4.3.2.4 Practical implications

X-ray transmission measurements serve as basis for radiometric determination of area density ρ_A [kg/m²] as well as raw density ρ [kg/m³], which, in turn, correspond to the radiation attenuation within the considered material. The results of the performed transmission measurements, however, unveil characteristics, which are considered to be attributed to both X-ray measuring and WBC material conditions. X-ray densitometry for ρ and ρ_A determination by means of the employed transmission measuring setups eventually follows Beer's law of attenuation as defined in eq. (II-10) as well as eq. (II-11) and their solution for ρ and ρ_A, respectively,

$$\rho = \frac{\ln \frac{I_0}{I_T}}{\frac{\mu}{\rho}(E) \cdot t}$$ (IV-35)

and with $\rho_A = \rho \cdot t$ it becomes

$$\rho_A = \frac{\ln \frac{I_0}{I_T}}{\frac{\mu}{\rho}(E)}$$ (IV-36).

Accordingly, density results are basically proportional to attenuation $\ln T^{-1}$ determined by X-ray transmission measurement as logarithmic ratio of initial to transmitted intensity with $I_T/I_0 = T$, where the energy-dependent reciprocal mass attenuation coefficient $\mu/\rho(E)^{-1}$ serves as constant of proportionality.

Contrary to the theoretical expectation as illustrated in Figure IV-29, it is found that μ/ρ at the individually applied energy level is not constant along the observed measuring range of ρ_A and ρ, respectively. Consequently, the direct influence of μ/ρ variations in the bottom of the fraction in eq. (IV-35) and eq. (IV-36) on the desired

evaluation result becomes obvious. The observed deviations from constant μ/ρ expectation along increasing ρ_A or ρ, respectively, would consequently be reflected on the very same evaluation results (ρ_A or ρ) in the respective order of magnitude of the relative deviation $\Delta\mu/\rho_{rel}$ from expected constancy. Accordingly, relative error $\Delta\mu/\rho_{rel}$ of an applied mass attenuation coefficient yields final error approximation $\Delta\rho_A$ of area density or $\Delta\rho$ of raw density determination by means of a respective X-ray measuring and evaluation setup. Moreover, the application of one single or mean mass attenuation coefficient for attenuation evaluation of X-ray measuring series on inhomogeneous WBC material is no appropriate means of choice. In this regard, the errors of density determination would increase with increasing distance of the actual measuring point in terms of ρ_A or ρ, respectively, from the corresponding density value, where the applied μ/ρ is valid. Eventually, X-ray densitometry on WBCs by means of attenuation measurements generally features no linear slope of $\ln T^{-1}$ and no constant μ/ρ as theoretically expected under ideal conditions (refer to Figure IV-29). Although the character of deviations depends on the actual conditions including, e. g., WBC material structure, transmission setup, and radiation energy, appropriate X-ray measurements on furnish mats and panels require the explicit consideration of the individual μ/ρ slope along the measuring range.

The findings facilitate to deduce the characteristic values for the deviation from ideal conditions of the individually applied X-ray transmission measuring setup, hence, to qualify the setup and its capability for X-ray densitometry. The evaluation comprises

- transmission ranging around $T \approx e^{-1}$, i. e.,
  T_{range} [–] ($T \in \mathbb{Q}^+$; $T \lesssim e^{-1}$),
- ordinate intercept of the exponential transmission T plots at $T < 1$ in comparison to theoretically expected $T = 1$, i. e.,
  $T_{intercept}$ [–] ($T \in \mathbb{Q}^+$; $T \leq 1$), which further reflects deviation of attenuation $\ln T^{-1}$ plots from linear slope, and

- relative variation of mass attenuation coefficient μ/ρ [m²/kg] computed toward μ/ρ_{max} at $\rho_{A,min}$ or ρ_{min}, respectively, of the considered density range, i. e.,
  $\Delta\mu/\rho_{rel}$ [–] $\left(\Delta\mu/\rho_{rel} \in \mathbb{Q}^+; \Delta\mu/\rho_{rel} \leq 1\right)$.

Table IV-28 compiles the respective values of all transmission measurements from both area density (Chapter IV–4.3.2.2) and raw density profile (Chapter IV–4.3.2.3) applications.

Beyond fundamental observations regarding measurements of one material type on the corresponding setup comprising non-linear attenuation and varying μ/ρ along the application range, differences of μ/ρ values are found re-

material device	T_{range} [–]	$T_{intercept}$ [–]	$\Delta\mu/\rho_{rel}$ [–]
ideal conditions	e^{-1}	1.00	1.00
Fmat			
W-mat-16-w/o	0.06...0.80	0.90	0.84
W-mat-20-w/o	0.07...0.63	0.82	0.77
W-mat-25-w/	0.10...0.79	0.98	0.96
indMDF			
W-panel-16-w/o	0.21...0.73	0.95	0.90
W-panel-20-w/o	0.10...0.35	0.83	0.88
W-panel-25-w/	0.15...0.31	0.99	0.99
W-panel-35-w/	0.47...0.93	1.00	1.01
SLmat, CLmat, CLmat			
W-mat-16-w/o	0.25...0.78	0.99	0.94
W-mat-20-w/o	0.07...0.61	0.83	0.80
W-mat-25-w/	0.20...0.82	0.98	0.96
labMDF			
Ag-RDP-55-w/o	0.11...0.39	0.90	0.95
Ag-RDP-55-w/	0.18...0.49	1.00	1.03
W-RDP-35-w/o	0.10...0.36	0.83	0.91
W-RDP-35-w/	0.16...0.47	0.94	0.96
W-RDP-50-w/o	0.17...0.46	0.88	0.92
W-RDP-50-w/	0.23...0.55	0.96	0.97

Table IV-28: Summary of the determined characteristic values for the deviation from ideal conditions of the individually applied X-ray transmission measuring setup, with the values of all transmission measurements from both area density (Chapter IV–4.3.2.2) and raw density profile (Chapter IV–4.3.2.3) applications; note, $\Delta\mu/\rho_{rel}$ was not extrapolated and corresponds to actual T_{range}.

garding equivalent setup and comparable material composition but varying material structure. Therefore, ready-pressed panels feature different μ/ρ compared to pre-compressed furnish mats, i. e., indMDF μ/ρ is roughly 85 ... 90 % that of Fmat considering the present investigations. With respect to RDP determination on panels with distinct raw density gradients, which are represented by the set of lab-made MDF, lab-MDF1056 μ/ρ is about 91 ... 97 % that of lab-MDF400. In both cases, the summarised range is attributed to respective energy and pre-filter conditions of the individual measuring setup. To conclude, decreasing raw density causes increasing mass attenuation coefficients, or vice versa, which will be explained with regard to radiation scattering and spectra elsewhere (Chapter IV–6).

Transferring the findings to common applications of X-ray measuring devices on WBCs in industry and science unveils potential measuring errors on a theoretical level. In the case of radiometric raw density profile determination by means of, e. g., W-RDP-35-w/o setup, the transmission measuring results in Figure IV-46 reveal maximum deviation from linear attenuation slope and theoretically constant μ/ρ of $\Delta\mu/\rho_{\mathrm{rel}} = -9.0$ % along the utilised raw density range $\rho_{\mathrm{nom}} = 400 ... 1056$ kg/m^3 (Figure IV-50). Hence, the application of a mean mass attenuation coefficient $\overline{\mu/\rho}$ for a conventional, e. g., MDF-19 specimen with a corresponding mean raw density about $\bar{\rho} = 750$ kg/m^3 would approximately yield measuring errors for SL ρ_{max} of $\Delta\rho = -40 ... 30$ kg/m^3, i. e., about -4 % raw density deviation in the exemplary case of MDF-19 from round robin test compared to actual $\rho \approx 910$ kg/m^3 SL mean (refer to Table IV-24). The like applies to X-ray measurements for ρ_{A} determination on furnish mats. Here, in-plane ρ_{A} variations within a typical measuring period on one produced product are rather small compared to the vertical gradient of panel RDP. But the total application range of the measuring system may be wide with $\rho_{\mathrm{A}} = 0.8 ... 30$ kg/m^2 considering a modern MDF production line. Here, the application of, e. g., W-mat-20-w/o device with $\mu/\rho = 0.1238$ m^2/kg at $\rho_{\mathrm{A}} = 14.6$ kg/m^2 in the middle of application range (in contrast to the actual

range $\mu/\rho = 0.1827 ... 0.1124$ m^2/kg) would, in turn, cause measuring errors in the order $\Delta\rho_{\mathrm{A}} = -47 ... + 9$ % for the limits of the application range. Let, furthermore, the calibration have been carried out by means of a panel instead of furnish material in the middle of the range ($\rho_{\mathrm{A}} = 14.6$ kg/m^2) corresponding to a customary MDF-19 yielding $\mu/\rho = 0.1084$ m^2/kg, the consequently determined area weight on the very same fibre mat were $\rho_{\mathrm{A}} = 16.7$ kg/m^2, i. e., about $+14$ % above the actual mat area density.

Beyond structural conditions, material composition may generally affect X-ray attenuation. A particular impact of MC on apparent radiation attenuation is found in Figure IV-41 to Figure IV-43 and Table IV-26. Here, the non-linearity of attenuation $\ln T^{-1}$ slope and μ/ρ values vary from OD to standard and moist conditions. Moistening is, nevertheless, just considered as an increase of material mass with comparable elemental composition in terms of mean atomic numbers, which will comprehensively be pointed out in Chapter IV–5.1. Subsequently, more hydrogen (H) is, however, present, where X-ray attenuation is predominated by (incoherent) scattering already in the low-energy range with mass attenuation coefficient for incoherent scattering mechanism $\mu_{\mathrm{incoh}}/\rho\,(12.7\ \mathrm{keV})_{\mathrm{H}} = 0.03630$ m^2/kg compared to the total one $\mu_{\mathrm{tot}}/\rho\,(12.7\ \mathrm{keV})_{\mathrm{H}} = 0.03801$ m^2/kg, which corresponds to 96 % (incoherent) scattering share of total mass attenuation process (refer to Figure VII-29, Table VII-3 in Appendix VII–4). Hence, transmission measuring results and consequently $\mu/\rho\,(\rho_{\mathrm{A}})$ are rather affected by increased scattering share in transmitted radiation with increasing MC. In addition to this practice-oriented observation, the theoretical MC impact will be evaluated in Chapter IV–5.1 and IV–5.2. At more or less constant MC levels, no distinct impact of customary material composition is found with particular respect to indMDF, where μ/ρ values just slightly vary in an equivalent order of magnitude. Nevertheless, further not clearly suppressible influence factors, e. g., material structure, superimpose potential differences between the sample types. Hence, the potential impact of elemental composition on μ/ρ variations will be theoretically pointed out and discussed in Chapter IV–5.2.

Finally, obviously non-ideal conditions of the present X-ray measurements and material-related radiation-physical effects cause deviations from ideal results, hence, yielding neither linear attenuation $\ln T^{-1}$ slope nor constant mass attenuation coefficient μ/ρ along the respective density (ρ_{A} and ρ) range. The transmission measuring results, however, indicate regarding X-ray densitometry on WBCs that

- measuring setup and parameter require reasonable adaption to the individual application range, which is not unlimited, in turn, and
- an approach is required to meet the comprehensive WBC material and X-ray measuring conditions.

4.3.3   Radiation spectra

4.3.3.1   Measurement

Result presentation of evaluated spectra from measurement by means of the spectrometer digiBASE 905-3 is limited to the exclusively applied energy level of Ag- and two representative tube potentials of W-target device, respectively. Note, results always comprise the impact of the $0.635\,\mathrm{mm}$ Al detector lid. Figure IV-51 provides an overview of the selected X-ray spectra, where analogously varied pre-filters and absorbers represent the comprehensively investigated measuring conditions regarding RDP determination. Vertical lines indicate mean energy $\bar{E}$ (dashed) following eq. (II-4) and intensity peak energy E_{peak} (dash-dotted), which facilitate spectra comparison beyond the shape of the plot. Complementarily, Table IV-29 compiles characteristic parameters from evaluation of all considered variations. Furthermore, Figure IV-52 exemplarily illustrates the impact of pre-filtering and varying absorbers, where the pre-filtered W spectra at two energy levels with predefined labMDF ($\rho_{\mathrm{nom}} = 400, 650, 1056\ \mathrm{kg/m^3}, \quad z_{\mathrm{nom}} = 50\,\mathrm{mm}$) as absorbers are compared toward likewise determined spectra without additional Al filter. However, all spectra plots are normalised to unity with $I(E)_{\mathrm{max}} = 1$ for comparison purpose of shifted spectra in consequence of beam hardening as pointed out below. Additionally, in Figure

IV-52 (bottom), spectra are referenced to the respective initial intensity I_0 without absorber for normalisation such that $I(E) = I(E)_{\mathrm{T}}/\sum I(E)_0$, thus, $\sum I(E)_0 = 1$ for initial (no absorber) I_0 spectrum $S_{\mathrm{D},0}(E)$.

As easily can be seen from the presented figures and the data in Table IV-29, all attenuating members within the X-ray beam, regardless of whether pre-filters or specimens as absorbers, affect the transmitted X-ray spectrum $S_{\mathrm{D,T}}(E)$ in comparison to the initially emitted $S_{\mathrm{D},0}(E)$. In this regard, the more or less distinct upward shift of the spectrum and its $\bar{E}$ as well as E_{peak} corresponding to low-energy absorption potential of irradiated matter is commonly known as beam hardening (refer to Chapter II–2.4) whereas E_{max} corresponding to tube potential remains unaltered. The effect considerably occurs in the case of low- to medium-energy continuous bremsstrahlung spectra without superimposed characteristic energies such as the applied W spectra. To this end, Figure IV-52 provides direct comparison of the transmitted spectra $S_{\mathrm{D,T}}(E, \rho_{\mathrm{A}})$ through labMDF (400, 650, and 1056) toward the corresponding initial spectrum $S_{\mathrm{D},0}(E)$ ('no absorber'). Furthermore, numerical evaluation of the upward shifted spectra via $\Delta\bar{E}$ [keV] and ΔE_{peak} [keV] (refer to Table IV-29) facilitates to comparatively quantify beam hardening in consequence of increasing area density $\rho_{\mathrm{A}} = \rho \cdot z$ of respective absorbers. Here, beam hardening appears strongest in case of 'open' spectra on both energy levels already with respect to low-density absorber (labMDF400) with $\Delta\bar{E}_{\mathrm{35kVp}} = 2.3\ \mathrm{keV}$ and $\Delta\bar{E}_{\mathrm{50kVp}} = 2.9\ \mathrm{keV}$, respectively. Pre-filtering with consequent pre-hardening of the initial spectrum, i. e., $\Delta\bar{E}_{\mathrm{35kVp}} = 2.7\ \mathrm{keV}$ and $\Delta\bar{E}_{\mathrm{50kVp}} = 2.9\ \mathrm{keV}$, reduces the beam hardening effect of the specimen (again labMDF) to $\Delta\bar{E}_{\mathrm{35kVp+Al}} = 1.2\ \mathrm{keV}$ and $\Delta\bar{E}_{\mathrm{50kVp+Al}} = 0.8\ \mathrm{keV}$, respectively. The effect is well-known to be amplified with increasing absorber ρ_{A}. However, beam hardening still occurs in case of pre-filtered radiation, but appears less distinct between the specimens, thus, with increasing ρ_{A} of the absorber. Analogous observations are to be found considering ΔE_{peak}. Beyond evaluation of spectrometer

energy resolution, $\mathrm{FWHM}\,[\mathrm{keV}]$ according to eq. (IV-30) is here applied to quantify the impact of beam hardening on bandwidth of the transmitted spectra. Table IV-29 lists the respective values supporting the obvious impression from Figure IV-51. Considering the evaluated continuous bremsstrahlung spectra regardless of AgK_α-lines, pre-filtered 35 kVp W-target tube provides most narrow-band energy distribution of the exemplarily evaluated spectra with $\mathrm{FWHM}_{35\mathrm{kVp+Al}} = 13.1\,\mathrm{keV}$. Subsequently, lab-MDF absorbers cause more narrow-band energy spectra with decreasing FWHM in consequence of increasing absorber ρ_A. Pre-filtered spectra reveal, in turn, less FWHM variations. In addition to evaluation of beam hardening via horizontal shift of the spectra, thus, $\bar{E}$ and E_peak upward variation, as well as analogously decreasing FWHM, I_0-referenced spectra in Figure IV-52 (bottom) facilitate to qualify energy-dependent attenuation by the absorbers, which is likewise quantified by I_T/I_0 in Table IV-29, regardless of uncalibrated intensities from spectrometer. Accordingly, both open and pre-filtered 50 kVp spectra reveal poor intensity contrast between the three absorbers. Furthermore, a pre-hardened spectrum leads to worse attenuation contrast already toward initial intensity. On the contrary, 35 kVp spectra with/without additional pre-filter yield more distinct energy-related radiation attenuation. Here, radiation attenuation occurs consistently over the total energy range whereas particularly pre-filtered 50 kVp spectra rather reveal unaltered $I(E)$ beyond E_peak. Apparently, appropriate application of the latter requires increased absorber ρ_A. Eventually, amongst W spectra, the pre-hardened 35 kVp spectrum appears to be most sufficient with respect to diminished beam hardening and enhanced energy-dependent radiation attenuation.
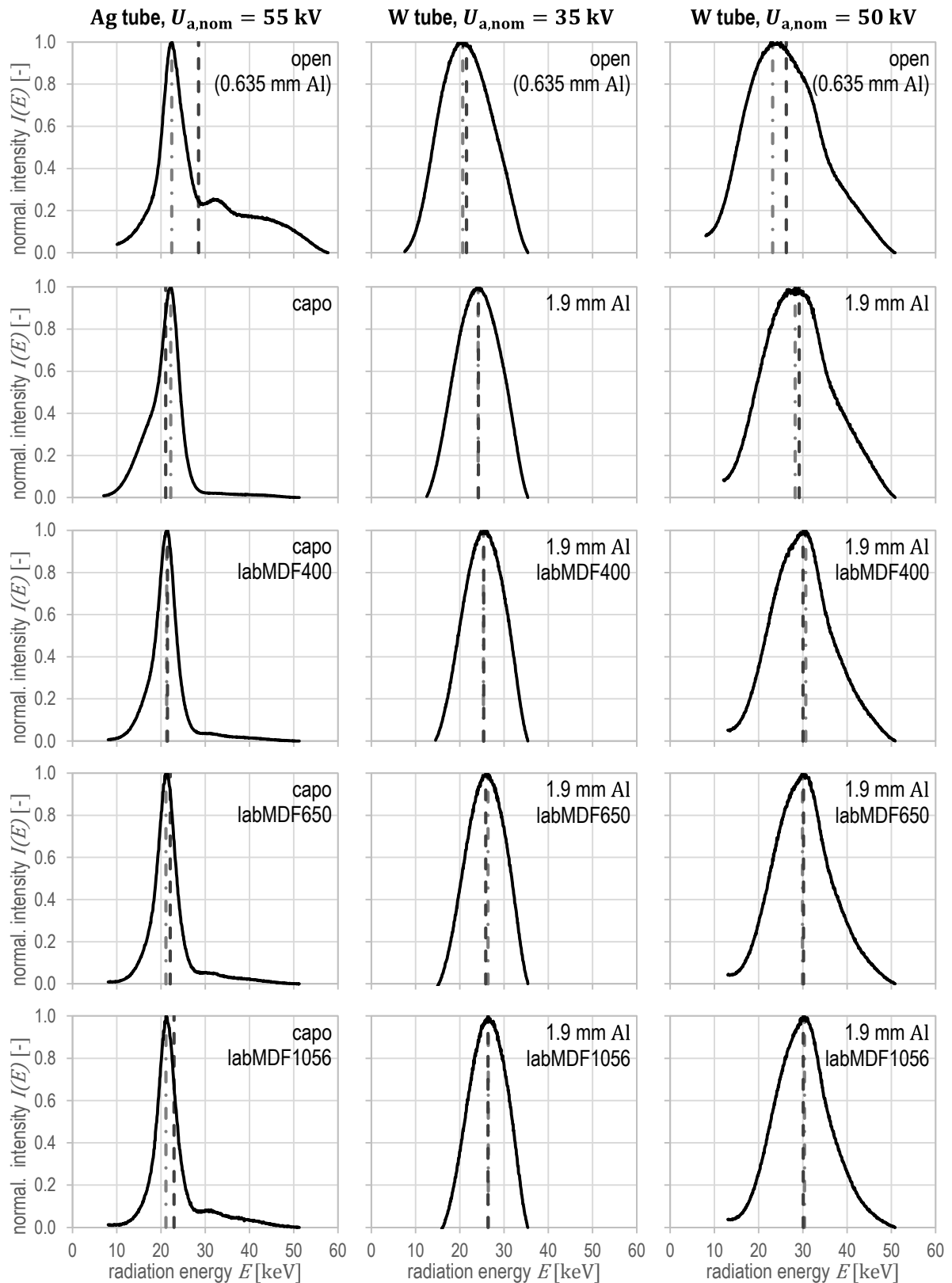
Figure IV-51: X-ray spectra (solid line) as normalised intensity with $I(E)_{\mathrm{max}} = 1$ over calibrated radiation energy E determined by spectrometer digiBASE 905-3 of the employed Ag- or W-target tube at varying $U_{\mathrm{a,nom}}$ directly emitted (open), collimated via capillary optics (capo) or with additional absorbers as pre-filter (Al) and labMDF ($z_{\mathrm{nom}} = 50\,\mathrm{mm}$) but always including $0.635\,\mathrm{mm}$ Al detector lid, complete with $\bar{E}$ (dashed line) and E_{peak} (dash-dotted line).

W tube, $U_{a,nom} = 35$ kV   **W tube, $U_{a,nom} = 50$ kV**
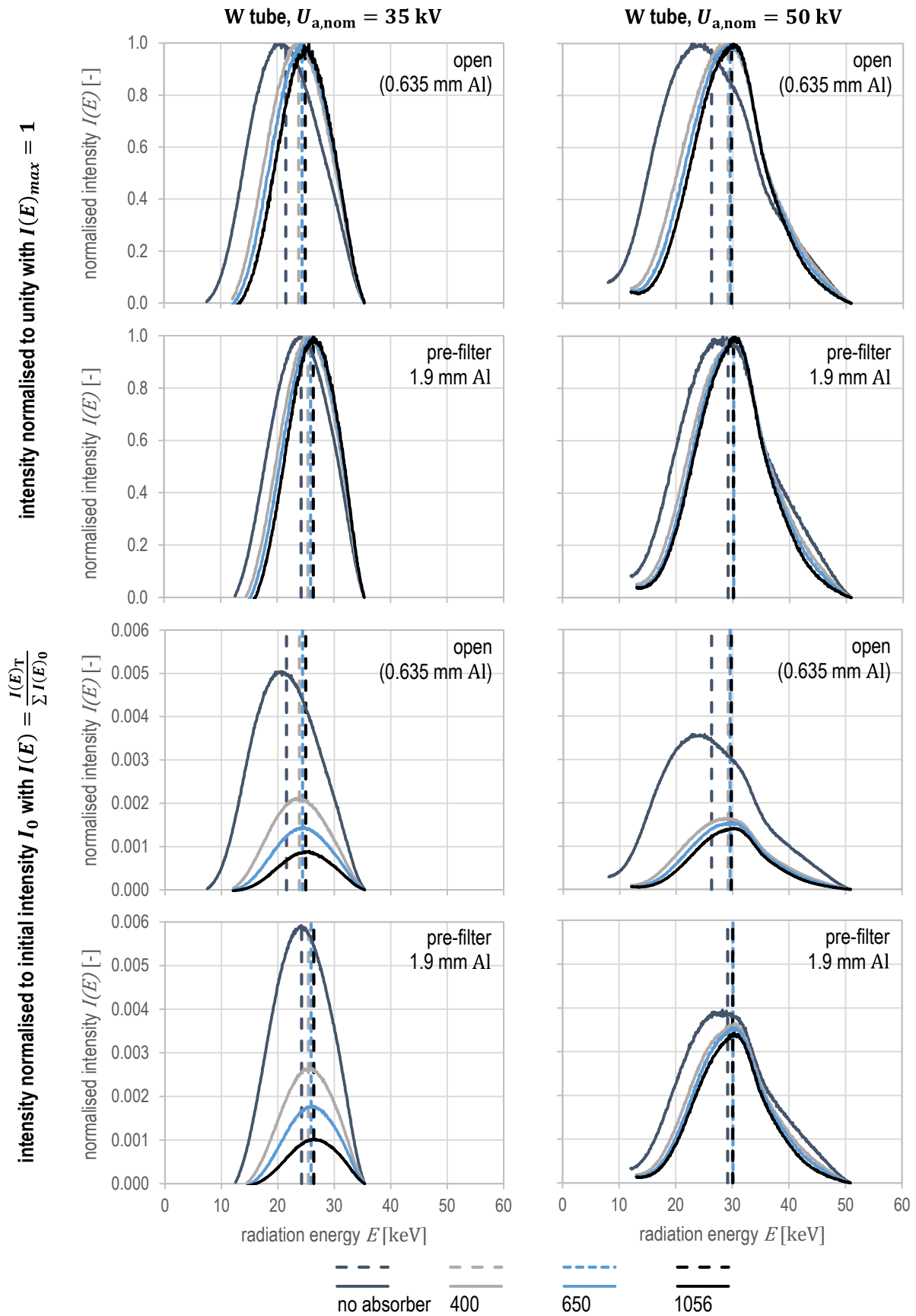
Figure IV-52: Comparison of X-ray spectra (solid lines) as normalised intensity with $I(E)_{max} = 1$ (top) or toward I_0 (bottom) over calibrated radiation energy E determined by spectrometer digiBASE 905-3 of the W-target tube at $U_{a,nom} = 35$ kV (left) or 50 kV (right) without (open) and with additional pre-filter (1.9 mm Al), respectively, but always incl. 0.635 mm Al detector lid, with additional absorbers labMDF ($z_{nom} = 50$ mm), complete with $\bar{E}$ (dashed lines).

X-ray tube target	$U_{a,nom}$ [kV]	pre-filter t [mm] Al	absorber labMDF	E_{max} [kVp]	$\bar{E}$ [keV]	$\Delta\bar{E}$ [keV] ref. to I_0	E_{peak} [keV]	ΔE_{peak} [keV] ref. to I_0	E_{min} [keV]	FWHM [keV]	$I = \sum I(E)$ [cps]	I_T/I_0 [-] = T
Ag	55	0.635	–	57.8	28.5	–	22.4	–	10.0	5.9	4223	–
+ capo		**0.635**	**–**	**51.3**	**21.1**	***-7.4**	**22.2**	***-0.3**	**7.0**	**5.3**	**8477**	I_0
		0.635	400	51.3	21.5	0.4	21.3	-0.9	8.0	4.6	2433	0.29
		0.635	650	51.3	22.1	1.0	21.1	-1.1	8.0	4.6	1285	0.15
		0.635	1056	51.3	22.9	1.8	21.1	-1.1	8.0	4.5	628	0.07
		1.635	–	51.3	21.5	0.5	21.6	-0.6	8.0	4.6	3730	–
W	35	**0.635**	**–**	**35.4**	**21.5**	**–**	**20.7**	**–**	**7.5**	**15.1**	**9874**	I_0
		0.635	400	35.4	23.8	2.3	23.7	3.0	12.0	12.9	3536	0.36
		0.635	650	35.4	24.4	2.9	24.8	4.1	12.0	12.4	2285	0.23
		0.635	1056	35.4	25.0	3.4	25.6	4.9	12.0	11.5	1315	0.13
		1.9	**–**	**35.4**	**24.2**	***2.7**	**24.2**	***3.5**	**12.5**	**13.1**	**11410**	I_0
		1.9	400	35.4	25.4	1.2	25.4	1.2	14.5	11.9	4627	0.41
		1.9	650	35.4	25.9	1.7	26.4	2.2	14.5	11.3	2980	0.26
		1.9	1056	35.4	26.4	2.1	26.4	2.3	14.5	10.7	1624	0.14
W	50	**0.635**	**–**	**50.9**	**26.3**	**–**	**23.2**	**–**	**8.0**	**19.7**	**15146**	I_0
		0.635	400	50.9	29.2	2.9	28.5	5.3	12.0	15.9	5774	0.38
		0.635	650	50.9	29.5	3.3	29.7	6.5	12.0	14.7	5056	0.33
		0.635	1056	50.9	29.8	3.5	30.1	7.0	12.0	13.9	4344	0.29
		1.9	**–**	**50.9**	**29.2**	***2.9**	**28.3**	***5.1**	**12.0**	**17.5**	**5271**	I_0
		1.9	400	50.9	30.0	0.8	30.7	2.4	13.0	15.0	4155	0.79
		1.9	650	50.9	30.1	1.0	29.9	1.7	13.0	14.0	3835	0.73
		1.9	1056	50.9	30.1	0.9	30.4	2.1	13.0	13.4	3515	0.67

Table IV-29: Compilation of characteristic parameters for X-ray spectra determined by spectrometer digi-BASE 905-3 of a Ag- or W-target tube at varying $U_{a,nom}$ considering variations of pre-filtering by Al (always including 0.635 mm Al detector lid) or beam collimation by capillary optics (capo, only Ag tube) and additional absorbers labMDF ($z_{nom} = 50$ mm); *reference to open value (I_0 measurement, resp. first row).

The intended X-ray spectra acquisition within original measuring device setup was only partly obtained. Whereas W-target spectra were acquired by simple replacement of the original detector and additional collimation of the spectrometer maintaining alignment and distances, the Ag-target device required a more elaborate setup modification. Therefore, the representativeness of the latter in comparison to regular measuring alignment is worth discussing. The acquisition of Ag spectra was characterised by crucially increased source-detector (open) and sample-detector distance as well as tight (pinhole) detector collimation (refer to Figure IV-20). Consequently, the measured spectra of transmitted radiation (with specimen) rather consist more or less exclusively of primary intensity I_P with minor scattered radiation I_s share due long specimen-detector distance according to assumptions (refer to Chapter II–2.5). Contrary to this, verifying measurements (short distance, no collimation) were not feasible owing to already mentioned spectrometer restrictions (Chapter IV–4.2.6.1). In the case of W-target device, the position and alignment of the spectrometer surface were equivalent to the original detector conditions but an additional lead aperture with < 1…1.5 mm was also required. Thus, a slightly increased scattering share is expected but again not further quantifiable by the spectrometer setup itself. Prospectively, another type of spectrometer allowing higher intensities facilitates to precisely quantify the contribution of scattered radiation to the transmitted spectrum by means of the aforementioned measures with regard to variations of collimation and travelling distance.

Eventually, the acquired transmission spectra $S_{\mathrm{D,T}}(E, \rho_{\mathrm{A}})$ as in the present case are considered to comprise considerably diminished scattered radiation, thus, more or less exclusively I_{P}, owing to employed setup with long specimen-detector distance (Ag) and pinhole-like collimation (both). Contrary to this, the actual measuring signal of the regular application is superimposed by respective scattering intensity I_{S}.

Beyond scattering considerations, the Ag-target device features capillary optics as quasi-parallel beam collimator, which are found to reveal a significant impact on the emitted spectra as obvious in Figure IV-51. On the other hand, the simplistic beam apertures of the W-target devices evidently have no influence on energy distribution. However, in contradiction to beam hardening, applied capillary optics diminish high-energy spectral share, actually K_β line, yielding $\Delta\bar{E} = -7.4\,\mathrm{keV}$ (Table IV-29) in comparison of 'capo' toward 'open' spectrum. Note, local peak at $32\,\mathrm{keV}$ occurred from another phenomenon, e. g., potential fluorescence, and does not correspond to any characteristic Ag-line whereas $E_{\mathrm{K}_{\beta 1}} = 24.94\,\mathrm{keV}$ (cf. KORTRIGHT, THOMPSON (2009)). Nevertheless, applied capillary optics cause apparent amplification of low-energy share below K_α line in consequence of increased low-energy transmission efficiency (cf. GAO, JANSSENS (2004)) as pointed out in Chapter II–1.3. Therefore, suppressed transmission of radiation with energies beyond $E(\theta_{\mathrm{c}})$ corresponding to the critical angle θ_{c} for total reflection according to eq. (II-7) occurs. However, actual bandpass properties cannot explicitly be presented, since particular optics design is not further specified by the device manufacturer and not obviously identifiable. Regardless of beam collimation, the diminished high-energy share beyond AgK_β-line, thus, the K-edge at $E = 25.51\,\mathrm{keV}$ (cf. HUBBELL, SELTZER (2004)), is to some extent furthermore attributed to the considerably flat radiation take-off angle (6°) from Ag target of the applied long-fine-focus tube, which emphasises the inherent filtering in terms of self-absorption within the target. Furthermore, the apparent impact on $E_{\max}$ is likewise observed. Whilst increased $E_{\max} = 57.8\,\mathrm{kVp}$ is found to remarkably exceed $U_{\mathrm{a,nom}} = 55\,\mathrm{kV}$ the in the case of freely emitted radiation (open), the applied capillary optics yield decreased $E_{\max} = 51.3\,\mathrm{kVp}$ (capo, Table IV-29). In the latter case, however, flat slope of diminished intensity plot toward the upper threshold made accurate $E_{\max}$ determination according to Figure IV-22 difficult. With particular respect to W-target devices, no special component-related conditions are observed.

The applied spectrometer is obviously found to inherently bias its results. During detector dead-time, coincident events on the detector remain uncounted and cause detector pile-up. However, dead-time was maintained reasonably low at appropriate total counting statistics. Thus, potential bias on the obtained results commonly corresponds to the method itself. Beyond that, TSOULFANIDIS (1995) considers dead-time as counting loss and suggests its correction via simple computation of the true counting rate. Nonetheless, he disregards energy-related origin of the counting loss to be corrected.

Furthermore, energy determination is fundamentally based on individual and repeated calibration by means of a known emitter, therefore, worthy of discussion. According to ZSCHERPEL (2015), deviations potentially originate from channel drift during and between temporally separated measurements owing to unstable parameters of PM tube and MCA. The phenomenon particularly becomes obvious from Ag-target results in Table IV-29, where E_{peak} corresponding to characteristic energy $E_{\mathrm{K}_{\alpha 1}} = 22.16\,\mathrm{keV}$ (cf. KORTRIGHT, THOMPSON (2009)) differs between the measuring series more or less considerably. The like is observed in terms of $E_{\max}$ determination, which is, notwithstanding that, consistently defined per energy level. However, apparently shifted characteristic parameters are likewise furthermore attributed to peak identification considering energy resolution of the spectrometer. Again with regard to energy resolution and holistic result quality, the applied spectrometer settings follow well-tested parameters. Note, e. g., maximum shaping time ($2\,\mu s$) yields improved energy resolution but coincidently causes increased dead-time. The applied detector inherently affects its

measuring results in consequence of energy-related scintillator efficiency as well as PM tube and MCA characteristics. Here, the actual detector response function $D(E)$ is unknown but expected to appear rather linear.

Beyond photon counting, 0.635 mm Al detector lid serves as permanent pre-filter with considerable impact on the acquired spectra in terms of consequent beam hardening owing to low-energy radiation absorption. Particularly $E < 10 \ldots 15$ keV, are found to be almost totally absorbed by the lid, thus, uncounted, which becomes obvious from the open spectra in Figure IV-51 (upper row) and all Ag spectra with infinitesimal low-energy intensities. Accordingly, a lower threshold $E_{\min}$ was defined (values in Table IV-29) to enhance subsequent spectral data processing, which was otherwise blurred by Compton background. In the case of further measured, but not yet presented, spectra employing W-target tube with $U_{\mathrm{a,nom}} < 20$ kV, application of the utilised spectrometer is found to be questionable. The inherently filtered low-energy radiation also causes information loss. For further comparative discussions, reference is made to Chapter IV–4.3.3.3. Nevertheless, additional pre-filter for W-target tube with final thickness of 1.9 mm (incl. detector lid) represents an actual device setup. Hence, despite $D(E)$, W spectra are close to real RDP measuring conditions. Furthermore, 1.5 mm Al filter was henceforth utilised for Ag-target device, where reference is made to complementary Ag-target results with 1.635 mm pre-filter in Table IV-29. In the end, however, no further spectrometer was available to verify the obtained results, which is prospectively suggested with particular regard to energy calibration and inherent filtering of the detector.

4.3.3.2   Simulation

Application of the sophisticated but coincidently also convenient XRayTools software facilitated comprehensive spectra modelling with particular consideration of labMDF specimens as predefined absorbers. However, a limited result presentation with corresponding figure and table content is selected in accordance with more time-consuming spectra measurements (Chapter IV–4.3.3.1). Analogously prepared plots again consistently comprise the impact of the similarly modelled 0.635 mm Al detector lid. In this regard, Figure IV-54 provides an overview of the selected Ag and W spectra, which were obtained considering both pre-filter and absorber (labMDF) variation at the respective energy levels. With particular focus on W-target tubes, Figure IV-56 compares spectra with predefined labMDF absorbers to illustrate the impact of increasing raw density at constant transmission distance on energy-dependent radiation attenuation and consequent beam hardening in dependence of pre-filtering. Regarding both figures, Table IV-30 summarises characteristic values to numerically evaluate transmission conditions. With respect to Figure IV-51 and Figure IV-52 as well as Table IV-29, all spectra plots are normalised to unity with $I(E)_{\max} = 1$. In addition, referencing toward corresponding initial intensity via $I(E) = I(E)_{\mathrm{T}}/\sum I(E)_0$ is performed in Figure IV-56 (bottom). Moreover, by default of the simulation software, spectra are modelled without explicit recording of scattered radiation, which likewise serves as preferential mode here. According to DERESCH (2013), inclusion of both coherent and incoherent scattering was initially implemented as a special case for particular applications with gamma-isotopes and is considered to be error-prone for general spectra modelling. Notwithstanding that, modelling of transmitted spectra $S_{\mathrm{T}}(E, \rho_{\mathrm{A}})$ comprising both coherently and incoherently scattered radiation of the respective labMDF absorbers was likewise performed and evaluated for comparative purposes. In analogous representation, Figure IV-55 and Figure IV-57 show all modelled spectra additionally with total recording of scattered radiation. Furthermore, Table IV-30 is extended by respective parameters to characterise the spectra numerically and to enable convenient comparison.

Beyond that, Figure IV-53 exemplarily provides an initial W-target spectrum without any pre-filtering except 0.2 mm Be tube window at $E_{\max} = 35$ kVp, which is obviously dominated by characteristic energies at L level with $E_{\mathrm{L}_{\alpha 1}} = 8.40$ keV and $E_{\mathrm{L}_{\beta 1}} = 9.67$ keV (cf. KORTRIGHT, THOMPSON (2009)). Owing to consistent pre-filtering in the

practical applications, the lines are considerably diminished already in the case of the 'open' spectrum with 0.635 mm Al and totally attenuated by additional absorbers (Figure IV-54). Accordingly, the application of pre-filtered W-target tubes at respectively low energy levels $E_{\max} < 70$ kVp, where K lines are not yet excited, exclusively exploits continuous bremsstrahlung radiation and allows certain adjustment of lower threshold by means of well-chosen pre-filters.

Comparing evaluation of transmitted spectra $S_T(E, \rho_A)$ without scattering recording (default by software) toward the corresponding initial spectrum $S_0(E)$ reveals a consistent impact from pre-filters and labMDF absorbers on the shape of the plot (Figure IV-54 and Figure IV-56), which results in the consequently computed characteristic parameters (Table IV-30). In this regard, modelled spectra fundamentally resemble corresponding measuring results, where, however, for comprehensive comparison reference is made to Chapter IV–4.3.3.3. A fundamental description of spectra appearance regarding applied conditions was already given for the measuring results in Chapter IV–4.3.3.1. Moreover, simulated spectra considering various target materials, tube potentials, pre-filters, and absorbers, correspondingly unveil ideal energy distributions modelled on basis of physical laws, which are implemented in the applied XRayTools software. However, a particularly distinct upward shift of the spectra in consequence of beam hardening becomes again obvious from alteration of mean energy $\bar{E}$ (dashed lines) following eq. (II-4) and intensity peak energy E_{peak} (dash-dotted lines) in Figure IV-54 whereby related values are listed in Table IV-30. The distance between those lines in the figures – particularly in the case of the exclusively continuous W bremsstrahlung spectra without characteristic energies within the applied range – serves furthermore as an estimation of spectra width; i. e., short distance or actually congruence between $\bar{E}$ and E_{peak} indicates comparatively more narrow-band and generally advantageous spectra, where mean energy and maximum intensity coincide. Particularly, FWHM [keV] following eq. (IV-30) in Table IV-30 provides the respective numerical evaluation fa-
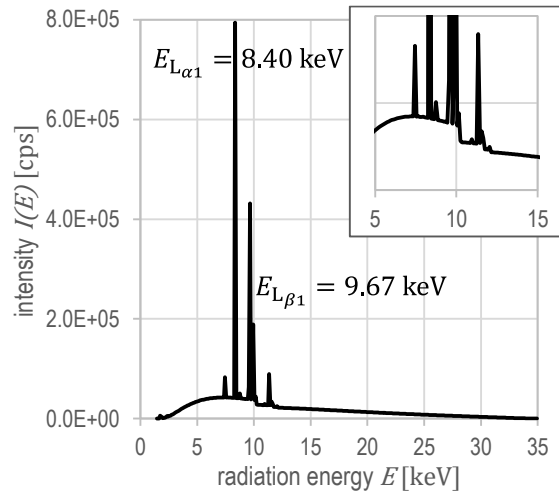
Figure IV-53: Exemplary X-ray spectrum simulated by XRayTools software of a W-target tube at $E_{\max} \equiv U_{\text{a,nom}} = 35$ kV without any additional pre-filter (except 0.2 mm Be tube window), complete with most dominant L energies and inset with respective close-up, without (default by software) recording of scattered radiation.

cilitating precise comparison of energy distribution width by means of an established figure. The aforementioned indication for beam hardening unveils the strongest effect in the case of 'open' spectra (without additional pre-filter but inherently including 0.635 mm Al detector lid) for all source types, where distinctness increases with increasing $\rho_A = \rho \cdot z$ of respective absorbers. Here, beam hardening already considerably occurs in consequence of radiation attenuation by low-density absorber (labMDF400) and reaches maximum for high-density absorber (labMDF1056) with $\Delta\bar{E}_{55kVp} = 6.8$ keV (Ag), $\Delta\bar{E}_{35kVp} = 4.8$ keV, and $\Delta\bar{E}_{50kVp} = 6.2$ keV, respectively. Moreover, pre-filtering causes intended pre-hardening and reduces, in turn, beam hardening in the same specimen to $\Delta\bar{E}_{35kVp+Al} = 2.6$ keV and $\Delta\bar{E}_{50kVp+Al} = 3.7$ keV, respectively, in the case of the W spectra. The effect, however, cannot be eliminated at all. The like respectively applies to ΔE_{peak} results.

Beyond evaluation of regularly modelled spectra without scattering, the simulation results with recording of both coherently and incoherently scattered radiation reveal comparable beam hardening characteristics (refer to '+S' in Figure IV-55 and Table IV-30 as well as total Figure IV-57),

where, nonetheless, slight but remarkable differences occur. Here, a decreased spectra shift in consequences of apparently diminished beam hardening is observable. The above considered high-density absorber (labMDF1056) yields $\Delta\bar{E}_{55\text{kVp+S}} = 5.6\ \text{keV}$ (Ag), $\Delta\bar{E}_{35\text{kVp+S}} = 4.3\ \text{keV}$, and $\Delta\bar{E}_{50\text{kVp+S}} = 5.3\ \text{keV}$, respectively. Regarding pre-filtered W-target spectra with recording of absorber scattering again, evaluation results in $\Delta\bar{E}_{35\text{kVp+Al+S}} = 2.1\ \text{keV}$ and $\Delta\bar{E}_{50\text{kVp+Al+S}} = 2.8\ \text{keV}$, respectively. Eventually, the recording of scattering causes individually decreased $\bar{E}$ (for all considered X-ray sources) and likewise downward shifted E_{peak} (except in case of Ag spectra). However, scattering intensities I_S superimpose transmitted primary intensities I_P behind the absorber. Due to incoherent (inelastic) scattering along with energy transition beyond coherent (elastic) interaction, total distribution of scattered radiation is rather shifted toward lower energies, which, in turn, potentially undergoes further attenuation processes. Consequently, scattered radiation from labMDF absorbers is considered to cause medium-energy apparent intensity increment. The effects become obvious from comparison of the lower spectra in Figure IV-56 (without) and Figure IV-57 (with scattering), respectively, which are normalised by referencing to corresponding $I(E)_0$, where $S_T(E, \rho_A)$ with scattering recording reveal considerably higher intensities in dependence of the virtually penetrated absorber. Table IV-30 provides particular intensity values $I = \sum I(E)$. Furthermore, computed total transmission $T = I_T/I_0$ facilitates evaluation of energy-related attenuation on basis of simulation data (last column in Table IV-30) to theoretically determine the most appropriate intensity contrast conditions for the intended transmission application.
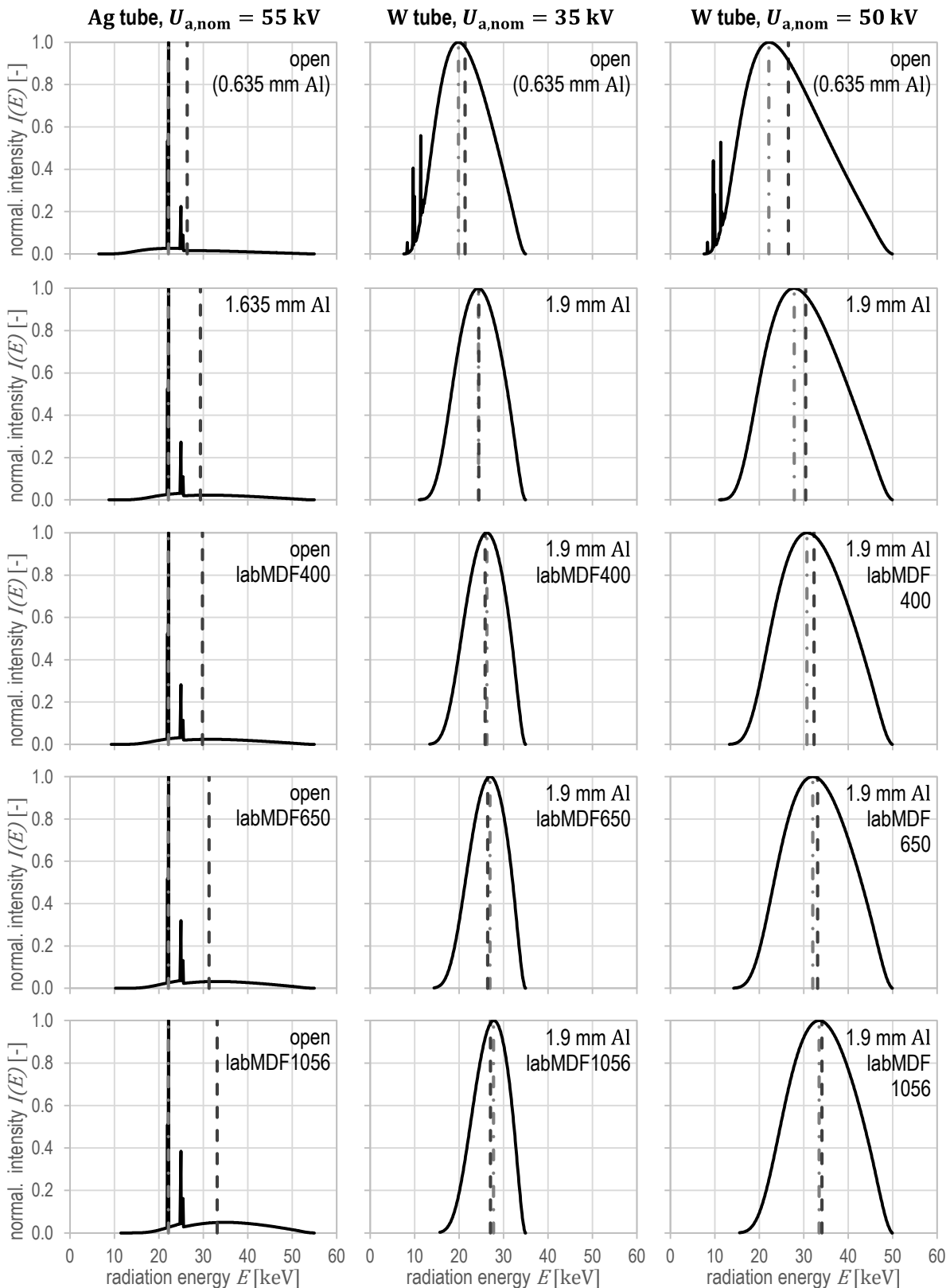
Figure IV-54: X-ray spectra (solid line) as normalised intensity with $I(E)_{\max} = 1$ over radiation energy E simulated by XRayTools software of a Ag- or W-target tube at varying $U_{a,\text{nom}}$ directly emitted (open) or with additional absorbers as pre-filter (Al) and labMDF ($z_{\text{nom}} = 50$ mm) but always including 0.635 mm Al (corresponding to spectrometer lid), complete with $\bar{E}$ (dashed line) and E_{peak} (dash-dotted line), without (default by software) recording of scattered radiation (in contrast to Figure IV-55).
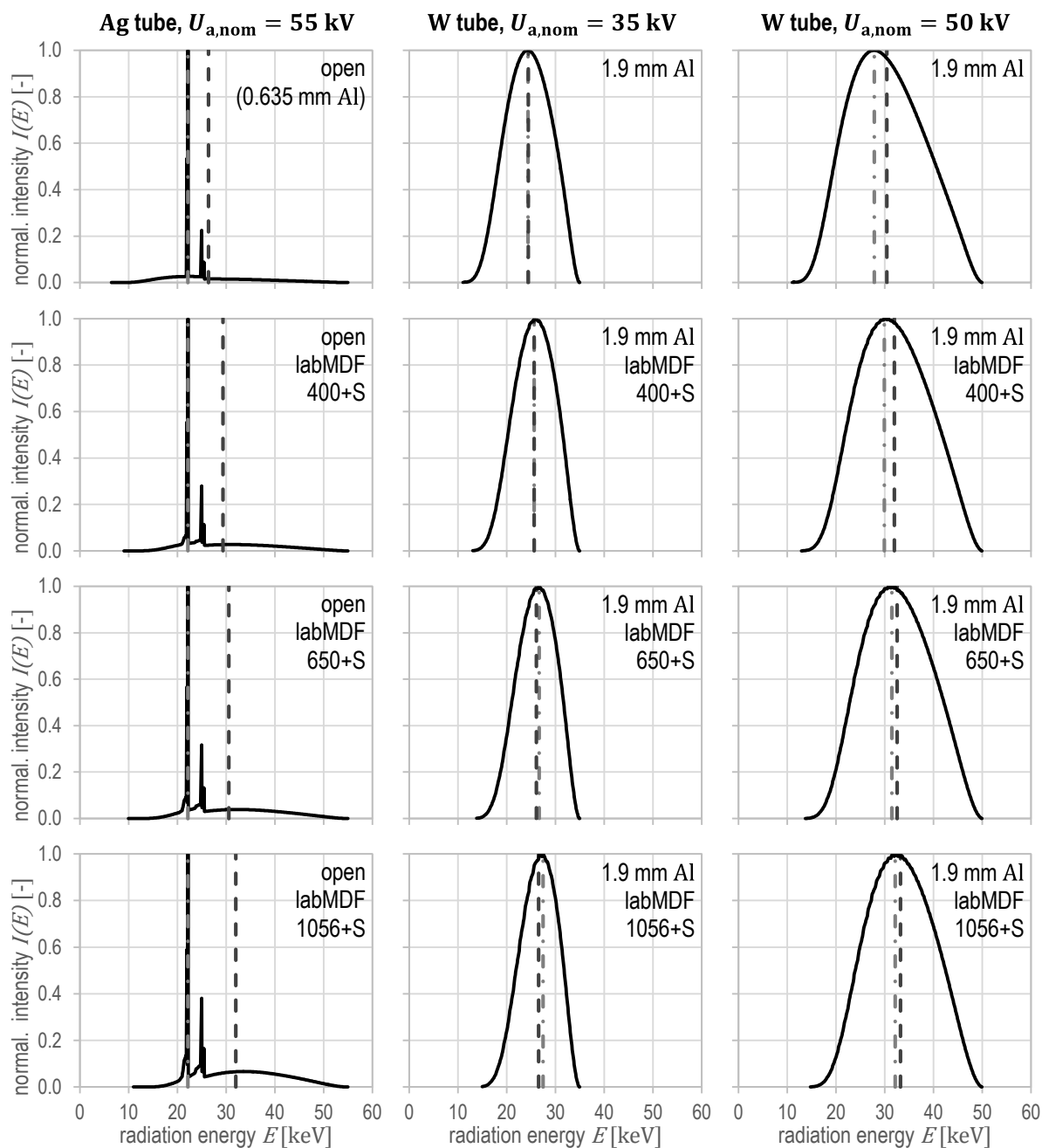
Figure IV-55: X-ray spectra (solid line) as normalised intensity with $I(E)_{\max} = 1$ over radiation energy E simulated by XRayTools software of a Ag- or W-target tube at varying $U_{\mathrm{a,nom}}$ directly emitted (open) or with additional absorbers as pre-filter (Al) and labMDF ($z_{\mathrm{nom}} = 50$ mm) but always including 0.635 mm Al (corresponding to spectrometer lid), complete with $\bar{E}$ (dashed line) and E_{peak} (dash-dotted line), with (+S) recording of scattered radiation (in contrast to Figure IV-54).

Figure IV-56: Comparison of X-ray spectra (solid lines) as normalised intensity with $I(E)_{max} = 1$ (top) or to I_0 (bottom) over radiation energy E simulated by XRayTools software of a W-target tube at $U_{a,nom} = 35$ kV (left) or 50 kV (right) without (open) and with additional pre-filter (1.9 mm Al), respectively, but always incl. 0.635 mm Al (corresp. to spectrometer lid), with additional absorbers labMDF ($z_{nom} = 50$ mm), complete with $\bar{E}$ (dashed lines), without (default by software) recording of scattered radiation (in contrast to Figure IV-57).

Figure IV-57: Comparison of X-ray spectra (solid lines) as normalised intensity with $I(E)_\mathrm{max} = 1$ (top) or to I_0 (bottom) over radiation energy E simulated by XRayTools software of a W-target tube at $U_\mathrm{a,nom} = 35$ kV (left) or 50 kV (right) without (open) and with additional pre-filter (1.9 mm Al), respectively, but always incl. 0.635 mm Al (corresp. to spectrometer lid), with additional absorbers labMDF ($z_\mathrm{nom} = 50$ mm), complete with $\bar{E}$ (dashed lines), with (+S) recording of scattered radiation (in contrast to Figure IV-56).

X-ray tube target	$U_{a,nom}$ [kV]	pre-filter t [mm] Al	absorber labMDF	E_{max} [kVp]	$\overline{E}$ [keV]	$\Delta\overline{E}$ [keV] ref. to I_0	E_{peak} [keV]	ΔE_{peak} [keV] ref. to I_0	E_{min} [keV]	FWHM [keV]	$I = \sum I(E)$ [cps]	I_T/I_0 [-] = T
Ag	55	0.635	–	55	26.4	–	22.2	–	6.4	< 1	8.558E+09	I_0
		0.635	400	55	29.8	3.4	22.2	0.0	9.2	< 1	3.183E+09	0.37
		0.635	650	55	31.3	4.9	22.2	0.0	10.2	< 1	1.984E+09	0.23
		0.635	1056	55	33.1	6.8	22.2	0.0	11.4	< 1	1.063E+09	0.12
		0.635	400+S	55	29.3	3.0	22.2	0.0	9.0	< 1	4.273E+09	0.50
		0.635	650+S	55	30.5	4.2	22.2	0.0	9.9	< 1	3.124E+09	0.37
		0.635	1056+S	55	32.0	5.6	22.2	0.0	10.9	< 1	2.099E+09	0.25
		1.635	–	55	29.4	3.0	22.2	0.0	8.7	< 1	4.852E+09	–
W	35	0.635	–	35	21.3	–	19.9	–	7.5	14.8	1.060E+06	I_0
		0.635	400	35	24.3	3.0	24.1	4.2	11.0	12.8	2.860E+05	0.27
		0.635	650	35	25.2	3.9	25.4	5.5	12.4	11.9	1.580E+05	0.15
		0.635	1056	35	26.1	4.8	26.7	6.8	14.0	10.9	7.226E+04	0.07
		0.635	400+S	35	24.1	2.7	23.8	3.9	10.8	12.7	3.933E+05	0.37
		0.635	650+S	35	24.8	3.5	24.8	4.9	12.0	11.8	2.587E+05	0.24
		0.635	1056+S	35	25.6	4.3	25.7	5.8	13.3	10.8	1.522E+05	0.14
		1.9	–	35	24.4	*3.1	24.4	*4.5	11.0	12.7	3.822E+05	I_0
		1.9	400	35	25.8	1.4	26.3	1.9	13.3	11.2	1.384E+05	0.36
		1.9	650	35	26.4	2.0	27.0	2.6	14.3	10.6	8.212E+04	0.21
		1.9	1056	35	27.1	2.6	27.8	3.4	15.6	9.8	4.016E+04	0.11
		1.9	400+S	35	25.6	1.2	25.7	1.3	13.0	11.1	1.879E+05	0.49
		1.9	650+S	35	26.1	1.6	26.7	2.3	13.8	10.6	1.324E+05	0.35
		1.9	1056+S	35	26.6	2.1	27.5	3.1	14.9	9.8	8.309E+04	0.22
W	50	0.635	–	50	26.6	–	22.2	–	7.5	21.6	2.661E+06	I_0
		0.635	400	50	30.3	3.7	27.6	5.4	11.0	21.1	1.005E+06	0.38
		0.635	650	50	31.5	4.9	29.5	7.3	12.4	20.6	6.423E+05	0.24
		0.635	1056	50	32.8	6.2	31.5	9.3	13.9	19.9	3.547E+05	0.13
		0.635	400+S	50	29.9	3.3	27.5	5.3	10.8	20.7	1.343E+06	0.50
		0.635	650+S	50	30.8	4.3	28.4	6.2	11.9	20.2	1.004E+06	0.38
		0.635	1056+S	50	31.9	5.3	30.0	7.8	13.2	19.3	6.950E+05	0.26
		1.9	–	50	30.4	*3.8	27.9	*5.7	11.0	21.0	1.369E+06	I_0
		1.9	400	50	32.3	1.9	30.8	2.9	13.2	20.0	6.343E+05	0.46
		1.9	650	50	33.1	2.7	32.1	4.2	14.2	19.6	4.264E+05	0.31
		1.9	1056	50	34.1	3.7	33.5	5.6	15.5	18.9	2.471E+05	0.18
		1.9	400+S	50	32.0	1.5	30.0	2.1	12.9	19.9	8.381E+05	0.61
		1.9	650+S	50	32.6	2.1	31.5	3.6	13.7	19.3	6.578E+05	0.48
		1.9	1056+S	50	33.2	2.8	32.2	4.3	14.7	18.5	4.765E+05	0.35

Table IV-30: Compilation of characteristic parameters for X-ray spectra simulated by XRayTools software of a Ag- or W-target tube at varying $U_{a,nom}$ considering variations of pre-filtering by Al (always including 0.635 mm Al corresponding to spectrometer lid) and additional absorbers labMDF ($z_{nom} = 50$ mm), without (default by software) and with (+S) recording of scattered radiation; *reference to open value (I_0 measurement, resp. first row).

Regarding simulation of the Ag-target spectra, the special setup modification required for spectra measurement were not explicitly modelled in terms of, e. g., distances and aperture diameters as described and discussed in Chapter IV–4.2.6.1 and Chapter IV–4.3.3.1, respectively. However, regarding modelling, geometric conditions are more a matter of eventually resulting intensities than of spectra shape or potential scattering impact. The same applies to modelling of the W-target device. Nonetheless, Ag spectra are dominated by the K lines within the lower third of the energy distribution. Moreover, energy resolution of the modelling software and a more detailed close-up on the plots facilitate to distinguish between K_{α} and K_{β} characteristic energies (refer to inset in Figure IV-59). From the increasing flat peak beyond the K lines of the plots around $E \approx 35\,\mathrm{keV}$ in Figure IV-54 and Figure IV-55, related diminution of low-energy intensities $I(E)$ becomes obvious clarifying beam hardening again. Hence, owing to intensity normalised to unity via $I(E)_{\max} = 1$, share of higher energies in attenuated spectra increases while lower are absorbed. The increment of $\Delta \bar{E}$ values in Table IV-30 supports this conclusion whereas constant $\Delta E_{\mathrm{peak}} = 0$ are attributed to $E_{\mathrm{peak}} = E_{K_{\alpha 1}} = 22.16\,\mathrm{keV}$ (cf. KORTRIGHT, THOMPSON (2009)). On the contrary, no explicit consideration of capillary optics was possible by the performed spectra modelling, hence, their impact cannot further be theoretically discussed beyond the measuring considerations above (Chapter IV–4.3.3.1).

To revisit the aforementioned impact of scattered radiation, which is recorded by spectra modelling in additional simulations, result validity requires critical discussion but can, ultimately, not be reliably verified. However, the results with scattering recording appear reasonable and facilitate an estimating evaluation of scattering impact from low-Z absorbers such as applied lab-MDF. Particularly, a comparison between analogously created Figure IV-56 (without) and Figure IV-57 (with scattering) reveals qualitative implications and Table IV-30 provides respective characteristic parameters. Accordingly, scattered radiation causes

- actually increased transmitted intensity I_{T} in terms of computed transmission $T = I_{\mathrm{T}}/I_0$, which is consistently beyond scattering-free spectra, and
- apparently diminished beam hardening with less distinct spectra upward shift according to decreased $\Delta \bar{E}$ and ΔE_{peak}

to summarise the observed impact with individual characteristic regarding the transmitted spectra. Furthermore, FWHM is more or less equivalent to the respective scattering-free spectra in consequence of an intensity increment again, which, in turn, primarily occurs within the mid-level energy range from scattered radiation behind the absorber. Nevertheless, modelled spectra including scattering serve as first theoretical approximation with convenient results whereas corresponding experimental determinations are elaborate and require careful consideration of result quality owing to setup (distance and collimation) and spectrometer impact. According to DERESCH (2013), default settings of XRayTools software without recording of scattered radiation rather yield reliable results whereas inclusion of both coherent and incoherent scattering was initially implemented as special case. Thus, scattering-free spectra have to be considered as more valid. However, beyond labMDF absorbers, the applied filters (including detector lid) were consistently modelled without scattering recording, where likewise potential fluorescence was omitted. Hence, particular variations within the final spectra with scattering recording are attributed to the impact of the labMDF specimens, where both coherent and incoherent scattering as attenuation mechanisms play a major role owing to the range of effective atomic numbers Z_{eff} and radiation energy.

Finally, the simulation results obtained using XRayTools software are considered to be free of methodical errors due to the established spectra modelling based on physical laws, where output reliability corresponds to input quality and proper operation. The set properties of the applied and likewise modelled components follow, as far as possible, manufacturer specifications and additional information. Filter material is simplified as pure Al. Absorber composition and physical

properties are based on comprehensive characterisations (Chapter IV–1.5) and analyses (Chapter IV–2, with all subsections). With respect to spectra measurements (refer to Chapter IV–4.3.3.1), 0.635 mm Al spectrometer lid was consistently taken into account leading to corresponding pre-hardening and causes, however, loss of low-energy information, which, in turn, becomes obvious from exemplarily modelled initial W spectrum in Figure IV-53 directly from the tube. On the contrary, practical applications without any pre-filter are rare and rather technically restricted. However, potential systematic result falsification is exclusively attributed to non-consideration of detectors for lack of particular information and potentially corresponding distorting effects by the respective detector response function $D(E)$ whereas following discussions in Chapter IV–4.3.3.3 partly reveal remarkable similarities to measurements. With further regard to the method, appropriately chosen energy resolution (0.1 keV) could actually be enhanced (by one power to ten) but yields already sufficient discretisation with clear distinguishability between K_α and K_β lines in coordination with convenient software performance. The validity of the modelled spectra with scattering recording from absorbers has generally not yet been verified but still provides, however, viable data for exploratory studies on energy-related scattering impact. Notwithstanding particular but minor insufficiencies, spectra simulation by means of XRayTools software serves as a convenient method for the estimation of radiation energy distributions based on precisely known or empirically varied component parameters in further dependency of transmission through likewise modelled filters and absorbers with actually analysed or virtually defined properties.

To eventually revisit the absorber conditions, labMDF was modelled using mechanically determined properties (refer to Table IV-23) of the measured specimens. In this regard, the simulation software assumingly considers the material to be a solid, homogenous, and non-porous body with the respectively predefined density and evenly distributed chemical elements along beam path. Such solid-body considerations fundamentally contradict the conceptual beam path

model through WBCs, which is developed in Chapter IV–3 and summarised in Figure IV-12, on mesoscopic, microscopic, and sub-microscopic scale. However, the conditions on the macroscopic level are met. Hence, the obtained simulation results are not able to viably reflect structural absorber conditions particularly regarding the transmission of scattered radiation. Neglecting scattered radiation, in turn, which potentially undergoes secondary or multiple attenuation processes, simulated spectra without recording of scattering, where exclusively primary intensities I_P are transmitted through the respective absorber, are considered not to be affected by actual absorber structures. Further empirically inferred, spectra with scattering recording solely represent the actual energy distribution to a limited extent because beyond radiation absorption, the likelihood of interaction and propagation of scattered photons considerably depends on structural conditions, such as porosity of the total body and true density of the condensed matter, along the beam path as well as its geometry. WBC structures as described in Chapter IV–3 are not considered, and actually not even known, by the modelling algorithms. Chapter IV–6 deepens this discussion with final implications regarding radiation propagation through WBCs.

4.3.3.3   Comparison

Figure IV-59 (Ag target) Figure IV-58 (W target) illustrate and compare the obtained results from spectra measurement and simulation exemplarily as transmitted spectra with $S_\mathrm{D,T}(E, \rho_\mathrm{A})$ and without detector impact $S_\mathrm{T}(E, \rho_\mathrm{A})$, respectively, through the medium-mass absorber labMDF650 and the applied pre-filter (1.9 mm Al only in case of W spectra). Note again, all plots and data inherently comprise the impact of the 0.635 mm Al spectrometer lid. In the case of Ag tube comparison (Figure IV-59), spectra plots with normalisation to respective I_0 was omitted owing to the dominance of the K_α line impeding any benefit from this method of presentation. Eventually, Table IV-31 provides a re-compilation of selected characteristic parameters from Table IV-29 and Table IV-30 for comparison in numbers.
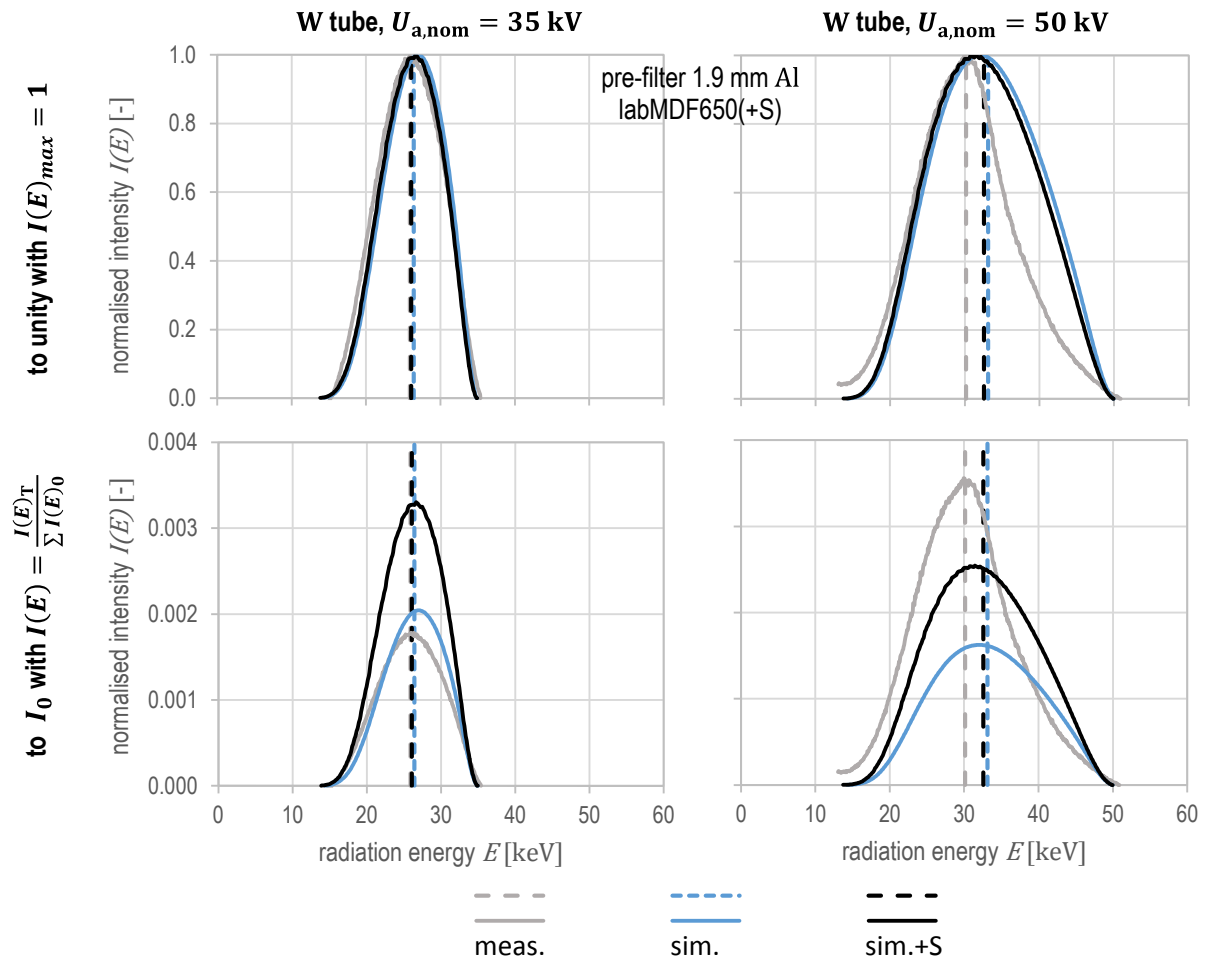
Figure IV-58: Comparison of X-ray spectra (solid lines) as normalised intensity with $I(E)_{\max} = 1$ (top) or to respective I_0 (bottom) over radiation energy E of a W-target tube at $U_{a,\mathrm{nom}} = 35\,\mathrm{kV}$ (left) or $50\,\mathrm{kV}$ (right) with pre-filter (1.9 mm Al incl. 0.635 mm Al spectrometer lid) and with absorber labMDF650 ($z_{\mathrm{nom}} = 50\,\mathrm{mm}$), measured by spectrometer digiBASE 905-3 (meas.) or simulated by XRayTools software (sim.) without (default by software) as well as with (+S) recording of scattered radiation, complete with $\bar{E}$ (dashed lines).

X-ray tube target	$U_{a,\mathrm{nom}}$ [kV]	pre-filter t [mm] Al	method (spectra)	$E_{\max}$ [kVp]	$\bar{E}$ [keV]	$\Delta\bar{E}$ [keV] to meas.	E_{peak} [keV]	ΔE_{peak} [keV] to meas.	$E_{\min}$ [keV]	FWHM [keV]	$I = \sum I(E)$ [cps]	I_T/I_0 [-] $= T$
Ag	55	0.635	meas.	51.3	22.1	–	21.1	–	8	4.6	1.285E+03	0.15
Ag	55	0.635	sim.	55	31.3	9.2	22.2	1.0	10.2	< 1	1.984E+09	0.23
Ag	55	0.635	sim.+S	55	30.5	8.5	22.2	1.0	9.9	< 1	3.124E+09	0.37
W	35	1.9	meas.	35.4	25.9	–	26.4	–	14.5	11.3	2.980E+03	0.26
W	35	1.9	sim.	35	26.4	0.5	27.0	0.6	14.3	10.6	8.212E+04	0.21
W	35	1.9	sim.+S	35	26.1	0.2	26.7	0.3	13.8	10.6	1.324E+05	0.35
W	50	1.9	meas.	50.9	30.1	–	29.9	–	13	14.0	3.835E+03	0.73
W	50	1.9	sim.	50	33.1	3.0	32.1	2.1	14.2	19.6	4.264E+05	0.31
W	50	1.9	sim.+S	50	32.6	2.5	31.5	1.5	13.7	19.3	6.578E+05	0.48

Table IV-31: Comparison of characteristic parameters for X-ray spectra of a Ag- or W-target tube at varying $U_{a,\mathrm{nom}}$ partly with pre-filter (1.9 mm Al incl. 0.635 mm Al spectrometer lid) or capillary optics (meas., only Ag tube) and with absorber labMDF650 ($z_{\mathrm{nom}} = 50\,\mathrm{mm}$), measured by spectrometer digiBASE 905-3 (meas.) or simulated by XRayTools software (sim.) without (default by software) as well as with (+S) recording of scattered radiation; re-compilation from Table IV-29 and Table IV-30 and re-evaluation of $\Delta\bar{E}$ and ΔE_{peak} (to meas.).
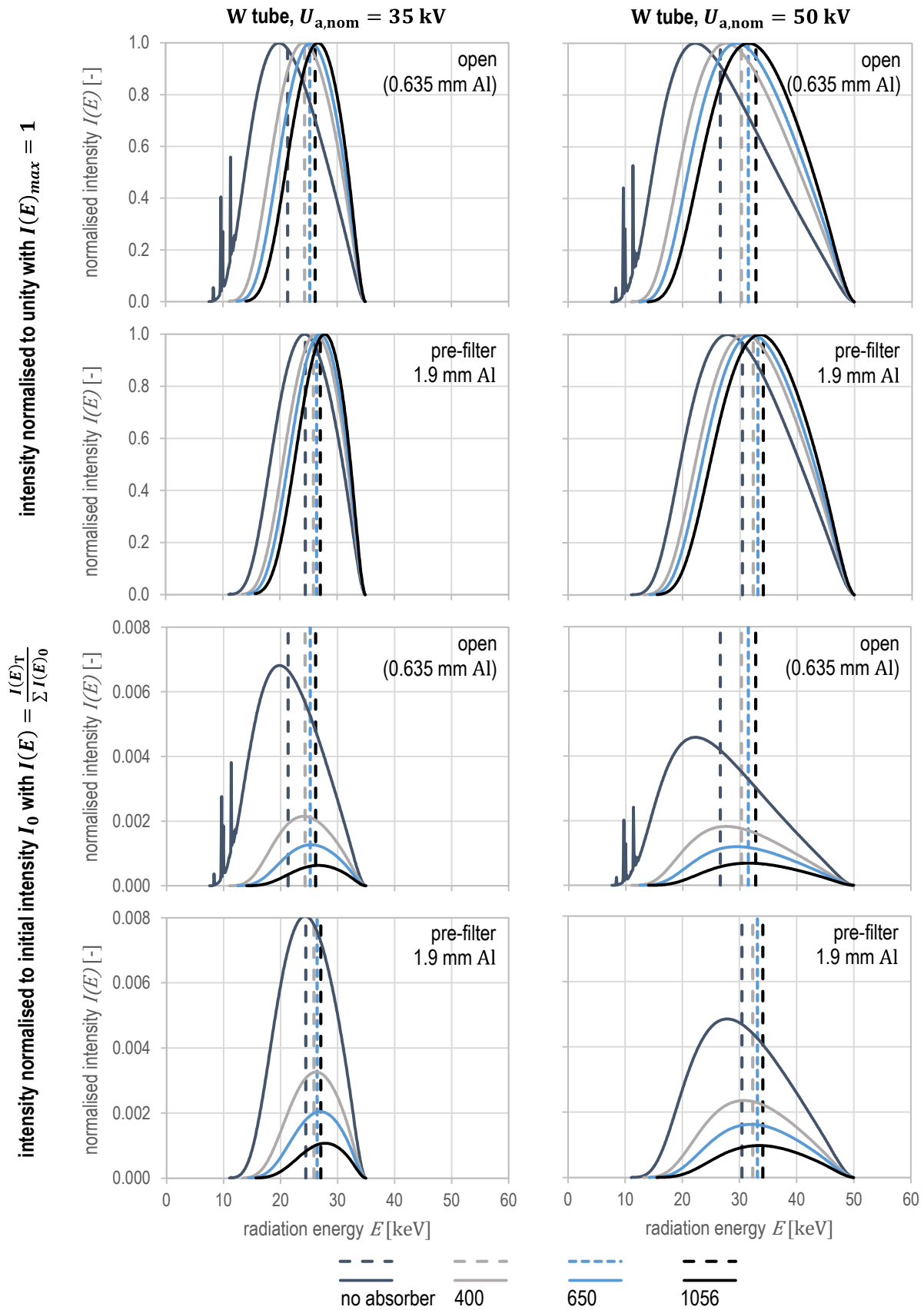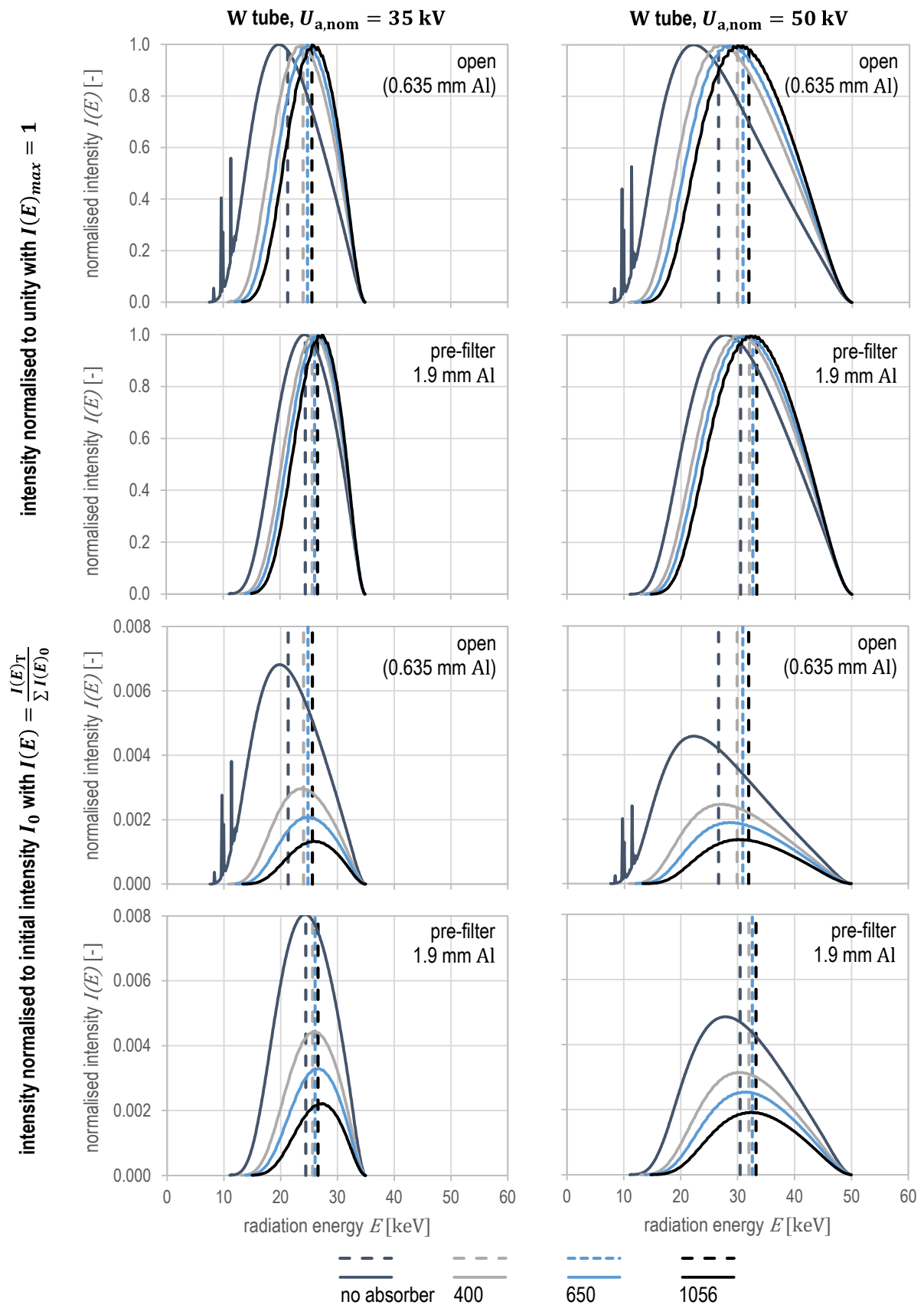
Ag tube, $U_{\mathrm{a,nom}} = 55\,\mathrm{kV}$
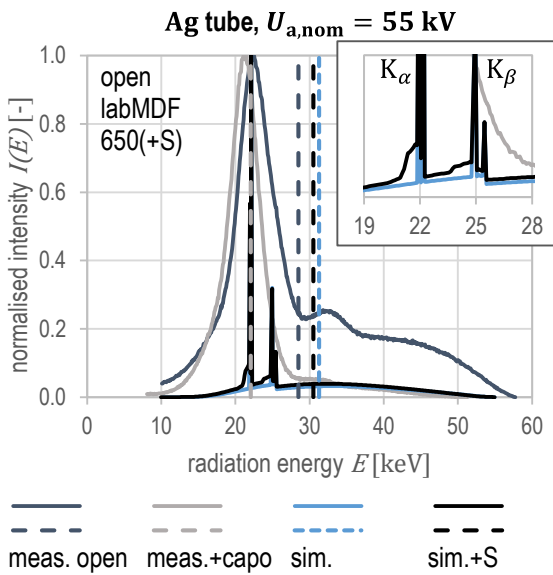
Figure IV-59: Comparison of X-ray spectra (solid lines) as normalised intensity with $I(E)_{\max} = 1$ over radiation energy E of a Ag-target tube at $U_{\mathrm{a,nom}} = 55\,\mathrm{kV}$ without pre-filter (but incl. 0.635 mm Al spectrometer lid) and with absorber labMDF650 ($z_{\mathrm{nom}} = 50\,\mathrm{mm}$), measured by spectrometer digiBASE 905-3 incl. capillary optics (meas.+capo) or simulated by XRayTools software (sim.) without (default by software) as well as with (+S) recording of scattered radiation, complete with $\bar{E}$ (dashed lines) and initial spectrum $S_{\mathrm{D,0}}(E)$ (meas. open); inset with close-up around the K lines with $E_{\mathrm{K}_{\alpha 1}} = 22.16\,\mathrm{keV}$ and $E_{\mathrm{K}_{\beta 1}} = 24.94\,\mathrm{keV}$.

In general, partly remarkable similarities between measurement and simulation are observable. Accordingly, both a limited impact of the detector behaviour $D(E)$ of the spectrometer as well as reliably modelled spectra are empirically to be concluded. Although, measuring results were generally considered to be biased due to methodical insufficiencies (Chapter IV–4.3.3.1). Obviously, the latter occurs, however, solely to some extent. Regardless of non-consideration of detector response $D(E)$, 0.635 mm Al spectrometer lid was consistently taken into account by both methods, which enhances comparability. Beyond that, simulation was performed neglecting detector impact, thus, inherently results in unbiased linear characteristic along the total energy range. Contrary to this, spectrometer data fundamentally comprise particular detector response function $D(E)$, which could not be precisely qualified but assumingly reveals, however,

a rather linear characteristic as well without obvious amplification of particular energies. Nevertheless, acquired spectra are particularly biased with respect to low-energy range $E < 15\,\mathrm{keV}$, where the characteristic W-target L-lines are totally eliminated by the spectrometer Al lid, which was likewise modelled. Further impact of the applied NaI(Tl) detector with subsequent PM and MCA from the very same components is far beyond regularly possible operator influence and only more or less variable in terms of replacement by another spectra acquisition method.

Despite all efforts to keep both methods systematically comparable, certain differences occur between spectra measuring and simulation results. General discrepancies potentially occurring between ideal expectation by simulation and actually measured spectra are attributed to both simulation as well as measuring aspects and their consequent combination such as

- inherent filtering of spectrometer lid (but additionally modelled) and scintillator with resulting lower energy threshold,
- disregarded and actually unknown $D(E)$ of spectrometer,
- energy resolution of spectrometer,
- slight inaccuracy in component modelling owing to missing parameters,
- scattering consideration, and,
- transmission setup with restricted distances and aperture dimensions.

Contrary to common insufficiencies, particular results of measurement and modelling are found to be in good agreement with and almost congruent to each other in the case of W-target tube at $U_{\mathrm{a,nom}} = 35\,\mathrm{kV}$ whereas considerable differences occur in the case of 50 kVp-spectra (W target). Furthermore, Ag-spectra comparison apparently unveils more discrepancies, which require further discussion. The measured spectra do not allow differentiation to be made between the K_{α} and K_{β} line, where the latter is included in the downward slope along increasing energy of the 'open' plot in Figure IV-51 in contrast to the steeper decline of the 'capo' plots. Complementarily, Figure IV-59 presents a direct comparison of the discussed spectra, where the applied capillary optics apparently diminish the K_{β} line like

also the energies beyond. Moreover, the measurement yields comparatively lower intensities of the K lines owing to the actual energy resolution, where the obtained $\mathrm{FWHM_{Ag,meas.}} = 4.6\,\mathrm{keV}$ is more than appropriate at all. Subsequently, e. g., K_α photons are, however, not precisely assigned to E_{K_α} resulting in widened energy distribution around the intensity peak and decrement of the very same. Despite this, $E_{\mathrm{peak}} = 22.16\,\mathrm{keV}$ remains equivalent for all obtained Ag spectra whereas observed $\Delta E_{\mathrm{peak}} = 1\,\mathrm{keV}$ is attributed to the aforementioned channel drift during measurement according to ZSCHERPEL (2015). Further detailed evaluation regarding the K lines surroundings (inset in Figure IV-59) unveils slightly increased intensity of the continuous energy distribution directly below each K line of the simulated spectrum with scattering recording toward the scattering-free one. The phenomenon is assumingly attributed to methodical insufficiencies of scattering recording by the modelling algorithm and henceforth neglected. Beyond peak intensity, total transmission $T = I_{\mathrm{T}}/I_0$ corresponds to the respective conditions. Here, the differences between both simulations with $T_{\mathrm{sim.}} = 0.23$ and $T_{\mathrm{sim.+S}} = 0.37$ are attributed to scattering recording whereas the considerably decreased measuring value $T_{\mathrm{meas.}} = 0.15$ clearly indicates impact of transmission setup with long distances and tight apertures, thus, diminished scattering recording, as well as capillary optics with energy-related radiation collimation characteristics. The latter furthermore causes $E_{\mathrm{max}} = 51.3\,\mathrm{keV}$ distinctly below $U_{\mathrm{a,nom}} = 55\,\mathrm{kV}$. Nevertheless, the impact of capillary optics with crucial attenuation of high-energy radiation beyond the K lines corresponding to the sophisticated properties (e. g. critical angle θ_{c} and intensity gain) of the very same could not be simulated by the applied version of the simulation software, since actual transmission efficiency as a function of radiation energy was not available. Obviously, enhanced low-energy transmission through capillary optics appears as a contrasting phenomenon to beam hardening, where low energies are absorbed by pre-filters of the specimens themselves.

Contrary to the Ag-spectra discussion above, the W-spectra comparison unveils less considerable discrepancies and has significant material-related implications. The observed differences between measured and simulated 50 kVp-spectra with labMDF absorbers as obvious from Figure IV-58 are attributed to actually recorded scattered radiation, which reaches the detector despite tight collimation and occurs from predominant Compton scattering as attenuation process within WBCs for $E > 25\,\mathrm{keV}$. Scattering recording, in turn, results in a remarkably apparent intensity increment at medium and lower energy level yielding increased radiation transmission $T_{\mathrm{50kVp,meas.}} = I_{\mathrm{T}}/I_0 = 0.73$ and the obviously irregular concave slope toward E_{max} of the normalised intensity distribution. Coincidently, scattering causes correspondingly decreased mean radiation energy again in consequence of incoherent (inelastic) Compton interaction with distinctly lower $\bar{E}_{\mathrm{50kVp,meas.}} = 30.1\,\mathrm{keV}$ and respective $\Delta\bar{E}_{\mathrm{50kVp,sim.}} = 3.0\,\mathrm{keV}$ as well as $\Delta\bar{E}_{\mathrm{50kVp,sim.+S}} = 2.5\,\mathrm{keV}$ compared to the measurement. Regarding simulation results, the observed phenomenon does not occur in the case of modelling with scattering recording, where, contrary to measurement, intensities are uniformly increased. Moreover, the observed concave slope toward E_{max} is commonly attributed to the effect of extrafocal radiation on spectra, where backscattered electrons within the X-ray tube cause emission of rather soft radiation beyond the focal spot (cf. NAGEL (2003)). The phenomena can, however, not be distinguished in the present case. As easily can be concluded regardless of extrafocal radiation, the findings are attributed to the structural material conditions of the investigated labMDF and consequently WBCs in general. In the case of spectra acquisition subsequent to actual radiation transmission through labMDF, scattered radiation previously undergoes secondary or multiple interaction processes within the specimen primarily with further incoherent scattering, which finally reaches the detector. Consequently, the additionally detected scattering intensity I_{S} superimposes the primary beam I_{P} on detector causing the remarkable downward shift of the observed energy dis-

tribution. On the contrary, equivalence of measured and both simulated 35 kVp-spectra (normalised to unity, top in Figure IV-58) is attributed to the energy range $E < 25\,\text{keV}$ with minor occurrence of Compton scattering and rather elastic photon scattering interaction beyond predominant photoelectric absorption. Hence, subsequently apparent intensity increment consistently occurs over the total energy range and corresponds, however, to the initial intensity $I(E)_0$. The intensity-related intensity increase becomes obvious in Figure IV-58 (bottom, normalised to I_0) comparing simulation results without and with scattering recording. Here, the simulation with scattering recording (sim.+S) indicates distinctly higher intensities with $T_{35\text{kVp,sim.+S}} = 0.35$ toward $T_{35\text{kVp,sim.}} = 0.21$ and $T_{35\text{kVp,meas.}} = 0.26$, because of the absence of any collimation in the modelling, whereas spectra measuring setup is characterised by pinhole-like detector collimation, which reduces the share of scattered radiation from the specimen (meas.) but does not eliminate its presence. Beyond the observed almost congruent energy distributions of the 35 kVp-spectra, respective mean energies $\bar{E} \approx 26\,\text{keV}$ (Table IV-31 and dashed lines in Figure IV-58) are approximately equal. Ultimately, spectra simulation results beyond common applications with homogenous absorbers always require critical evaluation and preferably metrological verification. Particularly in the case of X-ray transmission through inhomogeneous, porous low-Z composites such as WBCs, a remarkable structural impact on radiation attenuation, thus, transmitted spectra is found with subsequent detector influence.

4.3.3.4   Practical implications

As easily can be concluded from the performed spectra determination, the applied methods indicate different information content with respect to the actual X-ray measuring setup. Firstly, measured spectra represent both initially emitted as well transmitted radiation energy distributions behind a source, pre-filter or specimen but in front of the actual device detector. Since the latter was replaced by a spectrometer, actual detector behaviour is not taken into account by the

acquired spectra, which, in turn, comprise the response function $D(E)$ of the spectrometer. Despite pre-hardening by 0.635 mm Al spectrometer lid, results are considered to show unbiased energy distributions, which are either responsible for or caused by radiation interaction within specimen. However, measurements by an additional detector yield initial $S_{\text{D},0}(E)$ and transmitted $S_{\text{D,T}}(E, \rho_\text{A})$ X-ray spectra rather influenced by spectrometer than device detector. Beyond detection, spectra distortion by geometrical conditions occurs for reasons of spectrometer setup. Owing to the pinhole-like detector aperture and partly long specimen-detector distance required by the acquisition method, spectra measurements fail to record application-related scattered radiation commonly resulting in diminished scattering share. Secondly, spectra simulation yields results according to predefinitions and underlying physical conditions with potential consideration of all X-ray transmission setup members from source over pre-filters and absorbers to detector on demand. Hence, spectra modelling by means of a capable software (like the present) can, however, only provide as valuable results as the input parameters are comprehensively considered. Since the detector was omitted for reasons of simplification, simulation results represent initial $S_0(E)$ or transmitted $S_\text{T}(E, \rho_\text{A})$ X-ray spectra without the influence of a detector and consideration of actual geometrical conditions.

Beyond methodical conclusions, obtained results from spectra determination under consideration of varying labMDF absorbers indicate material-related beam hardening and facilitate quantifying its distinctness via spectra shift as a first approximation. For detailed WBC-related implications with further respect to quantified attenuation conditions, reference is made to Chapter IV–6. However, in the case of measurement as well as simulation with scattering recording, upward spectra shift with $\Delta\bar{E}$ and ΔE_{peak} in consequence of beam hardening by low-energy absorption is superimposed by rather low- and medium-energy scattered radiation emitted from the specimens in dependence of the very same, in turn.

To revisit the scattering discussion, the impact of scattering intensity I_S on actual spectra under regular measuring conditions has to be taken into account. In this regard, the effective energy distribution of scattered radiation $S_{T,S}(E, \rho_A)$ is unknown from measurement and not directly provided by simulation. However, comparison of respective sets of simulation data facilitates a quantification as first approximation, where the approach is explored in Chapter IV–6.3. Supposedly, evaluation will yield a similarly hardened continuous energy distribution ranging with its peak at rather low energy levels. Expected scattering spectrum is considered to correspond to energy range and predominant attenuation mechanisms (refer to Figure II-3 and Appendix VII–4), where consequently equivalent interaction effects with potentially multiple coherent and incoherent scattering as well as low-energy absorption occur. Prospectively, a verification by measurements via spectra acquisition with beam alignment closer to the real setup conditions, i. e., with particular respect to distances and detector collimation, is hardly realisable owing to the sensitive spectrometer detector with event limitation to approximately 10,000 cps.

Moreover, the findings from spectra investigations indicate that X-ray tube target and pre-filter material can be utilised to manipulate radiation energy distribution beyond the definition of $E_{\max}$ via $U_{a,\mathrm{nom}}$. Below their dominant characteristic energy $E_{K_{\alpha 1}} = 59.32\,\mathrm{keV}$ (cf. KORTRIGHT, THOMPSON (2009)), spectra from a W-target tube are found to enable rather free shaping of the employed energy distribution by means of appropriate pre-filter application. In this regard, e. g., the rather low $E_{\max}$ and excessive pre-filtering yields narrow-band continuous spectra with $\mathrm{FWHM} \approx 10\,\mathrm{keV}$, which is, however, not monoenergetic. Contrary to this, target materials with characteristic energies within the regularly applied energy range such as Ag limit the described flexibility but yield in combination with capillary optics, which rather absorb high- energy radiation, quasi-monoenergetic X-ray spectra with dominating characteristic lines. Accordingly, the high-Z target material W, which is widespread in NDT applications, provides maximum flexibility within low-energy range. Ag and further

medium-Z target materials such as Cr, Fe, Co, Cu, and Mo, which are common in analytical applications, concentrate energy distribution to the respective K_{α} energy with dominant intensity. Respective free selection of materials for an intended energy (cf. KORTRIGHT, THOMPSON (2009)) theoretically appears viable but is practically not applicable, since X-ray tube targets are restricted due to required durability and further physical properties. Beyond target material, geometrical aspects influence especially low-energy distribution of the spectra, where particularly flat anode angles cause increased inherent filtering with consequent pre-hardening. While W-target tubes provide comprehensive flexibility, devices for particular applications employing explicitly one energy level rather prefer appropriate narrow-band spectra with superimposed high-intensity characteristic line from corresponding material. Considering pre-filter material, Al is preferable to Cu because of an unfavourable absorption edge of the latter at $E = 8.98\,\mathrm{keV}$ (cf. HUBBELL, SELTZER (2004)) whereas Al comes without absorption edges in the considered energy range and consequently provides steady low-energy absorption without attenuation jumps. Regardless of this, absorption edges are specifically applied to cut out K_{β} radiation for particular purposes in analytical investigations. To this end, the pre-filter material is chosen following the rule $Z_{\mathrm{filter}} = Z_{\mathrm{target}} - 1$ resulting, e. g., in the inconvenient and rare metal $_{46}\mathrm{Pd}$ in case of $_{47}\mathrm{Ag}$-target. Pre-filter thickness, as easily can be seen from Figure IV-52 and Table IV-29, is appropriately chosen aiming at consequent pre-hardening in the order of open-beam hardening considering the raw density range of investigated specimens by the intended application. Nevertheless, beam hardening in consequence of radiation transmission through specimens cannot be eliminated but sufficiently diminished by material- and energy-adapted radiation pre-filtering as already discussed in Chapter II–2.4.2. Eventually, spectra simulation is a valuable method for providing an estimation regarding energy-related X-ray transmission conditions through WBCs. It conveniently facilitates also virtual variations. Nevertheless, exclusively spectra

measurements make it possible to actually consider the impact of structural conditions with significant impact on spectra characteristic in the case of the present inhomogeneous porous WBC matter. However, spectra acquisition procedures have to be considered to potentially be biased by themselves with respect to inherent beam hardening and detector response $D(E)$.

Henceforth, conclusions made on the basis of the findings from spectra investigations and further experimental and theoretical considerations are purposefully applied in Chapter IV–6.4 for practice-oriented energy choice and spectra modelling. To this end, as pointed out above, XRayTools software serves as convenient method for the estimation of radiation energy distributions in dependence of adjustable parameters of radiation generation, virtually variable pre-filters, and further absorbers representing the specimens, which cause radiation attenuation. Consequently, simulation is a rapid tool for theoretical pre-selection of process parameters in terms of X-ray energy choice and spectra shape but requires individual experimental verification. Finally, the most appropriate spectra are characterised by pre-filtered, rather narrow-band energy distributions evaluated by FWHM and E_{max} corresponding to the maximum material amount in terms of area density ρ_{A} to be penetrated aiming at sufficient transmission conditions indicated by total transmission $T = I_{\mathrm{T}}/I_0$. In this regard, intensity loss from pre-filter absorption is to be compensated by respective tube current I_{a} increment, which, in turn, is restricted by maximum power and heat generation. Well-chosen predefined filters consequently cause more or less equivalent beam hardening like the maximum area density of the considered measuring range, where beam hardening is, in turn, not totally eliminated but diminished at best within the area density range under investigation. However, distinct gradients of ρ and ρ_{A} within the investigated cross-section or area of the specimens cause correspondingly varying beam hardening characteristic. The same applies to scattered radiation superimposing the spectra. Both effects become obvious from Figure IV-51 to Figure IV-52 and Figure IV-54 to Figure IV-57 as well as Table IV-29 and Table IV-30, where

comparison of the three investigated nominal raw density levels reveals consistently increasing $\Delta\bar{E}$ and ΔE_{peak} with increasing raw density of the labMDF absorbers. Furthermore, a diminished energy shift is observed in the case of spectra with scattering recording. Eventually, X-ray measurements on WBCs fundamentally feature raw density dependent beam hardening and scattering superposition of the transmitted radiation. Moreover, the spectra characteristic consequently alters along the actual beam path.

Beyond the performed spectra measurements and simulations, a fundamentally different approach is explored and consequently proposed as a complementary practice-oriented method as well as for prospective verification of the obtained results. Since measured spectra contain the spectrometer characteristics (Chapter IV–4.2.6.1) and detector behaviour is not explicitly considered in simulations (Chapter IV–4.2.6.2), comprehensive description of the actual setup conditions is still pending and more or less attributed to applied methods. The like applies to structural conditions of WBC absorbers, where their impact is not consistently considered so far owing to detector collimation and distance restrictions from spectrometer and unfeasible modelling in first convenient attempt. Hence, the appropriate approach introduced by SILBERSTEIN (1932) as pointed out in Chapter II–1.2 was explored as follows. Notwithstanding the latest highly sophisticated methods for spectra simulation and metrological determination by means of energy-discriminating detectors, which require respective equipment, X-ray spectra are accordingly estimated, in turn, by means of acquired filtration curves; i. e., spectra are deduced from simple transmission measurements. Regardless of rigorous enhancement by SILBERSTEIN (1933), the initial approximate solution of integral equation by SILBERSTEIN (1932), however, is henceforth examined for simplicity. The approach provides rather rough estimations but involves nondemanding and affordable data acquisition, which inherently comprises characteristics of all setup components, i. e., even the applied detector, and beam geometry.

Owing to consistently performed energy-related transmission considerations in this thesis, the

wavelength-based historic approaches according to eq. (II-5) and (II-6) were respectively transformed and linear attenuation $\mu \cdot t$ was further replaced by equivalent mass attenuation $\mu/\rho \cdot \rho_A$ accomplishing the system of linear equations

$$f(E_1) + f(E_2) + \cdots + f(E_5) = 1$$

$$e^{-\frac{\mu}{\rho}(E_1)\cdot\rho_{A,2}} \cdot f(E_1) + e^{-\frac{\mu}{\rho}(E_2)\cdot\rho_{A,2}} \cdot f(E_2) + \cdots + e^{-\frac{\mu}{\rho}(E_5)\cdot\rho_{A,2}} \cdot f(E_5) = T_2 \quad \text{(IV-37)}$$

$$\text{...} \quad \text{...}$$

$$e^{-\frac{\mu}{\rho}(E_1)\cdot\rho_{A,5}} \cdot f(E_1) + e^{-\frac{\mu}{\rho}(E_2)\cdot\rho_{A,5}} \cdot f(E_2) + \cdots + e^{-\frac{\mu}{\rho}(E_5)\cdot\rho_{A,5}} \cdot f(E_5) = T_5$$

with $\rho_{A,i} = \rho \cdot t_i$ representing single layer filter thickness in terms of area density. For the performed measurements, the number of equations and unknowns $n = 5$ is particularly attributed to applied $n - 1 = 4$ layers of filters and free transmission through air ($i = 1$). Filters as predefined absorbers of $t_{\text{nom}} = 1.0$ mm Al were specified following SILBERSTEIN (1933) with respect to present radiation penetration potential, sufficiently low first-layer thickness t_2, and, however, coincidently reduced effort. Regardless of not further specified Al alloy, common $\rho_{\text{Al}} = 2.7$ g/cm^3 was taken into account. Exploratory measurements were performed by means of a W-target tube at $U_{\text{a,nom}} = 50$ kV resulting in simple transmission data $T(\rho_{A,i}) = I_T/I_0$ for each sequentially stacked filter layer. For evaluation, the system of linear equations of eq. (IV-37) was solved computer aided yielding $f(E_i)$. The obtained $n = 5$ data points correspond to discrete energy steps of $\Delta E = (E_{\text{max}} - E_{\text{min}})/n = 10$ keV, where $f(E_i) \equiv I(E_i)$ represent the intensities at predefined E_i. Exemplary results for measurements without (open) and with initial pre-filter (1.9 mm Al) are plotted in Figure IV-60, where the W-target device for RDP measurement with its actual operating setup and conditions as described in Chapter IV–4.2.3 was employed. Regarding precise solution of eq. (IV-37), the method was found to be crucially sensible toward accurate $\mu/\rho (E_i)$ for the energy steps of the calculation matrix, where inappropriate values bias particulary $I(E_i)$ and peak position of the computed spectrum; hence, $\mu/\rho (E_i)$ [m^2/kg] values were specifically determined by means of XCOM (2010) facilitating intermediate energies beyond standard grid of common tables (cf. HUBBELL,

SELTZER (2004) or MUPLOT (2006)), which enables to avoid data interpolation. Nevertheless, for the purpose of plotting the final energy distribution, intermediate intensities were interpolated aiming at continuous slope in Figure IV-60. Lower threshold energy was not further limited and consistently defined at $E_{\text{min}} = 0$ kVp. Consequently, $\mu/\rho (E_1) = 19.34$ m^2/kg at $E_1 = 5$ keV exceeds low-energy Al absorption edge at $E = 1.56$ keV (cf. HUBBELL, SELTZER (2004)), which is considered to bias the solution of the equation system owing to preferentially continuous decrement of $\mu/\rho (E)$. Regarding the upper limit, E_{max} was determined via U_a [kVp], where plot data was extended toward $E_{\text{max}} = 50$ kVp, since the last data point was computed at $E = 45$ keV. However, Figure IV-60 illustrates convenient shapes of free and pre-filtered, respectively, bremsstrahlung spectra. Comparison to respective spectra measuring results by spectrometer in Figure IV-52 (top right) reveals rough similarities toward both corresponding plots ('open' and 'pre-filter 1.9 mm Al' without absorber). Obviously, beam hardening in consequence of pre-filter application causes comparable effects, where position and shift of E_{peak} are in appropriate agreement. The same applies to low-energy downward slope. Note, 'open' spectra in Figure IV-52 inherently comprise 0.635 mm Al detector lid of the spectrometer. On the contrary, high-energy intensities of pre-filtered spectrum (black line) appear overestimated and further slight methodical insufficiencies were found. However, the explored historic approach by means of filtration curves facilitates to maintain regular measuring parameters, which are likewise set for typical applications of the evaluated setup, i. e., X-ray tube current and detector integration time

as well as aperture width and distances considering beam geometry. Contrary to advantageous direct application of actual device setup, Silberstein (1932) approach initially presumes narrow-beam conditions; hence, future work requires evaluation of the very same beam geometry impact. Beyond the performed experiments, a supposed optimisation toward WBC applications, where metal filters are to be replaced by wood- or WBC-related material in terms of Z_{eff} to obtain comparable attenuation conditions, are considered to be misleading regarding the intention to apply low-Z material. Moreover, material with predominant photoelectric absorption within the considered energy range in absence of secondary radiation transmission such as scattering is required. Hence, absorber material for filter stacks features monotonically and rather rapidly decreasing mass attenuation coefficient $\mu/\rho\,(E)$ along increasing energy likewise pointed out by Delgado (2007). Finally, the performed first exploratory but not further detailed studies reveal the viability of the Silberstein (1932) approach with respect to the considered setup and energy range of bremsstrahlung. Solving the system of linear equations in combination with increment data points $f(E_i) \equiv I(E_i)$ eventually requires enhancement considering hitherto research with corresponding mathematical as well as physical concepts regarding the ill-conditioned problem.
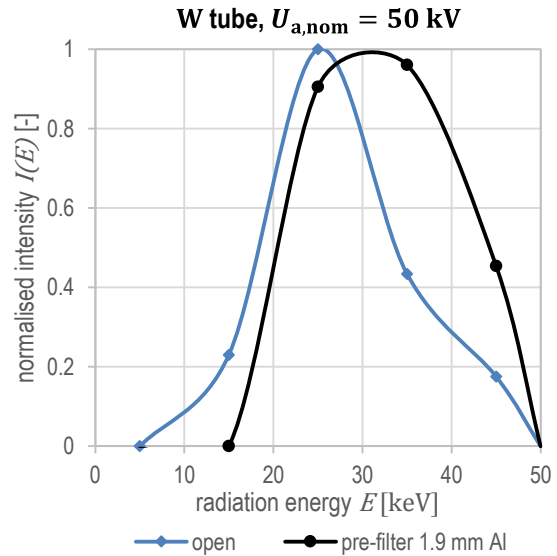
Figure IV-60: Exemplary X-ray spectra in first approximation determined via filter curves following the estimation approach of Silberstein (1932), interpolated plot as normalised intensity with $I(E)_{\max} = 1$ over radiation energy E of a W-target tube at $U_{\text{a,nom}} = 50$ kV, with $n = 5$ data points at $E = 5 \ldots 45$ keV.

5   X-ray attenuation computations

5.1   Effective atomic number

5.1.1   General remarks on the performance

As already pointed out in Chapter II–2.2, the determination of an effective atomic number Z_{eff} conduces as a vivid measure to compare radiation attenuation potential of composite materials and the effect of varying mixtures. Thus, the concepts are comprehensively applied with the aim to directly quantify the effective attenuation potential of WBCs considered as a mixture of compounds and the impact of fractional abundance of the actually present constituents as well as to evaluate effective X-ray interaction with WBC matter on sub-microscopic scale. To this end,

- simple and common, but limited power law method with $m = 2.94$ according to MAYNEORD (1937) and SPIERS (1946) yielding $\bar{Z}_{\text{eff}}$ and
- robust and more sophisticated Auto-Z_{eff} software introduced by TAYLOR et al. (2012) with energy-related results $Z_{\text{eff}}(E)$

are utilised for computations on the basis of both actual analysis data as elemental mass fraction $\omega(i)$ from Chapters IV–2.3 and IV–2.4 as well as virtual variation referring to the very same in an extreme but practice-oriented range. Moreover, the latter is particularly performed to virtually evaluate the impact of resin and moisture content as well as ash content and its composition on the radiation attenuation potential of WBCs. However, both applied methods are further evaluated regarding their practicability with focus on less elaborate procedures with few preconditions such as mass attenuation data.

The power law method is applied free from explicit energy dependence but, as aforementioned, rather valid at low energy levels. However, the actual range falls below $E_{\text{max}} < 55$ kVp. With $m = 2.94$, eq. (II-24) is applied and turns into

$$\bar{Z}_{\text{eff}} = \sqrt[2.94]{\sum_{i=1}^{k} \epsilon(i) \cdot Z_i^{2.94}} \qquad \text{(IV-38)}$$

taking the electron fraction $\epsilon(i)$ according to eq. (II-25) of all k elements of the mixture respectively into account. The choice of the value of m as exponent, however, can obviously be considered as Z-weighting, where increasing m amplify $\bar{Z}_{\text{eff}}$ toward the high Z_i in the present mixture. Data input for individual computations solely requires $\omega(i)$ from elemental analysis or theory as well as commonly available A_i and Z_i. Notwithstanding the well-known insufficiency of this single-valued expression of Z_{eff} as stated by HINE (1952) and elsewhere, the simplistic power law method is applied considering counterbalanced limitation and practicability.

Auto-Z_{eff} software Version 1.7 by TAYLOR et al. (2012) is employed, where $Z_{\text{eff}}(E)$ computation again solely requires predefinition of considered $\omega(i)$ and, for the purpose of $Z_{\text{eff}}(\bar{E})$ determination, $S(E)$. The latter is performed via eq. (II-30) apart from Auto-Z_{eff} software. Though bremsstrahlung spectra from X-ray tubes are inherently continuous with potentially superimposed discrete characteristic energies, eq. (II-30) is applied owing to discrete character of the data from spectra measurement as well as simulation (for results, refer to Chapter IV–4.3.2.4) and due to subsequently simplified computation. Advantageously, the method facilitates to explicitly take particular X-ray spectra into account, where lacking knowledge of the very same and subsequent assumptions potentially cause biased results.

Here, the power law method via eq. (IV-38) conduces for the evaluation of elemental compositions whereas complementary Auto-Z_{eff} software provides energy related results. For comparison between determination methods (Auto-Z_{eff} vs. power law), investigated matter (TMP, labMDF etc.), and virtual variations of the conditions of the very same, the simple difference

$$\Delta Z_{\text{eff}} = Z_{\text{eff},j} - Z_{\text{eff,ref}} \qquad \text{(IV-39)}$$

or ratio as quotient

$$QZ_{\text{eff}} = \frac{Z_{\text{eff},j}}{Z_{\text{eff,ref}}} \qquad \text{(IV-40)}$$

is calculated, where Z_{eff} may refer to $\bar{Z}_{\text{eff}}$, $Z_{\text{eff}}(E)$ or $Z_{\text{eff}}(\bar{E})$ and subscript j denotes the considered and ref the reference quantity.

5.1.2   Results and discussion

Table IV-32 summarises the results of atomic number computations by means of both methods, i. e., determination via power law ($\bar{Z}_{\text{eff}}$) and Auto-Z_{eff} software ($Z_{\text{eff}}(E)$), for the applied WBCs and respective constituents based on actual elemental analysis data or common compound values as well as generalised elemental compositions from past literature according to Table IV-14. To facilitate a convenient overview, result presentation is limited to selected but representative materials. In general, $\bar{Z}_{\text{eff}}$ of all WBC members is in the order of around nitrogen $Z_N = 7$ with a total (unweighted) mean $\bar{Z}_{\text{eff,mean}} = 6.94$. Total range covers $\bar{Z}_{\text{eff}} = 6.53 \ldots 7.42$ with $\Delta\bar{Z}_{\text{eff}} = 0.89$ and $Q\bar{Z}_{\text{eff}} = 1.14$ as comparison between the extremes, where maximum and minimum is attributed to water and lignin, respectively, revealing slightly more distinct deviations. However, the results differ $< 7.2\,\%$ from $\bar{Z}_{\text{eff,TMP}}$. Though the relative ratio appears high, all values are in the range of one atomic number, i. e., $\Delta\bar{Z}_{\text{eff,mean}} < \pm 0.5$. Further comparisons are pointed out later.

Auto-Z_{eff} software facilitates particular energy consideration and provides discrete $Z_{\text{eff}}(E)$ data in steps of 10 keV (15 keV additionally), where, however, intermediate values can sufficiently be interpolated. The results are presented as energy-dependent line plots of $Z_{\text{eff}}(E)$ in Figure IV-61 covering a practice-relevant range of radiation energy $E = 10 \ldots 100$ keV. Note, the charts focus on labMDF and its respective constituents with actual elemental analysis data as basis as well as the results calculated therefrom for labMDF at common conditions with $MC = 9.5\,\%$. Additionally, Table IV-32 summarises the corresponding $Z_{\text{eff}}(E)$ results by means of particular consideration of both an exemplary single energy $E = 10$ keV and a spectral-weighted mean

single-valued $Z_{\text{eff}}(\bar{E})$ via eq. (II-30). Whereas the former is attributed to the energy minimum of Auto-Z_{eff} software, the latter refers to a selected pre-filtered tungsten X-ray spectrum with $U_{\text{a,nom}} = 50$ kV, i. e., W-RDP-50-w/ with measured $E_{\max} = 50.9$ kVp and $\bar{E} = 29.2$ keV (Chapter IV–4.3.3.1), and is henceforth denoted as $Z_{\text{eff}}(\bar{E}, 50\,\text{kVp})$. At the lower energy limit, the total result range covers $Z_{\text{eff}}(10\,\text{keV}) = 5.83 \ldots 6.18$ with $\Delta Z_{\text{eff}}(10\,\text{keV}) = 0.35$ and $QZ_{\text{eff}}(10\,\text{keV}) = 1.06$ as comparison between the extremes, which is actually narrower compared to $\bar{Z}_{\text{eff}}$. Analogously, for all materials, in turn, spectral-weighted mean values yield $Z_{\text{eff}}(\bar{E}, 50\,\text{kVp}) = 5.21 \ldots 5.57$ where comparison within the range reveals slightly the same relations with $\Delta Z_{\text{eff}}(\bar{E}, 50\,\text{kVp}) = 0.37$ and $QZ_{\text{eff}}(\bar{E}, 50\,\text{kVp}) = 1.07$. Obviously, the best agreement of $\bar{Z}_{\text{eff}}$ with $Z_{\text{eff}}(E)$ is found at $E = 10$ keV. Here, the $Z_{\text{eff}}(10\,\text{keV})$ results of all materials taken into account differ toward $\bar{Z}_{\text{eff}}$, nevertheless, with $\Delta Z_{\text{eff}} = -0.83$ and $QZ_{\text{eff}} = 0.88$. For a detailed comparison, reference is made to Table IV-32 and Figure IV-61, where the latter additionally shows $\bar{Z}_{\text{eff}}$ as respective single values drawn at the ordinate (♦). Accordingly, difference between the methods increases with increment radiation energy owing to coincidently decreasing $Z_{\text{eff}}(E)$. Likewise, MARASHDEH et al. (2015) imply in their results, that a maximum $Z_{\text{eff}}(E)$ is found at low energies due to the predominant interaction mechanism of photoelectric absorption. Hence, an increasing share of scattering interactions on the total attenuation with increasing energy causes decreasing $Z_{\text{eff}}(E)$. Nonetheless, a similar slope can generally be observed for the considered materials in the lower energy range. More detailed, Figure IV-62 and Figure IV-61 unveil significant divergence of the water slope with increasing energy owing to approximately double $\omega(H)$ in water compared to dry WBC constituents and a corresponding high scattering share at higher energy levels. With particular focus on labMDF (dashed line), $Z_{\text{eff}}(E)$ slope is compared to its main components TMP, UF resin, and water in Figure IV-62. Obviously, the resulting labMDF at common $MC = 9.5\,\%$ (dotted line) is undistinguishable from its constituents at lower energies whereas the plots

material, substance	$\overline{Z}_{\text{eff}}$	$\Delta\overline{Z}_{\text{eff}}$ ref.: TMP	$Q\overline{Z}_{\text{eff}}$ ref.: TMP	$Z_{\text{eff}}(E)$ 10 keV	$\Delta Z_{\text{eff}}(E)$ ref.: $\overline{Z}_{\text{eff}}$	$QZ_{\text{eff}}(E)$ ref.: $\overline{Z}_{\text{eff}}$	$Z_{\text{eff}}(\overline{E})$ 50 kVp	$\Delta Z_{\text{eff}}(\overline{E})$ ref.: $\overline{Z}_{\text{eff}}$	$QZ_{\text{eff}}(\overline{E})$ ref.: $\overline{Z}_{\text{eff}}$
TMP	6.92			6.12	-0.80	0.884	5.50	-1.42	0.795
labMDF	6.93	0.01	1.001	6.13	-0.80	0.885	5.51	-1.41	0.796
labMDF 9.5 % MC	6.97	0.05	1.008	6.13	-0.85	0.879	5.48	-1.49	0.786
Fmat	7.01	0.09	1.013	6.17	-0.84	0.880	5.57	-1.44	0.794
UF-C	6.82	-0.10	0.985	6.07	-0.75	0.890	5.45	-1.37	0.799
indMDF	6.94	0.02	1.002	6.12	-0.82	0.883	5.50	-1.44	0.793
insulation	6.88	-0.05	0.993	6.09	-0.78	0.887	5.47	-1.41	0.796
WBC (UF, mean)	7.06	0.14	1.020	6.18	-0.87	0.876	5.57	-1.48	0.790
WBC (other, mean)	7.03	0.11	1.016	6.17	-0.86	0.878	5.55	-1.48	0.790
water	7.42	0.50	1.072	6.14	-1.28	0.827	5.21	-2.21	0.702
wood (simplistic)	6.79	-0.13	0.982	6.05	-0.74	0.890	5.40	-1.39	0.795
wood (total mean)	6.98	0.06	1.009	6.15	-0.84	0.880	5.52	-1.46	0.791
cellulose (mean)	6.89	-0.03	0.996	6.10	-0.79	0.885	5.45	-1.44	0.791
hemicelluloses (mean)	6.89	-0.03	0.996	6.11	-0.78	0.887	5.48	-1.41	0.795
lignin (mean)	6.53	-0.39	0.943	5.83	-0.69	0.894	5.22	-1.31	0.799
breast tissue	7.01	+0.09	1.013	5.80	-1.21	0.827	4.87	-2.14	0.695

Table IV-32: Effective atomic numbers determined via power law ($\overline{Z}_{\text{eff}}$) or by Auto-$Z_{\text{eff}}$ software ($Z_{\text{eff}}(E)$) for single energy $E = 10$ keV and as spectral-weighted mean via eq. (II-30) for a pre-filtered 50 kVp W spectrum (see Chapter IV–4.3.2.4) of applied WBCs and respective constituents based on actual elemental analysis data (upper rows) as well as common compound values and generalised literature figures, complete with comparison via ΔZ_{eff} eq. (IV-39) and QZ_{eff} eq. (IV-40) toward respective reference.
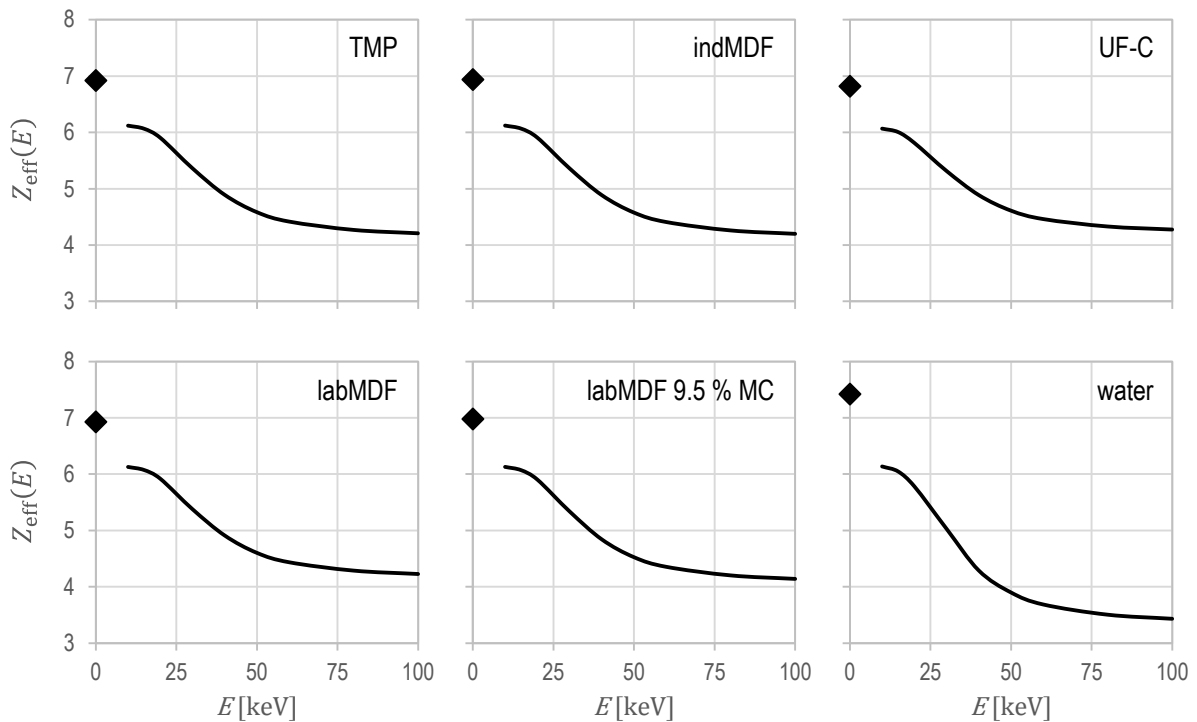
Figure IV-61: Effective atomic numbers $Z_{\text{eff}}(E)$ over a practice-relevant range of radiation energy E determined by Auto-Z_{eff} software (solid lines) of selected WBC and respective constituents based on actual elemental analysis data, complete with $\overline{Z}_{\text{eff}}$ (♦) via power law method independent from E for comparison, for summarised single values refer to Table IV-32.

slightly diverge with increasing radiation energy. Despite the distant water plot, low MC in a practice-relevant order is of minor impact on $Z_{\mathrm{eff}}(E)$ due to the non-dominant contribution of MC to total WBC mass, particularly of H from H_2O to WBC elemental composition at MC. Moreover, considerable moisture influence arises far beyond FSP as exploratory studies with more extreme virtually varied MC unveiled. However, regarding adhesive resin, UF-C plot reveals negligible difference from $Z_{\mathrm{eff}}(E)_{\mathrm{labMDF}}$. Furthermore, discussions on impact independent from energy of varying WBC constituents are continued later by means of $\bar{Z}_{\mathrm{eff}}$. In further comparison of $Z_{\mathrm{eff}}(E)$ toward $\bar{Z}_{\mathrm{eff}}$ it can be generalised that both single values for particular energy and consequently spectral-weighted mean $Z_{\mathrm{eff}}(\bar{E})$ consistently fall below $\bar{Z}_{\mathrm{eff}}$ with, e. g., $\Delta Z_{\mathrm{eff}}(10\,\mathrm{keV}) = -0.80$ up to $\Delta Z_{\mathrm{eff}}(100\,\mathrm{keV}) = -2.70$ in the case of labMDF or $\Delta Z_{\mathrm{eff}}(10\,\mathrm{keV}) = -1.28$ to $\Delta Z_{\mathrm{eff}}(100\,\mathrm{keV}) = -3.99$ for water. Notwithstanding the range of difference values, the ratio on prevailing rather low energy level approximates $QZ_{\mathrm{eff}} \approx 0.8\ldots0.9$, thus, $Z_{\mathrm{eff}}(E)$ is about 85 % that of $\bar{Z}_{\mathrm{eff}}$. Eventually, as also expected, the observed result differences between the methods are attributed to explicit consideration of all energy-related attenuation mechanisms by the methodical approach behind Auto-Z_{eff} software. Contrary to this, $\bar{Z}_{\mathrm{eff}}$ results rather correspond to actual radiation absorption omitting scattering interactions. Regarding intended evaluation of varying elemental compositions impact on attenuation potential at low energy levels, both methods are comparably conclusive. Beyond that, energy-dependent $Z_{\mathrm{eff}}(E)$ determination requires a comprehensive data basis, which is inherently included in Auto-Z_{eff} software. Consequently, both applied methods require, in turn, the same input, i. e., elemental composition, resulting in comparably convenient applicability. The complementary consideration of the applied radiation spectra is more elaborate owing to the determination of the very same (refer to Chapter IV–4.2.6.1).

To evaluate the impact of actually present and virtually varied elemental composition, result presentation and consequent discussion is henceforth focused on $\bar{Z}_{\mathrm{eff}}$ via eq. (IV-38). In this regard, $\bar{Z}_{\mathrm{eff}}$ results are compared to each other
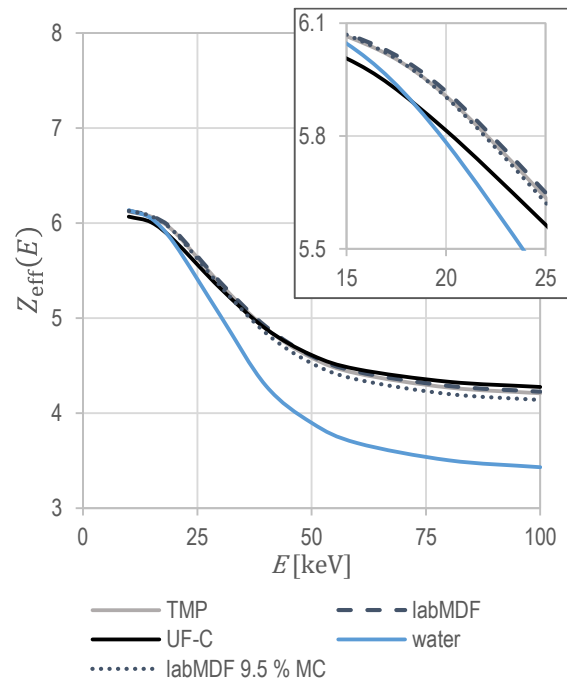
Figure IV-62: Effective atomic numbers $Z_{\mathrm{eff}}(E)$ over a practice-relevant range of radiation energy E determined by Auto-Z_{eff} software of labMDF and respective constituents based on actual elemental analysis data, inset with magnified $Z_{\mathrm{eff}}(E)$ plots between $E = 15\ldots25\,\mathrm{keV}$, for summarised single values refer to Table IV-32; note undistinguishable charts of TMP, labMDF (OD), and labMDF 9.5 % MC.

with $\bar{Z}_{\mathrm{eff,TMP}} = 6.92$ as the fundamental reference for comparisons following eq. (IV-39) and eq. (IV-40) to clarify expected infinitesimal and particularly negligible influence of variations of resin content $\omega(\mathrm{UF})_{\mathrm{OD}}$, MC, and $\omega(a)$. To this end, Table IV-32 compares $\bar{Z}_{\mathrm{eff}}$ results of all materials toward TMP, as aforementioned, where, regardless of lignin and water values, analysis-based results range $\Delta\bar{Z}_{\mathrm{eff}} = \pm0.14$ around $\bar{Z}_{\mathrm{eff,TMP}}$ in general. Beyond computations by means of analysis data from Chapter IV–2.4.2 complete with determined ash content in Chapter IV–2.3.2, Figure IV-63 illustrates virtual variation of $\bar{Z}_{\mathrm{eff,labMDF}}$ within an extreme but practice-oriented range of resin content via nitrogen content $\omega(\mathrm{N})$, moisture content MC, ash content $\omega(a)$, and effective atomic number of ash $\bar{Z}_{\mathrm{eff,ash}}$, where Table IV-33 summarises the upper and lower limit values around actual figures. As easily can be seen, the total range of virtual variation falls roughly below $\Delta\bar{Z}_{\mathrm{eff}} = -0.15\ldots+0.3$ around $\bar{Z}_{\mathrm{eff,TMP}}$ and is particularly caused by
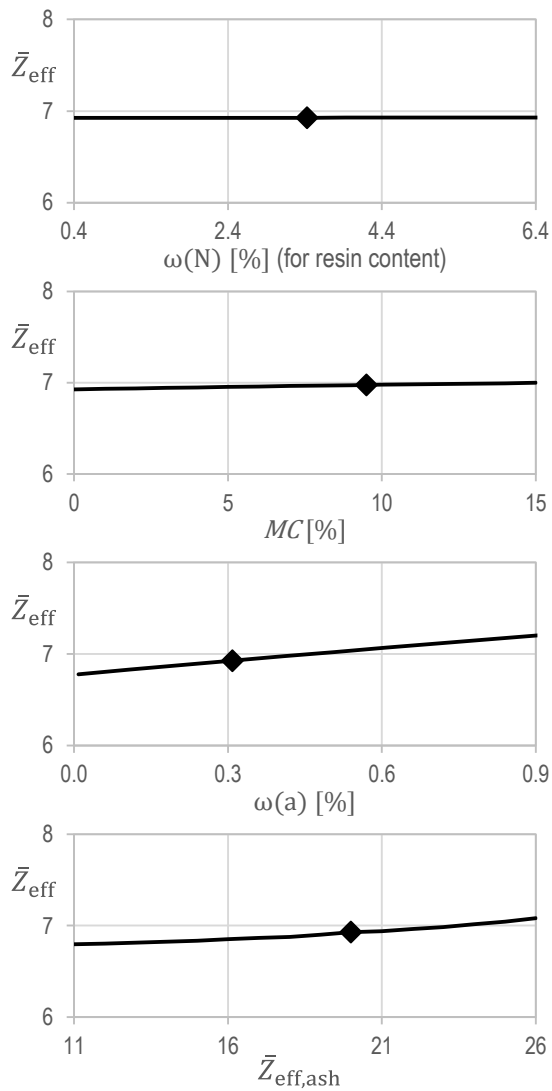
Figure IV-63: Effective atomic numbers $\bar{Z}_{eff}$ of labMDF (oven-dry) based on virtual variation (solid lines) of actual elemental analysis data ($\blacklozenge$) within an extreme but practice-oriented range of resin content via nitrogen content $\omega(N)$ [%], moisture content MC [%], ash content $\omega(a)$ [%], and effective atomic number of ash $\bar{Z}_{eff,ash}$.

parameter variation (abs.)		$\bar{Z}_{eff}$	$\Delta\bar{Z}_{eff}$	$Q\bar{Z}_{eff}$
+	6.4	6.929	+0.002	1.000
$\omega(N)$ [%]	3.4	6.927		
−	0.4	6.925	-0.002	1.000
FSP	27	7.04	+0.11	1.016
+	14.5	7.00	+0.02	1.003
MC [%]	9.5	6.97	+0.05	1.007
−	4.5	6.95	-0.02	0.997
OD	0.0	6.93		
+	0.9	7.21	+0.28	1.040
$\omega(a)$ [%]	0.309	6.93		
−	0.0	6.78	-0.15	0.979
+	26 (Fe)	7.08	+0.15	1.022
$\bar{Z}_{eff,ash}$	20 (Ca)	6.93		
−	11 (Na)	6.80	-0.13	0.981

Table IV-33: Effective atomic numbers $\bar{Z}_{eff}$ of labMDF (oven-dry) based on virtual variation with upper (+) and lower (−) limit value around actual elemental analysis data with comparison via $\Delta\bar{Z}_{eff}$ eq. (IV-39) and $Q\bar{Z}_{eff}$ eq. (IV-40) toward the respective actual value.

potential $\omega(a)$ variation. Nevertheless, detailed considerations reveal the following findings and consequent implications.

In comparison to clean wood (simplistic), elemental composition of UF adhesive resin is governed by fractional abundance of nitrogen (see UF-types in Table IV-15) independently from curing state. Here, UF-C roughly reveals a counterbalanced ratio C : N : O and $\bar{Z}_{eff,UF-C} = 6.82$. Figuratively, TMP resination adds N with $Z = 7$ to the elemental composition in between C ($Z = 6$)

and O ($Z = 8$) where $\bar{Z}_{eff,labMDF} = 6.93$ finally approximates in the order of N, which becomes obvious from the computational $\bar{Z}_{eff}$ results likewise aforementioned. Here, a negligible variation toward TMP of $\Delta\bar{Z}_{eff} = 0.01$ and $Q\bar{Z}_{eff} = 1.001$ is found to exist. The like applies to MDI-bonded insulation boards, where increased $\omega(C)$ merely decreases $\bar{Z}_{eff,insulation} = 6.88$, i. e., infinitesimal variation toward TMP of $\Delta\bar{Z}_{eff} = -0.05$ and $Q\bar{Z}_{eff} = 0.993$. However, as illustrated by Figure IV-63 (upper plot), virtual variations of resin content $\omega(UF)_{OD}$ in terms of total nitrogen fraction around labMDF value in the range $\omega(N)_{labMDF} = (3.4 \pm 3)$ % yields potential variations of $\Delta\bar{Z}_{eff} = \pm 0.002$ and $Q\bar{Z}_{eff} = 1.000$; hence, $\bar{Z}_{eff,labMDF} = 6.93$ remains unaffected by varying UF resin content in a practice-oriented extreme range. Moreover, transferred conclusions on industrial WBCs bonded with conventional types of organic adhesive resins with potential organic additives such as hydrophobic agents appear sufficient in general since $\bar{Z}_{eff,indMDF} = 6.94$ ranges in the equal order. Finally, $\bar{Z}_{eff}$ is totally unaffected by resination regarding the considered cases.

Regularly applied $MC_{labMDF} = 9.5$ % corresponding to 20/65 conditioning (refer to Table IV-5 in

Chapter IV–1.5) represents roughly the order of EMC of customary MDF in consequence of common ambient conditions. Accordingly computed $\bar{Z}_{\text{eff,labMDF9.5\%MC}} = 6.97$ reveals negligible variation toward oven-dry labMDF of $\Delta\bar{Z}_{\text{eff}} = +0.04$ and $Q\bar{Z}_{\text{eff}} = 1.007$. Likewise summarised in Table IV-33, virtual variations of $MC_{\text{labMDF}} = (9.5 \pm 5.0)$ % result in $\Delta\bar{Z}_{\text{eff}} = \pm 0.02$ and $Q\bar{Z}_{\text{eff}} = 0.997 \ldots 1.003$ in comparison to the mean. Obviously, as illustrated by the almost horizontal plot in Figure IV-63 (second from top), the practice-relevant MC range causes a slight but not substantial impact of EMC on $\bar{Z}_{\text{eff}}$. Moreover, further MC increment up to $MC_{\text{FSP}} = 27$ % (fibre saturation point) solely yields marginally increase of $\bar{Z}_{\text{eff}}$ in comparison to oven-dry state of $\Delta\bar{Z}_{\text{eff}} = +0.11$ and $Q\bar{Z}_{\text{eff}} = 1.016$ owing to $\bar{Z}_{\text{eff,water}} = 7.42$ close to oven-dry labMDF. Contrary to the present findings, KULLENBERG et al. (2010) state a dependence of Z_{eff} of a mixture of elements on the amount of water. However, the absence of a report on their likewise according to eq. (IV-38) computed $\bar{Z}_{\text{eff}}$ inhibits further evaluation of their findings. Nevertheless, their discovered context belongs to $MC = 33 \ldots 142$ % ranging beyond FSP and appears sufficient, in turn. In this regard, e. g., the energy-dependent $Z_{\text{eff}}(\bar{E}, 50\,\text{kVp})$ of labMDF with virtual $MC = 100$ % is about 0.92 times that of oven-dry material, i. e., actually in the middle compared to water with a factor of 0.85 toward oven-dry labMDF. Apparently, differences between dry wood or WBC matter and water arise with increasing radiation energy as aforementioned and obvious from Figure IV-62. Whereas $Z_{\text{eff}}(E > 15\,\text{keV})$ of moist matter fall below dry state values, virtual $\bar{Z}_{\text{eff,labMDF100\%MC}} = 7.19$ exceeds the dry state with $\Delta\bar{Z}_{\text{eff}} = +0.26$ and $Q\bar{Z}_{\text{eff}} = 1.037$ but less distinctly. Eventually, the dual-energy X-ray application of KULLENBERG et al. (2010) for MC measurement and, however, the topic in general claims fundamental discussions regarding issues below FSP and WBCs in general to be reported elsewhere.

Variations in WBC ash content are generally attributed to several material- and process-related parameters but commonly expected not to exceed $\omega(a) \approx 1$ % according to Table IV-11 and Table IV-12 in case of customary European

WBCs. Subsequently, ash constituents with Z_i beyond organic wood matter are fundamentally expected to raise $\bar{Z}_{\text{eff}}$. However, virtually tripling $\omega(a)_{\text{labMDF}}$ as the upper limit value in Table IV-33 causes 1.04 times higher $\bar{Z}_{\text{eff}}$ with $\Delta\bar{Z}_{\text{eff}} = +0.28$ and $Q\bar{Z}_{\text{eff}} = 1.040$ compared to the actually present composition of labMDF. Furthermore, labMDF virtually free of inorganic components, i. e., $\omega(a)_{\text{labMDF}} = 0$ %, yields downward $\bar{Z}_{\text{eff}}$ shift of $\Delta\bar{Z}_{\text{eff}} = -0.15$ and $Q\bar{Z}_{\text{eff}} = 0.979$ with potential $\bar{Z}_{\text{eff}} = 6.78$ in good agreement with $\bar{Z}_{\text{eff,wood(sim)}} = 6.79$ for simplistically considered wood as listed in Table IV-32. Figure IV-63 (second from bottom) illustrates the minor but undeniable $\bar{Z}_{\text{eff}}$ increment with increasing $\omega(a)$. Regardless of missing actual analysis data of ash composition, virtual alteration of mineral abundance in ash in terms of its analogously computed $\bar{Z}_{\text{eff,ash}}$ from $\bar{Z}_{\text{eff,ash}} = 11$ (corresponding to Na) up to $\bar{Z}_{\text{eff,ash}} = 26$ (Fe) cause $\Delta\bar{Z}_{\text{eff}} = -0.13 \ldots + 0.15$ and $Q\bar{Z}_{\text{eff}} = 0.981 \ldots 1.040$. Obviously from the plot in Figure IV-63 (bottom) with remarkable non-linear slope, virtual variations of ash composition are comparable but less markedly than in the case of $\omega(a)$.

To summarise, the impact of variations in WBC composition within a conventional range on $\bar{Z}_{\text{eff}}$ of the very same substance considered as mixture of chemical elements is rather negligible. The same applies to energy-related data as vividly illustrated by Figure IV-62, where, despite divergent $Z_{\text{eff}}(E)_{\text{water}}$ slope along increment E and marginal difference of $Z_{\text{eff}}(E)_{\text{UF-C}}$ plot at low-energy level, the line graphs of TMP as well as labMDF at oven-dry and $MC = 9.5$ % state are congruent and start to slightly diverge above $E < 40\,\text{keV}$.

Beyond virtual variation, further comparison of results based on elemental analysis with computations based on elemental composition data from both literature and empirical determination unveils no crucial differences as summarised in Table IV-32. The deviations are less distinct than the virtual range presented in Table IV-33 and discussed above considering the example of $\bar{Z}_{\text{eff}}$, where the findings analogously apply to $Z_{\text{eff}}(E)$. More detailed, $\bar{Z}_{\text{eff}}$ of WBCs (mean) bonded with UF as well as by other means differ

from each other in a negligible order and slightly exceed TMP with $\Delta \bar{Z}_{\mathrm{eff}} = +0.11 \ldots 0.14$ and $Q\bar{Z}_{\mathrm{eff}} \approx 1.02$ owing to higher mean ash content $\omega(a) \approx 0.5\,\%$ (see Table IV-14). Pure cell-wall constituents comprise inherently no minerals resulting in marginally lower $\bar{Z}_{\mathrm{eff}}$ compared to TMP with $\Delta \bar{Z}_{\mathrm{eff}} = -0.03$ and $Q\bar{Z}_{\mathrm{eff}} = 0.996$ for all celluloses and aforementioned more obvious difference of $\bar{Z}_{\mathrm{eff,lignin}}$ corresponding to increased $\omega(C) \approx 63.4\,\%$ (see Table IV-14). The same applies to clean wood (simplistic) with assumed ideal elemental composition (6/50/44 %), which consequently falls below all other values (except lignin).

Owing to underrepresented Z_{eff} investigations on wood and WBC in a technological context, comparison of the present computational results to data from further research is minimised. However, Hussein et al. (1997) report $\bar{\bar{Z}}_{\mathrm{eff,maple}} = 6.66$ as comparison to their investigated narcotics. Corresponding to computation following eq. (II-26), the single value appears disproportionally low whereas applied elemental composition is not further specified. Notwithstanding that Macedo et al. (2002) performed actually no elemental analysis and subsequent Z_{eff} computation, they point out an influence of chemical composition on linear attenuation coefficient even at equal density and consider corresponding dependence on atomic number at low radiation energies. Complementary to rare wood data, Marashdeh et al. (2015) summarise the results of almost all of their mangrove wood (*Rhizophora* spp.) samples in the range $Z_{\mathrm{eff}}(E)_{\mathrm{mangrove}} = 3.5 \ldots 7.5$ over the energy range $E = 10 \ldots 60\,\mathrm{keV}$, which is, accordingly, in good agreement with $\bar{Z}_{\mathrm{eff,mangrove}} = 7.09$ calculated by Banjade et al. (2001), in turn. However, a closer review of their findings (refer to Chapter II–2.2) partly unveils fundamental discrepancies in the work of Marashdeh et al. (2015) due to obviously invalid elemental analysis data. Note, the studies of both Banjade et al. (2001) and Marashdeh et al. (2015) were, however, performed in a medical context, where mangrove wood potentially serves as tissue equivalent phantom for dosimetric purposes. Primarily, Z_{eff} considerations commonly occur from medico-

physical application and research issues. Hence, relating comparisons of the present results are obvious, where breast tissue appears most suitable amongst human tissues regarding both its comparable elemental composition (cf. Taylor et al. (2012)) and aforementioned methodical investigation problems (e. g. mammography, refer to Chapter II–3.3). Here, breast tissue with $\bar{Z}_{\mathrm{eff,breast}} = 7.01$ is in good agreement with (moist) labMDF as well as common WBCs (from literature), where the difference toward TMP of $\Delta \bar{Z}_{\mathrm{eff}} = +0.09$ and $Q\bar{Z}_{\mathrm{eff}} = 1.013$ is likewise in the same order. On the contrary with respect to radiation energy, $Z_{\mathrm{eff}}(E)_{\mathrm{breast}}$ yields downward shifted computation results with almost congruent slope in comparison to WBC plots in Figure IV-61 owing to higher $\omega(H)_{\mathrm{breast}}$.

5.1.3 Concluding remarks

The concept of condensing the elemental composition of an actually present or virtually estimated composite into one value, i. e., computing the effective atomic number weighted by electron fraction following the simplistic approach via eq. (IV-38), serves as viable measure for comparative evaluation of WBCs regarding their radiation attenuation potential. Regardless of Z_{eff} determination method, both applied computation procedures facilitate rapid estimation of the X-ray attenuation potential of varying WBC compositions. Moreover, Z_{eff} highlights the elemental composition by a single number. Consequent quantification of effective radiation attenuation depends, however, on matter condensation of the constituent elements. In this regard, e. g., $\bar{Z}_{\mathrm{eff,air}} = 7.70$ (cf. Mayneord (1937)) is in the neighbourhood of water with $\bar{Z}_{\mathrm{eff,H_2O}} = 7.42$ but, obviously, its effective attenuation is related to the present amount of matter. Hence, direct $\bar{Z}_{\mathrm{eff}}$ comparison is advantageous in the case of matter with similar true density ρ_{t}, which is, to some extent, given with respect to WBC constituents (see Table IV-6 and Table IV-7). However, radiation attenuation corresponds to the mass of penetrated matter, thus, its area density ρ_{A}. Eventually, Z_{eff} based attenuation considerations are fundamentally enabled by the smooth

correlation between atomic number Z and interaction cross-sections σ for X-rays (refer to Chapter II–2.1, Table II-1). Note here, the Z dependence of the linear attenuation coefficient μ_{lin} with individual consideration of the single attenuation processes photoelectric absorption and incoherent scattering as pointed out in Chapter II–2.1 (refer to eq. (II-18) to eq. (II-21)) allows to compute a mean mass attenuation coefficient of the compound or mixture by means of Z_{eff}. However, the approach is, on the contrary, inexpedient for neutrons owing to the lack of a clear context between atomic number and radiation attenuation, which rather occurs vice versa and reveals individual characterisations for particular chemical elements.

Referring to both applied computation procedures, i. e., power law method eq. (IV-38) and Auto-Z_{eff} software, differences in resulting Z_{eff}, i. e., between $\bar{Z}_{\text{eff}}$ and $Z_{\text{eff}}(E)$, respectively, are found as summarised in Table IV-32. Consequently, comparison is reserved to the same method to be chosen according to particular purpose and potential restrictions. At this, regarding power law method, exponent was defined with $m = 2.94$ according to historically prevalent application but rather low compared to all hitherto extents. Nonetheless, increasing m amplifies high-Z constituents (likewise a weighted mean in general or the Lehmer mean, eq. (IV-21), particularly); thus, chosen m is found to be appropriate for composition comparison purpose at low energy levels. As aforementioned, $\bar{Z}_{\text{eff}}$ results via power law method are generally considered to overestimate the effective atomic number Z_{eff} of the investigated mixture with respect to energy-related $Z_{\text{eff}}(E)$. Here, $\bar{Z}_{\text{eff}}$ consistently falls below $Z_{\text{eff}}(E)$, where minimum differences, thus, maximum $Z_{\text{eff}}(E)$, are found at the lowest considered energy. The marked downward slope of the $Z_{\text{eff}}(E)$ plots in Figure IV-62 and Figure IV-61 with increasing energy is particularly attributed to constituent hydrogen and correspondingly predominant scattering interactions within the considered energy range since X-ray attenuation depends on radiation energy and photoelectric absorption gains reduced dominance along with increment energy.

Referring to the investigated actually measured and virtually varied elemental compositions, non-distinctive alteration of $\bar{Z}_{\text{eff}}$ with minor extent is found in consequence of variations in elemental composition as comprehensively discussed above and summarised in Figure IV-63 and Table IV-33. Consequently, regular raw-material- and process-related variations in general are, in turn, claimed to be negligible for effective mass attenuation as analogously investigated in Chapter IV–5.2. Considering organic binders for WBC, $\bar{Z}_{\text{eff}}$ is found to be independent from adhesive resin content and even type (refer to results for MDI-bonded insulation boards), where results reveal no relevant differences. Moreover, pure UF-C resin is in a comparable order to TMP and WBCs. Furthermore, upward MC variations below FSP cause infinitesimal increment of $\bar{Z}_{\text{eff}}$. Nonetheless, computed $\bar{Z}_{\text{eff,labMDF9.5\%MC}}$ representing mean moisture conditions is in good agreement with the value from oven-dry state $\bar{Z}_{\text{eff,labMDF}}$. Slightly more markedly but not tremendously, ash content affects $\bar{Z}_{\text{eff}}$ due to its constituent elements with $\Delta\bar{Z}_{\text{eff}} > 13$ on average compared to clean wood (simplistic). Eventually, the same applies to $Z_{\text{eff}}(E)$ over total relevant energy range regarding all considered WBC constituents.

Finally, no crucial differences in Z_{eff} are found to computationally result from varying elemental compositions of WBCs, where ΔZ_{eff} between variously (organic) resin-bonded WBCs remains equally negligible within relevant radiation energy range. Consequently, according to comprehensive computations based on actual analysis data, reported elemental compositions, and virtual variation of the very same as well as in comparison to rare literature values, all customary WBCs bonded with organic resins (without inorganic additives) at EMC due to common environmental conditions are more or less equal in terms of effective atomic numbers considering low radiation energy level with $\bar{Z}_{\text{eff,WBC,EMC}} \approx 7$. Likewise, water equivalence is a requirement for phantom materials or dosimeters for medical applications and commonly evaluated via Z_{eff} computations (cf. TAYLOR (2011)), equivalence of varying WBC compositions to common wood

values facilitates generalisation of X-ray attenuation consideration. Obviously, with respect to power law values ($\bar{Z}_{\mathrm{eff}}$), infinitesimal deviations from equality of the ratio of all virtually investigated WBC compositions (see Figure IV-63 and Table IV-33) in the total order of $Q\bar{Z}_{\mathrm{eff}} = 0.98 \dots 1.04$ (particularly attributed to ash variations) unveil the wood equivalence of WBCs considering practice-relevant extremes of resin, ash, and moisture content. Furthermore, wood equivalence is also found for $Z_{\mathrm{eff}}(E)$ over the considered energy range, where values marginally diverge at high energies. Beyond this, increasing MC starts to distort this consistency distinctly beyond FSP.

5.2   Mass attenuation coefficient

5.2.1   General remarks on the performance

As already pointed out in Chapter II–2.3, the computation of mass-fraction-weighted total mean mass attenuation coefficients $\mu/\rho\,(E)_{\mathrm{mix}}$ via mixture rule serves as a clear quantification of radiation attenuation within a compound or mixture. In addition to attenuation potential estimation of WBCs via Z_{eff} calculations in Chapter IV–5.1, application of the mixture rule for $\mu/\rho\,(E)_{\mathrm{mix}}$ computation is considered to provide enhanced quantification of potential impact of varying WBC elemental composition on effective radiation attenuation of the material under investigation.

To this end, the mixture rule following eq. (II-31) is utilised according to basic explanations in Chapter II–2.3.2 for computations on the basis of both actual analysis data as elemental mass fractions $\omega(i)$ from Chapters IV–2.3 and IV–2.4 as well as virtual variation referring to the very same in an extreme but practice-oriented range. Analogously to Z_{eff} determination in Chapter IV–5.1, particularly the latter provides virtual evaluation of resin, moisture, and ash content impact on radiation attenuation potential of WBCs. Virtually each material with (empirically) known elemental composition can theoretically be investigated regarding the impact of its composition variation on radiation attenuation potential of the

material in terms of $\mu/\rho\,(E)_{\mathrm{mix}}$ for all considered energies. However, material selection for computation and result presentation in Chapter IV–5.2.2 basically corresponds to the available analysis data (Table IV-15) as well as some reported and empirically determined compositions (Table IV-14), where respectively summarised mean values are taken into account. Nevertheless, elemental analysis leaves ash composition unspecified. The literature review (Chapter IV–2.3.2) shows, however, that non-combustible residues are dominated by CaO. Moreover, $\bar{Z}_{\mathrm{eff,ash}}$ variations in Chapter IV–5.1.2 yield no considerable impact on WBC $\bar{Z}_{\mathrm{eff}}$ in a certain range. Therefore and for simplification purpose, mass fraction $\omega(a)$ values from ash content determination are henceforth attributed to the chemical element $_{20}\mathrm{Ca}$ and the respective single mass attenuation coefficients $\mu/\rho\,(E)_{\mathrm{Ca}}$ unless otherwise stated like in the case of virtual variation of $\bar{Z}_{\mathrm{eff,ash}}$ (refer to Figure IV-70 and Table IV-37). Nevertheless, the considered material range is more or less congruent to the Z_{eff} evaluation, where reference is made to Table IV-32. Here, the charts and data compilations particularly focus on labMDF and its respective constituents with actual elemental analysis data at oven-dry (OD) conditions as basis as well as the results calculated therefrom for moist labMDF at standard 20/65 conditions with $MC = 9.5\,\%$, henceforth referred to as labMDF 9.5 % MC.

As already justified in Chapter II–2.1, tabulated data for $\mu/\rho\,(E)_i$ from XCOM (2010) is utilised, which is equivalent to HUBBELL, SELTZER (2004), but allows, moreover, to enter additional energies beyond standard grid. For reasons of reproducibility, all applied single values $\mu/\rho\,(E)_i$ of the chemical elements $_1\mathrm{H}$, $_6\mathrm{C}$, $_7\mathrm{N}$, $_8\mathrm{O}$, $_{16}\mathrm{S}$, and $_{20}\mathrm{Ca}$ are comprehensively listed in Appendix VII–4 Table VII-3 to Table VII-9. Accordingly, virtual variation of energy ranging $E = 5 \dots 100\,\mathrm{keV}$ in increments of $\Delta E = 1\,\mathrm{keV}$ (likewise for $Z_{\mathrm{eff}}(E)$) serves to more or less continuously illustrate the energy impact on radiation attenuation over a practice-oriented range. Beyond this, additional values (bold values in energy grid) are included exemplarily representing applied single mean energies $\bar{E}$; i.e., four particular energies $\bar{E}$ on

three levels with corresponding devices are compiled in Table IV-34 including the radioisotope ^{241}Am, which was commonly applied for RDP determination and in further previous investigations on wood (refer to Chapter II–2.3.3 and Table II-3). Here, $\bar{E}$ from spectra measurements (Chapter IV–4.3.3.1, no simulation data) employing respective initial beams (partly incl. pre-filters) was taken into account not the energy spectra after transmission through the individual specimens, which are also listed in Table IV-29. For further available values of $\bar{E}$ and $E_{\max}$ from the spectra evaluation of all device setups, reference is made to Table VII-2.

For comparison between investigated materials (TMP, labMDF etc.) and virtual variation of the conditions of the very same matter, simple mass attenuation coefficient difference $[\mathrm{m}^2/\mathrm{kg}]$

$$\Delta \frac{\mu}{\rho}(E)_{\mathrm{mix}} = \frac{\mu}{\rho}(E)_{\mathrm{mix},j} - \frac{\mu}{\rho}(E)_{\mathrm{mix,ref}} \qquad \text{(IV-41)}$$

or ratio as nondimensional quotient $[-]$

$$Q \frac{\mu}{\rho}(E)_{\mathrm{mix}} = \frac{\dfrac{\mu}{\rho}(E)_{\mathrm{mix},j}}{\dfrac{\mu}{\rho}(E)_{\mathrm{mix,ref}}} \qquad \text{(IV-42)}$$

is calculated, where $\mu/\rho(E)_{\mathrm{mix}}$ refers to the total mean mass attenuation coefficient of the considered (subscript j) and the reference (ref) material or quantity, respectively. Furthermore, particularly the evaluated virtual composition variations facilitate to deduce generalisations. To accordingly evaluate fundamental trends within the utilised practice-oriented range by means of a clear measure per variable constituent and energy level, the differential mass attenuation coefficient of the mixture

$$\delta \frac{\mu}{\rho}(E)_{\mathrm{mix}} = \frac{Q \dfrac{\mu}{\rho}(E)_{\mathrm{mix}+} - Q \dfrac{\mu}{\rho}(E)_{\mathrm{mix}-}}{\omega(i+) - \omega(i-)} \cdot 100$$
$$\text{(IV-43)}$$

is introduced with $Q\,\mu/\rho(E)_{\mathrm{mix}}\,[-]$ from eq. (IV-42) and $\omega(i)\,[\%]$ as percentage abundance of the considered constituent i, where $+$ and $-$ denote the upper and lower limit of variation range. The computation of $\delta\,\mu/\rho(E)_{\mathrm{mix}}$ yields percent per percentage parameter variation $[\%/\%\Delta\omega(i)]$, where the fractional content $\omega(i)$ may also refer to $MC\,[\%]$ or other particular

Energy level	E [keV]	type	device label
low	12.7	$\bar{E}$	W-mat-16-w/o
		$\bar{E}$	W-panel-16-w/o
medium	21.5	$\bar{E}$	Ag-RDP-55-w/
		$\bar{E}$	W-RDP-35-w/o
	29.2	$\bar{E}$	W-RDP-50-w/
high	59.5	E_γ	^{241}Am

Table IV-34: Radiation energies (classified on three levels) with corresponding X-ray device and setup labels (Chapter IV–4.2.2 and IV–4.2.3) utilised for $\mu/\rho(E)_{\mathrm{mix}}$ computation following eq. (II-31), individually measured mean energy $\bar{E}$ by means of X-ray spectrometry (Chapter IV–4.2.6.1 and IV–4.3.3.1), complete with radioisotope ^{241}Am; extract from Table VII-2.

compound concentrations within the mixture beyond elemental mass fraction as well as to, moreover, absolute variation of quantities such as $\bar{Z}_{\mathrm{eff}}$ of trace elements.

Computational $\mu/\rho(E)_{\mathrm{mix}}$ estimations according to eq. (II-31) considering a single (mean) energy cannot comprehensively represent actual attenuation conditions of polychromatic radiation in terms of X-ray transmission measurements. X-ray spectra data explicitly considering the employed measuring setup is rarely available in common practice and further affected by detection and the investigated material itself. However, measured spectra $S(E)$ (Chapter IV–4.3.3.1) are taken into account for additional computation of spectral-weighted total mean mass attenuation coefficient $\mu/\rho\big(S(E)\big)_{\mathrm{mix}}$ via eq. (II-35), where discrete data $S(E_j)$ is adapted to $\mu/\rho(E)_i$ raw data energy grid (Appendix VII–4) with $\Delta E = 1\,\mathrm{keV}$ such that individual $\sum_n S(E_j) = 1$. Spectra parameters such as $\bar{E}$ and $E_{\max}$ (Table IV-29), remain, however, unchanged. The results from integration over the measured spectral distributions are compared to $\mu/\rho(E)_{\mathrm{mix}}$ for $E = \bar{E}$ of the respective initial spectrum $S_{\mathrm{D},0}(E)$.

As commonly known and basically pointed out in Chapter II–2.1, total (tot) radiation attenuation during transmission through material comprises the single mechanisms photoelectric absorption (photo) as well as coherent (coh) and incoherent

(incoh) scattering within the considered energy range $E \leq 100\,\text{keV}$. Single attenuation mechanisms are strictly additive according to eq. (II-14) resulting in total mass attenuation coefficient $\mu_{\text{tot}}/\rho\,(E) = \mu/\rho\,(E)$. Therefore, $\mu/\rho\,(E)_{\text{mix}}$ computation is extended to single attenuation process consideration by mixture rule application via eq. (II-31) on the basis of already utilised elemental compositions. The applied elemental raw data for standard $\Delta E = 1\,\text{keV}$ grid (with additional device-specific energies) from XCOM (2010) provides also single mechanism values, which are likewise compiled in Table VII-3 to Table VII-9. Note, basic XCOM (2010) energy grid was used in terms of data determination, where no occurrence of absorption edges is found in the considered range $E = 5 \dots 100\,\text{keV}$ for the HCNOS-elements and calcium, which is confirmed by the tables available from HUBBELL, SELTZER (2004). However, single process attenuation data further facilitates to evaluate individual contribution to total attenuation via computation of attenuation fraction $\xi(i)$ following eq. (II-15).

Finally, computation results from Chapter IV–5.2.2 by means of both single mean energies $\mu/\rho\,(\bar{E})_{\text{mix}}$ as well measured X-ray spectra $\mu/\rho\,(S(E))_{\text{mix}}$ are compared toward mean mass attenuation coefficient $\overline{\mu/\rho}$ data from X-ray transmission measurements (Chapter IV–4.3.2). Corresponding values individually consider the respective device setup regarding measuring conditions, mean radiation energy $\bar{E}$ or X-ray spectrum $S(E)$. All computations are, in turn, performed on the basis of actually determined elemental compositions corresponding to the very same measured material. Comparison results are presented in Chapter IV–5.2.3.

5.2.2   Results and discussion

Mass-fraction-weighted total mean mass attenuation coefficients $\mu/\rho\,(E)_{\text{mix}}$ were computed for single energies within the range $E = 5 \dots 100\,\text{keV}$ for selected materials with the abundances $\omega(i)$ based on both elemental analyses (TMP, labMDF, Fmat, UF-C, indMDF, and insulation) as well as empirical and reviewed data (water,

wood (simplistic), wood (total mean), cellulose (mean), hemicelluloses (mean), and lignin (mean)). In addition to oven-dry material, labMDF at $MC = 9.5\,\%$ is taken into account and henceforth referred to as labMDF 9.5 % MC, where its elemental composition is computed following inverse moisture correction as described in Chapter IV–2.4.2. The moisture state is considered to correspond to standard conditions (refer to Chapter IV–1.5), i. e., virtual conditioning at 20/65, with consequent $MC = 9.5\,\%$ likewise measured for labMDF (refer to Table IV-5 in Chapter IV–1.5).

For comprehensive result presentation, reference is made to Appendix VII–4 complete with single $\mu/\rho\,(E)_i$ of the constituent elements as raw data. However, Figure IV-64 summarises computation results via compilation of selected attenuation plots in one chart over radiation energy E. Additionally, Figure IV-65 individually presents the same plots (and indMDF) with superimposed data points at low $E = 12.7\,\text{keV}$ (♦), medium $E = 21.5\,\text{keV}$ (■) and $E = 29.2\,\text{keV}$ (▲), as well as high $E = 59.5\,\text{keV}$ (●) energy level analogously to the selection in Table IV-34. Corresponding $\mu/\rho\,(E)_{\text{mix}}$ values for the very same energies are compiled in Table IV-35, where further materials come in addition. All graphs on logarithmic vertical axis fundamentally reveal the typical slope for mass attenuation coefficient plots over radiation energy, here, with steep decrement up to the region of $E = 25\,\text{keV}$ and with comparably slight diminution beyond.

All results can obviously be found in a comparable order without distinct differences, as expected, since elemental compositions and effective atomic numbers ($\bar{Z}_{\text{eff}}$ computation results, Chapter IV–5.1.2) are similarly close. Only water exceeds the other plots and cured adhesive resin (UF-C) slightly falls below, in both cases with decreasing distance along increasing energy, which is highlighted by means of the inset in Figure IV-64. Here, common composition of WBCs and the influence of present constituents on $\mu/\rho\,(E)_{\text{mix}}$ become obvious. Adhesive resin results summarised in UF-C with mean composition of both resin types (Table IV-3) as thermally cured structure without additional hardener

(Table IV-4) reveal lowest $\mu/\rho\,(E)_{\mathrm{mix}}$ values along the energy. Regardless of considerably higher nitrogen fraction $\omega(\mathrm{N})$ (Figure IV-11) of UF-C, the observed difference in its $\mu/\rho\,(E)_{\mathrm{mix}}$ is attributed to negligibly low ash content $\omega(a) <$ 0.1 %, where comparative calculations by means of TMP $\omega(a) = 0.309$ % would reveal $\mu/\rho\,(E)_{\mathrm{mix}}$ equivalent to TMP along total energy range. The composition of lab-made panels with a resin content of $\omega_{\mathrm{UF,OD}} = 10$ % (Chapter IV–1.2) yields, however, congruent plots of oven-dry (OD) lab-MDF (dashed line in Figure IV-64) and its raw material TMP (solid grey line). Thus, well-dispersed UF adhesive resin in cured state and common concentration is found not to significantly affect $\mu/\rho\,(E)_{\mathrm{mix}}$ of the final panel. Therefore, likewise indMDF plot in Figure IV-65 is more or less undistinguishable from labMDF (both OD). Computed water values are, in turn, higher than all others. Eventually, lab-MDF 9.5 % MC results (dotted line in Figure IV-64) are affected by the moisture but can be found, however, not far beyond OD labMDF.

So far, the result evaluation refers to visible perception at an axis scale of the magnified inset in Figure IV-64 of ± 0.021 m^2/kg, i. e., ± 34 %, around the vertical midpoint within this limited energy range $E = 20 \dots 25$ keV. Actual difference between labMDF at OD state and $MC = 9.5$ % can, moreover, be quantified with $\Delta\,\mu/\rho\,(E)_{\mathrm{mix}} =$ $+0.0011$ m^2/kg, where moist panels, therefore, exceed OD raw material values about 2 % at $E =$ 21.5 keV. To this end and beyond particular $\mu/\rho\,(E)_{\mathrm{mix}}$ results, Table IV-35 furthermore presents corresponding comparative figures $\Delta\,\mu/\rho\,(E)_{\mathrm{mix}}$ and $Q\,\mu/\rho\,(E)_{\mathrm{mix}}$ according to eq. (IV-41) and eq. (IV-42), respectively, on the four considered energy levels. Here, TMP data applies as reference representing clean wood. Accordingly and with equivalent extremes on all energy levels, $\mu/\rho\,(E)_{\mathrm{mix}}$ ranges between maximum (water) and minimum (lignin) with differences toward TMP of $\Delta\,\mu/\rho\,(12.5\ \mathrm{keV})_{\mathrm{mix}} =$ $-0.0343 \dots + 0.0607$ m^2/kg at the lowest and of $\Delta\,\mu/\rho\,(59.5\ \mathrm{keV})_{\mathrm{mix}} = -0.0004 \dots$ $+0.0014$ m^2/kg at the highest considered energy, i. e., basically decreasing $\Delta\,\mu/\rho\,(E)_{\mathrm{mix}}$ toward TMP along increasing E. The like applies to relative consideration with the ratios
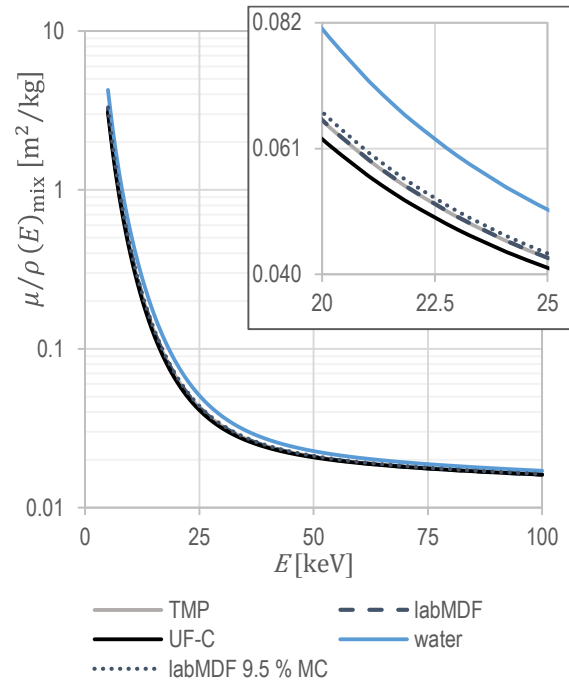
Figure IV-64: Total mean mass attenuation coefficients $\mu/\rho\,(E)_{\mathrm{mix}}$ over a practice-relevant range of radiation energy E computed via eq. (II-31) for labMDF and respective constituents based on actual elemental analysis data, inset with magnified $\mu/\rho\,(E)_{\mathrm{mix}}$ plot between $E = 20 \dots 25$ keV, for summarised single values refer to Table IV-35; note undistinguishable charts of TMP, labMDF (OD), and labMDF 9.5 % MC.

$Q\,\mu/\rho\,(12.7\ \mathrm{keV})_{\mathrm{mix}} = 0.833 \dots 1.296$ and $Q\,\mu/\rho\,(59.5\ \mathrm{keV})_{\mathrm{mix}} = 0.981 \dots 1.071$, respectively. Whilst the clean wood constituents cellulose as well as hemicelluloses are more or less equal and reveal no considerable differences toward TMP, lignin as further component drops below. Consequently, wood with the simplistic composition $\omega(\mathrm{H}) = 6$ %, $\omega(\mathrm{C}) = 50$ %, and $\omega(\mathrm{O}) =$ 44 % falls between. It is, moreover, ash content $\omega(a)$, which causes individual $\mu/\rho\,(E)_{\mathrm{mix}}$ differences between comparable materials apart from that. Considering WBC composition, cured adhesive resin UF-C $\mu/\rho\,(E)_{\mathrm{mix}}$ is 94.6 %, 95.5 %, 96.9 %, and 99.3 % that of TMP depending on the energy level ($E = 12.7, 21.5, 29.2, 59.5$ keV). Analogously, pure water exceeds TMP values about 29.6 %, 21.9 %, 15.8 %, and 7.1 %. The value characteristics prove the already observed decreasing distance between the plots with increasing energy, thus, mass attenuation coefficients of the investigated materials converge with increasing energy. The like applies to

$\frac{\mu}{\rho}(E)_{mix}$	μ/ρ $\left[\frac{m^2}{kg}\right]$	$\Delta\mu/\rho$ $\left[\frac{m^2}{kg}\right]$	$Q\mu/\rho$ $[-]$	μ/ρ $\left[\frac{m^2}{kg}\right]$	$\Delta\mu/\rho$ $\left[\frac{m^2}{kg}\right]$	$Q\mu/\rho$ $[-]$	μ/ρ $\left[\frac{m^2}{kg}\right]$	$\Delta\mu/\rho$ $\left[\frac{m^2}{kg}\right]$	$Q\mu/\rho$ $[-]$	μ/ρ $\left[\frac{m^2}{kg}\right]$	$\Delta\mu/\rho$ $\left[\frac{m^2}{kg}\right]$	$Q\mu/\rho$ $[-]$
energy E [keV]	12.7			21.5			29.2			59.5		
material, substance												
TMP	0.2050			0.0565			0.0338			0.0193		
labMDF	0.2055	+0.0004	1.002	0.0566	+0.0001	1.001	0.0338	0.0000	1.001	0.0193	0.0000	1.000
labMDF 9.5 % MC	0.2107	+0.0057	1.028	0.0576	+0.0011	1.020	0.0342	+0.0005	1.014	0.0194	+0.0001	1.006
Fmat	0.2136	+0.0086	1.042	0.0584	+0.0019	1.033	0.0345	+0.0008	1.023	0.0194	+0.0001	1.005
UF-C	0.1940	-0.0111	0.946	0.0540	-0.0025	0.955	0.0327	-0.0010	0.969	0.0192	-0.0001	0.993
indMDF	0.2067	+0.0017	1.008	0.0569	+0.0004	1.007	0.0339	+0.0002	1.005	0.0193	0.0000	1.001
insulation	0.2009	-0.0042	0.980	0.0556	-0.0009	0.985	0.0334	-0.0003	0.990	0.0193	0.0000	0.998
WBC (UF, mean)	0.2182	+0.0132	1.064	0.0593	+0.0028	1.050	0.0349	+0.0011	1.034	0.0194	+0.0001	1.008
WBC (other, mean)	0.2157	+0.0107	1.052	0.0588	+0.0023	1.041	0.0347	+0.0009	1.028	0.0194	+0.0001	1.007
water	0.2657	+0.0607	1.296	0.0689	+0.0124	1.219	0.0391	+0.0053	1.158	0.0207	+0.0014	1.071
wood (simplistic)	0.1931	-0.0119	0.942	0.0538	-0.0027	0.953	0.0327	-0.0011	0.968	0.0192	-0.0001	0.994
wood (total mean)	0.2115	+0.0064	1.031	0.0579	+0.0014	1.025	0.0343	+0.0006	1.017	0.0194	+0.0001	1.005
cellulose (mean)	0.2022	-0.0028	0.986	0.0557	-0.0008	0.985	0.0334	-0.0004	0.990	0.0193	0.0000	1.000
hemicellu. (mean)	0.2017	-0.0033	0.984	0.0555	-0.0010	0.983	0.0333	-0.0004	0.987	0.0193	0.0000	0.998
lignin (mean)	0.1707	-0.0343	0.833	0.0494	-0.0071	0.874	0.0309	-0.0028	0.916	0.0189	-0.0004	0.981

Table IV-35: Total mean mass attenuation coefficients $\mu/\rho(E)_{mix}$ at four energy levels E (corresponding to $\bar{E}$ of W-mat-16-w/o, W-RDP-35-w/o, and W-RDP-50-w/ device (Table IV-29) as well as ^{241}Am) computed via eq. (II-31) of applied WBCs and respective constituents based on actual elemental analysis data (upper rows) as well as common compound values and generalised literature figures (lower rows), complete with comparison via $\Delta\mu/\rho(E)_{mix}$ eq. (IV-41) and $Q\mu/\rho(E)_{mix}$ eq. (IV-42) toward respective TMP data as reference.
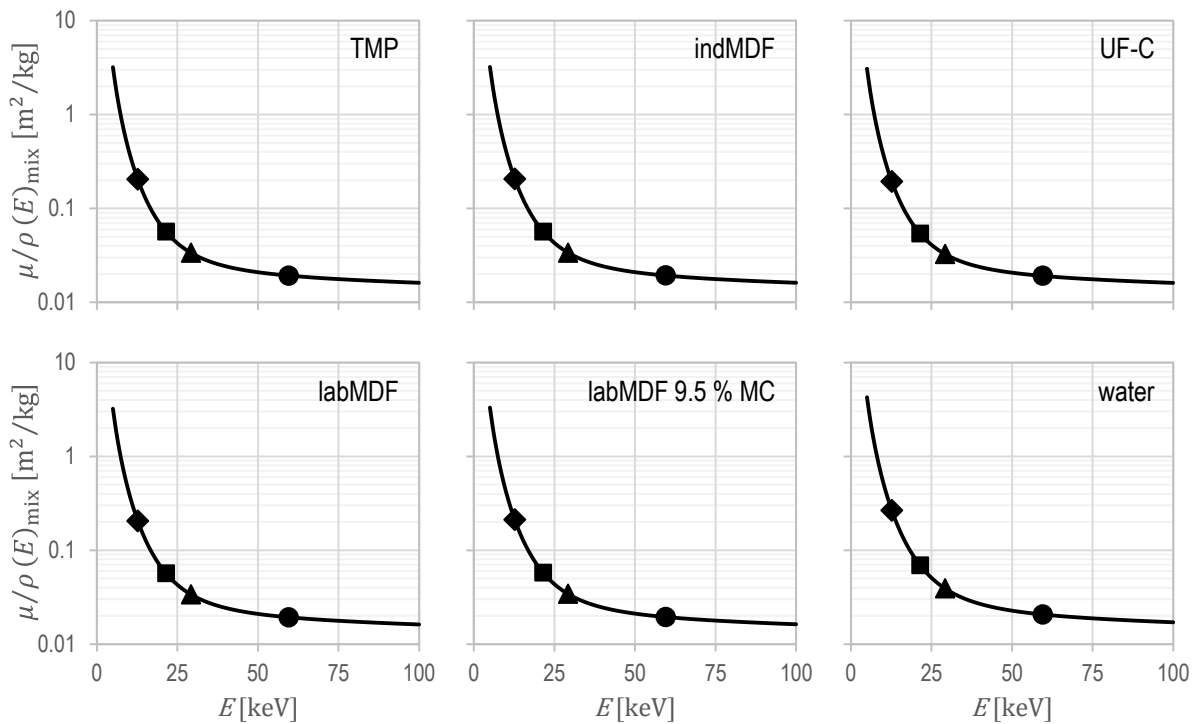
Figure IV-65: Total mean mass attenuation coefficients $\mu/\rho(E)_{mix}$ over a practice-relevant range of radiation energy E (solid lines) computed via eq. (II-31) of applied WBCs and respective constituents based on actual elemental analysis data, complete with superimposed data points at low $E = 12.7$ keV (♦), medium $E = 21.5$ keV (■) and $E = 29.2$ keV (▲), as well as high $E = 59.5$ keV (●) energy level, for summarised single values refer to Table IV-35.

actually moist material including adhesive resin, i. e., labMDF 9.5 % MC, but with considerably decreased extent, hence, computed $\mu/\rho\,(E)_{\mathrm{mix}}$ exceed TMP reference values by about 2.8 %, 2.0 %, 1.4 %, and 0.6 % (again at $E = 12.7, 21.5, 29.2, 59.5\,\mathrm{keV}$). On the contrary, exclusive resin addition resulting in labMDF causes no significant $\mu/\rho\,(E)_{\mathrm{mix}}$ variations with negligible $Q\,\mu/\rho\,(E)_{\mathrm{mix}} = 1.0\ldots1.002$ at OD conditions. The like applies to PMDI-bonded insulation, where slight differences are only observed around the low energy level and are considered to be rather attributed to lower $\omega(a)$ of the performed analysis.

To conclude computed total mean mass attenuation coefficients $\mu/\rho\,(E)_{\mathrm{mix}}$,

- a negligible impact of adhesive resin is proven,
- low-energy $\mu/\rho\,(E)_{\mathrm{mix}}$ reveal individual variations up to 3 % above clean TMP depending on MC and ash content $\omega(a)$,
- whereas all computed values except water are roughly equal at 59.5 keV level with $\mu/\rho\,(E)_{\mathrm{mix}} \approx 0.0193\,\mathrm{m^2/kg}$.

The latter, in turn, is in good agreement with some of the reviewed values compiled in Table II-3. However, for comparison with underrepresented literature values and particularly measured $\overline{\mu/\rho}$, reference is made to Chapter IV–5.2.3.

Beyond fundamental $\mu/\rho\,(E)_{\mathrm{mix}}$ results, the mass-fraction-weighted attenuation contribution $\eta(i)$ is computed following eq. (II-33) again at the four energy levels. The result presentation is, however, focused on similar material selection like in Figure IV-64 and Figure IV-65, i. e., applied OD WBCs (labMDF, indMDF, and insulation) and the respective raw material (TMP, UF-C, and Fmat) as well as water and, consequently, moist labMDF 9.5 % MC. Figure IV-66 presents $\eta(i)$ results as stacked horizontal bar charts transferred to 100 % scale. For corresponding values reference is made to Table IV-36.

material	mass-fraction-weighted attenuation contribution $\eta(i)$ [%]					
	$_1$H	$_6$C	$_7$N	$_8$O	$_{16}$S	a
energy E	12.7 keV					
TMP	1.1	30.5	0.4	60.7	0.1	7.2
labMDF	1.1	29.4	3.2	58.9	0.2	7.2
labMDF 9.5 % MC	1.1	26.2	2.9	63.2	0.2	6.4
Fmat	1.1	28.5	2.9	56.1	0.4	11.1
UF-C	1.1	19.4	35.0	43.3	0.0	1.1
indMDF	1.1	29.1	4.0	57.3	0.5	8.0
insulation	1.1	32.0	0.5	59.8	0.0	6.5
water	1.6	0.0	0.0	98.4	0.0	0.0
energy E	21.5 keV					
TMP	3.9	35.3	0.4	54.6	0.1	5.8
labMDF	3.8	34.0	3.2	53.0	0.2	5.8
labMDF 9.5 % MC	4.1	30.5	2.9	57.2	0.2	5.2
Fmat	3.7	33.2	2.9	50.8	0.3	9.0
UF-C	3.9	22.2	34.3	38.6	0.0	0.9
indMDF	3.9	33.8	4.0	51.6	0.4	6.4
insulation	3.9	36.9	0.5	53.5	0.0	5.2
water	6.0	0.0	0.0	94.0	0.0	0.0
energy E	29.2 keV					
TMP	6.3	39.8	0.4	49.5	0.0	4.0
labMDF	6.2	38.3	3.2	48.0	0.1	4.0
labMDF 9.5 % MC	6.6	34.5	2.9	52.2	0.1	3.6
Fmat	6.2	37.8	2.9	46.6	0.2	6.3
UF-C	6.3	24.7	33.9	34.5	0.0	0.6
indMDF	6.3	38.1	4.0	46.9	0.3	4.5
insulation	6.3	41.3	0.5	48.2	0.0	3.6
water	10.2	0.0	0.0	89.8	0.0	0.0
energy E	59.5 keV					
TMP	10.1	46.5	0.4	42.0	0.0	1.1
labMDF	10.0	44.9	3.2	40.8	0.0	1.1
labMDF 9.5 % MC	10.7	40.7	2.9	44.6	0.0	1.0
Fmat	10.0	45.0	3.0	40.2	0.1	1.7
UF-C	9.9	28.2	33.2	28.6	0.0	0.2
indMDF	10.1	44.7	4.0	39.9	0.1	1.2
insulation	10.0	47.9	0.5	40.6	0.0	1.0
water	17.7	0.0	0.0	82.3	0.0	0.0

Table IV-36: Mass-fraction-weighted attenuation contribution $\eta(i)$ [%] following eq. (II-33) of constituent elements and ash ($a = {}_{20}$Ca) for applied WBCs and respective raw material based on actual elemental analysis data, at four energy levels E (corresponding to $\bar{E}$ of W-mat-16-w/o, W-RDP-35-w/o, and W-RDP-50-w/ device (Table IV-29) as well as ^{241}Am); note, all materials oven-dry except labMDF 9.5 % MC (virtually conditioned at 20/65) and water.
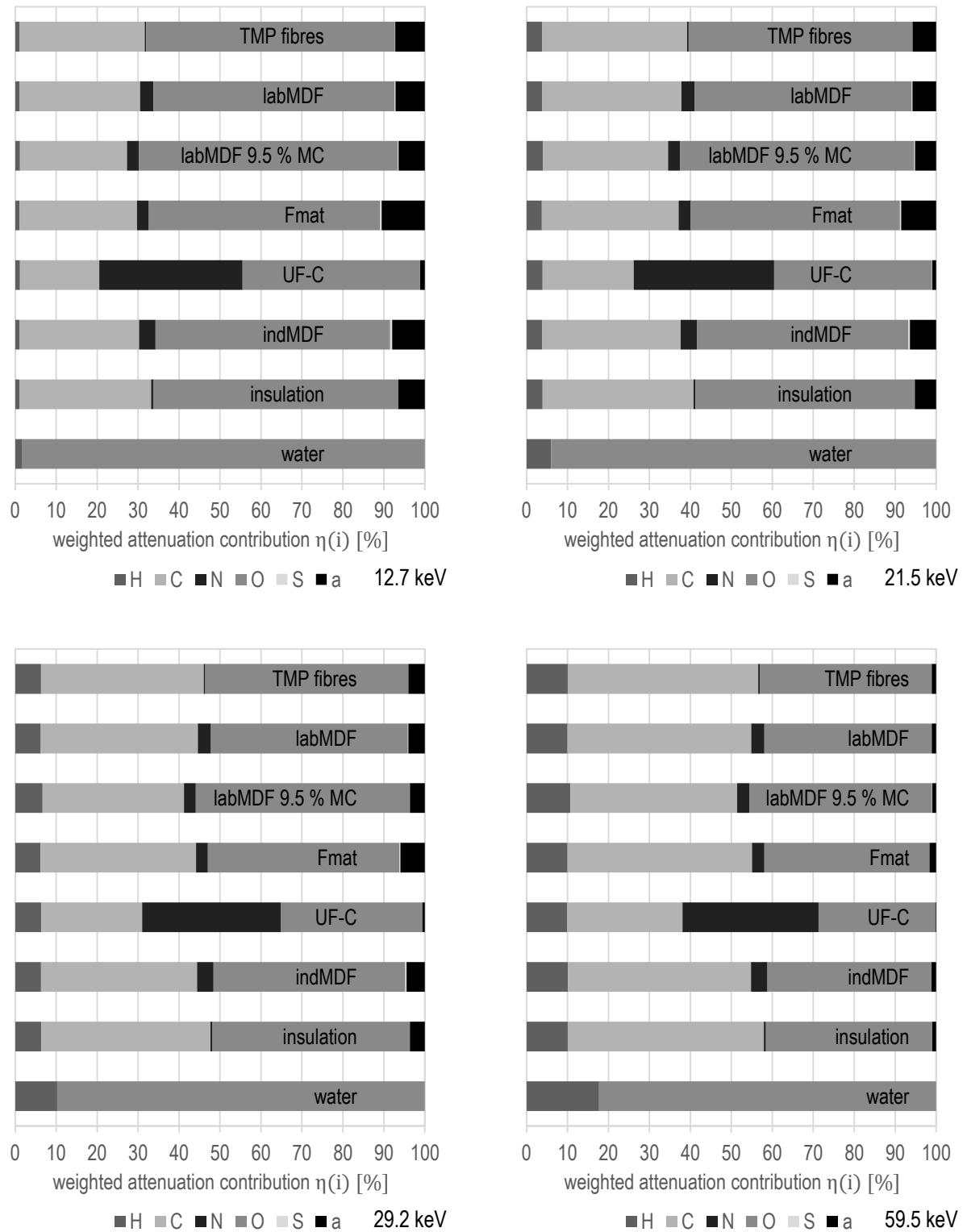
Figure IV-66: Mass-fraction-weighted attenuation contribution $\eta(i)$ [%] following eq. (II-33) of constituent elements and ash ($a = {}_{20}Ca$) for applied WBCs and respective raw material based on actual elemental analysis data, at four energy levels E (corresponding to $\bar{E}$ of W-mat-16-w/o, W-RDP-35-w/o, and W-RDP-50-w/ device (Table IV-29) as well as ${}^{241}Am$); note, all materials oven-dry except labMDF 9.5 % MC (virtually conditioned at 20/65) and water; for detailed values refer to Table IV-36.

The charts and values of $\eta(i)$ obviously differ from $\omega(i)$ (refer to Figure IV-11) since ith mass fraction is combined with actual attenuation potential of the single constituent. Accordingly, bar widths are weighted by $\mu/\rho(E)_i$ (additionally presented in Figure IV-69), hence radiation energy dependency comes in addition. With increasing energy, major attenuation contribution is generally found to be shifted from right to left in the shown order of chemical elements, i. e., from high-Z to low-Z constituents. Increasing contribution of hydrogen H with increasing energy E becomes particularly obvious from water charts and data. The like applies to the other materials. Contrary to this, considerably decreasing $\eta(i)$ values with increasing E particularly toward high energy level can be observed for ash a contribution, which is considered as elemental Ca as already pointed out elsewhere. Again, sulphur is negligible with $\eta(S) \leq 1\,\%$, where already $\omega(S)$ was rather close to detection limit of elemtal analysis as pointed out in Chapter IV–2.4.2.

Beyond the result presentation in Figure IV-66, Pareto charts are further utilised to illustrate mass-fraction-weighted contribution character of the investigated mixtures and particular difference between the four energy levels. To this end, Figure IV-67 and Figure IV-68 show both $\eta(i)$ [−] in descending order (bars) and its cumulation $\sum \eta(i)$ [%] (■ line plot) for applied WBCs and raw TMP fibres. Obviously, all charts reveal a common situation of Pareto analysis, where few members govern the overall result. The elements O and C significantly dominate the total attenuation of all materials on every energy level and yield, e. g. for labMDF 9.5 % MC, a cumulated contribution of $\sum \eta(i) = 89\,\%, 88\,\%, 87\,\%,$ and $85\,\%$ at $E = 12.7, 21.5, 29.2,$ and $59.5\,\mathrm{keV}$, respectively. Here, both constituents are consistently found in the same descending order $\eta(O) > \eta(C)$ where, however, $\eta(O)$ decreases with increasing energy in support of $\eta(C)$. Moreover, different $\mu/\rho(E)_i$, slopes in Figure IV-69, where initially distant CNO-element plots converge with increasing energy, enable understanding of energy-dependent attenuation contribution within the considered WBC materials. Therefore, low-energy $\eta(i)$ Pareto chart results are amplified by $\mu/\rho(E)_i$ diversity whereas high-energy figures

more or less represent elemental composition. Accordingly, 59.5 keV chart in Figure IV-66 appears equivalent to stacked horizontal bar charts of $\omega(i)$ in Figure IV-11. Likewise, the contribution and order of the other elements H, N, (and S) and ash a varies not only depending on material, thus, composition, but also due to energy level. With further respect to Figure IV-69, hydrogen H attenuation reveals different behaviour toward CNO-elements as well as Ca. Accordingly, H plot and data unveil low $\mu/\rho(E)$ at low and low-medium energy level with considerably lower diminution about 25 % along the considered energy range, and values beyond CNO-elements from medium energy level about $E = 27\,\mathrm{keV}$ (refer to Table VII-3 and Figure VII-29 in Appendix VII–4). Total attenuation, however, is dominated by scattering and features practically no absorption for $E \geq 5\,\mathrm{keV}$. Regardless of attenuation mechanisms, hydrogen is the third-strongest contributor at the high energy level with $\eta(H) \approx 10\,\%$ in contrast to low energy, where $\eta(H) = 1.1\,\%$ is negligible as directly compared in Figure IV-67. On the contrary, ash contribution is on third position with $\eta(a) \approx 6\,\%$ up to low-medium energy level and negligible, in turn, at highest energy with $\eta(a) = 1\,\%$. With regard to investigated material containing UF adhesive resin, i. e., labMDF (OD and 9.5 % MC), Fmat, and indMDF, contribution of nitrogen reveals equivalent results on all considered energy levels with $\eta(N) \approx 3 \ldots 4\,\%$. Eventually, actual contribution of elements besides C and O to total attenuation by WBCs around standard conditions is obviously rather small and partly negligible in strong dependence on applied radiation energy.
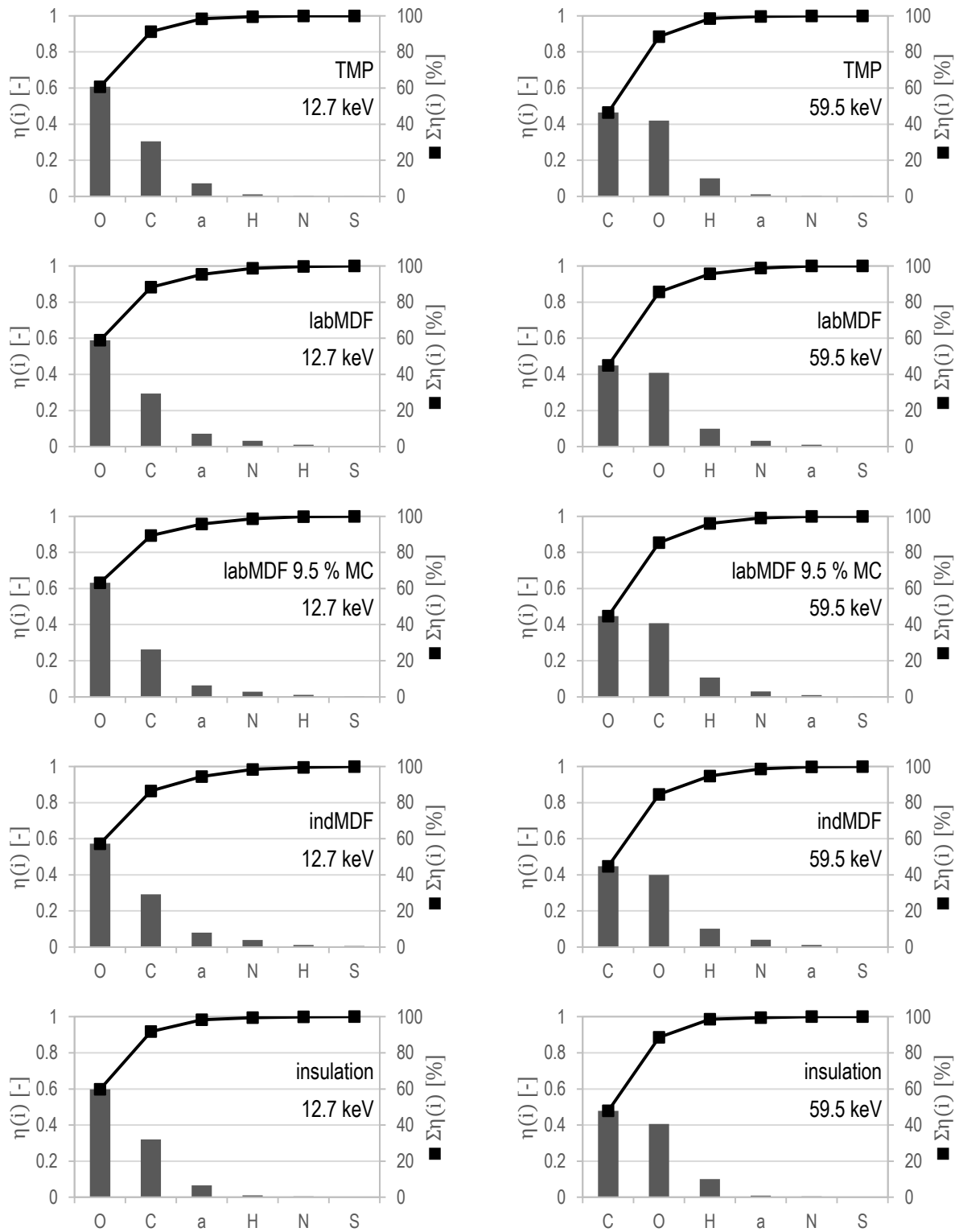
Figure IV-67: Pareto charts of mass-fraction-weighted attenuation contribution $\eta(i)$ [–] (bars, left vertical axis) following eq. (II-33) and its cumulation $\sum \eta(i)$ [%] (■, right vertical axis) of constituent elements and ash ($a = {}_{20}\mathrm{Ca}$) for applied WBCs and raw TMP fibres based on actual elemental analysis data, at low and high energy level $E = 12.7\,\mathrm{keV}$ and $E = 59.5\,\mathrm{keV}$ (corresponding to $\bar{E}$ of W-mat-16-w/o device (Table IV-29) and ${}^{241}\mathrm{Am}$); note, all materials oven-dry except labMDF 9.5 % MC (virtually conditioned at 20/65); for detailed values refer to Table IV-36.
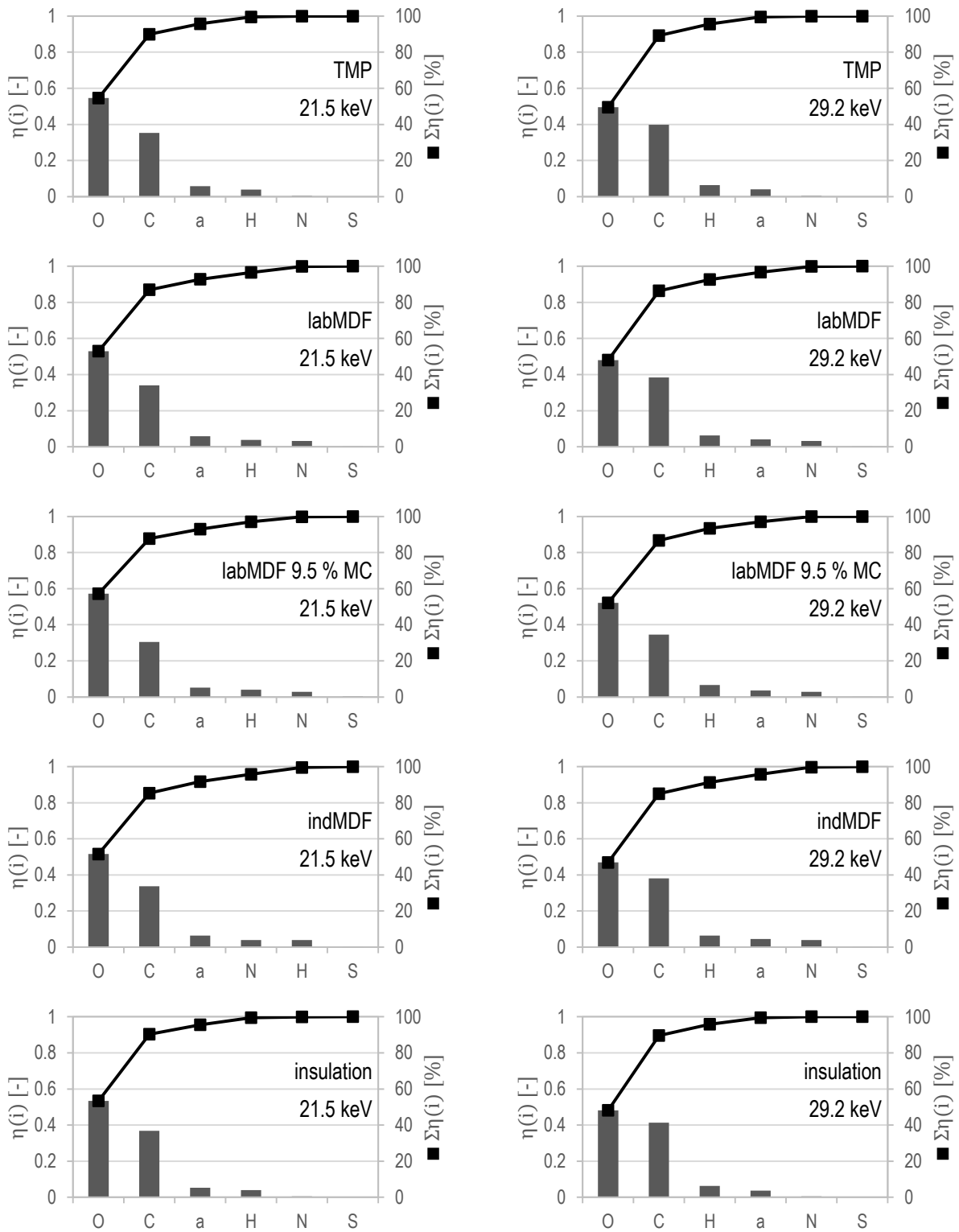
Figure IV-68: Pareto charts of mass-fraction-weighted attenuation contribution $\eta(i)$ [–] (bars, left vertical axis) following eq. (II-33) and its cumulation $\sum \eta(i)$ [%] (■, right vertical axis) of constituent elements and ash ($a = {}_{20}\text{Ca}$) for applied WBCs and raw TMP fibres based on actual elemental analysis data, at medium energy level $E = 21.5 \, \text{keV}$ and $E = 29.2 \, \text{keV}$ (corresponding to $\bar{E}$ of W-RDP-35-w/o and W-RDP-50-w/ device (Table IV-29)); note, all materials oven-dry except labMDF 9.5 % MC (virtually conditioned at 20/65); for detailed values refer to Table IV-36.
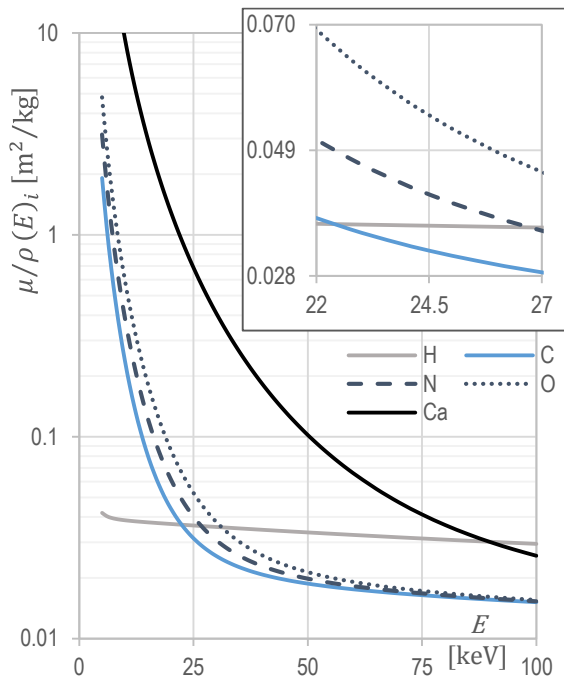
Figure IV-69: Single mass attenuation coefficients $\mu/\rho\,(E)_i$ of constituent HCNO-elements complete with Ca for ash over a practice-relevant range of radiation energy E as raw data from XCOM (2010), inset with magnified $\mu/\rho\,(E)_i$ plot between $E = 20 \ldots 25$ keV, for single values refer to Table VII-3 to Table VII-9.

Notwithstanding the above investigation of mass-fraction-weighted attenuation contribution $\eta(i)$ based on actual elemental analysis data, the virtual variation of WBC composition exemplarily for labMDF (oven-dry) serves as further basis for $\mu/\rho\,(E)_{\mathrm{mix}}$ computation via mixture rule to evaluate influence of $\omega(\mathrm{N})$ (for resin content), MC, $\omega(a)$, and $\bar{Z}_{\mathrm{eff,ash}}$ (for ash composition) within a practice-oriented range with extreme character considering conventional WBCs. Figure IV-70 illustrates virtually computed $\mu/\rho\,(E)_{\mathrm{mix}}$ results along respective parameter variation at low $E = 12.7$ keV, medium $E = 21.5$ keV and $E = 29.2$ keV, as well as high $E = 59.5$ keV energy level. Table IV-37 summarises chart data with particular focus on virtual lower $(-)$ and upper $(+)$ limits complete with comparison via $\Delta\,\mu/\rho\,(E)_{\mathrm{mix}}$ eq. (IV-41) and $\mathrm{Q}\,\mu/\rho\,(E)_{\mathrm{mix}}$ eq. (IV-42) toward respective $\mu/\rho\,(E)_{\mathrm{mix}}$ values from actual analysis data. To this end, result presentation corresponds to $\bar{Z}_{\mathrm{eff}}$ charts in Figure IV-63 as well as the data in Table IV-33 considering range of virtual variation. Accordingly, com-

parison toward $\bar{Z}_{\mathrm{eff}}$ reveals equivalent tendencies for $\mu/\rho\,(E)_{\mathrm{mix}}$ results in general whereas particular extent differs in dependency of energy level of $\mu/\rho\,(E)_{\mathrm{mix}}$ computation owing to its energy dependency and the calculation of $\bar{Z}_{\mathrm{eff}}$ independent from any energy consideration. Relative quantification of variation effects by the non-dimensional quotients $Q\bar{Z}_{\mathrm{eff}}$ and $\mathrm{Q}\,\mu/\rho\,(E)_{\mathrm{mix}}$, respectively, unveils a comparable impact of composition variations around high-medium to high radiation energies. The individual character, however, requires a differentiated consideration of the constituents.

Regarding adhesive resin content, more or less equal $\mu/\rho\,(E)_{\mathrm{mix}}$ values can be found on each energy level unaffected by $\omega(\mathrm{N})_{\mathrm{labMDF}} = (3.4 \pm 3)\,\%$ variation. On the upper limit $(+)$, there is no quantifiable difference with $\Delta\,\mu/\rho\,(E)_{\mathrm{mix}} = 0$. Infinitesimal differences can be observed on the lower limit $(-)$ with $\Delta\,\mu/\rho\,(E)_{\mathrm{mix}} \leq +0.0003$ m^2/kg. Hence, relative variation reveals a negligible range of $\mathrm{Q}\,\mu/\rho\,(E)_{\mathrm{mix}} = 1.0 \ldots 1.002$, which falls even below indMDF difference toward TMP (clean wood) in Table IV-35 with $\mathrm{Q}\,\mu/\rho\,(E)_{\mathrm{mix}} < 1.008$.

Virtual variation of the moisture conditions around $MC_{\mathrm{labMDF}} = 9.5\,\%$ corresponding to standard conditions 20/65 reveals minor but partly considerable differences within the limits particularly on low energy level with $\Delta\,\mu/\rho\,(E)_{\mathrm{mix}} = -0.0026 \ldots +0.0024$ m^2/kg. Toward oven-dry (OD) state at the very same energy $E = 12.7$ keV labMDF 9.5 % MC differs, in turn, with $\Delta\,\mu/\rho\,(E)_{\mathrm{mix}} = +0.0052$ m^2/kg and maximum moisture limit with assumed $MC_{\mathrm{FSP}} = 27\,\%$ (fibre saturation point) would exceed OD attenuation values with $\Delta\,\mu/\rho\,(E)_{\mathrm{mix}} = +0.0128$ m^2/kg. However, the impact of MC on $\mu/\rho\,(E)_{\mathrm{mix}}$ decreases with increasing energy. Moreover, primarily considered $\Delta MC = \pm 5\,\%$ causes no more than the relative deviation of $\pm 1.2\,\%$ on low and medium energy level. Moisture variations within the common limits are negligible in case of high energy $E = 59.5$ keV with $\mathrm{Q}\,\mu/\rho\,(E)_{\mathrm{mix}} = 0.997 \ldots 1.003$.

The greatest impact with the steepest slope of the plots in Figure IV-70 can be observed for the variation of both ash content $\omega(a)$ and composition via $\bar{Z}_{\text{eff,ash}}$, however, again decreasing with increasing energy. In consequence of virtual elimination of any mineral constituents, i. e., $\omega(a) = 0\,\%$, $\mu/\rho\,(E)_{\text{mix}}$ falls consistently below labMDF (OD) values on EA basis with $Q\,\mu/\rho\,(E)_{\text{mix}} = 0.933\ldots0.993$ along the considered energy range. Virtually threefold increase of ash content to $\omega(a) = 0.9\,\%$ yields, in turn, considerably increased $\mu/\rho\,(E)_{\text{mix}}$ due to larger abundance of high-attenuating $_{20}$Ca, where computed mass attenuation coefficients exceed analysed labMDF (OD) values about $1.5\ldots13.4\,\%$ depending on considered radiation energy. In contradiction to aforementioned parameters, virtual ash composition variation reveals non-linear slope of corresponding $\mu/\rho\,(E)_{\text{mix}}$ plots (last row in Figure IV-70) on each energy level. The extent, however, can be found below ash content impact. Particularly the decrement of $\bar{Z}_{\text{eff,ash}}$ is of practical relevance due to increased abundance of light ash elements like $_{14}$Si in consequence of, e. g., utilisation of annual plants with typically higher silicate content. Accordingly, $\mu/\rho\,(E)_{\text{mix}}$ could fall up to 6 % below conventional labMDF (OD) values but may further be counterbalanced by increased $\omega(a)$.

Finally, moisture and ash content are found to have a potentially considerable impact on WBC $\mu/\rho\,(E)_{\text{mix}}$ at low energies. However, all virtually evaluated composition variations become negligible at high energy levels.

energy E [keV]		12.7			21.5			29.2			59.5		
$\frac{\mu}{\rho}(E)_{\text{mix}}$ parameter variation (abs.)		μ/ρ $\left[\frac{m^2}{kg}\right]$	$\Delta\mu/\rho$ $\left[\frac{m^2}{kg}\right]$	$Q\mu/\rho$ $[-]$	μ/ρ $\left[\frac{m^2}{kg}\right]$	$\Delta\mu/\rho$ $\left[\frac{m^2}{kg}\right]$	$Q\mu/\rho$ $[-]$	μ/ρ $\left[\frac{m^2}{kg}\right]$	$\Delta\mu/\rho$ $\left[\frac{m^2}{kg}\right]$	$Q\mu/\rho$ $[-]$	μ/ρ $\left[\frac{m^2}{kg}\right]$	$\Delta\mu/\rho$ $\left[\frac{m^2}{kg}\right]$	$Q\mu/\rho$ $[-]$
+	6.4	0.2055	0.0000	1.000	0.0566	0.0000	1.000	0.0338	0.0000	1.000	0.0193	0.0000	1.000
$\omega(\mathbf{N})$ [%]	3.4	0.2055			0.0566			0.0338			0.0193		
−	0.4	0.2058	+0.0003	1.002	0.0567	+0.0001	1.002	0.0338	+0.0001	1.002	0.0193	0.0000	1.002
FSP	27	0.2183	+0.0128	1.062	0.0592	+0.0026	1.046	0.0349	+0.0011	1.033	0.0196	+0.0003	1.015
+	14.5	0.2131	+0.0024	1.011	0.0581	+0.0005	1.009	0.0345	+0.0002	1.006	0.0195	+0.0001	1.003
$\mathbf{MC}$ [%]	9.5	0.2107	+0.0052	1.025	0.0576	+0.0011	1.019	0.0342	+0.0005	1.014	0.0194	+0.0001	1.006
−	4.5	0.2081	-0.0026	0.988	0.0571	-0.0005	0.991	0.0340	-0.0002	0.993	0.0194	-0.0001	0.997
OD	0.0	0.2055			0.0566			0.0338			0.0193		
+	0.9	0.2330	+0.0275	1.134	0.0626	+0.0060	1.107	0.0362	+0.0024	1.073	0.0196	+0.0003	1.015
$\omega(\mathbf{a})$ [%]	0.309	0.2055			0.0566			0.0338			0.0193		
−	0.0	0.1917	-0.0138	0.933	0.0536	-0.0030	0.947	0.0326	-0.0012	0.964	0.0192	-0.0001	0.993
+	26 (Fe)	0.2185	+0.0130	1.063	0.0598	+0.0032	1.057	0.0352	+0.0014	1.040	0.0195	+0.0002	1.009
$\bar{Z}_{\text{eff,ash}}$	20 (Ca)	0.2055			0.0566			0.0338			0.0193		
−	11 (Na)	0.1931	-0.0124	0.940	0.0538	-0.0028	0.951	0.0327	-0.0011	0.967	0.0192	-0.0001	0.993

Table IV-37: Total mean mass attenuation coefficients $\mu/\rho\,(E)_{\text{mix}}$ of labMDF (oven-dry) based on virtual variation with upper (+) and lower (−) limit value around actual elemental analysis data with comparison via $\Delta\mu/\rho\,(E)_{\text{mix}}$ eq. (IV-41) and $Q\,\mu/\rho\,(E)_{\text{mix}}$ eq. (IV-42) toward the respective actual value.
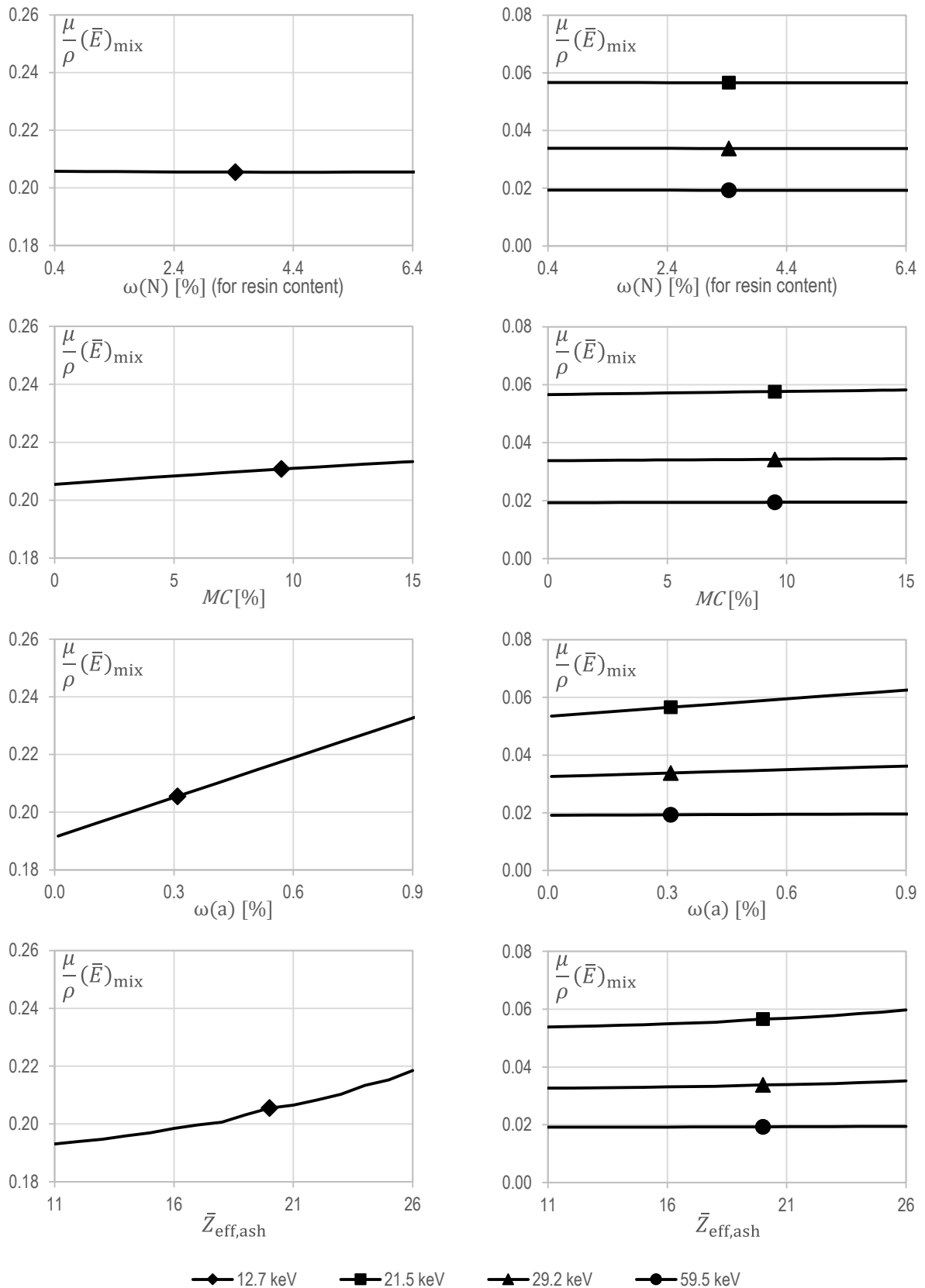
Figure IV-70: Total mean mass attenuation coefficients $\mu/\rho\,(E)_{\mathrm{mix}}$ of labMDF (oven-dry) based on virtual variation of actual elemental analysis data (points ♦, ■, ▲, ●) within an extreme but practice-oriented range of resin content via nitrogen content $\omega(N)$ [%], moisture content MC [%], ash content $\omega(a)$ [%], and effective atomic number of ash $\bar{Z}_{\mathrm{eff,ash}}$ at low $E = 12.7$ keV (♦), medium $E = 21.5$ keV (■) and $E = 29.2$ keV (▲), as well as high $E = 59.5$ keV (●) energy level.

For further quantitative evaluation of composition variation with exclusive respect to one factor at a time, the differential mass attenuation coefficient $\delta \mu/\rho\,(E)_{\mathrm{mix}}$ is introduced. The figure virtually expresses relative variation of $\mu/\rho\,(E)_{\mathrm{mix}}$ in consequence of composition variation with respect to the discussed aspects of resin content (via nitrogen content $\omega(\mathrm{N})$), MC, and ash content $\omega(a)$ as well as ash composition in terms of effective atomic number of the ash $\bar{Z}_{\mathrm{eff,ash}}$. Consequent computation following eq. (IV-43) takes $\mu/\rho\,(E)_{\mathrm{mix}}$ ranges with respect to the variables in Table IV-37 and their limits on the very same energy levels into account. Here, the bottom of the unit fraction [%/…] represents a respectively utilised calculation reference. Since $\delta \mu/\rho\,(E)_{\mathrm{mix}}$ presumes linear context in the considered range, its calculation is only partly applicable to virtual $\bar{Z}_{\mathrm{eff,ash}}$ variation (last-row charts in Figure IV-70), which obviously reveals a non-linear and rather progressively increasing slope. For the purpose of comparison and estimation of ash composition impact on different energy levels, it, however, is considered to serve as an appropriate figure for potential $\bar{Z}_{\mathrm{eff,ash}}$ variation effects on radiation attenuation.

The results of $\delta \mu/\rho\,(E)_{\mathrm{mix}}$ in Table IV-38 for virtual variation of labMDF (oven-dry) composition parameters in Table IV-37 unveil generally decreasing impact of WBC composition variation with increasing radiation energy in terms of decreasing $\delta \mu/\rho\,(E)_{\mathrm{mix}}$ values; hence, confirm hitherto findings. Negligible influence of adhesive resin content variation evaluated via $\omega(\mathrm{N})$ becomes obvious with consistent $\delta \mu/\rho\,(E)_{\mathrm{mix}} = -0.03\,\%/\%\Delta\omega(\mathrm{N})$ along total energy range. Thus, considering urea-based types of adhesive resin, no quantifiable impact of content and recipe apart from further additives can be stated by way of calculation. Increasing MC causes slightly increasing attenuation coefficients on low and low-medium energy levels with $\delta \mu/\rho\,(E)_{\mathrm{mix}} \approx 0.2\,\%/\%\Delta MC$. At higher energy levels, $\delta \mu/\rho\,(E)_{\mathrm{mix}}$ is more or less half the number and moisture variations in common application range yield no significant variation of WBC mass attenuation coefficients. The quantified influences of ash content variation appear tremendous but,

	energy E [keV]			
$\delta\dfrac{\mu}{\rho}(E)_{\mathrm{mix}}$	**12.7**	**21.5**	**29.2**	**59.5**
$[\%/\%\Delta\omega(\mathbf{N})]$	-0.03	-0.03	-0.03	-0.03
$[\%/\%\Delta\boldsymbol{MC}]$	0.23	0.18	0.13	0.06
$[\%/\%\Delta\omega(\boldsymbol{a})]$	22.33	17.78	12.11	2.44
$\left[\%/\Delta\bar{Z}_{\mathbf{eff,ash}}\right]$	0.82	0.71	0.49	0.11

Table IV-38: Differential mass attenuation coefficients $\delta \mu/\rho\,(E)_{\mathrm{mix}}$ acc. to eq. (IV-43) for virtual variation of labMDF (oven-dry) composition parameters in Table IV-37 on the very same energy levels.

note, the unit is related to one percent ash content variation. Breaking the figure down into $\Delta\omega(a) = 0.1\,\%$ as basis, the differential mass attenuation coefficient would range in the order of 1…2 % at low and medium energy levels, which can, nevertheless, not necessarily be neglected for particular WBC applications. However, the total range of consideration comprises, e. g., $\Delta\omega(a) = 0.9\,\%$ for European wood species (for details reference is made to Table IV-11). Moreover, increasing ash content will cause severe impact in the case of, e. g., tropical hardwoods or increment bark fraction in WBCs as well as regarding other lignocellulosic material such as bamboo and annual plants like rice straw (cf. LAMPERT (1967)). In this regard, the lower Z_{eff} of the constituent ash elements in consequence of commonly increased $_{14}\mathrm{Si}$ content in annual plants, will, in turn, affect $\mu/\rho\,(E)_{\mathrm{mix}}$ of WBCs made off such raw material. Differential variation in the order of $\delta \mu/\rho\,(E)_{\mathrm{mix}} = 0.5\ldots1.0\,\%/\Delta\bar{Z}_{\mathrm{eff,ash}}$ at low and medium energy levels is considered not to reveal a distinct impact in the case of European wood species with similar ash compositions. However, in WBC production rather a decrement of applied $\bar{Z}_{\mathrm{eff,ash}} = 20$ corresponding to $_{20}\mathrm{Ca}$ can be expected due to bark content (sand) or application of annual plants as well as the addition of 10…20 % fire retardants (on OD wood basis, on demand of fire-protection effect (cf. DEPPE, ERNST (1996)), which are commonly based on ammonium phosphate $(\mathrm{NH}_4)_3\mathrm{PO}_4$, where the impact is dominated by $_{15}\mathrm{P}$ as a highly-attenuating constituent.

Beyond application of the simplistic mixture rule considering single (mean) energies, spectral-weighted total mean mass attenuation coefficient $\mu/\rho \left(S(E) \right)_{\mathrm{mix}}$ is exclusively computed for the composition labMDF 9.5 % MC. Consequent result presentation is focused on comprehensively available spectra data (Chapter IV–4.3.3.1) from measurements by means of Ag- and W-RDP devices (the latter without and with pre-filter). Here, both the initial $S_{\mathrm{D},0}(E)$ and transmitted spectra $S_{\mathrm{D,T}}(E, \rho_{\mathrm{A}})$ are employed. The latter were acquired (Chapter IV–4.2.6.1) by radiation transmission through $z_{\mathrm{nom}} = 50$ mm of lab-MDF as absorber with varying ρ_{nom} [kg/m³] (Table IV-2) at $MC = 9.5$ % corresponding to standard conditions 20/65. Computation via eq. (II-35) is carried out within the energy range $E_{\min} \ldots E_{\max}$ according to Table IV-29, which is again listed in Table IV-39.

The results of $\mu/\rho \left(S(E) \right)_{\mathrm{mix}}$ in Figure IV-71 given as a vertical bar chart serve to illustrate the more or less consistently decreasing character along the displayed order of the device setup spectra and particularly within the very same. Furthermore, the chart reveals differences between $\mu/\rho \left(S_{\mathrm{D},0}(E) \right)_{\mathrm{mix}}$ and $\mu/\rho \left(\bar{E} \right)_{\mathrm{mix}}$ computed for corresponding $\bar{E} = E_{\mathrm{mean}}$ from initial spectrum $S_{\mathrm{D},0}(E)$. Table IV-39 summarises spectral-weighted computation results complete with comparison to corresponding $\mu/\rho \left(\bar{E} \right)_{\mathrm{mix}}$ data by means of $\Delta \mu/\rho \left(E \right)_{\mathrm{mix}}$ via eq. (IV-41) and $Q \mu/\rho \left(E \right)_{\mathrm{mix}}$ via eq. (IV-42).

Obviously, integration of $\mu/\rho \left(S_{\mathrm{D},0}(E) \right)_{\mathrm{mix}}$ across measured spectral distribution does not result in equal values like computation of $\mu/\rho \left(\bar{E} \right)_{\mathrm{mix}}$ for the mean energy of the respectively very same initial spectrum $S_{\mathrm{D},0}(E)$, where $\mu/\rho \left(\bar{E} \right)_{\mathrm{mix}}$ consistently drops below $\mu/\rho \left(S_{\mathrm{D},0}(E) \right)_{\mathrm{mix}}$ considering the initial spectra without labMDF absorber. Regardless of the potential bias from spectra determination itself as already comprehensively discussed in Chapter IV–4.3.3.1, there are methodical reasons for the found differences. Thus, weighting by energy distribution of the initial spectrum yields fundamentally higher $\mu/\rho \left(S_{\mathrm{D},0}(E) \right)_{\mathrm{mix}}$ values, which are emphasised by generally increasing $\mu/\rho \left(E \right)$
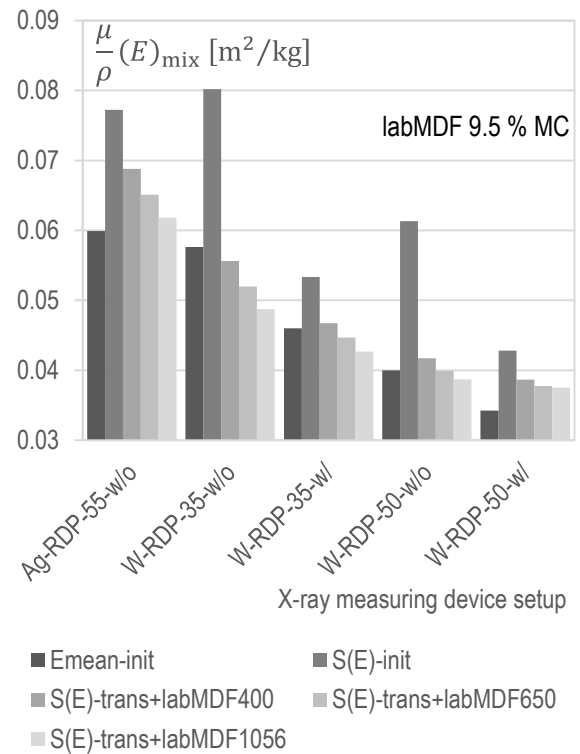
Figure IV-71: Spectral-weighted total mean mass attenuation coefficients $\mu/\rho \left(S(E) \right)_{\mathrm{mix}}$ exclusively for the composition labMDF 9.5 % MC computed via eq. (II-35) by means of respective $S(E)$ from spectra measurements employing Ag- and W-RDP device setups (Chapter IV–4.3.3.1) in the energy range $E_{\min} \ldots E_{\max}$ (Table IV-29) with discrete $\Delta E = 1.0$ keV considering initial (init, $S_{\mathrm{D},0}(E)$) and transmitted spectra (trans, $S_{\mathrm{D,T}}(E, \rho_{\mathrm{A}})$, through $z_{\mathrm{nom}} = 50$ mm labMDF absorber with ρ_{nom} [kg/m³] (Table IV-2) at $MC = 9.5$ %), complete with respective $\mu/\rho \left(\bar{E} \right)_{\mathrm{mix}}$ (computed via eq. (II-31) for $\bar{E} = E_{\mathrm{mean}}$ from $S_{\mathrm{D},0}(E)$); for data refer to Table IV-39.

with decreasing radiation energy (cf. Figure IV-64 and Figure IV-69) in comparison to mean energy attenuation coefficients $\mu/\rho \left(\bar{E} \right)_{\mathrm{mix}}$ of the very same spectrum. Particularly initial spectra without pre-filter and absorber impact commonly reveal right-skewed energy distributions (refer to Figure IV-52). Hence, higher low-energy $\mu/\rho \left(E \right)$ are additonally emphasised by larger low-energy share. Accordingly, W-device spectra without pre-filter application on both energy levels reveal maximum difference and exceed corresponding $\mu/\rho \left(\bar{E} \right)_{\mathrm{mix}}$ about 39.1 % and 53.3 % on nominal 35 keV and 50 keV level, respectively. Pre-filter application diminishes the relative difference to $Q \mu/\rho \left(E \right)_{\mathrm{mix}} = 1.160$ (W-RDP-35-w/)   and

X-ray spectrum	$S_D(E)$	with absorber	E_{max}	E_{min}	$\bar{E}$	$\frac{\mu}{\rho}(\bar{E})_{mix}$	$\frac{\mu}{\rho}(S(E))_{mix}$	$\Delta\mu/\rho$	$Q\,\mu/\rho$
measuring device setups	type	labMDF ρ_{nom}	[kVp]	[keV]	[keV]	[m²/kg]	[m²/kg]	[m²/kg]	[−]
Ag-RDP-55-w/o	init	–	51.3	7.0	21.1	0.0599	0.0772	0.0173	1.290
	trans	400	51.3	8.0	21.5		0.0688	0.0089	1.149
	trans	650	51.3	8.0	22.1		0.0651	0.0052	1.087
	trans	1056	51.3	8.0	22.9		0.0618	0.0019	1.032
W-RDP-35-w/o	init	–	35.4	7.5	21.5	0.0576	0.0802	0.0225	1.391
	trans	400	35.4	12.0	23.8		0.0556	-0.0020	0.965
	trans	650	35.4	12.0	24.4		0.0520	-0.0057	0.902
	trans	1056	35.4	12.0	25.0		0.0487	-0.0089	0.846
W-RDP-35-w/	init	–	35.4	12.5	24.2	0.0460	0.0534	0.0073	1.160
	trans	400	35.4	14.5	25.4		0.0468	0.0007	1.016
	trans	650	35.4	14.5	25.9		0.0447	-0.0013	0.972
	trans	1056	35.4	14.5	26.4		0.0427	-0.0033	0.928
W-RDP-50-w/o	init	–	50.9	8.0	26.3	0.0400	0.0613	0.0213	1.533
	trans	400	50.9	12.0	29.2		0.0417	0.0017	1.043
	trans	650	50.9	12.0	29.5		0.0399	-0.0001	0.998
	trans	1056	50.9	12.0	29.8		0.0387	-0.0013	0.968
W-RDP-50-w/	init	–	50.9	12.0	29.2	0.0342	0.0428	0.0086	1.251
	trans	400	50.9	13.0	30.0		0.0387	0.0044	1.129
	trans	650	50.9	13.0	30.1		0.0378	0.0035	1.103
	trans	1056	50.9	13.0	30.1		0.0375	0.0033	1.095

Table IV-39: Spectral-weighted total mean mass attenuation coefficients $\mu/\rho\left(S(E)\right)_{mix}$ exclusively for the composition labMDF 9.5 % MC computed via eq. (II-35) by means of respective $S(E)$ from spectra measurements employing Ag- and W-RDP device setups (Chapter IV–4.3.3.1) in the energy range $E_{min} \ldots E_{max}$ (Table IV-29) with discrete $\Delta E = 1.0$ keV considering initial (init, $S_{D,0}(E)$) and transmitted spectra (trans, $S_{D,T}(E,\rho_A)$, through $z_{nom} = 50$ mm lab-MDF absorber with ρ_{nom} [kg/m³] (Table IV-2) at $MC = 9.5$ %), complete with comparison toward respective $\mu/\rho\,(\bar{E})_{mix}$ (computed via eq. (II-31) for $\bar{E}$ from $S_{D,0}(E)$) by additional means of $\Delta\mu/\rho\,(E)_{mix}$ via eq. (IV-41) and $Q\,\mu/\rho\,(E)_{mix}$ via eq. (IV-42).

$Q\,\mu/\rho\,(E)_{mix} = 1.251$ (W-RDP-50-w/). Ag-RDP-55-w/o values are in a similar order like the latter with $Q\,\mu/\rho\,(E)_{mix} = 1.290$. The differences considerably decrease with regard to the results from integration over measured spectra $S_{D,T}(E,\rho_A)$ from transmitted radiation through respective labMDF specimen of varying nominal raw density ρ_{nom} as absorbers. Here, individual absorbers on each energy level obviously yield more or less equivalent $\mu/\rho\left(S_{D,T}(E,\rho_A)\right)_{mix}$ and $\mu/\rho\,(\bar{E})_{mix}$ values with relative deviations of less than ±5 % toward the mean energy results $\mu/\rho\,(\bar{E})_{mix}$, i. e.,

- Ag-RDP-55-w/o+labMDF1056,
- W-RDP-35-w/o+labMDF400 (rather close with raw density below),
- W-RDP-35-w/+labMDF400,
- W-RDP-50-w/o+labMDF650,
- and for W-RDP-50-w/ an absorber with raw density beyond labMDF1056.

Notwithstanding the same purpose, the two calculation methods by either considering single mean energy for $\mu/\rho\,(\bar{E})_{mix}$ via simplistic mixture rule eq. (II-31) or integration across polychromatic X-ray spectrum for $\mu/\rho\left(S(E)\right)_{mix}$ via extended mixture rule eq. (II-35) ultimately yield apparent differences. Since computation data serves as a theoretical estimation for X-ray measurements by means of the considered setup in common practical applications, the question arises regarding the most appropriate results in terms of representing actual measuring

conditions. The above exclusively theoretical basis, however, does not enable a conclusion to be made on this discrepancy. It, moreover, requires comparison toward measured $\overline{\mu/\rho}$, where reference is made to Chapter IV–5.2.3.

All mass attenuation coefficient computations above exclusively consider total (tot) attenuation as sum of the single processes. Likewise, single coefficients $\mu_i/\rho\,(E)_{\mathrm{mix}}$ are computed via simplistic mixture rule according to eq. (II-31) for particular energies with $\Delta E = 1\,\mathrm{keV}$ within the already applied range $E = 5 \dots 100\,\mathrm{keV}$. Here and beyond the three basic mechanisms photoelectric absorption (photo), coherent (coh) and incoherent (incoh) scattering, let the sum of the two latter be the scattering coefficient (scat = coh + incoh). Figure IV-72 presents resulting attenuation charts of selected materials, i. e., TMP (clean wood, OD) as well as oven-dry and moist labMDF. Table IV-41 provides an extraction of corresponding data at the four previously considered particular radiation energies complete with the attenuation fractions $\xi(i)$ of the single mechanisms following eq. (II-15). For comprehensive data, reference is made to Appendix VII–4, particularly Figure VII-36 to Figure VII-48 as well as Table VII-10 to Table VII-22.

Obviously, all plots of corresponding attenuation processes in Figure IV-72 reveal comparable or rather congruent slopes. Likewise, only slight differences in the third decimal place and, moreover, partly equal values particularly with increasing energy can be found in the summarised data in Table IV-41. Nevertheless, fundamentally decreasing total $\mu/\rho\,(E)$ along increasing radiation energy is equal to the plots in Figure IV-64. To distinguish between the three attenuation processes, the single mechanism plots can generally be characterised for WBCs by

- continuously decreasing photoelectric absorption with partly steep slope (grey solid line in Figure IV-72),
- less progressively decreasing coherent scattering (dotted line), and
- first increasing then slightly decreasing incoherent scattering (dashed line).
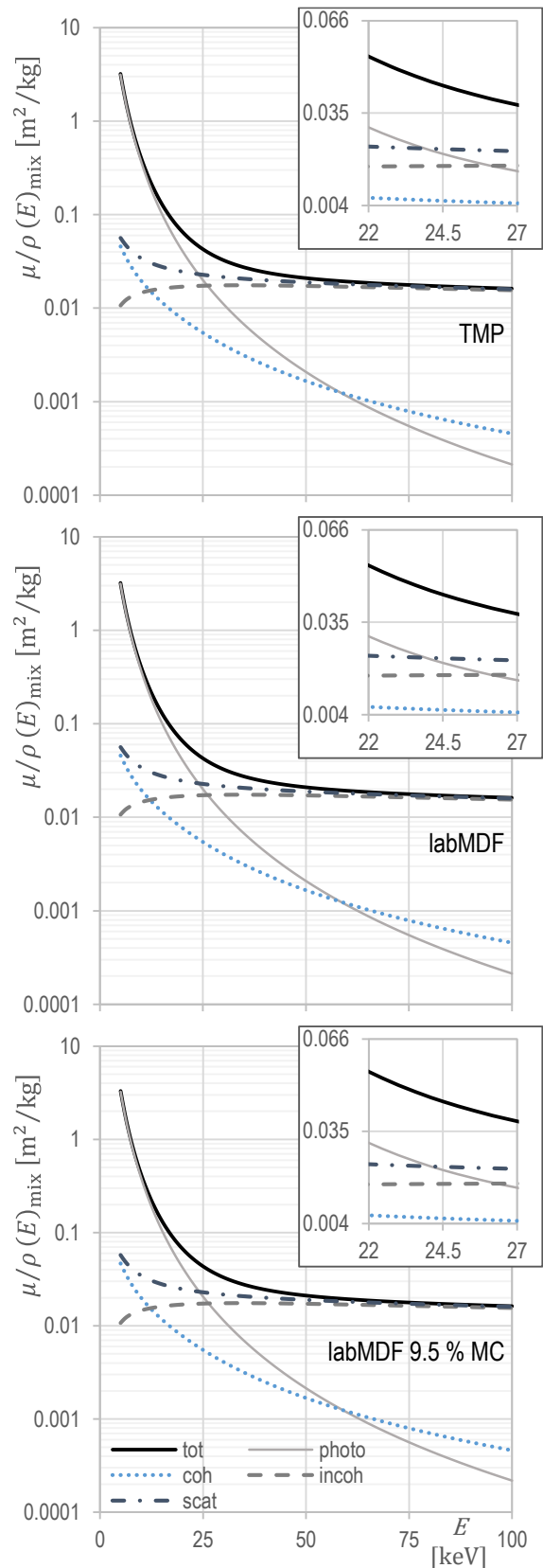
Figure IV-72: Total mean mass attenuation coefficient $\mu/\rho\,(E)_{\mathrm{mix}}$ over radiation energy E of selected lab-made material incl. attenuation processes photoelectric absorption, coherent and incoherent scattering, as well as scattering (scat = coh + incoh) determined like Table IV-41; data from Table VII-10 to Table VII-12.

Notwithstanding the described variations of single $\mu_i/\rho\,(E)$, the fraction of coherent scattering remains on an equivalently low order of magnitude with $\xi(\mathrm{coh}) = 0.06\,...\,0.13$ along total energy range. However, exemplary $\xi(i)$ results of the considered materials are equal on the respective energy level with a few exceptions particularly with respect to lab MDF 9.5 % MC. The same applies to indMDF as well as insulation, where reference is made to Table VII-15 and Table VII-16, respectively. Consequently, attenuation conditions within conventional WBCs at common moisture level can be concluded with exemplary values for the four considered energies as

-   almost exclusive photoelectric absorption on low energy level with $\xi(\mathrm{photo}) \approx 0.85$,
-   increasing scattering fraction on low-medium energy level with $\xi(\mathrm{scat}) \approx 0.42$,
-   dominating scattering on high-medium energy level particularly from incoherent process with $\xi(\mathrm{incoh}) \approx 0.52$, and
-   total attenuation predominated by total scattering with $\xi(\mathrm{scat}) \approx 0.94$ and more or less negligible absorption fraction with $\xi(\mathrm{photo}) \approx 0.06$.

Beyond the above estimations and visual perception (refer also to magnification in the respective inset in Figure IV-72), the point of intersection of absorption (grey solid line, photo) and scattering (dash-dotted line, scat) plots is calculated and the resulting energies are listed in Table IV-40. Resulting energies (x-values) represent equivalence of absorption and scattering fraction with $\xi(\mathrm{photo}) = \xi(\mathrm{scat}) = 0.5$ (y-value). The revealed energy range is likewise considered as the limit between low-medium and high-medium energy levels. However, the results in Table IV-40 additionally comprise relevant elemental data, where hydrogen H plots yield no intersection within the considered energy range $E \geq 5\,\mathrm{keV}$. For the other elements, intercept energy basically increases with increasing atomic number. With respect to the evaluated WBC materials, point of intersection is found on the same level with $E = 24 \pm 0.3\,\mathrm{keV}$. UF-C, however, slightly falls below with $E = 23.3\,\mathrm{keV}$ and water value exceeds all others with absorption-scattering intercept at $E = 25.7\,\mathrm{keV}$.

chemical element or material	$\boldsymbol{\xi(\mathrm{photo}) = \xi(\mathrm{scat}) = 0.5}$ at energy $\boldsymbol{E}$ [keV]
$_1$H	n. a.
$_6$C	19.8
$_7$N	23.6
$_8$O	27.4
$_{16}$S	60.4
$_{20}$Ca for ash	79.1
TMP	23.9
labMDF	23.9
labMDF 9.5 % MC	24.1
Fmat	24.4
UF-C	23.3
indMDF	24.0
insulation	23.7
water	25.7

Table IV-40: Radiation energy E where attenuation fractions $\xi(i)$ [–] eq. (II-15) of photoelectric absorption (photo) and scattering (scat = coh + incoh) equal 0.5 for applied WBCs and respective raw materials as well as constituent chemical elements, based on comprehensive data in Appendix VII–4.

Eventually, total radiation attenuation by conventional WBCs is dominated by scattering, which comprises the attenuation mechanisms coherent and incoherent scattering, for energies beyond $E \geq 24\,\mathrm{keV}$, where scattering fraction equals photoelectric absorption, i. e., $\xi(\mathrm{photo}) = \xi(\mathrm{scat}) = 0.5$. Moreover, on high energy level with $E \geq 50\,\mathrm{keV}$, photoelectric absorption plays a negligible role with fractions $\xi(\mathrm{photo}) \leq 0.1$. Nevertheless, particular knowledge of the ratio between absorption and scattering contribution is considered to be required to evaluate impact of radiation attenuation itself on X-ray measuring results in case of non-ideal conditions (no narrow-beam setup), which will comprehensively be discussed in Chapter IV–6.

Energy	$\frac{\mu_i}{\rho}(E)_{\text{mix}}$ [m^2/kg]					$\xi(i)$ [−]			
E [keV]	total	photo	coh	incoh	scat	photo	coh	incoh	scat
TMP oven-dry									
12.7	0.2050	0.1751	0.0145	0.0156	0.0300	0.85	0.07	0.08	0.15
21.5	0.0565	0.0325	0.0069	0.0171	0.0240	0.58	0.12	0.30	0.42
29.2	0.0338	0.0121	0.0042	0.0175	0.0217	0.36	0.13	0.52	0.64
59.5	0.0193	0.0012	0.0012	0.0169	0.0181	0.06	0.06	0.88	0.94
labMDF oven-dry									
12.7	0.2055	0.1755	0.0145	0.0155	0.0300	0.85	0.07	0.08	0.15
21.5	0.0566	0.0326	0.0069	0.0171	0.0240	0.58	0.12	0.30	0.42
29.2	0.0338	0.0121	0.0042	0.0175	0.0217	0.36	0.13	0.52	0.64
59.5	0.0193	0.0012	0.0012	0.0169	0.0181	0.06	0.06	0.88	0.94
labMDF at $MC = 9.5$ %									
12.7	0.2107	0.1805	0.0147	0.0156	0.0303	0.86	0.07	0.07	0.14
21.5	0.0576	0.0335	0.0070	0.0171	0.0241	0.58	0.12	0.30	0.42
29.2	0.0342	0.0124	0.0043	0.0175	0.0218	0.36	0.13	0.51	0.64
59.5	0.0194	0.0012	0.0012	0.0170	0.0182	0.06	0.06	0.87	0.94

Table IV-41: Total mass attenuation coefficients $\mu/\rho\,(E)_{\text{mix}}$ of selected lab-made material with TMP and labMDF at oven-dry conditions as well as labMDF at $MC = 9.5$ % as sum of the single coefficients following eq. (II-14) for the attenuation processes photoelectric absorption (photo), coherent scattering (coh), and incoherent scattering (incoh) as well as scattering coefficient (scat = coh + incoh) at low $E = 12.7$ keV, medium $E = 21.5$ keV and $E = 29.2$ keV, as well as high $E = 59.5$ keV energy level (refer to Table IV-34) determined on basis of analysis data (Table IV-15) via eq. (II-31) by means of XCOM (2010) elemental data (Table VII-3 to Table VII-9), complete with the attenuation fractions $\xi(i)$ following eq. (II-15) of the single mechanisms; extract from Table VII-10 to Table VII-12.

5.2.3 Comparison of computation and measurement

A compilation of computed and measured mean mass attenuation coefficients is presented in Table IV-42. Here, WBC material and radiation energies in terms of measuring device setups are taken into account, where comprehensive data is available. Therefore, lab-made fibreboard (labMDF), industrial MDF (indMDF, total mean of all panel thicknesses), and insulation board is selected with data corresponding to both Ag- and W-RDP device setups (with and without pre-filters) on medium energy level. Furthermore, on low energy level, data considering W-mat and W-panel device setups (without pre-filter) are utilised for cured fibre mats (Fmat) and indMDF, respectively. For computation with spectra consideration via eq. (II-35), not only initial spectra

$S_{\text{D},0}(E)$ but also transmitted $S_{\text{D,T}}(E, \rho_\text{A})$ are applied, where exclusively transmission data from labMDF with $\rho_{\text{nom}} = 650$ kg/m^3 is selected[35]. Since X-ray transmission measurements were performed employing specimens, which were conditioned to constant mass at standard 20/65, all computation results are transformed to the respective moisture level likewise already labMDF 9.5 % MC. For this purpose, elemental composition is adapted following inverse moisture correction as described in Chapter IV–2.4.2 with individual MC from Table IV-5 in Chapter IV–1.5, to facilitate comparability. However, the difference $\Delta\,\mu/\rho\,(E)_{\text{mix}}$ via eq. (IV-41) and the ratio $Q\,\mu/\rho\,(E)_{\text{mix}}$ via eq. (IV-42) yields calculational comparison toward respective measuring data as reference. In addition to tabulated data, Figure IV-73 illustrates labMDF 9.5 % MC results comparing measurements and corresponding computations.

---

[35] Note, transmitted spectra are not available on low energy level.

measuring device	measure-ment	computation, eq. (II-31), single mean energy			computation, eq. (II-35), initial spectrum			computation, eq. (II-35), labMDF650 spectrum		
setup / energy	$\overline{\mu/\rho}$	$\frac{\mu}{\rho}(\bar{E})_{\mathrm{mix}}$			$\frac{\mu}{\rho}\left(S_{\mathrm{D,0}}(E)\right)_{\mathrm{mix}}$			$\frac{\mu}{\rho}\left(S_{\mathrm{D,T}}(E,\rho_{\mathrm{A}})\right)_{\mathrm{mix}}$		
$\bar{E}$ [keV]	μ/ρ $\left[\frac{\mathrm{m}^2}{\mathrm{kg}}\right]$	μ/ρ $\left[\frac{\mathrm{m}^2}{\mathrm{kg}}\right]$	$\Delta\,\mu/\rho$ $\left[\frac{\mathrm{m}^2}{\mathrm{kg}}\right]$	$Q\,\mu/\rho$ $[-]$	μ/ρ $\left[\frac{\mathrm{m}^2}{\mathrm{kg}}\right]$	$\Delta\,\mu/\rho$ $\left[\frac{\mathrm{m}^2}{\mathrm{kg}}\right]$	$Q\,\mu/\rho$ $[-]$	μ/ρ $\left[\frac{\mathrm{m}^2}{\mathrm{kg}}\right]$	$\Delta\,\mu/\rho$ $\left[\frac{\mathrm{m}^2}{\mathrm{kg}}\right]$	$Q\,\mu/\rho$ $[-]$
Fmat 9.4 % MC										
W-mat-16-w/o 12.7	0.2039	0.2181	+0.0142	1.070	0.2472	+0.0433	1.213	n/a	n/a	n/a
indMDF 8.1 % MC										
W-panel-16-w/o 12.7	0.1749	0.2111	+0.0362	1.207	0.2394	+0.0645	1.369	n/a	n/a	n/a
labMDF 9.5 % MC										
Ag-RDP-55-w/o 21.1	0.0485	0.0599	+0.0114	1.235	0.0772	+0.0287	1.592	0.0651	+0.0166	1.342
W-RDP-35-w/o 21.5	0.0466	0.0576	+0.0110	1.236	0.0802	+0.0336	1.720	0.0520	+0.0054	1.115
W-RDP-35-w/ 24.2	0.0384	0.0460	+0.0076	1.198	0.0534	+0.0150	1.389	0.0447	+0.0063	1.164
W-RDP-50-w/o 26.3	0.0360	0.0400	+0.0040	1.112	0.0613	+0.0253	1.705	0.0399	+0.0039	1.110
W-RDP-50-w/ 29.2	0.0300	0.0342	+0.0042	1.139	0.0428	+0.0128	1.427	0.0378	+0.0078	1.259
indMDF 8.1 % MC										
Ag-RDP-55-w/o 21.1	0.0457	0.0600	+0.0143	1.314	0.0774	+0.0318	1.696	0.0653	+0.0196	1.430
W-RDP-35-w/o 21.5	0.0460	0.0578	+0.0118	1.257	0.0804	+0.0344	1.747	0.0521	+0.0061	1.133
W-RDP-35-w/ 24.2	0.0385	0.0461	+0.0076	1.196	0.0535	+0.0149	1.388	0.0448	+0.0063	1.163
W-RDP-50-w/o 26.3	0.0359	0.0401	+0.0042	1.116	0.0614	+0.0255	1.709	0.0400	+0.0040	1.112
W-RDP-50-w/ 29.2	0.0303	0.0343	+0.0040	1.134	0.0429	+0.0127	1.419	0.0378	+0.0076	1.251
insulation 9.1 % MC										
Ag-RDP-55-w/o 21.1	0.0468	0.0589	+0.0121	1.257	0.0759	+0.0290	1.620	0.0640	+0.0172	1.367
W-RDP-35-w/o 21.5	0.0514	0.0567	+0.0053	1.104	0.0788	+0.0274	1.534	0.0512	-0.0002	0.997
W-RDP-35-w/ 24.2	0.0403	0.0454	+0.0051	1.127	0.0526	+0.0123	1.304	0.0441	+0.0038	1.094
W-RDP-50-w/o 26.3	0.0394	0.0395	+0.0001	1.001	0.0603	+0.0209	1.529	0.0394	-0.0000	0.999
W-RDP-50-w/ 29.2	0.0314	0.0339	+0.0025	1.079	0.0423	+0.0109	1.346	0.0373	+0.0059	1.189

Table IV-42: Comparison between mean mass attenuation coefficients of fibre mats (Fmat), lab-made and industrial MDF, as well as insulation board at EMC in consequence of 20/65 conditioning with data from X-ray measurements $\overline{\mu/\rho}$ (Table IV-27) and computed values by single mean energies $\mu/\rho\,(\bar{E})_{\mathrm{mix}}$ (Table IV-35) as well as initial $\mu/\rho\left(S_{\mathrm{D,0}}(E)\right)_{\mathrm{mix}}$ and transmitted $\mu/\rho\left(S_{\mathrm{D,T}}(E,\rho_{\mathrm{A}})\right)_{\mathrm{mix}}$ (through $z_{\mathrm{nom}}=50\ \mathrm{mm}$ labMDF650) spectra (both Table IV-39), respectively considering W-mat and W-panel (without pre-filter) as well as Ag- and W-RDP (with and without pre-filters) device setups; complete with comparison via $\Delta\,\mu/\rho\,(E)_{\mathrm{mix}}$ eq. (IV-41) and $Q\,\mu/\rho\,(E)_{\mathrm{mix}}$ eq. (IV-42) toward respective measuring data as reference; note, $\bar{E}$ applies not to last column with labMDF650 spectra (Table IV-29), and the very same do not represent transmission conditions for insulation (only $\rho\approx 218\ \mathrm{kg/m^3}$).

Let the measured mean mass attenuation coefficients $\overline{\mu/\rho}$ be reliable data representing both material and measuring conditions. To consequently summarise comparison in general, computation data consistently exceeds measuring results with, however, particular exceptions and, moreover, partly considerable differences. Computed $\mu/\rho\left(S_{\mathrm{D,T}}(E,\rho_{\mathrm{A}})\right)_{\mathrm{mix}}$ results considering labMDF650 transmission spectra are found more or less consistently in the order of $\mu/\rho\,(\bar{E})_{\mathrm{mix}}$ data, why those spectra are selected, as already pointed out in Chapter IV–5.2.2 with respect to Table IV-39 and Figure IV-71. Moreover, $\mu/\rho\left(S_{\mathrm{D,T}}(E,\rho_{\mathrm{A}})\right)_{\mathrm{mix}}$ reveal lower differences toward measured $\overline{\mu/\rho}$ than initial spectra based $\mu/\rho\left(S_{\mathrm{D,0}}(E)\right)_{\mathrm{mix}}$, where the respective transmission conditions with consequently influenced spectra are considered to appropriately represent actual energy distributions during measure-
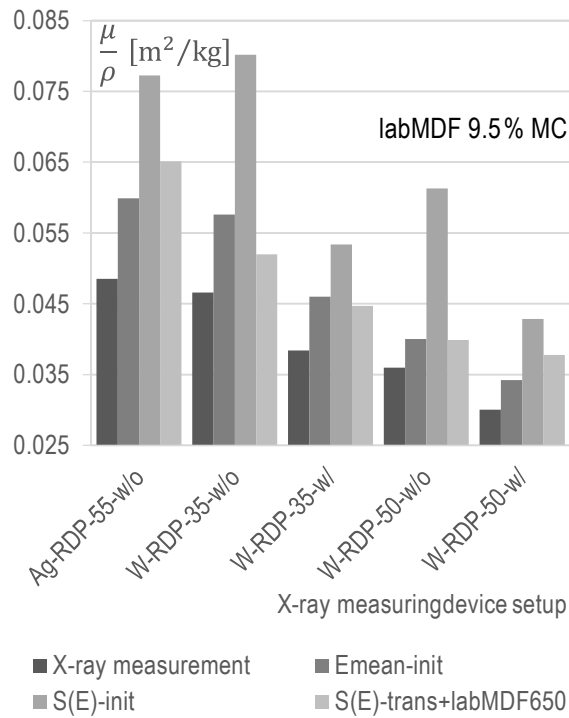
Figure IV-73: Comparison between mean mass attenuation coefficients of labMDF at $MC = 9.5\,\%$ from X-ray measurements $\overline{\mu/\rho}$ (Table IV-27) and computed values by single mean energies $\mu/\rho\,(\bar{E})_{\mathrm{mix}}$ (Table IV-35) as well as initial $\mu/\rho\left(S_{\mathrm{D,0}}(E)\right)_{\mathrm{mix}}$ and transmitted $\mu/\rho\left(S_{\mathrm{D,T}}(E,\rho_{\mathrm{A}})\right)_{\mathrm{mix}}$ (through $z_{\mathrm{nom}} = 50$ mm labMDF650) spectra (both Table IV-39), respectively considering Ag- and W-RDP device setups (with and without pre-filters); for data refer to Table IV-42.

ment. As already pointed out in terms of measuring and computation result presentation of labMDF and indMDF, comparison data of the very same is likewise found more or less congruent regardless of the only exception Ag-RDP-55-w/o data sets, where measuring results differ owing to potential insufficiencies during the measurement itself as already discussed (refer to Chapter IV–4.3.2.3). Respective insulation measuring results differ toward labMDF and indMDF at individual energies, which is already discussed with regard to structural conditions. The same applies to Fmat and indMDF values on low energy level.

However, consequent focus is on comparison of computation and measurement, since material related discussions can be found elsewhere. To this end, a preferably relative comparison via $\mathrm{Q}\,\mu/\rho\,(E)_{\mathrm{mix}}$ is taken into account, since $\mu/\rho\,(E)$ values basically vary due to energy level. For

labMDF 9.5 % MC (Figure IV-73) and apart from Ag-RDP-55-w/o data, initial spectra computations $\mu/\rho\left(S_{\mathrm{D,0}}(E)\right)_{\mathrm{mix}}$ reveal maximum deviations toward measurements. Here, both considered setups without pre-filter W-RDP-35-w/o and W-RDP-50-w/o exceed measured $\overline{\mu/\rho}$ in the order >70 %. Pre-filter application reduces the difference to about $\mathrm{Q}\,\mu/\rho\,(E)_{\mathrm{mix}} \approx 1.4$ for both energies. Deviations, furthermore, decrease in the case of transmission spectra application for computation of $\mu/\rho\left(S_{\mathrm{D,T}}(E,\rho_{\mathrm{A}})\right)_{\mathrm{mix}}$, where data exceeds measurements about 11…16 %, except W-RDP-50-w/ with $\mathrm{Q}\,\mu/\rho\,(E)_{\mathrm{mix}} = 1.26$. A similar pattern can be found for indMDF 8.1 % MC. Ag-RDP-55-w/o data likewise follows the tendency with decreasing deviation toward measurement in the case of transmission spectra application, where differences are found generally higher compared to the W-RDP setup results. Notwithstanding particular exceptions, computation of mass attenuation coefficients employing explicit transmission spectra is considered to rather agree with measurement with comparably minor differences of 10…15 % above. However, remaining deviations occur since applied labMDF650 spectra do obviously not consistently represent radiation attenuation conditions by the respective specimens. The exception W-RDP-50-w/ can furthermore be affected by measuring conditions like the detector linearity characteristic. Setup geometries, e. g., no narrow-beam, come in addition, which are considered to apparently decrease measured $\overline{\mu/\rho}$ by tendency. Beyond spectra considerations, $\mu/\rho\,(\bar{E})_{\mathrm{mix}}$ results reveal deviations toward measurements in a comparable order and decrease with increment mean energy $\bar{E}$. Again with few exceptions, however, a tendency becomes obvious with about 20…25 % deviation in case of W-RDP-35 setups and 10…15 % for W-RDP-50. Moreover, no distinct dependency of pre-filter application can be observed, which is, however, just indirectly considered by computation in terms of radiation energy for single coefficients $\mu/\rho\,(\bar{E})_i$.

The deviations of computation results toward measurements for insulation 9.1 % MC, reveal comparable character like labMDF and indMDF

but feature diminished extent, where, however, $\mu/\rho\,(\bar{E})_{\mathrm{mix}}$ data exceeds measurements in the order of <13 %. Fundamental differences, in turn, occur between the two spectra based computations. Nevertheless, pre-filter application yields decreased deviation in the case of $\mu/\rho\left(S_{\mathrm{D,0}}(E)\right)_{\mathrm{mix}}$. Transmission spectra based computations of $\mu/\rho\left(S_{\mathrm{D,T}}(E,\rho_{\mathrm{A}})\right)_{\mathrm{mix}}$ reveal a more or less opposite patern. Note, labMDF650 spectra do not represent transmission conditions for insulation with distinctly lower raw density $\rho \approx 218$ kg/m^3, where panel structure considerably differs from common MDF, which, in turn, affects measurements as already discussed. However, particular insulation computation results are found to actually equal corresponding measurements.

On low energy level, measuring data of fibre mats exceeds industrial MDF values due to reasons of material structure and radiation transmission conditions as already stated in Chapter IV–4.3.2.2. Differences of both corresponding computation results are attributed to higher Fmat ash content as already pointed out in Chapter IV–5.2.2. However, computation results, in turn, consistently exceed measuring values. Individual comparison reveals minor deviation of $\mu/\rho\,(\bar{E})_{\mathrm{mix}}$ with $\mathrm{Q}\,\mu/\rho\,(E)_{\mathrm{mix}} = 1.070$ for Fmat 9.4 % MC and $\mathrm{Q}\,\mu/\rho\,(E)_{\mathrm{mix}} = 1.207$ in case of indMDF 8.1 % MC. Likewise found in case of labMDF and indMDF considering the RDP devices, initial spectra $\mu/\rho\left(S_{\mathrm{D,0}}(E)\right)_{\mathrm{mix}}$ further exceed single mean energy computations with values about 21 % (Fmat) and 37 % (indMDF) above the measurements.

In addition to tabulated data for low and medium energy levels, only particular measuring values are available for $E = 59.5$ keV (radioisotope ^{241}Am) representing the high energy level of the raytest device in terms of round robin test on RDP determination (refer to Table IV-22 in Chapter IV–4.2.5). Therefore, the mean value from the transmission measurements considering all $n = 5$ MDF specimens results in $\overline{\mu/\rho} = 0.0166$ m^2/kg. In comparison, exclusive computation via simple mixture rule yields $\mu/\rho\,(E)_{\mathrm{mix}} = 0.0194$ m^2/kg, where no spectra consideration

is required due to monoenergetic isotope radiation source. Consequent relative calculational comparison reveals $\mathrm{Q}\,\mu/\rho\,(E)_{\mathrm{mix}} = 1.169$ toward measurement, which is in the rough order of $\mu/\rho\left(S_{\mathrm{D,T}}(E,\rho_{\mathrm{A}})\right)_{\mathrm{mix}}$ deviations in Table IV-42. However, setup conditions of the rather old raytest device are considered to particularly differ.

Besides present μ/ρ measurement and computation results, reviewed data from literature are taken into account for further comparison with focus on high energy level by means of ^{241}Am with $E = 59.5$ keV. As already pointed out in Chapter II–3.3, WBC measuring data is exclusively available for particleboard, where MAY et al. (1976) report $\overline{\mu/\rho} = 0.0172$ m^2/kg and RANTA, MAY (1978) $\overline{\mu/\rho} = 0.0189$ m^2/kg, which differ already about 10 %. Regarding clean wood, literature measuring data ranges in the order $\overline{\mu/\rho} = 0.0183$ m^2/kg (cf. LAUFENBERG (1986)), hence, in between the WBC values. In case of computation via mixture rule for clean wood, LAUFENBERG (1986) reports $\mu/\rho\,(E)_{\mathrm{mix}} = 0.0183$ m^2/kg, whereas $\mu/\rho\,(E)_{\mathrm{mix}} = 0.0193$ m^2/kg can be found from OLSON, ARGANBRIGHT (1981) as already presented in Table II-3 completed with further available values. However, the latter is in good agreement with above indMDF 8.1 % MC computation of $\mu/\rho\,(E)_{\mathrm{mix}} = 0.0194$ m^2/kg, which, in turn, exceeds particleboard values of about 2.6 % and 12.8 %, respectively. Present raytest measurements on MDF with $\overline{\mu/\rho} = 0.0166$ m^2/kg further fall below all literature data and $\overline{\mu/\rho}$ is 88…97 % that of reported particleboard measurements. Nevertheless, a congruent context is found, where computation results generally exceed measuring data even in case of monochromatic high energy radiation from ^{241}Am radioisotope source.

5.2.4   Concluding remarks

Notwithstanding several hitherto investigations on computational determination of mass attenuation coefficients with partial comparison to corresponding measurements, results are rarely available for WBCs (refer to Chapter II–2.3.3) and the impact of constituents is rather superficially evaluated. Hence, the present rather holistic investigations via the simplistic and extended mixture rule fill the gap and yield computed mass attenuation coefficients $\mu/\rho\,(E)_{\mathrm{mix}}$ based on actual elemental analysis data and virtual variation of the very same for single energies and further considering employed radiation spectra resulting in $\mu/\rho\left(S(E)\right)_{\mathrm{mix}}$ all in comparison toward $\overline{\mu/\rho}$ measuring data (refer to Chapter IV–4.3.2) from corresponding specimens. As obvious from Chapter IV–5.2.3, differences of computed toward measured μ/ρ occur for the very same material (elemental composition considering EMC during measurement). The extent, however, depends on the considered energy level and spectrum as well as the measuring conditions themselves. In this regard, fundamental investigations of μ/ρ by measurements must employ ideal setups ("good-architecture" conditions, cf. LIU et al. (1988)), which is not the case in all present measurements. However, all results reveal differences as expected, where measurements fall below computations with few exceptions. Further investigations facilitate estimations on how measuring conditions can be described in terms of radiation attenuation, where $\mu/\rho\left(S(E)\right)_{\mathrm{mix}}$ computation based on transmitted spectra is found to approach to the measurement for transmission spectra $S_{\mathrm{D,T}}(E,\rho_{\mathrm{A}})$ particularly from labMDF 650. On the contrary, $\mu/\rho\left(S(E)\right)_{\mathrm{mix}}$ results considering lower raw density spectra partly still exceed measuring data. Beyond X-ray spectra, computations based on single (mean) energies with particular consideration of the single attenuation mechanisms unveil increasing fraction of scattering (coherent as well as incoherent) with increasing energy. Here, practically no difference is found between investigated WBCs but toward water. The evaluated point of intersection of the single process attenuation plots quantifies, where scattering starts to

predominate and can be generalised for WBCs at common conditions with $E \approx 24\ \mathrm{keV}$. The consequent impact and corresponding context

- of non-narrow beam geometry,
- polychromatic radiation,
- variation of transmission spectra, and
- scattering fraction

need to be pointed out hereafter with focus on radiation-physical interdependencies.

Notwithstanding the above, mixture rule application evaluates radiation attenuation on the atomic level, where it happens, i. e., sub-microscopic scale (refer to Figure IV-12 and Chapter–3.5) for computation and microscopic scale (Chapter IV–3.4) regarding WBC composition and MC. It further facilitates to quantify the contribution of the single constituents, which is found to vary in dependence of the energy level and to be dominated by the elements C and O with total mass fraction $\omega(C+O)_{\mathrm{labMDF,9.5\,\%\,MC}} = 90\,\%$ (refer to Chapter IV–2.5) as illustrated in Figure IV-67 and Figure IV-68, which corresponds to found $\bar{Z}_{\mathrm{eff}} = 6.97$ for labMDF 9.5 % MC (Table IV-32) lying in between $_6C$ and $_8O$. Virtual variations based on actual elemental analysis investigates extreme but practice-oriented ranges of material compositions regarding their radiation attenuation potential. Moreover, since a primarily linear context is found between $\mu/\rho\,(E)_{\mathrm{mix}}$ and content variations of nitrogen (for UF resin), moisture, and ash, differential mass attenuation coefficient $\delta\,\mu/\rho\,(E)_{\mathrm{mix}}\ [\%/\%\Delta\omega(i)]$ is introduced, to quantify potential impact of composition variation on radiation attenuation. Therefore, computed $\mu/\rho\,(E)_{\mathrm{mix}}$ conduces as a clear measure for fundamental comparison of WBC recipes, e. g., regarding influence of additives such as hydrophobic agents or fire retardants on X-ray transmission measurements at various energies. To conclude the findings in general, the impact of varying MC and ash content $\omega(a)$ within practice-relevant ranges on lower energy levels is more or less considerable, decreases with increasing radiation energy, and turns negligible on high energy level. On the contrary, no considerable influence of (organic) adhesive resin is found. Particularly mineral constituents and trace elements (ash), which have no impact on

gravimetric raw density determination owing to their minor mass fraction, evidently affect radiation attenuation, thus, radiometric raw density measurement, likewise already concluded by KOURIS et al. (1981). An actual impact, however, is found to depend on radiation energy and ash content, where the latter typically ranges in non-dominant order with mass fractions $\omega(a) < 1\,\%$ for wood and WBCs considering European species. In addition to inherent wood mineral content, there are further sources in WBC production such as impurities from the wood-yard as commonly known. Beyond this, fibre and particle drying by directly flame-fuelled dryers (cf. THOEMEN et al. (2010)) is commonly discussed to influence furnish mat composition and consequent inline area density X-ray measurement owing to soot and further combustion residues, which are supposed to be incorporated into dried furnish material. Since soot mainly consists of carbon without considerable ash fraction in case of well-controlled furnace, direct flame-fuelled drying is empirically concluded not to considerably influence furnish mat composition, thus, X-ray measurements. The like applies to additives with purpose to increase electric conductivity, which conventionally just comprise carbon, where, e. g., DUNKY, NIEMZ (2002) report about typically 1 % soot addition. However, elemental compositions have to fundamentally be considered in terms of X-ray transmission measurements on WBCs. Actual impact of variations on consequent radiation attenuation may, nevertheless, be negligible. In this regard, already SALINAS et al. (2006) concluded that density and radiation energy primarily affect μ/ρ whereas variations in chemical composition yield minor influence as long as constituent elements are of similar atomic number, which is confirmed by the present investigations.

Beyond all material-related and, moreover, radiation-physical considerations, differences between measured and computed μ/ρ have to be discussed in context of the validity of the mixture rule referring to Chapter II–2.3.4. Accordingly, computed results may not represent the actual matter since binding state of the atoms is not explicitly taken into account (cf. JACKSON (1982)) and rather considered as free atoms. WBCs comprise, in turn, wood constituents, adhesive resin, and potential further additives, i. e., several compounds where the main chemical elements H, C, N, and O exist in various binding states. Notwithstanding that, present data allows not to evaluate this particular impact, since measuring conditions considerably deviate from ideal narrow-beam conditions and spectra were considered but are affected by the measurement itself. Thus, performed transmission measurements do not claim to verify the validity of the mixture rule. However, the predominant organic constituents as well as further main trace elements such as Ca and Si reveal no absorption edges within the considered energy range $E = 5 \dots 100\,\mathrm{keV}$. Hence, mixture rule can be considered not to break down as already stated elsewhere.

Moreover, conclusion on most appropriate computation results by either simple mixture rule via eq. (II-31) with $\mu/\rho\,(E)_{\mathrm{mix}}$ for one single (mean) energy or spectral-weighted computation of $\mu/\rho\left(S(E)\right)_{\mathrm{mix}}$ via eq. (II-35) aims at equivalent representation of actual measuring conditions by means of a reliable measure. Here, both methods yield obviously different mass attenuation coefficients for one and the same composition and comparison to corresponding measuring data reveals further differences. In comparison of both computation methods, it is found that spectra-based results differ from $\mu/\rho\,(\bar{E})_{\mathrm{mix}}$ although explicit mean energies of the very same spectra are taken into account whilst the extent of deviation depends on the width of energy distribution and basic energy level. In the case of narrow-band spectra, single mean energy attenuation coefficients $\mu/\rho\,(\bar{E})_{\mathrm{mix}}$ appear as sufficient, since the crucial low-energy share is diminished by pre-filter application. However, to conclude with respect to proposition in Chapter II–2.3.2, spectral-weighted total mean mass attenuation coefficient $\mu/\rho\left(S(E)\right)_{\mathrm{mix}}$ is found to yield more appropriate estimations. Employing appropriate transmission spectra for $\mu/\rho\left(S_{\mathrm{D,T}}(E,\rho_{\mathrm{A}})\right)_{\mathrm{mix}}$ computation, deviation toward corresponding measuring results can be reduced below ±5 %. This is accomplished by application of transmission spectra representing

mean material conditions in terms of, e. g., structure and raw density. However, particular transmission spectra are rarely available from measurements of the very same X-ray setup. Alternatively, enhanced X-ray spectra simulations (refer to Chapter IV–4.2.6.2 and Chapter IV–4.3.3.2) are considered to yield appropriate estimations as long as all component and material characteristics are comprehensively taken into account. Finally, $\mu/\rho\,(E)_{\mathrm{mix}}$ computation by either mixture rule method is considered as an indispensable estimation procedure, e. g., in terms of X-ray transmission measuring device setup design and feasibility studies regarding X-ray measurements on particular materials.

6 Radiation-physical interdependencies within porous composites

6.1 Introduction

In contrast to some of the hitherto investigations aiming at μ/ρ determination via measurements in comparison to computations (refer to Chapter II–2.3.3, partly with coincident evaluation of the mixture rule validity), the present experiments employ no monoenergetic narrow-beam geometry but utilise partly modified setups more or less congruent to X-ray measuring devices for the respective applications in WBC industry, e. g., area density or raw density profile determination. Thus, particular phenomena occur during measurements and yield differences in comparison to theoretical considerations. Accordingly, above observations and conclusions were already partly attributed to interdependent radiation-physical effects and can be summarised as

- deviations of measured vertical raw density profile (RDP) slope from reference in SL and CL of the panel as varyingly distinct flattened shapes with apparently decreased SL/CL ratio,
- non-linear slope of X-ray transmission plot $\ln T^{-1}$ (with $T = I_\mathrm{T}/I_0$) from measurement and consequently non-constant (i. e., decreasing) μ/ρ along increasing ρ_A and ρ, respectively,
- difference between measured $\overline{\mu/\rho}$ and computed $\mu/\rho\,(E)_\mathrm{mix}$ of the very same material with further influence of energy spectra $S(E)$ consideration, where measurements fall below corresponding computation on equivalent energy level,
- impact of WBC composition particularly regarding MC and ash content $\omega(a)$, which decreases with increasing radiation energy whereas low-Z variations due to resin content are negligible, and
- upward shift of transmitted spectra $S_\mathrm{D,T}(E, \rho_\mathrm{A})$ and respective mean energies in comparison to initial spectra $S_\mathrm{D,0}(E)$ without respective labMDF absorbers of predefined raw densities and dependence on the very same.

In the subsequent chapters, all findings come together and provide the basis for consequent implications. The interdependent radiation-physical effects like beam hardening, multiple scattering, and radiation build-up occur in natural consequence of the application of non-ideal measuring conditions, i. e., without realisation of "good-architecture" conditions, which is, nevertheless, not feasible in common measuring practice. Moreover, the interaction between radiation and matter during transmission and related information content of the measuring results is further considered on distinct scales to follow up on the radiation transmission concept through porous composites of Chapter IV–3. Eventually, conventional Beer's law of attenuation is found to break down for the considered WBC applications as to be comprehensively deduced in Chapter IV–6.6.

To some extent, the findings regarding radiation-physical interdependencies in terms of WBC X-ray densitometry were already published by SOLBRIG et al. (2015a). However, the considerations and conclusions will be deepened and discussed in detail hereafter.

6.2 Beam hardening

The upward shift of mean radiation energy and respective variations of the applied X-ray spectrum in consequence of attenuation of polychromatic radiation is commonly known as beam hardening. For general basics, fundamental effects, and discussion of hitherto findings, reference is made to Chapter II–2.4. Accordingly, beam hardening is considered to cause non-linear attenuation characteristics owing to variation of the energy-dependent mass attenuation coefficient, in turn, depending on transmission conditions such as material and thickness or area density.

In general, beam hardening unavoidably occurs, where X-ray spectra with a certain width are applied for transmission measurements. The extent of the energy shift, however, depends on the

particular measuring and material conditions. The former is attributed to individual radiation parameters and character of the applied X-ray spectrum as well as the transmission measuring setup itself. The latter is related to both chemical and structural material parameters. Pre-filters are common practice in both medical as well as technical X-ray applications and utilise the beam hardening effect to particularly influence initial energy spectrum by diminishment of low-energy fraction to a certain extent, which, in turn, depends on pre-filter material (metal alloy) and layer thickness and can accordingly be predefined. Therefore, a distinction has to be drawn between deliberately obtained beam hardening of the initial spectrum by pre-filtering, thus, referred to as pre-hardening, and undesirable energy shift during transmission measurement. The latter is unavoidable but reducible by proper pre-filter application.

Beam hardening is prevalent for X-ray transmission through all materials. The extent, however, depends on absorber elemental composition and atomic numbers of the constituents as well as fundamental radiation energy level, thus, on effective mass attenuation coefficient $\mu/\rho\,(E)$. As easily can be seen from Figure IV-69 in comparison between CNO-elements and Ca as well as particularly in Figure VII-30 to Figure VII-32 toward Figure VII-35 considering photoelectric absorption, not only the basic range of $\mu/\rho\,(E)$ but also the slope of attenuation plots differ between light elements and metals. To comprehensively evaluate attenuation conditions regarding beam hardening with focus on wood and WBCs as low-Z matter, Figure IV-74 combines $\mu/\rho\,(E)$ plots (incl. single processes) of lab-MDF 9.5 % MC and measured initial X-ray spectra $S_{D,0}(E)$ (partly incl. pre-filter) of selected device setups. Note, the more or less wide radiation energy spectra on levels corresponding to their application are superimposed by the steeply increasing slope of total $\mu/\rho\,(E)$ toward the lower energies and particularly with predominant photoelectric absorption (solid grey line, 'photo' in Figure IV-74) as interaction mechanism besides coherent and incoherent scattering. Consequently, beam hardening is particularly considerable for the energy range below
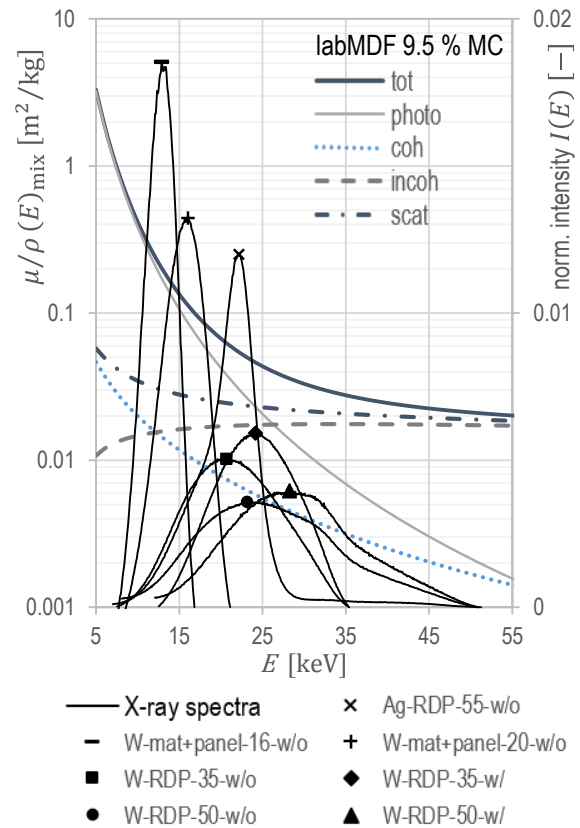
Figure IV-74: Total mean mass attenuation coefficient $\mu/\rho\,(E)$ (tot) over radiation energy E of lab-MDF 9.5 % MC incl. single attenuation processes photoelectric absorption (photo), coherent (coh) and incoherent (incoh) scattering, as well as scattering (scat = coh + incoh) determined on basis of analysis data (Table IV-15) via mixture rule eq. (II-31) by means of XCOM (2010) elemental data (for complete data refer to Table VII-12), in combination with measured initial X-ray spectra $S_{D,0}(E)$ (partly incl. pre-filter) of selected device setups (Table IV-18 to Table IV-20) as normalised intensities such that $\sum_n I(E_j) = 1$ (Chapter IV–4.3.3.1), with mark on intensity peak $I(E)_{max} = I(E_{peak})$.

$E \approx 24\ \mathrm{keV}$ (refer to Table IV-40), where photoelectric absorption still dominates beyond scattering. Hence, the comparatively narrow spectra on low and low-medium energy range in Figure IV-74 (W-mat+panle-16+20-w/o as well as Ag-RDP-55-w/o) will still be affected by energy shifts during specimen transmission. The wide spectra without additional pre-filter (W-RDP-35+50-w/o) are considered to yield strongest beam hardening effects in terms of measurement. Moreover, in case of W-RDP-50-w/ spectrum, impact of well-designed pre-filter becomes obvious and beam hardening is more or less completed with

respect to the illustrated labMDF 9.5 % MC as absorber, where further radiation attenuation will consequently be dominated by (incoherent) scattering, which is additionally attributed to the higher energy level. W-RDP-35-w/ spectrum, in turn, is similarly pre-filtered, a considerable extent of beam hardening is, however, expected, since large fraction of normalised energy distribution falls below considered threshold of $E \approx 24$ keV.

Beyond material composition, beam hardening depends on further transmission conditions. For homogeneous, non-porous, and isotropic material, attenuation, depends on transmission distance s_T at uniform density. The like consequently applies to beam hardening, which therefore increases along increasing path lengths s_T. For WBCs as inhomogeneous, porous, and anisotropic material, on the contrary, material structure comes in addition considering macroscopic and mesoscopic scale as illustrated in Figure IV-12. Nevertheless, the amount of irradiated material along the X-ray beam path through the specimen equals the area weight (macroscopic scale, refer to Chapter IV–3.2). With $\rho_\mathrm{A} = \rho \cdot s_\mathrm{T}$, it corresponds to the raw density ρ at uniform transmission distance or – vice versa – to the transmission distance s_T (e. g. mat heigth) at uniform raw density. Hence, both raw density or thickness variation cause varying beam hardening for X-ray transmission measuring applications on WBCs. Severe raw density differences, e. g., between the pre-compressed fibre mat and ready-pressed panel with the very same ρ_A, do, nevertheless, not necessarily cause varying beam hardening, likewise FUCHS (2010) points out, according to presumed varying low-energy absorption. In this regard, transmission distance differs but material amount equals, hence, primary absorption equals, too. As firstly stated by FUCHS (2010), refined by SOLBRIG et al. (2014b), and verified above (Table IV-26), measured μ/ρ fundamentally differ between equivalent mat and panel of equal ρ_A. Eventually, corresponding transmission spectra likewise differ, which is, notwithstanding the above, considered to be rather attributed to scattering issues than beam hardening, as to be pointed out in Chapter IV–6.3.

Above summarised observations (Chapter IV–6.1) in consequence of radiation-physical interdependencies are partly attributed to beam hardening, where impact can be estimated via own characteristic values to some extent. Fundamentally, upward shift of the measured spectra $S_{\mathrm{D,T}}(E, \rho_\mathrm{A})$ transmitted through labMDF absorbers of predefined raw density and corresponding increment of mean energies in comparison to initial spectra $S_{\mathrm{D,0}}(E)$ is found as typical beam hardening characteristic. The extent becomes obvious from the charts in Chapter IV–4.3.3.1 resulting from the performed radiation spectra measurements. The characteristic parameters in Table IV-29 facilitate quantification of the beam hardening effect:

- Energy shift is directly quantified via the individually calculated differences of mean energy $\Delta\bar{E}$ as well as energy at intensity peak ΔE_{peak}, respectively, considering the particular setup and specimens as absorber.
- Moreover, comparison of lower threshold energies E_{min} reveals the actually absorbed energy range, where the values are found to likewise increase with increasing material amount in the beam.
- The parameter full width at half maximum (FWHM, eq. (IV-30)) represents the width of the investigated spectra and provides an estimation for appropriate pre-filtering.

However, particularly $\Delta\bar{E}$ and E_{min} unveil the increasing penetration potential of the radiation due to more extensive beam hardening along area density ρ_A increment and practically quantify the effect on X-ray transmission measurements and related mass attenuation coefficients. Therefore, and to accordingly evaluate fundamental trends within an investigated ρ_A range on a basic energy level E by means of a clear measure, the beam hardening index

$$BHi(E, \rho_\mathrm{A}) = \frac{\dfrac{\Delta\bar{E}_\mathrm{T}}{\bar{E}_0}}{\dfrac{\Delta\rho_\mathrm{A}}{M\rho_\mathrm{A}}} \cdot 100 \qquad \text{(IV-44)}$$

is introduced as differential energy shift with $\Delta\bar{E}_\mathrm{T} = \bar{E}_{\mathrm{T,max}} - \bar{E}_{\mathrm{T,min}}$ related to initial mean energy $\bar{E}_0$ per corresponding incremental change of area density $\Delta\rho_\mathrm{A} = \rho_{\mathrm{A,max}} - \rho_{\mathrm{A,min}}$ related to

the mid-range $M\rho_\mathrm{A} = 0.5 \cdot \left(\rho_\mathrm{A,max} + \rho_\mathrm{A,min}\right)$ of the range. The computation of $BHi(E, \rho_\mathrm{A})$ yields percentage energy increment per percent area weight increase $[\%\Delta\bar{E}/\%\Delta\rho_\mathrm{A}]$. Consequent results facilitate comparison of X-ray transmission measuring applications regarding their individual beam hardening effects.

Nevertheless, $BHi(E, \rho_\mathrm{A})$ computation requires knowledge of transmission spectra $S_\mathrm{T}(E, \rho_\mathrm{A})$ from measurement or simulation considering the ρ_A range under investigation as well as corresponding initial spectra $S_0(E)$. Therefore, Table IV-43 provides exemplarily computed $BHi(E, \rho_\mathrm{A})$ results for the available RDP measuring device spectra from measurement (refer to Chapter IV–4.3.3.1) as well as simulation (Chapter IV–4.3.3.2, without scattering consideration). Moreover, Figure IV-75 illustrates the context of $BHi(E, \rho_\mathrm{A})$ with relative variations of mean transmitted energy $\bar{E}_\mathrm{T}$ along incremental changes of area weight ρ_A (refer to Table IV-23) for both measured and simulated X-ray spectra. It further shows linear regression plots considered as appropriate first approximation, where the slope (multiplied by 100 [%]), in turn, is found to more or less equal computed $BHi(E, \rho_\mathrm{A})$ in Table IV-43. With respect to spectra measurement, the exemplary results reveal obviously decreasing $BHi(E, \rho_\mathrm{A})$ in the displayed order of device setups (Table IV-43) corresponding to increasing

Figure IV-75: Relative shift of measured and simulated mean radiation energy $\Delta\bar{E}_\mathrm{rel}$ (bottom and top, respectively, simulation w/o scattering consideration) of transmitted spectra $S_\mathrm{D,T}(E, \rho_\mathrm{A})$ toward initial $S_\mathrm{D,0}(E)$ (for RDP setups refer to Table IV-29) over incremental change of area density $\Delta\rho_\mathrm{A}/M\rho_\mathrm{A}$ related to its mid-range, with linear regression plots (dashed lines) indicating the trend and respective slope illustrating the beam hardening index $BHi(E, \rho_\mathrm{A})$ (Table IV-43).

X-ray measuring device setup	$S_{\mathrm{D,0}}(E)$ $\bar{E}$ [keV]		$BHi(E, \rho_\mathrm{A})$ $[\%\Delta\bar{E}/\%\Delta\rho_\mathrm{A}]$	
	meas.	sim.	meas.	sim.
Ag-RDP-55-w/o	21.1	26.4	8.43	15.64
W-RDP-35-w/o	21.5	21.3	6.60	10.62
W-RDP-35-w/	24.2	24.4	4.72	6.14
W-RDP-50-w/o	26.3	26.6	2.79	11.65
W-RDP-50-w/	29.2	30.4	0.35	7.11

Table IV-43: Results of beam hardening index $BHi(E, \rho_\mathrm{A})$ computation acc. to eq. (IV-44) for applied RDP measuring setups based on measured (meas.) or simulated (sim., without scattering consideration) X-ray spectra $S_\mathrm{D,0}(E)$ (with initial mean energy $\bar{E}$) and $S_\mathrm{D,T}(E, \rho_\mathrm{A})$ considering labMDF 9.5 % MC as absorbers with varying area densities ρ_A (Table IV-23) at equivalent transmission distances $s_\mathrm{T} = z_\mathrm{nom} = 50$ mm.

mean initial energy $\bar{E}_0$. This is, however, not considered as an exclusive dependence of $BHi(E, \rho_A)$ on (mean) radiation energy, since individual width of energy distribution comes in addition. With particular focus on the W-target setups, $BHi(E, \rho_A)$ is found to decrease with pre-filter application (device labels …-w/) on the respective energy level $U_{a,nom} = 35$ kVp and $U_{a,nom} = 50$ kVp. Here, appropriately predefined pre-filter of W-RDP-50-w/ setup becomes obvious again, since $BHi(E, \rho_A) = 0.35 \ \%\Delta\bar{E}/\%\Delta\rho_A$ converges toward zero corresponding to minimised energy variation along the considered density range, hence, minimised beam hardening effects for the measuring application. Regarding simulated spectra, in turn, $BHi(E, \rho_A)$ reveals fundamentally different values. Note for Ag-RDP-55-w/o results, no similarities are expected, since simulation is not able to consider capillary optics, which is part of measuring setup. However, a trend of decreasing $BHi(E, \rho_A)$ with pre-filter application in the case of W-target setups is found again. Likewise, comparable levels of initial beam hardening corresponding to ordinate intercept with $\Delta E_T/E_0 = 0.02 \ldots 0.03$ (w/, lower) and $\Delta E_T/E_0 = 0.07 \ldots 0.10$ (w/o, upper) become obvious from the two groups in both charts in Figure IV-75, respectively, neglecting Ag-RDP-55-w/o plots. Notwithstanding this, the comparison between measurement and simulation unveils a different characteristic in some details. Note, decreasing $BHi(E, \rho_A)$ with increasing $\bar{E}$ of measured spectra is not featured by simulation results. Obviously, recorded radiation of transmission spectra is superimposed by further radiation-physical effects beyond simulation conditions. Since simulation data without consideration of scattering is applied (as software default, for discussion reference is made to Chapter IV–4.3.3.2), the observed phenomena in spectra measurement and consequent $BHi(E, \rho_A)$ differences are considered to be attributed to scatter radiation impinging on the respective detector, as to be discussed elsewhere. Eventually, $BHi(E, \rho_A)$ results based on simulation can be concluded to represent fundamental beam hardening of the evaluated application whereas measuring data rather considers setup conditions and can be superimposed by further

radiation-physical effects. Note, the introduced representation of BHi is not connected in any way to the beam hardening index $BIdx$ as utilised by LIN, SAMEI (2014) (refer to Chapter II–2.4). Moreover, BHi is introduced to quantify beam hardening in terms of transmitted spectra mean energy shift due to area density inhomogeneity, whereas LIN, SAMEI (2014) quantify accuracy of CT voxel values in consequence of beam hardening artefacts and noise by means of $BIdx$ and $NIdx$ (noise index).

Beyond quantified energy variations in dependence of ρ_A via $BHi(E, \rho_A)$, observed differences between measured $\overline{\mu/\rho}$ and correspondingly computed $\mu/\rho\,(E)_{mix}$ are already attributed to the applied spectra and mean energies, respectively, for computation. Accordingly, beam hardening is considered to cause the fundamental differences between theoretically equivalent mass attenuation coefficients in the case of inappropriate utilisation of initial spectra $S_{D,0}(E)$ and corresponding $\bar{E}_0$, respectively. The evaluation by means of $BHi(E, \rho_A)$ and particularly the ordinate intersects in Figure IV-75 represent the initial energy shift from the initial X-ray beam toward beginning radiation attenuation within the specimen under investigation. Moreover, the results obviously reveal the distinct difference between the two groups of open (upper) and pre-filtered (lower plots) X-ray beams regardless of Ag-RDP-55-w/o plot. Since beam hardening increases mean radiation energy, which, in turn, yields lower $\mu/\rho\,(E)$, the measurements of $\overline{\mu/\rho}$ falling bellow corresponding computations of $\mu/\rho\,(E)_{mix}$ are considered as proven. Moreover, transmission conditions are supposed to feature higher mean energies than applied for correspondingly computed values in Table IV-42. Therefore, further comparison of measuring results with comprehensive computation data, e. g., in Table VII-12 for labMDF 9.5 % MC, and interpolation within the discretisation step $\Delta E = 1$ keV facilitates to imply on the (mean) radiation energy, where $\mu/\rho\,(E)_{mix}$ computations equal $\overline{\mu/\rho}$ measurements. Table IV-44 exemplarily presents the radiation energies E from computation, which virtually correspond to the respec-

tively measured mean mass attenuation coefficients $\overline{\mu/\rho}$ of labMDF650 (Table IV-42 at $MC =$ 9.5 %) considering both total attenuation $\mu_{\text{tot}}/\rho\,(E)_{\text{mix}}$ as well as exclusive photoelectric absorption $\mu_{\text{photo}}/\rho\,(E)_{\text{mix}}$. With respect to total attenuation, virtually corresponding energies from computation consistently exceed $\bar{E}$ of initial spectra $S_{\text{D},0}(E)$ and range rather close to $\bar{E}$ of transmitted labMDF650 spectra $S_{\text{D,T}}(E, \rho_{\text{A}})$ (Table IV-29) with non-specific differences toward the latter (partly higher and lower). On the contrary, utilisation of single mechanism attenuation coefficient of photoelectric absorption yields lower energy values in the order of $\bar{E}$ from $S_{\text{D},0}(E)$. However, virtually corresponding single mechanism energies are found not to appropriately represent actual attenuation conditions, since $\mu_{\text{photo}}/\rho\,(E)_{\text{mix}}$ exclusively considers real absorption by the very same process whereas consequently scattered radiation impinges on the detector in an undefinable extent in terms of measurement and is, thus, part of detection signal. Although the exemplary computation results in Table IV-44 are not considered as precise determination of mean transmission energies, the context obviously represents beam hardening during X-ray transmission measurements. Accordingly, the calculated virtually corresponding mean energies considering total attenuation $\mu_{\text{tot}}/\rho\,(E)_{\text{mix}}$ may serve as a rough estimation of the energy shift, where X-ray spectra measurements are not available.

Referring to the above summarised observations (Chapter IV–6.1) with particular respect to WBC composition, no clear relation or quantifiable impact on beam hardening can be concluded. Considerable increment of high-Z element content due to ash or additives is, however, supposed to increase actual fraction of photoelectric absorption $\xi(\text{photo})$, hence, potentially yielding stronger beam hardening within the material under investigation. Partly found MC impact is rather an issue of scatter radiation.

Non-constant μ/ρ, i. e., decreasing slope along increasing ρ_{A} (and ρ, respectively) is found in X-ray transmission measuring results (cf. Figure IV-36 and Figure IV-50) and already discussed

| X-ray transmission measurement | virt. corresp. mean energy considering | | measured mean spectra energy | |
| | | μ_{tot} | μ_{photo} | $S_{\text{D},0}$ | $S_{\text{D,T}}$ |
RDP device setup	$\overline{\mu/\rho}$ $\left[\frac{\text{m}^2}{\text{kg}}\right]$	E [keV]	E [keV]	$\bar{E}$ [keV]	$\bar{E}$ [keV]
Ag-55-w/o	0.0485	23.5	22.3	21.1	22.1
W-35-w/o	0.0466	24.0	22.5	21.5	24.4
W-35-w/	0.0384	27.0	24.3	24.2	25.9
W-50-w/o	0.0360	28.2	25.1	26.3	29.5
W-50-w/	0.0300	32.4	27.5	29.2	30.1

Table IV-44: Measured mean mass attenuation coefficients $\overline{\mu/\rho}$ of labMDF650 (Table IV-42) with virtually corresponding radiation energies E from computation (interpolated from Table VII-12) considering both total attenuation $\mu_{\text{tot}}/\rho\,(E)_{\text{mix}}$ as well as exclusive photoelectric absorption $\mu_{\text{photo}}/\rho\,(E)_{\text{mix}}$, complete with measured mean radiation energy $\bar{E}$ of the employed initial $S_{\text{D},0}(E)$ and transmitted $S_{\text{D,T}}(E, \rho_{\text{A}})$ (through 50 mm labMDF650) spectra (Table IV-29).

in Chapter IV–4.3.2.4. The observations are particularly attributed to beam hardening, since $\mu/\rho\,(E)$ fundamentally decreases with increasing energy, but the characteristic is coincidently superimposed by scattering phenomena to be pointed out elsewhere. However, comparison of the plots in Figure IV-75 ($BHi(E, \rho_{\text{A}})$) and Figure IV-50 (relative μ/ρ) unveils obvious similarities. Again, and except Ag-RDP-55-w/o data, there are the two groups without (w/o) and with (w/) additional pre-filter, respectively. The individual slope turns steeper (up, Figure IV-75 and down, Figure IV-50, respectively) without pre-filter application due to higher $BHi(E, \rho_{\text{A}})$ of the respective setup. Within each group, in turn, the respective measuring conditions with lower energy level reveal higher $BHi(E, \rho_{\text{A}})$, thus, stronger beam hardening and coincidently steeper slope of relative μ/ρ variation along increasing ρ. Note, detector behaviour considering potential non-linearities in energy characteristic comes in addition, where, however, individual detector response function $D(E)$ is unknown.

Consequent deviations in RDP measurement as discussed in terms of the performed round robin test (refer to Chapter IV–4.3.1) are found to depend on the employed device. The respective

beam hardening effects are considered to be attributed to individually applied radiation parameters and partly unknown pre-filter utilisation basically resulting in varyingly distinct energy shifts during measurement of the raw density gradients. Accordingly, different $BHi(E, \rho_A)$ values have to be expected, where maximum is supposed to be found in the case of maximum raw density deviation from reference (i. e., device E in Table IV-24 and Table IV-25).

Notwithstanding the above, beam hardening does not necessarily cause measuring insufficiencies by itself. Moreover, the impact on quantitative X-ray applications, i. e., transmission measurements, particularly occurs in the case of inhomogeneous materials and distinct raw density or thickness (transmission distance) gradients under investigation, which, in turn, yield a varying extent of beam hardening partly within one measuring data set. On the other hand, X-ray applications for measurement of small area density variations on an equivalent level are rather affected by a corresponding level of initial beam hardening whereas no considerable variations within the measuring series have to be expected.

Eventually, WBC X-ray densitometry is individually affected by beam hardening due to the particular measuring application. Considering, e. g., area density ρ_A measurement, beam hardening effects depend on the application range with respect to the material amount. Let area density measurement on the furnish mat or panel raw density determination be carried out by an inline setup employing one single X-ray parameter setting (energy level and pre-filtering) for a wide ρ_A range. Furthermore, solely single sample calibration is performed, i. e., one single (mean) μ/ρ corresponding to ρ_A in the middle of application range is utilised. Nevertheless, actual transmission measuring conditions reveal decreasing μ/ρ plots along the respective ρ_A range with the slope depending on the individual X-ray setup (for exemplary results reference is made to Chapter IV–4.3.2.2 with summary in Figure

IV-36). Consequently, measuring results are biased by beam hardening effects, thus, deviate from trueness, where low-range ρ_A results are expected to be overestimated, i. e., higher readings compared to true ρ_A values and, vice versa, upper-range ρ_A results beyond calibration setpoint will be underestimated, i. e., displayed too low compared to trueness. Hence, beam hardening reduces measuring accuracy regarding desired ρ_A results.

Beyond that, the occurence of varying beam hardening across the vertical RDP of WBC panels is considered as one of the most vivid and coincidently crucial examples regarding X-ray densitometry. Therefore, common ratios of surface (SL) to core layer (CL) mean raw density with $\mathrm{SL/CL} = 1.4 \ldots 2.0$ for customary WBCs such as MDF and PB are found to be apparently reduced with resulting flattened RDP shapes owing to radiation-physical interdependencies. Likewise stated regarding the example of furnish mat ρ_A measurements, μ/ρ decreases along the investigated raw density range (for exemplary results reference is made to Chapter IV–4.3.2.3 with summary in Figure IV-50). Here, common but insufficient self-calibration (refer to Figure II-14) by means of one single (mean) μ/ρ corresponding to specimen's mean raw density $\bar{\rho}$ does not explicitly consider potential μ/ρ variations due to varying beam hardening along the density gradient. Dependent on local raw density, Figure IV-76 illustrates the context and summarises the consequences for X-ray RDP measurement by the example of specimen MDF1 from round robin test (refer to Chapter IV–4.3.1), which is virtually measured by W-RDP-50-w/o device. To this end, X-ray spectra were specifically simulated[36] (without scattering consideration, for method refer to Chapter IV–4.2.6.2) considering RDP sections of the specimen MDF1 ($z = 49.91\,\mathrm{mm}$) with $\bar{\rho} = 723\,\mathrm{kg/m^3}$, $\rho_{\min} = 622\,\mathrm{kg/m^3}$, and $\rho_{\max} = 933\,\mathrm{kg/m^3}$ (from gravimetric reference, Table IV-24). Corresponding characteristic parameters are compiled in Table IV-45. Let X-ray transmission measurement for

---

[36] Note, labMDF 9.5 % MC elemental composition is applied as common WBC composition, where reference is made to Chapter IV–2.4.2.

RDP determination be performed by regular intensity recording as cumulation over initial $S_0(E)$ and transmitted $S_T(E, \rho)$ spectra, respectively, and subsequent calculation of $T = I_T/I_0$. Coincidently, acquired intensity I corresponds to mean radiation energy $\bar{E}$ computed as spectral-weighted mean value. Note, E_{max} is bound to tube potential and, thus, unaffected by radiation transmission. Obviously, transmitted mean energy $\bar{E}_{T,\rho}$ is found to considerably exceed initial energy $\bar{E}_0$ at all RDP sections. The extent of energy shift depends, in turn, on local raw density within the profile under investigation and increases from CL min toward SL max with increasing raw density. The beam hardening index computed on the basis of simulated spectra considering the particular setup W-RDP-50-w/o and the measuring range $\rho = 622 \ldots 933$ kg/m^3 results in $BHi(E, \rho_A) = 11.76$ %$\Delta\bar{E}$/%$\Delta\rho_A$, which is found in the order of W-RDP-50-w/o device evaluation considering labMDF density range (Table IV-43). Accordingly, local radiation attenuation is governed by respective energy conditions resulting in analogously varying $\mu/\rho\left(\bar{E}_{T,\rho}\right)$, which considerably falls below theoretically computed value corresponding to initial energy spectrum and further decreases from CL min toward SL max. Moreover, actually transmitted intensity is found to deviate from theoretical expectation under ideal conditions, with locally decreased (CL min) or increased (SL max) values, respectively, due to RDP section. Since employed mean mass attenuation coefficient $\overline{\mu/\rho}$ from self-calibration expects linear attenuation $\ln T^{-1}$, final density ρ results and RDP slope are biased owing to actually non-linear transmission and varying $\mu/\rho\left(\bar{E}_{T,\rho}\right)$ along the measuring range. Thus, beam hardening effects cause deviations from trueness, where low-range ρ results are expected to be overestimated, i. e., higher readings compared to true ρ values and, vice versa, upper-range ρ results beyond $\bar{\rho}$ (calibration setpoint) will be underestimated, i. e., displayed too low compared to trueness.

To fundamentally conclude, beam hardening effects cause considerable bias of X-ray densitometry results, where one single mass attenuation coefficient as calibration parameter is applied for a wide range of area density and on specimens featuring distinct raw density gradients. The impact can sufficiently be reduced by appropriate pre-filter application for pre-hardening. Nonetheless, beam hardening effects cannot be totally eliminated for X-ray densitometry. Hence, beam hardening diminishes measuring accuracy regarding desired density results and has to consequently be considered otherwise.

Radiation parameters

$$I = \int_{E_{\min}}^{E_{\max}} I(E)\,dE \ [\text{a.u.}]$$

$$\bar{E} = \int_{E_{\min}}^{E_{\max}} E \cdot S(E)\,dE \ [\text{keV}]$$

$$E_{\max} \equiv U_{\mathrm{a}}[\text{kVp}]$$

Attenuation parameters

$$T = \frac{I_T}{I_0} \ [-]$$

$$\overline{\left(\frac{\mu}{\rho}\right)} = \frac{\overline{\ln T^{-1}}}{\bar{\rho}_{\mathrm{grav}} \cdot z} \ \left[\frac{\mathrm{m}^2}{\mathrm{kg}}\right]$$

Beam hardening consequences dependent on local raw density

air	**CL ρ_{min}**	**Mean $\bar{\rho}$**	**SL ρ_{max}**
$\bar{E}_0$	$\ll \quad \bar{E}_{\mathrm{T},\rho_{\min}}$	$< \quad \bar{E}_{\mathrm{T},\bar{\rho}}$	$< \quad \bar{E}_{\mathrm{T},\rho_{\max}}$
$\frac{\mu}{\rho}(\bar{E}_0)$	$\gg \quad \frac{\mu}{\rho}(\bar{E}_{\mathrm{T},\rho_{\min}})$	$> \quad \frac{\mu}{\rho}(\bar{E}_{\mathrm{T},\bar{\rho}}) = \overline{\left(\frac{\mu}{\rho}\right)}$	$> \quad \frac{\mu}{\rho}(\bar{E}_{\mathrm{T},\rho_{\max}})$
I_0	$I_{\mathrm{T},\rho_{\min}} \downarrow$	$I_{\mathrm{T},\bar{\rho}} =$	$I_{\mathrm{T},\rho_{\max}} \uparrow$
	$\rho_{min} \uparrow$	$\bar{\rho} =$	$\rho_{max} \downarrow$
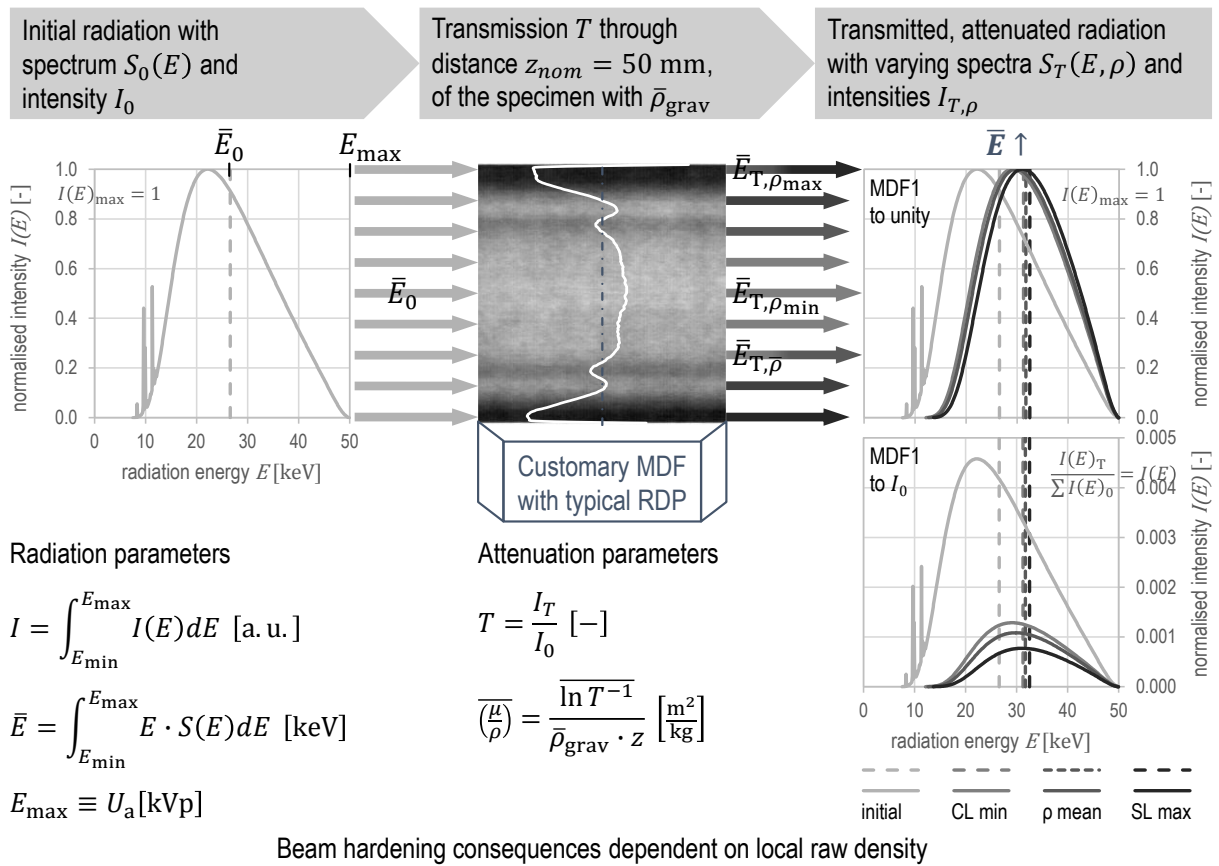
Figure IV-76: Illustration of context and consequences of varyingly distinct beam hardening in terms of X-ray RDP measurement on customary WBCs resulting in local variations of mean transmitted energy $\bar{E}_{T,\rho}$, mass attenuation coefficient $\mu/\rho\,(\bar{E}_{T,\rho})$, and effectively transmitted radiation intensity $I_{T,\rho}$ due to local raw density ρ; X-ray spectra simulated considering RDP sections of MDF1 ($z = 49.91\,\mathrm{mm}$) from round robin test (Chapter IV–4.3.1) with $\bar{\rho} = 723\,\mathrm{kg/m^3}$, $\rho_{\min} = 622\,\mathrm{kg/m^3}$, and $\rho_{\max} = 933\,\mathrm{kg/m^3}$ (from gravimetric reference, Table IV-24) with initial spectrum of W-RDP-50-w/o device (left) and transmitted spectra (right) normalised to unity (upper, $I(E)_{\max} = 1$) as well as to initial intensity I_0 (lower, $I(E) = I(E)_{\mathrm{T}}/\sum I(E)_0$), for characteristic parameters refer to Table IV-45.

target	$U_{\mathrm{a,nom}}$	pre-filter	absorber	$E_{\max}$	$\bar{E}$	$\Delta\bar{E}$	E_{peak}	ΔE_{peak}	$E_{\min}$	FWHM	$I = \sum I(E)$	I_{T}/I_0
	[kV]	t [mm]	MDF ρ	[kVp]	[keV]	[keV]	[keV]	[keV]	[keV]	[keV]	[cps]	[-]
			Al [kg/m^3]			ref. to I_0		ref. to I_0				$= T$
W	**50**	**0.635**	**–**	**50**	**26.6**	**–**	**22.2**	**–**	**7.5**	**21.6**	**2.661E+06**	I_0
		0.635	622	50	31.3	4.7	29.2	7.0	12.1	20.7	6.940E+05	0.26
		0.635	723	50	31.7	5.1	29.9	7.7	12.6	20.5	5.788E+05	0.22
		0.635	933	50	32.5	5.9	31.1	8.9	13.6	20.0	4.028E+05	0.15

Table IV-45: Simulation of beam hardening in terms of X-ray RDP measurement as compilation of characteristic parameters (like in Table IV-30) for W-RDP-50-w/o device radiation spectra simulated by XRayTools software (Chapter IV–4.2.6.2), with initial spectrum I_0 and transmission spectra considering RDP sections of MDF1 ($z = 49.91\,\mathrm{mm}$) from round robin test (Chapter IV–4.3.1) with $\bar{\rho} = 723\,\mathrm{kg/m^3}$, $\rho_{\min} = 622\,\mathrm{kg/m^3}$, and $\rho_{\max} = 933\,\mathrm{kg/m^3}$ (from gravimetric reference, Table IV-24); without (default by software) recording of scattered radiation, always including 0.635 mm Al corresponding to spectrometer lid.

6.3   Scattering and radiation build-up

The occurrence of scattering as an attenuation mechanism in consequence of coherent and incoherent interaction and resulting intensity of scattered radiation reveals particular dependencies such as radiation energy, material Z_{eff}, and angular direction as comprehensively discussed in Chapter II–2.5.1. For X-ray transmission measurements, no impact has to be considered in the case of ideal narrow-beam conditions with tight collimation of both source and detector. Accordingly, IEC 60050-881 (1983) defines narrow-beam attenuation measurement as a condition, where scattered radiation is negligible. On the contrary, broad-beam attenuation measurement always includes a certain amount of scattered radiation. Notwithstanding that, broad-beam geometry is mainly to be found in practice of technical X-ray applications. Beyond blurring as general consequence in X-ray imaging, scattering is considered to cause non-linear attenuation characteristics in terms of transmission measurement, i. e., contributes to non-linear slope of X-ray transmission plot $\ln T^{-1}$, due to bias of registered radiation intensity, following the fundamental discussion of hitherto findings in Chapter II–2.5. The like applies to all performed transmission measurements (Chapter IV–4.3.2), which belong to broad-beam applications, since all employed setups (Table IV-18 and Table IV-19) do not fulfil ideal conditions owing to solely slit or no collimation of the detector as well as initial beams with certain extent. Consequently, transmitted beams unavoidably comprise scattered radiation, which is assigned to secondary radiation and, thus, not primarily expected in the acquired signal. Hence, forward-scattered radiation, which somehow reaches the transmission detector of the setup, has to be taken into account. Moreover, any scattering from the specimen has to be considered such that backward-scattered radiation may undergo multiple interaction and could, thus, be redirected toward the transmitted beam. The like applies vice versa to forward-scattered radiation. Therefore, all scattering considerations below refer to multiple scattering.

As already illustrated in Figure II-10 with respect to measurements by means of extended beam and detector area, scattering superimposes the directly transmitted beam and contributes to the recorded total intensity on the detector. Note, Figure IV-77 serves as an enhancement of Figure II-10 and comprises relevant scattering phenomena (beyond absorption and unaffected transmission) to fundamentally distinguish between scattering directly from the central beam over the detector area (referred to as detector field of view (FOV)) and the radiation indirectly scattered in from outside FOV impinging on the detector. Beyond this, radiation may be scattered out, thus, removed from the transmitted beam and to be considered as actual attenuation fraction. Moreover, the beam diverges, where radiation may undergo multiple interactions within the specimen. Beyond scattered radiation reaching the detector from the material under investigation (inside or outside FOV), there are further potential sources of scatter radiation considering the setup and its surroundings. In industrial radiology, HALMSHAW (1995), e. g., mentions

- backscatter from the support of the film after beam has passed the very same or
- scatter originating from the primary beam hitting walls or other adjacent objects.

In the present case of the employed setups (Table IV-18 and Table IV-19), minor scattering from the surroundings except the material under investigation is expected due to the construction mainly made of metal and the applied low to medium energy range. Nevertheless, aluminium reveals a scattering fraction in the order of $\xi(\mathrm{scat}) = 0.16$ at $E = 25\,\mathrm{keV}$ (refer to Table

radiation source with broad-beam geometry

$I_{\mathrm{S-in}}$ I_{T} ↑

I_{P}

D-FOV

$I_{\mathrm{S-out}}$

$I_{\mathrm{T}} = I_{\mathrm{P}} + I_{\mathrm{S}}$
$I_{\mathrm{S}} = I_{\mathrm{S,coh}} + I_{\mathrm{S,incoh}}$
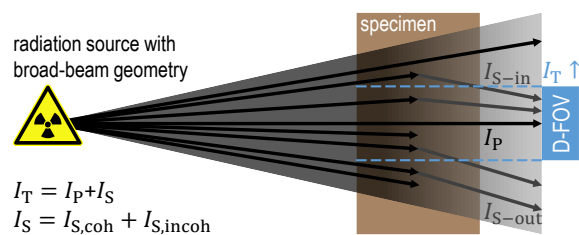
Figure IV-77: Broad-beam geometry following Figure II-10 enhanced with interaction processes beyond detector FOV illustrating scatter superimposition and consequent I_{T} increment from different secondary sources within the specimen.

VII-7) but yields strong self-absorption, in turn. On the contrary, the applied detector type of all W-target devices comprises plastic components carrying and covering the scintillator. Therefore, a considerable amount of scatter is supposed to contribute to the detection signal. Nevertheless, beam geometry hitting the detector is equal for I_T as well as I_0 determination. Thus, equivalent scattering contribution from irradiated detector components is expected for both I_T and I_0 measurement on the one hand. However, on the other hand, SPR values are considered to differ with $SPR_0 < SPR_T$, i. e., zero signal SPR without any attenuator in the direct beam is supposed to considerably fall below the very same of the attenuated beam, since transmission yields lower primary intensity. Moreover, transmitted spectra $S_\mathrm{T}(E, \rho_\mathrm{A})$ differ from the initial one $S_0(E)$, hence, cause different scattering due to energy-dependence of radiation interaction. Obviously, the actual scattering impact from close surroundings such as the detector housing cannot be clarified without particular determination of the respective scattering intensities, which is, in turn, elaborate considering the required masking setup or even unfeasible regarding appropriate accuracy. Eventually, there is a demand to consider inherent scattering otherwise. Consequently, beam and transmission geometry, hence, total X-ray measuring setup, fundamentally affects actual scattering conditions, thus, measuring results and effective mass attenuation coefficients. Here, ATTIX (2004) points out that any effective μ/ρ from a broad-beam attenuation measurement allways falls below the theoretical value (from computation and tabulation), where measured μ/ρ, in turn, comes close to computed values with setup conditions approaching narrow-beam geometry.

Regardless of image blur, scattering considerations in terms of the present quantitative applications, i. e, X-ray densitometry, preferably draw on radiation build-up as bias of detector signal compared to ideal expectation. Notwithstanding this, the build-up factor B for quantification of the effect is, however, not explicitly determined on the basis of measuring data. Note, the determination appears feasible by simple transformation of eq. (II-47) toward $B = I_\mathrm{T}/I_0 \cdot e^{\frac{\mu}{\rho}(E) \cdot \rho \cdot t}$ (likewise

SIEGEL et al. (1985) do), with $I_\mathrm{T}/I_0 = T$ from transmission measurements, ρ and t as gravimetrical specimen data, and $\mu/\rho(E) = \mu/\rho(E)_\mathrm{mix}$ from theoretical computation considering elemental composition and radiation energy E. However, the discussion in Chapter IV–5.2.3 unveils questionable validity of $\mu/\rho(E)_\mathrm{mix}$ no matter what computation method is used as a direct substitute for correspondingly measured μ/ρ. There is no obvious conclusion, which $\mu/\rho(E)_\mathrm{mix}$ values are applicable aiming at appropriate accuracy. Therefore, the $\mu/\rho(E)_\mathrm{mix}$ error would propagate to B computed thereof. Accordingly, no computation of B is performed on the basis of transmission measurements. Further methods by means of explicit determination of I_S or I_P, respectively, are associated with erroneous and elaborate measurement of such intensity fractions with regard to the particularly employed setups. Already HALMSHAW (1995) discusses methods for measurement of scattering intensity I_S, which feature certain difficulties and requirements to yield appropriate accuracy in determination. Consequently, no such measurements are performed and, thus, no values of B for the respective setups can be presented.

The above summarised observations (Chapter IV–6.1) in consequence of radiation-physical interdependencies are partly attributed to scattering. In contrast to the discussion on beam hardening in Chapter IV–6.2, obviously no particular numerical evaluations are feasible on the measuring data basis to directly quantify the scattering phenomena. However, further comparison of both measured and computed mass attenuation coefficients μ/ρ considering single interaction mechanisms provides an indirect indication for scattering conditions of the individual measuring setups. As earlier pointed out in Chapter II–2.5.4, such comparisons are already discussed by COPPOLA, REINIGER (1974), MIDGLEY (2006), or SARITHA, NAGESWARA RAO (2013), where the latter present deviations between their experimental and theoretical μ/ρ results of only $-0.05 \dots 1.54\,\%$ due to their tightly collimated setup comprising four apertures along the beam path. In addition to the earlier comparison of μ/ρ computation toward measurement in Chapter

IV–5.2.3, single attenuation processes with respective values in Table IV-41 are further taken into account. To this end, Table IV-46 provides a compilation of Table IV-42 data complete with computed single coefficients $\mu_i/\rho\,(\bar{E})_{\mathrm{mix}}$ at single mean energies $\bar{E}$ considering photoelectric absorption and scattering (sum of coherent and incoherent interaction) as well as corresponding attenuation fractions $\xi(i)$ following eq. (II-15). Figure IV-78 illustrates the data for labMDF650 at $MC = 9.5\,\%$. Note, although $\mu/\rho\,(E)_{\mathrm{mix}}$ computation of spectral-weighted total mean mass attenuation coefficient via application of corresponding transmitted spectra $S_{\mathrm{D,T}}(E,\rho_\mathrm{A})$, thus, $\mu/\rho\left(S_{\mathrm{D,T}}(E,\rho_\mathrm{A})\right)_{\mathrm{mix}}$, is found to yield more appropriate estimations (refer to Chapter IV–5.2.4), comparison in Table IV-46 and corresponding single process coefficient computation is performed on the basis of $\bar{E}$, thus, $\mu/\rho\,(\bar{E})_{\mathrm{mix}}$, which is considered a more practice-oriented index due to the general lack of both initial and particularly transmission spectra in the case of applications beyond present investigations.

However, $\overline{\mu/\rho}$ measuring results consistently range somewhere between computed $\mu_{\mathrm{photo}}/\rho\,(\bar{E})_{\mathrm{mix}}$ and $\mu_{\mathrm{tot}}/\rho\,(\bar{E})_{\mathrm{mix}}$, where the latter (total) represents ideal conditions, i. e., maximum attenuation in narrow-beam geometry on the respective energy level. Obviously, an individual partial addition of $\mu_{\mathrm{scat}}/\rho\,(\bar{E})_{\mathrm{mix}}$ to $\mu_{\mathrm{photo}}/\rho\,(\bar{E})_{\mathrm{mix}}$ would represent the practical case, such that after scattering interaction, radiation is not necessarily removed from the beam but partly reaches the detector due to beam geometry and collimation. The difference $\Delta\,\mu_{\mathrm{photo}}/\rho$ of photoelectric absorption toward measured (mean) $\overline{\mu/\rho}$ gives a quantitative indication for additional attenuation by scattering, which, however, actually removes the considered radiation portion from the transmitted beam by scattering out of FOV. The differences increase with increasing $\bar{E}$, thus, scattering contribution to total attenuation increases. Moreover, relative evaluation via the quotient $Q\,\mu_{\mathrm{photo}}/\rho$ appears more practicable. Therefore, $1 - Q\,\mu_{\mathrm{photo}}/\rho$ is considered as scattering contribution and likewise increases for the respective panel type, where labMDF and indMDF results
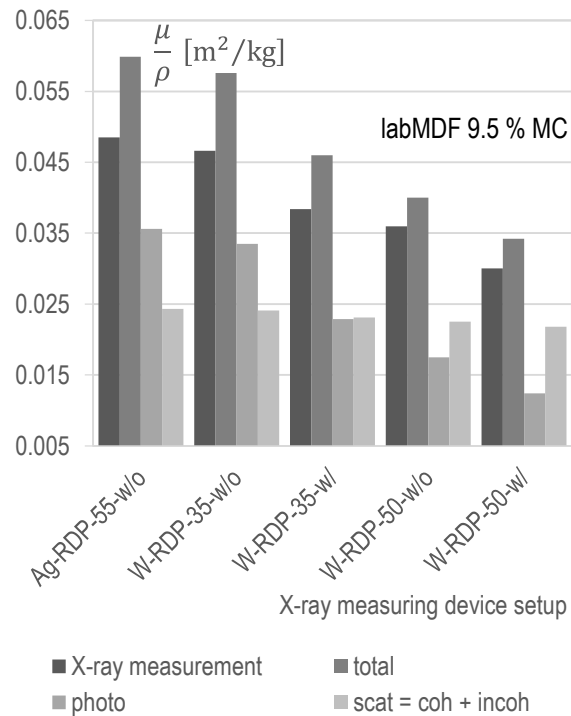
Figure IV-78: Comparison between mean mass attenuation coefficients of labMDF650 at $MC = 9.5\,\%$ from X-ray measurements $\overline{\mu/\rho}$ (Table IV-27) and computed values by single mean energies $\mu_i/\rho\,(\bar{E})_{\mathrm{mix}}$ (Table IV-35) for both total attenuation as well as single interaction processes photoelectric absorption and scattering (as sum of coherent and incoherent), respectively considering Ag- and W-RDP device setups; for data refer to Table IV-46.

are found in the same order. The values of insulation with considerably lower raw density, however, exceed the densified panel results owing to the different material structure, since the more porous insulation enables stronger divergence of the beam such that out-scattering diminishes secondary radiation reaching the detector. Eventually, $1 - Q\,\mu_{\mathrm{photo}}/\rho$ reveals an equivalent tendency like $\xi(\mathrm{scat})$ but falls below the theoretical scattering fraction, since not the total scattering contributes to real attenuation. The residual interaction causes in-scattered radiation, which is considered to be registered by the detector. Here, $1 - Q\,\mu_{\mathrm{tot}}/\rho$, i. e., the relative difference between measured and computed total $\mu_{\mathrm{tot}}/\rho\,(\bar{E})_{\mathrm{mix}}$, may serve as indication for scattering fraction in the transmitted beam of the respective measurement. Obviously, the results tend to decrease with increasing energy whereas the pattern shows some irregularities. Insulation values fall, in turn, below labMDF and

indMDF results, hence, a lower scattering fraction is considered to be emitted from the more porous material. Note, all discussed data above belongs to the applied RDP devices with slit collimation in front of the detector. However, the like observations are found for comparison of Fmat and indMDF data at $\bar{E} = 12.7\,\mathrm{keV}$, where fibre mat measurements obviously yield lower scattering fraction in transmitted radiation on detector compared to the panel measuring conditions (further discussions follow below). Note, all observed effects considering both ρ_A and RDP devices in comparison of measured toward computed μ/ρ are superimposed or even rather dominated by beam hardening, which is found to yield decreased μ/ρ compared to expectation as comprehensively discussed in Chapter IV–5.2.3 as well as Chapter IV–6.2. Therefore, no clear distinction, thus, no conclusion on the actual scattering impact, is possible based solely on μ/ρ considerations. Further implications considering energy spectra and the interdependencies of both effects scattering as well as beam hardening follow below.

measuring device		measure-ment			$\dfrac{\mu_i}{\rho}(\bar{E})_{\mathrm{mix}}$ computation, eq. (II-31), single mean energy				$\xi(i)\,[-]$	
setup	energy	$\overline{\mu/\rho}$		total			photo	scat	photo	scat
	$\bar{E}$ [keV]	μ/ρ $\left[\frac{\mathrm{m}^2}{\mathrm{kg}}\right]$	μ/ρ $\left[\frac{\mathrm{m}^2}{\mathrm{kg}}\right]$	$1 - Q\,\mu/\rho$ $[-]$	μ/ρ $\left[\frac{\mathrm{m}^2}{\mathrm{kg}}\right]$	$\Delta\,\mu/\rho$ $\left[\frac{\mathrm{m}^2}{\mathrm{kg}}\right]$	$1 - Q\,\mu/\rho$ $[-]$	μ/ρ $\left[\frac{\mathrm{m}^2}{\mathrm{kg}}\right]$		
Fmat 9.4 % MC										
W-mat-16-w/o	12.7	0.2039	0.2181	-0.070	0.1878	-0.0161	0.079	0.0304	0.86	0.14
indMDF 8.1 % MC										
W-panel-16-w/o	12.7	0.1749	0.2111	-0.207	0.1809	+0.0060	-0.034	0.0303	0.86	0.14
labMDF 9.5 % MC										
Ag-RDP-55-w/o	21.1	0.0485	0.0599	-0.235	0.0356	-0.0129	0.266	0.0243	0.59	0.41
W-RDP-35-w/o	21.5	0.0466	0.0576	-0.236	0.0335	-0.0131	0.281	0.0241	0.58	0.42
W-RDP-35-w/	24.2	0.0384	0.0460	-0.198	0.0229	-0.0155	0.404	0.0231	0.50	0.50
W-RDP-50-w/o	26.3	0.0360	0.0400	-0.112	0.0175	-0.0185	0.513	0.0225	0.44	0.56
W-RDP-50-w/	29.2	0.0300	0.0342	-0.139	0.0124	-0.0176	0.587	0.0218	0.36	0.64
indMDF 8.1 % MC										
Ag-RDP-55-w/o	21.1	0.0457	0.0600	-0.314	0.0358	-0.0099	0.216	0.0243	0.60	0.40
W-RDP-35-w/o	21.5	0.0460	0.0578	-0.257	0.0337	-0.0123	0.267	0.0241	0.58	0.42
W-RDP-35-w/	24.2	0.0385	0.0461	-0.196	0.0230	-0.0155	0.403	0.0231	0.50	0.50
W-RDP-50-w/o	26.3	0.0359	0.0401	-0.116	0.0176	-0.0183	0.510	0.0225	0.44	0.56
W-RDP-50-w/	29.2	0.0303	0.0343	-0.134	0.0125	-0.0178	0.587	0.0218	0.36	0.64
raytest	59.5	0.0166	0.0194	-0.169	0.0012	-0.0154	0.928	0.0182	0.06	0.94
insulation 9.1 % MC										
Ag-RDP-55-w/o	21.1	0.0468	0.0589	-0.257	0.0347	-0.0121	0.259	0.0242	0.59	0.41
W-RDP-35-w/o	21.5	0.0514	0.0567	-0.104	0.0327	-0.0187	0.363	0.0241	0.58	0.42
W-RDP-35-w/	24.2	0.0403	0.0454	-0.127	0.0223	-0.0180	0.447	0.0231	0.49	0.51
W-RDP-50-w/o	26.3	0.0394	0.0395	-0.001	0.0170	-0.0224	0.569	0.0225	0.43	0.57
W-RDP-50-w/	29.2	0.0314	0.0339	-0.079	0.0121	-0.0193	0.615	0.0218	0.36	0.64

Table IV-46: Comparison between mean mass attenuation coefficients (acc. to Table IV-42) of fibre mats (Fmat), lab-made (labMDF650) and industrial MDF, as well as insulation board at EMC in consequence of 20/65 conditioning with data from X-ray measurements $\overline{\mu/\rho}$ (Table IV-27) and computed values $\mu_i/\rho\,(\bar{E})_{\mathrm{mix}}$ at single mean energies $\bar{E}$ (Table IV-35) for both total attenuation as well as single interaction processes photoelectric absorption and scattering (scat = coh + incoh), respectively considering W-mat and W-panel (without pre-filter) as well as Ag- and W-RDP (with and without pre-filters) device setups plus raytest; complete with comparison via selected $\Delta\,\mu_i/\rho\,(E)_{\mathrm{mix}}$ eq. (IV-41) and $1 - Q\,\mu_i/\rho\,(E)_{\mathrm{mix}}$ eq. (IV-42) toward respective measuring data as reference; additionally, attenuation fractions $\xi(i)$ following eq. (II-15) of the single mechanisms acc. to Table IV-41.

Several anti-scatter methods are discussed in Chapter II–2.5.2. To avoid having scattered radiation from the surrounding specimen material reach the detector from beyond FOV, masking is recommended in common practice of radiography (cf. HALMSHAW (1995)), which corresponds to detector collimation in X-ray measuring applications. Both employed RDP devices (Table IV-18 and Table IV-19) feature respective slit collimators, which are, however, considered to let a certain amount of scattered radiation pass through the width and particularly over the length of the slit aperture. Moreover, W-target ρ_A setup detectors (mat and panel, Table IV-19) with considerable dimensions support no reasonable possibility for tight collimation in the regular application of the devices with furnish mats or panels moving beyond, thus, scattered radiation would reach the detector anyway. However, collimation fundamentally diminishes the transmission intensity, thus, the acquired signal. The loss is potentially to be compensated by an increment of the initial intensity via tube current or detector integration time. The same applies to anti-scatter grids, which could be an option for the large detectors but would considerably reduce signal yield. Moreover, particularly focussing grids are elaborate to adjust and maintain, and thus inappropriate for the regular application of the utilised devices under industrial conditions. Already NEITZEL (1992) recommended using cheap and reliable air gaps rather than grids, i. e., specifically increased s_{S-D}. Note, the distance increment likewise decreases measuring signal yield. However, ATTIX (2004) illustrates and discusses various broad-beam geometries. Accordingly, the case of a detector as close as possible to the specimen backside causes out-scattered radiation to be maximally replaced by in-scattered secondaries, i. e., no beneficial conditions. Moreover, an increment of specimen-backside-detector-surface distance s_{S-D} is well-known to reduce scattered radiation on the detector. Considering the beam width w covering at least the detector, ATTIX (2004) further points out that an increasing ratio s_{S-D}/w facilitates to approach narrow-beam conditions. Accordingly, the employed W-mat-ρ_A device particularly in the case of thin specimens with $s_{S-D} < 400$ mm can

be considered to reveal the most appropriate conditions with reduced scattering in contrast to the comparable W-panel-ρ_A setup featuring, however, a wide fan beam and low $s_{S-D} = 36$ mm. Eventually, both RDP devices appear well-equipped with a slit collimator and certain distance to the detector $s_{S-D} \approx 50$ mm, which, however, does not avoid registration of scattered radiation as μ/ρ measuring results indicate. The ρ_A setups for both mat and panel feature an open detector without any collimation, where the prior provides particular but varying s_{S-D}. Thus, different scattering conditions become likewise obvious from corresponding transmission measuring results in comparison between mat and panel data with

- varying $B(\rho_A)$ in case of W-mat-ρ_A results along increasing ρ_A obvious from rather non-linear slope of μ/ρ in Figure IV-36 and
- fundamentally stronger scattering impact, thus, higher $B(E)$, in case of W-panel-ρ_A measurements obvious from lower μ/ρ values at the same energy level in Figure IV-36 and Table IV-26

according to evaluations in Chapter IV–4.3.2.2 and first implications in Chapter IV–4.3.2.4.

Beyond beam geometry and measuring setup, the investigated material itself with structure and composition is considered to influence scattering conditions, thus, SPR according to eq. (II-44) and consequently B following eq. (II-48). In this regard, low-Z material such as WBCs with coincidently rather low true density of the wood matter reveals minor self-absorption of secondary radiation from coherent and incoherent scattering interaction. Contrary to this, scattering from high-Z metals (e. g. Fe) in the applied energy range undergoes most likely subsequent absorption within the high-density material itself due to energy loss of the secondaries in consequence of predominant incoherent Compton scattering and strong photoelectric absorption. Therefore, WBC specimens emit a considerable portion of secondary radiation, thus, may yield considerable SPR and B in terms of X-ray transmission measurements. However, increased self-absorption for both kinds of scattered radiation likewise applies to long transmission distances within light

and porous materials such as WBCs. Thus, the likelihood of secondary or even multiple interaction increases with increasing thickness of the absorber. Hence, a diminished amount of scattered radiation as I_S on the detector is expected. The phenomenon is considered to particularly occur in case of equivalent area density with increasing porosity, i. e., low densification (refer to beam path model Figure IV-12). This context is considered as further reason for the aforementioned differences between W-target device ρ_A results on Fmat and indMDF. At equivalent ρ_A, there are longer transmission distances through the pre-pressed furnish mat in comparison to the densified panel, e. g., about factor 10 in case of MDF. On the longer beam path, secondary radiation may undergo multiple interactions and, moreover, the beam is particularly enabled to more strongly diverge in the coarse structure of the wood-particle-resin-matrix (refer to mesoscopic level, Chapter IV–3.3), i. e., in the pores between particles or TMP fibres of the pre-pressed mat. Contrary to possible divergence in the case of ρ_A measurement, RDP determination features rather short but constant transmission distances along the profile. Note here, high raw densities in SL compared to CL are assumed to reveal higher SPR due to the higher amount of material, where radiation undergoes multiple interaction. In contrast to the aforementioned attenuation characteristic of metal, an increment of self-absorption fails to appear owing to the comparatively low true density of wood matter and non-dominance of photoelectric absorption in the applied medium energy range. Further implications on RDP measurement regarding scattering conditions follow below. To conclude for WBC structures, SPR and B increase with increasing raw density at equal specimen depth and decreasing transmission distance s_T (mat or panel thickness) at equal area density ρ_A. Moreover (refer to beam path model Figure IV-12), true density of WBC matter remains equal where solely porosity is diminished during densification.

Radiation build-up on detector and consequent increment of measured I_T compared to expectation of narrow-beam attenuation is illustrated in Figure IV-77, where scattering considerations further need to be related to corresponding energy distributions. To this end, eq. (II-43) is extended by explicit consideration of transmission spectra at detector surface to

$$S_T(E, \rho_A) = S_{T,P}(E, \rho_A) + S_{T,S}(E, \rho_A) \qquad \text{(IV-45)}$$

as sum of primary and scatter spectrum, where all spectral distributions depend on both energy E and area density ρ_A of the attenuating material. Again, detector response function $D(E)$ comes in addition according to eq. (IV-33). As easily can be seen, varying scattering fractions of the transmitted beam influence the spectra reaching the detector. Thus, in addition to the aforementioned energy shift (Chapter IV–6.2), transmitted spectra are found not to exclusively be affected by beam hardening, which is known to cause an upward shift of $\bar{E}_T$ and likewise E_{min}. Owing to broad-beam attenuation, coincidently recorded scatter radiation likewise contributes to the detected spectrum $S_{D,T}(E, \rho_A)$, however, inverse to beam hardening. Here, ATTIX (2004) points out that scattering generally tends to decrease the energy of the radiation reaching the detector. Hence, transmission spectra are particularly blurred by incoherent scattering such that an increment of low-energy fraction is observed within the energy distribution. This decrement of radiation energy is sometimes referred to as Compton shift due to the predominant incoherent interaction mechanism (cf. IEC 60050-881 (1983)). Similar observations are revealed from the comparison of simulated transmission spectra considering labMDF650 and particular RDP devices in Figure IV-58. As additionally quantified in Table IV-31, all energy distributions of the simulation with scattering consideration fall below the spectra without scattering registration. Further characteristic parameters in Table IV-30 for the comparison of scatter-free (Figure IV-56) and scatter (Figure IV-57) data considering further raw densities of labMDF verify the findings, where $\Delta\bar{E}$, ΔE_{peak} (both toward respective initial spectra $S_{D,0}(E)$), as well as E_{min} including scattering fall below the figures without recording of scatter radiation. The deviation of scattering spectra from scatter-free data, thus, the low-energy shift, increases with increasing raw density of the specimen at respectively the same energy

level in terms of X-ray device configuration. Furthermore, the difference increases with increasing initial energy of the simulated setups at equivalent specimen raw densities. Note, the observed downward shift of the energy spectra due to scattering is individually superimposed by density- and energy-dependent beam hardening. Notwithstanding this, INANC (1999) point out in their computational experiments on X-ray scattering, that no generalisation can easily be made regarding the energy distribution of scattering spectra. For increasing specimen thickness, peak of the spectrum is, however, found to tend to be shifted to lower energy levels. Eventually, implications regarding scattering impact on transmission spectra are rather considered as educated guesses on basis of the measuring observations and simulations above, where complex radiation-physical interdependencies need to be taken into account.

However, in addition to generally discussed lab-MDF simulation data above, results from extra simulation of scattering impact in terms of X-ray RDP measurement on customary MDF are presented in Table IV-48 as a compilation of characteristic parameters (analogously to scatter-free data in Table IV-45 considering beam hardening). Furthermore, Figure IV-79 illustrates context and consequences of scattering registration by the example of the specimen MDF1 from round robin test (refer to Chapter IV–4.3.1) and virtual application of W-RDP-50-w/o (Table IV-20) device. To this end, X-ray spectra were specifically simulated[37] with scattering consideration (for method refer to Chapter IV–4.2.6.2) for RDP sections of the specimen MDF1 ($z = 49.91\,\mathrm{mm}$) with $\bar\rho = 723\,\mathrm{kg/m^3}$, $\rho_{\min} = 622\,\mathrm{kg/m^3}$, and $\rho_{\max} = 933\,\mathrm{kg/m^3}$ (from gravimetric reference, Table IV-24). Note, as already discussed in Chapter IV–4.3.3.2, the validity of simulated scatter recording may be questionable according to DERESCH (2013), since all scattering angles are virtually registered without any possibility to consider particular beam geometry. The data, however, facilitates a first appropriate estimation of scattering impact in terms of RDP

measurement in comparison to analogously computed scatter-free data (default simulation). With regard to transmitted radiation spectra through considered RDP sections, Table IV-47 provides a quantitative comparison as difference of scatter toward scatter-free data. Note, all characteristic energy parameters $\bar E$, E_{peak}, as well as $E_{\min}$ consistently fall below the very same without scatter registration for all raw density values, respectively, owing to the contribution of low-energy scattered radiation, where the extent ranges $\Delta E = -1.1 \dots -0.5\,\mathrm{keV}$. The differences increase along the RDP slope toward SL with increasing raw density due to increasing impact of low-energy I_S (roughly constant in contrast to decreasing I_P, Table IV-48) on the spectra with a consequent downward shift of energy, which supports the implications for scattering consequences in Figure IV-79; i. e., increasing radiation build-up $B(E,\rho)$ with increasing raw density. Contrary to the expectation, the parameter full width at half maximum FWHM for characterisation of spectra width likewise decreases, which is assumingly attributed to the scatter impact on energy distribution (normalised to unity, right plots in Figure IV-79) toward constant $E_{\max}$, where the donward slope is obviously shifted to lower energies. This observation in simulation data appears similar to the effect of extrafocal radiation on spectra, where backscattered electrons within the X-ray tube cause emission of rather soft radiation beyond the focal spot (cf. NAGEL (2003)), likewise obvious from spectra measuring results in Figure IV-51 and Figure

absorber	$\Delta\bar E$	ΔE_{peak}	$\Delta E_{\min}$	ΔFWHM
MDF ρ	[keV]	[keV]	[keV]	[keV]
[kg/m³]	difference of scatter to scatter-free data			
622	-0.6	-0.8	-0.5	-0.5
723	-0.7	-0.7	-0.5	-0.5
933	-0.8	-1.1	-0.6	-0.4

Table IV-47: Comparison of simulated spectra with scattering consideration (Table IV-48) toward scatter-free data (Table IV-45) as difference between respective characteristic energy parameters.

---

[37] Note again, labMDF 9.5 % MC elemental composition is applied as common WBC composition (refer to Chapter IV–2.4.2).

IV-52 (particularly the 50 kVp-spectra). Further evaluation of simulation data including scattering reveal a decreased beam hardening index within the raw density range for the exemplarily simulated transmission data with $BHi(E, \rho_A)_S = 9.32 \ \%\Delta\bar{E}/\%\Delta\rho_A$ in comparison to $BHi(E, \rho_A) = 11.76 \ \%\Delta\bar{E}/\%\Delta\rho_A$ without scattering consideration. However, this does not necessarily indicate reduced beam hardening but rather a distinct scattering impact superimposing transmission spectra. Obviously, the occurrence and recording of scatter radiation owing to the particular measuring setup counteracts beam hardening by increment of the spectrum's low-energy share. The impact, however, of beam hardening rather dominates the detected transmission spectrum, thus, a fundamental upward energy shift is still present but diminished by scattering. To conclude, the beam hardening effect is considered to increase for setups with minor scatter radiation impinging on detector by means of close to narrow-beam design or respective specimen-detector distance s_{S-D}. Moreover, diminished radiation build-up and consequent effects on X-ray densitometry results are considered to occur. Consequently, the energetic impact of both beam hardening and multiple scattering with radiation build-up is reflected in $\mu/\rho\,(E)$ plots over ρ_A or ρ. Obviously and as partly discussed above, some of the charts in Chapter IV–4.3.2.2 and Chapter IV–4.3.2.3, respectively, reveal altering slope starting rather steep and turning slightly flatter as SPR, thus, B, increases and beam hardening is finished to a certain extent. Likewise, HALMSHAW (1995) concludes a similar characteristic in the reported experimental results related to an energy range with incoherent scattering as predominant attenuation mechanism, which confirms the above implications. The low-energy fraction of the primary beam is filtered out but replaced by similar low-energy radiation from multiple (mainly incoherent) scattering emerging from the specimen, which builds up an approximate equilibrium on the detector, which, in turn, yields an approximately equal $\mu/\rho\,(E)$ in the evaluated example.

Regardless of the above indirect implications on measuring data basis for estimated scattering contribution to attenuation (Table IV-46), spectra simulation results without and with scattering registration facilitate numerical evaluation of indices such as SPR and B for the considered RDP sections of MDF1. In addition to energy discussion of scattering impact, Table IV-48 comprises characteristic parameters related to scattering intensity I_S deduced from simulation data without (Table IV-45, considered as I_P) and with (Table IV-48, considered as I_T) scattering following eq. (IV-45), where Figure IV-79 concludes on scattering consequences dependent on local raw density. Accordingly, computed I_S is more or less equal along increasing ρ with solely slight decrement about 3.6 % at $\rho_{max} = 933 \ \text{kg/m}^3$ owing to increased multiple interaction (both scattering and absorption), thus, slight self-attenuation of scattered radiation. However, SPR computed via eq. (II-44) increases with increasing raw density, since primary intensity I_P decreases along with decreasing total intensity I_T whereas scattering intensity I_S is found to remain more or less equal. The like applies to STR according to eq. (II-46). Thus, B following the computation approach of eq. (II-48) likewise increases and yields overestimated detector readings. Consequently, recorded intensity $I_{T,D}$ on the detector exceeds expected values considering narrow-beam attenuation. Eventually, the extent of radiation build-up $B(E, \rho)$ varies along RDP and is found to increase with increasing local raw density. Hence, common RDP evaluation yields underestimated raw density values particularly considering ρ_{max} in panel surface layer (SL).

Finally, the occurrence and registration of any scattered radiation causes non-linearities in terms of X-ray transmission measurement and evaluation of measured attenuation $\ln T^{-1} = \ln(I_0/I_T)$. Notwithstanding the illustration in Figure IV-79 refers to RDP determination, the context and consequences of varying scattering impact can be transferred to ρ_A measurement or related applications. The scattering impact on transmission measuring results is expressed via SPR or B and yields overestimation of transmitted intensity and consequent underestimation of evaluated ρ or ρ_A, where linear attenuation is expected. Moreover, energy distribution of scattered radiation contributes to transmitted spectra such that its rather low energy fraction yields a

W target, $U_{a,nom} = E_{max} = 50$ kVp, 0.635 mm Al pre-filter

absorber MDF ρ [kg/m^3]	$\overline{E}$ [keV]	$\Delta\overline{E}$ [keV] ref. to I_0	E_{peak} [keV]	ΔE_{peak} [keV] ref. to I_0	E_{min} [keV]	FWHM [keV]	$I = \sum I(E)$ [cps]	I_T/I_0 [-] $= T$	I_S [cps] $= I_T - I_P$	SPR [-]	STR [-]	B [-]
–	26.6	–	22.2	–	7.5	21.6	2.661E+06	I_0	n/s	n/s	n/s	n/s
622	30.7	4.1	28.4	6.2	11.6	20.2	1.055E+06	0.40	3.612E+05	0.52	0.34	1.52
723	31.0	4.5	29.2	7.0	12.1	20.0	9.403E+05	0.35	3.615E+05	0.62	0.38	1.62
933	31.7	5.1	30.0	7.8	13.0	19.6	7.509E+05	0.28	3.481E+05	0.86	0.46	1.86

Table IV-48: Simulation of scattering impact in terms of X-ray RDP measurement as compilation of characteristic parameters (like in Table IV-30 and Table IV-45) for W-RDP-50-w/o device radiation spectra simulated by XRay-Tools software (Chapter IV–4.2.6.2), with initial spectrum I_0 and transmission spectra considering RDP sections of MDF1 ($z = 49.91$ mm) from round robin test (Chapter IV–4.3.1) with $\bar{\rho} = 723$ kg/m^3, $\rho_{min} = 622$ kg/m^3, and $\rho_{max} = 933$ kg/m^3 (from gravimetric reference, Table IV-24); with recording of scattered radiation, always including 0.635 mm Al corresponding to spectrometer lid.

slight but not negligible downward shift. This is considered to slightly counteract beam hardening whereas the latter, however, is further considered to dominate with a consequent upward energy shift of total transmission spectrum. To conclude discussion of scattering phenomena with respect to X-ray transmission measurements and determined μ/ρ, particular issues focusing on densitometry on WBC can be pointed out; i. e.,

- scattering in dependence of material amount in terms of ρ_A,
- further dependency on densification (hence, structure) of the porous material, thus,
- varying scattering across RDP, likewise
- varying scattering between panel and furnish mat with
- further dependency on transmission distance.

Preferably WBC structure is implied to cause varying scattering impact and corresponding non-linearities. Accordingly, the observed fundamental difference between measured μ/ρ (Table IV-26) of equivalent mat and panel with equal ρ_A are found to be caused by scattering impact as proposed by SOLBRIG et al. (2014b). As already discussed in Chapter IV–6.2, the phenomenon is not related to beam hardening as proposed by FUCHS (2010), since equal material amount ρ_A is considered to cause equal primary absorption whereas out-scattering and beam divergence potential increases with decreasing raw density,

thus, increasing porosity. Eventually, the scattering impact on transmission measuring results is more difficult to control compared to beam hardening effects, where appropriate pre-filter application avoids bias to a certain extent. The aforementioned scattering reduction methods, in turn, always diminish the signal yield from transmitted radiation with a partly insufficient benefit. Explicit scattering consideration by means of precise scattering quantification via B is found not to be feasible under practical conditions considering WBC densitometry. The like applies to consequently elaborate correction methods. Thus, scattering impact on measuring results has to be taken into account otherwise.

Initial radiation	Transmission T through distance $z_{nom} = 50$ mm, of the specimen with $\bar{\rho}_{grav}$	Transmitted, attenuated radiation with varying spectra $S_T(E, \rho)$ and intensities $I_{T,\rho}$, including primary I_P and secondary (scattered) I_S radiation

Radiation parameters

$$I = \int_{E_{\min}}^{E_{\max}} I(E)\,dE \;\; [\text{a.u.}]$$

$$I_T = I_P + I_S \text{ with } I_P \cap I_S = \emptyset$$

Scattering parameters

$$I_S = I_{S,\text{coh}} + I_{S,\text{incoh}}$$

$$SPR = \frac{I_S}{I_P} \geq 0 \; [-]$$

$$B = 1 + SPR \geq 1 \; [-]$$

Scattering consequences dependent on local raw density

	air		**CL** ρ_{min}		**Mean** $\bar{\rho}$		**SL** ρ_{max}
I_0	$\gg$		$I_{T,\rho_{min}}$	$>$	$I_{T,\bar{\rho}}$	$>$	$I_{T,\rho_{max}}$
			$I_{S,\rho_{min}}$	$\approx$	$I_{S,\bar{\rho}}$	$\approx$	$I_{S,\rho_{max}}$
			$I_{P,\rho_{min}}$	$>$	$I_{P,\bar{\rho}}$	$>$	$I_{P,\rho_{max}}$
			$SPR_{\rho_{min}}$	$<$	$SPR_{\bar{\rho}}$	$<$	$SPR_{\rho_{max}}$
			$B(\bar{E}_{T,\rho_{min}})$	$<$	$B(\bar{E}_{T,\bar{\rho}})$	$<$	$B(\bar{E}_{T,\rho_{max}})$
			$I_{T,\rho_{min}} \uparrow$		$(I_{T,\bar{\rho}} \uparrow)$		$I_{T,\rho_{max}} \uparrow\uparrow$
			$\rho_{min} \downarrow$		$\bar{\rho} =$		$\rho_{max} \downarrow\downarrow$

Energy parameters

$$\bar{E} = \int_{E_{\min}}^{E_{\max}} E \cdot S(E)\,dE \;\; [\text{keV}]$$

$$E_{\max} \equiv U_a [\text{kVp}]$$

Figure IV-79: Illustration of context and consequences of varyingly distinct scattering in terms of X-ray RDP measurement on customary WBCs resulting in local variations of scatter-to-primary ratio SPR, radiation build-up factor B, and effectively transmitted radiation intensity $I_{T,\rho}$ due to local raw density ρ; X-ray spectra simulated (in accordance with Figure IV-76) considering RDP sections of MDF1 ($z = 49.91$ mm) from round robin test (Chapter IV–4.3.1) with $\bar{\rho} = 723$ kg/m³, $\rho_{min} = 622$ kg/m³, and $\rho_{max} = 933$ kg/m³ (from gravimetric reference, Table IV-24) with initial spectrum of W-RDP-50-w/o device and transmitted spectra normalised to unity (right, $I(E)_{\max} = 1$) as well as to initial intensity I_0 (left, $I(E) = I(E)_T / \sum I(E)_0$), for characteristic parameters refer to Table IV-48.

6.4   X-ray energy

The radiation source as X-ray tube with well-defined pre-filter has to be suited to the application as already partly pointed out in terms of practical implications on spectra determination in Chapter IV–4.3.2.4, where, moreover, SOLBRIG et al. (2015a) propose individual X-ray property design with respect to the particular measuring application. Their initial approach is deepened below. Accordingly, knowledge about employed energy spectra $S(E)$ is an indispensable basis for sophisticated energy definition. The hitherto state of the art featured by rough estimation of rather too high X-ray energy is, however, rarely brought into question so far. Nevertheless, reliable densitometry requires individual radiation energies on an optimal level to increase measuring accuracy and sensitivity. To this end, RÓZSA (1987) suggests to adapt radiation properties to actually measured area density ρ_A such that corresponding mass attenuation coefficient $\mu/\rho\,(E)$ meets the optimal condition

$$\frac{\mu}{\rho}(E)_{\text{opt.}} = \rho_A^{-1} \tag{IV-46}$$

which, in turn, corresponds to a relative transmission of about $I_T/I_0 = T = e^{-1}$. Already WALTER, WIECHMANN (1961) apply the context of eq. (IV-46) for area density investigations on fibre- and particleboard, where they refer to reciprocal μ/ρ as penetration density, which is recommended to be $1 \dots 1.5 \cdot \rho_A$ to obtain minimum device-related measuring error. With further regard to RDP determination, OLSON et al. (1988) propose a similar approach aiming at maximum attenuation contrast in relation to maximum raw density ρ range (subscript R) at equivalent transmission distance s_T. Accordingly, optimal attenuation condition has to be individually found with

$$\frac{\mu}{\rho}(E)_{\text{opt.,R}} = \frac{\ln\left(\frac{\rho_{\max}}{\rho_{\min}}\right)}{(\rho_{\max} - \rho_{\min}) \cdot s_T} \tag{IV-47}$$

again, via fitting of the radiation energy, which can easily be transferred to a respective area density ρ_A range (R) such that

$$\frac{\mu}{\rho}(E)_{\text{opt.,R}} = \frac{\ln\left(\frac{\rho_{A,\max}}{\rho_{A,\min}}\right)}{\rho_{A,\max} - \rho_{A,\min}} \tag{IV-48}.$$

Note, for one and the same ρ_A range, the results of eq. (IV-46) considering arithmetic mean $\bar{\rho}_A = (\rho_{A,\max} - \rho_{A,\min})/2$ differ from the very same of eq. (IV-48) such that $\mu/\rho\,(E)_{\text{opt.}} < \mu/\rho\,(E)_{\text{opt.,R}}$, since eq. (IV-48) is obviously nothing else than the reciprocal logarithmic mean of the considered ρ_A range. Thus, higher radiation energy would be required to obtain $\mu/\rho\,(E)_{\text{opt.}}$ compared to $\mu/\rho\,(E)_{\text{opt.,R}}$. Notwithstanding this, a comparison of actual evaluation results may reveal differing observations due to the origin of $\bar{\rho}_A$ as to be discussed below. However, the deduction of eq. (IV-46) by RÓZSA (1987) and likewise eq. (IV-47) by OLSON et al. (1988) follow the mathematical consideration of maximum sensitivity by method of extrema, i. e., highest possible relative intensity change ΔT toward considered $\Delta\rho_A$ or $\Delta\rho$, which, in turn, yields maximum measuring resolution of ρ_A or ρ, respectively. Moreover, OLSON et al. (1988) illustrate the context of energy-dependent transmission probability on an exemplary wood cross-section with typical raw density variations over the tree rings. For optimal energy considering eq. (IV-47), transmission probability yields its maximum range corresponding to resulting intensity range, which is, in turn, diminished for both too low as well as too high energy levels, where measuring resolution decreases.

Therefore, relevant transmission measuring results from Chapter IV–4.3.2 are further evaluated in combination with $\mu/\rho\,(E)_{\text{mix}}$ computation data following Chapter IV–5.2. For total ρ_A measuring range of Fmat and indMDF at EMC in consequence of common conditioning at 20 °C and 65 % RH, Figure IV-80 presents respective plots of $\mu/\rho\,(E)_{\text{opt.}}$ according to eq. (IV-46) with corresponding radiation energies E from $\mu_{\text{tot}}/\rho\,(E)_{\text{mix}}$ computation determined via interpolation of, e. g., Table VII-12 data. Obviously, a steep decrement of $\mu/\rho\,(E)_{\text{opt.}}$ (note, logarithmic scale) can particularly be observed in the lower range up to $\rho_A \approx 15$ kg/m^2. Likewise, corresponding energy plots reveal an initially steep but later degressive incline in the low-energy range up to $E \approx 7.5$ keV, which turns linear up to $E \approx 30$ keV with a more or less equal slope of both Fmat and

indMDF plot. However, due to simple computation on the basis of actual ρ_A regardless of any structural conditions, furnish mat and panel plots in Figure IV-80 are found to be more or less congruent. In addition to total ρ_A consideration, Table IV-49 summarises evaluation results considering the three measuring ranges as applied in Chapter IV–4.3.2.2. Note, individually computed $\mu/\rho\,(E)_{\text{opt.}}$ according to eq. (IV-46) takes respective ρ_A at $T = e^{-1}$ from Table IV-26 into account, where Fmat results are found to slightly exceed indMDF values owing to lower scattering registration in the case of transmission measurements on furnish mats by means of the employed setup as comprehensively discussed in Chapter IV–6.3. In comparison to computation via eq. (IV-48), $\mu/\rho\,(E)_{\text{opt.,R}}$ differs from single-point values of $\mu/\rho\,(E)_{\text{opt.}}$ due to the following reasons. The computation via eq. (IV-48) is obviously associated with different weighting of the measuring range whereas $\mu/\rho\,(E)_{\text{opt.}}$ applies ρ_A at a particular transmission of $T = e^{-1}$. Moreover, and with regard to the result plots in Chapter IV–4.3.2.2, individual width of the measuring ranges varies due to applied set of samples, where indMDF ranges are not as wide as Fmat ranges on the respective energy level. Above mathematically derived context of $\mu/\rho\,(E)_{\text{opt.}} < \mu/\rho\,(E)_{\text{opt.,R}}$ is not fulfilled, since applied ρ_A is not the arithmetic mean of the measuring range. However, particularly in the case of Fmat evaluation results, the corresponding energies in comparison of $\mu/\rho\,(E)_{\text{opt.}}$ and $\mu/\rho\,(E)_{\text{opt.,R}}$ are respectively found in an equivalent order.

Moreover, the determined energies for optimal attenuation conditions are close to actual $\bar{E}$ values (refer to Table IV-26), hence, utilised setups are considered to feature appropriate energy conditions within the respective ρ_A measuring range. Eventually, the determined apparently optimal energy $E = 17.8\,\text{keV}$ from total range consideration obviously suits to middle range level and is, however, furthermore supposed to generally cause insufficiencies all around, i. e., in lower and upper ρ_A range due to both decreased sensitivity in terms of measuring contrast as well as detector behaviour in terms of potential non-linearities. The displayed total measuring range
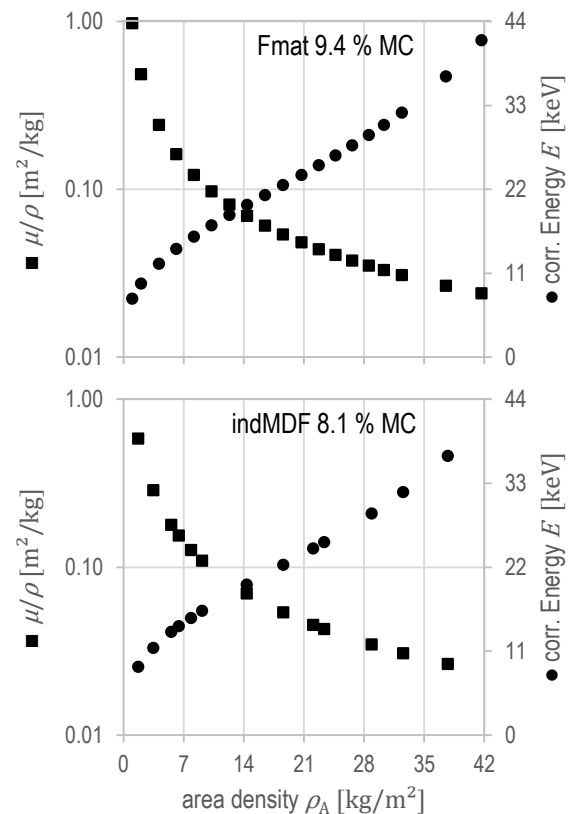
Figure IV-80: Plot of optimal mass attenuation coefficients $\mu/\rho\,(E)_{\text{opt.}}$ acc. to eq. (IV-46) and corresponding radiation energies E from $\mu_{\text{tot}}/\rho\,(E)_{\text{mix}}$ computation considering elemental composition of Fmat and indMDF, respectively, at EMC (20/65) over total ρ_A range from transmission measurements (Chapter IV–4.3.2.2).

of $\rho_A \approx 1\ldots42\,\text{kg/m}^2$ covers, in turn, an energy range of about $\Delta E = 34\,\text{keV}$. Toward the limits, no appropriate transmission conditions are, therefore, considered to be achievable. Such boundary conditions are, however, not considered by any means of eq. (IV-48) computation. Consequently, the above evaluation to determine optimal attenuation conditions for ρ_A measurement via corresponding energy selection following eq. (IV-46) and particularly eq. (IV-48) with explicit consideration of the present ρ_A range as well as the Figure IV-80 illustration unveil the inevitable necessity of energy adaption to the intended ρ_A measuring range, which needs further to be initially limited to an individually small width. In the case of, e. g., lower Fmat measuring range with $\rho_A = 1.0\ldots15.5\,\text{kg/m}^2$, computation reveals corresponding $\Delta E = 13\,\text{keV}$, which is distinctly more narrow com-

material	ρ_A measuring range			
	lower	middle	upper	total
Fmat 9.4 % MC				
$\rho_{A,max}$	15.5	23.8	41.7	41.7
$\rho_{A,min}$	1.0	3.1	4.1	1.0
$\mu/\rho_{opt.}$	0.2039	0.1369	0.0559	
corr. E	13.0	15.1	22.1	
$\mu/\rho_{opt.,R}$	0.1870	0.0987	0.0615	0.0911
corr. E	13.5	17.2	21.1	17.8
ΔE	13.0	14.8	29.3	33.9
indMDF 8.1 % MC				
$\rho_{A,max}$	9.2	22.1	37.8	37.8
$\rho_{A,min}$	1.7	9.2	23.4	1.7
$\mu/\rho_{opt.}$	0.1749	0.1154	0.0508	
corr. E	13.6	15.9	23.0	
$\mu/\rho_{opt.,R}$	0.2245	0.0680	0.0334	0.0858
corr. E	12.4	19.9	29.8	18.0
ΔE	7.4	8.2	11.3	27.6

Table IV-49: Summary of optimal mass attenuation coefficients for ρ_A [kg/m^2] measurements (in comparison of furnish mat and panel) and corresponding radiation energies E [keV] from $\mu_{tot}/\rho\,(E)_{mix}$ computation considering elemental composition of Fmat and indMDF, respectively, at EMC (20/65), with $\mu/\rho\,(E)_{opt.}$ [m^2/kg] acc. to eq. (IV-46) by means of ρ_A @ $T = e^{-1}$ from Table IV-26 as well as with $\mu/\rho\,(E)_{opt.,R}$ [m^2/kg] acc. to eq. (IV-48) by means of respective and total ρ_A ranges from transmission measurements (Chapter IV–4.3.2.2) complete with corresponding energy ranges ΔE considerin respective ρ_A limit values.

pared to the total range above but still considered to be rather wide with respect to the comparably steep $\mu/\rho\,(E)$ slope on low-energy level. On the contrary, lower indMDF covers just $\Delta E = 7.4\,\mathrm{keV}$ due to decreased ρ_A range. Therefore, ρ_A ranges of Fmat measurements appear comparably too wide as already pointed out in terms of transmission measuring result evaluation in Chapter IV–4.3.2.2. For further such evaluation data, reference is made to Table IV-49. These energy ranges resulting from optimal attenuation conditions considering both individual ρ_A limits are, however, not necessarily associated with a particular energy range of an applied X-ray spectrum as to be discussed below.

Regarding RDP measurement, Table IV-50 provides a summary of optimal attenuation conditions and corresponding radiation energies again considering both computation approaches according to eq. (IV-46) with mean area density $\bar{\rho}_A$ along beam axis considering total specimen cross-section via its mean raw density $\bar{\rho}$ with nominal $s_T = 50\,\mathrm{mm}$ and eq. (IV-47) considering individual transmission distances s_T at ρ_{min} and ρ_{max}, respectively. The deduced corresponding radiation energies E take again respective elemental composition of labMDF, indMDF, and insulation at EMC (20/65 conditioning) into account. The labMDF results clarify attenuation conditions depending on the amount of matter along the beam axis, i. e., ρ_A, since eq. (IV-46) computation again does not consider any structural conditions. Therefore, $\mu/\rho\,(E)_{opt.}$ decreases and corresponding energy increases with increasing raw density at equivalent transmission distance, since more matter requires higher penetration potential of the applied radiation. Regardless of some exceptions, comparison of both computation methods reveals that $\mu/\rho\,(E)_{opt.,R}$ falls bellow $\mu/\rho\,(E)_{opt.}$, thus, consideration of total raw density range including the extrema of the RDP is found to rather take stronger attenuating sections into account and consequently requires respectively higher radiation energy to obtain optimal attenuation contrast conditions along total RDP. Hence, $\mu/\rho\,(E)_{opt.,R}$ following eq. (IV-47) is to be preferred for estimation of appropriate energy conditions for X-ray RDP measurement. Note, the observation is contrary to mathematical expectation $\mu/\rho\,(E)_{opt.} < \mu/\rho\,(E)_{opt.,R}$, since $\bar{\rho}_A$ is not computed as arithmetic mean of the range's extrema but originates from individual mean gravimetric determination, thus, resulting $\mu/\rho\,(E)_{opt.}$ is weighted by actual mass distribution along the measured panel cross-section, whereas $\mu/\rho\,(E)_{opt.,R}$, however, explicitly considers the extrema of the profile, i. e., boundary attenuation conditions. However, in case of all indMDF evaluation results except round robin test samples, the energy corresponding to $\mu/\rho\,(E)_{opt.,R}$ is roughly in a comparable order around $E \approx 41\,\mathrm{keV}$ whereas ΔE considering ρ_{min} and ρ_{max}

material (specimen type)	$\bar{\rho}$ [kg/m³]	$\bar{\rho}_A$ [kg/m²]	ρ_{min} [kg/m³]	ρ_{max} [kg/m³]	$\mu/\rho_{opt.}$ [m²/kg]	corr. E [keV]	$\mu/\rho_{opt.,R}$ [m²/kg]	corr. E [keV]	ΔE [keV]
400	403	20.3			0.0492	23.4			
650	628	31.7			0.0315	31.1			
1056	961	47.9			0.0209	51.0			
labMDF	**664**	**33.3**	**403**	**961**	**0.0300**	**32.4**	**0.0311**	**31.5**	**27.6**
MDF-3	785	39.3	791	820	0.0255	38.2	0.0249	39.3	1.7
MDF-8	802	40.1	751	989	0.0249	39.2	0.0231	43.3	18.1
MDF-10	757	37.9	689	992	0.0264	36.7	0.0240	41.1	21.5
MDF-12	758	37.9	685	1018	0.0264	36.7	0.0238	41.5	24.7
MDF-19	741	37.1	645	1036	0.0270	35.9	0.0242	40.6	28.8
MDF-25	745	37.3	644	990	0.0268	36.1	0.0249	39.3	22.9
MDF-30	766	38.3	653	1116	0.0261	37.2	0.0232	43.1	41.7
indMDF	**765**	**38.2**	**644**	**1116**	**0.0261**	**37.1**	**0.0233**	**42.8**	**42.1**
MDF round robin	725	36.2	625	936	0.0276	35.1	0.0260	37.3	18.1
PB round robin	665	33.2	463	976	0.0301	32.4	0.0293	33.2	27.2
insulation	218	10.9	171	429	0.0920	17.3	0.0713	19.3	8.1
customary WBC panel, characterised via $\bar{\rho}$, percentage ρ_{min}, and extrema ratio SL_{max}/CL_{min}									
generalisation	**750**	**37.5**	**638**	**1020**	**0.0267**	**36.3**	**0.0246**	**39.9**	**26.9**

Table IV-50: Summary of optimal mass attenuation coefficients for RDP measurements (in comparison of lab-made (labMDF) and customary (indMDF, round robin test, and insulation) panels) and corresponding radiation energies E [keV] from $\mu_{tot}/\rho\,(E)_{mix}$ computation considering elemental composition of labMDF, indMDF, and insulation, respectively, at EMC (20/65), with $\mu/\rho\,(E)_{opt.}$ [m²/kg] acc. to eq. (IV-46) by means of $\bar{\rho}_A$ at nominal transmission distance $s_T = 50$ mm as well as with $\mu/\rho\,(E)_{opt.,R}$ [m²/kg] acc. to eq. (IV-47) by means of respective ρ ranges at mean transmission distance $\bar{s}_T$ from transmission measurements (Chapter IV–4.3.2.3 W-RDP-50-w/ RDP results) complete with corresponding energy ranges ΔE considerin respective ρ limit values.

considerably varies due to varying distinctness of the specimen's RDPs.

Moreover, evaluation results of MDF and PB from round robin test fall below both indMDF figures, i. e., respectively reveal a lower energy level and range around owing to lower mean raw density $\bar{\rho}$. Nevertheless, summarised indMDF attenuation conditions with $E = 42.8\,\text{keV}$ are considered to more or less represent appropriate requirements for X-ray RDP determination on customary MDF as well as PB and OSB. On the contrary, $\bar{E}$ values of all employed RDP device setups (refer to Table IV-27) obviously fall below the determined optimal energy level. Eventually, insulation evaluation results reveal considerably higher $\mu/\rho\,(E)_{opt.}$ and $\mu/\rho\,(E)_{opt.,R}$, thus, different optimal attenuation conditions with lower corresponding energies. Hence, RDP measurements on such low raw density material require particularly different X-ray setups from the ener-

getic point of view. Here, the lowest energy levels of the employed devices (refer to Table IV-27) with, e. g., $\bar{E} = 21.5\,\text{keV}$ of W-RDP-35-w/o setup approaches optimal conditions with $E = 19.2\,\text{keV}$ whereas measured $\overline{\mu/\rho} = 0.0514\,\text{m}^2/\text{kg}$ still significantly differs from $\mu/\rho_{opt.,R} = 0.0713\,\text{m}^2/\text{kg}$. Thus, none of the employed RDP devices is applicable to obtain optimal attenuation conditions for measurements on insulation or comparably light low-Z material, since lower radiation energy is required. To finally conclude energy predefinition for radiometric RDP determination on customary WBCs, a generalisation is possible by panel characterisation via mean raw density $\bar{\rho}$, percentage ρ_{min}, and surface to core layer ratio, which likewise serve as target values in panel production. Note, computation of the latter serves as a figure for the raw density contrast as introduced in Chapter IV–4.3.1, whereas here in contrast to Figure

IV-24 the raw density extrema are taken into account, i. e., $\mathrm{SL_{max}/CL_{min}}$ $[-]$, instead of respective mean values of the layer to explicitly consider boundary attenuation conditions of the total raw density gradient. However, empirical values are commonly found in the order $\rho_{\min} = 0.8 \ldots 0.9 \cdot \bar{\rho}$ and $\mathrm{SL_{max}/CL_{min}} = 1.4 \ldots 1.8$, where $\rho_{\min} = 0.85 \cdot \bar{\rho}$ and $\mathrm{SL_{max}/CL_{min}} = 1.5$ by further assumption of $\bar{\rho} = 750 \ \mathrm{kg/m^3}$ are exemplarily applied for a generalisation in Table IV-50 resulting in a mean energy level of about $E \approx 40 \ \mathrm{keV}$ for X-ray RDP measurement under optimal attenuation conditions with $\mu/\rho \, (E)_{\mathrm{opt.,R}} \approx 0.025 \ \mathrm{m^2/kg}$ determined on theoretical basis.

Beyond fundamental energy levels, likewise, the utilised X-ray spectra have to meet certain conditions. Here, clear standards exist in the medical field for a comparable range of applied energies with exemplary specifications of radiation qualities in Table II-4. However, no such particular recommendations are available in NDT, where mainly imaging techniques are common and quantitative applications on low-Z material are rather underrepresented so far as discussed in Chapter II–2.4.2. Therefore, recommendations for X-ray densitometry on WBCs are deduced from the above investigations and practical implications aiming at more or less unbiased transmission measuring results. To minimise beam hardening effects, a narrow-band energy distribution is required, which can be defined via the parameters FWHM and $E_{\max}$, on an appropriate basic level considering resulting attenuation such that mean energy $\bar{E}$ of the spectrum with corresponding $\mu/\rho \, (\bar{E})$ fulfils the conditions of eq. (IV-46), eq. (IV-47) or eq. (IV-48), respectively. To illustrate the context between energy dependent attenuation and radiation spectra, Figure IV-74 combines $\mu/\rho \, (E)$ plots including single mechanisms of labMDF 9.5 % MC as well as a selection of measured initial X-ray spectra $S_{\mathrm{D,0}}(E)$. The slope of total mass attenuation coefficient including the single interaction mechanisms over radiation energy reveals that obviously all spectra will be affected by beam hardening particularly in the low and low-medium energy range up to $E \approx 24 \ \mathrm{keV}$. Above, scattering fraction $\xi \, (\mathrm{scat})$ acc. to eq. (II-15) starts to dominate the attenuation processes (refer to Chapter

IV–5.2.2), which, nevertheless, is found to affect the transmission spectra $S_{\mathrm{T}}(E, \rho_{\mathrm{A}})$ as discussed in Chapter IV–6.3. Whilst feasible with respect to the required penetration potential, a basic energy level is considered to be beneficial, where photoelectric absorption of the investigated material predominates, thus, the occurrence of scattered radiation, which may be registered by the detector can consequently be diminished. However, to completely avoid beam hardening effects, monoenergetic radiation would be ideal, which is, in turn, considered to cause further insufficiencies with respect to application for WBC densitometry. This apparent energy optimum can be obtained by means of radioisotopes or a monochromator in addition to the X-ray tube. Both are less convenient and provide comparably low radiation flux (i. e. intensity) depending on isotope activity or tube power, respectively. Nevertheless, two practicable solutions exist. Quasi-monoenergetic spectra are obtainable by appropriate target material choice resulting in high intensity characteristic K_{α} energy (optimisable by filter application for pre-hardening and K_{β}-filtering, respectively). Such configuration is common practise for analytical X-ray applications (e. g. XRD, XRF, cf. Tsuji et al. (2004)) but less flexible and limited to one energy each because of restricted choice of target materials, which is furthermore rather too low for higher ρ_{A}. Notwithstanding this, energy setting is preferably carried out via adjustment of the tube voltage U_{a} [kV] of one installed X-ray tube including an appropriate target material in combination with pre-filter application on demand, to realise a lean total measuring system design affordable by industrial customers as likewise Solbrig et al. (2015a) point out. Regardless of cost aspects, available X-ray sources with multi-metal targets (cf. Hoffman, de Beer (2012)), which provide specific spectra on various energy levels with high-intensity characteristic lines on demand, are considered to be a highly sophisticated solution. However, a continuous bremsstrahlung spectrum preferably from common W target with well-defined pre-filter application for spectrum pre-hardening facilitates more or less flexible adaption of narrow-band energy distributions to the present requirements. Note, its application is

to be limited to high-voltage potential with $E_{\mathrm{max}} <$ 60 kVp to avoid occurrence of W-target characteristic lines with dominant $E_{\mathrm{K}_{\alpha 1}} = 59.32\ \mathrm{keV}$ (cf. KORTRIGHT, THOMPSON (2009)). However, lower threshold E_{min} is controlled via pre-filter design on both computational as well as empirical basis. In contrast to the above mathematic-physical deduction of optimal basic energy, no clear suggestion can be provided for appropriate spectra width definition via FWHM, which highly depends on the very same energy level and the requirements for signal yield from radiation intensity in relation to tube current I_{a}. Empirical findings exist from performed spectra measurements (Table IV-29) and simulations (Table IV-30), where narrow-band spectra can be obtained on low-energy level with, e. g., FWHM $= 4.6\ \mathrm{keV}$ of W-mat+panel-16-w/o device at $\bar{E} = 12.7\ \mathrm{keV}$ increasing toward high-medium energy with FWHM $= 17.5\ \mathrm{keV}$ of W-RDP-50-w/ device at $\bar{E} = 29.2\ \mathrm{keV}$ (refer to Figure IV-74). The latter is, however, not necessarily considered to cause considerable beam hardening. The individual pre-filter optimisation is claimed to minimise beam hardening expressed via $BHi(E, \rho_{\mathrm{A}})$ following eq. (IV-44) in a reasonable order along the respective measuring range taking account of the transmission spectra $S_{\mathrm{T}}(E, \rho_{\mathrm{A}})$ with, e. g., $BHi(E, \rho_{\mathrm{A}}) = 0.35\ \%\Delta\bar{E}/\%\Delta\rho_{\mathrm{A}}$ obtained by W-RDP-50-w/ device, thus, considered as best-practise RDP setup. Furthermore, a certain congruence between the width of individually applied spectrum and the theoretical energy range corresponding to present ρ_{A} (Table IV-49) or ρ (Table IV-50) range may yield beneficial attenuation conditions, where further investigations are required. Eventually, the utilised XRayTools software serves as convenient method for spectra estimation considering relevant variables such as tube properties, high voltage settings, and pre-filters as earlier implied in Chapter IV–4.3.3.4. However, all individual predefinitions are recommended to be experimentally verified, since none of the above theoretical considerations facilitates to take WBC structure and actual setup conditions explicitly into account. Obviously, X-ray property design for WBC densitometry requires coordination between partly contradictory practical conditions. Moreover, radiation

intensity is finally adapted via X-ray tube current I_{a} to individual requirements, where already WALTER, WIECHMANN (1961) bring up for consideration that rather low intensities are of dosimetric interest whereas sufficient signal statistics require an appropriate intensity level particularly depending on detector type and integration time.

6.5   Concluding remarks

The explanatory conceptual model for radiation transmission through porous composites with its propositions in Chapter IV–3 and the illustration in Figure IV-12 empirically considering four distinct scales of radiation-matter interaction serve as basis for consequent conclusions. Therefore, the concept is enhanced by the above findings in due consideration of

- radiation source and energy distribution,
- interaction within the material,
- its composition and structure,
- detection of transmitted radiation, as well as
- radiation-physical interdependencies between all parameters,

which provides a guidance for X-ray densitometry design considering WBCs and similar materials. Note, the descriptions of the proposed and verified beam path model do not draw on elasto-mechanical properties of the wood-particle-resin matrix with further regard to the hot-pressing process of WBCs with heat and mass transfer, where fundamental studies exist such as THOEMEN (2008) with all corresponding investigations or DROLET, DAI (2010) and others. Thus, there is no claim on comprehensive modelling of WBC properties. Moreover, the present radiation transmission concept draws on conditions and effects from the beam's point of view as radiation passes through WBC matter as earlier introduced in Chapter IV–3.1.

The review of all results in combination of comprehensive investigations on material (Chapter IV–2), X-ray measurements including transmission and spectra (Chapter IV–4), theoretical attenuation considerations (Chapter IV–5) as well as respective first practical implications leads to the conclusion that the proposal for a radiation

transmission concept through porous composites such as WBCs in Chapter IV–3 comprising radiation-matter interaction on distinct scales is considered to be verified by the above findings. The fundamental understanding of transmission measurements in general, where initial radiation intensity is diminished in consequence of the energy-dependent attenuation processes photoelectric absorption as well as coherent and incoherent scattering as illustrated in Figure II-5 is, however, found to be insufficient for X-ray transmission measurements on inhomogeneous and porous low-Z matter, hence, (wood and) WBCs. In consequence of the above investigations, the basic understanding of radiation transmission as in Figure II-5 is extended by consideration of the findings to the illustration in Figure IV-81 comprising

- inhomogeneous and porous matter, where the raw density $\rho = \rho_A/t$ affects effective radiation transmission,
- initial spectrum $S_0(E)$ with individual pre-filtering,
- beam hardening in consequence of low-energy absorption with mean-energy shift quantifiable via introduced beam hardening index $BHi(E, \rho_A)$ [%$\Delta\bar{E}$/%$\Delta\rho_A$] acc. to eq. (IV-44),

- internal scattering with an energy-dependent scattering fraction $\xi(\text{scat})$,
- external scattering yielding radiation build-up $B(E)$ following eq. (II-48) on basis of SPR via eq. (II-44),
- superimposition of primary and scattered intensity $I_T = I_P + I_S$ acc. to eq. (II-43),
- transmitted spectrum $S_T(E, \rho_A)$ depending on ρ_A-dependent beam hardening with further impact from scattering superimposition following eq. (IV-45),
- characteristic detector output considered as detector response function $D(E)$ yielding detected spectra $S_{D,0}(E)$ and $S_{D,T}(E)$ acc. to eq. (IV-32) and eq. (IV-33), respectively,
- and their individual interdependencies.

The latter occur such that the extent of a single radiation-physical effect reveals mutual dependencies between

- measuring conditions,
- setup parameters,
- material properties, and
- the consequent effects themselves

as illustrated in Figure IV-81. Note here, e. g., particularly the radiation-matter interaction processes within the specimen with consequent beam hardening and radiation build-up depend

$$I_T = I_0 \cdot \int_E S_0(E) \cdot B(E) \cdot D(E) \cdot e^{-\frac{\mu}{\rho}(E) \cdot \rho_A} dE$$
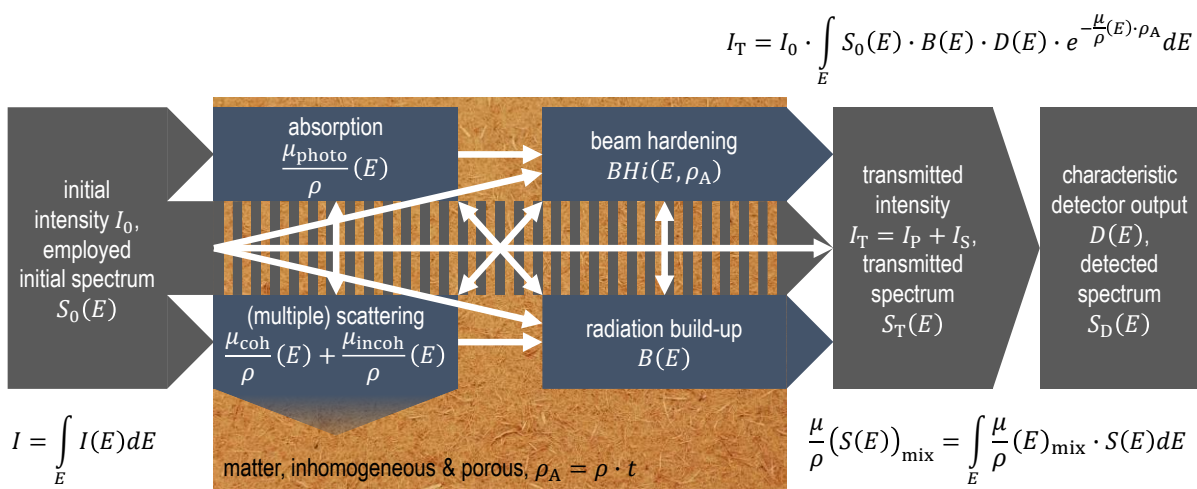
Figure IV-81: Schematic illustration of the extended understanding of radiation transmission through inhomogeneous and porous low-Z matter, i. e., WBCs, and the application for X-ray densitometry based on Figure II-5, additionally considering radiation-physical interdependencies (white arrows), with integrated radiation intensity I, spectral-weighted total mean mass attenuation coefficients $\mu/\rho\left(S(E)\right)_{\text{mix}}$ acc. to eq. (II-34), superimposed transmitted intensity I_T following eq. (II-43), and Beer's law of attenuation following eq. (II-10) extended by integration of initial spectrum $S_0(E)$, build-up factor $B(E)$, and detector response function $D(E)$ over radiation energy acc. to eq. (IV-49).

on each other, resulting in a transmitted spectrum with certain intensity influenced by beam geometry whereas final measuring signal is, in turn, affected by the detector and signal processing itself. However, in terms of transmission intensity I_T, context of most of the influence parameters under such non-ideal conditions are commonly described by means of

$$I_T = I_0 \cdot \int_E S_0(E) \cdot B(E) \cdot D(E) \cdot e^{-\frac{\mu}{\rho}(E) \cdot \rho_A} dE$$

(IV-49)

where attenuation law following eq. (II-10) is extended by integration of initial spectrum $S_0(E)$, build-up factor $B(E)$, and detector response function $D(E)$ over radiation energy E. With respect to above investigations, the coefficients are considered as non-trivial to determine and implement and, however, still not covering all variable effects and particularly their mutual relation. As exemplary discussion of the factors in eq. (IV-49), already Musílek et al. (1980) (p.623) consider B as "[…] quantity of questionable usefulness in many situations" depending on the determination method with partly elaborate equations and requirements of information, where, consequently, simple calculation of calibration curves is rather impossible. Hence, they recommend experimental measurement of B for relevant geometrical conditions, which is, nevertheless, likewise elaborate

Regardless of eq. (IV-49) and corresponding insufficiencies, consequent effects of radiation-physical interdependencies on X-ray densitometry on WBCs can now be empirically described or even quantified by the above findings and introduced parameters. To this end, Figure IV-82 combines the essentials of Figure IV-76 and Figure IV-79 to summarise the impact on RDP measurement, which is, moreover, transferable to comparable density gradients and measuring conditions. Therefore, biased measuring and evaluation results occur, since acquired transmission intensity I_T differs from linear expectation under ideal, i. e., monochromatic, narrow-beam, good-architecture conditions. Assuming appropriate energy conditions with regard to Chapter IV–6.4 considerations, particularly
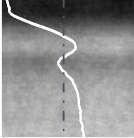
raw density profile		BH	scat	$\Rightarrow$	ρ_{result}
	$\rho_{\text{max,SL}}$	$I_T \uparrow$	$I_T \uparrow\uparrow$	with	$\downarrow\downarrow$
	$\bar{\rho}$	–	$(I_T \uparrow)$	$\frac{\mu}{\rho}(\bar{E}_{T,\bar{\rho}}) = \bar{\rho}_{\text{grav}}$	$= \bar{\rho}_{\text{grav}}$
	$\rho_{\text{min,CL}}$	$I_T \downarrow$	$I_T \uparrow$	$= \overline{\mu/\rho}$	$\uparrow$

Figure IV-82: Summary of radiation-physical effects on X-ray densitometry on WBCs considered as variation of transmitted intensity I_T in comparison to expectation under ideal conditons with particular impact from beam hardening (BH) as well as scattering (scat) and consequent bias of raw density evaluation results due to application of one single mean mass attenuation coefficient $\overline{\mu/\rho}$, by the example of radiometric RDP determination.

beam hardening and scattering as comprehensively discussed in Chapter IV–6.2 and Chapter IV–6.3, respectively, as well as their interdependencies are responsible for the observed deviations from true RDP (refer to results from reference method in Chapter IV–4.3.1), where only one single $\overline{\mu/\rho}$ following the calibration illustrated in Figure II-14 is individually applied. Here, beam hardening is well-known to cause decreasing $\mu/\rho(E)$ and consequent non-linearity of attenuation $\ln T^{-1}$, where the effect is found to increase with increasing mass of the same material, i. e., area density ρ_A, along the beam axis. In the case of RDP measurement as exemplarily illustrated in Figure IV-82, the density gradient causes varying beam hardening, thus, varying $\mu/\rho(E)$ over the specimen's cross-section. Moreover, since $\overline{\mu/\rho}$ corresponding to $\bar{\rho}$ is applied for evaluation,

- in surface layer (SL) with $\rho_{\text{max}} > \bar{\rho}$, underestimated I_T with correspondingly overestimated $\overline{\mu/\rho}$ yields underestimated ρ_{SL} as biased measuring results whereas
- in core layer (CL) with $\rho_{\text{min}} < \bar{\rho}$, overestimated I_T with correspondingly underestimated $\overline{\mu/\rho}$ yields overestimated ρ_{CL} with bias in opposite direction,
- however, without any effect on $\bar{\rho}$ corresponding to the specimen's gravimetric mean raw density $\bar{\rho}_{\text{grav}}$.

Scattering as attenuation mechanism is, in turn, well-known not to absorb but just to change direction (and energy in the case of incoherent scattering) of the considered radiation portion and yields additional intensity in the transmitted beam, i. e., radiation build-up, with consequent non-linearity of attenuation $\ln T^{-1}$, where the effect is found to increase with increasing densification of the porous material. Regarding RDP measurement (Figure IV-82), radiation build-up occurs along total specimen cross-section, where underestimated I_T, i. e., higher intensities than expected, yield underestimated raw density values ρ. Moreover, the effect increases with increasing ρ from CL minimum toward SL maximum. The impact from both phenomena on density measuring results is considered as varyingly strong whereas individual contribution cannot be distinguished via simple transmission measurement. Furthermore, consequent interdependencies appear in terms of energy conditions by spectral variations along the beam path. Here, beam hardening, i. e., low-energy absorption, shifts energy spectrum toward higher energies whereupon the scattering share of total attenuation increases (particularly beyond $E \approx 24\,\mathrm{keV}$), which, in turn, yields increment of low-energy fraction in case of incoherent scattering. Finally, mutual relation of both effects causes combined non-linearity of total attenuation $\ln T^{-1} = \ln(I_0/I_\mathrm{T})$ (refer to Figure IV-29) along increasing raw density at equivalent transmission distance or increasing material thickness at equivalent raw density, i. e., along increasing area density ρ_A in general. Eventually, the bias increases, and thus, the measuring accuracy decreases, in the respective sections along the profile and declines further at the extrema with more distinctness of the investigated density gradient, e. g., vertical RDP, where flattened shapes with decreased SL/CL ratio occur as observed in round robin test results (Chapter IV–4.3.1). Beyond the exemplary consideration of RDP measuring accuracy, radiation-physical interdependent effects on ρ_A measurement on pre-compressed furnish mats in comparison to ready-pressed panels are likewise attributed to the particularly differing structural conditions. Note, different μ/ρ are found for mat and panel with equivalent ρ_A determined by means of similar X-ray setups at identical energetic conditions. As earlier discussed in Chapter IV–6.2, the phenomenon is considered not to be attributed to varying beam hardening, since irradiated material amount ρ_A equals. It is rather an issue of scattering conditions, which obviously differ between mat and panel, as pointed out in Chapter IV–6.3.

Obviously, radiation-physical interdependent effects occur below the macroscopic scale (refer to Chapter IV–3.2), where an appropriate explanation is provided on distinct levels of consideration, i. e., the mesoscopic (Chapter IV–3.3), the microscopic (Chapter IV–3.4), and the sub-microscopic (Chapter IV–3.5) scale. To focus again on the material, let the amount in terms of ρ_A as well as its elemental composition including MC be appropriately considered for energy selection according to Chapter IV–6.4 via optimal attenuation conditions employing tabulated $\mu/\rho\,(E)$ of the elements present and the mixture rule following the findings in Chapter IV–5.2. The particular specimen structure, in turn, has to be considered via individual experimental verification of the pre-definitions, since no comprehensive simulation is available due to lack of prerequisites. However, for radiation transmission and interaction within WBC mater, the following empirical description is concluded. The (partly coarse) structure on the mesoscopic scale comprising intra- and inter-cellular pores is relevant for free propagation of scatter radiation. On the microscopic scale with condensed matter of mainly cell-wall tissue and resin layers with adsorbed water, interaction occurs, which partly yields secondary (i. e., scatter) radiation, however, governed by elemental composition on sub-microscopic scale. Obviously, both local and global material structure is considered to individually affect radiation propagation, where pores facilitate divergence off the primary beam axis. Accordingly, more or less free radiation propagation occurs through intra- as well as inter-cellular pores without any interaction due to distinctly lower attenuation in air owing to its considerably lower density (cf. Veigele (1970)). Moreover, present water vapour according to actual MC level, and thus,

sorption state below FSP is considered to negligibly increase interaction probability. Particularly the free space between the fibres facilitates free divergence of (also low-energy) radiation in the pores of furnish mats. Consequently, lower fraction of scatter radiation is finally considered to impinge within the detector FOV in the case of low-density WBC matter such as furnish mats with additionally longer transmission distance compared to a respective panel with equal ρ_A. However, a certain extent of the detector area is required to reduce integration time considering the demanding measuring conditions in WBC applications while appropriate noise characteristics are obtained. Thus, sufficient but not overstated beam collimation with respect to beam axis maintenance is recommended. Note, the design of the employed devices and their components are already suited to the application. Eventually, coincident registration of scattered radiation of unknown origin, i. e., no distinction whether within or beside detector FOV, appears unavoidable in WBC densitometry practice.

To briefly summarise the findings, the comprehensively discussed radiation transmission concept is supported by various theoretical as well as practical investigation results. Single radiation-physical effects can be described and partly quantified, likewise their interdependencies, where, nonetheless, a holistic parameter for total quantification is lacking. However, the deduced recommendations facilitate to establish an appropriate basis for good X-ray measuring practice on WBCs meeting individual requirements. On the contrary, a theoretical description and particular transmission measuring data evaluation by means of eq. (IV-49) is practically impossible due to the unfeasible quantification of the variables. Thus, to appropriately cover all individual radiation-physical interdependencies and to facilitate correspondingly valid measuring result evaluation in terms of X-ray densitometry, the concept illustrated in Figure IV-81 is still considered as incomplete and practically not applicable. Hence, a practice-oriented description of X-ray attenuation in WBCs is finally required.

6.6   Enhanced law of attenuation

Beer's general law of attenuation according to eq. (II-10) and with $\rho_A = \rho \cdot t$ likewise eq. (II-11) both expecting linear attenuation by means of one $\mu/\rho\,(E)$ is considered to break down in the case of transmission measurements on WBCs employing non-ideal transmission conditions, i. e, X-rays with broad-beam geometry on inhomogeneous material. Hence, an applied functional context for the obviously still strong relationship of transmission measuring results along increasing area density ρ_A taking the conditions explicitly into account is required serving further as a quantification of the impact. Because of the error-prone and time-consuming metrological determination of energy spectra, scattering, detector characteristics, and further conditions as well as the inherent difficulty to define and implement $S_0(E)$, $B(E)$, and $D(E)$ comprehensively into eq. (IV-49), SOLBRIG et al. (2015a) propose a rather practice-oriented approach, which is again deduced and applied below. Note, none of the considerations are connected in any way to other modified versions of Beer's law, which are, e. g., applied in optical physics (cf. KOCSIS et al. (2006)). Moreover, the introduction of an enhanced law of attenuation is explicitly related to the above findings and X-ray densitometry on WBCs. However, under ideal transmission conditions with monoenergetic narrow-beam attenuation in homogeneous material and without further bias from signal acquisition, the transformation of attenuation law eq. (II-11) is well-known to yield linear attenuation

$$\ln T^{-1} = \frac{\mu}{\rho}(E) \cdot \rho_A \qquad\qquad (IV\text{-}50)$$

with transmission $T = I_T/I_0$ and energy-dependent mass attenuation coefficient $\mu/\rho\,(E)$ as constant of proportionality, where the plot yields, furthermore, an intersection in the point of origin $(0;0)$. With reference to the first evaluation and discussion of the transmission measurements in Chapter IV–4.3.2, the result plots of $\ln T^{-1}$ over ρ_A and ρ, respectively, are found to obviously deviate from this relation. Moreover, a non-linear slope is observed considering the total range from maximum toward zero owing to decreasing

μ/ρ in dependence of ρ_{A}, which is, however, expected as $\mu/\rho\,(E) = \mathrm{const.}$ per energy level. Likewise, apparently shifted exponential transmission reveals ordinate intercepts $T \neq 1$ in contradiction to expectation under ideal conditions (refer to Table IV-28).

Notwithstanding that the determined attenuation plots do not comprehensively comply with eq. (IV-50), a mathematically valid linear equation to describe the relation between $\ln T^{-1}$ and ρ_{A} is assumed to be easily found in a limited range with even an appropriate coefficient of determination (R^2) but with an ordinate intercept $\ln T^{-1} \neq 0$, thus, considered as physically invalid to describe the actual context of the variables. A linear fitting of the individual transmission measuring results following the general form

$$\ln T^{-1}\,(\rho_{\mathrm{A}}) = a \cdot \rho_{\mathrm{A}} + b \qquad \text{(IV-51)}$$

with a as slope of the function and constant of proportionality in physical units of μ/ρ [m^2/kg] as well as the ordinate intercept b [–] results in the coefficients compiled in Table IV-51 from the linear regression analysis of selected transmission measuring data from both ρ_{A} (Chapter IV–4.3.2.2) and RDP (Chapter IV–4.3.2.3) setups. Obviously, linear regression is found in good agreement with individual scatter plots not least due to high coefficients of determination with $R^2 > 0.996$, respectively. However, b consistently reveals $\ln T^{-1} \neq 0$ at $\rho_{\mathrm{A}} = 0$ kg/m^2, where decreasing b is supposed to indicate aforementioned correspondingly decreasing impact from beam hardening, scattering, and further interdependent transmission conditions. In comparison of the setups, the plots approach but do not intersect the point of origin $(0; 0)$. For the context of increasing attenuation over increasing area density considering the above transmission measurements, general linear regression with exemplary results in Table IV-51 is, thus, concluded to provide a mathematically appropriate but radiation-physically insufficient description. Moreover, predefinition of $b = 0$, i.e., the expected coordinates origin intercept, would still yield appropriate regression even with high $R^2 > 0.99$ whilst slope a is individually increased. Nevertheless, any ill-suited linear approach will, in

| material | a | b | R^2 |
device	[m^2/kg]	[–]	[–]
Fmat			
W-mat-16-w/o	0.1795	0.1014	0.998
W-mat-20-w/o	0.1084	0.1956	0.997
W-mat-25-w/	0.0544	0.0223	1.0
indMDF			
W-panel-16-w/o	0.1652	0.0505	0.999
W-panel-20-w/o	0.0966	0.1649	0.999
W-panel-25-w/	0.0506	0.0060	0.998
SLmat, CLmat, CLmat			
W-mat-16-w/o	0.2164	0.0140	1.0
W-mat-20-w/o	0.1121	0.1848	0.997
W-mat-25-w/	0.0576	0.0172	1.0
labMDF			
Ag-RDP-55-w/o	0.0452	0.0944	0.999
W-RDP-35-w/o	0.0413	0.1635	1.0
W-RDP-35-w/	0.0367	0.0518	1.0
W-RDP-50-w/o	0.0323	0.1134	1.0
W-RDP-50-w/	0.0289	0.0322	1.0

Table IV-51: Coefficients from linear fitting acc. to eq. (IV-51) with a as slope of the function and the ordinate intercept b, corresponding to actual T_{range} (refer to Table IV-28) of selected transmission measuring results from both ρ_{A} (Chapter IV–4.3.2.2) and RDP (Chapter IV–4.3.2.3) setups; note, linear approach is henceforth rejected.

turn, not facilitate the subsequently deduced description of exponential transmission, which is likewise biased by radiation-physical interdependencies. Thus, any linear approach is henceforth rejected.

However, further evaluation of Chapter IV–4.3.2 data via regression analysis unveils a power function approach for the context between $\ln T^{-1}$ and ρ_{A} such that eq. (IV-50) is enhanced to

$$\ln T^{-1} = \left(\frac{\mu}{\rho}\,(E)_{\kappa} \cdot \rho_{\mathrm{A}}\right)^{\kappa} \qquad \text{(IV-52)}$$

in which the exponent $\kappa\,\{\kappa \in \mathbb{Q}^+ | \kappa \leq 1\}$ (lowercase Greek letter kappa) is introduced to consider actually non-linear slope of transmission measuring data while keeping $(0; 0)$ intercept and mass attenuation coefficient $\mu/\rho\,(E)_{\kappa}$ corresponds to eq. (IV-52) regression analysis as indicated by the subscript κ. Thus, the introduced exponent κ further serves as a dimensionless

measure for deviation from the close linear context of eq. (IV-50) caused by comprehensively discussed radiation-physical interdependencies in consequence of non-ideal attenuation conditions during irradiation of inhomogeneous and porous low-Z matter such as WBCs. Note, the special case $\kappa = 1$ is considered to represent ideal conditions. Decreasing κ, in turn, indicates increasing deviation from the very same whereas the plots always yield intersection through $(\mu/\rho\,(E)_\kappa^{-1}; \ln e)$, where attenuation is considered as optimal following eq. (IV-46) regarding energy choice (refer to Chapter IV–6.4). Consequently, conversion of the inverse function of eq. (IV-52) into the pattern of attenuation law yields the double-exponential function

$$I_{\mathrm{T}} = I_0 \cdot e^{-\left(\frac{\mu}{\rho}(E)_\kappa \cdot \rho_{\mathrm{A}}\right)^\kappa} \qquad (\text{IV-53})$$

introduced as enhanced law of attenuation with κ as additional exponent equal to the very same in eq. (IV-52). The mathematical representation is considered to provide an appropriate radiation-physical description for the biased exponential transmission T over increasing ρ_{A} considering aforementioned attenuation conditions on WBCs. However, a general exponential equation $T = c \cdot e^{-d}$ would yield appropriate regression of some measuring points but fails toward $\rho_{\mathrm{A}} = 0 \ \mathrm{kg/m^2}$, where according to this ill-suited mathematical context certain attenuation with $T < 1$ would computationally occur, which is, in turn, physically impossible, since no attenuating body is present. On the contrary, eq. (IV-53) subsequently yields $T = 1$ intersection according to expectation and further provides a mathematic-physically appropriate solution of the problem. Eventually, for the observed decrement of μ/ρ with increasing ρ_{A}, a further equation can be deduced from the above double-exponential approach. Initially, $\mu/\rho\,(E)$ is expected to be constant at equal energy for the same material with increasing ρ_{A}, i. e., $\mu/\rho\,(\rho_{\mathrm{A}}) = \mu/\rho\,(E) = const.$, thus,

$$\frac{\mu}{\rho}(\rho_{\mathrm{A}}) = \frac{\mu}{\rho}(E) \cdot \rho_{\mathrm{A}} \cdot \rho_{\mathrm{A}}^{-1} \qquad (\text{IV-54})$$

to bring area density ρ_{A} into consideration. Since non-linearity of $\ln T^{-1}$ is found and appropriately

described by eq. (IV-52), the context is transferred and the exponent κ likewise applied to the linear term $(\mu/\rho\,(E) \cdot \rho_{\mathrm{A}})$ to change eq. (IV-54) into

$$\frac{\mu}{\rho}(\rho_{\mathrm{A}}) = \left(\frac{\mu}{\rho}(E)_\kappa \cdot \rho_{\mathrm{A}}\right)^\kappa \cdot \rho_{\mathrm{A}}^{-1} \qquad (\text{IV-55}),$$

thus, $\mu/\rho\,(\rho_{\mathrm{A}})$ becomes reciprocally dependent from varying ρ_{A} with further $\lim_{\rho_{\mathrm{A}} \to 0} \mu/\rho\,(\rho_{\mathrm{A}}) = \infty$.

To apply and verify the approach, Figure IV-84 to Figure IV-94 present again selected transmission measuring result charts from both ρ_{A} (Chapter IV–4.3.2.2) and RDP (Chapter IV–4.3.2.3) setups extended with additional plots of individual regression function following

- eq. (IV-53) for relative transmission $T = I_{\mathrm{T}}/I_0$ [–] (dotted line),
- eq. (IV-52) for logarithmic of reciprocal transmission $\ln T^{-1} = \ln(I_0/I_{\mathrm{T}})$ [–] as measured attenuation (dashed line), and
- eq. (IV-55) for the mass attenuation coefficient $\mu/\rho\,(\rho_{\mathrm{A}})$ (dash-dotted line)

all depending on actual transmission in terms of the measured ρ_{A} or ρ range. The corresponding coefficients following power function approach of eq. (IV-52) are summarised in Table IV-52. Here, an obviously close fit to describe the non-linear slope of $\ln(T^{-1})$ over increasing ρ_{A} by the factor μ/ρ_κ and the exponent κ can be observed from all charts. Moreover, the individual power function regression analysis consistently yields a high coefficient of determination with $R^2 > 0.997$, respectively. Likewise, transmission T as an initial measuring result closely follows the introduced double-exponential description according to eq. (IV-53) represented by the dotted line in the figures. The deduced $\mu/\rho\,(\rho_{\mathrm{A}})$ description, in turn following eq. (IV-55), finally yields appropriate regression considering both mathematical as well as radiation-physical context. Notwithstanding that, the fit of some μ/ρ points from measurement is obviously found not as close to the regression computation as in the case of T and $\ln(T^{-1})$ charts. Note for the plots of decreasing $\mu/\rho\,(\rho_{\mathrm{A}})$ over increasing ρ_{A}, deviations of measured $\mu/\rho\,(\rho_{\mathrm{A}})$ in the scatter chart compared to

power fit are primarily attributed to errors in gravimetric ρ_A determination as earlier discussed regarding the respective plots in Chapter IV–4.3.2.

However, the exponent κ distinctly varies in Table IV-52, where decreasing κ, i. e., deviation from one, corresponds to a stronger curvature of the respective plots. Note here, κ is found to decrease in comparison between the devices, where no pre-filter is applied, thus, the initial spectrum is less pre-hardened, which becomes particularly obvious from the different W-RDP setups and in comparison of the 20 kV and 25 kV plots determined by W-mat and -panel devices, respectively. In the case of the corresponding 16 kV results, the initial spectrum is already narrower and the scattering impact is reduced due to the lower energy level, hence, resulting in higher κ values. Obviously, the pattern of κ variation in Table IV-52 corresponds to the very same of $T_{\mathrm{intercept}}$ and $\Delta\mu/\rho_{\mathrm{rel}}$ in Table IV-28 indicating respective deviations from ideal conditions, where κ is considered to be a more sophisticated index for comparison of individual radiation transmission conditions. To generally illustrate the effect of decreasing κ, Figure IV-83 (solid lines) shows theoretical transmission data considering non-ideal conditions computed via eq. (IV-53), eq. (IV-52), and eq. (IV-55) with assumed $\kappa = 0.85$ (just below Table IV-52 minimum) in comparison to ideal expectation from Figure IV-29 (dashed lines), where the basic energy and attenuation level is kept equal with $\mu/\rho = \mu/\rho_\kappa = 0.1125$ m^2/kg. Nevertheless, values of κ approaching toward one do not necessarily indicate improved transmission conditions according to earlier discussions of the setups. Such results may also be attributed to interdependency phenomena, where effects compensate each other particularly considering superimposition of low-energy fractions from scattering on hardened transmission spectra as discussed in Chapter IV–6.3 and, e. g., as partly illustrated in Figure IV-82 with respect to RDP determination. Moreover, the determined coefficients are found to reveal individually appropriate regressions but may partly not represent expected characteristics (according to earlier discussions) of the respective setups and energy levels owing

material device	μ/ρ_κ [m^2/kg]	κ [–]	R^2 [–]
Fmat			
W-mat-16-w/o	0.2008	0.9386	0.999
W-mat-20-w/o	0.1357	0.8661	0.999
W-mat-25-w/	0.0558	0.9858	1.0
indMDF			
W-panel-16-w/o	0.1752	0.9419	0.999
W-panel-20-w/o	0.1142	0.8982	0.999
W-panel-25-w/	0.0509	0.9950	0.998
SLmat, CLmat, CLmat			
W-mat-16-w/o	0.2193	0.9667	0.999
W-mat-20-w/o	0.1374	0.8790	0.999
W-mat-25-w/	0.0588	0.9906	0.999
labMDF			
Ag-RDP-55-w/o	0.0505	0.9276	0.999
W-RDP-35-w/o	0.0496	0.8842	1.0
W-RDP-35-w/	0.0392	0.9473	0.999
W-RDP-50-w/o	0.0370	0.8938	1.0
W-RDP-50-w/	0.0302	0.9566	0.999

Table IV-52: Coefficients from power function fitting acc. to eq. (IV-52) with the mass attenuation coefficient μ/ρ_κ as slope of the function and the exponent κ, corresponding to actual T_{range} (refer to Table IV-28) of selected transmission measuring results from both ρ_A (Chapter IV–4.3.2.2) and RDP (Chapter IV–4.3.2.3) setups; note, the coefficients likewise refer to eq. (IV-53) as enhanced law of attenuation and eq. (IV-55).

to limited ρ_A measuring ranges of some measuring series particularly in the case of indMDF measurements. The observed curvature of the derived power function is assumed to be straighter than expected and does, therefore, not represent the actual $\ln(T^{-1})$ slope affected by radiation-physical interdependencies. This may, e. g., be the case regarding W-panel-20-w/o and W-panel-25-w/ plots, where the lower ρ_A range is not covered in comparison to corresponding Fmat results. However, this discrepancy may not be clarified on the basis of the present data and, thus, requires more well-defined measuring series.

All μ/ρ_κ values in Table IV-52 consistently exceed the related slope a in Table IV-51 (note, rejected), thus, μ/ρ_κ reveals a more distinct increment of attenuation, which is, in turn, flattened by

the exponent κ along increasing ρ_A due to the typical characteristic from beam hardening and scatter registration. Considering the individual ρ_A range, μ/ρ_κ of the W-mat and -panel devices more or less equal the respective $\mu/\rho_{\text{opt.}}$ values in Table IV-49, i. e., optimal mass attenuation coefficient on the respective energy level owing to equivalent mathematical background with $1 = \mu/\rho \cdot \rho_A$ at $T = e^{-1}$. Moreover, the results from power function fitting μ/ρ_κ, which obviously represent reciprocal ρ_A at $T = e^{-1}$, nearly equal the corresponding μ/ρ in Table IV-26 determined via interpolation of the measuring data, where the minor differences are attributed to slight inaccuracy and linear assumption of the latter. Regarding RDP devices, μ/ρ_κ determined for W-RDP-50-w/ is roughly equal to $\mu/\rho_{\text{opt.}}$ considering $\bar{\rho}$ of labMDF in Table IV-50 again due to congruent ρ_A ranges of transmission measurement and computation. On the contrary, optimal attenuation values as generalised for customary WBC panels fall below μ/ρ_κ based on measurement. Thus, higher energy is required to obtain optimal attenuation conditions for RDP measurement as already concluded in Chapter IV–6.4. Moreover, the variation of μ/ρ in dependence of ρ_A by the exponent κ is considered to tend toward the order of $\mu/\rho\,(E)_{\text{mix}}$ (refer to individual energies in Table VII-12) whereas respective values with spectra consideration (Table IV-42) still exceed μ/ρ_κ. However, according to the respective slope of $\mu/\rho\,(\rho_A)$ in Figure IV-84 to Figure IV-94, one individual ρ_A is, thus, considered to exist, where $\mu/\rho\,(\rho_A)$ equals correspondingly computed $\mu/\rho\,(E)$ depending on the method following Chapter IV–5.2. Furthermore, the slope of $\mu/\rho\,(\rho_A)$ according to eq. (IV-55) with rapidly increasing μ/ρ in the lower ρ_A range toward the limit reveals the well-known condition, that beam hardening predominates on the respective energy level in low ρ_A transmission, i. e., at the beginning of the beam path through the material of respective thickness s_T.
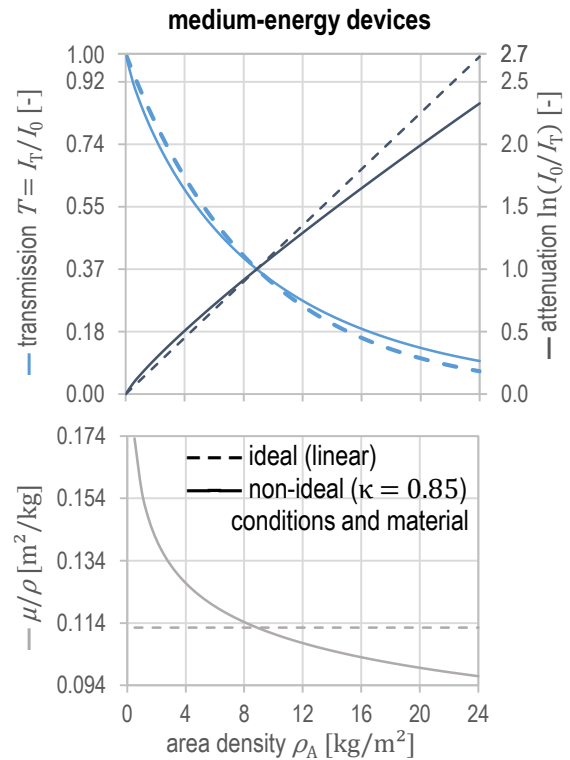
Figure IV-83: Theoretical transmission data considering non-ideal conditions (solid lines) computed via eq. (IV-53), eq. (IV-52), and eq. (IV-55) with assumed $\kappa = 0.85$ and $\mu/\rho = \mu/\rho_\kappa = 0.1125\ \text{m}^2/\text{kg}$ in comparison to ideal expectation from Figure IV-29 (dashed lines).
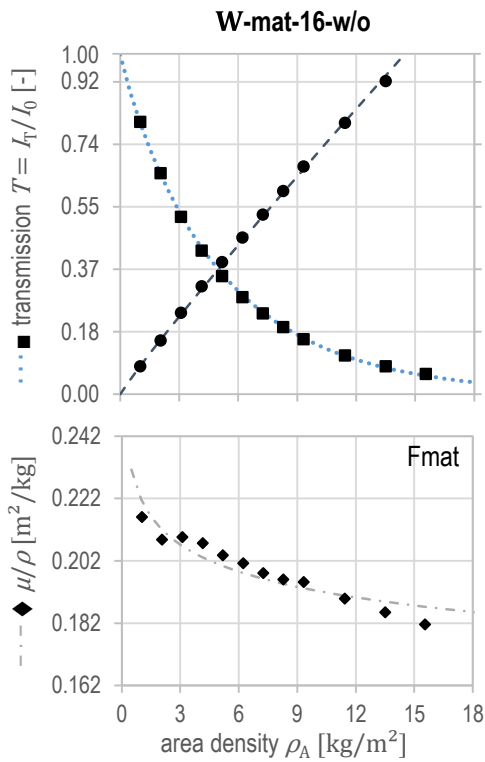
Figure IV-84: Transmission measuring results from Figure IV-30 (■, ●, ♦) extended with individual regression plots via eq. (IV-53) for T (dotted line), eq. (IV-52) for $\ln T^{-1}$ (dashed line), and eq. (IV-55) for μ/ρ (ρ_A) (dash-dotted line) with coefficients from Table IV-52.
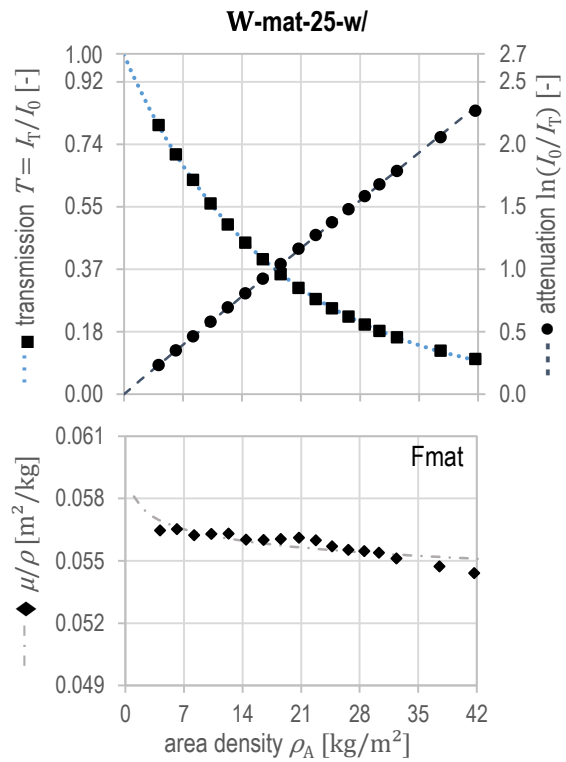
Figure IV-86: Transmission measuring results from Figure IV-32 (■, ●, ♦) extended with individual regression plots acc. to Figure IV-84.
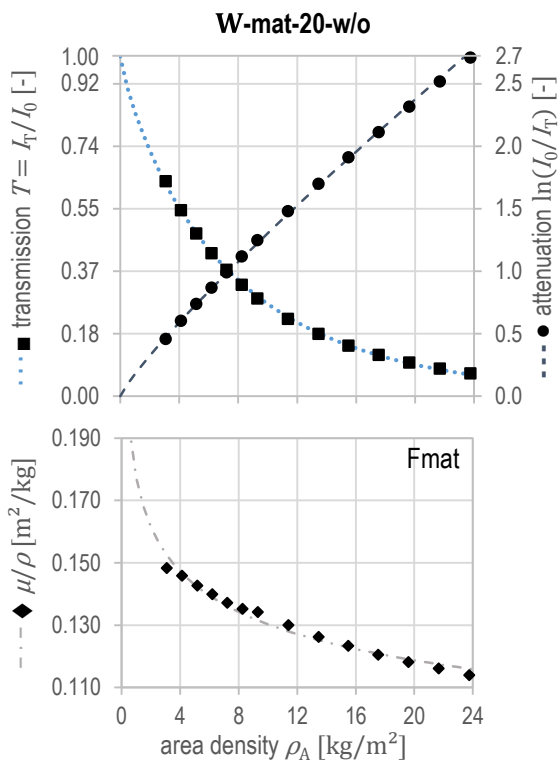
Figure IV-85: Transmission measuring results from Figure IV-31 (■, ●, ♦) extended with individual regression plots acc. to Figure IV-84.
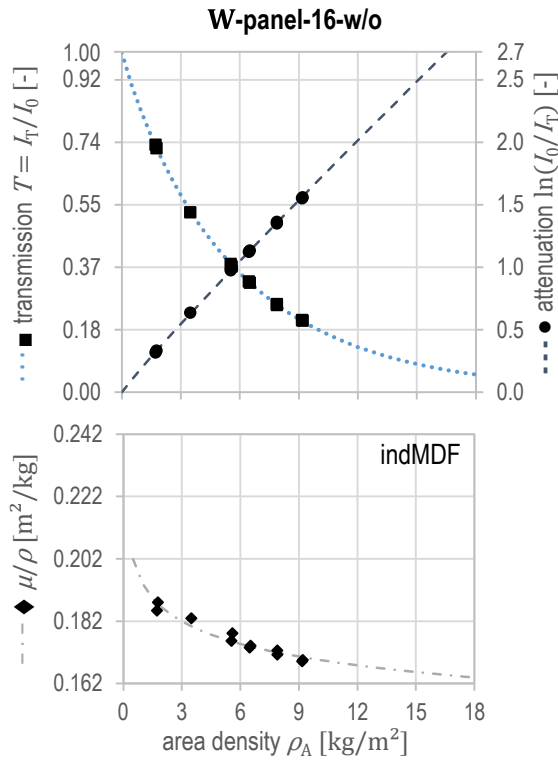
Figure IV-87: Transmission measuring results from Figure IV-33 (■, ●, ♦) extended with individual regression plots acc. to Figure IV-84.
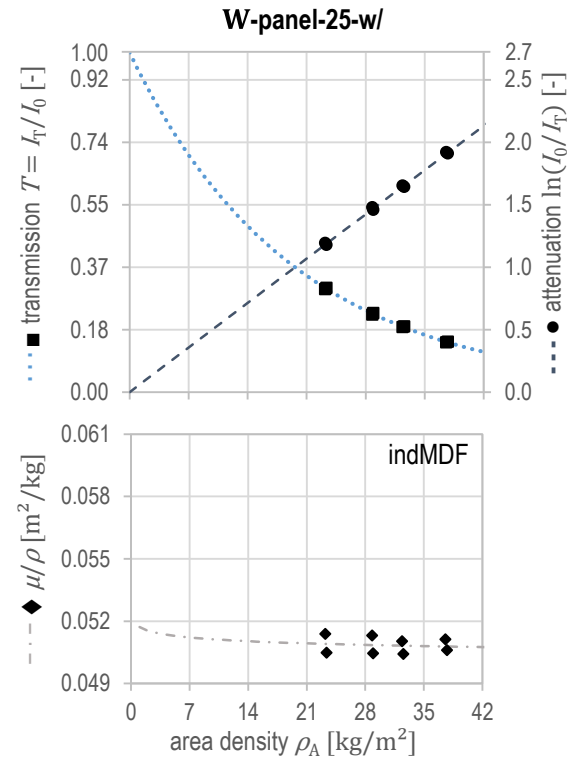
Figure IV-89: Transmission measuring results from Figure IV-35 (■, ●, ♦) extended with individual regression plots acc. to Figure IV-84.
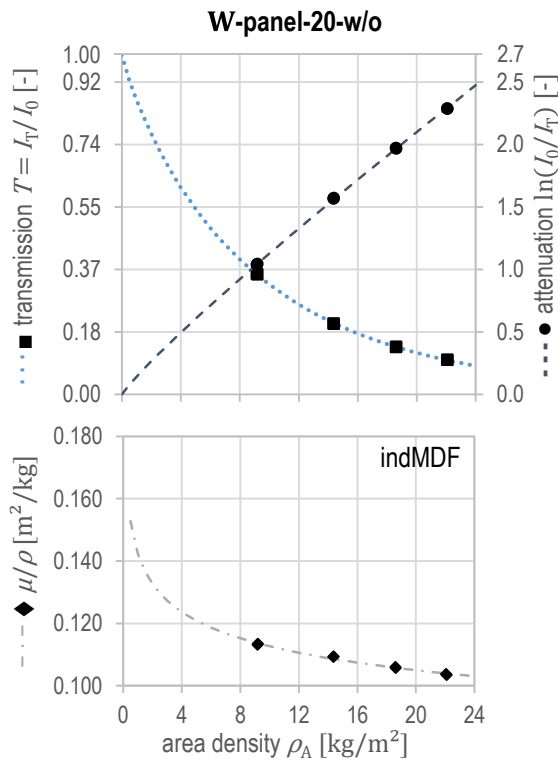
Figure IV-88: Transmission measuring results from Figure IV-34 (■, ●, ♦) extended with individual regression plots acc. to Figure IV-84.
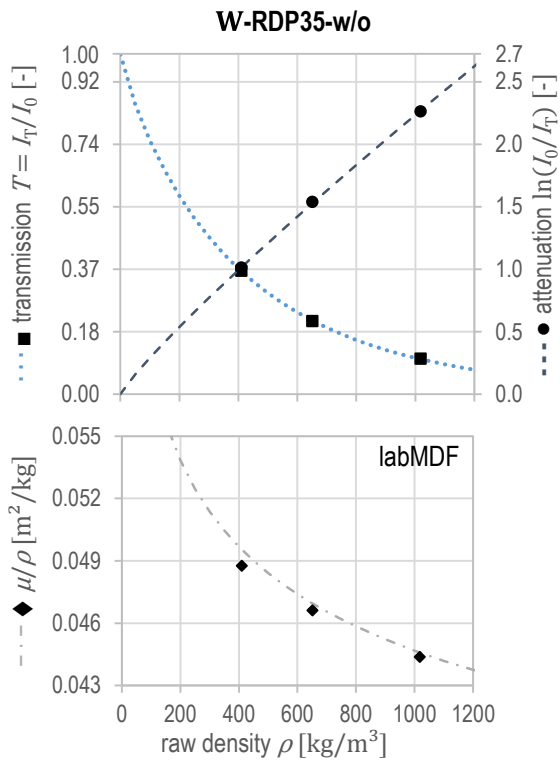
Figure IV-90: Transmission measuring results from Figure IV-46 (■, ●, ♦) extended with individual regression plots acc. to Figure IV-84.
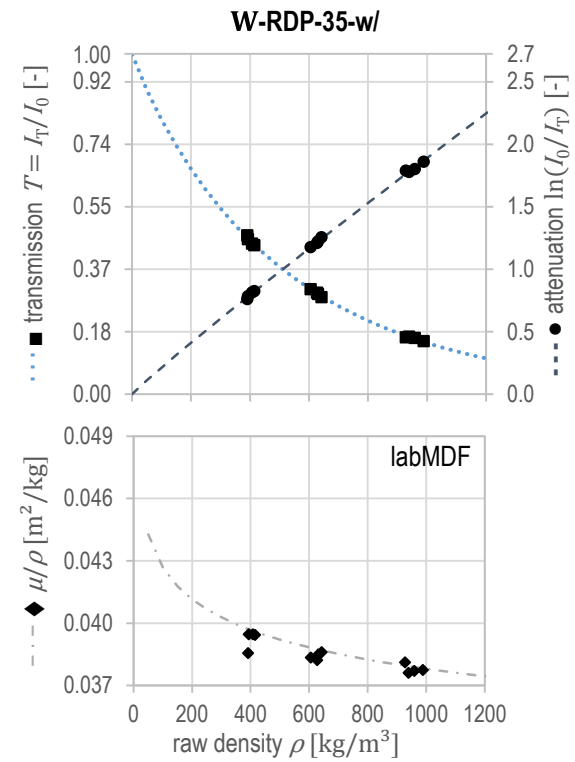
Figure IV-92: Transmission measuring results from Figure IV-48 (■, ●, ♦) extended with individual regression plots acc. to Figure IV-84.
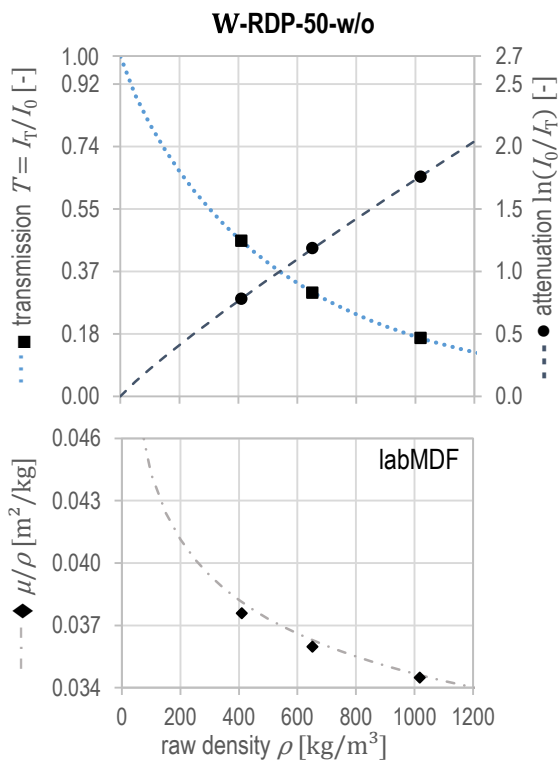
Figure IV-91: Transmission measuring results from Figure IV-47 (■, ●, ♦) extended with individual regression plots acc. to Figure IV-84.
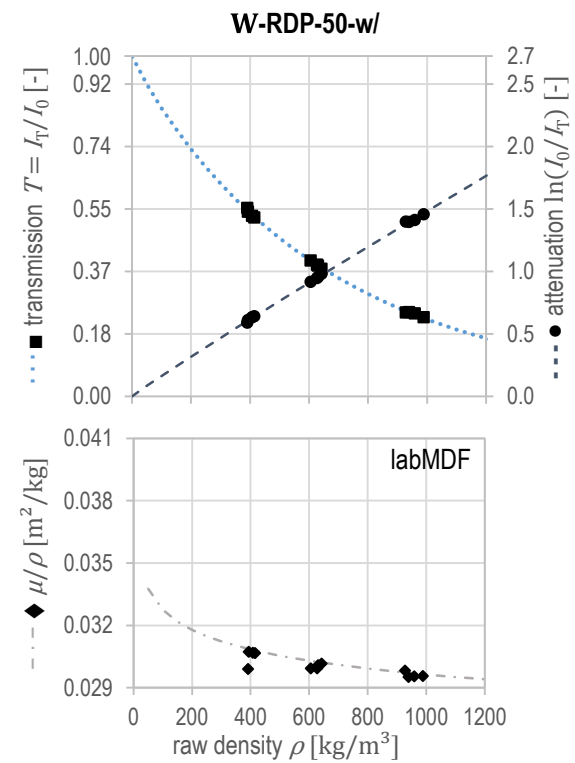
Figure IV-93: Transmission measuring results from Figure IV-49 (■, ●, ♦) extended with individual regression plots acc. to Figure IV-84.
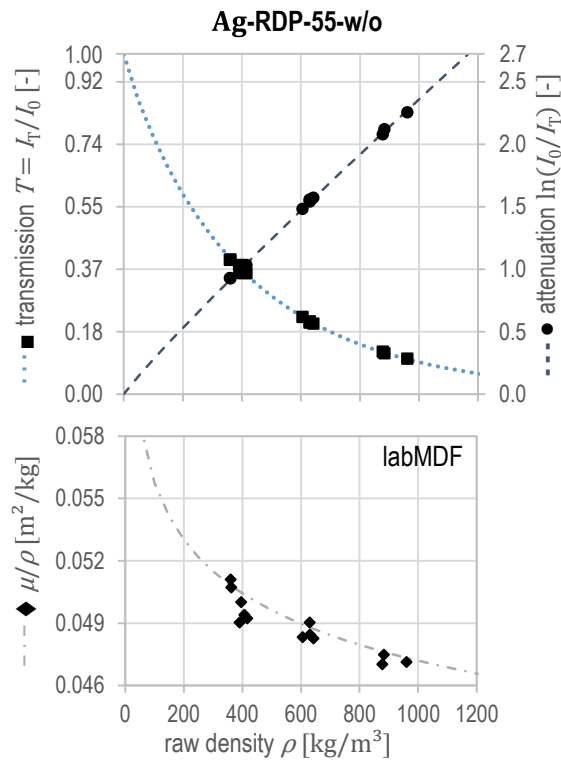
Figure IV-94: Transmission measuring results from Figure IV-44 (■, ●, ♦) extended with individual regression plots acc. to Figure IV-84.

To conclude, the introduced approach based on power function instead of linear attenuation considering decreasing μ/ρ along the beam path is found to serve as a viable description for X-ray transmission through WBCs by means of the double-exponential law of attenuation. The proof of its holistic validity is, nevertheless, still pending. All deduced equations with corresponding coefficients in Table IV-52, however, appropriately follow the scatter charts from measuring data as illustrated in Figure IV-84 to Figure IV-94. Note, an individual prediction by the plots needs to be verified by respectively enhanced measurements particularly with regard to the lower limits, i. e., considering present extrapolation of $\mu/\rho\,(\rho_A)$ for ρ_A toward zero. Such consideration of non-linear attenuation is indispensable to avoid errors in area and raw density determination on the basis of X-ray transmission measurements. Likewise already RUDMAN et al. (1969) consider non-linear measuring results from one of their setups as too large for accurate raw density determinations, thus, they improved the very same. However, the present thesis aims to explore existing X-ray transmission setups and to

describe the measuring conditions. Consequently, Figure IV-81 is enhanced to Figure IV-95 by substitution of eq. (IV-49) with eq. (IV-53) as well as by consideration of registered radiation intensity (both initial and transmitted) as integration along the energy spectrum and over the detector area. The resulting intensity is furthermore weighted by the detector response function $D(E)$, which, however, does not necessarily need to be known, since it is inherently included in the detector output, and thus part of the respective measurement itself. Therefore, Figure IV-95 is considered a comprehensive scheme for polychromatic radiation transmission through inhomogeneous and porous low-Z matter and measurement comprising radiation-physical interdependencies from both material and setup, and thus as a practice-oriented basis for X-ray densitometry on WBCs.

Beyond WBCs, correction of non-linearity due to beam hardening or scattering is discussed in Chapter II–2.4.3 and Chapter II–2.5.2, respectively. In comparison to existing correction methods such as applied in X-ray CT, the above approach by mathematical estimation of the non-linear function is, e. g., similar to the pre-processing linearisation method for beam hardening correction utilised by KASPERL (2005) and mathematically established by HERMAN (1979). Here, the non-linear slope of the attenuation plot $-\ln\big(H_S(L)\big)$ (refer to Figure II-6) measured by means of step wedges made of homogeneous material is approximated by a characteristic curve for beam hardening $H_S(L)$, of which the inverse function yields the correction H_S^{-1}. However, with its requirements, this linearisation method is limited to homogenous reference bodies with properties equal to the objects under investigation, and thus not applicable to WBCs. Moreover, step wedges as substitution for an actual material raw density range are found to cause insufficiencies with respect to WBC densitometry – particularly RDP measurement – as to be discussed in Chapter V–1. Beyond CT correction methods, further approaches exist to consider the non-linearities particularly by means of polynomial solutions. BJÄRNGARD, SHACKFORD (1994) propose a beam hardening coefficient, which extends exponential function

by a second-degree polynomial of penetration depth with an additional factor in the exponent of attenuation law such as in eq. (II-40). On the contrary, SOLBRIG et al. (2011) and likewise SOLBRIG (2012) apply second-degree polynomial fitting of the transmission measuring results from step wedges made of MDF for the context of decreasing μ/ρ over the measuring signal in terms of attenuation $\ln T^{-1}$ corresponding, in turn, to increasing ρ_A and, however, conclude already the polynomial to be an insufficient means of choice with respect to limit values of the function. In general, polynomials serve as simplistic means to fit non-linearity with apparently high coefficients of determination whereas true functional relation is well-known not to be represented in most of the cases. Hence, the found double-exponential approach is considered to be an appropriate mathematic-physical solution particularly considering the limits of the function. Accordingly, the exponential decrease of transmission $T(\rho_A)$ in dependence of area density with the double-exponent $-(\mu/\rho\,(E)_\kappa \cdot \rho_A)^\kappa$ in eq. (IV-53) yields $\lim_{\rho_A \to 0} T(\rho_A) = 1$, i. e., expected ordinate intercept, and converges toward zero with increasing ρ_A, i. e., $\lim_{\rho_A \to \infty} T(\rho_A) = 0$. Such limits obviously fit with reality as SOLBRIG et al. (2015a) also conclude whereas a polynomial fit would yield ordinate intercept at $T \neq 1$. Moreover, since the double-exponential approach is considered to represent physical background, already a few data points from appropriate measurements, like in the case of RDP data Figure IV-90 to Figure IV-94, obviously facilitate to model the mass attenuation coefficient variations along increasing raw and area density in consequence of radiation-physical interdependencies.

Regardless of the appropriate mathematic-physical description, κ claims no individual quantification of the single impact factors, thus, no explicit distinction between, e. g., beam hardening or scattering. However, κ is rather considered to be a total index for the transmission conditions of the setup including the material under investigation. In contradiction to prevalent correction approaches by means of, e. g., linearisation in technical X-ray CT, the approach above purposefully performs no individual correction of non-linearities from single effects by respective algorithms, which may bias the results in the case of ill-defined correction parameters. It instead describes the superimposition of the effects by means of the introduced double-exponential attenuation equation, which is intended for further utilisation in densitometry. The enhanced law of attenuation is, moreover, considered to be a practice-oriented approach particularly regarding the avoidance of X-ray spectra application due to their elaborate acquisition exclusively via special equipment as well as their superimposition by scattered radiation and comprehensive dependence on WBC raw density or actual transmission distance on the beam path. Furthermore, no computed attenuation coefficients based on elemental composition are required for application. Eventually, the coefficients $\mu/\rho\,(E)_\kappa$ and κ for the enhanced law of attenuation considering all present radiation-physical interdependencies are solely determined on the basis of transmission measurements employing the regular setup and respective specimens. Thus, individually determined $\mu/\rho\,(E)_\kappa$ and κ values are exclusively valid for the very same or a comparable combination of X-ray transmission setup, material, and corresponding parameters.

$$I = \int_{A_D} \int_E I(E, A)\, dE\, dA$$

$$I_T = I_0 \cdot e^{-\left(\frac{\mu}{\rho}(E)_\kappa \cdot \rho_A\right)^\kappa}$$

- initial intensity I_0, employed initial spectrum $S_0(E)$
- absorption $\frac{\mu_{photo}}{\rho}(E)$
- (multiple) scattering $\frac{\mu_{coh}}{\rho}(E) + \frac{\mu_{incoh}}{\rho}(E)$
- beam hardening $BHi(E, \rho_A)$
- radiation build-up $B(E)$
- transmitted intensity $I_T = I_P + I_S$, transmitted spectrum $S_T(E)$
- characteristic detector output $D(E)$, detected spectrum $S_D(E)$
- matter, inhomogeneous & porous, $\rho_A = \rho \cdot t$
- $\frac{\mu}{\rho}(E)_\kappa$
- κ $\{\kappa \in \mathbb{R} \,|\, 0 < \kappa\}$ setup, irradiated geometry
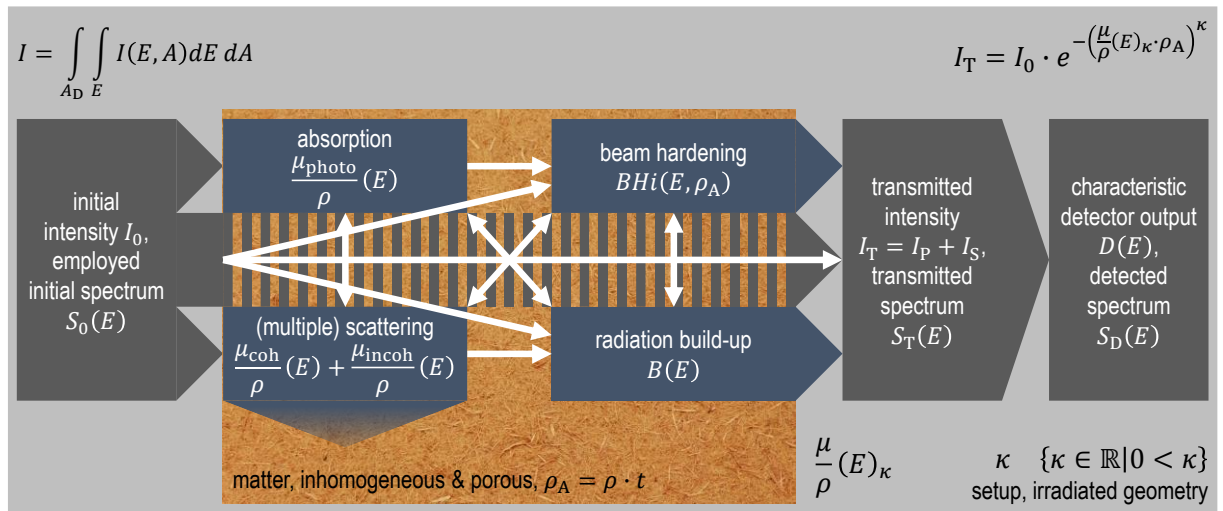
Figure IV-95: Final schematic illustration of the enhanced understanding based on Figure IV-81 of polychromatic radiation transmission with non-narrow beam geometry through inhomogeneous and porous low-Z matter, described by the double-exponential attenuation law as introduced in eq. (IV-53) considering radiation-physical interdependencies (white arrows) via the determined mass attenuation coefficient $\mu/\rho\,(E)_\kappa$ and the corresponding exponent κ, as practice-oriented basis for X-ray densitometry on WBCs.

1   Implications regarding the methods

X-ray densitometry on wood-based composites (WBCs) is influenced by various factors with respect to both radiation and material as well as their interdependencies. The context is illustrated in Figure IV-95 and described by the introduced double-exponential attenuation law following eq. (IV-53). It can be concluded as the main findings of the present thesis that

- non-linearities bias the transmission measuring results, where a linear context is generally expected,
- beam hardening occurs and varies in dependence on the varying attenuation potential of the investigated inhomogeneous material and the character of the applied X-ray energy spectrum,
- scattering phenomena superimpose all measurements and depend on both beam geometry and WBC densification,
- such impact from structural conditions increases with wide area density measuring ranges or more distinct raw density profiles (RDPs), and
- WBC composition has an impact on radiation attenuation but markedly depends on the type of the varying constituent as well as the employed radiation energy level.

For detailed discussion, reference is made to the respective chapters. However, comprehensive conclusions follow below.

Regarding the composition of customary WBCs with organic binders, an effective atomic number Z_{eff} remains more or less equal with resin addition. A variation in radiation attenuation depending on resination as reported by HILBERS (2006) is fundamentally questionable but may instead be attributed to structural material conditions of the respective measurements. Although the elemental composition alters, the effective mean

mass attenuation coefficients $\overline{\mu/\rho}$ remain similar. Moreover, already LAUFENBERG (1986) found that there is no significant impact on the radiometric raw density determination on WBCs from variations of resin content, (European softwood) wood species, and equilibrium moisture content (EMC) within normal ranges. Accordingly, hitherto findings can be generally confirmed by the present results regarding high energy applications with $E \geq 50\,\text{keV}$. The same applies to the RDP measurements on high-medium energy level $25 \leq E < 50\,\text{keV}$, where no significant variation of $\overline{\mu/\rho}$ with varying compositions is observed. With decreasing energy, in turn, the impact of moisture and ash content variations on the computational mass attenuation coefficient $\mu/\rho\,(E)_{\text{mix}}$ increases, which is considered to be relevant for area density measuring applications on light furnish mats and thin panels. However, $\mu/\rho\,(E)_{\text{mix}}$ is consistently unaffected by variations of (organic) adhesive resin content on all energy levels.

Regarding the applied methods for computational estimation of the attenuation potential of varying material compositions, the conclusion turns out to be different for the calculation of an effective atomic number Z_{eff} and the application of the mixture rule with a total mean mass attenuation coefficient for one energy $\mu/\rho\,(E)_{\text{mix}}$ or its spectral-weighted extension $\mu/\rho\,\big(S(E)\big)_{\text{mix}}$. Here, Z_{eff} is a vivid means to compare compounds regarding their attenuation potential by bringing them into line with elemental atomic numbers, where no energy consideration is required in the case of the simplistic power law method. The results are beneficial for a better understanding of WBCs regarding their composition from an X-ray beam's point of view, however, less applicable in the common densitometry practice. The computation via mixture rule

yields instead a more or less precise approximation of a total mean mass attenuation coefficient with explicit consideration of one energy (e. g. mean value or monochromatic source) or weighted by the energy distribution. The results are available for subsequent applications such as further computations or for energy definition. According to the different energy considerations of the approximation methods, the implication on the evaluated attenuation potential for one and the same compound may vary particularly in dependence on the corresponding energy level and spectrum.

Beyond the method of computation, an impact of the moisture content (MC) on radiation attenuation is concluded to exist but markedly depends on the radiation energy. The effect on densitometry, however, needs to be discussed. MC increment is considered to simply increase the WBC mass by water with Z_{eff} similar to wood. Here, no significant variation of WBC Z_{eff} occurs in the range below fibre saturation point (FSP) and until $MC \gg MC_{\mathrm{FSP}}$. Thus, X-ray measurement of the area density ρ_{A} distribution across the mat or panel is practically unaffected by the global MC level, regardless of local moisture variations. The measuring results correspond to the actual MC. A distinction is impossible by simple transmission measurements as to be discussed elsewhere. Regarding RDP measurement, the phenomenon is observed with increasing MC, that swelling and corresponding volume increment (in direction of the panel thickness) is counterbalanced by the mass increment, i. e., the increasing mass from moisture is homogeneously distributed over the specimen volume resulting, in turn, in an equal amount of matter in beam direction. Here, the specimen thickness increases due to swelling primarily along the cross-section (not in-plane). Likewise, the number of measuring layers with constant step size increases, where ρ_{A} of the layer along the beam path remains equal. Accordingly, the equivalent RDP shape is expanded along the higher panel thickness after swelling. The same, but vice versa, applies to specimen shrinkage in the case of dehydration. Obviously, the effective radiation attenuation comprises the individual moisture and material structure conditions. In Chapter II–2.4.4

it was reported, that PEASE et al. (2012) propose a coupled effective attenuation coefficient of water in porous substrates. The coefficient considers the influence of water on beam hardening and is recommended to be directly measured for the respective investigation instead of utilisation of tabulated water values. Hence, the mass attenuation coefficients for high-precision densitometry on WBCs (considered to be a porous material with complex composition and adsorbed water) must be determined via transmission measurements instead of computation via mixture rule, where the values were already concluded to be rather applicable for estimations and comparison of the attenuation characteristic.

Obviously, the equivalent attenuation potential of the WBC constituents provide a practical benefit for simple densitometry, since the measuring results represent ρ_{A} and ρ of the mat or panel at the respective MC of the composite considered to be a mixture of elements (refer to macroscopic scale, Chapter IV–3.2). However, a significant contrast between water and the dry WBC matter may be required to measure or visualise the moisture distribution for several purposes. According to the computed values (refer to Table IV-35), $\mu/\rho\,(E)_{\mathrm{mix}}$ of wood, adhesive resin, and water are found in a comparable order but reveal certain differences depending on the energy level (decreasing with increasing energy), where particularly water values differ. Therefore, the discrimination of, e. g., moisture accumulations in dry WBC matter appears feasible. Likewise, measurements of amount and distribution of moisture uptake in comparison between significantly different states, i. e., below and far beyond FSP, can be carried out. Here, XU et al. (1996) propose a procedure via difference method and by consideration of thickness swelling to determine the water absorption distribution along the RDP after 24 h (and 168 h) immersion in water. Nevertheless, the determination of sorptive moisture distributions within the material in terms of reliable MC determination below FSP (on mesoscopic and microscopic scale, Chapter IV–3.3 and IV–3.4) are considered to fail by means of X-ray transmission, since $\mu/\rho\,(E)$ values are too close. The hygroscopically bound water causes further material variation due to swelling

and shrinkage, thus, the resulting X-ray contrast may be superimposed by ρ_A and ρ variations, which interfere, in turn, clear distinction between moisture and WBC matter variations via X-ray densitometry.

However, similar atomic numbers are the reason for the poor discriminability. Here, NAYDENOV et al. (2004) deal with X- and gamma-ray multi-energy applications and point out that it is impossible to reliably distinguish between water ($Z_{\text{eff}} \approx$ 7.5) and organic materials ($Z_{\text{eff}} \approx 6 \dots 8$). Such methods require differences in Z_{eff} by about 50 % between the constituents. On the contrary, and with regard to the computed values in Table IV-32, water ($\bar{Z}_{\text{eff}} = 7.42$) just slightly exceeds dry labMDF ($\bar{Z}_{\text{eff}} = 6.93$) by about 7 %. Moreover, JACKSON (1982) discusses the possibility of increasing the attenuation contrast (for imaging) by measurements with energies near to the absorption K-edge of a considered element, preferably with much higher Z than the surrounding matter. Regarding low-Z matter, she reports that there is a "window" for C and O discrimination within $E = 0.28 \dots 0.53$ keV corresponding to the K-edges, thus, to obtain contrast between water and material with high C mass fractions (such as wood). This energy range is obviously far below practical ranges for X-ray transmission measurements on relevant layer thicknesses and is instead applied for X-ray microscopy. Hence, the K-edge absorption method is not applicable for densitometry on WBCs to obtain further sensitivity toward the moisture distribution. However, the utilisation of two (or multiple) radiation energy levels, thus, different $\mu/\rho\,(E)$, is a well-known method for distinguishing between the constituents of mixtures or composites, which provide correspondingly different attenuation potential (cf. MIDGLEY (2011)). Here, a varying ratio of the constituent's linear attenuation coefficients $\mu(E)$ on at least two energy levels is applied for discrimination, where transmission measurements with only one energy level yield no appropriate image contrast. The method is referred to as dual-energy X-ray absorptiometry and common practice for medical applications such as the determination of bone mineral content (cf. GILSANZ (1998)) and soft tissue composition (cf. MAZESS

et al. (1990)). Furthermore, multi-energy techniques are well-known for inspection of both luggage and cargo containers (cf. REBUFFEL, DINTEN (2007), ZENTAI (2008), KOLKOORI et al. (2014), where material discrimination is a considerable issue in terms of security. However, KULLENBERG et al. (2010) and HULTNÄS, FERNANDEZ-CANO (2012) propose dual-energy X-ray absorptiometry on medical energy levels (40 kVp and 90 kVp) for MC determination in wood chips by means of a commercially available dual-energy X-ray device. Here, further studies exist. TANAKA (2015) suggests 20 kVp and 100 kVp as an appropriate pair of X-ray tube voltages. KIM et al. (2015) apply 45 kVp and 60 kVp without pre-filter variation, which appears too close together. LINDGREN et al. (2016) transfer the approach to CT applications on wood and propose to divide the reconstructed voxel matrices acquired at 60 kVp and 200 kVp. They conclude their results from scans of wet pine cubes, where the voxel values are supposed to vary along the specimen cross-section due to moisture profiles, to show the feasibility of dual-energy X-ray CT for MC determination with sufficient contrast. However, a full calibration over a relevant MC range and quantification of the supposed moisture distribution was not performed. Virtually all dual-energy examinations apply wide MC ranges, focus on $MC \gg MC_{\text{FSP}}$, and imply the applicability of their proposed procedures or devices for MC determination on wood, where low standard errors of estimate around 2 % are claimed. Nevertheless, the results from various studies lead to the conclusion, that the uncertainty of dual-energy X-ray absorptiometry MC determination toward oven-dry method increases with decreasing MC, particularly below FSP. To an extent it turns out that there is no significant correlation between radiometric results and the gravimetric reference. Apart from wet wood chips, there is virtually no relevant application in WBC production. Moreover, dual-energy X-ray methods are consequently concluded to be not applicable for obtaining an appropriate contrast between adsorbed moisture and dry wood as well as WBC matter in the relevant MC range below FSP.

Hence, other radiometric methods are required, which are either more sensitive to moisture or increase the absorption contrast of one of the constituents. Here, SOLBRIG et al. (2015c) and other researchers before propose neutron radiography to obtain an appropriate contrast between dry wood matter and moisture in order to be visualised and quantified. Beyond X-ray and neutron radiography, magnetic resonance imaging (MRI) is an alternative without ionising radiation and considered to be an applicable method for scientific purposes (cf. WANG, CHANG (2007), PASSARINI et al. (2015)), since it is sensitive to hydrogen atoms. On the other hand, moisture discrimination may be supported by means of contrast agents with respect to the scope of investigation. Regarding the radiometric observation of RDP formation (refer to GRUCHOT (2009)), gold particles are proposed to be incorporated in terms of mat forming and to serve as marking of particular panel layers during hot-pressing as contrast toward the water vapour movement superimposed to densification and relaxation. Likewise, WANG et al. (2007) add 1 % (by weight) gold nano- and micro-particles to their wood plastic composites and achieve improved X-ray CT contrast. Moisture contrast may be increased by adding medical contrast agents to the water, e. g., based on iodine or barium. However, the substances must be considered to potentially bias the moisture movement due to interdependencies and the rather large size of their chemical compounds compared to the H_2O molecule.

Beyond composition and MC, the impact of WBC structure, particularly regarding densification, is pointed out in terms of the transmission measurements and result discussions in Chapter IV–4.3.2.4 and IV–6.5. Accordingly, the commonly utilised step or reference wedges are inferred to be inappropriate for both calibration and as representative reference owing to structural conditions. Step wedges were generally applied in radiography as reference parallel to the object in the image (on a film). Material type and the range of step height (i. e. transmission distance s_T) correspond to the attenuation potential of the investigated specimens. This was also common practise in former film densitometry on wood, e. g., by RUDMAN et al. (1969), who improved previous

procedures, where cellulose acetate step wedges are simultaneously irradiated on the X-ray film to obtain a calibration of the optical contrast toward the material raw density. POLGE, LUTZ (1969) applied such methods for RDP determination on particleboard. GRUCHOT (2009) utilised specimens of lab-made MDF with homogeneous RDP and increasing transmission distances $s_T = 5 \ldots 70\,\text{mm}$ for the calibration of his X-ray device via measuring series at different EMC. SOLBRIG et al. (2011) propose a step wedge as calibration sample for their RDP measurements, which is stacked out of stripes of customary thin MDF ($\bar{\rho} = 928\,\text{kg/m}^3$) with a panel thickness of $t_{\text{nom}} = \Delta s_T = 3\,\text{mm}$ and radiation transmission perpendicular to the panel plane. As already pointed out in Chapter IV–6.6, step wedges are, however, found to be insufficient as calibration or reference in WBC densitometry. With particular respect to RDP measurement, a step wedge made of homogenous material with varying s_T does not represent the actual structure of the panel specimen considering the raw density gradient along its cross-section. Even though ρ_A along the beam path in a considered layer of the specimen is equivalent to the corresponding step of the wedge, the respective densification, and thus, the porosity, may crucially differ. Consequently, the scattering conditions differ between step wedge material and WBC specimen structure, hence, there will be different radiation build-up, as comprehensively discussed in Chapter IV–6.3. Eventually, a calibration curve from a step wedge made of homogeneous material is considered not to be valid for the intended raw density range of the inhomogeneous specimens, where the significance of the bias depends on the individual beam geometry of the measuring setup. Moreover, the validity decreases, where considerably different raw densities of the calibration material are applied in comparison to the measured samples, e. g., in the case of ρ_A device calibration by means of ready-pressed panels for measurements on just pre-densified furnish mats. Regardless of structural conditions and radiation build-up, a reference wedge made of homogeneous material with predefined density may serve to verify an

RDP measuring device (with self-calibration according to Figure II-14) regarding its beam hardening impact. To this end, a PMMA[38] specimen with $s_T = 50$ mm is to be machined such that a wedge profile is obtained mimicking a common RDP shape. Here, the small section with total s_T corresponds to a surface layer and should yield measuring results equal to $\rho_{PMMA} = 1189$ kg/m^3. Beam hardening yields a density decrement (refer to Figure IV-76) depending on the impact.

Beam hardening is an unavoidable consequence of X-ray application even with pre-filters and quantified via the introduced beam hardening index $BHi(E, \rho_A)$ [%$\Delta\bar{E}$/%$\Delta\rho_A$] (refer to Chapter IV–6.2). Its determination requires systematic X-ray spectra measuring series or sophisticated simulations considering both transmission spectra through predefined absorbers with particular density steps as well as recording of the initial spectrum. Hence, it is considered to be a method for application in research and development as well as for re-design processes of X-ray densitometry systems rather than for evaluation of common measuring practice. The same applies to beam hardening correction. As basically pointed out in Chapter II–2.4, several correction methods exist for various applications with respective restrictions. Regardless of their potential benefits, none was directly applied. Since any correction potentially distorts the actual measuring information, correction of the transmission measuring results was avoided. The intention was not to correct the influence parameters but instead to evaluate them. Moreover, VDI/VDE 2630-1.2 (2018) considers the mostly empirical correction algorithms for non-linearity not to yield absolute measuring values. Any correction of non-linearities or corresponding simulation of the ideal conditions can only be as good as its algorithm (i. e. its representation of the real conditions) and its data input. An appropriate description of the mathematic-physical context is instead preferred. Here, boundary conditions, i. e., toward zero and infinity, must be considered. Such determinations must further

apply both the actual material and measuring setup. This is ultimately achieved by the enhanced law of attenuation based on a power function approach for the context between measured attenuation $\ln T^{-1}$ and area density ρ_A.

---

[38] PMMA with $\rho = 1189$ kg/m^3 in the order of wood or labMDF with $\rho_{nom} = 1056$ kg/m^3 (refer to Chapter IV–1.2).

2   Prospects

All findings and the deduced approach, to describe radiation attenuation by means of a double-exponential law, enhance the understanding of X-ray densitometry on wood-based composites (WBCs). The beneficial application of improved radiometric methods for wood and WBCs in research and industry is clarified in Chapter V–3. However, the present thesis does not claim to provide an extensive measuring series. Instead, it serves as an exploratory study to determine the relevant context. Therefore, prospective investigations are needed to verify the findings and consequent implications. To this end, comprehensive measuring series are pending with application of the proposed methods and systematic variation of the identified influence parameters with respect to the material such as

- WBC structure (mat vs. panel and panel RDP),
- ash content,
- partly MC,
- further additives (e. g. hydrophobic agents or fire retardants)

as well as those factors, which are inferred not to significantly affect $\mu/\rho\,(E)_{\mathrm{mix}}$ such as (organic) adhesive resins or (European) wood species without bark and apart from tropical hardwoods, bamboo, and annual plants with high ash contents. Here, numerous measuring series can be performed on predefined lab-made panels. Moreover, some of the verifications can be carried out in industrial environments with the application of typical ranges of conditions by means of X-ray measuring device installations in regular production lines. Correspondingly determined measuring ranges following the recommendations for energy definition are to be utilised for verification of the double-exponential approach by further measurements. With respect to boundary conditions, the validity of the individually found additional exponent κ needs to be evaluated toward zero and respectively high ρ_{A} of the range. Particularly the estimation of the energy-dependent $\mu/\rho\,(E)$ via extrapolation of eq. (IV-55) toward low $\rho_{\mathrm{A}} = 0 \ \mathrm{kg/m^2}$ requires a verification, since it represents the conditions

(particularly governed by beam hardening) at the beginning of the beam path through the specimen under investigation.

The same applies to radiation parameters with systematic measuring series considering

- beam geometry (incl. apertures),
- energy level,
- X-ray spectra and
- corresponding pre-filter application.

The results from (initial and transmission) spectra measurement should be verified by means of a further (measuring) method, i. e., a further spectrometer. In comprehensive series, the particular consideration of scattering conditions, energy calibration, and inherent filtering of the detector is required, thus, the avoidance to modify the original setup of the X-ray device in terms of distances, apertures, and beam collimation. Regarding beam hardening impact, RDP results are to be compared from repeat measurements with and without pre-filtering on both customary WBCs and specifically lab-made panels with predefined RDPs as well as new composites with extreme raw density ranges along the gradients, e. g., sandwich panels with foam cores (cf. SHALBAFAN et al. (2012)). Here, scattering is also considered to contribute to variations in the RDP results depending on the beam geometry. The individual evaluation of the radiation-physical effects beam hardening and scattering is considered to be valuable information. The examination is, however, elaborate due to the superimposition of the phenomena highly depending on the X-ray setup. Instead, the results would correspond to the employed device with general validity only to a limited extent. However, scattering estimations and beam hardening corrections are still part of current CT research as partly pointed out in Chapter II–2.4 and II–2.5 particularly in the context of industrial applications (cf. SHEDLOCK et al. (2015), WÜRFL et al. (2018) or SHIROMA et al. (2019)). The applicability of such new methods on wood and WBC investigation should be evaluated. Ultimately, the proposed explanatory conceptual model for radiation transmission through porous composites can be applied and

refined. To this end, an enhancement with respect to a more sophisticated modelling of photon transport through the WBC mat or panel and interaction with the matter is required. Here, actual structural models should be utilised based on available (refer to examples in Chapter IV–3.3) or explicitly determined μXCT data. Beyond radiometric methods, other structural characterisation should be considered, e. g., by means of microtomed cross-sections (cf. REBOLLEDO et al. (2018)).

X-ray measurements and general NDT (by means of ionising radiation) on wood and WBCs are comparable to medical applications. This is not only with regards to the energy range. Moreover, particular methodical problems are similar, i. e., contrast considerations owing to the low-Z soft matter with solely slight variation of the constituents as in mammography. Therefore, respective medical findings are worth reviewing for potential adaption to scientific or even industrial X-ray densitometry on wood and WBCs. Regarding measuring tasks such as wood-moisture discrimination, where simple X-ray transmission measurements fail, a method combination is expected to serve as prospective means of choice. The combined evaluation (i. e. data fusion) of measuring data from complementary methods is rising in current research and generally feasible since general computation performance and the potential of particular algorithms for data evaluation has considerably increased. Particularly in the field of applied sciences, the adaption of methods appears reasonable rather than the fundamental development of new techniques. Such method combination approaches generally exist and were partly already applied on wood, e. g., by

- HASENSTAB et al. (2009) with ultrasonic echo, X-ray backscattering, as well as X-ray and neutron radiography,
- SANABRIA et al. (2013) with air-coupled ultrasound and X-ray,
- LANVERMANN et al. (2014b) with neutron radiography and digital image correlation,

- SCHICKERT et al. (2017) with CT by means of ultrasound, radar, and X-ray, respectively, and
- TIITTA et al. (2017) with air-coupled ultrasound and electrical impedance spectroscopy,

or on other sophisticated composite material such as reinforced concrete by COTIČ et al. (2013) with multimodal data fusion. Regarding radiometric methods, neutron and X-ray radiography is increasingly combined to provide additional information of the investigated object, e. g., where only one of the methods is not able to resolve particular internal structures or yield sufficient contrast. Some of the available neutron beamlines at large-scale facilities already include an additional X-ray transmission setup, which either may be moved in line with the neutron beam axis (sequential) or is installed across the neutron beamline (simultaneous acquisition) according to the report of KAESTNER et al. (2017). Note the different neutron energies, and thus the corresponding penetration potential at the respective beamlines. However, appropriate method combination utilises the benefits of the one to overcome the insufficiencies of the other and to gain additional information, which would not be revealed by exclusive application of one of the considered techniques. Note here, LAHAT et al. (2015) point out the opportunities and challenges of multimodality across various disciplines. With focus on measuring tasks on WBCs, the combination of X-rays and neutrons appears advantageous for further examination of densification and water vapour movement in WBCs during hot-pressing, thus, to enhance the distinction of dry wood matter and moisture, and therefore, to continue the work of SOLBRIG et al. (2015b). To this end, neutron beamlines should be equipped with a complementary X-ray transmission setup vertically aligned to the neutron beamline, i. e., simultaneous X-ray and neutron data acquisition as holistic approach for the dynamic in-situ investigation of the hot-pressing process.

3 Implications regarding the application in research and industry

Most of the considered aspects and findings of the present thesis are apparently far beyond daily business of X-ray measuring system applications on WBCs. Nevertheless, practice-oriented implications can be derived for both science and industry, since the found radiation-physical interdependencies are considerable to reliably fulfil the respective measuring tasks. This is not only relevant for WBCs, the findings may be transferred to solid wood and virtually all other lignocellulosic materials as well as comparable low-Z matter and composites made therefrom with various possible material combinations. Regarding the utilisation of densitometry devices, the individual conditions differ depending on the field of application. In WBC production, inline X-ray measuring systems are common in the forming and press line but come with different technical levels to fulfil the measuring task depending on the age and manufacturer of the devices. However, with general technical progress and demand for improvements, the requirements on the measuring systems likewise increase. The lab devices for RDP measurement are prevalent in both industry and institutes associated with wood research. The latter often feature a considerably wider material range to be investigated. Beyond existing systems, research studies also require modified or particularly developed X-ray setups with regard to the various densitometry applications or related examinations. For RDP determination in WBC research and development, however, commercially available densitometry lab devices are employed for panel characterisation rather than to individually develop such X-ray equipment.

In wood science, a further challenge for X-ray densitometry is the application on decayed wood. Here, it is considered to be non-trivial to detect inner rod in the early state of decay, since a raw density decrement during degradation is associated with a MC increment. Thus, there is no distinct variation from the X-ray beam's point of view, which makes in-situ investigations of early-state fungal wood decay difficult by means of X-ray densitometry. Here, HERVÉ et al. (2014) were only able to measure a raw density loss by means of X-ray CT on the oven-dry specimens of incubated beech blocks after up to 150 days of wood degradation. In the fresh state, no clear detection of decayed areas was possible. Accordingly, MACCHIONI et al. (2007) compute the raw density decrement as difference between the decayed and non-degraded reference specimens. The measuring task of (in-situ) early-state wood decay identification is considered to be not manageable by simple transmission measurements on one energy level. On the contrary, an aforementioned method combination may provide improved solutions in particular cases. The same applies to the reliable in-situ discrimination of moisture and wood matter (particularly below FSP), where the components reveal similar attenuation potential on certain energy levels following the comprehensive implications in Chapter V–1. The difference method between the moist and the previous dry state may be applied as far as there is a respective reference condition. However, such computation does not enable the in-situ investigation of moisture movement with superimposed raw density variations.

Regarding ordinary measuring series for RDP determination in terms of research applications, the common lab devices are confronted with considerably different raw densities of the investigated materials ranging from foams to minerally-bonded WBCs. Thus, X-ray energy predefinition cannot be limited to one setting for the different samples. It has to follow the recommendations in Chapter IV–6.4 for the appropriate definition of individual measuring and energy ranges. For standard applications in the WBC industry with conventional panels, the customary RDP measuring devices may be sufficient for the task commonly employing one energy level, as long as their X-ray design and data evaluation follows above findings regarding X-ray energy predefinition, beam hardening prevention, and scattering consideration. Moreover, extreme raw density ranges (in terms of distinct SL/CL ratios) may occur within one specimen in the case of new composites such as PB with foam cores (cf.

SHALBAFAN et al. (2012)) or comparable sandwich panels. Regarding such composites with extreme RDPs (i. e. thin high-density surface layers (SL) on low-density core layers (CL) dominating the cross-section), inappropriate X-ray devices yield underestimated SL maxima with more significant measuring errors compared to MDF or PB with typical RDPs (refer to Chapter IV–4.3.1). The same applies to RDP determination on special lignocellulosic material such as palm wood, where a preliminary test revealed the ratio $\rho_{max}/\rho_{min} \approx 3$ (oil palm), which is about twice that of typical MDF SL/CL ratios (refer to Table IV-24). Furthermore, even more extreme differences, with up to factor five, occur between the structural members of palm wood, i. e., vascular bundles with $\rho = 940 \ \mathrm{kg/m^3}$ and parenchyma with $\rho = 190 \ \mathrm{kg/m^3}$ according to FATHI (2014) with exemplary values for one board of coconut palm. Here, both RDP measurement devices and X-ray CT systems for more detailed structural evaluations must consider the identified radiation-physical interdependencies to yield valid raw density results. Moreover, FRÜHWALD-KÖNIG (2019) proposes the application of X-ray densitometry for grading of oil palm lumber as basis for the optimisation of lengthwise ripping and cross cutting of in order to obtain products with homogeneous properties. A further field of latest research with RDP determination is the solid wood modification. LI et al. (2018) preferably apply an X-ray RDP measuring system for characterisations of their sandwich compressed wood regarding the impact of preheating. Note here, no reference method for result verification is performed. Hence, the employed device must be reliable and appropriate for the measuring task with respect to the partly extreme RDPs. Otherwise, implications from such studies may be considered as questionable regarding the impact of the varied parameters of the applied wood processing techniques. Here, RAUTKARI et al. (2011) also identify specimen heterogeneity to bias densitometry results of their employed X-ray device, where wood composites with discrete layers of varying raw density were studied. However, there is a growing occurrence of such research applications with

solid wood densification and resulting RDP evaluation in the context of processing parameters or further material properties (cf. KUTNAR et al. (2009), RAUTKARI (2012), DÖMÉNY et al. (2018), KÚDELA et al. (2018), and GAO et al. (2019)). Such processing via consolidation of low-density lignocellulosic material may also be applied to the aforementioned palm wood or low-density softwood in general. Here, FITCH (2018) points out the demand for innovations in the Southeast Asian wood industry.

Consequently, reliable X-ray measurements and valid densitometry results are inevitable for the significance of research data based on RDP determination. This applies not only to special composites. Also the evaluation of regular WBC modifications regarding the effects on RDP requires such appropriate X-ray densitometry systems. Numerous examinations regarding the process and material parameters exist, e. g.,

- IŽDINSKÝ, ŠTEFKA (2009) via press diagram modification or
- BELINI et al. (2014) considering WBC development,

where further reference is made to the listing of relevant reports, theses, and textbooks in Chapter I. As already pointed out by SOLBRIG et al. (2014a), true RDP data is, furthermore, required for modelling and computation of elasto-mechanical panel properties according to PLATH (1971). Moreover, the simulation of the RDP formation during hot-pressing following THOEMEN, HUMPHREY (2006) and THOEMEN et al. (2006) as well as the integration of the enhanced algorithms into the process control system of modern WBC plants following THÖMEN, HOMERIN (2017) and BERNARDY, STEFFEN (2017) with internal calibration of the modelling based on RDP laboratory results would be crucially affected by poor densitometry data.

To conclude, with regard to the relevance of reliable and valid RDP determination, inappropriate devices may yield biased measuring results. Here, more extreme RDPs cause, in turn, severer bias of the resulting slopes due to beam hardening and radiation build-up (scattering), since the effects and the interdependencies depend on ρ_A or ρ. The same applies to wide raw

density ranges of the investigated specimens in general. Consequently, the measured RDP shapes produced by inappropriate devices may appear flattened and particularly the ρ_{max} values are underestimated, thus, the significance of any panel property correlations particularly to the raw density extrema must be considered to be likewise underestimated. Ultimately, all RDP measuring results of previous studies are considered to be error-prone and correspondingly determined correlations are recommended for revision regarding the validity particularly of extreme RDPs, which were determined by supposedly insufficient measuring devices.

Reliability of the devices and validity of the results are the fundamental requirements for the employment of X-ray measuring systems in the WBC industry both for inline installation and in the quality lab. Here, reliability and validity must be measurable and verifiable by respective quantities. The evaluation of radiometric systems regarding their accuracy and precision for particular applications is a rising topic in wood and WBC research, where RAUTKARI et al. (2011), SOLBRIG et al. (2014a), and DIRESKE et al. (2017) discuss the RDP determination. Such comparative investigations are not yet published considering inline systems for ρ_A measurements except SOLBRIG et al. (2015d). They propose a procedure to determine the achievable measuring precision by means of the total uncertainty based on a statistical measuring signal analysis. For the exemplarily employed setup, ρ_A measuring precision is found in the range of +/-0.2 % (repeatability on 99.73 % confidence level). Accordingly, SOLBRIG et al. (2015d) propose an approach to verify the measuring system capability via adaption of common methods for measuring system analysis in terms of process qualification. However, such methods need to be refined and established as regular procedures in the WBC industry, e. g., for site acceptance tests and for X-ray measuring system verification on a regular basis.

For further theoretical evaluation of the expectable measuring accuracy, two of the introduced characteristic values can be applied. Based on a virtual or known variation range of the material composition, the differential mass attenuation coefficient of the mixture $\delta\,\mu/\rho\,(E)_{\mathrm{mix}}$ is applied to compute the corresponding range of $\mu/\rho\,(E)$. Here, Table IV-38 provides exemplary values for four energies or further $\delta\,\mu/\rho\,(E)_{\mathrm{mix}}$ are computed following eq. (IV-43). Moreover, such estimations of $\mu/\rho\,(E)$ variation considering energy variations depending on $\Delta\rho_A$ can be deduce from the beam hardening index BHi according to eq. (IV-44) with exemplary values in Table IV-43 (note, only valid for the corresponding X-ray setups). With the energy range for a considered ρ_A range, the respective $\mu/\rho\,(E)$ ranges are determined by means of tabulated data for the material under investigation (e. g. in Table VII-12 for labMDF at $MC = 9.5$ %). Regarding both composition and energy, the potential range of $\mu/\rho\,(E)$ is applied in the transformation of the attenuation law eq. (II-11) to compute the resulting uncertainty or error of ρ_A measurement. Particularly the latter via BHi is considered to be best suited in terms of X-ray device development whereas measuring uncertainties via $\delta\,\mu/\rho\,(E)_{\mathrm{mix}}$ due to material composition variations are relevant in the common densitometry practice.

In general, the quality of measuring data should be critically evaluated in practice, since consequent conclusions can only be as good as their data basis. Valid measuring results from reliable devices are indispensable with regards to inline as well as laboratory X-ray densitometry in WBC production and research. Considerations for improving the evaluation of process data for quality assurance and process control have existed for decades. Here, particularly the approaches for process modelling (cf. LOBENHOFFER (1991), BERNARDY, SCHERFF (1997), HASENER (2004)) and panel property simulation (cf. THOEMEN (2000)) require appropriate data quality in order to make good decisions. The same applies to the regular process control by the operators in a WBC production plant. However, data quality is still a crucial aspect, since there is a growing demand for inline measuring systems in the WBC production process and their integration into automated process control with increasing requirements on the panel properties. Here, e. g., thickness gauges are already well-integrated into the hot-press control loop to automatically maintain

the target thickness. Likewise, X-ray area density gauges will be integrated in the forming line automation to provide the actual value distribution within the furnish mat (cf. SOLBRIG (2018)). Notwithstanding the above and regardless of automation, technologists may be familiar with their (potentially poor) measuring results and determined density gradients as likewise discussed by SOLBRIG et al. (2014a). Accordingly, their knowledge of the individual relation between process parameters and panel properties may be sufficient for appropriate quality assurance within the production plant. However, a comparability of the results is not ensured between the plants (of the manufacturer group) or toward competitors. The round robin test in Chapter IV–4.3.1 unveiled considerable differences between lab devices, which is considered to likewise occur in the case of hitherto inline densitometry systems. Hence, and as already concluded, the capability of X-ray densitometry systems must be verified in terms of practical application in research and industry by appropriate validation procedures with well-defined acceptance criteria for the individual measuring processes.

Finally, and from a historical viewpoint, the basic principle of transmission measurements by means on ionising radiation and the application for densitometry on WBCs has existed for decades. There was continuous development of the devices, where also monoenergetic radioisotopes (such as ^{241}Am) were replaced by polychromatic X-ray tubes. Several radiation-physical issues remained, however, unconsidered, thus, insufficiencies occurred. Beyond that, the technical progress in further components as well as increasing requirements regarding measuring accuracy and precision are reported, i. e., there is an increasing demand for capable measuring equipment in the WBC sector instead of former rough indicators. Hence, X-ray transmission measurement is not considered to be inappropriate as method for densitometry on WBCs. On the contrary, the peculiarities of the applied radiation in combination with the investigated material should be explicitly considered to increase the capability of modern X-ray measuring systems for WBC production and science. Accord-

ingly, the realisation of the findings and implications of the present thesis will result in capable X-ray densitometry devices for the various measuring tasks on WBCs likewise concluded by SOLBRIG et al. (2015a). Therefore, measuring device manufacturers are encouraged to develop appropriate equipment and algorithms. Here, SOLBRIG (2017) points out some concepts of modern inline X-ray measuring systems and how they are employed according to their different measuring tasks in the forming and press line. SOLBRIG (2018) reports about practical experiences with a capable X-ray measuring and inspection system for furnish mats. Ultimately, capable X-ray densitometry systems provide a practical benefit in WBC industry with process and product enhancements. As commonly known (cf. SOLBRIG et al. (2014b)), the proper integration of reliable measuring equipment into process and quality control facilitates to avoid overdosing and consequently to achieve savings in raw material (wood furnish and adhesive resin) and energy consumption, therefore, production costs, as well as to maintain or to improve panel properties, and to meet the growing requirements in general.

Section VI
Bibliography

1 Literature

A COSTA et al. (1999)
Acosta, E.; Llovet, X.; Coleoni, E.; Salvat, F.; Riveros, J. A. – Simulation of x-ray spectra generated by electron impact on solids. X-Ray Spectrometry 28 (1999) 2. pp. 121-127.

A KÇA, E RZENEOĞLU (2014)
Akça, B.; Erzeneoğlu, S. Z. – The Mass Attenuation Coefficients, Electronic, Atomic, and Molecular Cross Sections, Effective Atomic Numbers, and Electron Densities for Compounds of Some Biomedically Important Elements at 59.5 keV. Science and Technology of Nuclear Installations 2014 (2014) pp. 1-8.

A LLES, M UDDE (2007)
Alles, J.; Mudde, R. F. – Beam hardening: Analytical considerations of the effective attenuation coefficient of x-ray tomography. Medical Physics 34 (2007) 7. pp. 2882-2889.

A LS-N IELSEN, M CM ORROW (2011)
Als-Nielsen, J.; McMorrow, D. – Elements of Modern X-ray Physics. 2nd ed. John Wiley & Sons, Ltd: The Atrium, Southern Gate, Chichester, West Sussex, 2011. 434 p.

A LVAREZ, M ACOVSKI (1976)
Alvarez, R. E.; Macovski, A. – Energy-selective reconstructions in X-ray computerised tomography. Physics in Medicine & Biology 21 (1976) 5. pp. 733.

A NAGNOSTOPOULOS (2006)
Anagnostopoulos, G. – Untersuchung des Einflusses der Patientenkörperanatomie auf die Dosimetrie und Entwicklung eines analytischen Dosisberechnungsmodells für die 192-Ir HDR Brachytherapie. Diss. Ruprecht-Karls-Universität, Naturwissenschaftlich-Mathematische Gesamtfakultät, Heidelberg, 2006. 166 p.

A NKERHOLD et al. (1999)
Ankerhold, U.; Berens, R.; Ambrosi, P. – X Ray Spectrometry of Low Energy Photons for Determining Conversion Coefficients from Air Kerma, Ka, to Personal Dose Equivalent, Hp(10), for Radiation Qualities of the ISO Narrow Spectrum Series. Radiation Protection Dosimetry 81 (1999) 4. pp. 247-258.

A NKERHOLD (2000)
Ankerhold, U. – Catalogue of X-ray spectra and their characteristic data - ISO and DIN radiation qualities, therapy and diagnostic radiation qualities, unfiltered X-ray spectra. PTB-Bericht, PTB-Dos-34. Physikalisch-Technische Bundesanstalt, Braunschweig, Germany, 2000. 121 p.

A NON. (1992)
Anon. – ComScan - X-Ray System for Non-Destructive Testing. Aircraft Engineering and Aerospace Technology 64 (1992) 3. pp. 14.

A NSELL (2015)
Ansell, M. P. (Ed.) – Wood composites. Elsevier: Amsterdam, 2015. 455 p.

A RUNMUTHU et al. (2013)
Arunmuthu, K.; Ashish, M.; Saravanan, T.; Philip, J.; Rao, B. P. C.; Jayakumar, T. – Simulation of beam hardening in X-ray tomography and its correction using linearisation and pre-filtering approaches. Insight - Non-Destructive Testing and Condition Monitoring 55 (2013) 10. pp. 540-547.

ATTIX (2004)
Attix, F. H. – Introduction to radiological physics and radiation dosimetry. WILEY-VCH Verlag: Weinheim, 2004. 628 p.

AUTORENKOLLEKTIV (1988)
Autorenkollektiv – Lexikon der Holztechnik. 3rd ed. Fachbuchverlag: Leipzig, 1988. 928 p.

BAETTIG et al. (2006)
Baettig, R.; Rémond, R.; Perré, P. – Measuring moisture content profiles in a board during drying: a polychromatic X-ray system interfaced with a vacuum/pressure laboratory kiln Wood Science and Technology 40 (2006) 4. pp. 261-274.

BALAIC et al. (1995)
Balaic, D. X.; Nugent, K. A.; Barnea, Z.; Garrett, R.; Wilkins, S. W. – Focusing of X-rays by Total External Reflection from a Paraboloidally Tapered Glass Capillary. Journal of Synchrotron Radiation 2 (1995) 6. pp. 296-299.

BANDEL (1995)
Bandel, A. – Gluing Wood. ed. catas: Udine, 1995. 303 p.

BANJADE et al. (2001)
Banjade, D. P.; Tajuddin, A. A.; Shukri, A. – A study of Rhizophora spp wood phantom for dosimetric purposes using high-energy photon and electron beams. Applied Radiation and Isotopes 55 (2001) 3. pp. 297-302.

BARBU et al. (2014)
Barbu, M. C.; Hasener, J.; Bernardy, G. – Modern Testing of Wood-Based Panels, Process Control, and Modeling. In: Aguilera, A.; Davim, J. P. (Eds.) Research Developments in Wood Engineering and Technology. IGI Global: Hershey PA, USA, 2014. pp. 90-130.

BARRETT, SWINDELL (1996)
Barrett, H. H.; Swindell, W. – Radiological imaging - The theory of image formation, detection, and processing. Revised ed. Academic Press: San Diego Boston New York London Sydney Tokyo Toronto, 1996. 706 p.

BAYER (2005)
Bayer, A. – X-ray attenuation techniques to explore the dynamics of water in porous media. Diss. Ruperto Carola University of Heidelberg, Combined Faculties for the Natural Sciences and for Mathematics, Heidelberg, Germany, 2005. 116 p.

BEALL (2000)
Beall, F. C. – Subsurface Sensing of Properties and Defects in Wood and Wood Products. Subsurface Sensing Technologies and Applications 1 (2000) 2. pp. 181-204.

BEALL (2007)
Beall, F. C. – Industrial application and opportunities for nondestructive evaluation of structural wood members. Maderas. Ciencia y tecnología 9 (2007) 2. pp. 127-134.

BECKMANN et al. (2008)
Beckmann, F.; Herzen, J.; Haibel, A.; Müller, B.; Schreyer, A. – High density resolution in synchrotron-radiation-based attenuation-contrast microtomography. In: Proc. SPIE 7078, Developments in X-Ray Tomography VI, 70781D, Optical Engineering + Applications. San Diego, California, United States. SPIE, 2008. pp. 1-13.

BELINI et al. (2014)
Belini, U. L.; Fiorelli, J.; Savastano Jr, H.; Tomazello Filho, M. – Density profile as a tool in assessing quality of new composite. Materials Research 17 (2014) pp. 138-145.

BENTHIEN et al. (2014a)
Benthien, J. T.; Heldner, S.; Seppke, B.; Bähnisch, C.; Ohlmeyer, M. – Innovativer Ansatz zur Bestimmung der Faserlänge - Automatisierte und reproduzierbare Methode zur Vermessung von Faserstoff entwickelt. Holz-Zentralblatt 140 (2014a) 41. pp. 1000.

BENTHIEN et al. (2014b)
Benthien, J. T.; Bähnisch, C.; Heldner, S.; Ohlmeyer, M. – Effect of Fiber Size Distribution on Medium-Denstiy Fiberboard Properties Caused by Varied Steaming Time and Temperature of Defibration Process. Wood and Fiber Science 46 (2014b) 2. pp. 175-185.

BENTHIEN, OHLMEYER (2017)
Benthien, J. T.; Ohlmeyer, M. – Influence of face-to-core layer ratio and core layer resin content on the properties of density-decreased particleboards. European Journal of Wood and Wood Products 75 (2017) 1. pp. 55-62.

BERGSTEN et al. (2001)
Bergsten, U.; Lindeberg, J.; Rindby, A.; Evans, R. – Batch measurements of wood density on intact or prepared drill cores using x-ray microdensitometry. Wood Science and Technology 35 (2001) 5. pp. 435-452.

BERGSTROM JR, PRATT (1997)
Bergstrom Jr, P. M.; Pratt, R. H. – An overview of the theories used in compton scattering calculations. Radiation Physics and Chemistry 50 (1997) 1. pp. 3-29.

BERNARDY, SCHERFF (1997)
Bernardy, G.; Scherff, B. – Prozessmodellierung führt zur Online-Qualitätskontrolle und Prozessoptimierung bei der Span- und Faserplattenproduktion. Holz als Roh- und Werkstoff 55 (1997) 2. pp. 133-140.

BERNARDY, STEFFEN (2017)
Bernardy, G.; Steffen, A. – Modernste Prozessleittechnik - der Weg zur selbstoptimierenden Holzwerkstoffproduktionsanlage mit "Prod-IQ® Next". In: IHD (Ed.) 12. Holzwerkstoffkolloquium. Dresden. Institut für Holztechnologie Dresden gemeinnützige GmbH (IHD), 2017. pp. 166-176.

BETZ et al. (2002)
Betz, M.; Coen, D.; Deimling, S.; Kreißig, J. – Thermische Verwertung von Holzprodukten - Inputabhängige Modellierung der End-of-Life Prozesse von Holz. PE Europe GmbH: Leinfelden-Echterdingen, 2002. 119 p.

BEYER et al. (2018)
Beyer, M.; Kránitz, D.; Bremer, M.; Peters, J.; Fischer, S.; Bues, C.-T.; Niemz, P. – Effect of natural aging on the chemical composition of Norway spruce, fir, and European oak wood. PRO LIGNO 14 (2018) 2. pp. 3-19.

BILDERBACK, FONTES (1997)
Bilderback, D. H.; Fontes, E. – Glass capillary optics for making x-ray beams of 0.1 to 50 microns diameter. AIP Conference Proceedings 417 (1997) 1. pp. 147-155.

BILLIANI et al. (1990)
Billiani, J.; Lederer, K.; Dunky, M. – Untersuchung der Molmassenverteilung von Harnstoff-Formaldehyd-Leimharzen durch GPC gekoppelt mit Lichtstreuung. Die Angewandte Makromolekulare Chemie 180 (1990) 1. pp. 199-208.

BIZIKS et al. (2019)
Biziks, V.; Van Acker, J.; Militz, H.; Grinins, J.; Van den Bulcke, J. – Density and density profile changes in birch and spruce caused by thermo-hydro treatment measured by X-ray computed tomography. Wood Science and Technology 53 (2019) 2. pp. 491-504.

BJÄRNGARD, SHACKFORD (1994)
Bjärngard, B. E.; Shackford, H. – Attenuation in high-energy x-ray beams. Medical Physics 21 (1994) 7. pp. 1069-1073.

BJEOUMIKHOV et al. (2005)
Bjeoumikhov, A.; Bjeoumikhova, S.; Wedell, R. – Capillary Optics in X-Ray Analytics. Particle & Particle Systems Characterization 22 (2005) 6. pp. 384-390.

BJEOUMIKHOV et al. (2009)
Bjeoumikhov, A.; Bjeoumikhova, S.; Wedell, R. – New Developments and Applications of X-Ray Capillary Optics. Particle & Particle Systems Characterization 26 (2009) 3. pp. 97-106.

BLAŽEJ et al. (1979)
Blažej, A.; Šutý, L.; Krkoška, P.; Weiss, E.; Zeppenfeld, G. – Chemie des Holzes. VEB Fachbuchverlag: Leipzig, 1979. 208 p.

BLOHM (2015)
Blohm, J.-H. – Holzqualität und Eigenschaften des juvenilen und adulten Holzes der Douglasie (Pseudotsuga menziesii (Mirb.) Franco) aus süddeutschen Anbaugebieten. Diss. Universität Hamburg, Fakultät für Mathematik, Informatik und Naturwissenschaften, Fachbereich Biologie, Hamburg, 2015. 174 p.

BOEHME (1992)
Boehme, C. – Die Bedeutung des Rohdichteprofils für MDF. European Journal of Wood and Wood Products 50 (1992) 1. pp. 18-24.

BOSSHARD (1974)
Bosshard, H. H. – Holzkunde. Band 2: Zur Biologie, Physik und Chemie des Holzes. Birkhäuser Verlag: Basel, Stuttgart, 1974. 312 p.

BOSSI et al. (1988)
Bossi, R.; Friddell, K.; Nelson, J. – Backscatter X-ray imaging. Materials evaluation 46 (1988) 11. pp. 1462-1467.

BRADLEY et al. (1991)
Bradley, D. A.; Tajuddin, A. A.; Che Wan Sudin, C. W. A.; Bauk, S. – Photon attenuation studies on tropical hardwoods. International Journal of Radiation Applications and Instrumentation. Part A. Applied Radiation and Isotopes 42 (1991) 8. pp. 771-773.

BRAGG, PEIRCE (1914)
Bragg, W. H.; Peirce, S. E. – LXIV. The absorption coefficients of X rays. The London, Edinburgh, and Dublin Philosophical Magazine and Journal of Science 28 (1914) 166. pp. 626-630.

BRAR et al. (1994)
Brar, G. S.; Sandhu, A. K.; Singh, M.; Mudahar, G. S. – Exposure buildup factors for bakelite, perspex and magnox-A12 up to 40 m.f.p. using the interpolation method. Radiation Physics and Chemistry 44 (1994) 5. pp. 459-466.

BRAR, MUDAHAR (1996)
Brar, G. S.; Mudahar, G. S. – Energy dependence of the energy absorption buildup factor of HCO-materials. Radiation Physics and Chemistry 47 (1996) 6. pp. 795-799.

BRAR et al. (1999)
Brar, G. S.; Sidhu, G. S.; Singh, P. S.; Mudahar, G. S. – Buildup factor studies of HCO-materials as a function of weight fraction of constituent elements. Radiation Physics and Chemistry 54 (1999) 2. pp. 125-129.

BRASHAW et al. (2009)
Brashaw, B. K.; Bucur, V.; Divos, F.; Goncalves, R.; Lu, J.; Meder, R.; Pellerin, R. F.; Potter, S.; Ross, R. J.; Wang, X. – Nondestructive testing and evaluation of wood: a worldwide research update. Forest products journal 59 (2009) 3. pp. 7-14.

BROOKS, CHIRO (1976)
Brooks, R. A.; Chiro, G. D. – Beam hardening in X-ray reconstructive tomography. Physics in Medicine & Biology 21 (1976) 3. pp. 390-398.

BROWN et al. (1974)
Brown, D. J.; Nolan, P. F.; Rothwell, E. – Automatic continuous density determination using gamma radiometry. Non-Destructive Testing 7 (1974) 2. pp. 76-81.

BRÜNING et al. (2006)
Brüning, R.; Kuettner, A.; Flohr, T. (Eds.) – Protocols for multislice CT. 3rd ed. Springer: Berlin Heidelberg, 2006. 311 p.

BRUNO et al. (2005)
Bruno, L.; Christian, G. S.; Marion, K.; Boris, B.; Til Florian, G.; Olga, K.; Federico, Z.; Anatoly, S.; Irina, S. – Refractive x-ray lenses. Journal of Physics D: Applied Physics 38 (2005) 10A. pp. A218.

BÜCHERL, LIERSE VON GOSTOMSKI (2011)
Bücherl, T.; Lierse von Gostomski, C. – Real-time radiography at the NECTAR facility. Nuclear Instruments and Methods in Physics Research Section A: Accelerators, Spectrometers, Detectors and Associated Equipment 651 (2011) 1. pp. 175-179.

BUCK (1996)
Buck, J. – Schnelles Relionstruktionsverfahren für die 3D-Röntgen-Computertomographie in der Materialprüfung. Diss. Universität des Saarlandes, Technische Fakultät, Saarbrücken, 1996. 129 p.

BUCUR, LEWARK (1987)
Bucur, V.; Lewark, S. – Physical properties of beechwood increment cores. Holz als Roh- und Werkstoff 45 (1987) 1. pp. 36.

BUCUR et al. (1998)
Bucur, V.; Ansell, M. P.; Barlow, C. Y.; Pritchard, J.; Garros, S.; Deglise, X. – Physical Methods for Characterizing Wood Composite Panel Products. Holzforschung 52 (1998) 5. pp. 553-561.

BUCUR (2003a)
Bucur, V. – Techniques for high resolution imaging of wood structure: a review. Measurement Science and Technology 14 (2003a) 12. pp. R91.

BUCUR (2003b)
Bucur, V. – Nondestructive characterization and imaging of wood. Springer-Verlag: Berlin, Heidelberg, 2003b. 354 p.

BUDDRUS (1990)
Buddrus, J. – Grundlagen der organischen Chemie. 2nd ed. de Gruyter: Berlin, 1990. 861 p.

BUNBURY (1925)
Bunbury, H. M. – Die trockene Destillation des Holzes. Springer: Berlin, 1925. 351 p.

CAI (2008)
Cai, Z. – A new method of determining moisture gradient in wood. Forest products journal 58 (2008) 7-8. pp. 41-45.

CAMARA et al. (2008)
Camara, C. G.; Escobar, J. V.; Hird, J. R.; Putterman, S. J. – Correlation between nanosecond X-ray flashes and stick-slip friction in peeling tape. Nature 455 (2008) 7216. pp. 1089-1092.

CAO et al. (2018)
Cao, W.; Fardell, G.; Price, B.; Dewulf, W. – Simulation based study on the influence of deviations between the assumed and actual X-ray spectra on the performance of the Alvarez dual-energy method for beam-hardening correction. In: 8th Conference on Industrial Computed Tomography (iCT). Wels, Austria. 2018. pp. 1-8.

CHAPMAN (2004)
Chapman, K. M. – A study of two aspects of medium density fibreboard manufacture. University of Canterbury. Chemical and Process Engineering, 2004. 189 p.

CHEN et al. (2010)
Chen, S.; Liu, X.; Fang, L.; Wellwood, R. – Digital X-ray analysis of density distribution characteristics of wood-based panels. Wood Science and Technology 44 (2010) 1. pp. 85-93.

CLAUSON, WILSON (1991)
    Clauson, M. L.; Wilson, J. B. – Comparison of video and x-ray for scanning wood density. Forest products journal 41 (1991) 3. pp. 58-62.

COMPTON (1923)
    Compton, A. H. – CXVII. The total reflexion of X-rays. Philosophical Magazine Series 6 45 (1923) 270. pp. 1121-1131.

COPPOLA, REINIGER (1974)
    Coppola, M.; Reiniger, P. – Influence of the Chemical Composition on the Gamma-Ray Attenuation By Soils. Soil Science 117 (1974) 6. pp. 331-335.

COTIČ et al. (2013)
    Cotič, P.; Niederleithinger, E.; Bosiljkov, V.; Jagličič, Z. – NDT Data Fusion for the Enhancement of Defect Visualization in Concrete. Key Engineering Materials 569-570 (2013) pp. 175-182.

COWN, CLEMENT (1983)
    Cown, D. J.; Clement, B. C. – A wood densitometer using direct scanning with X-rays. Wood Science and Technology 17 (1983) 2. pp. 91-99.

COX (2016)
    Anon. – Itrax Multiscanner, 2016. http://www.coxsys.se/product-line/itrax-multiscanner/. Access date 28.08.2016.

CROUDACE et al. (2006)
    Croudace, I. W.; Rindby, A.; Rothwell, R. G. – ITRAX: description and evaluation of a new multi-function X-ray core scanner. In: Rothwell, R. G. (Ed.) New techniques in sediment core analysis - Geological Society special publication, 267. Geological Society: London, 2006. pp. 51-63.

DANKELMAN et al. (1976)
    Dankelman, W.; Daemen, J. M. H.; de Breet, A. J. J.; Mulder, J. L.; Huysmans, W. G. B.; de Wit, J. – Modern methods for the analysis of urea formaldehyde resins. Die Angewandte Makromolekulare Chemie 54 (1976) 1. pp. 187-201.

DAUBE (1883)
    Daube, W. – Chemische Analysen des Kern- und Splintholzes wichtiger Waldbäume. Forstliche Blätter - Zeitschrift für Forst- und Jagdwesen 20 (1883) 6. pp. 177-192.

DAVIDSON et al. (2003)
    Davidson, D. W.; Fröjdh, C.; O'Shea, V.; Nilsson, H. E.; Rahman, M. – Limitations to flat-field correction methods when using an X-ray spectrum. Nuclear Instruments and Methods in Physics Research Section A: Accelerators, Spectrometers, Detectors and Associated Equipment 509 (2003) 1–3. pp. 146-150.

DAVIS, ELLIOTT (2006)
    Davis, G. R.; Elliott, J. C. – Artefacts in X-ray microtomography of materials. Materials Science and Technology 22 (2006) 9. pp. 1011-1018.

DAVIS, WELLS (1992)
    Davis, J.; Wells, P. – Computed tomographymeasurements on wood. Industrial Metrology 2 (1992) 3-4. pp. 195-218.

DEETZ (2009)
    Deetz, R. – Asche- und Silicatgehalt von Einjahrespflanzen in Abhängigkeit vom phänologischen Entwicklungsstadium. Diplomarbeit Fachhochschule Eberswalde, Fachbereich Holztechnik, Eberswalde, 2009. 142 p.

DELGADO (2007)
    Delgado, V. – Determination of x-ray spectra from attenuation data by imposing a priori positiveness and bounded support: Theory and experimental validation. Medical Physics 34 (2007) 3. pp. 994-1006.

DELGADO (2009)
    Delgado, V. – Determination of x-ray spectra from Al attenuation data by imposing a priori physical features of the spectrum: Theory and experimental validation. Medical Physics 36 (2009) 1. pp. 142-148.

DEPAULA (1992)
    DePaula, E. V. C. M. – Design and fabrication of a mechanical device for "in-situ" measurement of density of a wood particle mat during pressing. The University of Tennessee, Knoxville, 1992. 95 p.

DEPPE, ERNST (1991)
    Deppe, H.-J.; Ernst, K. – Taschenbuch der Spanplattentechnik. 3rd ed. DRW-Verlag: Leinfelden-Echterdingen, 1991. 467 p.

DEPPE, ERNST (1996)
    Deppe, H.-J.; Ernst, K. – MDF - Mitteldichte Faserplatten. DRW-Verlag: Leinfelden-Echterdingen, 1996. 200 p.

DERESCH et al. (2010)
    Deresch, A.; Jaenisch, G. R.; Bellon, C.; Warrikhoff, A. – Simulation and Experimental Verification of X-Ray Spectra. In: Thompson, D. O.; Chimenti, D. E. (Eds.) Review of progress in quantitative nondestructive evaluation, volume 29, AIP Conference Proceedings. Kingston (Rhode Island). AIP, 2010. pp. 535-540.

DERESCH (2013)
    Deresch, A. – Personal communication: Discussion on X-ray spectra modelling by means of XRayTools. BAM, Berlin, Division 8.3: Non-destructive Testing, Radiological Methods, 19.03.2013.

DEROME et al. (2011)
    Derome, D.; Griffa, M.; Koebel, M.; Carmeliet, J. – Hysteretic swelling of wood at cellular scale probed by phase-contrast X-ray tomography. Journal of Structural Biology 173 (2011) 1. pp. 180-190.

DEROME et al. (2012)
    Derome, D.; Rafsanjani, A.; Patera, A.; Guyer, R.; Carmeliet, J. – Hygromorphic behaviour of cellular material: hysteretic swelling and shrinkage of wood probed by phase contrast X-ray tomography. Philosophical Magazine 92 (2012) 28-30. pp. 3680-3698.

DESLATTES (1969)
    Deslattes, R. – Estimates of X-ray attenuation coefficients for the elements and their compounds. Acta Crystallographica Section A 25 (1969) 1. pp. 89-93.

DIRESKE et al. (2017)
    Direske, M.; Schaaf, A.; Stephani, B.; Wenderdel, C. – Genauigkeit radiometrischer Messverfahren zur Rohdichteprofilanalyse von dreischichtigen zementgebundenen Spanplatten. Holztechnologie 58 (2017) 6. pp. 50-54.

DIVÓS et al. (1996)
    Divós, F.; Szegedi, S.; Raics, P. – Local densitometry of wood by gamma back-scattering. Holz als Roh- und Werkstoff 54 (1996) 4. pp. 279-281.

DÖMÉNY et al. (2018)
    Dömény, J.; Čermák, P.; Koiš, V.; Tippner, J.; Rousek, R. – Density profile and microstructural analysis of densified beech wood (Fagus sylvatica L.) plasticized by microwave treatment. European Journal of Wood and Wood Products 76 (2018) 1. pp. 105-111.

DONALDSON (2008)
    Donaldson, L. – Microfibril Angle: Measurement, Variation and Relationships – A Review. IAWA Journal 29 (2008) 4. pp. 345-386.

DROLET, DAI (2010)

Drolet, F.; Dai, C. – Three-dimensional modeling of the structure formation and consolidation of wood composites. Holzforschung 64 (2010) 5. pp. 619-626.

DU PLESSIS et al. (2013)

du Plessis, A.; Meincken, M.; Seifert, T. – Quantitative Determination of Density and Mass of Polymeric Materials Using Microfocus Computed Tomography. Journal of Nondestructive Evaluation 32 (2013) 4. pp. 413-417.

DUEHOLM (1995)

Dueholm, S. – Bestimmung des Rohdichteprofils von Holzwerkstoffplatten. HK (1995) 11. pp. 1394-1398.

DUEHOLM (1996)

Dueholm, S. – Determination of Density Profiles of Wood-Based Panels: From Traditional Off-Line Laboratory Techniques to Continuous, In-Line, Real-Time Monitoring. In: Wolcott, M. P. (Ed.) Proceedings of the Thirtieth Washington State University International Particleboard/Composite Materials Symposium. Pullman, Washington. 1996. pp. 45-57.

DUNKY, LEDERER (1982)

Dunky, M.; Lederer, K. – Untersuchungen der Molgewichtsverteilung von Harnstoff-Formaldehyd-Leimharzen. Die Angewandte Makromolekulare Chemie 102 (1982) 1. pp. 199-213.

DUNKY (1998)

Dunky, M. – Urea-formaldehyde (UF) adhesive resins for wood. International Journal of Adhesion and Adhesives 18 (1998) 2. pp. 95-107.

DUNKY, NIEMZ (2002)

Dunky, M.; Niemz, P. – Holzwerkstoffe und Leime: Technologie und Einflussfaktoren. Springer-Verlag: Berlin, 2002. 954 p.

EHRENBERGER (1991)

Ehrenberger, F. – Quantitative organische Elementaranalyse - Analysenmethoden zur Bestimmung der Elemente im Makro-, Mikro- und Spurenbereich in organischer und anorganischer Matrix. VCH Verlagsgesellschaft mbH: Weinheim, 1991. 884 p.

EL-KATEB, ABDUL-HAMID (1991)

El-Kateb, A. H.; Abdul-Hamid, A. S. – Photon attenuation coefficient study of some materials containing hydrogen, carbon and oxygen. International Journal of Radiation Applications and Instrumentation. Part A. Applied Radiation and Isotopes 42 (1991) 3. pp. 303-307.

EL-KHAYATT (2011)

El-Khayatt, A. M. – NXcom - A program for calculating attenuation coefficients of fast neutrons and gamma-rays. Annals of Nuclear Energy 38 (2011) 1. pp. 128-132.

ELDRIDGE et al. (1990)

Eldridge, H. B.; Pray, H. L.; Yee, B. – An X-ray wood densitometer. In: McGonnagle, W. J. (Ed.) International Advances in Nondestructive Testing Volume 15. Routledge Gordon & Breach: New York, NY, 1990. pp. 15-26.

ELEMENTAR (2016)

Elementar Analysensysteme GmbH – vario MACRO cube - The art of elemental analysis, 2016. https://www.elementar.de/en/products/organic-elemental-analysis/vario-macro-cube.html. Access date 05.02.2016.

ENGSTRÖM et al. (1996)

Engström, P.; Rindby, A.; Vincze, L. – Capillary Optics. ESRF-Newsletter (1996) July. pp. 30-31.

ESCHBACH et al. (1995)

Eschbach, W.; Nogler, P.; Schär, E.; Schweingruber, F. H. – Technical advances in the radiodensitometrical determination of wood density. Dendrochronologia 13 (1995) pp. 155-168.

EVANS (1994)
> Evans, R. – Rapid Measurement of the Transverse Dimensions of Tracheids in Radial Wood Sections from Pinus radiata. Holzforschung 48 (1994) 2. pp. 168-172.

EVANS (1999)
> Evans, R. – A variance approach to the x-ray diffractometric estimation of microfibril angle in wood. Appita journal 52 (1999) 4. pp. 283-289.

EVANS (1955)
> Evans, R. D. – The atomic nucleus. Tata McGraw-Hill Publishing Company Ltd.: Bombay, New Delhi, India, 1955. 987 p.

EWERT et al. (2008a)
> Ewert, U.; Beckmann, J.; Bellon, C.; Jaenisch, G.-R.; Großer, A. – Fehlergrößenabhängige Kontrastreduktion und zusätzliche Unschärfe durch Streustrahlung reduzieren die Bildqualität radiologischer Abbildungen. In: DACH-Jahrestagung 2008. St. Gallen, Schweiz. Deutsche Gesellscahft für Zerstörungsfreie Prüfung e.V. (DGZfP), 2008a. pp. 1-12.

EWERT et al. (2008b)
> Ewert, U.; Redmer, B.; Rädel, C.; Osterloh, K.; Schnars, U.; Henrich, R.; Schimmelmann, O.; Bavendiek, K.; Jahn, M. – Mobile X-ray Inspection of light weight materials. In: International Symposium on NDT in Aerospace. Fürth, Germany. DGZfP, 2008b. pp. 99-111.

FAESSEL et al. (2005)
> Faessel, M.; Delisée, C.; Bos, F.; Castéra, P. – 3D Modelling of random cellulosic fibrous networks based on X-ray tomography and image analysis. Composites Science and Technology 65 (2005) 13. pp. 1931-1940.

FAHRNI (1956)
> Fahrni, F. – Das Verpressen von Spanplatten bei gefeuchteten oder feuchteren Deckspänen. Holz als Roh- und Werkstoff 14 (1956) 1. pp. 8-10.

FATHI (2014)
> Fathi, L. – Structural and mechanical properties of the wood from coconut palms, oil palms and date palms. Diss. Universität Hamburg, Fachbereich Biologie der Fakultät für Mathematik, Informatik und Naturwissenschaften, Hamburg, 2014. 248 p.

FENGEL, GROSSER (1975)
> Fengel, D.; Grosser, D. – Chemische Zusammensetzung von Nadel- und Laubhölzern - Eine Literaturübersicht. Holz als Roh- und Werkstoff 33 (1975) 1. pp. 32-34.

FENGEL, WEGENER (1983)
> Fengel, D.; Wegener, G. – Wood: chemistry, ultrastructure, reactions. Walter de Gruyter: Berlin, New York, 1983. 613 p.

FERNÁNDEZ et al. (2007a)
> Fernández, J. E.; Badiali, M.; Guidetti, A.; Scot, V. – Density profile unfolding from Compton scattering measurements in reflection geometry. X-Ray Spectrometry 36 (2007a) 1. pp. 20-26.

FERNÁNDEZ et al. (2007b)
> Fernández, J. E.; Badiali, M.; Guidetti, A.; Scot, V. – Multiple scattering corrections for density profile unfolding from Compton scattering signals in reflection geometry. Nuclear Instruments and Methods in Physics Research Section A: Accelerators, Spectrometers, Detectors and Associated Equipment 580 (2007b) 1. pp. 77-80.

FITCH (2018)
> Fitch, P. – Malaysia's timber dilemma - Why the industry needs innovation. Panels & Furniture Asia (2018) 6. pp. 69-70.

FREYBURGER et al. (2009)
> Freyburger, C.; Longuetaud, F.; Mothe, F.; Constant, T.; Leban, J.-M. – Measuring wood density by means of X-ray computer tomography. Annals of forest science 66 (2009) 8. pp. 804-804.

FRIEDMAN (2000)

> Friedman, W. D. – The criteria for measuring average density by X-ray attenuation: The role of spatial resolution. AIP Conference Proceedings 509 (2000) 1. pp. 1939-1946.

FRÜHWALD-KÖNIG (2019)

> Frühwald-König, K. – Properties and Grading of Oil Palm Lumber. In: Wang, X.; Sauter, U. H.; Ross, R. J. (Eds.) 21st International Nondestructive Testing and Evaluation of Wood Symposium. General Technical Report FPL–GTR–272. Freiburg, Germany. U.S. Department of Agriculture, Forest Service, Forest Products Laboratory, Madison, WI, 2019. pp. 204-212.

FUCHS (2010)

> Fuchs, M. – Neues Kalibrierverfahren an MDF-Matten vor dem Pressvorgang. Holztechnologie 51 (2010) 1. pp. 42-45.

GAO (1990)

> Gao, H. – X-ray computerized tomography of particleboard to predict through-thickness density profile. Master Thesis Oregon State University, Forest Products, Corvallis, OR, USA, 1990. 113 p.

GAO, JANSSENS (2004)

> Gao, N.; Janssens, K. – Polycapillary X-ray Optics. In: Tsuji, K.; Injuk, J.; Grieken, R. V. (Eds.) X-Ray Spectrometry: Recent Technological Advances. John Wiley & Sons Ltd: The Atrium, Southern Gate, Chichester, West Sussex, 2004. pp. 89-110.

GAO et al. (2019)

> Gao, Z.; Huang, R.; Chang, J.; Li, R.; Wu, Y.; Wang, Y. – Sandwich compression of wood: effects of preheating time and moisture distribution on the formation of compressed layer(s). European Journal of Wood and Wood Products 77 (2019) 2. pp. 219-227.

GERWARD (1993)

> Gerward, L. – X-ray attenuation coefficients: Current state of knowledge and availability. Radiation Physics and Chemistry 41 (1993) 4-5. pp. 783-789.

GERWARD et al. (2001)

> Gerward, L.; Guilbert, N.; Bjørn Jensen, K.; Levring, H. – X-ray absorption in matter. Reengineering XCOM. Radiation Physics and Chemistry 60 (2001) 1–2. pp. 23-24.

GIBBON, TUNDAK (1989)

> Gibbon, M. C.; Tundak, T. P. – Using density profilometer for quality and consistency measurements in MDF manufacturing. In: Particleboard/Composite Materials Symposium. Washington State University, Pullman, Washington. 1989.

GILSANZ (1998)

> Gilsanz, V. – Bone density in children: a review of the available techniques and indications. European Journal of Radiology 26 (1998) 2. pp. 177-182.

GIUDICEANDREA et al. (2011)

> Giudiceandrea, F.; Ursella, E.; Vicario, E. – A high speed CT scanner for the sawmill industry. In: Divos, F. (Ed.) Proceedings of the 17th international nondestructive testing and evaluation of wood symposium. Sopron, Hungary. University of West Hungary, 2011. pp. 105-112.

GONIS, BUTLER (2000)

> Gonis, A.; Butler, W. H. – Multiple Scattering in Solids. Springer: New York, 2000. 298 p.

GOTTLIEB (1883)

> Gottlieb, E. – Untersuchung über die elementare Zusammensetzung einiger Holzsorten in Verbindung mit calorimetrischen Versuchen über ihre Verbrennungsfähigkeit. Journal für Praktische Chemie 28 (1883) 1. pp. 385-421.

GRECON (2018)
Anon. – GreCon STENOGRAPH - Inline raw density profile measurement with X-ray technology, 2018. https://www.fagus-grecon.com/en/solutions/measuring-technology/stenograph/. Access date 01.11.2018.

GRETEN (1982)
Greten, E. – Der Einsatz der Meß- und Regeltechnik zur Kosteneinsparung in Spanplattenwerken. European Journal of Wood and Wood Products 40 (1982) 10. pp. 377-380.

GRODSTEIN (1957)
Grodstein, G. W. – X-ray attenuation coefficients from 10 keV to 100 MeV. NBS Circular 583, National Bureau of Standards, 1957. 58 p.

GROSSWENDT (1999)
Grosswendt, B. – Basic aspects of photon transport through matter with respect to track structure formation. Radiation and Environmental Biophysics 38 (1999) 3. pp. 147-161.

GRUCHOT (2009)
Gruchot, M. – In situ-Untersuchungen des Rohdichteprofils von Holzwerkstoffen am Beispiel von MDF. Diss. Universität Hamburg, Fakultät für Mathematik, Informatik und Naturwissenschaften, Fachbereich Biologie, Hamburg, 2009. 437 p.

GRUDD (2008)
Grudd, H. – Torneträsk tree-ring width and density AD 500 - 2004: a test of climatic sensitivity and a new 1500-year reconstruction of north Fennoscandian summers. Climate Dynamics 31 (2008) 7-8. pp. 843-857.

GRUNDBERG et al. (1995)
Grundberg, S.; Grönlund, A.; Grönlund, U. – The Swedish stem bank: a database for different silvicultural and wood properties. Research report, TULEA 1995:31. Luleå University of Technology, 1995.

GUAN et al. (2001)
Guan, N.; Wang, Y.-J.; Gu, H. – Specimen Orientation for the Calibration of Direct Scanning X-Ray Wood Densitometers. Wood and fiber science 33 (2001) 1. pp. 26-30.

GÜNTHER et al. (2015)
Günther, K.; Charwat-Pessler, J.; Barbu, M.-C.; Plank, B.; Richter, K.; Petutschnigg, A. – Analyzing wood bark insulation board structure using X-ray computed tomography and modeling its thermal conductivity by means of finite difference method. Journal of Composite Materials 50 (2015) 6. pp. 795-806.

HAAS (1998)
Haas, G. v. – Untersuchungen zur Heißpressung unter besonderer Berücksichtigung des Verdichtungsverhaltens, der Permeabilität, der Temperaturleitfähigkeit und der Sorptionsgeschwindigkeit. Diss. Universität Hamburg, Fakultät für Mathematik, Informatik und Naturwissenschaften, Fachbereich Biologie, Hamburg, 1998. 264 p.

HÄGGLUND (1951)
Hägglund, E. – Chemistry of Wood. Academic Press Inc.: New York, 1951. 631 p.

HALMSHAW (1995)
Halmshaw, R. – Industrial radiology - Theory and practice. 2nd ed. Chapman & Hall: London, 1995. 317 p.

HÄNSCH et al. (1983)
Hänsch, G.; Henze, W.; Winzmann, F. – Schwerpunkte der Meßtechnik in einer Produktionslinie für Spanplatten. Holz als Roh- und Werkstoff 41 (1983) 1. pp. 7-11.

HANSSON, CHEREPANOVA (2012)
    Hansson, L.; Cherepanova, E. – Determination of wood moisture properties using a CT-scanner
    in a controlled low-temperature environment. Wood Material Science & Engineering 7 (2012) 2.
    pp. 87-92.

HAPLA (1985)
    Hapla, F. – Radiographisch-densitometrische Holzeigenschaftsuntersuchungen an Douglasien
    aus unterschiedlich durchforsteten Versuchsflächen. Holz als Roh- und Werkstoff 43 (1985) 1.
    pp. 9-15.

HARDING (1997)
    Harding, G. – Inelastic photon scattering: Effects and applications in biomedical science and
    industry. Radiation Physics and Chemistry 50 (1997) 1. pp. 91-111.

HARDING, HARDING (2010)
    Harding, G.; Harding, E. – Compton scatter imaging: A tool for historical exploration. Applied
    Radiation and Isotopes 68 (2010) 6. pp. 993-1005.

HARTMANN et al. (2006)
    Hartmann, H.; Böhm, T.; Daugbjerg Jensen, P.; Temmerman, M.; Rabier, F.; Golser, M. –
    Methods for size classification of wood chips. Biomass and Bioenergy 30 (2006) 11. pp. 944-953.

HASCH (2002)
    Hasch, J. – Ökologische Betrachtungen von Holzspan- und Holzfaserplatten. Diss. Universität
    Hamburg, Fakultät für Mathematik, Informatik und Naturwissenschaften, Fachbereich Biologie,
    Hamburg, 2002. 288 p.

HASENER (2004)
    Hasener,   J. – Statistische   Methoden   der   industriellen   Prozessmodellierung   zur
    Echtzeitqualitätskontrolle am Beispiel einer kontinuierlichen Produktion von Faserplatten. Diss.
    Universität Hamburg, Fakultät für Mathematik, Informatik und Naturwissenschaften, Fachbereich
    Biologie, Hamburg, 2004. 242 p.

HASENER, BARBU (2009)
    Hasener, J.; Barbu, M. C. – Overview on NDT technologies for on-line control in the wood- based
    panel industry and an outlook for future trends. In: Alma, M. H.; Kalaycioglu, H. (Eds.) Proceedings
    of the COST Action E49 Processes and Performance of Wood-Based Panels - Workshop
    Proceedings Adding value through physical functionality. Istanbul, Turkey. 2009. pp. 2-14.

HASENSTAB et al. (2009)
    Hasenstab, A.; Ewert, U.; Jechow, M.; Osterloh, K.; Zscherpel, U.; Bücherl, T. – Untersuchung
    von Brettschichtholz (BSH) mit Entlastungsnuten mit Ultraschallecho, Radiografie und Neutronen.
    In: DGZfP-Jahrestagung 2009. Münster. 2009. pp. 1-12.

HASNÍKOVÁ, KUKLÍK (2014)
    Hasníková, H.; Kuklík, P. – Various non-destructive methods for investigation of timber members
    from a historical structure. Wood research - Drevarsky výskum 59 (2014) 3. pp. 411-420.

HAWKES, JACKSON (1980)
    Hawkes, D. J.; Jackson, D. F. – An accurate parametrisation of the X-ray attenuation coefficient.
    Physics in Medicine & Biology 25 (1980) 6. pp. 1167-1171.

HELLIER (2001)
    Hellier, C. – Handbook of Nondestructive Evaluation. McGraw-Hill: New York, 2001. 603 p.

HELMS, NIEMZ (1993)
    Helms, D.; Niemz, P. – Bohrwiderstandsmessung zur Qualitätsbeurteilung von Holz und
    Holzwerkstoffen. Die Holzbearbeitung: HOB (1993) 3. pp. 78-80.

HENKEL (1969)
    Henkel, M. – Ermittlung von Dichteprofilen an Span- und Faserplatten mit Röntgenstrahlen.
    Holztechnologie 10 (1969) 2. pp. 93-96.

HERMAN (1979)
  Herman, G. T. – Correction for beam hardening in computed tomography. Physics in Medicine and Biology 24 (1979) 1. pp. 81-106.

HERTRICH (2004)
  Hertrich, P. H. – Röntgenaufnahmetechnik: Grundlagen und Anwendungen. Publicis Corporate Publishing: Erlangen, 2004. 344 p.

HERTRICH (2005)
  Hertrich, P. H. – Practical radiography: principles and applications. Publicis Kommunikationsagentur GmbH, GWA: Erlangen, 2005. 316 p.

HERVÉ et al. (2014)
  Hervé, V.; Mothe, F.; Freyburger, C.; Gelhaye, E.; Frey-Klett, P. – Density mapping of decaying wood using X-ray computed tomography. International Biodeterioration & Biodegradation 86, Part C (2014) pp. 358-363.

HEYDEN (2000)
  Heyden, S. – Network modelling for the evaluation of mechanical properties of cellulose fibre fluff. Doctoral Thesis Lund University, Department of Mechanics and Materials, Structural Mechanics, Lund, Sweden, 2000. 209 p.

HILBERS (2006)
  Hilbers, U. – Untersuchungen zur Flächengewichtsmessung von Faserplatten mittels Röntgentechnik. Diplomarbeit Universität Hamburg, Fakultät für Mathematik, Informatik und Naturwissenschaften, Department Biologie, Hamburg, 2006. 135 p.

HILBERS et al. (2011)
  Hilbers, U.; Thoemen, H.; Hasener, J.; Fruehwald, A. – Effects of panel density and particle type on the ultrasonic transmission through wood-based panels. Wood Science and Technology (2011) pp. 1-14.

HINE (1952)
  Hine, G. J. – The effective atomic numbers of materials for various gamma-ray interactions. In: Physical Review 85(4), Minutes of the Meeting. Chicago, October 24-27, 1951. American Physical Society, 1952. pp. 725.

HO, HUSSEIN (2000)
  Ho, A. C.; Hussein, E. M. A. – Quantification of gamma-ray Compton-scatter nondestructive testing. Applied Radiation and Isotopes 53 (2000) 4–5. pp. 541-546.

HOAG, MCKIMMY (1988)
  Hoag, M.; McKimmy, M. D. – Direct scanning x-ray densitometry of thin wood sections. Forest products journal 38 (1988) 1. pp. 23-26.

HOAG, KRAHMER (1991)
  Hoag, M.; Krahmer, R. – Polychromatic X-Ray Attenuation Characteristics and Wood Densitometry Applications. Wood and fiber science 23 (1991) 1. pp. 23-31.

HOFFMAN, DE BEER (2012)
  Hoffman, J. W.; de Beer, F. C. – Characteristics of the Micro-Focus X-ray Tomography Facility (MIXRAD) at Necsa in South Africa. In: 18th World Conference on Nondestructive Testing. Durban, South Africa. South African Institute for Non-Destructive Testing (SAINT), 2012. pp. 1-12.

HOLLOWAY, BAKER (1972)
  Holloway, M. G.; Baker, C. P. – How the barn was born. Physics Today 25 (1972) 7. pp. 9.

HOLT et al. (1984)
  Holt, R. S.; Cooper, M. J.; Jackson, D. F. – Gamma-ray scattering techniques for non-destructive testing and imaging. Nuclear Instruments and Methods in Physics Research 221 (1984) 1. pp. 98-104.

HOSSEINPOURPIA et al. (2016)
Hosseinpourpia, R.; Adamopoulos, S.; Mai, C. – Dynamic vapour sorption of wood and holocellulose modified with thermosetting resins. Wood Science and Technology 50 (2016) 1. pp. 165-178.

HUBBELL, SELTZER (2004)
Hubbell, J. H.; Seltzer, S. M. – Tables of X-Ray Mass Attenuation Coefficients and Mass Energy-Absorption Coefficients from 1 keV to 20 MeV for Elements Z = 1 to 92 and 48 Additional Substances of Dosimetric Interest (version 1.4), 2004. http://www.nist.gov/pml/data/xraycoef/index.cfm. Access date 06.01.2018.

HUDDLESTON (1988)
Huddleston, A. L. – Quantitative methods in bone densitometry. Kluwer Academic Publishers: Boston, 1988. 224 p.

HULTNÄS, FERNANDEZ-CANO (2012)
Hultnäs, M.; Fernandez-Cano, V. – Determination of the moisture content in wood chips of Scots pine and Norway spruce using Mantex Desktop Scanner based on dual energy X-ray absorptiometry. Journal of Wood Science 58 (2012) 4. pp. 309-314.

HUMPHREY (1994)
Humphrey, P. E. – Engineering composites from oriented natural fibres: A strategy. In: Kennedy, J. F.; Phillips, G. O.; Williams, P. A. (Eds.) The chemistry and processing of wood and plant fibrous materials: Proceedings of the international Cellucon Conference, University of Wales, Bangor, UK, 1994. Woodhead Publishing Limited: Cambridge, 1994. pp. 213-220.

HUNT et al. (2017)
Hunt, J. F.; Leng, W.; Tajvidi, M. – Vertical density profile and internal bond strength of wet-formed particleboard bonded with cellulose nanofibrils. Wood and Fiber Science 49 (2017) 4. pp. 413-423.

HUSSEIN (1989)
Hussein, A. M. A. – Radiation scattering methods for non-destructive testing and imaging. In: McGonnagle, W. J. (Ed.) International Advances in Non-Destructive Testing. Gordon and Breach Science Publishers: New York, 1989. pp. 301-321.

HUSSEIN et al. (1997)
Hussein, E. M. A.; Gokhale, P.; Arendtsz, N. V.; Lawrence, A. H. – Inspection of cargo containers using gamma radiation. In: Pennella, L. O. M. J. J. (Ed.) Proc. SPIE 2936, Physics-Based Technologies for the Detection of Contraband, 210 (February 6, 1997). Boston, MA, USA. 1997. pp. 210-218.

HUSSEIN (2003a)
Hussein, E. M. A. – Handbook on Radiation Probing, Gauging, Imaging and Analysis - Volume I: Basics and Techniques. Kluwer Academic Publishers: Dordrecht, 2003a.

HUSSEIN (2003b)
Hussein, E. M. A. – Handbook on Radiation Probing, Gauging, Imaging and Analysis - Volume II: Applications and Design. Kluwer Academic Publishers: Dordrecht, 2003b.

HUSSEIN (2007)
Hussein, E. M. A. – Radiation Mechanics - Principles and Practice. Elsevier: Amsterdam, 2007. 342 p.

HUSSEIN (2011)
Hussein, E. M. A. – Computed radiation imaging - Physics and mathematics of forward and inverse problems. Elsevier: London, Waltham, 2011. 302 p.

IHD (2014)
    IHD – Echtzeit-Charakterisierung von Holzpartikeln für die Qualitätssicherung und Prozessoptimierung bei der Herstellung von Holzpartikelwerkstoffen in der Holzwerkstoffindustrie - Quick Wood Particle Size. Abschlussbericht. Unter Mitarbeit von A. Weber, A. Rapthel, U. Sonntag und C. Wenderdel., IHD, IWM, GFAI, Dresden, Halle, Berlin, 2014. 16-17 p.

ILLMAN, DOWD (1999)
    Illman, B. L.; Dowd, B. A. – High-resolution microtomography for density and spatial information about wood structures. In: Bonse, U. (Ed.) Proc. SPIE 3772, Developments in X-Ray Tomography II, 198. Denver, CO, USA. SPIE - The International Society for Optical Engineering, 1999. pp. 198-204.

IMAL (2018)
    Anon. – On-Line Density Profile Meter - CDP700, 2018. http://www.imal-pal.com/en/scheda.php?pr=96. Access date 01.11.2018.

IMAMURA, FUJII (1981)
    Imamura, K.; Fujii, M. – Empirical beam hardening correction in the measurement of vertebral bone mineral content by computed tomography. Radiology 138 (1981) 1. pp. 223-226.

INANC (1999)
    Inanc, F. – Analysis of X-Ray and Gamma Ray Scattering Through Computational Experiments. Journal of Nondestructive Evaluation 18 (1999) 2. pp. 73-82.

IVANOVA (2009)
    Ivanova, S. – Prüfverfahren zur schnellen Beurteilung der Spanplattenqualität durch indirekte Bestimmung der mineralischen Verunreinigungen. Diss. Universität Stuttgart, Fakultät Konstruktions-, Produktions- und Fahrzeugtechnik, Stuttgart, 2009. 136 p.

IŽDINSKÝ, ŠTEFKA (2009)
    Iždinský, J.; Štefka, V. – Density profile of particleboard produced by modified pressing diagram with the temperature of the pressing plates 190, 200, 210 °C and high moisture content of surface particles. In: Alma, M. H.; Kalaycioglu, H. (Eds.) Proceedings of the COST Action E49 Processes and Performance of Wood-Based Panels - Workshop Proceedings Adding value through physical functionality. Istanbul, Turkey. 2009. pp. 150-159.

JACKSON, HAWKES (1981)
    Jackson, D. F.; Hawkes, D. J. – X-ray attenuation coefficients of elements and mixtures. Physics Reports 70 (1981) 3. pp. 169-233.

JACKSON (1982)
    Jackson, D. F. – Chemical effects in X-ray transmission measurements. Nuclear Instruments and Methods in Physics Research 193 (1982) 1. pp. 387-389.

JACQUIN et al. (2019)
    Jacquin, P.; Mothe, F.; Longuetaud, F.; Billard, A.; Kerfriden, B.; Leban, J.-M. – CarDen: A software for fast measurement of wood density on increment cores by CT scanning. Computers and Electronics in Agriculture 156 (2019) pp. 606-617.

JAENISCH et al. (2016)
    Jaenisch, G.-R.; Kolkoori, S.; Bellon, C. – Quantitative Simulation of Back Scatter X-ray Imaging and Comparison to Experiments. In: 19th World Conference on Non-Destructive Testing (WCNDT 2016). Munich, Germany. German Society for Non-Destructive Testing (DGZfP), 2016. pp. 1-11.

JENSEN et al. (2002)
    Jensen, S.; Damkilde, L.; Krabbenhøft, K. – Non-destructive assessment and FEM simulations of moisture profiles in Sitka Spruce (Picea sitchensis) during drying. In: Proceeding of the 3rd European COST E. 2002.

JENSEN, KEHR (1995)
    Jensen, U.; Kehr, E. – Quantitative Auswertung der Rohdichteprofile von Spanplatten und MDF. European Journal of Wood and Wood Products 53 (1995) 1. pp. 16.

KAESTNER et al. (2017)
    Kaestner, A. P.; Hovind, J.; Boillat, P.; Muehlebach, C.; Carminati, C.; Zarebanadkouki, M.; Lehmann, E. H. – Bimodal Imaging at ICON Using Neutrons and X-rays. Physics Procedia 88 (2017) pp. 314-321.

KAK, SLANEY (1988)
    Kak, A. C.; Slaney, M. – Principles of computerized tomographic imaging. IEEE Press: New York, 1988. 344 p.

KALENDER (2011)
    Kalender, W. A. – Computed tomography fundamentals, system technology, image quality, applications. 3rd ed. Publicis Publishing: Erlangen, Germany, 2011. 372 p.

KALTSCHMITT et al. (2009)
    Kaltschmitt, M.; Hartmann, H.; Hofbauer, H. – Energie aus Biomasse - Grundlagen, Techniken und Verfahren. 2nd ed. Springer-Verlag: Berlin, Heidelberg, 2009. 1061 p.

KASAL, ANTHONY (2004)
    Kasal, B.; Anthony, R. W. – Advances in in situ evaluation of timber structures. Progress in Structural Engineering and Materials 6 (2004) 2. pp. 94-103.

KASPERL (2005)
    Kasperl, S. – Qualitätsverbesserungen durch referenzfreie Artefaktreduzierung und Oberflächennormierung in der industriellen 3D-Computertomographie. Diss. Technische Fakultät der Universität, Erlangen-Nürnberg, 2005. 172 p.

KAUFFMANN et al. (2006)
    Kauffmann, G. W.; Moser, E.; Sauer, R. – Radiologie. 3rd ed. Elsevier: München, 2006. 772 p.

KAUR et al. (2006)
    Kaur, P.; Singh, T.; Singh, P. S. – Effective Atomic Numbers and Electron Densities of Some HCO Materials as a Function of Weight Fraction of Constituent Elements. Asian Journal of Chemistry 18 (2006) 5. pp. 3340-3343.

KELLY (1977)
    Kelly, M. W. – Critical literature review of relationships between processing parameters and physical properties of particleboard - Gerneral Technical Report FPL-10. Forest Products Laboratory, U.S. Department of Agriculture Forest Service: Madison, Wisconsin, 1977. 70 p.

KERMANI, FEGHHI (2017)
    Kermani, A.; Feghhi, S. A. H. – Scatter Signal Elimination by Localized Primary Modulation in Industrial Computed Radiography. Journal of Nondestructive Evaluation 36 (2017) 4. pp. 71.

KERMANI, FEGHHI (2018)
    Kermani, A.; Feghhi, S. A. H. – Experimental Measurement of Scatter to Primary Ratio by Localized Primary Modulation in Industrial Computed Radiography. Journal of Nondestructive Evaluation 37 (2018) 1. pp. 9.

KERUR et al. (1993)
    Kerur, B. R.; Thontadarya, S. R.; Hanumaiah, B. – X-ray attenuation coefficients at 6.46 keV and the validity of the mixture rule for compounds. X-Ray Spectrometry 22 (1993) 1. pp. 13-16.

KEUNECKE et al. (2010)
    Keunecke, D.; Mannes, D.; Niemz, P.; Lehmann, E.; Evans, R. – Silviscan vs. neutron imaging to generate radial softwood density profiles. Wood Research 55 (2010) 3. pp. 49-60.

KEYLWERTH, KLEUTERS (1962)
    Keylwerth, R.; Kleuters, W. – Beitrag zur isotopentechnischen Jahrringanalyse. Holz als Roh- und Werkstoff 20 (1962) 5. pp. 173-181.

KIJEWSKI, BJÄRNGARD (1978)
Kijewski, P. K.; Bjärngard, B. E. – Correction for beam hardening in computed tomography. Medical Physics 5 (1978) 3. pp. 209-214.

KIM et al. (2013)
Kim, C.-K.; Oh, J.-K.; Lee, J.-J. – Influence of Wood Thickness on Attenuation of Soft X-ray for Developing Portable X-ray CT. In: Ross, R. J.; Wang, X. (Eds.) Proceedings 18th International Nondestructive Testing and Evaluation of Wood Symposium. Madison, Wisconsin, USA. USDA Forest Service, Products Laboratory, General Technical Report, FPL-GTR-226, 2013. pp. 602-609.

KIM et al. (2014)
Kim, C.-K.; Oh, J.-K.; Hong, J.-P.; Lee, J-J. – Density calculation of wood by portable X-ray tube with consideration of penetrating depth. Journal of Wood Science 60 (2014) 2. pp. 105-110.

KIM et al. (2015)
Kim, C.-K.; Oh, J.-K.; Hong, J.-P.; Lee, J.-J. – Dual-energy X-ray absorptiometry with digital radiograph for evaluating moisture content of green wood. Wood Science and Technology 49 (2015) 4. pp. 713-723.

KLEIN, NISHINA (1929)
Klein, O.; Nishina, Y. – Über die Streuung von Strahlung durch freie Elektronen nach der neuen relativistischen Quantendynamik von Dirac. Zeitschrift für Physik 52 (1929) 11. pp. 853-868.

KLEINSCHMIDT (1999)
Kleinschmidt, C. – Analytical considerations of beam hardening in medical accelerator photon spectra. Medical Physics 26 (1999) 9. pp. 1995-1999.

KLEINSCHMIDT, HÄNSCH (1985)
Kleinschmidt, H.-P.; Hänsch, G. – Gleichmäßiges Spänevlies durch flexiblen Rechen für die Formstation in Verbindung mit einer On-Line-Messung des Querprofils. European Journal of Wood and Wood Products 43 (1985) 10. pp. 429-431.

KLEUTERS (1964)
Kleuters, W. – Optimal Test Conditions for Determining Local Density of Wood By the Beta-Ray Method. Forest Products Journal XIV (1964) 9. pp. 414-420.

KNIGGE, SCHULZ (1966)
Knigge, W.; Schulz, H. – Grundriss der Forstbenutzung - Entstehung, Eigenschaften, Verwertung und Verwendung des Holzes und anderer Forstprodukte. Verlag Paul Parey: Hamburg, 1966. 584 p.

KOCSIS et al. (2006)
Kocsis, L.; Herman, P.; Eke, A. – The modified Beer–Lambert law revisited. Physics in Medicine & Biology 51 (2006) 5. pp. N91.

KOHLRAUSCH et al. (1996)
Kohlrausch, F.; Kose, V.; Wagner, S. – Praktische Physik Band 2. 24th ed. B. G. Teubner: Stuttgart, 1996. 909 p.

KOLKOORI et al. (2014)
Kolkoori, S.; Wrobel, N.; Deresch, A.; Redmer, B.; Ewert, U. – Dual High-Energy X-ray Digital Radiography for Material Discrimination in Cargo Containers. In: 11th European Conference on Non-Destructive Testing (ECNDT 2014). Prague, Czech Republic. 2014.

KOLLMANN (1951)
Kollmann, F. – Technologie des Holzes und der Holzwerkstoffe - Erster Band Anatomie und Pathologie, Chemie, Physik, Elastizität und Festigkeit. 2nd ed. Springer-Verlag; J. F. Bergmann: Berlin, Göttingen, Heidelberg; München, 1951. 1050 p.

KOLLMANN (1965)

    Kollmann, F. – Die Bedeutung der Gaußschen Normalverteilung für Struktur, Sorption und Rheologie von Holz. Holz als Roh- und Werkstoff 23 (1965) 5. pp. 165-173.

KORNELSEN, YOUNG (1981)

    Kornelsen, R. O.; Young, M. E. J. – Brachytherapy build-up factors. British Journal of Radiology 54 (1981) 638. pp. 136.

KORTRIGHT, THOMPSON (2009)

    Kortright, J. B.; Thompson, A. C. – X-ray emission energies. In: Thompson, A. C. (Ed.) X-Ray Data Booklet. 3rd ed. Lawrence Berkeley National Laboratory University of California: Berkeley, California, 2009. pp. 1.8-1.27.

KORTÜM, RIEGEL (2017)

    Kortüm, C.; Riegel, A. – Maschinenabnahmen und Prozessfähigkeitsuntersuchungen in der Holz- und Möbelindustrie. holztechnologie 58 (2017) 3. pp. 31.39.

KOSANETZKY, HARDING (1987)

    Kosanetzky, J.; Harding, G. – Materialprüfung mit Röntgen-Rückstreustrahlung. Materialprüfung 29 (1987) 7/8. pp. 217-221.

KOTWALIWALE et al. (2006)

    Kotwaliwale, N.; Weckler, P. R.; Brusewitz, G. H. – X-ray Attenuation Coefficients using Polychromatic X-ray Imaging of Pecan Components. Biosystems Engineering 94 (2006) 2. pp. 199-206.

KOTWALIWALE et al. (2007)

    Kotwaliwale, N.; Subbiah, J.; Weckler, P.; Brusewitz, G.; Kranzler, G. – Calibration of a Soft X-Ray Digital Imaging System for Biological Materials. Transactions of the ASABE 50 (2007) 2. pp. 661-666.

KOURIS et al. (1981)

    Kouris, K.; Tout, R. E.; Gilboy, W. B.; Spyrou, N. M. – Effect of constituent elements in wood on X-ray densitometry measurement. Archaeometry 23 (1981) 1. pp. 95-101.

KRIEGER (2012)

    Krieger, H. – Grundlagen der Strahlungsphysik und des Strahlenschutzes. 4th ed. Springer Spektrum: Wiesbaden, 2012. 813 p.

KRIEGER (2013)

    Krieger, H. – Strahlungsmessung und Dosimetrie. 2nd ed. Springer Spektrum: Wiesbaden, 2013. 722 p.

KRÖCKEL (2017)

    Kröckel, K. – Einfluss der Rohstoffsortierung auf das vertikale Dichteprofil von Bambus Scrimber. Bachelor Thesis Universität Hamburg, Fakultät für Mathematik, Informatik und Naturwissenschaften, Fachbereich Biologie, Hamburg, 2017. 83 p.

KRUG (2010)

    Krug, D. – Einfluss der Faserstoff-Aufschlussbedingungen und des Bindemittels auf die Eigenschaften von mitteldichten Faserplatten (MDF) für eine Verwendung im Feucht- und Außenbereich. Diss. Universität Hamburg, Fakultät für Mathematik, Informatik und Naturwissenschaften, Fachbereich Biologie, Hamburg, 2010. 293 p.

KRUGLOWA et al. (2010)

    Kruglowa, T.; Sandin, Y.; Kliger, R. – Density Calibration Using X-ray Equipment for In-Situ Assessment of Timber Structures. In: Proceedings of WCTE 2010-The 11th World Conference on Timber Engineering. Riva del Garda, Trentino, Italy. 2010.

KRUMM et al. (2008)
> Krumm, M.; Kasperl, S.; Franz, M. – Referenceless Beam Hardening Correction in 3D Computed Tomography Images of Multi-Material Objects. In: 17th World Conference on Nondestructive Testing, 25-28 Oct 2008. Shanghai, China. 2008. pp. 1-7.

KRUMM et al. (2010)
> Krumm, M.; Kasperl, S.; Franz, M. – Beam Hardening Correction of Multi-Material Objects. In: 10th European conference and exhibition on non-destructive testing (10thECNDT). Moscow, Russia. 2010. pp. 1-7.

KRUSE et al. (1996)
> Kruse, K.; Bröker, F.-W.; Frühwald, A. – Zusammenhang zwischen Querzugfestigkeit, Rohdichteprofil und Ultraschallgeschwindigkeit von Spanplatten. European Journal of Wood and Wood Products 54 (1996) 5. pp. 295-300.

KÚDELA et al. (2018)
> Kúdela, J.; Rousek, R.; Rademacher, P.; Rešetka, M.; Dejmal, A. – Influence of pressing parameters on dimensional stability and density of compressed beech wood. European Journal of Wood and Wood Products 76 (2018) 4. pp. 1241-1252.

KULLENBERG et al. (2010)
> Kullenberg, R.; Hultnäs, M.; Fernandez, V.; Nylinder, M.; Toft, S.; Danielsson, F. – Dual-Energy X-Ray Absorptiometry Analysis for the Determination of Moisture Content in Biomass. Journal of Biobased Materials and Bioenergy 4 (2010) 4. pp. 363-366.

KUMAR et al. (2006)
> Kumar, A.; Singh, S.; Thind, K. S.; Mudahar, G. S. – A Study of Buildup Factor under Different Geometrical Conditions for 1332 keV Gamma Rays. Asian Journal of Chemistry 18 (2006) 5. pp. 3348-3351.

KUMAR, REDDY (1997)
> Kumar, T. K.; Reddy, K. V. – Effective atomic numbers for materials of dosimetric interest. Radiation Physics and Chemistry 50 (1997) 6. pp. 545-553.

KUMAR (1958)
> Kumar, V. B. – Non-Destructive Test for Quality Evaluation of Fibre Boards. Svensk Papperstidning 61 (1958) 15. pp. 461-470.

KURUDIREK et al. (2011)
> Kurudirek, M.; Dogan, B.; Özdemir, Y.; Moreira, A. C.; Appoloni, C. R. – Analysis of some Earth, Moon and Mars samples in terms of gamma ray energy absorption buildup factors: Penetration depth, weight fraction of constituent elements and photon energy dependence. Radiation Physics and Chemistry 80 (2011) 3. pp. 354-364.

KÜSTNER (1931)
> Küstner, H. – Die Erzeugung intensiver monochromatischer Röntgenstrahlen mit Hilfe technischer Röhren ohne Spektralapparat. Zeitschrift für Physik 70 (1931) 5. pp. 324-347.

KUTNAR et al. (2009)
> Kutnar, A.; Kamke, F. A.; Sernek, M. – Density profile and morphology of viscoelastic thermal compressed wood. Wood Science and Technology 43 (2009) 1. pp. 57.

LAHAT et al. (2015)
> Lahat, D.; Adali, T.; Jutten, C. – Multimodal Data Fusion: An Overview of Methods, Challenges, and Prospects. Proceedings of the IEEE 103 (2015) 9. pp. 1449-1477.

LAMPERT (1967)
> Lampert, H. – Faserplatten - Rohstoffe, Herstellungsverfahren, Eigenschaften. VEB Fachbuchverlag: Leipzig, 1967. 453 p.

LANVERMANN et al. (2013)
      Lanvermann, C.; Evans, R.; Schmitt, U.; Hering, S.; Niemz, P. – Distribution of structure and lignin
      within growth rings of Norway spruce. Wood Science and Technology 47 (2013) 3. pp. 627-641.

LANVERMANN et al. (2014a)
      Lanvermann, C.; Wittel, F. K.; Niemz, P. – Full-field moisture induced deformation in Norway
      spruce: intra-ring variation of transverse swelling. European Journal of Wood and Wood Products
      72 (2014a) 1. pp. 43-52.

LANVERMANN (2014)
      Lanvermann, C. – Sorption and swelling within growth rings of norway spruce and implications on
      the macroscopic scale. Diss. Eidgenössische Technische Hochschule ETH Zürich, Departement
      Bau, Umwelt und Geomatik, Zürich, 2014.

LANVERMANN et al. (2014b)
      Lanvermann, C.; Sanabria, S. J.; Mannes, D.; Niemz, P. – Combination of neutron imaging (NI)
      and digital image correlation (DIC) to determine intra-ring moisture variation in Norway spruce.
      Holzforschung 68 (2014b) 1. pp. 113-122.

LASKE (1961)
      Laske, H. – Untersuchungsverfahren zur Charakterisierung fester Brennstoffe. VEB Dt. Verl. für
      Grundstoffindustrie: Leipzig, 1961. 373 p.

LAUDON et al. (2013)
      Laudon, N.; Baumgartner, R.; Hoyos-Montoya, D. C.; Brüchert, F.; Sauter, U. H. – Automatic
      Detection of Resin Pockets in High Speed Industrial CT Images of Norway Spruce. In: Ross, R.
      J.; Wang, X. (Eds.) Proceedings 18th International Nondestructive Testing and Evaluation of
      Wood Symposium. Madison, Wisconsin, USA. USDA Forest Service, Products Laboratory,
      General Technical Report, FPL-GTR-226, 2013. pp. 15-21.

LAUFENBERG (1986)
      Laufenberg, T. L. – Using gamma radiation to measure density gradients in reconstituted wood
      products. Forest Products Journal 36 (1986) 2. pp. 59-62.

LAUTNER, BECKMANN (2012)
      Lautner, S.; Beckmann, F. – Analysis of wood microstructure by synchrotron radiation-based x-ray
      microtomography (SRµCT). In: Stock, S. R. (Ed.) Proc. SPIE 8506, Developments in X-Ray
      Tomography VIII, 85060F. San Diego, California, USA. 2012. pp. 85060F-85060F-6.

LEBAN et al. (2016)
      Leban, J.-M.; Hervé, J.-C.; Bontemps, J.-D.; Longuetaud, F.; Mothe, F.; Jacquin, P. –
      Measurement of the annual biomass increment of the French forests, XyloDensMap project. In:
      Modelling Wood Quality, Supply and Value Chain Networks - Wood QC 2016. Quebec, Canada.
      2016.

LEHMANN, MANNES (2012)
      Lehmann, E. H.; Mannes, D. – Wood investigations by means of radiation transmission
      techniques. Journal of Cultural Heritage 13 (2012) 3, Supplement. pp. 35-43.

LEMASTER, DORNFELD (1990)
      LeMaster, R. L.; Dornfeld, D. A. – Determining vertical density profiles in wood composites unsing
      acoustic emission. In: dos Reis, H. L. M. (Ed.) Nondestructive testing and evaluation for
      manufacturing and construction - papers presented at the Nondestructive Testing and Evaluation
      for Manufacturing and Construction Conference, 9.-12. August 1988. University of Illinois at
      Urbana-Champaign. Hemisphere Publishing Corperation: New York, 1990. pp. 161-175.

LEMASTER, GREEN (1992)
      LeMaster, R. L.; Green, A. – The Use of Air-Coupled AE Sensors to Measure Densitiy Profiles in
      Wood-based Products. In: NPA Pressline Technology Seminars: 4. - 5. November 1992, Sheraton
      Portland Airport, Portland, Oregon und 2. - 3. Dezember 1992, Sheraton Airport Plaza, Charlotte,
      North Carolina. National Particleboard Association, Gaithersburg, Maryland. 1992. pp. 65-68.

LENZ et al. (1976)
Lenz, O.; Schär, E.; Schweingruber, F. H. – Methodische Probleme bei der radiographisch-densitometrischen Bestimmung der Dichte und der Jahrringbreiten von Holz. Holzforschung 30 (1976) 4. pp. 114-123.

LEROY, RANCOITA (2004)
Leroy, C.; Rancoita, P.-G. – Principles of radiation interaction in matter and detection. World Scientific Publishing Co. Pte. Ltd.: Singapore, 2004. 715 p.

LEWARK (1986)
Lewark, S. – Die Methode der Röntgendensitometrie von Holz und ihre Anwendung an Holz Immissionen ansgesetzter Bäume. Forstarchiv 57 (1986) 3. pp. 105-107.

LI et al. (2018)
Li, R.; Gao, Z.; Feng, S.; Chang, J.; Wu, Y.; Huang, R. – Effects of preheating temperatures on the formation of sandwich compression and density distribution in the compressed wood. Journal of Wood Science 64 (2018) 6. pp. 751-757.

LI et al. (2016)
Li, W.; Van den Bulcke, J.; De Schryver, T.; Van Acker, J. – Investigating water transport in MDF and OSB using a gantry-based X-ray CT scanning system. Wood Science and Technology 50 (2016) 6. pp. 1197-1211.

LICHTENEGGER et al. (1999)
Lichtenegger, H.; Reiterer, A.; Stanzl-Tschegg, S. E.; Fratzl, P. – Variation of Cellulose Microfibril Angles in Softwoods and Hardwoods—A Possible Strategy of Mechanical Optimization. Journal of Structural Biology 128 (1999) 3. pp. 257-269.

LIN, SAMEI (2014)
Lin, Y.; Samei, E. – A fast poly-energetic iterative FBP algorithm. Physics in medicine and biology 59 (2014) 7. pp. 1655-1678.

LINDEBERG (2004)
Lindeberg, J. – X-ray based tree ring analyses. Diss. Swedish University of Agricultural Sciences, Department of Silviculture, Umeå, 2004. 25 p.

LINDGREN (1991)
Lindgren, L. O. – Medical CAT-scanning: X-ray absorption coefficients, CT-numbers and their relation to wood density. Wood Science and Technology 25 (1991) 5. pp. 341-349.

LINDGREN et al. (1992)
Lindgren, O.; Davis, J.; Wells, P.; Shadbolt, P. – Non-destructive wood density distribution measurements using computed tomography. European Journal of Wood and Wood Products 50 (1992) 7. pp. 295-299.

LINDGREN (1992)
Lindgren, O. – Medical CT-scanners for non-destructive wood density and moisture content measurements. Diss. Luleå University of Technology, Department of Wood Technology, Skellefteå, 1992. 24 p.

LINDGREN et al. (2016)
Lindgren, O.; Seifert, T.; Du Plessis, A. – Moisture content measurements in wood using dual-energy CT scanning – a feasibility study. Wood Material Science & Engineering 11 (2016) 5. pp. 312-317.

LISTER (2004)
Lister, P. F. – Applications of X-ray computed tomography in the wood products industry. In: 16th World Conference on Nondestructive Testing. Montreal, Canada. 2004.

LIU et al. (1988)
Liu, C. J.; Olson, J. R.; Tian, Y.; Shen, Q. – Theoretical wood densitometry. I: Mass attenuation equations and wood density models. Wood and fiber science 20 (1988) 1. pp. 22-34.

LIU, TIAN (1991)
> Liu, C. J.; Tian, Y. – Theoretical wood densitometry. III: Mean density and density variation on stem cross-sections. Wood and fiber science 23 (1991) 2. pp. 273-289.

LOBENHOFFER (1990)
> Lobenhoffer, H. – Qualitätsbedingte Regelung eines Spanplattenformstrangs. Diss. Georg-August-Universität Göttingen, Fachbereich Wirtschaftswissenschaften, Göttingen, 1990. 289 p.

LOBENHOFFER (1991)
> Lobenhoffer, H. – Qualitätsbestimmte Regelung in der Spanplattenindustrie. Holz als Roh- und Werkstoff 49 (1991) 1. pp. 7-12.

LOHMANN (2010)
> Lohmann, U. (Ed.) – Holzlexikon. 4th ed. Nikol Verlag: Hamburg, 2010. 1423 p.

LOOS (1961)
> Loos, W. E. – The Relationship between Gamma Ray Absorption and Wood Moisture Content and Density. Forest Products Journal 11 (1961) 5. pp. 145-149.

LU, LAM (1999)
> Lu, C.; Lam, F. – Study on the X-ray calibration and overlap measurements in robot formed flakeboard mats. Wood Science and Technology 33 (1999) 2. pp. 85-95.

LUX et al. (2006)
> Lux, J.; Delisée, C.; Thibault, X. – 3D characterization of wood based fibrous materials: an application. 2011 25 (2006) 1. pp. 25-35.

MACCHIONI et al. (2007)
> Macchioni, N.; Palanti, S.; Rozenberg, P. – Measurements of fungal wood decay on Scots pine and beech by means of X-ray microdensitometry. Wood Science and Technology 41 (2007) 5. pp. 417-426.

MACEDO et al. (2002)
> Macedo, A.; Vaz, C. M. P.; Pereira, J. C. D.; Naime, J. M.; Cruvinel, P. E.; Crestana, S. – Wood Density Determination by X- and Gamma-Ray Tomography. Holzforschung 56 (2002) 5. pp. 535-540.

MAISL et al. (2010)
> Maisl, M.; Porsch, F.; Schorr, C. – Computed laminography for X-ray inspection of lightweight constructions. In: 2nd International Symposium on NDT in Aerospace. 2010. pp. 1-7.

MALAN, MARAIS (1992)
> Malan, F. S.; Marais, P. G. – Some Notes on the Direct Gamma Ray Densitometry of Wood. Holzforschung 46 (1992) 2. pp. 91-97.

MALONEY (1993)
> Maloney, T. M. – Modern particleboard & dry-process fiberboard manufacturing. Updated ed. Miller Freeman: San Francisco, 1993. 688 p.

MANNES et al. (2009)
> Mannes, D.; Sonderegger, W.; Hering, S.; Lehmann, E.; Niemz, P. – Non-destructive determination and quantification of diffusion processes in wood by means of neutron imaging. Holzforschung 63 (2009) 5. pp. 589-596.

MANOHARA et al. (2008)
> Manohara, S. R.; Hanagodimath, S. M.; Thind, K. S.; Gerward, L. – On the effective atomic number and electron density: A comprehensive set of formulas for all types of materials and energies above 1 keV. Nuclear Instruments and Methods in Physics Research Section B: Beam Interactions with Materials and Atoms 266 (2008) 18. pp. 3906-3912.

MARASHDEH et al. (2011)
    Marashdeh, M. W.; Hashim, R.; Tajuddin, A. A.; Bauk, S.; Sulaiman, O. – Effect of particle size on the characterization of binderless particleboard made from Rhizophora spp. mangrove wood for use as phantom material. BioResources 6 (2011) 4. pp. 4028-4044.

MARASHDEH et al. (2012)
    Marashdeh, M. W.; Bauk, S.; Tajuddin, A. A.; Hashim, R. – Measurement of mass attenuation coefficients of Rhizophora spp. binderless particleboards in the 16.59–25.26 keV photon energy range and their density profile using x-ray computed tomography. Applied Radiation and Isotopes 70 (2012) 4. pp. 656-662.

MARASHDEH et al. (2015)
    Marashdeh, M. W.; Al-Hamarneh, I. F.; Abdel Munem, E. M.; Tajuddin, A. A.; Ariffin, A.; Al-Omari, S. – Determining the mass attenuation coefficient, effective atomic number, and electron density of raw wood and binderless particleboards of Rhizophora spp. by using Monte Carlo simulation. Results in Physics 5 (2015) pp. 228-234.

MARUTZKY, SEEGER (2002)
    Marutzky, R.; Seeger, K. – Energie aus Holz und anderer Biomasse - Grundlagen, Technik, Emissionen, Wirtschaftlichkeit, Entsorgung, Recht. 1st reprint ed. DRW-Verlag Weinbrenner: Leinfelden-Echterdingen, 2002. 362 p.

MAY (1977)
    May, H.-A. – Zur Mechanik der Holzspanplatten unter besonderer Berücksichtigung der Rohdichte-Differenzierung und Rohstoffzusammensetzung. Holz als Roh- und Werkstoff 35 (1977) 10. pp. 385-387.

MAY (1983)
    May, H.-A. – Zusammenhänge zwischen Eigenschaften, Rohstoffkomponenten und dem Dichteprofil von Spanplatten - Teil 3: Auswertung von Dichteprofilen und industrielle Anwendungsmöglichkeiten zur Abschliffüberwachung. Holz als Roh- und Werkstoff 41 (1983) 5. pp. 189-192.

MAY et al. (1976)
    May, H. A.; Schätzler, H. P.; Kühn, W. – Measurement of the density profile of chipboard by means of gamma rays. Kerntechnik 18 (1976) 11. pp. 491-494.

MAYNEORD (1937)
    Mayneord, W. V. – The Significance of the Röntgen. Acta/Unio Internationalis contra Cancrum 2 (1937) pp. 271-282.

MAZESS et al. (1990)
    Mazess, R. B.; Barden, H. S.; Bisek, J. P.; Hanson, J. – Dual-energy x-ray absorptiometry for total-body and regional bone- mineral and soft-tissue composition. Am J Clin Nutr 51 (1990) 6. pp. 1106-1112.

McCULLOUGH (1975)
    McCullough, E. C. – Photon attenuation in computed tomography. Medical Physics 2 (1975) 6. pp. 307-320.

McFARLANE et al. (2000)
    McFarlane, N. J. B.; Bull, C. R.; Tillett, R. D.; Speller, R. D.; Royle, G. J.; Johnson, K. R. A. – The Potential for Compton Scattered X-rays in Food Inspection: The Effect of Multiple Scatter and Sample Inhomogeneity. Journal of Agricultural Engineering Research 75 (2000) 3. pp. 265-274.

MEDVED et al. (1998)
    Medved, S.; Budnar, M.; Pirkmaier, S. – Ermittlung des Feuchtigkeitsprofils von Spanplatten mit Gammastrahlen. Holzforschung und Holzverwertung 50 (1998) 1. pp. 7-10.

MEYER (1979)
    Meyer, B. – Urea-Formaldehyde Resins. Addison-Wesley Publishing Company: Reading, Massachusetts, 1979.

MEYER (2007)

  Meyer, N. T. – Einfluss von Druckänderungen während des Heißpressprozesses auf die mechanischen Eigenschaften von Holzwerkstoffen. Diss. Universität Hamburg, Department Biologie der Fakultät für Mathematik, Informatik und Naturwissenschaften, Hamburg, 2007. 238 p.

MIDGLEY (2006)

  Midgley, S. – Angular width of a narrow beam for X-ray linear attenuation coefficient measurements. Radiation Physics and Chemistry 75 (2006) 9. pp. 945-953.

MIDGLEY (2004)

  Midgley, S. M. – A parameterization scheme for the x-ray linear attenuation coefficient and energy absorption coefficient. Physics in Medicine and Biology 49 (2004) 2. pp. 307.

MIDGLEY (2005)

  Midgley, S. M. – Measurements of the X-ray linear attenuation coefficient for low atomic number materials at energies 32-66 and 140 keV. Radiation Physics and Chemistry 72 (2005) 4. pp. 525-535.

MIDGLEY (2011)

  Midgley, S. M. – A model for multi-energy x-ray analysis. Physics in Medicine and Biology 56 (2011) 10. pp. 2943-2962.

MIETTUNEN et al. (1991)

  Miettunen, R.; Korhola, O.; Savikurki, S. – The scatter-to-primary ratio as a function of varying X-ray absorption measured by computed radiography. European Journal of Radiology 13 (1991) 2. pp. 156-159.

MIETTUNEN, KORHOLA (1991)

  Miettunen, R. H.; Korhola, O. A. – The effect of scatter reduction on the signal-to-noise ratio in computed radiography. European Journal of Radiology 12 (1991) 3. pp. 167-170.

MINCONG et al. (2008)

  Mincong, C.; Hongmei, L.; Ziyu, C.; Ji, S. – An examination of mass thickness measurements with X-ray sources. Applied Radiation and Isotopes 66 (2008) 10. pp. 1387-1391.

MÖRATH (1950)

  Mörath, E. – Die chemische Zusammensetzung des Holzes. In: Liese, J. (Ed.) Handbuch der Holzkonservierung. 3rd ed. Springer: Berlin, Heidelberg, 1950. pp. 37-43.

MOSCHLER JR, WINISTORFER (1990)

  Moschler Jr, W. W.; Winistorfer, P. M. – Direct scanning densitometry: an effect of sample heterogeneity and aperture area. Wood and fiber science 22 (1990) 1. pp. 31-38.

MOSCHLER, DOUGAL (1988)

  Moschler, J. W.; Dougal, E. – Calibration Procedure For A Direct Scanning Densitometer Using Gamma Radiation. Wood and fiber science 20 (1988) 3. pp. 297-303.

MUPLOT (2006)

  – MuPlot v. 1.03 - A software tool for the computation of x-ray attenuation coefficients, 2006. http://shape.ing.unibo.it/html/muplot.htm. Access date 01.06.2015.

MURTY (1965)

  Murty, R. C. – Effective Atomic Numbers of Heterogeneous Materials. Nature 207 (1965) 4995. pp. 398-399.

MURTY (2004)

  Murty, V. R. K. – Effective atomic numbers for W/Cu alloy for total photon attenuation. In: Proceedings of the Seventh Radiation Physics and Protection Conference (RPC-2004). Ismailia (Egypt). 2004. pp. 249-252.

MUSÍLEK et al. (1980)
> Musílek, L.; Čechák, T.; Šeda, J. – Empirical formulae for build-up factor calculations in wide conical γ-ray beams. The International Journal of Applied Radiation and Isotopes 31 (1980) 10. pp. 623-627.

NAGEL (2003)
> Nagel, H. D. (Ed.) – Strahlenphysikalische Grundlagen der Röntgendiagnostik. Philips Medizin Systeme Abt. Wissenschaft & Technik: Hamburg, 2003.

NAYDENOV et al. (2004)
> Naydenov, S. V.; Ryzhikov, V. D.; Smith, C. F. – Direct reconstruction of the effective atomic number of materials by the method of multi-energy radiography. Nuclear Instruments and Methods in Physics Research Section B: Beam Interactions with Materials and Atoms 215 (2004) 3–4. pp. 552-560.

NEARN, BASSETT (1968)
> Nearn, W. T.; Bassett, K. – X-Ray Determination and Use Of Surface-to-Surface Density Profile in Fiberboard. Forest Products Journal 18 (1968) 1. pp. 73-74.

NEITZEL (1992)
> Neitzel, U. – Grids or air gaps for scatter reduction in digital radiography: A model calculation. Medical Physics 19 (1992) 2. pp. 475-481.

NICKERSON (1958)
> Nickerson, R. A. – The Fundamentals Of Differential Radiation Measurements. J. Soc. Non-Destructive Testing 16 (1958) 2. pp. 24-7, 41.

NIEMZ, SANDER (1990)
> Niemz, P.; Sander, D. (Eds.) – Prozeßmeßtechnik in der Holzindustrie. Fachbuchverlag: Leipzig, 1990. 288 p.

NIEMZ (1995)
> Niemz, P. – Entwicklungen in der zerstörungsfreien Werkstoffprüfung. Ihre Bedeutung bei Untersuchungen von Holz und Holzwerkstoffen, Teil 2. Holz-Zentralblatt 121 (1995) 73. pp. 1242-1244.

NIEMZ et al. (1999)
> Niemz, P.; Tenisch, W.; Kucera, L. – Entwicklungen bei der zerstörungsfreien Prüfung von Holz. Holz-Forschung, Holz-Verwertung: Mitteilungen der Österreichischen Gesellschaft für Holzforschung Wien 51 (1999) 6. pp. 101-105.

NIEMZ, MANNES (2012)
> Niemz, P.; Mannes, D. – Non-destructive testing of wood and wood-based materials. Journal of Cultural Heritage 13 (2012) 3, Supplement. pp. 26-34.

OH et al. (2009)
> Oh, J.-K.; Shim, K.; Kim, K.-M.; Lee, J.-J. – Quantification of knots in dimension lumber using a single-pass X-ray radiation. Journal of Wood Science 55 (2009) 4. pp. 264-272.

OLIVEIRA et al. (2016)
> Oliveira, V.; Van den Bulcke, J.; Van Acker, J.; de Schryver, T.; Pereira, H. – Cork structural discontinuities studied with X-ray microtomography. Holzforschung 70 (2016) 1. pp. 87-94.

OLSON, ARGANBRIGHT (1981)
> Olson, J. R.; Arganbright, D. G. – Prediction of Mass Attenuation Coefficients of Wood. Wood Science 14 (1981) 2. pp. 86-90.

OLSON et al. (1988)
> Olson, J. R.; Liu, C. J.; Tian, Y.; Shen, Q. – Theoretical wood densitometry. II. Optimal x-ray energy for wood density measurement. Wood and fiber science 20 (1988) 2. pp. 187-196.

ÖSTERÅS (2004)
      Österås, A. H. – Interactions between calcium and heavy metals in norway spruce - Accumulation
      and binding of metals in wood and bark. Diss. Stockholm University, Department of Botany,
      Sweden, 2004. 52 p.

OSTERLOH et al. (2007)
      Osterloh, K.; Zscherpel, U.; Rädel, C.; Weidemann, G.; Meinel, D.; Goebbels, J.; Ewert, U.;
      Hasenstab, A.; Bücherl, T. – Durchstrahlungsprüfung von Holz. In: DGZfP-Jahrestagung 2007.
      Fürth. Deutsche Gesellscahft für Zerstörungsfreie Prüfung e.V. (DGZfP), 2007. pp. 1-12.

OSTERLOH et al. (2008)
      Osterloh, K.; Rädel, C.; Zscherpel, U.; Meinel, D.; Ewert, U.; Bücherl, T.; Hasenstab, A. – Fast
      neutron radiography and tomography of wood. Insight 50 (2008) 6. pp. 307-311.

OSTERLOH et al. (2010)
      Osterloh, K.; Zscherpel, U.; Jechow, M.; Fratzscher, D.; Wrobel, N.; Ewert, U. – X-ray backscatter
      imaging with a novel twisted slit collimator. In: 10 th European Conference on Nondestructive
      Testing (ECNDT). Moscow, Russia. 2010. pp. 1-8.

PAKI AMOUZOU et al. (2006)
      Paki Amouzou, P.; Gertsenshteyn, M.; Jannson, T.; Shnitser, P.; Savant, G. – Inelastic scattering
      measurements of low energy x-ray photons by organics, soil, water, wood, and metals. In: Franks,
      L. A.; Burger, A.; James, R. B.; Barber, H. B.; Doty, F. P.; Roehrig, H. (Eds.) Proc. SPIE 6319,
      Hard X-Ray and Gamma-Ray Detector Physics and Penetrating Radiation Systems VIII, 63190V.
      San Diego, California, USA. SPIE - The International Society for Optical Engineering, 2006. pp.
      63190V-63190V-13.

PARETZKE (1987)
      Paretzke, H. G. – Radiation Track Structure Theory. In: Freeman, G. R. (Ed.) Kinetics of
      nonhomogeneous processes - a practical introduction for chemists, biologists, physicists, and
      material scientists. Wiley: New York, 1987. pp. 89-170.

PARIS et al. (2015)
      Paris, J. L.; Kamke, F. A.; Xiao, X. – X-ray computed tomography of wood-adhesive bondlines:
      attenuation and phase-contrast effects. Wood Science and Technology 49 (2015) 6. pp. 1185-
      1208.

PARKER, JOZSA (1973)
      Parker, M. L.; Jozsa, L. A. – X-ray scanning machine for tree-ring width and density analyses.
      Wood and Fiber Science 5 (1973) 3. pp. 192-197.

PARKER et al. (1973)
      Parker, M. L.; Schoorlemmer, J.; Carver, L. J. – Computerized scanning densitometer for
      automatic recording of tree-ring width and density data from X-ray negatives. Wood and Fiber
      Science 5 (1973) 3. pp. 237-248.

PARTHASARADHI (1968)
      Parthasaradhi, K. – Effective atomic numbers in compounds. Indian journal of pure and applied
      physics 6 (1968) 10. pp. 574-575.

PASSARINI et al. (2015)
      Passarini, L.; Malveau, C.; Hernández, R. E. – Distribution of the equilibrium moisture content in
      four hardwoods below fiber saturation point with magnetic resonance microimaging. Wood
      Science and Technology 49 (2015) 6. pp. 1251-1268.

PAULITSCH, MEHLHORN (1973)
      Paulitsch, M.; Mehlhorn, L. – Neues Verfahren zur Bestimmung des Rohdichteprofils von
      Holzspanplatten. Holz als Roh- und Werkstoff 31 (1973) 10. pp. 393-397.

PAULITSCH, BARBU (2015)
      Paulitsch, M.; Barbu, M. C. – Holzwerkstoffe der Moderne. DRW-Verlag Weinbrenner GmbH &
      Co. KG: Leinfelden-Echterdingen, 2015. 524 p.

PEASE et al. (2012)
Pease, B. J.; Scheffler, G. A.; Janssen, H. – Monitoring moisture movements in building materials using X-ray attenuation: Influence of beam-hardening of polychromatic X-ray photon beams. Construction and Building Materials 36 (2012) pp. 419-429.

PERRE, THIERCELIN (2004)
Perre, P.; Thiercelin, F. – Evidence of dual scale porous mechanisms during fluid migration in hardwood species - (I) - Using the attenuation of a polychromatic X-ray beam to determine the evolution of moisture content during imbibition of beech. Chinese Journal of Chemical Engineering 12 (2004) 6. pp. 773-782.

PERRIN (1948)
Perrin, F. H. – Whose Absorption Law? Journal of the Optical Society of America 38 (1948) 1. pp. 72-74.

PFRIEM et al. (2009)
Pfriem, A.; Zauer, M.; Wagenführ, A. – Alteration of the pore structure of spruce (Picea abies (L.) Karst.) and maple (Acer pseudoplatanus L.) due to thermal treatment as determined by helium pycnometry and mercury intrusion porosimetry. Holzforschung 63 (2009) 1. pp. 94-98.

PHELPS et al. (1975)
Phelps, M. E.; Gado, M. H.; Hoffman, E. J. – Correlation of Effective Atomic Number and Electron Density with Attenuation Coefficients Measured with Polychromatic X Rays. Radiology 117 (1975) 3. pp. 585-588.

PIZZI, MITTAL (2003)
Pizzi, A.; Mittal, K. L. – Handbook of Adhesive Technology. Marcel Dekker: New York, Basel, 2003. 1036 p.

PLANK et al. (2017)
Plank, B.; Salaberger, D.; Rao, G.; Amirkhanov, A.; Kastner, J. – 4D Röntgen-Computertomografie mittels konventioneller Labor CTs: Möglichkeiten und Einschränkungen. In: DGZfP-Jahrestagung 2017. Koblenz, Germany. 2017. pp. 1-9.

PLATH (1971)
Plath, E. – Beitrag zur Mechanik der Holzspanplatten. European Journal of Wood and Wood Products 29 (1971) 10. pp. 377-382.

PLATH, SCHNITZLER (1974)
Plath, E.; Schnitzler, E. – Das Rohdichteprofil als Beurteilungsmerkmal von Spanplatten. European Journal of Wood and Wood Products 32 (1974) 11. pp. 443-449.

PLINKE et al. (2012)
Plinke, B.; Schirp, A.; Weidenmüller, I. – Methoden der Holzpartikelgrößenmessung - Von der technologischen Fragestellung zur aussagefähigen Statistik. holztechnologie 53 (2012) 4. pp. 11-17.

PLINKE et al. (2018)
Plinke, B.; Bittner, F.; Endres, H.-J. – Messung der Dichteverteilung in Holzpartikelwerkstoffen in drei Dimensionen mit Computertomographie. In: Wagenführ, A. (Ed.) 18. Holztechnologischen Kolloquium. Dresden. TU Dresden, Institut für Holz- und Papiertechnik, 2018. pp. 208-217.

POLGE, LUTZ (1969)
Polge, H.; Lutz, P. – Über die Möglichkeit der Dichtemessung von Spanplatten senkrecht zur Plattenebene mit Hilfe von Röntgenstrahlen. holztechnologie 10 (1969) 2. pp. 75-79.

POLGE (1970)
Polge, H. – The use of X-ray densitometric methods in dendrochronology. Tree-Ring Bulletin 30 (1970) 1-4. pp. 1-10.

POLGE (1978)
Polge, H. – Fifteen years of wood radiation densitometry. Wood Science and Technology 12 (1978) 3. pp. 187-196.

POLLER, KNAPPE (1988)
Poller, S.; Knappe, R. – Über die Elementarzusammensetzung von Dendromassen der Kiefer. holztechnologie 29 (1988) 4. pp. 205-207.

POLUDNIOWSKI (2007)
Poludniowski, G. G. – Calculation of x-ray spectra emerging from an x-ray tube. Part II. X-ray production and filtration in x-ray targets. Medical Physics 34 (2007) 6. pp. 2175-2186.

POLUDNIOWSKI, EVANS (2007)
Poludniowski, G. G.; Evans, P. M. – Calculation of x-ray spectra emerging from an x-ray tube. Part I. Electron penetration characteristics in x-ray targets. Medical Physics 34 (2007) 6. pp. 2164-2174.

RACKWITZ (1954)
Rackwitz, G. – Ein Beitrag zur Kenntnis der Vorgänge bei der Verleimung von Holzspänen zu Holzspanplatten in beheizten hydaulischen Pressen. Diss. Technische Hochschule, Braunschweig, 1954.

RACZKOWSKI, STEMPIEŃ (1967)
Raczkowski, J.; Stempień, C. – On the relation between the density of wood and the density of the solid wood substance. Holz als Roh- und Werkstoff 25 (1967) 10. pp. 380-383.

RANTA, MAY (1978)
Ranta, L.; May, H.-A. – Zur Messung von Rohdichteprofilen an Spanplatten mittels Gammastrahlen. European Journal of Wood and Wood Products 36 (1978) 12. pp. 467-474.

RAUTKARI et al. (2011)
Rautkari, L.; Kamke, F.; Hughes, M. – Potential error in density profile measurements for wood composites. European Journal of Wood and Wood Products 69 (2011) 1. pp. 167-169.

RAUTKARI (2012)
Rautkari, L. – Surface modification of solid wood using different techniques. Diss. Aalto University, Department of Forest Products Technology, Espoo, Finland, 2012. 126 p.

REBOLLEDO et al. (2018)
Rebolledo, P.; Cloutier, A.; Yemele, M.-C. – Effect of Density and Fiber Size on Porosity and Thermal Conductivity of Fiberboard Mats. Fibers 6 (2018) 4. pp. 81.

REBUFFEL, DINTEN (2007)
Rebuffel, V.; Dinten, J. M. – Dual-energy X-ray imaging: benefits and limits. Insight - Non-Destructive Testing and Condition Monitoring 49 (2007) 10. pp. 589-594.

REIMERS et al. (2008)
Reimers, W.; Pyzalla, A. R.; Schreyer, A.; Clemens, H. (Eds.) – Neutrons and synchrotron radiation in engineering materials science. Wiley-VCH: Weinheim, 2008. 460 p.

REINPRECHT, ŠUPINA (2015)
Reinprecht, L.; Šupina, P. – Comparative evaluation of inspection techniques for impregnated wood utility poles: ultrasonic, drill-resistive, and CT-scanning assessments. European Journal of Wood and Wood Products 73 (2015) 6. pp. 741-751.

RIEGEL (1997)
Riegel, A. – Gefügeschädigungen durch spanende Bearbeitung - Stand der Erkenntnisse und mögliche Meßmethoden. European Journal of Wood and Wood Products 55 (1997) 2. pp. 111-117.

Riggio et al. (2014)
Riggio, M.; Anthony, R. W.; Augelli, F.; Kasal, B.; Lechner, T.; Muller, W.; Tannert, T. – In situ assessment of structural timber using non-destructive techniques. Materials and Structures 47 (2014) 5. pp. 749-766.

Rindby (1986)
Rindby, A. – Applications of fiber technique in the X-ray region. Nuclear Instruments and Methods in Physics Research Section A: Accelerators, Spectrometers, Detectors and Associated Equipment 249 (1986) 2-3. pp. 536-540.

Rindby et al. (1989)
Rindby, A.; Engström, P.; Larsson, S.; Stocklassa, B. – X-Ray Microbeam Spectrometer. Patentschrift WO 89/12817, IPC G01N 23/223. Inhaber Rindby, Anders; Engström, Per; Larsson, Sturre; Stocklassa, Bengt, Schweden. 1989. 13 p.

Rindfleisch (1937)
Rindfleisch, H. – Über den K-Sprung von Al(13) bis W(74). Annalen der Physik 420 (1937) 5. pp. 409-437.

Rinn et al. (1996)
Rinn, F.; Schweingruber, F. H.; Schär, E. – RESISTOGRAPH and X-Ray Density Charts of Wood - Comparative Evaluation of Drill Resistance Profiles and X-ray Density Charts of Different Wood Species. Holzforschung 50 (1996) 4. pp. 303-311.

Rinnhofer et al. (2003)
Rinnhofer, A.; Petutschnigg, A.; Andreu, J.-P. – Internal log scanning for optimizing breakdown. Computers and Electronics in Agriculture 41 (2003) 1–3. pp. 7-21.

Ritchings, Pullan (1979)
Ritchings, R. T.; Pullan, B. R. – A technique for simultaneous dual energy scanning. Journal of computer assisted tomography 3 (1979) 6. pp. 842-846.

Roberts (1964)
Roberts, A. F. – Ultimate analyses of partially decomposed wood samples. Combustion and Flame 8 (1964) 4. pp. 345-346.

Robertson et al. (1999)
Robertson, G.; Olson, J.; Allen, P.; Chan, B.; Seth, R. – Measurement of fiber length, coarseness, and shape with the fiber quality analyzer. Tappi journal 82 (1999) 10. pp. 93-98.

Roffael (1982)
Roffael, E. – Die Formaldehyd-Abgabe von Spanplatten und anderen Werkstoffen. DRW-Verlag Weinbrenner-KG: Leinefelden-Echterdingen, 1982. 154 p.

Roffael et al. (2009)
Roffael, E.; Bär, G.; Behn, C.; Dix, B. – Einfluss der Aufschlusstemperatur auf die morphologischen Eigenschaften von TMP aus Kiefernholz. European Journal of Wood and Wood Products 67 (2009) 1. pp. 119-120.

Röntgen (1898a)
Röntgen, W. C. – Weitere Beobachtungen über die Eigenschaften der X-Strahlen (Dritte Mittheilung). Annalen der Physik 300 (1898a) 1. pp. 18-37.

Röntgen (1898b)
Röntgen, W. C. – Ueber eine neue Art von Strahlen (Erste Mittheilung). Annalen der Physik 300 (1898b) 1. pp. 1-11.

Ross (2015)
Ross, R. J. (Ed.) – Nondestructive Evaluation of Wood - Second Edition - General Technical Report FPL-GTR-238. 2nd ed. U.S. Department of Agriculture, Forest Service, Forest Products Laboratory: Madison, WI, 2015. 176 p.

ROWELL (2005)
Rowell, R. M. – Handbook of wood chemistry and wood composites. CRC Press: Boca Raton, Fla., 2005. 487 p.

RÓZSA (1987)
Rózsa, S. – Radiometrische Messungen in der Industrie - Grundlagen und Meßmethoden. Franzis: München, 1987. 292 p.

RUDMAN et al. (1969)
Rudman, P.; McKinnell, F.; Higgs, M. – Quantitative determination of wood density by X-ray densitometry. Journal of the Institute of Wood Science 24 (1969) 6. pp. 37-43.

RUHRKOHLE-VERKAUF GMBH (1984)
Ruhrkohle-Verkauf GmbH (Ed.) – Ruhrkohlen-Handbuch - Anhaltszahlen, Erfahrungswerte und praktische Hinweise für industrielle Verbraucher. 6th ed. Verlag Glückauf: Essen, 1984. 404 p.

RUSSO (2018)
Russo, P. (Ed.) – Handbook of X-ray imaging - physics and technology. CRC Press Taylor & Francis Group: Boca Raton, FL, 2018. 1419 p.

RUTH, JOSEPH (1997)
Ruth, C.; Joseph, P. M. – Estimation of a photon energy spectrum for a computed tomography scanner. Medical Physics 24 (1997) 5. pp. 695-702.

SALINAS et al. (2006)
Salinas, I. C. P.; Conti, C. C.; Lopes, R. T. – Effective density and mass attenuation coefficient for building material in Brazil. Applied Radiation and Isotopes 64 (2006) 1. pp. 13-18.

SALO (2018)
Salo, R. (Ed.) – MDF Yearbook 2017/2018 - Global Industry Review. AWA Alexander Watson Associates BV: Amsterdam, 2018. 76 p.

SANABRIA et al. (2011)
Sanabria, S. J.; Wyss, P.; Neuenschwander, J.; Niemz, P.; Sennhauser, U. – Assessment of glued timber integrity by limited-angle microfocus X-ray computed tomography. European Journal of Wood and Wood Products 69 (2011) 4. pp. 605-617.

SANABRIA et al. (2013)
Sanabria, S. J.; Hilbers, U.; Neuenschwander, J.; Niemz, P.; Sennhauser, U.; Thömen, H.; Wenker, J. L. – Modeling and prediction of density distribution and microstructure in particleboards from acoustic properties by correlation of non-contact high-resolution pulsed air-coupled ultrasound and X-ray images. Ultrasonics 53 (2013) 1. pp. 157-170.

SARITHA, NAGESWARA RAO (2012)
Saritha, B.; Nageswara Rao, A. S. – Z dependence of photon interactions in wood materials. Canadian Journal of Physics 91 (2012) 3. pp. 221-225.

SARITHA, NAGESWARA RAO (2013)
Saritha, B.; Nageswara Rao, A. S. – Determination of attenuation coefficients of some wood materials based on thickness and chemical composition. Canadian Journal of Physics 92 (2013) 9. pp. 968-972.

SAUTER et al. (2015)
Sauter, U. H.; Bertolini, N.; Laudon, N.; Baumgartner, R.; Hoyos-Montoya, D. C.; Stängle, S. M.; Brüchert, F. – Automated wood species identification by CT-technology. In: Ross, R. J.; Gonçalves, R.; Wang, X. (Eds.) 19th International Nondestructive Testing and Evaluation of Wood Symposium. General Technical Report FPL–GTR–239. Rio de Janeiro, Brazil. U.S. Department of Agriculture, Forest Service, Forest Products Laboratory, Madison, WI, 2015. pp. 558-561.

SCHAJER (2001)
Schajer, G. S. – Lumber strength grading using X-ray scanning. Forest products journal 51 (2001) 1. pp. 43-50.

SCHÄTZLER (1979)
Schätzler, H. P. – Basic aspects on the use of elastic and inelastic scattered gamma radiation for the determination of binary systems with effective atomic numbers of less than 10. The International Journal of Applied Radiation and Isotopes 30 (1979) 2. pp. 115-121.

SCHEFFLER, BLÜTHGEN (2017)
Scheffler, R.; Blüthgen, L. – Orientierende radiometrische Untersuchungen zur Bestimmung der Rohdichte an den Bambusarten Phyllostachys pubescens und Guadua angustifolia. holztechnologie 58 (2017) 4. pp. 11-15.

SCHICKERT et al. (2017)
Schickert, M.; Bonitz, F.; Ulanov, A.; Müller, B.; Chmara, S.; Ruminski, N.; Rehpenning, P.-E.; Blüthgen, L.; Flade, P.; Wiedemann, J. – Tomographische Abbildung mit Ultraschall, Radar und Röntgen zur Detektion von Fäule in Holzstämmen. In: DGZfP-Jahrestagung 2017. Koblenz, Germany. 2017. pp. 1-11.

SCHIEBOLD (2015)
Schiebold, K. – Zerstörungsfreie Werkstoffprüfung - Durchstrahlungsprüfung ein Lehr- und Arbeitsbuch für Ausbildung und Prüfpraxis. Springer Vieweg: Berlin, Heidelberg, 2015. 308 p.

SCHMITT et al. (1987)
Schmitt, W. G. H.; Mahmalat, M. O.; Beyer, H. K. – Die Meßgenauigkeit der computertomographischen Densitometrie in der Nachbarschaft des Beckenskeletts. RöFo - Fortschritte auf dem Gebiet der Röntgenstrahlen und der bildgebenden Verfahren 146 (1987) 1. pp. 34-38.

SCHÖRNER et al. (2011)
Schörner, K.; Goldammer, M.; Stephan, J. – Comparison between beam-stop and beam-hole array scatter correction techniques for industrial X-ray cone-beam CT. Nuclear Instruments and Methods in Physics Research Section B: Beam Interactions with Materials and Atoms 269 (2011) 3. pp. 292-299.

SCHRIEVER, BOEHME (1984)
Schriever, E.; Boehme, C. – Bestimmung von mineralischen Bestandteilen in Spanplatten. Holz als Roh- und Werkstoff 42 (1984) 2. pp. 51-54.

SCHWEINGRUBER et al. (1988)
Schweingruber, F. H.; Bartholin, T.; Schaur, E.; Briffa, K. R. – Radiodensitometric-dendroclimatological conifer chronologies from Lapland (Scandinavia) and the Alps (Switzerland). Boreas 17 (1988) 4. pp. 559-566.

SEIFERT (1972)
Seifert, J. – Zur Sorption und Quellung von Holz und Holzwerkstoffen - Dritte Mitteilung: Die Volumenkontraktion zwischen Holz und Wasser. Holz als Roh- und Werkstoff 30 (1972) 9. pp. 332-342.

SEPPKE et al. (2015)
Seppke, B.; Bähnisch, C.; Benthien, J.; Heldner, S.; Ohlmeyer, M. – A Concurrent Skeleton-based Approach for the Characterization of Wood Fibers with Sub-pixel Precision For Fiber Board Production. In: Perner, P. (Ed.) Proceedings of Advances in Mass Data Analysis of Image and Signals in Medicine, Biotechnology, Chemistry and Food Industry (MDA), 2015, draft version - to appear. 2015.

SERGEJEWA (1959)
Sergejewa, A. S. – Chemie des Holzes und der Cellulose. Verlag Theodor Steinkopff: Dresden, 1959. 151 p.

SHAH et al. (1996)
Shah, G. A.; Hassam, G.; Newman, D. L. – The effectiveness of antiscatter techniques. Radiography 2 (1996) 3. pp. 191-197.

SHALBAFAN et al. (2012)
Shalbafan, A.; Luedtke, J.; Welling, J.; Thoemen, H. – Comparison of foam core materials in innovative lightweight wood-based panels. European Journal of Wood and Wood Products 70 (2012) 1. pp. 287-292.

SHANI (2001)
Shani, G. – Radiation dosimetry - instrumentation and methods. 2nd ed. CRC Press LLC: 2001. 506 p.

SHARAF (2001)
Sharaf, J. M. – Practical aspects of Compton scatter densitometry. Applied Radiation and Isotopes 54 (2001) 5. pp. 801-809.

SHEDLOCK et al. (2015)
Shedlock, D.; Wang, A.; Nisius, D.; Hu, M.; Yoon, S.; Brooks, A.; Shapiro, E.; Star-lack, J. – Refinement of Imaging Processing of Scatter Correction and Beam Hardening Tools for Industrial Radiography and Cone Beam CT. In: International Symposium on Digital Industrial Radiology and Computed Tomography (DIR 2015). Ghent, Belgium. Gent BC Administratieve informatie, 2015. pp. 1-10.

SHEIKH et al. (2008)
Sheikh, A. M.; Khokhar, I.; Anwar, M. S.; Khan, M. N.; Akhtar, H. – Studies on synthesis and properties of urea formaldehyde adhesives. Journal of the Chemical Society of Pakistan 30 (2008) 1. pp. 20-22.

SHIRAKAWA (2000)
Shirakawa, Y. – A build-up treatment for thickness gauging of steel plates based on gamma-ray transmission. Applied Radiation and Isotopes 53 (2000) 4–5. pp. 581-586.

SHIROMA et al. (2019)
Shiroma, A.; Star-Lack, J.; Holt, K.; Hu, M.; Hoelzer, S.; Yoon, S.; Sosnovsky, E.; GregoryFailla; Wang, A.; Kokkonen, P.; Ruprech, M.; Maslowski, A.; Nisiu, D. – Scatter Correction for Industrial Cone-Beam Computed Tomography (CBCT) Using 3D VSHARP, a fast GPU-Based Linear Boltzmann Transport Equation Solve. In: 9th Conference on Industrial Computed Tomography (iCT). Padova, Italy. 2019. pp. 1-9.

SIDHU et al. (1999)
Sidhu, G. S.; Singh, P. S.; Mudahar, G. S. – Energy Absorption Buildup Factor Studies in Biological Samples. Radiation Protection Dosimetry 86 (1999) 3. pp. 207-216.

SIDHU et al. (2000)
Sidhu, G. S.; Singh, P. S.; Mudahar, G. S. – A study of energy and effective atomic number dependence of the exposure build-up factors in biological samples. Journal of Radiological Protection 20 (2000) 1. pp. 53-68.

SIDKY et al. (2005)
Sidky, E. Y.; Yu, L.; Pan, X.; Zou, Y.; Vannier, M. – A robust method of x-ray source spectrum estimation from transmission measurements: Demonstrated on computer simulated, scatter-free transmission data. Journal of Applied Physics 97 (2005) 12. pp. 124701.

SIEGEL et al. (1985)
Siegel, J. A.; Wu, R. K.; Maurer, A. H. – The buildup factor: effect of scatter on absolute volume determination. Journal of nuclear medicine : official publication, Society of Nuclear Medicine 26 (1985) 4. pp. 390-394.

SILBERSTEIN (1932)
Silberstein, L. – Determination of the spectral composition of X-ray radiation from filtration data. Journal of the Optical Society of America 22 (1932) 5. pp. 265-278.

SILBERSTEIN (1933)
Silberstein, L. – XXXIV. Spectral composition of an X-ray radiation determined from its filtration curve. Philosophical Magazine Series 7 15 (1933) 98. pp. 375-394.

SINGH et al. (2004)
Singh, C.; Singh, T.; Kumar, A.; Mudahar, G. S. – Energy and chemical composition dependence of mass attenuation coefficients of building materials. Annals of Nuclear Energy 31 (2004) 10. pp. 1199-1205.

SINGH et al. (1996)
Singh, K.; Kaur, R.; Vandana; Kumar, V. – Study of effective atomic numbers and mass attenuation coefficients in some compounds. Radiation Physics and Chemistry 47 (1996) 4. pp. 535-541.

SINGH et al. (1993)
Singh, M.; Sandhu, A. K.; Brar, G. S.; Mudahar, G. S. – Effect of weight fractions of H, C and O on the total mass attenuation coefficients of HCO-materials. Applied Radiation and Isotopes 44 (1993) 7. pp. 1073-1076.

SINGH et al. (2009)
Singh, T.; Kumar, N.; Singh, P. S. – Chemical composition dependence of exposure buildup factors for some polymers. Annals of Nuclear Energy 36 (2009) 1. pp. 114-120.

SINGH et al. (2014a)
Singh, V. P.; Badiger, N. M.; Kucuk, N. – Assessment of methods for estimation of effective atomic numbers of common human organ and tissue substitutes: waxes, plastics and polymers. Radioprotection 49 (2014a) 02. pp. 115-121.

SINGH et al. (2014b)
Singh, V. P.; Badiger, N. M.; Kucuk, N. – Determination of Effective Atomic Numbers Using Different Methods for Some Low-Z Materials. Journal of Nuclear Chemistry 2014 (2014b) Article ID 725629. pp. 1-7.

SINKA et al. (2004)
Sinka, I. C.; Burch, S. F.; Tweed, J. H.; Cunningham, J. C. – Measurement of density variations in tablets using X-ray computed tomography. International Journal of Pharmaceutics 271 (2004) 1–2. pp. 215-224.

SKAAR (1988)
Skaar, C. – Wood-water relations. Springer-Verlag: Berlin u.a., 1988. 292 p.

SLISERIS et al. (2017)
Sliseris, J.; Andrä, H.; Kabel, M.; Dix, B.; Plinke, B. – Virtual characterization of MDF fiber network. European Journal of Wood and Wood Products 75 (2017) 3. pp. 397-407.

SOINÉ (1990)
Soiné, H. – Neues Dichte-Meßgerät erweitert die Möglichkeiten. HK (1990) 02. pp. 119-193.

SOLBRIG (2009)
Solbrig, K. – Optimierung und Evaluierung eines radiometrischen Dichtemessarbeitsplatzes am Beispiel des Itrax Wood Scanners. Masterarbeit Hochschule Ostwestfalen-Lippe, Fachbereich Produktion und Wirtschaft, Lemgo, 2009. 125 p.

SOLBRIG et al. (2010)
Solbrig, K.; Frühwald, K.; Gruchot, M.; Ressel, J. B. – Rohdichteprofilbestimmung bei Holzwerkstoffen - "Itrax Woodscanner" als radiometrischer Labor-Dichtemessplatz für Holzwerkstoffe und Sonderanwendungen. Holz-Zentralblatt 136 (2010) 36. pp. 895-896.

SOLBRIG et al. (2011)
Solbrig, K.; Frühwald, K.; Ressel, J. B.; Gruchot, M. – Radiometrische Untersuchungen an Holz und Holzwerkstoffen unter Einsatz ionisierender Strahlung. In: DGZfP-Jahrestagung 2011. Bremen. 2011. pp. 1-11.

SOLBRIG (2012)
Solbrig, K. – Process monitoring in particle board production – looking very deep inside? In: Riegel, A.; Nicolich, M. (Eds.) 2nd International Conference Production Engineering and Management for Furniture Industry, 27th and 28th September 2012. Lemgo, Germany. Schriftenreihe Logistik Fachbereich Produktion und Wirtschaft, Hochschule Ostwestfalen-Lippe, Lemgo, 2012. pp. 41-56.

SOLBRIG et al. (2013)
Solbrig, K.; Krause, B.; Frühwald, K.; Fuchs, M.; Ressel, J. B. – Beitrag zur Genauigkeit radiometrischer Messmethoden zur Bestimmung von Rohdichtegradienten an Holzwerkstoffen. In: IHD (Ed.) 10. Holzwerkstoffkolloquium. Dresden. Institut für Holztechnologie Dresden gemeinnützige GmbH (IHD), 2013. pp. 159-175.

SOLBRIG et al. (2014a)
Solbrig, K.; Fuchs, M.; Frühwald, K.; Ressel, J. B. – Accuracy of the radiometric determination of raw density gradients on wood-based composites. holztechnologie 55 (2014a) 6. pp. 27-34.

SOLBRIG et al. (2014b)
Solbrig, K.; Fuchs, M.; Frühwald, K.; Ressel, J. B. – X-ray based process and quality control in wood-based composites production - needs and benefits. In: Villmer, F.-J.; Padoano, E. (Eds.) 4th International Conference Production Engineering and Management, 25th and 26th September 2014. Lemgo, Germany. Schriftenreihe Logistik Fachbereich Produktion und Wirtschaft, Hochschule Ostwestfalen-Lippe, Lemgo, 2014b. pp. 179-192.

SOLBRIG et al. (2015a)
Solbrig, K.; Frühwald, K.; Ressel, J. B.; Fuchs, M. – Wood-based composite X-ray densitometry – attenuation effects on measurements. In: Ross, R. J.; Gonçalves, R.; Wang, X. (Eds.) 19th International Nondestructive Testing and Evaluation of Wood Symposium. General Technical Report FPL–GTR–239. Rio de Janeiro, Brazil. U.S. Department of Agriculture, Forest Service, Forest Products Laboratory, Madison, WI, 2015a. pp. 303-313.

SOLBRIG et al. (2015b)
Solbrig, K.; Frühwald, K.; Ressel, J. B.; Mannes, D.; Schillinger, B.; Schulz, M. – Dampfbewegung in Holzwerkstoffen – Visualisierung und Quantifizierung der Siedewelle mittels Neutronenradiographie. In: IHD (Ed.) 11. Holzwerkstoffkolloquium. Dresden. Institut für Holztechnologie Dresden gemeinnützige GmbH (IHD), 2015b. pp. 89-108.

SOLBRIG et al. (2015c)
Solbrig, K.; Frühwald, K.; Ressel, J. B.; Mannes, D.; Schillinger, B.; Schulz, M. – Radiometric investigation of water vapour movement in wood-based composites by means of cold and thermal neutrons. In: 10th World Conference on Neutron Radiography 5-10 October 2014 WCNR-10. Grindelwald, Switzerland. Elsevier Physics Procedia, 2015c. pp. 583-592.

SOLBRIG et al. (2015d)
Solbrig, K.; Fuchs, M.; Frühwald, K.; Ressel, J. B. – Zuverlässiger Einsatz quantitativer Röntgenmesstechnik zur Prozess- und Qualitätskontrolle in der Holzwerkstoffindustrie. In: DACH-Jahrestagung 2015 - ZfP in Forschung, Entwicklung und Anwendung. Salzburg, Austria. Deutsche Gesellschaft für Zerstörungsfreie Prüfung DGZfP, Berlin, 2015d. pp. 1-13.

SOLBRIG (2017)
Solbrig, K. – Erkennungs-Dienst - Spezialisierte Röntgentechnik für verschiedene Messaufgaben bei der Holzwerkstoffproduktion. MDF-Magazin - Supplement von Holz-Zentralblatt und HK 23 (2017) pp. 38-45.

SOLBRIG (2018)
Solbrig, K. – Best Practice - Einsatz von EWS-Hochleistungs-Röntgenmesstechnik in der Formstarße von MDF & Co. MDF-Magazin - Supplement von Holz-Zentralblatt und HK 24 (2018) pp. 48-57.

SPIERS (1946)
Spiers, F. W. – Effective Atomic Number and Energy Absorption in Tissues. The British Journal of Radiology 19 (1946) 218. pp. 52-63.

STAMM, SEBORG (1934)
Stamm, A. J.; Seborg, R. M. – Adsorption Compression on Cellulose and Wood. I. Density Measurements in Benzene. The Journal of Physical Chemistry 39 (1934) 1. pp. 133-142.

STAMM, HANSEN (1937)
Stamm, A. J.; Hansen, L. A. – The Bonding Force of Cellulosic Materials for Water (from Specific Volume and Thermal Data). The Journal of Physical Chemistry 41 (1937) 7. pp. 1007-1016.

STANDFEST et al. (2009)
Standfest, G.; Petutschnigg, A.; Dunky, M.; Zimmer, B. – Rohdichtebestimmung von Holzwerkstoffen mittels Computertomographie. Holz als Roh- und Werkstoff 67 (2009) 1. pp. 83-87.

STANDFEST (2011)
Standfest, G. – Hohlräume in Holzwerkstoffen. Diss. Universität für Bodenkultur, Department für Materialwissenschaften und Prozesstechnik, Institut für Holzforschung, Vienna, Austria, 2011. 77 p.

STANDFEST et al. (2013)
Standfest, G.; Kutnar, A.; Plank, B.; Petutschnigg, A.; Kamke, F.; Dunky, M. – Microstructure of viscoelastic thermal compressed (VTC) wood using computed microtomography. Wood Science and Technology 47 (2013) 1. pp. 121-139.

STÄNGLE et al. (2015)
Stängle, S. M.; Brüchert, F.; Heikkila, A.; Usenius, T.; Usenius, A.; Sauter, U. H. – Potentially increased sawmill yield from hardwoods using X-ray computed tomography for knot detection. Annals of Forest Science 72 (2015) 1. pp. 57-65.

STEFFENREM et al. (2014)
Steffenrem, A.; Kvaalen, H.; Dalen, K. S.; Høibø, O. A. – A high-throughput X-ray-based method for measurements of relative wood density from unprepared increment cores from Picea abies. Scandinavian Journal of Forest Research 29 (2014) 5. pp. 506-514.

STEGEMANN (1995)
Stegemann, D. – Zerstörungsfreie Prüfverfahren Radiografie und Radioskopie. Vieweg+Teubner Verlag: Wiesbaden, 1995. 177 p.

STEINER et al. (1978)
Steiner, P. R.; Jozsa, L. A.; Parker, M. L.; Chow, S. – Application of x-ray densitometry to determine density profile in waferboard: relationship of density to thickness expansion and internal bond strength under various cycles. Wood science 11 (1978) 1. pp. 48-55.

STEVENS (1978)
Stevens, R. R. – Slicing apparatus aids in determination of layer density of particleboard. Forest products journal 28 (1978) 2. pp. 51-52.

SUCHSLAND, WOODSON (1987)
Suchsland, O.; Woodson, G. E. – Fiberboard manufacturing practices in the United States. U.S. Dept. of Agriculture, Forest Service: 1987.

SUGIMORI, LAM (1999)
Sugimori, M.; Lam, F. – Macro-void distribution analysis in strand-based wood composites using an X-ray computer tomography technique. Journal of Wood Science 45 (1999) 3. pp. 254-257.

SUTEAU, CHIRON (2005)
Suteau, C.; Chiron, M. – An iterative method for calculating gamma-ray build-up factors in multi-layer shields. Radiation Protection Dosimetry 116 (2005) 1-4. pp. 489-492.

TAJUDDIN et al. (1996)
Tajuddin, A. A.; Che Wan Sudin, C. W. A.; Bradley, D. A. – Radiographic and scattering investigation on the suitability of Rhizophora sp. as tissue-equivalent medium for dosimetric study. Radiation Physics and Chemistry 47 (1996) 5. pp. 739-740.

TANAKA et al. (2009)
Tanaka, T.; Avramidis, S.; Shida, S. – Evaluation of moisture content distribution in wood by soft X-ray imaging. Journal of Wood Science 55 (2009) 1. pp. 69-73.

TANAKA (2015)
Tanaka, T. – Improved method based on dual-energy X-ray absorptiometry for nondestructive evaluation of solid wood moisture content. Holzforschung 69 (2015) 9. pp. 1133-1136.

TANNERT et al. (2014)
Tannert, T.; Anthony, R. W.; Kasal, B.; Kloiber, M.; Piazza, M.; Riggio, M.; Rinn, F.; Widmann, R.; Yamaguchi, N. – In situ assessment of structural timber using semi-destructive techniques. Materials and Structures 47 (2014) 5. pp. 767-785.

TAYLOR et al. (2013)
Taylor, A.; Plank, B.; Standfest, G.; Petutschnigg, A. – Beech wood shrinkage observed at the micro-scale by a time series of X-ray computed tomographs (µXCT). Holzforschung 67 (2013) 2. pp. 201-205.

TAYLOR et al. (2008)
Taylor, M. L.; Franich, R. D.; Trapp, J. V.; Johnston, P. N. – The effective atomic number of dosimetric gels. Australasian Physics & Engineering Sciences in Medicine 31 (2008) 2. pp. 131-138.

TAYLOR (2011)
Taylor, M. L. – Robust determination of effective atomic numbers for electron interactions with TLD-100 and TLD-100H thermoluminescent dosimeters. Nuclear Instruments and Methods in Physics Research Section B: Beam Interactions with Materials and Atoms 269 (2011) 8. pp. 770-773.

TAYLOR et al. (2012)
Taylor, M. L.; Smith, R. L.; Dossing, F.; Franich, R. D. – Robust calculation of effective atomic numbers: The Auto-Zeff software. Medical Physics 39 (2012) 4. pp. 1769-1778.

TENORIO et al. (2015)
Tenorio, C.; Moya, R.; Filho, M. T.; Valaert, J. – Application of the X-ray densitometry in the evaluation of the quality and mechanical properties of biomass pellets. Fuel Processing Technology 132 (2015) 0. pp. 62-73.

THOEMEN (2000)
Thoemen, H. – Modeling the physical processes in natural fiber composites during batch and continuous pressing. Diss. Oregon State University, Forest Products Department, Corvallis, 2000. 187 p.

THOEMEN et al. (2006)
Thoemen, H.; Haselein, C. R.; Humphrey, P. E. – Modeling the physical processes relevant during hot pressing of wood-based composites. Part II. Rheology. European Journal of Wood and Wood Products 64 (2006) 2. pp. 125-133.

THOEMEN, HUMPHREY (2006)
Thoemen, H.; Humphrey, P. E. – Modeling the physical processes relevant during hot pressing of wood-based composites. Part I. Heat and mass transfer. European Journal of Wood and Wood Products 64 (2006) 1. pp. 1-10.

THOEMEN (2008)
Thoemen, H. – Grundlegende Untersuchungen zur Herstellung und Mikrostruktur von Holzwerkstoffen. Forschungsbericht zum Antrag auf kumulative Habilitation Universität Hamburg, Department Biologie, Fakultät für Mathematik, Informatik und Naturwissenschaften, Hamburg, 2008. 250 p.

THOEMEN (2010)
Thoemen, H. – Vom Holz zum Werkstoff - Grundlegende Untersuchungen zur Herstellung und Struktur von Holzwerkstoffen. Berner Fachhochschule Architektur, Holz und Bau: Biel (Schweiz), 2010. 152 p.

THOEMEN et al. (2010)
Thoemen, H.; Irle, M.; Sernek, M. (Eds.) – Wood-Based Panels - An Introduction for Specialists. Brunel University Press: London, England, 2010. 304 p.

THÖMEN, VIEMEISTER (2015)
Thömen, H.; Viemeister, D. – Bestimmung der Klebstoffverteilung im industriellen Holzwerkstoffprozess. In: IHD (Ed.) 11. Holzwerkstoffkolloquium. Dresden. Institut für Holztechnologie Dresden gemeinnützige GmbH (IHD), 2015. pp. 109-116.

THÖMEN, HOMERIN (2017)
Thömen, H.; Homerin, B. – Modernste Prozessleittechnik - Integration eines mathematisch-physikalischen Modells in ein industrielles Prozessleitsystem. In: IHD (Ed.) 12. Holzwerkstoffkolloquium. Dresden. Institut für Holztechnologie Dresden gemeinnützige GmbH (IHD), 2017. pp. 157-164.

THOMPSON et al. (1989)
Thompson, R.; Pineau, J.; Zerkus, M. – Design and construction of a profile density measurement system for the composite wood products industry. In: Southeastcon '89. Proceedings. Energy and Information Technologies in the Southeast., IEEE. Columbia, SC , USA 1989. pp. 1366-1371.

THUNELL (1955)
Thunell, B. – Gütebestimmung und zerstörungsfreie Prüfung von Bauholz. Holz als Roh- und Werkstoff 13 (1955) 3. pp. 101-111.

TI (2015)
TI – Untersuchung der Faserqualität von TMP für die MDF-Produktion. Abschlussbericht zum FNR-Vorhaben „Fiber-Impact" (FKZ: 22013211), Thünen Report 34. Johann Heinrich von Thünen-Institut, Braunschweig, 2015. 74 p.

TIEMANN (1906)
Tiemann, H. D. – Effect of moisture upon the strength and stiffness of wood. U.S. Dept. of Agriculture, Forest Service: Washington, D. C., 1906.

TIITTA et al. (1993)
Tiitta, M.; Olkkonen, H.; Lappalainen, T.; Kanko, T. – Automated low energy photon absorption equipment for measuring internal moisture and density distributions of wood samples. European Journal of Wood and Wood Products 51 (1993) 6. pp. 417-421.

TIITTA et al. (1996)
Tiitta, M.; Olkkonen, H.; Kanko, T. – Veneer sheet density measurement by the 55Fe gamma attenuation method. Holz als Roh- und Werkstoff 54 (1996) 2. pp. 81-84.

TIITTA (2006)
Tiitta, M. – Non-destructive methods for characterisation of wood material. Diss. University of Kuopio, Faculty of Natural and Enviromental Sciences, Department of Physics, 2006. 70 p.

TIITTA et al. (2017)
Tiitta, M.; Tomppo, L.; Möttönen, V.; Marttila, J.; Antikainen, J.; Lappalainen, R.; Heräjärvi, H. – Predicting the bending properties of air dried and modified Populus tremula L. wood using combined air-coupled ultrasound and electrical impedance spectroscopy. European Journal of Wood and Wood Products 75 (2017) 5. pp. 701-709.

TILLACK, BELLON (2000)
Tillack, G.-R.; Bellon, C. – Röntgenspektren – Ein Modell zur Beschreibung. MP Materialprüfung 42 (2000) 5. pp. 155-159.

TORELLI, ČUFAR (1995)
   Torelli, N.; Čufar, K. – Mexican tropical hardwoods. Comparative study of ash and silica content. Holz als Roh- und Werkstoff 53 (1995) 1. pp. 61-62.

TOUSI et al. (2014)
   Tousi, E. T.; Bauk, S.; Hashim, R.; Jaafar, M. S.; Abuarra, A.; Aldroobi, K. S. A.; Al-Jarrah, A. M. – Measurement of mass attenuation coefficients of Eremurus–Rhizophora spp. particleboards for X-ray in the 16.63–25.30 keV energy range. Radiation Physics and Chemistry 103 (2014) pp. 119-125.

TRENDELENBURG (1939)
   Trendelenburg, R. – Das Holz als Rohstoff - Seine Entstehung, stoffliche Beschaffenheit und chemische Verwertung. J. F. Lehmanns: München, Berlin, 1939. 435 p.

TSAI, CHO (1976)
   Tsai, C. M.; Cho, Z. H. – Physics of contrast mechanism and averaging effect of linear attenuation coefficients in a computerized transverse axial tomography (CTAT) transmission scanner. Physics in Medicine and Biology 21 (1976) 4. pp. 544-559.

TSOULFANIDIS (1995)
   Tsoulfanidis, N. – Measurement and detection of radiation. 2nd ed. Taylor & Francis: Washington, DC, 1995. 636 p.

TSUJI et al. (2004)
   Tsuji, K.; Injuk, J.; Grieken, R. V. (Eds.) – X-Ray Spectrometry: Recent Technological Advances. John Wiley & Sons Ltd: The Atrium, Southern Gate, Chichester, West Sussex, 2004. 615 p.

TUCKER et al. (1991)
   Tucker, D. M.; Barnes, G. T.; Chakraborty, D. P. – Semiempirical model for generating tungsten target x-ray spectra. Medical Physics 18 (1991) 2. pp. 211-218.

TURGUT et al. (2002)
   Turgut, Ü.; Şimşek, Ö.; Büyükkasap, E.; Ertuğrul, M. – X-Ray attenuation coefficients at different energies and the validity of the mixture rule for compounds around the absorption edge. Spectrochimica Acta Part B: Atomic Spectroscopy 57 (2002) 2. pp. 261-266.

TZSCHERLICH (1988)
   Tzscherlich, S. – Vergleich verschiedener Verfahren der Feuchte- und Dichtemessung von Hackschnitzeln mit Neutronen- und Gammastrahlung. Diss. Technischen Universität Dresden, Fakultät für Bau-, Wasser- und Forstwesen, Dresden, 1988. 187 p.

VAHEY et al. (2006)
   Vahey, D. W.; Zhu, J. Y.; Scott, C. T. – Comparison of SilviScan and optical imaging measurements of tracheid dimensions and wood density. In: Proceedings of 2006 progress in paper physics. Oxford. 2006. pp. 73-76.

VAZIRI et al. (2011)
   Vaziri, M.; Lindgren, O.; Pizzi, A. – Influence of Weldling Parameters on Weldline Density and Its Relation to Crack Formation in Welded Scots Pine Joints. Journal of Adhesion Science and Technology 25 (2011) 15. pp. 1819-1828.

VEIGELE (1970)
   Veigele, W. J. – X-Ray Attenuation Cross Sections of Air between 0.1 keV and 1 MeV. Journal of Applied Physics 41 (1970) 7. pp. 3178-3181.

VIGUIER et al. (2017)
   Viguier, J.; Bourreau, D.; Bocquet, J.-F.; Pot, G.; Bléron, L.; Lanvin, J.-D. – Modelling mechanical properties of spruce and Douglas fir timber by means of X-ray and grain angle measurements for strength grading purpose. European Journal of Wood and Wood Products 75 (2017) 4. pp. 527-541.

VINCZE et al. (1998)
Vincze, L.; Janssens, K.; Adams, F.; Rindby, A.; Engström, P. – Interpretation of capillary generated spatial and angular distributions of x rays: Theoretical modeling and experimental verification using the European Synchrotron Radiation Facility Optical beam line. Review of Scientific Instruments 69 (1998) 10. pp. 3494-3503.

VOLLMERT (1985)
Vollmert, B. – Grundriß der makromolekularen Chemie - Band 2 Polymersynthesen II [Polykondensation], Polymer-Reaktionen. E. Vollmert: Karlsruhe, 1985. 308 p.

VÖLZ (2001)
Völz, H. G. – Industrielle Farbprüfung - Grundlagen und Methoden. 2nd ed. Wiley-VCH Verlag: Weinheim, 2001. 402 p.

VOROB'EV et al. (1971)
Vorob'ev, A. A.; Vorob'ev, V. A.; Tarasov, G. P. – Behavior of the energy factor in the bremsstrahlung buildup behind a plane layer of a homogeneous material. Soviet Physics Journal 14 (1971) 1. pp. 69-72.

VÖSSING, NIEDERLEITHINGER (2018)
Vössing, K., J.; Niederleithinger, E. – Nondestructive assessment and imaging methods for internal inspection of timber. A review. Holzforschung 72 (2018) 6. pp. 467-477.

WAGENFÜHR, SCHOLZ (2012)
Wagenführ, A.; Scholz, F. (Eds.) – Taschenbuch der Holztechnik. 2nd ed. Fachbuchverlag Leipzig im Carl Hanser Verlag: München, 2012. 567 p.

WAGENFÜHR (1989)
Wagenführ, R. – Anatomie des Holzes - unter besonderer Berücksichtigung der Holztechnik. 4th ed. VEB Fachbuchverlag: Leipzig, 1989. 334 p.

WAGNER et al. (2018)
Wagner, R.; Fuchs, T.; Scholz, G.; Kretzer, C.; Schielein, R.; Firsching, M.; Kirsch, S.; Wolters, M.; Raquet, M.; Bär, F. P. – Dual-energy computed tomography of historical musical instruments made of multiple materials. In: 8th Conference on Industrial Computed Tomography (iCT). Wels, Austria. 2018. pp. 1-6.

WALKER (2006a)
Walker, J. C. F. – Basic wood chemistry and cell wall ultrastructure. In: Walker, J. C. F. (Ed.) Primary Wood Processing: Principles and Practice. 2nd ed. Springer Netherlands: Dordrecht, 2006a. pp. 23-67.

WALKER (2006b)
Walker, J. C. F. (Ed.) – Primary wood processing: principles and practice. 2nd ed. Springer-Verlag: Dordrecht, 2006b. 596 p.

WALTER (1929)
Walter, B. – Über die besten Formeln zur Berechnung der Absorption der Röntgenstrahlen in einem beliebigen Stoff. Fortschritte auf dem Gebiet der Röntgenstrahlen 35 (1929) 5. pp. 929-947.

WALTER, WIECHMANN (1961)
Walter, F.; Wiechmann, H. – Dichteuntersuchungen an Faser- und Spanplatten. Holztechnologie 2 (1961) 2. pp. 172-178.

WALTHER (2006)
Walther, T. – Methoden zur qualitativen und quantitativen Analyse der Mikrostruktur von Naturfaserwerkstoffen. Diss. Universität Hamburg, Fakultät für Mathematik, Informatik und Naturwissenschaften, Fachbereich Biologie, Hamburg, 2006. 232 p.

WALTHER, THOEMEN (2009)
Walther, T.; Thoemen, H. – Synchrotron X-ray microtomography and 3D image analysis of medium density fiberboard (MDF). Holzforschung 63 (2009) 5. pp. 581-587.

WANG, CHANG (2007)
Wang, P. C.; Chang, S. J. – Nuclear magnetic resonance imaging of wood. Wood and fiber science 18 (2007) 2. pp. 308-314.

WANG et al. (2005)
Wang, X.; Salenikovich, A.; Mohammad, M.; Hu, L. J. – Evaluation of density distribution in wood-based panels using X-ray scanning. In: Bröker, F.-W. (Ed.) Proceedings of the 14th International Symposium on Nondestructive Testing of Wood: May 2005. University of Applied Science, Eberswalde, Germany. Shaker Verlag: Aachen, 2005. pp. 29-38.

WANG et al. (2007)
Wang, Y.; Muszynski, L.; Simonsen, J. – Gold as an X-ray CT scanning contrast agent: Effect on the mechanical properties of wood plastic composites. Holzforschung 61 (2007) 6. pp. 723-730.

WARNECKE (1995)
Warnecke, T. – Neuartige Rohdichteprofilmessung an MDF-Platten. HK (1995) 11. pp. 1380-1383.

WATANABE et al. (2008)
Watanabe, K.; Saito, Y.; Avramidis, S.; Shida, S. – Non-destructive Measurement of Moisture Distribution in Wood during Drying Using Digital X-ray Microscopy. Drying Technology: An International Journal 26 (2008) 5. pp. 590 - 595.

WAŻNY, WAŻNY (1964)
Ważny, H.; Ważny, J. – Über das Auftreten von Spurenelementen im Holz. Holz als Roh- und Werkstoff 22 (1964) 8. pp. 299-304.

WEI et al. (2011)
Wei, Q.; Leblon, B.; La Rocque, A. – On the use of X-ray computed tomography for determining wood properties: a review. Canadian Journal of Forest Research 41 (2011) 11. pp. 2120-2140.

WELLING (1998)
Welling, J. (Ed.) – EUR 18489 - Directory of non-destructive testing methods for the wood-based panel industry. Office for Official Publications of the European Communities: Luxembourg, 1998. 130 p.

WENDERDEL, KRUG (2010)
Wenderdel, C.; Krug, D. – Untersuchung zum Einfluss der Aufschlussbedingungen auf die morphologische Ausprägung von aus Kiefernholz hergestelltem TMP-Faserstoff. European Journal of Wood and Wood Products 70 (2010) 1-3. pp. 85-89.

WENDERDEL, KRUG (2011)
Wenderdel, C.; Krug, D. – Analysemethode zur Bewertung der Faser-Bindemittel-Wechselwirkung bei der MDF-Herstellung - Theoretischer Ansatz und Arbeitshypothesen. Holztechnologie 52 (2011) 1. pp. 44-50.

WENDERDEL et al. (2014)
Wenderdel, C.; Weber, A.; Pfaff, M.; Sonntag, U.; Theumer, T. – Spezielle Methoden zur morphologischen Charakterisierung lignocelluloser Faserstoffe - Teil 1: Stand der Technik und theoretische Ableitung einer Partikelklassifizierung. holztechnologie 55 (2014) 6. pp. 12-19.

WENDERDEL (2015)
Wenderdel, C. – Herstellung mehrschichtiger Faserplatten im Trockenverfahren mit kartonähnlichen Eigenschaften. Diss. ETH-Zürich, Eidgenössische Technische Hochschule, Zürich, 2015. 221 p.

WENDERDEL (2016)
> Wenderdel, C. – Personal communication: Discussion on fibre morphology characterisation and analysis results. IHD, Dresden, Scientist, topics: MDF, PB, Inorganic binders, Particle analyses, 02.03.2016.

WENDERDEL et al. (2016)
> Wenderdel, C.; Weber, A.; Hielscher, M.; Pfaff, M.; Sonntag, U. – Spezielle Methoden zur morphologischen Charakterisierung lignocelluloser Faserstoffe - Teil 2: Faserstofferzeugung und morphologische Charakterisierung. holztechnologie 57 (2016) 3. pp. 16-22.

WHITE, ROSS (2014)
> White, R. H.; Ross, R. J. (Eds.) – Wood Condition Assessment Manual - Second Edition - General Technical Report FPL-GTR-234. 2nd ed. U.S. Department of Agriculture, Forest Service, Forest Products Laboratory: Madison, WI, 2014. 102 p.

WIBERG, MORÉN (1999)
> Wiberg, P.; Morén, T. J. – Moisture flux determination in wood during drying above fibre saturation point using CT-scanning and digital image processing. European Journal of Wood and Wood Products 57 (1999) 2. pp. 137-144.

WICKIZER et al. (1976)
> Wickizer, R.; Zacher, R.; Krippner, K.; Liu, Y.-Y. – A Comparison of Some Models of X-Ray Beam Hardening. In: Dubuque, G.; Gray, J. E.; Hendee, W. R.; Rossi, R. P.; Haus, A.; Cacak, R. K.; Carson, P. L. (Eds.) SPIE 0096, Application of Optical Instrumentation in Medicine V. Washington, D.C. 1976. pp. 276-282.

WIJNENDAELE (2018)
> Wijnendaele, K. (Ed.) – EPF Annual Report 2017 - 2018. European Panel Federation: Brussels, 2018. 264 p.

WILSON (1980)
> Wilson, C. R. – Quantitative Computed Tomography. In: Fullerton, G. D.; Zagzebski, J. A. (Eds.) Medical Physics of CT and ultrasound tissue imaging and characterization. American Institute of Physics: New York, N.Y., 1980. pp. 163-175.

WINANDY, KAMKE (2003)
> Winandy, J. E.; Kamke, F. A. – Fundamentals of Composite Processing - Proceedings of a Workshop. General Technical Report, FPL-GTR-149, USDA Forest Service, Forest Products Laboratory, Madison, WI, USA, 2003. 126 p.

WINDEISEN et al. (2007)
> Windeisen, E.; Strobel, C.; Wegener, G. – Chemical changes during the production of thermo-treated beech wood. Wood Science and Technology 41 (2007) 6. pp. 523-536.

WINISTORFER et al. (1996)
> Winistorfer, P.; Young, T.; Walker, E. – Modeling and Comparing Vertical Density Profiles. Wood and fiber science 28 (1996) 1. pp. 133-141.

WINISTORFER et al. (2000)
> Winistorfer, P.; Moschler, W.; Wang, S.; DePaula, E.; Bledsoe, B. – Fundamentals of Vertical Density Profile Formation in Wood Composites. Part I. In-Situ Density Measurement of the Consolidation Process. Wood and fiber science 32 (2000) 2. pp. 209-219.

WINISTORFER et al. (1986)
> Winistorfer, P. M.; Davis, W. C.; Moschler, W. W., Jr. – A direct scanning densitometer to measure density profiles in wood composite products. Forest Products Journal 36 (1986) 11/12. pp. 82-86.

WINISTORFER et al. (1995)
> Winistorfer, P. M.; Xu, W.; Wimmer, R. – Application of a drill resistance technique for density profile measurement in wood composite panels. Forest Products Journal 45 (1995) 6. pp. 90-93.

WITTENBERGER, FRITZ (1991)
    Wittenberger, W.; Fritz, W. – Physikalisch-chemisches Rechnen mit einer Einführung in die höhere Mathematik. 2nd ed. Springer-Verlag: Wien, New York, 1991. 481 p.

WONG et al. (1999)
    Wong, E.-D.; Zhang, M.; Wang, Q.; Kawai, S. – Formation of the density profile and its effects on the properties of particleboard. Wood Science and Technology 33 (1999) 4. pp. 327-340.

WONG et al. (1998)
    Wong, E. D.; Zhang, M.; Wang, Q.; Kawai, S. – Effects of mat moisture content and press closing speed on the formation of density profile and properties of particleboard. Journal of Wood Science 44 (1998) 4. pp. 287-295.

WONG (1999)
    Wong, E. D. – Effects of Density Profile on the Mechanical Properties of Particleboard and Fiberboard. Wood research: bulletin of the Wood Research Institute Kyoto University 86 (1999) pp. 19-33.

WORBES et al. (1995)
    Worbes, M.; Klosa, D.; Lewark, S. – Rohdichtestruktur von Jahresringen tropischer Hölzer aus zentralamazonischen Überschwemmungswäldern. Holz als Roh- und Werkstoff 53 (1995) 1. pp. 63-67.

WU et al. (2009)
    Wu, Y.; Wang, S.; Zhou, D.; Xing, C.; Zhang, Y. – Use of nanoindentation and silviscan to determine the mechanical properties of 10 hardwood species. Wood and fiber science 41 (2009) 1. pp. 64-73.

WÜRFL et al. (2018)
    Würfl, T.; Maaß, N.; Dennerlein, F.; Maier, A. K. – A new calibration-free beam hardening reduction method for industrial CT. In: 8th Conference on Industrial Computed Tomography (iCT). Wels, Austria. 2018. pp. 1-7.

XCOM (2010)
    Berger, M. J.; Hubbell, J. H.; Seltzer, S. M.; Chang, J.; Coursey, J. S.; Sukumar, R.; Zucker, D. S.; Olsen, K. – XCOM: Photon Cross Section Database (version 1.5), 2010. https://www.nist.gov/pml/xcom-photon-cross-sections-database. Access date 01.01.2018.

XING et al. (2005)
    Xing, C.; Riedl, B.; Cloutier, A.; Shaler, S. M. – Characterization of urea-formaldehyde resin penetration into medium density fiberboard fibers. Wood Science and Technology 39 (2005) 5. pp. 374-384.

XU et al. (1996)
    Xu, W.; Winistorfer, P.; Moschler, W. – A Procedure To Determine Water Absorption Distribution In Wood Composite Panels. Wood and fiber science 28 (1996) 3. pp. 286-294.

YANG et al. (1987)
    Yang, N. C.; Leichner, P. K.; Hawkins, W. G. – Effective atomic numbers for low-energy total photon interactions in human tissues. Medical physics 14 (1987) 5. pp. 759-766.

ZAUER et al. (2013)
    Zauer, M.; Pfriem, A.; Wagenführ, A. – Toward improved understanding of the cell-wall density and porosity of wood determined by gas pycnometry. Wood Science and Technology 47 (2013) 6. pp. 1197-1211.

ZENTAI (2008)
    Zentai, G. – X-ray imaging for homeland security. In: International Workshop on Imaging Systems and Techniques. Crete, Greece. IEEE, 2008. pp. 1-6.

Zeppenfeld, Grunwald (2005)

    Zeppenfeld, G.; Grunwald, D. – Klebstoffe in der Holz- und Möbelindustrie. 2nd ed. DRW-Verlag Weinbrenner: Leinfelden-Echterdingen, 2005. 363 p.

Zhang et al. (2015)

    Zhang, X.; Li, L.; Zhang, F.; Xi, X.; Deng, L.; Yan, B. – Improving the accuracy of CT dimensional metrology by a novel beam hardening correction method. Measurement Science and Technology 26 (2015) 015007. pp. 1-11.

Zhou et al. (2009)

    Zhou, R.-F.; Wang, J.; Chen, W.-M. – X-ray beam hardening correction for measuring density in linear accelerator industrial computed tomography. Chinese Physics C 33 (2009) 7. pp. 599-602.

Zhukovskiy et al. (2012)

    Zhukovskiy, M. E.; Jaenisch, G.-R.; Deresch, A.; Podoliako, S. V. – Mathematical Modeling of Radiography Experiments. In: 18th World Conference on Nondestructive Testing. Durban, South Africa. 2012. pp. 1-7.

Zscherpel (2015)

    Zscherpel, U. – Personal communication: Discussion on X-ray spectra measurement and data evaluation. BAM, Berlin, Division 8.3: Non-destructive Testing, Radiological Methods, 30.11.2015.

2 Standards and guidelines

ASTM D1102-84 (2013)
ASTM D1102-84:2013 – Standard Test Method for Ash in Wood – ASTM International: West Conshohocken, PA, USA, 2 p.

ASTM D 5373 (2014)
ASTM D 5373:2014 – Standard Test Methods for Determination of Carbon, Hydrogen and Nitrogen in Analysis Samples of Coal and Carbon in Analysis Samples of Coal and Coke – ASTM International: West Conshohocken, PA, USA, 11 p.

DIN 1306 (1984)
DIN 1306:1984 – Dichte – Begriffe, Angaben. Beuth Verlag: Berlin, 2 p.

DIN 6811-1 (1987)
DIN 6811-1:1987 – Medizinische Röntgeneinrichtungen bis 300 kV – Strahlenschutzregeln für die Herstellung; Röntgenanwendungsgeräte und deren Komponenten für die Röntgendiagnostik. Beuth Verlag: Berlin, 56 p.

DIN 6814-2 (2000)
DIN 6814-2:2000 – Begriffe in der radiologischen Technik – Teil 2: Strahlungsphysik. Beuth Verlag: Berlin, 30 p.

DIN 6814-3 (2016)
DIN 6814-3:2016 – Begriffe in der radiologischen Technik – Teil 3: Dosimetrie. Beuth Verlag: Berlin, 40 p.

DIN 6818-1 (2004)
DIN 6818-1:2004 – Strahlenschutzdosimeter – Teil 1: Allgemeine Regeln. Beuth Verlag: Berlin, 46 p.

DIN 50014 (1985)
DIN 50014:1985 – Klimate und ihre technische Anwendung – Normalklimate. Beuth Verlag: Berlin, 2 p.

DIN 50014 (2018)
DIN 50014:2018 – Normalklimate für Vorbehandlung und/oder Prüfung – Festlegungen. Beuth Verlag: Berlin, 7 p.

DIN 51719 (1997)
DIN 51719:1997 – Prüfung fester Brennstoffe – Bestimmung des Aschegehaltes. Beuth Verlag: Berlin, 3 p.

DIN 51913 (2013)
DIN 51913:2013 – Prüfung von Kohlenstoffmaterialien – Bestimmung der Dichte mit dem Gaspyknometer (volumetrisch) unter Verwendung von Helium als Messgas - Feststoffe. Beuth Verlag: Berlin, 7 p.

DIN 51918 (2012)
DIN 51918:2012 – Prüfung von Kohlenstoffmaterialien – Bestimmung der Rohdichte und der offenen Porosität. Beuth Verlag: Berlin, 10 p.

DIN 54113-1 (2018)
DIN 54113-1:2018 – Zerstörungsfreie Prüfung - Strahlenschutzregeln für die technische Anwendung von Röntgeneinrichtungen bis 1 MV – Teil 1: Sicherheitstechnische Anforderungen und Prüfungen für Herstellung, Errichtung und Betrieb. Beuth Verlag: Berlin, 24 p.

DIN 54370 (2007)
DIN 54370:2007 – Prüfung von Papier und Pappe – Bestimmung des Glührückstandes. Beuth Verlag: Berlin, 7 p.

DIN 66137-1 (2003)
DIN 66137-1:2003 – Bestimmung der Dichte fester Stoffe – Teil 1: Grundlagen. Beuth Verlag: Berlin, 6 p.

DIN 66137-2 (2004)
DIN 66137-2:2004 – Bestimmung der Dichte fester Stoffe – Teil 2: Gaspyknometrie. Beuth Verlag: Berlin, 9 p.

DIN 68100 (2010)
DIN 68100:2010 – Toleranzsytem für Holzbe- und -verarbeitung – Begriffe, Toleranzreihen, Schwind- und Quellmaße. Beuth Verlag: Berlin, 25 p.

DIN 68364 (2003)
DIN 68364:2003 – Kennwerte von Holzarten – Rohdichte, Elastizitätsmodul und Festigkeiten. Beuth Verlag: Berlin, 8 p.

DIN CEN/TS 15405 (DIN SPEC 1152) (2010)
DIN CEN/TS 15405 (DIN SPEC 1152):2010 – Feste Sekundärbrennstoffe - Bestimmung der Dichte von Pellets und Briketts – Beuth Verlag: Berlin, 17 p.

DIN EN 300 (2006)
DIN EN 300:2006 – Platten aus langen, flachen, ausgerichteten Spänen (OSB) – Definitionen, Klassifizierung und Anforderungen. Beuth Verlag: Berlin, 22 p.

DIN EN 310 (1993)
DIN EN 310:1993 – Holzwerkstoffe – Bestimmung des Biege-Elastizitätsmoduls und der Biegefestigkeit. Beuth verlag: Berlin, 8 p.

DIN EN 319 (1993)
DIN EN 319:1993 – Spanplatten und Faserplatten – Bestimmung der Zugfestigkeit senkrecht zur Plattenebene. Beuth Verlag: Berlin, 6 p.

DIN EN 322 (1993)
DIN EN 322:1993 – Holzwerkstoffe – Bestimmung des Feuchtegehaltes. Beuth verlag: Berlin, 5 p.

DIN EN 323 (1993)
DIN EN 323:1993 – Holzwerkstoffe – Bestimmung der Rohdichte. Beuth verlag: Berlin, 5 p.

DIN EN 325 (2012)
DIN EN 325:2012 – Holzwerkstoffe – Bestimmung der Maße der Prüfkörper. Beuth Verlag: Berlin, 8 p.

DIN EN 444 (1994)
DIN EN 444:1994 – Zerstörungsfreie Prüfung – Grundlagen für die Durchstrahlungsprüfung von metallischen Werkstoffen mit Röntgen- und Gammastrahlen. Beuth Verlag: Berlin, 12 p.

DIN EN 1246 (1998)
DIN EN 1246:1998 – Klebstoffe - Bestimmung des Aschegehaltes und des Sulfat-Aschegehaltes – Beuth Verlag: Berlin, 6 p.

DIN EN 1330-3 (1997)
DIN EN 1330-3:1997 – Zerstörungsfreie Prüfung - Terminologie – Teil 3: Begriffe der industriellen Durchstrahlungsprüfung. Beuth Verlag: Berlin, 30 p.

DIN EN 1330-11 (2007)
    DIN EN 1330-11:2007 – Zerstörungsfreie Prüfung - Terminologie – Teil 11: Begriffe der Röntgendiffraktometrie von polykristallinen und amorphen Materialien. Beuth Verlag: Berlin, 64 p.

DIN EN 12085 (2013)
    DIN EN 12085:2013 – Wärmedämmstoffe für das Bauwesen - Bestimmung der linearen Maße von Probekörpern – Beuth Verlag: Berlin, 11 p.

DIN EN 12543-1 (1999)
    DIN EN 12543-1:1999 – Zerstörungsfreie Prüfung - Charakterisierung von Brennflecken in Industrie-Röntgenanlagen für die zerstörungsfreie Prüfung – Teil 1: Scan-Verfahren. Beuth Verlag: Berlin, 8 p.

DIN EN 12544-2 (2000)
    DIN EN 12544-2:2000 – Zerstörungsfreie Prüfung - Messung und Auswertung der Röntgenröhrenspannung – Teil 2: Konstanzprüfung mit dem Dickfilter-Verfahren. Beuth Verlag: Berlin, 7 p.

DIN EN 12544-3 (1999)
    DIN EN 12544-3:1999 – Zerstörungsfreie Prüfung - Messung und Auswertung der Röntgenröhrenspannung – Teil 3: Spektrometer-Verfahren. Beuth Verlag: Berlin, 7 p.

DIN EN 13068-1 (2000)
    DIN EN 13068-1:2000 – Zerstörungsfreie Prüfung - Radioskopische Prüfung – Teil 1: Quantitative Messung der bildgebenden Eigenschaften. Beuth Verlag: Berlin, 19 p.

DIN EN 16016-1 (2011)
    DIN EN 16016-1:2011 – Zerstörungsfreie Prüfung - Durchstrahlungsverfahren - Computertomografie – Teil 1: Terminologie. Beuth Verlag: Berlin, 17 p.

DIN EN 16016-2 (2012)
    DIN EN 16016-2:2012 – Zerstörungsfreie Prüfung - Durchstrahlungsverfahren - Computertomografie – Teil 2: Grundlagen, Geräte und Proben. Beuth Verlag: Berlin, 25 p.

DIN EN 16016-3 (2012)
    DIN EN 16016-3:2012 – Zerstörungsfreie Prüfung - Durchstrahlungsverfahren - Computertomografie – Teil 3: Durchführung und Auswertung. Beuth Verlag: Berlin, 28 p.

DIN EN 16785 (2014)
    DIN EN 16785:2014 – Biobasierte Produkte – Bestimmung des biobasierten Gehalts unter Verwendung der Radiokarbon- und Elementaranalyse. Beuth Verlag: Berlin, 20 p.

DIN EN 60601-1-3 (2014)
    DIN EN 60601-1-3:2014 – Medizinische elektrische Geräte – Teil 1-3: Allgemeine Festlegungen für die Sicherheit einschließlich der wesentlichen Leistungsmerkmale. Beuth Verlag: Berlin, 63 p.

DIN EN 60627 (2016)
    DIN EN 60627:2016 – Bildgebende Geräte für die Röntgendiagnostik – Kenngrößen von Streustrahlenrastern für die allgemeine Anwendung und für die Mammographie. Beuth Verlag: Berlin, 41 p.

DIN EN ISO 1 (2016)
    DIN EN ISO 1:2016 – Geometrische Produktspezifikationen (GPS) - Standardreferenztemperatur für die Geometrische Produktspezifikation und -prüfung – Beuth Verlag: Berlin, 11 p.

DIN EN ISO 1183-1 (2013)
    DIN EN ISO 1183-1:2013 – Kunststoffe - Verfahren zur Bestimmung der Dichte von nicht verschäumten Kunststoffen – Teil 1: Eintauchverfahren, Verfahren mit Flüssigkeitspyknometer und Titrationsverfahren. Beuth Verlag: Berlin, 15 p.

DIN EN ISO 1183-3 (2000)
    DIN EN ISO 1183-3:2000 – Kunststoffe - Verfahren zur Bestimmung der Dichte von nicht verschäumten Kunststoffen – Teil 3: Gas-Pyknometer-Verfahren. Beuth Verlag: Berlin, 8 p.

DIN EN ISO 3451-1 (2008)
    DIN EN ISO 3451-1:2008 – Kunststoffe - Bestimmung der Asche – Teil 1: Allgemeine Grundlagen Beuth Verlag: Berlin, 11 p.

DIN EN ISO 5579 (2014)
    DIN EN ISO 5579:2014 – Zerstörungsfreie Prüfung – Durchstrahlungsprüfung von metallischen Werkstoffen mit Film und Röntgen- oder Gammastrahlen – Grundlagen. Beuth Verlag: Berlin, 20 p.

DIN EN ISO 16371-2 (2018)
    DIN EN ISO 16371-2:2018 – Zerstörungsfreie Prüfung - Industrielle Computer-Radiographie mit Phosphor-Speicherfolien – Teil 2: Grundlagen für die Prüfung von metallischen Werkstoffen mit Röntgen- und Gammastrahlen. Beuth Verlag: Berlin, 43 p.

DIN EN ISO 17636-2 (2013)
    DIN EN ISO 17636-2:2013 – Zerstörungsfreie Prüfung von Schweißverbindungen - Durchstrahlungsprüfung – Teil 2: Röntgen- und Gammastrahlungstechniken mit digitalen Detektoren. Beuth Verlag: Berlin, 63 p.

DIN ISO 3310-1 (2017)
    DIN ISO 3310-1:2017 – Analysensiebe - Technische Anforderungen und Prüfung – Teil 1: Analysensiebe mit Metalldrahtgewebe. Beuth Verlag: Berlin, 22 p.

DIN ISO 9276-1 (2004)
    DIN ISO 9276-1:2004 – Darstellung der Ergebnisse von Partikelgrößenanalysen – Teil 1: Grafische Darstellung. Beuth Verlag: Berlin, 13 p.

DIN 51903 (2012)
    DIN 51903:2012 – Prüfung von Kohlenstoffmaterialien – Bestimmung des Aschewertes - Feststoffe. Beuth Verlag: Berlin, 9 p.

IEC 60050-395 (2014)
    IEC 60050-395:2014 – International Electrotechnical Vocabulary – Chapter 395. Nuclear instrumentation: Physical phenomena, basic concepts, instruments, systems, equipment and detectors. International Electrotechnical Commission IEC: Geneva, Switzerland, 397 p.

IEC 60050-881 (1983)
    IEC 60050-881:1983 – International Electrotechnical Vocabulary – Chapter 881. Radiology and radiological physics. International Electrotechnical Commission IEC: Geneva, Switzerland, 226 p.

ISO 291 (2008)
    ISO 291:2008 – Plastics – Standard atmospheres for conditioning and testing. Beuth Verlag: Berlin, 16 p.

ISO 554 (1976)
    ISO 554:1976 – Standard atmospheres for conditioning and/or testing – Specifications. Beuth Verlag: Berlin, 4 p.

ISO 3340 (1976)
    ISO 3340:1976 – Fibre building boards - Determination of sand content – International Organization for Standardization: 5 p.

ISO 5576 (1997)
    ISO 5576:1997 – Non-destructive testing - Industrial X-ray and gamma-ray radiology - Vocabulary – Beuth Verlag: Berlin, 40 p.

ISO 13061-1 (2014)
    ISO 13061-1:2014 – Physical and mechanical properties of wood - Test methods for small clear
    wood specimens – Part 1: Determination of moisture content for physical and mechanical tests.
    ISO copyright office: Vernier, Geneva, Switzerland, 12 p.

ISO 13061-2 (2014)
    ISO 13061-2:2014 – Physical and mechanical properties of wood - Test methods for small clear
    wood specimens – Part 2: Determination of density for physical and mechanical tests. ISO
    copyright office: Vernier, Geneva, Switzerland, 12 p.

ISO 13061-3 (2014)
    ISO 13061-3:2014 – Physical and mechanical properties of wood - Test methods for small clear
    wood specimens – Part 3: Determination of ultimate strength in static bending. ISO copyright
    office: Vernier, Geneva, Switzerland, 12 p.

ISO 15708-1 (2017)
    ISO 15708-1:2017 – Non-destructive testing - Radiation methods for computed tomography –
    Part 1: Terminology. ISO copyright office: Vernier, Geneva, Switzerland, 12 p.

ISO 15708-2 (2017)
    ISO 15708-2:2017 – Non-destructive testing - Radiation methods for computed tomography –
    Part 2: Principles, equipment and samples. ISO copyright office: Vernier, Geneva, Switzerland,
    24 p.

ISO 15708-3 (2017)
    ISO 15708-3:2017 – Non-destructive testing - Radiation methods for computed tomography –
    Part 3: Operation and interpretation. ISO copyright office: Vernier, Geneva, Switzerland, 28 p.

ISO/DIS 4037-1 (2017)
    ISO/DIS 4037-1:2017 – Radiological protection - X and gamma reference radiation for calibrating
    dosemeters and doserate meters and for determining their response as a function of photon
    energy – Part 1: Radiation characteristics and production methods. Beuth Verlag: Berlin, 55 p.

TAPPI T 211 (2016)
    TAPPI T 211:2016 – Ash in wood, pulp, paper and paperboard – combustion at 525 °C. Technical
    Association of the Pulp and Paper Industry: Peachtree Corners, GA, 5 p.

TAPPI T 413 (2017)
    TAPPI T 413:2017 – Ash in wood, pulp, paper and paperboard – combustion at 900 °C. Technical
    Association of the Pulp and Paper Industry: Peachtree Corners, GA, 5 p.

TGL 11369 (1977)
    TGL 11369:1977 – Prüfung von Span- und Faserplatten – Bestimmung der Dicke, Winkligkeit,
    Flächendichte und Rohdichte. Verlag für Standardisierung der DDR: Leipzig, 5 p.

VDI/VDE 2630-1.1 (2016)
    VDI/VDE 2630-1.1:2016 – Computed tomography in dimensional measurement – Part 1.1:
    Fundamentals and definitions. Beuth Verlag: Berlin, 32 p.

VDI/VDE 2630-1.2 (2018)
    VDI/VDE 2630-1.2:2018 – Computed tomography in dimensional measurement – Part 1.2:
    Influencing variables on measurement results and recommendations for computed tomography
    dimensional measurements. Beuth Verlag: Berlin, 27 p.

VDI/VDE 5575-1 (2017)
    VDI/VDE 5575-1:2017 – X-ray optical systems – Part 1: Terms and definitions. Beuth Verlag:
    Berlin, 12 p.

VDI/VDE 5575-2 (2015)
    VDI/VDE 5575-2:2015 – X-ray optical systems – Part 2: Measurement methods, Measurement
    set-up and methods for the evaluation of X-ray optical systems. Beuth Verlag: Berlin, 31 p.

VDI/VDE 5575-3 (2018)
> VDI/VDE 5575-3:2018 – X-ray optical systems – Part 3: Capillary X-ray lenses. Beuth Verlag: Berlin, 10 p.

VDI/VDE 5575-9 (2018)
> VDI/VDE 5575-9:2018 – X-ray optical systems – Part 9: X-ray filters. Beuth Verlag: Berlin, 8 p.

1 Material

1.1 Lab-made furnish mats

Figure VII-1: Photographic documentation of the densification setup for manufacturing of lab-made furnish mats (Chapter IV–1.1) with exemplary photographs for Fmat2 (top) and SLmat (bottom).

1.2　Lab-made homogeneous fibreboards
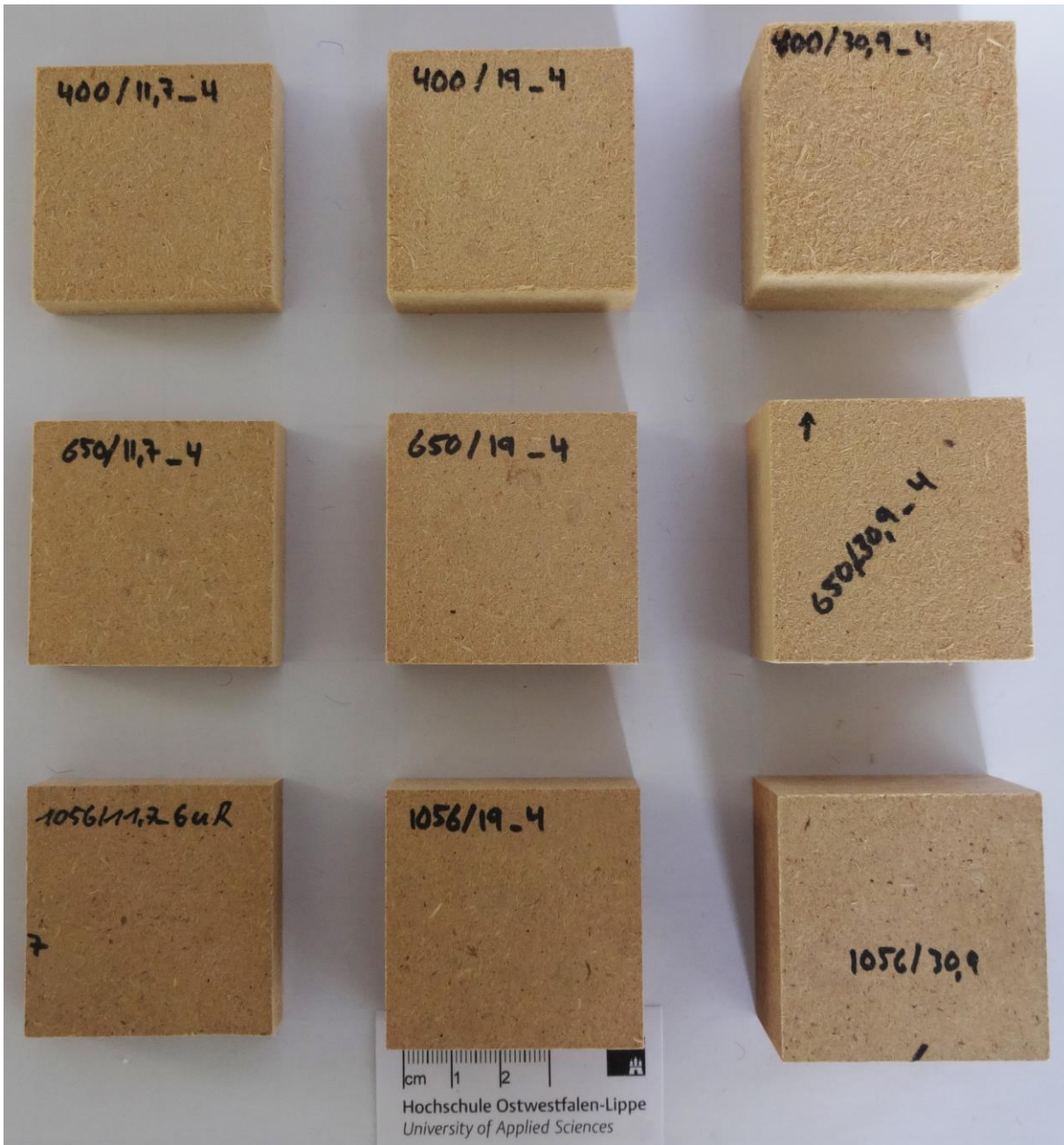
Figure VII-2: Lab-made MDF (labMDF) specimens with the nominal dimensions of $50 \times 50 \times t_{panel}$ mm^3 as set of all manufactured types according to Table IV-2, panel surface.
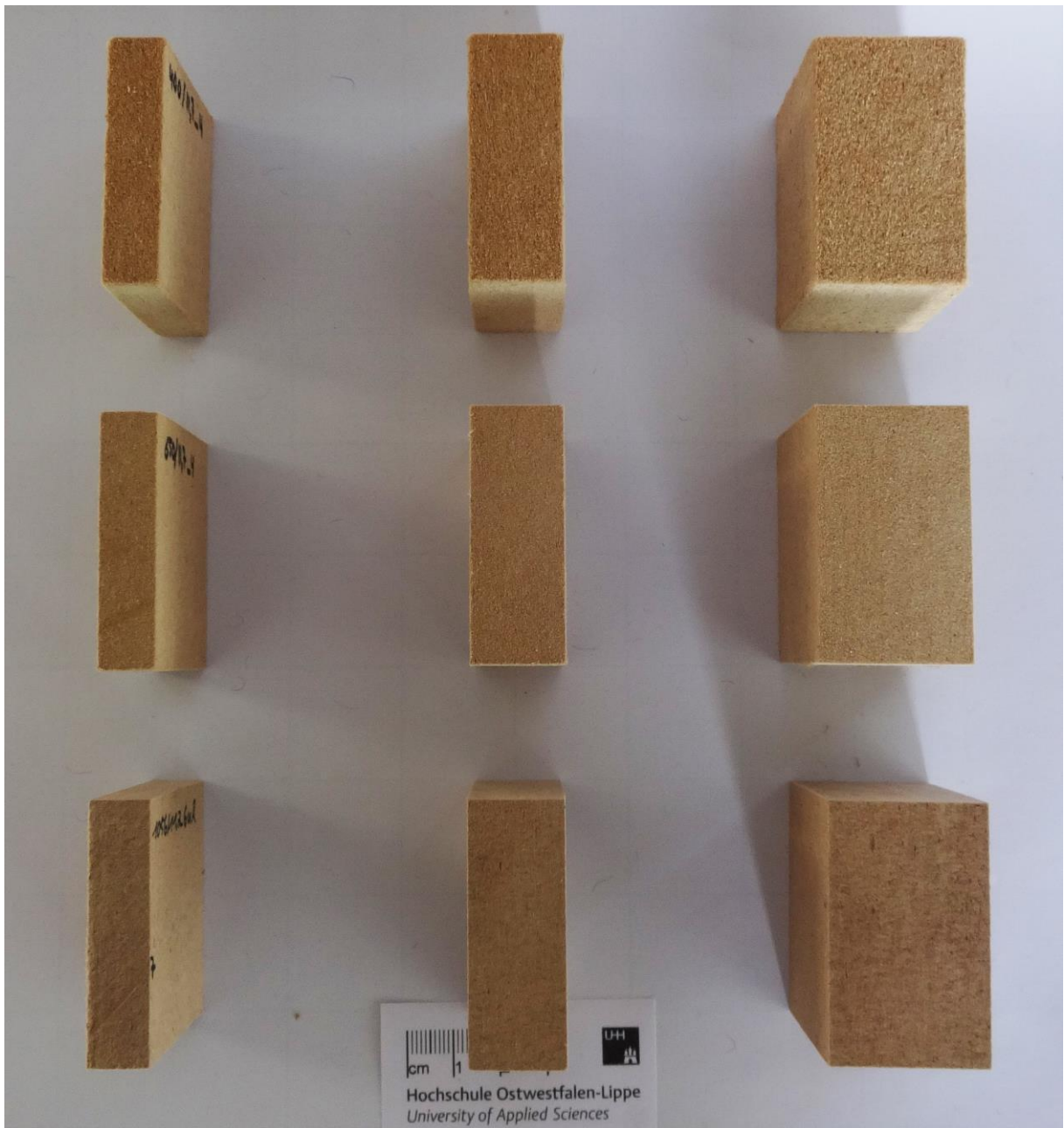
Figure VII-3: Lab-made MDF (labMDF) specimens with the nominal dimensions of $50 \times 50 \times t_{\mathrm{panel}}$ mm^3 as set of all manufactured types according to Table IV-2, panel edge.

1.3 Customary industrial panels

The shown raw density profiles (RDPs) represent respectively one exemplary specimen of the sample set. For RDPs of the lab-made homogeneous fibreboards (labMDF), reference is made to Figure IV-5. Exemplary RDPs of the lab-made fibre mats (Fmat) are shown in Figure IV-3. The RDPs presented in this chapter correspond to the customary industrial panels described in Chapter IV–1.3 with MDF (Figure VII-7) and wood-fibre insulation board (Figure VII-5).

Figure VII-4: Wood-fibre insulation board specimen with the nominal dimensions of $50 \times 50 \times 40\ \text{mm}^3$.
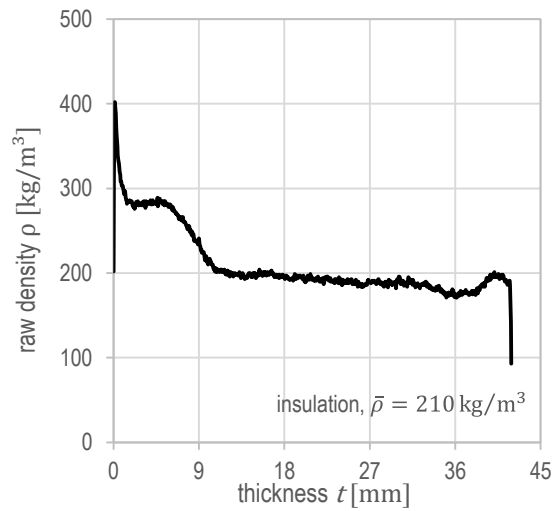
Figure VII-5: Exemplary RDP of wood-fibre insulation board measured by the W-target RDP device (Chapter IV–4.2.3) at standard conditions 20 °C/65 % RH with mean specimen raw density $\bar{\rho}$ (all panel values in Table IV-5).
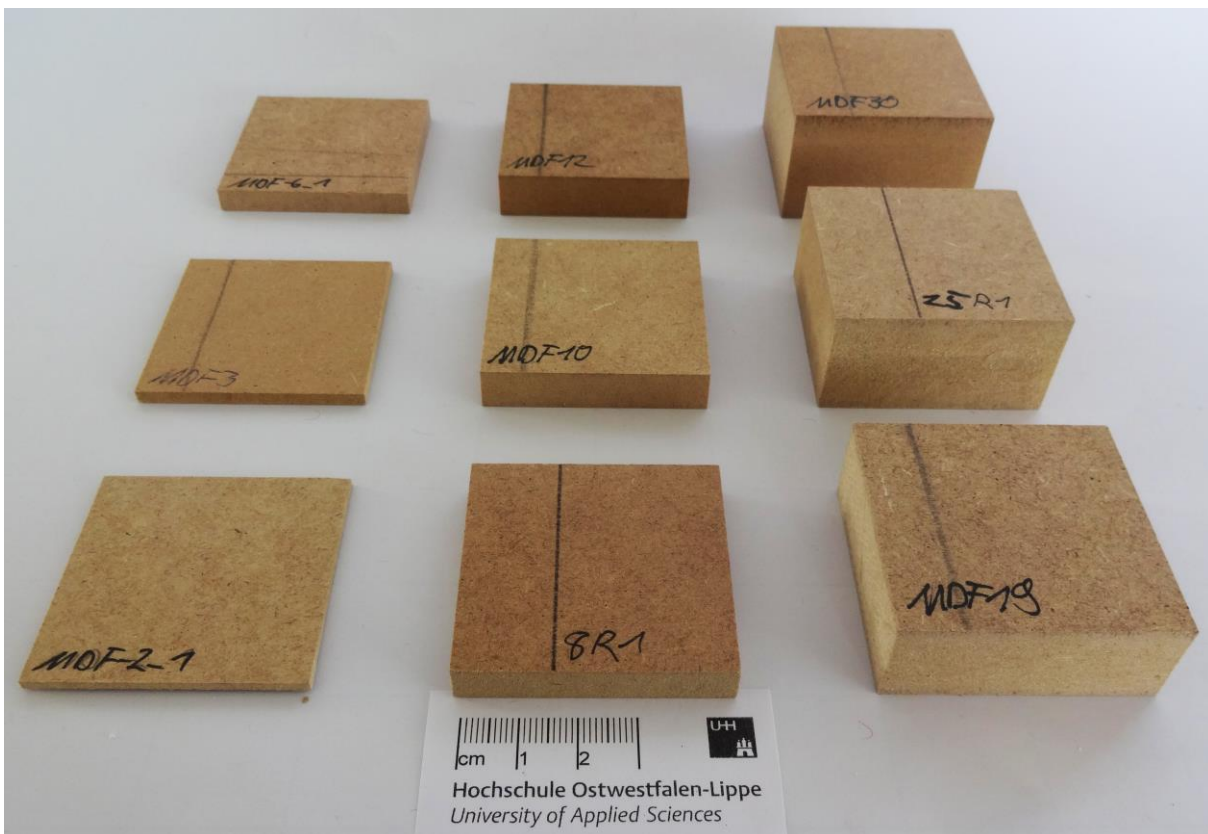
Figure VII-6: MDF specimens from customary panels of industrial origin (indMDF) with the nominal dimensions of $50 \times 50 \times t_{\text{panel}}\ \text{mm}^3$.
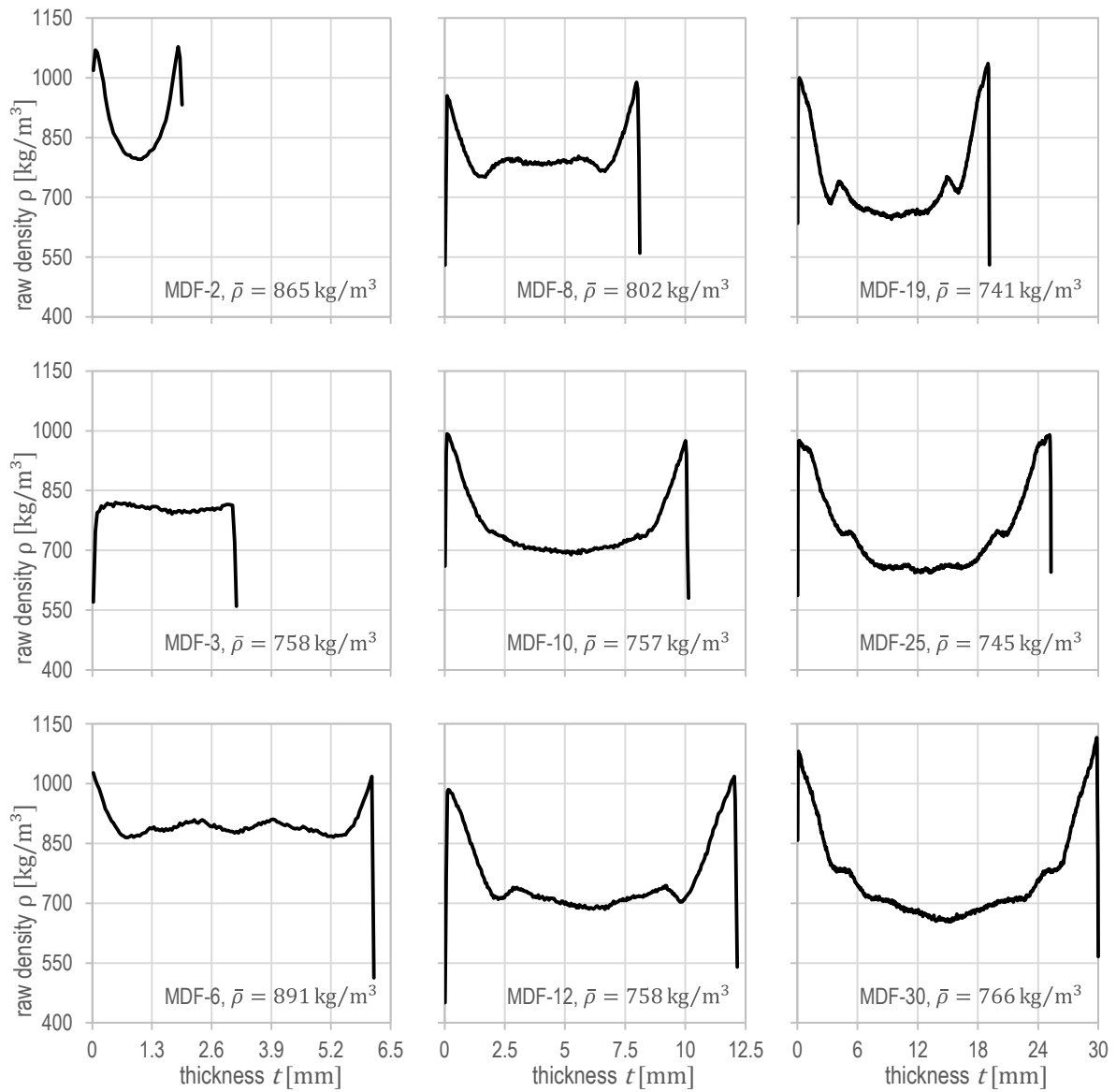
Figure VII-7: Exemplary RDPs of customary industrial MDF (indMDF) of random origin measured by the W-target RDP device (Chapter IV–4.2.3) at standard conditions 20 °C/65 % RH with mean specimen raw density $\bar{\rho}$ (all panel values in Table IV-5).

1.4   Adhesive resin

Figure VII-9: Urea-formaldehyde adhesive resin sample in the solid state as type UF1-D (dried without additional hardener) acc. to Table IV-3 and Table IV-4.
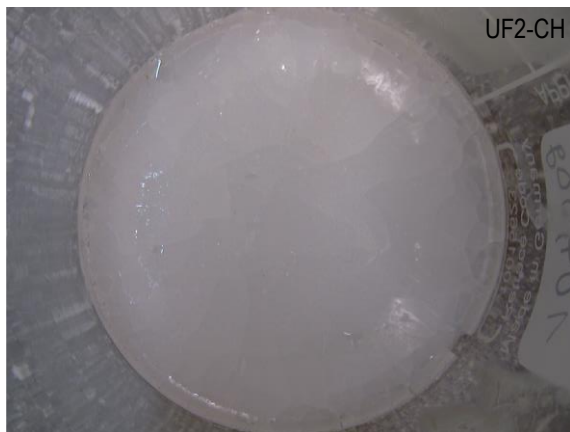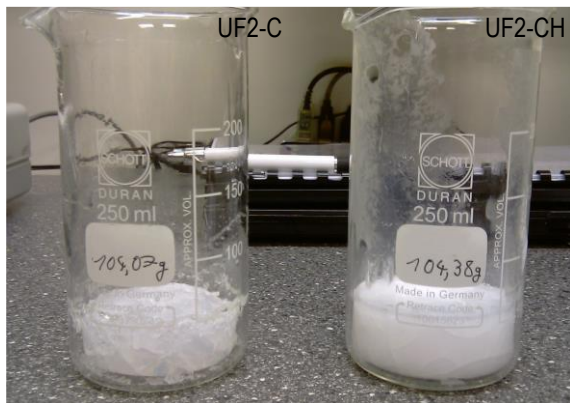
Figure VII-8: Urea-formaldehyde adhesive resin samples in the solid state as type UF2-C and UF2-CH (cured without and with additional hardener, respectively) acc. to Table IV-3 and Table IV-4.

2 Material characterisation

2.1 True density and porosity

Figure VII-10: Sample preparation for true density determination via gas pycnometry on panel material with 10 mm wide parallel offcuts (top), cutting of single specimens by band-saw with nominal dimensions of $2\ldots3 \times 10 \times 19$ mm^3 ($l \times w \times t_{\text{panel}}$) (middle), and randomly mixed material (bottom); for fibrous material see Appendix VII–2.2.
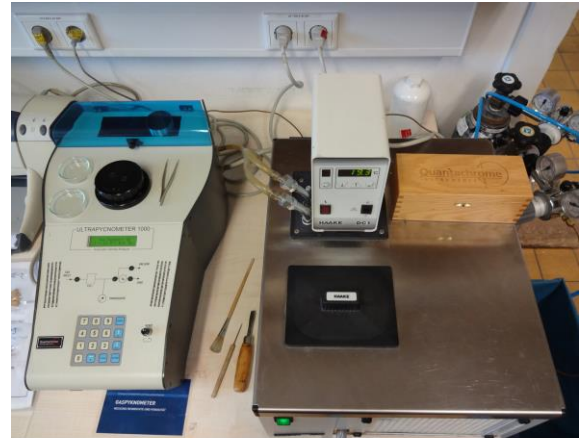
Figure VII-11: Analysis equipment for true density determination via gas pycnometry at the Institute of Wood and Paper Technology, Technische Universität Dresden, Germany with the gas pycnometer ULTRAPYCNOMETER 1000, QUANTACHROME GmbH & Co. KG, Odelzhausen, Germany complete with peripheral equipment for supply and conditioning of Helium (He) as displacement gas at 1.31 bar pressure and $\vartheta_{set} = 20\,°\mathrm{C}$; exemplary specimens of labMDF (middle), PB-19 (bottom left), and raw TMP fibres (resin-unblended) of labMDF (bottom right) within the measuring cell.

Figure VII-12: Analysis equipment for additional density determination on dry adhesive resin by means of immersion method following DIN EN ISO 1183-1 (2013) via Archimedes' principle (i. e. buoyancy method) with purified water (without wetting agent) as immersion liquid (IL), with analytical balance XS205DU, Mettler-Toledo GmbH, Giessen, Germany, equipped with the corresponding density kit.

2.2   Fibre and particle morphology

Figure VII-13: Photographic documentation for visual comparison of both fibre types TMP-F (top, for lab-made furnish mats Fmat) and TMP-H (middle, for lab-made homogeneous fibreboards labMDF) as well as milled fibres TMP-h (bottom, type TMP-H as prepared for analyses).
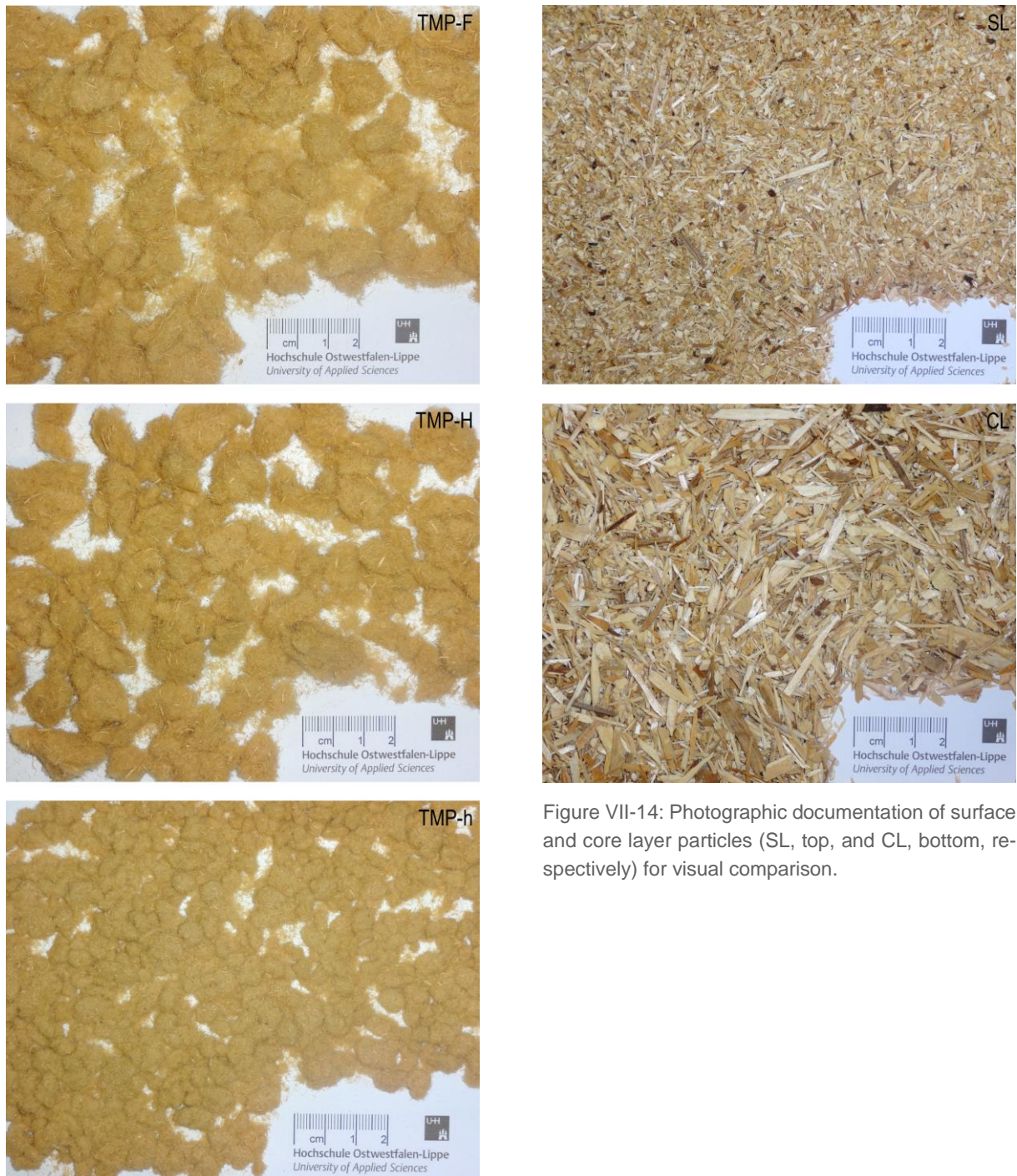
Figure VII-14: Photographic documentation of surface and core layer particles (SL, top, and CL, bottom, respectively) for visual comparison.
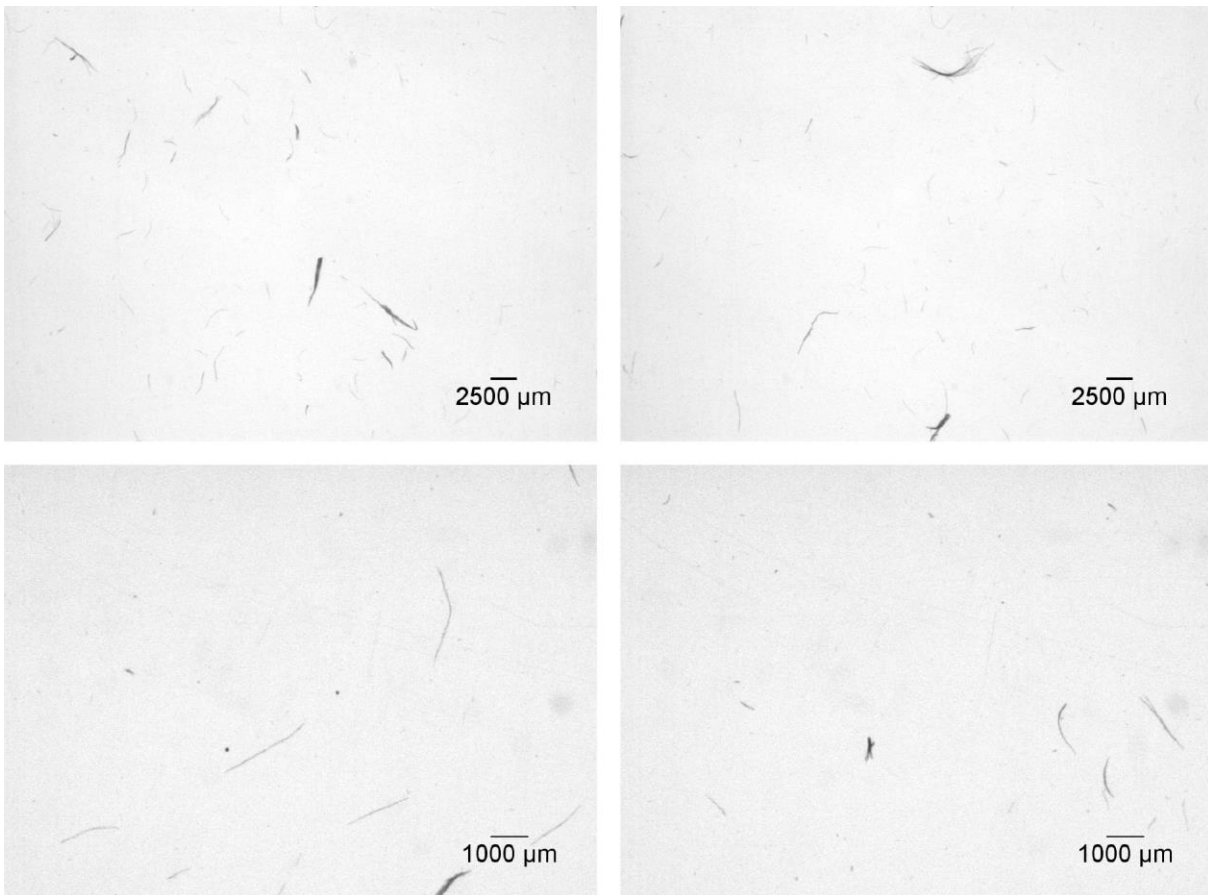
Figure VII-15: Exemplary raw images of fibre morphology analysis via IHD method acquired on material in water suspension by both basic (top, 2500 μm ≈ FBc mean length) and zoom (bottom, 1000 μm ≈ SFs mean length) camera of the employed CamSizer device; note, scale bar length and thickness roughly correspond to mean length and width of FBc and SFs; by courtesy of IHD, Dresden, WENDERDEL (2016).
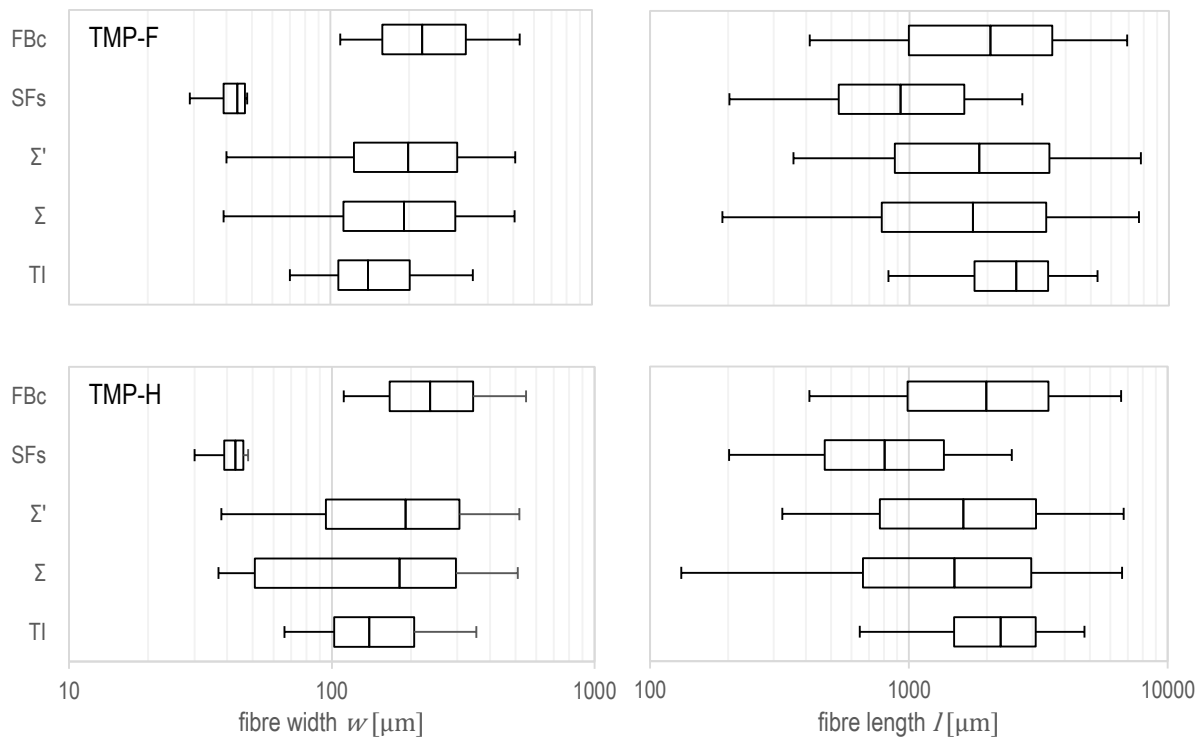
Figure VII-16: Summary of fibre width w [µm] (left) and length l [µm] (right) variation within selected predominant structural fibre types short single fibres (SFs) and compact fibre bundles (FBc) as well as total sample with (Σ) and without (Σ') dust determined by IHD method (upper four, volume-weighted) and undifferentiated results from TI method (bottom, double width- or length-weighted) of TMP-F (top) and TMP-H (bottom) as box plots with $Q1$, $median$, and $Q3$, as well as 5 % quantiles as whiskers $Q(0.05)$ and $Q(0.95)$; note camera resolution of 15 µm (IHD method) and 23,2 µm (TI method) pixel size.

Complementarily to the main investigations in fibre morphology characterisation (IHD method, Chapter IV–2.2), a fibre size determination method was employed featuring dry separation of TMP fibres to be analysed. The automated system with complex data evaluation at that time available at TI, Hamburg, Germany, and referred to as FibreCube was developed by TI (2015) together with partners, referred to as TI method henceforth. The method is introduced by BENTHIEN et al. (2014a) and applied by, e. g., BENTHIEN et al. (2014b). For methodical and technical details, reference is made to the latter. During device performance, fibres are separated within an air stream by combined application of compressed air and ultrasound and, subsequently, left on a rotating glass plate, where image acquisition is performed. Besides common initial image correction, data evaluation features

a fibre extraction process and yields length and number of fibres. SEPPKE et al. (2015) describe the skeleton-based fibre characterisation software approach. Subsequently, a relative frequency of the so-called double length-weighted fibre length (cf. ROBERTSON et al. (1999)) is computed via squared length and data provided by common device output following DIN ISO 9276-1 (2004). On the contrary to primarily applied morphology characterisation via IHD method, the TI method (as applied at that time) does not involve explicit distinction between inherent types of structural elements within the fibrous material. On request, beyond regular device operation, fibre width was additionally evaluated and analogously made available as final frequency distribution of double width-weighted values. Accordingly and following the established procedure of the laboratory[39], fibrous material

---

[39] Fibre size determination was performed at the Thünen Institute (TI) of Wood Research, Hamburg-Bergedorf, Germany by the local staff. Their support and special evaluation effort is highly appreciated.

was analysed at ambient conditions, roughly equal to 20/65. To this end, repeat determinations on $n = 3$ samples with nominal mass of 0.5 g each were performed.

Table VII-1 and Figure VII-17 show the results of the complementary fibre size determination by TI method on both raw TMP fibre types F and H complete with milled fibres TMP-h. The values and charts represent the combined data from $n = 3$ samples as summary according to the FibreCube output and evaluation on double width- or length-weighted basis.

	TMP-F	TMP-H	TMP-h
Numbre of fibres [pcs/mg]	357	389	579
Fibre length [mm]	2.77	2.44	1.43
50 % quantile [mm]	2.58	2.26	1.27
Fibre length classes [%]			
a) 0...0.3 mm	0.45	0.87	2.08
b) 0.3...1 mm	7.03	11.22	31.56
c) 1...3 mm	55.72	60.67	62.67
d) 3...6 mm	33.74	25.46	3.67
e) > 6 mm	3.05	1.78	0.02
Fibre width [mm]	0.165	0.163	0.155

Table VII-1: Results of the complementary fibre size determination by TI method on both raw TMP fibre types F and H complete with milled fibres TMP-h, combined data from $n = 3$ samples as summary acc. to FibreCube output and evaluation on double width- or length-weighted basis.
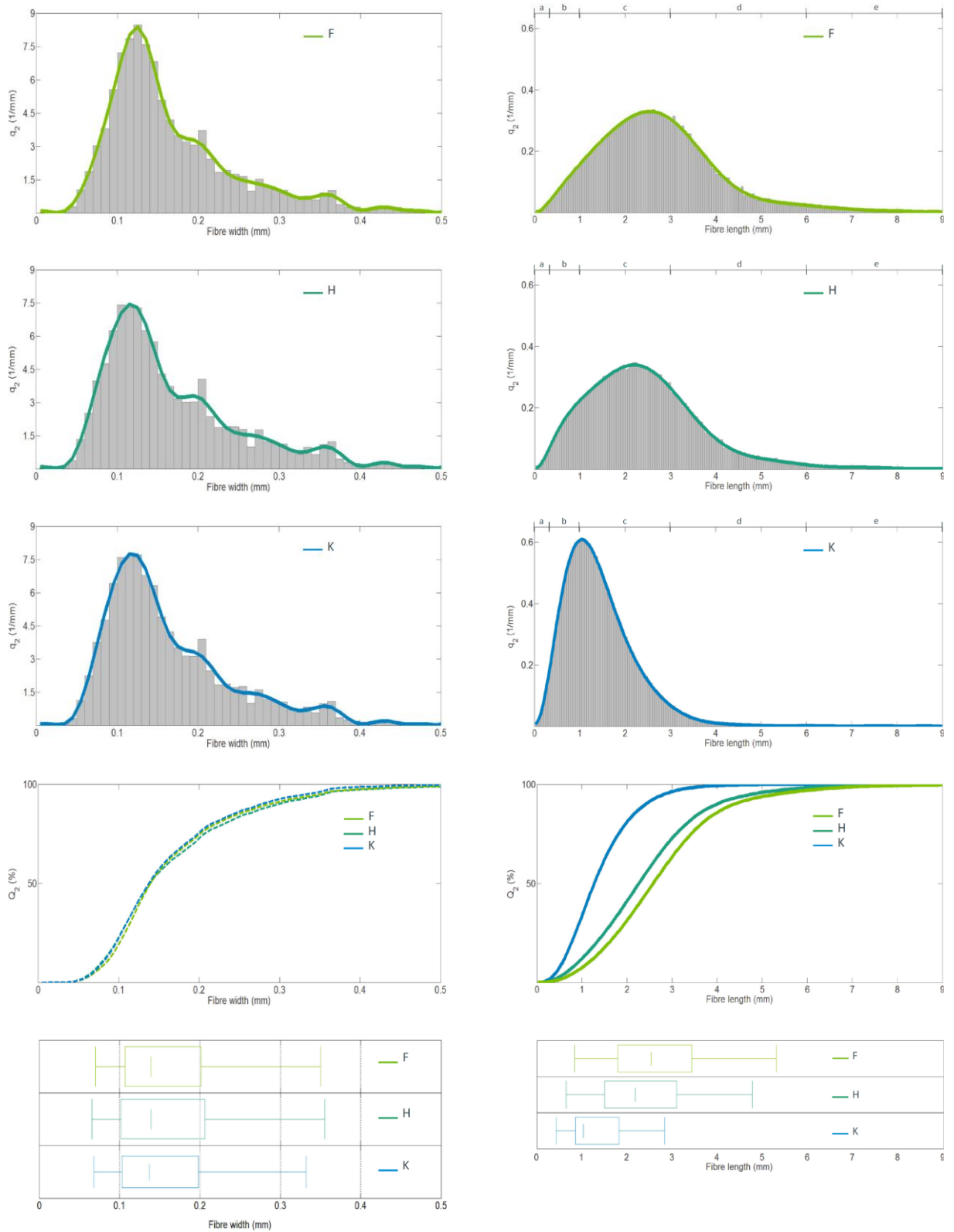
Figure VII-17: Results of the complementary fibre size determination by TI method on both raw TMP fibre types F (top) and H (second from top) complete with milled fibres TMP-h (third from top, label 'K') as normalised frequency q_2 [1/mm] as well as cumulative frequency Q_3 [%] (second from bottom) and box plot (bottom, $Q1$, $Q2$, and $Q3$ with 5 % quantiles as whiskers) with fibre width (left) and length (right), combined data from $n = 3$ samples as charts acc. to FibreCube output and evaluation on double width- or length-weighted basis.

2.3   Ash content

Figure VII-18: Analysis equipment for ash content determination via complete combustion according to the procedure in Table IV-10, with analytical balance AE240, Mettler-Toledo (left), desiccator, microwave laboratory system StarT Pyro T-1640, MLS GmbH, Leutkirch, Germany as exhaust air high-temperature furnace (middle and right) complete with porcelain combustion crucibles with lid.

Figure VII-19: Photographic documentation of the ash content determination procedure via complete combustion according to Table IV-10.
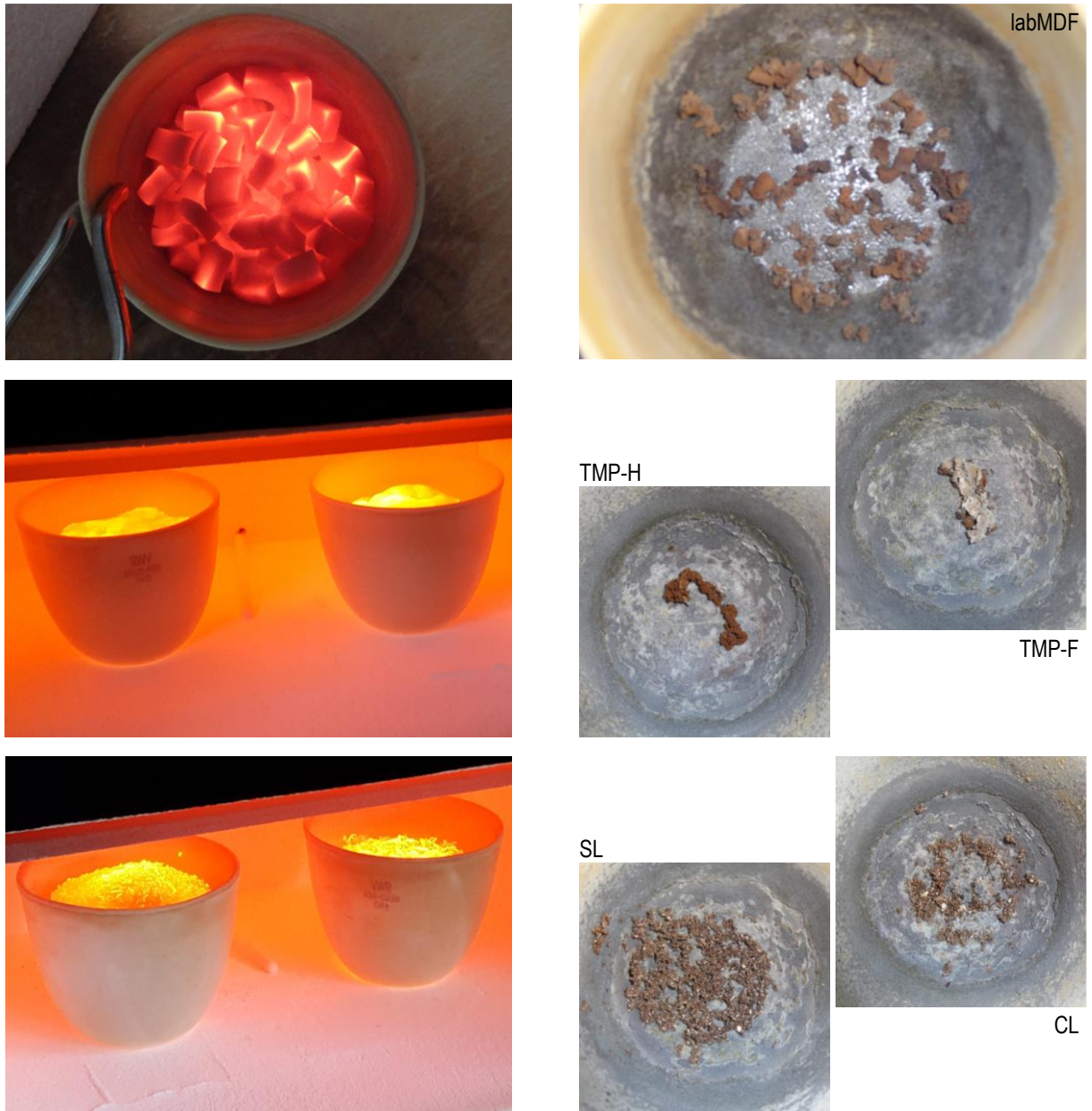
Figure VII-20: Exemplary photographs of the samples during ash content determination via complete combustion, filled crucibles with removed lid after 1 h of incomplete combustion (steps 7 and 8 Table IV-10) in the furnace followed by further 5 h at 900 °C (left column), corresponding final ash (non-combustible residue, right column) of labMDF (top), TMP-H (for lab-made homogeneous fibreboards labMDF) and TMP-F (for lab-made furnish mats Fmat) (middle), as well as SL and CL particles (bottom); note, weighed portion, and thus, ash amount differs.

2.4 Elemental composition

Figure VII-21: Analysis equipment for determination of mass fractions of the non-metallic chemical elements C, H, N, and S (elemental analysis) by means of the vario MACRO cube CHNS, Elementar Analysensysteme GmbH, Hanau, Germany.

Figure VII-22: Photographic documentation of specimen preparation for elemental analysis by means of the Figure VII-21 device as described in Chapter IV–2.4.1, with milled particles (top), labMDF shavings made by fine-toothed saw, weighing and packing in thin tin foil, and sample feeder loading.

3   Gravimetric reference method
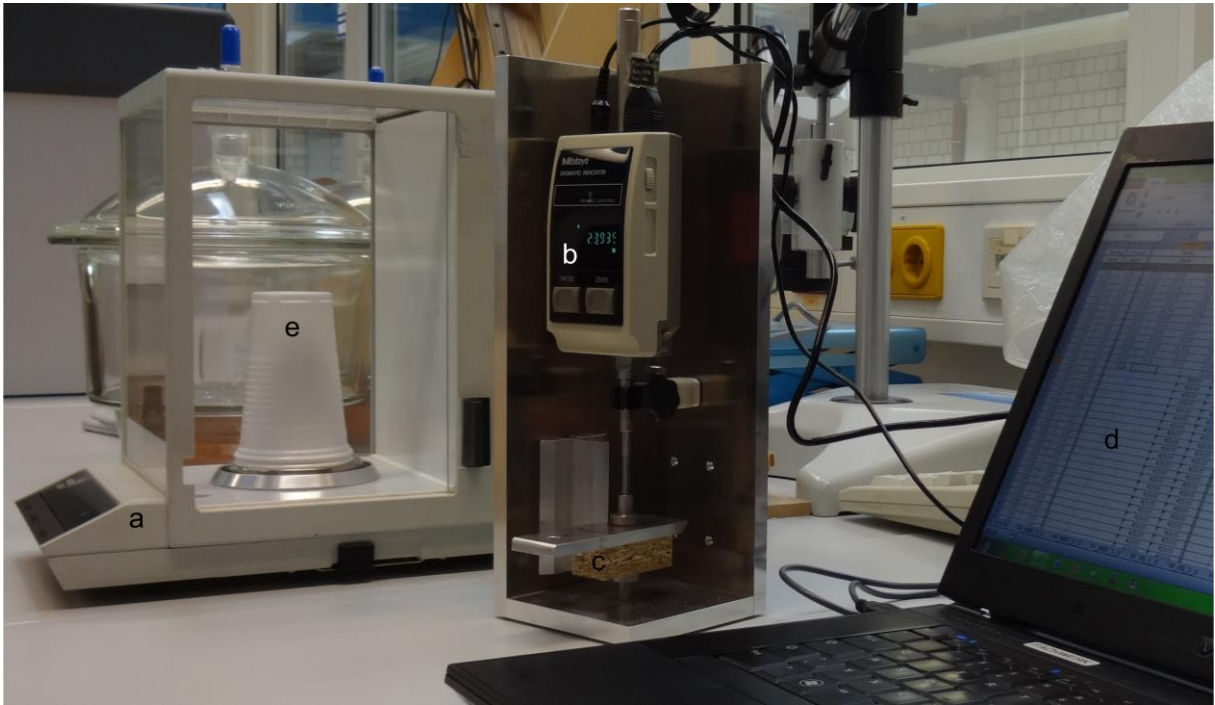
Figure VII-23: Peripheral equipment for gravimetric reference method for RDP measurement by determination of raw density per layer of the specimen after milling (Figure IV-15) via residual mass and thickness measurement by analytical balance AE240, Mettler-Toledo (a), digital dial gauge Digimatic Indicator, Mitutoyo (b) with tip Ø16 mm according to DIN EN 325 (2012), specimen fixed by PVA glue on aluminium holder (c), PC for data acquisition via interface (d); raised weighing position to avoid impact of holder magnet (e).
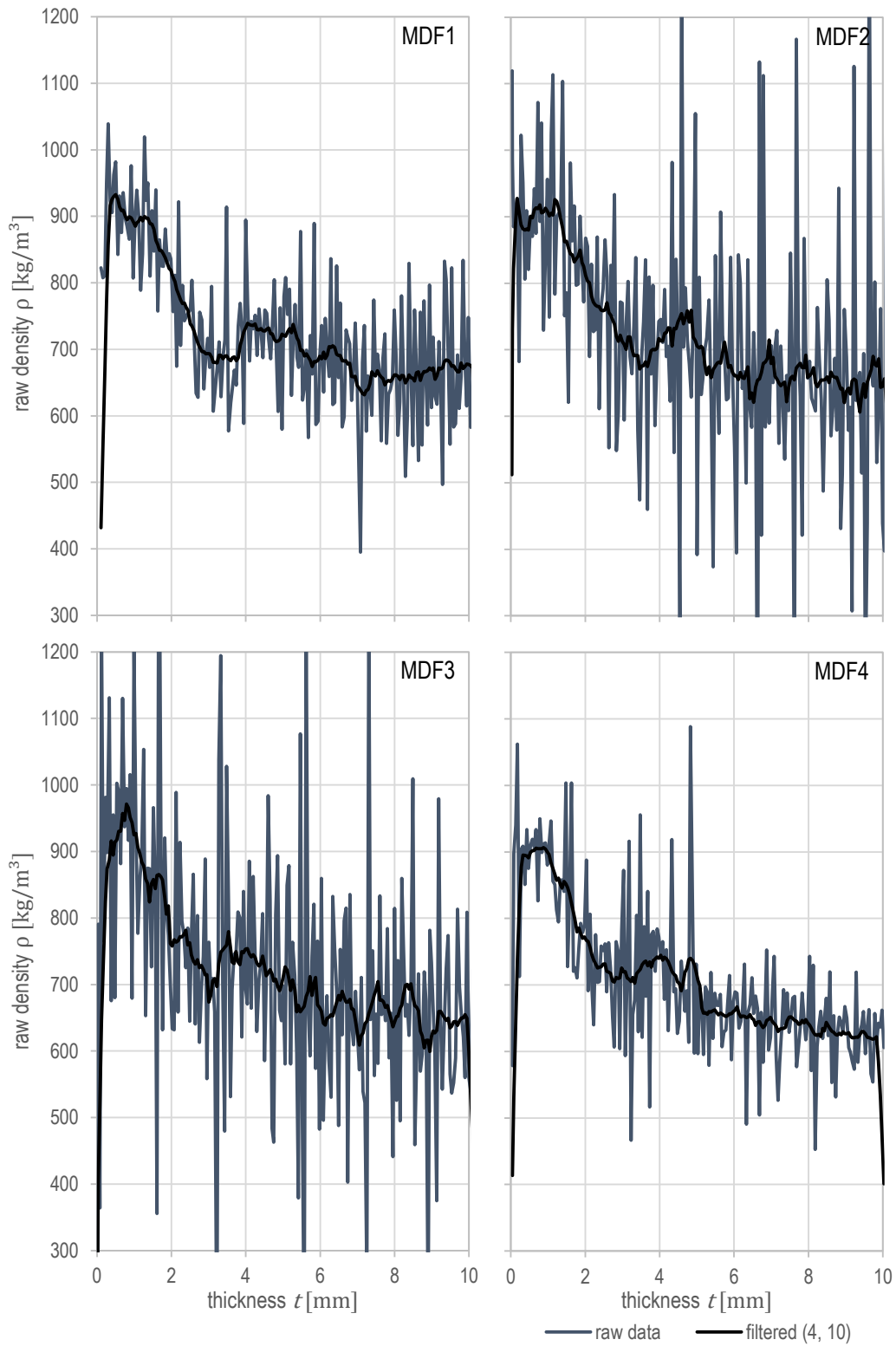
Figure VII-24: Gravimetric RDPs of MDF-19 from round robin test as raw data and filtered via Gaussian smoothing by convolution kernel $\sigma = 4$, $w_K = 10$; for results of the specimen MDF5 refer to Figure IV-18.
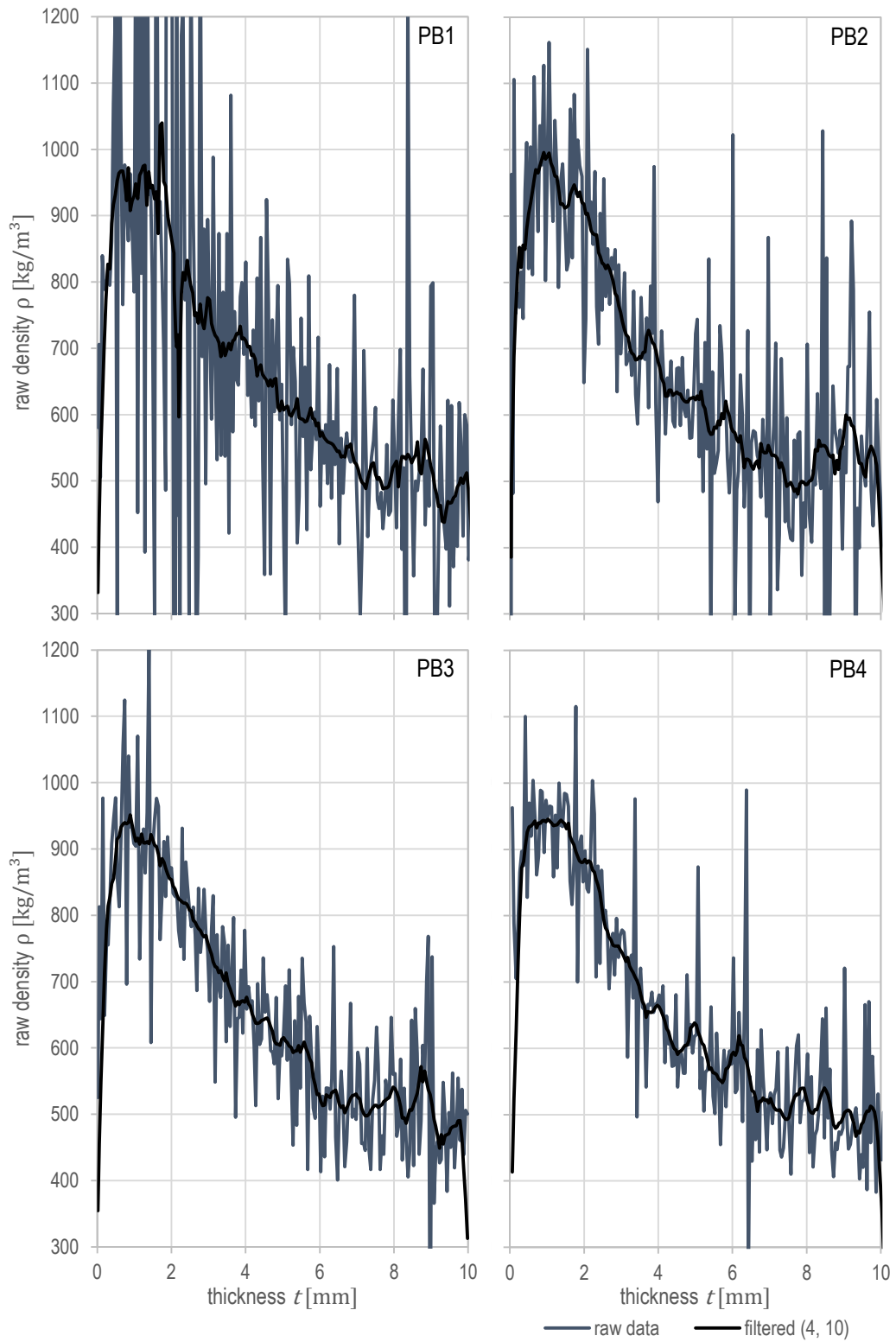
Figure VII-25: Gravimetric RDPs of PB-19 from round robin test as raw data and filtered via Gaussian smoothing by convolution kernel $\sigma = 4$, $w_\mathrm{K} = 10$; for results of the specimen PB5 refer to Figure IV-18.
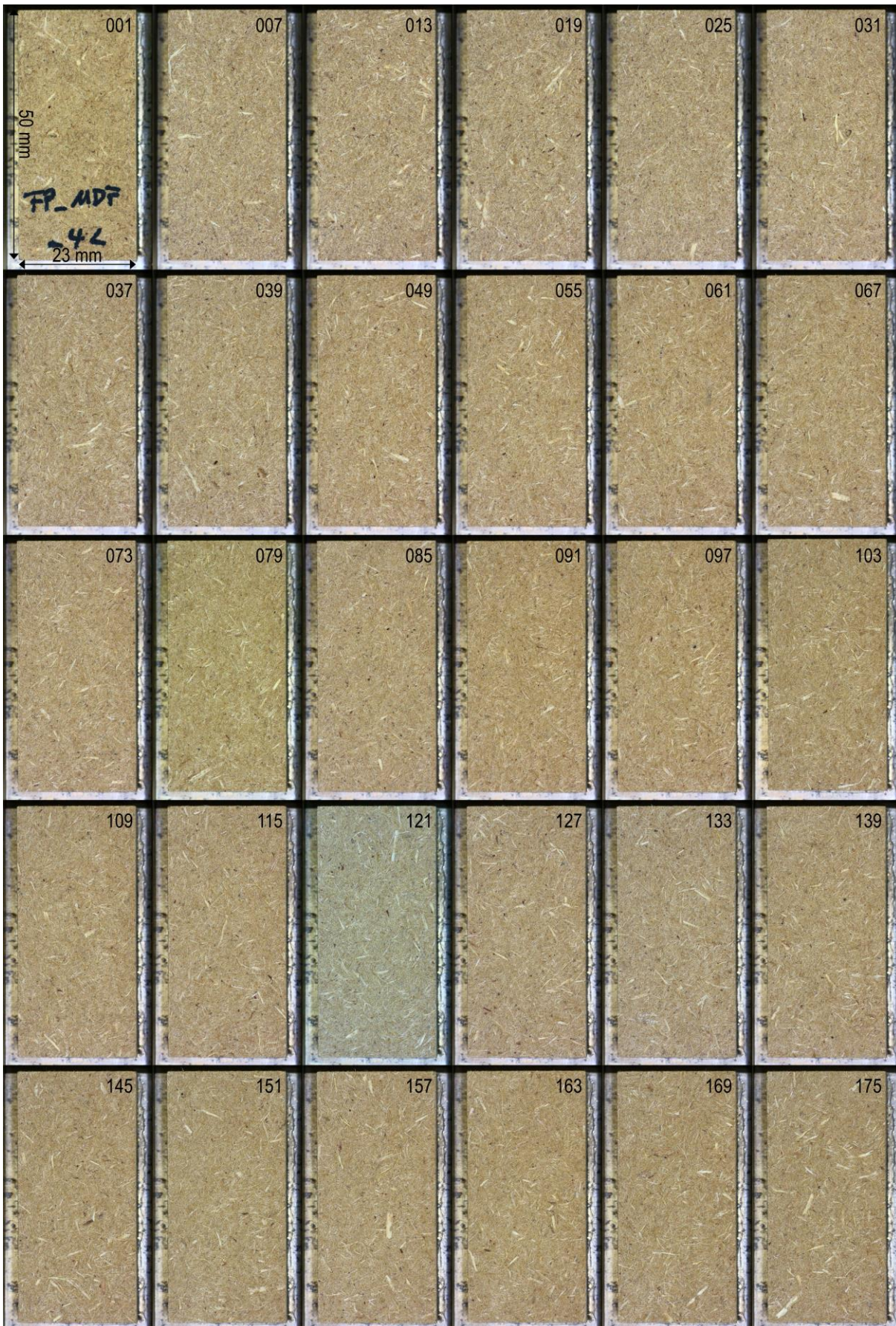
Figure VII-26: Selection of images per layer from RDP reference method (Chapter IV–4.2.4.2, left specimen halves 23 × 50 mm² on aluminium baseplate) after milling in 50 µm steps of the exemplary specimen MDF4, every seventh layer with 0.3 mm distance between the images; note, colour variations due to camera automatic white balance.
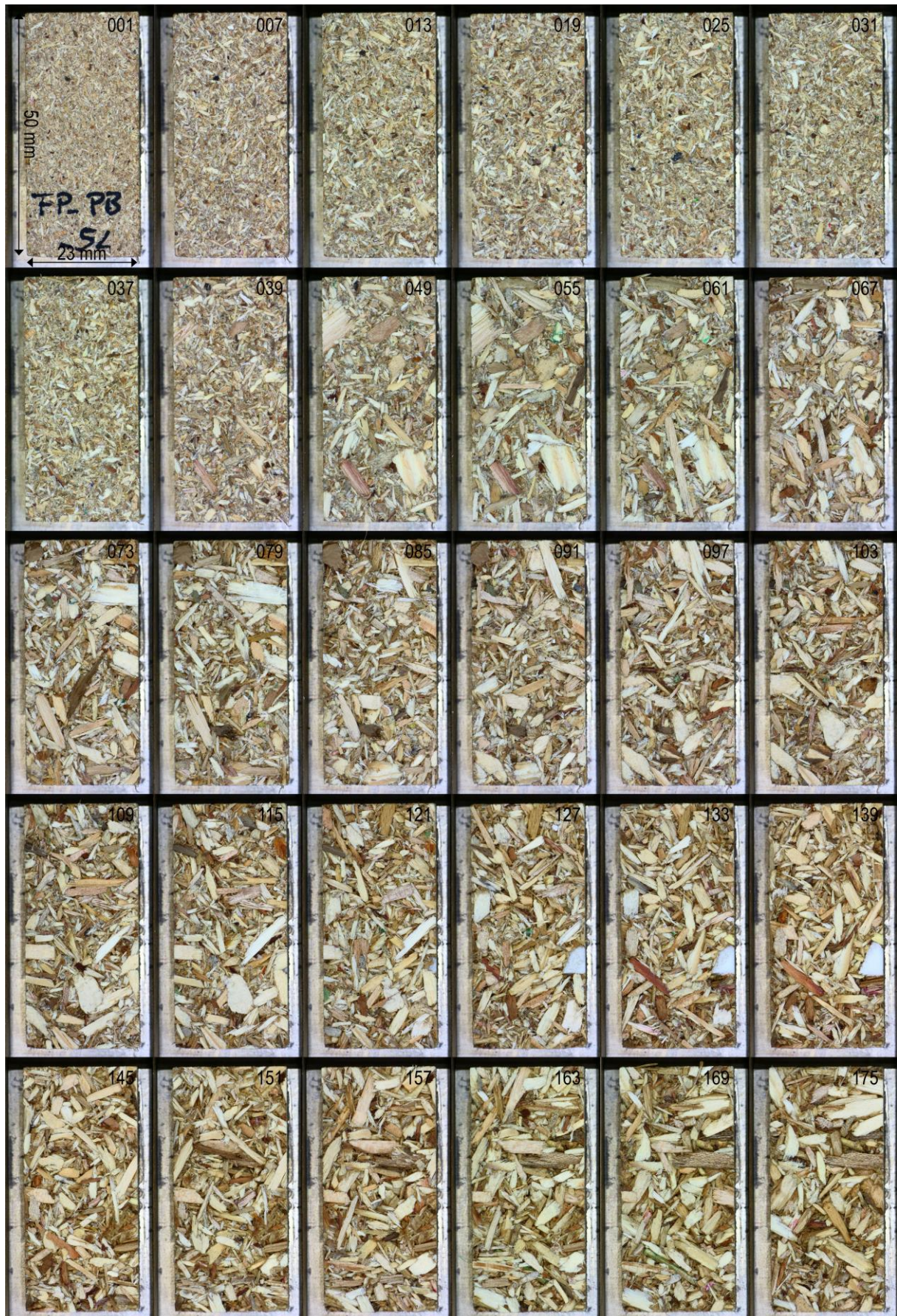
Figure VII-27: Selection of images per layer from RDP reference method (Chapter IV–4.2.4.2, left specimen halves 23 × 50 mm² on aluminium baseplate) after milling in 50 µm steps of the exemplary specimen PB5, every seventh layer with 0.3 mm distance between the images; note, colour variations due to camera automatic white balance.
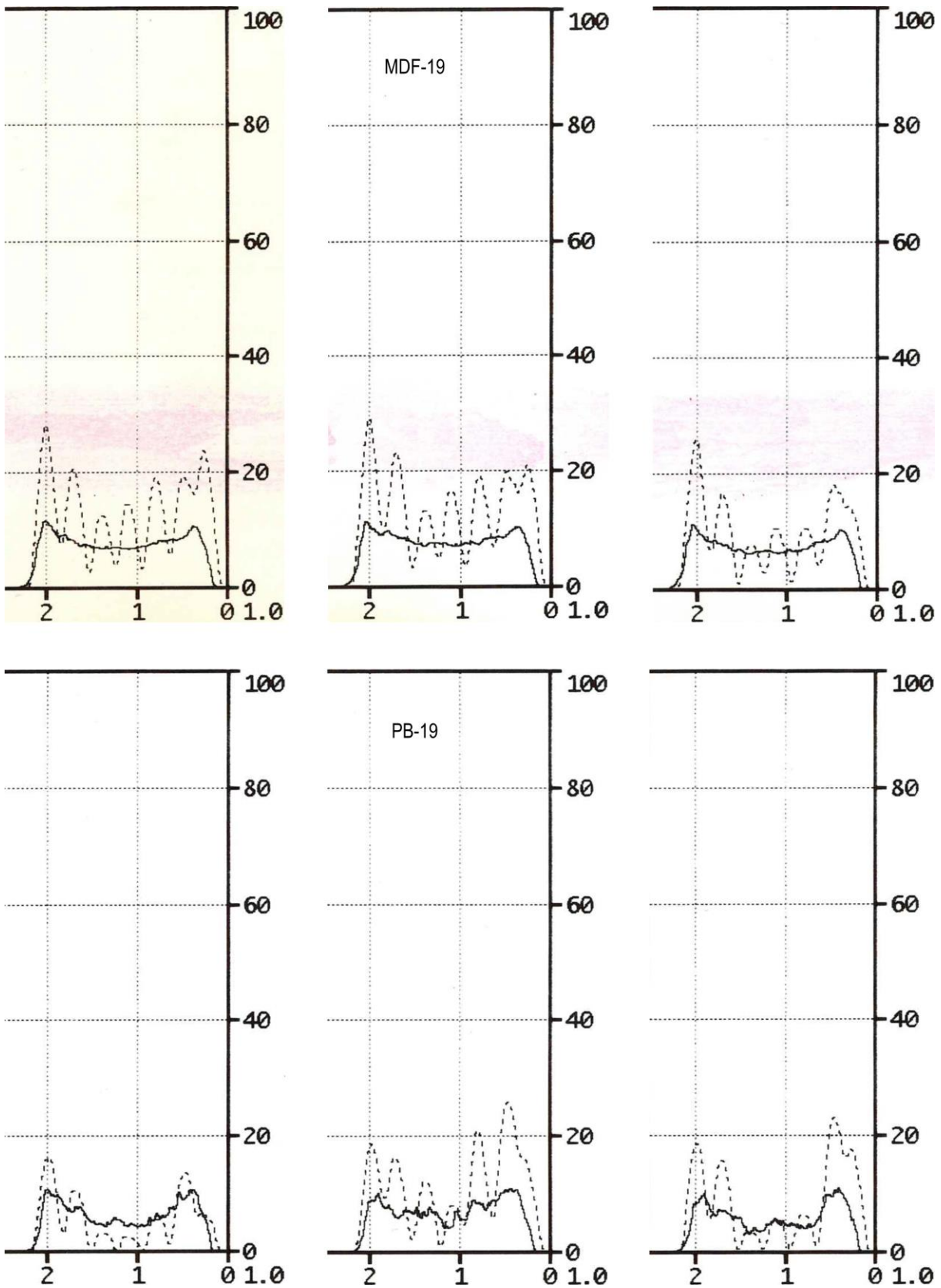
Figure VII-28: Exploratory application of drilling resistance method for vertical RDP determination on WBCs by means of the IML RESI PowerDrill® handheld device (a rather old model with only a profile printout), with needle $n = 2500 \ \text{min}^{-1}$ and $v_f = 15 \ \text{cm/min}$; exemplary printouts of MDF-19 (top) and PB-19 (bottom) with relative profiles corresponding to RDPs (vertical axis) along the panel thickness (horizontal axis [cm]) directly from device evaluation and output (scanned printouts).

4 Mass attenuation coefficient computation

The data compilation in this chapter comprises the relevant chemical elements

- $_1$H in Figure VII-29 and Table VII-3
- $_6$C in Figure VII-30 and Table VII-4,
- $_7$N in Figure VII-31 and Table VII-5,
- $_8$O in Figure VII-32 and Table VII-6,
- $_{13}$Al in Figure VII-33 and Table VII-7,
- $_{16}$S in Figure VII-34 and Table VII-8,
- $_{20}$Ca in Figure VII-35 and Table VII-9 (for ash),

as well as materials and mixtures with composition data based on elemental analyses (Table IV-15 and Table IV-16)

- TMP oven-dry (OD) in Figure VII-36 and Table VII-10,
- labMDF OD in Figure VII-37 and Table VII-11,
- labMDF at $MC = 9.5\,\%$ in Figure VII-38 and Table VII-12,
- Fmat OD in Figure VII-39 and Table VII-13,
- UF-C in Figure VII-40 and Table VII-14,
- indMDF OD in Figure VII-41 and Table VII-15,
- insulation OD in Figure VII-42 and Table VII-16,

and on the basis of empirical compositions complete with data from literature review (Table IV-14)

- water in Figure VII-43 and Table VII-17,
- wood (simplistic) OD in Figure VII-44 and Table VII-18,
- wood (total mean) OD in Figure VII-45 and Table VII-19,
- cellulose (mean) in Figure VII-46 and Table VII-20,
- hemicelluloses (mean) in Figure VII-47 and Table VII-21, and
- lignin (mean) in Figure VII-48 and Table VII-22.

Energy level	E [keV]	type	device label
low	12.7	$\bar{E}$	W-mat-16-w/o
		$\bar{E}$	W-panel-16-w/o
medium	15.5	$\bar{E}$	W-mat-20-w/o
		$\bar{E}$	W-panel-20-w/o
	16.9	$E_{\max}$	W-mat-16-w/o
		$E_{\max}$	W-panel-16-w/o
	21.1	$\bar{E}$	Ag-RDP-55-w/o
	21.2	$E_{\max}$	W-mat -20-w/o
		$E_{\max}$	W-panel-20-w/o
	21.5	$\bar{E}$	Ag-RDP-55-w/
		$\bar{E}$	W-RDP-35-w/o
	24.2	$\bar{E}$	W-RDP-35-w/
	26.3	$\bar{E}$	W-RDP-50-w/o
	27.3	$\bar{E}$	W-panel-35-w/
	29.2	$\bar{E}$	W-RDP-50-w/
	35.1	$E_{\max}$	W-panel-35-w/
	35.4	$E_{\max}$	W-RDP-35-w/o
		$E_{\max}$	W-RDP-35-w/
high	50.9	$E_{\max}$	W-RDP-50-w/o
		$E_{\max}$	W-RDP-50-w/
	51.3	$E_{\max}$	Ag-RDP-55-w/o
		$E_{\max}$	Ag-RDP-55-w/
	59.5	E_γ	^{241}Am

Table VII-2: Particular radiation energies (classified on three levels) with corresponding X-ray device and setup label (Chapter IV–4.2.2 and IV–4.2.3) beyond standard grid of subsequent mass attenuation coefficient $\mu/\rho\,(E)$ tables, individually measured mean energy $\bar{E}$ and maximum Energy $E_{\max}$ by means of X-ray spectrometry (Chapter IV–4.2.6.1 and IV–4.3.3.1), complete with radioisotope ^{241}Am.
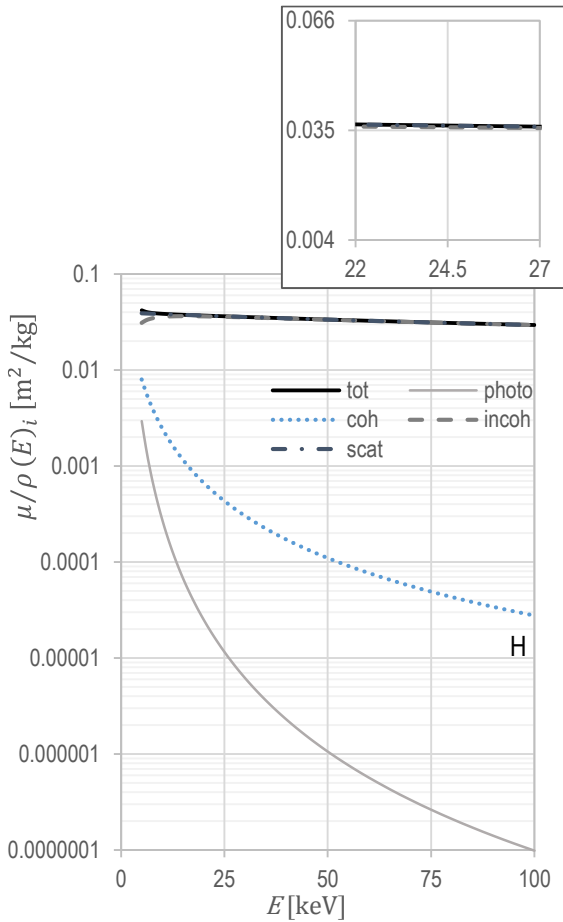
Figure VII-29: Total mass attenuation coefficients $\mu/\rho\,(E)_i$ of the element hydrogen $_1$H over radiation energy E incl. attenuation processes photoelectric absorption, coherent and incoherent scattering, as well as scattering (scat = coh + incoh) with corresponding data in Table VII-3.
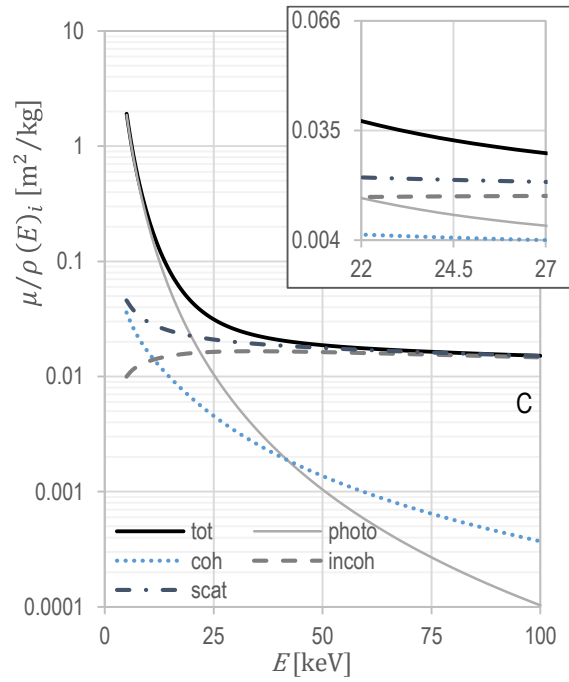
Figure VII-30: Total mass attenuation coefficients $\mu/\rho\,(E)_i$ of the element carbon $_6$C over radiation energy E incl. attenuation processes photoelectric absorption, coherent and incoherent scattering, as well as scattering (scat = coh + incoh) with corresponding data in Table VII-4.
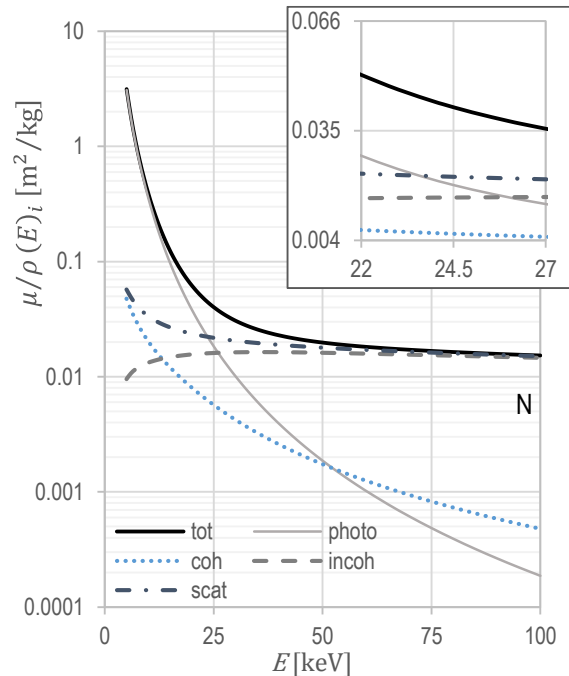
Figure VII-31: Total mass attenuation coefficients $\mu/\rho\,(E)_i$ of the element nitrogen $_7$N over radiation energy E incl. attenuation processes photoelectric absorption, coherent and incoherent scattering, as well as scattering (scat = coh + incoh) with corresponding data in Table VII-5.
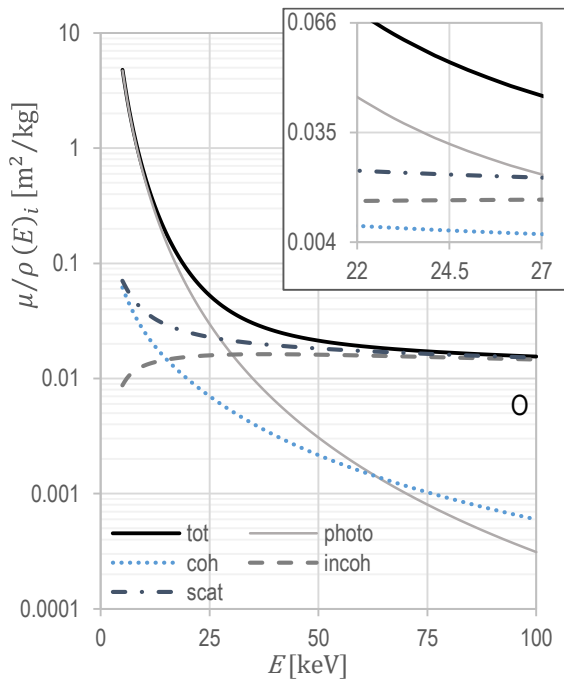
Figure VII-32: Total mass attenuation coefficients $\mu/\rho\,(E)_i$ of the element oxygen $_8$O over radiation energy E incl. attenuation processes photoelectric absorption, coherent and incoherent scattering, as well as scattering (scat = coh + incoh) with corresponding data in Table VII-6.
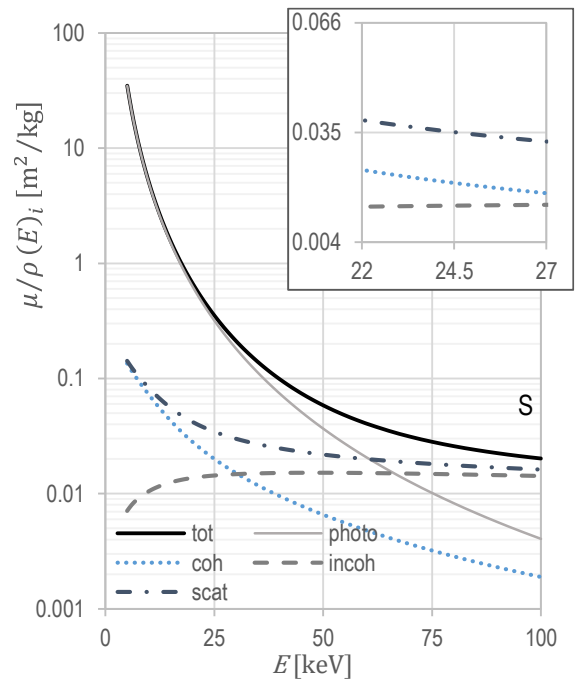
Figure VII-34: Total mass attenuation coefficients $\mu/\rho\,(E)_i$ of the element sulphur $_{16}$S over radiation energy E incl. attenuation processes photoelectric absorption, coherent and incoherent scattering, as well as scattering (scat = coh + incoh) with corresponding data in Table VII-8.
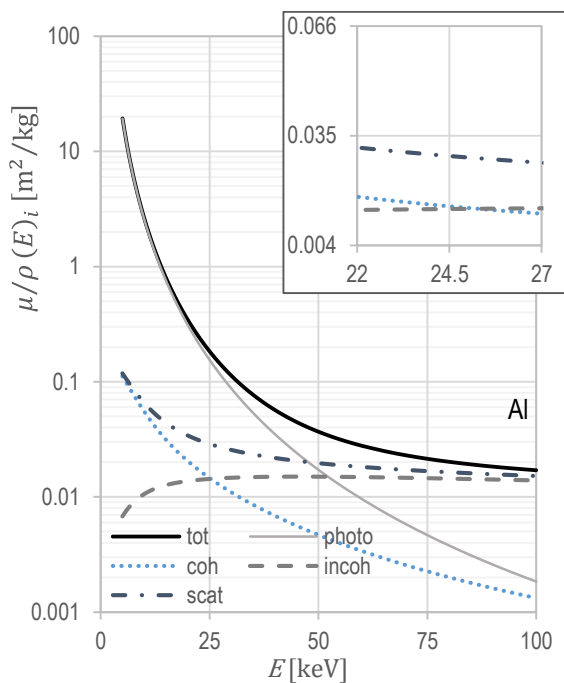
Figure VII-33: Total mass attenuation coefficients $\mu/\rho\,(E)_i$ of the element aluminium $_{13}$Al over radiation energy E incl. attenuation processes photoelectric absorption, coherent and incoherent scattering, as well as scattering (scat = coh + incoh) with corresponding data in Table VII-8.
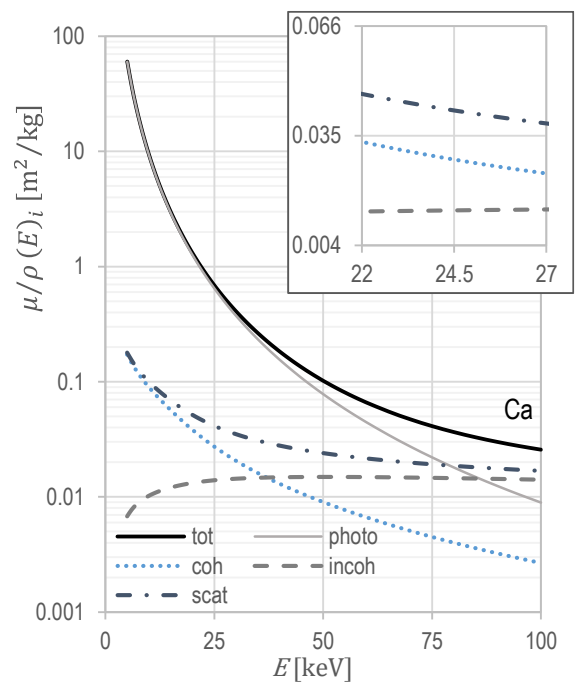
Figure VII-35: Total mass attenuation coefficients $\mu/\rho\,(E)_i$ of the element calcium $_{20}$Ca over radiation energy E incl. attenuation processes photoelectric absorption, coherent and incoherent scattering, as well as scattering (scat = coh + incoh) with corresponding data in Table VII-9.
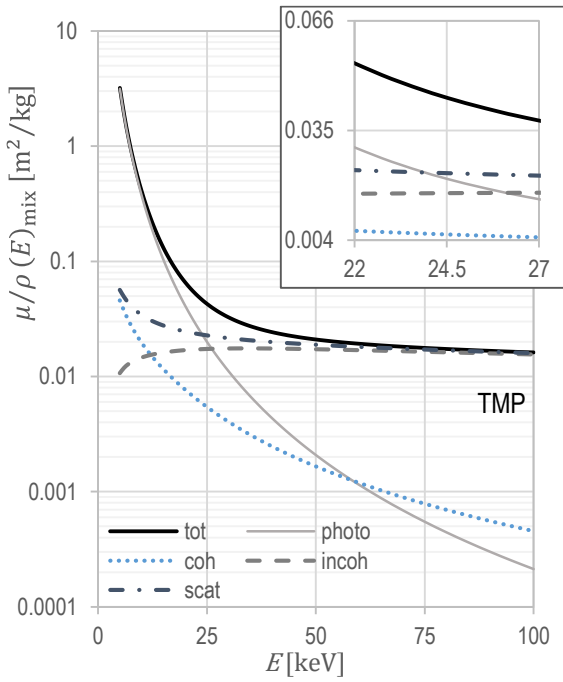
Figure VII-36: Total mean mass attenuation coefficient $\mu/\rho\,(E)_{\mathrm{mix}}$ of oven-dry TMP over radiation energy E incl. attenuation processes photoelectric absorption, coherent and incoherent scattering, as well as scattering (scat = coh + incoh) determined like corresponding data in Table VII-10.
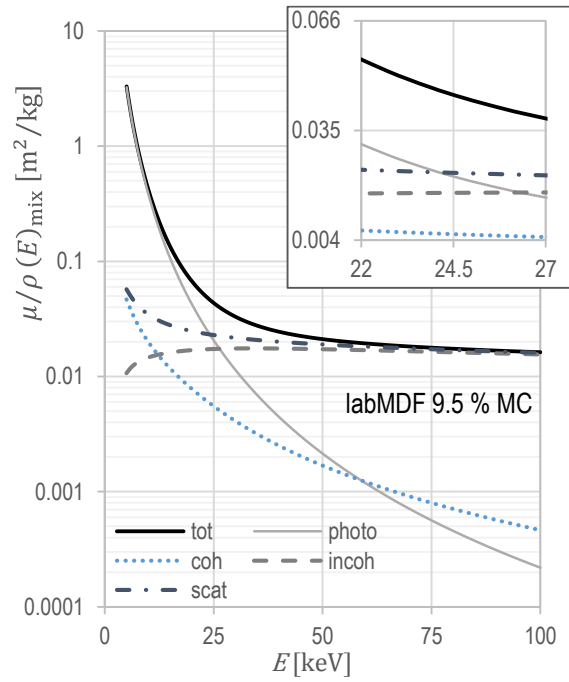
Figure VII-38: Total mean mass attenuation coefficient $\mu/\rho\,(E)_{\mathrm{mix}}$ of moist labMDF at $MC = 9.5\,\%$ over radiation energy E incl. attenuation processes photoelectric absorption, coherent and incoherent scattering, as well as scattering (scat = coh + incoh) determined like corresponding data in Table VII-12.
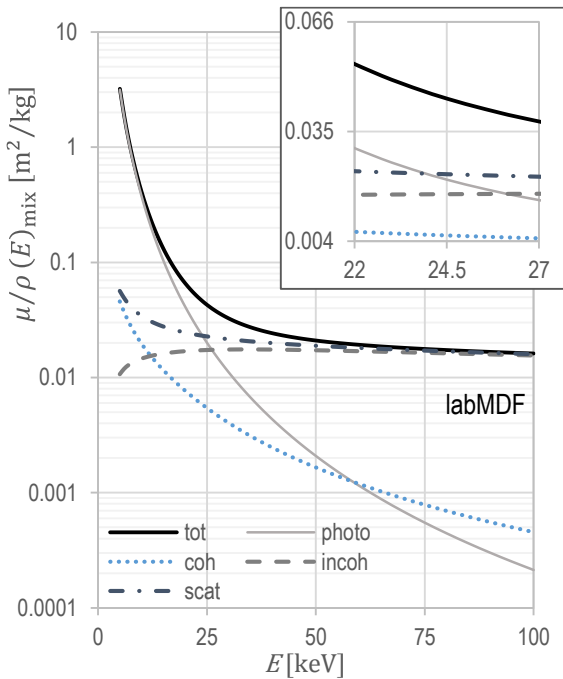
Figure VII-37: Total mean mass attenuation coefficient $\mu/\rho\,(E)_{\mathrm{mix}}$ of oven-dry labMDF over radiation energy E incl. attenuation processes photoelectric absorption, coherent and incoherent scattering, as well as scattering (scat = coh + incoh) determined like corresponding data in Table VII-11.
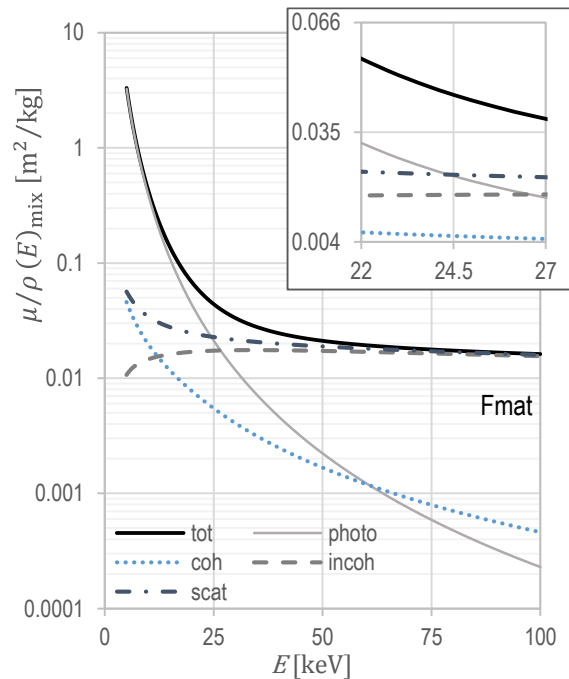
Figure VII-39: Total mean mass attenuation coefficient $\mu/\rho\,(E)_{\mathrm{mix}}$ of oven-dry Fmat over radiation energy E incl. attenuation processes photoelectric absorption, coherent and incoherent scattering, as well as scattering (scat = coh + incoh) determined like corresponding data in Table VII-13.
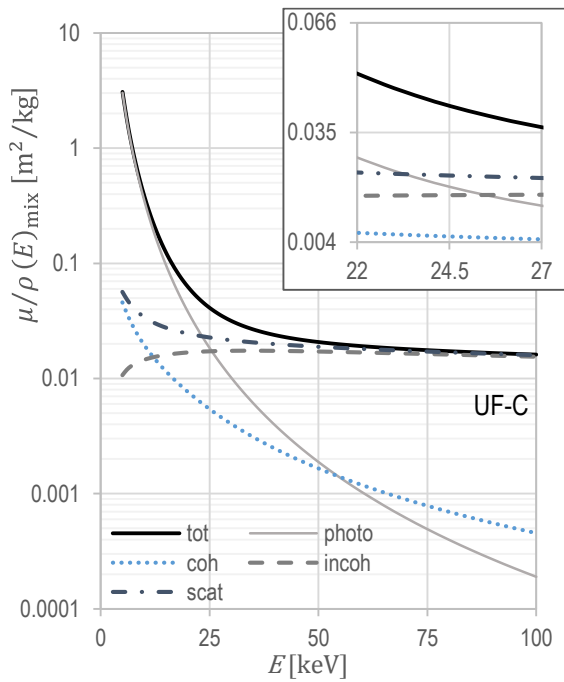
Figure VII-40: Total mean mass attenuation coefficient $\mu/\rho\,(E)_{\mathrm{mix}}$ of UF-C over radiation energy E incl. attenuation processes photoelectric absorption, coherent and incoherent scattering, as well as scattering (scat = coh + incoh) determined like corresponding data in Table VII-14.
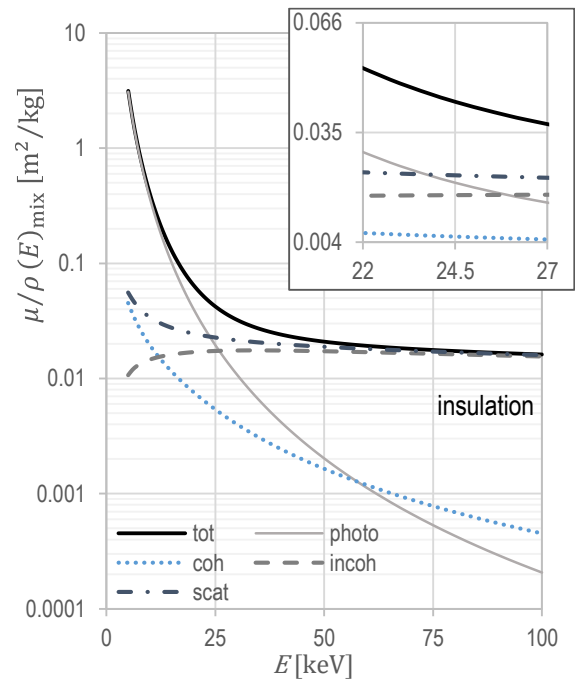
Figure VII-42: Total mean mass attenuation coefficient $\mu/\rho\,(E)_{\mathrm{mix}}$ of oven-dry insulation over radiation energy E incl. attenuation processes photoelectric absorption, coherent and incoherent scattering, as well as scattering (scat = coh + incoh) determined like corresponding data in Table VII-16.
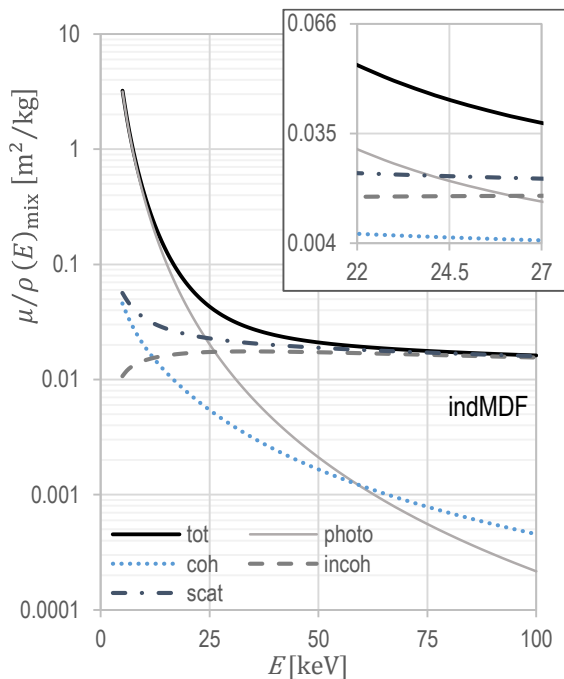
Figure VII-41: Total mean mass attenuation coefficient $\mu/\rho\,(E)_{\mathrm{mix}}$ of oven-dry indMDF over radiation energy E incl. attenuation processes photoelectric absorption, coherent and incoherent scattering, as well as scattering (scat = coh + incoh) determined like corresponding data in Table VII-15.
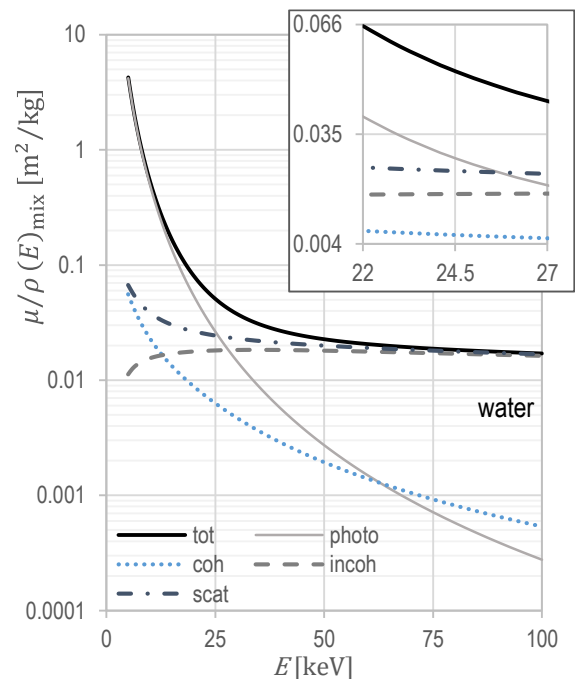
Figure VII-43: Total mean mass attenuation coefficient $\mu/\rho\,(E)_{\mathrm{mix}}$ of water H_2O over radiation energy E incl. attenuation processes photoelectric absorption, coherent and incoherent scattering, as well as scattering (scat = coh + incoh) determined like corresponding data in Table VII-17.
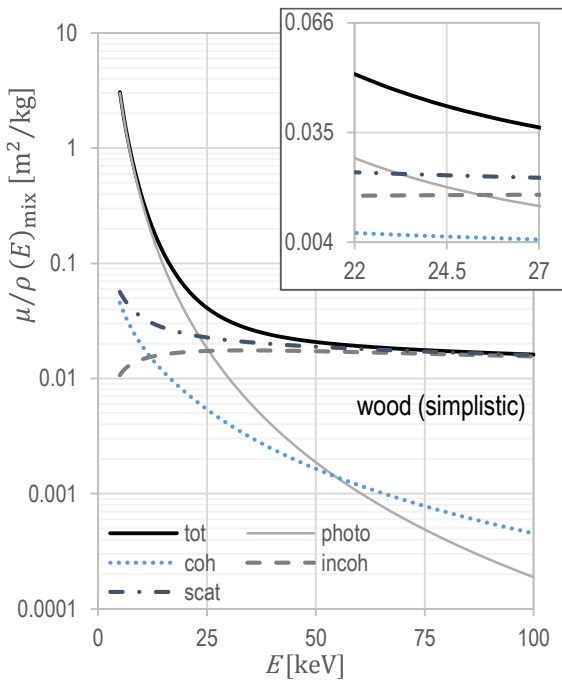
Figure VII-44: Total mean mass attenuation coefficient $\mu/\rho\,(E)_{\mathrm{mix}}$ of oven-dry wood (simplistic) over radiation energy E incl. attenuation processes photoelectric absorption, coherent and incoherent scattering, as well as scattering (scat = coh + incoh) determined like corresponding data in Table VII-18.
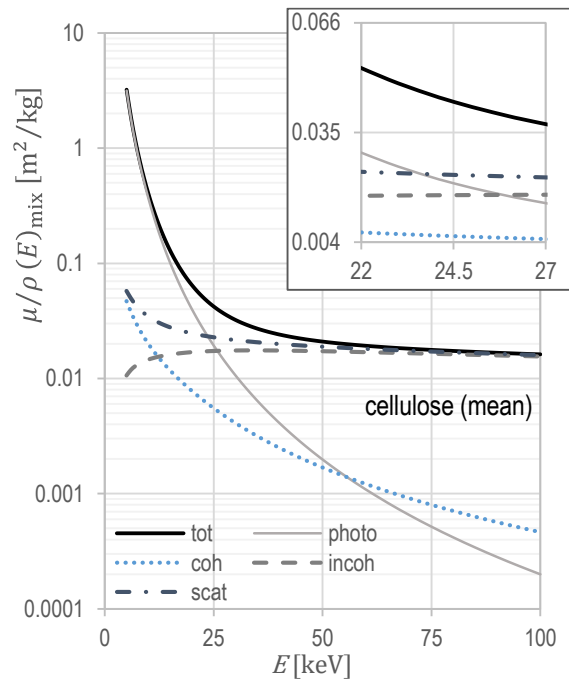
Figure VII-46: Total mean mass attenuation coefficient $\mu/\rho\,(E)_{\mathrm{mix}}$ of cellulose (mean) over radiation energy E incl. attenuation processes photoelectric absorption, coherent and incoherent scattering, as well as scattering (scat = coh + incoh) determined like corresponding data in Table VII-20.
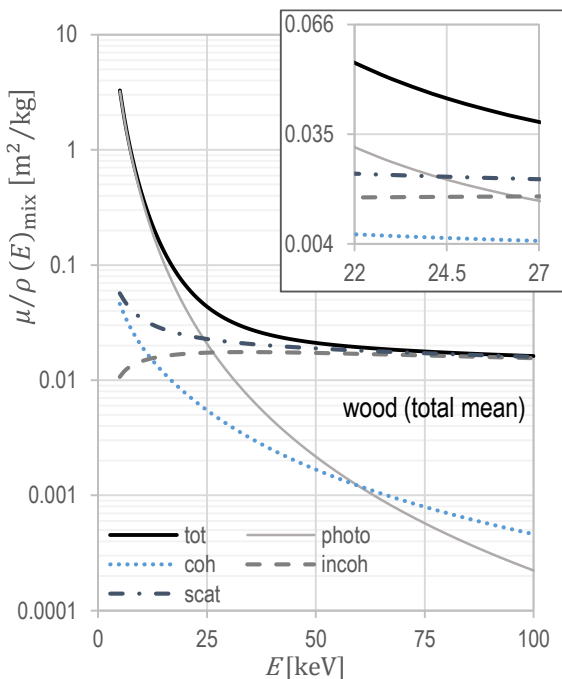
Figure VII-45: Total mean mass attenuation coefficient $\mu/\rho\,(E)_{\mathrm{mix}}$ of oven-dry wood (total mean) over radiation energy E incl. attenuation processes photoelectric absorption, coherent and incoherent scattering, as well as scattering (scat = coh + incoh) determined like corresponding data in Table VII-19.
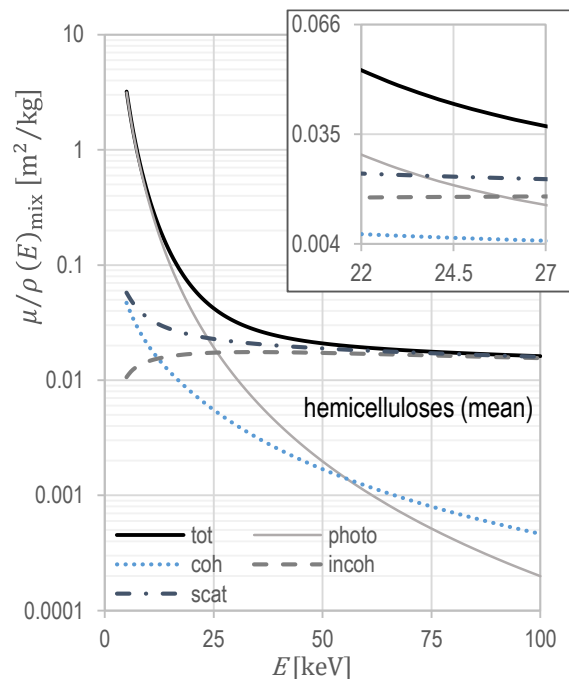
Figure VII-47: Total mean mass attenuation coefficient $\mu/\rho\,(E)_{\mathrm{mix}}$ of hemicelluloses (mean) over radiation energy E incl. attenuation processes photoelectric absorption, coherent and incoherent scattering, as well as scattering (scat = coh + incoh) determined like corresponding data in Table VII-21.
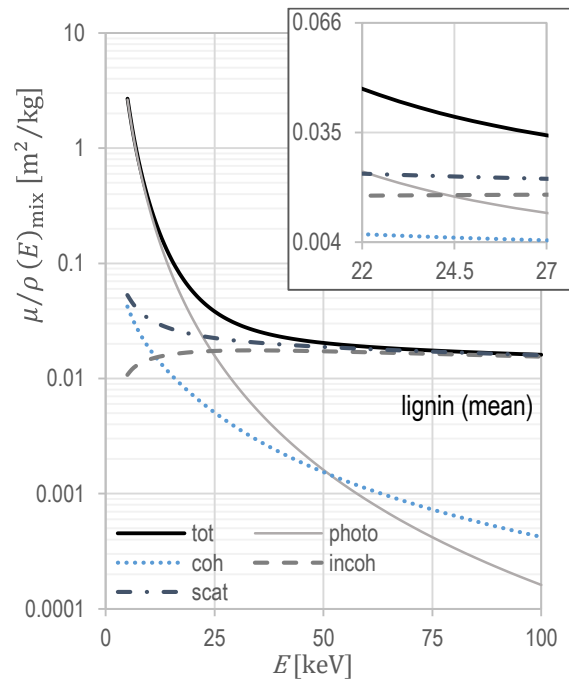
Figure VII-48: Total mean mass attenuation coefficient $\mu/\rho\,(E)_{\mathrm{mix}}$ of lignin (mean) over radiation energy E incl. attenuation processes photoelectric absorption, coherent and incoherent scattering, as well as scattering (scat = coh + incoh) determined like corresponding data in Table VII-22.

Hydrogen $_1$H

Energy			$\frac{\mu_i}{\rho}(E)$ [m²/kg]			$\xi(i)$ [−]			
E [keV]	total	photo	coh	incoh	scat	photo	coh	incoh	scat
5	0.0419	0.0029	0.0080	0.0310	0.0390	0.07	0.19	0.74	0.93
6	0.0404	0.0016	0.0060	0.0329	0.0388	0.04	0.15	0.81	0.96
7	0.0396	0.0009	0.0046	0.0341	0.0387	0.02	0.12	0.86	0.98
8	0.0391	0.0006	0.0037	0.0349	0.0386	0.01	0.09	0.89	0.98
9	0.0388	0.0004	0.0030	0.0354	0.0384	0.01	0.08	0.91	0.99
10	0.0385	0.0003	0.0025	0.0358	0.0383	0.01	0.06	0.93	0.99
11	0.0383	0.0002	0.0021	0.0361	0.0381	0.01	0.05	0.94	0.99
12	0.0381	0.0001	0.0018	0.0362	0.0380	0.00	0.05	0.95	1.00
12.7	**0.0380**	**0.0001**	**0.0016**	**0.0363**	**0.0379**	**0.00**	**0.04**	**0.96**	**1.00**
13	0.0380	0.0001	0.0015	0.0363	0.0379	0.00	0.04	0.96	1.00
14	0.0378	0.0001	0.0013	0.0364	0.0377	0.00	0.04	0.96	1.00
15	0.0376	0.0001	0.0012	0.0364	0.0376	0.00	0.03	0.97	1.00
15.5	**0.0376**	**0.0001**	**0.0011**	**0.0364**	**0.0375**	**0.00**	**0.03**	**0.97**	**1.00**
16	0.0375	0.0001	0.0010	0.0364	0.0374	0.00	0.03	0.97	1.00
16.9	**0.0374**	**0.0000**	**0.0009**	**0.0364**	**0.0373**	**0.00**	**0.02**	**0.97**	**1.00**
17	0.0374	0.0000	0.0009	0.0364	0.0373	0.00	0.02	0.97	1.00
18	0.0372	0.0000	0.0008	0.0364	0.0372	0.00	0.02	0.98	1.00
19	0.0371	0.0000	0.0007	0.0363	0.0370	0.00	0.02	0.98	1.00
20	0.0370	0.0000	0.0007	0.0363	0.0369	0.00	0.02	0.98	1.00
21	0.0368	0.0000	0.0006	0.0362	0.0368	0.00	0.02	0.98	1.00
21.1	**0.0368**	**0.0000**	**0.0006**	**0.0362**	**0.0368**	**0.00**	**0.02**	**0.98**	**1.00**
21.2	**0.0368**	**0.0000**	**0.0006**	**0.0362**	**0.0368**	**0.00**	**0.02**	**0.98**	**1.00**
21.5	**0.0368**	**0.0000**	**0.0006**	**0.0362**	**0.0367**	**0.00**	**0.02**	**0.98**	**1.00**
22	0.0367	0.0000	0.0006	0.0361	0.0367	0.00	0.02	0.98	1.00
23	0.0366	0.0000	0.0005	0.0360	0.0365	0.00	0.01	0.99	1.00
24	0.0364	0.0000	0.0005	0.0360	0.0364	0.00	0.01	0.99	1.00
24.2	**0.0364**	**0.0000**	**0.0005**	**0.0359**	**0.0364**	**0.00**	**0.01**	**0.99**	**1.00**
25	0.0363	0.0000	0.0004	0.0359	0.0363	0.00	0.01	0.99	1.00
26	0.0362	0.0000	0.0004	0.0358	0.0362	0.00	0.01	0.99	1.00
26.3	**0.0362**	**0.0000**	**0.0004**	**0.0358**	**0.0361**	**0.00**	**0.01**	**0.99**	**1.00**
27	0.0361	0.0000	0.0004	0.0357	0.0361	0.00	0.01	0.99	1.00
27.3	**0.0360**	**0.0000**	**0.0004**	**0.0357**	**0.0360**	**0.00**	**0.01**	**0.99**	**1.00**
28	0.0359	0.0000	0.0003	0.0356	0.0359	0.00	0.01	0.99	1.00
29	0.0358	0.0000	0.0003	0.0355	0.0358	0.00	0.01	0.99	1.00
29.2	**0.0358**	**0.0000**	**0.0003**	**0.0355**	**0.0358**	**0.00**	**0.01**	**0.99**	**1.00**
30	0.0357	0.0000	0.0003	0.0354	0.0357	0.00	0.01	0.99	1.00
31	0.0356	0.0000	0.0003	0.0353	0.0356	0.00	0.01	0.99	1.00
32	0.0355	0.0000	0.0003	0.0352	0.0355	0.00	0.01	0.99	1.00
33	0.0354	0.0000	0.0003	0.0351	0.0354	0.00	0.01	0.99	1.00
34	0.0352	0.0000	0.0002	0.0350	0.0352	0.00	0.01	0.99	1.00
35	0.0351	0.0000	0.0002	0.0349	0.0351	0.00	0.01	0.99	1.00
35.1	**0.0351**	**0.0000**	**0.0002**	**0.0349**	**0.0351**	**0.00**	**0.01**	**0.99**	**1.00**
35.4	**0.0351**	**0.0000**	**0.0002**	**0.0349**	**0.0351**	**0.00**	**0.01**	**0.99**	**1.00**

Hydrogen $_1$H

Energy	$\frac{\mu_i}{\rho}(E)$ [m^2/kg]					$\xi(i)$ [−]			
E [keV]	total	photo	coh	incoh	scat	photo	coh	incoh	scat
36	0.0350	0.0000	0.0002	0.0348	0.0350	0.00	0.01	0.99	1.00
37	0.0349	0.0000	0.0002	0.0347	0.0349	0.00	0.01	0.99	1.00
38	0.0348	0.0000	0.0002	0.0346	0.0348	0.00	0.01	0.99	1.00
39	0.0347	0.0000	0.0002	0.0345	0.0347	0.00	0.01	0.99	1.00
40	0.0346	0.0000	0.0002	0.0344	0.0346	0.00	0.00	1.00	1.00
41	0.0345	0.0000	0.0002	0.0343	0.0345	0.00	0.00	1.00	1.00
42	0.0344	0.0000	0.0002	0.0342	0.0344	0.00	0.00	1.00	1.00
43	0.0343	0.0000	0.0001	0.0341	0.0343	0.00	0.00	1.00	1.00
44	0.0342	0.0000	0.0001	0.0340	0.0342	0.00	0.00	1.00	1.00
45	0.0341	0.0000	0.0001	0.0339	0.0341	0.00	0.00	1.00	1.00
46	0.0340	0.0000	0.0001	0.0338	0.0339	0.00	0.00	1.00	1.00
47	0.0339	0.0000	0.0001	0.0337	0.0339	0.00	0.00	1.00	1.00
48	0.0338	0.0000	0.0001	0.0336	0.0337	0.00	0.00	1.00	1.00
49	0.0337	0.0000	0.0001	0.0335	0.0336	0.00	0.00	1.00	1.00
50	0.0336	0.0000	0.0001	0.0334	0.0335	0.00	0.00	1.00	1.00
50.9	**0.0335**	**0.0000**	**0.0001**	**0.0334**	**0.0335**	**0.00**	**0.00**	**1.00**	**1.00**
51	0.0335	0.0000	0.0001	0.0334	0.0335	0.00	0.00	1.00	1.00
51.3	**0.0334**	**0.0000**	**0.0001**	**0.0333**	**0.0334**	**0.00**	**0.00**	**1.00**	**1.00**
52	0.0334	0.0000	0.0001	0.0333	0.0334	0.00	0.00	1.00	1.00
53	0.0333	0.0000	0.0001	0.0332	0.0333	0.00	0.00	1.00	1.00
54	0.0332	0.0000	0.0001	0.0331	0.0332	0.00	0.00	1.00	1.00
55	0.0331	0.0000	0.0001	0.0330	0.0331	0.00	0.00	1.00	1.00
56	0.0330	0.0000	0.0001	0.0329	0.0330	0.00	0.00	1.00	1.00
57	0.0329	0.0000	0.0001	0.0328	0.0329	0.00	0.00	1.00	1.00
58	0.0328	0.0000	0.0001	0.0327	0.0328	0.00	0.00	1.00	1.00
59	0.0327	0.0000	0.0001	0.0326	0.0327	0.00	0.00	1.00	1.00
59.5	**0.0327**	**0.0000**	**0.0001**	**0.0326**	**0.0326**	**0.00**	**0.00**	**1.00**	**1.00**
60	0.0326	0.0000	0.0001	0.0325	0.0326	0.00	0.00	1.00	1.00
65	0.0322	0.0000	0.0001	0.0321	0.0322	0.00	0.00	1.00	1.00
70	0.0317	0.0000	0.0001	0.0317	0.0317	0.00	0.00	1.00	1.00
75	0.0313	0.0000	0.0000	0.0313	0.0313	0.00	0.00	1.00	1.00
80	0.0309	0.0000	0.0000	0.0309	0.0309	0.00	0.00	1.00	1.00
85	0.0305	0.0000	0.0000	0.0305	0.0305	0.00	0.00	1.00	1.00
90	0.0302	0.0000	0.0000	0.0301	0.0301	0.00	0.00	1.00	1.00
95	0.0298	0.0000	0.0000	0.0298	0.0298	0.00	0.00	1.00	1.00
100	0.0294	0.0000	0.0000	0.0294	0.0294	0.00	0.00	1.00	1.00

Table VII-3: Total mass attenuation coefficients $\mu/\rho\,(E)_i$ of the element hydrogen $_1$H as sum of the single coefficients following eq. (II-14) for the attenuation processes photoelectric absorption (photo), coherent scattering (coh), and incoherent scattering (incoh) as well as scattering coefficient (scat = coh + incoh) for a practice-oriented energy range (incl. particular device energies, bold, refer to Table VII-2) determined via XCOM (2010), complete with the attenuation fractions $\xi(i)$ following eq. (II-15) of the single mechanisms.

Carbon $_6$**C**

Energy						$\frac{\mu_i}{\rho}(E)$ [m^2/kg]			$\xi(i)$ [$-$]
E [keV]	total	photo	coh	incoh	scat	photo	coh	incoh	scat
5	1.9120	1.8660	0.0360	0.0099	0.0459	0.98	0.02	0.01	0.02
6	1.0950	1.0540	0.0292	0.0110	0.0402	0.96	0.03	0.01	0.04
7	0.6846	0.6483	0.0244	0.0119	0.0363	0.95	0.04	0.02	0.05
8	0.4576	0.4241	0.0210	0.0125	0.0335	0.93	0.05	0.03	0.07
9	0.3225	0.2911	0.0183	0.0131	0.0314	0.90	0.06	0.04	0.10
10	0.2373	0.2076	0.0162	0.0135	0.0297	0.87	0.07	0.06	0.13
11	0.1811	0.1527	0.0145	0.0139	0.0284	0.84	0.08	0.08	0.16
12	0.1426	0.1153	0.0130	0.0143	0.0273	0.81	0.09	0.10	0.19
12.7	**0.1226**	**0.0960**	**0.0122**	**0.0145**	**0.0267**	**0.78**	**0.10**	**0.12**	**0.22**
13	0.1153	0.0890	0.0118	0.0146	0.0264	0.77	0.10	0.13	0.23
14	0.0955	0.0699	0.0107	0.0149	0.0256	0.73	0.11	0.16	0.27
15	0.0807	0.0559	0.0098	0.0151	0.0249	0.69	0.12	0.19	0.31
15.5	**0.0748**	**0.0502**	**0.0094**	**0.0152**	**0.0246**	**0.67**	**0.13**	**0.20**	**0.33**
16	0.0695	0.0452	0.0090	0.0153	0.0243	0.65	0.13	0.22	0.35
16.9	**0.0616**	**0.0378**	**0.0083**	**0.0155**	**0.0238**	**0.61**	**0.13**	**0.25**	**0.39**
17	0.0608	0.0371	0.0082	0.0155	0.0237	0.61	0.14	0.25	0.39
18	0.0540	0.0308	0.0076	0.0157	0.0233	0.57	0.14	0.29	0.43
19	0.0486	0.0258	0.0070	0.0158	0.0228	0.53	0.14	0.33	0.47
20	0.0442	0.0218	0.0065	0.0160	0.0224	0.49	0.15	0.36	0.51
21	0.0406	0.0185	0.0060	0.0161	0.0221	0.46	0.15	0.40	0.54
21.1	**0.0403**	**0.0183**	**0.0060**	**0.0161**	**0.0220**	**0.45**	**0.15**	**0.40**	**0.55**
21.2	**0.0400**	**0.0180**	**0.0059**	**0.0161**	**0.0220**	**0.45**	**0.15**	**0.40**	**0.55**
21.5	**0.0391**	**0.0172**	**0.0058**	**0.0161**	**0.0219**	**0.44**	**0.15**	**0.41**	**0.56**
22	0.0377	0.0159	0.0056	0.0162	0.0218	0.42	0.15	0.43	0.58
23	0.0352	0.0137	0.0052	0.0162	0.0215	0.39	0.15	0.46	0.61
24	0.0331	0.0119	0.0049	0.0163	0.0212	0.36	0.15	0.49	0.64
24.2	**0.0327**	**0.0116**	**0.0048**	**0.0163**	**0.0211**	**0.35**	**0.15**	**0.50**	**0.65**
25	0.0314	0.0104	0.0046	0.0164	0.0209	0.33	0.15	0.52	0.67
26	0.0299	0.0092	0.0043	0.0164	0.0207	0.31	0.14	0.55	0.69
26.3	**0.0295**	**0.0088**	**0.0042**	**0.0164**	**0.0206**	**0.30**	**0.14**	**0.56**	**0.70**
27	0.0286	0.0081	0.0040	0.0165	0.0205	0.28	0.14	0.58	0.72
27.3	**0.0282**	**0.0078**	**0.0039**	**0.0165**	**0.0204**	**0.28**	**0.14**	**0.58**	**0.72**
28	0.0275	0.0072	0.0038	0.0165	0.0203	0.26	0.14	0.60	0.74
29	0.0265	0.0064	0.0036	0.0165	0.0201	0.24	0.13	0.62	0.76
29.2	**0.0263**	**0.0062**	**0.0035**	**0.0165**	**0.0201**	**0.24**	**0.13**	**0.63**	**0.76**
30	0.0256	0.0057	0.0034	0.0166	0.0199	0.22	0.13	0.65	0.78
31	0.0249	0.0051	0.0032	0.0166	0.0197	0.21	0.13	0.67	0.79
32	0.0242	0.0046	0.0030	0.0166	0.0196	0.19	0.12	0.68	0.81
33	0.0236	0.0042	0.0029	0.0166	0.0194	0.18	0.12	0.70	0.82
34	0.0231	0.0038	0.0027	0.0166	0.0193	0.16	0.12	0.72	0.84
35	0.0226	0.0034	0.0026	0.0166	0.0192	0.15	0.11	0.73	0.85
35.1	**0.0225**	**0.0034**	**0.0026**	**0.0166**	**0.0192**	**0.15**	**0.11**	**0.74**	**0.85**
35.4	**0.0224**	**0.0033**	**0.0025**	**0.0166**	**0.0191**	**0.15**	**0.11**	**0.74**	**0.85**

Carbon $_6$C

Energy	$\frac{\mu_i}{\rho}(E)$ [m^2/kg]					$\xi(i)$ [−]			
E [keV]	total	photo	coh	incoh	scat	photo	coh	incoh	scat
36	0.0222	0.0031	0.0025	0.0166	0.0190	0.14	0.11	0.75	0.86
37	0.0218	0.0028	0.0023	0.0166	0.0189	0.13	0.11	0.76	0.87
38	0.0214	0.0026	0.0022	0.0166	0.0188	0.12	0.10	0.77	0.88
39	0.0211	0.0024	0.0021	0.0165	0.0187	0.11	0.10	0.79	0.89
40	0.0208	0.0022	0.0020	0.0165	0.0186	0.11	0.10	0.80	0.89
41	0.0205	0.0020	0.0020	0.0165	0.0185	0.10	0.10	0.81	0.90
42	0.0202	0.0019	0.0019	0.0165	0.0184	0.09	0.09	0.82	0.91
43	0.0200	0.0017	0.0018	0.0165	0.0183	0.09	0.09	0.82	0.91
44	0.0198	0.0016	0.0017	0.0165	0.0182	0.08	0.09	0.83	0.92
45	0.0196	0.0015	0.0017	0.0164	0.0181	0.08	0.08	0.84	0.92
46	0.0194	0.0014	0.0016	0.0164	0.0180	0.07	0.08	0.85	0.93
47	0.0192	0.0013	0.0015	0.0164	0.0179	0.07	0.08	0.85	0.93
48	0.0190	0.0012	0.0015	0.0164	0.0178	0.06	0.08	0.86	0.94
49	0.0189	0.0011	0.0014	0.0163	0.0177	0.06	0.08	0.87	0.94
50	0.0187	0.0010	0.0014	0.0163	0.0177	0.06	0.07	0.87	0.94
50.9	**0.0186**	**0.0010**	**0.0013**	**0.0163**	**0.0176**	**0.05**	**0.07**	**0.88**	**0.95**
51	0.0186	0.0010	0.0013	0.0163	0.0176	0.05	0.07	0.88	0.95
51.3	**0.0185**	**0.0010**	**0.0013**	**0.0163**	**0.0176**	**0.05**	**0.07**	**0.88**	**0.95**
52	0.0184	0.0009	0.0013	0.0162	0.0175	0.05	0.07	0.88	0.95
53	0.0183	0.0009	0.0012	0.0162	0.0174	0.05	0.07	0.89	0.95
54	0.0182	0.0008	0.0012	0.0162	0.0174	0.04	0.07	0.89	0.96
55	0.0181	0.0008	0.0012	0.0161	0.0173	0.04	0.06	0.89	0.96
56	0.0179	0.0007	0.0011	0.0161	0.0172	0.04	0.06	0.90	0.96
57	0.0178	0.0007	0.0011	0.0161	0.0172	0.04	0.06	0.90	0.96
58	0.0177	0.0006	0.0010	0.0161	0.0171	0.04	0.06	0.91	0.96
59	0.0176	0.0006	0.0010	0.0160	0.0170	0.03	0.06	0.91	0.97
59.5	**0.0176**	**0.0006**	**0.0010**	**0.0160**	**0.0170**	**0.03**	**0.06**	**0.91**	**0.97**
60	0.0175	0.0006	0.0010	0.0160	0.0170	0.03	0.06	0.91	0.97
65	0.0171	0.0004	0.0008	0.0158	0.0167	0.03	0.05	0.93	0.97
70	0.0167	0.0003	0.0007	0.0157	0.0164	0.02	0.04	0.94	0.98
75	0.0164	0.0003	0.0006	0.0155	0.0161	0.02	0.04	0.94	0.98
80	0.0161	0.0002	0.0006	0.0153	0.0159	0.01	0.04	0.95	0.99
85	0.0158	0.0002	0.0005	0.0152	0.0157	0.01	0.03	0.96	0.99
90	0.0156	0.0001	0.0005	0.0150	0.0154	0.01	0.03	0.96	0.99
95	0.0154	0.0001	0.0004	0.0148	0.0152	0.01	0.03	0.97	0.99
100	0.0151	0.0001	0.0004	0.0147	0.0150	0.01	0.02	0.97	0.99

Table VII-4: Total mass attenuation coefficients $\mu/\rho\,(E)_i$ of the element carbon $_6$C as sum of the single coefficients following eq. (II-14) for the attenuation processes photoelectric absorption (photo), coherent scattering (coh), and incoherent scattering (incoh) as well as scattering coefficient (scat = coh + incoh) for a practice-oriented energy range (incl. particular device energies, bold, refer to Table VII-2) determined via XCOM (2010), complete with the attenuation fractions $\xi(i)$ following eq. (II-15) of the single mechanisms.

Nitrogen $_7$N

E [keV]	$\frac{\mu_i}{\rho}(E)$ [m^2/kg]					$\xi(i)$ [−]			
	total	photo	coh	incoh	scat	photo	coh	incoh	scat
5	3.1440	3.0870	0.0477	0.0096	0.0573	0.98	0.02	0.00	0.02
6	1.8080	1.7590	0.0384	0.0107	0.0491	0.97	0.02	0.01	0.03
7	1.1320	1.0890	0.0317	0.0116	0.0433	0.96	0.03	0.01	0.04
8	0.7559	0.7167	0.0269	0.0123	0.0391	0.95	0.04	0.02	0.05
9	0.5306	0.4946	0.0232	0.0128	0.0360	0.93	0.04	0.02	0.07
10	0.3879	0.3543	0.0203	0.0133	0.0336	0.91	0.05	0.03	0.09
11	0.2934	0.2617	0.0180	0.0137	0.0317	0.89	0.06	0.05	0.11
12	0.2283	0.1982	0.0161	0.0140	0.0302	0.87	0.07	0.06	0.13
12.7	**0.1945**	**0.1653**	**0.0150**	**0.0143**	**0.0293**	**0.85**	**0.08**	**0.07**	**0.15**
13	0.1822	0.1533	0.0146	0.0143	0.0289	0.84	0.08	0.08	0.16
14	0.1486	0.1208	0.0132	0.0146	0.0278	0.81	0.09	0.10	0.19
15	0.1236	0.0967	0.0121	0.0148	0.0269	0.78	0.10	0.12	0.22
15.5	**0.1135**	**0.0870**	**0.0115**	**0.0149**	**0.0265**	**0.77**	**0.10**	**0.13**	**0.23**
16	0.1046	0.0785	0.0111	0.0150	0.0261	0.75	0.11	0.14	0.25
16.9	**0.0912**	**0.0658**	**0.0102**	**0.0152**	**0.0255**	**0.72**	**0.11**	**0.17**	**0.28**
17	0.0899	0.0646	0.0102	0.0152	0.0254	0.72	0.11	0.17	0.28
18	0.0784	0.0536	0.0094	0.0154	0.0248	0.68	0.12	0.20	0.32
19	0.0692	0.0450	0.0087	0.0155	0.0242	0.65	0.13	0.22	0.35
20	0.0618	0.0381	0.0080	0.0157	0.0237	0.62	0.13	0.25	0.38
21	0.0557	0.0325	0.0075	0.0158	0.0233	0.58	0.13	0.28	0.42
21.1	**0.0552**	**0.0320**	**0.0074**	**0.0158**	**0.0232**	**0.58**	**0.13**	**0.29**	**0.42**
21.2	**0.0547**	**0.0315**	**0.0074**	**0.0158**	**0.0232**	**0.58**	**0.13**	**0.29**	**0.42**
21.5	**0.0531**	**0.0301**	**0.0072**	**0.0158**	**0.0231**	**0.57**	**0.14**	**0.30**	**0.43**
22	0.0508	0.0279	0.0070	0.0159	0.0229	0.55	0.14	0.31	0.45
23	0.0466	0.0241	0.0065	0.0160	0.0225	0.52	0.14	0.34	0.48
24	0.0431	0.0210	0.0061	0.0161	0.0221	0.49	0.14	0.37	0.51
24.2	**0.0425**	**0.0204**	**0.0060**	**0.0161**	**0.0221**	**0.48**	**0.14**	**0.38**	**0.52**
25	0.0402	0.0184	0.0057	0.0161	0.0218	0.46	0.14	0.40	0.54
26	0.0377	0.0162	0.0054	0.0162	0.0215	0.43	0.14	0.43	0.57
26.3	**0.0370**	**0.0156**	**0.0053**	**0.0162**	**0.0215**	**0.42**	**0.14**	**0.44**	**0.58**
27	0.0355	0.0143	0.0050	0.0162	0.0213	0.40	0.14	0.46	0.60
27.3	**0.0350**	**0.0138**	**0.0049**	**0.0162**	**0.0212**	**0.39**	**0.14**	**0.46**	**0.61**
28	0.0337	0.0127	0.0047	0.0163	0.0210	0.38	0.14	0.48	0.62
29	0.0321	0.0113	0.0045	0.0163	0.0208	0.35	0.14	0.51	0.65
29.2	**0.0318**	**0.0110**	**0.0044**	**0.0163**	**0.0207**	**0.35**	**0.14**	**0.51**	**0.65**
30	0.0307	0.0101	0.0042	0.0163	0.0206	0.33	0.14	0.53	0.67
31	0.0294	0.0091	0.0040	0.0164	0.0204	0.31	0.14	0.56	0.69
32	0.0283	0.0082	0.0038	0.0164	0.0202	0.29	0.13	0.58	0.71
33	0.0274	0.0074	0.0036	0.0164	0.0200	0.27	0.13	0.60	0.73
34	0.0265	0.0067	0.0034	0.0164	0.0198	0.25	0.13	0.62	0.75
35	0.0257	0.0061	0.0033	0.0164	0.0197	0.24	0.13	0.64	0.76
35.1	**0.0257**	**0.0060**	**0.0032**	**0.0164**	**0.0197**	**0.23**	**0.13**	**0.64**	**0.77**
35.4	**0.0255**	**0.0059**	**0.0032**	**0.0164**	**0.0196**	**0.23**	**0.13**	**0.64**	**0.77**

Nitrogen $_7$N

Energy				$\frac{\mu_i}{\rho}(E)$ [m^2/kg]				$\xi(i)$ [$-$]
E [keV]	total	photo	coh	incoh	scat	photo	coh	incoh	scat
36	0.0251	0.0055	0.0031	0.0164	0.0195	0.22	0.12	0.66	0.78
37	0.0244	0.0051	0.0030	0.0164	0.0194	0.21	0.12	0.67	0.79
38	0.0239	0.0046	0.0028	0.0164	0.0192	0.19	0.12	0.69	0.81
39	0.0233	0.0042	0.0027	0.0164	0.0191	0.18	0.12	0.70	0.82
40	0.0229	0.0039	0.0026	0.0164	0.0190	0.17	0.11	0.72	0.83
41	0.0225	0.0036	0.0025	0.0164	0.0188	0.16	0.11	0.73	0.84
42	0.0221	0.0033	0.0024	0.0164	0.0187	0.15	0.11	0.74	0.85
43	0.0217	0.0031	0.0023	0.0163	0.0186	0.14	0.10	0.75	0.86
44	0.0214	0.0029	0.0022	0.0163	0.0185	0.13	0.10	0.76	0.87
45	0.0211	0.0026	0.0021	0.0163	0.0184	0.13	0.10	0.77	0.87
46	0.0208	0.0025	0.0020	0.0163	0.0183	0.12	0.10	0.78	0.88
47	0.0205	0.0023	0.0019	0.0163	0.0182	0.11	0.09	0.79	0.89
48	0.0203	0.0021	0.0019	0.0162	0.0181	0.11	0.09	0.80	0.89
49	0.0200	0.0020	0.0018	0.0162	0.0180	0.10	0.09	0.81	0.90
50	0.0198	0.0019	0.0017	0.0162	0.0179	0.09	0.09	0.82	0.91
50.9	**0.0196**	**0.0018**	**0.0017**	**0.0162**	**0.0179**	**0.09**	**0.09**	**0.82**	**0.91**
51	0.0196	0.0017	0.0017	0.0162	0.0178	0.09	0.09	0.83	0.91
51.3	**0.0195**	**0.0017**	**0.0017**	**0.0162**	**0.0178**	**0.09**	**0.08**	**0.83**	**0.91**
52	0.0194	0.0016	0.0016	0.0161	0.0178	0.08	0.08	0.83	0.92
53	0.0192	0.0015	0.0016	0.0161	0.0177	0.08	0.08	0.84	0.92
54	0.0190	0.0014	0.0015	0.0161	0.0176	0.08	0.08	0.84	0.92
55	0.0189	0.0014	0.0015	0.0161	0.0175	0.07	0.08	0.85	0.93
56	0.0187	0.0013	0.0014	0.0160	0.0174	0.07	0.08	0.86	0.93
57	0.0186	0.0012	0.0014	0.0160	0.0174	0.07	0.07	0.86	0.93
58	0.0184	0.0011	0.0013	0.0160	0.0173	0.06	0.07	0.87	0.94
59	0.0183	0.0011	0.0013	0.0159	0.0172	0.06	0.07	0.87	0.94
59.5	**0.0182**	**0.0010**	**0.0013**	**0.0159**	**0.0172**	**0.06**	**0.07**	**0.87**	**0.94**
60	0.0182	0.0010	0.0012	0.0159	0.0172	0.06	0.07	0.88	0.94
65	0.0176	0.0008	0.0011	0.0158	0.0168	0.04	0.06	0.89	0.96
70	0.0171	0.0006	0.0009	0.0156	0.0165	0.04	0.05	0.91	0.96
75	0.0167	0.0005	0.0008	0.0154	0.0163	0.03	0.05	0.92	0.97
80	0.0164	0.0004	0.0007	0.0153	0.0160	0.02	0.04	0.93	0.98
85	0.0161	0.0003	0.0007	0.0151	0.0158	0.02	0.04	0.94	0.98
90	0.0158	0.0003	0.0006	0.0149	0.0155	0.02	0.04	0.95	0.98
95	0.0155	0.0002	0.0005	0.0148	0.0153	0.01	0.03	0.95	0.99
100	0.0153	0.0002	0.0005	0.0146	0.0151	0.01	0.03	0.96	0.99

Table VII-5: Total mass attenuation coefficients $\mu/\rho\,(E)_i$ of the element nitrogen $_7$N as sum of the single coefficients following eq. (II-14) for the attenuation processes photoelectric absorption (photo), coherent scattering (coh), and incoherent scattering (incoh) as well as scattering coefficient (scat = coh + incoh) for a practice-oriented energy range (incl. particular device energies, bold, refer to Table VII-2) determined via XCOM (2010), complete with the attenuation fractions $\xi(i)$ following eq. (II-15) of the single mechanisms.

Oxygen $_8$O

Energy								
			$\frac{\mu_i}{\rho}(E)$ [m^2/kg]					$\xi(i)$ [$-$]
E [keV]	total	photo	coh	incoh	scat	photo	coh	incoh	scat
5	4.7910	4.7200	0.0618	0.0087	0.0705	0.99	0.01	0.00	0.01
6	2.7700	2.7100	0.0498	0.0100	0.0598	0.98	0.02	0.00	0.02
7	1.7400	1.6880	0.0410	0.0110	0.0520	0.97	0.02	0.01	0.03
8	1.1630	1.1170	0.0345	0.0118	0.0463	0.96	0.03	0.01	0.04
9	0.8160	0.7741	0.0295	0.0124	0.0419	0.95	0.04	0.02	0.05
10	0.5953	0.5567	0.0257	0.0129	0.0386	0.94	0.04	0.02	0.06
11	0.4485	0.4125	0.0226	0.0134	0.0360	0.92	0.05	0.03	0.08
12	0.3472	0.3134	0.0201	0.0137	0.0338	0.90	0.06	0.04	0.10
12.7	**0.2944**	**0.2619**	**0.0186**	**0.0140**	**0.0326**	**0.89**	**0.06**	**0.05**	**0.11**
13	0.2753	0.2432	0.0181	0.0140	0.0321	0.88	0.07	0.05	0.12
14	0.2227	0.1921	0.0163	0.0143	0.0306	0.86	0.07	0.06	0.14
15	0.1836	0.1542	0.0149	0.0145	0.0294	0.84	0.08	0.08	0.16
15.5	**0.1677**	**0.1388**	**0.0142**	**0.0147**	**0.0289**	**0.83**	**0.08**	**0.09**	**0.17**
16	0.1538	0.1254	0.0136	0.0148	0.0284	0.82	0.09	0.10	0.18
16.9	**0.1328**	**0.1053**	**0.0126**	**0.0149**	**0.0275**	**0.79**	**0.09**	**0.11**	**0.21**
17	0.1307	0.1033	0.0125	0.0150	0.0274	0.79	0.10	0.11	0.21
18	0.1126	0.0860	0.0115	0.0151	0.0266	0.76	0.10	0.13	0.24
19	0.0982	0.0723	0.0107	0.0153	0.0259	0.74	0.11	0.16	0.26
20	0.0865	0.0612	0.0099	0.0154	0.0253	0.71	0.11	0.18	0.29
21	0.0770	0.0523	0.0092	0.0155	0.0247	0.68	0.12	0.20	0.32
21.1	**0.0762**	**0.0515**	**0.0091**	**0.0155**	**0.0247**	**0.68**	**0.12**	**0.20**	**0.32**
21.2	**0.0754**	**0.0507**	**0.0091**	**0.0155**	**0.0246**	**0.67**	**0.12**	**0.21**	**0.33**
21.5	**0.0729**	**0.0485**	**0.0089**	**0.0156**	**0.0245**	**0.66**	**0.12**	**0.21**	**0.34**
22	0.0692	0.0450	0.0086	0.0156	0.0242	0.65	0.12	0.23	0.35
23	0.0627	0.0390	0.0080	0.0157	0.0237	0.62	0.13	0.25	0.38
24	0.0573	0.0339	0.0075	0.0158	0.0233	0.59	0.13	0.28	0.41
24.2	**0.0563**	**0.0330**	**0.0074**	**0.0158**	**0.0232**	**0.59**	**0.13**	**0.28**	**0.41**
25	0.0527	0.0297	0.0070	0.0159	0.0229	0.56	0.13	0.30	0.44
26	0.0487	0.0262	0.0066	0.0160	0.0226	0.54	0.14	0.33	0.46
26.3	**0.0477**	**0.0252**	**0.0065**	**0.0160**	**0.0225**	**0.53**	**0.14**	**0.34**	**0.47**
27	0.0454	0.0231	0.0062	0.0160	0.0222	0.51	0.14	0.35	0.49
27.3	**0.0445**	**0.0223**	**0.0061**	**0.0160**	**0.0221**	**0.50**	**0.14**	**0.36**	**0.50**
28	0.0425	0.0206	0.0059	0.0161	0.0219	0.48	0.14	0.38	0.52
29	0.0400	0.0183	0.0055	0.0161	0.0216	0.46	0.14	0.40	0.54
29.2	**0.0395**	**0.0179**	**0.0055**	**0.0161**	**0.0216**	**0.45**	**0.14**	**0.41**	**0.55**
30	0.0378	0.0164	0.0052	0.0161	0.0214	0.43	0.14	0.43	0.57
31	0.0359	0.0147	0.0050	0.0162	0.0211	0.41	0.14	0.45	0.59
32	0.0342	0.0133	0.0047	0.0162	0.0209	0.39	0.14	0.47	0.61
33	0.0327	0.0120	0.0045	0.0162	0.0207	0.37	0.14	0.50	0.63
34	0.0314	0.0109	0.0043	0.0162	0.0205	0.35	0.14	0.52	0.65
35	0.0302	0.0099	0.0040	0.0162	0.0203	0.33	0.13	0.54	0.67
35.1	**0.0301**	**0.0098**	**0.0040**	**0.0162**	**0.0203**	**0.33**	**0.13**	**0.54**	**0.67**
35.4	**0.0298**	**0.0095**	**0.0040**	**0.0162**	**0.0202**	**0.32**	**0.13**	**0.55**	**0.68**

continued from page 372

Oxygen $_8$O

Energy	$\frac{\mu_i}{\rho}(E)$ [m²/kg]					$\xi(i)$ [−]			
E [keV]	total	photo	coh	incoh	scat	photo	coh	incoh	scat
36	0.0291	0.0090	0.0039	0.0162	0.0201	0.31	0.13	0.56	0.69
37	0.0282	0.0083	0.0037	0.0163	0.0199	0.29	0.13	0.58	0.71
38	0.0273	0.0076	0.0035	0.0163	0.0198	0.28	0.13	0.59	0.72
39	0.0266	0.0070	0.0034	0.0163	0.0196	0.26	0.13	0.61	0.74
40	0.0259	0.0064	0.0032	0.0162	0.0195	0.25	0.12	0.63	0.75
41	0.0252	0.0059	0.0031	0.0162	0.0193	0.23	0.12	0.64	0.77
42	0.0246	0.0054	0.0030	0.0162	0.0192	0.22	0.12	0.66	0.78
43	0.0241	0.0050	0.0028	0.0162	0.0190	0.21	0.12	0.67	0.79
44	0.0236	0.0047	0.0027	0.0162	0.0189	0.20	0.12	0.69	0.80
45	0.0231	0.0043	0.0026	0.0162	0.0188	0.19	0.11	0.70	0.81
46	0.0227	0.0040	0.0025	0.0162	0.0187	0.18	0.11	0.71	0.82
47	0.0223	0.0038	0.0024	0.0162	0.0186	0.17	0.11	0.72	0.83
48	0.0220	0.0035	0.0023	0.0161	0.0185	0.16	0.11	0.73	0.84
49	0.0216	0.0033	0.0022	0.0161	0.0184	0.15	0.10	0.74	0.85
50	0.0213	0.0031	0.0022	0.0161	0.0183	0.14	0.10	0.75	0.86
50.9	**0.0211**	**0.0029**	**0.0021**	**0.0161**	**0.0182**	**0.14**	**0.10**	**0.76**	**0.86**
51	0.0210	0.0029	0.0021	0.0161	0.0182	0.14	0.10	0.76	0.86
51.3	**0.0210**	**0.0028**	**0.0021**	**0.0161**	**0.0181**	**0.13**	**0.10**	**0.77**	**0.87**
52	0.0208	0.0027	0.0020	0.0161	0.0181	0.13	0.10	0.77	0.87
53	0.0205	0.0025	0.0020	0.0160	0.0180	0.12	0.10	0.78	0.88
54	0.0203	0.0024	0.0019	0.0160	0.0179	0.12	0.09	0.79	0.88
55	0.0200	0.0022	0.0018	0.0160	0.0178	0.11	0.09	0.80	0.89
56	0.0198	0.0021	0.0018	0.0160	0.0177	0.11	0.09	0.80	0.89
57	0.0196	0.0020	0.0017	0.0159	0.0176	0.10	0.09	0.81	0.90
58	0.0194	0.0019	0.0017	0.0159	0.0175	0.10	0.09	0.82	0.90
59	0.0193	0.0018	0.0016	0.0159	0.0175	0.09	0.08	0.82	0.91
59.5	**0.0192**	**0.0017**	**0.0016**	**0.0159**	**0.0174**	**0.09**	**0.08**	**0.83**	**0.91**
60	0.0191	0.0017	0.0016	0.0158	0.0174	0.09	0.08	0.83	0.91
65	0.0183	0.0013	0.0013	0.0157	0.0170	0.07	0.07	0.86	0.93
70	0.0177	0.0010	0.0012	0.0155	0.0167	0.06	0.07	0.88	0.94
75	0.0172	0.0008	0.0010	0.0154	0.0164	0.05	0.06	0.89	0.95
80	0.0168	0.0006	0.0009	0.0152	0.0161	0.04	0.05	0.91	0.96
85	0.0164	0.0005	0.0008	0.0151	0.0159	0.03	0.05	0.92	0.97
90	0.0161	0.0004	0.0007	0.0149	0.0156	0.03	0.05	0.93	0.97
95	0.0158	0.0004	0.0007	0.0148	0.0154	0.02	0.04	0.94	0.98
100	0.0155	0.0003	0.0006	0.0146	0.0152	0.02	0.04	0.94	0.98

Table VII-6: Total mass attenuation coefficients $\mu/\rho\,(E)_i$ of the element oxygen $_8$O as sum of the single coefficients following eq. (II-14) for the attenuation processes photoelectric absorption (photo), coherent scattering (coh), and incoherent scattering (incoh) as well as scattering coefficient (scat = coh + incoh) for a practice-oriented energy range (incl. particular device energies, bold, refer to Table VII-2) determined via XCOM (2010), complete with the attenuation fractions $\xi(i)$ following eq. (II-15) of the single mechanisms.

Aluminium $_{13}$Al

Energy				$\frac{\mu_i}{\rho}(E)$ [m²/kg]					$\xi(i)$ [−]
E [keV]	total	photo	coh	incoh	scat	photo	coh	incoh	scat
5	19.3400	19.2200	0.1116	0.0068	0.1184	0.99	0.01	0.00	0.01
6	11.5300	11.4300	0.0964	0.0077	0.1041	0.99	0.01	0.00	0.01
7	7.4080	7.3160	0.0834	0.0085	0.0919	0.99	0.01	0.00	0.01
8	5.0320	4.9500	0.0723	0.0093	0.0816	0.98	0.01	0.00	0.02
9	3.5690	3.4960	0.0630	0.0100	0.0729	0.98	0.02	0.00	0.02
10	2.6210	2.5560	0.0551	0.0106	0.0657	0.98	0.02	0.00	0.03
11	1.9810	1.9220	0.0486	0.0111	0.0597	0.97	0.02	0.01	0.03
12	1.5340	1.4790	0.0431	0.0116	0.0547	0.96	0.03	0.01	0.04
12.7	**1.2980**	**1.2460**	**0.0398**	**0.0119**	**0.0517**	**0.96**	**0.03**	**0.01**	**0.04**
13	1.2120	1.1610	0.0386	0.0120	0.0505	0.96	0.03	0.01	0.04
14	0.9744	0.9274	0.0347	0.0123	0.0470	0.95	0.04	0.01	0.05
15	0.7955	0.7515	0.0314	0.0127	0.0440	0.94	0.04	0.02	0.06
15.5	**0.7225**	**0.6798**	**0.0299**	**0.0128**	**0.0427**	**0.94**	**0.04**	**0.02**	**0.06**
16	0.6583	0.6168	0.0285	0.0129	0.0415	0.94	0.04	0.02	0.06
16.9	**0.5609**	**0.5214**	**0.0263**	**0.0131**	**0.0394**	**0.93**	**0.05**	**0.02**	**0.07**
17	0.5513	0.5121	0.0261	0.0132	0.0392	0.93	0.05	0.02	0.07
18	0.4667	0.4294	0.0240	0.0134	0.0373	0.92	0.05	0.03	0.08
19	0.3990	0.3634	0.0221	0.0136	0.0357	0.91	0.06	0.03	0.09
20	0.3442	0.3100	0.0205	0.0137	0.0342	0.90	0.06	0.04	0.10
21	0.2993	0.2665	0.0190	0.0139	0.0329	0.89	0.06	0.05	0.11
21.1	**0.2953**	**0.2626**	**0.0189**	**0.0139**	**0.0327**	**0.89**	**0.06**	**0.05**	**0.11**
21.2	**0.2913**	**0.2587**	**0.0187**	**0.0139**	**0.0326**	**0.89**	**0.06**	**0.05**	**0.11**
21.5	**0.2799**	**0.2477**	**0.0183**	**0.0139**	**0.0323**	**0.88**	**0.07**	**0.05**	**0.12**
22	0.2623	0.2306	0.0177	0.0140	0.0317	0.88	0.07	0.05	0.12
23	0.2314	0.2007	0.0166	0.0141	0.0307	0.87	0.07	0.06	0.13
24	0.2055	0.1758	0.0155	0.0142	0.0297	0.86	0.08	0.07	0.14
24.2	**0.2008**	**0.1713**	**0.0153**	**0.0142**	**0.0295**	**0.85**	**0.08**	**0.07**	**0.15**
25	0.1836	0.1547	0.0146	0.0143	0.0289	0.84	0.08	0.08	0.16
26	0.1649	0.1368	0.0137	0.0144	0.0281	0.83	0.08	0.09	0.17
26.3	**0.1598**	**0.1320**	**0.0135**	**0.0144**	**0.0279**	**0.83**	**0.08**	**0.09**	**0.17**
27	0.1489	0.1215	0.0129	0.0145	0.0274	0.82	0.09	0.10	0.18
27.3	**0.1446**	**0.1174**	**0.0127**	**0.0145**	**0.0272**	**0.81**	**0.09**	**0.10**	**0.19**
28	0.1351	0.1084	0.0122	0.0145	0.0267	0.80	0.09	0.11	0.20
29	0.1232	0.0971	0.0116	0.0146	0.0262	0.79	0.09	0.12	0.21
29.2	**0.1210**	**0.0950**	**0.0114**	**0.0146**	**0.0260**	**0.78**	**0.09**	**0.12**	**0.22**
30	0.1128	0.0872	0.0110	0.0146	0.0256	0.77	0.10	0.13	0.23
31	0.1037	0.0787	0.0104	0.0147	0.0251	0.76	0.10	0.14	0.24
32	0.0958	0.0711	0.0099	0.0147	0.0246	0.74	0.10	0.15	0.26
33	0.0887	0.0645	0.0094	0.0148	0.0242	0.73	0.11	0.17	0.27
34	0.0825	0.0587	0.0090	0.0148	0.0238	0.71	0.11	0.18	0.29
35	0.0770	0.0536	0.0086	0.0148	0.0234	0.70	0.11	0.19	0.30
35.1	**0.0764**	**0.0531**	**0.0085**	**0.0149**	**0.0234**	**0.69**	**0.11**	**0.19**	**0.31**
35.4	**0.0749**	**0.0517**	**0.0084**	**0.0149**	**0.0232**	**0.69**	**0.11**	**0.20**	**0.31**

Aluminium $_{13}$Al

Energy									$\xi(i)$ [−]
				$\frac{\mu_i}{\rho}(E)$ [m²/kg]					
E [keV]	total	photo	coh	incoh	scat	photo	coh	incoh	scat
36	0.0720	0.0490	0.0082	0.0149	0.0230	0.68	0.11	0.21	0.32
37	0.0676	0.0449	0.0078	0.0149	0.0227	0.66	0.12	0.22	0.34
38	0.0636	0.0413	0.0075	0.0149	0.0224	0.65	0.12	0.23	0.35
39	0.0601	0.0380	0.0072	0.0149	0.0221	0.63	0.12	0.25	0.37
40	0.0568	0.0350	0.0069	0.0149	0.0218	0.62	0.12	0.26	0.38
41	0.0539	0.0324	0.0066	0.0150	0.0215	0.60	0.12	0.28	0.40
42	0.0513	0.0300	0.0063	0.0150	0.0213	0.59	0.12	0.29	0.41
43	0.0489	0.0278	0.0061	0.0150	0.0210	0.57	0.12	0.31	0.43
44	0.0467	0.0259	0.0058	0.0150	0.0208	0.55	0.13	0.32	0.45
45	0.0447	0.0241	0.0056	0.0150	0.0206	0.54	0.13	0.34	0.46
46	0.0428	0.0224	0.0054	0.0150	0.0204	0.52	0.13	0.35	0.48
47	0.0411	0.0209	0.0052	0.0150	0.0202	0.51	0.13	0.36	0.49
48	0.0396	0.0196	0.0050	0.0150	0.0200	0.49	0.13	0.38	0.51
49	0.0381	0.0183	0.0048	0.0150	0.0198	0.48	0.13	0.39	0.52
50	0.0368	0.0172	0.0047	0.0150	0.0196	0.47	0.13	0.41	0.53
50.9	**0.0357**	**0.0162**	**0.0045**	**0.0150**	**0.0195**	**0.45**	**0.13**	**0.42**	**0.55**
51	0.0356	0.0161	0.0045	0.0150	0.0195	0.45	0.13	0.42	0.55
51.3	**0.0352**	**0.0158**	**0.0045**	**0.0150**	**0.0194**	**0.45**	**0.13**	**0.42**	**0.55**
52	0.0345	0.0152	0.0044	0.0149	0.0193	0.44	0.13	0.43	0.56
53	0.0334	0.0143	0.0042	0.0149	0.0192	0.43	0.13	0.45	0.57
54	0.0324	0.0134	0.0041	0.0149	0.0190	0.41	0.13	0.46	0.59
55	0.0315	0.0127	0.0040	0.0149	0.0189	0.40	0.13	0.47	0.60
56	0.0307	0.0119	0.0038	0.0149	0.0187	0.39	0.12	0.49	0.61
57	0.0299	0.0113	0.0037	0.0149	0.0186	0.38	0.12	0.50	0.62
58	0.0291	0.0107	0.0036	0.0149	0.0185	0.37	0.12	0.51	0.63
59	0.0284	0.0101	0.0035	0.0149	0.0183	0.36	0.12	0.52	0.65
59.5	**0.0281**	**0.0098**	**0.0034**	**0.0148**	**0.0183**	**0.35**	**0.12**	**0.53**	**0.65**
60	0.0278	0.0096	0.0034	0.0148	0.0182	0.34	0.12	0.53	0.66
65	0.0251	0.0074	0.0029	0.0147	0.0177	0.29	0.12	0.59	0.71
70	0.0230	0.0058	0.0026	0.0146	0.0172	0.25	0.11	0.64	0.75
75	0.0214	0.0047	0.0023	0.0145	0.0168	0.22	0.11	0.68	0.78
80	0.0202	0.0038	0.0020	0.0144	0.0164	0.19	0.10	0.71	0.81
85	0.0192	0.0031	0.0018	0.0143	0.0161	0.16	0.09	0.74	0.84
90	0.0183	0.0026	0.0016	0.0141	0.0158	0.14	0.09	0.77	0.86
95	0.0176	0.0022	0.0015	0.0140	0.0155	0.12	0.08	0.79	0.88
100	0.0170	0.0018	0.0013	0.0139	0.0152	0.11	0.08	0.81	0.89

Table VII-7: Total mass attenuation coefficients $\mu/\rho(E)_i$ of the element aluminium $_{13}$Al as sum of the single coefficients following eq. (II-14) for the attenuation processes photoelectric absorption (photo), coherent scattering (coh), and incoherent scattering (incoh) as well as scattering coefficient (scat = coh + incoh) for a practice-oriented energy range (incl. particular device energies, bold, refer to Table VII-2) determined via XCOM (2010), complete with the attenuation fractions $\xi(i)$ following eq. (II-15) of the single mechanisms.

Sulphur $_{16}$S

E [keV]	total	photo	coh	incoh	scat	photo	coh	incoh	scat
				$\frac{\mu_i}{\rho}(E)$ [m^2/kg]				$\xi(i)$ [−]	
5	34.8700	34.7300	0.1353	0.0071	0.1424	1.00	0.00	0.00	0.00
6	21.1600	21.0300	0.1172	0.0079	0.1251	0.99	0.01	0.00	0.01
7	13.7800	13.6700	0.1029	0.0087	0.1116	0.99	0.01	0.00	0.01
8	9.4640	9.3640	0.0911	0.0094	0.1004	0.99	0.01	0.00	0.01
9	6.7750	6.6840	0.0810	0.0100	0.0910	0.99	0.01	0.00	0.01
10	5.0130	4.9300	0.0723	0.0105	0.0828	0.98	0.01	0.00	0.02
11	3.8110	3.7350	0.0647	0.0110	0.0757	0.98	0.02	0.00	0.02
12	2.9640	2.8940	0.0581	0.0114	0.0695	0.98	0.02	0.00	0.02
12.7	**2.5150**	**2.4490**	**0.0540**	**0.0117**	**0.0657**	**0.97**	**0.02**	**0.00**	**0.03**
13	2.3500	2.2860	0.0523	0.0119	0.0642	0.97	0.02	0.01	0.03
14	1.8950	1.8350	0.0473	0.0122	0.0596	0.97	0.02	0.01	0.03
15	1.5500	1.4950	0.0430	0.0125	0.0556	0.96	0.03	0.01	0.04
15.5	**1.4090**	**1.3550**	**0.0411**	**0.0127**	**0.0537**	**0.96**	**0.03**	**0.01**	**0.04**
16	1.2840	1.2320	0.0392	0.0128	0.0521	0.96	0.03	0.01	0.04
16.9	**1.0950**	**1.0460**	**0.0362**	**0.0131**	**0.0493**	**0.96**	**0.03**	**0.01**	**0.05**
17	1.0760	1.0270	0.0359	0.0131	0.0490	0.95	0.03	0.01	0.05
18	0.9114	0.8650	0.0330	0.0133	0.0464	0.95	0.04	0.01	0.05
19	0.7787	0.7347	0.0305	0.0135	0.0440	0.94	0.04	0.02	0.06
20	0.6709	0.6290	0.0282	0.0137	0.0419	0.94	0.04	0.02	0.06
21	0.5824	0.5423	0.0262	0.0139	0.0401	0.93	0.04	0.02	0.07
21.1	**0.5744**	**0.5345**	**0.0260**	**0.0139**	**0.0399**	**0.93**	**0.05**	**0.02**	**0.07**
21.2	**0.5666**	**0.5269**	**0.0258**	**0.0139**	**0.0398**	**0.93**	**0.05**	**0.02**	**0.07**
21.5	**0.5441**	**0.5048**	**0.0253**	**0.0140**	**0.0393**	**0.93**	**0.05**	**0.03**	**0.07**
22	0.5091	0.4706	0.0244	0.0140	0.0385	0.92	0.05	0.03	0.08
23	0.4479	0.4109	0.0228	0.0142	0.0370	0.92	0.05	0.03	0.08
24	0.3964	0.3607	0.0214	0.0143	0.0357	0.91	0.05	0.04	0.09
24.2	**0.3870**	**0.3516**	**0.0211**	**0.0143**	**0.0354**	**0.91**	**0.05**	**0.04**	**0.09**
25	0.3527	0.3182	0.0201	0.0144	0.0345	0.90	0.06	0.04	0.10
26	0.3155	0.2821	0.0189	0.0145	0.0334	0.89	0.06	0.05	0.11
26.3	**0.3054**	**0.2723**	**0.0186**	**0.0145**	**0.0331**	**0.89**	**0.06**	**0.05**	**0.11**
27	0.2835	0.2511	0.0178	0.0146	0.0324	0.89	0.06	0.05	0.11
27.3	**0.2748**	**0.2427**	**0.0175**	**0.0146**	**0.0321**	**0.88**	**0.06**	**0.05**	**0.12**
28	0.2560	0.2245	0.0168	0.0147	0.0315	0.88	0.07	0.06	0.12
29	0.2321	0.2014	0.0159	0.0147	0.0307	0.87	0.07	0.06	0.13
29.2	**0.2277**	**0.1972**	**0.0158**	**0.0147**	**0.0305**	**0.87**	**0.07**	**0.06**	**0.13**
30	0.2113	0.1814	0.0151	0.0148	0.0299	0.86	0.07	0.07	0.14
31	0.1930	0.1638	0.0144	0.0148	0.0292	0.85	0.07	0.08	0.15
32	0.1770	0.1485	0.0137	0.0149	0.0286	0.84	0.08	0.08	0.16
33	0.1629	0.1349	0.0130	0.0149	0.0280	0.83	0.08	0.09	0.17
34	0.1504	0.1230	0.0124	0.0150	0.0274	0.82	0.08	0.10	0.18
35	0.1392	0.1124	0.0118	0.0150	0.0269	0.81	0.09	0.11	0.19
35.1	**0.1382**	**0.1114**	**0.0118**	**0.0150**	**0.0268**	**0.81**	**0.09**	**0.11**	**0.19**
35.4	**0.1351**	**0.1084**	**0.0116**	**0.0150**	**0.0267**	**0.80**	**0.09**	**0.11**	**0.20**

Sulphur $_{16}$S

Energy				$\frac{\mu_i}{\rho}(E)$ [m²/kg]				$\xi(i)$ [−]	
E [keV]	total	photo	coh	incoh	scat	photo	coh	incoh	scat
36	0.1293	0.1029	0.0113	0.0151	0.0264	0.80	0.09	0.12	0.20
37	0.1204	0.0945	0.0108	0.0151	0.0259	0.78	0.09	0.13	0.22
38	0.1124	0.0869	0.0104	0.0151	0.0255	0.77	0.09	0.13	0.23
39	0.1052	0.0801	0.0099	0.0151	0.0251	0.76	0.09	0.14	0.24
40	0.0987	0.0740	0.0095	0.0152	0.0247	0.75	0.10	0.15	0.25
41	0.0929	0.0685	0.0092	0.0152	0.0243	0.74	0.10	0.16	0.26
42	0.0875	0.0635	0.0088	0.0152	0.0240	0.73	0.10	0.17	0.27
43	0.0827	0.0590	0.0085	0.0152	0.0237	0.71	0.10	0.18	0.29
44	0.0783	0.0549	0.0082	0.0152	0.0234	0.70	0.10	0.19	0.30
45	0.0742	0.0512	0.0079	0.0152	0.0231	0.69	0.11	0.20	0.31
46	0.0705	0.0477	0.0076	0.0152	0.0228	0.68	0.11	0.22	0.32
47	0.0671	0.0446	0.0073	0.0152	0.0225	0.66	0.11	0.23	0.34
48	0.0640	0.0417	0.0071	0.0152	0.0223	0.65	0.11	0.24	0.35
49	0.0611	0.0391	0.0068	0.0152	0.0220	0.64	0.11	0.25	0.36
50	0.0585	0.0367	0.0066	0.0152	0.0218	0.63	0.11	0.26	0.37
50.9	**0.0563**	**0.0347**	**0.0064**	**0.0152**	**0.0216**	**0.62**	**0.11**	**0.27**	**0.38**
51	0.0560	0.0345	0.0064	0.0152	0.0216	0.62	0.11	0.27	0.38
51.3	**0.0553**	**0.0338**	**0.0063**	**0.0152**	**0.0215**	**0.61**	**0.11**	**0.27**	**0.39**
52	0.0538	0.0324	0.0062	0.0152	0.0214	0.60	0.11	0.28	0.40
53	0.0517	0.0305	0.0060	0.0152	0.0212	0.59	0.12	0.29	0.41
54	0.0497	0.0288	0.0058	0.0152	0.0210	0.58	0.12	0.31	0.42
55	0.0479	0.0272	0.0056	0.0152	0.0208	0.57	0.12	0.32	0.43
56	0.0462	0.0256	0.0054	0.0152	0.0206	0.55	0.12	0.33	0.45
57	0.0447	0.0242	0.0052	0.0152	0.0204	0.54	0.12	0.34	0.46
58	0.0432	0.0229	0.0051	0.0152	0.0202	0.53	0.12	0.35	0.47
59	0.0418	0.0217	0.0049	0.0151	0.0201	0.52	0.12	0.36	0.48
59.5	**0.0412**	**0.0212**	**0.0049**	**0.0151**	**0.0200**	**0.51**	**0.12**	**0.37**	**0.49**
60	0.0405	0.0206	0.0048	0.0151	0.0199	0.51	0.12	0.37	0.49
65	0.0352	0.0160	0.0042	0.0151	0.0192	0.45	0.12	0.43	0.55
70	0.0312	0.0126	0.0036	0.0150	0.0186	0.40	0.12	0.48	0.60
75	0.0282	0.0101	0.0032	0.0149	0.0181	0.36	0.11	0.53	0.64
80	0.0259	0.0083	0.0029	0.0147	0.0176	0.32	0.11	0.57	0.68
85	0.0240	0.0068	0.0026	0.0146	0.0172	0.28	0.11	0.61	0.72
90	0.0225	0.0057	0.0023	0.0145	0.0168	0.25	0.10	0.65	0.75
95	0.0212	0.0048	0.0021	0.0144	0.0165	0.22	0.10	0.68	0.78
100	0.0202	0.0041	0.0019	0.0143	0.0161	0.20	0.09	0.71	0.80

Table VII-8: Total mass attenuation coefficients $\mu/\rho\,(E)_i$ of the element sulphur $_{16}$S as sum of the single coefficients following eq. (II-14) for the attenuation processes photoelectric absorption (photo), coherent scattering (coh), and incoherent scattering (incoh) as well as scattering coefficient (scat = coh + incoh) for a practice-oriented energy range (incl. particular device energies, bold, refer to Table VII-2) determined via XCOM (2010), complete with the attenuation fractions $\xi(i)$ following eq. (II-15) of the single mechanisms.

Calcium $_{20}$Ca

| E [keV] | $\frac{\mu_i}{\rho}(E)$ [m²/kg] | | | | | $\xi(i)$ [−] | | | |
	total	photo	coh	incoh	scat	photo	coh	incoh	scat
5	60.2500	60.0700	0.1720	0.0068	0.1788	1.00	0.00	0.00	0.00
6	37.3100	37.1600	0.1465	0.0077	0.1542	1.00	0.00	0.00	0.00
7	24.7400	24.6000	0.1268	0.0085	0.1353	0.99	0.01	0.00	0.01
8	17.2700	17.1400	0.1116	0.0092	0.1208	0.99	0.01	0.00	0.01
9	12.5100	12.4000	0.0995	0.0097	0.1093	0.99	0.01	0.00	0.01
10	9.3410	9.2410	0.0895	0.0102	0.0998	0.99	0.01	0.00	0.01
11	7.1590	7.0670	0.0811	0.0107	0.0918	0.99	0.01	0.00	0.01
12	5.6070	5.5220	0.0738	0.0111	0.0849	0.98	0.01	0.00	0.02
12.7	**4.7780**	**4.6980**	**0.0693**	**0.0113**	**0.0806**	**0.98**	**0.01**	**0.00**	**0.02**
13	4.4730	4.3940	0.0674	0.0114	0.0789	0.98	0.02	0.00	0.02
14	3.6260	3.5520	0.0618	0.0118	0.0735	0.98	0.02	0.00	0.02
15	2.9790	2.9110	0.0567	0.0121	0.0688	0.98	0.02	0.00	0.02
15.5	**2.7130**	**2.6470**	**0.0544**	**0.0122**	**0.0666**	**0.98**	**0.02**	**0.00**	**0.02**
16	2.4780	2.4130	0.0522	0.0123	0.0645	0.97	0.02	0.00	0.03
16.9	**2.1190**	**2.0580**	**0.0485**	**0.0126**	**0.0611**	**0.97**	**0.02**	**0.01**	**0.03**
17	2.0830	2.0220	0.0481	0.0126	0.0607	0.97	0.02	0.01	0.03
18	1.7680	1.7110	0.0444	0.0128	0.0573	0.97	0.03	0.01	0.03
19	1.5140	1.4590	0.0412	0.0130	0.0542	0.96	0.03	0.01	0.04
20	1.3060	1.2550	0.0382	0.0132	0.0515	0.96	0.03	0.01	0.04
21	1.1350	1.0860	0.0356	0.0134	0.0490	0.96	0.03	0.01	0.04
21.1	**1.1190**	**1.0710**	**0.0353**	**0.0134**	**0.0488**	**0.96**	**0.03**	**0.01**	**0.04**
21.2	**1.1040**	**1.0560**	**0.0351**	**0.0134**	**0.0485**	**0.96**	**0.03**	**0.01**	**0.04**
21.5	**1.0600**	**1.0130**	**0.0344**	**0.0135**	**0.0479**	**0.96**	**0.03**	**0.01**	**0.05**
22	0.9925	0.9458	0.0332	0.0136	0.0468	0.95	0.03	0.01	0.05
23	0.8733	0.8285	0.0311	0.0137	0.0448	0.95	0.04	0.02	0.05
24	0.7726	0.7297	0.0291	0.0138	0.0429	0.94	0.04	0.02	0.06
24.2	**0.7544**	**0.7118**	**0.0288**	**0.0139**	**0.0426**	**0.94**	**0.04**	**0.02**	**0.06**
25	0.6871	0.6458	0.0274	0.0140	0.0413	0.94	0.04	0.02	0.06
26	0.6139	0.5741	0.0257	0.0141	0.0398	0.94	0.04	0.02	0.06
26.3	**0.5940**	**0.5546**	**0.0253**	**0.0141**	**0.0394**	**0.93**	**0.04**	**0.02**	**0.07**
27	0.5509	0.5125	0.0243	0.0142	0.0384	0.93	0.04	0.03	0.07
27.3	**0.5338**	**0.4958**	**0.0239**	**0.0142**	**0.0380**	**0.93**	**0.04**	**0.03**	**0.07**
28	0.4965	0.4593	0.0229	0.0142	0.0372	0.93	0.05	0.03	0.07
29	0.4492	0.4132	0.0217	0.0143	0.0360	0.92	0.05	0.03	0.08
29.2	**0.4405**	**0.4047**	**0.0215**	**0.0143**	**0.0358**	**0.92**	**0.05**	**0.03**	**0.08**
30	0.4079	0.3729	0.0206	0.0144	0.0350	0.91	0.05	0.04	0.09
31	0.3717	0.3377	0.0196	0.0145	0.0340	0.91	0.05	0.04	0.09
32	0.3398	0.3067	0.0186	0.0145	0.0331	0.90	0.05	0.04	0.10
33	0.3116	0.2793	0.0177	0.0146	0.0323	0.90	0.06	0.05	0.10
34	0.2866	0.2551	0.0169	0.0146	0.0315	0.89	0.06	0.05	0.11
35	0.2643	0.2335	0.0161	0.0147	0.0308	0.88	0.06	0.06	0.12
35.1	**0.2622**	**0.2315**	**0.0161**	**0.0147**	**0.0307**	**0.88**	**0.06**	**0.06**	**0.12**
35.4	**0.2561**	**0.2256**	**0.0158**	**0.0147**	**0.0305**	**0.88**	**0.06**	**0.06**	**0.12**

continued from page 378

Calcium $_{20}$Ca

Energy	$\frac{\mu_i}{\rho}(E)$ [m²/kg]					$\xi(i)$ [−]			
E [keV]	total	photo	coh	incoh	scat	photo	coh	incoh	scat
36	0.2444	0.2143	0.0154	0.0147	0.0301	0.88	0.06	0.06	0.12
37	0.2266	0.1971	0.0148	0.0147	0.0295	0.87	0.07	0.07	0.13
38	0.2105	0.1816	0.0141	0.0148	0.0289	0.86	0.07	0.07	0.14
39	0.1961	0.1678	0.0136	0.0148	0.0283	0.86	0.07	0.08	0.14
40	0.1830	0.1552	0.0130	0.0148	0.0278	0.85	0.07	0.08	0.15
41	0.1712	0.1439	0.0125	0.0148	0.0273	0.84	0.07	0.09	0.16
42	0.1605	0.1336	0.0120	0.0148	0.0269	0.83	0.07	0.09	0.17
43	0.1507	0.1243	0.0116	0.0149	0.0264	0.82	0.08	0.10	0.18
44	0.1418	0.1158	0.0112	0.0149	0.0260	0.82	0.08	0.10	0.18
45	0.1337	0.1080	0.0108	0.0149	0.0256	0.81	0.08	0.11	0.19
46	0.1262	0.1009	0.0104	0.0149	0.0253	0.80	0.08	0.12	0.20
47	0.1194	0.0945	0.0100	0.0149	0.0249	0.79	0.08	0.12	0.21
48	0.1131	0.0885	0.0097	0.0149	0.0246	0.78	0.09	0.13	0.22
49	0.1073	0.0830	0.0093	0.0149	0.0243	0.77	0.09	0.14	0.23
50	0.1019	0.0780	0.0090	0.0149	0.0240	0.77	0.09	0.15	0.24
50.9	**0.0975**	**0.0738**	**0.0088**	**0.0149**	**0.0237**	**0.76**	**0.09**	**0.15**	**0.24**
51	0.0970	0.0734	0.0087	0.0149	0.0237	0.76	0.09	0.15	0.24
51.3	**0.0956**	**0.0720**	**0.0087**	**0.0149**	**0.0236**	**0.75**	**0.09**	**0.16**	**0.25**
52	0.0925	0.0691	0.0085	0.0149	0.0234	0.75	0.09	0.16	0.25
53	0.0882	0.0651	0.0082	0.0149	0.0231	0.74	0.09	0.17	0.26
54	0.0843	0.0615	0.0079	0.0149	0.0228	0.73	0.09	0.18	0.27
55	0.0807	0.0580	0.0077	0.0149	0.0226	0.72	0.10	0.18	0.28
56	0.0773	0.0549	0.0075	0.0149	0.0224	0.71	0.10	0.19	0.29
57	0.0741	0.0520	0.0073	0.0149	0.0221	0.70	0.10	0.20	0.30
58	0.0711	0.0492	0.0070	0.0149	0.0219	0.69	0.10	0.21	0.31
59	0.0684	0.0467	0.0068	0.0149	0.0217	0.68	0.10	0.22	0.32
59.5	**0.0671**	**0.0455**	**0.0067**	**0.0149**	**0.0216**	**0.68**	**0.10**	**0.22**	**0.32**
60	0.0658	0.0443	0.0066	0.0149	0.0215	0.67	0.10	0.23	0.33
65	0.0551	0.0345	0.0058	0.0148	0.0206	0.63	0.11	0.27	0.37
70	0.0472	0.0274	0.0051	0.0147	0.0198	0.58	0.11	0.31	0.42
75	0.0412	0.0220	0.0045	0.0146	0.0191	0.54	0.11	0.36	0.46
80	0.0366	0.0180	0.0040	0.0145	0.0186	0.49	0.11	0.40	0.51
85	0.0329	0.0149	0.0036	0.0144	0.0180	0.45	0.11	0.44	0.55
90	0.0300	0.0124	0.0032	0.0143	0.0176	0.41	0.11	0.48	0.59
95	0.0277	0.0105	0.0029	0.0142	0.0172	0.38	0.11	0.51	0.62
100	0.0257	0.0089	0.0027	0.0141	0.0168	0.35	0.10	0.55	0.65

Table VII-9: Total mass attenuation coefficients $\mu/\rho\,(E)_i$ of the element calcium $_{20}$Ca as sum of the single coefficients following eq. (II-14) for the attenuation processes photoelectric absorption (photo), coherent scattering (coh), and incoherent scattering (incoh) as well as scattering coefficient (scat = coh + incoh) for a practice-oriented energy range (incl. particular device energies, bold, refer to Table VII-2) determined via XCOM (2010), complete with the attenuation fractions $\xi(i)$ following eq. (II-15) of the single mechanisms.

TMP oven-dry

Energy								
				$\frac{\mu_i}{\rho}(E)\ [\mathrm{m^2/kg}]$				$\xi(i)\ [-]$
E [keV]	total	photo	coh	incoh	scat	photo	coh	incoh	scat
5	3.2056	3.1489	0.0457	0.0107	0.0564	0.98	0.01	0.00	0.02
6	1.8566	1.8074	0.0369	0.0119	0.0488	0.97	0.02	0.01	0.03
7	1.1695	1.1261	0.0306	0.0128	0.0434	0.96	0.03	0.01	0.04
8	0.7847	0.7453	0.0260	0.0135	0.0395	0.95	0.03	0.02	0.05
9	0.5532	0.5167	0.0224	0.0141	0.0365	0.93	0.04	0.03	0.07
10	0.4059	0.3717	0.0196	0.0146	0.0342	0.92	0.05	0.04	0.08
11	0.3079	0.2755	0.0174	0.0150	0.0324	0.89	0.06	0.05	0.11
12	0.2403	0.2094	0.0156	0.0153	0.0309	0.87	0.06	0.06	0.13
12.7	**0.2050**	**0.1751**	**0.0145**	**0.0156**	**0.0300**	**0.85**	**0.07**	**0.08**	**0.15**
13	0.1922	0.1626	0.0140	0.0156	0.0297	0.85	0.07	0.08	0.15
14	0.1571	0.1285	0.0127	0.0159	0.0286	0.82	0.08	0.10	0.18
15	0.1309	0.1032	0.0116	0.0161	0.0277	0.79	0.09	0.12	0.21
15.5	**0.1202**	**0.0929**	**0.0111**	**0.0162**	**0.0273**	**0.77**	**0.09**	**0.13**	**0.23**
16	0.1109	0.0840	0.0106	0.0163	0.0269	0.76	0.10	0.15	0.24
16.9	**0.0968**	**0.0705**	**0.0098**	**0.0165**	**0.0263**	**0.73**	**0.10**	**0.17**	**0.27**
17	0.0954	0.0692	0.0097	0.0165	0.0262	0.73	0.10	0.17	0.27
18	0.0832	0.0576	0.0090	0.0167	0.0256	0.69	0.11	0.20	0.31
19	0.0735	0.0484	0.0083	0.0168	0.0251	0.66	0.11	0.23	0.34
20	0.0657	0.0411	0.0077	0.0169	0.0246	0.63	0.12	0.26	0.37
21	0.0593	0.0351	0.0071	0.0170	0.0242	0.59	0.12	0.29	0.41
21.1	**0.0587**	**0.0346**	**0.0071**	**0.0170**	**0.0241**	**0.59**	**0.12**	**0.29**	**0.41**
21.2	**0.0581**	**0.0340**	**0.0070**	**0.0170**	**0.0241**	**0.59**	**0.12**	**0.29**	**0.41**
21.5	**0.0565**	**0.0325**	**0.0069**	**0.0171**	**0.0240**	**0.58**	**0.12**	**0.30**	**0.42**
22	0.0540	0.0302	0.0066	0.0171	0.0238	0.56	0.12	0.32	0.44
23	0.0496	0.0262	0.0062	0.0172	0.0234	0.53	0.13	0.35	0.47
24	0.0459	0.0228	0.0058	0.0173	0.0231	0.50	0.13	0.38	0.50
24.2	**0.0452**	**0.0222**	**0.0057**	**0.0173**	**0.0230**	**0.49**	**0.13**	**0.38**	**0.51**
25	0.0427	0.0200	0.0054	0.0173	0.0228	0.47	0.13	0.41	0.53
26	0.0401	0.0176	0.0051	0.0174	0.0225	0.44	0.13	0.43	0.56
26.3	**0.0393**	**0.0170**	**0.0050**	**0.0174**	**0.0224**	**0.43**	**0.13**	**0.44**	**0.57**
27	0.0378	0.0156	0.0048	0.0174	0.0222	0.41	0.13	0.46	0.59
27.3	**0.0372**	**0.0150**	**0.0047**	**0.0174**	**0.0221**	**0.40**	**0.13**	**0.47**	**0.60**
28	0.0358	0.0138	0.0045	0.0174	0.0220	0.39	0.13	0.49	0.61
29	0.0341	0.0123	0.0043	0.0175	0.0217	0.36	0.13	0.51	0.64
29.2	**0.0338**	**0.0121**	**0.0042**	**0.0175**	**0.0217**	**0.36**	**0.13**	**0.52**	**0.64**
30	0.0326	0.0111	0.0040	0.0175	0.0215	0.34	0.12	0.54	0.66
31	0.0313	0.0099	0.0038	0.0175	0.0213	0.32	0.12	0.56	0.68
32	0.0301	0.0090	0.0036	0.0175	0.0211	0.30	0.12	0.58	0.70
33	0.0291	0.0081	0.0034	0.0175	0.0210	0.28	0.12	0.60	0.72
34	0.0281	0.0074	0.0033	0.0175	0.0208	0.26	0.12	0.62	0.74
35	0.0273	0.0067	0.0031	0.0175	0.0206	0.24	0.11	0.64	0.76
35.1	**0.0272**	**0.0066**	**0.0031**	**0.0175**	**0.0206**	**0.24**	**0.11**	**0.64**	**0.76**
35.4	**0.0270**	**0.0064**	**0.0030**	**0.0175**	**0.0206**	**0.24**	**0.11**	**0.65**	**0.76**

TMP oven-dry

Energy				$\frac{\mu_i}{\rho}(E)$ [m²/kg]				$\xi(i)$ [−]	
E [keV]	total	photo	coh	incoh	scat	photo	coh	incoh	scat
36	0.0266	0.0061	0.0030	0.0175	0.0205	0.23	0.11	0.66	0.77
37	0.0259	0.0056	0.0028	0.0175	0.0203	0.22	0.11	0.68	0.78
38	0.0253	0.0051	0.0027	0.0175	0.0202	0.20	0.11	0.69	0.80
39	0.0248	0.0047	0.0026	0.0175	0.0201	0.19	0.10	0.71	0.81
40	0.0242	0.0043	0.0025	0.0175	0.0199	0.18	0.10	0.72	0.82
41	0.0238	0.0040	0.0024	0.0174	0.0198	0.17	0.10	0.73	0.83
42	0.0234	0.0037	0.0023	0.0174	0.0197	0.16	0.10	0.75	0.84
43	0.0230	0.0034	0.0022	0.0174	0.0196	0.15	0.09	0.76	0.85
44	0.0226	0.0032	0.0021	0.0174	0.0195	0.14	0.09	0.77	0.86
45	0.0223	0.0029	0.0020	0.0174	0.0194	0.13	0.09	0.78	0.87
46	0.0220	0.0027	0.0019	0.0173	0.0193	0.12	0.09	0.79	0.88
47	0.0217	0.0025	0.0019	0.0173	0.0192	0.12	0.09	0.80	0.88
48	0.0214	0.0024	0.0018	0.0173	0.0191	0.11	0.08	0.81	0.89
49	0.0212	0.0022	0.0017	0.0173	0.0190	0.10	0.08	0.81	0.89
50	0.0210	0.0021	0.0017	0.0172	0.0189	0.10	0.08	0.82	0.90
50.9	**0.0208**	**0.0020**	**0.0016**	**0.0172**	**0.0188**	**0.09**	**0.08**	**0.83**	**0.91**
51	0.0207	0.0019	0.0016	0.0172	0.0188	0.09	0.08	0.83	0.91
51.3	**0.0207**	**0.0019**	**0.0016**	**0.0172**	**0.0188**	**0.09**	**0.08**	**0.83**	**0.91**
52	0.0205	0.0018	0.0015	0.0172	0.0187	0.09	0.08	0.84	0.91
53	0.0203	0.0017	0.0015	0.0171	0.0186	0.08	0.07	0.84	0.92
54	0.0202	0.0016	0.0014	0.0171	0.0185	0.08	0.07	0.85	0.92
55	0.0200	0.0015	0.0014	0.0171	0.0185	0.08	0.07	0.85	0.92
56	0.0198	0.0014	0.0013	0.0170	0.0184	0.07	0.07	0.86	0.93
57	0.0197	0.0014	0.0013	0.0170	0.0183	0.07	0.07	0.86	0.93
58	0.0195	0.0013	0.0013	0.0170	0.0182	0.07	0.06	0.87	0.93
59	0.0194	0.0012	0.0012	0.0169	0.0182	0.06	0.06	0.87	0.94
59.5	**0.0193**	**0.0012**	**0.0012**	**0.0169**	**0.0181**	**0.06**	**0.06**	**0.88**	**0.94**
60	0.0192	0.0011	0.0012	0.0169	0.0181	0.06	0.06	0.88	0.94
65	0.0186	0.0009	0.0010	0.0167	0.0178	0.05	0.06	0.90	0.95
70	0.0181	0.0007	0.0009	0.0166	0.0174	0.04	0.05	0.91	0.96
75	0.0177	0.0005	0.0008	0.0164	0.0172	0.03	0.04	0.92	0.97
80	0.0173	0.0004	0.0007	0.0162	0.0169	0.03	0.04	0.93	0.97
85	0.0170	0.0004	0.0006	0.0160	0.0166	0.02	0.04	0.94	0.98
90	0.0167	0.0003	0.0006	0.0158	0.0164	0.02	0.03	0.95	0.98
95	0.0164	0.0003	0.0005	0.0157	0.0162	0.02	0.03	0.95	0.98
100	0.0162	0.0002	0.0005	0.0155	0.0160	0.01	0.03	0.96	0.99

Table VII-10: Total mean mass attenuation coefficients $\mu/\rho\,(E)_{\mathrm{mix}}$ of oven-dry TMP as sum of the single coefficients following eq. (II-14) for the attenuation processes photoelectric absorption (photo), coherent scattering (coh), and incoherent scattering (incoh) as well as scattering coefficient (scat = coh + incoh) for a practice-oriented energy range (incl. particular device energies, bold, refer to Table VII-2) determined on basis of analysis data (Table IV-15) via eq. (II-31) by means of XCOM (2010) elemental data (Table VII-3 to Table VII-9), complete with the attenuation fractions $\xi(i)$ following eq. (II-15) of the single mechanisms.

labMDF oven-dry

Energy				$\frac{\mu_i}{\rho}(E)$ [m²/kg]			$\xi(i)$ [−]	
E [keV]	total	photo	coh	incoh	scat	photo	coh	incoh	scat
5	3.2131	3.1565	0.0458	0.0107	0.0564	0.98	0.01	0.00	0.02
6	1.8610	1.8117	0.0370	0.0119	0.0489	0.97	0.02	0.01	0.03
7	1.1722	1.1288	0.0307	0.0128	0.0435	0.96	0.03	0.01	0.04
8	0.7866	0.7471	0.0260	0.0135	0.0395	0.95	0.03	0.02	0.05
9	0.5545	0.5180	0.0224	0.0141	0.0365	0.93	0.04	0.03	0.07
10	0.4068	0.3726	0.0197	0.0146	0.0342	0.92	0.05	0.04	0.08
11	0.3086	0.2762	0.0174	0.0150	0.0324	0.89	0.06	0.05	0.10
12	0.2408	0.2100	0.0156	0.0153	0.0309	0.87	0.06	0.06	0.13
12.7	**0.2055**	**0.1755**	**0.0145**	**0.0155**	**0.0300**	**0.85**	**0.07**	**0.08**	**0.15**
13	0.1926	0.1630	0.0140	0.0156	0.0297	0.85	0.07	0.08	0.15
14	0.1574	0.1288	0.0127	0.0159	0.0286	0.82	0.08	0.10	0.18
15	0.1312	0.1035	0.0116	0.0161	0.0277	0.79	0.09	0.12	0.21
15.5	**0.1205**	**0.0932**	**0.0111**	**0.0162**	**0.0273**	**0.77**	**0.09**	**0.13**	**0.23**
16	0.1111	0.0842	0.0106	0.0163	0.0269	0.76	0.10	0.15	0.24
16.9	**0.0970**	**0.0707**	**0.0098**	**0.0165**	**0.0263**	**0.73**	**0.10**	**0.17**	**0.27**
17	0.0956	0.0694	0.0097	0.0165	0.0262	0.73	0.10	0.17	0.27
18	0.0834	0.0578	0.0090	0.0166	0.0256	0.69	0.11	0.20	0.31
19	0.0736	0.0486	0.0083	0.0168	0.0251	0.66	0.11	0.23	0.34
20	0.0658	0.0412	0.0077	0.0169	0.0246	0.63	0.12	0.26	0.37
21	0.0593	0.0352	0.0071	0.0170	0.0242	0.59	0.12	0.29	0.41
21.1	**0.0588**	**0.0347**	**0.0071**	**0.0170**	**0.0241**	**0.59**	**0.12**	**0.29**	**0.41**
21.2	**0.0582**	**0.0341**	**0.0070**	**0.0170**	**0.0241**	**0.59**	**0.12**	**0.29**	**0.41**
21.5	**0.0566**	**0.0326**	**0.0069**	**0.0171**	**0.0240**	**0.58**	**0.12**	**0.30**	**0.42**
22	0.0540	0.0303	0.0067	0.0171	0.0238	0.56	0.12	0.32	0.44
23	0.0496	0.0262	0.0062	0.0172	0.0234	0.53	0.13	0.35	0.47
24	0.0459	0.0229	0.0058	0.0172	0.0231	0.50	0.13	0.38	0.50
24.2	**0.0453**	**0.0223**	**0.0057**	**0.0173**	**0.0230**	**0.49**	**0.13**	**0.38**	**0.51**
25	0.0428	0.0200	0.0054	0.0173	0.0227	0.47	0.13	0.40	0.53
26	0.0401	0.0176	0.0051	0.0174	0.0225	0.44	0.13	0.43	0.56
26.3	**0.0394**	**0.0170**	**0.0050**	**0.0174**	**0.0224**	**0.43**	**0.13**	**0.44**	**0.57**
27	0.0378	0.0156	0.0048	0.0174	0.0222	0.41	0.13	0.46	0.59
27.3	**0.0372**	**0.0151**	**0.0047**	**0.0174**	**0.0221**	**0.40**	**0.13**	**0.47**	**0.60**
28	0.0358	0.0139	0.0045	0.0174	0.0220	0.39	0.13	0.49	0.61
29	0.0341	0.0124	0.0043	0.0175	0.0217	0.36	0.13	0.51	0.64
29.2	**0.0338**	**0.0121**	**0.0042**	**0.0175**	**0.0217**	**0.36**	**0.13**	**0.52**	**0.64**
30	0.0326	0.0111	0.0040	0.0175	0.0215	0.34	0.12	0.54	0.66
31	0.0313	0.0100	0.0038	0.0175	0.0213	0.32	0.12	0.56	0.68
32	0.0301	0.0090	0.0036	0.0175	0.0211	0.30	0.12	0.58	0.70
33	0.0291	0.0081	0.0034	0.0175	0.0209	0.28	0.12	0.60	0.72
34	0.0282	0.0074	0.0033	0.0175	0.0208	0.26	0.12	0.62	0.74
35	0.0273	0.0067	0.0031	0.0175	0.0206	0.25	0.11	0.64	0.75
35.1	**0.0272**	**0.0066**	**0.0031**	**0.0175**	**0.0206**	**0.24**	**0.11**	**0.64**	**0.76**
35.4	**0.0270**	**0.0065**	**0.0031**	**0.0175**	**0.0206**	**0.24**	**0.11**	**0.65**	**0.76**

labMDF oven-dry

Energy				$\frac{\mu_i}{\rho}(E)$ [m²/kg]					$\xi(i)$ [−]
E [keV]	total	photo	coh	incoh	scat	photo	coh	incoh	scat
36	0.0266	0.0061	0.0030	0.0175	0.0205	0.23	0.11	0.66	0.77
37	0.0259	0.0056	0.0028	0.0175	0.0203	0.22	0.11	0.67	0.78
38	0.0253	0.0051	0.0027	0.0175	0.0202	0.20	0.11	0.69	0.80
39	0.0248	0.0047	0.0026	0.0175	0.0201	0.19	0.10	0.71	0.81
40	0.0243	0.0043	0.0025	0.0175	0.0199	0.18	0.10	0.72	0.82
41	0.0238	0.0040	0.0024	0.0174	0.0198	0.17	0.10	0.73	0.83
42	0.0234	0.0037	0.0023	0.0174	0.0197	0.16	0.10	0.75	0.84
43	0.0230	0.0034	0.0022	0.0174	0.0196	0.15	0.09	0.76	0.85
44	0.0226	0.0032	0.0021	0.0174	0.0195	0.14	0.09	0.77	0.86
45	0.0223	0.0029	0.0020	0.0174	0.0194	0.13	0.09	0.78	0.87
46	0.0220	0.0027	0.0019	0.0173	0.0193	0.12	0.09	0.79	0.88
47	0.0217	0.0026	0.0019	0.0173	0.0192	0.12	0.09	0.80	0.88
48	0.0214	0.0024	0.0018	0.0173	0.0191	0.11	0.08	0.81	0.89
49	0.0212	0.0022	0.0017	0.0172	0.0190	0.11	0.08	0.81	0.89
50	0.0210	0.0021	0.0017	0.0172	0.0189	0.10	0.08	0.82	0.90
50.9	**0.0208**	**0.0020**	**0.0016**	**0.0172**	**0.0188**	**0.09**	**0.08**	**0.83**	**0.91**
51	0.0207	0.0020	0.0016	0.0172	0.0188	0.09	0.08	0.83	0.91
51.3	**0.0207**	**0.0019**	**0.0016**	**0.0172**	**0.0188**	**0.09**	**0.08**	**0.83**	**0.91**
52	0.0205	0.0018	0.0015	0.0172	0.0187	0.09	0.08	0.84	0.91
53	0.0203	0.0017	0.0015	0.0171	0.0186	0.08	0.07	0.84	0.92
54	0.0202	0.0016	0.0014	0.0171	0.0185	0.08	0.07	0.85	0.92
55	0.0200	0.0015	0.0014	0.0171	0.0185	0.08	0.07	0.85	0.92
56	0.0198	0.0014	0.0014	0.0170	0.0184	0.07	0.07	0.86	0.93
57	0.0197	0.0014	0.0013	0.0170	0.0183	0.07	0.07	0.86	0.93
58	0.0195	0.0013	0.0013	0.0170	0.0182	0.07	0.06	0.87	0.93
59	0.0194	0.0012	0.0012	0.0169	0.0182	0.06	0.06	0.87	0.94
59.5	**0.0193**	**0.0012**	**0.0012**	**0.0169**	**0.0181**	**0.06**	**0.06**	**0.88**	**0.94**
60	0.0192	0.0011	0.0012	0.0169	0.0181	0.06	0.06	0.88	0.94
65	0.0186	0.0009	0.0010	0.0167	0.0177	0.05	0.06	0.90	0.95
70	0.0181	0.0007	0.0009	0.0165	0.0174	0.04	0.05	0.91	0.96
75	0.0177	0.0005	0.0008	0.0164	0.0172	0.03	0.04	0.92	0.97
80	0.0173	0.0004	0.0007	0.0162	0.0169	0.03	0.04	0.93	0.97
85	0.0170	0.0004	0.0006	0.0160	0.0166	0.02	0.04	0.94	0.98
90	0.0167	0.0003	0.0006	0.0158	0.0164	0.02	0.03	0.95	0.98
95	0.0164	0.0003	0.0005	0.0157	0.0162	0.02	0.03	0.95	0.98
100	0.0162	0.0002	0.0005	0.0155	0.0160	0.01	0.03	0.96	0.99

Table VII-11: Total mean mass attenuation coefficients $\mu/\rho(E)_{\mathrm{mix}}$ of oven-dry labMDF as sum of the single coefficients following eq. (II-14) for the attenuation processes photoelectric absorption (photo), coherent scattering (coh), and incoherent scattering (incoh) as well as scattering coefficient (scat = coh + incoh) for a practice-oriented energy range (incl. particular device energies, bold, refer to Table VII-2) determined on basis of analysis data (Table IV-15) via eq. (II-31) by means of XCOM (2010) elemental data (Table VII-3 to Table VII-9), complete with the attenuation fractions $\xi(i)$ following eq. (II-15) of the single mechanisms.

labMDF at $MC = 9.5$ %

Energy								
				$\frac{\mu_i}{\rho}(E)$ [m^2/kg]				$\xi(i)$ [−]
E [keV]	total	photo	coh	incoh	scat	photo	coh	incoh	scat
5	3.3039	3.2463	0.0466	0.0107	0.0574	0.98	0.01	0.00	0.02
6	1.9134	1.8634	0.0377	0.0120	0.0496	0.97	0.02	0.01	0.03
7	1.2050	1.1609	0.0312	0.0129	0.0441	0.96	0.03	0.01	0.04
8	0.8083	0.7684	0.0264	0.0136	0.0400	0.95	0.03	0.02	0.05
9	0.5696	0.5327	0.0228	0.0142	0.0370	0.94	0.04	0.02	0.06
10	0.4178	0.3832	0.0199	0.0147	0.0346	0.92	0.05	0.04	0.08
11	0.3168	0.2840	0.0177	0.0151	0.0327	0.90	0.06	0.05	0.10
12	0.2471	0.2159	0.0158	0.0154	0.0312	0.87	0.06	0.06	0.13
12.7	**0.2107**	**0.1805**	**0.0147**	**0.0156**	**0.0303**	**0.86**	**0.07**	**0.07**	**0.14**
13	0.1975	0.1676	0.0142	0.0157	0.0299	0.85	0.07	0.08	0.15
14	0.1613	0.1325	0.0129	0.0160	0.0289	0.82	0.08	0.10	0.18
15	0.1343	0.1064	0.0117	0.0162	0.0279	0.79	0.09	0.12	0.21
15.5	**0.1233**	**0.0958**	**0.0112**	**0.0163**	**0.0275**	**0.78**	**0.09**	**0.13**	**0.22**
16	0.1137	0.0865	0.0107	0.0164	0.0271	0.76	0.09	0.14	0.24
16.9	**0.0992**	**0.0727**	**0.0100**	**0.0165**	**0.0265**	**0.73**	**0.10**	**0.17**	**0.27**
17	0.0977	0.0713	0.0099	0.0166	0.0264	0.73	0.10	0.17	0.27
18	0.0852	0.0594	0.0091	0.0167	0.0258	0.70	0.11	0.20	0.30
19	0.0752	0.0499	0.0084	0.0169	0.0253	0.66	0.11	0.22	0.34
20	0.0671	0.0423	0.0078	0.0170	0.0248	0.63	0.12	0.25	0.37
21	0.0605	0.0362	0.0072	0.0171	0.0243	0.60	0.12	0.28	0.40
21.1	**0.0599**	**0.0356**	**0.0072**	**0.0171**	**0.0243**	**0.59**	**0.12**	**0.29**	**0.41**
21.2	**0.0593**	**0.0351**	**0.0071**	**0.0171**	**0.0242**	**0.59**	**0.12**	**0.29**	**0.41**
21.5	**0.0576**	**0.0335**	**0.0070**	**0.0171**	**0.0241**	**0.58**	**0.12**	**0.30**	**0.42**
22	0.0550	0.0311	0.0067	0.0172	0.0239	0.57	0.12	0.31	0.43
23	0.0505	0.0270	0.0063	0.0172	0.0235	0.53	0.12	0.34	0.47
24	0.0467	0.0235	0.0059	0.0173	0.0232	0.50	0.13	0.37	0.50
24.2	**0.0460**	**0.0229**	**0.0058**	**0.0173**	**0.0231**	**0.50**	**0.13**	**0.38**	**0.50**
25	0.0435	0.0206	0.0055	0.0174	0.0229	0.47	0.13	0.40	0.53
26	0.0407	0.0181	0.0052	0.0174	0.0226	0.45	0.13	0.43	0.55
26.3	**0.0400**	**0.0175**	**0.0051**	**0.0174**	**0.0225**	**0.44**	**0.13**	**0.44**	**0.56**
27	0.0384	0.0160	0.0049	0.0175	0.0223	0.42	0.13	0.45	0.58
27.3	**0.0377**	**0.0155**	**0.0048**	**0.0175**	**0.0223**	**0.41**	**0.13**	**0.46**	**0.59**
28	0.0363	0.0143	0.0046	0.0175	0.0221	0.39	0.13	0.48	0.61
29	0.0346	0.0127	0.0043	0.0175	0.0219	0.37	0.13	0.51	0.63
29.2	**0.0342**	**0.0124**	**0.0043**	**0.0175**	**0.0218**	**0.36**	**0.13**	**0.51**	**0.64**
30	0.0330	0.0114	0.0041	0.0175	0.0216	0.34	0.12	0.53	0.66
31	0.0317	0.0102	0.0039	0.0176	0.0214	0.32	0.12	0.55	0.68
32	0.0305	0.0092	0.0037	0.0176	0.0212	0.30	0.12	0.58	0.70
33	0.0294	0.0083	0.0035	0.0176	0.0211	0.28	0.12	0.60	0.72
34	0.0285	0.0076	0.0033	0.0176	0.0209	0.27	0.12	0.62	0.73
35	0.0276	0.0069	0.0032	0.0176	0.0207	0.25	0.11	0.64	0.75
35.1	**0.0275**	**0.0068**	**0.0031**	**0.0176**	**0.0207**	**0.25**	**0.11**	**0.64**	**0.75**
35.4	**0.0273**	**0.0066**	**0.0031**	**0.0176**	**0.0207**	**0.24**	**0.11**	**0.64**	**0.76**

labMDF at $MC = 9.5$ %

Energy									$\xi(i)$ [−]
				$\frac{\mu_i}{\rho}(E)$ [m²/kg]					
E [keV]	total	photo	coh	incoh	scat	photo	coh	incoh	scat
36	0.0269	0.0063	0.0030	0.0176	0.0206	0.23	0.11	0.65	0.77
37	0.0262	0.0057	0.0029	0.0176	0.0204	0.22	0.11	0.67	0.78
38	0.0256	0.0053	0.0027	0.0176	0.0203	0.21	0.11	0.69	0.79
39	0.0250	0.0048	0.0026	0.0175	0.0202	0.19	0.10	0.70	0.81
40	0.0245	0.0045	0.0025	0.0175	0.0200	0.18	0.10	0.72	0.82
41	0.0240	0.0041	0.0024	0.0175	0.0199	0.17	0.10	0.73	0.83
42	0.0236	0.0038	0.0023	0.0175	0.0198	0.16	0.10	0.74	0.84
43	0.0232	0.0035	0.0022	0.0175	0.0197	0.15	0.10	0.75	0.85
44	0.0228	0.0033	0.0021	0.0174	0.0196	0.14	0.09	0.76	0.86
45	0.0225	0.0030	0.0020	0.0174	0.0195	0.13	0.09	0.78	0.87
46	0.0222	0.0028	0.0020	0.0174	0.0194	0.13	0.09	0.78	0.87
47	0.0219	0.0026	0.0019	0.0174	0.0193	0.12	0.09	0.79	0.88
48	0.0216	0.0024	0.0018	0.0173	0.0192	0.11	0.08	0.80	0.89
49	0.0213	0.0023	0.0017	0.0173	0.0191	0.11	0.08	0.81	0.89
50	0.0211	0.0021	0.0017	0.0173	0.0190	0.10	0.08	0.82	0.90
50.9	**0.0209**	**0.0020**	**0.0016**	**0.0173**	**0.0189**	**0.10**	**0.08**	**0.83**	**0.90**
51	0.0209	0.0020	0.0016	0.0173	0.0189	0.10	0.08	0.83	0.90
51.3	**0.0208**	**0.0020**	**0.0016**	**0.0172**	**0.0189**	**0.09**	**0.08**	**0.83**	**0.91**
52	0.0207	0.0019	0.0016	0.0172	0.0188	0.09	0.08	0.83	0.91
53	0.0205	0.0018	0.0015	0.0172	0.0187	0.09	0.07	0.84	0.91
54	0.0203	0.0017	0.0015	0.0172	0.0186	0.08	0.07	0.85	0.92
55	0.0201	0.0016	0.0014	0.0171	0.0185	0.08	0.07	0.85	0.92
56	0.0199	0.0015	0.0014	0.0171	0.0185	0.07	0.07	0.86	0.93
57	0.0198	0.0014	0.0013	0.0171	0.0184	0.07	0.07	0.86	0.93
58	0.0196	0.0013	0.0013	0.0170	0.0183	0.07	0.07	0.87	0.93
59	0.0195	0.0012	0.0012	0.0170	0.0182	0.06	0.06	0.87	0.94
59.5	**0.0194**	**0.0012**	**0.0012**	**0.0170**	**0.0182**	**0.06**	**0.06**	**0.87**	**0.94**
60	0.0193	0.0012	0.0012	0.0170	0.0182	0.06	0.06	0.88	0.94
65	0.0187	0.0009	0.0010	0.0168	0.0178	0.05	0.06	0.90	0.95
70	0.0182	0.0007	0.0009	0.0166	0.0175	0.04	0.05	0.91	0.96
75	0.0178	0.0006	0.0008	0.0164	0.0172	0.03	0.04	0.92	0.97
80	0.0174	0.0005	0.0007	0.0163	0.0170	0.03	0.04	0.93	0.97
85	0.0171	0.0004	0.0006	0.0161	0.0167	0.02	0.04	0.94	0.98
90	0.0168	0.0003	0.0006	0.0159	0.0165	0.02	0.03	0.95	0.98
95	0.0165	0.0003	0.0005	0.0157	0.0162	0.02	0.03	0.95	0.98
100	0.0163	0.0002	0.0005	0.0156	0.0160	0.01	0.03	0.96	0.99

Table VII-12: Total mean mass attenuation coefficients $\mu/\rho\,(E)_{\mathrm{mix}}$ of moist labMDF at $MC = 9.5$ % as sum of the single coefficients following eq. (II-14) for the attenuation processes photoelectric absorption (photo), coherent scattering (coh), and incoherent scattering (incoh) as well as scattering coefficient (scat = coh + incoh) for a practice-oriented energy range (incl. particular device energies, bold, refer to Table VII-2) determined on basis of analysis data (Table IV-15) via eq. (II-31) by means of XCOM (2010) elemental data (Table VII-3 to Table VII-9), complete with the attenuation fractions $\xi(i)$ following eq. (II-15) of the single mechanisms.

Fmat oven-dry

Energy					$\frac{\mu_i}{\rho}(E)$ [m^2/kg]				$\xi(i)$ [−]
E [keV]	total	photo	coh	incoh	scat	photo	coh	incoh	scat
5	3.3117	3.2549	0.0459	0.0107	0.0566	0.98	0.01	0.00	0.02
6	1.9228	1.8734	0.0371	0.0119	0.0490	0.97	0.02	0.01	0.03
7	1.2136	1.1700	0.0308	0.0128	0.0436	0.96	0.03	0.01	0.04
8	0.8156	0.7760	0.0261	0.0135	0.0396	0.95	0.03	0.02	0.05
9	0.5756	0.5390	0.0225	0.0141	0.0366	0.94	0.04	0.02	0.06
10	0.4227	0.3884	0.0197	0.0146	0.0343	0.92	0.05	0.03	0.08
11	0.3208	0.2883	0.0175	0.0150	0.0325	0.90	0.05	0.05	0.10
12	0.2504	0.2194	0.0157	0.0153	0.0310	0.88	0.06	0.06	0.12
12.7	**0.2136**	**0.1836**	**0.0145**	**0.0155**	**0.0301**	**0.86**	**0.07**	**0.07**	**0.14**
13	0.2003	0.1706	0.0141	0.0156	0.0297	0.85	0.07	0.08	0.15
14	0.1636	0.1350	0.0128	0.0159	0.0287	0.82	0.08	0.10	0.18
15	0.1363	0.1085	0.0117	0.0161	0.0278	0.80	0.09	0.12	0.20
15.5	**0.1251**	**0.0977**	**0.0111**	**0.0162**	**0.0274**	**0.78**	**0.09**	**0.13**	**0.22**
16	0.1154	0.0884	0.0107	0.0163	0.0270	0.77	0.09	0.14	0.23
16.9	**0.1006**	**0.0743**	**0.0099**	**0.0165**	**0.0264**	**0.74**	**0.10**	**0.16**	**0.26**
17	0.0992	0.0729	0.0098	0.0165	0.0263	0.73	0.10	0.17	0.27
18	0.0864	0.0607	0.0090	0.0167	0.0257	0.70	0.10	0.19	0.30
19	0.0762	0.0511	0.0083	0.0168	0.0251	0.67	0.11	0.22	0.33
20	0.0680	0.0434	0.0077	0.0169	0.0246	0.64	0.11	0.25	0.36
21	0.0613	0.0371	0.0072	0.0170	0.0242	0.61	0.12	0.28	0.39
21.1	**0.0607**	**0.0365**	**0.0071**	**0.0170**	**0.0242**	**0.60**	**0.12**	**0.28**	**0.40**
21.2	**0.0601**	**0.0360**	**0.0071**	**0.0170**	**0.0241**	**0.60**	**0.12**	**0.28**	**0.40**
21.5	**0.0584**	**0.0344**	**0.0069**	**0.0171**	**0.0240**	**0.59**	**0.12**	**0.29**	**0.41**
22	0.0557	0.0319	0.0067	0.0171	0.0238	0.57	0.12	0.31	0.43
23	0.0511	0.0277	0.0062	0.0172	0.0234	0.54	0.12	0.34	0.46
24	0.0472	0.0241	0.0058	0.0173	0.0231	0.51	0.12	0.37	0.49
24.2	**0.0465**	**0.0235**	**0.0058**	**0.0173**	**0.0230**	**0.51**	**0.12**	**0.37**	**0.49**
25	0.0440	0.0212	0.0055	0.0173	0.0228	0.48	0.12	0.39	0.52
26	0.0412	0.0187	0.0051	0.0174	0.0225	0.45	0.12	0.42	0.55
26.3	**0.0404**	**0.0180**	**0.0050**	**0.0174**	**0.0224**	**0.45**	**0.12**	**0.43**	**0.56**
27	0.0388	0.0165	0.0048	0.0174	0.0222	0.43	0.12	0.45	0.57
27.3	**0.0381**	**0.0159**	**0.0048**	**0.0174**	**0.0222**	**0.42**	**0.12**	**0.46**	**0.58**
28	0.0367	0.0147	0.0046	0.0174	0.0220	0.40	0.12	0.48	0.60
29	0.0349	0.0131	0.0043	0.0175	0.0218	0.38	0.12	0.50	0.62
29.2	**0.0345**	**0.0128**	**0.0043**	**0.0175**	**0.0217**	**0.37**	**0.12**	**0.51**	**0.63**
30	0.0333	0.0117	0.0041	0.0175	0.0215	0.35	0.12	0.53	0.65
31	0.0319	0.0106	0.0038	0.0175	0.0213	0.33	0.12	0.55	0.67
32	0.0307	0.0095	0.0036	0.0175	0.0212	0.31	0.12	0.57	0.69
33	0.0296	0.0086	0.0035	0.0175	0.0210	0.29	0.12	0.59	0.71
34	0.0286	0.0078	0.0033	0.0175	0.0208	0.27	0.11	0.61	0.73
35	0.0278	0.0071	0.0031	0.0175	0.0206	0.26	0.11	0.63	0.74
35.1	**0.0277**	**0.0071**	**0.0031**	**0.0175**	**0.0206**	**0.25**	**0.11**	**0.63**	**0.75**
35.4	**0.0274**	**0.0069**	**0.0031**	**0.0175**	**0.0206**	**0.25**	**0.11**	**0.64**	**0.75**

Fmat oven-dry

Energy				$\frac{\mu_i}{\rho}(E)$ [m²/kg]				$\xi(i)$ [−]	
E [keV]	total	photo	coh	incoh	scat	photo	coh	incoh	scat
36	0.0270	0.0065	0.0030	0.0175	0.0205	0.24	0.11	0.65	0.76
37	0.0263	0.0059	0.0028	0.0175	0.0203	0.23	0.11	0.67	0.77
38	0.0256	0.0054	0.0027	0.0175	0.0202	0.21	0.11	0.68	0.79
39	0.0251	0.0050	0.0026	0.0175	0.0201	0.20	0.10	0.70	0.80
40	0.0245	0.0046	0.0025	0.0175	0.0199	0.19	0.10	0.71	0.81
41	0.0241	0.0043	0.0024	0.0174	0.0198	0.18	0.10	0.72	0.82
42	0.0236	0.0039	0.0023	0.0174	0.0197	0.17	0.10	0.74	0.83
43	0.0232	0.0036	0.0022	0.0174	0.0196	0.16	0.09	0.75	0.84
44	0.0229	0.0034	0.0021	0.0174	0.0195	0.15	0.09	0.76	0.85
45	0.0225	0.0031	0.0020	0.0174	0.0194	0.14	0.09	0.77	0.86
46	0.0222	0.0029	0.0019	0.0173	0.0193	0.13	0.09	0.78	0.87
47	0.0219	0.0027	0.0019	0.0173	0.0192	0.12	0.09	0.79	0.88
48	0.0216	0.0025	0.0018	0.0173	0.0191	0.12	0.08	0.80	0.88
49	0.0214	0.0024	0.0017	0.0172	0.0190	0.11	0.08	0.81	0.89
50	0.0211	0.0022	0.0017	0.0172	0.0189	0.11	0.08	0.82	0.89
50.9	**0.0209**	**0.0021**	**0.0016**	**0.0172**	**0.0188**	**0.10**	**0.08**	**0.82**	**0.90**
51	0.0209	0.0021	0.0016	0.0172	0.0188	0.10	0.08	0.82	0.90
51.3	**0.0208**	**0.0020**	**0.0016**	**0.0172**	**0.0188**	**0.10**	**0.08**	**0.83**	**0.90**
52	0.0207	0.0020	0.0016	0.0172	0.0187	0.09	0.08	0.83	0.91
53	0.0205	0.0018	0.0015	0.0171	0.0186	0.09	0.07	0.84	0.91
54	0.0203	0.0017	0.0015	0.0171	0.0186	0.09	0.07	0.84	0.92
55	0.0201	0.0016	0.0014	0.0171	0.0185	0.08	0.07	0.85	0.92
56	0.0199	0.0015	0.0014	0.0170	0.0184	0.08	0.07	0.85	0.92
57	0.0198	0.0014	0.0013	0.0170	0.0183	0.07	0.07	0.86	0.93
58	0.0196	0.0014	0.0013	0.0170	0.0182	0.07	0.07	0.87	0.93
59	0.0195	0.0013	0.0012	0.0169	0.0182	0.07	0.06	0.87	0.93
59.5	**0.0194**	**0.0013**	**0.0012**	**0.0169**	**0.0181**	**0.06**	**0.06**	**0.87**	**0.94**
60	0.0193	0.0012	0.0012	0.0169	0.0181	0.06	0.06	0.87	0.94
65	0.0187	0.0009	0.0010	0.0167	0.0178	0.05	0.06	0.89	0.95
70	0.0182	0.0007	0.0009	0.0165	0.0175	0.04	0.05	0.91	0.96
75	0.0178	0.0006	0.0008	0.0164	0.0172	0.03	0.04	0.92	0.97
80	0.0174	0.0005	0.0007	0.0162	0.0169	0.03	0.04	0.93	0.97
85	0.0170	0.0004	0.0006	0.0160	0.0166	0.02	0.04	0.94	0.98
90	0.0167	0.0003	0.0006	0.0158	0.0164	0.02	0.03	0.95	0.98
95	0.0165	0.0003	0.0005	0.0157	0.0162	0.02	0.03	0.95	0.98
100	0.0162	0.0002	0.0005	0.0155	0.0160	0.01	0.03	0.96	0.99

Table VII-13: Total mean mass attenuation coefficients $\mu/\rho\,(E)_{\mathrm{mix}}$ of oven-dry Fmat as sum of the single coefficients following eq. (II-14) for the attenuation processes photoelectric absorption (photo), coherent scattering (coh), and incoherent scattering (incoh) as well as scattering coefficient (scat = coh + incoh) for a practice-oriented energy range (incl. particular device energies, bold, refer to Table VII-2) determined on basis of analysis data (Table IV-15) via eq. (II-31) by means of XCOM (2010) elemental data (Table VII-3 to Table VII-9), complete with the attenuation fractions $\xi(i)$ following eq. (II-15) of the single mechanisms.

UF-C

Energy	$\frac{\mu_i}{\rho}(E)$ [m²/kg]					$\xi(i)$ [−]			
E [keV]	total	photo	coh	incoh	scat	photo	coh	incoh	scat
5	3.0824	3.0258	0.0459	0.0107	0.0566	0.98	0.01	0.00	0.02
6	1.7776	1.7285	0.0370	0.0119	0.0489	0.97	0.02	0.01	0.03
7	1.1157	1.0724	0.0306	0.0128	0.0434	0.96	0.03	0.01	0.04
8	0.7466	0.7072	0.0259	0.0135	0.0394	0.95	0.03	0.02	0.05
9	0.5252	0.4887	0.0223	0.0141	0.0365	0.93	0.04	0.03	0.07
10	0.3847	0.3506	0.0196	0.0146	0.0341	0.91	0.05	0.04	0.09
11	0.2916	0.2593	0.0173	0.0150	0.0323	0.89	0.06	0.05	0.11
12	0.2274	0.1966	0.0155	0.0153	0.0308	0.86	0.07	0.07	0.14
12.7	**0.1940**	**0.1641**	**0.0144**	**0.0155**	**0.0299**	**0.85**	**0.07**	**0.08**	**0.15**
13	0.1818	0.1523	0.0140	0.0156	0.0296	0.84	0.08	0.09	0.16
14	0.1486	0.1201	0.0127	0.0159	0.0285	0.81	0.09	0.11	0.19
15	0.1239	0.0963	0.0116	0.0161	0.0276	0.78	0.09	0.13	0.22
15.5	**0.1139**	**0.0866**	**0.0110**	**0.0162**	**0.0272**	**0.76**	**0.10**	**0.14**	**0.24**
16	0.1051	0.0782	0.0106	0.0163	0.0269	0.74	0.10	0.15	0.26
16.9	**0.0918**	**0.0656**	**0.0098**	**0.0164**	**0.0262**	**0.71**	**0.11**	**0.18**	**0.29**
17	0.0905	0.0643	0.0097	0.0165	0.0262	0.71	0.11	0.18	0.29
18	0.0791	0.0535	0.0090	0.0166	0.0256	0.68	0.11	0.21	0.32
19	0.0699	0.0449	0.0083	0.0168	0.0250	0.64	0.12	0.24	0.36
20	0.0626	0.0380	0.0077	0.0169	0.0245	0.61	0.12	0.27	0.39
21	0.0566	0.0325	0.0071	0.0170	0.0241	0.57	0.13	0.30	0.43
21.1	**0.0560**	**0.0320**	**0.0071**	**0.0170**	**0.0241**	**0.57**	**0.13**	**0.30**	**0.43**
21.2	**0.0555**	**0.0315**	**0.0070**	**0.0170**	**0.0240**	**0.57**	**0.13**	**0.31**	**0.43**
21.5	**0.0540**	**0.0301**	**0.0069**	**0.0170**	**0.0239**	**0.56**	**0.13**	**0.32**	**0.44**
22	0.0516	0.0279	0.0066	0.0171	0.0237	0.54	0.13	0.33	0.46
23	0.0475	0.0241	0.0062	0.0171	0.0233	0.51	0.13	0.36	0.49
24	0.0440	0.0210	0.0058	0.0172	0.0230	0.48	0.13	0.39	0.52
24.2	**0.0434**	**0.0205**	**0.0057**	**0.0172**	**0.0230**	**0.47**	**0.13**	**0.40**	**0.53**
25	0.0411	0.0184	0.0054	0.0173	0.0227	0.45	0.13	0.42	0.55
26	0.0386	0.0162	0.0051	0.0173	0.0224	0.42	0.13	0.45	0.58
26.3	**0.0379**	**0.0156**	**0.0050**	**0.0173**	**0.0224**	**0.41**	**0.13**	**0.46**	**0.59**
27	0.0365	0.0143	0.0048	0.0174	0.0222	0.39	0.13	0.48	0.61
27.3	**0.0359**	**0.0138**	**0.0047**	**0.0174**	**0.0221**	**0.38**	**0.13**	**0.48**	**0.62**
28	0.0346	0.0127	0.0045	0.0174	0.0219	0.37	0.13	0.50	0.63
29	0.0330	0.0113	0.0043	0.0174	0.0217	0.34	0.13	0.53	0.66
29.2	**0.0327**	**0.0111**	**0.0042**	**0.0174**	**0.0217**	**0.34**	**0.13**	**0.53**	**0.66**
30	0.0316	0.0101	0.0040	0.0174	0.0215	0.32	0.13	0.55	0.68
31	0.0304	0.0091	0.0038	0.0175	0.0213	0.30	0.13	0.57	0.70
32	0.0293	0.0082	0.0036	0.0175	0.0211	0.28	0.12	0.60	0.72
33	0.0283	0.0074	0.0034	0.0175	0.0209	0.26	0.12	0.62	0.74
34	0.0275	0.0067	0.0033	0.0175	0.0207	0.24	0.12	0.64	0.76
35	0.0267	0.0061	0.0031	0.0175	0.0206	0.23	0.12	0.65	0.77
35.1	**0.0266**	**0.0060**	**0.0031**	**0.0175**	**0.0206**	**0.23**	**0.12**	**0.66**	**0.77**
35.4	**0.0264**	**0.0059**	**0.0030**	**0.0175**	**0.0205**	**0.22**	**0.12**	**0.66**	**0.78**

UF-C

Energy	$\frac{\mu_i}{\rho}(E)$ [m²/kg]					$\xi(i)$ [−]			
E [keV]	total	photo	coh	incoh	scat	photo	coh	incoh	scat
36	0.0260	0.0056	0.0030	0.0175	0.0204	0.21	0.11	0.67	0.79
37	0.0254	0.0051	0.0028	0.0175	0.0203	0.20	0.11	0.69	0.80
38	0.0248	0.0047	0.0027	0.0175	0.0202	0.19	0.11	0.70	0.81
39	0.0243	0.0043	0.0026	0.0174	0.0200	0.18	0.11	0.72	0.82
40	0.0238	0.0039	0.0025	0.0174	0.0199	0.17	0.10	0.73	0.84
41	0.0234	0.0036	0.0024	0.0174	0.0198	0.15	0.10	0.74	0.84
42	0.0230	0.0033	0.0023	0.0174	0.0197	0.15	0.10	0.76	0.85
43	0.0226	0.0031	0.0022	0.0174	0.0195	0.14	0.10	0.77	0.86
44	0.0223	0.0029	0.0021	0.0174	0.0194	0.13	0.09	0.78	0.87
45	0.0220	0.0027	0.0020	0.0173	0.0193	0.12	0.09	0.79	0.88
46	0.0217	0.0025	0.0019	0.0173	0.0192	0.11	0.09	0.80	0.89
47	0.0214	0.0023	0.0019	0.0173	0.0191	0.11	0.09	0.81	0.89
48	0.0212	0.0022	0.0018	0.0172	0.0190	0.10	0.08	0.81	0.90
49	0.0210	0.0020	0.0017	0.0172	0.0189	0.10	0.08	0.82	0.90
50	0.0207	0.0019	0.0017	0.0172	0.0189	0.09	0.08	0.83	0.91
50.9	**0.0205**	**0.0018**	**0.0016**	**0.0172**	**0.0188**	**0.09**	**0.08**	**0.84**	**0.91**
51	0.0205	0.0018	0.0016	0.0172	0.0188	0.09	0.08	0.84	0.91
51.3	**0.0205**	**0.0017**	**0.0016**	**0.0172**	**0.0187**	**0.08**	**0.08**	**0.84**	**0.92**
52	0.0203	0.0017	0.0015	0.0171	0.0187	0.08	0.08	0.84	0.92
53	0.0201	0.0016	0.0015	0.0171	0.0186	0.08	0.07	0.85	0.92
54	0.0200	0.0015	0.0014	0.0171	0.0185	0.07	0.07	0.85	0.93
55	0.0198	0.0014	0.0014	0.0170	0.0184	0.07	0.07	0.86	0.93
56	0.0196	0.0013	0.0013	0.0170	0.0184	0.07	0.07	0.87	0.93
57	0.0195	0.0012	0.0013	0.0170	0.0183	0.06	0.07	0.87	0.94
58	0.0194	0.0012	0.0013	0.0169	0.0182	0.06	0.07	0.88	0.94
59	0.0192	0.0011	0.0012	0.0169	0.0181	0.06	0.06	0.88	0.94
59.5	**0.0192**	**0.0011**	**0.0012**	**0.0169**	**0.0181**	**0.06**	**0.06**	**0.88**	**0.94**
60	0.0191	0.0010	0.0012	0.0169	0.0181	0.05	0.06	0.88	0.95
65	0.0185	0.0008	0.0010	0.0167	0.0177	0.04	0.06	0.90	0.96
70	0.0180	0.0006	0.0009	0.0165	0.0174	0.03	0.05	0.92	0.97
75	0.0176	0.0005	0.0008	0.0163	0.0171	0.03	0.04	0.93	0.97
80	0.0173	0.0004	0.0007	0.0162	0.0169	0.02	0.04	0.94	0.98
85	0.0169	0.0003	0.0006	0.0160	0.0166	0.02	0.04	0.94	0.98
90	0.0166	0.0003	0.0006	0.0158	0.0164	0.02	0.03	0.95	0.98
95	0.0164	0.0002	0.0005	0.0157	0.0162	0.01	0.03	0.96	0.99
100	0.0161	0.0002	0.0005	0.0155	0.0159	0.01	0.03	0.96	0.99

Table VII-14: Total mean mass attenuation coefficients $\mu/\rho\,(E)_{\text{mix}}$ of UF-C as sum of the single coefficients following eq. (II-14) for the attenuation processes photoelectric absorption (photo), coherent scattering (coh), and incoherent scattering (incoh) as well as scattering coefficient (scat = coh + incoh) for a practice-oriented energy range (incl. particular device energies, bold, refer to Table VII-2) determined on basis of analysis data (Table IV-15) via eq. (II-31) by means of XCOM (2010) elemental data (Table VII-3 to Table VII-9), complete with the attenuation fractions $\xi(i)$ following eq. (II-15) of the single mechanisms.

indMDF oven-dry

Energy					$\frac{\mu_i}{\rho}(E)$ [m²/kg]				$\xi(i)$ [−]
E [keV]	total	photo	coh	incoh	scat	photo	coh	incoh	scat
5	3.2247	3.1681	0.0457	0.0107	0.0564	0.98	0.01	0.00	0.02
6	1.8688	1.8195	0.0369	0.0119	0.0488	0.97	0.02	0.01	0.03
7	1.1777	1.1343	0.0306	0.0128	0.0434	0.96	0.03	0.01	0.04
8	0.7905	0.7511	0.0259	0.0136	0.0395	0.95	0.03	0.02	0.05
9	0.5575	0.5209	0.0224	0.0141	0.0365	0.93	0.04	0.03	0.07
10	0.4091	0.3749	0.0196	0.0146	0.0342	0.92	0.05	0.04	0.08
11	0.3104	0.2780	0.0174	0.0150	0.0324	0.90	0.06	0.05	0.10
12	0.2423	0.2114	0.0156	0.0153	0.0309	0.87	0.06	0.06	0.13
12.7	**0.2067**	**0.1767**	**0.0145**	**0.0156**	**0.0300**	**0.85**	**0.07**	**0.08**	**0.15**
13	0.1938	0.1641	0.0140	0.0156	0.0297	0.85	0.07	0.08	0.15
14	0.1584	0.1298	0.0127	0.0159	0.0286	0.82	0.08	0.10	0.18
15	0.1319	0.1042	0.0116	0.0161	0.0277	0.79	0.09	0.12	0.21
15.5	**0.1212**	**0.0939**	**0.0111**	**0.0162**	**0.0273**	**0.77**	**0.09**	**0.13**	**0.23**
16	0.1118	0.0848	0.0106	0.0163	0.0269	0.76	0.09	0.15	0.24
16.9	**0.0976**	**0.0713**	**0.0098**	**0.0165**	**0.0263**	**0.73**	**0.10**	**0.17**	**0.27**
17	0.0961	0.0699	0.0097	0.0165	0.0262	0.73	0.10	0.17	0.27
18	0.0839	0.0582	0.0090	0.0167	0.0256	0.69	0.11	0.20	0.31
19	0.0741	0.0490	0.0083	0.0168	0.0251	0.66	0.11	0.23	0.34
20	0.0661	0.0415	0.0077	0.0169	0.0246	0.63	0.12	0.26	0.37
21	0.0597	0.0355	0.0071	0.0170	0.0242	0.59	0.12	0.29	0.41
21.1	**0.0591**	**0.0350**	**0.0071**	**0.0170**	**0.0241**	**0.59**	**0.12**	**0.29**	**0.41**
21.2	**0.0585**	**0.0344**	**0.0070**	**0.0170**	**0.0241**	**0.59**	**0.12**	**0.29**	**0.41**
21.5	**0.0569**	**0.0329**	**0.0069**	**0.0171**	**0.0240**	**0.58**	**0.12**	**0.30**	**0.42**
22	0.0543	0.0306	0.0067	0.0171	0.0238	0.56	0.12	0.32	0.44
23	0.0499	0.0265	0.0062	0.0172	0.0234	0.53	0.12	0.34	0.47
24	0.0461	0.0231	0.0058	0.0173	0.0231	0.50	0.13	0.37	0.50
24.2	**0.0455**	**0.0225**	**0.0057**	**0.0173**	**0.0230**	**0.49**	**0.13**	**0.38**	**0.51**
25	0.0430	0.0202	0.0054	0.0173	0.0228	0.47	0.13	0.40	0.53
26	0.0403	0.0178	0.0051	0.0174	0.0225	0.44	0.13	0.43	0.56
26.3	**0.0396**	**0.0172**	**0.0050**	**0.0174**	**0.0224**	**0.43**	**0.13**	**0.44**	**0.57**
27	0.0380	0.0158	0.0048	0.0174	0.0222	0.41	0.13	0.46	0.58
27.3	**0.0373**	**0.0152**	**0.0047**	**0.0174**	**0.0221**	**0.41**	**0.13**	**0.47**	**0.59**
28	0.0360	0.0140	0.0045	0.0174	0.0220	0.39	0.13	0.48	0.61
29	0.0342	0.0125	0.0043	0.0175	0.0217	0.36	0.12	0.51	0.64
29.2	**0.0339**	**0.0122**	**0.0042**	**0.0175**	**0.0217**	**0.36**	**0.12**	**0.52**	**0.64**
30	0.0327	0.0112	0.0040	0.0175	0.0215	0.34	0.12	0.53	0.66
31	0.0314	0.0101	0.0038	0.0175	0.0213	0.32	0.12	0.56	0.68
32	0.0302	0.0091	0.0036	0.0175	0.0211	0.30	0.12	0.58	0.70
33	0.0292	0.0082	0.0034	0.0175	0.0210	0.28	0.12	0.60	0.72
34	0.0282	0.0074	0.0033	0.0175	0.0208	0.26	0.12	0.62	0.74
35	0.0274	0.0068	0.0031	0.0175	0.0206	0.25	0.11	0.64	0.75
35.1	**0.0273**	**0.0067**	**0.0031**	**0.0175**	**0.0206**	**0.25**	**0.11**	**0.64**	**0.75**
35.4	**0.0271**	**0.0065**	**0.0031**	**0.0175**	**0.0206**	**0.24**	**0.11**	**0.65**	**0.76**

indMDF oven-dry

Energy			$\frac{\mu_i}{\rho}(E)$ [m²/kg]					$\xi(i)$ [−]	
E [keV]	total	photo	coh	incoh	scat	photo	coh	incoh	scat
36	0.0267	0.0062	0.0030	0.0175	0.0205	0.23	0.11	0.66	0.77
37	0.0260	0.0057	0.0028	0.0175	0.0203	0.22	0.11	0.67	0.78
38	0.0254	0.0052	0.0027	0.0175	0.0202	0.20	0.11	0.69	0.80
39	0.0248	0.0048	0.0026	0.0175	0.0201	0.19	0.10	0.70	0.81
40	0.0243	0.0044	0.0025	0.0175	0.0199	0.18	0.10	0.72	0.82
41	0.0239	0.0040	0.0024	0.0174	0.0198	0.17	0.10	0.73	0.83
42	0.0234	0.0037	0.0023	0.0174	0.0197	0.16	0.10	0.74	0.84
43	0.0230	0.0035	0.0022	0.0174	0.0196	0.15	0.09	0.76	0.85
44	0.0227	0.0032	0.0021	0.0174	0.0195	0.14	0.09	0.77	0.86
45	0.0223	0.0030	0.0020	0.0174	0.0194	0.13	0.09	0.78	0.87
46	0.0220	0.0028	0.0019	0.0173	0.0193	0.13	0.09	0.79	0.87
47	0.0217	0.0026	0.0019	0.0173	0.0192	0.12	0.09	0.80	0.88
48	0.0215	0.0024	0.0018	0.0173	0.0191	0.11	0.08	0.80	0.89
49	0.0212	0.0023	0.0017	0.0173	0.0190	0.11	0.08	0.81	0.89
50	0.0210	0.0021	0.0017	0.0172	0.0189	0.10	0.08	0.82	0.90
50.9	**0.0208**	**0.0020**	**0.0016**	**0.0172**	**0.0188**	**0.10**	**0.08**	**0.83**	**0.90**
51	0.0208	0.0020	0.0016	0.0172	0.0188	0.10	0.08	0.83	0.91
51.3	**0.0207**	**0.0019**	**0.0016**	**0.0172**	**0.0188**	**0.09**	**0.08**	**0.83**	**0.91**
52	0.0206	0.0019	0.0015	0.0172	0.0187	0.09	0.08	0.83	0.91
53	0.0204	0.0017	0.0015	0.0171	0.0186	0.09	0.07	0.84	0.91
54	0.0202	0.0016	0.0014	0.0171	0.0186	0.08	0.07	0.85	0.92
55	0.0200	0.0015	0.0014	0.0171	0.0185	0.08	0.07	0.85	0.92
56	0.0198	0.0015	0.0014	0.0170	0.0184	0.07	0.07	0.86	0.93
57	0.0197	0.0014	0.0013	0.0170	0.0183	0.07	0.07	0.86	0.93
58	0.0195	0.0013	0.0013	0.0170	0.0182	0.07	0.06	0.87	0.93
59	0.0194	0.0012	0.0012	0.0169	0.0182	0.06	0.06	0.87	0.94
59.5	**0.0193**	**0.0012**	**0.0012**	**0.0169**	**0.0181**	**0.06**	**0.06**	**0.88**	**0.94**
60	0.0193	0.0012	0.0012	0.0169	0.0181	0.06	0.06	0.88	0.94
65	0.0187	0.0009	0.0010	0.0167	0.0178	0.05	0.06	0.90	0.95
70	0.0181	0.0007	0.0009	0.0166	0.0175	0.04	0.05	0.91	0.96
75	0.0177	0.0006	0.0008	0.0164	0.0172	0.03	0.04	0.92	0.97
80	0.0173	0.0004	0.0007	0.0162	0.0169	0.03	0.04	0.93	0.97
85	0.0170	0.0004	0.0006	0.0160	0.0166	0.02	0.04	0.94	0.98
90	0.0167	0.0003	0.0006	0.0159	0.0164	0.02	0.03	0.95	0.98
95	0.0164	0.0003	0.0005	0.0157	0.0162	0.02	0.03	0.95	0.98
100	0.0162	0.0002	0.0005	0.0155	0.0160	0.01	0.03	0.96	0.99

Table VII-15: Total mean mass attenuation coefficients $\mu/\rho\,(E)_{\mathrm{mix}}$ of oven-dry indMDF as sum of the single coefficients following eq. (II-14) for the attenuation processes photoelectric absorption (photo), coherent scattering (coh), and incoherent scattering (incoh) as well as scattering coefficient (scat = coh + incoh) for a practice-oriented energy range (incl. particular device energies, bold, refer to Table VII-2) determined on basis of analysis data (Table IV-15) via eq. (II-31) by means of XCOM (2010) elemental data (Table VII-3 to Table VII-9), complete with the attenuation fractions $\xi(i)$ following eq. (II-15) of the single mechanisms.

insulation oven-dry

Energy					$\frac{\mu_i}{\rho}(E)$ $[\mathrm{m}^2/\mathrm{kg}]$				$\xi(i)$ $[-]$
E [keV]	total	photo	coh	incoh	scat	photo	coh	incoh	scat
5	3.1428	3.0866	0.0453	0.0107	0.0560	0.98	0.01	0.00	0.02
6	1.8193	1.7704	0.0366	0.0119	0.0485	0.97	0.02	0.01	0.03
7	1.1455	1.1024	0.0303	0.0128	0.0432	0.96	0.03	0.01	0.04
8	0.7684	0.7293	0.0257	0.0135	0.0393	0.95	0.03	0.02	0.05
9	0.5417	0.5053	0.0222	0.0141	0.0363	0.93	0.04	0.03	0.07
10	0.3974	0.3634	0.0195	0.0146	0.0341	0.91	0.05	0.04	0.09
11	0.3015	0.2693	0.0173	0.0150	0.0323	0.89	0.06	0.05	0.11
12	0.2354	0.2046	0.0154	0.0153	0.0308	0.87	0.07	0.07	0.13
12.7	**0.2009**	**0.1710**	**0.0143**	**0.0156**	**0.0299**	**0.85**	**0.07**	**0.08**	**0.15**
13	0.1883	0.1588	0.0139	0.0156	0.0295	0.84	0.07	0.08	0.16
14	0.1540	0.1255	0.0126	0.0159	0.0285	0.81	0.08	0.10	0.19
15	0.1284	0.1007	0.0115	0.0161	0.0276	0.78	0.09	0.13	0.22
15.5	**0.1179**	**0.0907**	**0.0110**	**0.0162**	**0.0272**	**0.77**	**0.09**	**0.14**	**0.23**
16	0.1088	0.0820	0.0105	0.0163	0.0268	0.75	0.10	0.15	0.25
16.9	**0.0950**	**0.0688**	**0.0097**	**0.0165**	**0.0262**	**0.72**	**0.10**	**0.17**	**0.28**
17	0.0937	0.0675	0.0097	0.0165	0.0262	0.72	0.10	0.18	0.28
18	0.0818	0.0562	0.0089	0.0167	0.0256	0.69	0.11	0.20	0.31
19	0.0723	0.0472	0.0082	0.0168	0.0250	0.65	0.11	0.23	0.35
20	0.0646	0.0401	0.0076	0.0169	0.0245	0.62	0.12	0.26	0.38
21	0.0583	0.0342	0.0071	0.0170	0.0241	0.59	0.12	0.29	0.41
21.1	**0.0578**	**0.0337**	**0.0070**	**0.0170**	**0.0241**	**0.58**	**0.12**	**0.29**	**0.42**
21.2	**0.0572**	**0.0332**	**0.0070**	**0.0170**	**0.0240**	**0.58**	**0.12**	**0.30**	**0.42**
21.5	**0.0556**	**0.0317**	**0.0068**	**0.0171**	**0.0239**	**0.57**	**0.12**	**0.31**	**0.43**
22	0.0532	0.0295	0.0066	0.0171	0.0237	0.55	0.12	0.32	0.45
23	0.0489	0.0255	0.0062	0.0172	0.0233	0.52	0.13	0.35	0.48
24	0.0453	0.0222	0.0058	0.0173	0.0230	0.49	0.13	0.38	0.51
24.2	**0.0446**	**0.0216**	**0.0057**	**0.0173**	**0.0230**	**0.49**	**0.13**	**0.39**	**0.51**
25	0.0422	0.0195	0.0054	0.0173	0.0227	0.46	0.13	0.41	0.54
26	0.0396	0.0172	0.0051	0.0174	0.0224	0.43	0.13	0.44	0.57
26.3	**0.0389**	**0.0165**	**0.0050**	**0.0174**	**0.0224**	**0.43**	**0.13**	**0.45**	**0.58**
27	0.0373	0.0152	0.0048	0.0174	0.0222	0.41	0.13	0.47	0.59
27.3	**0.0367**	**0.0146**	**0.0047**	**0.0174**	**0.0221**	**0.40**	**0.13**	**0.47**	**0.60**
28	0.0354	0.0135	0.0045	0.0174	0.0219	0.38	0.13	0.49	0.62
29	0.0337	0.0120	0.0042	0.0175	0.0217	0.36	0.13	0.52	0.64
29.2	**0.0334**	**0.0118**	**0.0042**	**0.0175**	**0.0217**	**0.35**	**0.13**	**0.52**	**0.65**
30	0.0323	0.0108	0.0040	0.0175	0.0215	0.33	0.12	0.54	0.67
31	0.0310	0.0097	0.0038	0.0175	0.0213	0.31	0.12	0.57	0.69
32	0.0298	0.0087	0.0036	0.0175	0.0211	0.29	0.12	0.59	0.71
33	0.0288	0.0079	0.0034	0.0175	0.0209	0.27	0.12	0.61	0.73
34	0.0279	0.0072	0.0032	0.0175	0.0208	0.26	0.12	0.63	0.74
35	0.0271	0.0065	0.0031	0.0175	0.0206	0.24	0.11	0.65	0.76
35.1	**0.0270**	**0.0065**	**0.0031**	**0.0175**	**0.0206**	**0.24**	**0.11**	**0.65**	**0.76**
35.4	**0.0268**	**0.0063**	**0.0030**	**0.0175**	**0.0205**	**0.23**	**0.11**	**0.65**	**0.77**

insulation oven-dry

Energy	$\frac{\mu_i}{\rho}(E)$ [m²/kg]					$\xi(i)$ [−]			
E [keV]	total	photo	coh	incoh	scat	photo	coh	incoh	scat
36	0.0264	0.0059	0.0029	0.0175	0.0204	0.23	0.11	0.66	0.77
37	0.0257	0.0054	0.0028	0.0175	0.0203	0.21	0.11	0.68	0.79
38	0.0251	0.0050	0.0027	0.0175	0.0202	0.20	0.11	0.70	0.80
39	0.0246	0.0046	0.0026	0.0175	0.0200	0.19	0.10	0.71	0.81
40	0.0241	0.0042	0.0024	0.0175	0.0199	0.17	0.10	0.72	0.83
41	0.0237	0.0039	0.0023	0.0174	0.0198	0.16	0.10	0.74	0.84
42	0.0233	0.0036	0.0022	0.0174	0.0197	0.15	0.10	0.75	0.85
43	0.0229	0.0033	0.0022	0.0174	0.0196	0.15	0.09	0.76	0.85
44	0.0225	0.0031	0.0021	0.0174	0.0194	0.14	0.09	0.77	0.86
45	0.0222	0.0029	0.0020	0.0174	0.0193	0.13	0.09	0.78	0.87
46	0.0219	0.0027	0.0019	0.0173	0.0192	0.12	0.09	0.79	0.88
47	0.0216	0.0025	0.0018	0.0173	0.0191	0.11	0.08	0.80	0.89
48	0.0214	0.0023	0.0018	0.0173	0.0190	0.11	0.08	0.81	0.89
49	0.0211	0.0022	0.0017	0.0172	0.0190	0.10	0.08	0.82	0.90
50	0.0209	0.0020	0.0016	0.0172	0.0189	0.10	0.08	0.82	0.90
50.9	**0.0207**	**0.0019**	**0.0016**	**0.0172**	**0.0188**	**0.09**	**0.08**	**0.83**	**0.91**
51	0.0207	0.0019	0.0016	0.0172	0.0188	0.09	0.08	0.83	0.91
51.3	**0.0206**	**0.0019**	**0.0016**	**0.0172**	**0.0188**	**0.09**	**0.08**	**0.83**	**0.91**
52	0.0205	0.0018	0.0015	0.0172	0.0187	0.09	0.07	0.84	0.91
53	0.0203	0.0017	0.0015	0.0171	0.0186	0.08	0.07	0.84	0.92
54	0.0201	0.0016	0.0014	0.0171	0.0185	0.08	0.07	0.85	0.92
55	0.0199	0.0015	0.0014	0.0171	0.0184	0.07	0.07	0.86	0.93
56	0.0198	0.0014	0.0013	0.0170	0.0184	0.07	0.07	0.86	0.93
57	0.0196	0.0013	0.0013	0.0170	0.0183	0.07	0.07	0.87	0.93
58	0.0195	0.0012	0.0013	0.0170	0.0182	0.06	0.06	0.87	0.94
59	0.0193	0.0012	0.0012	0.0169	0.0181	0.06	0.06	0.88	0.94
59.5	**0.0193**	**0.0011**	**0.0012**	**0.0169**	**0.0181**	**0.06**	**0.06**	**0.88**	**0.94**
60	0.0192	0.0011	0.0012	0.0169	0.0181	0.06	0.06	0.88	0.94
65	0.0186	0.0009	0.0010	0.0167	0.0177	0.05	0.05	0.90	0.95
70	0.0181	0.0007	0.0009	0.0166	0.0174	0.04	0.05	0.91	0.96
75	0.0177	0.0005	0.0008	0.0164	0.0171	0.03	0.04	0.93	0.97
80	0.0173	0.0004	0.0007	0.0162	0.0169	0.02	0.04	0.94	0.97
85	0.0170	0.0004	0.0006	0.0160	0.0166	0.02	0.04	0.94	0.98
90	0.0167	0.0003	0.0006	0.0158	0.0164	0.02	0.03	0.95	0.98
95	0.0164	0.0002	0.0005	0.0157	0.0162	0.01	0.03	0.96	0.99
100	0.0162	0.0002	0.0005	0.0155	0.0160	0.01	0.03	0.96	0.99

Table VII-16: Total mean mass attenuation coefficients $\mu/\rho\,(E)_{\mathrm{mix}}$ of oven-dry insulation as sum of the single coefficients following eq. (II-14) for the attenuation processes photoelectric absorption (photo), coherent scattering (coh), and incoherent scattering (incoh) as well as scattering coefficient (scat = coh + incoh) for a practice-oriented energy range (incl. particular device energies, bold, refer to Table VII-2) determined on basis of analysis data (Table IV-15) via eq. (II-31) by means of XCOM (2010) elemental data (Table VII-3 to Table VII-9), complete with the attenuation fractions $\xi(i)$ following eq. (II-15) of the single mechanisms.

Water H$_2$O

Energy					$\frac{\mu_i}{\rho}(E)$ [m^2/kg]		$\xi(i)$ [$-$]		
E [keV]	total	photo	coh	incoh	scat	photo	coh	incoh	scat
5	4.2596	4.1922	0.0558	0.0112	0.0670	0.98	0.01	0.00	0.02
6	2.4646	2.4069	0.0449	0.0126	0.0575	0.98	0.02	0.01	0.02
7	1.5497	1.4992	0.0369	0.0136	0.0505	0.97	0.02	0.01	0.03
8	1.0372	0.9921	0.0310	0.0144	0.0454	0.96	0.03	0.01	0.04
9	0.7290	0.6875	0.0265	0.0150	0.0415	0.94	0.04	0.02	0.06
10	0.5330	0.4944	0.0231	0.0155	0.0386	0.93	0.04	0.03	0.07
11	0.4026	0.3664	0.0203	0.0159	0.0362	0.91	0.05	0.04	0.09
12	0.3126	0.2783	0.0181	0.0162	0.0343	0.89	0.06	0.05	0.11
12.7	**0.2657**	**0.2326**	**0.0167**	**0.0165**	**0.0332**	**0.88**	**0.06**	**0.06**	**0.12**
13	0.2487	0.2160	0.0162	0.0165	0.0327	0.87	0.07	0.07	0.13
14	0.2020	0.1706	0.0147	0.0168	0.0314	0.84	0.07	0.08	0.16
15	0.1673	0.1370	0.0133	0.0170	0.0303	0.82	0.08	0.10	0.18
15.5	**0.1531**	**0.1233**	**0.0127**	**0.0171**	**0.0298**	**0.80**	**0.08**	**0.11**	**0.19**
16	0.1408	0.1114	0.0122	0.0172	0.0294	0.79	0.09	0.12	0.21
16.9	**0.1221**	**0.0935**	**0.0113**	**0.0173**	**0.0286**	**0.77**	**0.09**	**0.14**	**0.23**
17	0.1203	0.0917	0.0112	0.0174	0.0285	0.76	0.09	0.14	0.24
18	0.1042	0.0764	0.0103	0.0175	0.0278	0.73	0.10	0.17	0.27
19	0.0913	0.0642	0.0095	0.0176	0.0272	0.70	0.10	0.19	0.30
20	0.0810	0.0544	0.0089	0.0177	0.0266	0.67	0.11	0.22	0.33
21	0.0725	0.0465	0.0082	0.0178	0.0261	0.64	0.11	0.25	0.36
21.1	**0.0718**	**0.0458**	**0.0082**	**0.0178**	**0.0260**	**0.64**	**0.11**	**0.25**	**0.36**
21.2	**0.0710**	**0.0451**	**0.0081**	**0.0178**	**0.0260**	**0.63**	**0.11**	**0.25**	**0.37**
21.5	**0.0689**	**0.0431**	**0.0080**	**0.0179**	**0.0258**	**0.63**	**0.12**	**0.26**	**0.37**
22	0.0656	0.0400	0.0077	0.0179	0.0256	0.61	0.12	0.27	0.39
23	0.0598	0.0346	0.0072	0.0180	0.0252	0.58	0.12	0.30	0.42
24	0.0549	0.0301	0.0067	0.0181	0.0248	0.55	0.12	0.33	0.45
24.2	**0.0540**	**0.0293**	**0.0066**	**0.0181**	**0.0247**	**0.54**	**0.12**	**0.33**	**0.46**
25	0.0508	0.0264	0.0063	0.0181	0.0244	0.52	0.12	0.36	0.48
26	0.0473	0.0232	0.0059	0.0182	0.0241	0.49	0.13	0.38	0.51
26.3	**0.0464**	**0.0224**	**0.0058**	**0.0182**	**0.0240**	**0.48**	**0.13**	**0.39**	**0.52**
27	0.0443	0.0206	0.0056	0.0182	0.0238	0.46	0.13	0.41	0.54
27.3	**0.0435**	**0.0198**	**0.0055**	**0.0182**	**0.0237**	**0.46**	**0.13**	**0.42**	**0.54**
28	0.0417	0.0183	0.0053	0.0182	0.0235	0.44	0.13	0.44	0.56
29	0.0395	0.0163	0.0050	0.0183	0.0232	0.41	0.13	0.46	0.59
29.2	**0.0391**	**0.0159**	**0.0049**	**0.0183**	**0.0232**	**0.41**	**0.13**	**0.47**	**0.59**
30	0.0376	0.0146	0.0047	0.0183	0.0230	0.39	0.12	0.49	0.61
31	0.0358	0.0131	0.0044	0.0183	0.0227	0.37	0.12	0.51	0.63
32	0.0343	0.0118	0.0042	0.0183	0.0225	0.34	0.12	0.53	0.66
33	0.0330	0.0107	0.0040	0.0183	0.0223	0.32	0.12	0.56	0.68
34	0.0318	0.0097	0.0038	0.0183	0.0221	0.30	0.12	0.58	0.70
35	0.0307	0.0088	0.0036	0.0183	0.0219	0.29	0.12	0.60	0.71
35.1	**0.0306**	**0.0087**	**0.0036**	**0.0183**	**0.0219**	**0.28**	**0.12**	**0.60**	**0.72**
35.4	**0.0304**	**0.0085**	**0.0036**	**0.0183**	**0.0219**	**0.28**	**0.12**	**0.60**	**0.72**

Water H_2O

Energy				$\frac{\mu_i}{\rho}(E)\ [\text{m}^2/\text{kg}]$					$\xi(i)\ [-]$
E [keV]	total	photo	coh	incoh	scat	photo	coh	incoh	scat
36	0.0298	0.0080	0.0034	0.0183	0.0218	0.27	0.12	0.61	0.73
37	0.0289	0.0073	0.0033	0.0183	0.0216	0.25	0.11	0.63	0.75
38	0.0282	0.0067	0.0031	0.0183	0.0214	0.24	0.11	0.65	0.76
39	0.0275	0.0062	0.0030	0.0183	0.0213	0.22	0.11	0.67	0.78
40	0.0268	0.0057	0.0029	0.0183	0.0211	0.21	0.11	0.68	0.79
41	0.0262	0.0052	0.0028	0.0183	0.0210	0.20	0.10	0.70	0.80
42	0.0257	0.0048	0.0026	0.0182	0.0209	0.19	0.10	0.71	0.81
43	0.0252	0.0045	0.0025	0.0182	0.0207	0.18	0.10	0.72	0.82
44	0.0248	0.0042	0.0024	0.0182	0.0206	0.17	0.10	0.73	0.83
45	0.0244	0.0039	0.0023	0.0182	0.0205	0.16	0.10	0.75	0.84
46	0.0240	0.0036	0.0022	0.0181	0.0204	0.15	0.09	0.76	0.85
47	0.0236	0.0033	0.0022	0.0181	0.0203	0.14	0.09	0.77	0.86
48	0.0233	0.0031	0.0021	0.0181	0.0202	0.13	0.09	0.78	0.87
49	0.0230	0.0029	0.0020	0.0181	0.0201	0.13	0.09	0.79	0.87
50	0.0227	0.0027	0.0019	0.0180	0.0200	0.12	0.09	0.79	0.88
50.9	**0.0224**	**0.0026**	**0.0019**	**0.0180**	**0.0199**	**0.11**	**0.08**	**0.80**	**0.89**
51	0.0224	0.0026	0.0019	0.0180	0.0199	0.11	0.08	0.80	0.89
51.3	**0.0223**	**0.0025**	**0.0018**	**0.0180**	**0.0198**	**0.11**	**0.08**	**0.81**	**0.89**
52	0.0222	0.0024	0.0018	0.0180	0.0198	0.11	0.08	0.81	0.89
53	0.0219	0.0022	0.0017	0.0179	0.0197	0.10	0.08	0.82	0.90
54	0.0217	0.0021	0.0017	0.0179	0.0196	0.10	0.08	0.83	0.90
55	0.0215	0.0020	0.0016	0.0179	0.0195	0.09	0.08	0.83	0.91
56	0.0213	0.0019	0.0016	0.0178	0.0194	0.09	0.07	0.84	0.91
57	0.0211	0.0018	0.0015	0.0178	0.0193	0.08	0.07	0.84	0.92
58	0.0209	0.0017	0.0015	0.0178	0.0193	0.08	0.07	0.85	0.92
59	0.0208	0.0016	0.0014	0.0177	0.0192	0.08	0.07	0.85	0.92
59.5	**0.0207**	**0.0015**	**0.0014**	**0.0177**	**0.0191**	**0.07**	**0.07**	**0.86**	**0.93**
60	0.0206	0.0015	0.0014	0.0177	0.0191	0.07	0.07	0.86	0.93
65	0.0199	0.0011	0.0012	0.0175	0.0187	0.06	0.06	0.88	0.94
70	0.0193	0.0009	0.0010	0.0173	0.0184	0.05	0.05	0.90	0.95
75	0.0188	0.0007	0.0009	0.0172	0.0181	0.04	0.05	0.91	0.96
80	0.0184	0.0006	0.0008	0.0170	0.0178	0.03	0.04	0.92	0.97
85	0.0180	0.0005	0.0007	0.0168	0.0175	0.03	0.04	0.93	0.97
90	0.0177	0.0004	0.0007	0.0166	0.0173	0.02	0.04	0.94	0.98
95	0.0173	0.0003	0.0006	0.0164	0.0170	0.02	0.03	0.95	0.98
100	0.0171	0.0003	0.0005	0.0163	0.0168	0.02	0.03	0.95	0.98

Table VII-17: Total mean mass attenuation coefficients $\mu/\rho\,(E)_{\text{mix}}$ of water H_2O as sum of the single coefficients following eq. (II-14) for the attenuation processes photoelectric absorption (photo), coherent scattering (coh), and incoherent scattering (incoh) as well as scattering coefficient (scat = coh + incoh) for a practice-oriented energy range (incl. particular device energies, bold, refer to Table VII-2) determined on basis of empirical and literature data (Table IV-14) via eq. (II-31) by means of XCOM (2010) elemental data (Table VII-3 to Table VII-9), complete with the attenuation fractions $\xi(i)$ following eq. (II-15) of the single mechanisms.

Wood (simplistic) oven-dry

Energy			$\frac{\mu_i}{\rho}(E)$ [m^2/kg]					$\xi(i)$ [−]	
E [keV]	total	photo	coh	incoh	scat	photo	coh	incoh	scat
5	3.0666	3.0100	0.0456	0.0107	0.0563	0.98	0.01	0.00	0.02
6	1.7687	1.7195	0.0369	0.0119	0.0488	0.97	0.02	0.01	0.03
7	1.1103	1.0669	0.0305	0.0128	0.0434	0.96	0.03	0.01	0.04
8	0.7429	0.7036	0.0259	0.0136	0.0394	0.95	0.03	0.02	0.05
9	0.5226	0.4862	0.0223	0.0141	0.0364	0.93	0.04	0.03	0.07
10	0.3829	0.3488	0.0195	0.0146	0.0341	0.91	0.05	0.04	0.09
11	0.2902	0.2579	0.0173	0.0150	0.0323	0.89	0.06	0.05	0.11
12	0.2264	0.1956	0.0155	0.0154	0.0308	0.86	0.07	0.07	0.14
12.7	**0.1931**	**0.1632**	**0.0144**	**0.0156**	**0.0299**	**0.85**	**0.07**	**0.08**	**0.16**
13	0.1811	0.1515	0.0139	0.0156	0.0296	0.84	0.08	0.09	0.16
14	0.1480	0.1195	0.0126	0.0159	0.0285	0.81	0.09	0.11	0.19
15	0.1234	0.0958	0.0115	0.0161	0.0276	0.78	0.09	0.13	0.22
15.5	**0.1134**	**0.0862**	**0.0110**	**0.0162**	**0.0272**	**0.76**	**0.10**	**0.14**	**0.24**
16	0.1047	0.0778	0.0105	0.0163	0.0269	0.74	0.10	0.16	0.26
16.9	**0.0915**	**0.0652**	**0.0097**	**0.0165**	**0.0262**	**0.71**	**0.11**	**0.18**	**0.29**
17	0.0902	0.0640	0.0097	0.0165	0.0262	0.71	0.11	0.18	0.29
18	0.0788	0.0532	0.0089	0.0167	0.0256	0.68	0.11	0.21	0.32
19	0.0697	0.0447	0.0082	0.0168	0.0250	0.64	0.12	0.24	0.36
20	0.0624	0.0378	0.0076	0.0169	0.0246	0.61	0.12	0.27	0.39
21	0.0564	0.0323	0.0071	0.0170	0.0241	0.57	0.13	0.30	0.43
21.1	**0.0559**	**0.0318**	**0.0070**	**0.0170**	**0.0241**	**0.57**	**0.13**	**0.31**	**0.43**
21.2	**0.0554**	**0.0313**	**0.0070**	**0.0171**	**0.0240**	**0.57**	**0.13**	**0.31**	**0.43**
21.5	**0.0538**	**0.0299**	**0.0068**	**0.0171**	**0.0239**	**0.56**	**0.13**	**0.32**	**0.44**
22	0.0515	0.0278	0.0066	0.0171	0.0237	0.54	0.13	0.33	0.46
23	0.0474	0.0240	0.0062	0.0172	0.0234	0.51	0.13	0.36	0.49
24	0.0439	0.0209	0.0058	0.0173	0.0230	0.48	0.13	0.39	0.52
24.2	**0.0433**	**0.0203**	**0.0057**	**0.0173**	**0.0230**	**0.47**	**0.13**	**0.40**	**0.53**
25	0.0410	0.0183	0.0054	0.0173	0.0227	0.45	0.13	0.42	0.55
26	0.0385	0.0161	0.0051	0.0174	0.0224	0.42	0.13	0.45	0.58
26.3	**0.0379**	**0.0155**	**0.0050**	**0.0174**	**0.0224**	**0.41**	**0.13**	**0.46**	**0.59**
27	0.0364	0.0142	0.0048	0.0174	0.0222	0.39	0.13	0.48	0.61
27.3	**0.0358**	**0.0137**	**0.0047**	**0.0174**	**0.0221**	**0.38**	**0.13**	**0.49**	**0.62**
28	0.0346	0.0126	0.0045	0.0174	0.0219	0.37	0.13	0.50	0.63
29	0.0330	0.0113	0.0042	0.0175	0.0217	0.34	0.13	0.53	0.66
29.2	**0.0327**	**0.0110**	**0.0042**	**0.0175**	**0.0217**	**0.34**	**0.13**	**0.53**	**0.66**
30	0.0316	0.0101	0.0040	0.0175	0.0215	0.32	0.13	0.55	0.68
31	0.0304	0.0090	0.0038	0.0175	0.0213	0.30	0.13	0.58	0.70
32	0.0293	0.0082	0.0036	0.0175	0.0211	0.28	0.12	0.60	0.72
33	0.0283	0.0074	0.0034	0.0175	0.0209	0.26	0.12	0.62	0.74
34	0.0275	0.0067	0.0032	0.0175	0.0208	0.24	0.12	0.64	0.76
35	0.0267	0.0061	0.0031	0.0175	0.0206	0.23	0.12	0.66	0.77
35.1	**0.0266**	**0.0060**	**0.0031**	**0.0175**	**0.0206**	**0.23**	**0.12**	**0.66**	**0.77**
35.4	**0.0264**	**0.0058**	**0.0030**	**0.0175**	**0.0206**	**0.22**	**0.11**	**0.66**	**0.78**

continued from page 396

Wood (simplistic) oven-dry

Energy				$\frac{\mu_i}{\rho}(E)$ [m^2/kg]				$\xi(i)$ [$-$]
E [keV]	total	photo	coh	incoh	scat	photo	coh	incoh	scat
36	0.0260	0.0055	0.0029	0.0175	0.0205	0.21	0.11	0.67	0.79
37	0.0254	0.0051	0.0028	0.0175	0.0203	0.20	0.11	0.69	0.80
38	0.0248	0.0046	0.0027	0.0175	0.0202	0.19	0.11	0.71	0.81
39	0.0243	0.0043	0.0026	0.0175	0.0200	0.17	0.11	0.72	0.82
40	0.0238	0.0039	0.0024	0.0175	0.0199	0.16	0.10	0.73	0.84
41	0.0234	0.0036	0.0023	0.0175	0.0198	0.15	0.10	0.75	0.85
42	0.0230	0.0033	0.0022	0.0174	0.0197	0.14	0.10	0.76	0.86
43	0.0227	0.0031	0.0022	0.0174	0.0196	0.14	0.10	0.77	0.86
44	0.0223	0.0029	0.0021	0.0174	0.0195	0.13	0.09	0.78	0.87
45	0.0220	0.0027	0.0020	0.0174	0.0194	0.12	0.09	0.79	0.88
46	0.0217	0.0025	0.0019	0.0173	0.0193	0.11	0.09	0.80	0.89
47	0.0215	0.0023	0.0018	0.0173	0.0192	0.11	0.09	0.81	0.89
48	0.0212	0.0021	0.0018	0.0173	0.0191	0.10	0.08	0.82	0.90
49	0.0210	0.0020	0.0017	0.0173	0.0190	0.10	0.08	0.82	0.90
50	0.0208	0.0019	0.0016	0.0172	0.0189	0.09	0.08	0.83	0.91
50.9	**0.0206**	**0.0018**	**0.0016**	**0.0172**	**0.0188**	**0.09**	**0.08**	**0.84**	**0.91**
51	0.0205	0.0018	0.0016	0.0172	0.0188	0.09	0.08	0.84	0.91
51.3	**0.0205**	**0.0017**	**0.0016**	**0.0172**	**0.0188**	**0.08**	**0.08**	**0.84**	**0.92**
52	0.0204	0.0016	0.0015	0.0172	0.0187	0.08	0.08	0.84	0.92
53	0.0202	0.0015	0.0015	0.0171	0.0186	0.08	0.07	0.85	0.92
54	0.0200	0.0015	0.0014	0.0171	0.0185	0.07	0.07	0.86	0.93
55	0.0198	0.0014	0.0014	0.0171	0.0185	0.07	0.07	0.86	0.93
56	0.0197	0.0013	0.0013	0.0170	0.0184	0.07	0.07	0.87	0.93
57	0.0195	0.0012	0.0013	0.0170	0.0183	0.06	0.07	0.87	0.94
58	0.0194	0.0011	0.0013	0.0170	0.0182	0.06	0.06	0.88	0.94
59	0.0192	0.0011	0.0012	0.0169	0.0182	0.06	0.06	0.88	0.94
59.5	**0.0192**	**0.0011**	**0.0012**	**0.0169**	**0.0181**	**0.05**	**0.06**	**0.88**	**0.95**
60	0.0191	0.0010	0.0012	0.0169	0.0181	0.05	0.06	0.88	0.95
65	0.0185	0.0008	0.0010	0.0167	0.0178	0.04	0.05	0.90	0.96
70	0.0181	0.0006	0.0009	0.0166	0.0174	0.03	0.05	0.92	0.97
75	0.0177	0.0005	0.0008	0.0164	0.0172	0.03	0.04	0.93	0.97
80	0.0173	0.0004	0.0007	0.0162	0.0169	0.02	0.04	0.94	0.98
85	0.0170	0.0003	0.0006	0.0160	0.0166	0.02	0.04	0.94	0.98
90	0.0167	0.0003	0.0006	0.0159	0.0164	0.02	0.03	0.95	0.98
95	0.0164	0.0002	0.0005	0.0157	0.0162	0.01	0.03	0.96	0.99
100	0.0162	0.0002	0.0005	0.0155	0.0160	0.01	0.03	0.96	0.99

Table VII-18: Total mean mass attenuation coefficients $\mu/\rho\,(E)_{\mathrm{mix}}$ of oven-dry wood (simplistic) as sum of the single coefficients following eq. (II-14) for the attenuation processes photoelectric absorption (photo), coherent scattering (coh), and incoherent scattering (incoh) as well as scattering coefficient (scat = coh + incoh) for a practice-oriented energy range (incl. particular device energies, bold, refer to Table VII-2) determined on basis of empirical and literature data (Table IV-14) via eq. (II-31) by means of XCOM (2010) elemental data (Table VII-3 to Table VII-9), complete with the attenuation fractions $\xi(i)$ following eq. (II-15) of the single mechanisms.

Wood (total mean) oven-dry

Energy								
				$\frac{\mu_i}{\rho}(E)$ $[\text{m}^2/\text{kg}]$				$\xi(i)$ $[-]$
E [keV]	total	photo	coh	incoh	scat	photo	coh	incoh	scat
5	3.2925	3.2355	0.0461	0.0107	0.0568	0.98	0.01	0.00	0.02
6	1.9096	1.8600	0.0372	0.0119	0.0491	0.97	0.02	0.01	0.03
7	1.2041	1.1604	0.0309	0.0128	0.0437	0.96	0.03	0.01	0.04
8	0.8086	0.7690	0.0262	0.0136	0.0397	0.95	0.03	0.02	0.05
9	0.5704	0.5337	0.0226	0.0141	0.0367	0.94	0.04	0.02	0.06
10	0.4186	0.3842	0.0198	0.0146	0.0344	0.92	0.05	0.03	0.08
11	0.3176	0.2851	0.0175	0.0150	0.0325	0.90	0.06	0.05	0.10
12	0.2479	0.2168	0.0157	0.0154	0.0310	0.87	0.06	0.06	0.13
12.7	**0.2115**	**0.1814**	**0.0146**	**0.0156**	**0.0301**	**0.86**	**0.07**	**0.07**	**0.14**
13	0.1982	0.1685	0.0141	0.0157	0.0298	0.85	0.07	0.08	0.15
14	0.1619	0.1332	0.0128	0.0159	0.0287	0.82	0.08	0.10	0.18
15	0.1349	0.1071	0.0117	0.0161	0.0278	0.79	0.09	0.12	0.21
15.5	**0.1238**	**0.0964**	**0.0111**	**0.0162**	**0.0274**	**0.78**	**0.09**	**0.13**	**0.22**
16	0.1142	0.0872	0.0107	0.0164	0.0270	0.76	0.09	0.14	0.24
16.9	**0.0996**	**0.0732**	**0.0099**	**0.0165**	**0.0264**	**0.74**	**0.10**	**0.17**	**0.26**
17	0.0982	0.0719	0.0098	0.0165	0.0263	0.73	0.10	0.17	0.27
18	0.0856	0.0599	0.0090	0.0167	0.0257	0.70	0.11	0.20	0.30
19	0.0755	0.0503	0.0084	0.0168	0.0252	0.67	0.11	0.22	0.33
20	0.0674	0.0427	0.0077	0.0169	0.0247	0.63	0.11	0.25	0.37
21	0.0608	0.0365	0.0072	0.0170	0.0242	0.60	0.12	0.28	0.40
21.1	**0.0602**	**0.0360**	**0.0071**	**0.0171**	**0.0242**	**0.60**	**0.12**	**0.28**	**0.40**
21.2	**0.0596**	**0.0354**	**0.0071**	**0.0171**	**0.0242**	**0.59**	**0.12**	**0.29**	**0.41**
21.5	**0.0579**	**0.0339**	**0.0069**	**0.0171**	**0.0240**	**0.58**	**0.12**	**0.30**	**0.42**
22	0.0553	0.0314	0.0067	0.0171	0.0238	0.57	0.12	0.31	0.43
23	0.0507	0.0272	0.0063	0.0172	0.0235	0.54	0.12	0.34	0.46
24	0.0469	0.0238	0.0058	0.0173	0.0231	0.51	0.12	0.37	0.49
24.2	**0.0462**	**0.0231**	**0.0058**	**0.0173**	**0.0231**	**0.50**	**0.12**	**0.37**	**0.50**
25	0.0436	0.0208	0.0055	0.0173	0.0228	0.48	0.13	0.40	0.52
26	0.0409	0.0183	0.0051	0.0174	0.0225	0.45	0.13	0.43	0.55
26.3	**0.0401**	**0.0177**	**0.0051**	**0.0174**	**0.0225**	**0.44**	**0.13**	**0.43**	**0.56**
27	0.0385	0.0162	0.0048	0.0174	0.0223	0.42	0.13	0.45	0.58
27.3	**0.0379**	**0.0157**	**0.0048**	**0.0174**	**0.0222**	**0.41**	**0.13**	**0.46**	**0.59**
28	0.0364	0.0144	0.0046	0.0175	0.0220	0.40	0.13	0.48	0.60
29	0.0347	0.0129	0.0043	0.0175	0.0218	0.37	0.12	0.50	0.63
29.2	**0.0343**	**0.0126**	**0.0043**	**0.0175**	**0.0217**	**0.37**	**0.12**	**0.51**	**0.63**
30	0.0331	0.0115	0.0041	0.0175	0.0216	0.35	0.12	0.53	0.65
31	0.0317	0.0104	0.0039	0.0175	0.0214	0.33	0.12	0.55	0.67
32	0.0305	0.0094	0.0037	0.0175	0.0212	0.31	0.12	0.57	0.69
33	0.0295	0.0085	0.0035	0.0175	0.0210	0.29	0.12	0.60	0.71
34	0.0285	0.0077	0.0033	0.0175	0.0208	0.27	0.12	0.62	0.73
35	0.0277	0.0070	0.0031	0.0175	0.0207	0.25	0.11	0.63	0.75
35.1	**0.0276**	**0.0069**	**0.0031**	**0.0175**	**0.0207**	**0.25**	**0.11**	**0.64**	**0.75**
35.4	**0.0273**	**0.0067**	**0.0031**	**0.0175**	**0.0206**	**0.25**	**0.11**	**0.64**	**0.75**

Wood (total mean) oven-dry

Energy				$\frac{\mu_i}{\rho}(E)$ [m²/kg]				$\xi(i)$ [−]
E [keV]	total	photo	coh	incoh	scat	photo	coh	incoh	scat
36	0.0269	0.0064	0.0030	0.0175	0.0205	0.24	0.11	0.65	0.76
37	0.0262	0.0058	0.0028	0.0175	0.0204	0.22	0.11	0.67	0.78
38	0.0256	0.0053	0.0027	0.0175	0.0202	0.21	0.11	0.68	0.79
39	0.0250	0.0049	0.0026	0.0175	0.0201	0.20	0.10	0.70	0.80
40	0.0245	0.0045	0.0025	0.0175	0.0200	0.18	0.10	0.71	0.82
41	0.0240	0.0042	0.0024	0.0175	0.0198	0.17	0.10	0.73	0.83
42	0.0236	0.0039	0.0023	0.0175	0.0197	0.16	0.10	0.74	0.84
43	0.0232	0.0036	0.0022	0.0174	0.0196	0.15	0.09	0.75	0.85
44	0.0228	0.0033	0.0021	0.0174	0.0195	0.15	0.09	0.76	0.86
45	0.0225	0.0031	0.0020	0.0174	0.0194	0.14	0.09	0.77	0.86
46	0.0222	0.0029	0.0019	0.0174	0.0193	0.13	0.09	0.78	0.87
47	0.0219	0.0027	0.0019	0.0173	0.0192	0.12	0.09	0.79	0.88
48	0.0216	0.0025	0.0018	0.0173	0.0191	0.12	0.08	0.80	0.88
49	0.0213	0.0023	0.0017	0.0173	0.0190	0.11	0.08	0.81	0.89
50	0.0211	0.0022	0.0017	0.0173	0.0189	0.10	0.08	0.82	0.90
50.9	**0.0209**	**0.0021**	**0.0016**	**0.0172**	**0.0188**	**0.10**	**0.08**	**0.82**	**0.90**
51	0.0209	0.0020	0.0016	0.0172	0.0188	0.10	0.08	0.83	0.90
51.3	**0.0208**	**0.0020**	**0.0016**	**0.0172**	**0.0188**	**0.10**	**0.08**	**0.83**	**0.90**
52	0.0207	0.0019	0.0016	0.0172	0.0187	0.09	0.08	0.83	0.91
53	0.0205	0.0018	0.0015	0.0172	0.0187	0.09	0.07	0.84	0.91
54	0.0203	0.0017	0.0015	0.0171	0.0186	0.08	0.07	0.85	0.92
55	0.0201	0.0016	0.0014	0.0171	0.0185	0.08	0.07	0.85	0.92
56	0.0199	0.0015	0.0014	0.0171	0.0184	0.08	0.07	0.86	0.92
57	0.0198	0.0014	0.0013	0.0170	0.0183	0.07	0.07	0.86	0.93
58	0.0196	0.0013	0.0013	0.0170	0.0183	0.07	0.07	0.87	0.93
59	0.0195	0.0013	0.0012	0.0170	0.0182	0.07	0.06	0.87	0.93
59.5	**0.0194**	**0.0012**	**0.0012**	**0.0169**	**0.0182**	**0.06**	**0.06**	**0.87**	**0.94**
60	0.0193	0.0012	0.0012	0.0169	0.0181	0.06	0.06	0.88	0.94
65	0.0187	0.0009	0.0010	0.0168	0.0178	0.05	0.06	0.90	0.95
70	0.0182	0.0007	0.0009	0.0166	0.0175	0.04	0.05	0.91	0.96
75	0.0178	0.0006	0.0008	0.0164	0.0172	0.03	0.04	0.92	0.97
80	0.0174	0.0005	0.0007	0.0162	0.0169	0.03	0.04	0.93	0.97
85	0.0171	0.0004	0.0006	0.0160	0.0167	0.02	0.04	0.94	0.98
90	0.0167	0.0003	0.0006	0.0159	0.0164	0.02	0.03	0.95	0.98
95	0.0165	0.0003	0.0005	0.0157	0.0162	0.02	0.03	0.95	0.98
100	0.0162	0.0002	0.0005	0.0155	0.0160	0.01	0.03	0.96	0.99

Table VII-19: Total mean mass attenuation coefficients $\mu/\rho\,(E)_{\mathrm{mix}}$ of oven-dry wood (total mean) as sum of the single coefficients following eq. (II-14) for the attenuation processes photoelectric absorption (photo), coherent scattering (coh), and incoherent scattering (incoh) as well as scattering coefficient (scat = coh + incoh) for a practice-oriented energy range (incl. particular device energies, bold, refer to Table VII-2) determined on basis of empirical and literature data (Table IV-14) via eq. (II-31) by means of XCOM (2010) elemental data (Table VII-3 to Table VII-9), complete with the attenuation fractions $\xi(i)$ following eq. (II-15) of the single mechanisms.

Cellulose (mean)

E [keV]	total	photo	coh	incoh	scat	photo	coh	incoh	scat
			$\frac{\mu_i}{\rho}(E)$ [m^2/kg]					$\xi(i)$ [−]	
5	3.2185	3.1606	0.0470	0.0107	0.0576	0.98	0.01	0.00	0.02
6	1.8572	1.8070	0.0379	0.0119	0.0498	0.97	0.02	0.01	0.03
7	1.1661	1.1219	0.0314	0.0128	0.0442	0.96	0.03	0.01	0.04
8	0.7802	0.7402	0.0266	0.0136	0.0401	0.95	0.03	0.02	0.05
9	0.5487	0.5117	0.0229	0.0141	0.0370	0.93	0.04	0.03	0.07
10	0.4019	0.3672	0.0200	0.0146	0.0346	0.91	0.05	0.04	0.09
11	0.3044	0.2716	0.0177	0.0150	0.0327	0.89	0.06	0.05	0.11
12	0.2372	0.2060	0.0158	0.0154	0.0312	0.87	0.07	0.06	0.13
12.7	**0.2022**	**0.1720**	**0.0147**	**0.0156**	**0.0303**	**0.85**	**0.07**	**0.08**	**0.15**
13	0.1896	0.1597	0.0143	0.0157	0.0299	0.84	0.08	0.08	0.16
14	0.1548	0.1260	0.0129	0.0159	0.0288	0.81	0.08	0.10	0.19
15	0.1289	0.1010	0.0118	0.0161	0.0279	0.78	0.09	0.13	0.22
15.5	**0.1184**	**0.0909**	**0.0112**	**0.0162**	**0.0275**	**0.77**	**0.09**	**0.14**	**0.23**
16	0.1092	0.0820	0.0108	0.0163	0.0271	0.75	0.10	0.15	0.25
16.9	**0.0953**	**0.0688**	**0.0100**	**0.0165**	**0.0265**	**0.72**	**0.10**	**0.17**	**0.28**
17	0.0939	0.0675	0.0099	0.0165	0.0264	0.72	0.11	0.18	0.28
18	0.0819	0.0561	0.0091	0.0167	0.0258	0.69	0.11	0.20	0.31
19	0.0724	0.0471	0.0084	0.0168	0.0252	0.65	0.12	0.23	0.35
20	0.0647	0.0399	0.0078	0.0169	0.0247	0.62	0.12	0.26	0.38
21	0.0584	0.0341	0.0073	0.0170	0.0243	0.58	0.12	0.29	0.42
21.1	**0.0578**	**0.0336**	**0.0072**	**0.0171**	**0.0243**	**0.58**	**0.12**	**0.30**	**0.42**
21.2	**0.0573**	**0.0330**	**0.0071**	**0.0171**	**0.0242**	**0.58**	**0.12**	**0.30**	**0.42**
21.5	**0.0557**	**0.0316**	**0.0070**	**0.0171**	**0.0241**	**0.57**	**0.13**	**0.31**	**0.43**
22	0.0532	0.0293	0.0068	0.0171	0.0239	0.55	0.13	0.32	0.45
23	0.0489	0.0254	0.0063	0.0172	0.0235	0.52	0.13	0.35	0.48
24	0.0453	0.0221	0.0059	0.0173	0.0232	0.49	0.13	0.38	0.51
24.2	**0.0446**	**0.0215**	**0.0058**	**0.0173**	**0.0231**	**0.48**	**0.13**	**0.39**	**0.52**
25	0.0422	0.0193	0.0055	0.0173	0.0229	0.46	0.13	0.41	0.54
26	0.0396	0.0170	0.0052	0.0174	0.0226	0.43	0.13	0.44	0.57
26.3	**0.0389**	**0.0164**	**0.0051**	**0.0174**	**0.0225**	**0.42**	**0.13**	**0.45**	**0.58**
27	0.0373	0.0150	0.0049	0.0174	0.0223	0.40	0.13	0.47	0.60
27.3	**0.0367**	**0.0145**	**0.0048**	**0.0174**	**0.0222**	**0.39**	**0.13**	**0.47**	**0.61**
28	0.0354	0.0133	0.0046	0.0175	0.0221	0.38	0.13	0.49	0.62
29	0.0337	0.0119	0.0043	0.0175	0.0218	0.35	0.13	0.52	0.65
29.2	**0.0334**	**0.0116**	**0.0043**	**0.0175**	**0.0218**	**0.35**	**0.13**	**0.52**	**0.65**
30	0.0323	0.0106	0.0041	0.0175	0.0216	0.33	0.13	0.54	0.67
31	0.0310	0.0096	0.0039	0.0175	0.0214	0.31	0.13	0.57	0.69
32	0.0298	0.0086	0.0037	0.0175	0.0212	0.29	0.12	0.59	0.71
33	0.0288	0.0078	0.0035	0.0175	0.0210	0.27	0.12	0.61	0.73
34	0.0279	0.0071	0.0033	0.0175	0.0209	0.25	0.12	0.63	0.75
35	0.0271	0.0064	0.0032	0.0175	0.0207	0.24	0.12	0.65	0.76
35.1	**0.0270**	**0.0064**	**0.0031**	**0.0175**	**0.0207**	**0.24**	**0.12**	**0.65**	**0.77**
35.4	**0.0268**	**0.0062**	**0.0031**	**0.0175**	**0.0206**	**0.23**	**0.12**	**0.65**	**0.77**

Cellulose (mean)

Energy									$\xi(i)$ [$-$]
				$\dfrac{\mu_i}{\rho}(E)$ [m²/kg]					
E [keV]	total	photo	coh	incoh	scat	photo	coh	incoh	scat
36	0.0264	0.0058	0.0030	0.0175	0.0205	0.22	0.11	0.66	0.78
37	0.0257	0.0053	0.0029	0.0175	0.0204	0.21	0.11	0.68	0.79
38	0.0252	0.0049	0.0027	0.0175	0.0203	0.19	0.11	0.70	0.81
39	0.0246	0.0045	0.0026	0.0175	0.0201	0.18	0.11	0.71	0.82
40	0.0241	0.0041	0.0025	0.0175	0.0200	0.17	0.10	0.72	0.83
41	0.0237	0.0038	0.0024	0.0175	0.0199	0.16	0.10	0.74	0.84
42	0.0233	0.0035	0.0023	0.0175	0.0198	0.15	0.10	0.75	0.85
43	0.0229	0.0033	0.0022	0.0174	0.0196	0.14	0.10	0.76	0.86
44	0.0225	0.0030	0.0021	0.0174	0.0195	0.13	0.09	0.77	0.87
45	0.0222	0.0028	0.0020	0.0174	0.0194	0.13	0.09	0.78	0.87
46	0.0219	0.0026	0.0020	0.0174	0.0193	0.12	0.09	0.79	0.88
47	0.0216	0.0024	0.0019	0.0173	0.0192	0.11	0.09	0.80	0.89
48	0.0214	0.0023	0.0018	0.0173	0.0191	0.11	0.08	0.81	0.89
49	0.0211	0.0021	0.0017	0.0173	0.0190	0.10	0.08	0.82	0.90
50	0.0209	0.0020	0.0017	0.0173	0.0189	0.09	0.08	0.82	0.91
50.9	**0.0207**	**0.0019**	**0.0016**	**0.0172**	**0.0189**	**0.09**	**0.08**	**0.83**	**0.91**
51	0.0207	0.0019	0.0016	0.0172	0.0189	0.09	0.08	0.83	0.91
51.3	**0.0206**	**0.0018**	**0.0016**	**0.0172**	**0.0188**	**0.09**	**0.08**	**0.83**	**0.91**
52	0.0205	0.0017	0.0016	0.0172	0.0188	0.08	0.08	0.84	0.92
53	0.0203	0.0016	0.0015	0.0172	0.0187	0.08	0.07	0.85	0.92
54	0.0201	0.0015	0.0015	0.0171	0.0186	0.08	0.07	0.85	0.92
55	0.0200	0.0014	0.0014	0.0171	0.0185	0.07	0.07	0.86	0.93
56	0.0198	0.0014	0.0014	0.0171	0.0184	0.07	0.07	0.86	0.93
57	0.0196	0.0013	0.0013	0.0170	0.0184	0.07	0.07	0.87	0.93
58	0.0195	0.0012	0.0013	0.0170	0.0183	0.06	0.07	0.87	0.94
59	0.0194	0.0011	0.0012	0.0170	0.0182	0.06	0.06	0.88	0.94
59.5	**0.0193**	**0.0011**	**0.0012**	**0.0170**	**0.0182**	**0.06**	**0.06**	**0.88**	**0.94**
60	0.0192	0.0011	0.0012	0.0169	0.0181	0.06	0.06	0.88	0.94
65	0.0186	0.0008	0.0010	0.0168	0.0178	0.04	0.06	0.90	0.96
70	0.0181	0.0006	0.0009	0.0166	0.0175	0.04	0.05	0.91	0.96
75	0.0177	0.0005	0.0008	0.0164	0.0172	0.03	0.05	0.93	0.97
80	0.0174	0.0004	0.0007	0.0162	0.0169	0.02	0.04	0.93	0.98
85	0.0170	0.0003	0.0006	0.0161	0.0167	0.02	0.04	0.94	0.98
90	0.0167	0.0003	0.0006	0.0159	0.0164	0.02	0.03	0.95	0.98
95	0.0165	0.0002	0.0005	0.0157	0.0162	0.01	0.03	0.95	0.99
100	0.0162	0.0002	0.0005	0.0155	0.0160	0.01	0.03	0.96	0.99

Table VII-20: Total mean mass attenuation coefficients $\mu/\rho\,(E)_{\mathrm{mix}}$ of cellulose (mean) as sum of the single coefficients following eq. (II-14) for the attenuation processes photoelectric absorption (photo), coherent scattering (coh), and incoherent scattering (incoh) as well as scattering coefficient (scat = coh + incoh) for a practice-oriented energy range (incl. particular device energies, bold, refer to Table VII-2) determined on basis of empirical and literature data (Table IV-14) via eq. (II-31) by means of XCOM (2010) elemental data (Table VII-3 to Table VII-9), complete with the attenuation fractions $\xi(i)$ following eq. (II-15) of the single mechanisms.

Hemicelluloses (mean)

Energy			$\frac{\mu_i}{\rho}(E)$ [m^2/kg]				$\xi(i)$ [−]		
E [keV]	total	photo	coh	incoh	scat	photo	coh	incoh	scat
5	3.2105	3.1527	0.0469	0.0106	0.0576	0.98	0.01	0.00	0.02
6	1.8525	1.8023	0.0379	0.0119	0.0497	0.97	0.02	0.01	0.03
7	1.1630	1.1189	0.0314	0.0128	0.0442	0.96	0.03	0.01	0.04
8	0.7781	0.7382	0.0265	0.0135	0.0401	0.95	0.03	0.02	0.05
9	0.5473	0.5103	0.0229	0.0141	0.0370	0.93	0.04	0.03	0.07
10	0.4008	0.3662	0.0200	0.0146	0.0346	0.91	0.05	0.04	0.09
11	0.3036	0.2709	0.0177	0.0150	0.0327	0.89	0.06	0.05	0.11
12	0.2366	0.2055	0.0158	0.0153	0.0312	0.87	0.07	0.06	0.13
12.7	**0.2017**	**0.1715**	**0.0147**	**0.0155**	**0.0302**	**0.85**	**0.07**	**0.08**	**0.15**
13	0.1891	0.1592	0.0142	0.0156	0.0299	0.84	0.08	0.08	0.16
14	0.1544	0.1256	0.0129	0.0159	0.0288	0.81	0.08	0.10	0.19
15	0.1286	0.1007	0.0118	0.0161	0.0279	0.78	0.09	0.13	0.22
15.5	**0.1181**	**0.0906**	**0.0112**	**0.0162**	**0.0274**	**0.77**	**0.10**	**0.14**	**0.23**
16	0.1089	0.0818	0.0108	0.0163	0.0271	0.75	0.10	0.15	0.25
16.9	**0.0950**	**0.0686**	**0.0100**	**0.0165**	**0.0264**	**0.72**	**0.10**	**0.17**	**0.28**
17	0.0937	0.0673	0.0099	0.0165	0.0264	0.72	0.11	0.18	0.28
18	0.0817	0.0560	0.0091	0.0166	0.0258	0.68	0.11	0.20	0.32
19	0.0722	0.0470	0.0084	0.0168	0.0252	0.65	0.12	0.23	0.35
20	0.0645	0.0398	0.0078	0.0169	0.0247	0.62	0.12	0.26	0.38
21	0.0582	0.0340	0.0072	0.0170	0.0243	0.58	0.12	0.29	0.42
21.1	**0.0577**	**0.0335**	**0.0072**	**0.0170**	**0.0242**	**0.58**	**0.12**	**0.30**	**0.42**
21.2	**0.0571**	**0.0329**	**0.0071**	**0.0170**	**0.0242**	**0.58**	**0.13**	**0.30**	**0.42**
21.5	**0.0555**	**0.0315**	**0.0070**	**0.0171**	**0.0241**	**0.57**	**0.13**	**0.31**	**0.43**
22	0.0531	0.0292	0.0068	0.0171	0.0238	0.55	0.13	0.32	0.45
23	0.0488	0.0253	0.0063	0.0172	0.0235	0.52	0.13	0.35	0.48
24	0.0451	0.0220	0.0059	0.0172	0.0231	0.49	0.13	0.38	0.51
24.2	**0.0445**	**0.0214**	**0.0058**	**0.0173**	**0.0231**	**0.48**	**0.13**	**0.39**	**0.52**
25	0.0421	0.0193	0.0055	0.0173	0.0228	0.46	0.13	0.41	0.54
26	0.0395	0.0169	0.0052	0.0174	0.0225	0.43	0.13	0.44	0.57
26.3	**0.0388**	**0.0163**	**0.0051**	**0.0174**	**0.0225**	**0.42**	**0.13**	**0.45**	**0.58**
27	0.0373	0.0150	0.0049	0.0174	0.0223	0.40	0.13	0.47	0.60
27.3	**0.0366**	**0.0144**	**0.0048**	**0.0174**	**0.0222**	**0.39**	**0.13**	**0.47**	**0.61**
28	0.0353	0.0133	0.0046	0.0174	0.0220	0.38	0.13	0.49	0.62
29	0.0337	0.0119	0.0043	0.0175	0.0218	0.35	0.13	0.52	0.65
29.2	**0.0333**	**0.0116**	**0.0043**	**0.0175**	**0.0217**	**0.35**	**0.13**	**0.52**	**0.65**
30	0.0322	0.0106	0.0041	0.0175	0.0216	0.33	0.13	0.54	0.67
31	0.0309	0.0095	0.0039	0.0175	0.0214	0.31	0.13	0.57	0.69
32	0.0298	0.0086	0.0037	0.0175	0.0212	0.29	0.12	0.59	0.71
33	0.0288	0.0078	0.0035	0.0175	0.0210	0.27	0.12	0.61	0.73
34	0.0279	0.0070	0.0033	0.0175	0.0208	0.25	0.12	0.63	0.75
35	0.0271	0.0064	0.0032	0.0175	0.0207	0.24	0.12	0.65	0.76
35.1	**0.0270**	**0.0063**	**0.0031**	**0.0175**	**0.0207**	**0.23**	**0.12**	**0.65**	**0.77**
35.4	**0.0268**	**0.0062**	**0.0031**	**0.0175**	**0.0206**	**0.23**	**0.12**	**0.65**	**0.77**

continued from page 402

Hemicelluloses (mean)

Energy	$\frac{\mu_i}{\rho}(E)$ [m²/kg]					$\xi(i)$ [−]			
E [keV]	total	photo	coh	incoh	scat	photo	coh	incoh	scat
36	0.0263	0.0058	0.0030	0.0175	0.0205	0.22	0.11	0.66	0.78
37	0.0257	0.0053	0.0029	0.0175	0.0204	0.21	0.11	0.68	0.79
38	0.0251	0.0049	0.0027	0.0175	0.0202	0.19	0.11	0.70	0.81
39	0.0246	0.0045	0.0026	0.0175	0.0201	0.18	0.11	0.71	0.82
40	0.0241	0.0041	0.0025	0.0175	0.0200	0.17	0.10	0.73	0.83
41	0.0236	0.0038	0.0024	0.0174	0.0198	0.16	0.10	0.74	0.84
42	0.0232	0.0035	0.0023	0.0174	0.0197	0.15	0.10	0.75	0.85
43	0.0229	0.0032	0.0022	0.0174	0.0196	0.14	0.10	0.76	0.86
44	0.0225	0.0030	0.0021	0.0174	0.0195	0.13	0.09	0.77	0.87
45	0.0222	0.0028	0.0020	0.0174	0.0194	0.13	0.09	0.78	0.87
46	0.0219	0.0026	0.0020	0.0173	0.0193	0.12	0.09	0.79	0.88
47	0.0216	0.0024	0.0019	0.0173	0.0192	0.11	0.09	0.80	0.89
48	0.0213	0.0023	0.0018	0.0173	0.0191	0.11	0.08	0.81	0.89
49	0.0211	0.0021	0.0017	0.0172	0.0190	0.10	0.08	0.82	0.90
50	0.0209	0.0020	0.0017	0.0172	0.0189	0.09	0.08	0.82	0.91
50.9	**0.0207**	**0.0019**	**0.0016**	**0.0172**	**0.0188**	**0.09**	**0.08**	**0.83**	**0.91**
51	0.0207	0.0018	0.0016	0.0172	0.0188	0.09	0.08	0.83	0.91
51.3	**0.0206**	**0.0018**	**0.0016**	**0.0172**	**0.0188**	**0.09**	**0.08**	**0.83**	**0.91**
52	0.0205	0.0017	0.0016	0.0172	0.0187	0.08	0.08	0.84	0.92
53	0.0203	0.0016	0.0015	0.0171	0.0187	0.08	0.07	0.85	0.92
54	0.0201	0.0015	0.0015	0.0171	0.0186	0.08	0.07	0.85	0.92
55	0.0199	0.0014	0.0014	0.0171	0.0185	0.07	0.07	0.86	0.93
56	0.0198	0.0014	0.0014	0.0170	0.0184	0.07	0.07	0.86	0.93
57	0.0196	0.0013	0.0013	0.0170	0.0183	0.07	0.07	0.87	0.93
58	0.0195	0.0012	0.0013	0.0170	0.0183	0.06	0.07	0.87	0.94
59	0.0193	0.0011	0.0012	0.0169	0.0182	0.06	0.06	0.88	0.94
59.5	**0.0193**	**0.0011**	**0.0012**	**0.0169**	**0.0181**	**0.06**	**0.06**	**0.88**	**0.94**
60	0.0192	0.0011	0.0012	0.0169	0.0181	0.06	0.06	0.88	0.94
65	0.0186	0.0008	0.0010	0.0167	0.0178	0.04	0.06	0.90	0.96
70	0.0181	0.0006	0.0009	0.0166	0.0175	0.04	0.05	0.91	0.96
75	0.0177	0.0005	0.0008	0.0164	0.0172	0.03	0.05	0.93	0.97
80	0.0173	0.0004	0.0007	0.0162	0.0169	0.02	0.04	0.93	0.98
85	0.0170	0.0003	0.0006	0.0160	0.0167	0.02	0.04	0.94	0.98
90	0.0167	0.0003	0.0006	0.0159	0.0164	0.02	0.03	0.95	0.98
95	0.0164	0.0002	0.0005	0.0157	0.0162	0.01	0.03	0.95	0.99
100	0.0162	0.0002	0.0005	0.0155	0.0160	0.01	0.03	0.96	0.99

Table VII-21: Total mean mass attenuation coefficients $\mu/\rho\,(E)_\mathrm{mix}$ of hemicelluloses (mean) as sum of the single coefficients following eq. (II-14) for the attenuation processes photoelectric absorption (photo), coherent scattering (coh), and incoherent scattering (incoh) as well as scattering coefficient (scat = coh + incoh) for a practice-oriented energy range (incl. particular device energies, bold, refer to Table VII-2) determined on basis of empirical and literature data (Table IV-14) via eq. (II-31) by means of XCOM (2010) elemental data (Table VII-3 to Table VII-9), complete with the attenuation fractions $\xi(i)$ following eq. (II-15) of the single mechanisms.

Lignin (mean)

Energy	$\frac{\mu_i}{\rho}(E)$ [m^2/kg]					$\xi(i)$ [$-$]			
E [keV]	total	photo	coh	incoh	scat	photo	coh	incoh	scat
5	2.6920	2.6386	0.0423	0.0108	0.0531	0.98	0.02	0.00	0.02
6	1.5507	1.5040	0.0342	0.0120	0.0462	0.97	0.02	0.01	0.03
7	0.9729	0.9316	0.0284	0.0129	0.0413	0.96	0.03	0.01	0.04
8	0.6510	0.6133	0.0241	0.0136	0.0377	0.94	0.04	0.02	0.06
9	0.4583	0.4233	0.0209	0.0142	0.0350	0.92	0.05	0.03	0.08
10	0.3362	0.3033	0.0183	0.0146	0.0330	0.90	0.05	0.04	0.10
11	0.2553	0.2240	0.0163	0.0150	0.0313	0.88	0.06	0.06	0.12
12	0.1997	0.1697	0.0146	0.0154	0.0299	0.85	0.07	0.08	0.15
12.7	**0.1707**	**0.1416**	**0.0135**	**0.0156**	**0.0291**	**0.83**	**0.08**	**0.09**	**0.17**
13	0.1602	0.1314	0.0131	0.0157	0.0288	0.82	0.08	0.10	0.18
14	0.1314	0.1036	0.0119	0.0159	0.0278	0.79	0.09	0.12	0.21
15	0.1100	0.0830	0.0109	0.0162	0.0270	0.75	0.10	0.15	0.25
15.5	**0.1013**	**0.0746**	**0.0104**	**0.0163**	**0.0266**	**0.74**	**0.10**	**0.16**	**0.26**
16	0.0937	0.0674	0.0099	0.0164	0.0263	0.72	0.11	0.17	0.28
16.9	**0.0822**	**0.0565**	**0.0092**	**0.0165**	**0.0257**	**0.69**	**0.11**	**0.20**	**0.31**
17	0.0810	0.0554	0.0091	0.0165	0.0257	0.68	0.11	0.20	0.32
18	0.0711	0.0460	0.0084	0.0167	0.0251	0.65	0.12	0.23	0.35
19	0.0632	0.0386	0.0078	0.0168	0.0246	0.61	0.12	0.27	0.39
20	0.0568	0.0327	0.0072	0.0170	0.0241	0.58	0.13	0.30	0.42
21	0.0516	0.0279	0.0067	0.0171	0.0237	0.54	0.13	0.33	0.46
21.1	**0.0512**	**0.0275**	**0.0066**	**0.0171**	**0.0237**	**0.54**	**0.13**	**0.33**	**0.46**
21.2	**0.0507**	**0.0270**	**0.0066**	**0.0171**	**0.0237**	**0.53**	**0.13**	**0.34**	**0.47**
21.5	**0.0494**	**0.0258**	**0.0064**	**0.0171**	**0.0236**	**0.52**	**0.13**	**0.35**	**0.48**
22	0.0473	0.0240	0.0062	0.0171	0.0234	0.51	0.13	0.36	0.49
23	0.0438	0.0207	0.0058	0.0172	0.0230	0.47	0.13	0.39	0.53
24	0.0408	0.0180	0.0054	0.0173	0.0227	0.44	0.13	0.42	0.56
24.2	**0.0402**	**0.0175**	**0.0054**	**0.0173**	**0.0227**	**0.44**	**0.13**	**0.43**	**0.56**
25	0.0382	0.0158	0.0051	0.0173	0.0224	0.41	0.13	0.45	0.59
26	0.0360	0.0139	0.0048	0.0174	0.0222	0.39	0.13	0.48	0.61
26.3	**0.0355**	**0.0134**	**0.0047**	**0.0174**	**0.0221**	**0.38**	**0.13**	**0.49**	**0.62**
27	0.0342	0.0123	0.0045	0.0174	0.0219	0.36	0.13	0.51	0.64
27.3	**0.0337**	**0.0118**	**0.0044**	**0.0174**	**0.0219**	**0.35**	**0.13**	**0.52**	**0.65**
28	0.0326	0.0109	0.0042	0.0175	0.0217	0.33	0.13	0.54	0.67
29	0.0312	0.0097	0.0040	0.0175	0.0215	0.31	0.13	0.56	0.69
29.2	**0.0309**	**0.0095**	**0.0039**	**0.0175**	**0.0214**	**0.31**	**0.13**	**0.57**	**0.69**
30	0.0300	0.0087	0.0038	0.0175	0.0213	0.29	0.13	0.58	0.71
31	0.0289	0.0078	0.0036	0.0175	0.0211	0.27	0.12	0.61	0.73
32	0.0279	0.0070	0.0034	0.0175	0.0209	0.25	0.12	0.63	0.75
33	0.0271	0.0063	0.0032	0.0175	0.0207	0.23	0.12	0.65	0.77
34	0.0263	0.0057	0.0030	0.0175	0.0206	0.22	0.12	0.67	0.78
35	0.0257	0.0052	0.0029	0.0175	0.0204	0.20	0.11	0.68	0.80
35.1	**0.0256**	**0.0052**	**0.0029**	**0.0175**	**0.0204**	**0.20**	**0.11**	**0.69**	**0.80**
35.4	**0.0254**	**0.0050**	**0.0028**	**0.0175**	**0.0204**	**0.20**	**0.11**	**0.69**	**0.80**

Lignin (mean)

Energy	$\frac{\mu_i}{\rho}(E)$ [m²/kg]					$\xi(i)$ [−]			
E [keV]	total	photo	coh	incoh	scat	photo	coh	incoh	scat
36	0.0250	0.0048	0.0028	0.0175	0.0203	0.19	0.11	0.70	0.81
37	0.0245	0.0043	0.0026	0.0175	0.0201	0.18	0.11	0.71	0.82
38	0.0240	0.0040	0.0025	0.0175	0.0200	0.17	0.10	0.73	0.83
39	0.0236	0.0037	0.0024	0.0175	0.0199	0.16	0.10	0.74	0.84
40	0.0231	0.0034	0.0023	0.0175	0.0198	0.15	0.10	0.76	0.85
41	0.0228	0.0031	0.0022	0.0175	0.0197	0.14	0.10	0.77	0.86
42	0.0224	0.0029	0.0021	0.0174	0.0195	0.13	0.09	0.78	0.87
43	0.0221	0.0026	0.0020	0.0174	0.0194	0.12	0.09	0.79	0.88
44	0.0218	0.0025	0.0019	0.0174	0.0193	0.11	0.09	0.80	0.89
45	0.0215	0.0023	0.0019	0.0174	0.0192	0.11	0.09	0.81	0.89
46	0.0212	0.0021	0.0018	0.0173	0.0191	0.10	0.08	0.82	0.90
47	0.0210	0.0020	0.0017	0.0173	0.0190	0.09	0.08	0.82	0.91
48	0.0208	0.0018	0.0017	0.0173	0.0189	0.09	0.08	0.83	0.91
49	0.0206	0.0017	0.0016	0.0172	0.0189	0.08	0.08	0.84	0.92
50	0.0204	0.0016	0.0015	0.0172	0.0188	0.08	0.08	0.85	0.92
50.9	**0.0202**	**0.0015**	**0.0015**	**0.0172**	**0.0187**	**0.07**	**0.07**	**0.85**	**0.93**
51	0.0202	0.0015	0.0015	0.0172	0.0187	0.07	0.07	0.85	0.93
51.3	**0.0201**	**0.0015**	**0.0015**	**0.0172**	**0.0187**	**0.07**	**0.07**	**0.85**	**0.93**
52	0.0200	0.0014	0.0014	0.0172	0.0186	0.07	0.07	0.86	0.93
53	0.0198	0.0013	0.0014	0.0171	0.0185	0.07	0.07	0.86	0.93
54	0.0197	0.0012	0.0013	0.0171	0.0184	0.06	0.07	0.87	0.94
55	0.0195	0.0012	0.0013	0.0171	0.0184	0.06	0.07	0.87	0.94
56	0.0194	0.0011	0.0013	0.0170	0.0183	0.06	0.06	0.88	0.94
57	0.0193	0.0010	0.0012	0.0170	0.0182	0.05	0.06	0.88	0.95
58	0.0191	0.0010	0.0012	0.0170	0.0181	0.05	0.06	0.89	0.95
59	0.0190	0.0009	0.0011	0.0169	0.0181	0.05	0.06	0.89	0.95
59.5	**0.0189**	**0.0009**	**0.0011**	**0.0169**	**0.0180**	**0.05**	**0.06**	**0.89**	**0.95**
60	0.0189	0.0009	0.0011	0.0169	0.0180	0.05	0.06	0.89	0.95
65	0.0183	0.0007	0.0010	0.0167	0.0177	0.04	0.05	0.91	0.96
70	0.0179	0.0005	0.0008	0.0165	0.0174	0.03	0.05	0.92	0.97
75	0.0175	0.0004	0.0007	0.0164	0.0171	0.02	0.04	0.93	0.98
80	0.0172	0.0003	0.0006	0.0162	0.0168	0.02	0.04	0.94	0.98
85	0.0169	0.0003	0.0006	0.0160	0.0166	0.02	0.03	0.95	0.98
90	0.0166	0.0002	0.0005	0.0158	0.0163	0.01	0.03	0.96	0.99
95	0.0163	0.0002	0.0005	0.0157	0.0161	0.01	0.03	0.96	0.99
100	0.0161	0.0002	0.0004	0.0155	0.0159	0.01	0.03	0.96	0.99

Table VII-22: Total mean mass attenuation coefficients $\mu/\rho\,(E)_{\mathrm{mix}}$ of lignin (mean) as sum of the single coefficients following eq. (II-14) for the attenuation processes photoelectric absorption (photo), coherent scattering (coh), and incoherent scattering (incoh) as well as scattering coefficient (scat = coh + incoh) for a practice-oriented energy range (incl. particular device energies, bold, refer to Table VII-2) determined on basis of empirical and literature data (Table IV-14) via eq. (II-31) by means of XCOM (2010) elemental data (Table VII-3 to Table VII-9), complete with the attenuation fractions $\xi(i)$ following eq. (II-15) of the single mechanisms.

5 Related publications

Publications resulting from the investigations of the present thesis

Scientific Papers

Accuracy of the radiometric determination of raw density gradients on wood-based composites.
Solbrig, K.; Fuchs, M.; Frühwald, K.; Ressel, J. B. – holztechnologie 55 (2014) 6. p. 27-34.

Conference Proceedings

Radiometrische Untersuchungen an Holz und Holzwerkstoffen unter Einsatz ionisierender Strahlung.
Solbrig, K.; Frühwald, K.; Ressel, J. B.; Gruchot, M. – In: DGZfP-Jahrestagung 2011. Bremen. 2011.
p. 1-11.

Process monitoring in particle board production – looking very deep inside?
Solbrig, K. – In: Riegel, A.; Nicolich, M. (eds.) 2nd International Conference Production Engineering
and Management for Furniture Industry, 27th and 28th September 2012. Lemgo, Germany. Schriften-
reihe Logistik Fachbereich Produktion und Wirtschaft, Hochschule Ostwestfalen-Lippe, Lemgo, 2012.
p. 41-56.

Beitrag zur Genauigkeit radiometrischer Messmethoden zur Bestimmung von Rohdichtegradienten an
Holzwerkstoffen.
Solbrig, K.; Krause, B.; Frühwald, K.; Fuchs, M.; Ressel, J. B. – In: IHD (ed.) 10. Holzwerkstoffkollo-
quium. Dresden. Institut für Holztechnologie Dresden gemeinnützige GmbH (IHD), 2013. p. 159-175.

X-ray based process and quality control in wood-based composites production - needs and benefits.
Solbrig, K.; Fuchs, M.; Frühwald, K.; Ressel, J. B. – In: Villmer, F.-J.; Padoano, E. (eds.) 4th Interna-
tional Conference Production Engineering and Management, 25th and 26th September 2014. Lemgo,
Germany. Schriftenreihe Logistik Fachbereich Produktion und Wirtschaft, Hochschule Ostwestfalen-
Lippe, Lemgo, 2014. p. 179-192.

Zuverlässiger Einsatz quantitativer Röntgenmesstechnik zur Prozess- und Qualitätskontrolle in der
Holzwerkstoffindustrie.
Solbrig, K.; Fuchs, M.; Frühwald, K.; Ressel, J. B. – In: DACH-Jahrestagung 2015 - ZfP in Forschung,
Entwicklung und Anwendung. Salzburg, Austria. Deutsche Gesellschaft für Zerstörungsfreie Prüfung
DGZfP, Berlin, 2015. p. 1-13.

Wood-based composite X-ray densitometry – attenuation effects on measurements.
Solbrig, K.; Frühwald, K.; Ressel, J. B.; Fuchs, M. – In: Ross, R. J.; Gonçalves, R.; Wang, X. (eds.)
19th International Nondestructive Testing and Evaluation of Wood Symposium. General Technical Re-
port FPL–GTR–239. Rio de Janeiro, Brazil. U.S. Department of Agriculture, Forest Service, Forest
Products Laboratory, Madison, WI, 2015. p. 303-313.

Related studies in the context of radiometric investigations on wood-based composites

Scientific Papers

Analyses using neutrons and positrons.
Revay, Z.; Gerstenberg, H.; Schulz, M.; Solbrig, K.; Hugenschmidt, C.; Voit, A. – Neutron News 26 (2015) 1. p. 23-28.

Conference Proceedings

Grundlegende Untersuchung zur Anwendung der Millimeterwellen- und Terahertz-Technologie an Holz und Holzwerkstoffen.
Demming, M.; Solbrig, K.; Frühwald, K.; Hilger, T. – In: DGZfP-Jahrestagung 2013. Dresden. 2013. p. 1-11.

Comparison of Computed Tomography on wood based composites by means of cold neutrons and X-ray.
Solbrig, K.; Frühwald, K.; Ressel, J. B.; Schillinger, B.; Schulz, M.; Plank, B. – Conference poster. In: Kastner, J. (ed.) 5th conference on industrial computed tomography 2014 (iCT2014). Wels, Austria. Shaker Verlag, 2014.

Process qualification in the wood industry.
Riegel, A.; Kortüm, C.; Solbrig, K. – In: Padoano, E.; Villmer, F.-J. (eds.) 5th International Conference Production Engineering and Management, October 1 and 2, 2015. Trieste, Italy. Schriftenreihe Logistik Fachbereich Produktion und Wirtschaft, Hochschule Ostwestfalen-Lippe, Lemgo, 2015. p. 89-98.

Radiometric investigation of water vapour movement in wood-based composites by means of cold and thermal neutrons.
Solbrig, K.; Frühwald, K.; Ressel, J. B.; Mannes, D.; Schillinger, B.; Schulz, M. – In: 10th World Conference on Neutron Radiography 5-10 October 2014 WCNR-10. Grindelwald, Switzerland. Elsevier Physics Procedia, 2015. p. 583-592.

Dampfbewegung in Holzwerkstoffen – Visualisierung und Quantifizierung der Siedewelle mittels Neutronenradiographie.
Solbrig, K.; Frühwald, K.; Ressel, J. B.; Mannes, D.; Schillinger, B.; Schulz, M. – In: IHD (ed.) 11. Holzwerkstoffkolloquium. Dresden. Institut für Holztechnologie Dresden gemeinnützige GmbH (IHD), 2015. p. 89-108.

6   Curriculum vitae

Curriculum vitae not included for reasons of data protection.